Challa S. S. R. Kumar *Editor*

Transmission Electron Microscopy Characterization of Nanomaterials

INCLUDED IN SPRINGERMATERIALS.COM

Springer

Transmission Electron Microscopy Characterization of Nanomaterials

Challa S. S. R. Kumar
Editor

Transmission Electron Microscopy Characterization of Nanomaterials

With 403 Figures and 15 Tables

Springer

Editor
Challa S. S. R. Kumar
Center for Advanced Microstructures and Devices
Baton Rouge, LA, USA

ISBN 978-3-642-38933-7 ISBN 978-3-642-38934-4 (eBook)
DOI 10.1007/ 978-3-642-38934-4
Springer Heidelberg New York Dordrecht London

Library of Congress Control Number: 2013955568

© Springer-Verlag Berlin Heidelberg 2014
This work is subject to copyright. All rights are reserved by the Publisher, whether the whole or part of the material is concerned, specifically the rights of translation, reprinting, reuse of illustrations, recitation, broadcasting, reproduction on microfilms or in any other physical way, and transmission or information storage and retrieval, electronic adaptation, computer software, or by similar or dissimilar methodology now known or hereafter developed. Exempted from this legal reservation are brief excerpts in connection with reviews or scholarly analysis or material supplied specifically for the purpose of being entered and executed on a computer system, for exclusive use by the purchaser of the work. Duplication of this publication or parts thereof is permitted only under the provisions of the Copyright Law of the Publisher's location, in its current version, and permission for use must always be obtained from Springer. Permissions for use may be obtained through RightsLink at the Copyright Clearance Center. Violations are liable to prosecution under the respective Copyright Law.
The use of general descriptive names, registered names, trademarks, service marks, etc. in this publication does not imply, even in the absence of a specific statement, that such names are exempt from the relevant protective laws and regulations and therefore free for general use. While the advice and information in this book are believed to be true and accurate at the date of publication, neither the authors nor the editors nor the publisher can accept any legal responsibility for any errors or omissions that may be made. The publisher makes no warranty, express or implied, with respect to the material contained herein.

Printed on acid-free paper

Springer is part of Springer Science+Business Media (www.springer.com)

Contents

1 TEM Characterization of Biological and Inorganic Nanocomposites 1
Penghe Qiu, Lin Wang, and Chuanbin B. Mao

2 Electron Microscopy of Thin Film Inorganic and Organic Photovoltaic Materials 43
Aidan A. Taylor and Budhika G. Mendis

3 TEM for Characterization of Semiconductor Nanomaterials 89
Elvio Carlino

4 Study on Polymeric Nano-Composites by 3D-TEM and Related Techniques 139
Atsushi Kato, Yoshinobu Isono, Kazuya Nagata, Atsushi Asano, and Yuko Ikeda

5 TEM for Characterization of Nanowires and Nanorods 195
Sarah K. St. Angelo

6 TEM for Characterization of Core-Shell Nanomaterials 243
Yiqian Wang and Chao Wang

7 Valence Electron Spectroscopy for Transmission Electron Microscopy 287
Masami Terauchi

8 TEM Characterization of Nanocomposite Materials 333
Kenji Kaneko, Yoshio Sakka, and Yoshizumi Ishikawa

9 High Resolution in STEM Mode: Individual Atom Analysis in Semiconductor Nanowires 375
María de la Mata and Jordi Arbiol

10 Electron Microscopy for Characterization of Thermoelectric Nanomaterials 427
Haijun Wu and Jiaqing He

11 TEM for Characterization of Nanocomposite Oxide Thin Films: A Case Study on Solution-Derived Lanthanum Strontium Manganites 537
Patricia Abellán, César Moreno, Felip Sandiumenge, and Xavier Obradors

12 TEM Characterization of Metallic Nanocatalysts 577
Dong Su

13 3D Electron Microscopy Applied to Nanoscience 619
Ileana Florea, Ovidiu Ersen, and Charles Hirlimann

14 Transmission Electron Microscopy of 1D-Nanostructures 657
Teresa Ben, Rabie Fath Allah, David L. Sales, David González, and Sergio I. Molina

Erratum E1

Index 703

Contributors

Patricia Abellán Physical Sciences Division, Pacific Northwest National Laboratory, Richland, WA, USA

Jordi Arbiol Institut de Ciència de Materials de Barcelona, ICMAB–CSIC, Campus de la UAB, Bellaterra, CAT, Spain

Institució Catalana de Recerca i Estudis Avançats (ICREA), Barcelona, CAT, Spain

Atsushi Asano Department of Applied Chemistry, National Defense Academy, Yokosuka, Kanagawa, Japan

Teresa Ben Departamento de Ciencia de los Materiales e I. M. y Q. I. Facultad de Ciencias, Universidad de Cádiz, Puerto Real, Cádiz, Spain

Elvio Carlino Centro di Microscopia Elettronica – Consiglio Nazionale delle Ricerche – Istituto di Officina dei Materiali (CNR-IOM-TASC), Trieste, Italy

Ovidiu Ersen Institut de Physique et Chimie des Matériaux de Strasbourg (IPCMS), UMR 7504 CNRS – Université de Strasbourg, Strasbourg, France

Rabie Fath Allah Departamento de Ciencia de los Materiales e I. M. y Q. I. Facultad de Ciencias, Universidad de Cádiz, Puerto Real, Cádiz, Spain

Ileana Florea Institut de Physique et Chimie des Matériaux de Strasbourg (IPCMS), UMR 7504 CNRS – Université de Strasbourg, Strasbourg, France

David González Departamento de Ciencia de los Materiales e I. M. y Q. I. Facultad de Ciencias, Universidad de Cádiz, Puerto Real, Cádiz, Spain

Jiaqing He Department of Physics, South University of Science and Technology of China, Shenzhen, People's Republic of China

Charles Hirlimann Institut de Physique et Chimie des Matériaux de Strasbourg (IPCMS), UMR 7504 CNRS – Université de Strasbourg, Strasbourg, France

Yuko Ikeda Graduate School of Science and Technology, Kyoto Institute of Technology, Kyoto, Japan

Yoshizumi Ishikawa Advanced Materials Research Group, New Technology Research Laboratory, Sumitomo Osaka Cement Co., LTD, Chiba, Japan

Yoshinobu Isono Department of Materials Science and Technology, Nagaoka University of Technology, Nagaoka, Niigata, Japan

Kenji Kaneko Department of Materials Science and Engineering, Kyushu University, Fukuoka, Japan

Atsushi Kato Department of Material Analysis, NISSAN ARC, LTD, Yokosuka, Kanagawa, Japan

Chuanbin B. Mao Department of Chemistry and Biochemistry, Stephenson Life Sciences Research Center, University of Oklahoma, Norman, OK, USA

María de la Mata Institut de Ciència de Materials de Barcelona, ICMAB-CSIC, Campus de la UAB, Bellaterra, CAT, Spain

Budhika G. Mendis Physics Department, Durham University, Durham, UK

Sergio I. Molina Departamento de Ciencia de los Materiales e I. M. y Q. I. Facultad de Ciencias, Universidad de Cádiz, Puerto Real, Cádiz, Spain

César Moreno International Center for Young Scientist, National Institute for Materials Science, Tsukuba, Ibaraki, Japan

Kazuya Nagata Department of Advanced Technology Development, Laboratory of Plastics, Asahikasei Chemicals Corporation, Kawasaki-ku Kawasaki, Kanagawa, Japan

Xavier Obradors Institut de Ciencia de Materials de Barcelona, CSIC, Bellaterra, Spain

Penghe Qiu Department of Chemistry and Biochemistry, Stephenson Life Sciences Research Center, University of Oklahoma, Norman, OK, USA

Yoshio Sakka Advanced Ceramics Group, Materials Processing Unit, National Institute for Materials Science, Tsukuba, Japan

David L. Sales Departamento de Ciencia de los Materiales e I. M. y Q. I. Facultad de Ciencias, Universidad de Cádiz, Puerto Real, Cádiz, Spain

Felip Sandiumenge Institut de Ciencia de Materials de Barcelona, CSIC, Bellaterra, Spain

Sarah K. St. Angelo Department of Chemistry, Dickinson College, Carlisle, PA, USA

Dong Su Center for Functional Nanomaterials, Brookhaven National Laboratory, Upton, NY, USA

Aidan A. Taylor Physics Department, Durham University, Durham, UK

Masami Terauchi Institute of Multidisciplinary Research for Advanced Materials, Tohoku University, Aoba-ku, Sendai, Japan

Chao Wang The Cultivation Base for State Key Laboratory, Qingdao University, Qingdao, People's Republic of China

Lin Wang Department of Chemistry and Biochemistry, Stephenson Life Sciences Research Center, University of Oklahoma, Norman, OK, USA

Yiqian Wang The Cultivation Base for State Key Laboratory, Qingdao University, Qingdao, People's Republic of China

Haijun Wu Department of Physics, South University of Science and Technology of China, Shenzhen, People's Republic of China

TEM Characterization of Biological and Inorganic Nanocomposites

1

Penghe Qiu, Lin Wang, and Chuanbin B. Mao

Contents

1 Definition of the Topic 1
2 Overview 2
3 Introduction 2
4 Experimental and Instrumental Methodology 3
4.1 Ultramicrotome 3
4.2 Specimen Staining 4
5 Use of TEM in Bio-nano Research 5
5.1 Naturally Occurring Bio-inorganic Nanocomposites 5
5.2 Synthetic Inorganic Nanomaterials Templated by Biological Nanostructures 12
5.3 Externally Introduced Inorganic Nanoparticles in Cells and Tissues 27
6 Concluding Remarks and Future Perspective 35
References 35

1 Definition of the Topic

Transmission electron microscopy (TEM) is a microscopy technique that employs a beam of high-energy electrons to transmit through a specimen of nanometer thickness. Information on the various aspects of a specimen, including but not limited to materials size, shape, crystallinity, composition, and elemental mapping, can be collected during the interaction of the electron beam with the specimen. This chapter presents an overview of the recent applications of TEM in characterizing biological and inorganic nanocomposites.

An erratum to this chapter can be found at http://dx.doi.org/10.1007/978-3-642-38934-4_15

P. Qiu • L. Wang • C.B. Mao (✉)
Department of Chemistry and Biochemistry, Stephenson Life Sciences Research Center, University of Oklahoma, Norman, OK, USA
e-mail: cbmao@ou.edu

C.S.S.R. Kumar (ed.), *Transmission Electron Microscopy Characterization of Nanomaterials*, DOI 10.1007/978-3-642-38934-4_1,
© Springer-Verlag Berlin Heidelberg 2014

2 Overview

Bio-inorganic nanocomposites are materials containing both biological and inorganic components, at least one of which has features on the nanometer scale. Bio-inorganic nanocomposites exist universally in nature. Most often they are seen in macroscopic, hierarchical structures but are constructed from nano-sized fundamental units. These materials are usually mechanically strong so that they can provide the necessary support and protection for life. In the past decade, great advance has been made in nanotechnology research. A number of synthetic strategies have been developed to fabricate nanomaterials of different sizes and shapes as well as tunable physical and chemical properties. Among them, biological template-based synthesis is considered one of the most important methods. Many inorganic nanomaterials, such as metals, semiconductors, and oxides, have been fabricated with biotemplates of various types; these materials also meet the definition of bio-inorganic nanocomposites and thus are the subject of discussion in this chapter. Inorganic nanoparticles have been actively employed for biological therapeutic and diagnostic applications both in vivo and in vitro. In such research, TEM is used to examine ultra-sectioned samples of cells and tissues containing inorganic nanoparticles; some important conclusions were obtained almost exclusively based on the TEM instrumentation. This part of research is also worth a review under the current topic. In addition, naturally occurring bio-inorganic nanocomposites have been under intensive research by scientists in the areas of biology, medicine, and materials science for decades. Most of the previous discoveries had been reviewed and compiled into several relevant books [1–4]; so here we will only cover some of the most recent TEM findings of the naturally occurring bio-inorganic nanocomposites. It should be noted that, since this chapter covers a broad range of research topics and each research topic involves a number of characterization techniques, it is difficult to provide a full picture of all the studies mentioned here simply by interpreting the TEM data.

3 Introduction

TEM is one of the most powerful techniques to characterize materials with nanometer-scale features. Due to the small de Broglie wavelength of electrons, TEM is capable of imaging specimens at resolutions up to the atomic level. TEM has multiple imaging modes that enable examination of specimens from various aspects. Bright-field TEM, in which images are generated directly by transmitted electrons, is the most commonly employed imaging mode seen in the literature. Under this mode, the size, shape, uniformity, and dispersity of nanomaterials can be directly observed. Dark-field TEM allows one to use diffracted electrons from a specific set of crystal planes to image materials and is often used to locate defects in crystals. High-resolution TEM (HRTEM) has been extensively used to study the lattice structure of crystals. It is very useful in discovering the crystallinity and crystal defects, like stacking faults and twinning, of nanomaterials as well as in studying the kinetic processes in materials transformation in which changes usually begin at the atomic level. Electron diffraction (ED) is associated with the

TEM imaging mode and can be used to determine the crystal structure and phase of nanomaterials based on the spacing and symmetry of diffraction patterns. Unlike the conventional TEM, the scanning transmission electron microscope (STEM) generates images by performing a raster scan of a narrow electron beam over the sample. When coupled with a high-angle annular dark-field (HAADF) detector, the STEM is capable of imaging by the atomic number of elements in the sample, which is also known as Z-contrast imaging. The HAADF-STEM mode is ideal for distinguishing components in nanocomposites. Qualitative and relatively quantitative elemental analysis can be carried out by both the energy-dispersive X-ray spectroscopy (EDX or EDS) and electron energy loss spectroscopy (EELS). However, EELS is more powerful in that it can not only generate spectra from certain sample areas showing the compositions of the materials but also map data showing the actual element distribution in a nanostructure. In addition, cryo-TEM provides an option to examine biological samples under cryogenic temperature, preventing them from structural deformation caused by electron beams and by the conventional sample treatment during ultra-sectioning. Finally, three-dimensional (3D) images can be generated in TEM equipped with proper detectors and software.

The investigation of bio-inorganic nanocomposites has been heavily dependent on the TEM, and all the above-mentioned TEM imaging modes are actively involved in the characterization. In studying the naturally occurring bio-inorganic nanocomposites, TEM is employed to uncover the components and structures as well as the structure–function relationships of the materials. The inorganic nanomaterials synthesized by biological templates usually contain features of a few nanometers buried inside a thick shell; thus, they are almost exclusively characterized by the TEM. TEM is also unique in the study of inorganic nanoparticles–cell/tissue composite materials, because it is not only capable of observing inorganic nanoparticles at very high resolution but can also discern organelles of an ultra-sectioned cell clearly.

4 Experimental and Instrumental Methodology

This part introduces some of the most commonly used sample sectioning and staining techniques.

4.1 Ultramicrotome

Ultramicrotome refers to cutting materials into extremely thin sections for electron microscope observation. A complete ultramicrotome process includes a set of consecutive treatments of specimens including fixation, dehydration, embedding, sectioning, and staining. Fixation is done to stabilize the materials so that their structure can be maintained in the subsequent processing steps. Primary fixation can be done by glutaraldehyde ($1 \sim 3$ %) or formaldehyde ($3.7 \sim 4.0$ %) in phosphate-buffered saline (PBS) buffer. Secondary fixation is normally finished with $0.5 \sim 1.0$ % of osmium

tetroxide in cacodylate buffer. Both fixations can be carried out under room temperature in the dark and repeated wash with buffer. Water should be applied after each step. Dehydration is done to remove free water in the specimens and replace it with solvents compatible with the embedding resins. Ethanol and acetone are two common solvents used in the dehydration process. The removal of water is done by suspending the specimens consecutively in a gradient concentration (starting from below 70 % v/v, ending with 100 %) of one of the solvents. Sometimes, an additional dehydration step using propylene oxide is applied following the ethanol or acetone treatment. Specimens are immobilized in a hard resin-based matrix by the embedding treatment. Depending on the objective of study and the nature of specimens, numerous embedding media with different formulas have been produced commercially. Epoxy and acrylic resins are the two major resins used in the formulation of commercial embedding media. In an embedding treatment, specimens are first suspended into infiltration solutions to allow resin monomers to penetrate the biological tissues. This is normally repeated a few times with increasing content of resin monomers in the solutions. Embedding is then accomplished by polymerization of the final embedding mixture containing the specimen under either heat (epoxy resin) or UV light (acrylic resin) in a mold. Sectioning is a process in which resin-embedded specimens are cut into extremely thin slices with a microtome. The dried resin blocks should be first trimmed to include most of the sample in a small trapezoid. Sections are obtained by slicing the trapezoid over a knife in an appropriate angle. The thickness of the sections can be adjusted through a sophisticated advancement mechanism. A typical section for TEM observation should have thickness between 40 nm and 150 nm. Glass blades are used most frequently in sectioning biological samples, while diamond blades are needed for hard materials, such as bone, seashells, and teeth. The slices, which float on the water after the cut, should be manipulated with care by an eyelash brush. By dipping an empty TEM grid into the water right under the slice and lifting up, the slices can be collected onto the TEM grids. At least five to ten sections should be collected for one sample to secure a successful observation of the objects of interest. The staining process is described in the following section.

4.2 Specimen Staining

Since most biological specimens are mainly composed of low-atomic-weight elements, such as hydrogen, carbon, oxygen, and nitrogen, direct TEM observation of these specimens is practically difficult. In practice, this problem is resolved by preferential introduction of some high-atomic-weight metal ions into or surrounding the specimens during the preparation of TEM samples. This treatment is known as staining. Generally, there are two types of staining, positive staining and negative staining, depending on where the heavy metal ions are introduced.

Positive staining. In positive staining, the heavy metal ions interact with the body of biological specimens, resulting in an increased average density and therefore an enhanced contrast of the specimen. Visually, under the TEM, the specimen itself is dark

with a bright surrounding background. Positive staining is often applied to sectioned biological specimens. The staining is commonly accomplished by a 2 % aqueous or alcoholic solution of uranyl acetate and optionally a second staining by lead citrate. There have been several procedures to carry out the staining. In one approach, for example, a small drop (about 5–10 μL) of uranyl acetate is placed onto the sample side of the TEM grid, being held at the end of a pair of fine-tipped tweezers. After a certain amount of interaction time, the staining droplet is wicked away by a filter paper and followed immediately by several gentle rinses with water. Alternatively, the TEM grid can be floated onto a larger drop of the uranyl acetate solution or immersed into a pool of staining solution. The staining time varies from several minutes up to 1–2 h depending on the types of embedding resins. If a small drop of staining solution is employed, the TEM grid should be placed in a highly moisturized environment to prevent any precipitation of salt caused by evaporation of water. In case a second staining by lead citrate is necessary, it should be finished by floating the TEM grid onto a drop of staining solution in a protected CO_2-free environment, usually achieved by placing NaOH pellets inside a closed petri dish. After immediate and sufficient wash with CO_2-free water, the TEM grid is air dried and ready for TEM examination.

Negative staining. In contrast to positive staining, macromolecules are usually unstained in negative staining but are outlined by a thin film of the heavy metal ions. Therefore, the specimen is bright under the electron beam, against a dark background. Because the macromolecule itself is relatively untouched, negative staining can generate better structural resolution in imaging biological specimens. For this reason, negative staining is preferred over positive staining in the TEM study of biological specimens with independent structures, such as DNA, virus, and bacteria. The two most often used stains are 1–2 % aqueous solutions of uranyl acetate and phosphotungstic acid. In a negative staining procedure, a droplet of the sample is added to the formvar side of a TEM grid to allow adsorption of the former to the latter. The adsorption time can last from 30 s to 15 min depending on the concentration of the sample, but the grid should never be dried out. Afterward, without removing the remaining liquid, a droplet of the staining solution is placed onto the TEM grid, and the liquid is then wicked away by a piece of filter paper, leaving a thin liquid film on the grid. Once the grid is air dried, the negatively stained sample is ready for the TEM observation. As was the case with positive staining, the whole process can also be done by floating the TEM grid onto a drop of the corresponding liquids. Besides, instead of being added separately twice, the sample solution and the stains can be premixed in a 1:1 volume ratio, and the rest can be accomplished as usual.

5 Use of TEM in Bio-nano Research

5.1 Naturally Occurring Bio-inorganic Nanocomposites

For life on earth, inorganic materials play important roles in maintaining their biological activities. Solid inorganic minerals are critical components engaged in the

construction of many mechanically strong tissues, such as bone, teeth, and seashells. Nature is able to assemble inorganic solids and biological macromolecules into versatile structures that are strong enough to provide the necessary protection and support for life. It is of great significance to study the detailed structures of these naturally occurring bio-inorganic composites as well as the underlying mechanisms that lead to the formation of such structures as their knowledge will contribute directly to a number of research fields, such as biology, medicine, and materials engineering. Although the overall structure of most naturally occurring bio-inorganic composites is macroscopic, the fundamental building blocks to make these materials are on the nanometer scale. For this reason, TEM has been an indispensable tool to study various aspects of such bio-inorganic nanocomposites.

5.1.1 Hydroxyapatite–Collagen Bio-inorganic Nanocomposites in Bone and Fish Scales

Bone is perhaps the most abundant naturally occurring bio-inorganic nanocomposite on earth. TEM had been used to investigate the structure of bone shortly after its invention. The bone has a hierarchical structure with several levels of organizations of materials, although the fundamental building blocks to make the bone were found to be the mineralized collagen fibrils. An individual collagen fibril in the bone is about 80–100 nm in diameter when observed under the TEM. The collagen fibrils are further assembled from a triple helix of polypeptides, which are about 1.5 nm in diameter and 300 nm in length. The triple-helical molecules assemble in parallel to the long axis of the bone but slightly offset to each neighboring molecule to form a periodic structure which repeats every 68 nm [5]. The mineral present in the bone is known as hydroxyapatite (HAP). The HAP appears as nanoplates, which are only a few nanometers thick and about 50-nm long and 25-nm wide on an average. In a higher level of bone structure, collagen fibrils are seen to assemble into parallel bundles, and HAP nanoplates are located in the space in between each collagen bundle as well as in the gap zone of the collagen fibrils [6, 7].

In addition to studying the basic structure of the naturally grown bones, TEM has also been actively employed to discover the nucleation mechanism of the hydroxyapatite in the bone. Due to the complicated nature of the in vivo environment, such investigation has been predominately carried out by using in vitro models [8–10]. The role of bone proteins in nucleating HAP is controversial. Either collagen or non-collagenous proteins are proposed to nucleate HAP [11]. In a model research, a cryo-TEM analysis showed that a natural bone apatite-like structure can be successfully obtained by incubating the collagen fibrils in a buffered HAP precursor solution containing polyaspartic acid or fetuin, inhibitors of HAP crystallization, but without any non-collagenous proteins (Fig. 1.1) [9]. A detailed TEM study revealed that the collagen acted synergistically with HAP inhibitors to achieve the bone apatite-like structure: the amorphous calcium phosphate clusters, formed in the presence of inhibitors, can be infiltrated into collagen fibrils and be transformed into oriented HAP crystals by charges in the collagen molecules. In another example, the predominant role of collagen in apatite crystallization was further confirmed [10]. This model simply involved stirring a high-density collagen matrix,

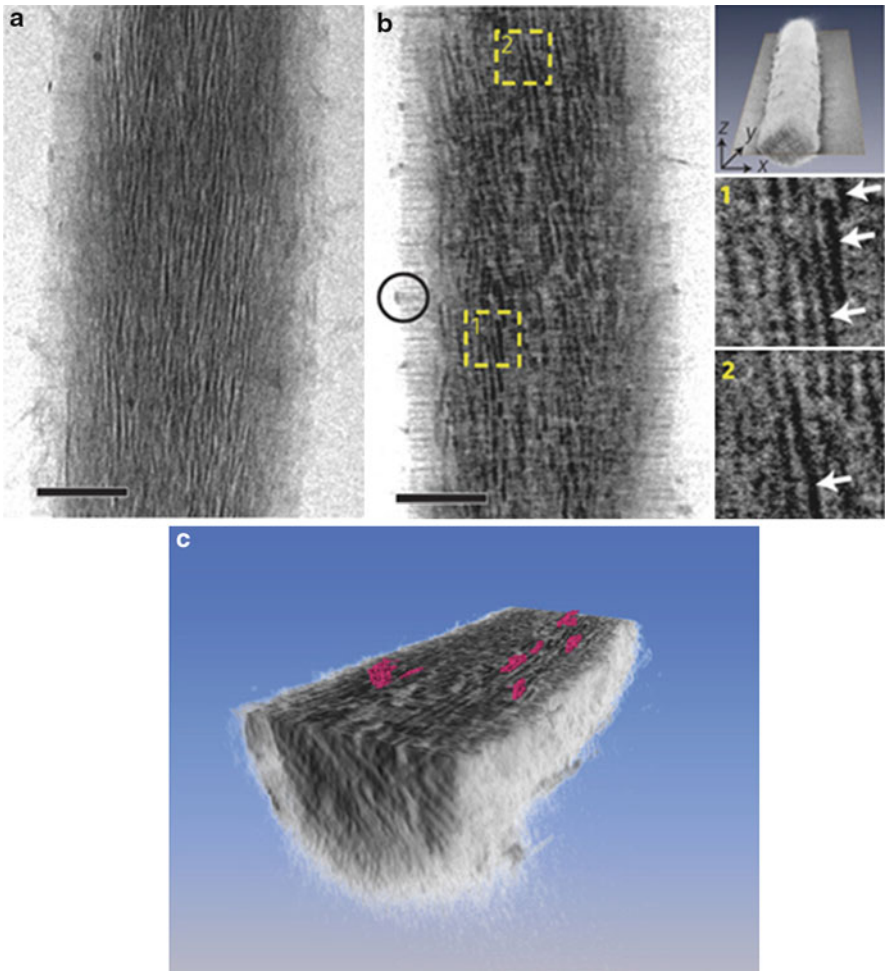


Fig. 1.1 Cryo-TEM examination of a negatively stained collagen fibril incubated in a buffered mineralization solution containing 10 μg/mL of pAsp for 72 h. (**a**) A 2D cryo-TEM image of a mineralized fibril. (**b**) A longitudinal slice of the 3D volume (top *inset* in the *right panel*, sectioned along the *xy* plane) of the collagen fibril. Areas marked by dashed squares are magnified in *insets* 1 and 2, in which plate-shaped crystals are visible in a direction horizontal to the plate plane (*white arrows*). *Circled area* suggests the amorphous calcium phosphate infiltrating the collagen fibril. (**c**) 3D sectional view of a mineralized collagen fibril generated by computer. The 3D model suggests that apatite plates (*pink colored*) are inserted into the collagen matrix. Scale bars: 100 nm (Adapted from Ref. [9])

which was self-assembled from collagen and calcium phosphate precursors during a coprecipitation process, in a simulated body fluid (SBF). It turned out that the apatite can still nucleate and grow in an oriented manner in the collagen matrix, as observed by TEM, even in the absence of non-collagenous proteins or HAP

inhibitors. Moreover, the resultant collagen–apatite structure mimicked well the long-range hierarchical organization in the real bone tissues.

Another area of bone research where TEM is actively involved is bone diseases such as osteoporosis and abnormal bone mineralization. Osteoporosis is a disease in which the bone turns brittle and fragile; it is characterized by reduced bone mineral density and thinning in the trabecular struts in the bone. Although it is still not quite clear how osteoporosis takes place, the apatite crystal shape and size in the osteoporotic bone has been well studied by the TEM. Surprisingly, a comparative structure examination has suggested that on the nanoscale there is no significant difference between normal and osteoporotic bones, including human fibula, tibia, and lumbar and thoracic vertebra samples, in the apatite crystal morphology, size, and orientation in the collagen matrix [12, 13]. Abnormal bone mineralization has also been observed on mutant fish [14]. For example, several mutants of adult zebrafish were identified with phenotype body difference. When the bone structures of normal and mutant zebrafish were compared by the TEM, significant differences were noticed in both the diameter of collagen fibrils and the shape of apatite crystals. The diameter of thin collagen fibrils in the mutant fish bone is about two times as large as that in the bone of normal fish, and the bone apatite crystals in mutant fish are larger in size, with irregular rather than plated shape.

Fish scale is another naturally occurring material that contains collagen–apatite bio-inorganic nanocomposites. A bright-field TEM examination of a thin section of tilapia fish scale uncovered that there are two different layers, normally referred to as internal layer and external layer, with totally different collagen- and apatite-assembled structures (Fig. 1.2). In the external layer, the collagen fibers, 20–30 nm in diameter, are randomly oriented, with needle-like calcium-based crystals embedded in the collagen matrix. The internal layer is composed of several sub-layers; the collagen fibrils, 70–120 nm in diameter, in each sub-layer are oriented toward one direction but are positioned at an angle of about 90° to the fibrils in the neighboring sub-layers [15, 16]. Each collagen sub-layer has a thickness on the micron order, and several of them are packed together to form the plywood-like internal layer of the fish scale. The EELS spectrum obtained from the internal layer suggested that there are calcium, oxygen, carbon, and phosphorous elements, and the Selected Area Electron Diffraction (SAED) pattern obtained from the same layer confirmed the presence of apatite crystals [16, 17]. In a further investigation, carried out by a combination of bright-field, dark-field, and energy-filtered TEM, on the longitudinal and transversal view of the collagen fibrils in the internal layer, it was discovered that (1) the apatite crystals and other calcium-containing materials exist universally in the space among each collagen fibril and that (2) there are also minerals on each collagen fibril, but most of the minerals are present on the surface of the gap zones rather than deep inside the fibril [16].

5.1.2 Calcium Carbonate–Containing Bio-inorganic Nanocomposites

Nacre is a bio-inorganic composite material that can be found in the inner layer of many mollusk shells. The inorganic component in nacre is aragonite-type calcium carbonate, which takes about 95 % of the total volume. In materials science, nacre is

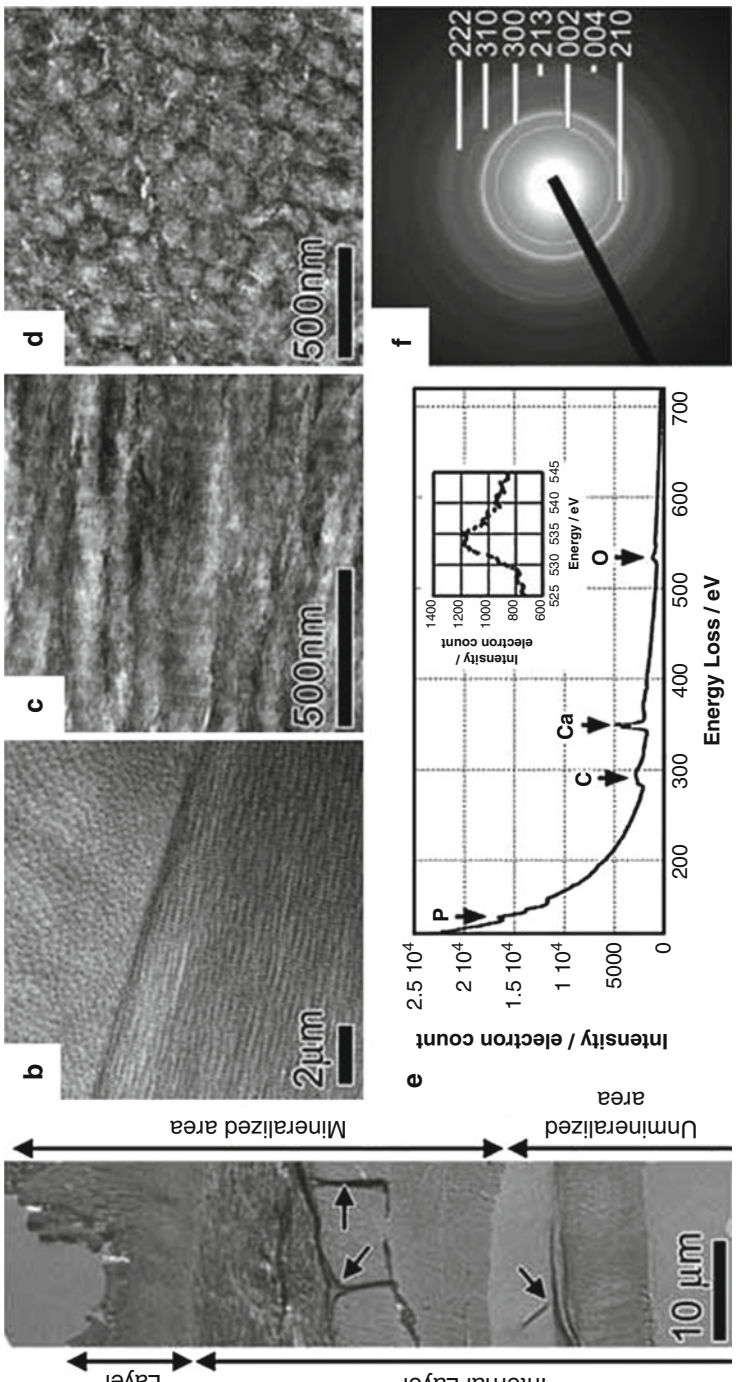


Fig. 1.2 TEM characterization of a fish scale from a tilapia (*Oreochromis niloticus*). (**a**) Distinct double-layered structure of the fish scale. (**b**) The internal layer is composed of several sub-layers; the collagen fibrils in each sub-layer are oriented toward one direction but are positioned at an angle of about 90° to the fibrils in the neighboring sub-layers. (**c**, **d**) Longitudinal and transverse views of mineralized collagen fibrils in a sub-layer. (**e**, **f**) EELS and SAED data suggest the presence of apatite in the collagen matrix (Adapted from Ref. [16])

well known for its magnificent mechanical strength and fracture resistance, which are the result of the so-called brick-and-mortar-assembled structure of aragonite and biopolymers [18]. As revealed by Scanning Electron Microscopy (SEM), the hierarchical structure of nacre is assembled by layer-by-layer stacking of aragonite platelets. An individual aragonite platelet, which is roughly hexagonal shaped, has an edge length of about 5 μm and a thickness of 200–500 nm. The biopolymer layer, which is about 5–20 nm in thickness, is sandwiched in between neighboring layers of aragonite platelets. When a single aragonite platelet is studied under the TEM, it shows a characteristic diffraction pattern of a single crystal. However, the lattice structure obtained from the HRTEM denied that the individual aragonite platelet is a whole piece of monocrystal, but instead it is assembled from numerous small aragonite nanocrystals and amorphous nanoparticles [19, 20]. The assembly process is manipulated by the mechanism of screw dislocation and amorphous aggregation. It is the preferential orientation of aragonite nanocrystals that results in a pseudo-single-crystal-like behavior of aragonite platelets.

The mechanical strength and fracture resistance of nacre are roughly two to three orders of magnitude higher than those of pure aragonite materials [21]. In an attempt to understand the mechanisms that contribute to such mechanical enhancement, TEM is employed as the primary investigating tool. It has been used to discover some minor yet important changes in the crystal structure of aragonite, which has led to the proposal of new mechanisms. In one example, the nacre from California, red abalone, was subjected to two different types of mechanical tests, namely, quasi-static and dynamic uniaxial compression tests, and after tests, the samples were examined by TEM [22]. A significant crystal rearrangement was observed in quasi-statically deformed nacre. Instead of being a quasi-single-crystal-like structure in the aragonite of pristine nacre, the nanocrystals had become disorganized and randomly oriented. When high-strain-rate dynamic deformation was applied, disorganization on the atomic level, including partial dislocation and twinning, was further seen in individual aragonite nanocrystals (Fig. 1.3). These structural changes were termed “partial dislocation emission” and “deformation twinning,” and it is believed that they are two of the mechanisms responsible for the enhanced mechanical properties of nacre. In another work, in the examination of a cross-section of a nacre sample by TEM, a mineral bridge was discovered in the interlayer organic matrix of aragonite platelets [23–25]. The presence of the mineral bridge might play a role in the fracture resistance property of nacre.

Sea urchin (SU) spine is another type of naturally occurring material that contains calcium carbonate–based bio-inorganic nanocomposites. Just like many other materials fabricated by nature, SU spine has a hierarchical structure that is constructed from nanometer-scale building blocks. The overall morphology of SU spine is porous and sponge-like, which is a typical structure for amorphous materials [26]. However, when characterized by several different techniques, including electron diffraction, X-ray diffraction, and polarized optical microscopy, the calcite component inside the SU spine actually showed patterns of single crystals [27, 28]. The HRTEM examination of an ultrathin section of SU spine revealed its mesocrystalline nature: the calcite appears as nano-sized crystals embedded in an

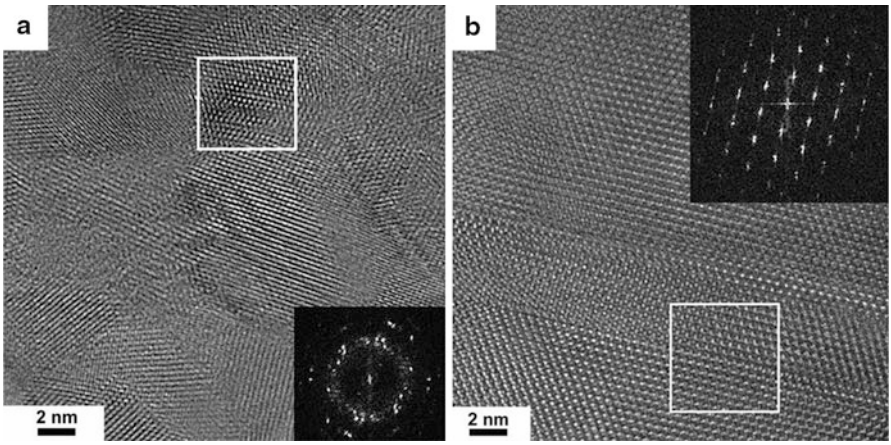


Fig. 1.3 HRTEM images showing partial dislocations (**a**) and deformation twinning (**b**) in the dynamically deformed nacre. *White boxes* indicate typical spots of dislocations and twinning. *Inset* in (**a**) Ring-like diffraction pattern suggests disordering of the aragonite nanoparticles. *Inset* in (**b**) Fast Fourier Transform (FFT) analysis confirms the presence of twinning in the nanoparticles (Adapted from Ref. [22])

amorphous matrix in a highly oriented manner. This type of crystal assembly is very similar to the pattern observed in the aforementioned aragonite platelet in nacre. It is also suggested by the TEM observation of sectioned samples of different treatments that there is a thick layer composed of amorphous calcium carbonate (ACC) and/or macromolecules covering the calcite mesocrystals [29]. These ACC particles could possibly be where the calcite nanocrystals originated. Cavities, with an average diameter of 50–60 nm, were discovered by bright-field TEM to be homogeneously distributed in the calcite crystals of *Lytechinus variegates* SU spines [30]. These cavity structures can be very important for the fracture toughness of the SU spines as the cavities absorb/deflect the stress of a propagating crack and prevent the structural deformation.

5.1.3 Silica in Plants and Microorganisms

Silicon is one of the most abundant elements on earth. The natural form of silicon includes silicate compounds, polysilicic acids, and silica. Due to its abundance in nature, silicon has been used by many organisms, especially plants and microorganisms, to build their skeleton structure for support and protection of life. The silicon compound discovered in the biological system is usually amorphous silica, which can be referred to as biosilica. In the research of biosilica, optical and scanning electron microscopes have been used heavily to discover the hierarchical structure in which silica is present, but TEM has been preferentially employed for various investigations on the subcellular level [31].

Maryna umbrellata is a type of ciliate, normally inhabiting in ephemeral pools and having an umbrella shape; it has an average size of about 10 μm. The presence

of biosilica in *M. umbrellata* can be confirmed by several characterization techniques, including EDS, EELS, and bright-field TEM [32, 33]. Under the TEM, silica granules appeared as many dark spots in an ultrathin section of the cell; after being treated with hydrofluoric acid, silica was dissolved away, leaving only the fracture pattern of the organic matrix. Further TEM examination revealed that the distribution of silica granules in the cell differs dramatically in different cell stages, namely, trophic and cystic stages. In the trophic stage, silica was found to mainly gather in the anterior half of the cell, while during the transition to the cystic stage, most of the silica granules were excreted from inside the cell to form a thick cover over the resting cyst. In an investigation to uncover the detailed biosilicification process, it was discovered that the synthesis of silica has taken place in the Golgi apparatus. Silica nanoparticles of a size of 20–40 nm first accumulated in the silica deposition vesicles (SDVs), which were fused by vesicles in the Golgi apparatus. The densely packed silica nanoparticles in the SDVs were then fused together to form silica gel and eventually transformed into fracture-patterned silica granules with an average size of about 630–819 nm. Biosilica granules with a similar fractured pattern were also discovered in plants like the palm tree [34].

Diatoms are another type of unicellular microorganisms that are well known for using silica to build their main skeleton structure – the cell wall, also known as frustule. The frustules show extremely diverse and sophisticated patterns, such as pores, ribs, and marginal ridges, in nature. It is the frustule pattern as well as the overall morphology of the diatoms that define the genera and species of such microorganisms. It is expected that there are about 10,000 different species of diatoms living primarily in open water. The most straightforward and simple application of TEM in diatom research is to group them into different species. For example, in a survey of diatoms belonging to the *Pseudo-nitzschia* genus in the western North Pacific Ocean, 11 different species were identified by TEM based on the difference in various morphological parameters, such as apical axis, transapical axis, fibulae, valve striae, poroids, and band striae [35]. TEM is also a very helpful tool in studying the biosilicification process of the diatoms. When *Thalassiosira punctigera* and *Thalassiosira weissflogii* diatoms were cultured in media of different salinity, significant biosilica nanostructural change was discovered by direct TEM observation. For diatoms cultured in a low-salinity medium, the density of pores in the silica nanostructures was higher than that observed for diatoms cultured in a high-salinity medium [36].

5.2 Synthetic Inorganic Nanomaterials Templated by Biological Nanostructures

In the past decade, great advance has been made in nanotechnology research. A number of synthetic strategies are developed to fabricate nanomaterials of different sizes and shapes as well as tunable physical and chemical properties. Benefiting from the success in synthetic chemistry, a variety of nanoparticles-based applications have been explored. Among the synthetic strategies,

biotemplate-based synthesis is considered one of the most important methods. Many inorganic nanomaterials, such as metals, semiconductors, and oxides, are fabricated with biotemplates of various types. Generally, as templates, biological nanostructures have at least three advantages that make them attractive. First, most biotemplates are highly uniform in size and shape, which provides a simple mechanism in controlling the monodispersity of the resultant inorganic nanomaterials. Second, biotemplates can be purified in a relatively large quantity, making it possible to mass-produce the desired inorganic nanomaterials. Finally, the native charges on biotemplates offer interacting sites for the inorganic precursors. More importantly, the surface chemistry of certain types of biotemplates can be manipulated by genetic means, so that they can be employed as a universal platform to fabricate various inorganic nanomaterials simply by displaying the corresponding target-specific peptides on the surface of templates.

Together, the biotemplates and the inorganic nanomaterials growing on them form the bio-inorganic nanocomposite materials. In the investigation of such bio-inorganic nanocomposites, TEM has been the primary tool. TEM is capable of discerning both the inorganic components and the stained biological templates. The variety of imaging modes in the TEM enables it to characterize the bio-inorganic nanocomposites from various aspects. Here, the discussion is based on biological templates of four different categories, including 0D protein cages, 1D nanofibers, self-assembled hierarchically structured biotemplates, and DNA-based templates.

5.2.1 0D Protein Cage Templates

Protein cages are self-assembled spherical protein shell architectures composed of a limited number of subunits. Often these symmetrical assemblies have strong nanostructures and precisely defined inner and outer diameters. Thus, as containers, protein cages can physically limit the size of particles growing in the cavity and promise the production of nanoparticles with uniform shape and size. Moreover, the interior part of the protein unit can be genetically modified with tunable electrostatic charges or peptides affinitive to a specific inorganic material, which further facilitates the growth of nanoparticles inside the protein cages. Recently, a series of protein cages, such as DNA-binding proteins from starved cells (DPS), small heat-shock proteins, ferritin (Fn), MS2 bacteriophage, Cowpea chlorotic mottle virus (CCMV), and Cowpea mosaic virus (CPMV), have been exploited as biotemplates in nanoparticle synthesis. These biotemplates covered the cavity diameter range of 4.5–24 nm [37, 38].

Here is a typical example in which TEM is actively used to characterize the inorganic/protein cage core–shell nanostructures. Iwahori et al. used the self-assembled apoferritin protein from horse spleen (HSAFn) as size-constrained reaction cages to mineralize ZnSe nanoparticles [39]. The synthesis started with the electrostatic condensation of zinc precursor ions into the cage cavities by incubating them together for some time, followed by addition of selenium ions to form ZnSe. As shown in the TEM images of a negatively stained sample, the as-prepared ZnSe nanoparticles were monodisperse and spherical with an average diameter consistent with the inner size of the HSAFn cages. Each ZnSe nanoparticle was surrounded by an intact ferritin cage which appeared white after

negative staining under the bright-field TEM, while in the TEM image of an unstained sample, only ZnSe nanoparticles are visible. The crystallinity of gold nanoparticles was studied by both the HRTEM and SAED. The biological template can also be visualized under TEM without negative staining, using instead the HAADF-STEM mode. In this mode, each element composition exhibits a contrast depending on their atomic weight; thus, a heavy inorganic core appears bright while a dark shell surrounding the core indicates low-atomic-weight protein cages [40]. EELS is also capable of analyzing bio-inorganic nanocomposites prepared from protein cages. For example, in the atomic layer deposition (ALD) of titanium oxide (TiO_2) onto apoferritin cage templates, it was discovered that TiO_2 can be selectively deposited onto the outer and inner surfaces of the protein cage through thermal pretreatment and osmotic dehydration. Although hollow and core–shell TiO_2 nanostructures can be seen under the bright-field TEM, the STEM coupled with EELS provides instant confirmation of titanium distribution across the nanoparticles (Fig. 1.4d–i) [41].

5.2.2 1D Filamentous Biological Templates

Besides 0D protein cages, 1D fibrous biological nanostructures can also be used as templates for the synthesis or assembly of nanorods, nanowires, and nanotubes. 1D nanostructures, due to their unique electronic, optical, thermal, and mechanical properties, are expected to be applied as both interconnects and functional units in nanoscale electronics [42]. The biological fibrous templates include tobacco mosaic virus (TMV), M13 and fd filamentous bacteriophage, bacterial flagella, microtubules, and collagen [43–45]. Most of the templates are nanofibers precisely self-assembled from thousands of same subunits and with uniform diameter and identical length. This section will focus on the inorganic 1D nanomaterials produced on TMV, phage, and flagella, which present genetically modifiable surface chemistry. TEM is the first choice to observe the linear hybrid structures produced with or without negative staining. Meanwhile, the crystalline phase and structure as well as the chemical composition are analyzed by TEM.

Tobacco Mosaic Virus Templates

TMV is a plant virus with rod-like appearance. Its capsid is composed of 2,130 copies of identical coat proteins, and there is a single-stranded helical RNA in the cavity. The virion is about 300 nm in length and 18 and 4 nm in outer and inner diameter, respectively. TMV is superior as a template for nanomaterial synthesis since it is extraordinarily stable. It is able to withstand high temperatures of up to 90 °C and can maintain a broad pH range from 3.5 to 9 over several hours, and its structural integrity is maintained even in some organic solvents, such as ethanol and dimethylsulfoxide (DMSO) [46, 47].

So far, a variety of materials were fabricated into linear nanostructures through TMV. Shenton et al. synthesized CdS and PdS nanotubes on the external surface of TMV [44]. TEM revealed the mineralized tubular structures of CdS. The dense outer mineral layer and the light internal TMV core were obvious. EDS analysis confirmed the presence of Cd and S elements. The lattice structures in the HRTEM image

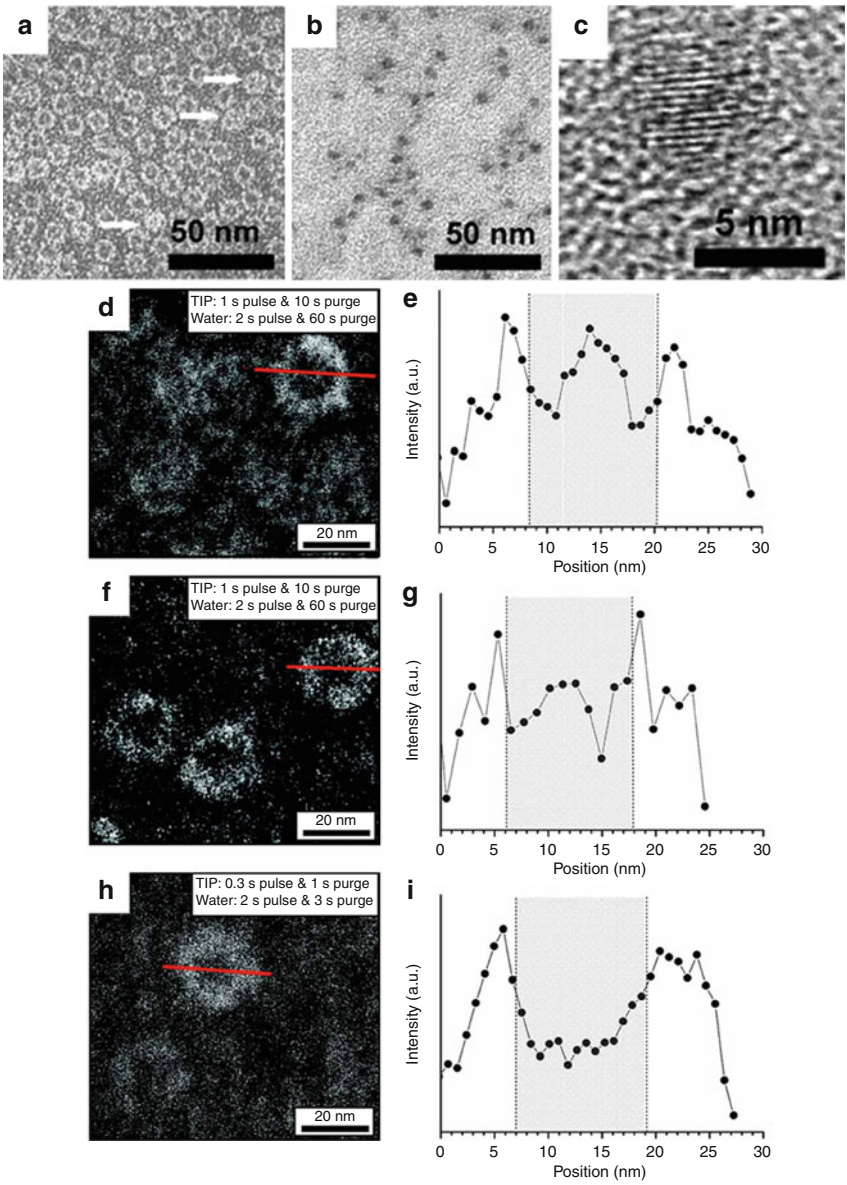


Fig. 1.4 TEM characterization of bio-inorganic nanocomposites synthesized by templating against protein cages. (**a**–**c**) ZnSe nanoparticles synthesized in the apoferritin protein from horse spleen (HSAFn). (**a**, **b**) Bright-field TEM images of stained and unstained ZnSe nanoparticles, respectively. (**c**) HRTEM image. (**d**–**i**) Dark-field STEM (**d**, **f**, **h**) and EELS (**e**, **g**, **i**) characterization of TiO_2 nanostructures fabricated by atomic layer deposition of TiO_2 onto HSAFn templates. The titanium intensity profiles on the *right panel* are obtained along the *red lines* in the corresponding images on their *left*. These results suggest that TiO_2 can be selectively deposited onto the outer and inner surfaces of the protein cages (Adapted from Ref. [39] (**a**–**c**) and Ref. [41] (**d**–**i**))

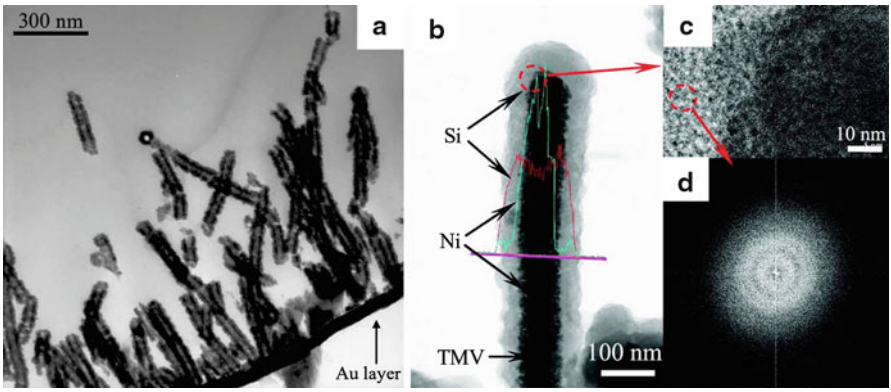


Fig. 1.5 TEM characterization of anode material of a lithium-ion battery prepared by a vertical array of a TMV template. (**a**) TEM image of a vertical array of nickel-coated TMV nanorods on gold substrate. (**b**) TEM image of a TMV–Ni–Si nanowire prepared by physical vapor deposition (PVD) of silicon. The superimposed EDS profile shows distribution of Si and Ni elements across the nanowire. (**c**, **d**) HRTEM and FFT pattern of circled areas in **b** and **c**, indicating the amorphous nature of silicon (Adapted from Ref. [53] (**a**) and Ref. [54] (**b–d**))

indicated the zinc blende crystal structure and the disordered aggregation of CdS nanoparticles. Similar results were obtained with PbS nanotubes. Besides CdS and PbS, Au, Pt, Ag, Pd, Ni, Co, SiO_2, and iron oxide nanoparticle arrays or nanotubes have been organized or synthesized through TMV templating [48–50]. An interesting phenomenon was observed during the research of this hybrid that TMV virions self-assembled head to tail into long nanotubes along the long axis when mineralizing SiO_2 from tetraethoxysilane (TEOS) in an acidified solvent [48]. It is believed that the complementary hydrophobic interactions between two ends of the helical structure give rise to the assembly just like the interactions to assemble protein subunits together into a TMV capsid at any cross section [51]. This highly ordered long fiber structure is not stable, but with the coating of inorganic shell or polymer layer, it becomes robust and suitable for further applications [52]. An important application of inorganic–TMV nanocomposites is as anode material for lithium-ion batteries (LIBs) [53–56]. In these studies, TMVs were engineered to display a cysteine motif at the N-terminal of each coat protein subunit. The strong covalent interactions between thiol groups on cysteine and metallic atoms enabled the dense, vertical assembly of these virus rods on solid metal substrates (Fig. 1.5a). The virus rods were then coated subsequently with a thin layer of metal, as current collector, and another layer of active anode material, like Si or TiO_2, for lithium-ion batteries (Fig. 1.5b–d). The 3D virus-based bio-inorganic nanocomposite anode materials have enhanced dramatically the capacity and cycling stability of lithium-ion batteries.

The 4-nm central channel of TMV has also been used as a reaction vessel for the growth of nanowires just like in the case of 0D protein cage templates. Linear Ag nanoparticle arrays were formed within the channels of the virions [49]. Ni and Co nanowires of about 3 nm diameter were synthesized selectively in the narrow

channel by first activating the TMV with Pd(II) or Pt(II) ions [57]. Then the activated TMVs were metallized by the electroless deposition method in a bath solution containing a reductant and nickel or cobalt ions. The nanowires were about 300-nm long, but the ones up to 600 nm were observed which suggested the end-to-end assembly of TMVs. By changing the reaction condition and the reductant, the spatial selectivity (exterior and/or interior) of metallization can be achieved [48, 50, 57]. In addition, bimetallic alloy nanowires, like CoPt and $FePt_3$, synthesized inside the TMV channel have also been reported [58].

Filamentous Bacteriophage Templates

Bacteriophage is a type of virus that specifically infects bacteria. Wild-type M13 and fd phages are linear, flexible nanofibers, about 6 nm in diameter and 900 nm in length. They are the two major types of phage frequently employed as templates in the synthesis of 1D inorganic nanomaterials. Structurally, the sidewall of M13 and fd phages is self-assembled from a few thousand copies of major coat protein (pVIII), while four types of minor coat protein (pIII, pVI, pVII, and pIX) are at the two distal ends of the nanofibers. It is reported that all five coat proteins can be genetically engineered to display foreign peptides [59–63]. Moreover, unlike the genetic modification on other protein assemblies, which can only introduce one type of exogenous peptide, two or three different peptides can be simultaneously displayed on different phage coat proteins, and these are known as double- and triple-display techniques [64–67]. This technology bestows phage with multiple functionalities on a single nanoscale structure. One of the biggest advantages of using filamentous phage as a template to make linear nanostructures is that peptide sequences binding specifically to a target material can be selected directly through a so-called biopanning process. In this process, a phage library, which contains billions of randomly displayed foreign peptides on the phage surface, is allowed to interact with the target in the first affinity selection. The unbound phages are then washed away and the binding phages are eluted and used as phage input for the second round of selection. After several further rounds of selection, the phages that still bind to the target are considered to have the highest affinity. A variety of inorganic materials, including metals, metal oxides, and semiconductors, have been applied as targets for biopanning, and a pool of peptides with specific affinity have been established, which confer huge potential on bacteriophages as templates for 1D nanomaterial synthesis [68–71]. So far, the bacteriophage-templated inorganic nanofibers have been explored for applications such as lithium-ion battery, photocatalytic water oxidation, hydrogen production, gas and humidity sensing, and electroconductive films [72–76].

Mao et al. reported a pioneer work of synthesizing single-crystal semiconducting nanowires (ZnS and CdS) and ordered magnetic nanowires (CoPt and FePt) based on genetically engineered M13 phage templates [71]. The peptides displayed on the major coat protein of M13 phage were selected through a screening process from the phage library and were considered to control the composition and phase during nanoparticle nucleation. Taking ZnS as an example (Fig. 1.6), ZnS nanocrystals were first mineralized onto the virus surface from a metal salt precursor under reduced

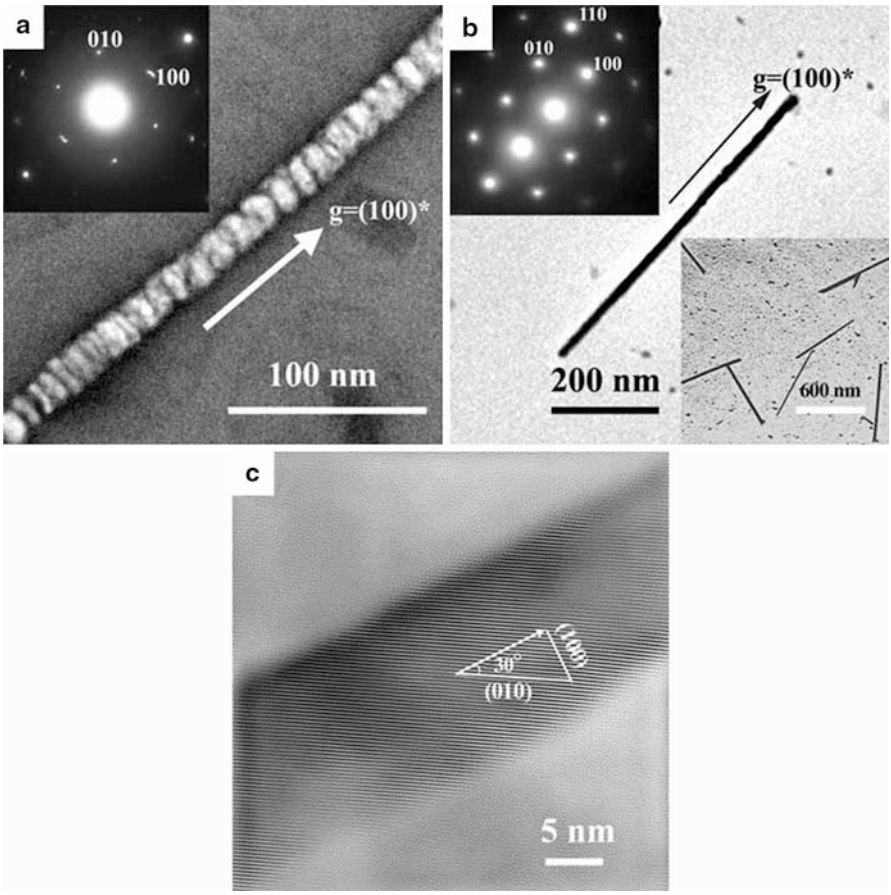


Fig. 1.6 TEM characterization of ZnS nanowires by using engineered M13 phage as templates. (**a**) Dark-field diffraction contrast image of the as-synthesized ZnS nanowires using the (100) reflection. (**b**) Bright-field TEM image of a single ZnS nanowire after annealing. Electron diffraction in the *inset* in (**a**) shows the wurtzite-type, polycrystalline nature of the as-synthesized ZnS nanowires, which became single crystal after annealing, as indicated by the electron diffraction pattern (*inset* in **b**) and the HRTEM (**c**) (Adapted from Ref. [71])

temperature. From the dark-field TEM observation, using the (100) reflection, of an as-synthesized nanowire, it was clear that although in close contact, the nucleated ZnS nanocrystals were not fused together probably due to the blocking effect of the functional peptides. The electron diffraction data showed that the as-synthesized ZnS nanowires are polycrystalline with a wurtzite-type structure and that the (100) plane of the ZnS nanocrystals is preferentially oriented perpendicular to the longitudinal direction of the nanowires. After annealing, as revealed by HRTEM and electron diffraction, the polycrystalline assemblies were transformed to single-crystal nanowires and the preferred orientation of crystal planes in the as-synthesized ZnS

nanowires was also retained. Similarly, by fusing different nucleating peptides onto M13 phage, CdS, CoPt, and FePt nanowires were obtained through either mineralization or chemical reduction. This work represents a universal strategy for the synthesis and TEM characterization of the 1D nanostructure of various inorganic materials, such as CeO_2, $FePO_4$, Au–Ag alloy, IrO_2, Rh, Ru, and Pd, based on the genetically modified phage templates.

Double-display phage system was also explored as templates for hybrid nanomaterial synthesis and assembly. In one example, M13 phage major coating protein pVIII was genetically modified with cobalt nucleation motif and gold-binding motif [73]. As a result, Au and Co_3O_4 nanomaterials can be subsequently deposited onto the phage nanofibers (Fig. 1.7a–c). TEM examination showed that Au appeared as spherical nanoparticles embedded in the solid Co_3O_4 nanowire matrix. When the Au–Co_3O_4 hybrid nanowires were applied as anode material of lithium-ion battery (LIB), they exhibited remarkably higher capacity and much slower capacity degradation through many cycles of charging and discharging. Instead of fusing foreign peptides only onto one type of protein, the major coating protein pVIII and tip protein pIII were also modified as bifunctional templates to form cathode material for LIB [64]. The inserted motif on pVIII is used to help the nucleation and growth of amorphous iron phosphate (a-$FePO_4$) nanowires, the major functional components of LIB cathode, and the modified pIII can specifically bind to carbon nanotubes (CNTs). The formed complex structure was an a-$FePO_4$ nanowire with the virus tip (pIII protein) tethering with CNTs (Fig. 1.7d–f). The addition of CNTs enhanced the electronic conductivity of the cathode and, thus, resulted in a significant increase in the specific capacity of LIB under high discharging rates.

5.2.3 Bacterial Flagella Templates

Bacterial flagella are motion organs protruding from the surface of bacteria. They are protein fibers self-assembled helically from more than 20,000 copies of identical protein subunits called flagellin. The outer diameter of flagella is about 12–25 nm, while the inner is only 2 nm, and the length is tunable depending on the number of subunits. Unlike the major coat proteins of TMV and bacteriophage, which can only display no more than 10 amino acids, flagellin can be modified with up to 302 amino acids at the highly variable, solvent-exposed domains (D2 and D3) [77–80]. And this would bring higher tunability over the charge and surface chemistry of the flagella, making them very suitable as templates for nanomaterial synthesis and assembly. So far, as characterized almost exclusively by bright-field TEM, nanoparticle arrays and nanowires of metal (Co, Cu, Cd, Ag, Au, and Pd) and quantum dots (ZnS and CdTe) have been successfully produced by templating against wild-type or genetically engineered flagella [81, 82]. Moreover, flagella exhibit diverse morphologies under different pH values, temperature, and ion strength [83]. Based on this phenomenon, we synthesized silica nanotubes (SNTs) templated by flagella, and the resultant nanotubes exhibited variable morphologies at different pH values under TEM (Fig. 1.8) [84]. At pH 4, SNTs were curly and coiled bundles. SNTs exhibited the sinusoidal wave morphology at both pH 8 and 9, but with a shorter wavelength at pH 9.

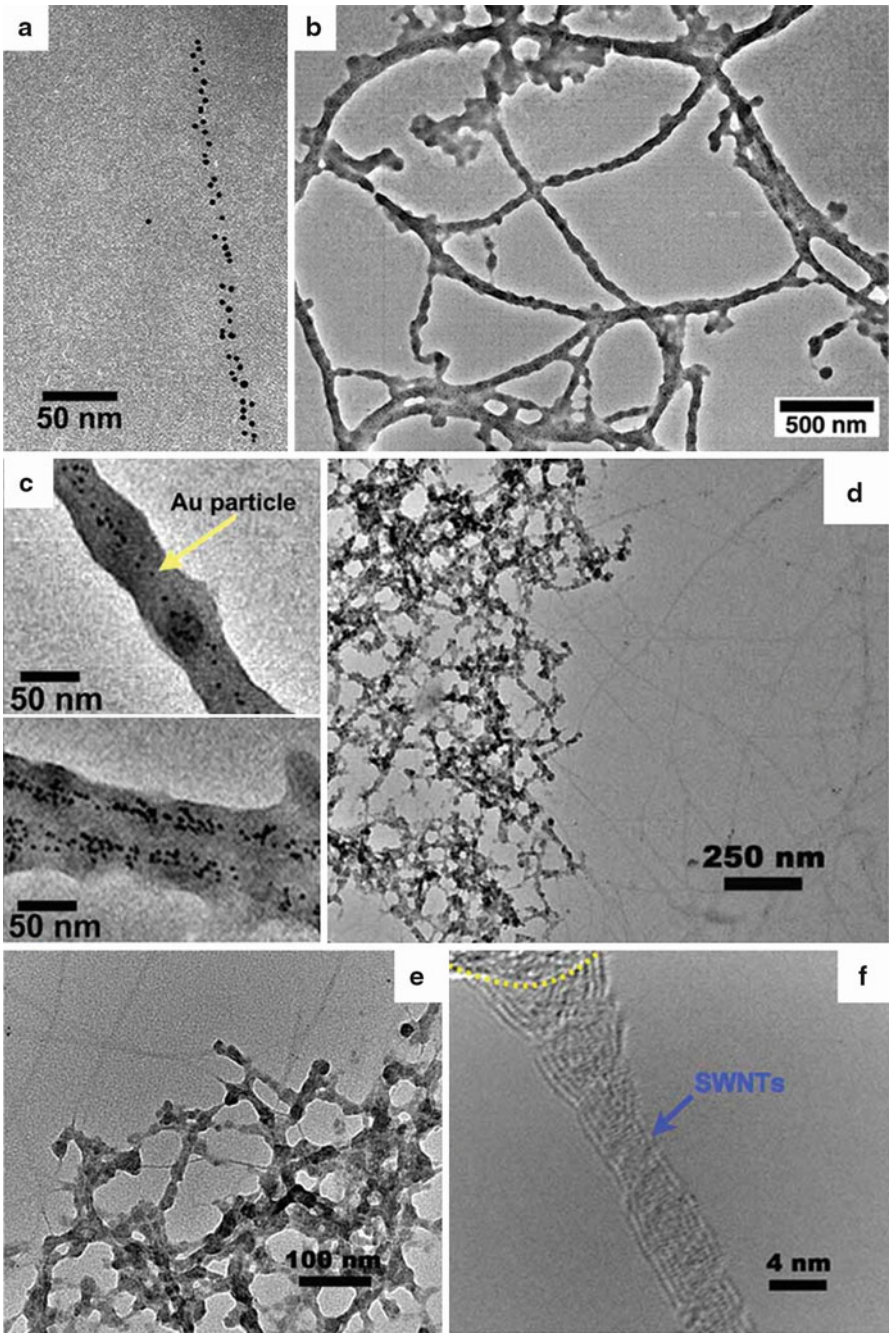


Fig. 1.7 TEM images of lithium-ion battery electrode materials fabricated by using engineered M13 phage as templates. (**a**–**c**) Au–Co_3O_4 hybrid nanowires prepared by M13 phage displayed

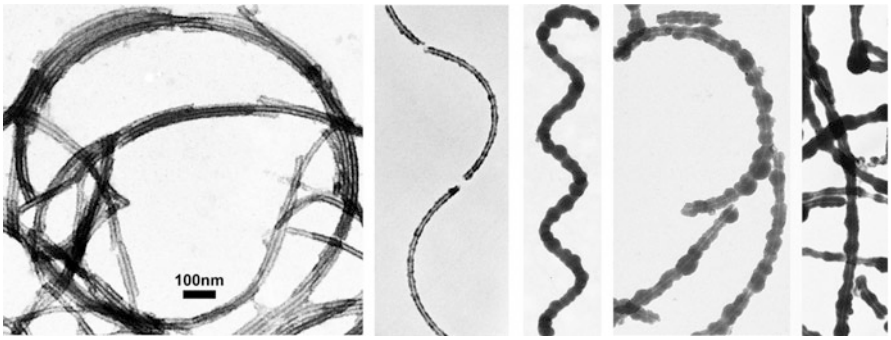


Fig. 1.8 Morphology manipulation of flagella-templated silica nanotubes synthesized under different pH values. TEM images from *left* to *right* correspond to silica nanotubes synthesized at a pH of 4, 8, 9, 10.5, and 11, respectively (Adapted from Ref. [84])

When the pH value was increased to 10.5, SNTs were coiled but containing a single flagella nanofiber in the channel, which was different from the flagella bundles observed at pH 4. Further increasing the pH to 11, the coiled SNTs became straight. In addition, the peptide sequences displayed on the flagella surface also alter the morphology of SNTs.

5.2.4 Self-assembled Hierarchically Structured Biotemplates

Both the protein cages and fibrous biological templates are capable of self-assembling into highly ordered 2D or 3D structures, which are also ideal scaffolds for making inorganic nanomaterials with hierarchical organization. Various strategies have been developed to construct the complex structures from starting building blocks, such as self-assembly at a liquid/solid or liquid/liquid interface, evaporation-induced self-assembly, dip-coating, and layer-by-layer method. These strategies greatly rely on the inherent properties of building units including uniform size and shape, exquisite symmetry, modifiable surface chemistry, and liquid crystal structure at high concentrations [51].

Protein cages were able to organize themselves into ordered hexagonal 2D arrays by interfacial methods, and the nanoparticles grown or assembled in the cages were thus organized into a monolayer of close-packed arrays without aggregation. Ferritin molecules were reported to make 2D arrays at air/water interfaces, and the array of

Fig. 1.7 (continued) both the gold-binding and cobalt nucleation motifs on the pVIII major coat proteins. Gold nanoparticles of 5 nm were first assembled onto the phage (**a**), followed by a direct nucleation and growth of Co_3O_4 nanowires (**b**, **c**). (**d**–**f**) Low- and high-magnification TEM images of a-$FePO_4$ nanowire and single-walled carbon nanotubes (SWNTs) complex prepared by double-displayed M13 phage template. The pVIII major coat proteins were displayed with a-$FePO_4$ nucleation peptides and the pIII tip proteins were engineered with SWNT-binding peptides. TEM images show that a-$FePO_4$ nanowires were nucleated and grown on the main body of phage template, while the SWNTs were tethered to one end of the a-$FePO_4$ nanowires (Adapted from Ref. [73] (**a**–**c**) and Ref. [64] (**d**–**e**))

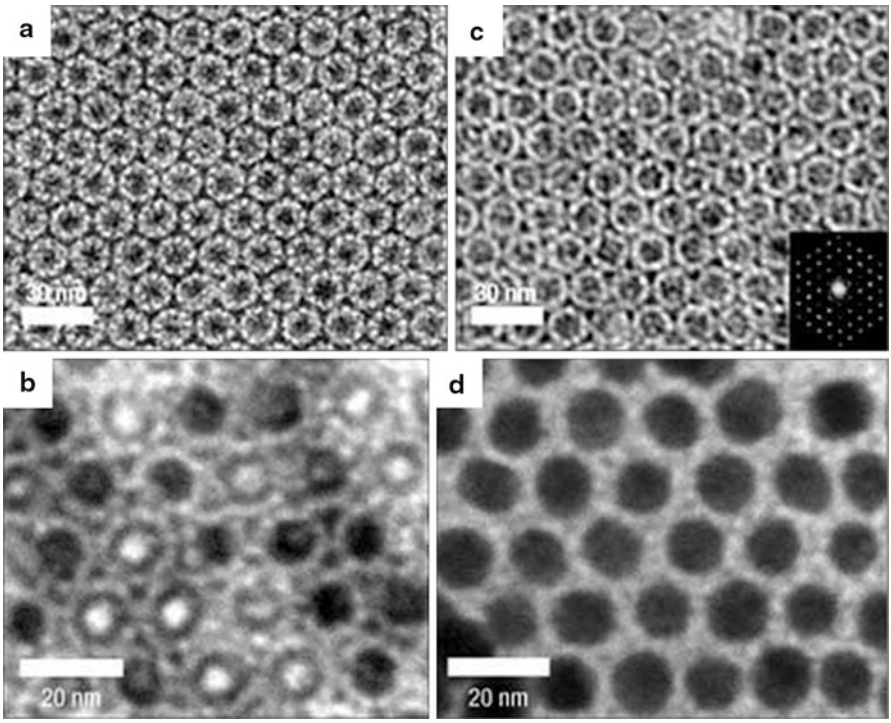


Fig. 1.9 TEM characterization of the assembled 2D arrays of AuNPs–protein bio-inorganic nanocomposites. (**a**, **c**) 2D array of the beta chaperonins corresponding to a pore size of 3 and 9 nm, respectively. The chaperonin proteins have been genetically modified with chemically reactive motifs. (**b**, **d**) Uptake of 5- and 10-nm AuNPs onto the apical pores of chaperonins resulted in a 2D ordered array of AuNPs (Adapted from Ref. [86])

iron oxide cores could be easily obtained by heat treatment [85]. Chaperonin, a hollow double-ring structure composed of 18 identical subunit proteins, was also used to form this kind of structure. Mcmillan et al. introduced a cysteine residue at the central pore position of each subunit of chaperonin and thus formed a reactive ring of nine thiols, which was able to capture gold nanoparticles [86]. The 2D chaperonin crystalline template was produced by direct deposition and the ordered range was up to 20 μm (Fig. 1.9a, b). After incubation with 5- and 10-nm gold nanoparticle solutions, the hexagonally packed array was observed clearly under the TEM (Fig. 1.9c, d). In addition, virus-like particles (VLPs), which are composed of virus proteins coating over an inorganic nanoparticle core, exhibited the same self-assembly behavior to form 2D array patterns [87].

Fibrous biological nanomaterials were also reported to self-assemble into ordered structures, which were then employed as templates to fabricate inorganic nanostructures. For example, bacterial pili are rigid, rod-like protein assemblies, growing on the surface of bacteria. They are usually 1–2 μm in length and 6–7 nm in diameter. It was discovered

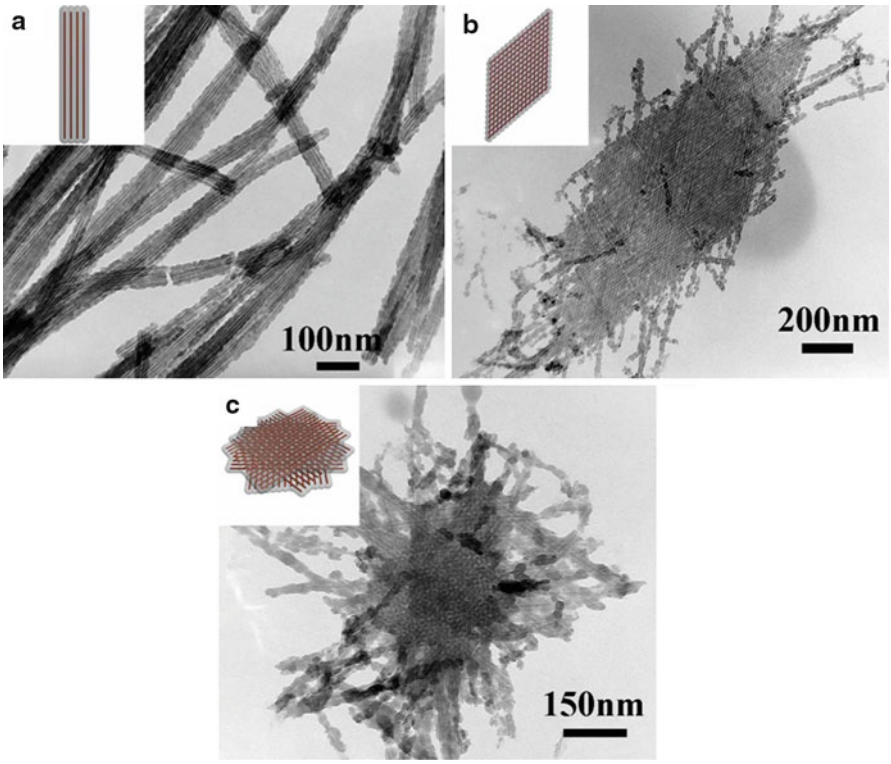


Fig. 1.10 Silica–pili bio-inorganic nanocomposites fabricated by templating against the pili assemblies. Silica nanostructures of multichannels (**a**), nanorhombuses (**b**), and nanoflowers (**c**), which were prepared by using pili bundles and double- and multiple-layer lattices as templates, respectively. *Insets* are a sketch depiction of the corresponding nanostructures (Adapted from Ref. [88])

that pili are able to assemble into hierarchical structures in some inducer solutions, such as hexamethylenediamine, pimelic acid, and 1,3-propanedisulfonic acid [88]. Depending on the concentration and types of inducers, pili can form several different assemblies, including bundles and double-, triple-, and multiple-layer lattices. In the lattice structure, the angle between pili nanofibers in the neighboring layers was found always to be 42°, which is the result of the groove–ridge interlocking fit of the pili fibers. The pili assemblies were then served as biotemplates to synthesize silica nanomaterials. Silica nanostructures, like multichannels, nanorhombuses, and nanoflowers, were obtained by templating against pili bundles and double- and multiple-layer lattices, respectively (Fig. 1.10).

5.2.5 DNA-Based Biotemplates

The diameter of a single-stranded DNA (ssDNA) is less than 1 nm and that of a double-stranded DNA (dsDNA) is about 2 nm. The tiny size and the precise

control of length and sequence make DNA molecules very intriguing scaffolds for nanostructures. Some types of nanomaterials have been directly synthesized on DNA molecules and mainly focused on metals such as Au, Ag, Pd, Cu, Ni, and Co and semiconductors such as CdS, CuS, and Fe_3O_4 [89–98]. But the applications of most of these works were limited since the produced deposits were not continuous and thus not electrically conductive. It is believed that the small number of nucleation sites resulted in this deficiency, and some strategies have been employed to solve this problem, such as an enhancement step for further growth of the formed nanoparticles or multistranded templates (bundles or nanotubes) to increase nucleation sites [98–100]. Actually, a great part of this section is not on the direct synthesis of nanoparticles or nanowires on DNA templates but on assembling the DNA molecules into specific structures first and then using the assemblies as templates for a programmed assembly of functional nanoparticles. Until now, considerable 1D, 2D, and 3D DNA structures including strictly periodic lattices, cylindrical tubes, and diverse geometric shapes have been generated [101–104]. These structures are mostly built up from repeating tiles or DNA origami on the basis of specific interaction between complementary sequences [101, 105]. Gold nanoparticles were the most used inorganic nanomaterial organized on DNA scaffolds. The precise addressing of nanoparticles was contributed from the Au–S covalent bonding, biotin–streptavidin interaction, or complementary DNA binding. The generated inorganic–DNA hybrid composites with accurately positioned, distanced, and patterned nanoparticles are of considerable importance for both photonic and electronic applications [106–108].

Very recently, 3D finite and infinite organization of DNA has been reported by several groups through different approaches. The 3D DNA structures make it possible to assemble nanoparticles into 3D arrays through the templating strategy. So far, the only example of DNA-templated 3D assembly of nanoparticles was reported by the Yan et al. [109]. In their work, they discovered that when gold nanoparticles were linked onto one of the four types of tiles, whose self-assembly forms 2D nanosheets, they could induce the rolling up of DNA sheets to form tubular structures, and simultaneously the nanoparticles were transformed into periodic 3D arrays. The formation of DNA tubes was the result of unfavorable electrostatic repulsion forces and the steric effect among closely approaching gold nanoparticles on the tiles; by curling up, the nanoparticles could be separated from each other and the unfavorable forces were minimized. The assembled pattern of gold nanoparticles is correlated to their sizes. The 5-nm gold nanoparticles could be assembled into several types of 3D arrays, including stacked rings, single spirals, double spirals, and nested spirals, corresponding to the different association manners of the DNA tiles during rolling up, while with increased size (10 and 15 nm) of gold nanoparticles, the stacked ring conformation was preferentially formed.

In addition to the DNA substrates assembled from DNA tiles with sticky ends, the DNA origami can also be used independently as templates to achieve precise assembly of nanoparticles. Ding et al. developed a strategy of assembling exactly six gold nanoparticles of different sizes into an array with a triangular-shaped DNA origami template (Fig. 1.11a) [110]. They designed

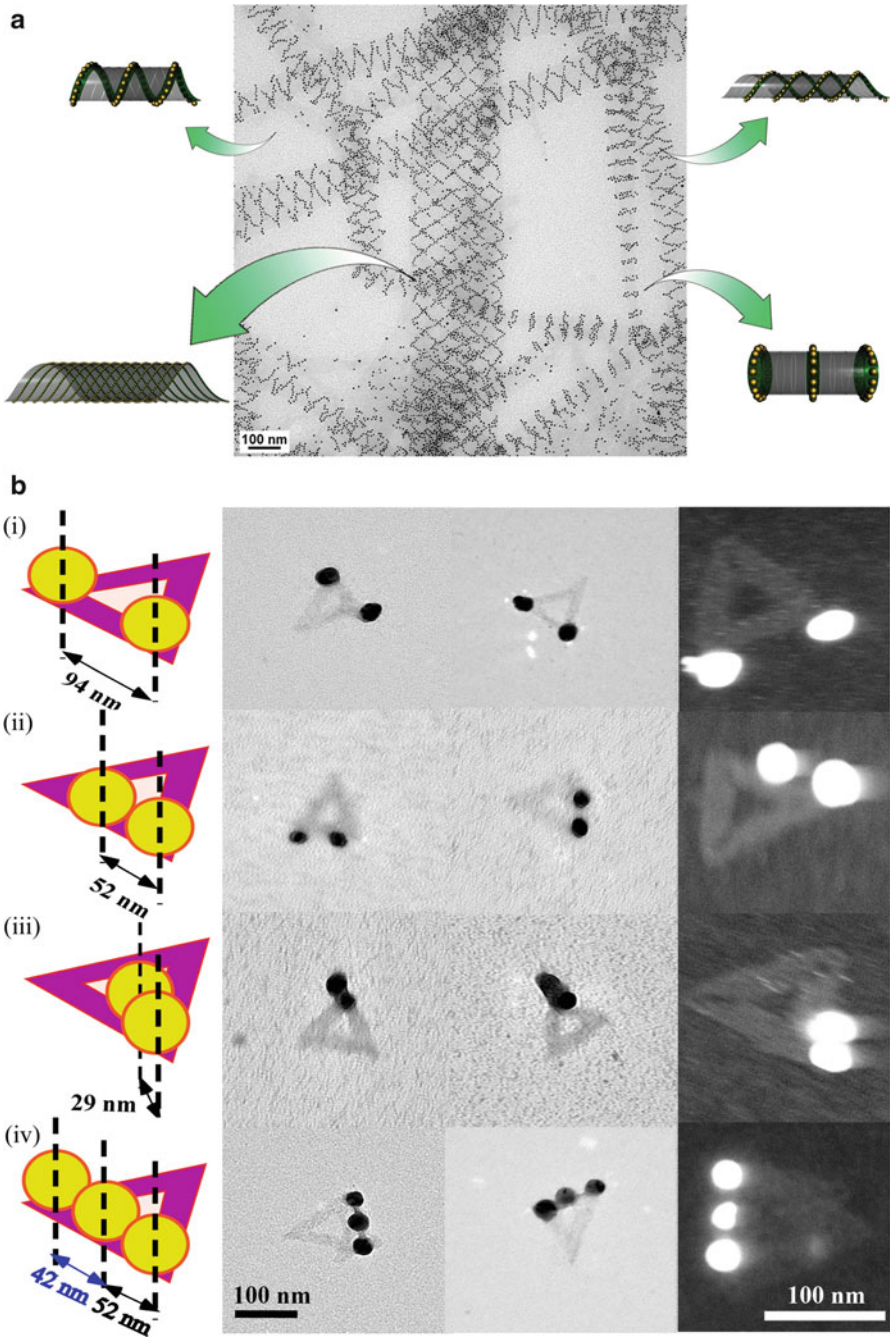


Fig. 1.11 (continued)

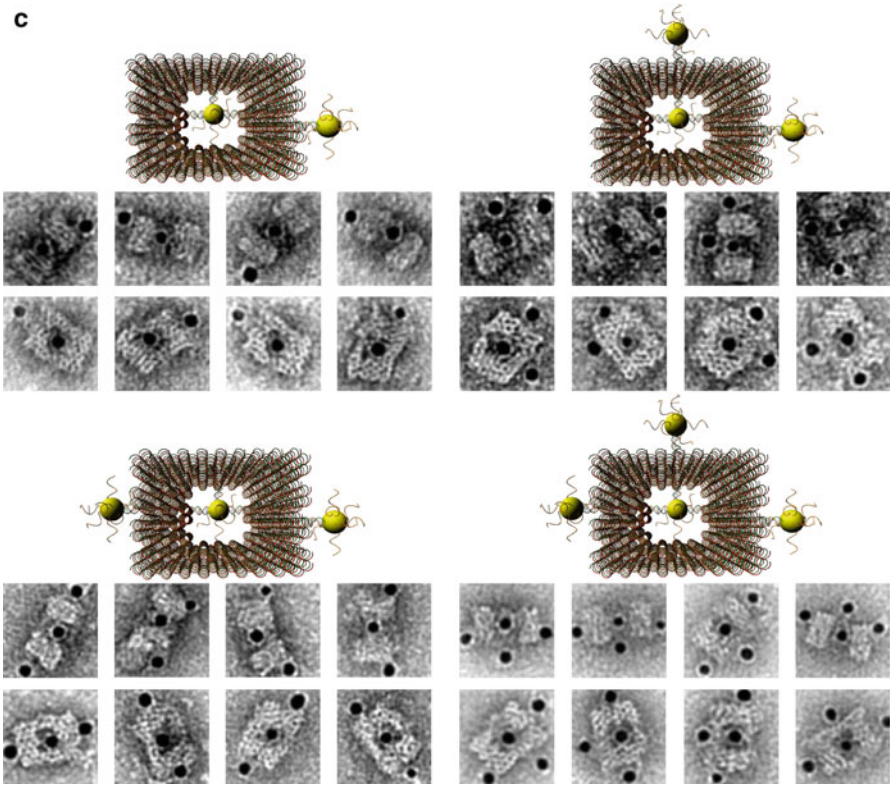


Fig. 1.11 Controlled assembly of AuNPs and AgNPs by using DNA hierarchical nanostructures as templates. The DNA templates are usually constructed from DNA tiles and origami. In a rationally designed DNA template, the number and locations of nanoparticle capture strands can be well manipulated, leading to the controlled assembly of nanoparticles. (**a**) Several different tubular conformations of AuNPs. The AuNPs were first co-assembled with DNA tiles to form 2D arrays; the steric and electrostatic repulsion between neighboring AuNPs then forced the 2D arrays curling up into tubular structures of different conformations. (**b**) Controlled assembly of AgNPs onto a triangular-shaped DNA origami. The *middle* two columns show two typical AgNPs assembled patterns. DNA origami was negatively stained and shows gray contrast under the bright-field TEM. The fourth column is the STEM images of each assembly, and no negative staining was applied. (**c**) Manipulable arrangement of 5-nm AuNPs inside and outside DNA cages. The DNA cages were assembled from DNA origami. The AuNPs capture strands were selectively placed on the inner and outer walls of the DNA cages, resulting in several different patterns of assembly. Negative staining was applied to make DNA visible under the bright-field TEM (Adapted from Ref. [109] (**a**), Ref. [111] (**b**), and Ref. [112] (**c**))

six different naked DNA oligomers by extending the sequence of staple strands at specific sites along one edge of the triangular template. Six gold nanoparticles with each modified with one type of complementary sequence can be placed at the desired location on the template after hybridization. In a following work, through a similar design, a controlled number of silver nanoparticles (one, two, and three nanoparticles) were assembled onto the

triangular origami template, and both the interparticle distance and their positions relative to the template were demonstrated to be manipulable (Fig. 1.11b) [111]. In another work reported by the Yan et al., a single gold nanoparticle was successfully encapsulated inside the cavity of each DNA origami cage through hybridization with the oligomers designed on the inner surface of the cages [112]. Moreover, by displaying free oligomers on selected outer surfaces of the template, they were able to assemble nanoparticles into patterns of different symmetry (Fig. 1.11c).

5.3 Externally Introduced Inorganic Nanoparticles in Cells and Tissues

Nanoparticles, including soft polymeric nanoparticles and hard inorganic nanoparticles, have been the subject of intensive research as drug carriers in recent years. One of the most valuable advantages of the nanoparticles-based drug delivery is that the surface of nanoparticles can be chemically modified with specific targeting molecules, so that drugs can be delivered more effectively to the desired sites in the body. Ideally, it is expected that the nanoparticles will be degraded or excreted from the body after drug release is completed. However, due to the complexity of the biological systems, there is a tremendous uncertainty in the fate of nanoparticles once injected in vivo. For long-term safety, it is highly essential to study the biological behaviors of nanoparticles, such as toxicity, organ distribution, and in vivo degradation [113, 114]. Most often, such study is carried out relying on the biological experimental techniques. For example, toxicity of nanoparticles is usually evaluated by an MTT assay and hematoxylin and eosin (HE) staining has been a very useful tool to confirm the biocompatibility of nanoparticles. These characterization techniques focus almost exclusively on the biological changes taking place after the introduction of nanoparticles, and what happens to the nanoparticles is unknown. Fortunately, TEM is not only capable of observing inorganic nanoparticles at very high resolution but can also discern organelles of an ultra-sectioned cell clearly. Therefore, TEM has been very useful in the study of inorganic nanoparticles–cell/tissue composite materials, and together with the conventional biological characterization techniques, they contribute to a more comprehensive understanding of the fate of nanoparticles both in vivo and in vitro.

5.3.1 Degradation of Nanoparticles In Vivo and In Vitro

Silica is well known as a biodegradable material, and mesoporous silica nanoparticles (MSNPs) are considered as ideal drug carriers due to their extremely large surface-to-volume ratio, easily modifiable surface chemistry, and size tunability. However, not much detail is known about how silica gets decomposed inside cells. In a research by Zhai et al., MSNPs were cocultured with the human umbilical vein endothelial cells (HUVECs); the biodegradation behavior of the MSNPs was then studied based on the TEM observation of ultra-sectioned

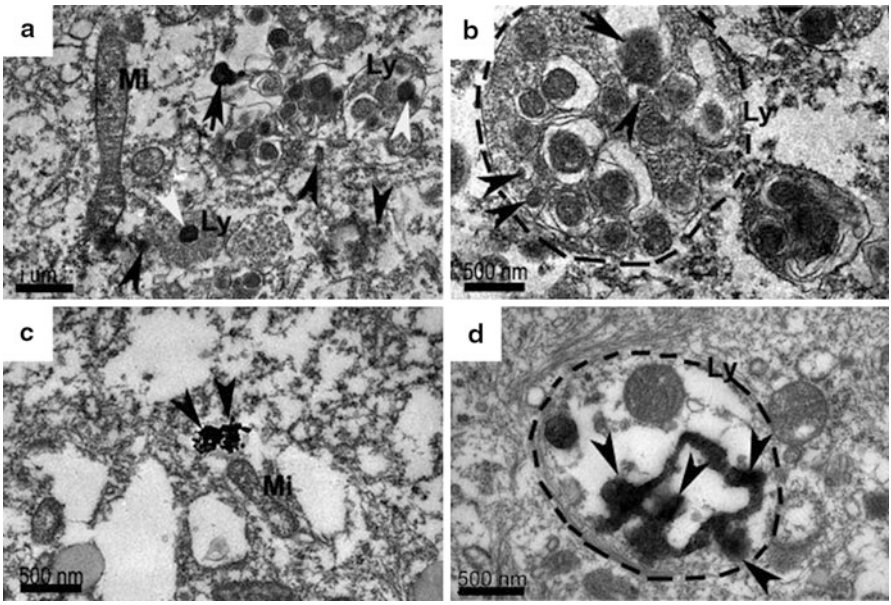


Fig. 1.12 TEM characterization of the degradation behavior of mesoporous silica nanoparticles (MSNPs) in human umbilical vein endothelial cells (HUVEC). (**a**, **b**) After 2 days of culture, some of the MSNPs inside and outside lysosomes showed significantly reduced size, indicating partial dissolution of silica inside cells. (**c**, **d**) After 4 days of culture, MSNPs in the cytoplasm have broken down into many smaller nanoparticles (**c**), while in the lysosome, the MSNPs have decomposed and fused to form some irregular-shaped structure (**d**). *Black arrow heads*: decomposed MSNPs; *black arrows*: nondegraded MSNPs; *white arrow heads*: MSNPs in lysosome. *Mi* mitochondrion, *Ly* lysosome (Adapted from Ref. [115])

MSNPs–cell composites (Fig. 1.12) [115]. The MSNPs were seen in the cytoplasm and lysosome of cells in both free and aggregated forms within the first 24 h of coculture. The nanoparticles remained spherical inside the cells 2 days after culture, but silica had been partially dissolved as evidenced by reduced contrast of the nanoparticles under the TEM. Significant decomposition was observed after 4 days of culture: the spherical MSNPs in the cytoplasm had broken down into many smaller nanoparticles and those in the lysosome had fused together to form an irregular ring structure.

In addition to the in vitro study, TEM has also been employed as a unique tool to investigate the in vivo biodegradation of iron oxide nanoparticles (IONPs) (Fig. 1.13) [116]. The TEM observation of spleen samples from 1 day post injection revealed that the IONPs were not ubiquitous inside the organs studied, including spleen, liver, and adipose tissue, but were only present densely in a few macrophage-type cells in each organ. Down to the subcellular level, it was discovered that the IONPs were actually located exclusively inside the lysosomes of the macrophages. Seven days after the retro-orbital injection, both intact IONPs and

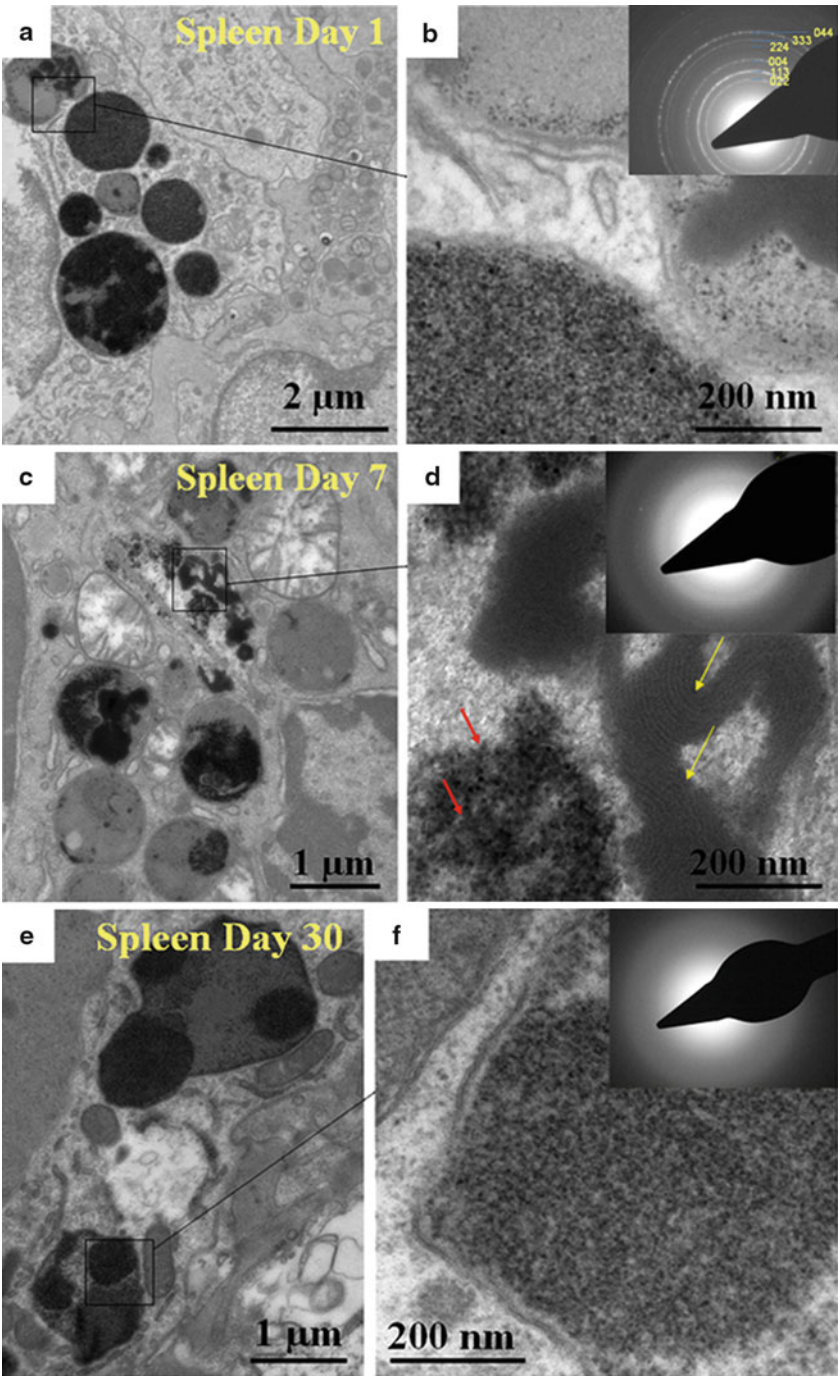


Fig. 1.13 (continued)

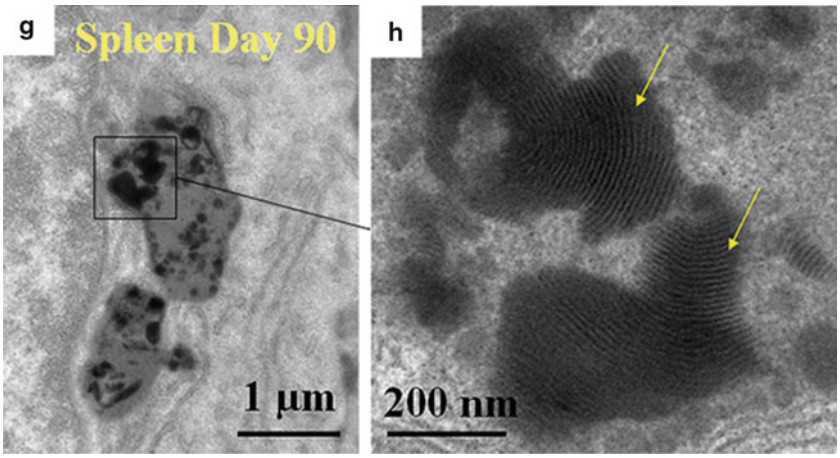


Fig. 1.13 Long-term transformation of iron oxide nanoparticles (IONPs) in the spleen of mice. The IONPs are located exclusively inside the lysosomes of the macrophages. Low- and high-magnification TEM images of IONPs in the spleen after 1 day (**a**, **b**), 7 days (**c**, **d**), 30 days (**e**, **f**), and 90 days (**g**, **h**). The electron diffraction patterns in the *insets* in **b**, **d**, and **f** suggest that the crystallized IONPs become completely amorphous after 30 days of in vivo biotransformation. No IONPs can be discerned after 90 days (**g**, **h**), but instead many fingerprint-like patterns are seen, indicating that the IONPs have been completely decomposed and the iron has been possibly stored in the ferritin/hemosiderin proteins (Adapted from Ref. [116])

fingerprint-like circular arrays, which are an indication of the presence of ferritin proteins, were seen in the lysosomes of the spleen macrophages by the TEM. The presence of ferritin proteins inside the lysosomes suggests that part of the IONPs had been decomposed and the iron derived from such decomposition could potentially be stored by the ferritin proteins. Although dense packing of the IONPs inside the lysosomes was still observable 30 days post injection, the individual nanoparticles could hardly be clearly discerned and more importantly the biodecomposition had caused a loss of crystallinity of the nanoparticles. The IONPs completely disappeared 90 days post injection, but instead, numerous fingerprint-like arrays appeared in the lysosomes, suggesting a thorough decomposition of IONPs. Based on the fact that, in the spleen, liver, and adipose tissue, there were always 5–7-nm iron-rich ferritin proteins associated with areas where IONPs had been highly degraded, the ongoing biotransformation of iron from IONPs to the ferritin proteins was further confirmed by the TEM.

5.3.2 Delivery of Nanoparticles Functionalized by Cell-Specific Motifs

Targeted delivery is one of the most important aspects of the nanoparticles-based drug delivery. In the in vitro study of the delivery of nanoparticles functionalized by cell-specific motifs, TEM has been applied to evaluate the effectiveness of the targeted delivery as well as to investigate changes of

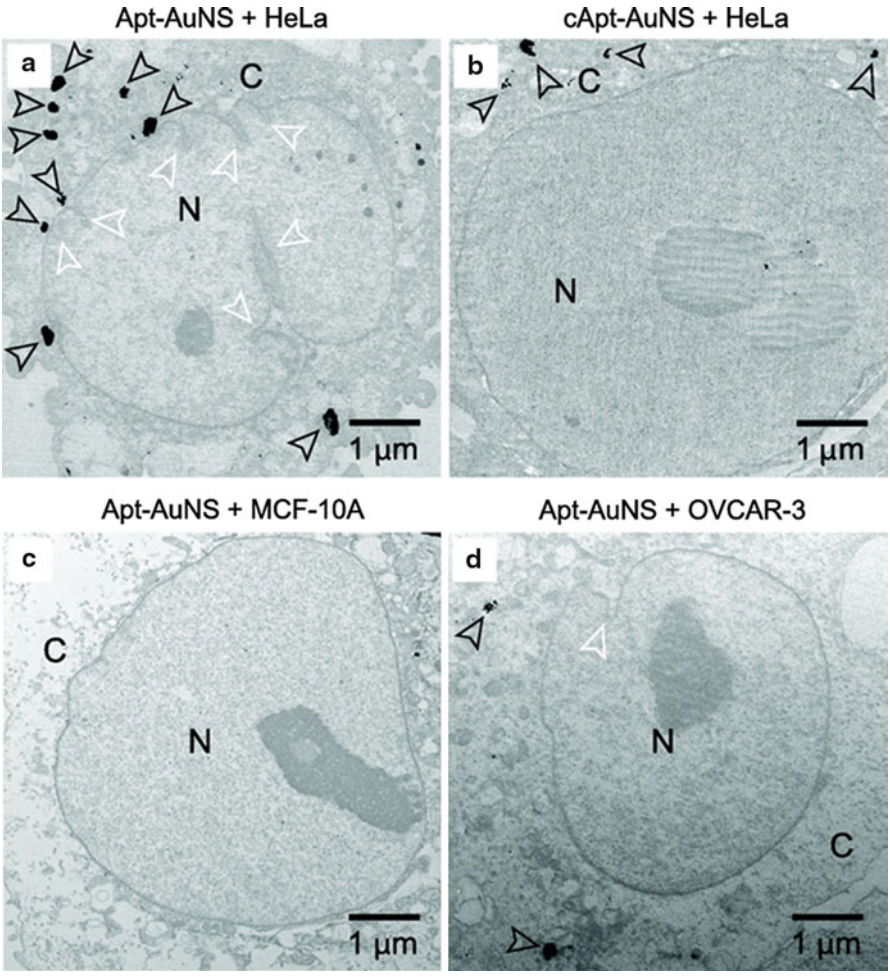


Fig. 1.14 TEM characterization of nuclear envelope (NE) invaginations as a result of the delivery of nucleus-targeting gold nanostars (AuNS) into the HeLa cervical cancer cells. (**a**) AS1411 aptamer–functionalized AuNS (Apt-AuNS) were successfully delivered to locations near the nucleus of HeLa cells, which caused a significant NE deformation. The HeLa cells express a high level of nucleolin, to which the AS1411 aptamer binds. (**b–d**) No significant NE deformation was observed in the delivery of (**b**) a control aptamer–functionalized AuNS (cApt-AuNS) into HeLa cells, (**c**) Apt-AuNS into nonspecific MCF-10A cells, and (**d**) Apt-AuNS into ovarian carcinoma cells (OVCAR-3), which have low surface expression of nucleolin (Adapted from Ref. [119])

cellular behaviors upon the delivery of nanoparticles to the desired cell organelles [117].

Trans-activating transcriptional activator (TAT) peptide is a cell penetration peptide that can facilitate translocation across the cell membranes. The cell

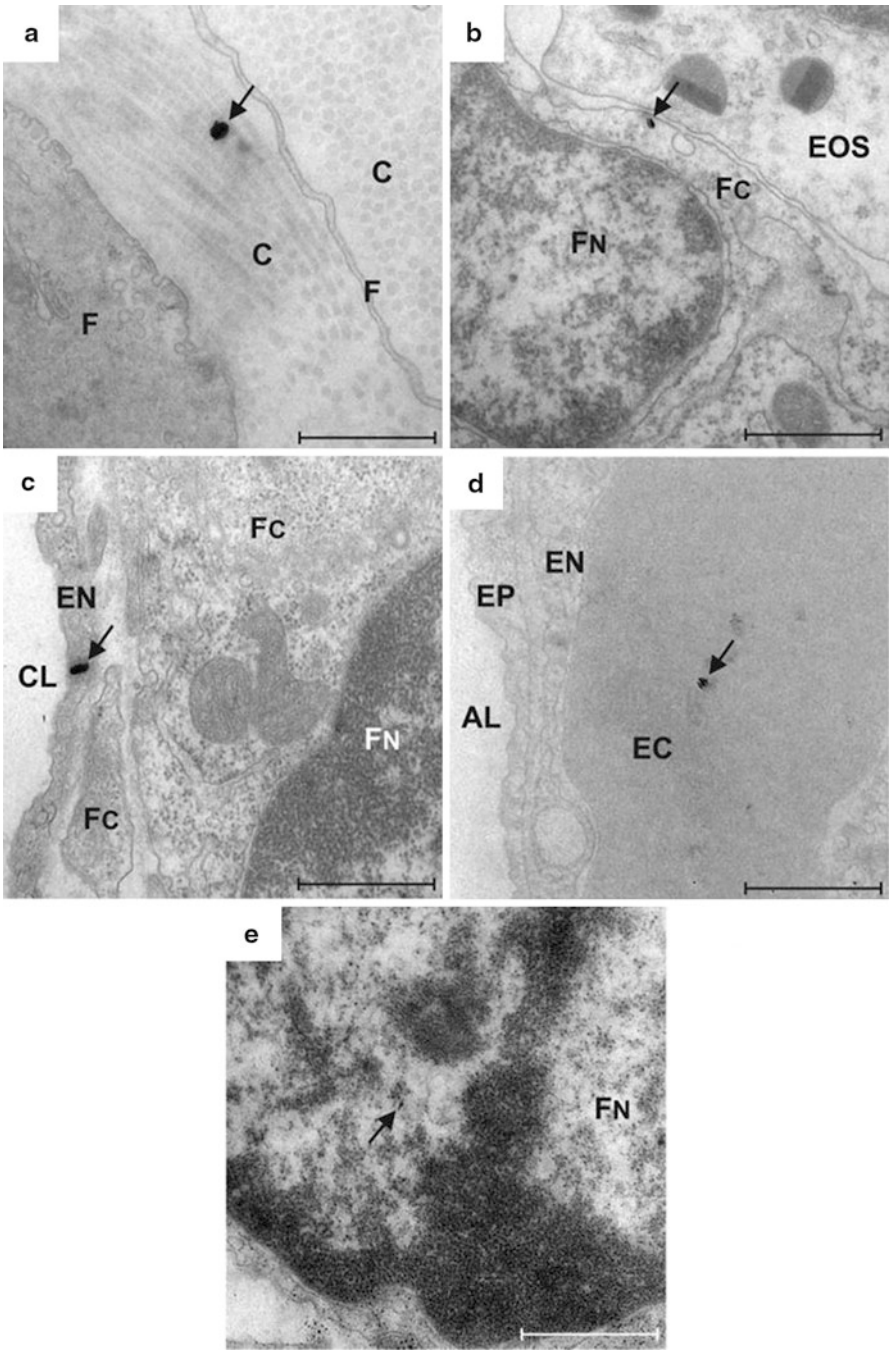


Fig. 1.15 Distribution of TiO_2 ultrafine particles (UFPs) in the lung parenchyma of experimental rats. TiO_2 UFPs were inhaled by rats in the form of aerosol. UFPs were found in several tissues of

internalization efficiency of TAT-functionalized gold nanostars (AuNS) was compared with that of the unmodified nanoparticles, namely, bare AuNS and polyethylene glycol (PEG)-coated AuNS, by examining the ultra-sectioned AuNS–cell composite samples with the TEM [118]. Numerous TAT-functionalized AuNS were found inside the cells, mainly in the vesicles and the cytoplasm, while in contrast, bare AuNS formed large aggregates in the vesicles and very few PEG-coated AuNS were seen in the sectioned cell samples under the experimental particle concentration. The results obtained from the TEM examination suggested that AuNS modified by TAT peptide can significantly increase their uptake by cells. Such enhanced cell uptake has enabled the AuNS to kill the disease-causing cells at a very low laser power density.

AS1411 is a single-stranded DNA aptamer, which is highly affinitive to nucleolin and can block several of its functions. For this reason, AS1411 has been used as a chemotherapeutic agent for cancer cells. Odom's et al. discovered that the AS1411 aptamer–functionalized gold nanostars (Apt-AuNS) can be trafficked to the perinuclear region of the HeLa cervical cancer cells [119]. TEM analysis on other control samples revealed that such targeted delivery of AuNS is a result of the functioning of AS1411 onto the nanoparticles. More importantly, with the assistance of high-resolution TEM, significant folding/deformation of the nuclear envelope (NE) was observed in more than 60 % of the HeLa cells upon introduction of the Apt-AuNS (Fig. 1.14). There were, on an average, 3 ± 0.5 folds formed on each nucleus. And the sites of foldings were strongly correlated with the location of Apt-AuNS: the foldings always appeared near to the nanoparticles. When the AS1411 aptamer was released from the AuNS by femtosecond near-infrared (NIR) pulse irradiation, TEM showed that both the percentage of cells containing NE folds and the number of folds in each cell were increased. Moreover, a viability analysis suggested death of a large population of the HeLa cells after release of the AS1411 aptamer, indicating the effectiveness of the Apt-AuNS both for nucleus-targeted delivery and as a chemotherapeutic agent for cancer treatment. In another work reported by Xu et al., TEM was also used to confirm the nucleus internalization of iron oxide nanoparticles functionalized by the KKKRKV nuclear localization signal peptide [120].

5.3.3 Internalization of Nanoparticles In Vivo and In Vitro

TEM has been the predominant characterization method in studying the pathways in the cellular uptake of nanoparticles. Because the nanoparticles used for biological research fall in the similar size range as that of the biomacromolecules, like

Fig. 1.15 (continued) the lung compartments, including (**a**) the connective tissue between collagen fibrils, (**b**) the fibroblast cytoplasm, (**c**) the cytoplasm of a capillary endothelial cell, (**d**) the erythrocyte in the capillary lumen, and (**e**) the fibroblast nucleus. In none of these TEM images, TiO_2 UFPs were membrane bound, indicating that they were internalized by nonphagocytic mechanisms. C, collagen fibril; F, fibroblast; FN, fibroblast nucleus; FC, fibroblast cytoplasm; EOS, eosinophil granulocyte; CL, capillary lumen; EN, capillary endothelial cell; EP, epithelium; AL, alveolar lumen; EC, erythrocyte. Scale bars: 500 nm (Adapted from Ref. [128])

proteins and virus, they can follow the same endocytic routes in terms of cell internalization. There are several endocytosis pathways, including phagocytosis, macropinocytosis, and clathrin-/caveolin-dependent/independent endocytosis [121]. In each internalization pathway, the size of endocytic vesicles and morphological changes of cells are different, and such differences can be easily identified by the TEM [122, 123]. In addition to the mechanism study, TEM has also been employed to study the effect of the size and shape of nanoparticles on cellular uptake [124].

Meng et al. investigated the internalization of rod-shaped mesoporous silica nanoparticles (MSNPs) of different aspect ratios into HeLa cancer cells [125]. They discovered that the MSNPs were internalized through the mechanism of macropinocytosis, as both filopodia and macropinocytotic vesicles were observed in the ultrastructure of the cell by TEM. Further investigation suggested that the average number of nanoparticles per cell, the number of filopodia, and the degree of cell membrane ruffling were strongly dependent on the aspect ratio of the MSNPs. They were all maximized with an MSNP aspect ratio of about 2.1–2.5, indicating that the macropinocytosis uptake mechanism is capable of distinguishing and preferentially endocytosing MSNPs of a specific aspect ratio. The size- and shape-dependent cellular uptake was also reported by other research groups on gold nanorods and particles prepared through the "particle replication in non-breaking templates" (PRINT) fabrication technique [126].

Cellular uptake through the macropinocytosis pathway was also discovered during the internalization of gadolinium-based silica nanoparticles (GBNs) [127]. The intermediate state during the formation of the macropinosome was successfully observed under the TEM. The macropinosome formation was initiated by the rising of lamellipodia at the site on the cell surface where nanoparticles were settled. The lamellipodia would then gradually bend and, eventually, form a circular protrusion, to include the nanoparticles inside. Finally, the protrusion was transformed into the macropinosome by fusing with the plasma membrane and penetrating into the cytoplasm.

Geiser et al. reported a non-endocytic pathway in investigating the in vivo distribution of TiO_2 ultrafine particles (UFPs) in lungs [128]. The experimental rats were exposed to the TiO_2 UFPs aerosol for a certain amount of time, and the intrapulmonary distribution of inhaled UFPs was studied by the TEM. The electron microscope analysis showed that the UFPs were present in every tissue compartment of the lung, including epithelial and endothelial cells, fibroblasts, connective tissues, blood capillaries, and red blood cells (Fig. 1.15). On the subcellular level, it was discovered that these particles were not membrane bound. Similar results were obtained in the in vitro study when UFPs were exposed to pulmonary macrophages and red blood cells. As it is true that when nanoparticles are internalized through the endocytic pathway into the cytoplasm, they are always surrounded by a membrane, the UFPs were not following this pathway. The authors suggested that the UFP uptake into cells might be through diffusion or adhesive interactions.

6 Concluding Remarks and Future Perspective

TEM has been demonstrated to be a powerful instrument in the characterization of bio-inorganic nanocomposites. It has a number of imaging modes that allow investigation to be conducted from various aspects. As revealed by many examples described in this chapter, TEM is indispensable in the examination of three major types of bio-inorganic nanocomposites, that is, naturally occurring composites, inorganic nanomaterials fabricated on biotemplates, and inorganic nanoparticles introduced into cells and tissues for biological research. Recently, in situ TEM, which refers to carrying out a sample treatment or a chemical process inside the TEM, has attracted intensive research interest to study the real-time structural evolution of materials in various processes. For example, the lithiation process of nanowires-based lithium-ion batteries' anode materials, like SnO_2, has been examined by the in situ TEM [129]. In this examination, a nano-cell was configured, on a specially designed sample stage, by employing a single SnO_2 nanowire as the anode, a drop of electrolyte, and a small piece of $LiCoO_2$ as the cathode. Once the SnO_2 nanowire was in contact with the electrolyte to start the discharge process, the morphology, structure, and phase transition of the lithiated nanowire could be observed in real time. Currently, the in situ TEM is rarely considered to study the kinetic process of the formation of bio-inorganic nanocomposites. However, along with the recent advance in technology, there are now liquid sample stages that even allow in situ TEM imaging of living organisms and biological reactions [130]. The same imaging technique could be readily applied to study the interaction between biological and inorganic materials, that is, the in vitro investigation of apatite mineralization onto collagen fibrils and the nucleation and growth of inorganic nanomaterials onto biological templates.

Acknowledgments We would like to acknowledge the financial support from the National Science Foundation (DMR-0847758, CBET-0854414, CBET-0854465, and CMMI-1234957), National Institutes of Health (5R01HL092526-02, 5R01DE01563309, 1R21EB015190-01A1, 4R03AR056848-03), Department of Defense's Peer Reviewed Medical Research Program (W81XWH-12-1-0384), Oklahoma Center for the Advancement of Science and Technology (HR11-006), and Oklahoma Center for Adult Stem Cell Research (434003).

References

1. Sigel A, Sigel H, Sigel RKO (eds) (2008) Biomineralization: from nature to application. Wiley, Chichester
2. Bonucci E (1992) Calcification in biological systems. CRC Press, Boca Raton
3. Cuif JP, Dauphin Y, Sorauf JE (eds) (2010) Biominerals and fossils through time. Cambridge University Press, Cambridge
4. Driessens FCM, Verbeeck RK (1990) Biominerals. CRC Press, Boca Raton
5. Weiner S, Wagner HD (1998) The material bone: structure mechanical function relations. Annu Rev Mater Sci 28:271–298
6. Cressey BA, Cressey G (2003) A model for the composite nanostructure of bone suggested by high-resolution transmission electron microscopy. Mineral Mag 67(6):1171–1182
7. McNally EA, Schwarcz HP, Botton GA, Arsenault AL (2012) A model for the ultrastructure of bone based on electron microscopy of Ion-milled sections. PLoS One 7(1)

8. Deshpande AS, Fang PA, Simmer JP, Margolis HC, Beniash E (2010) Amelogenin-collagen interactions regulate calcium phosphate mineralization in vitro. J Biol Chem 285(25): 19277–19287
9. Nudelman F, Pieterse K, George A, Bomans PHH, Friedrich H, Brylka LJ et al (2010) The role of collagen in bone apatite formation in the presence of hydroxyapatite nucleation inhibitors. Nat Mater 9(12):1004–1009
10. Wang Y, Azais T, Robin M, Vallee A, Catania C, Legriel P et al (2012) The predominant role of collagen in the nucleation, growth, structure and orientation of bone apatite. Nat Mater 11(8):724–733
11. George A, Veis A (2008) Phosphorylated proteins and control over apatite nucleation, crystal growth, and inhibition. Chem Rev 108(11):4670–4693
12. Rubin MA, Jasiuk I, Taylor J, Rubin J, Ganey T, Apkarian RP (2003) TEM analysis of the nanostructure of normal and osteoporotic human trabecular bone. Bone 33(3): 270–282
13. Suvorova EI, Petrenko PP, Buffat PA (2007) Scanning and transmission electron microscopy for evaluation of order/disorder in bone structure. Scanning 29(4):162–170
14. Wang XM, Cui FZ, Ge J, Wang Y (2004) Hierarchical structural comparisons of bones from wild-type and liliput(dtc232) gene-mutated zebrafish. J Struct Biol 145(3): 236–245
15. Ikoma T, Kobayashi H, Tanaka J, Walsh D, Mann S (2003) Microstructure, mechanical, and biomimetic properties of fish scales from pagrus major. J Struct Biol 142(3): 327–333
16. Okuda M, Ogawa N, Takeguchi M, Hashimoto A, Tagaya M, Chen S et al (2011) Minerals and aligned collagen fibrils in tilapia fish scales: structural analysis using dark-field and energy-filtered transmission electron microscopy and electron tomography. Microsc Microanal 17(5):788–798
17. Okuda M, Takeguchi M, Tagaya M, Tonegawa T, Hashimoto A, Hanagata N et al (2009) Elemental distribution analysis of type I collagen fibrils in tilapia fish scale with energy-filtered transmission electron microscope. Micron 40(5–6):665–668
18. Sun JY, Bhushan B (2012) Hierarchical structure and mechanical properties of nacre: a review. RSC Adv 2(20):7617–7632
19. Zhang XA, Wu WJ, Wang JF (2007) Dynamic analysis of preferential orientation of aragonite crystals in nacre from mollusk shell. Chin Sci Bull 52(24):3452–3456
20. Nassif N, Pinna N, Gehrke N, Antonietti M, Jager C, Colfen H (2005) Amorphous layer around aragonite platelets in nacre. Proc Natl Acad Sci USA 102(36):12653–12655
21. Wang RZ, Gupta HS (2011) Deformation and fracture mechanisms of bone and nacre. Ann Rev Mater Res 41:41–73
22. Huang ZW, Li HZ, Pan ZL, Wei QM, Chao YJ, Li XD (2011) Uncovering high-strain rate protection mechanism in nacre. Sci Rep 1
23. Song F, Zhang XH, Bai YL (2002) Microstructure and characteristics in the organic matrix layers of nacre. J Mater Res 17(7):1567–1570
24. Song F, Soh AK, Bai YL (2003) Structural and mechanical properties of the organic matrix layers of nacre. Biomaterials 24(20):3623–3631
25. Rousseau M, Lopez E, Stempfle P, Brendle M, Franke L, Guette A et al (2005) Multiscale structure of sheet nacre. Biomaterials 26(31):6254–6262
26. Su X, Kamat S, Heuer AH (2000) The structure of sea urchin spines, large biogenic single crystals of calcite. J Mater Sci 35(22):5545–5551
27. Moureaux C, Perez-Huerta A, Compere P, Zhu W, Leloup T, Cusack M et al (2010) Structure, composition and mechanical relations to function in sea urchin spine. J Struct Biol 170(1):41–49
28. Magdans U, Gies H (2004) Single crystal structure analysis of sea urchin spine calcites: systematic investigations of the Ca/Mg distribution as a function of habitat of the sea urchin and the sample location in the spine. Eur J Mineral 16(2):261–268

29. Seto J, Ma YR, Davis SA, Meldrum F, Gourrier A, Kim YY et al (2012) Structure–property relationships of a biological mesocrystal in the adult sea urchin spine. Proc Natl Acad Sci USA 109(10):3699–3704
30. Robach JS, Stock SR, Veis A (2005) Transmission electron microscopy characterization of macromolecular domain cavities and microstructure of single-crystal calcite tooth plates of the sea urchin *Lytechinus variegatus*. J Struct Biol 151(1):18–29
31. Asada R, Tazaki K (2001) Silica biomineralization of unicellular microbes under strongly acidic conditions. Can Mineral 39:1–16
32. Foissner W, Weissenbacher B, Krautgartner WD, Lutz-Meindl U (2009) A cover of glass: first report of biomineralized silicon in a ciliate, *Maryna umbrellata* (Ciliophora: Colpodea). J Eukaryot Microbiol 56(6):519–530
33. Foissner W (2009) The stunning, glass-covered resting cyst of *Maryna umbrellata* (Ciliophora, Colpodea). Acta Protozool 48(3):223–243
34. Lins U, Barros CF, da Cunha M, Miguens FC (2002) Structure, morphology, and composition of silicon biocomposites in the palm tree *Syagrus coronata* (Mart.) Becc. Protoplasma 220(1–2):89–96
35. Stonik IV, Orlova TY, Lundholm N (2011) Diversity of pseudo-nitzschia *H. Peragallo* from the western North Pacific. Diatom Res 26(1–2):121–134
36. Vrieling EG, Sun QY, Tian M, Kooyman PJ, Gieskes WWC, van Santen RA et al (2007) Salinity-dependent diatom biosilicification implies an important role of external ionic strength. Proc Natl Acad Sci USA 104(25):10441–10446
37. Stillman TJ, Upadhyay M, Norte VA, Sedelnikova SE, Carradus M, Tzokov S et al (2005) The crystal structures of *Lactococcus lactis* MG1363 Dps proteins reveal the presence of an N-terminal helix that is required for DNA binding. Mol Microbiol 57(4):1101–1112
38. Speir JA, Munshi S, Wang G, Baker TS, Johnson JE (1995) Structures of the native and swollen forms of cowpea chlorotic mottle virus determined by X-ray crystallography and cryo-electron microscopy. Structure 3(1):63–78
39. Iwahori K, Yoshizawa K, Muraoka M, Yamashita I (2005) Fabrication of ZnSe nanoparticles in the apoferritin cavity by designing a slow chemical reaction system. Inorg Chem 44(18):6393–6400
40. Hennequin B, Turyanska L, Ben T, Beltran AM, Molina SI, Li M et al (2008) Aqueous near-infrared fluorescent composites based on apoferritin-encapsulated PbS quantum dots. Adv Mater 20(19):3592–+
41. Kim H, Pippel E, Gosele U, Knez M (2009) Titania nanostructures fabricated by atomic layer deposition using spherical protein cages. Langmuir 25(23):13284–13289
42. Xia YN, Yang PD, Sun YG, Wu YY, Mayers B, Gates B et al (2003) One-dimensional nanostructures: synthesis, characterization, and applications. Adv Mater 15(5):353–389
43. Meegan JE, Aggeli A, Boden N, Brydson R, Brown AP, Carrick L et al (2004) Designed self-assembled beta-sheet peptide fibrils as templates for silica nanotubes. Adv Funct Mater 14(1):31–37
44. Ono Y, Kanekiyo Y, Inoue K, Hojo J, Nango M, Shinkai S (1999) Preparation of novel hollow fiber silica using collagen fibers as a template. Chem Lett 6:475–476
45. Behrens S, Wu J, Habicht W, Unger E (2004) Silver nanoparticle and nanowire formation by microtubule templates. Chem Mater 16(16):3085–3090
46. Perham RN, Wilson TM (1978) The characterization of intermediates formed during the disassembly of tobacco mosaic virus at alkaline pH. Virology 84(2):293–302
47. Niu Z, Liu J, Lee LA, Bruckman MA, Zhao D, Koley G et al (2007) Biological templated synthesis of water-soluble conductive polymeric nanowires. Nano Lett 7(12):3729–3733
48. Shenton W, Douglas T, Young M, Stubbs G, Mann S (1999) Inorganic–organic nanotube composites from template mineralization of tobacco mosaic virus. Adv Mater 11(3):253–+
49. Dujardin E, Peet C, Stubbs G, Culver JN, Mann S (2003) Organization of metallic nanoparticles using tobacco mosaic virus templates. Nano Lett 3(3):413–417

50. Knez M, Sumser M, Bittner AM, Wege C, Jeske H, Martin TP et al (2004) Spatially selective nucleation of metal clusters on the tobacco mosaic virus. Adv Funct Mater 14(2):116–124
51. Rong JH, Niu ZW, Lee LA, Wang Q (2011) Self-assembly of viral particles. Curr Opin Colloid Interface Sci 16(6):441–450
52. Niu Z, Bruckman M, Kotakadi VS, He J, Emrick T, Russell TP et al (2006) Study and characterization of tobacco mosaic virus head-to-tail assembly assisted by aniline polymerization. Chem Commun 28:3019–3021
53. Royston E, Ghosh A, Kofinas P, Harris MT, Culver JN (2008) Self-assembly of virus-structured high surface area nanomaterials and their application as battery electrodes. Langmuir 24(3):906–912
54. Chen XL, Gerasopoulos K, Guo JC, Brown A, Wang CS, Ghodssi R et al (2010) Virus-enabled silicon anode for lithium-ion batteries. ACS Nano 4(9):5366–5372
55. Gerasopoulos K, McCarthy M, Banerjee P, Fan X, Culver JN, Ghodssi R (2010) Biofabrication methods for the patterned assembly and synthesis of viral nanotemplates. Nanotechnology 21(5)
56. Chen XL, Gerasopoulos K, Guo JC, Brown A, Wang CS, Ghodssi R et al (2011) A patterned 3D silicon anode fabricated by electrodeposition on a virus-structured current collector. Adv Funct Mater 21(2):380–387
57. Knez M, Bittner AM, Boes F, Wege C, Jeske H, Maiss E et al (2003) Biotemplate synthesis of 3-nm nickel and cobalt nanowires. Nano Lett 3(8):1079–1082
58. Tsukamoto R, Muraoka M, Seki M, Tabata H, Yamashita I (2007) Synthesis of CoPt and FePt3 nanowires using the central channel of tobacco mosaic virus as a biotemplate. Chem Mater 19(10):2389–2391
59. Huang WZ, Petrosino J, Palzkill T (1998) Display of functional beta-lactamase inhibitory protein on the surface of M13 bacteriophage. Antimicrob Agents Chemother 42(11):2893–2897
60. Lee SK, Yun DS, Belcher AM (2006) Cobalt ion mediated self-assembly of genetically engineered bacteriophage for biomimetic Co-Pt hybrid material. Biomacromolecules 7(1):14–17
61. Nam KT, Wartena R, Yoo PJ, Liau FW, Lee YJ, Chiang YM et al (2008) Stamped microbattery electrodes based on self-assembled M13 viruses. Proc Natl Acad Sci USA 105(45):17227–17231
62. Hufton SE, Moerkerk PT, Meulemans EV, de Bruine A, Arends JW, Hoogenboom HR (1999) Phage display of cDNA repertoires: the pVI display system and its applications for the selection of immunogenic ligands. J Immunol Methods 231(1–2):39–51
63. Gao CS, Mao SL, Kaufmann G, Wirsching P, Lerner RA, Janda KD (2002) A method for the generation of combinatorial antibody libraries using pIX phage display. Proc Natl Acad Sci USA 99(20):12612–12616
64. Lee YJ, Yi H, Kim WJ, Kang K, Yun DS, Strano MS et al (2009) Fabricating genetically engineered high-power lithium-ion batteries using multiple virus genes. Science 324(5930):1051–1055
65. Chen LM, Zurita AJ, Ardelt PU, Giordano RJ, Arap W, Pasqualini R (2004) Design and validation of a bifunctional ligand display system for receptor targeting. Chem Biol 11(8):1081–1091
66. Lee YJ, Lee Y, Oh D, Chen T, Ceder G, Belcher AM (2010) Biologically activated noble metal alloys at the nanoscale: for lithium ion battery anodes. Nano Lett 10(7):2433–2440
67. Nam KT, Peelle BR, Lee SW, Belcher AM (2004) Genetically driven assembly of nanorings based on the M13 virus. Nano Lett 4(1):23–27
68. Naik RR, Stringer SJ, Agarwal G, Jones SE, Stone MO (2002) Biomimetic synthesis and patterning of silver nanoparticles. Nat Mater 1(3):169–172
69. Umetsu M, Mizuta M, Tsumoto K, Ohara S, Takami S, Watanabe H et al (2005) Bioassisted room-temperature immobilization and mineralization of zinc oxide – the structural ordering of ZnO nanoparticles into a flower-type morphology. Adv Mater 17(21):2571–+

70. Whaley SR, English DS, Hu EL, Barbara PF, Belcher AM (2000) Selection of peptides with semiconductor binding specificity for directed nanocrystal assembly. Nature 405(6787): 665–668
71. Mao CB, Solis DJ, Reiss BD, Kottmann ST, Sweeney RY, Hayhurst A et al (2004) Virus-based toolkit for the directed synthesis of magnetic and semiconducting nanowires. Science 303(5655):213–217
72. Nam YS, Magyar AP, Lee D, Kim JW, Yun DS, Park H et al (2010) Biologically templated photocatalytic nanostructures for sustained light-driven water oxidation. Nat Nanotechnol 5(5):340–344
73. Nam KT, Kim DW, Yoo PJ, Chiang CY, Meethong N, Hammond PT et al (2006) Virus-enabled synthesis and assembly of nanowires for lithium ion battery electrodes. Science 312(5775):885–888
74. Mao CB, Liu AH, Cao BR (2009) Virus-based chemical and biological sensing. Angew Chem Int Ed 48(37):6790–6810
75. Niu ZW, Bruckman MA, Harp B, Mello CM, Wang Q (2008) Bacteriophage M13 as a scaffold for preparing conductive polymeric composite fibers. Nano Res 1(3): 235–241
76. Neltner B, Peddie B, Xu A, Doenlen W, Durand K, Yun DS et al (2010) Production of hydrogen using nanocrystalline protein-templated catalysts on M13 phage. ACS Nano 4(6):3227–3235
77. Westerlund-Wikstrom B, Tanskanen J, Virkola R, Hacker J, Lindberg M, Skurnik M et al (1997) Functional expression of adhesive peptides as fusions to *Escherichia coli* flagellin. Protein Eng 10(11):1319–1326
78. Iannolo G, Minenkova O, Petruzzelli R, Cesareni G (1995) Modifying filamentous phage capsid – limits in the size of the major capsid protein. J Mol Biol 248(4):835–844
79. Malik P, Tarry TD, Gowda LR, Langara A, Petukhov SA, Symmons MF et al (1996) Role of capsid structure and membrane protein processing in determining the size and copy number of peptides displayed on the major coat protein of filamentous bacteriophage. J Mol Biol 260(1):9–21
80. Petrenko VA, Smith GP, Gong X, Quinn T (1996) A library of organic landscapes on filamentous phage. Protein Eng 9(9):797–801
81. Kumara MT, Tripp BC, Muralidharan S (2007) Exciton energy transfer in self-assembled quantum dots on bioengineered bacterial flagella nanotubes. J Phys Chem C 111(14): 5276–5280
82. Kumara MT, Tripp BC, Muralidharan S (2007) Self-assembly of metal nanoparticles and nanotubes on bioengineered flagella scaffolds. Chem Mater 19(8):2056–2064
83. Asakura S (1970) Polymerization of flagellin and polymorphism of flagella. Adv Biophys 1:99–155
84. Li D, Qu XW, Newton SMC, Klebba PE, Mao CB (2012) Morphology-controlled synthesis of silica nanotubes through pH- and sequence-responsive morphological change of bacterial flagellar biotemplates. J Mater Chem 22(31):15702–15709
85. Yamashita I (2001) Fabrication of a two-dimensional array of nano-particles using ferritin molecule. Thin Solid Films 393(1–2):12–18
86. McMillan RA, Paavola CD, Howard J, Chan SL, Zaluzec NJ, Trent JD (2002) Ordered nanoparticle arrays formed on engineered chaperonin protein templates. Nat Mater 1(4): 247–252
87. Sun J, DuFort C, Daniel MC, Murali A, Chen C, Gopinath K et al (2007) Core-controlled polymorphism in virus-like particles. Proc Natl Acad Sci USA 104(4):1354–1359
88. Cao BR, Xu H, Mao CB (2011) Controlled self-assembly of rodlike bacterial pili particles into ordered lattices. Angew Chem Int Ed 50(28):6264–6268
89. Coffer JL, Bigham SR, Li X, Pinizzotto RF, Rho YG, Pirtle RM et al (1996) Dictation of the shape of mesoscale semiconductor nanoparticle assemblies by plasmid DNA. Appl Phys Lett 69(25):3851–3853

90. Dittmer WU, Simmel FC (2004) Chains of semiconductor nanoparticles templated on DNA. Appl Phys Lett 85(4):633–635
91. Nyamjav D, Ivanisevic A (2005) Templates for DNA-templated Fe_3O_4 nanoparticles. Biomaterials 26(15):2749–2757
92. Gu Q, Cheng CD, Haynie DT (2005) Cobalt metallization of DNA: toward magnetic nanowires. Nanotechnology 16(8):1358–1363
93. Becerril HA, Ludtke P, Willardson BM, Woolley AT (2006) DNA-templated nickel nanostructures and protein assemblies. Langmuir 22(24):10140–10144
94. Monson CF, Woolley AT (2003) DNA-templated construction of copper nanowires. Nano Lett 3(3):359–363
95. Ongaro A, Griffin F, Beeeher P, Nagle L, Iacopino D, Quinn A et al (2005) DNA-templated assembly of conducting gold nanowires between gold electrodes on a silicon oxide substrate. Chem Mater 17(8):1959–1964
96. Park SH, Prior MW, LaBean TH, Finkelstein G (2006) Optimized fabrication and electrical analysis of silver nanowires templated on DNA molecules. Appl Phys Lett 89(3)
97. Lund J, Dong JC, Deng ZX, Mao CD, Parviz BA (2006) Electrical conduction in 7 nm wires constructed on lambda-DNA. Nanotechnology 17(11):2752–2757
98. Braun E, Eichen Y, Sivan U, Ben-Yoseph G (1998) DNA-templated assembly and electrode attachment of a conducting silver wire. Nature 391(6669):775–778
99. Park SH, Barish R, Li HY, Reif JH, Finkelstein G, Yan H et al (2005) Three-helix bundle DNA tiles self-assemble into 2D lattice or 1D templates for silver nanowires. Nano Lett 5(4):693–696
100. Liu D, Park SH, Reif JH, LaBean TH (2004) DNA nanotubes self-assembled from triple-crossover tiles as templates for conductive nanowires. Proc Natl Acad Sci USA 101(3):717–722
101. Rothemund PWK (2006) Folding DNA, to create nanoscale shapes and patterns. Nature 440(7082):297–302
102. Zhang JP, Liu Y, Ke YG, Yan H (2006) Periodic square-like gold nanoparticle arrays templated by self-assembled 2D DNA nanogrids on a surface. Nano Lett 6(2):248–251
103. Goodman RP, Schaap IAT, Tardin CF, Erben CM, Berry RM, Schmidt CF et al (2005) Rapid chiral assembly of rigid DNA building blocks for molecular nanofabrication. Science 310(5754):1661–1665
104. Han DR, Pal S, Nangreave J, Deng ZT, Liu Y, Yan H (2011) DNA origami with complex curvatures in three-dimensional space. Science 332(6027):342–346
105. Winfree E, Liu F, Wenzler LA, Seeman NC (1998) Design and self-assembly of two-dimensional DNA crystals. Nature 394(6693):539–544
106. Li HY, Carter JD, LaBean TH (2009) Nanofabrication by DNA self-assembly. Mater Today 12(5):24–32
107. Kuzuya A, Komiyama M (2010) DNA origami: fold, stick, and beyond. Nanoscale 2(3):310–322
108. Samano EC, Pilo-Pais M, Goldberg S, Vogen BN, Finkelstein G, LaBean TH (2011) Self-assembling DNA templates for programmed artificial biomineralization. Soft Matter 7(7):3240–3245
109. Sharma J, Chhabra R, Cheng A, Brownell J, Liu Y, Yan H (2009) Control of self-assembly of DNA tubules through integration of gold nanoparticles. Science 323(5910):112–116
110. Ding BQ, Deng ZT, Yan H, Cabrini S, Zuckermann RN, Bokor J (2010) Gold nanoparticle self-similar chain structure organized by DNA origami. J Am Chem Soc 132(10):3248–+
111. Pal S, Deng ZT, Ding BQ, Yan H, Liu Y (2010) DNA-origami-directed self-assembly of discrete silver-nanoparticle architectures. Angew Chem Int Ed 49(15):2700–2704
112. Zhao Z, Jacovetty EL, Liu Y, Yan H (2011) Encapsulation of gold nanoparticles in a DNA origami cage. Angew Chem Int Ed 50(9):2041–2044
113. AshaRani PV, Mun GLK, Hande MP, Valiyaveettil S (2009) Cytotoxicity and genotoxicity of silver nanoparticles in human cells. ACS Nano 3(2):279–290

114. Zhang XD, Wu D, Shen X, Liu PX, Yang N, Zhao B et al (2011) Size-dependent in vivo toxicity of PEG-coated gold nanoparticles. Int J Nanomedicine 6:2071–2081
115. Zhai WY, He CL, Wu L, Zhou Y, Chen HR, Chang J et al (2012) Degradation of hollow mesoporous silica nanoparticles in human umbilical vein endothelial cells. J Biomed Mater Res B Appl Biomater 100B(5):1397–1403
116. Levy M, Luciani N, Alloyeau D, Elgrabli D, Deveaux V, Pechoux C et al (2011) Long term in vivo biotransformation of iron oxide nanoparticles. Biomaterials 32(16):3988–3999
117. Conde J, Ambrosone A, Sanz V, Hernandez Y, Marchesano V, Tian FR et al (2012) Design of multifunctional gold nanoparticles for in vitro and in vivo gene silencing. ACS Nano 6(9):8316–8324
118. Yuan H, Fales AM, Vo-Dinh T (2012) TAT peptide-functionalized gold nanostars: enhanced intracellular delivery and efficient NIR photothermal therapy using ultralow irradiance. J Am Chem Soc 134(28):11358–11361
119. Dam DHM, Lee JH, Sisco PN, Co DT, Zhang M, Wasielewski MR et al (2012) Direct observation of nanoparticle-cancer cell nucleus interactions. ACS Nano 6(4):3318–3326
120. Xu CJ, Xie J, Kohler N, Walsh EG, Chin YE, Sun SH (2008) Monodisperse magnetite nanoparticles coupled with nuclear localization signal peptide for cell-nucleus targeting. Chem Asian J 3(3):548–552
121. Doherty GJ, McMahon HT (2009) Mechanisms of endocytosis. Annu Rev Biochem 78:857–902
122. Schlachter EK, Widmer HR, Bregy A, Lonnfors-Weitzel T, Vajtai I, Corazza N et al (2011) Metabolic pathway and distribution of superparamagnetic iron oxide nanoparticles: in vivo study. Int J Nanomedicine 6:1793–1800
123. Garcia-Aonso J, Khan FR, Misra SK, Turmaine M, Smith BD, Rainbow PS et al (2011) Cellular internalization of silver nanoparticles in gut epithelia of the estuarine polychaete nereis diversicolor. Environ Sci Technol 45(10):4630–4636
124. Chithrani BD, Ghazani AA, Chan WCW (2006) Determining the size and shape dependence of gold nanoparticle uptake into mammalian cells. Nano Lett 6(4):662–668
125. Meng H, Yang S, Li ZX, Xia T, Chen J, Ji ZX et al (2011) Aspect ratio determines the quantity of mesoporous silica nanoparticle uptake by a small GTPase-dependent macropinocytosis mechanism. ACS Nano 5(6):4434–4447
126. Gratton SEA, Ropp PA, Pohlhaus PD, Luft JC, Madden VJ, Napier ME et al (2008) The effect of particle design on cellular internalization pathways. Proc Natl Acad Sci USA 105(33):11613–11618
127. Rima W, Sancey L, Aloy MT, Armandy E, Alcantara GB, Epicier T et al (2013) Internalization pathways into cancer cells of gadolinium-based radiosensitizing nanoparticles. Biomaterials 34(1):181–195
128. Geiser M, Rothen-Rutishauser B, Kapp N, Schurch S, Kreyling W, Schulz H et al (2005) Ultrafine particles cross cellular membranes by nonphagocytic mechanisms in lungs and in cultured cells. Environ Health Perspect 113(11):1555–1560
129. Huang JY, Zhong L, Wang CM, Sullivan JP, Xu W, Zhang LQ et al (2010) In situ observation of the electrochemical lithiation of a single SnO(2) nanowire electrode. Science 330(6010):1515–1520
130. Evans JE, Jungjohann KL, Wong PC, Chiu PL, Dutrow GH, Arslan I et al (2012) Visualizing macromolecular complexes with in situ liquid scanning transmission electron microscopy. Micron 43(11):1085–1090

Electron Microscopy of Thin Film Inorganic and Organic Photovoltaic Materials

2

Aidan A. Taylor and Budhika G. Mendis

Contents

1 Definition of the Topic 43
2 Overview 44
3 Background 44
3.1 The Case for Thin-Film Photovoltaics 44
3.2 Operating Principles 45
3.3 Inorganic Solar Cells 48
3.4 Organic Bulk Heterojunction Solar Cells 50
4 Materials Issues in Inorganic Solar Cells 52
4.1 CdTe 52
4.2 CIGS 56
4.3 CZTS 63
5 Measuring the Electrical Activity of Grain Boundaries 66
5.1 Background 66
5.2 Recombination Velocity Measurement 72
5.3 Barrier Height Measurement 75
6 Materials Issues in Organic Solar Cells 78
References 81

1 Definition of the Topic

Scanning and transmission electron microscopy have played an important role in the progress made by photovoltaic devices over the past two decades. With thin-film photovoltaic (PV) devices now accounting for more than 20 % of total PV sales, this chapter reviews the important insights into PV materials gleaned from electron microscopy.

A.A. Taylor • B.G. Mendis (✉)
Physics Department, Durham University, Durham, UK
e-mail: b.g.mendis@durham.ac.uk

C.S.S.R. Kumar (ed.), *Transmission Electron Microscopy Characterization of Nanomaterials*, DOI 10.1007/978-3-642-38934-4_2,
© Springer-Verlag Berlin Heidelberg 2014

2 Overview

Thin-film photovoltaic devices based on direct band gap semiconducting materials and photoactive organic materials offer a low-cost, high-volume, and renewable source of energy. Unfortunately, both of these prospects have yet to realize their potential and continue to lag some way behind conventional Si-based PV.

Electron microscopy is routinely used to characterize thin-film structures with regard to their thicknesses, homogeneities, and morphologies but possesses capabilities far in excess of this. The use of chemical analysis techniques such as energy dispersive X-ray analysis (EDS) and electron energy loss spectroscopy (EELS) enables nanometer-level composition evaluation, an important capability when investigating multilayer stacks. Cathodoluminescence (CL) and electron-beam-induced current (EBIC) techniques give insight into the electronic properties of materials, while electron-beam backscatter diffraction (EBSD) allows a more fundamental understanding of film crystallography and growth processes. The careful application of these more advanced electron microscopy methods opens an avenue to the superior understanding of structure–property relationships.

In this chapter a brief overview of the development of both inorganic and organic PV materials is given, and the most important findings of electron microscopy in relation to PV materials are reviewed. Additionally, several of the more advanced techniques for the quantitative evaluation of semiconductor electrical properties are described in more detail.

3 Background

3.1 The Case for Thin-Film Photovoltaics

If photovoltaic energy generation is to deliver a significant proportion (greater than 10 %) of the world's electricity needs, then the cost must be reduced significantly. The dominant photovoltaic (PV) technology is, at present, crystalline silicon. The indirect band gap of silicon means that a thick, up to 400 μm, layer is needed in order for most of the solar radiation to be absorbed. This large thickness means that, in turn, the crystalline quality, i.e., defect density, of the material must be favorable such that the electrons and holes generated on absorption of photons can reach the contacts where collection occurs. Additionally, the band gap of Si, 1.1 eV, is somewhat lower than the optimum band gap, 1.3–1.5 eV, calculated for solar energy generation from the sun's radiation [1] (these issues will be discussed in greater detail in the next section). The result of this is that solar panels from Si require either single crystals or very large, ~10 cm, grains. Producing material of this quality requires a great deal of energy input; this leads to high, and difficult to avoid, production costs. Thin-film PV materials are presently the most promising prospect for large-scale solar electricity generation.

The use of a direct band gap absorber material reduces the required thickness of the absorber by two orders of magnitude to 1–5 μm; this reduces the requirement for crystalline quality by a corresponding amount as the carriers generated by photon absorption only need to diffuse a few micrometers in order to be collected. The outcome of this for solar panel production is that far less photoactive material is required, making the construction of many solar power plants feasible, and a much greater range of possible production techniques is opened up. The efficiencies (η, the proportion of incident solar energy converted to electricity) of thin-film PV modules, 10–15 %, presently lag behind those of Si-based modules, up to 20 % [2]; closing this gap is key to the viability of large-scale PV electricity generation.

3.2 Operating Principles

The basic principle of thin-film PV electricity generation is the production and separation of electron–hole pairs in a p-n junction. First demonstrated in their present form in 1954 by Bell Laboratories, solar cells operate through the promotion, by an incident photon, of electrons from the valence to the conduction band of a semiconductor material. The separation of the electron and hole generated by the intrinsic field of a p-n junction leads to an output power defined by the potential drop of the junction and the average flux of electrons across it, ignoring other loss mechanisms. The nature of this architecture makes a number of parameters crucial to the performance of a PV cell. The first of these is the band gap, E_g, defined as the energy difference between the top of the valence band and the bottom of the conduction band, Fig. 2.1. The band gap plays an important role in PV as it defines the minimum photon energy necessary for electron–hole generation in the absorber and the maximum possible open-circuit voltage of the p-n junction. These two factors form the basis for the determination of the optimal band gap for a PV device to deliver the maximum power from solar radiation [1].

Figure 2.2a shows the spectrum of radiation from the sun reaching the Earth having passed through 1.5 atmospheric thicknesses; typical for Europe and North America, the form of this spectrum is due to a convolution of the black-body radiation of the sun with the various absorption spectra of gases in the atmosphere. The optimum energy conversion efficiency of a PV device with an absorber band gap of E_g can be seen in Fig. 2.2b; this relationship indicates an optimum band gap of 1.3-1.5 eV for the absorber.

The next important parameter for the operation of a PV device is the carrier lifetime of the absorber, the average time for electrons to recombine with holes. High carrier lifetimes are very favorable for device performance as this gives a greater time window for the carriers to diffuse to the p-n junction. The carrier lifetime is limited in practice by the presence of crystal defects in the absorber, whether these be zero-dimensional (vacancies, interstitial atoms, and anti-site atoms), one-dimensional (dislocations), or two-dimensional (surfaces, interfaces,

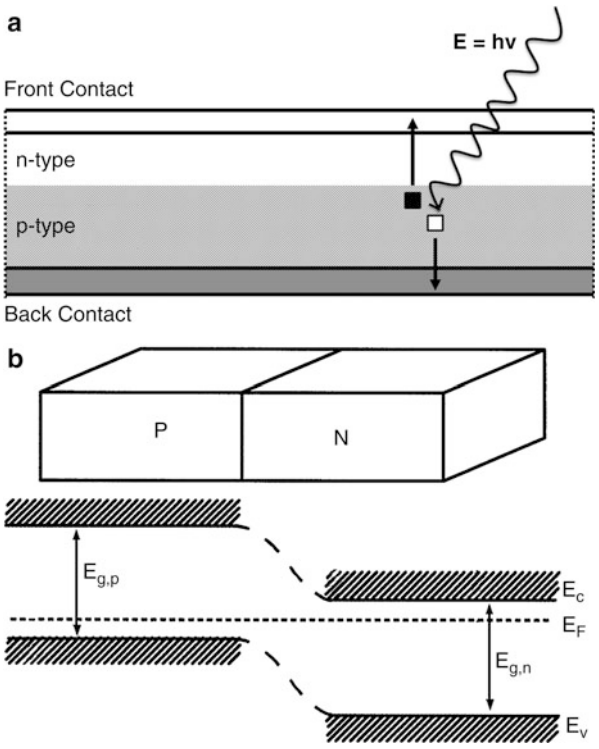


Fig. 2.1 Schematic of layers in a photovoltaic device, (**a**), and the p-n junction created by this architecture, (**b**). When a photon of energy hν is absorbed, it produces an electron–hole pair, as indicated in (**a**); the separation of these carriers by the field of the p-n junction in (**b**) can be utilized to generate electricity from light, the photovoltaic effect

grain boundaries, and twin boundaries). Reducing the influence of such defects while keeping production costs down is the single greatest challenge of PV research. Fortunately, the strong light absorption of the direct band gap materials used for PV absorbers results in the majority of the carriers being photogenerated very close to the junction; as a result a lifetime of only several nanoseconds is required in thin-film PV. The importance of the carrier lifetime is such that the majority of the research discussed in the following concerns the elimination of – or electrical passivation of – defects in the absorber (grain boundaries, etc.).

The most common means of characterizing a PV device is the J-V (current density-voltage) curve. The J-V curve, a schematic curve shown in Fig. 2.3, plots the current density versus the applied voltage for a solar cell under standardized illumination (AM1.5 [4], Fig. 2.2a). Other useful metrics of solar cell performance can be easily determined from the J-V curve; the most common are the short-circuit current density, J_{sc}; the open-circuit voltage, V_{oc}; the fill factor (FF); and the efficiency, η. V_{oc} and J_{sc} are defined as the voltage at zero current and vice versa (Fig. 2.3); the fill factor is the ratio between the area of the rectangle defined by the maximum power output point and the product of J_{sc} and V_{oc}. η is the ratio of the maximum power output to the incident solar power. Using the J-V curve and an equivalent curve for the device with no solar illumination together with simulation

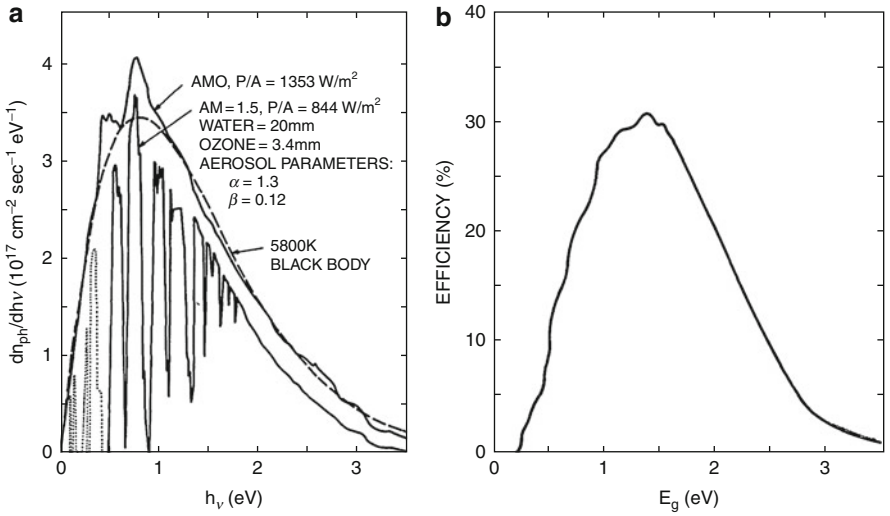


Fig. 2.2 Plot of the radiation spectrum from the sun that reaches the Earth's surface (**a**) and the maximum possible conversion efficiency of PV devices as a function of the absorber band gap (**b**). Also indicated in (**a**) are the radiation produced by a black body at 5,800 K, *dashed line*, and the radiation received by the outer limits of the Earth's atmosphere, relevant for electricity generation in space (Reprinted with permission from [3]. Copyright 1980, American Institute of Physics)

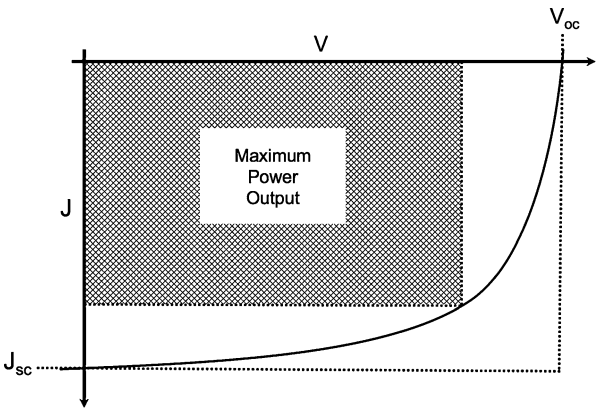


Fig. 2.3 A schematic J–V curve for an illuminated solar cell; the parameters J_{sc} and V_{oc} are indicated. The fill factor for a cell is determined from the area of the rectangle defined by the maximum power output, as indicated, divided by the product of J_{sc} and V_{oc}, indicated by the *larger rectangle*

software [5, 6], the series and shunt resistances of the device can be estimated. The series and shunt resistances of a PV device are defined in reference to an equivalent circuit of a device, Fig. 2.4. In this circuit the series resistance impedes the flow of the photocurrent to the p-n junction while the shunt resistance impedes the flow of photocurrent by-passing the junction; from these definitions it should be clear that a low series resistance and high shunt resistance are desirable.

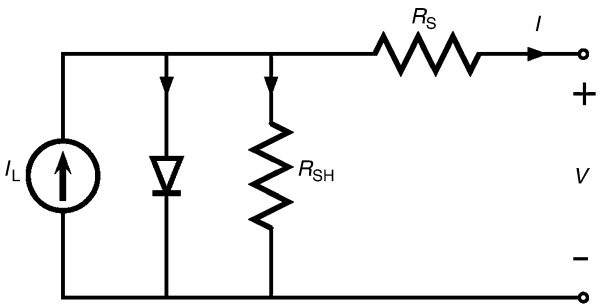


Fig. 2.4 An equivalent circuit for a PV device showing the roles played by the series, R_S, and shunt resistances, R_{SH}, for a photovoltaic current generator, I_L. The diode in the circuit represents the p-n junction of the PV device

3.3 Inorganic Solar Cells

At the time of writing, two thin-film technologies are in production, CdTe- and Cu(In,Ga)Se_2 (CIGS)-based devices. Often termed "second generation" photovoltaics, these cell systems utilize polycrystalline heterojunction architectures and compete directly with the existing Si-based technologies. CIGS devices are produced in the substrate configuration with multilayers deposited onto glass or metal foil, Fig. 2.5a, while CdTe devices are produced as a superstrate with multilayers effectively deposited onto the bottom of the glass, Fig. 2.5b. The schematic comparison between the two configurations in Fig. 2.5 shows reversal of the transparent conductive oxide (TCO) and back contact layers necessary for the different configurations; other than this the two architectures are very similar. An increasing level of research has focussed on producing CdTe in the substrate configuration [7, 8], but presently all solar panel production of CdTe is of the superstrate type.

The first PV cell based on CdTe (n-CdTe/p-Cu_2Te) was demonstrated in 1963 by the General Electric Research Laboratory [9], though 10 % efficiency was only achieved with a the switch to a p-CdTe/n-CdS superstrate structure [10, 11]. The realization that chlorine played an important role in device growth [12] and the optimization of the front and back contacts [13] led to the creation of a 16.5 % efficient device; recent refinements to the device architecture have improved upon this in the production of a 18.2 % cell [2].

The development of CIGS PV devices began in 1975 when Bell Laboratories announced a CdS/CIS cell with 12 % conversion efficiency [14]. This initial device was however based on single crystal CIS; it was not until 1984 that conversion efficiencies greater than 10 % were demonstrated for a thin film [15], at this point still based on CIS. Following two decades of close competition between the maximum demonstrated efficiencies of CIGS and CdTe, several developments in the early 1990s led to CIGS achieving an efficiency advantage over CdTe which has yet to be relinquished. The first of these developments was the realization that Na, diffusing through the Mo back contact from the soda-lime glass substrate, has a highly beneficial effect on the properties of CIS and CIGS devices. The other

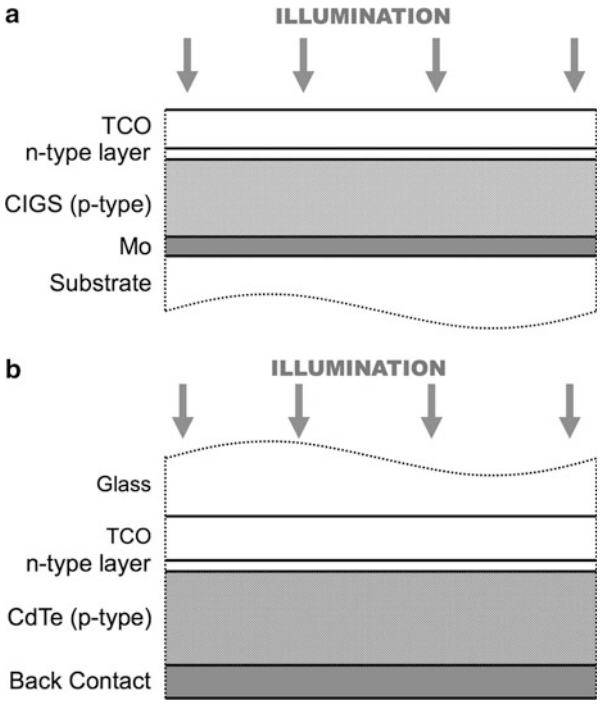


Fig. 2.5 Diagrams illustrating the substrate (**a**) and superstrate (**b**), configurations used in thin-film PV. The transparent conducting oxide (TCO) consists of high-resistance and low-resistance layers in modern high-efficiency devices; this is not indicated

development was the incorporation of Ga, substituting for a fraction of the In and grading this substitution through the thickness of the absorber [16].

CIGS-based cells lead the efficiency tables for thin-film polycrystalline PV for both individual cells (19.6 ± 0.6 %) and modules (15.7 ± 0.5 %) [2], but in both categories the difference between CIGS and CdTe is small. Both CIGS and CdTe have major drawbacks regarding their use in high-volume PV electricity generation. For CIGS the major drawback is the cost and limited supply of In; for CdTe the toxicity of Cd and the limited supply of Te are problematic. In order to overcome these problems, work has begun on the next generation inorganic PV absorber materials as well as organic PV materials. The leading next generation inorganic absorber is presently $Cu_2ZnSn(S,Se)_4$ (CZTS). This material uses only abundant, nontoxic, and low-cost elements; it also has an appropriate band gap (1.0–1.5 eV depending on the relative S and Se content [17]). A number of deposition techniques have already been demonstrated for CZTS, including evaporation [18, 19], solution processing [20, 21], and electrodeposition [22, 23], with a maximum efficiency of 11.1 % [21] achieved to date. Like CIGS, CZTS is produced in the substrate configuration, and it seems as though much of the cell architecture and processing research carried out for CIGS can be adapted [19, 24], if not directly transferred (CBD-CdS, TCOs), to CZTS.

3.4 Organic Bulk Heterojunction Solar Cells

Organic solar cells based on semiconducting polymers and fullerene molecules are an alternative to inorganic thin-film solar cells [25]. Their main advantages include low-cost, lightweight, rapid solution-based deposition, such as inkjet printing and roller casting, as well as compatibility with flexible substrates. The operating principle of organic solar cells is however different from its inorganic counterpart. The origin of this is the small dielectric constant of organic compounds, which means that the photogenerated electron–hole pair is tightly bound as an exciton. Since excitons are charge neutral, they cannot contribute to the electric current extracted from the device and must therefore be dissociated into free charge carriers (i.e., free electrons and free holes). This takes place at the interface between the polymer and fullerene molecule(s) as illustrated in Fig. 2.6a. In organic solids the intermolecular interactions are weak, so that the electronic structure consists of discrete molecular energy levels. Of fundamental importance is the highest occupied molecular orbital (HOMO) with π-bonding and the lowest unoccupied molecular orbital (LUMO) with π^*-antibonding. For exciton dissociation the polymer must have a relatively low ionization energy and the fullerene a relatively high electron affinity. Electron transfer takes place from the polymer (the donor) to the fullerene (the acceptor) [26]. Following electron transfer there can still be some Coulomb attraction between the electron in the acceptor and hole in the donor; this intermediate state is known as the charge transfer (CT) state [27]. It can either dissociate into free carriers or undergo recombination. The operating principle of an organic solar cell can therefore be illustrated schematically as in Fig. 2.6b. The absorber layer consists of a phase-separated mixture of polymer and fullerene, known as a bulk heterojunction configuration. An incoming photon is absorbed by the polymer (fullerenes absorb mainly in the near-UV region) to create a tightly bound exciton. The exciton diffuses through the polymer and dissociates into free electrons and holes at the donor-acceptor interface (provided the CT state is overcome). In organic materials the exciton diffusion length is typically $\sim$10 nm [28], so that phase separation on a similar length scale is required for efficient carrier generation. Once free carriers are generated, contiguous percolation pathways are required for carrier transport to the electrodes (i.e., electrons towards the cathode and holes towards the anode). This ideally requires a large domain size in the phase-separated microstructure.

The competing requirements for carrier generation and transport imply that the phase-separated microstructure of bulk heterojunction solar cells is of fundamental importance.

The field is progressing rapidly, and currently the highest efficiency for bulk heterojunction cells (non-tandem) is better than 8 % for a PTB7-PC71BM system [29, 30]. In the laboratory, devices are typically fabricated by spin coating a solution of the donor and acceptor phases; in this as-deposited state the device performance can be non-optimum. Several methods have been used to increase efficiency, such as thermal, solvent annealing, as well as solvent mixtures/additives. These methods will be described in relation to the poly(3-hexylthiophene) (P3HT)

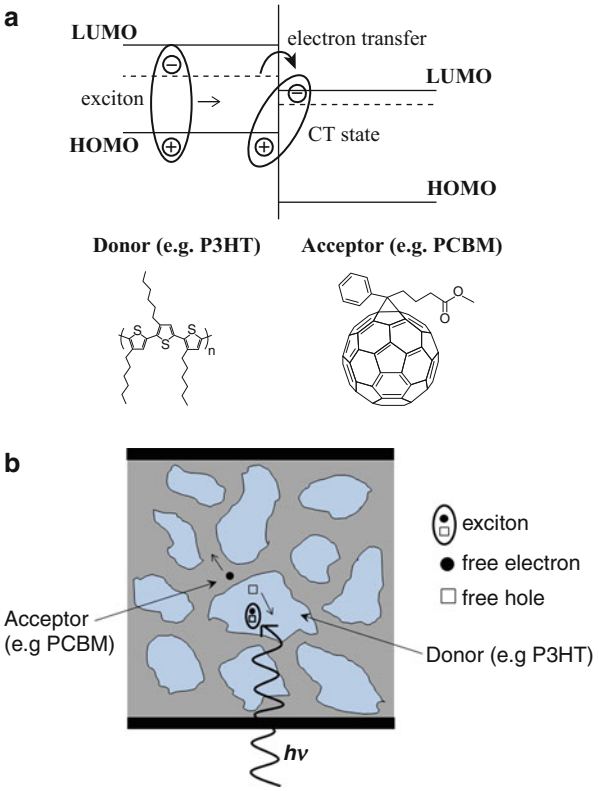


Fig. 2.6 (**a**) shows the molecular energy levels for exciton dissociation at the donor-acceptor (D–A) interface. Excitons created by photon absorption in the donor undergo electron transfer at the D–A interface due to the offset in LUMO levels. An intermediate charge transfer (CT) state is created due to Coulomb attraction between the electron in the acceptor and hole in the donor. The CT state must undergo further dissociation in order to generate free electrons and holes. (**b**) is a schematic illustrating the operating principles of a bulk heterojunction solar cell. An incoming photon of energy *hv* is absorbed by the donor phase, thereby generating a neutral exciton. The exciton can dissociate into free carriers provided it can diffuse to a neighboring donor-acceptor interface before undergoing recombination. Once free carriers are generated, contiguous percolation pathways are required in order to extract the electric current from the device

donor-[6, 6]-phenyl C61 butyric acid methyl ester (PCBM) acceptor system, which is widely studied and has thus far achieved 4–5 % efficiencies [31] (see Fig. 2.6a for molecular illustrations of P3HT and PCBM). During spin coating the solvent rapidly evaporates, and the finely dispersed PCBM molecules/aggregates inhibit the P3HT polymer chains from crystallization. Thermal annealing above the glass transition temperature of the polymer allows the system to approach equilibrium. Several effects have been observed during thermal annealing, such as residual solvent evaporation, volume relaxation of the absorber layer due to a change in free volume, and P3HT/PCBM phase separation [32, 33]. The improved crystallinity of P3HT can be detected by the presence of vibronic bands between ~510 and

610 nm in UV–vis absorption measurements and by the roughening of the film surface due to phase separation [34]. The P3HT crystals have a fibrillar structure, similar to nanowires, the high aspect ratio providing a large donor-acceptor interface area for carrier generation and an efficient percolation pathway for hole transport. Indeed Berson et al. [35] found an improvement in device efficiency with increasing volume fraction of P3HT fibers, except at very high loadings. In the solvent annealing approach, the spin coating process is terminated with the film still wet and covered with (say) a petri dish in order to slow the solvent evaporation rate. The P3HT polymer chains are free to move about in the residual solvent and will gradually crystallize [36]. An alternative approach is to use solvent mixtures/additives [37–39]. Here the principle is to have differential solubility of PCBM in the host solvent and additive as well as a higher boiling point for the additive. During drying the host solvent will evaporate more rapidly, so that the additive concentration within the wet film increases. If the solubility of PCBM is low in the additive, it will precipitate out of solution, thus enabling the P3HT to crystallize uninhibited.

4 Materials Issues in Inorganic Solar Cells

4.1 CdTe

Cadmium telluride has a band gap of 1.45 eV, and its equilibrium structure is the adamantine sphalerite structure. As an absorber it is p-type [10] and so is usually paired with the n-type CdS emitter; an example of a superstrate CdS/CdTe cell is shown in Fig. 2.7.

Electron microscopy, both scanning electron microscopy (SEM) and transmission electron microscopy (TEM), has been important in the development of CdTe-based PV. At the most basic level, SEM is an important tool for the assessment of coating morphologies and homogeneities; it can however deliver far more than this. Electron backscatter diffraction (EBSD) is an established method of measuring the grain sizes and crystallographic textures of thin films; for CdTe it has principally been used to investigate growth parameters [40, 41]. The accurate quantification of grain size, and the capability of EBSD to filter out the twin boundaries, makes it possible to see clear trends between grain size and cell performance [40]. The application of electron-beam-induced current (EBIC) and cathodoluminescence (CL) in the SEM is particularly important in the study of PV materials as they can be used to probe the electrical properties at the nanoscale.

One area where electron microscopy has made a major impact in the development of CdTe PV is chlorine activation. The incorporation of Cl has been very consistently demonstrated to greatly enhance the performance of CdTe cells [42–44]; understanding the processes occurring during Cl activation is key to optimizing this step. One of the earliest observations relating to Cl activation is that it can trigger impressive grain growth in small-grained CdS and CdTe [45, 47] when it is carried out by depositing $CdCl_2$ onto the CdTe and heating in air or inert

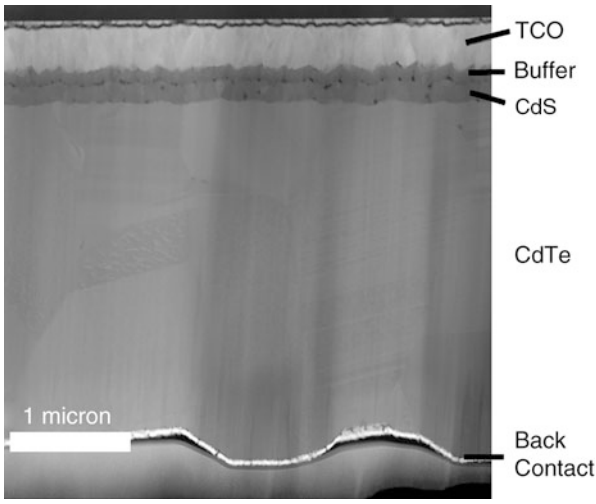


Fig. 2.7 Dark-field STEM image of a CdS/CdTe superstrate cell showing the device architecture (Figure is courtesy of AA Taylor and JD Major, unpublished results)

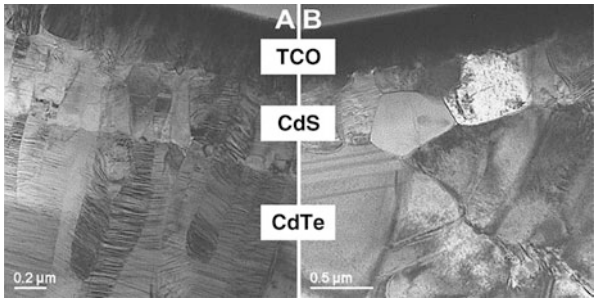


Fig. 2.8 Bright-field TEM micrographs showing the CdS/CdTe interface before, (**a**), and after, (**b**), Cl activation; note the significant reduction in twin density and increase in grain size (Reprinted with permission from [47]. Copyright 2004, Springer Science and Business Media)

gas [46]. This effect is most clearly seen in the work by Terheggen et al. [47] where highly twinned CdS and CdTe were observed to recrystallize following $CdCl_2$ treatment, Fig. 2.8. Another observation made by electron microscopy is that the CL emission from grain interiors and from grain boundaries is quite different [48–50], Fig. 2.9. The more uniform contrast over the grain interior and grain boundaries seen for the donor-acceptor pair energy region, Fig. 2.9c, indicates that the Cl becomes associated with the CdTe grain boundaries, passivating them. More details regarding the role of Cl at grain boundaries can be found in Sect. 5.1.

The physics of twin boundaries and dislocations in CdTe is a subject that has been extensively investigated with TEM [51–53]. Lamellar twins, intrinsic, and extrinsic planar defects are all regularly observed in CdTe, Fig. 2.10, and it is not unusual to observe regions of buried wurtzite (the hcp analogue to the sphalerite structure) where twinning is effectively occurring on every plane, Fig. 2.11. Comparisons between the structures as observed in the TEM and simulated structures indicate that while these defects are predicted to create additional energy levels within the band gap, these levels are relatively shallow, due to no "wrong" Cd–Cd

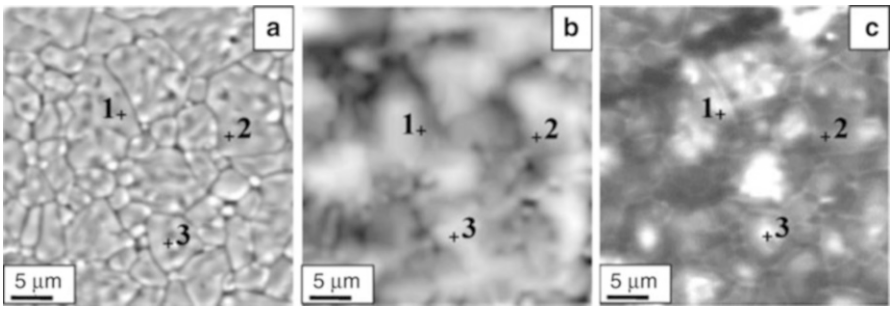


Fig. 2.9 Monochromatic CL images of (**b**) the excitonic region of the CdTe spectrum and (**c**) the donor-acceptor pair region. Note the greater contrast between grain boundaries and grain interiors in (**b**). The SEM image is shown in (**a**). (Reprinted with permission from [49]. Copyright 2002, John Wiley and Sons Ltd.)

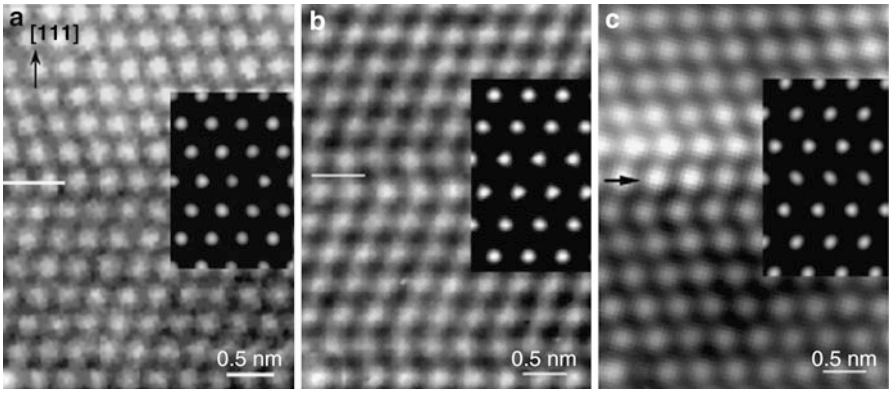


Fig. 2.10 HRTEM micrographs of a lamellar twin (**a**), intrinsic (**b**), and extrinsic (**c**), planar defects in CdTe. *Inset* are computer simulations of the images from the predicted structure showing excellent agreement between model and experiment (Reprinted with permission from [52]. Copyright 2007, Elsevier)

or Te–Te bonds being made, and thus are not predicted to be strongly detrimental to the collection of photocurrent [51, 52]. These observations are consistent with work correlating the grain size in the CdTe absorber of a CdS/CdTe cell with the cell efficiency [40] where a superior correlation between grain size and efficiency was found if the twin boundaries were ignored. This approach of combining high-resolution TEM with image simulation and ab initio calculations in order to determine the atomic positions and additional energy levels at defects has also been applied to dislocations [53] and double-positioning twin boundaries [51].

Another area in which electron microscopy has made an impact in CdTe PV research is in the study of sulfur diffusion. The pseudo-binary phase diagram for

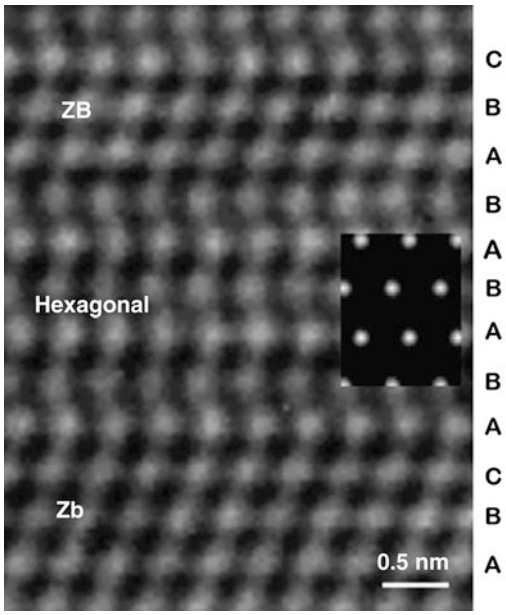


Fig. 2.11 HRTEM micrograph of a region of buried wurtzite in the more stable sphalerite structure of CdTe, the letters indicate the stacking sequence of the close-packed planes. *Inset* is a simulated image of the buried wurtzite structure showing excellent agreement between experiment and theory (Reprinted with permission from [52]. Copyright 2007, Elsevier)

CdTe and CdS indicates 15 % solubility of CdS in CdTe at 600 °C [54, 55], a common temperature for CdTe deposition on CdS; it is therefore expected that the CdS/CdTe interface will not be chemically sharp. Experimental determination of the diffusion coefficients [55] and modelling of the thermal processes during cell production [56] point towards the presence of a region several hundred nanometers in thickness at the CdS/CdTe interface and along CdTe grain boundaries where up to 4 at% sulfur substitutes for tellurium. TEM has found this prediction to be accurate [47, 53, 57], Fig. 2.12. Terheggen et al. [47], from which Fig. 2.12 is adapted, found that the degree of sulfur interdiffusion was influenced somewhat by the amount of $CdCl_2$ used for the Cl activation; the dominant effect however seems to be the additional thermal processing involved in Cl activation.

At the extreme end there is evidence that the CdS layer can be entirely consumed by the process of CdTe deposition [53, 58], Fig. 2.13. The exact role played by sulfur in CdS/CdTe cells remains a subject of some debate [59–61], but the total consumption of the CdS is detrimental to cell performance as it allows localized shunting of the photocurrent to the TCO. Work at NREL [53, 58] has shown that the presence of oxygen during the CdS deposition can stabilize this layer against consumption by CdTe but the mechanisms at work in this process remain unclear.

The development of back contacts to enhance the V_{OC} of CdTe cells [62–64], continued work on TCOs and window layers to reduce optical losses [65, 66], and the development of substrate configuration CdS/CdTe cells [7, 8] are all areas in which electron microscopy will play a future role.

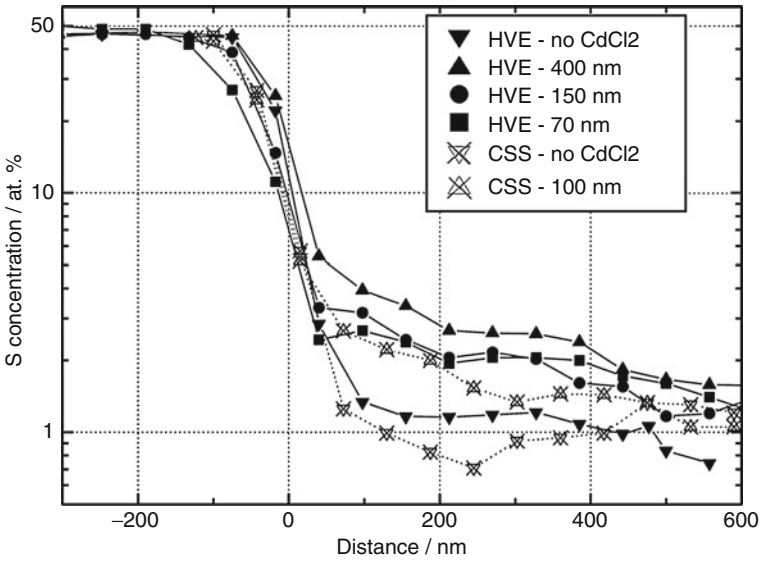


Fig. 2.12 EDS line profiles of the sulfur concentration in high-vacuum evaporated (*HVE*) and close-space sublimated (*CSS*) CdS; the thicknesses refer to the thickness of $CdCl_2$ used for Cl activation (Reprinted with modifications, with permission from [47]. Copyright 2004, Springer Science and Business Media)

4.2 CIGS

Alongside CdTe, CIGS forms the second generation of photovoltaic absorber materials. While the record efficiencies of CIGS cells have exceeded those of CdTe since the mid-1990s [2], the higher costs of a more complex deposition scheme [67] and instabilities in the supply of indium give CIGS modules a somewhat higher cost per Watt. $Cu(In,Ga)Se_2$ has the chalcopyrite structure, also an adamantine configuration, with a band gap of approximately 1.2 eV [68]. Unlike CdTe, CIGS is usually produced in the substrate configuration onto an Mo back contact with TCO and window layers deposited subsequently; an example of this is shown in Fig. 2.14.

A number of issues surround the deposition of CIGS onto Mo. An important aspect of the CIGS deposition is the formation of a $MoSe_2$ layer at the interface, Fig. 2.15. It has been found that the $MoSe_2$ layer between the Mo back contact and CIGS absorber leads to the formation of an ohmic contact [69]; if the deposition conditions are altered such that no $MoSe_2$ forms the contact becomes Schottky type (and hence detrimental to carrier collection and cell performance). As Fig. 2.15 indicates, the $MoSe_2$ layer is nanocrystalline, typically 100–200 nm in thickness, and it has been found that it usually forms with its c-axis (it has an hexagonal structure) perpendicular to the interface [69, 70]. By altering the composition of the CIGS deposited onto Mo, making it Cu, (In,Ga), or Se rich [69], it was demonstrated that (In,Ga)-rich compositions favor $MoSe_2$ growth while Cu-rich CIGS

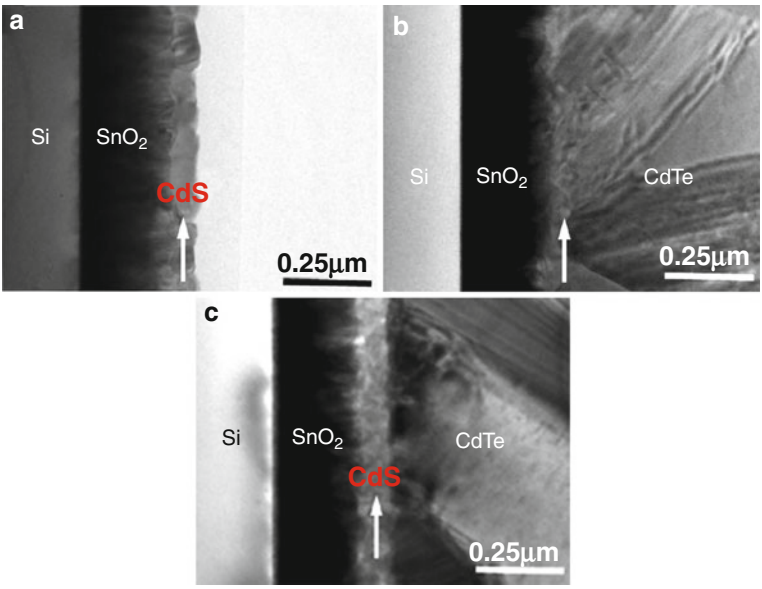


Fig. 2.13 Bright-field TEM micrographs of the SnO_2/CdS/CdTe interfaces, (**a**) is CSS-grown CdS, (**b**) is CSS-grown CdTe onto the coating in (**a**), and (**c**) is chemical-bath-deposited (CBD)-grown CdS and CSS-grown CdTe. The CdS layer is indicated by *white arrows*; in (**b**) the layer has been consumed during the growth of the CdTe absorber (Reprinted with permission from [53]. Copyright 2011, Elsevier)

suppresses it; this leads to the concept of multistage deposition processes [16]. Stoichiometric and Cu-rich CIGS coatings contain inclusions and/or a surface layer of binary Cu_xSe phases [71]; these are metallic in nature and hence detrimental to the cell. It has however been found that Cu-rich CIGS layers have significantly larger grain sizes [72] than their Cu-poor equivalents. A three-stage evaporation process combines these ideas by initially depositing a (In,Ga)-rich composition, to develop a $MoSe_2$ layer, followed by a Cu-rich composition to drive the growth of large grains before finishing with a second (In,Ga)-rich step to ensure that the resultant coating is Cu poor [73], Fig. 2.16. A final aspect of CIGS deposition is the generation of a Ga gradient in the resultant coating; the gradient in Ga content of the cell shown in Fig. 2.14 is shown in Fig. 2.17. The addition of Ga to CIS causes an increase in the band gap of the resultant semiconductor [74], leading to a better match to the solar spectrum [1], while the gradient in Ga content creates a highly beneficial back surface field [68].

As with CdTe, and thin-film growth in general, electron microscopy is a powerful tool in understanding the growth processes of CIGS. The influence of Ga content and deposition route on the grain size and texture of CIGS coatings have been extensively studied [75, 76]. It is found, Fig. 2.18, that the average grain size of the resultant absorber depends upon the Ga content with grain sizes decreasing as Ga content increases. It is also found that around 40 % of the boundaries in CIGS

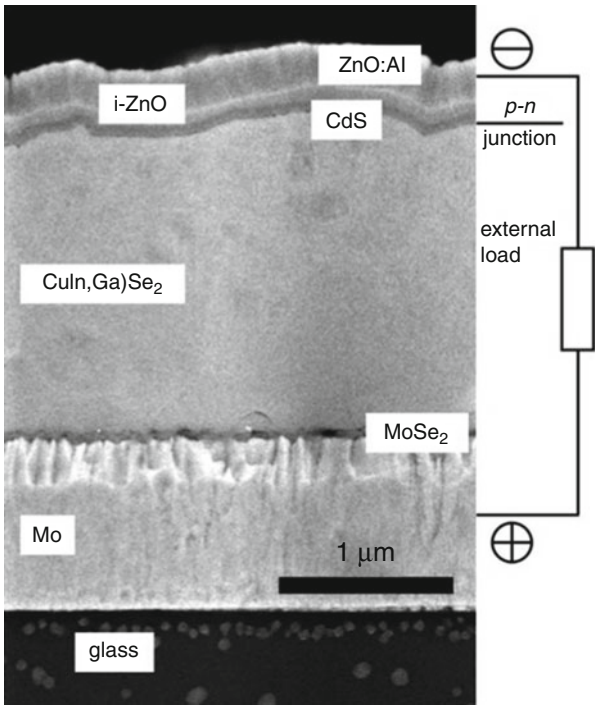


Fig. 2.14 SEM micrograph showing a typical CIGS cell in the substrate configuration; the circuit formed by this heterojunction is indicated schematically (Reprinted with permission from [75]. Copyright 2007, International Union of Crystallography)

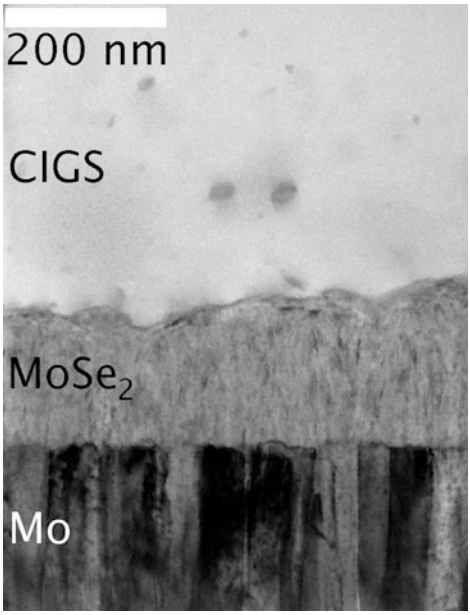


Fig. 2.15 Bright-field STEM micrograph showing the CIGS/Mo interface in CIGS cell. The presence of a nanocrystalline $MoSe_2$ layer between the CIGS absorber and the Mo back contact is evident (Figure is courtesy of AA Taylor and PJ Dale, unpublished results)

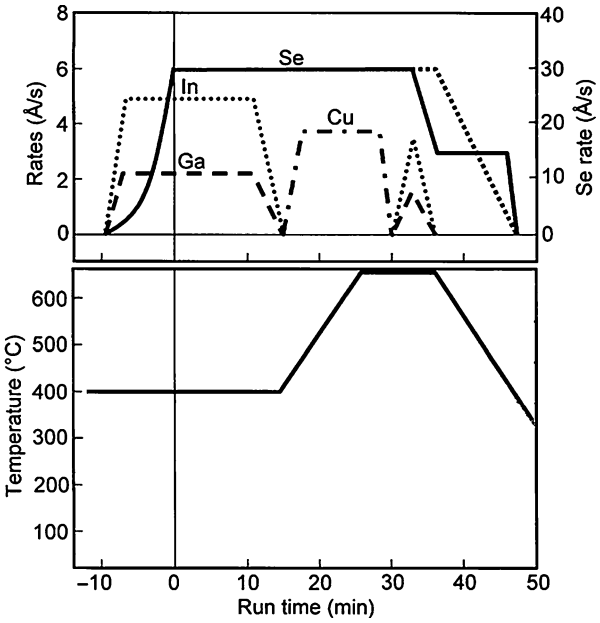


Fig. 2.16 Schematic profile of the three-stage deposition of CIGS absorber layers by evaporation (Reprinted in a modified form, with permission from [73]. Copyright 2001, Elsevier)

absorbers deposited by various means are Σ3-type boundaries with misorientations of 60° and 71°, Fig. 2.19. As with CdTe, it is demonstrated that these boundaries are not strongly electrically active [76, 77] (Fig. 2.20), the depletion in the CL signal in Fig. 2.20a at twin boundaries is clearly lower than that at random grain boundaries, and sometimes no depletion is evident. This observation is consistent with the presence of such boundaries in high-performing devices.

The investigation of grain boundaries in CIGS with CL has yielded a number of important results. In a comparison between a state-of-the-art 19.9 % device and a 13 % device, a stark difference in CL recombination losses at the grain boundaries has been observed [78]; losses of 5–10 % are observed in the more efficient device compared to 20–30 % in the 13 % device. Earlier work by Romero et al. [79] offers an explanation for this phenomenon. Examination of the CL spectra in grain interiors and at grain boundaries, Fig. 2.21a, highlights clear differences in the emission spectra; at the boundaries a maximum emission energy of 1.02 eV is observed while an addition peak at 1.08 eV is present in the grain interiors. Monochromated CL imaging of the same region serves to further highlight this effect; far more variation in the CL signal is present when imaging at 1.08 eV (Fig. 2.21b) compared to imaging at 1.02 eV (Fig. 2.21c). The invariance of the 1.02 eV emission with electron-beam current (carrier density) indicates [80] that it represents the dominant radiative recombination pathway during solar illumination, comparable with low electron-beam current. It can therefore be surmised that uniform CL emission at this lower energy is a good indicator for solar cell performance.

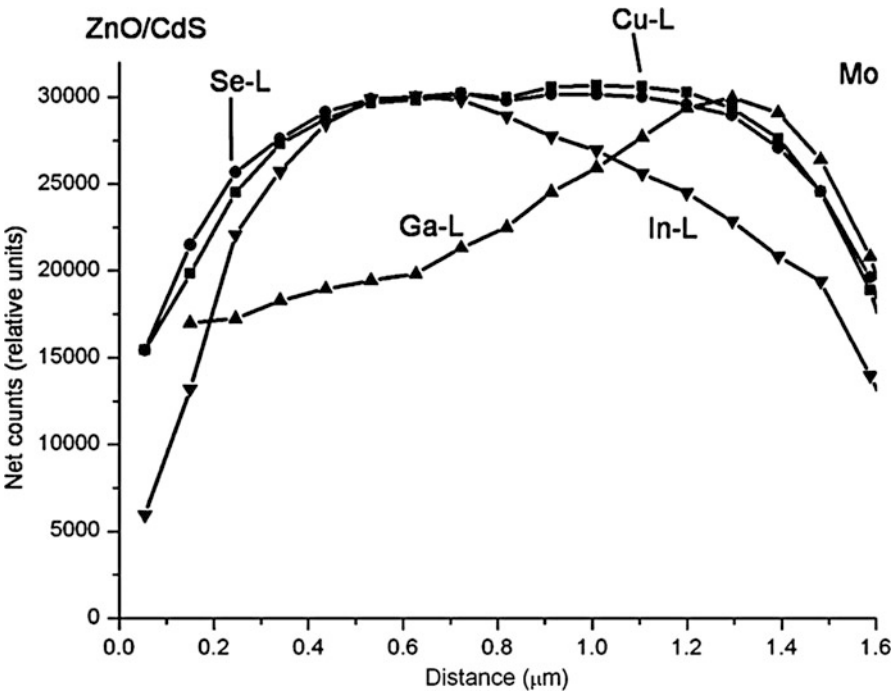


Fig. 2.17 The variation in content, as measured by SEM-EDS, of Cu, In, Ga, and Se across the height of the CIGS cell in Fig. 2.14; the positions of the front contact, ZnO/CdS, and back contact, Mo, are indicated (Reprinted with permission from [75]. Copyright 2007, International Union of Crystallography)

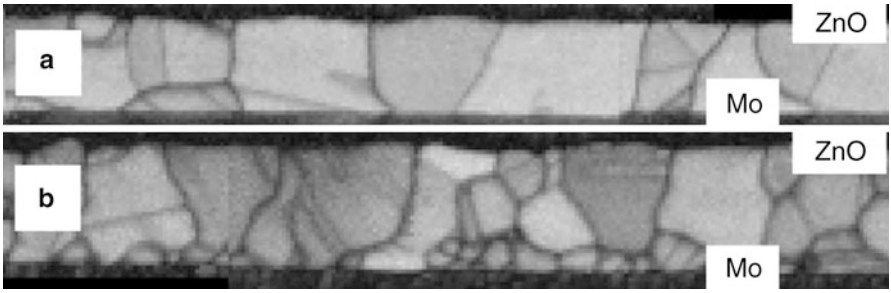


Fig. 2.18 EBSD image quality maps of (**a**), $Cu_{0.23}In_{0.17}Ga_{0.09}Se_{0.51}$, and (**b**), $Cu_{0.23}In_{0.11}Ga_{0.15}Se_{0.51}$; the average grain sizes of these absorbers are calculated to be 0.73 μm and 0.47 μm, respectively (Reprinted with permission from [75]. Copyright 2007, International Union of Crystallography)

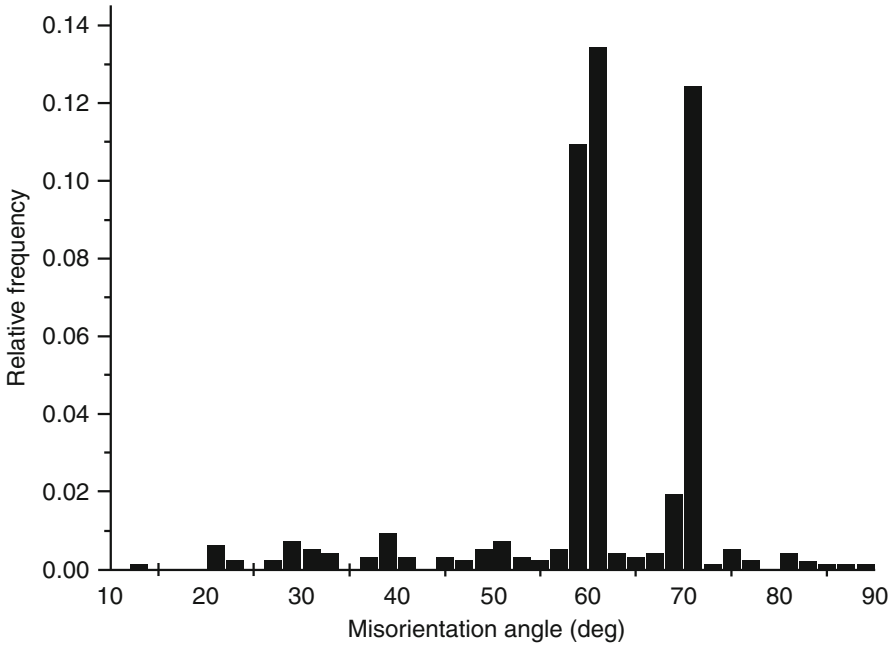


Fig. 2.19 The distribution of grain boundary misorientation angles in a $Cu_{0.23}In_{0.16}Ga_{0.10}Se_{0.51}$ absorber, as determined by EBSD. Note the very high, ~40 %, fraction of assessed boundaries with 60° or 71° misorientation (Reprinted with permission from [75]. Copyright 2007, International Union of Crystallography)

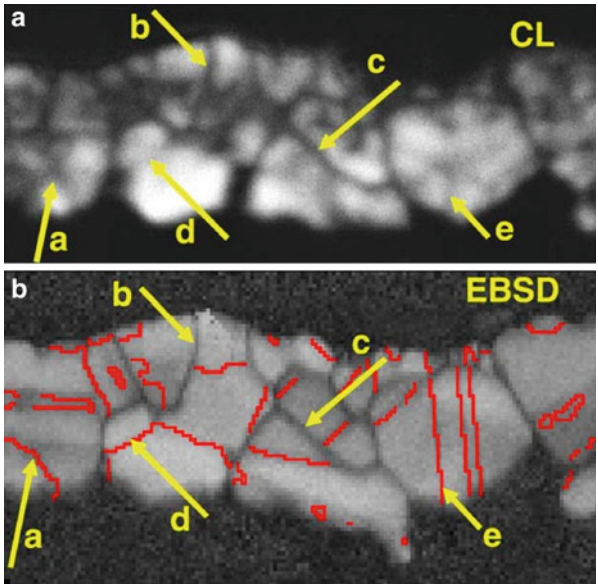


Fig. 2.20 SEM-CL (**a**) and EBSD image quality map (**b**) from the same region of a CIS absorber. The boundaries marked *a*, *d*, and *e* are Σ3 oriented while *b* and *c* are randomly oriented. The depletion of the CL signal is significantly greater at the randomly oriented boundaries (Reprinted with permission from [76]. Copyright 2009, Elsevier)

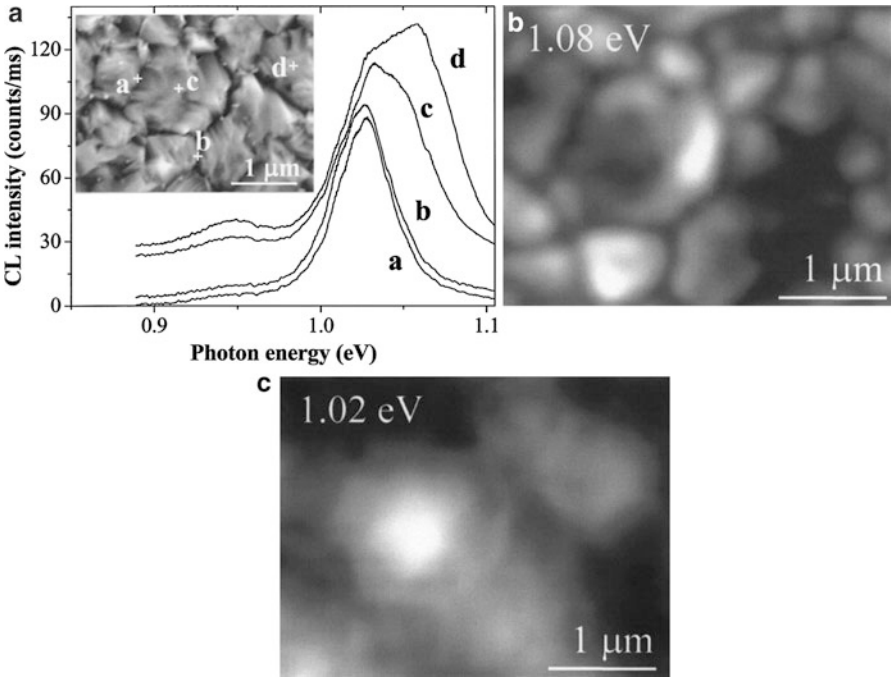


Fig. 2.21 CL of a 19.2 % efficient CIGS absorber layer; (**a**) shows the variation in CL spectra between grain boundaries and interiors, (**b**) is a monochromatic CL image acquired at 1.08 ± 0.01 eV, and (**c**) is a monochromatic CL image acquired at 1.02 ± 0.01 eV. Little depletion of the 1.02 eV emission is observed at grain boundaries (Reprinted with permission from [79]. Copyright 2003, American Institute of Physics)

Analogous to the role of chlorine in CdTe, sodium plays an important role in CIGS devices. As with Cl activation for CdTe, the exact role played by Na in CIGS is not clear, but it has been shown to influence the grain size during film growth [81–83] and increase the conductivity of the absorber [84, 85] and is predicted to passivate grain boundaries [86]. Extensive TEM-EDS analysis of CIGS absorbers from multiple sources did not detect any Na at the boundaries [87]; in fact no change in composition was observed at the boundaries, Fig. 2.22. More recent work using aberration-corrected scanning TEM (STEM) has succeeded in the detection of composition variation at CIGS grain boundaries [88], but the Na remains beyond the limits of even this advanced instrumentation. Other techniques, including SIMS mapping [81], scanning Auger electron spectroscopy [89], and atom probe tomography [90], have indicated the presence of Na at boundaries. The consensus is therefore that the high concentration of Na required for efficient devices is beyond the limit of solid solubility in CIGS, so the Na must segregate to grain boundaries [91].

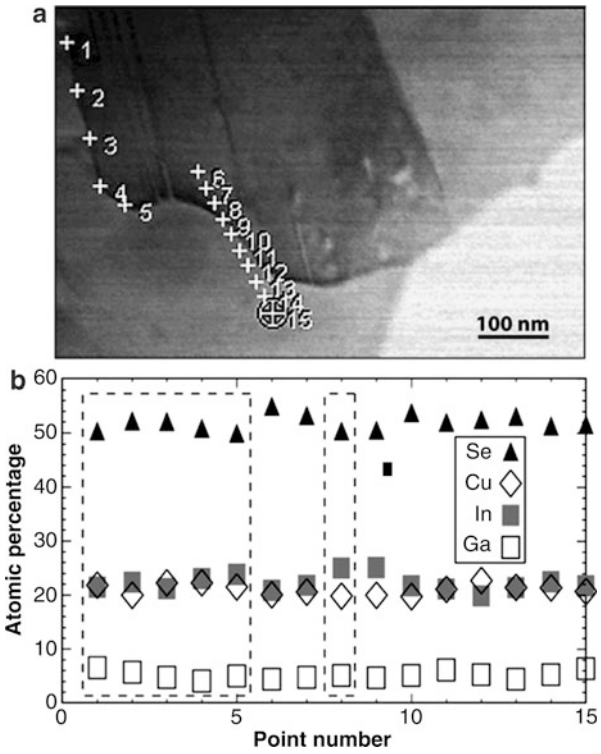


Fig. 2.22 TEM-EDS analysis of CIGS grain boundaries. (**a**) is a STEM bright-field micrograph of several grain boundaries in a CIGS absorber, the numbered crosses indicate the positions of EDS analysis, and the results of which are plotted in (**b**). The *dashed outlines* in (**b**) highlight those points acquired at grain boundaries; the size of the data points corresponds roughly to the uncertainty (Reprinted with permission from [87]. Copyright 2007, American Institute of Physics)

4.3 CZTS

While CZTS shows great promise and leads the field of third-generation photovoltaics [21], it presents some very challenging material issues. The problem begins with the crystal structure [17, 92]. First-principles calculations [17] suggest that the difference in energy between the kesterite and stannite (Fig. 2.23) structures is only ~3 meV/atom; this raises questions about which phase is present in the absorber and whether different deposition methods could create different phases. Both the kesterite and stannite structures are well suited to the role of absorber; cation disorder in the structure could however pose a problem due to the large number of point defects. Convergent beam electron diffraction (CBED) experiments [93] were not able to discern the phase while neutron diffraction of CZTS indicates ~30 % cation disorder between Cu and Zn [94]. In fact, direct evidence of such cation disorder has been provided in the TEM through STEM-EELS measurements [93], Fig. 2.24. From high angle annular dark field (HAADF) imaging alone there is no difference between the areas of CZTS in Fig. 2.24a, c; the bright columns are Sn while the other columns are Cu or Zn. In Fig. 2.24b both Cu and Zn signals are seen in the EELS spectra of the three darker atom columns indicated in Fig. 2.24a; in Fig. 2.24d only a signal for Zn was found. The atomic model shown in Fig. 2.23 indicates that the atom columns analyzed in Fig. 2.24b, d should

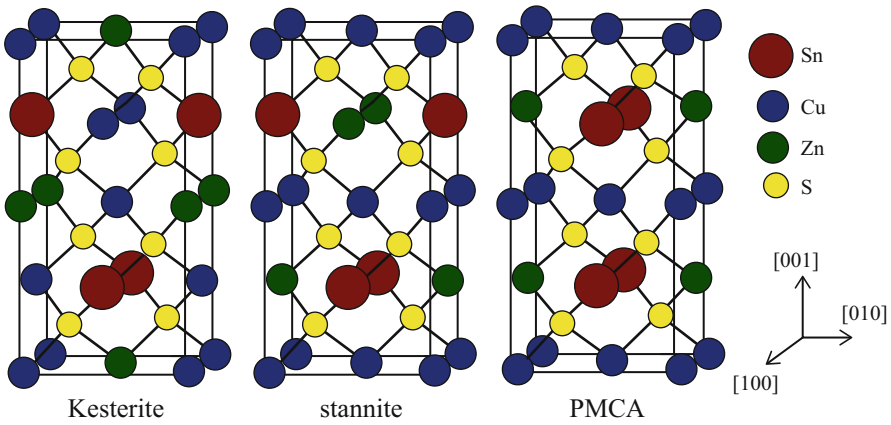


Fig. 2.23 Ball models of the kesterite, stannite, and primitive-mixed CuAu (PMCA) structures of CZTS. The kesterite and stannite structures are both tetragonal but vary in the positions of the Cu and Zn cations (Reprinted with permission from [93]. Copyright 2012, John Wiley and Sons Ltd.)

be either Sn–Zn–Cu–Cu–Sn for kesterite or Sn–Cu–Zn–Cu–Sn for stannite; while the mixed signal observed in Fig. 2.24b can be explained by beam broadening in the sample, the absence of a signal for Cu in Fig. 2.24d can only be explained by a clustering of Zn anti-site defects. The scale of this anti-site clustering was estimated to be between 1.5 and 5 nm.

A major obstacle facing the development of CZTS PV devices is the formation of secondary phases. These phases, which include ZnS, Cu_xS, Sn_xS, and $Cu_xSn_yS_z$, are highly detrimental to device performance [95]. Unfortunately, the detection of these phases, particularly ZnS and $Cu_xSn_yS_z$, by X-ray diffraction [96] and Raman spectroscopy [97, 98] is rendered deeply problematic by peak overlapping. Two factors contribute to the presence of secondary phases in CZTS absorbers, the limited phase-field stability of CZTS [99] and the thermodynamic instability of CZTS in contact with Mo [100, 101]. The problem of CZTS instability with respect to the Mo back contact has been particularly well illustrated by Wätjen et al. [101], Fig. 2.25. In Fig. 2.25a a TEM micrograph shows a CZTS-based device produced by reactive sputtering; the EDS maps for the area of the absorber indicated in the micrograph clearly show a homogeneous distribution of Cu, Zn, Sn, and S with no evidence of secondary phases in the absorber. Figure 2.25b shows a cell produced by the same method following a 550 °C anneal for 3 min; this time the EDS clearly shows the presence of the three binary sulfides of Cu, Zn, and Sn and a MoS_2 layer, as predicted by thermodynamic calculations [100]. In the study by Wätjen et al. [101], the processing was chosen such that secondary phases were expected to form; the presence of additional phases at the back contact has however also been noted in optimized devices [98].

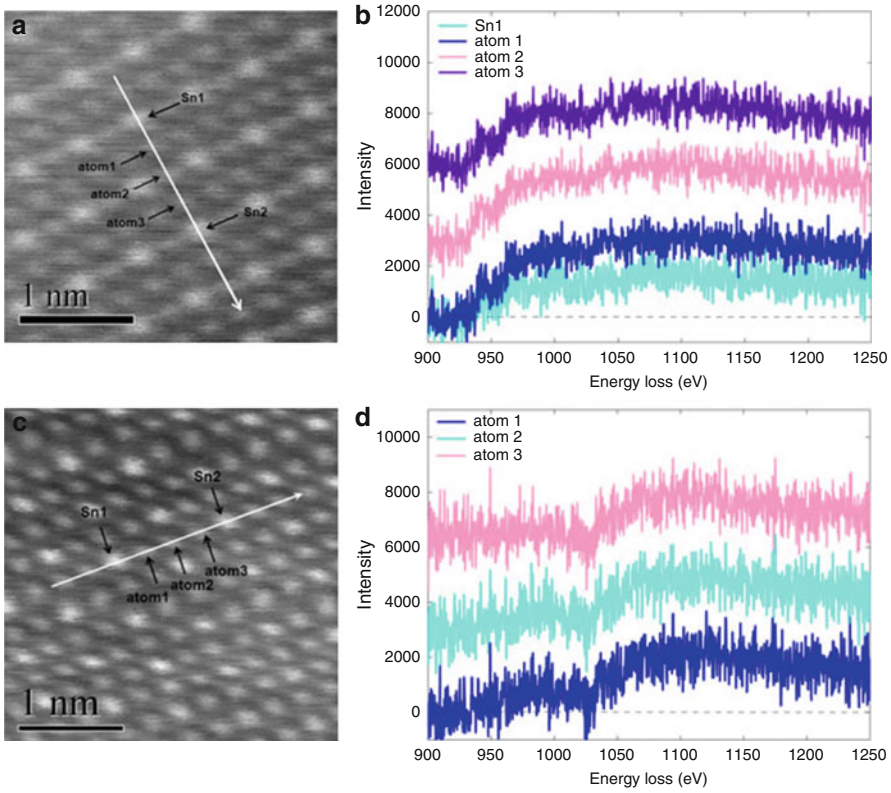


Fig. 2.24 STEM-EELS analysis of [010]-oriented CZTS; (**a**) and (**c**) are the HAADF images of two regions; (**b**) and (**d**) are EELS spectra of atom positions marked on the HAADF micrographs. In (**b**) the EELS edge due to Cu at 950 eV and that due to Zn at 1,050 eV are observed; in (**d**) only the Zn edge at 1,050 eV is present (Reprinted with permission from [93]. Copyright 2012, John Wiley and Sons Ltd.)

The record efficiencies for CdTe and CIGS cells have been achieved by physical vapor deposition (PVD) methods [13, 78]; this likely owes to the high level of control and reproducibility afforded by PVD techniques like sputtering and evaporation. For CZTS, however, the record-device efficiencies for the past few years have been repeatedly set by a solution-processing route [20, 21, 102]. A possible explanation for this effect is that the solution-processing route suppresses the formation of the secondary phases [20]. Figure 2.26 shows two CZTS cells, with different sulfur and selenium contents, processed by the IBM hydrazine solution route. While the TEM cross sections do show the presence of pores in the absorbers, Fig. 2.26b, c, no evidence of secondary phases other than $Mo(S,Se)_2$ is seen. The demonstrated capabilities of electron microscopy for the analysis of secondary phases make it an essential tool for the further development of CZTS devices.

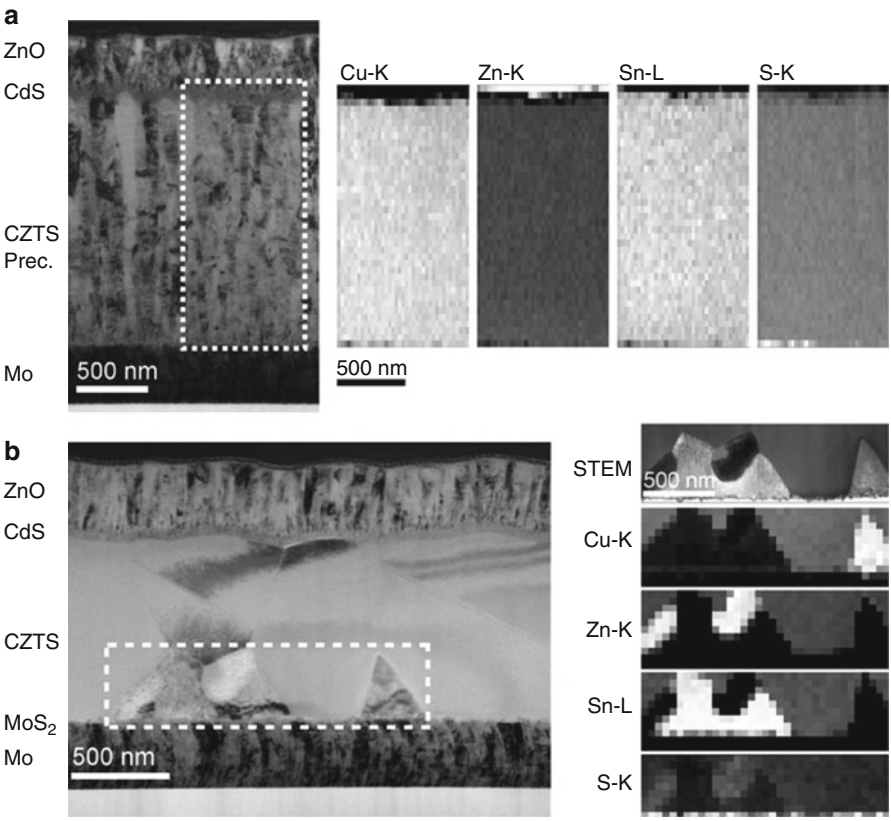


Fig. 2.25 TEM-EDS investigation of phase decomposition of CZTS in contact with Mo. In (**a**) a freshly reactive-sputter-deposited CZTS absorber is shown; EDS mapping of the absorber does not reveal the presence of any phases other than CZTS. In (**b**) a CZTS absorber following a 550 °C anneal for 3 min is shown; note the presence of the three binary sulfides at the CZTS/Mo interface (Reprinted with permission from [101]. Copyright 2012, Elsevier)

5 Measuring the Electrical Activity of Grain Boundaries

5.1 Background

Low-cost deposition processes for thin-film solar cells, such as close-space sublimation, evaporation, and electrodeposition, produce a high density of grain boundary defects in the absorber layer (see, e.g., Figs. 2.8, 2.18, and 2.26). In the case of CdTe and CIGS, it has been reported that polycrystalline material produces higher-efficiency devices than their single-crystal counterparts, though it must be noted that considerably more effort has gone into optimizing the former. This observation is inconsistent with the behavior of silicon-based solar cells and is counterintuitive

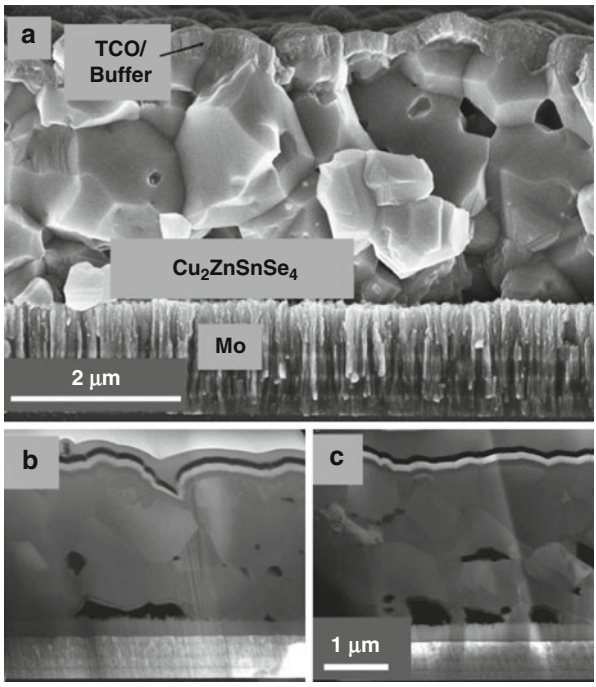


Fig. 2.26 SEM (**a**) and TEM (**b**) and (**c**) of CZTS devices produced by the hydrazine solution-processing route. The samples in (**b**) and (**c**) differ in their relative fractions of S and Se; note presence of pores but no secondary phases such as Zn (S,Se) (Reprinted with permission from [20]. Copyright 2010, John Wiley and Sons Ltd.)

to the idea that grain boundaries generally degrade the electrical activity of devices (not just solar cells). Nevertheless there is perhaps some truth in this claim; for example, grain boundaries could getter any impurity elements that are present in the starting material or introduced during deposition, thereby improving the crystal quality of the grain interiors. This leads to an increased carrier lifetime and diffusion length and hence better devices. Indeed numerical simulations by Taretto et al. [103] have shown that the efficiency of a solar cell for a given defect concentration is higher if the defects are accumulated at the grain boundaries rather than at the grain interiors (the simulated grain size was 2 μm, similar to real device structures). Nevertheless it is clear that once the crystal quality of the grain interiors is sufficiently improved, the performance-limiting feature of the absorber layer is the grain boundaries.

In order to understand the role of a grain boundary on solar cell performance, the key physical parameters need to be identified via an electronic band structure diagram. Consider an isolated grain boundary region in a p-type semiconductor (e.g., CdTe, CIGS) as shown schematically in Fig. 2.27a. The different bonding environment at the grain boundary, for example, dangling bonds, distorted interatomic bonds, and different bond coordination numbers, gives rise to electronic states within the band gap. The presence of additional defect states means that the region of grain boundary is charge neutral at the level φ_0 (called the "quasi-neutrality" level) which is different to the Fermi level of the neighboring perfect crystal grain interiors. At equilibrium the Fermi level must be constant throughout

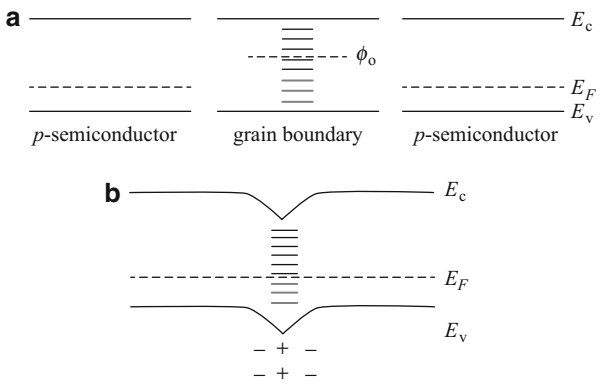


Fig. 2.27 (**a**) Electronic band structure of a grain boundary in isolation from p-type perfect crystal. E_c, E_v, and E_F denote the conduction band minimum, valence band maximum, and Fermi energy, respectively. In a neutral grain boundary, energy levels below φ_0 are filled. (**b**) shows the equilibrium band structure after the grain boundary makes contact with the perfect crystal (i.e., grain interiors). Electrons are transferred from the grain boundary into the grain interiors in order to maintain a constant Fermi energy level

the structure, and in the case of Fig. 2.27a this is achieved by electrons flowing from the grain boundary into the grain interiors, thereby forming a double Schottky barrier (Fig. 2.27b). The charged grain boundary results in band bending by an amount eV_{gb}, the sense of the bending being such that electrons are attracted and holes repelled. Electrons attracted to the grain boundary undergo Shockley-Read-Hall (SRH) recombination due to defect states, the local recombination rate under illumination being larger than the thermal generation rate (especially for mid-gap states). Hence, at steady state, electrons must diffuse from the grain interiors to the grain boundary at a rate determined by the recombination velocity (S). The precise relationship is given by the boundary condition $D_n(d\Delta n/dx) = S.\Delta n(0)$, where D_n is the diffusion coefficient and $\Delta n(0)$, $(d\Delta n/dx)$ are the excess minority carrier concentration and gradient at the grain boundary plane. $D_n(d\Delta n/dx)$ is the diffusive flux from the grain interior, and $S.\Delta n(0)$ is the SRH grain boundary recombination rate. Grain boundaries with large recombination velocities are strong minority carrier sinks and therefore degrade device performance. The barrier height V_{gb} acts as an obstacle to the hole current, so that grain boundaries affect collection of both minority and majority carriers in a solar cell device. It should also be noted that the quasi-neutrality level is not the only mechanism for producing a charged grain boundary. The grain boundary can act as a preferential segregation site for impurity atoms, which could locally change the donor or acceptor population. A net increase in (ionized) donor concentration leads to a positively charged grain boundary (similar to Fig. 2.27b) while the opposite is true for a net increase in (ionized) acceptors. For p-type semiconductors, where the Fermi level is close to the valence band edge, the effect of acceptors is small, while only a relatively small increase in donor concentration gives rise to a non-negligible barrier height.

Numerical simulations have been carried out to determine the effect of neutral [103, 104] as well as charged [105, 106] grain boundaries on the performance of thin-film CIGS solar cells. The short-circuit current density (J_{sc}), open-circuit voltage (V_{oc}), fill factor ($F\,F$), and efficiency decrease monotonically with increasing grain boundary defect density and recombination velocity (experimentally it is also observed that grain boundaries increase the series resistance in CdTe devices [107]). In the simulations by Taretto et al. [103] grain boundaries were found to decrease the overall cell efficiency by as much as 10 %. The effect on V_{oc} and $F\,F$ is more pronounced than J_{sc}. The decrease in V_{oc} is attributed to the higher recombination rate at the grain boundary while a larger diode ideality factor, due to increased SRH recombination within the space charge region, resulted in a lower $F\,F$. The relatively small change in J_{sc} is due to the fact that the recombination velocity is greatest when the concentration of electrons and holes is similar (this is a consequence of SRH recombination); the photogenerated carrier profile for a CIGS solar cell indicates that the absolute carrier concentration is relatively small in the region where this condition is satisfied, thus making only a small impact on J_{sc} [91]. A simulation of horizontal grain boundaries (i.e., normal to the film thickness direction) has shown that the decrease in cell properties is greatest when the grain boundary is located ∼50 nm from the CIGS-CdS heterojunction (i.e., within the space charge region), the position coinciding with the region where electron and hole concentrations under illumination are similar [104]. Grain boundaries within the quasi-neutral region of the device have very little effect on J_{sc}, since there the recombination velocity is small due to the low electron concentration in the p-type semiconductor (note that in CIGS the photogenerated carrier density in the quasi-neutral region is small due to most of the light being absorbed in the space charge region; this is however not the case for polycrystalline Si solar cells). For the same reason horizontal grain boundaries within the space charge region are thought to have a greater impact on device performance than vertical, columnar grain boundaries. Finally some authors (see, e.g., [108] (CdTe) and [109] (CIGS)) have suggested that the band bending profile for a positively charged grain boundary results in preferred transport channels for minority carrier electrons due to a reduced recombination rate arising from the hole barrier of the grain boundary. The simulations by Metzger and Gloeckler [105] and Gloeckler et al. [106] indicate that this is not the case. Hole repulsion means that the grain boundary and the adjacent region are less strongly p-doped compared to the perfect crystal and hence the recombination rate increases. Large degrees of band bending, for example, an inverted n-type boundary, are required before the hole concentration is sufficiently low to limit recombination. However, as discussed previously charged grain boundaries mainly affect V_{oc} rather than J_{sc}. Under forward bias the space charge region is wider at the positively charged grain boundary compared to the perfect crystal, and as a consequence a large recombination rate is obtained along a greater length segment of the grain boundary, thereby reducing V_{oc} [106]. The decrease in V_{oc} and fill factor offsets any increase in J_{sc} (for an inverted grain boundary), so that the net cell efficiency decreases.

Before describing electron microscopy methods to measure grain boundary recombination velocity and barrier height, a summary of grain boundary-related results for CdTe and CIGS will first be presented. In CdTe solar cells a post-deposition chlorine activation treatment is required to achieve the highest efficiency (Sect. 4.1). Several microstructural changes are reported to take place, one of which is grain boundary passivation due to chlorine segregation. Experimental evidence for grain boundary chlorine enrichment was obtained using energy-filtered TEM [47, 110], and theoretical simulations have also suggested the possibility of chlorine passivation [111, 112]. The luminescence spectrum for CdTe consists of a broad donor-acceptor pair (DAP) peak at ~1.4 eV, which is thought to (at least partly) involve transitions between a Cl_{Te}^{+} donor and chlorine A-centers, i.e., a (V_{Cd}^{2-} + Cl_{Te}^{+})-acceptor complex [113, 114]. Monochromatic cathodoluminescence imaging showed the DAP luminescence to originate from the grain interiors as well as grain boundaries, whereas exciton emission was strongest within the grain interiors [49], thus providing further indirect evidence for chlorine segregation to the grain boundaries. Grain boundaries in CdTe are considered to be charged, but there is controversy on the sign of band bending. Using electron-beam-induced current imaging, Durose and coworkers [115, 116] observed contrast reversal due to high injection conditions at lower electron-beam currents at the grain interiors compared to the grain boundaries and attributed this to higher p-doping at the grain boundaries. The grain boundaries are therefore negatively charged and repel minority carrier electrons. On the other hand, Visoly-Fisher et al. [108, 117] observed positively charged grain boundaries using scanning probe methods, i.e., scanning capacitance microscopy (SCM), scanning Kelvin probe microscopy (SKPM), and conductive probe AFM. In some cases the barrier height was sufficiently large to create an n-type inversion layer at the grain boundary. It should be noted however that for SCM measurements the sample surface needs to be oxidized which could lead to oxygen impurities at the grain boundaries. Woods et al. [118, 119] have proposed an alternative model based on current versus temperature measurements carried out on CdTe thin films lifted off from real devices. Here the grain boundary is positively charged (downward band bending), but the region neighboring the grain boundaries has a higher acceptor concentration (upward band bending). The band bending increases with chlorine activation (typical post-activation values are 952 meV for downward bending and 250 meV for upward bending). The model of Woods et al. combines features from both EBIC and scanning probe microscopy observations, and it is possible that either limited spatial resolution in the experiments or an asymmetry in the downward/upward barrier heights may have led to the conflicting results.

In contrast to CdTe, CIGS thin-film solar cells do not require any post-deposition doping or optimization treatments (cf. chlorine activation). However, it is recognized that Na diffusion from the underlying soda-lime glass substrate, through the Mo back contact into the absorber layer during deposition, is beneficial for device performance. Atom probe tomography has shown that Na preferentially segregates at the grain boundaries [90, 120] while SKPM measurements provide evidence for positively charged grain boundaries in CIGS [109]. The barrier height however

decreases rapidly to zero over the Ga/(In + Ga) composition range 28–38 % from a plateau value of ~150 meV at In-rich compositions [121, 122]. A direct correlation of device efficiency and barrier height is observed; the efficiency first increases on alloying $CuInSe_2$ (CIS) with Ga due to the increase in band gap but then decreases in the composition region where the barrier height collapses, despite the Ga composition in this region (i.e., 28–38 %) being below that required to produce the ideal Shockley-Queisser band gap of 1.3–1.5 eV. It was assumed that positively charged grain boundaries are therefore required for efficient devices, although as described earlier numerical simulations indicate the opposite trend due to a reduced V_{oc}. Yan et al. [123] have carried out ab initio simulations on a CIS grain boundary structure modified from the atomic configuration of a double-positioning twin boundary in CdTe [51]. The grain boundary contained dangling bonds, "wrong" bonds (i.e., bonds with unfavorable atoms), and atom coordination numbers larger than four. Despite this the relaxed grain boundary had no deep level states due to volume expansion at the grain boundary core, thereby minimizing the impact of high-energy bonding configurations (especially Se–Se bonds). This behavior is unique to CIS (it was not observed in the relaxed CdTe grain boundary) and suggests that CIS grain boundaries are neutral. Experimental evidence for the lack of grain boundary deep states in CIGS was obtained from scanning tunnelling spectroscopy [124] although a high density of shallow levels near the conduction band minimum was observed. However, Yan et al. [123] also found that Na has a favorable binding energy to the grain boundary, and it was suggested that Na creates shallow donor levels, which has little impact on carrier recombination but gives rise to a positive charge at the grain boundary. SKPM measurements on CIGS films deposited on soda-lime glass and borosilicate glass revealed positively charged grain boundaries in the former, while no band bending was detected in the latter [123], implying that grain boundaries in CIGS are intrinsically neutral but acquire charge when doped with Na.

Persson and Zunger [125] have also proposed a mechanism whereby CIGS grain boundaries can be charge neutral but at the same time act as hole barriers. This is based on observations of the low-energy {112} polar surfaces of chalcopyrites which require the creation of Cu vacancies (V_{Cu}) in order to maintain charge neutrality. The valence band maximum of CIGS is due to Cu *d*-Se *p* hybridization; at the Cu-deficient (112) surface the repulsion between Cu-*d* and Se-*p* orbitals is reduced, so that the valence band maximum is lowered with respect to the bulk (there is however no change in the conduction band minimum). The shift in valence band means that the grain boundaries act as hole barriers while minority carrier electrons are unaffected. Using aberration-corrected scanning transmission electron microscopy, Abou-Ras et al. [88] have indeed shown a decrease in Cu concentration on {112} twin boundaries in CIGS; in some cases the decrease in Cu was accompanied by an increase in In, possibly due to formation of low-energy ($2V_{Cu}^{-} + In_{Cu}^{2+}$) defect complexes [126]. However, for random grain boundaries, Cu enrichment and In depletion were observed or vice versa, the Cu and In concentrations always being anticorrelated. CIGS thin films have a high density of Σ3 {112} twins as well as random grain boundaries [75]. It is possible that two grain boundary

types are therefore present, the former being described by the model of Persson and Zunger [125] while the latter belonging to the model proposed by Yan et al. [123].

5.2 Recombination Velocity Measurement

There are two SEM methods for measuring the recombination velocity, one based on electron-beam-induced current (EBIC, [127]) and the other on cathodoluminescence (CL, [128]). The former can be applied to both indirect and direct band gap semiconductors, but as thin-film solar cells are invariably direct band gap, the CL method has the advantage that it can be applied to the absorber layer material directly without having to make a device structure. In the EBIC method it is assumed that (i) the grain boundary is end-on and (ii) the edge of the space charge region is at the electron-beam entrance surface, to which carriers generated by the electron beam must diffuse in order to generate an EBIC signal. The second assumption is not entirely accurate since in a real device the space charge region can extend an appreciable distance of (say) sub-micrometer to few micrometers into the material, and the excess carriers generated within this volume are readily collected by the built-in electric field. Nevertheless Donolato's EBIC method involves solving the continuity equation for a point source of electron–hole pair generation, which is then extended to the entire electron-beam generation volume using Green's function methods. The EBIC contrast profile across the grain boundary can be expressed in terms of a non-analytical solution where one of the parameters is the electron-beam carrier generation profile. Various approximations to the carrier generation profile (e.g., spherically symmetric Gaussian, pear shape; see, e.g., [129] and references therein) have been made to simplify the calculation, but with the advent of modern computers, more accurate Monte Carlo simulations can be used as part of a numerical solution. The expression for the EBIC contrast profile also contains the minority carrier diffusion length and reduced recombination velocity (i.e., the ratio of the recombination velocity to the bulk carrier diffusion velocity) as material parameters. These can be estimated by finding the best fit theoretical contrast profile to that obtained experimentally. In Donolato's [127] original method the comparison was restricted to the area and variance of the EBIC profile rather than its entire shape.

The CL method also extracts the minority carrier diffusion length and reduced recombination velocity from the intensity profile measured across the grain boundary. The method relies on the Van Roosbroeck [130] model for the steady-state carrier distribution profile normal to a free surface in a semi-infinite slab, where the excess carrier source is a plane parallel to and at a finite distance from the free surface. The CL intensity profile for such a scenario, with the free surface replaced by a grain boundary, is given by [128]

$$\ln\left[\Delta I(x_b)\right] = \ln\left[1 - \frac{I(x_b)}{I(\infty)}\right] = \ln\left(\frac{S_{red}}{S_{red}+1}\right) - \frac{x_b}{L} \tag{2.1}$$

where $I(x_b)$ is the CL intensity for an electron beam positioned a distance x_b from the grain boundary, $I(\infty)$ is the plateau intensity in the bulk, S_{red} is the reduced recombination velocity, and L is the minority carrier diffusion length. A plot of $\ln[\Delta I(x_b)]$ versus x_b is therefore a straight line with the gradient and intercept yielding values for L and S_{red}, respectively. In deriving the above equation, several assumptions are made: (i) the CL signal is proportional to the number of electron–hole pairs, (ii) there is no change in radiative recombination efficiency (η) across the grain boundary, (iii) carriers are not present in the grain opposite to that in which the electron beam is incident, and (iv) the electron-beam generation volume is approximated as a planar surface. The first assumption can be easily verified by monitoring the CL signal as a function of electron-beam current and carrying out the measurements in the linear regime. Assumptions (ii) and (iii) means that the $\ln[\Delta I(x_b)]$ versus x_b plot deviates from linear behavior close to the grain boundary (i.e., small x_b). This is observed in practice although the dominant contribution appears to be the carrier distribution (assumption iii) rather than any variations in η.

The fourth assumption on the shape of the electron-beam generation volume is clearly unrealistic. Despite this $\ln[\Delta I(x_b)]$ versus x_b plots for experimental CL profiles do show a linear trend at x_b large enough to avoid the complications of assumptions (ii) and (iii) discussed earlier. An example for a grain boundary in vapor grown CdTe is shown in Fig. 2.28. The $\ln[\Delta I(x_b)]$ versus x_b plot (Fig. 2.28d) is obtained from the integrated CL intensity profile (Fig. 2.28c) extracted from the box region in the panchromatic CL image (Fig. 2.28b) and shows linear behavior (0.98 regression coefficient) apart from a slight downward deviation close to the grain boundary. The extracted values for L and S_{red} are 0.55 ± 0.03 µm and 0.23 ± 0.02, respectively. The diffusion length is consistent with previous values reported in the literature for CdTe. The recombination velocity is smaller than the bulk diffusion velocity and is thought to be due to the low misorientation of the grain boundary, which is typical for vapor grown CdTe [131] (note also that the grain boundary is not even weakly observable in the secondary electron image of Fig. 2.28a). Apart from experimental evidence Monte Carlo simulations [132] have also shown Eq. 2.1 to be generally valid at large x_b. Here the L and S_{red} values extracted from the (simulated) $\ln[\Delta I(x_b)]$ versus x_b plot were compared with the input Monte Carlo simulation values, and the systematic deviations between the two found to be ~10 % for L and no more than ~15 % for S_{red}. Mendis and Bowen [133] have analyzed the effect of the electron-beam generation volume on the CL measurement in greater detail. The CL intensity profile for a uniform slab of excess carriers was shown to follow the Van Roosbroeck predictions within a constant multiplication factor, so that Eq. 2.1 is still valid. The electron beam does not produce excess carriers uniformly, but the above scenario is certainly closer to the real situation than the Van Roosbroeck model.

CL has also been used to measure the reduced recombination velocity of heterointerfaces such as secondary phase precipitates in Cu_2ZnSnS_4 (CZTS; [132]). CZTS is thermodynamically stable in only a narrow region of the phase diagram and other sulfides may be present in the microstructure, in particular ZnS which has a highly negative heat of formation. An example is shown in Fig. 2.29a.

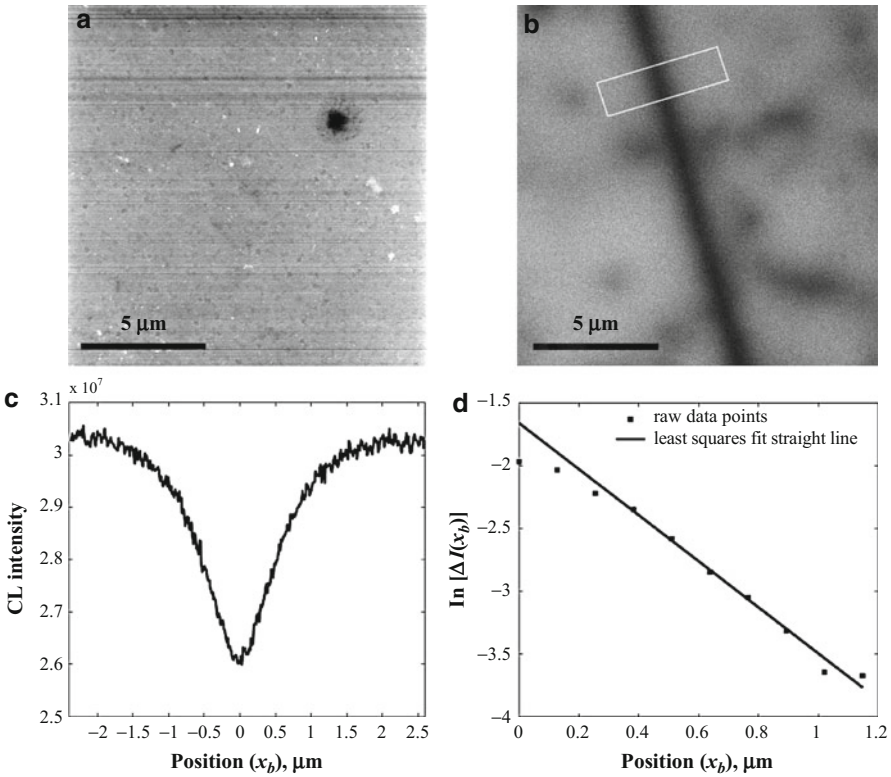


Fig. 2.28 (**a**) Secondary electron and (**b**) panchromatic CL image of a grain boundary in vapor grown CdTe. The integrated CL intensity profile extracted from the box region in (**b**) is shown in (**c**). The $\ln[\Delta I(x_b)]$ versus x_b plot for this profile is shown in (**d**) (Reproduced with permission from [128]; Copyright 2010 American Institute of Physics)

The monochromatic CL image of the ZnS-CZTS heterointerface acquired at the ZnS wavelength of 430 nm is shown in Fig. 2.29b. The integrated intensity profile extracted from the box region of Fig. 2.29b is shown in Fig. 2.29c and from this the $\ln[\Delta I(x_b)]$ versus x_b plot can be constructed (Fig. 2.29d). The extracted values for L and S_{red} are 309 ± 30 nm and 1.27 ± 0.20, respectively. Similar measurements for other ZnS-CZTS heterointerfaces gave recombination velocity values of the order of or less than the bulk diffusion velocity, i.e., the ZnS-CZTS heterointerface is electrically passive. The $Cu_xSn_yS_z$-CZTS heterointerface was also found to be electrically passive but not the SnS-CZTS heterointerface [132]. Secondary phases such as ZnS, Cu_2SnS_3 have a similar crystal structure and lattice parameters to CZTS, and it was assumed that the weak recombination is due to the formation of coherent heterointerfaces. Preliminary (unpublished) results by the authors using focussed ion-beam TEM cross-sectional samples, extracted from the ZnS-CZTS

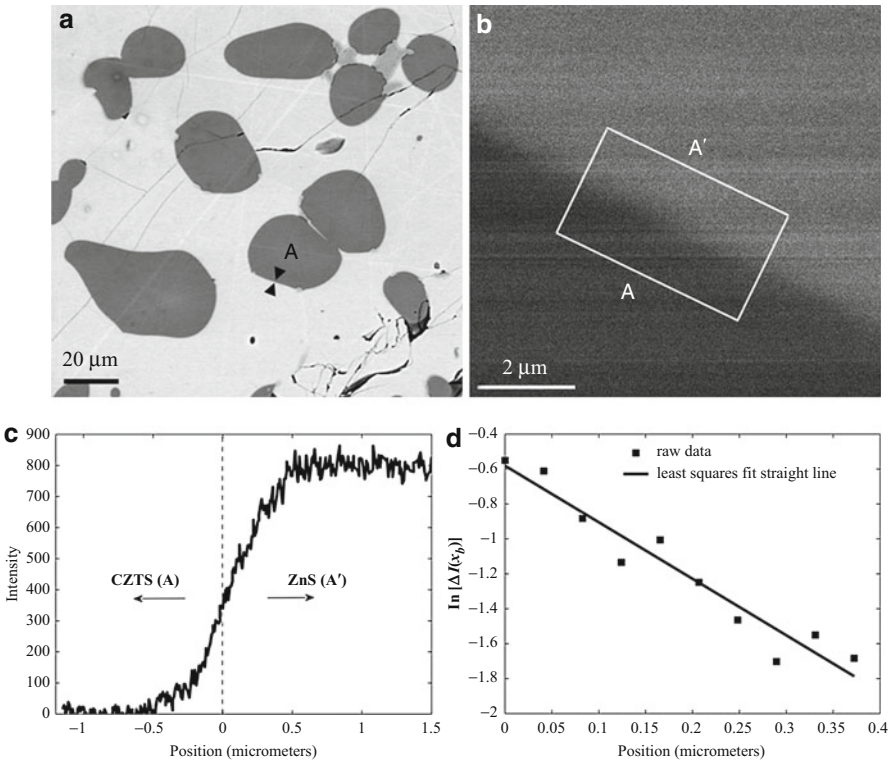


Fig. 2.29 (**a**) Backscattered electron image of ZnS precipitates in CZTS. The 430 nm monochromatic CL image of the heterointerface marked "A" in (**a**) is shown in (**b**). The integrated CL intensity from the *box region* in (**b**) is shown in (**c**) from which the $\ln[\Delta I(x_b)]$ versus x_b plot can be constructed (**d**) (Reproduced with permission [132]; Copyright 2012 American Institute of Physics)

heterointerfaces from which the SEM CL measurements were recorded, revealed only interfacial steps and no interfacial dislocations; furthermore the c-planes of the tetragonal CZTS grain were continuous with the (100) planes of ZnS. The high degree of lattice registry is consistent with a small recombination velocity.

5.3 Barrier Height Measurement

In the solar cell literature, band bending at a grain boundary is typically analyzed using scanning probe microscopy, most notably SKPM which measures the local variation in work function (see Sect. 5.1 for CdTe and CIGS references). Surface methods are influenced by contamination/adsorbed impurity atoms, surface dipole layers, and reconstruction of the grain boundary atomic structure at the free surface. In many cases measurements are carried out on the deposited thin film with no extra sample preparation, so that surface roughness also complicates the results.

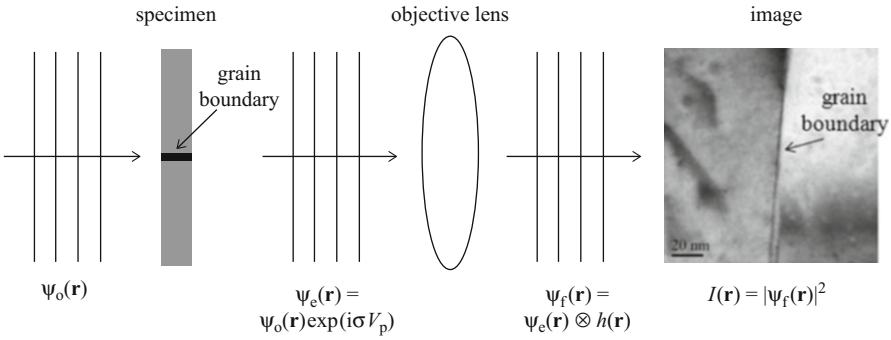


Fig. 2.30 Schematic illustrating the principle of Fresnel contrast imaging. The incident electron of wavefunction $\psi_0(\mathbf{r})$ undergoes a phase shift $\exp(i\sigma V_p)$ as it propagates through the specimen. Here σ is an interaction constant and V_p is the projected potential of the specimen. The objective lens convolves the exit wavefunction $\psi_e(\mathbf{r})$ with the point spread function $h(\mathbf{r})$, so that the image intensity $I(\mathbf{r})$ is given by the square modulus of this new wavefunction $\psi_f(\mathbf{r})$

In electron microscopy the Fresnel contrast method (also known as in-line holography) has been used to map potential variations. A schematic of this TEM-based technique is shown in Fig. 2.30. The electron beam with incident wavefunction $\psi_0(\mathbf{r})$ undergoes a phase shift that is proportional to the local projected potential $V_p(\mathbf{r})$ as it propagates through the specimen (phase object approximation) so that the specimen exit wavefunction is modified to $\psi_e(\mathbf{r})$, where $\mathbf{r}$ is the position vector. The projected potential is the specimen potential integrated along the thickness direction. As an example, a positively charged grain boundary with larger $V_p(\mathbf{r})$ will accelerate the electron, the smaller De Broglie wavelength leading to a phase shift with respect to the (quasi-)neutral grain interiors of smaller $V_p(\mathbf{r})$. Hence if the phase of the exit wave could be measured, information about potential variations within the sample can be extracted. This is however complicated by the fact that imaging by the objective lens is not perfect. Mathematically this is expressed as a convolution of $\psi_e(\mathbf{r})$ by the point spread function $h(\mathbf{r})$ of the objective lens. The image is the square modulus of this new wavefunction $\psi_f(\mathbf{r})$, i.e., no phase information is directly measured. However, phase information is indirectly present. To see this consider two specimen points, (say) one at the grain boundary and one in the grain interior. The spacing between the two points is less than the coherence length of the electron beam, so that the phase of the incident wavefunction can be treated as constant. Due to the point spread function, the individual points are broadened into discs in the image. Interference takes place in the region of disc overlap, such that the resultant intensity is a function of the phase difference in $\psi_e(\mathbf{r})$ for the two points as well as phase distortions introduced by the objective lens (i.e., $h(\mathbf{r})$). The Fresnel contrast method involves acquiring a series of images at different defocus values (i.e., different $h(\mathbf{r})$) and using the interference intensity (i.e., Fresnel fringe profile) to extract the phase of the exit wavefunction using numerical methods, such as the iterative wavefunction reconstruction (IWFR)

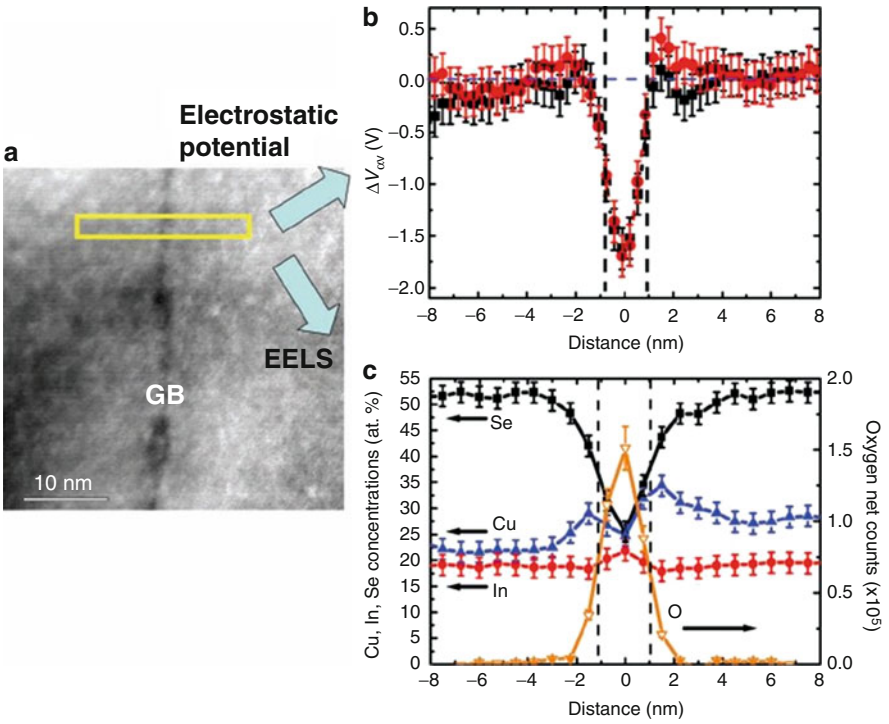


Fig. 2.31 (**a**) Image of a grain boundary in CIGS and the corresponding projected potential (**b**) reconstructed using the Fresnel contrast technique and (**c**) the chemical composition measured using EELS in an aberration-corrected STEM. The two projected potential curves in (**b**) were extracted from different regions of the same grain boundary (Reproduced with permission from [136]; Copyright 2012 Wiley [138])

algorithm (see, e.g., [134, 135]). Once the potential variation is extracted, then Poisson's equation can be used to calculate the electric field and charge density across the grain boundary.

Despite its promise, considerable care must be taken in correctly interpreting Fresnel contrast results. The focus series images are acquired with a small objective aperture that only includes the unscattered beam and the diffraction streak from the end-on grain boundary. Under these conditions the measured potential corresponds to the "mean inner potential" (V_o), which is the DC component of the crystal potential when expressed as a Fourier series.

V_o is proportional to $[\sum \boldsymbol{f}_{el}(0)]/\Omega$, where $\boldsymbol{f}_{el}(0)$ is the atom/ion scattering factor at zero angle and Ω is the unit cell volume (the summation of $\boldsymbol{f}_{el}(0)$ is over all atoms/ions in the unit cell). Apart from grain boundary charge, there are two other reasons why V_o can be different at the grain boundary compared to the grain interior: (i) a change in atomic density and (ii) a change in composition. This is evident from the results of Abou-Ras et al. [136] shown in Fig. 2.31. The projected potential extracted using the Fresnel contrast method is shown in Fig. 2.31b for the

CIGS grain boundary in Fig. 2.31a. A potential decrease of ~1.8 eV is observed at the grain boundary plane. The electron energy loss spectroscopy (EELS) measured composition profile across the grain boundary (Fig. 2.31c) shows large Se depletion and O enrichment. From the measured compositions a decrease in mean inner potential of 3.3 eV was calculated at the grain boundary, which is not significantly different from the measured value, given that O enrichment and changes in density were not included in the calculation. Experimental artifacts such as surface grooves [137] and fringing fields [138] outside the TEM specimen can also complicate the measurement. The fringing fields increase with relative permittivity of the specimen but should have a small effect on the projected potential measured provided the specimen thickness is greater than ~10 nm.

For recombination velocity and barrier height measurements, an important consideration is the effect of the high-energy electron beam, which creates electron–hole pairs in the material in addition to the intrinsic thermal generation rate. This is similar to a solar cell under working conditions, but there are several differences between electron illumination and solar illumination. First, electrons interact more strongly with matter due to their charge, and second, an electron can generate multiple electron–hole pairs compared to only one electron–hole pair per photon. As an example Galloway et al. [115] calculated that the photogenerated carrier profile in CdTe under AM1.5 illumination is similar to that of an 11 keV electron beam with only 1 pA current; in most experiments the electron–hole pairs generated by the electron beam will therefore exceed that of a solar cell under standard working conditions. The excess electron–hole pairs decrease the occupancy of defect states at the grain boundary, so that above a critical illumination intensity both the barrier height and recombination velocity decrease rapidly [139]. This is a potential problem for measuring the recombination velocity in the SEM, since the incident electron must lose all of its energy to the solid provided it is not backscattered out of the specimen. However, for TEM measurement of barrier heights, the use of high-energy electrons transmitted through a thin foil means that energy transfer is minimized, so that the grain boundary characteristics are likely to be closer to that of a real solar cell device. It can be argued therefore that the recombination velocity should also be measured in the TEM rather than SEM, but the presence of two free surfaces in a TEM thin foil means that the boundary conditions deviate significantly from the models used to extract the recombination velocity (Sect. 5.2).

6 Materials Issues in Organic Solar Cells

As mentioned in Sect. 3.4, the morphology of bulk heterojunction solar cells consists of phase-separated donor and acceptor components. A large donor-acceptor interface area is required for carrier generation through exciton dissociation while simultaneously creating efficient percolation pathways for the free carriers to drift/diffuse towards the collection electrodes. Several methods are used to optimize the microstructure, such as the use of solvent additives during

deposition and post-deposition processes such as thermal and solvent annealing. TEM is ideal for imaging the nanoscale phase separation but a simple 2D projection is insufficient to characterize the morphology in any great detail. In electron tomography a series of images is acquired at different specimen tilts and the resulting information used to reconstruct the 3D object (for reviews see, e.g., [140, 141]). It is ideally suited to characterize hybrid solar cells [142] where the acceptor is an inorganic semiconductor (e.g., CdSe, ZnO) and the donor a polymer such as P3HT. The high contrast between the inorganic material and polymer makes it relatively easy to distinguish the two components, using, for example, high-angle annular dark-field (HAADF) imaging in a scanning TEM (STEM). From the tomograms important parameters such as the distance between a polymer voxel and the nearest donor-acceptor interface (governs carrier generation), fraction of inorganic semiconductor forming percolation pathways to the cathode (carrier collection), etc. can be analyzed [143, 144].

Electron tomography of bulk heterojunction solar cells where the donor is a polymer (e.g., P3HT) and acceptor a small molecule (e.g., PCBM) is complicated by the low contrast between the two carbon-rich components. Nevertheless there are several studies in the literature where tomography is carried out using TEM bright-field images acquired with a defocussed objective lens in order to enhance amplitude contrast. TEM bright-field tomography is rarely used for inorganic materials due to the strong influence of diffraction contrast at discrete tilt angles. In organic materials however diffraction is typically not a problem, and in the case of (semi-)crystalline P3HT the crystallinity is rapidly destroyed on exposure to the electron beam, so that only the outlines of the more dense crystals remain, which are nevertheless stable to the electron doses required for a typical tomography experiment [141]. However, the fact that bright-field images must be defocussed means that the spatial resolution is degraded and Fresnel fringing artifacts are introduced into the reconstruction. Bright-field electron tomography has been used to examine the effects of processing on the microstructure of P3HT-PCBM solar cells [145]. Figure 2.32 shows the reconstructed volumes of the as-spin-coated, thermal-annealed (130 °C for 20 min), and solvent-annealed (3 h in *ortho*-dichlorobenzene) P3HT-PCBM absorber layer, together with slices extracted from the reconstruction from near the cathode, anode, and bulk regions. Long fiber-like features are observed for the thermal- and solvent-annealed material, which correspond to crystalline P3HT [146], but not for the as-spin-coated sample. The π-stacking within these fibers give better hole mobility leading to higher-efficiency devices [35]. Furthermore tomography revealed the P3HT fibers to be concentrated near the anode region which facilitates hole collection (it should be emphasized however that this trend is dependent on sample fabrication). Bright-field electron tomography has also been applied to another widely studied bulk heterojunction solar cell, MDMO-PPV/PCBM [147]. It was found that for the high efficiency, 80 wt% PCBM device thin PCBM strands linked the individual PCBM domains, thus forming efficient percolation pathways for electron transport. Similar interlinks were not observed for lower PCBM concentrations which could explain the lower device efficiencies.

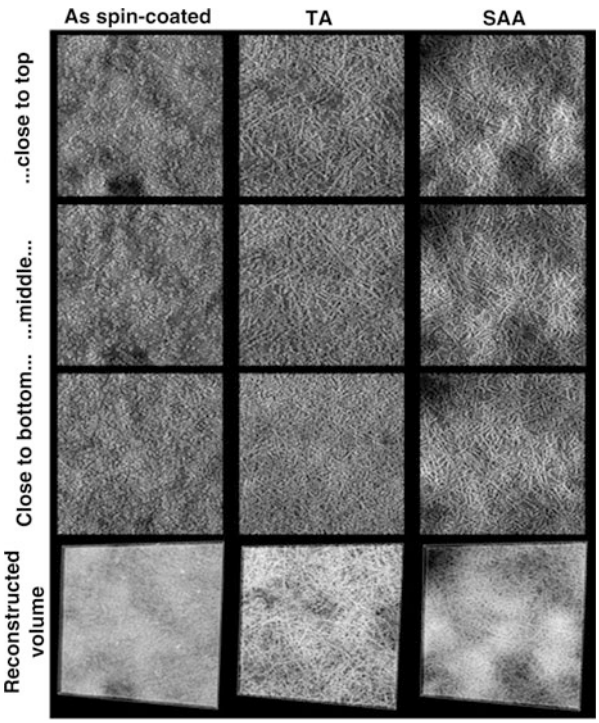


Fig. 2.32 Reconstructed bright-field electron tomograms of a P3HT-PCBM layer in the as- spin-coated, thermal-annealed (TA; 130 °C/20 min), and solvent-assisted-annealed (SAA; 3 h in *ortho*-dichlorobenzene) states. Also shown are extracted slices from the top region (i.e., close to the cathode), bottom region (i.e., close to the anode), and bulk for each specimen (Reproduced with permission from [145]. Copyright 2009 American Chemical Society)

A different approach to electron tomography of bulk heterojunction solar cells such as P3HT-PCBM was proposed by Herzing et al. [148]. Here the small difference in plasmon energy between P3HT (22.2 eV) and PCBM (25.5 eV) is used to generate contrast via energy-filtered imaging. Principal component analysis indicated that the contrast is strongest at 19 and 27 eV, respectively (Fig. 2.33a). An energy-filtered image acquired with a 5 eV wide slit centered at 19 eV revealed a higher intensity for the lower plasmon energy P3HT fibers (Fig. 2.33b). On the other hand, if the slit was centered at 27 eV, the higher-energy plasmon PCBM phase appeared brighter (Fig. 2.33c). The PCBM is seen to occupy the regions between the P3HT fibers. Importantly the contrast in these energy-filtered images is significantly greater than an in-focus bright-field TEM image, which enables electron tomography at much higher spatial resolutions (see Fig. 2.6 in [148] for a comparison of bright-field and energy-filtered tomograms). However, it is important to bear in mind that the plasmon signal does not satisfy the projection criterion for tomography, i.e., its intensity is not proportional to the projected specimen thickness. Multiple scattering is strong when the projected thickness exceeds the plasmon mean free path, a condition commonly observed at large specimen tilts (e.g., a 70° tilt increases the projected thickness by a factor of 3). This can be a problem for solar cells where the absorber layer thickness is typically of the order of the plasmon mean free path (∼100 nm) for efficient light absorption. Hence even at zero tilts the specimen is likely to exhibit multiple scattering.

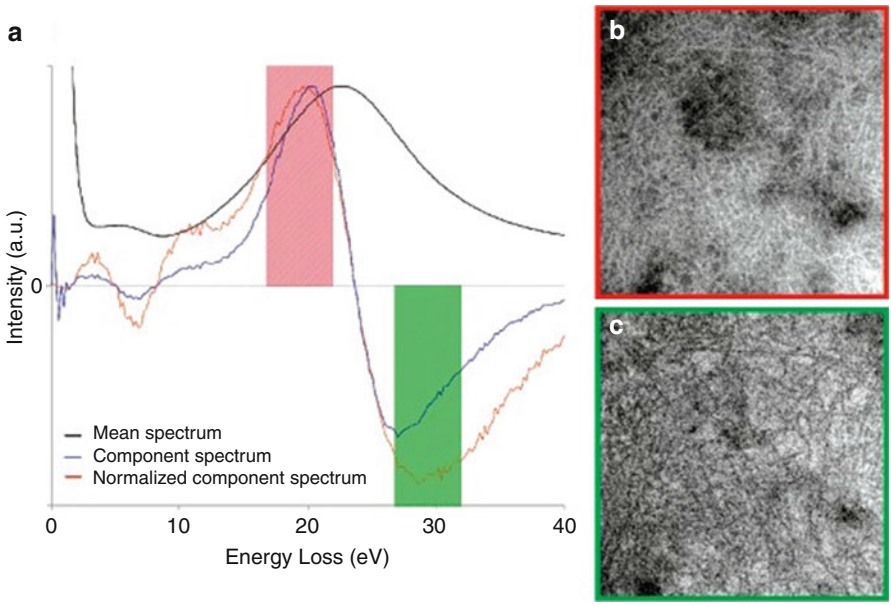


Fig. 2.33 (**a**) Mean electron energy loss spectrum for a P3HT-PCBM thin film (*black line*). The *blue line* is a spectral component from principal component analysis measuring the difference between spectra for pure P3HT and pure PCBM. To get an indication of contrast this curve is divided by the mean spectrum to generate the *red line* which has extrema at 19 and 27 eV. The energy-filtered images acquired at 19 and 27 eV are shown in (**b**) and (**c**) and highlight P3HT and PCBM regions, respectively. The energy selecting slit width is 5 eV (Adapted from [148]. Reproduced with permission; Copyright 2010 American Chemical Society)

References

1. Shockley W, Queisser HJ (1960) Detailed balance limit of efficiency of pn junction solar cells. J Appl Phys 32:510–519
2. Green MA, Emery K, Hishikawa Y, Warta W, Dunlop ED (2013) Solar cell efficiency tables (version 41). Prog Photovolt Res Appl 21:1–11
3. Henry CH (1980) Limiting efficiencies of ideal single and multiple energy gap terrestrial solar cells. J Appl Phys 51:4494
4. Riordan C, Hulstrom R (1990) What is an air mass 1.5 spectrum. Photovolt Spec Conf 21:1085–1088
5. Burgers AR, Eikelboom JA, Schoenecker A, Sinke WC (1996) Improved treatment of the strongly varying slope in fitting solar cell I-V curves. Photovolt Spec Conf 25:569–572
6. Hegedus SS, Shafarman WN (2004) Thin-film solar cells: device measurements and analysis. Prog Photovolt Res Appl 12:155–176
7. Dhere RG, Duenow JN, Dehart CM, Li JV, Kuciauskas D, Gessert TA (2012) Development of substrate structure CdTe photovoltaic devices with performance exceeding 10%. Photovolt Spec Conf 38:003208–003211
8. Wu JJ, Wu HC, Zhao CZ (2012) CdTe solar cells on flexible metallic substrates. Adv Mater Res 535:2075–2078

9. Cusano DA (1963) CdTe solar cells and photovoltaic heterojunctions in II-VI compounds. Solid State Electron 6:217–233
10. Bonnet D, Rabenhorst H (1972) New results on the development of a thin film p-CdTe- nCdS heterojunction solar cell. Photovolt Spec Conf 9:129–132
11. Tyan Y-S, Perez-Albuerne EA (1982) Integrated array of photovoltaic cells having minimized shorting losses. US Patent No. 4315096
12. Britt J, Ferekides C (1993) Thin-film CdS/CdTe solar cell with 15.8% efficiency. Appl Phys Lett 62:2851–2852
13. Wu X, Keane JC, Dhere RG, DeHart C, Duda A, Gessert TA, Sheldon P (2001) 16.5% efficient CdS/CdTe polycrystalline thin-film solar cell. In: Proceedings of the 17th European photovoltaic solar energy conference, Munich, p 995
14. Shay JL, Wagner S, Kasper HM (1975) Efficient $CuInSe_2$/CdS solar cells. Appl Phys Lett 27:89–90
15. Mickelsen RA, Chen WS, Hsiao YR, Lowe VE (1984) Polycrystalline thin-film $CuInSe_2$/CdZnS solar cells. Electron Devices 5:542–546
16. Gabor AM, Tuttle JR, Albin DS, Contreras MA, Noufi R, Hermann AM (1994) High-efficiency $CuIn_xGa_{1-x}Se_2$ solar cells made from $(In_xGa_{1-x})_2Se_3$ precursor films. Appl Phys Lett 65:198–200
17. Chen S, Gong XG, Walsh A, Wei S-H (2009) Crystal and electronic band structure of Cu_2ZnSnX_4 (X = S and Se) photovoltaic absorbers: first principles insights. Appl Phys Lett 94:041903
18. Wang K, Gunawan O, Todorov T, Shin B, Chey SJ, Bojarczuk NA, Mitzi D, Guha S (2010) Thermally evaporated Cu_2ZnSnS_4 solar cells. Appl Phys Lett 97:143508
19. Repins I, Beall C, Vora N, DeHart C, Kuciauskas D, Dippo P, To B, Mann J, Hsu W-C, Goodrich A, Noufi R (2012) Co-evaporated Cu_2ZnSnS_4 films and devices. Sol Energy Mater Sol Cells 101:154–159
20. Todorov TK, Reuter KB, Mitzi DB (2010) High-efficiency solar cell with earth- abundant liquid-processed absorber. Adv Energy Mater 22:E156–E159
21. Todorov TK, Tang J, Bag S, Gunawan O, Gokmen T, Zhu Y, Mitzi DB (2013) Beyond 11 % efficiency: characteristics of state-of-the-art $Cu_2ZnSn(S, Se)_4$ solar cells. Adv Energy Mater 3:34–38
22. Scragg JJ, Dale PJ, Peter LM (2009) Synthesis and characterization of Cu_2ZnSnS_4 absorber layers by an electrodeposition-annealing route. Thin Solid Films 517:2481–2484
23. Chan CP, Lam H, Surya C (2010) Preparation of Cu_2ZnSnS_4 films by electrodeposition using ionic liquids. Sol Energy Mater Sol Cells 94:207–211
24. Romero MJ, Dui H, Teeter G, Yan Y, Al-Jassim MM (2011) Comparative study of the luminescence and intrinsic point defects in the kesterite Cu_2ZnSnS_4 and chalcopyrite $Cu(In, Ga)Se_2$ thin films used in photovoltaic applications. Phys Rev B 84:165324
25. Thompson BC, Fréchet JMJ (2008) Polymer-fullerene composite solar cells. Ang Chem Int Ed 47:58–77
26. Sariciftci NS, Smilowitz LB, Heeger AJ, Wudl F (1992) Photoinduced electron transfer from a conducting polymer to buckminsterfullerene. Science 258:1474–1476
27. Clarke TM, Durrant JR (2010) Charge photogeneration in organic solar cells. Chem Rev 110:6736–6767
28. Haugeneder A, Neges M, Kallinger C, Spirkl W, Lemmer U, Feldmann J, Scherf U, Harth E, Gügel A, Mllen K (1999) Exciton diffusion and dissociation in conjugated polymer/fullerene blends and heterostructures. Phys Rev B 59:15346–15351
29. Liang Y, Xu Z, Xia J, Ting Tsai S, Wu Y, Li G, Ray C, Yu L (2010) For the bright future-bulk heterojunction polymer solar cells with power conversion efficiency of 7.4%. Adv Mater 22:E135–E138
30. He Z, Zhong C, Huang X, Wong WY, Wu H, Chen L, Su S, Cao Y (2011) Simultaneous enhancement of open circuit voltage, short circuit current density and fill factor in polymer solar cells. Adv Mater 23:4636–4643

31. Ma WL, Yang CY, Gong X, Lee K, Heeger AJ (2005) Thermally stable, efficient polymer solar cells with nanoscale control of the interpenetrating network morphology. Adv Funct Mater 15:1617–1622
32. Wang T, Pearson AJ, Lidzey DG, Jones RAL (2011) Evolution of structure, optoelectronic properties and device performance of polythiophene: fullerene solar cells during thermal annealing. Adv Funct Mater 21:1383–1390
33. Pearson AJ, Wang T, Jones RAL, Lidzey DG, Staniec PA, Hopkinson PE, Donald AM (2012) Rationalising phase transitions with thermal annealing temperatures for P3HT: PCBM organic photovoltaic devices. Macromolecules 45:1499–1508
34. Li G, Shrotriya V, Yao Y, Huang J, Yang Y (2007) Manipulating regioregular poly(3-hexylthiophene): [6, 6]-phenyl-C61-butyric acid methyl ester blends-route towards high efficiency polymer solar cells. J Mater Chem 17:3126–3140
35. Berson S, De Bettignies R, Bailly S, Guillerez S (2007) Poly(3-hexylthiophene) fibres for photovoltaic applications. Adv Funct Mater 17:1377–1384
36. Li G, Yao Y, Yang H, Shrotriya V, Yang G, Yang Y (2007) Solvent annealing effect in polymer solar cells based on poly(3-hexylthiophene) and methanofullerenes. Adv Funct Mater 17:1636–1644
37. Yao Y, Hou J, Xu Z, Li G, Yang Y (2008) Effect of solvent mixtures on the nanoscale phase separation in polymer solar cells. Adv Funct Mater 18:1783–1789
38. Lee JK, Ma WL, Brabec CJ, Yuen J, Moon JS, Kim JY, Lee K, Bazan GC, Heeger AJ (2008) Processing additives for improved efficiency from bulk heterojunction solar cells. J Am Chem Soc 130:3619–3623
39. De Sio A, Madena T, Huber R, Parisi J, Neyshtadt S, Deschler F, Da Como E, Esposito S, von Hauff E (2011) Solvent additives for tuning the photovoltaic properties of polymer-fullerene solar cells. Sol Energy Mater Sol Cells 95:3536–3542
40. Nowell MM, Scarpulla MA, Compaan AD, Liu X, Paudel NR, Kwon D, Wieland KA (2011) Electron backscatter diffraction and photoluminescence of sputtered CdTe thin films. Photovolt Spec Conf 37:001327–001332
41. Nowell MM, Wright SI, Scarpulla MA, Compaan AD, Liu X, Paudel NR, Wieland KA (2012) The correlation of performance in CdTe photovoltaics with grain boundaries. Phys Fail Anal Integ Circ 19:1–7
42. Wald FV, Entine G (1978) Crystal growth of CdTe for γ-ray detectors. Nucl Inst Methods 150:13–23
43. Toušková DK, Toušek J (1997) Preparation and characterisation of CdS/CdTe thin film solar cells. Thin Solid Films 293:272–276
44. Hommel D, Waag A, Scholl S, Landwehr G (1992) Chlorine: a new efficient n-type dopant in CdTe layers grown by molecular beam epitaxy. Appl Phys Lett 1:1546–1548
45. Romeo A, Bätzner DL, Zogg H, Tiwari AN (2000) Recrystallization in CdTe/CdS. Thin Solid Films 361-362:420–425
46. Niles DW, Waters D, Rose D (1998) Chemical reactivity of $CdCl_2$ wet-deposited on CdTe films studied by X-ray photoelectron spectroscopy. Appl Surf Sci 136:221–229
47. Terheggen M, Heinrich H, Kostorz G, Baetzner D, Romeo A, Tiwari AN (2004) Analysis of bulk and interface phenomena in CdTe/CdS thin-film solar cells. Interf Sci 12:259–266
48. Durose K, Edwards PR, Halliday DP (1999) Materials aspects of CdTe/CdS solar cells. J Cryst Growth 197:733–742
49. Romero MJ, Al-Jassim MM, Dhere RG, Hasoon FS, Contreras MA, Gessert TA, Moutinho HR (2002) Beam injection methods for characterizing thin-film solar cells. Prog Photovolt Res Appl 10:445–455
50. Consonni V, Feuillet G, Renet S (2006) Spectroscopic analysis of defects in chlorine doped polycrystalline CdTe. J Appl Phys 99:053502
51. Yan Y, Al-Jassim MM, Jones KM (2003) Structure and effects of double-positioning twin boundaries in CdTe. J Appl Phys 94:2976

52. Yan Y, Jones KM, Jiang CS, Wu XZ, Noufi R, Al-Jassim MM (2007) Understanding the defect physics in polycrystalline photovoltaic materials. Physica B 401–402:25–32
53. Yan Y, Jones KM, Al-Jassim MM, Dhere R, Wu X (2011) Transmission electron microscopy study of dislocations and interfaces in CdTe solar cells. Thin Solid Films 519:7168–7172
54. Ohata K, Saraie J, Tanaka T (1973) Phase diagram of the CdS-CdTe pseudobinary system. Jpn J Appl Phys 12:1198
55. Lane DW, Conibeer GJ, Wood DA, Capper P, Romani S, Hearne S (1999) Sulfur diffusion in CdTe and the phase diagram of the CdS-CdTe pseudo-binary alloy. J Cryst Growth 197:743–748
56. Lane DW, Rogers KD, Painter JD, Wood DA, Ozsan ME (2000) Structural dynamics in CdS-CdTe thin films. Thin Solid Films 361–362:1–8
57. Moutinho HR, Dhere RG, Jiang C-S, Yan Y, Albin DS, Al-Jassim MM (2010) Investigation of potential and electric field profiles in cross sections of CdTe/CdS solar cells using scanning Kelvin probe microscopy. J Appl Phys 108:074503
58. Albin DS, Yan Y, Al-Jassim MM (2002) The effect of oxygen on interface microstructure evolution in CdS/CdTe solar cells. Prog Photovolt Res Appl 10:309–322
59. Edwards PR, Halliday DP, Durose K, Richter H, Bonnet D (1997) The influence of $CdCl_2$ treatment and interdiffusion on grain boundary passivation in CdTe/CdS solar cells. In: Proceedings of the 14th European photovoltaic solar energy conference, Barcelona, pp 2083–2086
60. McCandless BE, Engelmann MG, Birkmire RW (2001) Interdiffusion of the CdS/CdTe thin films: modeling x-ray diffraction line profiles. J Appl Phys 89:988–994
61. Metzger WK, Albin D, Romero MJ, Dippo P, Young M (2006) $CdCl_2$ treatment, S diffusion and recombination in polycrystalline CdTe. J Appl Phys 99:103703
62. Gessert TA, Burst JM, Wei S-H, Ma J, Kuciauskas D, Rance WL, Barnes TM, Duenow JN, Reese MO, Li JV, Yound MR, Dippo P (2012) Pathways toward higher performance CdS/CdTe devices: Te exposure of CdTe surface before ZnTe:Cu/Ti contacting. Thin Solid Films 535:237–240
63. Jarkov A, Bereznev S, Laes K, Volobujeva O, Traksmaa R, ÖPik A, Mellikov E (2011) Conductive polymer PEDOT: PSS back contact for CdTe solar cell. Thin Solid Films 519:7449–7452
64. Taylor AA, Major JD, Phillips L, McLeod I, Durose K, Mendis B.G Manuscript in preparation
65. Irvine SJC, Barrioz V, Lamb D, Jones EW, Rowlands-Jones RL (2008) MOCVD of thin film photovoltaic solar cells – next generation production technology? J Cryst Growth 310:5198–5203
66. Swanson DE, Lutze RM, Sampath WS, Williams JD (2012) Plasma cleaning of TCO surfaces prior to CdS/CdTe deposition. Photovolt Spec Conf 38:000859–000863
67. Gabor AM, Tuttle JR, Bode MH, Franz A, Tennant AL, Contreras MA, Noufi R, Jensen DG, Hermann AM (1996) Band-gap engineering in Cu(In, Ga)Se_2 thin films grown from (In, Ga)$_2Se_3$ precursors. Sol Energy Mater Sol Cells 41:247–260
68. Dullweber T, Lundberg O, Malmström J, Bodegård M, Stolt L, Rau U, Schock H-W, Werner JH (2001) Back surface band gap gradings in Cu(In,Ga)Se_2 solar cells. Thin Solid Films 387:11–13
69. Wada T, Kohara N, Nishiwaki S, Negami T (2001) Characterization of the Cu(In, Ga)Se_2/Mo interface in CIGS solar cells. Thin Solid Films 387:118–122
70. Nishiwaki S, Kohara N, Negami T, Wada T (1998) $MoSe_2$ layer formation at Cu(In, Ga)Se_2/Mo interfaces in high efficiency Cu($In_{1-x}Gax$)Se_2 solar cells. Jpn J Appl Phys 37:L71–L73
71. Scheer R, Diesner K, Lewerenz H-J (1995) Experiments on the microstructure of evaporated $CuInS_2$ thin films. Thin Solid Films 268:130–136
72. Klenk R, Walter T, Schmid D, Schock HW (1993) Growth mechanisms and diffusion in multinary and multilayer chalcopyrite thin films. Jpn J Appl Phys 32:57–61

73. Hasoon FS, Yan Y, Althani H, Jones KM, Moutinho HR, Alleman J, Al- Jassim MM, Noufi R (2001) Microstructural properties of Cu(In,Ga)Se_2 thin films used in high-efficiency devices. Thin Solid Films 387:1–5
74. Wei S-H, Zunger A (1995) Band offsets and optical bowings of chalcopyrites and Zn- based II-VI alloys. J Appl Phys 78:3846–3856
75. Abou-Ras D, Schorr S, Schock H-W (2007) Grain-size distributions and grain boundaries of chalcopyrite-type thin films. J Appl Crystallogr 40:841–848
76. Abou-Ras D, Koch CT, Vüstner V, van Aken PA, Jahn U, Contreras MA, Ca-ballero R, Kaufmann CA, Scheer R, Unold T, Schock H-W (2009) Grain-boundary types in chalcopyrite-type thin films and their correlations with film texture and electrical properties. Thin Solid Films 517:2545–2549
77. Ott N, Hanna G, Rau U, Werner JH, Strunk HP (2004) Texture of Cu(In, Ga)Se_2 thin films and nanoscale cathodoluminescence. J Phys Condens Matter 16:S85
78. Repins I, Contreras M, Romero M, Yan Y, Metzger W, Li J, Johnston S, Egaas B, DeHart C, Scharf J, McCandless BE, Noufi R (2008) Characterization of 19.9% efficient CIGC absorbers. Photovolt Spec Conf 33:1–6
79. Romero MJ, Ramanathan K, Contreras MA, Al-Jassim MM, Noufi R, Sheldon P (2003) Cathodoluminescence of Cu(In, Ga)Se_2 thin films used in high-efficiency solar cells. Appl Phys Lett 83:4770–4772
80. Shklovskii BI, Efros AL (1984) Electronic properties of doped semiconductors. Springer, Germany.
81. Bodegård M, Stolt L, Hedstrom J (1994) The influence of sodium on the grain structure of $CuInSe_2$ films for photovoltaics applications. Eur Sol Energy Conf 12:1743–1746
82. Bodegård M, Granath K, Stolt L (2000) Growth of Cu(In,Ga)Se_2 thin films by coevaporation using alkaline precursors. Thin Solid Films 361:9–16
83. Rudmann D, Bilger G, Kaelin M, Haug F-J, Zogg H, Tiwari AN (2003) Effects of NaF coevaporation on the structural properties of Cu(In, Ga)Se_2 thin films. Thin Solid Films 431:37–40
84. Jasenek A, Rau U, Nadenau V, Schock H-W (2000) Electronic properties of CuGaSe- based heterojunction solar cells. Part II. Defect Spectroscopy. J Appl Phys 87:594
85. Rudmann D, Da Cunha AF, Kaelin M, Kurdesau F, Zogg H, Tiwari AN, Bilger G (2004) Efficiency enhancement of Cu(In, Ga)Se_2 solar cells due to post-deposition Na incorporation. Appl Phys Lett 84:1129–1131
86. Cahen D, Noufi R (1989) Defect chemical explanation for the effect of air anneal on CdS/$CuInSe_2$ solar cell performance. Appl Phys Lett 54:558–560
87. Lei C, Li CM, Rockett A, Robertson IM (2007) Grain boundary compositions in Cu(In, Ga)Se_2. J Appl Phys 101:024909
88. Abou-Ras D, Schaffer B, Schaffer M, Schmidt SS, Caballero R, Unold T (2012) Direct insight into grain boundary reconstruction in polycrystalline Cu(In, G)$Se_2$with atomic resolution. Phys Rev Lett 108:075502
89. Niles DW, Al-Jassim MM, Ramanathan K (1999) Direct observation of Na and O impurities at grain surfaces of $CuInSe_2$ thin films. J Vacuum Sci Technol A Vacuum, Surf Films 17:291–296
90. Cadel E, Barreau N, Kessler J, Pareige P (2010) Atom probe study of sodium distribution in polycrystalline Cu(In, Ga)Se_2 thin film. Acta Mater 58:2634–2637
91. Scheer R, Schock H-W (2011) Chalcogenide photovoltaics: physics, technologies and thin film devices. Wiley-VCH Verlag GmbH & Co. KGaA, Germany
92. Nagoya A, Asahi R, Wahl R, Kresse G (2010) Defect formation and phase stability of Cu_2ZnSnS_4 photovoltaic materials. Phys Rev B 81:113202
93. Mendis BG, Shannon MD, Goodman MCJ, Major JD, Claridge R, Halliday DP, Durose K (2012) Direct observation of Cu, Zn cation disorder in Cu_2ZnSnS_4 solar cell absorber material using aberration corrected scanning electron microscopy. Prog Photovolt Res Appl. doi:10.1002/pip.2279

94. Schorr S (2011) The crystal structure of kesterite type compounds: a neutron and X-ray diffraction study. Sol Energy Mater Sol Cells 95:1482–1488
95. Wätjen TW, Engman J, Edoff M, Platzer-Björkman C (2012) Direct evidence of current blocking by ZnSe in $Cu_2ZnSnSe_4$ solar cells. Appl Phys Lett 100:173510
96. Dale PJ, Hoenes K, Scragg JJ, Siebentritt S (2009) A review of the challenges facing kesterite based thin film solar cells. Photovolt Specialists Conf (PVSC) 34:002080–002085
97. Fontané X, Calvo-Barrio L, Izquierdo-Roca Z, Saucedo E, Pérez-Rodriguez A, Morante JR, Berg DM, Dale PJ, Siebentritt S (2011) In-depth resolved Raman scattering analysis for the identification of secondary phases: characterisation of Cu_2ZnSnS_4 layers for solar cell applications. Appl Phys Lett 98:181905
98. Wang K, Shin B, Reuter KB, Todorov T, Mitzi DB, Guha S (2011) Structural and elemental characterization of high efficiency Cu_2ZnSnS_4 solar cells. Appl Phys Lett 98:051912
99. Platzer-Björkman C, Scragg JJ, Flammersberger H, Kubart T, Edoff M (2012) Influence of precursor sulfur content on the film formation and compositional changes in Cu_2ZnSnS_4 films and solar cells. Sol Energy Mater Sol Cells 98:110–117
100. Scragg JJ, Dale PJ, Colombara D, Peter LM (2012) Thermodynamic aspects of the synthesis of then-film materials for solar cells. Chem Phys Chem 13:3035–3046
101. Wätjen TW, Scragg JJ, Ericson T, Edoff M, Platzer-Björkman C (2012) Secondary compound formation revealed by transmission electron microscopy at the Cu_2ZnSnS_4/Mo interface. Thin Solid Films 535:31–34
102. Barkhouse DAR, Gunawan O, Gokmen T, Todorov TK, Mitzi DB (2012) Device characteristics of a 10.1 % hydrazine-processed $Cu_2ZnSn(Se, S)_4$ solar cell. Prog Photovolt Res Appl 20:6–11
103. Taretto K, Rau U, Werner JH (2005) Numerical simulation of grain boundary effects in $Cu(In,Ga)Se_2$ thin film solar cells. Thin Solid Films 480–481:8–12
104. Nerat M, Černivec G, Smole F, Topič M (2008) Simulation study of the effects of grain shape and size on the performance of $Cu(In,Ga)Se_2$ solar cells. J Appl Phys 104:083706
105. Metzger WK, Gloeckler M (2005) The impact of charged grain boundaries on thin film solar cells and characterisation. J Appl Phys 98:063701
106. Gloeckler M, Sites JR, Metzger WK (2005) Grain boundary recombination in $Cu(In, Ga)Se_2$ solar cells. J Appl Phys 98:113704
107. Major JD, Proskuryakov YY, Durose K, Zoppi G, Forbes I (2010) Control of grain size in sublimation grown CdTe and the improvement in performance of devices with systematically increased grain size. Sol Energy Mater Sol Cells 94:1107–1112
108. Visoly-Fisher I, Cohen SR, Gartsman K, Ruzin A, Cahen D (2006) Understanding the beneficial role of grain boundaries in polycrystalline solar cells from single grain boundary scanning probe microscopy. Adv Funct Mater 16:649–660
109. Jiang CS, Noufi R, Ramanathan K, AbuShama JA, Moutinho HR, Al-Jassim MM (2004) Does the local built-in potential on grain boundaries of $Cu(In, Ga)Se_2$ thin films benefit photovoltaic performance of the device? Appl Phys Lett 85:2625–2627
110. Terheggen M, Heinrich H, Kostorz G, Romeo A, Baetzner D, Tiwari AN, Bosio A, Romeo N (2003) Structural and chemical interface characterisation of CdTe solar cells by transmission electron microscopy. Thin Solid Films 431–432:262–266
111. Yan Y, Al-Jassim MM, Jones KM (2004) Passivation of double positioning twin boundaries in CdTe. J Appl Phys 96:320–326
112. Zhang L, Da Silva JLF, Li J, Yan Y, Gessert TA, Huai Wei S (2008) Effect of co-passivation of Cl and Cu on CdTe grain boundaries. Phys Rev Lett 101:155501
113. Hofmann DM, Omling P, Grimmeiss HG, Meyer BK, Benz KW, Sinerius D (1992) Identification of the chlorine A-centre in CdTe. Phys Rev B 45:6247–6250
114. Halliday DP, Eggleston JM, Durose K (1998) A photoluminescence study of polycrystalline thin film CdTe/CdS solar cells. J Cryst Growth 186:543–549
115. Galloway SA, Edwards PR, Durose K (1999) Characterisation of thin film CdS/CdTe solar cells using electron and optical beam induced current. Sol Energy Mater Sol Cells 57:61–74

116. Edwards PR, Galloway SA, Durose K (2000) Erratum to EBIC and luminescence mapping of CdTe/CdS solar cells. Thin Solid Films 372:284–291
117. Visoly-Fisher I, Cohen SR, Cahen D (2003) Direct evidence for grain boundary depletion in polycrystalline CdTe from nanoscale resolved measurements. Appl Phys Lett 82:556–558
118. Woods LM, Levi DH, Kaydanov V, Robinson GY, Ahrenkiel RK (1998) Proceedings of 2nd world conference on photovoltaic solar energy conversion, vol 1. European Commission, Ispra, Italy, p 1043–1046
119. Woods LM, Robinson GY, Levi DH (2000) The effects of $CdCl_2$ on CdTe electrical properties using a new theory for grain boundary conduction. Proceedings of 28th IEEE photovoltaic specialists conference. IEEE, Piscataway, NJ, p 603–606
120. Cojocaru-Mirédin O, Choi P, Wuerz R, Raabe D (2011) Atomic scale distribution of impurities in $CuInSe_2$-based thin film solar cells. Ultramicroscopy 111:552–556
121. Jiang CS, Noufi R, AbuShama JA, Ramanathan K, Moutinho HR, Pankow J, Al-Jassim MM (2004) Local built-in potential on grain boundary of Cu(In, Ga)Se_2. Appl Phys Lett 84:3477
122. Azulay D, Balberg I, Millo O (2012) Microscopic evidence for the modification of the electronic structure at grain boundaries of $Cu(In_{1-x}Ga_x)Se_2$ films. Phys Rev Lett 108:076603
123. Yan Y, Jiang CS, Noufi R, Huai Wei S, Moutinho HR, Al-Jassim MM (2007) Electrically benign behaviour of grain boundaries in polycrystalline $CuInSe_2$ films. Phys Rev Lett 99:235504
124. Mönig H, Smith Y, Caballero R, Kaufmann CA, Lauermann I, Lux-Steiner MCH, Sadewasser S (2010) Direct evidence for a reduced density of deep level defects at grain boundaries of Cu(In,Ga)Se_2 thin films. Phys Rev Lett 105:116802
125. Persson C, Zunger A (2003) Anomalous grain boundary physics in polycrystalline $CuInSe_2$: the existence of a hole barrier. Phys Rev Lett 91:266401
126. Zhang SB, Huai Wei S, Zunger A, Katayama-Yoshida H (1998) Defect physics of the $CuInSe_2$ chalcopyrite semiconductor. Phys Rev B 57:9642–9655
127. Donolato C (1983) Theory of beam induced current characterisation of grain boundaries in polycrystalline solar cells. J Appl Phys 54:1314–1322
128. Mendis BG, Bowen L, Jiang QZ (2010) A contactless method for measuring the recombination velocity of an individual grain boundary in thin film photovoltaics. Appl Phys Lett 97:092112
129. Corkish R, Puzzer T, Sproul AB, Luke KL (1998) Quantitative interpretation of electron beam induced current grain boundary contrast profiles with application to silicon. J Appl Phys 84:5473–5481
130. Van Roosbroeck W (1955) Injected current carrier transport in a semi-infinite semiconductor and the determination of lifetimes and surface recombination velocities. J Appl Phys 26:380–391
131. Watson CCR, Durose K (1993) Cathodoluminescence microscopy of bulk CdTe crystals. J Cryst Growth 126:325–329
132. Mendis BG, Goodman MCJ, Major JD, Taylor AA, Durose K, Halliday DP (2012) The role of secondary phase precipitation on grain boundary electrical activity in Cu_2ZnSnS_4 (CZTS) photovoltaic absorber layer material. J Appl Phys 112:124508
133. Mendis BG, Bowen L (2011) Cathodoluminescence measurement of grain boundary recombination velocity in vapour grown p-CdTe. J Phys Conf Ser 326:012017
134. Allen LJ, McBride W, O'Leary NL, Oxley MP (2004) Exit wave reconstruction at atomic resolution. Ultramicroscopy 100:91–104
135. Bhattacharyya S, Koch CT, Rühle M (2006) Projected potential profiles across inter- faces obtained by reconstructing the exit face wavefunction from through focal series. Ultramicroscopy 106:525–538
136. Abou-Ras D, Schmidt SS, Caballero R, Unold T, Werner Schock H, Koch CT, Schaffer B, Schaffer M, Pa Choi P, Cojocaru-Mirédin O (2012) Confined and chemically flexible grain boundaries in polycrystalline compound semiconductors. Adv Energy Mater 2:992–998

137. Dunin-Borkowski RE (2000) The development of Fresnel contrast analysis and the interpretation of mean inner potential profiles at interfaces. Ultramicroscopy 83:193–216
138. Dunin-Borkowski RE, Saxton WO (1997) The electrostatic contribution to the forward scattering potential at a space charge layer in high energy electron diffraction. II fringing fields. Acta Crystallogr A 53:242–250
139. Oualid J, Singal CM, Dugas J, Crest JP, Amzil H (1984) Influence of illumination on the grain boundary recombination velocity in silicon. J Appl Phys 55:1195–1205
140. Midgley PA, Weyland M (2003) 3D electron microscopy in the physical sciences: the development of Z-contrast and EFTEM tomography. Ultramicroscopy 96:413–431
141. van Bavel SS, Loos J (2010) Volume organisation of polymer and hybrid solar cells as revealed by electron tomography. Adv Funct Mater 20:3217–3234
142. Huynh WU, Dittmer JJ, Alivisatos AP (2002) Hybrid nanorod-polymer solar cells. Science 295:2425–2427
143. Oosterhout SD, Wienk MM, van Bavel SS, Thiedmann R, Koster LJA, Gilot J, Loos J, Schmidt V, Janssen RAJ (2009) The effect of three-dimensional morphology on the efficiency of hybrid polymer solar cells. Nat Mater 8:818–824
144. Hindson JC, Saghi Z, Hernandez-Garrido JC, Midgley PA, Greenham NC (2011) Morphological study of nanoparticle-polymer solar cells using high angle annular dark field electron tomography. Nano Lett 11:904–909
145. van Bavel SS, Sourty E, de With G, Loos J (2009) Three dimensional nanoscale organisation of bulk heterojunction polymer solar cells. Nano Lett 9:507–513
146. Brinkmann M, Wittmann JC (2006) Orientation of regioregular poly(3-hexylthiophene) by directional solidification: a simple method to reveal the semicrystalline structure of a conjugated polymer. Adv Mater 18:860–863
147. Yang X, Loos J (2007) Toward high-performance polymer solar cells: the importance of morphology control. Macromolecules 40:1353–1362
148. Herzing AA, Richter LJ, Anderson IM (2010) 3D nanoscale characterisation of thin film organic photovoltaic device structures via spectroscopic contrast in the TEM. J Phys Chem C 114:17501–17508

TEM for Characterization of Semiconductor Nanomaterials

3

Elvio Carlino

Contents

1 Definition of the Topic 89
2 Overview 90
3 Introduction 91
4 Experimental Methodology 95
4.1 Notes on Sample Preparation 95
4.2 Imaging Experiments 97
4.3 Electron Diffraction Experiments 100
4.4 Spectroscopic Experiments 100
4.5 Simulation of TEM Results 103
5 Key Research Findings 107
5.1 TEM/STEM Studies of Heterostructures 107
5.2 Strained Nanostructured Semiconductors 114
5.3 Symmetries in Electron Diffraction and Their Applications 116
5.4 Studies of Clusters with Different Shape and Aspect Ratio 118
5.5 The Challenge of EDX and EELS at Atomic Resolution on Nanostructures 125
6 Conclusions and Future Perspective 132
References 133

1 Definition of the Topic

Transmission electron microscopy (TEM) provides a wide range of methods to study the morphology, the crystal structure and perfection, the chemistry, and the magnetic and the electronic properties of the matter at the highest spatial resolution.

E. Carlino
Centro di Microscopia Elettronica – Consiglio Nazionale delle Ricerche – Istituto di Officina dei Materiali (CNR-IOM-TASC), Trieste, Italy
e-mail: carlino@iom.cnr.it

C.S.S.R. Kumar (ed.), *Transmission Electron Microscopy Characterization of Nanomaterials*, DOI 10.1007/978-3-642-38934-4_3,
© Springer-Verlag Berlin Heidelberg 2014

In this chapter some TEM approaches to study nanostructured semiconductors will be described with the help of practical examples of their application to different kinds of material systems.

2 Overview

Semiconductors have revolutionized our life in the twentieth century, and this revolution is still going on producing devices smaller and smaller, powerful, and always present in our lives. The base of this revolution was the capability to design and produce new artificial materials by developing new methods for their growth capable of decreasing the size of the relevant devices. By decreasing the size of semiconductor materials and devices, a new world of quantum properties appears, and transmission electron microscopy (TEM) is the way to study at the highest spatial resolution the relationship between structural and electronic properties of new materials versus growth conditions. The properties of the semiconductor devices we use everyday are strongly related to several parameters bounded to their chemistry, crystal structure, strain status, and crystal defects. Transmission electron microscopy developed over the years different approaches to study each of these aspects improving along the time the spatial resolution limit to answer to the requirement of knowledge on the material properties with increasing precision, accuracy, and spatial resolution. Certainly semiconductor research and production owe to TEM a consistent portion of their success but at the same time represented a strong driving force to develop new equipment with better performances and new methods to explore subtle aspects of the properties of semiconducting materials. Nowadays, one of the aims of nanoscience is to produce semiconductor devices based on few atoms, and this requires TEM methods with resolution and accuracy on atomic scale, or even higher as the properties of clusters of few atoms can change dramatically due to small distortion in their crystal structure related, for example, to a capping layer or to the presence of an interstitial atom or a vacancy.

Here it will be shown how different TEM approaches can be used and combined together to understand the properties of semiconductor materials, their crystal structure, the kind of eventual extended defects, the interface status, the chemistry, its homogeneity, and the magnetic and electronic properties. The different TEM methodologies will be illustrated through examples of different kind of samples like 2-D heterostructures, quantum wires, quantum dots, and clusters with different degree of shape anisotropy like spheres, rods, and branched structures. The point of view used in writing this paper would like to mark how the different methods in transmission electron microscopy constitute a unique body in which the scientist can select the best approach to understand the properties of the specimen keeping in mind that, at least so far, a TEM is not an equipment in which by pressing a button we can have an automatic response on the features of the specimen. Along the chapter, a particular attention is devoted to highlight under which experimental condition the information can be achieved by transmission electron microscopy and properly interpreted. The aim here is also to mark how a TEM is not a rigid

equipment but a flexible optical bench that can be tuned in an unconventional way, designing new experimental setup to study subtle properties of the matter and generating new original approaches.

3 Introduction

A classic approach of physics to study an unknown object is by hitting the object with a well-known probe and reconstructing the unknown by analyzing the results of the interactions in the framework of a suitable theory. The electrons interact strongly with the matter; as an example, an electron has a probability of interaction with the matter about four orders of magnitude higher than an X-ray photon. This high probability of scattering practically means that few microns of a solid are enough to stop an electron with energy of hundreds of keV but in turns means that we can derive an enormous quantity of information about a thin section of a solid if we use a well-known and well-controlled electron probe and a suitable detector. A transmission electron microscope is capable to produce a coherent electron probe with a size ranging between some hundred of microns down to less than 1 Å, with an energy spread better than 0.2 eV, and to move the probe on the area of interest with sub-nanometer accuracy. As a rule of thumb, the spatial resolution achievable with any magnifying equipment is about directly proportional to the wavelength used to illuminate the object. This is well known since the end of nineteenth century and described by Abbe's work on imaging resolution limits due to diffraction effects [1]. As a consequence, the spatial resolution achievable illuminating an object by electrons is in principle about five orders of magnitude better than the resolution achievable by using photons in the visible light range [2]. For example, the wavelength of a 200 keV electron is 2.5 pm, well below the distance of two atoms in a solid, which is of the order of 100 pm. In practice, the aberrations of the electron lenses limit the resolution about two orders of magnitude above the diffraction limits. Only recently the introduction of new correctors for spherical and chromatic aberrations improved further the resolution of electron microscopes demonstrating so far a resolution of about 50 pm. A transmission electron microscope represents a tool suitable to study fundamental and subtle properties of the matter at atomic resolution by imaging its morphology and structure at atomic scale. From the area of interest imaged at atomic resolution, further properties can be studied at the same time by electron diffraction or by energy-dispersive X-ray spectroscopy (EDXS) or by electron energy-loss spectroscopy (EELS). We could divide the experiments performed by TEM in three big sets:

1. Experiments of imaging, in which the morphology, structure, and elemental distribution of the specimen are directly seen (or, better, are seen in the direct space) by using both elastic and inelastic scattered electrons. In fact, there are several ways to image a specimen, and the kind of information achievable depends on the experimental set up used. In Fig. 3.1 it is shown the simplified schematic diagram of a TEM equipment and the different configuration of the lenses to perform imaging or diffraction experiments.

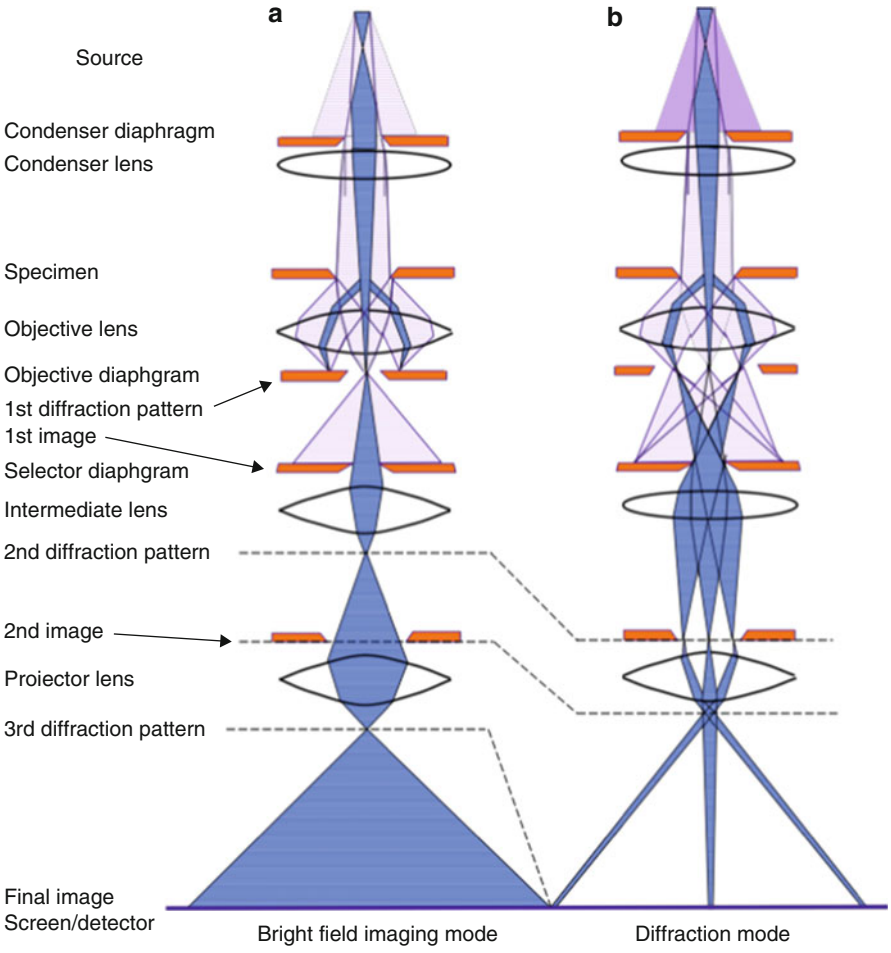


Fig. 3.1 Schematic layout of a TEM operated in diffraction contrast bright field imaging (*left*) and diffraction (*right*) modes, respectively

2. Experiments of diffractions in which the back focal plane of the objective lens is conjugated with the acquisition system (Fig. 3.1b). Also in the case of diffraction experiments, there are different kinds of electron optical setup to be used depending on the kind of information to be achieved. In Fig. 3.2a, b it is schematically shown how a diffraction pattern is formed in a TEM, when the Ewald's sphere cut some points of the reciprocal space, and the effect of tilting a specimen; Fig. 3.2c, d are the relevant experimental diffraction patterns as acquired in the different diffraction conditions in (a) and (b), respectively. It is worthwhile to note that, due to the reduced thickness of a TEM specimen in the direction perpendicular to the primary electron beam, the reciprocal space nodes

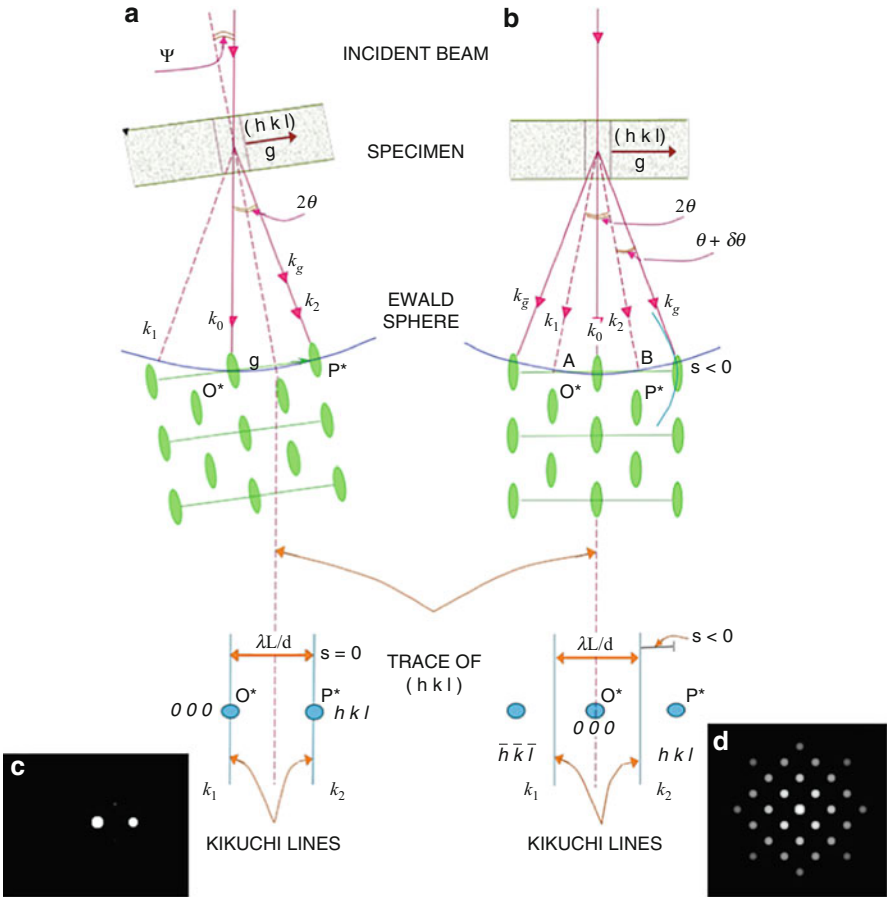


Fig. 3.2 Diffraction pattern formation in a TEM: (**a**, **b**) schematic layout, by using the Ewald's sphere construction, showing the effect of tilting the specimen; (**c**, **d**) relevant experimental diffraction patterns as obtained by using the experimental set up in (**a**) and (**b**), respectively. It should be noted how, by tilting the specimen with respect to the primary electron beam, it is possible to excite a large number of *diffracted spots*, as in the case of a zone axis orientation shown in (**d**) or it is possible to excite only one *diffracted spot* beside to the direct beam (so-called two-beam conditions), as shown in (**c**)

are elongated in the direction normal to the sample foil, and therefore diffraction spots in an electron diffraction experiments can be seen even if the relevant reciprocal space vectors are not precisely in Bragg's conditions (in Fig. 3.2 $s \neq 0$).

3. Experiments of spectroscopies based on inelastic interactions of the primary probe electrons with the specimen atoms, which are mainly EDXS and EELS experiments, to derive chemical, electronic, and magnetic information on the specimen.

Indeed, it would be helpful to consider a TEM not only a *microscope* but a flexible electron optical bench capable of handle a well-characterized electron probe on the specimen and to analyze the results of their interaction. This approach would make evident how flexible can be electron microscopy and how new methods could be developed depending on the properties of the matter, which we would like to shed light on. Since the introduction of the electron microscopy, in the first half of last century, a number of new methods based on TEM were developed, and certainly the need of understanding the properties of semiconducting materials represented, and still represents, a formidable driving force for the development of new methods in TEM; at the same time TEM has been, and it is, a basic tool for the study and development of semiconducting materials and devices.

The properties of a semiconductor are strongly related to its chemistry homogeneity, to the presence of chemical impurities or dopants, to its crystal structure and perfection, and to a wide range of structural defects like point defects (interstitials, substitutional, vacancies) or extended defects (dislocations, staking faults, twinning, etc.). Small distortion in the crystal structure changes the semiconductor band gap and is used to create new semiconducting materials, as demonstrated by growing epitaxial layers on a suitable substrate by controlling the crystal growth on a monolayer scale by using, for example, molecular beam epitaxy (MBE) [3] or metallorganic chemical vapor deposition (MOCVD) or other kind of methods capable of controlling the layer growth on an atomic scale [4]. A new class of semiconductors also discriminate the spin status of the charged carriers and are the subject of the spintronic [5] where electronic and magnetic properties are used together to set up the devices of the future. The study of semiconducting materials by TEM requires the application of a large number of methods of imaging, electron diffraction, and spectroscopies.

Here, the aim is to show by direct examples how TEM can be used to study the detail of the structural, chemical, electronic, and magnetic properties of a semiconductor at the origin of its performances. Indeed, among the large number of TEM methods used in microscopy of semiconducting materials, only some of them will be considered here, as a chapter would not be enough even only to briefly mention all the existing TEM-based methods. The choice of the methods considered in this paper is certainly not the only one possible; the methods here described were selected for the wide range of applications to nanostructured semiconducting materials and also, in our opinion, give a didactic flavor of the capability of transmission electron microscopy. Moreover, two recent examples of unconventional use of TEM, that we believe are particular instructive to show the flexibility of the methodology and the capability to generate new methods, were also considered. In Sect. 4 the experimental background of some fundamental TEM methods will be briefly described, whereas in Sect. 5 selected methods to address the properties of interest of a semiconducting material will be applied to nanostructured semiconductors. Some examples will be also dedicated to show how an unconventional use of a TEM can produce new unexpected methods to study at the highest spatial resolution the properties of a material and, in particular, of a semiconducting material.

4 Experimental Methodology

4.1 Notes on Sample Preparation

Due to the high cross section of the electron-matter interaction, the specimen for TEM experiments has to be thinned to a thickness which, in most of the experiments, should range between few nanometers to some hundred of nanometers [2]. The specimen preparation is extremely important for the relevant experiments, and any good TEM experiment starts with a good sample preparation. The aim is to obtain a sample conveniently thin and suitable for the TEM specimen holders, which, practically in all the TEM equipment, are designed to hold and handle a thin disk with a diameter of 3 mm. If the starting point is a bulk sample, like the case of a film epitaxially grown on a substrate, we have the choice to prepare the specimen in the geometry more suitable for the experiments we are planning; for example, if we wish to detect and measure the density of dislocations in a epilayer, we could gently cut a disk of 3 mm from the sample, thinning it to remove, partially or completely, the substrate and obtaining a plan view of the film. If the aim is to detect where the dislocations are originating, for example, at the interface between substrate and epilayer due to a cluster of impurities or to the mismatch between substrate and film, we have the choice to prepare the sample in cross-sectional geometry, gluing appropriate dummy layers to form a wafer containing in the center of the specimen to be studied (Fig. 3.3). The wafer is then cut perpendicularly to the stacking direction and thinned by mechanical grinding and polishing to about 10–40 μm, depending on the brittleness of the materials. The electron transparency is then obtained usually by chemical etching or ion beam milling [2]. We can achieve extremely good knowledge on a material by using a TEM, and we can apply tens of TEM approaches to understand subtle aspects of its nature, but we have to pay a cost in advance, which is a proper specimen preparation that always requires a high skillfulness and could be very time consuming, up to several days of work like in the case of the preparation of a cross section of an epitaxial film as the one sketched in the Fig. 3.3 and described in the relevant caption. The thinning process is always very intrusive, and of course it is necessary that the thinned specimen would have the same properties of the pristine one, and any eventual modification has to be well known to the experimentalist. Let us mark once again that there is no way to achieve reliable information by TEM experiments if the specimen is not properly prepared.

There are several approaches to thin a specimen down to electron transparency for TEM experiments (by chemical etching, jet thinning, mechanical grinding, ion beam milling, etc. [2]), and in many cases more methods are used together to achieve a good quality final result. More recently, the development of focused ion beam (FIB) milling allows one to cut and thin to the desired thickness a well-defined area of the specimen [6]. As in the modern FIB, the cutting and thinning process is monitored in situ by scanning electron microscopy (SEM) allowing to see directly the processed area with nanometer range resolution; this approach is particularly helpful when a high spatial accuracy is needed in extracting the region

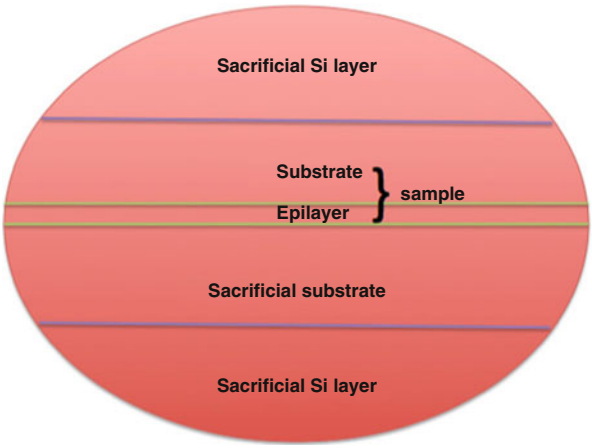


Fig. 3.3 TEM sample, prepared in cross-sectional geometry, of an *epilayer* grown on a *substrate*. The wafer for cross section is prepared gluing the specimen with the *epilayer* faced to a *sacrificial substrate* equal to the one used to grow the film to avoid preferential erosion in the proximity of the area of interest during the thinning process; the wafer is then glued to two *sacrificial Si layer* to obtain a total wafer width $\geq$3 mm. The use of Si at this step is due to have a fast monitor of the sample thickness during the mechanical grinding process as below 30 μm; the Si is transparent to the visible light and turn from *red*, at about 30 μm in thickness, to *pale yellow*, at about 10 μm in thickness. The wafer is then sliced perpendicular to the planes of gluing obtaining layers about 1 mm thick. The resulting specimen is therefore drilled by using a hollow drill and a disk 3 mm in diameter, as the one schematized in the figure, is finally obtained. The disk is hence grinded and polished down to 10–40 μm, depending on the brittleness of the material. The electron transparency is then obtained usually by chemical etching or ion beam milling

to be studied from the sample, like in the case of a semiconducting device when our interest is, for example, on the gate or on the oxide layer. For this reason some semiconducting industries installed FIB and TEM in the production clean room for quality test on the devices. In other cases the specimen preparation is relatively much more straightforward as, for example, in the case of nanostructures dispersed in a solvent. In the latter case the specimen preparation requires a relatively short time to deposit a drop of suspension, with a calibrated density of particles, on a TEM copper grid covered by thin carbon film and allowing the solvent to evaporate. There is no a general better approach to the TEM sample preparation, but it depends on the kind of specimen and on the kind of TEM experiments to be performed [2].

The specimen preparation for TEM requires a very high skillfulness, and there is a vast bibliography on this subject, which is behind the aim of this paper; here the aim is to give a hint of the complexity of the TEM sample preparation and of its importance. The influence of the specimen preparation on the measures performed in a TEM experiment is definitively important, and in some cases the specimen preparation could introduce unavoidable artifacts in the specimen that prevent

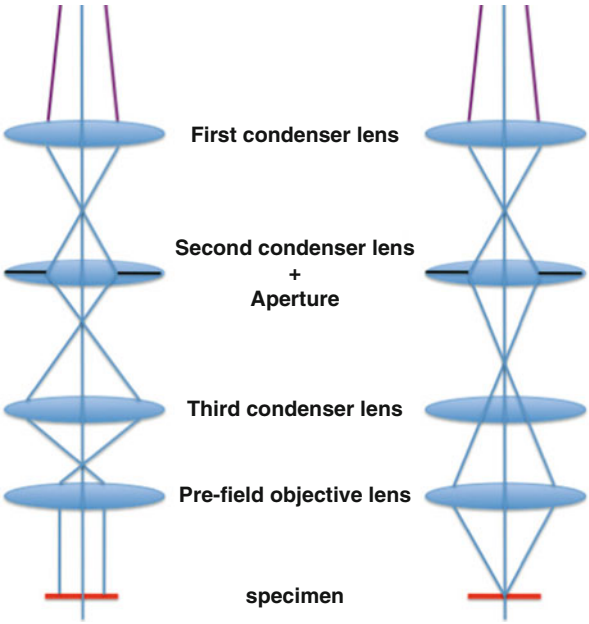


Fig. 3.4 Simplified schematic layout of different setup of the illumination system of a TEM to achieve parallel (*left*) or convergent (*right*) illumination on the specimen

a proper study of the materials unless the influence of specimen preparation is not quantified properly by modeling the effect of the thinning process on the sample.

4.2 Imaging Experiments

There are several ways to image a specimen in a TEM, and the use of a specific method depends on the information we would like to achieve from the specimen. The condenser lenses of a TEM can handle the electrons generated by the cathode with high accuracy, producing a parallel beam or a highly focused beam to illuminate the specimen (Fig. 3.4).

The parallel beam configuration is used for imaging in diffraction contrast [2] or in high-resolution transmission electron microscopy (HRTEM) phase contrast [7]. In the diffraction contrast method, the image is formed by selecting a specific diffracted beam placing an aperture in the back focal plane of the objective lens of the microscope (see Figs. 3.1 and 3.2). The image formed by selecting the direct beam, which is the beam that comes through the specimen but has the same direction of the incident beam, is called bright field (BF). The image formed by using one of the diffracted beams escaping from the sample is called dark field (DF). The amplitude and phase of the diffracted beams depend on the experimental setup and on the specimen nature and orientation and are well described by the dynamical theory of electron diffraction [2]. The sample manipulator is used to tilt

the specimen in different geometries exciting different diffracted beams according to the aim of the TEM investigation (Fig. 3.2). In paragraph 4.5 it will be shown how TEM images of any kind can be simulated by using algorithms based on dynamical theory of electron diffraction [2, 8, 9], and, in particular, it will be explained in which sense high-resolution transmission electron microscopy shows the positions of atomic columns in the specimen. Nevertheless, even intuitively, it should be expected that if we use a particular diffracted beam to form the image, the features of the relevant image would depend closely on the features of the lattice planes generating that specific diffracted beam. This feature is at the origin of the method of characterization of extended defects based on diffraction contrast used in electron microscopy.

When the image is obtained by allowing to all the diffracted beams to interfere each other and the specimen is thin enough to satisfy the so-called thin object approximation [10], and with a proper choice of the objective lens defocus value, the contrast of the resulting image, called HRTEM image, is directly related to the crystal potential projected on the plane of observation and hence is a direct image of the "atomic columns" seen in the chosen projection [7]. This aspect will be deepened in the par 4.5.

The focused beam setup of the condenser system can be used in conjunction with a set of scanning coils to move with high accuracy the beam on the specimen and acquiring the relevant electrons scattered forward by using detectors placed below the specimen (Fig. 3.5).

For each position of the focused electron beam on the sample, the resulting signal is acquired by a detector and represents one pixel of the whole image. In this case the equipment is operated in scanning transmission electron microscopy (STEM) mode [11]. The detectors for STEM imaging are of different kinds: there is mainly a central circular detector coaxial with the electron optical axis of the microscope, called bright field (BF) detector, used to acquire the electrons scattered at lower angles and one or more annular detectors around the central one called annular dark-field (ADF) detectors (Fig. 3.5). The use of BF STEM detector allows one to acquire images with features corresponding to the one obtained in TEM mode BF diffraction contrast or HRTEM; it depends if only the direct beam(BF) hits the detector, or a set of diffracted beams interferes on the central detector (HRTEM), respectively. This equivalence between TEM and STEM imaging finds its physics origin and explanation in the theorem of reciprocity of the electron-scattering theory [12]. ADF detector allows one to obtain images corresponding to the TEM DF mode. If the experimental setup of the STEM ADF experiments is such to allow only electrons diffracted at high angle (larger than 50–60 mrad) to be collected by the ADF detector, the relevant imaging mode is called high-angle annular dark-field (HAADF) imaging, and the resulting image contrast is strongly related to the atomic number of the species contained in the sample and hence represents a kind of chemical map of the specimen [11]. HAADF imaging is so sensitive to the atomic number that it can be used to detect isolated impurities in a semiconductor, as in the case of doping atoms [13]. Based on the sensitivity to the atomic number of HAADF imaging, there were developed also methods capable of

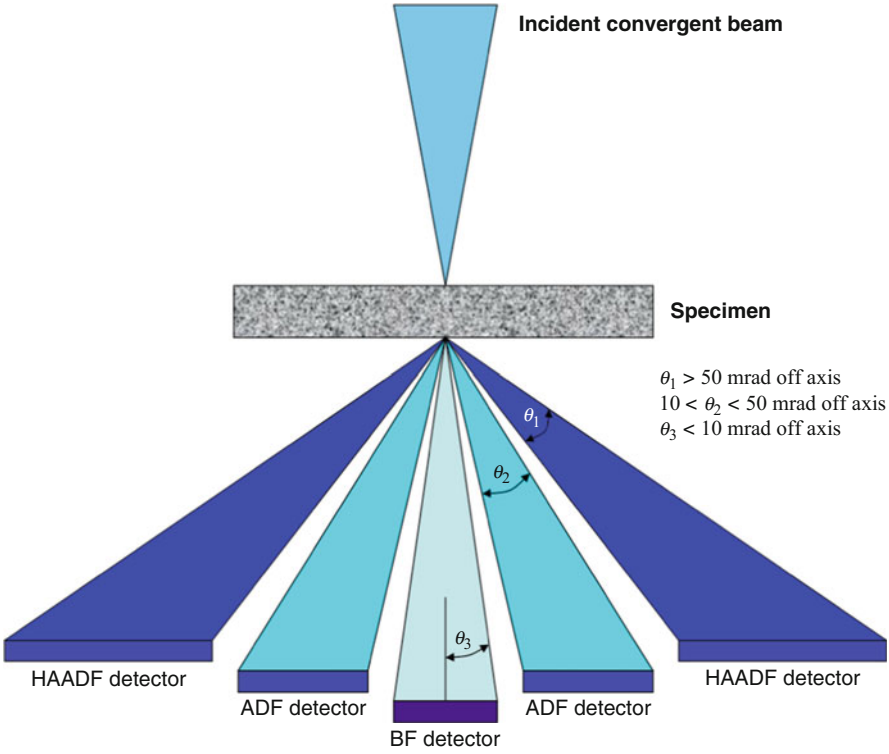


Fig. 3.5 Scanning transmission electron microscopy (STEM) imaging mode and relevant detectors as a function of the angles of scattering of the electrons within the specimen

measuring the distribution of atomic layers of guest atoms in a host matrix allowing an accurate determination of the chemical species gradient as, for example, in the case of delta doping of semiconducting materials [14].

The resolution in a TEM/STEM imaging experiment is physically limited by the diffraction aberration, but indeed the electron lens aberrations stop the resolution at two orders of magnitude worst. As an example, at 200 keV the electron wavelength is 2.5 pm, whereas the resolution of a high-quality TEM equipment with a spherical aberration coefficient (Cs) of 0.5 mm for the objective lens has a resolution, at optimum defocus, of 190 pm [7]. Only very recently [15–17] a way to correct the spherical and chromatic aberrations, based on the realization of special magneto-optical poles, has been found, pushing the resolution below the Angstrom [18] and hence closer to its diffraction limit but still away from it. It is also worthwhile to remark that the electron optical conditions of aberration-corrected experiments are intrinsically instable, and hence a great care has to be dedicated to monitor the experimental conditions to be able to achieve reliable information [19]. There are also other methodological approaches, not based on construction improvements, to increase the resolution of an imaging TEM experiment, for example, the exit

wave reconstruction [20], which demonstrated so far 100 pm resolution and electron coherent diffraction imaging (EDI) [21–23], which demonstrated so far 70 pm resolution, and hence can be used to study the specimen at subatomic resolution.

4.3 Electron Diffraction Experiments

The diffraction pattern formed in the back focal plane of the objective lens of a TEM can be easily acquired simply conjugating that plane to the acquisition system, usually the same coupled charged device (CCD), or photographic film or imaging plate [24, 25] used for image acquisition, by properly tuning the projection lens system of the equipment as schematized in Fig. 3.1 [26]. The flexibility of the illumination system and the possibility to tilt the specimen allow one to obtain diffraction patterns by using a parallel beam or a convergent beam (see Fig. 3.4) on the sample oriented as desired to explore its properties. The diffraction patterns can be obtained from well-defined areas of the specimen selected in imaging mode. The specimen-illuminated area diameters achievable by using a parallel beam (the so-called selected area diffraction, or micro-diffraction, or nano-diffraction pattern, depending on the way used to select the specimen area explored) are between about 100 μm and 10 nm [26, 27]. The diffraction patterns obtained by parallel electron beams are used mostly to measure the sample lattice parameters and for phase identification. Electron diffraction pattern obtained by focusing a conical electron beam onto the specimen is named convergent beam electron diffraction (CBED) [28]. The CBED pattern can be obtained illuminating small specimen area (below 1 Å in diameter) and, depending on the experimental set up, can be used to measure a wide range of specimen properties like point group, space group, strain, crystal potential, critical voltage, and defects [29–34].

4.4 Spectroscopic Experiments

So far we considered, in the imaging and diffraction methods, electrons scattered elastically by the specimen. The energy lost by electrons in the interaction with the specimens produced the spectroscopic signals used in TEM/STEM experiments. There are two main spectroscopic signals used in electron microscopy:

– Energy-dispersive X-rays, due to the emission of characteristic X-rays from the specimen atoms ionized by the primary high-energy electron beam (Fig. 3.6). The energy of the characteristic X-ray is specific of the kind of emitting atom, and their number is related to the intensity of the primary electron beam and to the number of the atoms illuminated by the electron beam. A detector placed close to the electron-specimen interaction point is used to measure the intensity and the energy of the X-ray signal, therefore, used to identify and quantify the chemical species inside the specimen [35]. The example in Fig. 3.6 shows the EDXS spectrum as acquired in a specimen area containing several chemical

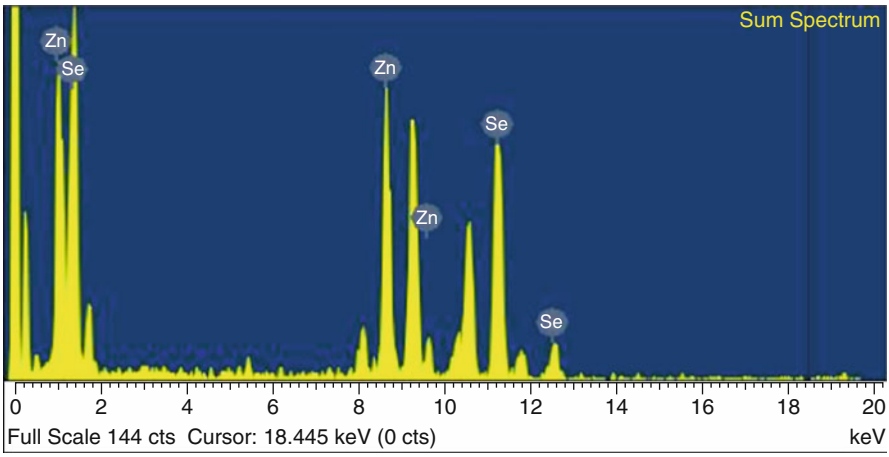


Fig. 3.6 EDXS spectrum showing several characteristic X-ray peaks belonging to different chemical elements. The X-ray peaks of *Zn* and *Se* are labeled in the figure

species, and each of them produces one or more fluorescence peaks at different energies. The relative heights of the peaks belonging to a chemical element are its fingerprints as they are related to its atomic structure. In Fig. 3.6 the peaks belonging to Se and Zn are marked. From the measure of the counts in the peaks, weighted by the relevant ionization cross section, it can be derived the relative content of the different atomic species in the specimen.

The number of excited atoms that decade emitting a characteristic X-rays depends on their atomic number, and it is higher for heavy atoms than for light atoms ($Z < 10$). Hence EDXS experiments are very good in detecting heavy atoms but show a low yield for light elements. Also the efficiency in the detector collection is relatively low, of the order of 1–3 %, and this further complicates the analysis of light elements. The typical spatial resolution depends on the beam size and specimen thickness and varies, in an accurate high spatial resolution experiment, from 1 to 10 nm [35].

It is worthwhile to mention that, in particular for semiconducting materials, the photons emitted at much smaller energy, in the range from infrared to ultraviolet, can be acquired and studied in the so-called cathode-luminescence spectroscopy [36, 37].

– The primary electrons after the inelastic interaction with the specimen atoms can be separated in energy by different kinds of magnetic systems and collected in parallel by a CCD array forming the electron energy-loss spectrum (Fig. 3.7). In Fig. 3.7 is shown an EELS spectrum as acquired on a SiO_2 sample. In the inset of Fig. 3.7, the schema of the oxygen K edge formation is shown. The peak at zero loss contains electrons interacting elastically with the specimen or those that do not interact with the specimen at all and are evidently the majority of the spectrum.

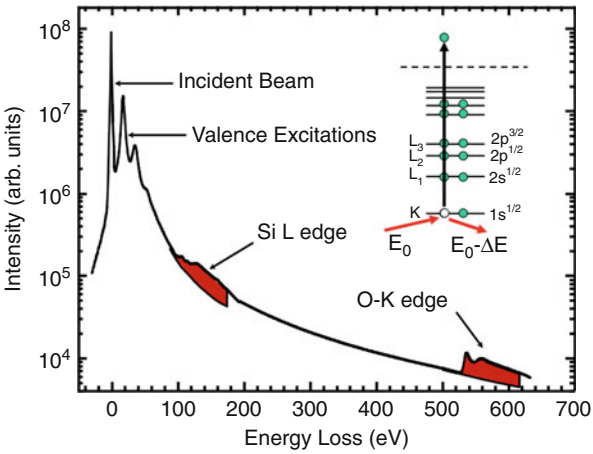


Fig. 3.7 EELS spectrum of a SiO_2 sample. The content of the peak at zero loss identifies the electrons that interact elastically with the specimen or those electrons that do not interact at all with the specimen. The *low-loss region* is conventionally between 0 and 50 eV. Above 50 eV there is the *high-loss region* where the ionization edges are located (Reproduced by courtesy permission of D. Muller from reference [122])

The analysis of the EELS spectrum can be used to identify and quantify the specimen chemistry [38] but also to achieve information on the bonds and electronic structure of the specimen [38, 39]. In particular for a semiconductor or an insulator, a transition from the valence band to the conduction band would produce a signal in the EELS low-loss region (from 0 to 50 eV) which is proportional to the number of unoccupied levels in the conduction band and gives evidence of the energy gap and of the eventual defects within the energy gap of the semiconductor (Fig. 3.7) [40–42]. The signal in a EELS spectrum is large for $Z < 33$ and has in principle no limits in the atomic number even if the measure of the edge intensity is not straightforward due to the presence of a large background that has to be modeled and removed accurately to quantify the real number of counts in the edge [38]. The typical efficiency detection of EELS detector is of about 90 %, and EELS can achieve routinely a spatial resolution from 0.1 to 1 nm. A good quantification of the EEL spectra would require relatively thin TEM specimen to limit plural scattering effect in the spectra [38]. The possibility to use a window to select a specific interval of energies in the EEL spectrum, and to form an image by using the inelastic electrons that lost those specific energies opens the world of inelastic imaging in the TEM [38]. Energy-filtered TEM (EFTEM) images and diffractions open another wide set of methods and can be used, for example, to map the chemistry of the specimen in a very direct way or to deconvolve the influence of inelastic scattering from TEM elastic images or diffractions, increasing the accuracy in deriving the specimen properties. More recently, it has been demonstrated that EELS spectra can also be used to study the dichroic properties of a specimen [43] by developing a method capable to map quantitatively the magnetic moment distribution on a sub-nanometer scale [44, 45]. This latter approach is becoming an important tool in the study of the spintronic properties of a material that represent a class of materials of high interest for the development of the electronic of the future.

The spectroscopic studies are gaining even more attention in the recent time when the possibility to use electron probe with a diameter smaller than one Angstrom in STEM configuration demonstrated the capability to achieve EDXS and EELS spectra at atomic resolution allowing to understand, as never before, fine details of interface properties in particular on nanostructured materials [46–50].

4.5 Simulation of TEM Results

One of the advantages of the TEM is that, in most of the cases, the information achieved is contained in images and images are more easily understood with respect to other information support. On the other hand this is also a risk as, in many cases, people tend to give an intuitive meaning to the features displayed in an image, and this produces a wrong interpretation in most of the cases in TEM. Following Severin Amelincks: "we can believe what we see as long as we understand how we see." Indeed, the aim of a TEM experiment is not to provide nice images but to produce quantitative information on the specimen, and in most of the cases these information need to be quantified with the help of computer simulation of images. This is of course true also in the case of the quantification of the spectra obtained by EDXS or EELS. Fortunately, even if the electron-specimen interaction is very strong and produces a wide range of secondary effects, it can be accurately simulated by many programs based on dynamical theory of electron-matter interaction [9, 51, 52]. In particular, the so-called multi-slice approach developed by Cowley and Moodie [53] enables to describe the electron-specimen interaction in a particularly intuitive way and suitable to be compiled for TEM/STEM image simulation. The method considers the specimen as made of n very thin slices, and in a thin slice it is possible to assume some approximations that simplify the calculation of the electron-matter interaction; the electron wave function escaping from the specimen is the result of the interaction of the incident wave function with all the slices and from slice to slice is applied a Fresnel wave propagator. The wave function after the specimen is modified by the interaction with the microscope objective lens, and the result is what we observe on the image acquisition system. The image formation in the TEM is schematized in Fig. 3.8.

As an example, if the specimen is extremely thin, we could directly calculate analytically the image contrast of an HRTEM image. Let us consider that the specimen has a thickness t between two infinite planes parallel to the plane (x, y) of an orthogonal Cartesian system of reference. The difference of phase δ between two waves of wavelength λ following a different optical path Δ is given in general by $\delta = 2\pi\Delta/\lambda$. In the case of a very thin sample, it can be assumed that the sample crystal electrostatic potential $\phi(\vec{r})$ only changes the phase of the incident electron wave-function (phase-object approximation [2]) and the difference of phase δ is given by $\delta = \frac{2\pi}{\lambda}\int_0^t \frac{\phi(\vec{r})}{2E}dz$ where t is the specimen thickness and E is the energy of the primary electrons propagating parallel down to the z-axis. If the sample is thin

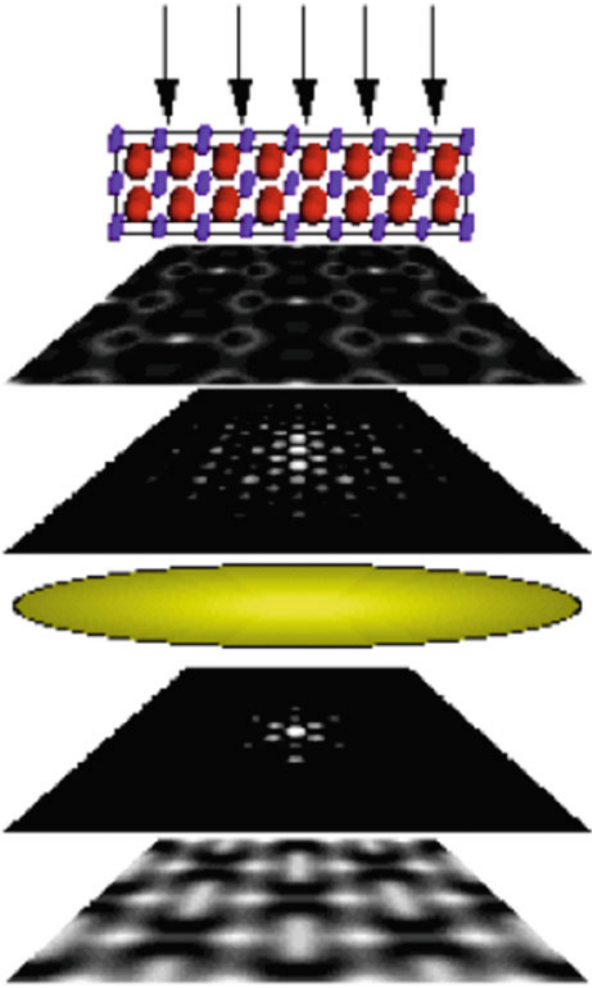


Fig. 3.8 Schema of the formation of HRTEM image: going from *top* to *bottom*: the *arrows* indicate the direction of the electron plane waves impinging on the specimen, then the *first plane below* the specimen shows the projected electron wave function, keep going, the specimen diffraction pattern is shown. The *yellow ellipse* indicates the objective lens and then in its back focal plane is formed the diffraction pattern that we can observe in the microscope and finally the HRTEM image

enough to consider that the crystal potential does not change along the z-direction (crystal projected potential approximation) [2] results $\delta = \pi\phi(x,\ y)t/\lambda E$. The object function describing the de-phasing due to the specimen crystal potential on the primary electron wave function is: $q(x,y) = e^{i\delta} = e^{i\sigma\phi(x,y)t}$, where $\sigma = 2me\lambda\pi/h^2$, e is the charge of the electron, and h is the Planck's constant. The action of the microscope objective lens is to form the diffraction pattern of the specimen in the objective lens back focal plane (see Figs. 3.1, 3.2, and 3.8) and to form the image of the specimen in the image plane. The diffracted amplitude pattern is the Fourier transform of the object function $q(x,\ y)$ [9] and hence is $Q(u,v) = \Im\{q(x,y)\} = \delta(u,v) + i\sigma\tilde{\phi}(u,v)$ where u and v are the coordinates in the reciprocal space. We can model the influence of the objective lens and of its aberrations as a further term of de-phasing depending on the angle α on which

the electron wave fronts impinge on the lens and it is represented by the function $\chi(\alpha) = \chi(u, v)$. What we measure in the reciprocal space is the intensity of the diffraction spots and hence the square modulus of the diffracted amplitudes R(u, v):

$$R(u,v) = Q(u,v)e^{i\chi(u,\,v)} = \delta(u,v) + \sigma\,\tilde{\phi}\,(u,v)e^{i(\chi(u,\,v)+\pi/2)}$$

The inverse Fourier transform of $R(u, v)$ would finally give the image amplitude in the image plane of the objective lens. An aperture in the back focal plane of the objective lens will select the beams contributing to the final image (Figs. 3.1 and 3.2). The role of the aperture is formalized by the function $A(u, v)$ where $A(u, v) = 1$ if $\sqrt{u^2 + v^2} \leq r_0$ or $A(u, v) = 0$ if $\sqrt{u^2 + v^2} > r_0$ where r_0 is the radius of the aperture in the reciprocal space. The wave function in the image plane is hence

$\Psi(x,y) = \Im^{-1}\{R(u,v)A(u,v)\} = 1 + \sigma\Im^{-1}\left\{\tilde{\phi}(u,v)e^{i[\pi/2+\chi(u,v)]}A(u,v)\right\}$ and the relevant intensity is $I(x,y) = \left|1 + \sigma\Im^{-1}\left\{\tilde{\phi}(u,v)T(u,v)A(u,v)\right\}\right|^2$ where $T(u, v) = e^{i[\chi(u,v)+\pi/2]}$ is called phase-contrast transfer function and accounts for the response of the objective lens. The value of the function $\chi(u, v) = \pi/2$ can be obtained by tuning properly the microscope objective lens defocus to the so-called optimum defocus, which depends on the electron wavelength and on the spherical aberration coefficient of the microscope objective lens [7], and if the aperture function value is $A(u, v) = 1$ results $I(x, y) = |1 - t\sigma\phi(-x, -y)|^2$. Neglecting the quadratic terms due to the validity of the weak phase-object approximation [53] it results $I(x, y) \cong |1 - 2t\sigma\phi(-x, -y)|$. From the last equation it is immediately evident how the minima in the HRTEM image contrast are directly related to the crystal projected potential, and in this sense the HRTEM is the image of the crystal atomic columns projected in the plane of view. The reader should be cautious that, in general, the minima in the HRTEM image contrast do not correspond to the positions of the real atomic column in the specimen and only by accurately knowing the image condition and modeling the specimen structure it is possible to correlate the maxima or minima in an HRTEM image to the true positions of the atomic columns seen in the chosen projection. Figure 3.9a shows, for example, how the contrast of the HRTEM image depends on specimen thickness and objective lens defocus in a nonobvious way, and the positions of the minima or maxima of the image could either represent the position of the projected atomic column. Hence, appropriate interpretation of HRTEM images does need always to be quantitatively compared to the relevant simulations. It is worthwhile to mark that, in most cases, atomic resolution HAADF STEM images are more easily interpretable as in a wide range of defocus and thickness the positions of the atomic columns coincide with the maxima of the experimental image, as shown through focus/thickness HAADF image simulation in Fig. 3.9b. Nevertheless, the quantification in the case of small variation in the crystal structure or in the case of quantification of chemistry of the sample from the HAADF images does require again detailed modeling and computer simulations [14, 46].

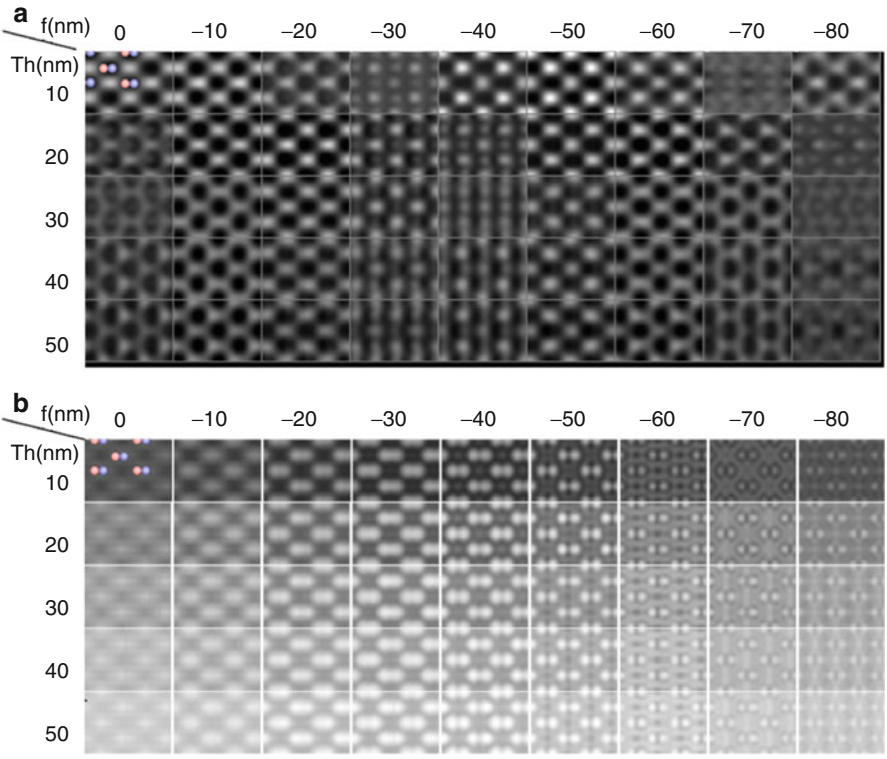


Fig. 3.9 (**a**) HRTEM image simulation and (**b**) HAADF STEM image simulation as a function of the thickness/defocus values for a GaAs crystal seen in the [1,1,0] projections, the *pink* and *pale-blue dots* in the inset in the *upper left part* of the images show the true positions of the Ga and As atomic columns

Up to 20 years ago, an accurate simulation of dynamical electron scattering would have required the use of a night of calculation on a mainframe. The development of more efficient calculation routines along with the tremendous increasing of calculation capabilities of modern workstations allows one to simulate an HRTEM image in few seconds, or less, depending on the complexity of the crystal model. The image contrast simulation, irrespective on the kind of imaging considered, requires a good modeling of the specimen. In some cases a good modeling of the specimen requires the use of appropriate physical approach, for example, modeling based on density functional theory [54, 55] capable to provide a reliable model as input for the TEM image simulation program finally compared with the experimental image. This approach is capable to produce highly accurate measurements of the properties of the specimen arriving to detect and recognize, for example, single atoms in a matrix in a HAADF STEM experiment [56].

5 Key Research Findings

5.1 TEM/STEM Studies of Heterostructures

The properties of the interfaces in a semiconductor are of fundamental importance as it can modify strongly the mechanical and electronic properties of a material. In some cases the growth conditions of the first few atomic layers of a film can change dramatically the properties of the relevant material or device. A case study particularly representative is, for example, the growth of II-VI epilayer on III-V substrate. II-VI/III-V heterostructures fabricated by MBE are crucial elements of a number of devices currently under development, ranging from spin transistors [57, 58] and spin filters [59] to blue-green emitters [60]. To develop high-quality heterostructures, much effort has been devoted to the reduction of the native defect concentration. Stacking faults (SFs) on {111} planes, propagating from the II-VI/III-V interface to the free surface of the II-VI epilayer, are the main types of native defects and have been extensively studied in prototype ZnSe/GaAs (001) heterostructures [61–66]. The defects characterization and the measure of their density are a typical problem solved by TEM. The presence of a defect in the foil influences the diffraction contrast image in a peculiar way. To model the problem we can consider that the undistorted crystal unit cell in a position $\vec{A}_{\vec{L}}$ due to the presence of the defect, is moved in a position $\vec{A}_{\vec{L}} + \vec{R}(\vec{r})$. The displacement vector $\vec{R}(\vec{r})$ can be modeled depending on the kind of defect considered [67]. If the TEM specimen were tilted to excite only one reciprocal space vector together with the direct beam (the so-called two-beam conditions; see Fig. 3.2a, c), the deformation vector would influence the relevant diffraction contrast image in a way that can be computed univocally from the dynamical theory of electron diffraction [68]. In particular, by selecting different diffraction conditions and forming the image with different excited vectors, the defect can be visible or not, as shown in Fig. 3.10, where a plan view of a ZnSe/GaAs heterostructure grown by MBE is displayed. The details of the heterostructure growth conditions can be found in A. Colli et al. [69]. The reason behind the visibility or not of a defect, or of some of its components, is related to the presence of scalar products between the excited reciprocal vector $\vec{g}$ and the deformation displacement vector $\vec{R}(\vec{r})$ in the expression of the diffracted intensities [2]; when the excited reciprocal vector is perpendicular to the displacement vector, the resulting zero value of their scalar product nullifies the relevant diffracted intensity.

It is worth to point out that all the images in Fig. 3.10 are taken in the same sample area, in two beams conditions, but with different tilt with respect to the primary electron beam to excite different reciprocal lattice vectors. The reciprocal vector **g** used to form the image is reported in the relevant picture. For example, in Fig. 3.10c the specimen was tilted to excite the (4,0,0) diffracted spot together with the direct beam, and then the latter was selected by the objective diaphragm (see Figs. 3.1 and 3.2) to form the image. With these diffraction conditions all the components of the staking fault are visible together with the relevant partial dislocations except the partial dislocation in the bottom-right part of the Fig. 3.10c,

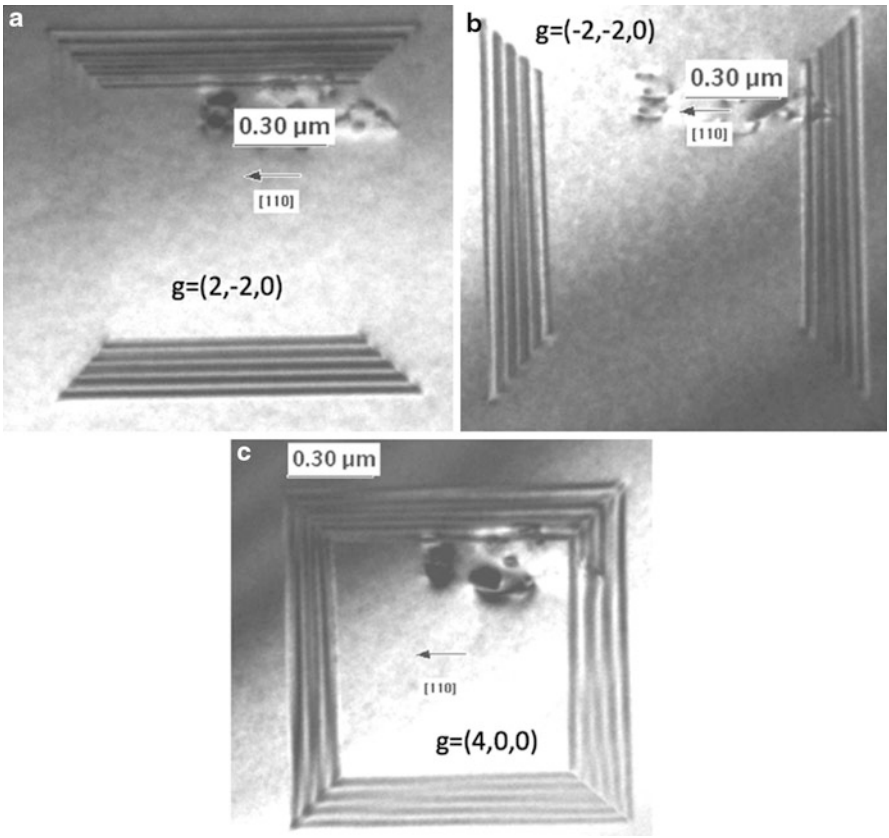


Fig. 3.10 Diffraction contrast two-beam conditions bright fields on staking faults in ZnSe/GaAs heterostructures. The presence of the different components of the staking fault and associated partial dislocations are visible, or not, depending on the chosen diffraction condition indicated on each image

which is invisible in these conditions [70] (note the white line in the right-bottom part of the square formed by the different components of the stacking faults). The diffraction conditions in the Fig. 3.10a, b make evident how the invisibility conditions are satisfied for perpendicular components of the stacking fault. The set of images allows one to univocally determine the nature of the stacking fault affecting the {1,1,1} planes. The density of these defects is strongly related to the conditions used for the first few monolayers of growth of ZnSe epilayer ranging from 10^4 up to 10^9 cm^{-2} [69]. The lifetime of the laser devices based on the heterostructures with lower defect density has a lifetime of four orders of magnitude higher than the devices with higher defect density. The formation of a higher defect density was believed due to the formation of GaSe dimers producing a 3-D growth, whereas the formation of Zn-As dimers was believed to produce a 2-D growth with a relevant low density of extended defects. Indeed, there are two procedures capable to produce

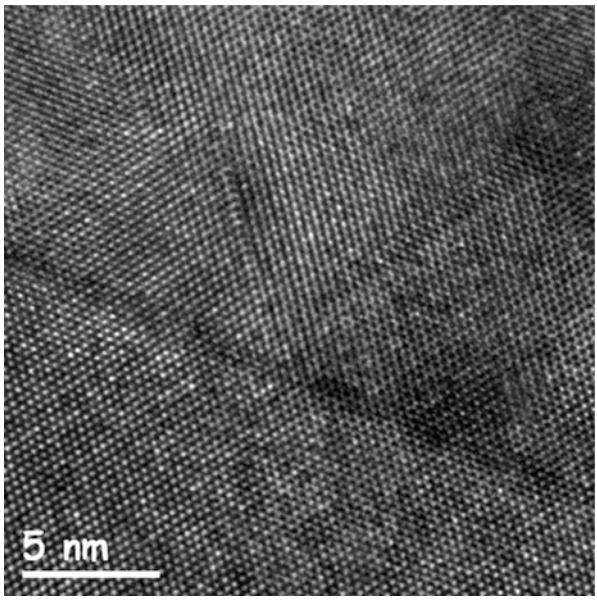


Fig. 3.11 Experimental HRTEM image in [1,1,0] zone axis of the interface of a ZnSe/GaAs heterostructure. In the center of the image are visible two of the components of a stacking fault along the <1,1,1> directions of the ZnSe epilayer with the vertex at the interface between the two materials

samples with defect density below 10^4 cm^{-2}. The first procedure involved preexposure of the GaAs surface to a Zn flux followed by migration-enhanced epitaxy (MEE) of ZnSe [71]. The second procedure involved fabrication of a 2-nm-thick ZnSe buffer layer at the interface in highly Se-rich conditions [71]. In both cases it was observed the formation of an interface layer about 1 nm thick. A combination of different TEM/STEM imaging techniques on ZnSe/GaAs specimens prepared in cross section [1,0,0] and [1,1,0] geometry together with EDXS experiments and theoretical constrains, related to the neutrality of the interface charge, enable to understand completely the chemistry and the structure of the interface layer [69] making clear that the GaSe reactions at the ZnSe/GaAs interface do not necessarily lead to high stacking fault densities. Furthermore, the observed reduction in the number of native defects in state-of-the-art heterostructures does not reflect the formation of Zn-As reaction products. Figure 3.11 is an HRTEM image in [1,1,0] zone axis of a ZnSe/GaAs heterostructure (the GaAs substrate is shown in the lower part of the image) with defect density $<10^4$ cm^{-2} grown by using Se predosing process [69]. The image has been focused in a region where a staking fault on the {1,1,1} is clearly visible together with the darker interface layer. No evidence of an interface cluster is detectable together with further defected areas. To position with high accuracy the electron beam to measure by EDXS the interface composition, the microscope was operated in STEM mode scanning an electron probe of 0.14 nm in a square of 10 nm centered onto the interface layer. The region to be measured was selected on the relevant atomic resolution HAADF image, and in Fig. 3.12 one of the areas studied is reported. Indeed, by using HAADF imaging further data on the interface composition are obtained at atomic resolution [11, 72] as the intensity I in an atomic resolution HAADF image is point to point related to the average atomic number

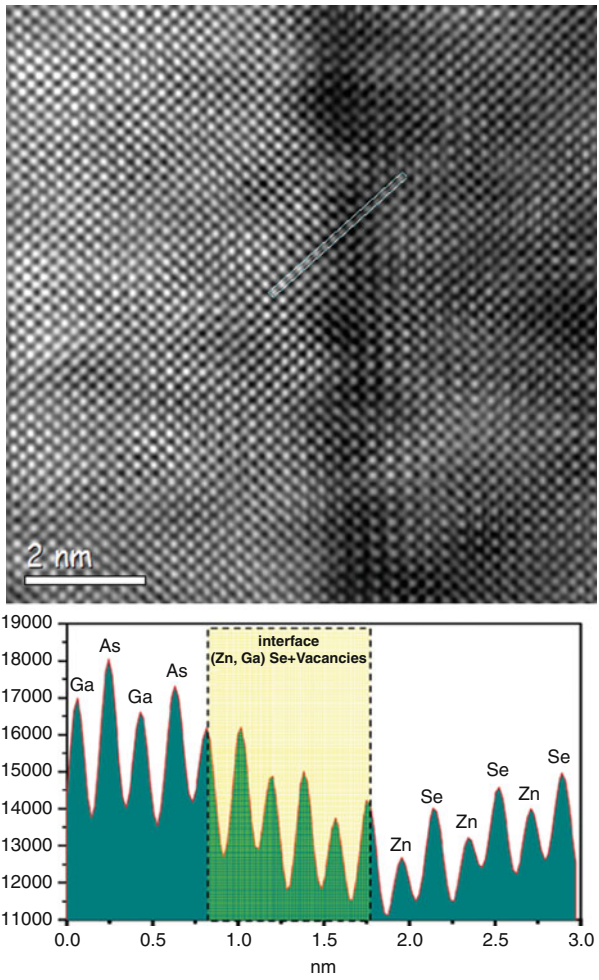


Fig. 3.12 Experimental HAADF images in [1,0,0] zone axis of a typical sample area where the EDXS maps were acquired. In the image it is also marked a region across the GaAs/ZnSe interface where the intensity profile was measured and shown below. In this projection every *white spot* in the HAADF image is the position of an atomic column of cations or anions, seen separately, projected in the image plane of the microscope. The different intensities due to the different atomic numbers of cations and anions enable to distinguish the polarity of the specimen

of the probed atomic column. The experiments were performed both on samples in [1,1,0] and [1,0,0] zone axes. The use of two different cross-sectional geometries enables to view different projections of cations and anions atomic columns; in the case of [1,1,0] projections, the cation-anion distance is of 0.14 nm, whereas in the case of [1,0,0] projection the cation-anion spacing is of 0.198 nm. The experimental conditions used for the HAADF experiments enable a resolution of 0.14 nm and hence in both projections the anions and cations can be distinguished as shown in Figs. 3.12 and 3.13d.

In Fig. 3.12 it is marked a region across the interface together with the relevant image intensity profile showing the position and the intensity of anions and cations atomic columns. As it can be seen, for example, atomic columns of Ga in the substrate can be immediately distinguished as having a lower intensity due to the Ga lower atomic number ($Z = 31$) with respect to As atomic columns ($Z = 33$).

The analysis is more complicated in the darker region between substrate and epilayer as possible intermixing of atomic species from the substrate and epilayer may occur. The eventual presence of a strain field could also complicate further the interpretation of the image contrast at the interface [48]. Indeed, the influence of the strain, due to the mismatch between GaAs and ZnSe, in the HAADF image has been simulated and shown in Fig. 3.13a.The experimental parameters used in the simulation are the same used to acquire the experimental image shown in the Fig. 3.13d. In particular the collection angle used in the acquisition of the experimental HAADF images is $84 \leq 2\vartheta \leq 224$ mrad and has been chosen to minimize the influence of long-range strain effect in the relevant image contrast [69]. As it can be seen, the presence of the strain at the interface of GaAs/ZnSe does not produce an appreciable contrast variation due to the relatively low value of the GaAs/ZnSe mismatch together with the high value of the HAADF image collection angle. The HAADF images in Fig. 3.13 have been simulated in the framework of multi-slice method and frozen phonon approximation [9].

Indeed, the darker region at the interface layers observed in the HAADF images (Figs. 3.12 and 3.13d) could be explained by the presence of vacancies within the interface layer as shown in the simulations in Fig. 3.13b, c. The presence of vacancies on the cation or anion sub-lattice at the ZnSe/GaAs interface was actually first postulated to explain the contrast shown by TEM diffraction contrast dark-field experiments by using (4,0,0) and (4,2,0) diffraction spots [73].

To investigate the local composition, EDXS spectra maps were recorded from regions as in Fig. 3.12 and in Fig. 3.13d. The specimens in the measured areas had a typical thickness of 15 nm – as measured by convergent beam electron diffraction – producing an estimated beam broadening of about 0.5 nm [35]. Because the thin samples examined produced relatively few X-ray photons due also to the very small size of the electron probe, the long acquisition times required made specimen drift of special concern. Therefore, the data were acquired for relatively short time intervals, then were recorded a STEM image to gauge drift, and continued EDXS data accumulation only if no relevant sample drift had been detected in the STEM image. This procedure was repeated on several regions of the specimen, and final composition variations from spectrum to spectrum were within 10 %. This value can be considered as an assessment of the overall experimental uncertainty in these EDXS data.

Taking into account the elemental X-ray emission cross sections the EDXS spectra showed only a minor As contribution – at the percent level – and a Ga to As ratio much larger than expected from stoichiometric GaAs [35]. By assuming that the residual As signal derived from the tail-end contribution of the GaAs substrate, it was inferred and subtracted the contribution to the overall Ga signal deriving from the same tail-end emission. The resulting average composition of the interface layer was 45 at.% Se, 34 at.% Zn, and 21 at.% Ga for the heterostructure incorporating a Se-rich CIL, and 50 at.% Se, 40 at.% Zn, and 10 at.% Ga for the interface fabricated through Zn predosing and MEE.

The above values, included in Table 3.1, could in principle be affected by minority contributions to the Se and Zn signals coming from the tail-end emission

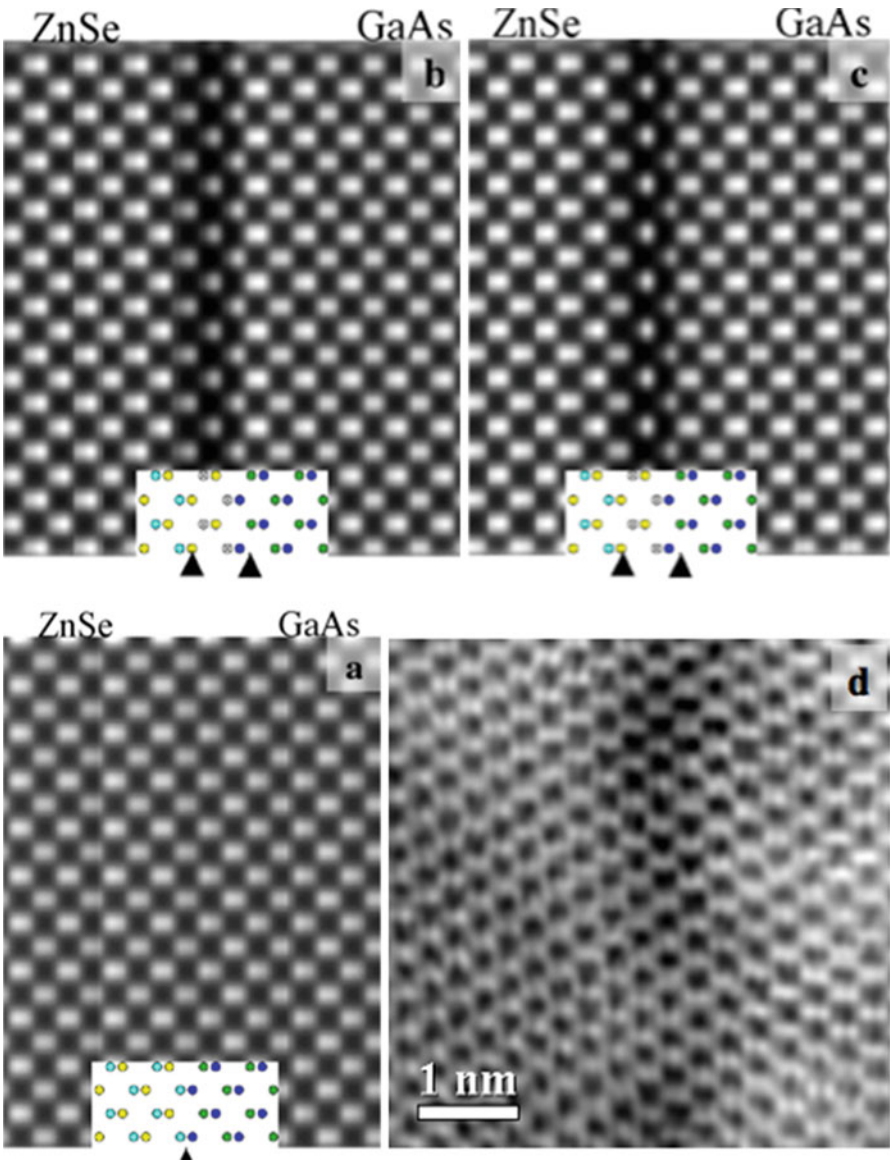


Fig. 3.13 Simulated (**a**–**c**), and experimental (**d**) HAADF images in [1,1,0] zone axis. The *insets* in (**a**), (**b**), and (**c**) mark the position of the atomic columns in *sky-blue* Zn, in *yellow* Se, in *green* Ga, and in *blue* As; the *open circles* with cross or point inside are vacancies on the cation sites. (**a**) GaAs/ZnSe simulation taking into account the strain due to the mismatch between substrate and epilayer, (**b**) simulation by considering the formation of a ternary interface layer (Zn,Ga,)Se with 8 % of vacancies on cation sites, (**c**) simulation by considering the formation of a ternary interface layer (Zn,Ga,)Se with 14 % of vacancies on cation sites, (**d**) experimental HAADF image

Table 3.1 Composition of (Zn, Ga)Se ternary reaction products observed in ZnSe/GaAs heterostructures incorporating a thin buffer layer grown in highly Se-rich conditions (rows 1–3) or with interface fabricated by predosing the GaAs surface with Zn flux followed by ZnSe MEE (rows 4–6). The relative concentrations are shown as determined experimentally by means of EDXS (rows 1 and 4), theoretical values consistent with charge neutrality that closely approximate the experimental EDXS data (rows 2 and 5), and the corresponding alloy composition in terms of Se, Zn, Ga, and cation vacancies V (rows 3 and 6)

Interface		Se	Zn	Ga	V
Se-rich CIL	EDXS	0.45	0.34	0.21	–
Theory	EDXS	0.54	0.31	0.15	–
Theory	Composition	1	0.58	0.28	0.14
Zn predosing	EDXS	0.50	0.40	0.10	–
Theory	EDXS	0.52	0.39	0.09	–
Theory	Composition	1	0.75	0.17	0.08

of the stoichiometric ZnSe epilayer, so that the Se-rich Zn/Se ratio measured by EDXS should be considered, in principle, as a lower limit of the true Se enrichment within the interface region. As indicated by the HAADF images, also the EDXS data suggest the presence of a substantial concentration of vacancies in the interface layer. This is because in the presence of a single type of anions within the sphalerite structure, charge neutrality specifies the average number of valence electrons present on the cation sites. For a Zn, Ga, and Se alloy, charge neutrality requires a concentration y of vacancies V on cation sites equal to half the concentration of Ga atoms, i.e., a composition $Zn_{1-3x/2}Ga_xV_{x/2}Se$. The different alloy compositions can be tabulated compatible with charge neutrality deriving the corresponding expected EDXS relative concentrations, i.e., $(2 - 3x)/(4 - x)$ for Zn, $2x/(4 - x)$ for Ga, and $2/(4 - x)$ for Se. In Table 3.1 are also included theoretical alloy compositions consistent with charge neutrality and with the experimental EDXS data for the two interfaces. The results indicate that for interfaces incorporating a Se-rich CIL, charge neutrality requires that lattice vacancies are present on about 14 % of the available cation sites within the sphalerite structure, while for interfaces fabricated through Zn predosing and MEE, the value decreases to about 8 %. In both cases, the cation vacancy concentration may account for the reduced contrast observed by HAADF imaging in Figs. 3.12 and 3.13d. This is shown in Fig. 3.13b, c where the HAADF contrast expected from the two different interface layers is simulated in the same framework of Fig. 3.13a. In Fig. 3.13b, c, the presence of vacancies within the ternary compound lowers the image intensity near the interface, in qualitative agreement with the experimental behavior observed in Figs. 3.12 and 3.13d. We caution the reader that, strictly speaking, the comparison between simulated and experimental HAADF images should be valid only for the Fig. 3.13d, as it has been acquired in the same zone axis of the simulated images. The results reported in Table 3.1 were also supported by several experimental evidences achieved by further investigations by X-ray photoelectron spectroscopy and synchrotron photoemission spectroscopy [69]. Summarizing, the use of atomic resolution HAADF images together with the relevant image simulation, the EDXS data

analysis, and the theoretical consideration about the charge neutrality of the interface allows one to derive the details of the interface composition at the interface of a heterostructure on atomic resolution level even if the primary beam broadening in the sample thickness would not allow atomic resolution in the EDXS data acquisition. It is also important to underline that accurate data can be obtained only if TEM specimen preparation process has been performed following a procedure designed to avoid preferential thinning in the TEM sample interface area [69].

5.2 Strained Nanostructured Semiconductors

The strain effect in semiconductors has a huge importance as it directly influences the properties of materials and devices and finds direct application in a wide range of applications, like in the case of strain-enhanced advanced CMOS technology or strain-based piezoresistive MEMS transducers [74], and a variety of methods were developed in the years to measure and model the strain status in a solid. What it is necessary to know in many cases is how the strain status is locally, for example, at the interface between two or more materials. Many methods were developed to measure strain in TEM on a sub-micrometer area, with a resolution that can reach the atomic scale, based on diffraction methods [75, 76] or on imaging methods by diffraction contrast [77, 78], HRTEM [79–81], or HAADF [82] imaging. It is worthwhile to remark that the thickness of the TEM sample is an important parameter to be considered to understand if the strain measurement made by TEM is representative of the bulk materials or devices or should be corrected for the effect of elastic strain relaxation induced by the thinning process necessary for the TEM specimen preparation [83]. Moreover, when nanostructures are involved [84–88], the only way to understand the strain status on a local scale is by atomic resolution TEM methods. For example, it has been demonstrated that by combining HRTEM images and geometric phase analysis (GPA) of the resulting micrographs using Fourier transform routine, the strain status can be fully measured [89]. This method is particularly important when applied to hybrid materials formed by two or more nanostructures as in the case of materials for spintronic. In Fig. 3.14 two particles, one of semiconductor TiO_2 and another particle of magnetic Fe oxide, are displayed at high resolution. The HRTEM images enable to understand the epitaxial relationship between the two particles and the strain field associated [90]. Fig. 3.14a, g are HRTEM images of heterostructures in different relative configurations, and Fig. 3.14b, c, h, i are the corresponding fast Fourier transform (FFT) analyses of the regions enclosed by the blue and the red boxes in panel (a), which correspond to brookite TiO_2 viewed along the <1,1,0> and <1,2,0> zone axis, and inverse spinel cubic Fe_xO_y down the <1,1,2> and <2,1,5> zone axis, respectively. In Fig. 3.14d, l are shown the joint diffractograms obtained by merging the FFTs in panels *b–c* and *h–i*, respectively, each traced by a different color. In Fig. 3.14e, m are magnified HRTEM views of the matchstick head in panels *a* and *g*. The relative orientations of the interfacial planes between the two material domains are marked

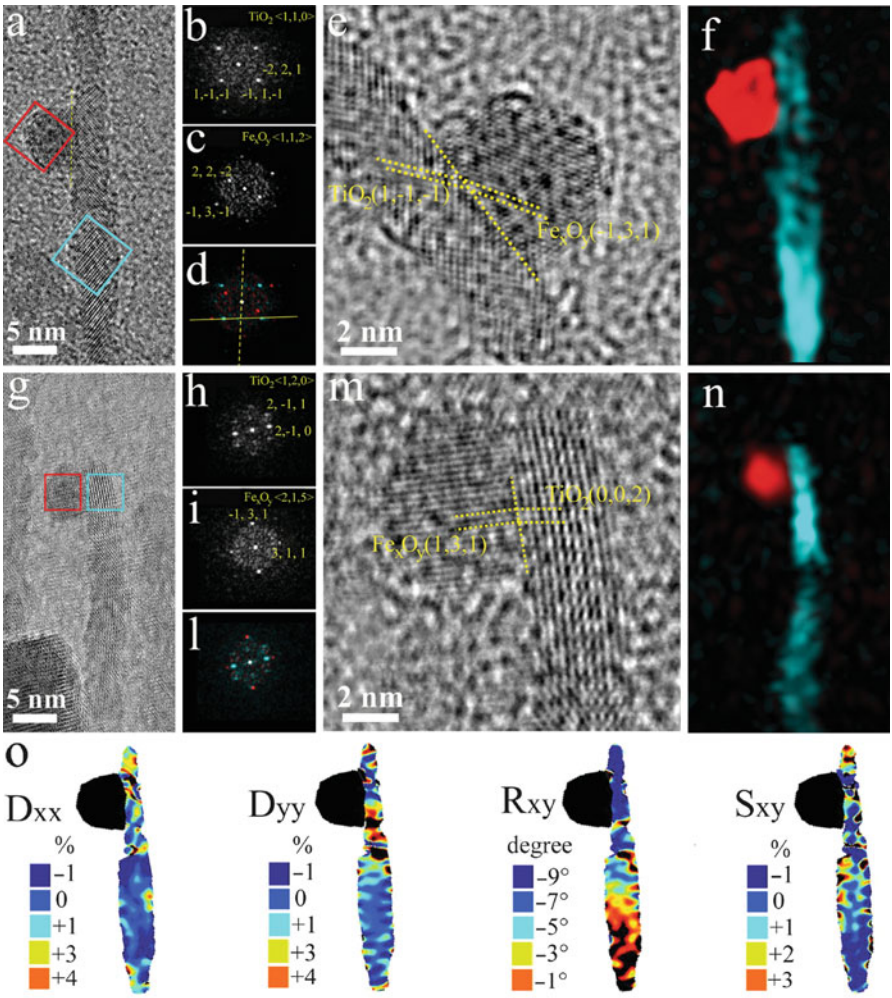


Fig. 3.14 HRTEM images of hybrid semiconductor-magnetic particles together with the relevant diffractograms and the strain analysis maps (see text) (Reprinted with permission from R. Buonsanti, et al. [90])

by dotted yellow lines. In Fig. 3.14e, the interface is perpendicular to the [2,−2,0] TiO_2 and the [0,4,−2] Fe_xO_y directions, while in Fig. 3.14m it is approximately perpendicular to the [2,−1,0] TiO_2 and [3,1,1] Fe_xO_y directions, respectively. The lattice mismatch in the two cases can be calculated as

$$\frac{d^{Fe_xO_y}_{-1,3,1}/\cos(60^\circ) - d^{TiO_2}_{1,-1,-1}/\cos(47^\circ)}{d^{TiO_2}_{1,-1,-1}/\cos(47^\circ)} = 0.2\% \quad \text{and} \quad \frac{d^{Fe_xO_y}_{1,3,1} - d^{TiO_2}_{0,0,2}}{d^{TiO_2}_{0,0,2}} = 1.5\%$$

Figure 3.14f, n are false-color crystal-phase amplitude maps obtained by HRTEM contrast analysis of the images in panels (a) and (g), respectively: the blue and red colors are related to the most intense fringes of the TiO_2 and Fe_xO_y lattices, respectively. Note that the black regions identifiable in the middle of the Fe_xO_y domains (red) in panel *f* correspond to an effective reduction of the fringe visibility thereon, possibly due to the presence of a partially amorphous region or a local variation in the dynamical diffraction condition. The disappearance of the TiO_2 fringes in panels *f* and *n* is due to a rotation and partial amorphization of the rod section in this region. Figure 3.14o is a false-color set of strain maps of fringe displacement in the direction perpendicular (D_{xx}) or parallel to the long nanorod axis (D_{yy}), of fringe rotation (R_{xy}), and of shear stress (S_{xy}) for the rodlike sections of the semiconductor-magnetic hybrid nanocrystal, obtained by GPA analyses of the HRTEM image in panel *a*.

Summarizing, the HRTEM images of nanostructured particles together with the GPA analysis allow a detailed analysis of the strain status along a nanorod and at the interface with another particle constituting a hybrid material. This knowledge represents an essential element for full understanding of the resulting electro-optical properties in view of the application of hybrid nanostructured particles for the realization of spintronic devices.

5.3 Symmetries in Electron Diffraction and Their Applications

The use of an electron probe with high-convergence angle ($\alpha > 10^{-2}$ rad) opens a wide range of applications. Furthermore the use of convergent beam geometries enables to get information from specimen volumes much smaller with respect to the volumes investigated by parallel beam diffraction as a minimum probe diameter of 0.2 nm in convergent beam geometry is easily achievable in most of modern microscope. One feature of a convergent beam electron diffraction (CBED) pattern from a crystal oriented in a low-index zone axis is immediately evident, and it is the high symmetry related to the symmetry of the crystal unit cell. Figure 3.15 shows the symmetries of a [0001] zone axis CBED whole pattern (WP) of a GaSe crystal acquired in a sample area where different polytypes are staked in the direction parallel to the primary electron beam.

The term whole pattern (WP) is used to indicate that we are considering the symmetries of all visible diffracted disks together. All the possible symmetries of all the crystal point groups produce a limited number of symmetries in the relevant CBED diffraction patterns [28] and can be used to probe the sample crystallographic properties on a small illuminated area. Small distortion in the crystal due to defects or variation in the chemistry or to a stress field would produce a variation in the crystal unit cell and can be probed by CBED experiments [91]. This is the case, for example, of the distortion produced by epitaxial relationship between two different grains of materials or to a stoichiometry variations. For example, specimens grown by different dopants can produce different polytypes; a typical case study is GaSe grown from the melt [31]. The polytypism is due to small



Fig. 3.15 Convergent beam electron diffraction pattern in [0001] zone axis of a crystal of GaSe

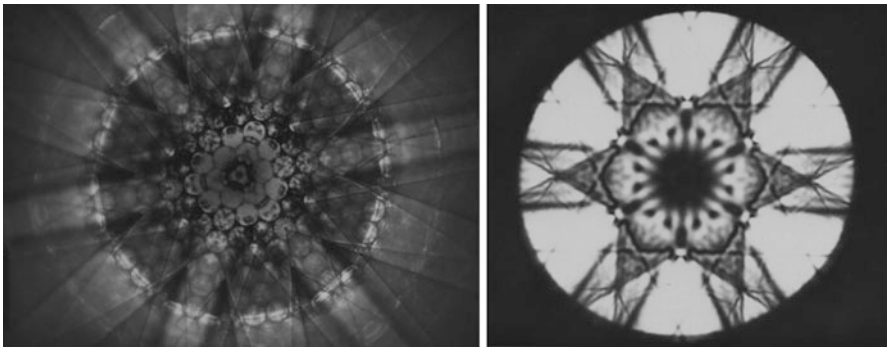


Fig. 3.16 WP CBED (*left*) and LACBED (*right*) as acquired on GaSe crystal doped by iodine and oriented with the [0001] direction parallel to the primary electron beam. The symmetry of the WP CBED is 3 m whereas the symmetry of the LACBED is 6 mm, which univocally identify the $P\bar{6}m2$ space group of the ε polytype of GaSe

modification in the stacking of slab of nearly identical composition but slightly tilted around the direction of grown or slightly shifted along a direction perpendicular to the growth direction. To a first glance, this small variations could appear difficult to be revealed and characterized even by sophisticated atomic resolution experiments performed on state-of-art aberration-corrected equipment. It should be noted that even if the crystal modifications are small, the resulting unit cell is changed along with the crystal symmetry. Indeed, many polytypes can exist within the same specimen forming small grains with sizes ranging from microns to few tents of nanometers and stacked one on the other. An experiment in CBED on thin samples orienting the crystal with the growth direction parallel to the electron beam allows an immediate detection of the symmetries modification as a function of the dopants. In Fig. 3.16 is shown a WP CBED in [0001] zone axis together with the large angle convergent beam electron diffraction (LACBED) in the same zone axis

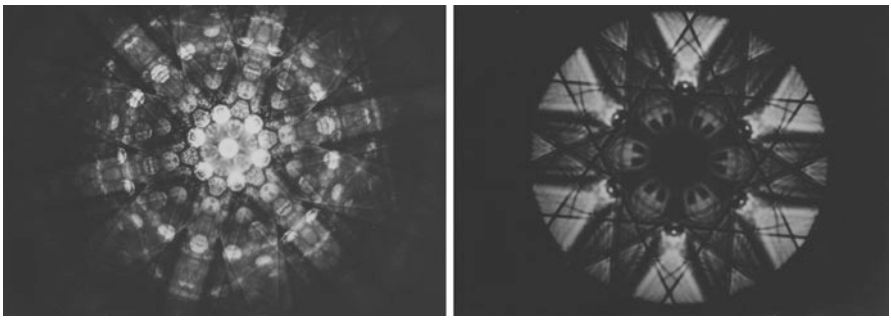


Fig. 3.17 WP CBED (*left*) and LACBED (*right*) as acquired on GaSe crystal doped by arsenic and oriented with the [0001] direction parallel to the primary electron beam. The symmetry of the WP CBED and the symmetry of the LACBED are both 3 mm, which univocally identify the $R3m$ space group of the rhombohedral γ polytype of GaSe

of GaSe crystal doped by iodine. The LACBED pattern is a technique used to mark and magnify the symmetries of the direct diffracted disk [92]. The symmetry of the diffraction on the left of Fig. 3.16 is 3 m, which means that the features of the pattern are repeated every 120° together with a mirror symmetry [29]. The symmetry of the LACBED on the right is higher and it is 6 mm, meaning that the features of the diffraction are repeated every 60° together with two perpendicular mirror planes. These symmetries univocally identify the space group $P\bar{6}m2$ and the relevant polytype of GaSe [31].

In Fig. 3.17 is shown the result of the CBED experiment performed on a GaSe specimen doped by arsenic. In this case the symmetry of the crystal structure is different, and hence the symmetry of the diffractions is consequently different being 3 m in the CBED WP and 3 m in the LACBED, which univocally identify the structure space group as $R3m$ and hence a rhombohedral γ polytype of GaSe [31].

Summarizing, among the vast application of convergent beam electron diffraction, here the attention is focused on how the symmetry of the relevant diffraction patterns can be used to disclose subtle but fundamental properties of a material by using a very straightforward and reliable approach based on CBED TEM experiments.

5.4 Studies of Clusters with Different Shape and Aspect Ratio

The synthesis of nanocrystals with complex shapes is an exciting development in nanoscience [86, 93] as it paves the way to materials with tailored, geometry-dependent properties and to new concepts of self-assembly arising from the mutual interaction of such nanocrystals. For example, semiconductor tetrapod-shaped nanocrystals present promising potential for building blocks in solar cells [94, 95] as active components in nanoscale transistors [96], as field emitters, and might open

up new possibilities to create unique architectures that cannot be realized with spherical or rod-shaped nanocrystals. The availability of chemical solution-grown fabrication process for colloidal nanocrystals has opened the way to production of nanocrystals with a wide range of composition and shapes. TEM-based approaches coupled with ab initio DFT calculations represent unique opportunities to study the properties of complex nanocrystals unveiling the relationship behind the performances of such fascinating materials and allowing to understand how a particular shape and/or properties can be obtained by properly tuning the growth conditions. For example, the properties of a tetrapod-shaped semiconductor are related to the structure of the different branches and of the core, which determine the propagation of the charged carriers [97]. In Fig. 3.18 are shown some HRTEM experiments on CdTe tetrapods with different orientations with respect to the primary electron beam, as sketched in the relevant insets of Fig. 3.18a, b. The contrast at the interface between the arm and the core, as marked by the rectangular in Fig. 3.18c, has been modeled in (d) and simulated in (e) by full dynamical calculations [97]. The atomistic model in Fig. 3.18d was built by joining three hexagonal wurtzite domains sharing the (1,1,−2,2) twin boundary. Two domains represent two of the wurtzite arms of the tetrapod joined to central wurtzite core.

The formation of the structures observed in Fig. 3.18 is sketched in Fig. 3.19. The left column shows an exploded view of three different types of nuclei (middle column) that could rationalize the formation of rods (a), dipods (b), and tetrapods (c). Two types of domains are considered in this model (as shown in a, left side). One domain exposes a (0,0,0,−1) facet (here defined as type I domain), whereas the other domain exposes a (0001) facet (type II domain). In a multiple-twin nanocrystal the two types of domains are connected to each other by a twin boundary. Of these two types of domains, only one can grow to an elongated structure, although at the present it is not yet understood which one of the two domains this will be. Let us assume that the "fast-growing" domain is of the type I. Therefore, the nucleus from which a rod (or a matchstick) evolves is composed of at least one domain which is of type I. This domain can be joined to one type II domain (as shown in a) or to more type II domains (up to three) by (1,1,−2,2) twin boundaries. These will be the slow-growing domains. Then, if a second twin boundary is generated between any of these type II domains and yet a new type I domain, a second arm will form (a possible case for this situation is shown in b). In the most crowded situation, eight domains can join together to form an octahedral crystal (as shown in c). Four of these domains can be of type I and four of type II, and in this case four arms will branch out from this core, forming a tetrapod like the one shown in the Fig. 3.18.

Indeed, the occurrence of the observed structure would require a low energy of formation to be thermodynamically favored. The calculations of the energy of formation of the (1,1,−2,2) twin boundaries with head to tail polarity configuration can be performed by ab initio LDA DFT calculations [97]. The simulations give for this kind of defect an energy on formation of 70 mJ/m^2, which is indeed not a low energy of formation [97, 98], and hence this kind of structure would not be formed unless the presence of other factors could promote their formation. This observation

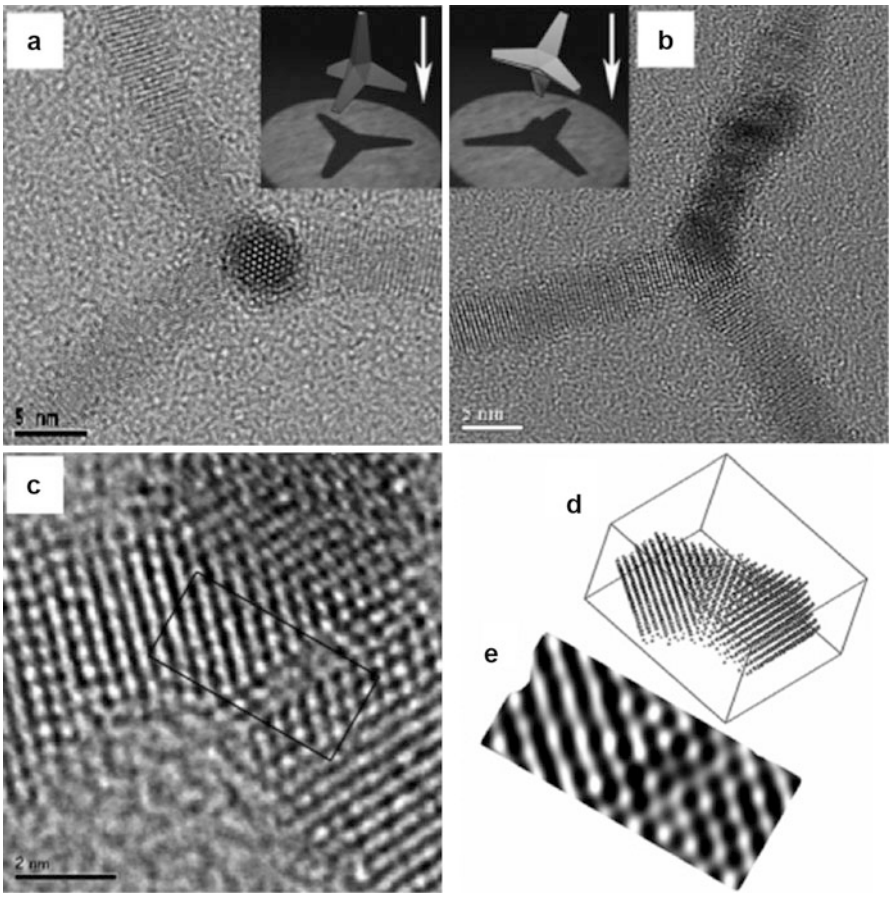


Fig. 3.18 (**a**) HRTEM image of a CdTe tetrapod with one arm pointing upward. Inset: orientation of the nanocrystal with respect to the electron beam (*white arrow*). The analysis of the symmetry and of the lattice spacing of the *arms of several tetrapods* indicates a wurtzite structure (space group $P6_3mc$) with lattice parameters corresponding to (**a**) 0.458 nm and (**c**) 0.75 nm, (respectively). (**b**) Tilted tetrapod. *Inset*: orientation of the nanocrystal with respect to the electron beam (*white arrow*). In particular, in this geometry *two arms* are superimposed. (**c**) Central region of the tetrapod shown in (**b**) is imaged here at higher magnification. The *rectangular contour* is the region that is the object of the image simulation. (**d**) Supercell containing the atomistic model used to simulate the HRTEM image of the *central region of the tetrapod*, viewed along its [−2,−4,−7] zone axis and rotated around this axis (which is perpendicular to the plane of the image) so that the model has the same orientation as the real nanocrystal in the HRTEM image in (**c**). (**e**) Simulated HRTEM image of the *core region of the tetrapod* contoured in (**c**) (Reprinted with permission from Carbone et al. [97]. Copyright 2006 American Chemical Society)

allows one to rationalize the role of the organic molecule capable of promoting anisotropy grown of nanostructures in solutions; in the case of tetrapod of CdTe, it was in fact observed that the factor promoting the formation of the twinned structure and the growth of highly anisotropic tetrapods is, in the case shown

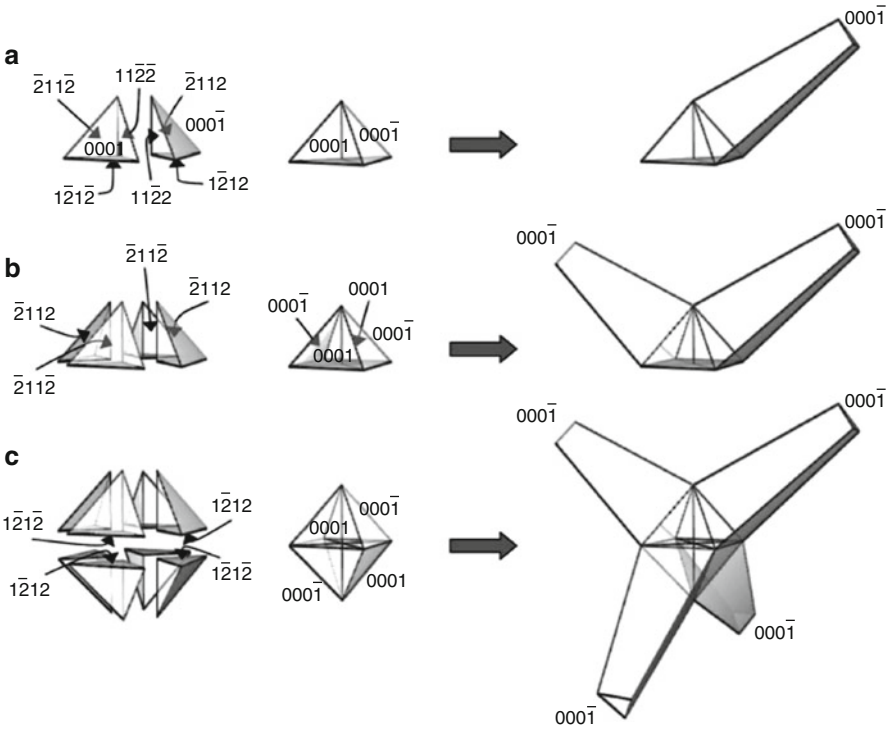


Fig. 3.19 Sketch of multiple-twinning model (Reprinted with permission from Carbone et al. [97]. Copyright 2006 American Chemical Society)

here, the presence of methylphosphonic acid that could bind to Cd^{2+} forming a highly mobile composite that promotes the fast growing of the crystals along preferential directions [97].

To unveil some important properties of nanostructures, it is in some cases necessary to have a resolution better than one Angstrom [16]. As we have seen before, even if the wavelength of electrons in the TEM is of few nanometers and hence the diffraction limit to spatial resolution is hundreds of times better than necessary for atomic resolution in crystalline solids, the presence of aberrations in the electron lenses limit the resolution slightly above the Angstrom. There is a statement of P. W. Hawks that concisely well explain this point [99]:

> Electron lenses are extremely poor: if glass lenses were as bad, we should see as well with the naked eye as with a microscope! The demonstration by Otto Scherzer in 1936 that skilful lens design could never eliminate the spherical and chromatic aberrations of rotationally symmetric electron lenses was therefore most unwelcome and the other great electron optician of those years, Walter Glaser, never ceased striving to find a loophole in Scherzer's proof. In the wartime and early post-war years, the first proposals for correcting Cs were made and in 1947, in a second milestone paper, Scherzer listed these and other ways of correcting lenses; soon after, Dennis Gabor invented holography for the same purpose.

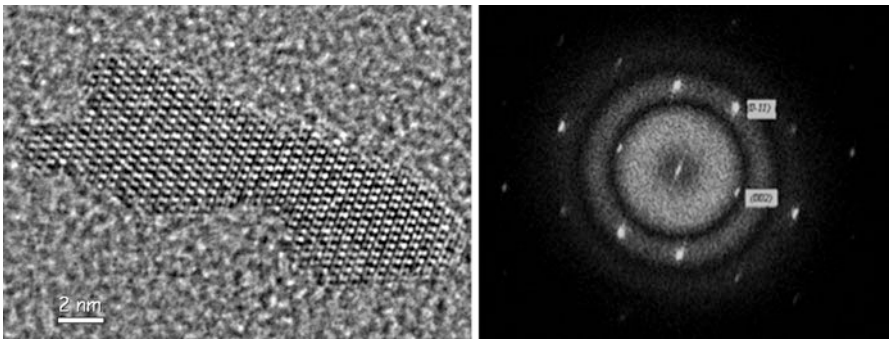


Fig. 3.20 HRTEM of anatase TiO_2 nanorod in [1,0,0] zone axis (*left*) along with the relevant diffractogram (*right*)

Therefore, along the time two different philosophies tried to overcome the limit related to the electron lens aberrations; one is instrumental and has produced only recently microscopes with spherical and chromatic aberration correctors [17] capable to achieve a resolution of about 50 pm [100, 101]. The development of aberration-corrected microscopes is definitely a revolution in the modern electron microscopy and will improve substantially our knowledge of the materials but once again mark how reliable information can be achieved only as a result of an accurate experiment. In fact, the information we obtain from a microscope it is always a convolution between the specimen and the microscope setup, and we cannot derive the true material properties if we do not know precisely the equipment conditions; this is especially true for the aberration-corrected microscopes whose conditions have a stability limited in time as they are intrinsically unstable [19]. The other way to overcome the limit induced by the electron lens aberrations is by developing physical methods, for example, the holography [102] cited above by Hawkes, which despite lens aberrations are capable to recover for their influences improving the resolution of TEM-imaging experiments [20–23, 103] to about 0.1 nm or below. As an example, coherent electron diffraction imaging enables to increase the resolution of a standard microscope to a resolution comparable with aberration-corrected equipments revealing features of the nanostructured material, otherwise unreachable, and extending so far the resolution of standard HRTEM experiments down to a resolution of 70 pm [22, 23]. This method is a typical example of the new ways that can be opened by using a TEM in a nonconventional manner to explore new ideas based on the fundaments of physics. In fact, by using the information in the phase-contrast HRTEM image, a combination of coherent electron diffractive imaging (EDI) and HRTEM can increase the resolution up to a limit set mainly by the highest spatial frequency contained in the electron diffraction pattern. As an example, let us consider the semiconducting nanoparticle in Fig. 3.20. In Fig. 3.20 is shown an HRTEM image of a nanorod of anatase TiO_2 obtained by using a standard TEM equipped by an objective lens with spherical aberration coefficient C_s of (0.47 ± 0.01) mm and operated at an accelerating

voltage of 200 kV and hence capable of a resolution in HRTEM imaging at optimum defocus of 0.19 nm [7].

The diffractogram shows the presence of <0,0,2> spots, which are forbidden for the $I4_1/amd$ tetragonal space group of a genuine anatase phase. Further experiments and calculations demonstrate that the {0,0,2} extra spots are not due to dynamical diffraction effects or mis-tilt of the rod with respect to the electron beam and should therefore be due to a crystal structural modification [22]. To investigate to a further detail, it was performed a coherent electron diffraction imaging experiment (EDI). In principle if intensity and phase of a diffraction pattern are known, it is possible to obtain the image of the diffracting object by the inverse Fourier transform of the whole diffraction pattern. Unfortunately, phases are lost in the experimental diffraction pattern (the well-known phase problem), and hence at least half of the information necessary to image the object is lost. If we consider an isolated object, we can recover the phase information by oversampling the measured diffraction pattern at a suitable frequency. This is equivalent to an a priori knowledge of as many zero scattering points in the object space as the unknown phases in the Fourier space to compensate for their loss in the measured diffraction pattern and to construct a system of equations with an equal number of unknowns. In practice, the reconstruction of the lost phases is performed by using iterative phasing algorithms [104, 105]. The iterative transform algorithm bounces back and forth between the real space object domain, where some constraints based on a priori knowledge of the object are applied, and the reciprocal space domain where the measured modulus data constraints is applied. However, in any diffraction experiments, some intensities are lost due to imperfection/saturation of the detectors or to low signal-to-noise ratio. This further lack of information can be also compensated by a priori information on the diffracting specimen, if available. The EDI approach requires that the diffracted waves emitted by the object have to be scattered from a spatial region of finite size-named support [106] as for a finite domain the Shannon's theorem can be applied and states that under appropriate oversampling conditions, the image of the domain by the action of a function f can be reconstructed univocally [107]. A strong a priori information is the knowledge of the finite support, which in the case of coherent diffraction imaging in a TEM can be known with high accuracy as we can acquire an HRTEM image of the investigated object. EDI approach combines both the HRTEM image information (object support and low-resolution object projected crystal electrostatic potential) with the electron diffraction pattern to realize a dual-space phase reconstruction. In practice, the EDI phasing approach aims to extend the relatively low-resolution crystal potential information already contained in the HREM image up to the maximum spatial resolution corresponding to the highest Miller index diffraction spots measured – with sufficient accuracy – in the electron diffraction pattern. Therefore, EDI requires experimentally the acquisition of an HRTEM of the object illuminating an area at least double the size of the particle to satisfy the oversampling conditions [22] and a nano-diffraction (n-DP) by using the same illumination conditions. Figure 3.21 shows (a) the n-DP with the central part missing due to the presence of the beam stopper used to avoid the damage of the detector by the

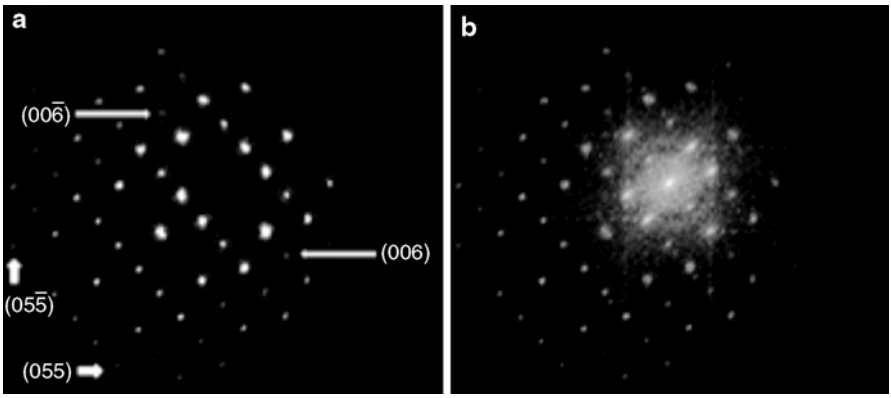


Fig. 3.21 (**a**) Experimental nano-diffraction pattern and (**b**) experimental nano-diffraction pattern merged to the FFT of the HRTEM image of the nanorod shown in Fig. 3.20

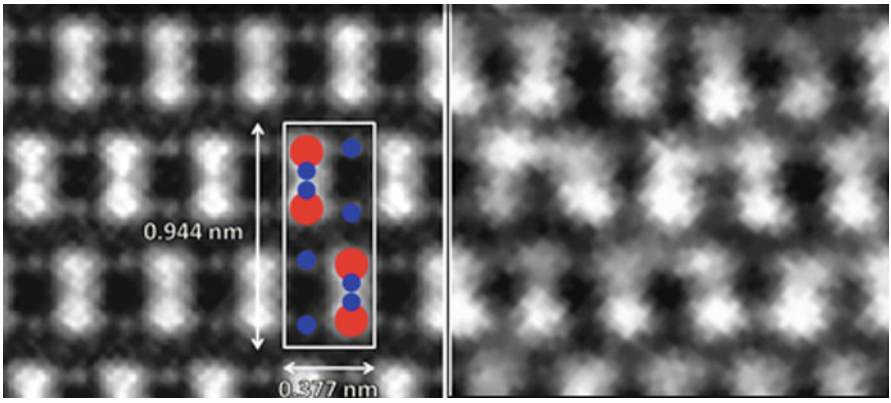


Fig. 3.22 (*Left*) Phase-retrieved image of the projected crystal potential of a magnified small portion of the rod in Fig. 3.20. In the inset the TiO_2 unit cell is reported with the Ti atoms in *red* and the oxygen atoms in *blue*. As can be seen all the atomic columns in the projection can be seen due to the enhanced resolution of the retrieved image. On the right is shown, for ease of comparison, a relevant area of the rod in the HRTEM, at 0.19 nm resolution, in Fig. 3.20

high intensity of the direct beam; the missing part is derived from the FFT of the HRTEM image and merged in the n-DP after scaling and rotation obtained by using as reference some common diffracted intensities [22] as result in Fig. 3.21b.

In the figure the white arrows indicate the {0,0,6} forbidden diffracted spots together with the {0,5,−5} spots which are the highest spatial frequencies in the diffraction pattern corresponding to a lattice spacing of 70 pm, which is therefore the resolution theoretically achievable in this case by EDI. Figure 3.22 shows (left) the phase-retrieved diffractive image of a portion of the TiO_2 nanocrystal shown in Fig. 3.20, which has been rotated to allow the c axis to be vertically oriented. A rectangular box has been superimposed, which depicts the tetragonal structure of

bulk anatase with the titanium and oxygen atomic columns in red and blue, respectively. By simulating the retrieved image, it is possible to measure accurately the resolution, which is of 70 pm, as theoretically expected [22] and allows to distinguish the oxygen atomic columns. For ease of comparison, on the right of Fig. 3.22 is reported, magnified, a portion of the HRTEM at 0.19 nm of resolution in Fig. 3.20.

The enhanced resolution enables to measure a distortion of the unit cell due to a reduction of the length of the c-axis of 0.57 % with respect to the c axis of bulk anatase. This reduction changes the symmetries of the anatase unit cell and makes visible the forbidden reflections as experimentally observed in the n-ED patterns. The distortion is possibly due to unusual local variation in titanium and/or oxygen occupancy and/or surface driven lattice strain in nanometer-sized crystal domain related to unusual properties of anatase TiO_2 in nano-sized particles [22].

Until very recently, the application of coherent electron diffraction imaging in the TEM was demonstrated only for isolated particles as the sampling requirement is more straightforwardly achieved for an isolated structure, and this is the reason why when the method was originally conceived for X-rays by Sayre [108] was for isolated structures. De Caro et al. [23] in 2012 demonstrated that the sampling requirement can be also satisfied by confining properly the electron beam in an area of an extended specimen and reconstructing, as a case study, the projected potential of a Si sample oriented in [1,1,2] zone axis at a resolution of 71 pm. This last experiment paves the way to the application of EDI at any kind of samples at subatomic resolution and enables to study, for example, the subtle structure of an interface or of an extended defect. This generalized EDI method was named Keyhole coherent Electron Diffraction Imaging (KEDI) [23].

5.5 The Challenge of EDX and EELS at Atomic Resolution on Nanostructures

The recent development of aberration correctors for TEM lenses, capable of focusing an electron beam in an area of 50 pm [18], poses the question if atomic resolution can be achieved not only in coherent and incoherent elastic imaging but also in EDXS and EELS spectroscopies and relevant mapping. There are two main effects to be considered as far as spatial resolution in spectroscopy concerns: the broadening of the primary beam in the interaction with the specimen and the delocalization of inelastic interactions, which means as follows: how far from an atom must be the electron probe before the atom edge can be detected? [109]. Indeed the question in this form could be misleading as the tails, even of relatively localized inelastic interaction, like the ionization of an atom, are on a scale at least one order of magnitude larger than the interatomic distances in a solid. A better way to pose the problem could be as follows: what is the degree of localization in inelastic scattering? This problem has been a source of debate on semiclassical [110, 111] and quantum mechanical calculations where the latter gives more localized results [112]. Indeed, even the second question could be ill posed as the

degree of the localization in a spectroscopic measurement in a TEM depends also on the experimental setup and on the kind of detector used, as it directly influences the physics of the interaction to be measured: it is one of those fascinating cases, well know in quantum physics, where we cannot divide the interaction to be measured from the influence of the experimentalist and of its experimental setup [113, 114]. The quantum mechanical perspective requires that the entire system of incident beam, specimen, and detector represents one quantum mechanical measurement system and that the view of the specimen does depend on how you look at it [115]. We can achieve EDXS and EELS measurement by using proper electro-optical design of the spectrometer and microscope column, choosing and controlling very accurately the experimental setup and always considering the factors, based on fundamental physics, limiting the achievement of a result [47]. Always the experimental conditions in which the results are obtained in a TEM investigation play a strong (and often very subtle) role and in particular when we approach the physics limit of what can be measured in an experiment. When the beam interacts with the specimen always spread laterally. Even if we do not consider the scattering with the atoms, the beam would broaden by $2\alpha t$ for a probe of convergence semi-angle α focused on the top surface of a specimen of thickness t. The broadening, for a highly focused probe and a thin specimen, easily exceeds 1nm [47]. EDXS experiment resolution is more strongly related to beam broadening with respect to EELS experiments, as in the latter the beam-broadening effect can be reduced by using an angle-limiting aperture that removes electrons that deviate from the optic axis by more than its semi-angle β. A proper choice of β can reduce the effect of the beam broadening to be comparable with interatomic distances in a solid [47]. Indeed, the channeling effect that occurs in crystalline specimen oriented along low-index zone axis reduces the beam broadening with respect to amorphous material, or not well-oriented crystalline specimens, and hence improves the spatial resolution of EELS but also of EDXS experiments. An accurate and convincing analysis of the limiting factors to the spatial resolution of the spectroscopies in TEM/STEM has been reported by R. F. Egerton [47] who considers the effect of beam broadening, chromatic aberration, inelastic delocalization, and radiation damage together with the use of a proper geometry for the detector. For example, in Fig. 3.23 is reported the localization distance as a function of the internal diameter of an annular detector as this shape maximizes the spatial resolution of an EELS experiment (Fig. 3.23).

Providing that the equipment is properly suited and the experimental set up is properly tuned and controlled, the aberration-corrected microscope provided very recently the evidence that both EDXS and EELS can map the chemistry of a semiconductor at an atomic level. This is shown in Fig. 3.24 where the EDXS map of a GaAs specimen is shown with a clear definition of the atomic cations and anions in the sphalerite structure seen in the [1,1,0] zone axis. In this projection, the distance between cations and anions within the dumbbells is of 0.14 nm. A similar result is shown in Fig. 3.25 in the case of an EELS map. On the other hand the spatial resolution depends on the physical phenomena to be studied. In Figs. 3.24 and 3.25 the atomic resolution maps were obtained in both EDXS and EELS by

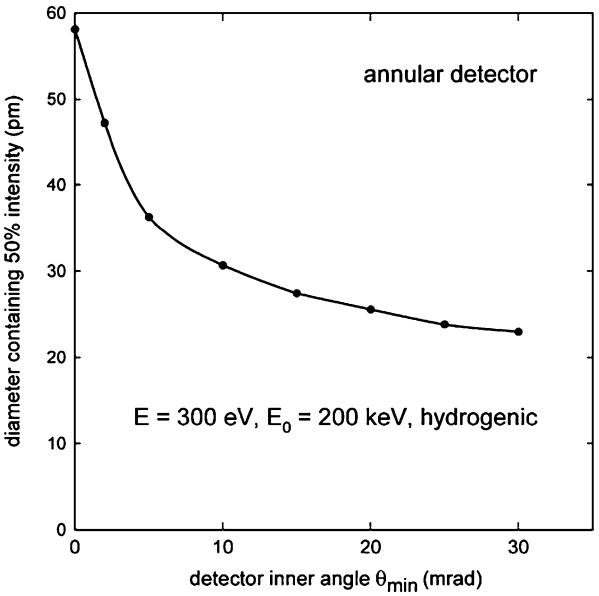


Fig. 3.23 Localization distance of EELS signal as a function of the internal diameter of an annular detector, for an external diameter corresponding to 45 mrad scattering angle. The calculation assumes parallel incident illumination and incoherent inelastic scattering [47]

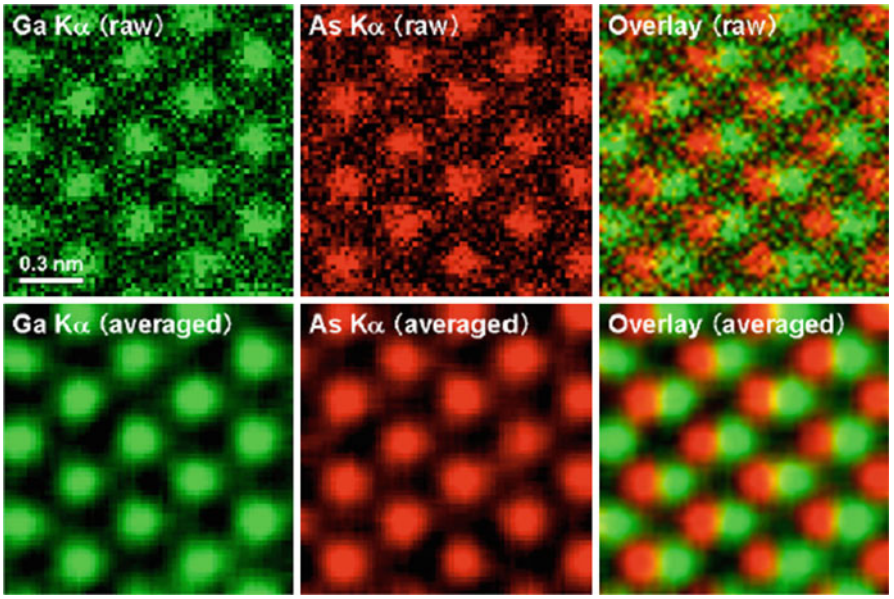


Fig. 3.24 EDXS maps by using K-edges of a GaAs sample seen in [1,1,0] zone axis. In the [1,1,0] projection, the spacing of cations and anions in the GaAs dumbbells is 0.14 nm (Reproduced by courtesy of Jeol Japan)

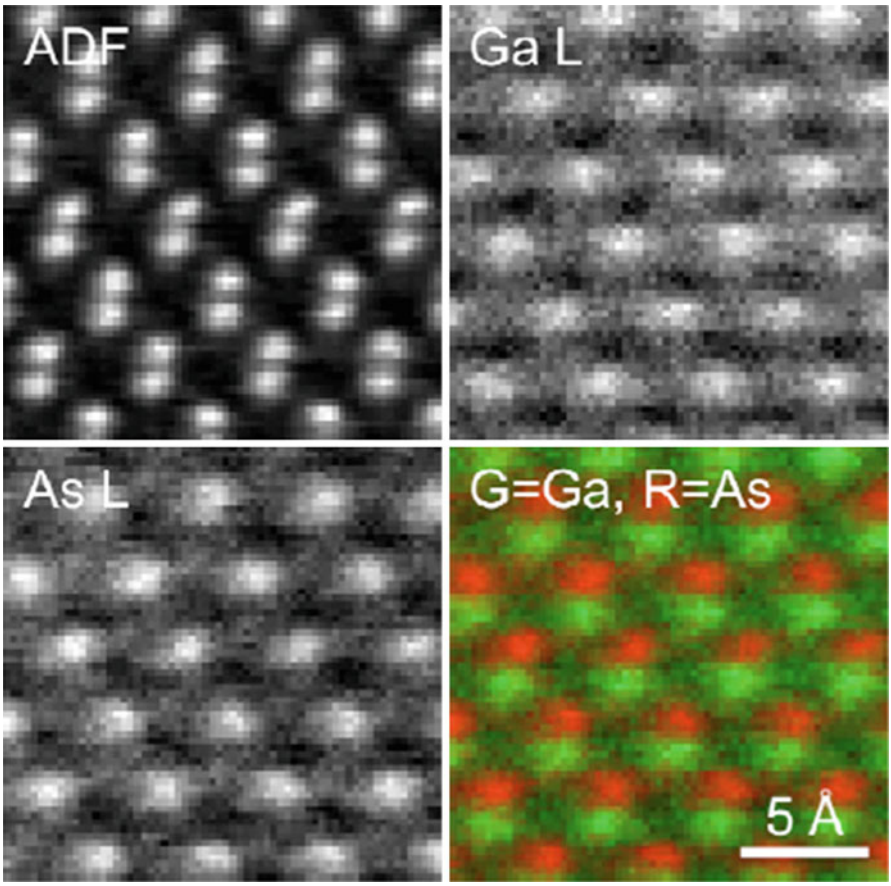


Fig. 3.25 EELS maps by using L-edges of a GaAs sample seen in [1,1,0] zone axis. In the [1,1,0] projection, the spacing of cations and anions in the GaAs dumbbells is 0.14 nm (Reprinted with permission from Krivanek et al. [123])

measuring high-energy edges of As and Ga, K-edges for the EDXS, and L-edges for EELS measurements, respectively. If the interactions to be measured are in the low-loss region of an EELS spectrum, the effect of the delocalization should prevent to achieve truly atomic resolution in the measurements.

A very recent methodology based on EELS, and named Electron energy-loss Magnetic Chiral Dichroism (EMCD), is capable to measure the distribution of the magnetic moments in a material and hence represents a very precious tool for the study of future materials for spintronic [43]. The method is the homologous X-ray Magnetic Circular Dichroism (XMCD), developed by using polarized X-ray photons produced by synchrotrons, resulting from the dependence of the absorption cross section as well as the absorptive/dispersive part of the scattering amplitudes for X-rays on the magnetization of the target [116]. These effects occur for energies close to an inner shell absorption edge and are intimately correlated to the spin and

orbital polarization of the empty density of states, resulting in a quantitative determination of local magnetic spin and orbital moments via sum rules and element-specific manners [117]. In the case of EMCD, the resolution of 1 nm demonstrated so far is one order of magnitude better with respect to the one achievable in an XMCD experiment. Based on theoretical evaluation of the delocalization phenomena in EMCD experiments, it should be possible to achieve a resolution of 0.2 nm and hence practically an atomic resolution in the measure of the distribution of the magnetic moment in a lattice [118] quantified by proper sum rules [44]. This method is another typical example of the new ways that can be opened by using a TEM in a nonconventional manner to explore new ideas based on the fundaments of physics. The ideas behind the EMCD emerge comparing the absorption cross section (Eq. 3.1) in the electron absorption, at the base of the Electron Energy-loss Near Edge structure (ELNES), to the absorption cross section (Eq. 3.2) for X-ray, the latter at the base of X-ray absorption near edge structure (XANES):

$$\frac{\partial^2\sigma}{\partial E\partial\Omega} = \sum_{i,f} \frac{4^2\gamma^2 k_f}{a_0^2 q^4 k_i} \left|\langle f|\vec{q}\cdot\vec{R}|i\rangle\right|^2 \delta\left(E_i - E_f + E\right) \tag{3.1}$$

where $|i\rangle$, $|f\rangle$ are the initial and final target states, $\vec{q} = \vec{k}_i - \vec{k}_f$ is the momentum transfer from the probe to the target in the interaction, a_0 is the Bohr radius, E is the energy loss, $\gamma = 1/\sqrt{1-\beta^2}$ is the relativistic correction factor, and $\vec{R}$ is the position operator of the target electron.

$$\sigma = \sum_{i,f} 4\pi^2 \hbar\alpha\omega \left|\langle f|\vec{\varepsilon}\cdot\vec{R}|i\rangle\right|^2 \delta(E_i - E_f + E) \tag{3.2}$$

where $\alpha = e^2/4\pi\varepsilon_0\hbar c$ is the fine structure constant and $\vec{\varepsilon}$ is the polarization vector of the adsorbed photon. From Eqs. 3.1 and 3.2 it results that, within the dipole approximation, the polarization vector of the adsorbed photon plays the same role of the momentum transfer in ELNES. The similarities between Eqs. 3.1 and 3.2 can be rationalized considering that the physical entity involved in both phenomena is the electric field: in the case of the ELNES, it is the electric field generated by the electrons of the beam and in the case of the XANES, it is the electric field of the electromagnetic wave of the X-ray beam. In the XMCD experiments the circularly polarized photon generates a rotating electric field at the atom position. The same should be generated in the relevant TEM EMCD experiment. From the formal point of view, we have in the XMCD the polarized vector as $\vec{\varepsilon} + i\vec{\varepsilon}'$, where $\vec{\varepsilon}\perp\vec{\varepsilon}'$, the imaginary part comes into play as the vertical and horizontal electric field components are shifted by $\lambda/4$ that makes a phase difference of $e^{ik\lambda/4} = i$. In the EMCD, in analogy, we should have $\vec{q} + i\vec{q}'$ with $\vec{q}\perp\vec{q}'$ and $|\vec{q}| = |\vec{q}'|$. The setup for the EMCD is therefore sketched in Fig. 3.26. In particular for the case study shown here, the sample to be measured is a thin layer of iron-grown epitaxial by MBE on a GaAs

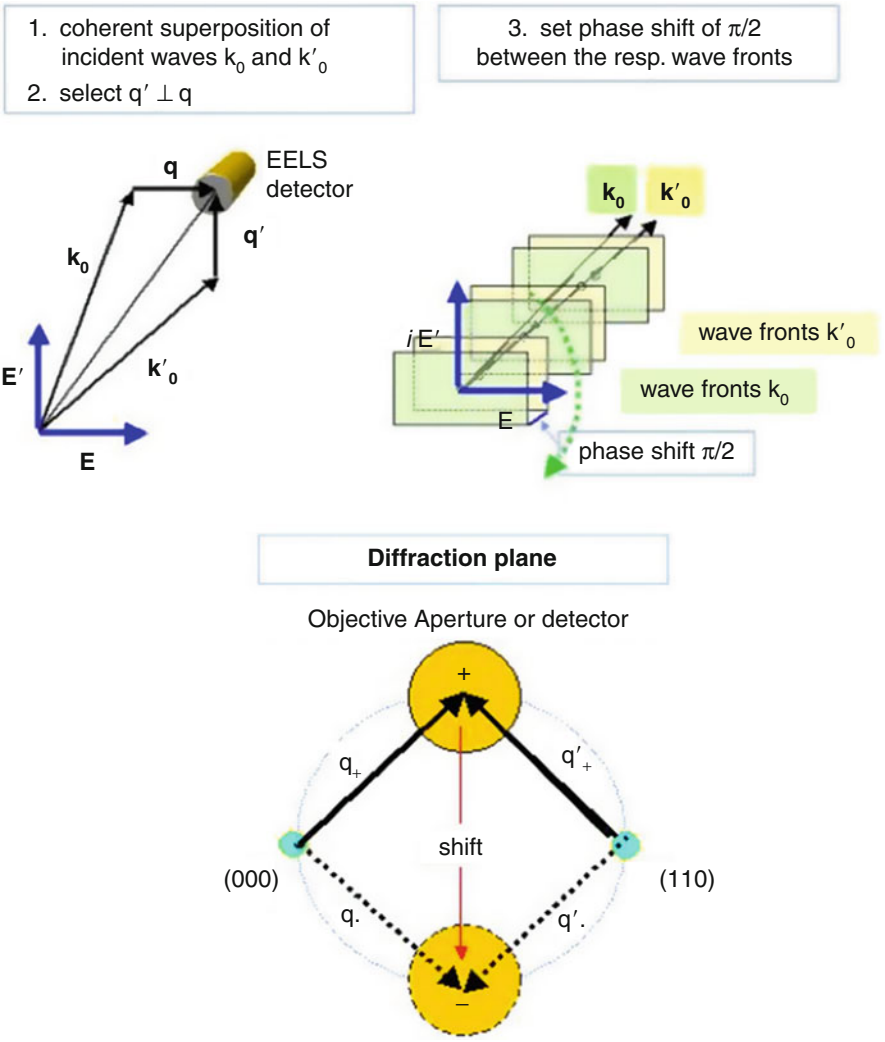


Fig. 3.26 Simplified scattering geometry, drawn in the diffraction plane of the TEM. *Left*: the detector (or a contrast aperture) selects $\vec{q}$ and $\vec{q}'$. *Center*: Bragg diffraction creates a coherent superposition of two incident plane waves (with wave vectors $\vec{k}_0$ and $\vec{k}'_0$ and electric field vectors $\vec{E}$ and $\vec{E}_0$) in the Fe crystal. A phase shift of $\pi/2$ is set between the two wave fronts by tilting the incoming beam. *Right*: the *larger circle* represents the points for which $\vec{q}$ is perpendicular to $\vec{q}'$. The *two smaller circles* show the two positions for which the condition $|\vec{q}| = |\vec{q}'|$ is also true and indicate the actual EMCD experimental setup. As the two positions "+" and "−" have opposite chirality, EMCD can be detected by simply acquiring spectra at the two positions and taking their difference (Reproduced from Suppl. Info of Schattschneider et al. [43])

(001) substrate [43]. The ELNES is measured in the diffraction plane in those positions where the conditions $\vec{q} \perp \vec{q}'$ and $|\vec{q}| = |\vec{q}'|$ are satisfied as shown in the right part of Fig. 3.26.

The chiral signal is the difference of two measured spectra with different chirality of the allowed transitions relative to the magnetic moments. This can be done by changing the phase shift from $\pi/2$ to $-\pi/2$; this would reverse the helicity of the electric perturbing field. However, definition of the phase of the excitation is not straightforward. According to the Bloch theory, the electron beam in the crystal is described by a superposition of several Bloch waves [2]. Their amplitudes and phases are determined by the boundary conditions, namely, the beam tilt and the specimen thickness. There are several diffracted intensities that can be generated in a crystalline specimen; for the EMCD experiments the diffraction condition in two-beam conditions need to have electron waves with a phase difference of $\pi/2$ to reproduce the situation used in the XMCD experiments. The condition of perpendicularity of transferred momenta would be fulfilled by any point located on a virtual circle drawn having, as a diameter, the segment connecting the two Bragg spots under examination (right panel of Fig. 3.26). Only two points in the circle fulfill also the condition $|\vec{q}| = |\vec{q}'|$ as shown in Fig. 3.26. The spectrometer entrance aperture is hence placed in those positions and the two spectra, with opposite chirality, are acquired and therefore subtracted revealing the dichroic signal [43].

In Fig. 3.27 it is reported the EMCD signal, and the relevant simulations, as measured in the first experimental evidence of the EMCD method. The experiment demonstrated the feasibility of a measure of dichroic signal in a magnetic layer of

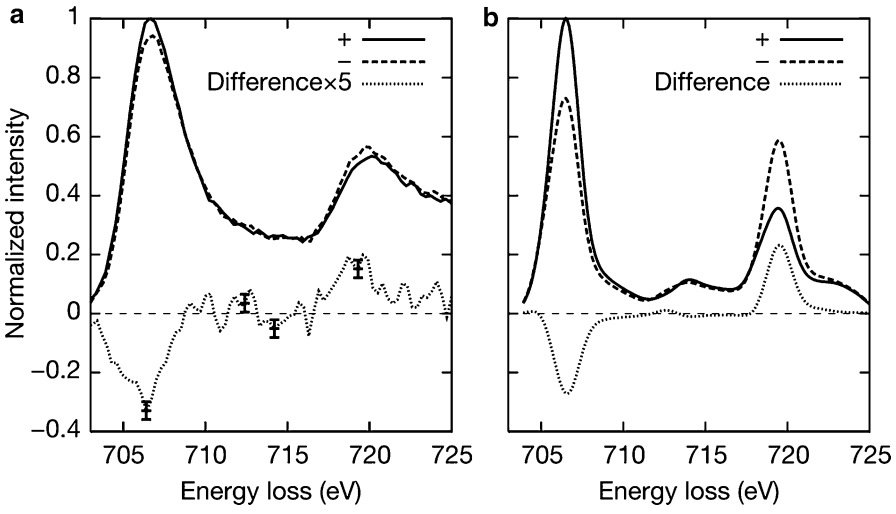


Fig. 3.27 Energy-loss magnetic chiral dichroism. Measured (**a**) and simulated (**b**) Fe L2,3 edges for 10 nm Fe on GaAs (001) in the two configurations "+" and "−" explained in Fig. 3.26. The difference (magnified by a factor of 5 in the figure) is 0.07 for the measured spectra and 0.32 for the simulations. The r.m.s. of the noise, indicated by the error bars in a, is ±8 % of the difference (Reproduced from Schattschneider et al. [43])

Fe grown epitaxially on GaAs (001) substrate performed in a TEM by using the experimental setup in Fig. 3.26.

Other experimental setup can be also used to perform EMCD experiments [119], and recently the use of electron vortex beams in the TEM has successfully been applied in the acquisition of EMCD data [120]. The results in Fig. 3.27 show also the high noise level of the first pioneeristic work; in the few years between the first experiment and now, the EMCD experiments have been repeated many times on different material systems, by different researchers all over the world, and by different experimental setup producing a definitive improvement of the signal-to-noise ratio and a reliable quantitative map of the distribution of the orbital and spin magnetic moments [44, 45] in the solid state. The EMCD is still a fast-growing approach and represents a new valuable tool in the study of magnetic properties of materials at the highest spatial resolution, but the approach also shows, once more, how the electron microscope can also be used to perform original experiments capable to investigate the fundaments of physics.

6 Conclusions and Future Perspective

TEM methods for the characterization of semiconductor nanomaterials are a vast topic as there are tens of different approaches developed to study the structural, chemical, electronic, optical, and magnetic properties of modern nanostructured semiconductors. Here, it has been tried to give an overview of the possibility of the investigations based on electron microscopy but, due to the dimension of the issue, only in relatively few cases the degree of deepening of TEM methods have been described with a bit more of detail and by practical examples. The choice of the examples and of the methods to be marked, certainly not exhaustive, has been guided by the aim to show how powerful is the set of methods based on electron microscopy to study fundamental and subtle properties of the semiconducting nanomaterials and how all the methods developed should be considered as a whole, because the more modern approaches, for example, aberration-corrected HRTEM or HAADF imaging, are extremely powerful investigating methods but cannot replace other older approaches like diffraction contrast imaging of convergent beam electron diffraction to investigate in a very elegant and effective way some aspects like defects characterization or determination of point group or space groups which are definitively important in the understanding of the properties of nanostructured semiconducting materials and devices. The other guideline in writing this chapter has been the need to mark how always in a TEM experiment what is measured is a convolution between the microscope and the sample, and hence the only way to achieve reliable information on the specimen is by knowing accurately the equipment setup, which is not always straightforward. The importance of the specimen preparation has been also marked; there is no way to achieve reliable information if the specimen has not been prepared properly, and a wrong specimen preparation could produce a sample whose properties are not the same of the pristine one. In a way, up to now, electron microscopy still

needs a well-trained scientist behind the experiment; otherwise the risk of a wrong interpretation of the experimental result is always very high. The modern equipment are much more friendly with respect to the past but still need a highly skillful microscopist to avoid artifacts. The recent discovery of intrinsic instability of aberration-corrected conditions is a warning that should be considered very carefully as super-equipment cannot produce reliable data if not properly used and monitored. On the other hand, some of the examples above try to underline how a TEM is a very flexible equipment suitable to be tuned, even in a not standard way, to reveal new and subtle properties of the matter. With this respect, besides the examples of the EDI and of the EMCD reported above, I would like only to mention here another famous and fundamental experiment performed some years ago in a TEM that demonstrated the self-interference of an electron. The experiment of self-interference of an electron for many years was believed to remain only a *gedankenexperiment*, but the skillfulness of some scientists and the flexibility of a TEM enabled to reveal in a very elegant way the deep quantistic wave-particle dualism of an electron [121]. The recent advances in the realization of aberration-corrected equipment together with further improvement of the new recently methods developed, and above described, will allow to study the properties of the matter and, in particular, of the nanostructured semiconducting materials to the ultimate resolution and accuracy enabling a knowledge of the physics behind the performance of materials and devices as never before.

Acknowledgments I would like to thank Alfonso Franciosi for the many inspiring discussions, Regina Ciancio for the careful reading of the paper and Ezio Cociancich for the help in the realization of some of the figures of the chapter.

References

1. Abbe E (1874) A contribution to the theory of the microscope and the nature of microscopic vision. Proc Bristol Nat Soc 1:200–261
2. Hirsch P, Howie A, Nicholson RB, Pashley DW, Whelan MJ (1977) Electron microscopy of thin crystals, 2nd edn. R. E. Krieger, Malabar
3. Herman A, Sitter H (1996) Molecular beam epitaxy: fundamental and current status. Springer series in materials science, vol **7**. Springer-Verlag Berlin and Heidelberg GmbH
4. Scheel HJ, Capper P (2008) Crystal growth technology: from fundamentals and simulation to large scale production. Wiley-VCH, Weinheim
5. Johnson M, Silsbee RH (1985) Interfacial charge-spin coupling: injection and detection of spin magnetization in metals. Phys Rev Lett 55(17):1790–1793. doi:PMID 10031924
6. Obst M, Gasser P, Mavrocordatos D, Dittrich M (2005) TEM-specimen preparation of cell/mineral interfaces by focused ion beam milling. Am Mineral 90:1270–1277
7. Spence JCH (1988) Experimental high-resolution electron microscopy, 2nd edn. Oxford University Press, New York
8. Stadelmann PA (1987) EMS – a software package for electron diffraction analysis and HREM image simulations in material science. Ultramicroscopy 21:131–145
9. Kirkland EJ (1998) Advanced computing in electron microscopy. Plenum, New York
10. Cowley JM (1990) Diffraction physics, 4th edn. North Holland Elsevier Science, Amsterdam

11. Pennycook SJ, Nellist PD (1999) Impact of electron microscopy on materials research. Kluwer, Dordrecht
12. Pogany AP, Turner PS (1968) Reciprocity in electron diffraction and microscopy. Acta Cryst A24:103–109
13. Voyles PM, Muller DA, Kirland EJ (2004) Depth-dependent imaging of individual dopant atoms in silicon. Microsc Microanal 10:291–300
14. Carlino E, Grillo V (2005) Atomic-resolution quantitative composition analysis using scanning transmission electron microscopy Z-contrast experiments. Phys Rev B 71:235303
15. Haider M, Rose H, Uhlemann S, Kabius B, Urban K (1998) Towards 0.1 nm resolution with the first spherically corrected transmission electron microscope. J Electron Microsc 47:395
16. Krivanek OL, Dellby N, Lupini AR (1999) Towards sub-Å electron beams. Ultramicroscopy 78:1
17. Rose HH (2008) Optics of high-performance electron microscopes. Sci Technol Adv Mater 9:014107–0141037
18. Nellist PD, Chisholm MF, Dellby N, Krivanek OL, Murfitt MF, Szilagyi ZS, Lupini AR, Borisevich A, Sides WH Jr, Pennycook SJ (2004) Direct sub-Angström imaging of a crystal lattice. Science 305:1741
19. Schramm SM, van der Molen SJ, Tromp RM (2012) Intrinsic instability of aberration-corrected electron microscopes. Phys Rev Lett 109:163901
20. Miedema MAO, van den Bos A, Buist A (1994) Experimental design of the exit wave reconstruction from a transmission electron microscope defocus series. IEEE Trans Inst Meas 43:181–186
21. Huang WJ, Zuo JM, Jiang B, Kwon KW, Shim M (2009) Sub-Ångström-resolution diffractive imaging of single nanocrystals. Nature Phys 5:129–133
22. De Caro L, Carlino E, Caputo G, Cozzoli PD, Giannini C (2010) Electron diffractive imaging of oxygen atoms in nanocrystals at sub-angstrom resolution. Nature Nanotech 5:360–365
23. De Caro L, Carlino E, Alessio Vittoria F, Siliqi D, Giannini C (2012) Keyhole electron diffractive imaging (KEDI). Acta Cryst A681-16
24. Williams DB, Carter CB (2009) Transmission electron microscopy: a textbook for material science, 2nd edn. Springer Science+Business Media, New York
25. Zuo JM (2000) Detection characteristics of a slow-scan CCD camera, imaging plates and film, and electron image restoration. Microsc Res Tech 49:245–268
26. Reimer L (1984) Transmission electron microscopy: physics of image formation and micro-analysis. Springer-Verlag Berlin Heidelberg, New York, Tokio
27. Loretto MH (1984) Electron beam analysis of materials. Chapman and Hall, London
28. Buxton BF, Eades JA, Steeds JW, Rackam GM (1976) Philos Trans Royal Soc Lond A 281:171
29. Steeds JW, Vincent R (1983) J Appl Cryst 16:317
30. Tanaka M, Saito R, Ueno K, Harada Y (1980) J Electron Microsc 29:408
31. Deblasi C, Mancini AM, Manno D, Rizzo A, Carlino E (1991) Convergent beam electron diffraction analysis of GaSe crystals grown from the melt by different doping elements. Il Nuovo Cimento 13D(2):233–246
32. Armigliato A, Balboni R, Corticelli F, Frabboni S (1995) Influence of experimental parameters on the determination of tetragonal distortion in heterostructures by LACBEDMicrosc. Microanal Microstruct 6(5–6):449–456
33. Matsuhata H, Gjonnes J (2002) Bloch wave degeneracies and critical voltage effect in CBED patterns. Microsc Microanal 8(S02):92–93
34. Morniroli J-P, Cherns D (1996) Analysis of grain boundary dislocations by large angle convergent beam electron diffraction. Ultramicroscopy 62:53–63
35. Goldstein JI, Williams DB, Cliff G (1989) In: Joy DC, Romigjr AD, Goldstein JI (eds) Quantitative X-ray analysis in principles of analytical electron microscopy, 2nd edn. Plenum Press, New York

36. Yamamoto N (1990) Characterization of crystal defects by cathodoluminescence detection system combined with TEM. Trans Jpn Inst Met 31:659–665
37. Wang JN, Steeds JW, Hopkinson M (1993) Microstructure and cathodoluminescence of MBE-grown (001) InGaP/GaAs strained-layer heterostructures. Semicond Sci Technol 8:502–508
38. Egerton RF (1989) Electron energy loss spectrometry in the electron microscope. Plenum, New York
39. Yamamoto Y, Tatsumiand K, Muto S (2007) Site-selective electronic structure of aluminum in oxide ceramics obtained by TEM-EELS analysis using the electron standing-wave method. Mater Trans 48(10):2590–2594
40. Rafferty B, Brown LM (1998) Direct and indirect transitions in the region of the band gap using electron-energy-loss spectroscopy. Phys Rev B 58:10326
41. Batson PE, Kavanah KL, Woodall JM, Mayer JM (1986) Electron-energy-loss scattering near a single misfit dislocation at the GaAs/GaInAs interface. Phys Rev Lett 57:2719
42. Lazar S, Botton GA, Tichelaar FD, Zandbergen HW (2003) Materials science applications of HREELS in near edge structure analysis and low-energy loss spectroscopy. Ultramicroscopy 96:535
43. Schattschneider P, Rubino S, Hébert C, Rusz J, Kune J, Novák P, Carlino E, Fabrizioli M, Panaccione G, Rossi G (2006) Experimental proof of circular magnetic dichroism in the electron microscope. Nature 441:486–488
44. Rusz J, Eriksson O, Novak P, Oppeneer PM (2007) Sum-rules for electron energy-loss near-edge spectra. Phys Rev B 76:060408. doi:10.1103/PhysRevB.76.060408
45. Schattschneider P, Hèbert C, Rubino S, Stöger-Pollach M, Rusz J, Novak P (2008) Magnetic circular dichroism in EELS: towards 10 nm resolution. Ultramicroscopy 108:433–438. doi:10.1016/j.ultramic.2007.07.002
46. Muller DA (2009) Structure and bonding at the atomic scale by scanning transmission electron microscopy. Nat Mater 8(4):263–270
47. Egerton RF (2007) Limits to the spatial, energy and momentum resolution of electron energy-loss spectroscopy. Ultramicroscopy 107:575–586
48. Mkhoyan KA, Kirkland EJ, Silcox J, Alldredge ES (2004) Atomic level scanning transmission electron microscopy characterization of GaN/AlN quantum wells. J Appl Phys 96(1):738–746
49. Varela M, Gazquez J, Pennycook SJ (2012) STEM-EELS imaging of complex oxides and interfaces. MRS Bull 37(01):29–35
50. Van Tendeloo G, Bals S, Van Aert S, Verbeeck J, Van Dyck D (2012) Advanced electron microscopy for advanced materials. Adv Mater 24:5655–5675
51. http://cime.epfl.ch/research/jems
52. http://totalresolution.com
53. Cowley JM, Moodie AF (1957) The scattering of electrons by atoms and crystals. I. A new theoretical approach. Acta Crystallogr 10:609–619
54. Perdew JP, Burke K, Ernzerhof M (1996) Generalized gradient approximation made simple. Phys Rev Lett 77:3865
55. Ciancio R, Carlino E, Rossi G, Aruta C, Scotti di Uccio U, Vittadini A, Selloni A (2012) Magnéli- like phases in epitaxial anatase TiO_2 thin films. Phys Rev B 86:104110
56. Krivanek OL, Chisholm MF, Nicolosi V, Pennycook TJ, Corbin GJ, Dellby N, Murfitt MF, Own CS, Szilagyi ZS, Oxley MP, Pantelides ST, Pennycook SJ (2010) Atom-by-atom structural and chemical analysis by annular dark-field electron microscopy. Nature 464:571–574. doi:10.1038/nature08879
57. Malajovich I, Berry JJ, Samarth N, Awschalom DD (2001) Persistant sourcing of coherent spins for multifunctional semiconductor spintronics. Nature 411:770
58. Wolf SA, Awschalom D, Buhrman RA, Daughton JM, von Molnar S, Roukes ML, Chtchelkanova AY, Treger DM (2001) Spintronics: a spin-based electronics vision for the future. Science 294:1488

59. Grabs P, Richter G, Fiederling R, Becker CR, Ossau W, Schmidt G, Molenkamp LW, Weigand W, Umbach E, Sedova IV, Ivanov SV (2002) Molecular-beam epitaxy of (Cd,Mn)Se on InAs, a promising material system for spintronics. Appl Phys Lett 80:3766, and references therein
60. Schulz O, Strassburg A, Rissoni T, Rodt S, Reissmann L, Pohl UW, Bimberg D, Klude M, Hommel D, Itoh S, Nakano K, Ishibashi A (2002) Operation and catastrophic optical degradation of II–VI laser diodes at output powers larger than 1 W. Phys Stat Sol B 229:943–948, and references therein
61. Guha S, DePuydt JM, Qiu J, Höfler GE, Haase MA, Wu BJ, Cheng H (1993) Role of stacking faults as misfit dislocation sources and nonradiative recombination centers in II-VI heterostructures and devices. Appl Phys Lett 63:3023
62. Hua GC, Otsuka N, Grillo DC, Fan Y, Han J, Ringle MD, Gunshor RL, Hovinen M, Nurmikko AV (1994) Microstructure study of a degraded pseudomorphic separate confinement heterostructure blue-green laser diode. Appl Phys Lett 65:1331
63. Kuo LH, Salamanca-Riba L, Wu BJ, Höfler BJ, DePuydt JM, Cheng H (1995) Dependence of the density and type of stacking faults on the surface treatment of the substrate and growth mode in ZnSxSe1 − x/ZnSe buffer layer/GaAs heterostructures. Appl Phys Lett 67:3298
64. Petruzzello J, Haberern KW, Herko SP, Marshall T, Gaines JM, Guha S, U'Ren S, Haugen JM (1996) Characterization of low defect density blue-green lasers. J Cryst Growth 159:573
65. Bonard J-M, Ganiere J-D, Heun S, Paggel JJ, Rubini S, Sorba L, Franciosi A (1997) Stacking faults in pseudomorphic ZnSe-GaAs and lattice-matched ZnSe-In0.04 Ga0.96 As layers. Phil Mag Lett 75:219
66. Wang N, Fung KK, Sou IK (2000) Direct observation of stacking fault nucleation in the early stage of ZnSe/GaAs pseudomorphic epitaxial layer growth. Appl Phys Lett 77:2846
67. Jackson AG (1991) Handbook of crystallography. Springer, New York
68. Amelinckx S (1992) Kinematical and dynamical diffraction theory in electron microscopy in materials science. In: Merli PG, Vittori Antisari M (eds) World Scientific - Singapore-New Jersey-London-Hong Kong
69. Colli A, Carlino E, Pelucchi E, Grillo V, Franciosi A (2004) Local interface composition and native stacking fault density in ZnSe/GaAs (001) heterostructures. Jour Appl Phys 96(5):2592–2602
70. Thomas G (1975) In: Valdre U, Ruedl E (eds) Introduction to transmission electron microscopy in electron microscopy in materials science. Commission of the European Communities, Directorate General, Luxembourg, EUR 5515e
71. Colli A, Pelucchi E, Franciosi A (2003) Controlling the native stacking fault density in II-VI/III-V heterostructures. Appl Phys Lett 83:81, and references therein
72. Nellist PD, Pennycook SJ (1999) Incoherent imaging using dynamically scattered coherent electrons. Ultramicroscopy 78:111
73. Li D, Gonsalves JM, Otsuka N, Qiu J, Kobayashi M, Gunshor RL (1990) Structure of the ZnSe/GaAs heteroepitaxial interface. Appl Phys Lett 57:449
74. Sun Y, Scott Thompson E, Nishida T (2010) Strain effect in semiconductors: theory and applications. Springer New York Dordrecht Heidelberg, London. ISBN 978-1-4419-0551-2
75. Spessot A, Frabboni S, Balboni R, Armigliato A (2007) Method for determination of the displacement field in patterned nanostructures by TEM/CBED analysis of split high-order Laue zone line profiles. J Microsc 226:140–155
76. Jacob D, Androussi Y, Lefebvre A (2001) LACBED measurement of the chemical composition of a thin InxGa1-x As layer buried in a GaAs matrix. Ultramicroscopy 89:299–303
77. Janssens KGF, Van der Biest O, Vanhellemont J, Maes HE (1997) Assessment of the quantitative characterization of localized strain by using electron diffraction contrast imaging. Ultramicroscopy 69:151–167
78. Miller PD, Liu CP, Murray Gibson J (2000) TEM measurement of strain in coherent quantum heterostructures. Ultramicroscopy 84:225–233

79. Hytch MJ, Snoeck E, Kilaas R (1998) Quantitative measurement of displacement and strain fields from HREM micrographs. Ultramicroscopy 4:131–146
80. Hytch MJ, Plamann T (2001) Imaging conditions for reliable measurement of displacement and strain in high-resolution electron microscopy. Ultramicroscopy 87:199–212
81. Niermann T, Park JB, Lehmann M (2011) Local estimation of lattice constants in HRTEM images. Ultramicroscopy 111:1083–1092
82. Liu CP, Preston AR, Boothroyd CB, Humphreys CJ (1999) Quantitative analysis of ultrathin doping layers in semiconductors using high-angle annular dark field images. J Microsc 194(1):171–182
83. De Caro L, Giuffrida A, Carlino E, Tapfer L (1997) Effect of the elastic stress relaxation on the hrtem image contrast of strained heterostructures. Acta Cryst A 53:168
84. Baker SN, Baker GA (2010) Luminescent carbon nanodots: emergent nanolights. Angew Chem Int Ed 49:6726–6744
85. Ojo W, Xu S, Delpech F, Nayral C, Chaudret B (2012) Room-temperature synthesis of air-stable and size-tunable luminescent ZnS-coated Cd3P2 nanocrystals with high quantum yields. Angew Chem Int Ed 51:738–741
86. KantaHaldar K, Sinha G, Lahtinen J, Patra A (2012) Hybrid colloidal Au-CdSe pentapod heterostructures synthesis and their photocatalytic properties. ACS Appl Mater Interfaces 4:6266–6272
87. Kim I, Haverinen HM, Wang Z, Madakuni S, Kim Y, Li J, Jabbour GE (2009) Efficient organic solar cells based on planar metallophthalocyanines. Chem Mater 21:4256–4260
88. Mirkovic T, Rossouw D, Botton GA, Gregory D (2011) Scholes broken band alignment in EuS-CdS nanoheterostructures. Chem Mater 23:181–187
89. Taraci JL, Hytch MJ, Clement T, Peralta P, McCartney MR, Drucker J, Picraux ST (2005) Strain mapping in nanowires. Nanotechnology 16:2365–2371
90. Buonsanti R, Grillo V, Carlino E, Giannini C, Gozzo F, Garcia-Hernandez M, Garcia MA, Cingolani R, Cozzoli PD (2010) Architectural control of seeded grown iron oxide/TiO_2 nanorod heterostructures: the role of seeds in topology selection. J Am Chem Soc 132(7):2437–2464
91. Hu GB, Peng L-M, Yu QF, Lu HQ (2000) Automated identification of symmetry in CBED patterns: a genetic approach. Ultramicroscopy 84:47–56
92. Tanaka M, Saito R, Sekii H (1983) Point-group determination by convergent-beam electron diffraction. Acta Cryst A 39:357
93. Burda C, Chen XB, Narayanan R, El-Sayed MA (2005) Chemistry and properties of nanocrystals of different shapes. Chem Rev 105(4):1025–1102
94. Huynh WU, Dittmer JJ, Alivisatos AP (2002) Hybrid nanorod-polymer solar cells. Science 295(5564):2425–2427
95. Sun BQ, Marx E, Greenham NC (2003) Photovoltaic devices using blends of branched CdSe nanoparticles and conjugated polymers. Nano Lett 3(7):961–963
96. Cui Y, Banin U, Bjork MT, Alivisatos AP (2005) Electrical transport through a single nanoscale semiconductor branch point. Nano Lett 5(7):1519–1523
97. Carbone L, Kudera S, Carlino E, Parak WJ, Cingolani R, Manna L (2006) Multiple wurtzite twinning in CdTe nanocrystals induced by methylphosphonic acid. J Am Chem Soc 128(3):748–755
98. Yan YF, Al-Jassim MM, Chisholm MF, Boatner LA, Pennycook SJ, Oxley M (2005) [1100]/[1102] twin boundaries in wurtzite ZnO and group-III-nitrides. Phys ReV B 71(4):041309
99. Hawkes PW (2009) Aberration correction past and present. Phil Trans R Soc A 28 367(1903):3637–3664
100. Kisielowski C, Freitag B, Bischoff M, van Lin H, Lazar S, Knippels G, Tiemeijer P, van der Stam M, von Harrach S, Stekelenburg M, Haider M, Uhlemann S, Muller H, Hartel P, Kabius B, Miller D, Petrov I, Olson EA, Donchev T, Kenik EA, Lupini AR, Bentley J, Pennycook SJ, Anderson IM, Minor AM, Schmid AK, Duden T, Radmilovic V,

Ramasse QM, Watanabe M, Erni R, Stach EA, Denes P, Dahmen U (2008) Atomic structure of core-shell precipitates in Al-Li-Sc-Zr alloys studied by analytical and aberration-corrected TEM/STEM. Microsc Microan 14:469
101. Meyer JC, Kisielowski C, Erni R, Rossel MD, Crommie MF, Zettl A (2008) Direct imaging of lattice atoms and topological defects in graphene membranes. Nano Lett 8:3582
102. Gabor D (1948) A new microscopic principle. Nature 161:777
103. Fan H, Zhong ZZ, Zheng C, Li F (1985) Image processing in high-resolution electron microscopy using direct method. Acta Crystallogr A41:163–165
104. Fienup JR (1982) Phase retrieval algorithms: a comparison. Appl Opt 21:2758–2769
105. Fienup JR (1987) Reconstruction of a complex-valued object from the modulus of its Fourier transform using a support constraint. J Opt Soc Am A4:118–127
106. Abbey B, Nugent KA, Williams GJ, Clark JN, Peele AG, Pfeifer MA, De Jonge M, McNulty I (2008) Keyhole coherent diffractive imaging. Nature 4:394–398
107. Shannon (1949) Communication in the presence of noise. Proc Inst Radio Eng 37(1):1021
108. Sayre D (1952) Some implications of a theorem due to Shannon. Acta Cryst 5:843
109. Muller DA, Silcox J (1995) Delocalization in inelastic scattering. Ultramicroscopy 59:195–213
110. Howie A (1979) Image-contrast and localized signal selection technique. J Microsc Oxford 117:11–23
111. Bourdillon AJ, Self PG, Stobbs WM (1981) Crystallographic orientation effects in energy dispersive X-ray analysis. Philos Mag A 44:1335–1350
112. Kohl H, Rose H (1985) Theory of image formation by inelastically scattered electrons in the electron microscope. Adv Electron Electron Phys 65:173
113. Messiah A (1999) Quantum mechanics. Dover, North-Holland Publishing Company, Amsterdam
114. Lupini AR, Pennycook SJ (2003) Localization in elastic and inelastic scattering. Ultramicroscopy 96:313–322
115. Pennycook SJ (2002) Structure determination through Z-contrast microscopy. Adv Imaging Electron Phys 123:173–206, P. G. Merli, G. Calestani, and M. Vittori-Antisari, Eds
116. Stöhr J, Wu Y, Dunham D, Tonner BP (1993) Element-specific magnetic microscopy with circularly polarized X-rays. Science 259:658–661
117. Carra P, Thole BT, Altarelli M, Wang X (1993) X-ray circular dichroism and local magnetic fields. Phys Rev Lett 70(5):694–697
118. Schattschneider P, Ennena I, Stoger-Pollach M, Verbeeck J, Mauchamp V, Jaouen M (2010) Real space maps of magnetic moments on the atomic scale: theory and feasibility. Ultramicroscopy 110:1038–1041
119. Lidbaum H, Rusz J, Rubino S, Liebig A, Hjorvarsson B, Oppeneer PM, Eriksson O, Leifer K (2010) Reciprocal and real space maps for EMCD experiments. Ultramicroscopy 110:1380–1389
120. Verbeeck J, Tian H, Schattschneider P (2010) Production and application of electron vortex beams. Nature 467:301–303
121. http://l-esperimento-piu-bello-della-fisica.bo.imm.cnr.it/english/index.html
122. http://www.ccmr.cornell.edu/igert/modular/docs/4_Chemical_Identification_at_Nanoscale.pdf
123. Krivanek OL, Dellby N. Murfitt MF (2011) Aberration-corrected scanning transmission electron microscopy of semiconductors. J Phys: Conf Ser 326:012005. Seventeenth international conference on microscopy of semiconducting materials, 2011. IOP Publishing. doi:10.1088/1742-6596/326/1/012005

Study on Polymeric Nano-Composites by 3D-TEM and Related Techniques

4

Atsushi Kato, Yoshinobu Isono, Kazuya Nagata, Atsushi Asano, and Yuko Ikeda

Contents

1 Definition of the Topic 140
2 Overview 140
3 Introduction 140
4 Experimental and Instrumental Methodology 143
4.1 Outline of 3D-TEM Observation 143
4.2 Original Pretreatment for Removing Rubber-Soluble Zn Compounds from Rubber Vulcanizates 144
5 Key Research Findings 145
5.1 Visualization of CB Network Structure in CB-Filled NR Vulcanizates 145
5.2 Rearrangement and Destruction of CB Network Structure 151
5.3 Visualization of CB/Rubber Interaction Layer and Relationship Between Its Parameters and Physical Properties 161
5.4 Dependence of Optical Properties on Silica Network of Silica-Filled Cured NR 168
5.5 High-Impact Mechanism of Polyketone/Polyamide Polymer Alloy 176
6 Conclusions and Future Perspective 188
References 189

A. Kato
Department of Material Analysis, NISSAN ARC, LTD, Yokosuka, Kanagawa, Japan

Y. Isono
Department of Materials Science and Technology, Nagaoka University of Technology, Nagaoka, Niigata, Japan

K. Nagata
Department of Advanced Technology Development, Laboratory of Plastics, Asahikasei Chemicals Corporation, Kawasaki-ku Kawasaki, Kanagawa, Japan

A. Asano
Department of Applied Chemistry, National Defense Academy, Yokosuka, Kanagawa, Japan

Y. Ikeda (✉)
Graduate School of Science and Technology, Kyoto Institute of Technology, Kyoto, Japan
e-mail: yuko@kit.ac.jp

C.S.S.R. Kumar (ed.), *Transmission Electron Microscopy Characterization of Nanomaterials*, DOI 10.1007/978-3-642-38934-4_4,
© Springer-Verlag Berlin Heidelberg 2014

1 Definition of the Topic

There are strong demands for controlling the morphologies of nanofiller aggregate dispersion and polymer phase separation in order to improve the performance of nanofiller-filled rubber and polymer alloys and to impart new functions to materials. To accomplish these subjects, it is essential to visualize the morphologies three-dimensionally and to have techniques for analyzing and evaluating them. In this chapter, we describe the visualization of the nanofiller network structure and the nanofiller/rubber interaction layer in rubber and the lamella network structure in polyketone/polyamide polymer alloys by using a three-dimensional transmission electron microscopy/electron tomography technique, which is abbreviated as 3D-TEM in this study. The relationship between their morphological parameters and physical properties is also described.

2 Overview

Filler loading, blending, and alloying are typical ways to obtain the desired properties of polymer materials. The structure of the dispersed filler phase significantly influences the characteristics obtained. A combination technique of three-dimensional transmission microscopy and electron tomography, which is abbreviated as 3D-TEM, is used as methods for visualizing and evaluating the dispersion structure. The 3D images obtained by 3D-TEM can be analyzed quantitatively, and the 3D morphological parameters can be extracted from the images. In this review, the relationship between the dispersion structure and physical properties of nanofillers (i.e., carbon black and silica) in cross-linked rubbers is described along with presenting a structural analysis of the polymer alloy of polyketone/polyamide 6 as an example of a high-impact polymer alloy.

3 Introduction

Polymer nanocomposites are unique materials in their physical and mechanical properties improved substantially with the addition of a small volume fraction of nanometer-sized filler particles [1–6]. The improvements are observed when the filler size is comparable to that of the polymer chains and to the average wall-to-wall distance between filler particles. Under such conditions, it is believed that a secondary network was formed by connecting the filler particles [2–5]. This transient network is assumed to be the reason for the large enhancement observed in viscoelastic properties. The transient network also produces rubberlike behavior in a certain range of frequencies [2]. The appearance and range of this regime depend on the polymer-filler affinity and, hence, on the lifetime of attachments between the filler particles and the bridging chains.

We now know that rubber vulcanizates filled with carbon black (CB) or particulate silica have a double network structure consisting of a rubber chain network

and a filler network [7–9]. The former network can be estimated by the equilibrium degree of swelling by a solvent and equilibrium modulus of the rubber vulcanizate [10–12]. With regard to the latter network, the authors have succeeded in observing the filler (i.e., CB and silica) network structure by means of 3D-TEM [13–24]. The skeleton of the filler network has been visualized for the first time by combining the closest distance (d_p) between the two neighboring nanofiller aggregates on a line between their centers of gravity, which is calculated from a 3D-TEM image, and the electric percolation behavior of the filler-filled rubber vulcanizate. On the basis of the visualization results, it was found that local filler aggregates were connected to one another, resulting in a dramatic decrease in the volume resistivity in a relatively low-filler-loading region. When the volume resistivity reaches almost a constant value in a high-CB-loading region, a three-dimensional filler network is formed. The filler network has a three-dimensional structure in which filler aggregates are interconnected with bound rubber around the aggregates. The filler network consists of cross-linked and branched chains of the aggregates, and isolated chains are also observed. Surprisingly, it is notable that a linear relationship is observed between the fraction of the CB network chain and the fraction of the dielectric relaxation strength of the filler-filled rubber vulcanizate [18]. It is also known that the filler network is ruptured and rearranged by an external stimulation such as heat treatment [24, 25] and large deformation [26–29].

Various research results have so far been reported regarding the thickness of bound rubber. For example, Priskin et al. [30] calculated 2–8 nm as the thickness of the bound rubber by employing the theory which separated truly absorbed rubber from the insoluble gel. Nishi [31] used pulsed nuclear magnetic resonance (NMR) to investigate the relaxation time constant (T_2) caused by several interactions between different spins of rubber molecules in CB-filled rubber. He measured T_2 of CB gels formed by kneading different types of CB (SAF, HAF, and SRF) and natural rubber and estimated the thickness of the glassy layer, i.e., short T_2 component, in bound rubber to be 0.6–4.3 nm. Recently, Litinov et al. [32] studied CB-filled ethylene propylene diene monomer (EPDM) vulcanizates using solid-state NMR and mechanical testing. Their results revealed that a very thin layer (thickness $\geq$ 0.6 nm) consisting of strong immobilized EPDM chain fragments on the CB surface formed a quasi-permanent CB network in the rubber matrix. Based on the measured viscoelasticity of CB-filled rubber, Smitt [33] estimated the thickness of the glassy layer around CB to be 2 nm. Nakajima et al. [34] used an atomic force microscope (AFM) to measure the force volume of CB-filled NR vulcanizates. They reported that bound rubber had a two-layer structure consisting of a glassy layer of about 2 nm in thickness and an uncured rubber layer of about several 10 nm in thickness. They also showed that both layers exhibited an elastic modulus higher than that of the matrix rubber. In another study, 3D-TEM and an image analysis technique were used to examine d_p between neighboring particles of CB aggregates in CB-filled NR vulcanizates. This approach made it possible to visualize the CB/NR interaction layer three-dimensionally and to assess its volume quantitatively for the first time. That is, the dependence of the viscoelastic behavior and the coefficient of thermal expansion on the volume fraction of the CB/NR

interaction layer (i.e., the immobilized rubber interfacial layer) were examined for the first time [35].

Notable features of silica-filled cured NR include optical transparency and the silica network structure. Optical transparent polymers have come into use in recent years in many applications, including organic glass for aquarium tanks, plastic lenses, transparent plastic roofs of automobiles, and plastic optical fiber. Various types of transparent polymer are in use as thermoplastics, such as acrylic resins, polystyrene, polyester, polycarbonate, and polyarylates. Epoxy resins, phenol resins, and polyimide resins are among the thermosetting polymers being used today. Most of these polymer materials exhibit optical transparency as a result of controlling their chemical purity and composition and/or higher-order structure [36]. Efforts are under way to develop new materials with outstanding mechanical properties, while still retaining their optical transparency, by compounding silica particles or glass fibers into these polymer resins [37, 38]. Since the optical transparency or nontransparency of particulate-silica-filled rubber has not been fully elucidated, we investigated the relationship between transparency and the morphology of the silica network [22]. To examine optical transparency, diffusion transmittance and haze were measured using the standard light C representing the average daylight. The results were interpreted on the basis of the network structure formed by the aggregations of particulate silica as observed by 3D-TEM.

There are also strong desires today for the development of impact-resistant plastic materials for automobiles [39–42], cameras, video cameras, mobile phones [43], and other products. Several mechanisms have been reported so far concerning the impact resistance of polymeric materials. According to Kuriyama [44], the mechanisms manifesting impact resistance in polymers that have been examined in recent years include the formation of crazes or cavitation, shear (yield) deformation, and absorption of impact energy by the fracturing of the adhesive interface between the matrix and the dispersed phase. Nagata et al. [43] reported that a polymer alloy of ethylene/propylene/carbon monoxide (polyketone, PK) and polyamide 6 (PA) exhibited stiffness equal to or greater than polycarbonate (PC) and higher Izod impact strength greater than 0.05–1 kJ/m of PC [45, 46]. Surprisingly, they found that the absorption of moisture markedly improved the impact strength of this alloy.

In this study [47, 48], the phase separation and higher-order structure of this alloy were observed by using a TEM and a 3D-TEM. The dispersion of nitrogen originating from PA was detected by electron energy loss spectroscopy (EELS). The lamella network structure and molecular motion of the PK/PA polymer alloy were also investigated by small-angle X-ray scattering (SAXS) measurement and a solid-state high-resolution NMR technique. Instrumented Charpy impact testing was used to examine the impact fracture mechanism of this polymer alloy. The macroscopic mechanism involved in improving impact resistance due to the absorption of moisture was examined based on the load-displacement behavior, crack generation energy, and crack propagation energy measured for dry and wet polymer alloy test samples with an instrumented Charpy impact testing machine. The relationship between the aforementioned morphology and impact properties is discussed below based on the results.

The following sections first focus on the network structure of nanofiller (i.e., CB and silica) aggregates and the relationship between the 3D-morphological parameters obtained by 3D-TEM observation and physical properties (electric and optical properties) of nanofiller-filled cured NR. By applying a two-phase mixing law (excluding CB) to find the volume fractions of the CB/NR interaction layer (i.e., the immobilized rubber interfacial layer) and the rubber matrix, we found that the viscoelastic behavior of CB-filled NR vulcanizates became explicable for the first time. The phase separation and high-impact mechanism of the PK/PA polymer alloy is then described. The mechanism of its high-impact resistance is discussed on the basis of the results of TEM and 3D-TEM observation, EELS, SAXS and solid-state high-resolution NMR measurements.

4 Experimental and Instrumental Methodology

4.1 Outline of 3D-TEM Observation

In a conventional TEM observation, a 3D sample object is projected onto a two-dimensional plane. Because the resulting 2D image does not represent the morphology of the sample along its thickness direction, it is not possible to discern the aggregation state of the particles and the phase separation of polymer alloys in that direction. A 3D-TEM image, on the other hand, provides information in the thickness direction to enable a fully 3D observation of particle aggregation and phase separation. In this connection, the thickness of the rubber samples used in this research was set at approximately 200 nm to allow the electron beam to pass through them easily, which results in a good contrast for TEM observation.

The principle of 3D-TEM is explained here briefly along with the observation conditions used in this work. A sample is subjected to TEM measurements while being tilted in 2° steps between −70° and +70°, resulting in a sequence of sliced images. The tilted images are not simply 2D image slices, but 2D projections of the mass-density distribution of the sample. Gold colloid particles of 10 nm in size are used as fiducial markers. By computerized positioning of the relationship between the images, the positions of the tilted images are aligned and the axis of rotation is determined. The continuous sequence of tilted images obtained in this way is then subjected to Radon transform (i.e., Fourier transform and inverse Fourier transform) operations to reconstruct 3D images. This procedure constitutes the principle of three-dimensional electron microscopy/electron tomography [49–52]. Volume rendering or surface rendering is also performed to construct 3D images on a nanometer scale [49–56]. The principle of 3D-TEM is fundamentally the same as that of X-ray computerized tomography (CT) used in the medical field. Because an electron beam is used, it is also called electron tomography. In the following discussion, it will be referred to simply as 3D-TEM.

The 3D-TEM observations were performed in this study using a Tecnai G2 F20 TEM (FEI Co.). The accelerating voltage of the electron beam was 200 kV. Samples were approximately 500 nm long, 500 nm wide, and 200 nm thick. After some pretreatment procedures, including removal of rubber-soluble zinc (Zn) compounds [57] and electron

staining, the samples were tilted in a range from −70° to +70° in 2° increments, and tilted images were obtained over this range of angles. This resulted in a series of 71 continuous tilted images that were automatically measured and loaded into the computer. It is well known that organic polymers are susceptible to damage by an electron beam [58, 59], which is an issue that requires care in 3D-TEM observation [20]. In this study, the same portion of a sample was irradiated by the electron beam for only a short time because the sample was continually tilted. Consequently, the damage was assumed to be negligible. Using the IMOD software (a program created at Colorado University) [50] installed on the Tecnai TEM, the continuous series of tilted images were converted to image slices showing the mass-density distribution of the sample at each angle. Then, 3D images were reconstructed from the image slices using the AMIRA program created by TGS Co. [60].

4.2 Original Pretreatment for Removing Rubber-Soluble Zn Compounds from Rubber Vulcanizates

Removal of Zn compounds from the rubbery matrix of NR vulcanizates is necessary to obtain clear 3D-TEM images of the aggregates. Here, CB-filled NR vulcanizate whose CB content was 20 parts per 100 rubber by weight (phr) was used to explain this procedure. A 3D-TEM image slice of the CB-filled NR before removing the Zn compounds is shown in Fig. 4.1a. This image slice has very low contrast, making it difficult to construct a clear 3D image. Let us consider the reason why the contrast of the 3D-TEM image slice is so low. The elements causing the electron beam to scatter are presumably contained in the NR vulcanizate and are heavier than sulfur, carbon, and hydrogen from which the rubber is made. Thus, it can be assumed that the heavier elements must be metallic ones. Considering the recipes of the sulfur-cured rubber compounds used in this study, a very likely candidate of a compound containing such elements is ZnO. According to Coran [57], ZnO reacts with stearic acid and the vulcanizing sulfur/accelerator (e.g., sulfenamide) in the sulfur-vulcanizing reactions to generate rubber-soluble Zn compounds and ZnS. Rubber-soluble Zn compounds may include Zn (II) stearate and Zn complexes with accelerator fragments. We have developed an original pretreatment method (called the NISSAN ARC-AK method) for removing Zn compounds from NR vulcanizates by using a special solvent comprised of diethyl ether/benzene/conc. hydrochloric acid (HCl) = 43/14/43 (vol%). Note that the ratios of the mixture must be modified to match the kind of rubber being examined. The solvent mixture is in two phases. The upper phase is a mixture of benzene and ether dissolved in hydrochloric acid. The lower phase is a mixture of hydrochloric acid. The rubber vulcanizate is swollen by benzene and floats in the upper phase.

The mechanism of removing rubber-soluble Zn compounds from rubber vulcanizates takes place as follows: Rubber vulcanizates are swollen by benzene. Ether is easily dissolved in benzene. HCl is partially dissolved in ether. Ether carries HCl into the rubber vulcanizate that is swollen by benzene. As a result, HCl reacts with Zn compounds. Ether moves the reaction product consisting of a compound of Zn and hydrochloric acid to the HCl-rich phase.

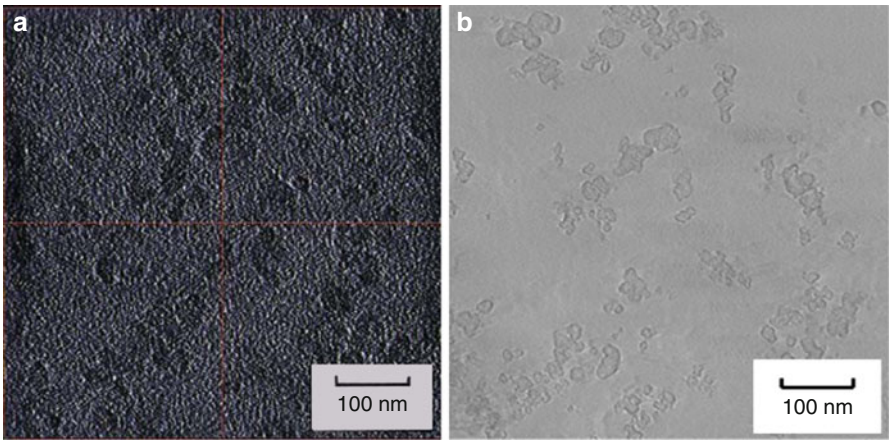


Fig. 4.1 3D-TEM image slices of CB-20 before and after removal of Zn compounds [18] (Reprinted from Rubber Chemistry Technology 79, Kato A., Shimanuki J., Kohjiya S., Ikeda Y., Three-dimensional morphology of carbon black in NR vulcanizates as revealed by 3D-TEM and dielectric measurements. 653–673, Copyright © (2006), with permission from the Rubber Division, American Chemical Society, Inc.)

In this study, this pretreatment was carried out accompanied by stirring at room temperature for about 12 h. The process was repeated twice. The samples were then left in a draft for about a day, after which they were dried using a vacuum dryer. Since bound rubber is in an immobilized phase and is insoluble in organic solvents at room temperature [30–35], it is presumably not damaged significantly by this mild pretreatment. Energy dispersive X-ray spectroscopy (EDX) results for nanofiller-filled natural rubber sulfur vulcanizates before and after this pretreatment revealed that Zn was almost entirely removed by this process [18, 20]. Based on the Si peak, the ratio of Zn removal was more than 90 % from silica-filled NR vulcanizates [20]. In addition, about 50 % of the unreacted residual sulfur was also removed. However, it is not avoided that a small amount of chlorine adds to the double bonds of the diene rubber. A 3D-TEM image slice of a CB-filled NR vulcanizate from which Zn compounds were removed is shown in Fig. 4.1b. Compared with the image in Fig. 4.1a, the 3D-TEM image in Fig. 4.1b has much higher contrast. CB aggregates appear white in the images. The results indicate that some Zn compounds were solubilized in the NR vulcanizate and disturbed the 3D-TEM observation of nanofiller aggregates.

5 Key Research Findings

5.1 Visualization of CB Network Structure in CB-Filled NR Vulcanizates

The compounding recipes of the CB-filled NR vulcanizates examined in this study are summarized in Table 4.1 The CB loading in this series of vulcanizate samples

Table 4.1 Recipes of carbon black-filled NR compounds [18] (Reprinted from Rubber Chemistry Technology 79, Kato A., Shimanuki J., Kohjiya S., Ikeda Y., Three-dimensional morphology of carbon black in NR vulcanizates as revealed by 3D-TEM and dielectric measurements. 653–673, Copyright © (2006), with permission from the Rubber Division, American Chemical Society, Inc.)

	Samples[*1]								
Ingredients/phr[*2]	CB0	CB5	CB10	CB20	CB30	CB40	CB50	CB60	CB80
NR (RSS#1)	100	100	100	100	100	100	100	100	100
Stearic acid (ST)	2	2	2	2	2	2	2	2	2
Active ZnO	1	1	1	1	1	1	1	1	1
CBS[*3]	1	1	1	1	1	1	1	1	1
Sulfur	1.5	1.5	1.5	1.5	1.5	1.5	1.5	1.5	1.5
Carbon black (CB)[*4]	0	5	10	20	30	40	50	60	80

[*1]Curing conditions: 140 °C, 15 min under pressure
[*2]Per 100 g of rubber
[*3]N-cyclohexyl-2-benzothiazole sulfenamide
[*4]HAF, dried at 120 °C for 2 h

was varied from 0 to 80 phr. The quantities of the other compounding agents were the same, specifically, 2 phr of stearic acid, 1 phr of active ZnO, 1 phr of *N*-cyclohexel-2-benzothiazole sulfenamide (CBS), and 1.5 phr of sulfur. The active ZnO used had a submicron particle size. Vulcanization was performed under pressure at 413 K (140 °C) for 15 min.

Figure 4.2 shows 3D-TEM images of the vulcanizate samples from which the Zn compounds had been removed. The CB loading of the samples denoted as CB-10, CB-20, CB-40, and CB-80 was 10, 20, 40, and 80 phr, respectively. CB aggregates consisting of a number of particles are observed even in CB-10 with the lowest CB loading. In contrast, many large aggregates packed closely together are seen in CB-80 with the highest CB loading. The images show that CB aggregates became larger in size with a higher CB loading. The 3D-TEM nanostructural parameters of the CB aggregates and networks visualized by image processing analysis are discussed below in relation to the physical properties.

Two distances between the aggregates were calculated from the 3D-TEM images. One is the closest distance (d_g) between the centers of the gravity of two neighboring CB aggregates. The other is the closest distance (d_p) between the two neighboring CB aggregates on a line between their centers of gravity. The two distances are illustrated in Fig. 4.3.

Figure 4.4 shows the dependence of the volume resistivity (ρ_v) and d_p on the CB loading. It is seen in Fig. 4.4a that d_p tends to converge to a constant level after the CB loading reaches around 40 phr. Considering that the thickness of the bound rubber around CB particles or aggregates is reported to range from a few to several nanometers, i.e., 2–8 nm [19, 30–34, 61], this saturation tendency presumably indicates that the CB aggregates are unable to come any closer together than approximately 3 nm even when the CB loading is higher than 40 phr. Figure 4.4b shows the volume resistivity (ρ_v) of the CB-filled cross-linked NR vulcanizates as

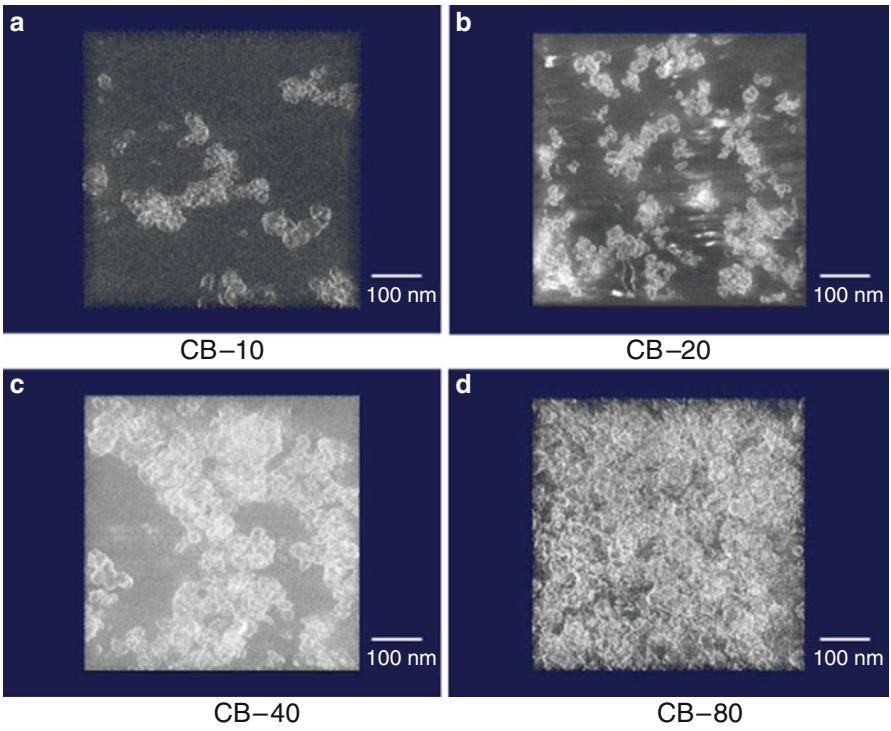


Fig. 4.2 3D-TEM images of CB-10, CB-20, CB-40, and CB-80 [18] (Reprinted from Rubber Chemistry Technology 79, Kato A., Shimanuki J., Kohjiya S., Ikeda Y., Three-dimensional morphology of carbon black in NR vulcanizates as revealed by 3D-TEM and dielectric measurements. 653–673, Copyright © (2006), with permission from the Rubber Division, American Chemical Society, Inc.)

a function of the CB loading at room temperature. It is seen that ρ_v decreased sharply with a higher CB loading up to 30 phr, after which it declined only gradually and tended to converge to a constant level, especially above 50 phr. The sharp drop in volume resistivity when the CB loading was increased is indicative of percolation.

Diagrams of the 3D skeletonized network structure of the CB aggregates in the CB-10, CB-40, and CB-80 vulcanizate samples are shown in Fig. 4.5. The individual networks are shown in different colors in order to make adjacent ones easier to distinguish. The closest distance (d_p) between the two neighboring CB aggregates in the diagrams is approximately 3 nm, the value at which volume resistivity and inter-aggregate distance as measured between the perimeters were found to saturate in the high-CB-loading region. In the case of low CB loadings of 20 phr or below, it is seen that independent CB aggregates existed locally, whereas at CB loadings of 40 phr or higher, the CB network structure was extended throughout the entire samples. Chain branching of the CB aggregates was observed in all of the samples examined. The high conductivity seen in the samples having a CB loading of 40 phr or higher is

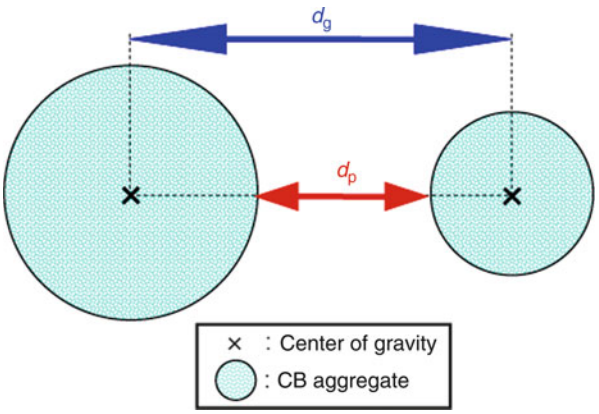


Fig. 4.3 Definitions of the closest distance (d_p) between two neighboring CB aggregates and the closest distance (d_g) between their centers of gravity as 3D parameters [22] (Reprinted from J Appl Polym Sci 122, Kato A., Suda T., Ikeda Y., Kohjiya S., Thermal destruction of carbon black network structure in natural rubber vulcanizate. J Appl Polym Sci 122:1300–1315, Copyright © (2011), with permission from John Wiley and Sons)

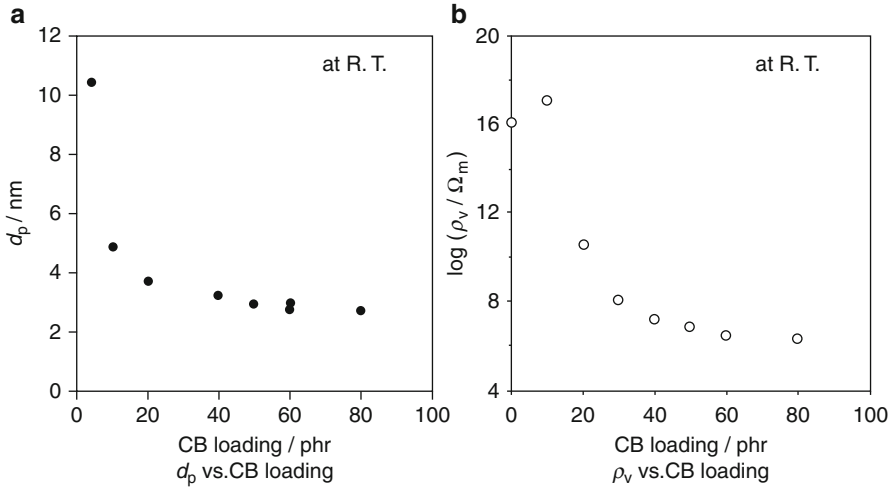


Fig. 4.4 Dependence of the closest distance (d_p) between two neighboring CB aggregates and volume resistivity (ρ_v) on CB loading [18] (Reprinted from Rubber Chemistry Technology 79, Kato A., Shimanuki J., Kohjiya S., Ikeda Y., Three-dimensional morphology of carbon black in NR vulcanizates as revealed by 3D-TEM and dielectric measurements. 653–673, Copyright © (2006), with permission from the Rubber Division, American Chemical Society, Inc.)

probably attributable to the movement of electrons through such a conductive network. It can be expected that this network structure linked by relatively strong interactions is also closely related to various properties in addition to electrical characteristics.

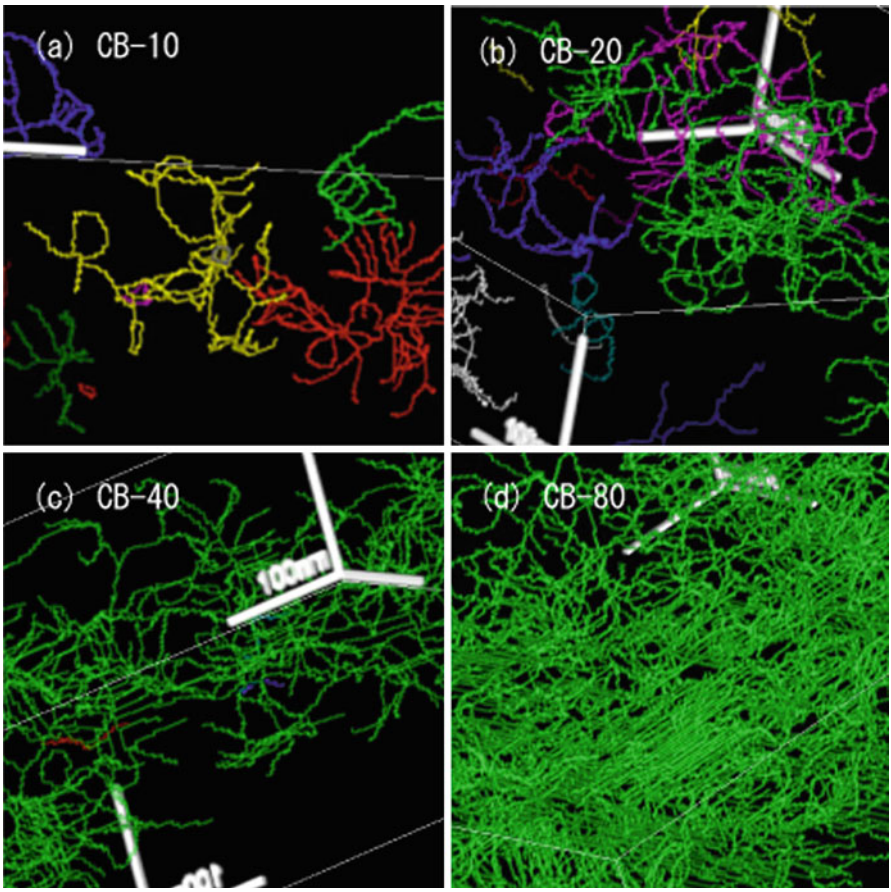


Fig. 4.5 Visualization of CB aggregate network structures and their characteristics for CB-10, CB-20, CB-40, and CB-80. The centers of gravity of CB aggregates are connected by a line. The aggregates are linked by a d_p of 3 nm. The unconnected patterns are shown in different colors [18] (Reprinted from Rubber Chemistry Technology 79, Kato A., Shimanuki J., Kohjiya S., Ikeda Y., Three-dimensional morphology of carbon black in NR vulcanizates as revealed by 3D-TEM and dielectric measurements. 653–673, Copyright © (2006), with permission from the Rubber Division, American Chemical Society, Inc.)

The nanofiller (such as CB and silica aggregate) network parameters must be defined. Figure 4.6 is a schematic diagram of the aggregate network. The circles are nanofiller aggregates. The arrows indicate the linkages to the network. The chains connecting the cross-linking points are cross-linked chains, and the chains extending outward like branches are branched chains. The two thick arrows show the cross-linking point (*Nd*) and the branching point (*Tm*) of the network, respectively. The fraction of the cross-linked chains (F_{cross}), the fraction

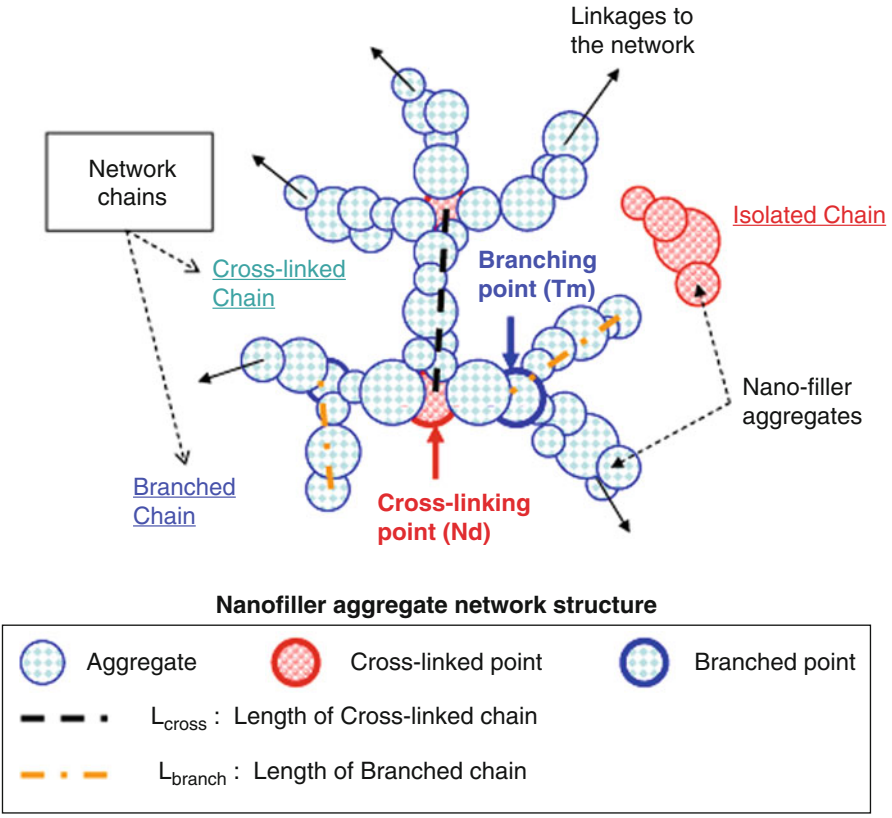


Fig. 4.6 Nanofiller aggregate network and its parameters [22] (Reprinted from J Opt Soc Am B, 25, Kato, A., Ikeda,Y., Kasahara, Y., Shimanuki, J., Suda, T., Hasegawa, T., Sawabe, H., Kohjiya, S., Optical transparency and silica network structure in cross-linked natural rubber as revealed by spectroscopic and three-dimensional transmission electron microscopy techniques, 1602–1615, Copyright © (2008), with permission from the Optical Society of America)

of the branched chains (F_{branch}), and the fraction of the isolated chains (F_{isolate}) are defined by the following equations [18, 20–24, 29, 35]:

$$F_{\text{cross}} = \frac{N.NdNd}{(N.NdNd + N.NdTm + N.Ni)} \tag{4.1}$$

$$F_{\text{branch}} = \frac{N.NdTm}{(N.NdNd + N.NdTm + N.Ni)} \tag{4.2}$$

$$F_{\text{isolate}} = \frac{N.Ni}{(N.NdNd + N.NdTm + N.Ni)} \tag{4.3}$$

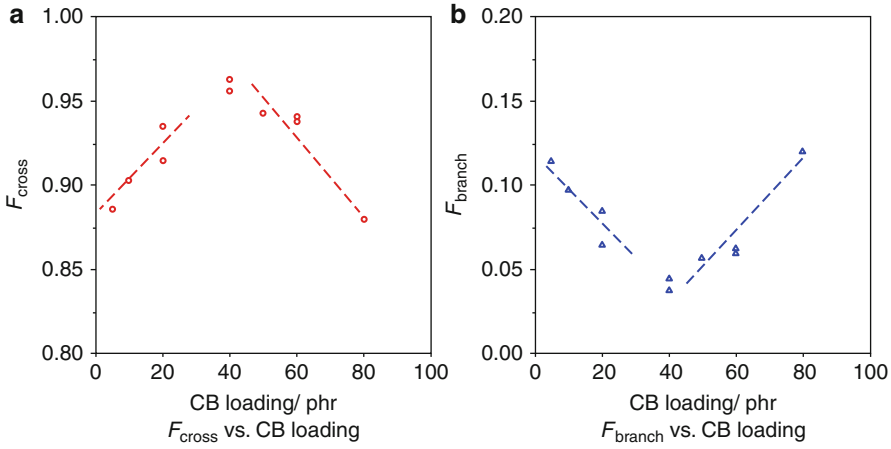


Fig. 4.7 Fractions of cross-linked (F_{cross}) and branched (F_{branch}) chains of CB aggregates as a function of CB loading. At CB loadings of 40 phr or larger, the fraction of cross-linked chains decreases linearly and the fraction of branched chains increases linearly with increasing CB loading [18] (Reprinted from Rubber Chemistry Technology 79, Kato A., Shimanuki J., Kohjiya S., Ikeda Y., Three-dimensional morphology of carbon black in NR vulcanizates as revealed by 3D-TEM and dielectric measurements. 653–673, Copyright © (2006), with permission from the Rubber Division, American Chemical Society, Inc.)

where *N. NdNd* is the number of cross-linked chains, *N.NdTm* is the number of branched chains, *N.Ni* is the number of isolated chains, and *N. NdNd* + *N.NdTm* + *N.Ni* is the total number of network chains. Since isolated chains hardly existed in these samples, i.e., $F_{isolate}$ was almost 0, the two fractions F_{cross} and F_{branch} were selected as the parameters to characterize the CB network structure. Figure 4.7 shows the dependence of F_{cross} and F_{branch} on the CB loading. F_{cross} increases almost linearly with lower CB loading, whereas F_{branch} decreases almost linearly in the low-CB-loading region of less than 40 phr. In contrast, F_{cross} decreases with increasing CB loading, whereas F_{branch} increases almost linearly in the high-CB-loading region of 40 phr or more. These results suggest that the network structure in the low-CB-loading (pregel) region differs from that in the high-CB-loading region after gelation.

5.2 Rearrangement and Destruction of CB Network Structure

5.2.1 Heat Treatment

In order to investigate the thermal destruction and rearrangement of the CB network consisting of CB aggregates in the rubbery matrix, a suitable heat-treatment temperature without any thermal decomposition of rubber matrix was examined by using differential scanning calorimetry (DSC), thermomechanical analysis (TMA) and thermal expansion measurements. As a result, 383 K (110 °C) was chosen as the heat-treatment temperature under a vacuum. The volume resistivity (ρ_v) of the 50 phr CB-filled natural rubber vulcanizate (CB-50) increased rapidly up to a heat-treatment

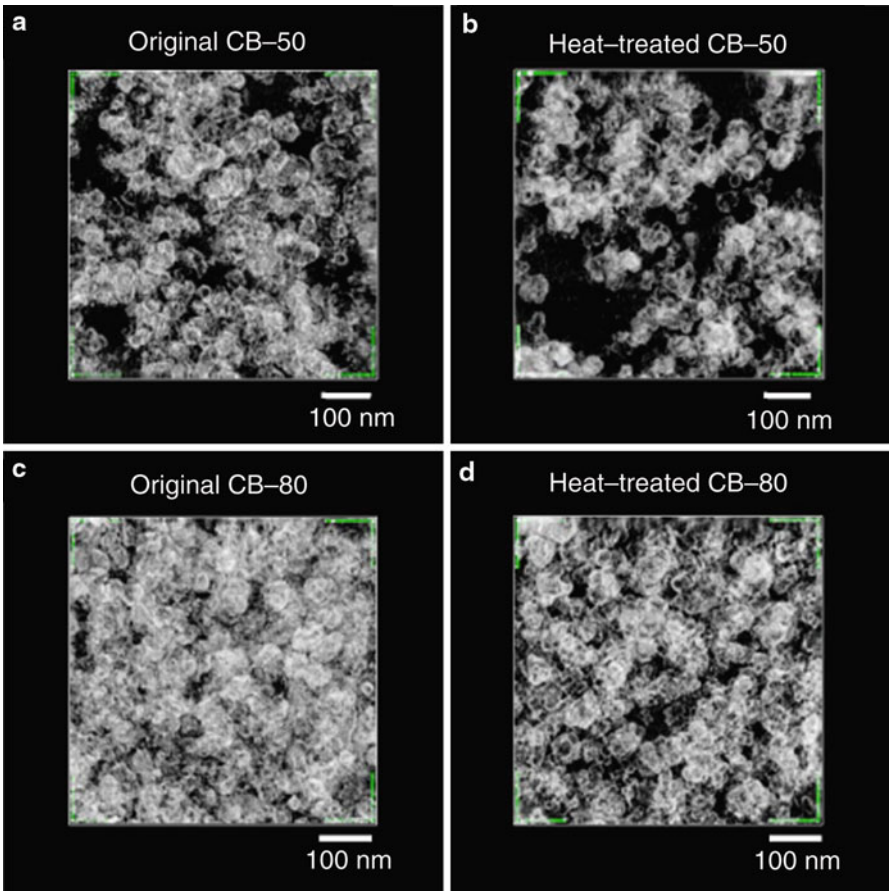


Fig. 4.8 3D-TEM images of CB-50 and CB-80 before/after heat treatment at 383 K (110 °C) for 75 h in a vacuum [24]

time of 24 h, after which it decreased with a longer heat-treatment time, whereas ρ_v of CB-80 remained almost constant without depending on the heating time [24]. Figure 4.8 shows 3D-TEM images of the CB aggregates of CB-50 and CB-80. The original CB-50 and CB-80 in (a) and (c) were not heat-treated, while the corresponding samples in (b) and (d) were heat-treated at 383 K for 75 h in a vacuum. The images were constructed and are displayed in black and white. CB aggregates appear as white forms in the images. Scale bars of 100 nm are indicated under the images on the right sides. Adjacent aggregates separated by about 1 nm, which is the resolution of 3D-TEM, are shown so that they can be distinguished. These images show that the distribution of the CB aggregates and the CB network changed before and after the heat treatment. Concretely, compared with the images of CB-50 and CB-80 before the heat treatment in (a) and (c), the CB aggregates and the CB networks in the images in (b) and (d) show pronounced heterogeneity. Diagrams of

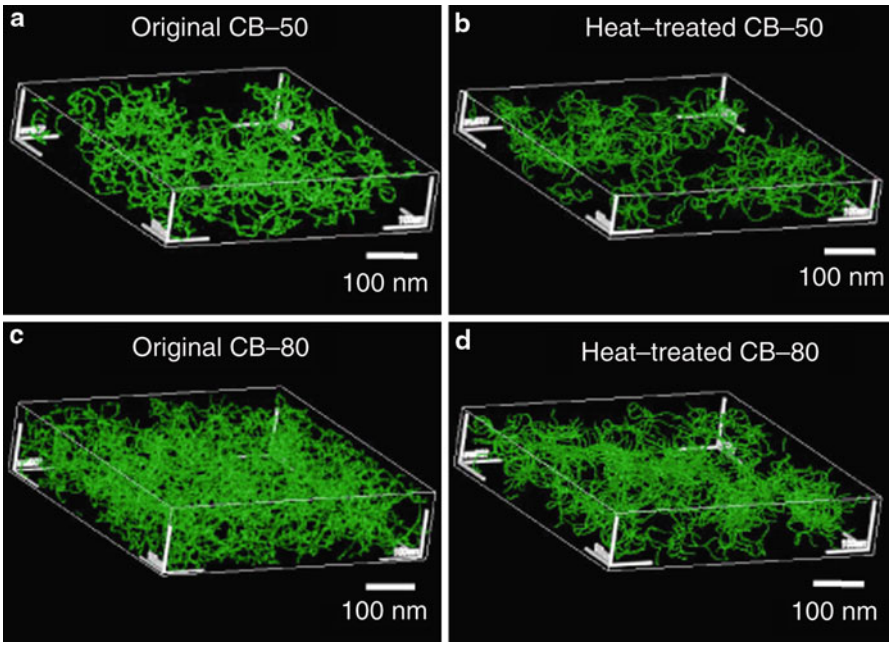


Fig. 4.9 3D-TEM image analysis results for the CB network of CB-50 and CB-80 before/after heat treatment at 383 K (110 °C) for 75 h in a vacuum [24]

the 3D skeletonized network structure of the CB aggregates in the original and the heat-treated samples of CB-50 and CB-80 are shown in Fig. 4.9. The CB network structure appears to extend throughout the entire original samples of CB-50 and CB-80, whereas the CB network in the heat-treated samples in (b) and (d) was markedly ruptured. It is noteworthy that the thermal destruction of the CB network structure is more pronounced in CB-50 than that in CB-80.

The length (L_{cross}) of the cross-linked chains is defined as the distance between two cross-linked points, and the length (L_{branch}) of the branched chains is defined as the distance from the branching point to the end of the branched chain. Isolated chains that were independent of the network were not found before or after the heat treatment. The densities (D_{cross} and D_{branch}) of the cross-linked points and the branched points are defined as follows:

$$D_{\text{cross}} = \frac{N.Nd}{TV} \tag{4.4}$$

$$D_{\text{branch}} = \frac{N.Tm}{TV} \tag{4.5}$$

where $N.Nd$ is the number of cross-linked points, $N.Tm$ is the number of branched points, and TV is the total volume containing the CB network [24].

Table 4.2 Characteristics of CB network of CB-50 and CB-80 before/after heat treatment at 383 K (110 °C) for 75 h in a vacuum obtained by 3D-image analysis of 3D-TEM images [24]

Samples		L_{cross}/nm	L_{branch}/nm	D_{cross}[a]/nm^{-3}	D_{branch}[b]/nm^{-3}	F_{cross}[c]	F_{branch}[d]
CB-50	Original	40	82	8.0×10^{-6}	6.7×10^{-7}	0.94	0.06
	Heat-treated	23	42	2.0×10^{-5}	1.1×10^{-5}	0.68	0.32
CB-80	Original	39	110	1.7×10^{-5}	3.1×10^{-6}	0.88	0.12
	Heat-treated	22	46	3.0×10^{-5}	1.7×10^{-5}	0.67	0.33

[a,b]Densities of cross-linking points and branching points of CB network, respectively
[c,d]Fractions of cross-linked chains and branched chains, respectively

Table 4.2 shows the characteristics of the CB network structures of the original CB-50 and CB-80 samples before the heat treatment and those of samples heat-treated at 383 K for 75 h in a vacuum. These characteristics were obtained by 3D image analysis of the 3D-TEM images. This table indicates the average lengths (L_{cross} and L_{branch}), D_{cross} and D_{branch}, and F_{cross} and F_{branch} of CB-50 and CB-80 before/after heat treatment. Compared with the original samples, the average lengths and D_{cross} of the heat-treated samples decreased. D_{branch} of the heat-treated CB-50 increased, whereas that of the heat-treated CB-80 was almost the same. These results reveal that the CB networks of CB-50 and CB-80 were broken and were rearranged by the heat treatment. In addition, after the heat treatment, F_{cross} of CB-50 and CB-80 decreased, whereas F_{branch} increased. These results suggest that the heat treatment changed the composition of their CB networks. It is notable that F_{branch} of CB-50 became larger than that of CB-80, while the decrease in F_{cross} of CB-50 was almost the same as that of CB-80 due to the heat treatment. Additionally, F_{cross} and F_{branch} of the heat-treated CB-50 showed the same values (F_{cross} and F_{branch} = ca. 0.7 and ca. 0.3, respectively) as those of the heat-treated CB-80. This implies that the CB network of CB-80 was more thermally stable than that of CB-50 and that the F_{cross} and F_{branch} values of ca. 0.7 and ca. 0.3 represented a more thermally stable composition. It should be noted that the CB network structure is closely related to the electrical paths in the rubber matrix. Therefore, these data suggest that the electrical paths in CB-50 were significantly severed in the heat-treatment process, whereas the damage to the electrical paths in CB-80 was much less. This supports the dependence of the volume resistivities of CB-50 and CB-80 on the heat-treatment time at 383 K in a vacuum [24].

5.2.2 Two-Step Curing Under Elongation

Two types of CB-filled cured SBR 1502 were prepared as reference samples and two-step cured samples. The compounding recipes of the reference samples are given in Table 4.3. The only ingredient changed in this series of SBR reference samples was the CB loading, which was varied in a range of 10–80 phr. The CB volume fraction (ϕ_{CB}) was calculated using 1.8 and 0.94 g/cm^3 as the densities of CB [62] and SBR [63], respectively. The quantity of the compounding agent was the same in all the reference samples at 3 phr of dicumyl peroxide (DCP). The reference samples were cured under pressure of 2 MPa at 443 K (170 °C) for 30 min in the mold.

Table 4.3 Recipes for preparation of CB-filled cured SBR reference samples and two-step cured sample [29] (Reprinted from J Appl Polym Sci 128, Kato A., Isono Y., Structural changes in the carbon black network in carbon-black-filled styrene-butadiene rubber samples cured with a two-step process. 2498–2507, Copyright © (2013), with permission from John Wiley and Sons)

	Sample					
Ingredient	CB10/ SBR[*1]	CB20/ SBR[*1]	CB40/ SBR[*1]	CB60/ SBR[*1]	CB80/ SBR[*1]	CB40/SBR (α^{*7})[*6]
SBR1502	100	100	100	100	100	100
DCP[*2] (phr[*3])	3	3	3	3	3	3
CB[*4] (phr)	10	20	40	60	80	40
CB volume fraction[*5]	0.050	0.095	0.17	0.24	0.30	0.17

[*1]Cureconditions: 30 min at 443 K (170 °C) under pressure of 2 MPa
[*2]Dicumyl peroxide
[*3]Parts by weight per 100 parts by weight of rubber
[*4]HAF (N330)
[*5]Calculated using that the densities of 1.8 and 0.94 for CB and SBR
[*6]Two-step curing conditions Pre-curing: 8.5 min. at 403 K (130 °C) under pressure of 2 MPa before elongation Post-curing: 15 min at 443 K (170 °C) after elongation
[*7]Initial elongation ratio after pre-curing and before post-curing

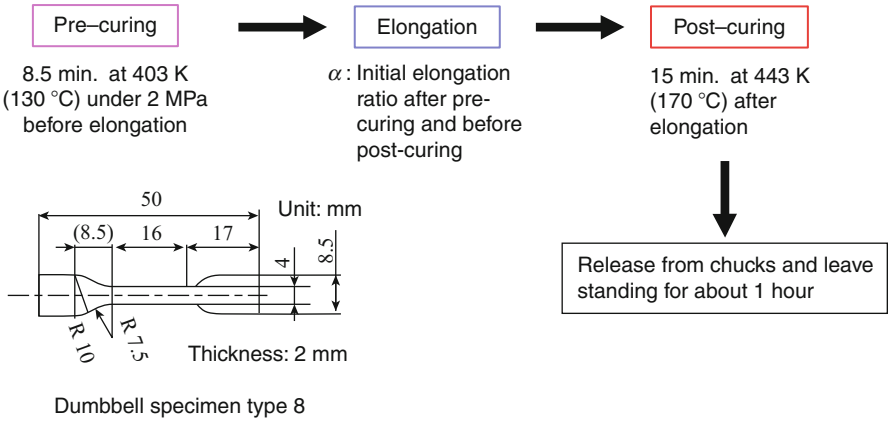


Fig. 4.10 Two-step curing process of CB-filled cured SBR samples [29] (Reprinted from J Appl Polym Sci 128, Kato A., Isono Y., Structural changes in the carbon black network in carbon-black-filled styrene-butadiene rubber samples cured with a two-step process. 2498–2507, Copyright © (2013), with permission from John Wiley and Sons)

The last column in Table 4.3 indicates the recipe of the two-step cured samples, and Fig. 4.10 shows the curing process. The DCP and CB loadings were 3 phr and 40 phr, respectively. Pre-curing was performed under pressure of 2 MPa at 403 K (130 °C) for 8.5 min in the mold. Dumbbell specimens (approximately 4 mm wide, 50 mm long, and 2 mm thick) were cut from pre-cured SBR sheets. After stretching the specimens between two marker lines at an arbitrary elongation ratio, the

Table 4.4 Residual elongation ratios of CB-filled cured SBR samples (α = 1–4) after two-step curing [29] (Reprinted from J Appl Polym Sci 128, Kato A., Isono Y., Structural changes in the carbon black network in carbon-black-filled styrene-butadiene rubber samples cured with a two-step process. 2498–2507, Copyright © (2013), with permission from John Wiley and Sons)

Sample	CB40/SBR (α = 1)	CB40/SBR (α = 2)	CB40/SBR (α = 3)	CB40/SBR (α = 4)
α^{*1}	1	2	3	4
$\alpha_{res}{}^{*2}$	1	1.82	2.82	3.77

*1Initial elongation ratio after pre-curing and before post-curing
*2Residual elongation ratio after two-step curing

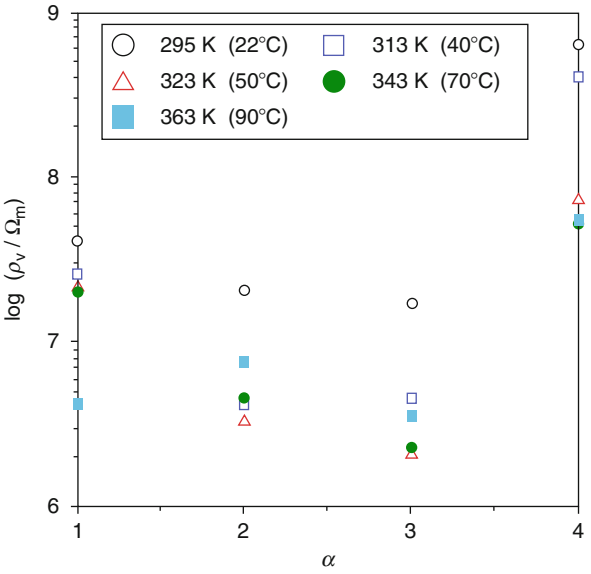


Fig. 4.11 Relationship between elongation ratio (α) and volume resistivity (ρ_v) [29] (Reprinted from J Appl Polym Sci 128, Kato A., Isono Y., Structural changes in the carbon black network in carbon-black-filled styrene-butadiene rubber samples cured with a two-step process. 2498–2507, Copyright © (2013), with permission from John Wiley and Sons)

stretched specimens were post-cured at 443 K (170 °C) for 15 min. After post-curing, the specimens were released from the chucks and held at room temperature for about 1 h before measuring the distance between the two marker lines. The elongation ratio (α) is defined here as the ratio of the length of a specimen before stretching to the length of the specimen after stretching. And, the residual elongation ratio is also defined (α_{res}) as the ratio of the length of a specimen before stretching to the residual length of the specimen held for about 1 h after post-curing. Table 4.4 shows the residual elongation ratios of CB-40/SBR samples after two-step curing, where α indicates the initial elongation ratio from 1 to 4 after pre-curing and before post-curing. The residual elongation ratios (α_{res}) of the specimens were 90 % or more of the initial α values. Taking into consideration the findings of Kohjiya et al. [17, 20, 21, 61], Kato et al. [18, 24], Ikeda et al. [19], and Satoh et al. [64], it is inferred that a CB network also formed in these CB-40/SBR samples, in spite of the different kinds of CB and rubber used and the differences in the vulcanizing or curing systems. Figure 4.11 shows the volume resistivity ρ_v

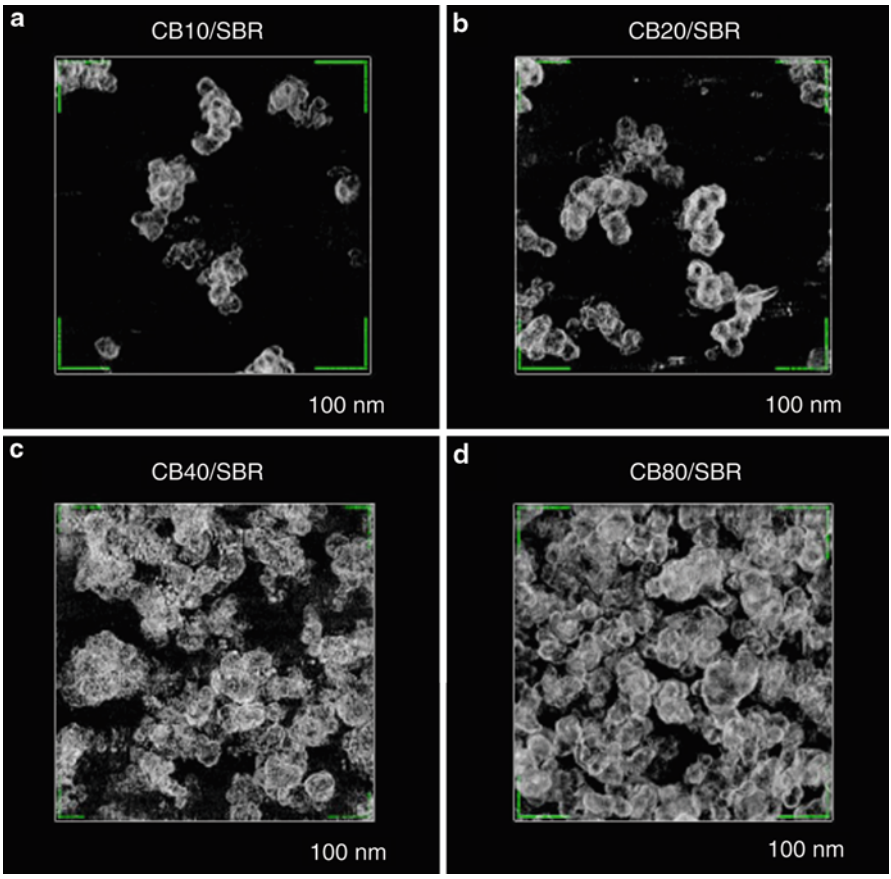


Fig. 4.12 3D-TEM images of CB-filled cured SBR reference samples [29] (Reprinted from J Appl Polym Sci 128, Kato A., Isono Y., Structural changes in the carbon black network in carbon-black-filled styrene-butadiene rubber samples cured with a two-step process. 2498–2507, Copyright © (2013), with permission from John Wiley and Sons)

measured in a temperature range of 295–363 K (22–90 °C) for CB-filled cross-linked SBR samples having a fixed elongation ratio α of 1 to 4, respectively. At 295 K (22 °C), the samples with α of 1–3 showed a slight decline in ρ_v with increasing α, whereas ρ_v increased markedly at $\alpha = 4$. These ρ_v tendencies are presumably attributable to changes in the distribution of CB aggregates. These characteristics will be described in more detail later in a discussion of the 3D-TEM observations.

Figure 4.12 shows 3D-TEM images of the CB-10, CB-20, CB-40, and CB-80/SBR reference samples. The white grains are CB aggregates. In the CB10/SBR sample, CB aggregates are seen here and there in the image. At CB loadings higher than 10 phr, the CB aggregate structures continued to grow larger in size and tended to be nearly uniformly distributed in the CB-80/SBR sample. By applying a 3D

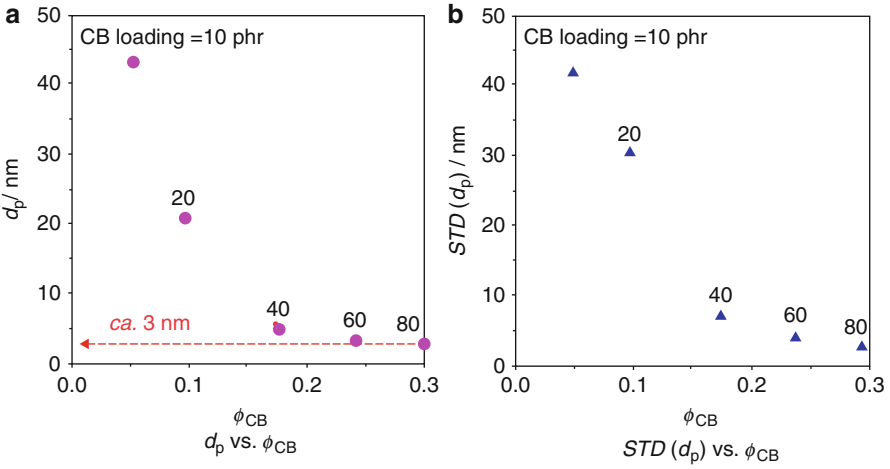


Fig. 4.13 Dependence of average closest interparticle distance (d_p) between CB aggregates and its standard deviation (*STD* (d_p)) on CB volume fraction (ϕ_{CB}) [29] (Reprinted from J Appl Polym Sci 128, Kato A., Isono Y., Structural changes in the carbon black network in carbon-black-filled styrene-butadiene rubber samples cured with a two-step process. 2498–2507, Copyright © (2013), with permission from John Wiley and Sons)

image analysis technique to these images, we can determine the closest interparticle distance (d_p) between CB aggregates and its standard deviation (*STD* (d_p)), as proposed by Kato et al. [17, 18, 21–24, 65, 66]. Figure 4.13 shows the dependence of d_p and *STD* (d_p) on the CB volume fraction (ϕ_{CB}). It is seen in Fig. 4.13a, b that d_p and *STD* (d_p) decreased as ϕ_{CB} was increased above 0.050 (10 phr) and that both values stabilized at ϕ_{CB} of 0.17 (40 phr) or higher. The stable value of d_p was approximately 3 nm, which is identical to the value reported for HAF-filled NR vulcanizates [17, 18, 21–24, 65, 66]. These results imply the presence of a CB/SBR interaction layer that prevents direct contact between CB aggregates even if ϕ_{CB} is increased. It is assumed that this interaction layer is closely related to the bound rubber phase. As will be described later, the linking of CB aggregates at a distance of 3 nm results in the formation of a CB network consisting of cross-linked, branched, and isolated chains. In Fig. 4.13b showing the dependence of *STD* (d_p) on ϕ_{CB}, the standard deviation of dp decreased rapidly with increases of CB loading more than ϕ_{CB}=0.050, and held the low constant value at CB loading of 40 phr or more. It is observed that the CB aggregates became more uniformly distributed at ϕ_{CB} above 0.050 (10 phr) and that the samples were filled with CB at approximately the distance of the CB/SBR interaction layer at ϕ_{CB} of 0.17 or higher.

Figure 4.14 shows 3D-TEM images of the two-step cured CB-40/SBR samples having α values in a range of 1–4. The elongation direction is along the horizontal axis, and the white grains are CB aggregates. It is seen that the gaps between the CB aggregates tended to increase with increasing α. In particular, at $\alpha = 4$, the CB aggregates exhibit a segmented morphology. These results presumably support the pronounced increase seen in ρ_v for $\alpha = 4$. Figure 4.15 shows d_p and the distance (d_g)

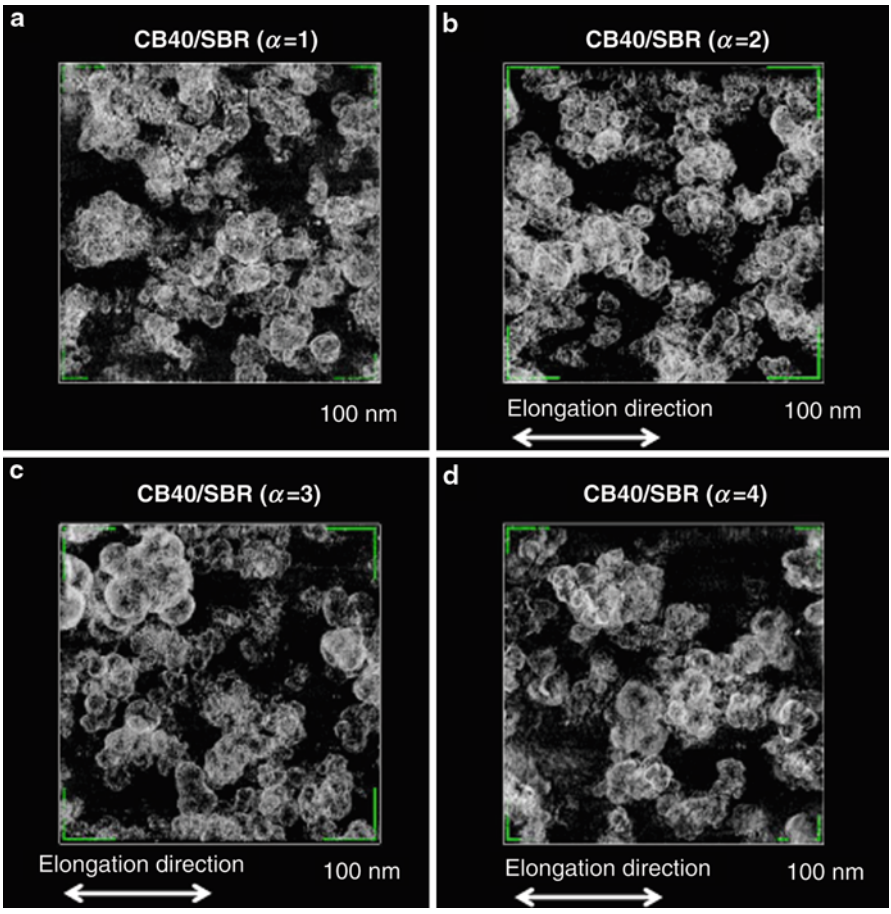


Fig. 4.14 3D-TEM images of two-step cured CB-filled SBR samples [29] (Reprinted from J Appl Polym Sci 128, Kato A., Isono Y., Structural changes in the carbon black network in carbon-black-filled styrene-butadiene rubber samples cured with a two-step process. 2498–2507, Copyright © (2013), with permission from John Wiley and Sons)

between the centers of gravity of the closest CB aggregates as a function of α. Surprisingly, d_p of the samples with α = 1–2 decreased slightly, whereas it increased for the samples with a larger α value. These results imply that for the samples with α of 1–2, their cross-sectional area decreased accompanying elongation, thereby pushing the CB aggregates toward the interior of the sample, resulting in a highly packed state that reduced d_p slightly and ρ_v also declined somewhat. At α values greater than 3, elongation probably pulled the CB aggregates apart, resulting in a pronounced increase in d_p, and ρ_v also increased markedly. Further, it is seen that d_g increased at α = 1–3 and decreased at α = 3–4. Here, let us consider that d_g reflects d_p and the size of the two closest CB aggregates. For the samples with α = 1–3, the reduction of the sample cross-sectional area accompanying

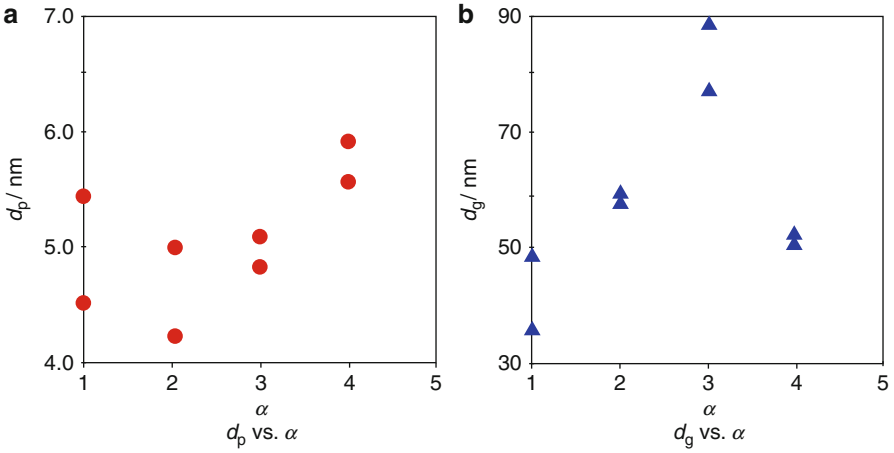


Fig. 4.15 Average closest distance (d_p) between CB aggregates and average minimum distance (d_g) between their centers of gravity as a function of elongation ratio (α) [29] (Reprinted from J Appl Polym Sci 128, Kato A., Isono Y., Structural changes in the carbon black network in carbon-black-filled styrene-butadiene rubber samples cured with a two-step process. 2498–2507, Copyright © (2013), with permission from John Wiley and Sons)

elongation promoted the coalescence of the CB aggregates, whereas with an α value greater than 3, the shear fields produced by the further reduction of the sample cross-sectional area presumably worked to divide finely the coarsened CB aggregates [29].

The results in Fig. 4.13 show that d_p displayed a constant value of approximately 3 nm when the CB loading was increased to 40 phr or higher. Since this value probably equaled the thickness of the CB/SBR interaction layer, it was assumed that the linking of the nearest neighbor CB aggregates at a distance of approximately 3 nm formed the CB network. Accordingly, the CB network can be visualized by drawing lines connecting the centers of gravity of the nearest CB aggregates [17, 18, 21–24, 65, 66]. Figure 4.16 presents images of the CB network thus obtained for the two-step cured CB-40/SBR samples with α values of 1–4. The elongation direction is along the horizontal axis, and bars representing 100 nm are indicted in the four corners of each rectangular parallelepiped view. CB networks that are not connected are shown in different colors. The CB network in the unelongated state ($\alpha = 1$) in Fig. 4.16a is almost entirely the same color, indicating that nearly all the CB aggregates were linked at a distance of approximately 3 nm. In contrast, as the samples were increasingly elongated, the CB network colors changed, implying that the CB network was broken by elongation. The CB-40/SBR sample with $\alpha = 4$ in Fig. 4.16d in particular was broken up into small fragments. In addition, the fractal dimension (*FD*) of the CB networks in Fig. 4.16 was calculated by the box-counting method [67–70] and found to decrease with increasing α [29]. This result suggests that the CB network was flattened as a result of elongation.

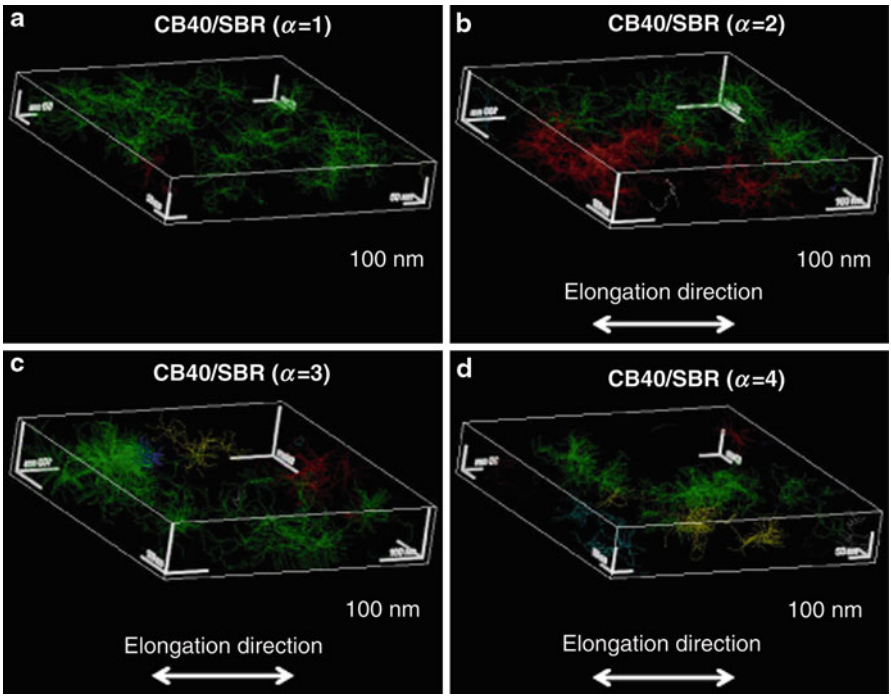


Fig. 4.16 CB network images of two-step cured CB-filled SBR samples [29] (Reprinted from J Appl Polym Sci 128, Kato A., Isono Y., Structural changes in the carbon black network in carbon-black-filled styrene-butadiene rubber samples cured with a two-step process. 2498–2507, Copyright © (2013), with permission from John Wiley and Sons)

Figure 4.17 shows the dependence of F_{cross}, F_{branch}, and F_{isolate} on α. It is seen that F_{cross} decreased almost linearly and F_{branch} increased almost linearly with increasing α. These results suggest that the cross-linked chains of the CB network were severed by elongation and that the number of branched chains increased. While F_{isolate} showed an overall tendency to increase with increasing α, the increase was more pronounced in the region of $3 < \alpha \leq 4$ than in the region of $1 \leq \alpha < 3$. This implies that when elongation destroyed the CB network, isolated chains were also generated in addition to branched chains and that isolated chains were markedly generated in the region of $\alpha \geq 3$. In addition, the change in F_{isolate} around $\alpha = 3$ corresponded closely to the remarkable change in ρ_{v} as well as to the changes in d_{p}, d_{g}, D_{CB}, and V_{CB} of the CB aggregates [29].

5.3 Visualization of CB/Rubber Interaction Layer and Relationship Between Its Parameters and Physical Properties

Figure 4.18a shows a portion of the atomic force microscope (AFM) phase image of the CB-20 sample obtained at a probe contact pressure of 10 nN. The light and dark

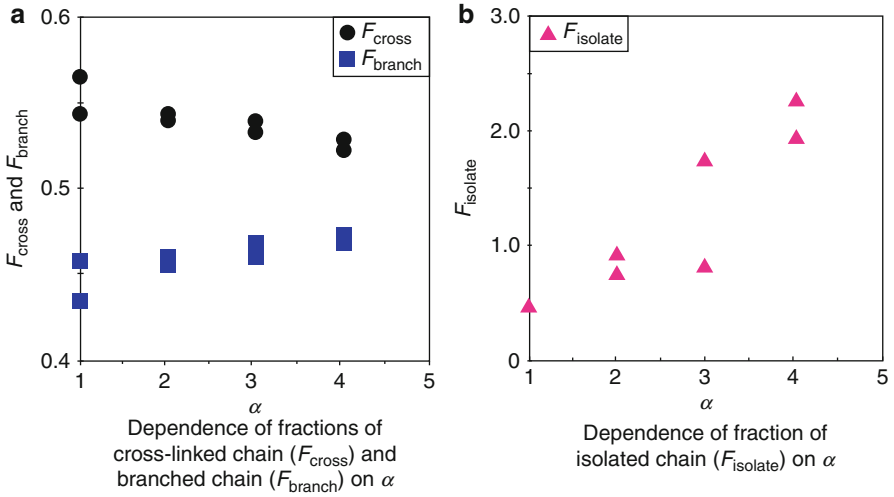


Fig. 4.17 Dependence of CB network parameters on elongation ratio (α) [29] (Reprinted from J Appl Polym Sci 128, Kato A., Isono Y., Structural changes in the carbon black network in carbon-black-filled styrene-butadiene rubber samples cured with a two-step process. 2498–2507, Copyright © (2013), with permission from John Wiley and Sons)

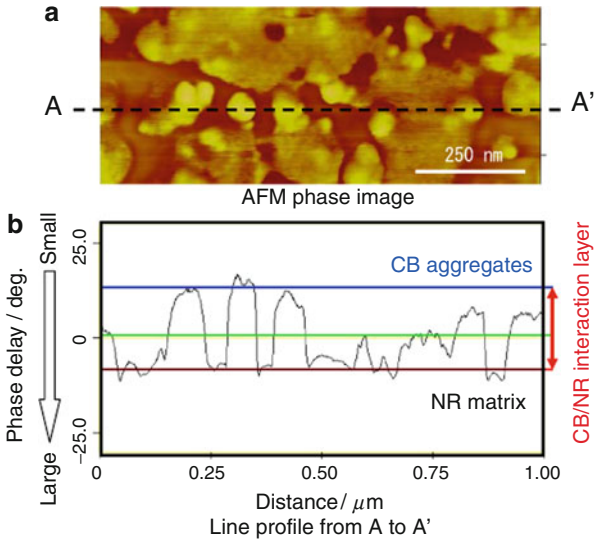


Fig. 4.18 Line profile of AFM phase image of CB-20 [35] (Reprinted from Colloid Polym Sci 291, Kato A, Ikeda Y, Tsushi R, Kokubo Y, Kojima N, A new approach to visualizing the carbon black/natural rubber interaction layer in carbon black-filled natural rubber vulcanizates and to elucidating the dependence of mechanical properties on quantitative parameters. 2101–2110, Copyright © (2013), with permission from Springer)

regions have small and large phase delays, respectively, indicating that the elastic modulus of the former is high, while that of the latter is low. Several large bright spots occupy the greater part of the measured surface of the CB-20 sample. Considering that CB particles are 20–30 nm in diameter, it is assumed that all

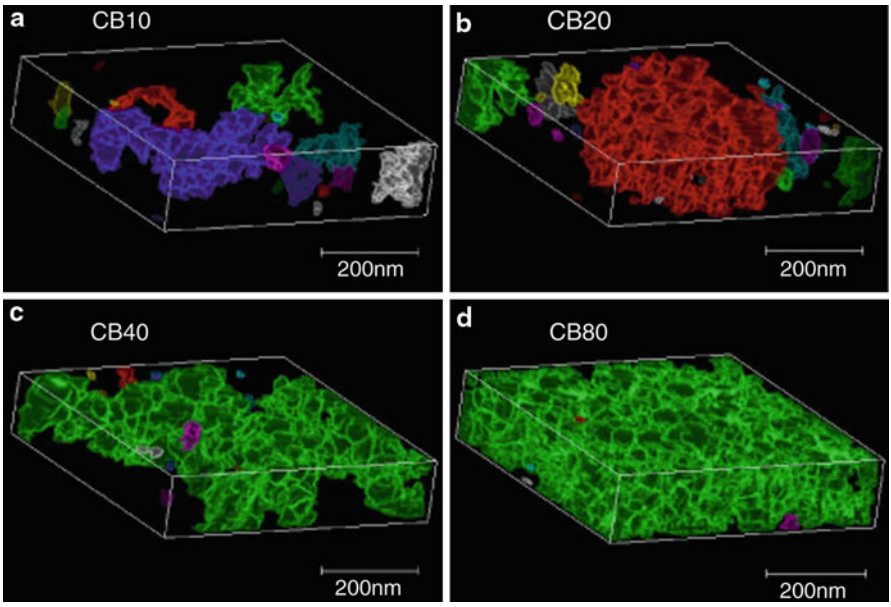


Fig. 4.19 3D images of CB/NR interaction layer [35] (Reprinted from Colloid Polym Sci 291, Kato A, Ikeda Y, Tsushi R, Kokubo Y, Kojima N, A new approach to visualizing the carbon black/natural rubber interaction layer in carbon black-filled natural rubber vulcanizates and to elucidating the dependence of mechanical properties on quantitative parameters. 2101–2110, Copyright © (2013), with permission from Springer)

these large spots do not correspond to CB aggregates, but rather reflect the CB/NR interaction layer (i.e., the immobilized rubber interfacial layer) containing CB aggregates. Figure 4.18b plots the phase delay along line A-A' as a function of the distance from the edge of the image. The portion showing the smallest phase delay may be the core of the CB aggregates, and that showing the largest phase delay may be due to the rubbery matrix. Accordingly, it is inferred that the interaction layer between the CB filler and the matrix rubber is the region between the smallest and the largest phase delay values.

Based on the foregoing 3D-TEM observation results, it is reasonable to consider that a layer ranging in depth from a minimum of 1.5 nm to a maximum of approximately 3 nm from the CB particle surface corresponds to the thickness of the CB/rubber interaction layer immobilized by the CB filler. In this regard, a d_p value of a few nm corresponds to the thickness of the NR glassy layer around CB as found by Nishi and Nakajima et al. [34] based on pulsed NMR and AFM measurements. Figure 4.19 shows 3D images of the CB/NR interaction layer of four CB-filled NR vulcanizate samples, assuming hypothetically that the thickness of the interaction layer is approximately 3 nm. The matrix rubber excluding CB and CB aggregates is shown uniformly in black, and the CB/NR interaction layers that are not interconnected are shown in different colors. As can be seen in Fig. 4.19,

CB aggregates in the sulfur-cured NR vulcanizates are linked via the CB/rubber interaction layer to form the CB network. The size of these large spots nearly corresponds to that of the region of the CB/rubber interaction layer of the CB-20 sample in Fig. 4.18a.

Letting V_i denote the volume of the CB/rubber interaction layer, V_s the volume of the CB-filled NR vulcanizate sample, and V_{CB} the volume of mixed CB, we defined the following volume ratios of the NR matrix, and the CB/rubber interaction layer, i.e., $\phi_{ui/s(\text{without CB})}$ and $\phi_{i/s(\text{without CB})}$ of two phases excluding the CB phase [35].

The volume fractions of the two phases are the following:

$$\phi_{ui/s(\text{without CB})} = 100\left(\frac{V_s - V_i - V_{CB}}{V_s - V_{CB}}\right) \tag{4.6}$$

$$\phi_{i/s(\text{without CB})} = 100\left(\frac{V_i}{V_s - V_{CB}}\right) \tag{4.7}$$

$$\phi_{ui/s(\text{without CB})} + \phi_{i/s(\text{without CB})} = 1 \tag{4.8}$$

Figure 4.20 shows the CB filler loading dependence of $\phi_{ui/s(\text{without CB})}$ and $\phi_{i/s(\text{without CB})}$. The value of $\phi_{i/s(\text{without CB})}$ increased nearly linearly, and that of $\phi_{ui(\text{without CB})}$ decreased linearly with increasing CB loading of 20 phr or below. The value of $\phi_{i/s(\text{without CB})}$ increased nonlinearly, and that of $\phi_{ui(\text{without CB})}$ decreased nonlinearly with increasing CB loading more than 30 phr. The linear increase in the values and the nonlinear decrease in the values presumably reflect percolation behavior in the formation process of the CB network. The results of Figs. 4.19 and 4.20 that for CB loadings of 20 phr or less, CB aggregates and the fragments of the CB network that are present locally increase as a result of the increase in CB loading, and some of them become linked together, while the total volume of the CB network increases. In contrast, near a CB loading of 30 phr or higher, the formation of the CB network is completed, so the number of branched chains increases more markedly than the number of cross-linked chains with a further increase in CB loading, owing to 3D constraints on the CB network [17–21, 23]. Assuming that two branched chains combine to form one linked chain, the CB/NR interaction layer increases more due to branched chains than to cross-linked chains on account of the former's free ends with an increase in the surface area. Accordingly, it is assumed that the total volume of the CB/NR interaction layer increases markedly with an increasing number of branched chains at CB filler loadings of 30 phr or more.

Figure 4.21 shows the dependence of the storage modulus (E') and the reciprocal of E' ($1/E'$) on the amount of CB loading of CB-filled NR vulcanizates at 293 K (20 °C). As the CB loading was increased, E' increased nonlinearly and $1/E'$ decreased nonlinearly. Figure 4.22 shows the dependence of E' and $1/E'$ on $\phi_{i/s(\text{without CB})}$. E' did not change significantly in 0 (0 phr) $\leq \phi_{i/s(\text{without CB})} \leq 0.132$

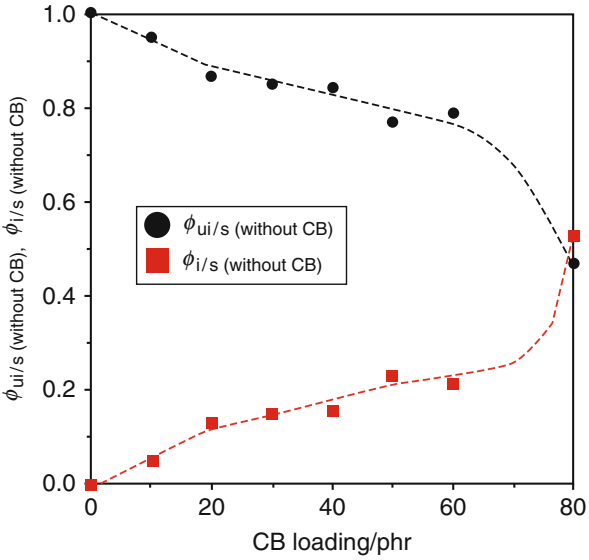


Fig. 4.20 Dependence of volume ratios [$\phi_{ui/s(without\ CB)}$, and $\phi_{i/s(without\ CB)}$] of NR matrix, and CB/NR interaction layer, without CB on CB loading. The *dotted lines* are for a visual guide. (Reprinted from Colloid Polym Sci 291, Kato A, Ikeda Y, Tsushi R, Kokubo Y, Kojima N, A new approach to visualizing the carbon black/natural rubber interaction layer in carbon black-filled natural rubber vulcanizates and to elucidating the dependence of mechanical properties on quantitative parameters. 2101–2110, Copyright © (2013), with permission from Springer)

(20 phr), while it increased almost linearly in 0.132 (20 phr) $<\phi_{i/s(without\ CB)} \leq 0.527$ (80 phr). Moreover, $1/E'$ decreased almost linearly in $0 \leq \phi_{i/s(without\ CB)} \leq 0.132$, while it did not change significantly in $0.132 < \phi_{i/s(without\ CB)} \leq 0.527$. These results show that the series and parallel mechanical models proposed by Fukahori [71] are applicable to the linear dependence of E' and $1/E'$ on $\phi_{i/s(without\ CB)}$ in the former and the latter regions, respectively. It suggests that a CB network, in which CB aggregates are connected through the CB/NR interaction layer, is formed in the rubber matrix and influences the viscoelastic properties of CB-filled rubber vulcanizates [35].

The foregoing results indicate that the reinforcement mechanisms of CB and fiber such as glass fiber (GF) and carbon fiber (CF) are essentially very different. Based on TEM observation results for CB-filled rubber vulcanizates, Medalia [72] reported that the aspect ratio (l/d) of CB aggregates was 1.7–1.9. Halpin et al. [73] found that the significant reinforcement effect of nylon-fiber-filled rubber vulcanizate occurred at l/d of more than 10. These findings imply that because the l/d of CB aggregates in rubber vulcanizates is much smaller than 10, CB aggregates cannot reinforce the rubber matrix directly. Rather, by applying the mixing law to the volume fractions of the NR matrix and the CB/NR interaction layer formed

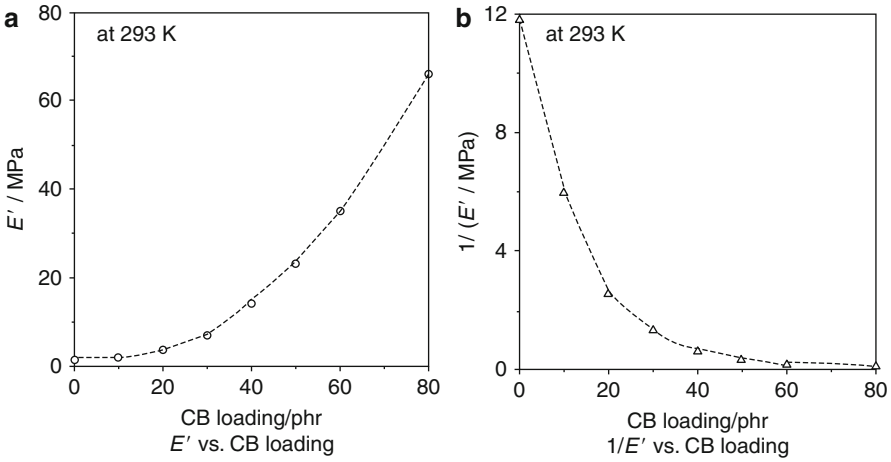


Fig. 4.21 Dependence of storage modulus (E') and reciprocal of E′(1/E') on CB loading of CB-filled NR vulcanizates. The *dotted lines* are for a visual guide [35] (Reprinted from Colloid Polym Sci. 291, Kato A, Ikeda Y, Tsushi R, Kokubo Y, Kojima N, A new approach to visualizing the carbon black/natural rubber interaction layer in carbon black-filled natural rubber vulcanizates and to elucidating the dependence of mechanical properties on quantitative parameters. 2101–2110, Copyright © (2013), with permission from Springer)

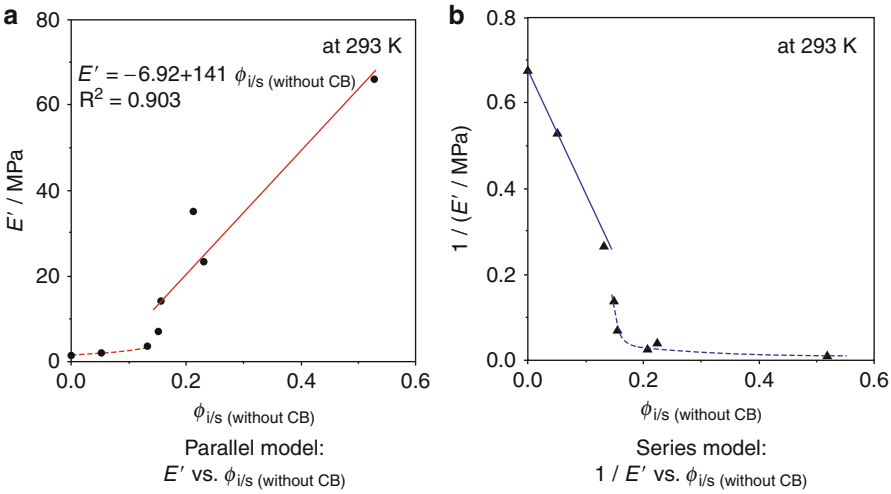


Fig. 4.22 Dependence of E' and $1/E'$ on $\phi_{i/s(without\ CB)}$. The *dotted* and *solid lines* are for a visual guide and the approximate linear line, respectively [35] (Reprinted from Colloid Polym Sci 291, Kato A, Ikeda Y, Tsushi R, Kokubo Y, Kojima N, A new approach to visualizing the carbon black/natural rubber interaction layer in carbon black-filled natural rubber vulcanizates and to elucidating the dependence of mechanical properties on quantitative parameters. 2101–2110, Copyright © (2013), with permission from Springer)

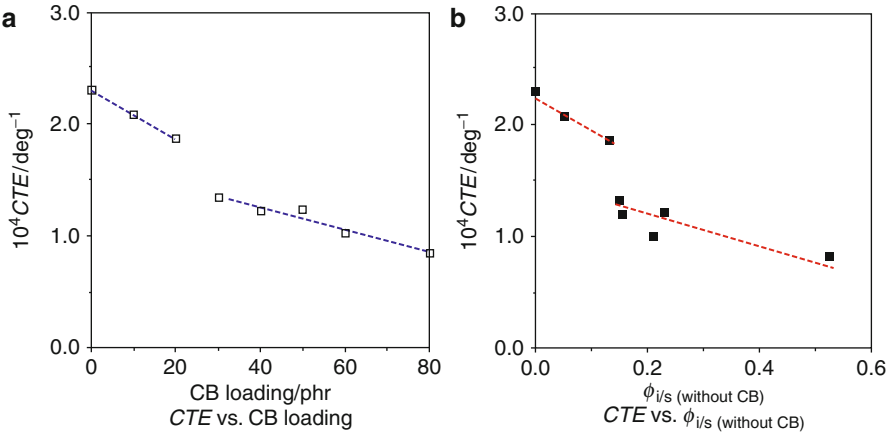


Fig. 4.23 Dependence of coefficient of thermal expansion (*CTE*) on CB loading and volume fraction ($\phi_{i/s(without\ CB)}$) of CNIL in CB-filled NR vulcanizates. The lines are for a visual guide [35] (Reprinted from Colloid Polym Sci 291, Kato A, Ikeda Y, Tsushi R, Kokubo Y, Kojima N, A new approach to visualizing the carbon black/natural rubber interaction layer in carbon black-filled natural rubber vulcanizates and to elucidating the dependence of mechanical properties on quantitative parameters. 2101–2110, Copyright © (2013), with permission from Springer)

around CB aggregates, the viscoelastic behavior of CB-filled NR vulcanizates can be explained for the first time. For CB loadings of 20 phr or less, the CB/NR interaction layer of local CB aggregates causes the reinforcement effect of the series mechanical model. In contrast, for CB loadings of 30 phr or more, the CB network is connected through the CB/NR interaction layer and grows in three dimensions to constitute the whole rubber matrix. The CB/NR interaction layer which forms the CB network generates the reinforcement effect of the parallel mechanical model. Therefore, it is assumed that the mechanical model of the mixing law changes from a series model to a parallel one before and after CB network formation. In addition, a typical mixing law for the volume fractions of fiber and the rubber matrix can be applied to determine the reinforcement effect of fibers because fibers with *l*/*d* of 10 or more serve to reinforce the rubber matrix.

Kato et al. [47, 74] investigated the relationship between the coefficient of thermal expansion (*CTE*) calculated from the temperature region of 298–348 K (25–75 °C) and the amount of CB loading. Their results are shown in Fig. 4.23a. The transition point that is closely related to the formation of the CB network is observed in the CB loading region from 20 to 30 phr. However, it is better to examine the relationship between the *CTE* and $\phi_{i/s(without\ CB)}$ because the transition is related to the volume ratio of the CB/NR interaction layer (i.e., the immobilized rubber interfacial layer) rather than that of CB. This relationship is shown in Fig. 4.23b. A sudden change (i.e., the transition point) in the *CTE* in the CB loading region of 20–30 phr is clearer in Fig. 4.23b than in Fig. 4.23a.

5.4 Dependence of Optical Properties on Silica Network of Silica-Filled Cured NR

The recipes for the particulate-silica-filled cross-linked NR examined in this study are shown in Table 4.5. Silica used in this study was conventional hydrophilic silica VN-3. The only ingredient that was changed in this series of cross-linked NR was the silica loading, which was varied from 0 to 80 phr. The loading of dicumyl peroxide (DCP) used as a cross-linking agent was the same in all the samples at 1 phr. The ingredients were mixed with NR (RSS No. 1 grade from Indonesia) in a two-roll mill and cross-linked in the mold at 428 K (155 °C) in a pressure range of 100–150 kg/cm^2 for 20–30 min to produce cross-linked NR sheets of approximately 1 mm in thickness. In the following discussion, the samples will be referred to by the designation NR-P-X, where P stands for peroxide curing and X indicates the silica content in phr.

In general, increasing the loading of inorganic particles or glass fibers mixed into a transparent polymer tends to cause the optical transmittance of the resulting composite material to decline, even if the refractive index difference is very small [37, 38]. The photographs in Fig. 4.24 show the optical transparency of the sheet-shaped particulate-silica-filled cross-linked NR samples (NR-P-10, NR-P-30, NR-P-40, and NR-P-80) placed on pieces of grid paper. For the sample with a silica loading of 10 phr, the pattern of the grid paper behind the sample can be seen, but it is virtually indiscernible for NR-P-30. In addition, polarized light was not observed in the latter sample. As the silica loading was increased from 40 to 80 phr, the pattern of the grid paper gradually became visible again. An optical transparency anomaly of this kind has never been reported before.

The concepts of diffusion transmittance and haze are both used effectively in optics-related industries as indices of transparency in the standard light C region, i.e., the average daylight region. Excluding the scattering of light caused by irregularities on the sample surface, two cases may be considered when a sample is opaque. In one case, incident light is absorbed or scattered inside the material, resulting in a shield effect that blocks the transmission of light. In the other case, light transmitted from the material is markedly diffused or scattered. Accordingly, the shield effect can be quantitatively examined in the former case, while diffusion transmittance and haze can be similarly examined in the latter case. The shield effect (T_{shield}), diffusion transmittance (T_{d}), and haze (H) are defined here using total transmittance (T_{t}) and parallel transmittance (T_{p}) as shown below [75]:

$$T_{\text{Shield}} = 1 - T_t \tag{4.9}$$

$$T_d = T_t - T_p \tag{4.10}$$

$$H = \frac{T_d}{T_t} \tag{4.11}$$

where $0 < T_{\text{d}}, T_{\text{p}} < T_{\text{t}} < 1$.

Table 4.5 Recipes of silica-filled cross-linked natural rubber [22] (Reprinted from J Opt Soc Am B, 25, Kato, A., Ikeda,Y., Kasahara, Y., Shimanuki, J., Suda, T., Hasegawa, T., Sawabe, H., Kohjiya, S., Optical transparency and silica network structure in cross-linked natural rubber as revealed by spectroscopic and three-dimensional transmission electron microscopy techniques, 1602–1615, Copyright © (2008), with permission from the Optical Society of America)

Ingredient (phr[*2])	Sample[*1]						
	NR–P–0	NR–P–10	NR–P–20	NR–P–30	NR–P–40	NR–P–60	NR–P–80
NR(RSS#1)	100	100	100	100	100	100	100
DCP[*3]	1	1	1	1	1	1	1
Silica[*4]	0	10	20	30	40	60	80

[*1]Cross-linking conditions: 20-30 min. at 155 °C under 100–150 kg/cm^2
[*2]Grams per one hundred grams of rubber
[*3]Dicumyl peroxide
[*4]Nipsil VN-3 obtained from Nippon Silica Industrial Co., Ltd.

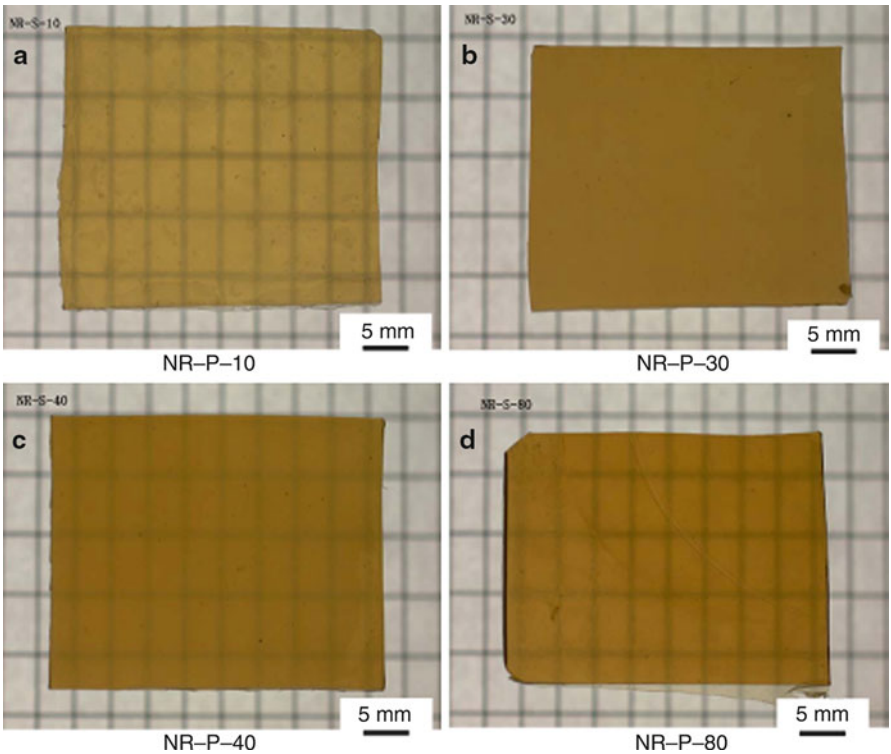


Fig. 4.24 Optical transparency of NR-P-10, NR-P-30, NR-P-40, and NR-P-80 films [22] (Reprinted from J Opt Soc Am B, 25, Kato, A., Ikeda,Y., Kasahara, Y., Shimanuki, J., Suda, T., Hasegawa, T., Sawabe, H., Kohjiya, S., Optical transparency and silica network structure in cross-linked natural rubber as revealed by spectroscopic and three-dimensional transmission electron microscopy techniques. 1602–1615, Copyright © (2008), with permission from the Optical Society of America)

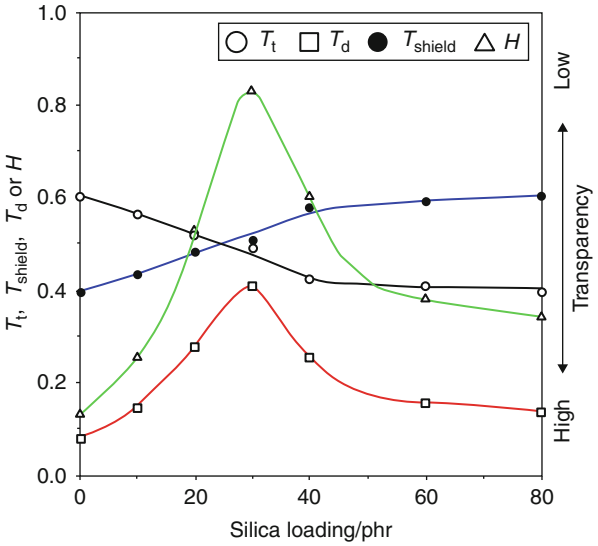


Fig. 4.25 Dependence of total transmittance (T_t), shield effect (T_{shield}), diffuse transmittance (T_d), and haze (H) on silica loading [22] (Reprinted from J Opt Soc Am B, 25, Kato, A., Ikeda,Y., Kasahara, Y., Shimanuki, J., Suda, T., Hasegawa, T., Sawabe, H., Kohjiya, S., Optical transparency and silica network structure in cross-linked natural rubber as revealed by spectroscopic and three-dimensional transmission electron microscopy techniques. 1602–1615, Copyright © (2008), with permission from the Optical Society of America)

It is noted that all these parameters (T_{shield}, T_t, T_d and T_p) are between unity and zero. The lower the values of T_{shield}, T_d, and H are, the higher is the transparency of the material. The dependence of T_{shield}, T_t, T_d, and H on the silica loading is shown in Fig. 4.25. As the silica loading was increased, T_{shield} gradually increased and T_t decreased, whereas T_d and H showed their smallest values in the regions of high and low silica loading and their maximum values at a silica loading of 30 phr. The presence of maximums in T_d and H agrees well with the results mentioned earlier, which implies that a shield effect or light scattering is enhanced the most at a silica loading of 30 phr.

Figure 4.26 shows 3D-TEM images of NR-P-10, NR-P-30, NR-P-40, and NR-P-80. The white particles seen in the images are silica. Because 3D-TEM provides information along the depth direction of the samples, the difference in the dispersion state of the silica aggregates, compared with that in Fig. 4.26, is obvious at a glance. Based on these silica aggregate dispersion patterns obtained by image processing, an investigation was made of the relationship between the particle dispersion state and T_{shield}, T_d, and H, the results of which are described below. It is notable that the 3D-TEM images obtained for these specimens are qualitatively in accord with those obtained for specimens that were cross-linked by sulfur, though the latter were not transparent at all [13, 15, 76]. The silica loading dependence of d_p and ρ_v found for the silica-filled cross-linked NR samples is shown in

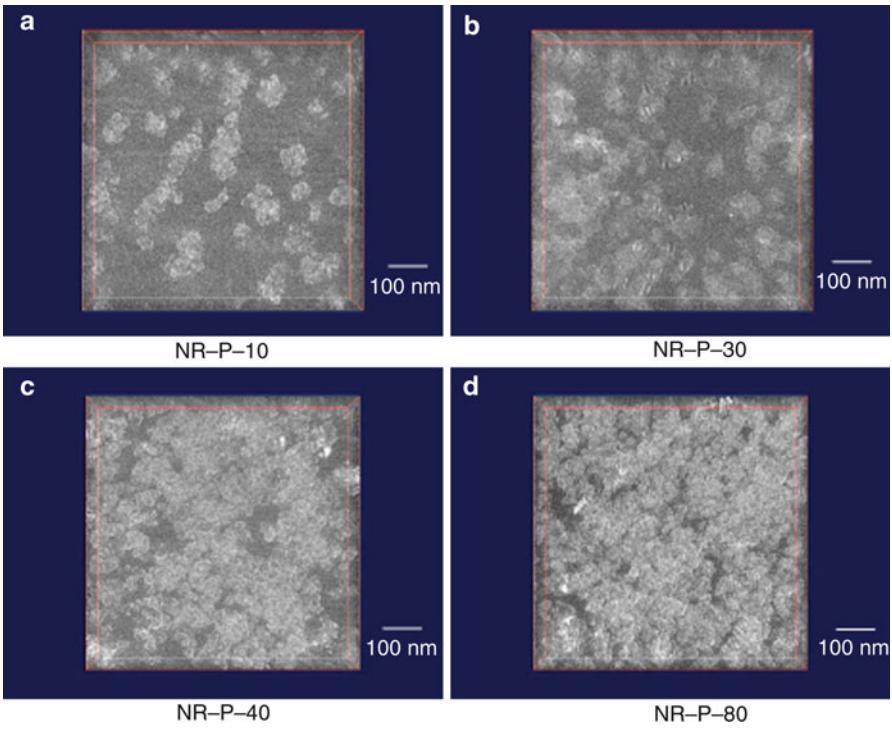


Fig. 4.26 3D-TEM images of NR-P-10, NR-P-30, NR-P-40, and NR-P-80 [22] (Reprinted from J Opt Soc Am B, 25, Kato, A., Ikeda,Y., Kasahara, Y., Shimanuki, J., Suda, T., Hasegawa, T., Sawabe, H., Kohjiya, S., Optical transparency and silica network structure in cross-linked natural rubber as revealed by spectroscopic and three-dimensional transmission electron microscopy techniques. 1602–1615, Copyright © (2008), with permission from the Optical Society of America)

Fig. 4.27a, b, respectively. In Fig. 4.27a, it is seen that d_p decreased sharply as the silica loading was increased and converged to its asymptotic value (1.3 nm) at a loading level of 30 phr or higher. It is presumed that this value of 1.3 nm indicates the smallest d_p that the silica aggregates could come close to one another. This value may be reasonable because the presence of a bound rubber layer on the silica surface has been presumed on the basis of the reinforcing effect of particulate silica [22, 77, 78]. Therefore, the thickness of the bound rubber layer may be 1.3 nm on the surface of silica (VN-3) aggregates. This is the first report of the thickness of the bound rubber layer on silica particles obtained by using 3D-TEM results. Electron diffusion in silica-filled rubber probably occurs due to hopping conduction when d_p between silica aggregates or the rubber layer between two silica aggregates is equal to or less than 1.3 nm.

It is observed in Fig. 4.27b that ρ_v declined sharply, i.e., conductivity increased sharply, as the silica loading was increased. This is a very interesting finding because silica is an electrical insulator. The increase in conductivity indicates that it became

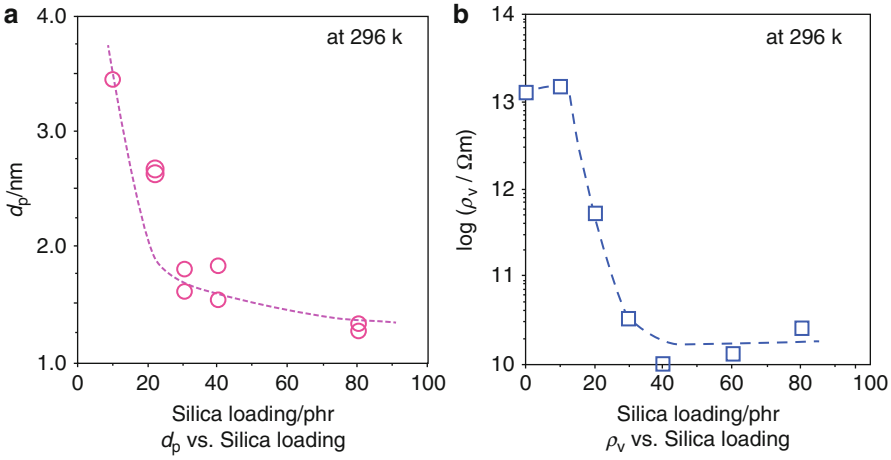


Fig. 4.27 (**a**) Silica loading dependence of the closest distance (d_p) between two neighboring silica aggregates and (**b**) volume resistivity (ρ_v) at room temperature [22] (Reprinted from J Opt Soc Am B, 25, Kato, A., Ikeda,Y., Kasahara, Y., Shimanuki, J., Suda, T., Hasegawa, T., Sawabe, H., Kohjiya, S., Optical transparency and silica network structure in cross-linked natural rubber as revealed by spectroscopic and three-dimensional transmission electron microscopy techniques. 1602–1615, Copyright © (2008), with permission from the Optical Society of America)

markedly easier for electrons to flow through the silica aggregates with the increase in silica loading. The reason for this result can presumably be understood as follows: Because hydroxyl functional groups (silanol) are present on the silica surface, it is assumed that water resulting from residual moisture tends to gather on the silica surface by hydrogen bonding to form the silica-NR interfaces. The exact interface structure has yet to be elucidated, but the copresence of moisture and a bound rubber layer due to strong absorption (i.e., chemisorption) is well established [15, 79–83]. Accordingly, when the silica aggregates come close enough together for electrons to jump the gap between them, a higher conductivity is observed on account of the small insulation distance of ca. 1.3 nm and the absorbed water molecules with some conductive impurities. The results indicate that ρ_v also converged to a constant value at a silica loading of 30 phr or higher. It can be inferred therefore that the percolated conductive network of the silica aggregates was formed at a silica loading of 30 phr.

The 3D network of silica aggregates such as that in Fig. 4.5 was visualized by drawing a line connecting their centers of gravity. The procedure is as follows: Firstly, the center of gravity of each aggregate is positioned in the 3D-TEM image. Secondly, when neighboring aggregates having a d_p value equal to or less than 1.3 nm are found, their centers of gravity are connected by a line to show the distance (d_g) between them. Thirdly, all possible pairs are connected in this way. Lastly, only the lines are shown, resulting in a skeleton that indicates the electron conductive paths. The network structures visualized in this way for the NR-P-10, NR-P-30, and NR-P-80 samples are shown in Fig. 4.28. Networks that are not mutually connected are shown in different colors from the percolated one. It is seen that localized networks were present in the NR-P-10 sample (Fig. 4.28a) and that

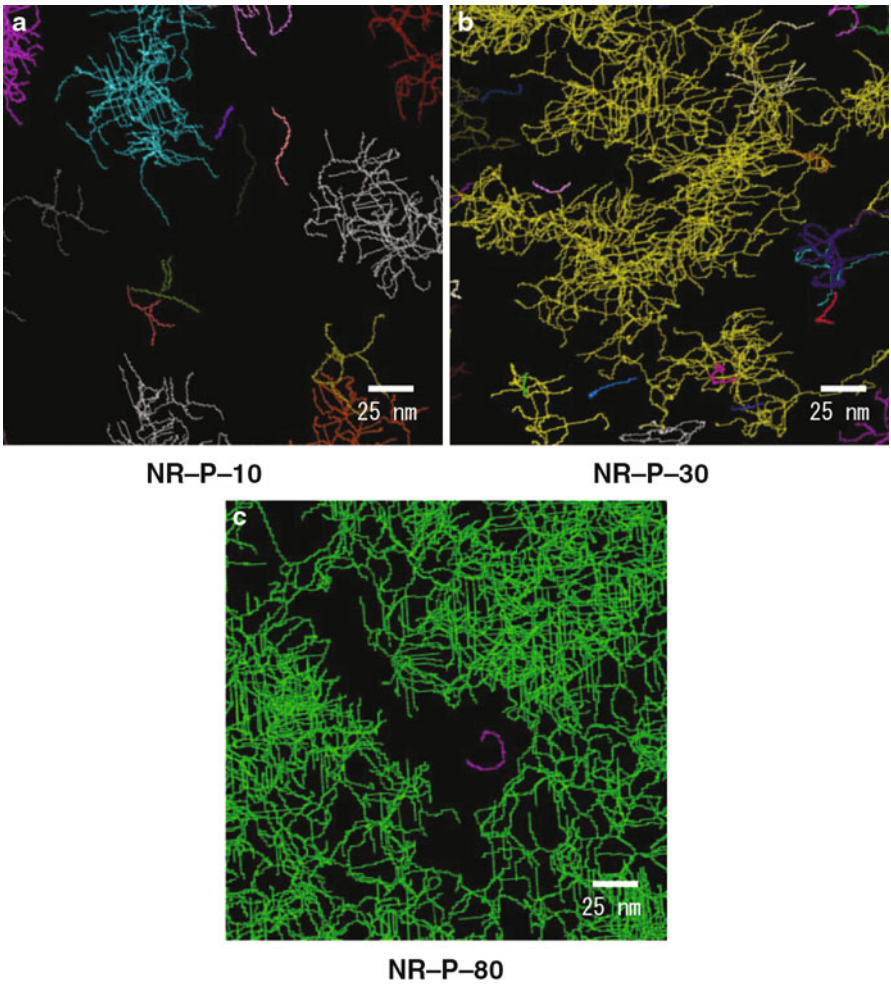


Fig. 4.28 Visualization of network structures of silica and of isolated chain structure of silica in NR matrix [22] (Reprinted from J Opt Soc Am B, 25, Kato, A., Ikeda,Y., Kasahara, Y., Shimanuki, J., Suda, T., Hasegawa, T., Sawabe, H., Kohjiya, S., Optical transparency and silica network structure in cross-linked natural rubber as revealed by spectroscopic and three-dimensional transmission electron microscopy techniques. 1602–1615, Copyright © (2008), with permission from the Optical Society of America)

these network structures were joined together as the silica loading was increased in the NR-P-30 sample (Fig. 4.28b). A further increase in the silica content resulted in the formation of a dense network structure in the NR-P-80 sample (Fig. 4.28c). It is also observed that the mesh size of the silica aggregate network structure was nearly uniform. The mean lengths of the cross-linked chains, branched chains, and isolated chains ranged from 9 to 24 nm, from 17 to 41 nm, and from 14 to 38 nm, respectively. No specific tendency was seen for the dependence of these lengths

on the silica loading. In short, the networks were composed of three types of chains: cross-linked chains with both ends connected to the network, branched chains having one end connected to the network and the other end free, and isolated chains with neither end connected to the network structure. Isolated chains were observed in all the samples and are easily recognized in NR-P-10 shown in Fig. 4.28a. It is assumed that these results are related to the formation mechanism of the silica aggregate networks. The mechanism will be elucidated and reported separately in the near future.

The optical transparency of hydrophilic silica-filled cross-linked NR was previously examined in a silica loading range of 0–80 phr, and it was found that samples were transparent at filler loadings above and below 30 phr, but were opaque at the intermediate level [22]. (Optical transparency in the average daylight region declined markedly or haze increased markedly.) The relationship between 3D-TEM image observation results and electrical percolation revealed that this optical anomaly was not caused by the dispersion state of silica aggregates, but rather originated from multiple scattering induced by the network, especially by the isolated chains of silica aggregates.

Based on these results, by making a comparison with a Monte Carlo experimental equation [84], the following equations are obtained concerning multiple light scattering caused by the dispersed particles. They show that the attenuation coefficient is equal to the scattering coefficient (μ_s) in a medium containing particles and isolated chains. Assuming that the silica particles are related to μ_s, it may reflect the diffusion transmittance (T_d) and haze (H). The length of the isolated chains is denoted by L ($2r$). Because n shows the number of particles per unit volume, it may be replaced by the chain density.

$$T_d(orH) \propto \mu_s = \pi K_p n r^2 \tag{4.12}$$

$$\begin{aligned} T_d(orH) &\propto \pi K_p n r^2 \\ &\propto \left(\frac{\pi K_p}{4}\right) n L^2 \end{aligned} \tag{4.13}$$

where T_d and H are both proportional to μ_s, π is ca. 3.14, K_p is the scattering factor for an aqueous spherical particle depending on its radius and the radiation wavelength, n is the number of isolated chains per unit volume, and r ($=L/2$) is the radius of the spherical particle. As a result, Eq. 4.14 for T_d and Eq. 4.15 for H can be deduced from Eq. 4.13.

$$T_d = CnL^2 + T_d(NR) \tag{4.14}$$

$$H = C'nL^2 + H(NR) \tag{4.15}$$

where C and C' are constants related to ($\pi K_p/4$) and T_d (NR) and H (NR) are coefficients that originate only from the NR matrix without any silica filler.

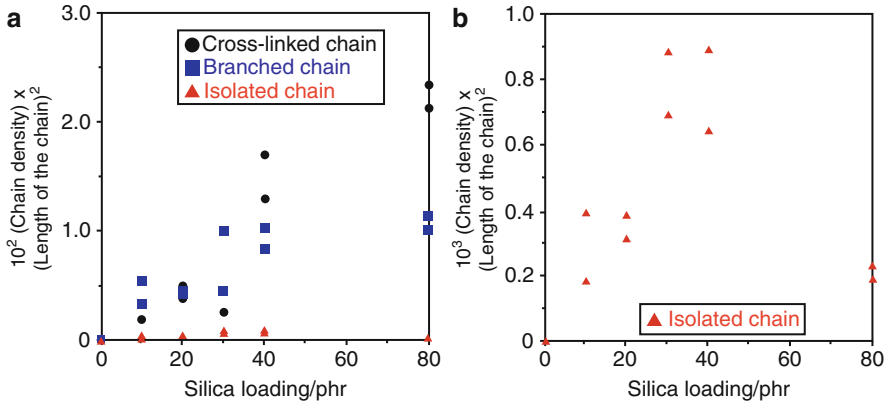


Fig. 4.29 (**a**) Dependence of product of chain density × chain length^2 of three types of network chains on silica loading and (**b**) dependence of product of chain density × chain length^2 of isolated chains on silica loading [22] (Reprinted from J Opt Soc Am B, 25, Kato, A., Ikeda,Y., Kasahara, Y., Shimanuki, J., Suda, T., Hasegawa, T., Sawabe, H., Kohjiya, S., Optical transparency and silica network structure in cross-linked natural rubber as revealed by spectroscopic and three-dimensional transmission electron microscopy techniques. 1602–1615, Copyright © (2008), with permission from the Optical Society of America)

The silica loading dependence of this product is shown in Fig. 4.29a for cross-linked and branched network chains and in Fig. 4.29b for isolated chains. The magnitude of the product of the number of chains and their squared length was found to decrease in the order of the cross-linked chains, branched chains and isolated chains, as seen in Fig. 4.29. As the silica loading was increased, the product values of the network chains increased significantly at silica loadings of 30 phr or higher. In contrast, the product values of the isolated chains in the latter figure increased with increasing silica loading up to 30 phr, after which they decreased, thus displaying unique behavior at 30 phr. This behavior suggests that the isolated chains may play an important role in determining the minimum transparency of the 30 phr loaded sample. The dependence of diffusion transmittance (T_d) and haze (H) on the product of the chain density times the chain length^2 of the isolated chains of silica aggregates is shown in Fig. 4.30. A linear relationship is clearly observed in this figure. The order of the samples with respect to transparency also shows good consistency, which suggests that the isolated chains are closely related to optical scattering, resulting in minimum transparency at a silica loading of 30 phr. From these results, it is inferred that light scattered by the isolated chains that were not attached to the network was heterogeneous for the material system as a whole, thus increasing diffusion transmittance and causing a loss of transparency.

Taking these results into account, it is assumed that the thermal motion of the cross-linked and branched network chains was constrained and that the light scattered by these chains was homogeneous for the material system as a whole on account of the homogeneous network structure. Diffusion transmittance did not

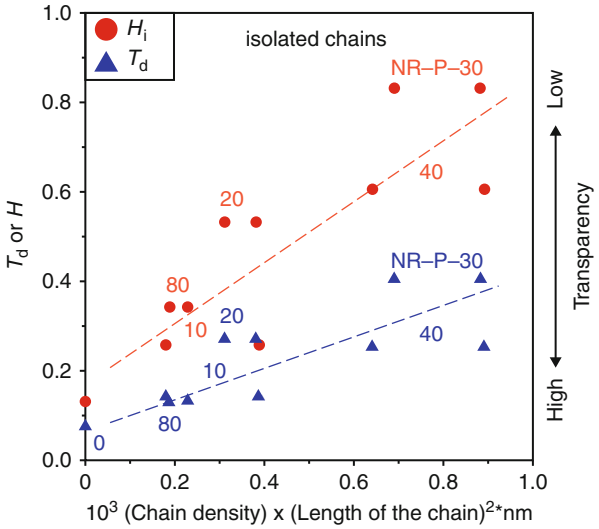


Fig. 4.30 Dependence of diffusion transmittance (T_d) and haze (H) on product of chain density × chain length^2 of isolated chains [22] (Reprinted from J Opt Soc Am B, 25, Kato, A., Ikeda,Y., Kasahara, Y., Shimanuki, J., Suda, T., Hasegawa, T., Sawabe, H., Kohjiya, S., Optical transparency and silica network structure in cross-linked natural rubber as revealed by spectroscopic and three-dimensional transmission electron microscopy techniques. 1602–1615, Copyright © (2008), with permission from the Optical Society of America)

fluctuate noticeably. It is interesting that the silica network system showed similar multiple scattering like that mentioned above, even though it is formed by the agglomeration of nanofiller aggregates in the NR matrix. This similarity between the two apparently different systems may be reasonable because the matrix NR is in a highly viscous yet liquid state. It is inferred from these observations that the product (i.e., the reciprocal of the scattering cross section) of the number and length squared of the isolated chains was the largest for the NR-P-30 sample, resulting in a pronounced increase in diffusion transmittance that markedly reduced its transparency as seen in Figs. 4.24 and 4.25.

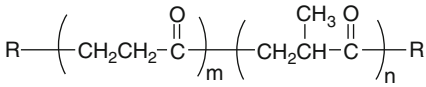
5.5 High-Impact Mechanism of Polyketone/Polyamide Polymer Alloy

The polymer alloys examined in this study consisted of an ethylene/propylene/CO copolymer (Carilon D26HM100, Shell Co.), i.e., PK and PA 6 (Amilan CM1017, Toray Ind.). Table 4.6 shows the mixing ratios of the polymer alloys used. The designation of each sample and its mixing ratio are indicated. For example, the sample indicated as K60A40 was blended of 60 mass % of PK (volume fraction 0.578) and 40 mass % of PA (volume fraction 0.422) by mechanical mixing using a twin-screw extruder (TEX-30a, Japan Steel Works) at 508 K (235 °C). Polymer alloy

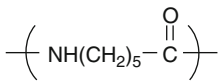
Table 4.6 Weight ratio of PK/PA polymer alloys [47] (Reprinted from J Appl Polym Sci 116, Kato A, Nishioka M, Takahashi Y, Suda T, Sawabe H, Isoda A, Drozdova O, Hasegawa T, Izumi T, Nagata K, Hikasa S, Iwabuki H, Asano A, Phase separation and mechanical properties of polyketone/polyamide polymer alloys. 3056–3069, Copyright © (2010), with permission from John Wiley and Sons)

	Ingredient (mass %)	
Sample	PK	PA
K100	100	0
K90A10	90	10
K80A20	80	20
K70A30	70	30
K60A40	60	40
K50A50	50	50
K40A60	40	60
K30A70	30	70
K20A80	20	80
K10A90	10	90
A100	0	100

Polyketone (PK)
Ethylene/propylene/CO copolymer
(Carilon D26HM100, Shell Co.)



Polyamide 6 (PA)
(Amilan CM101017, Toray Ind.)



impact test specimens (unnotched) were then molded at a resin temperature of 518 K (245 °C) and a mold temperature of 343 K (70 °C) using an injection molding machine (J50E II, Japan Steel Works). Wet test specimens were then moisture-conditioned by holding them at 50 % RH and a temperature of 296 K (23 °C) for 3 weeks. Dry test specimens were prepared by drying them in a vacuum at 373 K (100 °C) for 72 h. The moisture absorption rate of the test specimens was determined by measuring their water content with the Karl Fisher method. The test specimens were then hermetically sealed in aluminum foil-laminated bags and stored in a refrigerator until just before the Charpy impact test. To avoid any change in the notch shape due to moisture conditioning or drying, a Type A notch (opening angle, 45 ± 1°; notch radius, 0.25 ± 0.05 mm; depth, 2.0 ± 0.1 mm) was machined to prepare notched test specimens just before the impact test. This test specimen size conforms to Japanese Industrial Standard (JIS) K7111, "Testing method for determining Charpy impact strength of plastics."

The moisture absorption rates (M_{abs}) of the PK/PA polymer alloy samples are shown in Fig. 4.31 as a function of the PA mass fraction (MF_{PA}). For the wet samples, M_{abs} increased linearly from 0.6 to 1.7 % with MF_{PA} only in the range of 0 mass % $\leq MF_{PA} \leq$50 mass % and became constant of ca. 1.7 % for the higher MF_{PA} values. For the dry samples, M_{abs} seemed to be almost constant much smaller than 0.1 % for every MF_{PA}. The M_{abs} constancy for dry samples and the existence of two M_{abs} dependencies on MF_{PA} for wet samples suggest that M_{abs} was not simply dependent on MF_{PA}. These results imply that M_{abs} is affected from either compositions or the phase separation of the PK/PA polymer alloys. The change of M_{abs} also influences on the glass transition temperature (T_g) of an alloy.

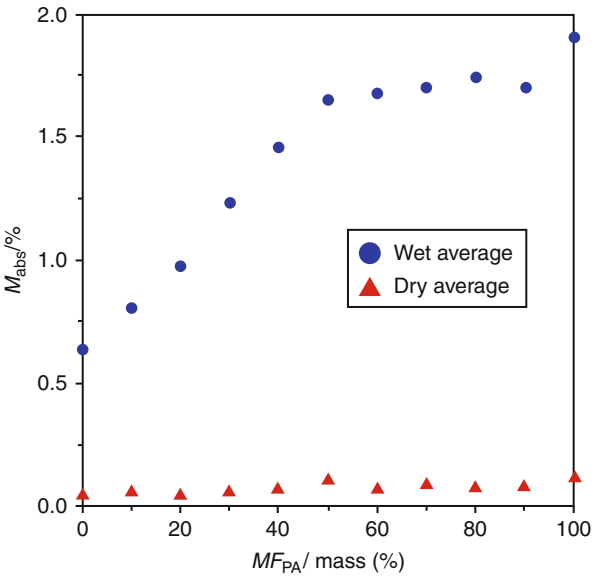


Fig. 4.31 Moisture absorption rate (M_{abs}) of PK/PA polymer alloy samples as a function of PA mass fraction (MF_{PA}) [47] (Reprinted from J Appl Polym Sci 116, Kato A, Nishioka M, Takahashi Y, Suda T, Sawabe H, Isoda A, Drozdova O, Hasegawa T, Izumi T, Nagata K, Hikasa S, Iwabuki H, Asano A, Phase separation and mechanical properties of polyketone/polyamide polymer alloys. 3056–3069, Copyright © (2010), with permission from John Wiley and Sons)

Feng et al. [85] reported that T_g of poly(methyl methacrylate) (PMMA) in the blends of an alternating ethylene-tetrafluorethylene copolymer (ETFE) moves to low temperatures when the ETFE content increases. They reported that this result confirms that only weak interactions take place between ETFE and PMMA.

First of all, we measured DSC curves to obtain information on miscibility and melting behavior in both crystalline phases of PK and PA in the PK/PA alloys. Figure 4.32 shows the DSC curves of pure PK, pure PA, and the K60A40 alloy under the dry condition. These curves were obtained in the second scan to avoid any background effect of the thermal history of the samples. Other alloys examined showed similar DSC curves. The left-hand graph in Fig. 4.32 represents the glass transition region and the right-hand graph the melting temperature (T_m) region. Usually, miscible and homogeneous blends or alloys show a single glass transition in the middle range of both distinct transitions [86]. However, the K60A40 alloy exhibits two different glass transitions, which are attributed to PK and PA, respectively, in the left-hand graph, although both T_g values become slightly closer. This indicates that the alloy is heterogeneous on a scale of several tens of nm [86, 87], but there are some interacting regions between PK and PA. The right-hand graph in Fig. 4.32 shows two endothermic transitions, ascribed to the T_m of both the α and γ crystalline phases of pure PA, at 498 and 483 K (225 and 210 °C), respectively. The endothermic transition of pure PK is observed in the middle of these melting points of pure PA, and T_m is 493 K (220 °C). There is also another transition at a higher temperature as a shoulder peak for pure PK. It is known that the endothermic transition of PK shows propylene unit dependence and doublet T_m peaks. PK has at least two kinds of crystallites, α (T_m = 518–523 K (245–250 °C)) and β (T_m = 483–513 K (210–240 °C)), and an increase in the propylene unit induces β

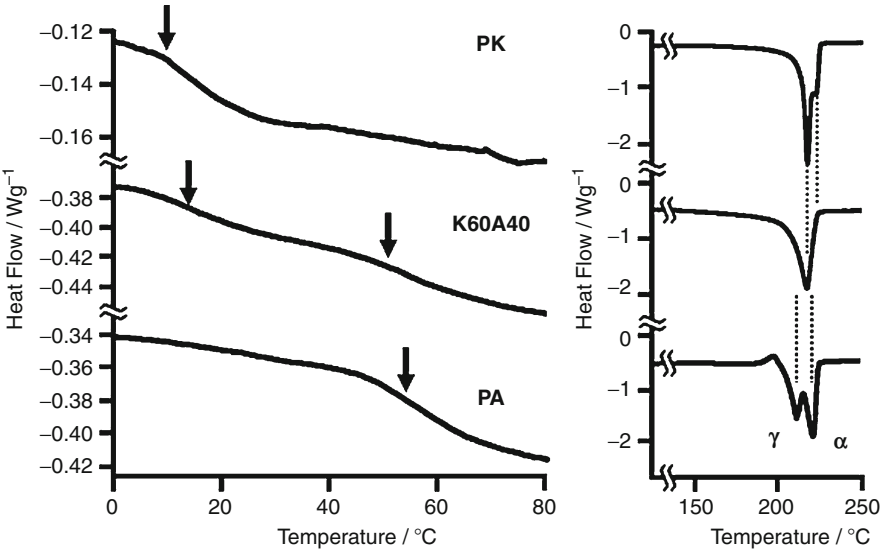


Fig. 4.32 Observed DSC curves for pure PK, K60A40, and pure PA. The *left-hand* graph is for the region from 273 to 353 K (0–80 °C), and the *right-hand* graph shows enlarged DSC curves for the melting endothermic peak region from 423 to 523 K (150–250 °C). The curves were obtained in the second scan [48] (Reprinted from Macromolecules, 42, Asano A, Nishioka M, Takahashi Y, Kato A, Hikasa S, Iwabuki H, Nagato K, Sato H, Hasegawa T, Sawabe H, Arao M, Suda T, Mukai M, Ishikawa D, Izumi T, High impact properties of polyketone/polyamide-6 alloys induced by characteristic morphology and water absorption. 9506–9514, Copyright © (2009), with permission from Am. Chem. Soc.)

crystallites from α crystallites [88, 89]. Judging from the T_m value, the crystalline phase is attributable to β crystallites. The reason for the small shoulder peak is unknown at present, but it may be related to the highly ordered crystalline phase of pure PK. For the K60A40 alloy, a broad peak is observed at the middle point between those of the α and γ crystalline phases of pure PA, and the T_m value is close to that of pure PK. The broad melting peak for the K60A40 alloy is shapeless and smooth. Therefore, the endothermic transition does not show any useful information about the morphology or change in crystalline phases of PA and PK.

Here, we will discuss the grass transition phenomenon for both dry and wet samples in detail. The left-hand graph in Fig. 4.32 shows the DSC thermograms of dry K100, A100, and K60A40 [48]. The thermograms of PK and PA show two distinguishable T_g values (ca. 283 K and ca. 328 K (ca. 10 °C and ca. 55 °C), respectively) corresponding to the respective neat polymers, whereas K60A40 has two T_g values (ca. 287 K and ca. 324 K (ca. 14 °C and ca. 51 °C)) located between the T_g of PK and that of PA. This result suggests that an interaction between PK and PA components occurred in K60A40. In order to investigate the effect of humidity on Tg, we conducted a thermomechanical analysis (TMA) of pure PK, pure PA, and the polymer alloys under both dry and wet conditions. Figure 4.33 shows the

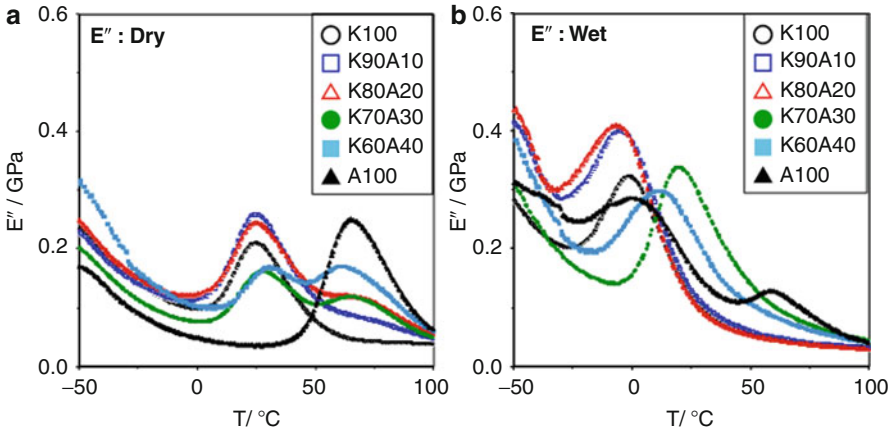


Fig. 4.33 Relationship between dynamic loss modulus (E'') of PK/PA polymer alloy and temperature (T) [48] (Reprinted from Macromolecules, 42, Asano A, Nishioka M, Takahashi Y, Kato A, Hikasa S, Iwabuki H, Nagato K, Sato H, Hasegawa T, Sawabe H, Arao M, Suda T, Mukai M, Ishikawa D, Izumi T, High impact properties of polyketone/polyamide-6 alloys induced by characteristic morphology and water absorption. 9506–9514, Copyright © (2009), with permission from Am. Chem. Soc.)

observed TMA curves (dynamic loss modulus: E'') in relation to temperature at a frequency of 10 Hz. The main dispersion corresponding to the glass transition is observed at approximately 298 K (25 °C) for pure PK and at 339 K (66 °C) for pure PA under the dry condition (Fig. 4.33a). The dispersion peaks for both pure PK and pure PA appear at different temperatures from the T_g values obtained by DSC. This shift presumably occurs because the change in the viscoelastic response of the test specimens affects the TMA curves in Fig. 4.33, whereas DSC measures the calorimetric change for a small quantity of a sample. These main dispersions are also observed for the K60A40 alloy at similar positions or with a slight shift toward an intermediate position. Each peak appears mostly at the same position but broadening occurs. For the wet condition shown in Fig. 4.33b, the intensity of the E'' curve of pure PA decreases compared with that of the dry condition, and a subdispersion at ca. 271 K (ca. −2 °C) is newly observed. The main dispersion peaks for both pure PK and pure PA shift to 271 and 331 K (−2 and 58 °C), respectively. These values are lower than those obtained under the dry condition. The E'' curve of the K60A40 alloy under the wet condition shows a broad hump in the temperature region from 223 to 373 K (−50 to 100 °C), and the main dispersion peak is observed at ca. 284 K (ca. 11 °C). The examination of the E'' curves indicates that humidity affected the T_g values to decrease for every sample. However, the impact strength values (total energy) obtained in the Charpy impact tests of both pure PK and pure PA do not show any effect of humidity at all, whereas the T_g values under the wet condition shift toward a lower temperature. This lower temperature shift suggests that the effect of the decrease in T_g, which causes plasticization of PA or PK due to humidity, limits the improvement of impact

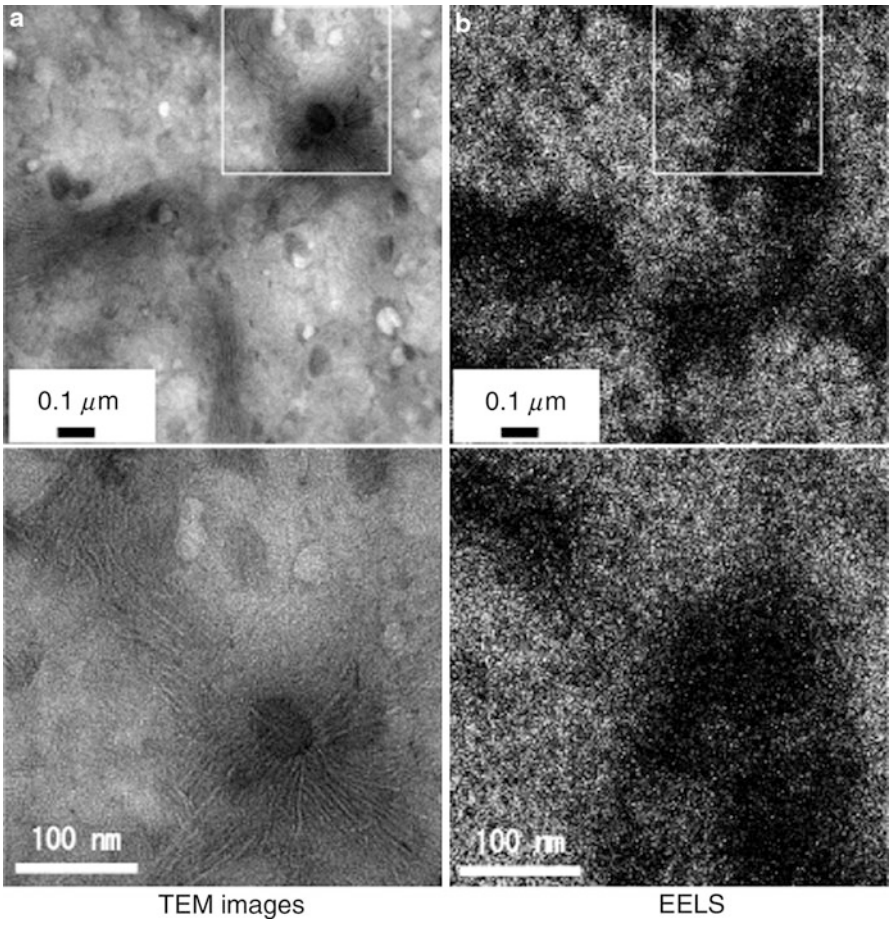


Fig. 4.34 TEM and EELS (electron energy loss spectroscopy) images of K60A40. EELS images indicate the distribution of N in PA6 [47] (Reprinted from J Appl Polym Sci 116, Kato A, Nishioka M, Takahashi Y, Suda T, Sawabe H, Isoda A, Drozdova O, Hasegawa T, Izumi T, Nagata K, Hikasa S, Iwabuki H, Asano A, Phase separation and mechanical properties of polyketone/polyamide polymer alloys. 3056–3069, Copyright © (2010), with permission from John Wiley and Sons)

strength. On the other hand, the subdispersions observed at a lower temperature than T_g presumably affect impact properties [90]. Therefore, it is also necessary to study the motional change of the local segment after alloying to elucidate the mechanism of the high-impact properties of polymers as well as to reveal the morphology. Thus, we first focused on revealing the morphological change related to humidity in the PK/PA alloys because an overall morphological investigation is helpful in analyzing local segmental motion after alloying.

Figure 4.34a shows TEM images of K60A40 observed at low and high magnification. The deep and light color regions are presumably the PA-rich phase stained

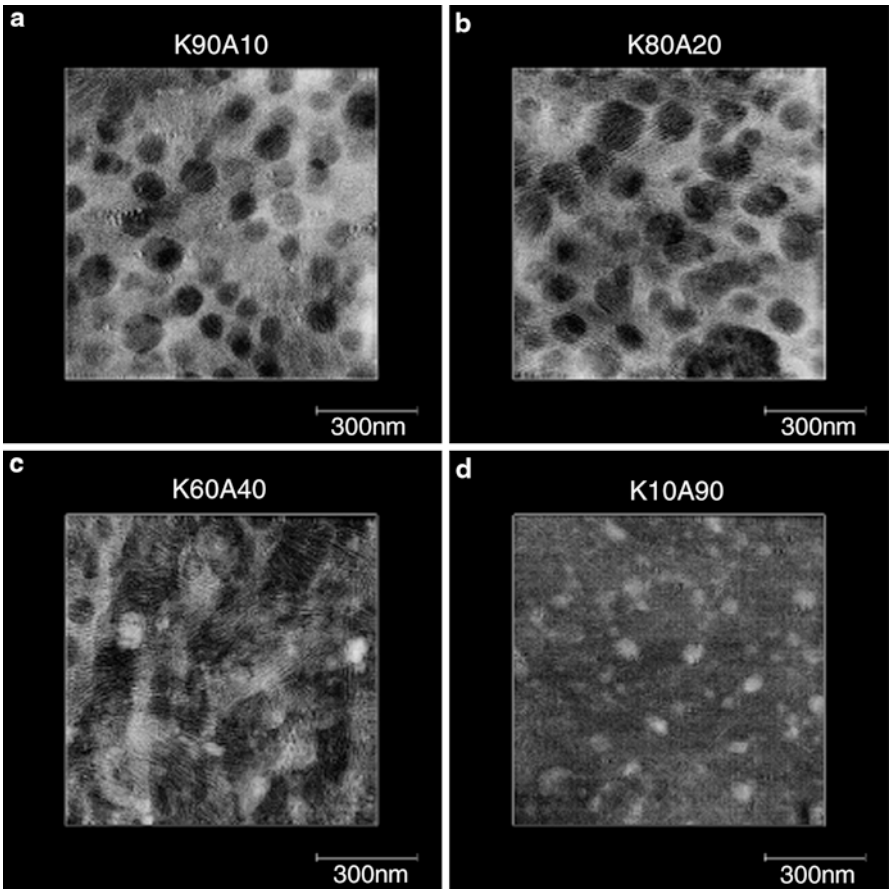


Fig. 4.35 3D-TEM images of (**a**) K90A10, (**b**) K80A20, (**c**) K60A40, and (**d**) K10A90 [47] (Reprinted from J Appl Polym Sci 116, Kato A, Nishioka M, Takahashi Y, Suda T, Sawabe H, Isoda A, Drozdova O, Hasegawa T, Izumi T, Nagata K, Hikasa S, Iwabuki H, Asano A, Phase separation and mechanical properties of polyketone/polyamide polymer alloys. 3056–3069, Copyright © (2010), with permission from John Wiley and Sons)

with phosphotungstic acid and the hard-to-stain PK-rich phase, respectively. Network and particle patterns can be observed in these images. The network in particular displayed a lamella pattern. Electron energy loss spectroscopy (EELS) mapping images of the same views as the TEM observations are shown in Fig. 4.34b. The white parts indicate the presence of N that originated from PA. A comparison of Fig. 4.34a, b reveals that N was noticeably scarce in the region of the lamella network. This result implies that the lamella network was formed in the PK-rich phase of K60A40. A 3D-TEM was used to observe 3D images of the lamella network at the nanometer level. Figure 4.35 shows 3D-TEM images of (a) K90A10, (b) K80A20, (c) K60A40, and (d) K10A90. The black and white

mapping is opposite to that in Fig. 4.34 to see morphology clearly, namely, white parts mainly relate to the lamella region. A lamella-filled spherical black region of 100–300 nm in size was observed in K90A10 and K80A20. The spherical black region was not observed in K60A40. The formation of a 3D co-continuous structure consisting of the lamella network of the PK-rich phase and the PA-rich phase at the nanometer level was observed in this sample. The lamella network was also observed in K10A90. Considering the PK loading (10 mass %), it is inconceivable that the entire lamella network was composed of the PK-rich phase. Let us look carefully at K60A40 and K10A90. Takahashi et al. [91] reported that the lamella thickness (about 14 nm) of K60A40 was larger than that (about 8 nm) of K10A90 from small-angle X-ray scattering (SAXS) measurements. This suggests that the components of the lamella network differed between the two samples. The lamella thickness of K60A40 might correspond to that of PK, whereas the lamella thickness of K10A90 might represent that of PA. The lamella network is also discussed below with respect to the SAXS measurement results.

Smith et al. [92] reported that phase inversion occurs when the minority component becomes the continuous phase and the majority component is dispersed and that this inversion, which is generally observed under melt-shear conditions, normally depends on the blend composition and the viscosities of the polymer components. According to Chuai et al. [93], with increasing volume fraction of one of the phases, in the case that a previously continuous phase becomes discontinuous (thus switching the role of "network" and "particles" in a polymer blend), the volume fraction at which the switching occurs is known as the "phase inversion" point. Considering these observations, the K90A10 and K80A20 alloys with a high PA loading probably consisted of one phase in the matrix of the second phase, the more balanced composition of the K60A40 alloy produced co-continuous structures at the phase inversion point, and the phase-inverted structure such as the K10A90 alloy formed at a volume fraction above that point. This speculation is supported by the 3D-TEM observation results.

Figure 4.36 shows the respective SAXS measurement results for the dry and wet PK/PA polymer alloys. The vertical and the horizontal axes indicate the X-ray diffraction strength and the scattering angle (2θ), respectively. For the dry K100 sample in Fig. 4.36a, a shoulder peak was observed at 2θ of 0.8°. The K90A10 and K60A40 samples had the peak at this 2θ degree, too. The peak strength increased with an increase in PA loading from K90A10 to K60A40. A calculation of the long period (d) for 2θ at about 0.8° by using the Bragg equation [$\lambda = 2d \sin\theta$, where d equals the lamella thickness, λ the wavelength of X-rays, and θ the scattering angle] yielded a value of approximately 13 nm. The peak strength decreased with an increase in PA loading from K70A30 to A100. In this loading region, the 2θ value at the peak gradually increased from about 0.8° with an increase in PA loading. An increase in 2θ means a decrease in the distance of the lamella (d). The d value of A100 was about 8 nm. These results suggest that PA loading promoted an increase in the lamella of the PK-rich phase in the region from K100 to K60A40. The amount of lamella decreased with increasing PA loading in the region from K70A30 to A100. There was a pronounced difference in the amount of lamella, especially between K10A90 and A100. The component of the lamella also changed from the PK-rich

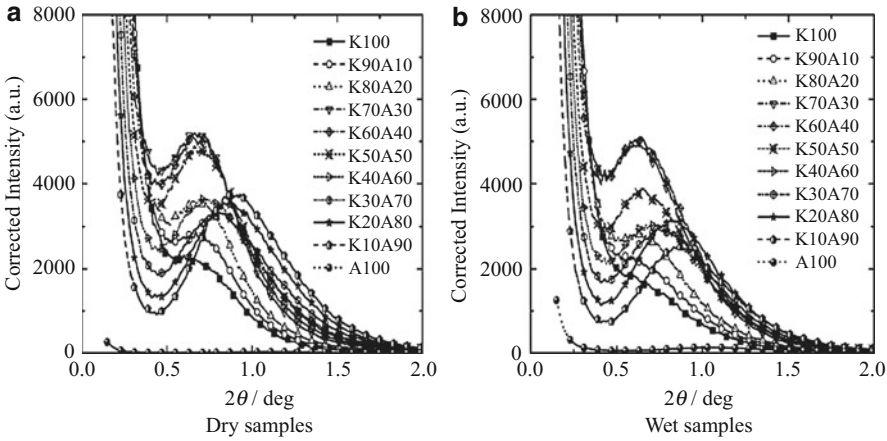


Fig. 4.36 SAXS measurement results for dry and wet PK/PA polymer alloys [47] (Reprinted from J Appl Polym Sci 116, Kato A, Nishioka M, Takahashi Y, Suda T, Sawabe H, Isoda A, Drozdova O, Hasegawa T, Izumi T, Nagata K, Hikasa S, Iwabuki H, Asano A, Phase separation and mechanical properties of polyketone/polyamide polymer alloys. 3056–3069, Copyright © (2010), with permission from John Wiley and Sons)

phase to the PA-rich phase in the region from K70A30 to A100. It is seen in Fig. 4.36b that the wet polymer alloys had almost the same amount of lamella as the dry ones, though 2θ at the peak decreased a little with an increase in moisture absorption. For example, the d value of the dry K60A40 sample was about 13 nm, whereas that of the wet K60A40 sample was about 14.5 nm. These results suggest that the amorphous regions between the crystal lamella, that is, the interlayer, contain a small amount of PA and are swollen by moisture.

Figure 4.37 shows the solid-state high-resolution cross-polarization/magic-angle spinning NMR (^{13}C CP/MAS NMR) spectra of the dry and wet K60A40 samples at room temperature. The signal strength is shown along the vertical axis in relation to the chemical shift along the horizontal axis. The solid and dotted lines are the wet and dry samples, respectively. PK had only two signal peaks at 37 and 210 ppm, which were independent of moisture absorption. The signal peaks at ca. 27, 29, 31, 41, 43, and 170 ppm, which are attributed to total, crystal, and amorphous PA, are indicated as PA, PA_{cry}, and PA_{amo} in the figure. It is known that the NMR signal strength decreases when molecular motion becomes higher than the strength of ^{1}H decoupling frequency. Notice that the PA and PA_{amo} signal strength of the wet K60A60 sample was lower than that of the dry one (marked by red circles). This implies that moisture absorption enhanced the motion of PA. Such higher molecular motion may follow quick stimulation such as that in impact testing and may be able to absorb more impact energy.

The load-displacement curve obtained from a Charpy impact test is diagrammed schematically in Fig. 4.38. This load-displacement curve has been simplified to an asymmetric conical pattern. The maximum stress (*MS*) was calculated from the

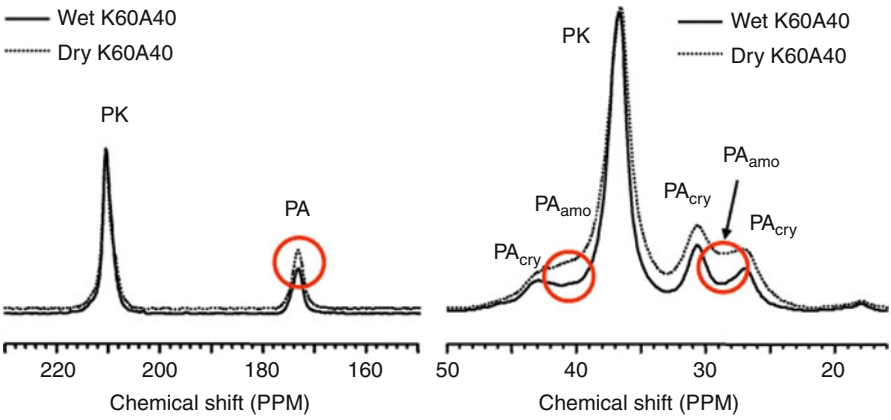


Fig. 4.37 ^{13}C CP MAS NMR spectra of wet and dry K60A40 samples [47] (Reprinted from J Appl Polym Sci 116, Kato A, Nishioka M, Takahashi Y, Suda T, Sawabe H, Isoda A, Drozdova O, Hasegawa T, Izumi T, Nagata K, Hikasa S, Iwabuki H, Asano A, Phase separation and mechanical properties of polyketone/polyamide polymer alloys. 3056–3069, Copyright © (2010), with permission from John Wiley and Sons)

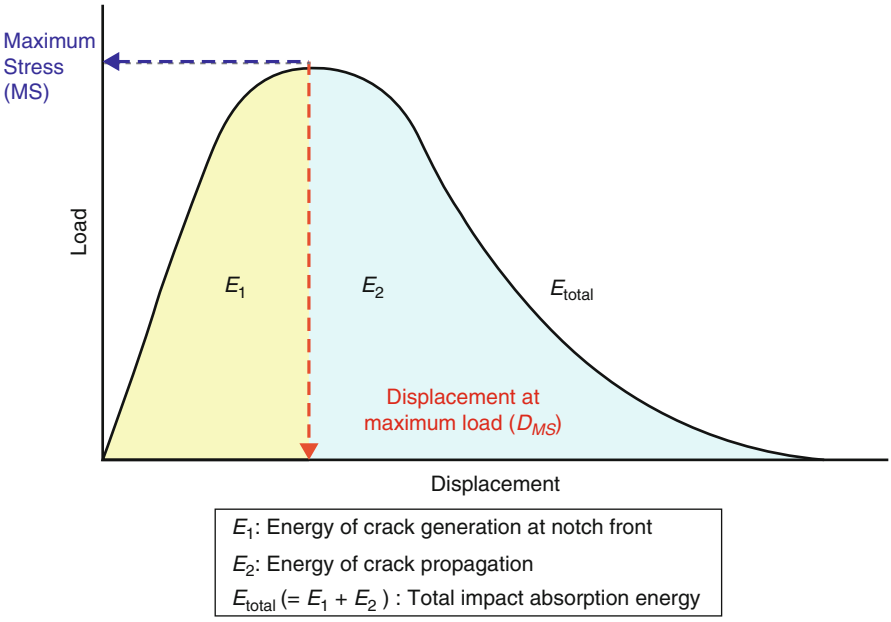


Fig. 4.38 Schematic diagram of load-displacement curve obtained from Charpy impact test [47] (Reprinted from J Appl Polym Sci 116, Kato A, Nishioka M, Takahashi Y, Suda T, Sawabe H, Isoda A, Drozdova O, Hasegawa T, Izumi T, Nagata K, Hikasa S, Iwabuki H, Asano A, Phase separation and mechanical properties of polyketone/polyamide polymer alloys. 3056–3069, Copyright © (2010), with permission from John Wiley and Sons)

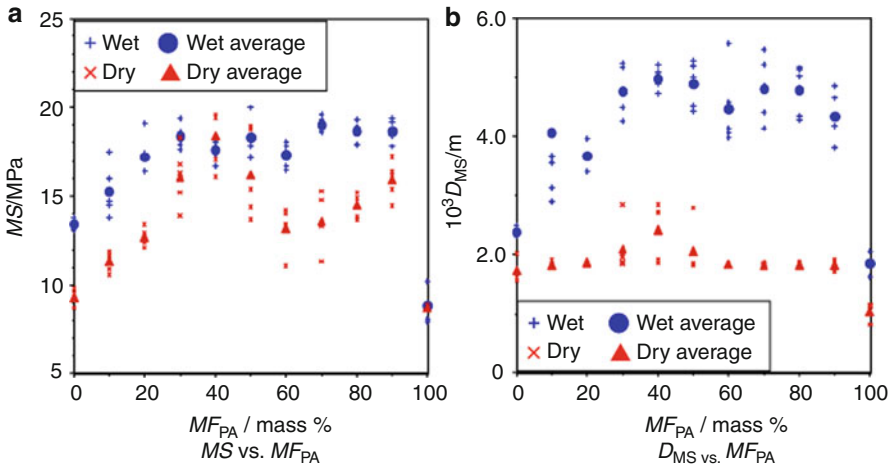


Fig. 4.39 Dependence of maximum stress (*MS*) and displacement (D_{MS}) at *MS* on PA mass fraction (MF_{PA}) [47] (Reprinted from J Appl Polym Sci 116, Kato A, Nishioka M, Takahashi Y, Suda T, Sawabe H, Isoda A, Drozdova O, Hasegawa T, Izumi T, Nagata K, Hikasa S, Iwabuki H, Asano A, Phase separation and mechanical properties of polyketone/polyamide polymer alloys. 3056–3069, Copyright © (2010), with permission from John Wiley and Sons)

maximum load at the peak top of the load-displacement curve in Fig. 4.38. The displacement at the *MS* was defined as the displacement (D_{MS}). The curve was divided into two portions at the peak top and the energy found for each area was defined as the energy (E_1) of crack generation at the notch front and the energy (E_2) of crack propagation. The sum of the two values is the total impact absorption energy (E_{total}). The *MS* and the D_{MS} of the dry and wet polymer alloy samples as a function of the PA mass fraction (MF_{PA}) are shown in Fig. 4.39a, b, respectively. The dry and wet K60A40 samples displayed nearly the same *MS* values, but the wet sample showed larger D_{MS} than the dry sample. These results indicate that MF_{PA} did not change the mechanical strength of the polymer alloys appreciably, but it did increase their deformation markedly. This result supports the ductile fracture exhibited by the wet polymer alloy sample [47]. With regard to the improved ductility of the PA phase due to moisture absorption, Nishioka et al. [94] and Asano et al. [48] investigated wet and dry K60A40 samples by ^{13}C-NMR spectroscopy and found that the mobility of PA molecules was markedly higher in the wet samples than in the dry ones. This implies that moisture absorption enhances the mobility of PA molecule chains, making it easier for large deformation to occur.

The E_{total}, E_1, and E_2 values found for the wet and dry polymer alloy samples are shown in Figs. 4.40 and 4.41, respectively. In the case of K70A30 and K60A40, the energy levels were higher for the wet samples than for the dry ones. The largest energy values are seen for the wet K60A40 sample. It is especially interesting that distinct increases in E_2 due to moisture absorption are seen in the order of K70A30 followed by K60A40, whereas the values of the other

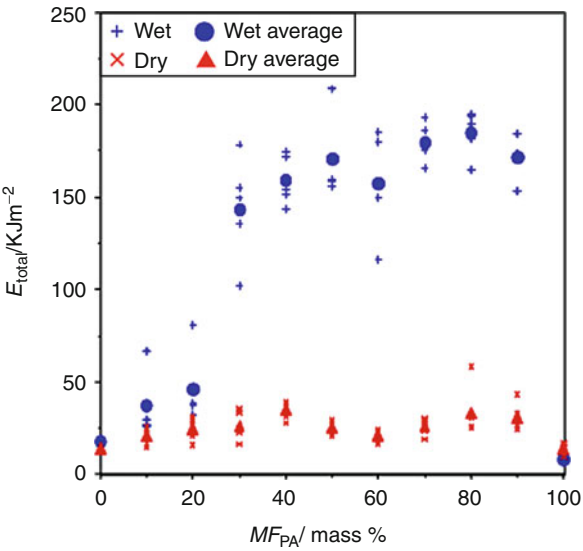


Fig. 4.40 Relationship between total impact absorption energy (E_{total}) and PA mass fraction (MF_{PA}) of wet and dry samples [47] (Reprinted from J Appl Polym Sci 116, Kato A, Nishioka M, Takahashi Y, Suda T, Sawabe H, Isoda A, Drozdova O, Hasegawa T, Izumi T, Nagata K, Hikasa S, Iwabuki H, Asano A, Phase separation and mechanical properties of polyketone/polyamide polymer alloys. 3056–3069, Copyright © (2010), with permission from John Wiley and Sons)

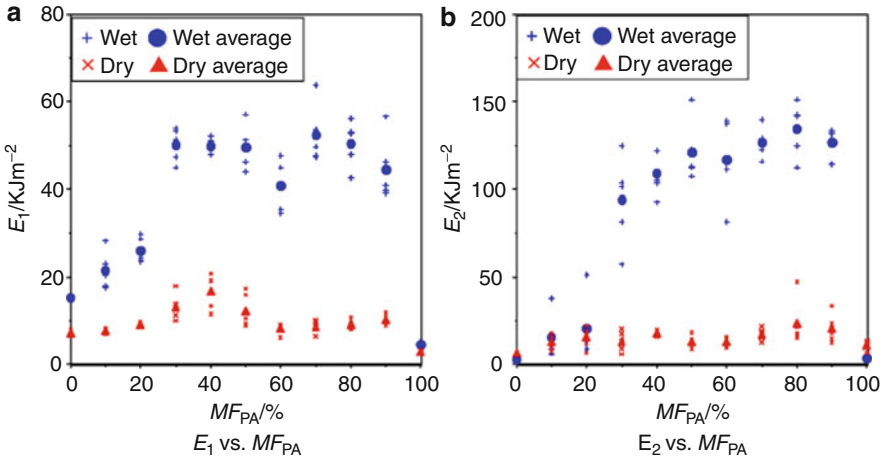


Fig. 4.41 Dependence of E_1 and E_2 on PA mass fraction (MF_{PA}) of wet and dry samples [47] (Reprinted from J Appl Polym Sci 116, Kato A, Nishioka M, Takahashi Y, Suda T, Sawabe H, Isoda A, Drozdova O, Hasegawa T, Izumi T, Nagata K, Hikasa S, Iwabuki H, Asano A, Phase separation and mechanical properties of polyketone/polyamide polymer alloys. 3056–3069, Copyright © (2010), with permission from John Wiley and Sons)

samples in both their wet and their dry states were nearly the same. These results indicate that in a range of MF_{PA} of 30–40 mass% (K70A30 and K60A40), the pronounced increase in E_2 due to moisture absorption, in addition to the increase in E_1, contributed to increasing E_{total}. Furthermore, taking into account the

magnitude of the energy, E_2 contributed more to increasing E_{total} than E_1 in this MF_{PA} range. The wet K70A30 and K60A40 samples in particular showed a marked increase in deformation, which increased the energy of crack generation at the notch front (E_1). Moreover, the energy of crack propagation (E_2) of these samples showed an even larger distinct increase for some reason, resulting in a noticeable increase in their E_{total} values as well. For example, the E_{total} value of PC is 10–80 kJ/m^2 [22, 46]. With regard to this particular increase in E_2, it is assumed that the PA phase became a stress concentrator following the large deformation of the test sample, causing crazes to form around it which promoted the absorption of energy.

If only the PA phase of the wet polymer alloy samples showed a marked increase in elongation and the PK phase was unable to follow that change, the test samples would fail at an early stage; thus, no increase in impact energy absorption could be expected. Accordingly, in order for the PK phase to be able to follow the change in elongation of the PA phase, it is necessary to consider the interface between the incompatible PK and PA phases. Inoue and Ougizawa [95] proposed that the size (d_{ip}) of the island phase in a system of two incompatible polymers is proportional to the interfacial tension (σ_i) between the two components. Broseta et al. [96] reported that d_{ip} in such polymer systems is proportional to the interaction parameter between the components (χ) and that χ is inversely proportional to the equilibrium interfacial thickness (λ_{ip}). These observations mean that λ_{ip} increases as d_{ip} decreases. In other words, in a polymer alloy composed of two incompatible constituent polymers, like the polymer alloy samples examined in this study, it can be inferred that the interfacial thickness of the two phases, i.e., the interaction between the phases, increases as the size of the island phase decreases. These results imply that the phase separation structure and higher-order structure are closely related to mechanical properties.

6 Conclusions and Future Perspective

The 3D-TEM tomography observation method combined with 3D image analysis is a unique technique that can visualize the nanofiller dispersion structure and phase separation structure in three dimensions at the nanometer level. This method was applied to a nanofiller-filled polymer and a polymer alloy in order to investigate the relationship between morphological and physical properties. First, with an increase in CB loading in CB-filled rubber, electrical percolation was observed. In the region of 0 phr $<$ CB loading $<$ 40 phr, percolation closely related to the formation of the CB network in the rubber matrix was observed. The physical properties before and after percolation differed significantly. By using the three-dimensional electron microscopy/electron tomography (3D-TEM) method, the CB network was visualized for the first time. The closest interparticle distance (d_p = ca. 3 nm) between CB aggregates forming the CB network is presumed to be the thickness of the immobilized CB/rubber interfacial layer. In the relationship between the volume fraction and the viscoelasticity of this layer, a parallel mechanical model

can be applied for CB loading of 30 phr or more, whereas a series mechanical model can be applied for CB loading of 20 phr or less. In the former case, by using extrapolation, it is possible to determine the complex modulus of the interface layer or the immobilized rubber interfacial layer. It was observed that the CB network was rearranged and broken under heat treatment or elongation.

Silica in rubber forms a silica network that is similar to the CB network. A silica network was formed at the same d_p = ca. 1.3 nm for hydrophilic silica. This finding suggests that an immobilized layer around silica was formed by the physical interaction between silica and rubber rather than by the action of a surface functional group of silica. Surprisingly, the optical transparency of hydrophilic silica-filled rubber was found to be due to multiple light scattering caused by isolated chains of the silica network at silica loading of 30 phr. Concretely, because the number density of isolated chains reached its maximum value, optical transparency was lowered notably.

On the other hand, after moisture absorption, the polymer alloy of polyketone (PK)/polyamide 6 (PA) showed 1.5–2 times greater impact resistance than polycarbonate. From the results of a solid-state ^{13}C NMR measurement, a small-angle X-ray scattering (SAXS) measurement, and 3D-TEM observation, it was found that both components of the co-continuous structure of the polymer exhibited markedly improved impact resistance. Specifically, the lamella network formed from PK or PA showed the reinforcement effect that prevents crack propagation. The PA amorphous phase that absorbed moisture displayed high molecular mobility to track quick deformation and absorb the impact energy. As a result, the polymer alloy showed a notably higher capacity to absorb impact energy. These results were made clear for the first time by using the 3D-TEM observation method.

In the near future, it is expected that 3D-TEM will be one of the most powerful and indispensable tools for the development of nanotechnology and new nanomaterials using not only rubber but also other components.

Acknowledgments The authors would like to thank Emeritus Prof. S. Kohjiya of Kyoto University; Dr. S. Hikasa, Dr. H. Iwabuki, and Mr. J. Ootake of the Industrial Technology Center of Okayama Prefecture; Messrs R. Tsushi, Y. Kokubo, and Y. Kasahara of the Kyoto Institute of Technology; Dr. O. Dorozdova of Renishaw K. K.; Mrs. M. Nishioka, and Messrs T. Suda, H. Sawabe, J. Shimanuki, T. Hasegawa, T. Izumi, M. Mukai, and T. Gotou, N. Kojima, M. Hashimoto, Dr. M. Arao, Dr. Y. Takahashi, Misses. M. Gonda, and A. Isoda of NISSAN ARC, LTD. for their valuable cooperation and advice.

References

1. Wei L, Tang T, Huang BJ (2004) Synthesis and characterization of polyethylene/clay-silica nanocomposites: a montmorillonite/silica-hybrid-supported catalyst and in situ polymerization. Polym Sci Pt A 42:941–949
2. Zhang Q, Archer L (2002) Poly(ethylene oxide)/silica nanocomposites: structure and rheology. Langmuir 18:10435–10442
3. Teinstein SS, Zhu A (2002) Reinforcement mechanism of nanofilled polymer melts as elucidated by nonlinear viscoelastic behavior. Macromolecules 35:7262–7273

4. Zhang Q, Archer L (2004) Optical polarimetry and mechanical rheometry of poly (ethylene oxide)-silica dispersions. Macromolecules 37:1928–1936
5. Zhu Z, Thompson T, Wang SQ, von Meerwall ED, Halasa A (2005) Investigating linear and nonlinear viscoelastic behavior using model silica-particle-filled polybutadiene. Macromolecules 38:8816–8824
6. Ozisik R, Zheng J, Dionne PJ, Picu CR, von Meerwall ED (2005) NMR relaxation and pulsed-gradient diffusion study of polyethylene nanocomposites. J Chem Phys 123:134901–134908
7. Karásek L, Meissner B, Asai S, Sumita M (1996) Percolation concept: polymer-filler gel formation, electrical conductivity and dynamic electrical properties of carbon-black-filled rubbers. Polymer J 28:121–126
8. Yamaguchi K, Busfield JJC, Thomas AG (2003) Electrical and mechanical behavior of filled elastomers I. The effect of strain. J Polym Sci Phys Pt B 41:2079–2089
9. Satoh Y, Suda K, Fujii S, Kawahara S, Isono Y, Kagami S (2007) Differential dynamic modulus of carbon black filled uncured SBR in single step large shearing deformation. J Soft Mater 3:29–40
10. Treloar LRG (1958) The physics of rubber elasticity, 2nd edn. Clarendon, Oxford
11. Tobolsky AV (1960) Properties and structure of polymers. Wiley, New York
12. Ferry JD (1980) Viscoelastic properties of polymers, 3rd edn. Wiley, New York
13. Ikeda Y, Kato A, Shimanuki J, Kohjiya S (2004) Nano-structural observation of in situ silica in natural rubber matrix by three dimensional transmission electron microscopy. Macromol Rapid Commun 25:1186–1190
14. Ikeda Y (2005) Characterization of rubber nano-composites by using 3D-TEM/electron tomography. Sen'I Gakkai-shi 61:34–38 (in Japanese)
15. Kohjiya S, Kato A, Shimanuki J, Hasegawa T, Ikeda Y (2005) Three-dimensional nanostructure of in situ silica in natural rubber as revealed by 3D-TEM/electron tomography. Polymer 46:4440–4446
16. Kato A, Ikeda Y, Kohjiya S (2005) Three-dimensional observation of nano filler-filled natural rubber vulcanizates by 3D-transmission electron microscope (3D-TEM). Nippon Gomu Kyoukaishi 78(5):180–186 (in Japanese)
17. Kohjiya S, Kato A, Suda T, Shimanuki J, Ikeda Y (2006) Visualisation of carbon black networks in rubbery matrix by 3D-TEM image. Polymer 47:3298–3301
18. Kato A, Shimanuki J, Kohjiya S, Ikeda Y (2006) Three-dimensional morphology of carbon black in NR vulcanizates as revealed by 3D-TEM and dielectric measurements. Rubber Chem Technol 79:653–673
19. Ikeda Y, Kato A, Shimanuki J, Kohjiya S, Tosaka M, Poompradub S, Toki S, Hsiao BS (2007) Nano-structural elucidation in carbon black loaded NR vulcanizate by 3D-TEM and in situ WAXD measurements. Rubber Chem Technol 80:251–264
20. Kohjiya S, Kato A, Ikeda Y (2008) Visualization of nanostructure of soft matter by 3D-TEM: nanoparticles in a natural rubber matrix. Prog Polym Sci 33:979–997
21. Kohjiya S, Ikeda Y, Kato A (2008) Visualization of nano-filler dispersion and morphology in rubbery matrix by 3D-TEM. In: Bhowmick AK (ed) Current topics in elastomers research. CRC Press, Boca Raton, pp 543–551 (Chap 19)
22. Kato A, Ikeda Y, Kasahara Y, Shimanuki J, Suda T, Hasegawa T, Sawabe H, Kohjiya S (2008) Optical transparency and silica network structure in cross-linked natural rubber as revealed by spectroscopic and three-dimensional transmission electron microscopy techniques. J Opt Soc Am B 25:1602–1615
23. Kato A, Ikeda Y, Kohjiya S (2012) Carbon black-filled natural rubber composites: physical chemistry and reinforcing mechanism. In: Thomas S, Joseph K, Malhotra SK, Goda K, Streekala MS (eds) Polymer composites, vol 1, Macro- and microcomposites. Wiley-VCH, Boscher, pp 515–543 (Chap 17)
24. Kato A, Suda T, Ikeda Y, Kohjiya S (2011) Thermal destruction of carbon black network structure in natural rubber vulcanizate. J Appl Polym Sci 122:1300–1315

25. Ghani AA, Eatha AI, Hassan AA (1985) Effect of carbon black and thermal aging on the conduction mechanism of natural and styrene butadiene rubbers. Angew Makromol Chem 129:1–9
26. Satoh Y, Suda K, Fujii S, Kawahara S, Isono Y, Kagami S (2007) Novel characterization of filler network in rubber materials using differential dynamic modulus in large compression and recovery. J Soft Mater 3:14–20
27. Gent AN (1992) Engineering with rubber. Hanser, Munich
28. Isono Y, Ferry JD (1984) Stress relaxation and differential dynamic modulus of carbon black filled styrene-butadiene. Rubber in large shearing deformations. Rubber Chem Technol 57:925–943
29. Kato A, Isono Y (2013) Structural changes in the carbon black network in carbon-black-filled styrene-butadiene rubber samples cured with a two-step process. J Appl Polym Sci 128:2498–2507
30. Piskin I, Tokita N (1972) Bound rubber in elastomers: analysis of elastomer-filler interaction and its effect on viscosity and modulus of composite systems. J Appl Polym Sci 16:473–492
31. Nishi T (1972) Effect of solvent and carbon black species on the rubber-carbon black interactions studied by pulsed NMR. J Polym Sci Polym Phys 12:685–693
32. Litvinov VM, Orza RA, Klüppel M, van Duin M, Magusin PCMM (2011) Rubber-filler interactions and network structure in relation to stress-strain behavior of vulcanized, carbon black filled EPDM. Macromolecules 44:4887–4900
33. Smit PPA (1968) Glass transition in carbon black reinforced rubber. Rubber Chem Technol 41:1194–1202
34. Nakajima K, Nishi T (2008) Recent developments in rubber research using atomic force microscopy. In: Bhomik AK (ed) Current topics in elastomers research. CRC Press, Boca Raton, pp 579–604 (Chap 21)
35. Kato A, Ikeda Y, Tsushi R, Kokubo Y, Kojima N (2013) A new approach to visualizing the carbon black/natural rubber interaction layer in carbon black-filled natural rubber vulcanizates and to elucidating the dependence of mechanical properties on quantitative parameters. Colloid Polym Sci 291:2101–2110
36. Schelm S, Smith GB (2005) Tuning the surface-plasmon resonance in nanoparticles for glazing application. J Appl Phys 97(1–8):124314
37. Naganuma T, Iba H, Kagawa Y (1999) Optothermal properties of glass particle-dispersed epoxy matrix composite. J Mater Sci Lett 18:1587–1589
38. Kagawa Y, Iba H (2000) Optically transparent composites. Materia Jpn 39:137–140
39. Charlesworth D (1981) Potential use for plastics in automobiles. Mater Des 2:149–156
40. Waterman NA, Neal M (1981) Plastics in automobiles at SITEV '81. Mater Des 2:250–259
41. Chen G, Jiang A, Lin Z, Li Y (2004) Experimental study of glass-fiber mat thermoplastic material impact properties and lightweight automobile body analysis. Mater Des 25:579–585
42. Edwards KL (2006) Materials for automobiles (2004) Elsevier 0-7506-5692-1 277 p. Mater Des 27:172
43. Nagata N, Hikasa S, Hirotani M, Nitto Y, Watanabe T (2006) Structure and physical properties of polyketone/polyamide polymer alloy-2. Polym Prep Jpn 55:4286–4287
44. Kuriyama S (1999) Physical properties of plastic molding- for example, high toughness. Seikei Kakou 11:273–277 (in Japanese)
45. Mechanical engineer's handbook. http//:www.docstoc.com >Technology> Other. (Citation on 10 Nov 2012)
46. Polycarbonate – Tarflon. http://www.idemitsu-chemicals.de/16-0-polycarbonate-tarflon.html. (Citation at 10 Nov 2012)
47. Kato A, Nishioka M, Takahashi Y, Suda T, Sawabe H, Isoda A, Drozdova O, Hasegawa T, Izumi T, Nagata K, Hikasa S, Iwabuki H, Asano A (2010) Phase separation and mechanical properties of polyketone/polyamide polymer alloys. J Appl Polym Sci 116:3056–3069

48. Asano A, Nishioka M, Takahashi Y, Kato A, Hikasa S, Iwabuki H, Nagato K, Sato H, Hasegawa T, Sawabe H, Arao M, Suda T, Mukai M, Ishikawa D, Izumi T (2009) High impact properties of polyketone/polyamide-6 alloys induced by characteristic morphology and water absorption. Macromolecules 42:9506–9514
49. Frank J (ed) (1992) Electron tomography: three-dimensional imaging with the transmission electron microscope. Plenum, New York
50. Kremer JR, Mastronarde DN, McIntosh JR (1996) Computer visualization of three-dimensional image data using IMOD. J Struct Biol 116:71–76
51. Marco S, Bouder T, Messaoudi C, Rigaud JL (2004) Electron tomography of biological samples. Biochemistry (Moscow) 69(11):1219–1225
52. Frank J (ed) (2006) Electron tomography methods for three-dimensional visualization of structures in the cell, 2nd edn. Springer, Berlin
53. Brian SK, David GH, Donald FB, Fishman EK (1996) Skeletal 3-D CT: advantages of volume rendering over surface rendering. Skeletal Radiol 25:207–214
54. Kim KH, Kwon MJ, Kwon SM, Ra JB, Park HW (2002) Biomedical paper: fast surface and volume rendering based on shear-warp factorization for a surgical simulator. Comput Aided Surg 7:268–278
55. The Japanese Society of Microscopy (2004) Feature articles: electron tomography. Microscopy 39(1):2–33
56. Johnson C, Hansen C (eds) (2005) The visualization handbook. Academic, San Diego
57. Coran AY (2003) Chemistry of the vulcanization and protection of elastomers: a review of the achievements. J Appl Polym Sci 87:24–30
58. Tsuji M, Kohjiya S (1995) Structural studies on crystalline polymer solids by high-resolution electron microscopy. Prog Polym Sci 20(2):259–308
59. Tsuji M, Fujita M, Kohjiya S (1997) On the correlation between modulus of polymer crystals and resistance against electron-beam irradiation. Nihon Reorogi Gakkaishi 25:193–194 (in Japanese)
60. Detlev S, Malte W, Hans-Christian H (2005) Amira: a highly interactive system for visual data analysis. In: Hansen CD, Johnson CR (eds) The visualization handbook. Elsevier, Amsterdam (Chap 38)
61. Kohjiya S, Kato A, Shimanuki J, Hasegawa T, Ikeda Y (2005) Three-dimensional nanostructure of in situ silica in natural rubber as revealed by 3D-TEM/electron tomography. J Mater Sci 40:2553–2555
62. The Carbon Black Association, Japan (1995) Handbook of carbon black. The Carbon Black Association, Tokyo, p 66 (in Japanese)
63. Nihon Gosei Gomu Co., Ltd (ed) (1985) JSR handbook. JSR, Tokyo, p 70 (in Japanese)
64. Satoh Y, Suda K, Fujii S, Kawahara S, Isono Y, Kagami S (2007) Novel characterization of filler network in rubber materials using differential dynamic modulus in large compression and recovery. J Soft Mater 3:14–20
65. Kohjiya S, Kato A (2005) Visualization of nanostructure in soft materials by 3D-TEM. Kobunshi Ronbunshu 62:467–475 (in Japanese)
66. Kato A, Kohjiya S, Ikeda Y (2006) Three-dimensional electron transmission microscopy. Koubunshi 55:616–619 (in Japanese)
67. Hirata M (2000) A fractal approach to the mixing-microstructure-property relationship for rubber compounds. J Appl Polym Sci 78:1555–1565
68. Jäger KM, McQueen DH (2001) Fractal agglomerates and electrical conductivity in carbon black polymer. Polymer 42:9575–9581
69. Usui MH, Ishizuki M, Shige I, Suzuki H (2003) Rheological characteristics of non-spherical suspensions. Kor-Aust Rheol J 15(1):19–25
70. Viswanathan R, Heaney MB (2005) Direct imaging of the percolation network in a three-dimensional disordered conductor-insulator composite. Phys Rev Lett 75:4433–4436
71. Fukahori Y (2008) Mechanism of the carbon black reinforcement of rubbers. In: Bhomik AK (ed) Current topics in elastomers research. CRC Press, Boca Raton, pp 517–539 (Chap 18)

72. Medalia AI (1972) Effective degree of immobilization of rubber occluded within carbon black aggregates. Rubber Chem Technol 45:1171–1194
73. Halpin JC, Kardos JL (1972) Moduli of crystalline polymers employing composite theory. J Appl Phys 43:2235–2241
74. Singh R, Mattoo A, Saigal A (2006) Optimizing the design and impact behavior of a polymeric enclosure. Mater Des 27:955–967
75. Miyasaka K (ed) (1992) Dictionary of plastics. Asakura Shoten, Tokyo (in Japanese)
76. Kato A, Kohjiya S, Ikeda Y (2007) Nanostructure in traditional composites of natural rubber and reinforcing silica. Rubber Chem Technol 80:690–700
77. Heinrich G, Kluppel M (2004) The role of polymer-filler-interphase in reinforcement of elastomers. Kautsch Gummi Kunstst 57:452–454
78. Song M, Ansarifar A, Nijhawan R, Nanapoolsin T (2003) Reinforcing effect of silica and silane fillers on the properties of some natural rubber vulcanizates. Rubber Chem Technol 76:1290–1310
79. Kohjiya S, Yamashita S (1992) Moisture cure and related processes of synthetic and natural rubber. J Appl Polym Sci Appl Polym Symp 50:213–221
80. Zhang W, Leonov AI (2001) IGC study of filler-filler and filler-rubber interaction in silica-filled compounds. J Appl Polym Sci 81(10):2517–2530
81. He N, Ge S, Yan G, Hu C, Gu M (2004) Investigation on the mechanism of the photoluminescence of MCM-41. Mater Res Bull 39:1931–1937
82. Kaijou R, Ito M, Ono S (2004) Filler gel and rubber gel in silica-filled rubber systems. Nippon Gomu Kyoukaishi 77:375–381 (in Japanese)
83. Yuan P, Yang D, Lin Z, He H, Wen X, Wang L, Den F (2006) Influences of pretreatment temperature on the surface silylation of diatomaceous amorphous silica with trimethylchlorosilane. J Non-Cryst Solids 352:3762–3771
84. Kandidov VP, Milisin VO, Bykov AV, Priezzhev AV (2006) Application of corpuscular and wave Monte-Carlo method in optics of dispersive media. Quantum Electron 36:1003–1008
85. Feng J, Chan CM (1997) Miscibility and properties of alternating ethylene-Tetrafluoroethylene copolymers and poly (methyl methacrylate) blends. Polymer 38:6371–6378
86. Utracki LA (1989) Polymer alloys and blends; thermodynamics and rheology. Carl Hanser, Münich
87. Asano A, Takegoshi K (1998) Polymer blends and miscibility. In: Ando I, Asakura T (eds) Solid state NMR of polymers. Elsevier Science B.V, Amsterdam, pp 351–414 (Chap 10)
88. Lagaron JM, Vickers ME, Powell AK, Davidson NS (2000) Crystalline structure in aliphatic polyketones. Polymer 41:3011–3017
89. Lagaron JM, Vickers ME, Powell AK, Bonner JG (2002) On the effect of the nature of the side chain over the crystalline structure in aliphatic polyketones. Polymer 43:1877–1886
90. Matsuoka S (1992) Relaxation phenomena in polymers. Carl Hanser, Münich
91. Takahashi Y, Nishioka M, Sawabe H, Sato H, Kato A, Nagata K, Iwabuki H, Hikasa S, Asano A (2009) Nano structure of polyketon/polyamide polymer alloy. Koubunshi Ronbunshu 66:577–584 (in Japanese)
92. Smith AP, Ade H, Smith SD, Koch CC, Spontak RJ (2001) Anomalous phase inversion in polymer blends prepared by cryogenic mechanical allying. Macromolecules 34:1536–1538
93. Chuai CZ, Almdal K, Lyngaae-Jorgensen J (2003) Phase continuity and inversion in polystyrene/poly(methyl methacrylate) blends. Polymer 44:481–493
94. Nishioka M, Takahshi Y, Kato A, Sawabe H, Sato H, Nagata K, Hikasa S, Iwabuki H, Asano A (2009) Influence of water absorption on high-impact properties of polyketon/polyamide polymer alloys. Koubunshi Ronbunshu 66:570–576 (in Japanese)
95. Inoue T, Ougizawa T, Society of Polymer Science, Japan (1995) Fundamentals of polymer experiments and analysis of molecular characteristics. In: New polymer experimentology 1. Kyoritsu Shuppan, Tokyo (in Japanese)
96. Broseta D, Fredrickson GH, Helfand E, Leiber L (1990) Molecular weight and polydispersity effects at polymer-polymer interfaces. Macromolecules 23:132–139

TEM for Characterization of Nanowires and Nanorods

5

Sarah K. St. Angelo

Contents

1 Definition of the Topic 195
2 Overview 196
3 Introduction 196
4 Experimental and Instrumental Methodology 198
5 Key Research Findings 199
5.1 Ex Situ TEM Techniques for Analysis of Nanowires 199
5.2 In Situ TEM Techniques for Analysis of Nanowires 216
6 Conclusions and Future Perspectives 234
References 235

1 Definition of the Topic

Transmission electron microscopy (TEM) and related techniques allow for imaging of nanomaterials to determine the material size, shape, composition, and crystal structure. In situ TEM measurements allow for observation of dynamic processes, such as nanowire growth. This chapter describes the application of ex situ and in situ TEM techniques to the analysis of nanowires/nanorods as a subset of nanomaterials. Nanowires refer to anisotropic metal, semiconductor, metal oxide, and/or alloyed structures that may be cylindrical solids, core-shell structures, or hollow tube-like structures. Herein, "bottom-up" nanowires – those synthesized by monomer addition or particle aggregation – are considered for how their analyses may be aided by TEM-based techniques. Lithographically defined wire-like structures, carbon nanotubes, and graphene-based scroll structures are not considered in this chapter.

S.K. St. Angelo
Department of Chemistry, Dickinson College, Carlisle, PA, USA
e-mail: stangels@dickinson.edu

C.S.S.R. Kumar (ed.), *Transmission Electron Microscopy Characterization of Nanomaterials*, DOI 10.1007/978-3-642-38934-4_5,
© Springer-Verlag Berlin Heidelberg 2014

2 Overview

Nanowires synthesized by chemical means, as opposed to those defined lithographically, are considered in this chapter for how they may be evaluated with TEM and associated techniques. In order to measure the size, shape, crystallinity, and composition of individual nanowires, TEM is often the method of choice, if not necessity, due to the resolution requirements of the sample.

Potential applications for nanowires related to energy generation and storage, medical treatments and devices, memory and computation, and sensors and actuators require thorough characterization and understanding of structural, compositional, or other changes experienced by the nanowires under various conditions. TEM performed ex situ has successfully provided much of the data in this regard. With the ex situ approach, nanowires are synthesized and then analyzed, or they are analyzed at particular stages of growth. Similarly, with nanowires undergoing thermal stress, for example, heat would be applied to the sample, and then it would be evaluated after the heat is removed. Researchers have successfully developed and tested numerous theories related to nanowire growth, structural change, defect formation and movement, decomposition, conductivity, etc., by assembling pieces of data without observing the processes directly. Examples of ex situ TEM analysis of nanowires will be discussed.

With in situ techniques, nanowire synthesis may be accomplished within the viewing chamber of a transmission electron microscope with use of liquid cells or environmental chambers that allow for control of gas pressure and composition. Nanowires synthesized in situ will be discussed, particularly examples regarding how in situ TEM informs the understanding of mechanisms by which nanowires may grow. In situ TEM techniques, such as those allowing for heating, electrical measurements, mechanical stress, and electrochemical reactions provide a real-time view of the nanowire sample experiencing dynamic conditions. Likewise, this approach to in situ imaging provides additional information regarding nanowire properties.

3 Introduction

In the characterization of nanomaterials, size and shape are of primary interest. Optical, electrical, and other properties are influenced by size and shape at the nanoscale. Transmission electron microscopy (TEM) is a fundamental characterization tool for individual nanoparticles and for populations of particles. High-resolution TEM (HR-TEM) provides a view of the internal structure – the crystal lattice – of the nanomaterial being interrogated. Crystal structure that influences the shape of nanostructures can be used to explain what is observed or to influence the growth of particular facets of the nanoparticle.

Beyond size and shape, concurrent analyses such as selected area electron diffraction (SAED), electron energy loss spectroscopy (EELS), and other composition-identifying techniques provide information regarding structure, phase, and chemical identity of nanoparticles or parts of nanoparticles. This aspect

of having multiple compositions or structures is of particular interest when considering nanowires. One-dimensional nanostructures may consist of single or multiple chemical components, depending on the synthetic or growth method. The various materials may be arranged in discrete "slices" or sections along the length of the wire, or they may be distributed radially in a core-shell configuration. Nanowires grown via a catalyst method (e.g., vapor–liquid–solid (VLS) growth) typically have gold nanoparticles at one end of single-crystalline bodies composed of one or more semiconductors.

In situ techniques greatly expand the analytical power of TEM because of the capability to view nanoparticles undergoing change. Video imaging at typical rates of 15–30 frames per second allows for essentially continuous imaging of processes whose fundamental steps occur at or below the frame rate. Environmental TEM and microscopes outfitted with liquid cells allow nanomaterials researchers to observe nanowire growth in real time. Mechanisms previously inferred via ex situ measurements can be confirmed, refined, or disputed with evidence from real-time observation. When HR-TEM imaging is used in conjunction with real-time observation, researchers can peer into the crystal structures of nanomaterials experiencing a dynamic process, such as growth by oriented attachment. Oriented attachment is a mechanism by which nanoparticles or nanorods may join together to form larger nanostructures, such as nanowires. The orientation of the building blocks may be "perfect" with complete alignment of the crystal lattices of two merging particles, or "imperfect" with dislocations or defects at the interface. High-resolution in situ observation of the process provides evidence of the mechanism when there are no defects at the location where two particles have merged. The rate at which two particles approach each other is often slow enough that reorientation to an energetically favorable orientation and the joining of the particles can be observed. Other processes of growth and change can be similarly observed.

In situ heating allows for the direct observation of phase changes at the nanoscale. Heating of the sample may be accomplished by heating with the electron beam, using a heated state, or Joule heating from contact with an STM (scanning tunneling microscopy) tip. Annealing, thermal breakdown, melting, defect motion, and amorphization of nanomaterials may be viewed. Reversible phase transformations between two (or more) solid phases can be controlled and observed with in situ heating. If electrical properties, such as conductivity, are of interest, contact with the STM tip allows for coordinated heating, electrical measurement, and imaging. Additionally, electrical measurements may be performed as a function of mechanical strain applied by a movable STM tip. Nanowires may be brought into contact, pressed together to effect structural changes, and the changing conductivity may be measured as images are taken. Atomic force microscope (AFM) tips may be similarly employed for in situ mechanical tests owing to their piezoelectric motion controls (as with STM) and force feedback capability. With in situ mechanical measurements, stress–strain may be correlated with changes in the nanowire crystalline structure. Nanowires of the same material but with varying dimensions may be compared for strength, flexibility, and structural changes, leading to a better understanding of which nanowires may be useful for applications in which mechanical properties are important.

Electrochemical measurements conducted in situ combine liquid cells and electrical measuring capabilities within TEM. This is of particular interest for nanomaterials considered for use in lithium ion batteries. Physical, chemical, and electrical changes can be monitored simultaneously. The structural evolution of nanowires serving as the anode under the dynamic charging is not directly observable by other means. Use of ionic liquid electrolytes circumvents the necessity of using sealed liquid cells due to the very low vapor pressure of ionic liquids. It also simplifies the construction of the electrochemical "cell" by requiring only the wicking contact of the ionic liquid between the anode (nanowire) and the cathode.

4 Experimental and Instrumental Methodology

For many nanowire or nanorod samples for which basic imaging is the goal, transmission electron microscopy is often the most appropriate analysis choice. Size, shape, and population distributions can be determined for samples of interest by analyzing the images obtained. Electron diffraction patterns obtained with TEM allow for the indexing of crystalline materials. High-resolution TEM (HR-TEM) afforded by improved electron optics and scanning transmission electron microscopy (STEM) allows for image-based evaluation of crystal structure with an achievable resolution at the sub-Ångstrom level [1, 2]. High-resolution images may be analyzed with two-dimensional Fourier transform to reveal lattice spacings that assist with confirming the chemical identity and/or crystal phase of the material. High-angle annular dark field (HAADF) imaging constructs high-resolution images that have enhanced contrast due to increased dependence of electron diffraction on atomic number. STEMs with very shallow depth of field (only a few nanometers) can be used to image "slices" at varying depths in a sample. The images can then be reconstructed to produce a three-dimensional representation of the sample [3]. Techniques often incorporated with transmission electron microscopes for elemental analysis are electron energy loss spectroscopy (EELS) and energy-dispersive x-ray spectroscopy (abbreviated variously as XEDS, EDS, EDX, EDXS, EDAX). With these techniques, structural and compositional data may be obtained.

In situ techniques provide opportunities for real-time imaging of nanomaterials undergoing dynamic processes or stresses [2, 4–11]. Environmental chambers that allow for control of gas pressure and type [5] and liquid cells that permit real-time imaging of fluid-based processes [8, 9] make possible TEM imaging and analysis of nanowire growth and change. When coupled with scanning probe techniques [10, 11] of scanning tunneling microscopy (STM) or atomic force microscopy (AFM), it is possible to investigate electrical and mechanical properties of nanomaterials with concurrent imaging. STM also provides the opportunity to use Joule heating to apply thermal stress to nanomaterials. Heating may be otherwise accomplished with heating of the sample with the electron beam or with a temperature-controlled sample holder. Imaging and other analyses (e.g., electron diffraction) allow for real-time evaluation of thermodynamic phase changes and changes in the crystal lattice.

In situ electrochemistry also relies on the spatial manipulation of in situ STM. Typically one electrode side of the electrochemical cell is stationary, and the other electrode approaches to make contact through an ionic liquid electrolyte [12, 13]. Voltage may then be varied and current measured while structural and chemical changes to the electrode of interest are monitored with TEM and elemental analysis.

5 Key Research Findings

5.1 Ex Situ TEM Techniques for Analysis of Nanowires

The most straightforward applications for TEM in the evaluation of nanowires is the ex situ evaluation of size, shape, structure, and/or composition. TEM can be used to confirm or augment other analyses, and is de rigueur for nanomaterials characterization. Quantitative description of size and shape of a nanowire population is necessary for understanding and controlling the synthetic procedure.

5.1.1 Determining Size, Shape, and Composition of Nanowires

The vapor–liquid–solid (VLS) mechanism for generating nanowires was first confirmed with real-time TEM imaging in 2001 by Yiying Wu and Peidong Yang [14]. Their observations confirmed that the wire growth mechanism consists of three main stages: alloying, nucleation, and growth. In VLS nanowire production, a metal nanoparticle serves as a catalyst for nanowire growth. Molecular precursor for the desired semiconductor nanowire is added via chemical vapor deposition (CVD) to reaction vessel, and the precursor forms a liquid alloy with the catalyst material. Upon saturation of the catalyst with the dissolved precursor, the nanowire grows out from the catalyst particle. The resulting nanowires have catalyst caps on one end. The VLS process has allowed for the production of nanowires of many compositions, and TEM analysis has contributed to further understanding of various growth mechanisms and the nanowires produced by VLS and related processes.

VLS catalysts may be of a different material than the nanowire, they may be a component material of the nanowire, or they may be spontaneously generated in the growth of the nanowires. PbS wires have been produced with a chemical vapor deposition VLS (CVD-VLS) procedure that relies on the spontaneous generation of Pb catalyst [15]. Unlike most other CVD-VLS methods, no catalyst material must be intentionally added or intentionally generated by a separate procedure. PbS wires are generated by sublimating bulk PbS and allowing it to redeposit on a Si substrate. The authors note the spontaneous formation of Pb spheres from which PbS wires can grow. Under the growth conditions used, the Pb spheres grew in diameter with the wires. A “reverse taper” in the wires was observed – the diameter at the catalyst end was wider than the diameter at the opposite end. The nanowires and Pb catalysts were characterized in part by TEM, HR-TEM, electron diffraction, and EDS. Due to the relatively large size of the wires (~1,000 nm diameter), a thinning procedure was performed before TEM analysis could be completed. TEM images show a sharp interface between the Pb cap and the nanowire body as seen in the

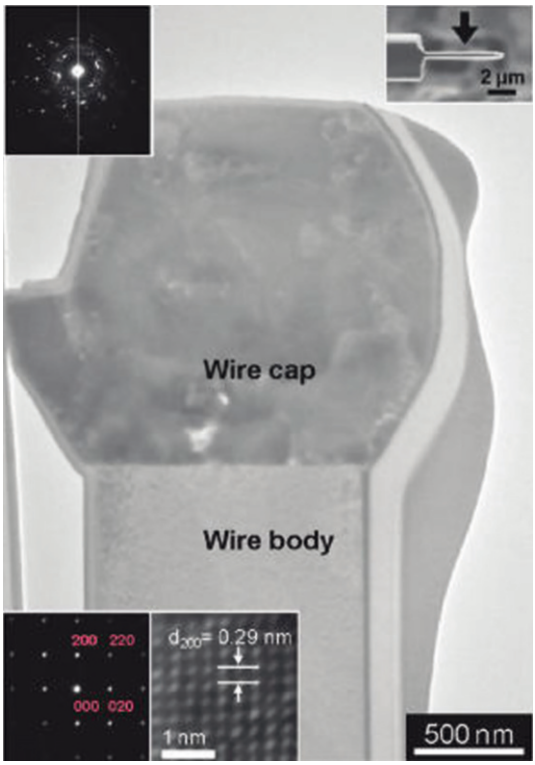


Fig. 5.1 TEM image of a PbS nanowire and catalyst cap (thinned for imaging). *Inset upper right*: SEM image of the nanowire with an *arrow* indicating the direction of the TEM electron beam. *Inset upper left*: Electron diffraction pattern for the nanowire cap. *Insets bottom left*: Electron diffraction pattern and HR-TEM image of the nanowire body. (Reprinted with Permission from *ACS Nano* 5(11): 8730–8738. Copyright 2011, American Chemical Society)

main image of Fig. 5.1. Electron diffraction of the Pb cap (Fig. 5.1, inset upper left) indicates a polycrystalline structure, while analysis of the nanowire body (Fig. 5.1, inset lower left) indicates a single-crystalline structure. Analysis of the lattice fringes in the nanowire body corroborates the presence of single-crystalline PbS. EDS was used to confirm the 1:1 stoichiometry of PbS in the wire body. A ratio of 1:8.4 S:Pb was found in the capping nanoparticle. The ratio indicates the presence of some PbS among, predominantly, Pb. XRD (x-ray diffraction) analysis of the wires had indicated the presence of PbS along with metallic Pb; however, the technique could not determine if there were regions of PbS and Pb or if the material was homogeneous. Analyses possible within TEM provided strong evidence for the Pb catalyst formation and subsequent PbS wire growth [15].

An alternate approach for obtaining catalyst and nanowire materials for VLS is to use laser ablation. In 1998, Morales and Lieber demonstrated that Si/SiO_2 and Ge nanowires with Fe catalysts could be produced with laser ablation-VLS [16]. This work spurred investigations with pulsed laser deposition-VLS (PLD-VLS) methods for producing nanowires and other high-aspect-ratio nanostructures. Iron oxides, α-Fe_2O_3 (hematite), ε-Fe_2O_3, and Fe_3O_4 (magnetite), have been generated as nanorods, nanowires, and nanobelts via PLD-VLS growth [17]. A pressed powder of magnetite was the target for laser ablation, and a 2-nm Au film supported on

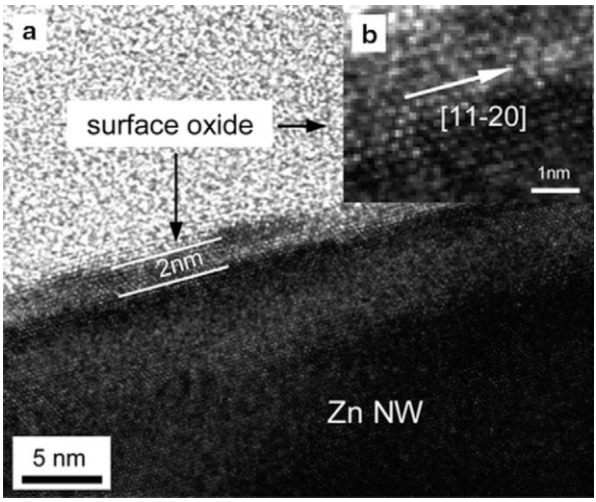


Fig. 5.2 (**a**) HR-TEM image of the side of a Zn nanowire with the 2-nm-thick oxide coating highlighted. (**b**) The high-resolution image of the oxide coating shows that it is single crystalline. (Reprinted with Permission from *Nano Lett* 7(8): 2540–2544. Copyright 2007, American Chemical Society)

polycrystalline alumina was used for the VLS catalyst particles. Nanorods, nanowires, and nanobelts were produced with approximate dimensions of 500 × 30 nm, 1–5 μm × 30 nm, and 7 μm × 100 nm, respectively. The nanobelts were defined by a rectangular cross section; whereas, the nanorods and nanowires were defined by their cylindrical shapes. HR-TEM was used to differentiate hematite and magnetite within the samples. Electron diffraction within TEM was used to determine lattice parameters for the nanostructures. Both hematite and magnetite phases were found in the bulk samples, and it was found that careful control of O_2 partial pressure in the synthesis allows for control of the phase produced. The authors determined that the nanostructures were crystalline throughout and that there was little to no detectable amorphous layer on the surface of the structures [17].

In characterizing nanowires for many possible applications, determining the internal structure is important. One strategy for producing nanowires is cold-wall physical vapor deposition for single crystalline Zn nanowires [18]. The method provides a means to produce metallic single crystalline wires in a manner analogous to the VLS method for the production of semiconductor or oxide nanowires. The vapor-solid method (VS) does not rely on a catalyst particle that remains attached to the nanowires for wire growth. Zn nanowires from the VS process have been shown to be single crystalline rather than polycrystalline or amorphous via electron diffraction patterns obtained turning TEM analyses. High-resolution TEM imaging allowed for lattice spacing measurements as well as the confirmation of the direction of crystal growth. The Zn nanowires produced in this work vary in diameter from 30 to 350 nm and have lengths up to 89 μm; however, HR-TEM reveals a 2-nm-thick zinc oxide coating on the wires, as shown in Fig. 5.2. The oxide is also shown to be single crystalline. EDX measurements provide analysis of the composition, and no impurities were detected [18].

Nanoparticles and nanowires are often candidates for the active surfaces in heterogeneous catalysis reactions. Co_3O_4 nanowires have been used as catalysts

for the gas phase oxidation of carbon monoxide at temperatures as low as −77 °C [19]. A simple synthetic procedure in which cobalt precursor was heated in ethylene glycol and then combined with aqueous Na_2CO_3 resulted in a cobalt hydroxide carbonate intermediate. The intermediate material was then calcined in air to produce Co_3O_4 nanorods having dimensions of 5–15 nm × 200–300 nm. TEM and HR-TEM (Fig. 5.3) were central for the structural characterization of the nanorods and for aiding in the description of a possible reaction mechanism for the CO reduction. In lower magnification images, many nanorods are shown to have straight, non-tapering sides that form nearly rectangular particles (Fig. 5.3b). Higher-resolution images (Fig. 5.3c–f) reveal lattice spacing that shows internally organized structure with nanorod growth along the [110] axis. By imaging several orientations, the authors were able to construct a model nanorod to use in their proposed CO reduction reaction mechanism. The model rectangular prism shape of the Co_3O_4 nanorods has four relatively long [110] planes along its length. Because of the dominance of this exposed plane and the chemical structure of the cobalt oxide, the nanorod surfaces have more Co^{3+} sites than other Co_3O_4 nanoparticle shapes. The Co^{3+} sites are active to CO reduction. Other shapes preferentially expose crystallographic planes which are less rich in active Co^{3+} sites and are more populated with less active Co^{2+} sites. Interestingly, the authors determined a similar value for activation energy for the CO reduction reaction between Co_3O_4 nanorods and nanoparticles; however, they determined that the pre-exponential factor for the Arrhenius equation serves to increase the reaction rate for nanorod catalysts. Essentially, the reaction is the same – CO is reduced at Co^{3+} sites in both cases – but the number of active sites is significantly increased with the nanorods. TEM and especially thorough analysis with HR-TEM allowed the authors to develop a reaction mechanism that could explain why their Co_3O_4 nanorods performed well as a catalyst for CO reduction whereas other Co_3O_4 nanoparticles did not [19].

Hollow nanowires, also called nanotubes or nanotubules, can be synthesized from a variety of materials, including metals [20–34], metal oxides [35–39], and semiconductors [40–43]. Methods for producing metal/alloy nanotubes and other hollow nanostructures via galvanic replacement of a less noble metal with a more noble metal were developed by Younan Xia and colleagues [44–47]. The nanotube structure provides greater surface area for possible catalytic applications owing to the additional surface area available on the interior of the nanotube [21–29, 44]. The thorough characterization of these structures must include imaging of their hollow structure, a measurement of the wall thickness and consistency and determination of composition, particularly with multi-component materials.

Nanotube arrays of anodized TiO_2 can be impregnated with BiOI to produce photoelectrocatalytic materials [48]. The TiO_2 arrays can be characterized before and after treatment with BiOI to provide evidence for successful modification of the nanostructure. The authors used TEM to image the nanotube sides, allowing for a view of the wall thickness along the nanotube length. When imaging TiO_2 prior to treatment with BiOI, the outer diameter of the tubes was 100 nm, with a wall thickness of about 20 nm. The tube walls appeared to have a consistent width. After treatment with BiOI, the outer diameter increased to 105 nm, and the wall thickness

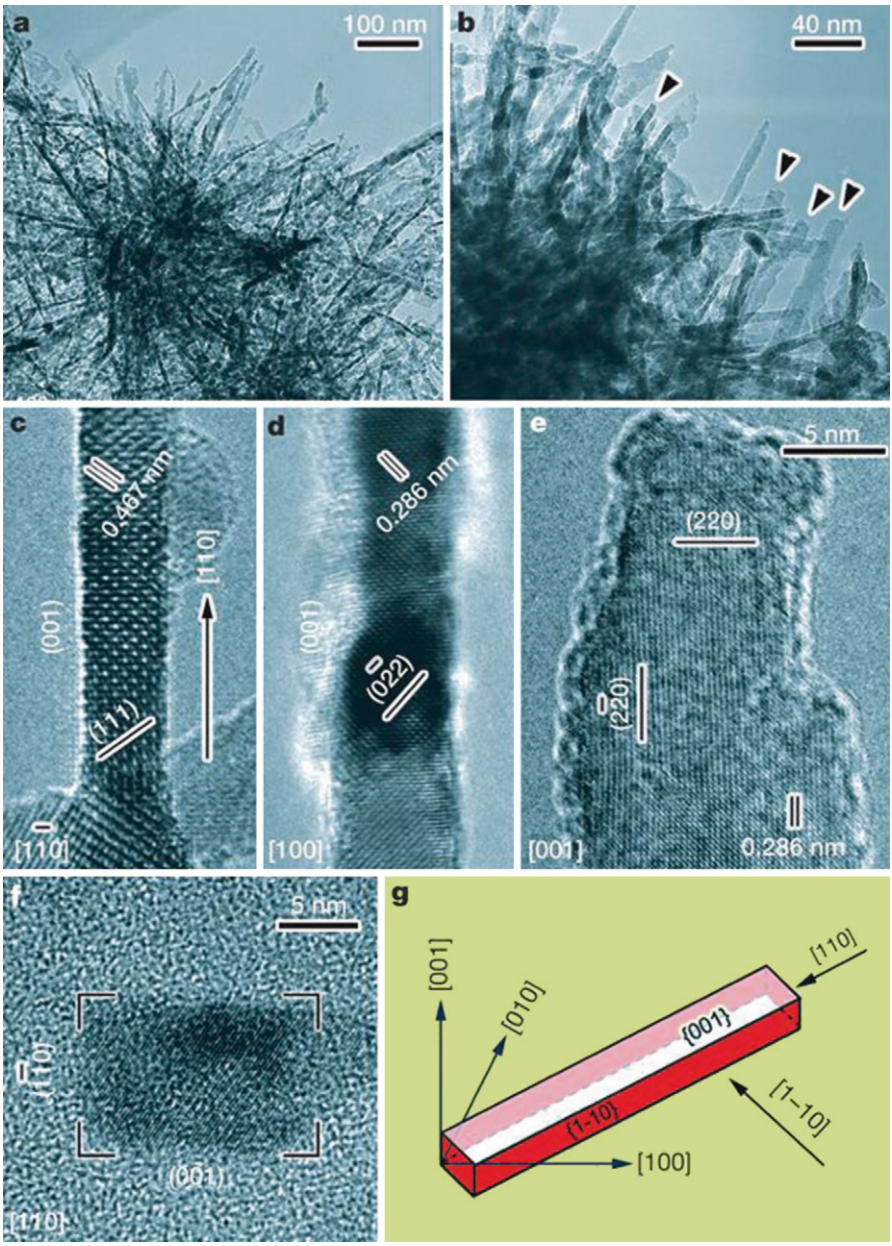


Fig. 5.3 TEM, HR-TEM images, and diagram of Co_3O_4 nanorods. (**a**, **b**) Lower- and higher-magnification TEM images of the nanorods. *Arrows* in **b** point to nanorods with straight sides and squared ends. (**c**–**f**) HR-TEM images showing crystal planes and growth directions. (**g**) The shape of ideal nanorods with catalytically active planes in *red*. (Reprinted by permission from Macmillan Publishers Ltd: *Nature* 458(7239): 746–749, Copyright 2009)

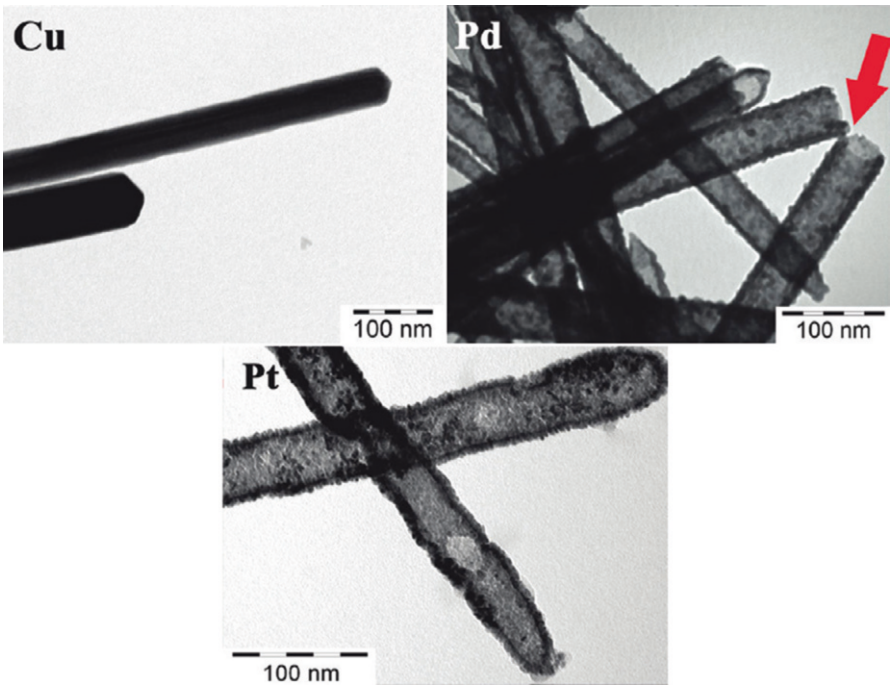


Fig. 5.4 TEM images of copper nanowires, CuPd and CuPt nanotubes. The ratio Pd or Pt precursor to Cu was 0.25. The *arrow* in the CuPd nanotube image points to the open ends of the nanotubes in the sample. (Reprinted with permission from *J Phys Chem C* 115(19): 9403–9409. Copyright 2011, American Chemical Society)

increased to about 27.5 nm. The inner diameter of the nanotube decreased from 60 to about 50 nm. The wall thickness remained consistent after treatment with no apparent difference in thickness along the nanotube length. The BiOI coating appeared to be consistent based on the TEM images with the addition of electron-dense material coating the entirety of the nanotube. EDX analysis confirmed the addition of Bi and I to the nanostructure [48]. Applications that depend on surface area, like catalysis, or contained volume, like drug delivery, need customizable nanomaterials. Once again, TEM and EDS allow for the thorough characterization of size, shape, and composition.

An example of hollow bimetallic nanotubes is found with CuPd and CuPt nanotubes generated via a galvanic replacement reaction [34]. In this procedure, solid copper nanowires were exposed to palladium and platinum salts. By controlling the mole ratios of the metals, the authors were able to control the final composition of the bimetallic nanotubes. As with the TiO_2-BiOI nanotubes [48], the "hollowness" of the nanotubes is readily analyzed with TEM as seen in Fig. 5.4. The sacrificial solid, single crystalline Cu nanowires have a consistently even, dark, and smooth appearance in TEM. After galvanic replacement with Pd and Pt, the resulting structures appear hollow and have obvious walls and open ends, as noted

by the arrow in the image labelled Pd in Fig. 5.4. Further, the nanotubes are roughened and appear polycrystalline although the authors offer electron diffraction as evidence for single crystallinity in the nanotubes. Of interest are the different results in terms of final mole ratio and final size for the two systems. EDS was used to quantify the compositions of a range of Pd:Cu and Pt:Cu mole ratios for galvanic replacement. Galvanic replacement of Cu with Pd was essentially complete at 1–1.5 Pd:Cu, but, at the same ratio, Pt only replaced about 70 % of the available Cu. Size changes were also different for the two systems. Addition of palladium salt caused a notable increase in diameter of the nanostructure. Pd tended to deposit on the nanowire surface during galvanic replacement. Pt tended to alloy with Cu, and the authors observed an unchanging diameter until there was more Pt than Cu in the system. They assert that additional Pt deposited onto the nanotube surface and then increased the observed diameter [34].

Another common mechanism for producing hollow nanostructures and nanotubes is the Kirkendall effect [49, 50]. The effect was first reported in the metallurgical literature related to diffusion at metal-alloy heterojunctions [51], and it was first applied to nanomaterials with the synthesis of cobalt-based hollow nanocrystals [52]. For nanotube formation to occur via the Kirkendall effect, the core-shell nanowire must consist of materials that have differing mutual diffusion rates such that the core material diffuses out more quickly than the shell material diffuses inward. Lattice vacancy defects at the interface facilitate the diffusion, and as the vacancies coalesce, voids within the faster-diffusing material form. Often, initial amounts of core and shell material are carefully determined based on the desired stoichiometry of the final product. To avoid unreacted material in the final structure, the amounts of core and shell must be carefully applied, grown, or deposited.

Recent examples of nanomaterials being produced by the Kirkendall effect include nanotubes of several oxide materials nanotubes [50, 53–56]. The interface between a metal nanowire and its thin metal oxide coating can result in appropriate mutual diffusion for the formation of nanotubes. The formation of SnO_2 nanotubes [53] and CeO_2 nanotubes [54] has been shown to proceed via the Kirkendall effect. For the Sn–SnO_2 system, the authors relied on TEM and HR-TEM to observe the nanomaterials at various times during the reaction that transforms the solid Sn nanorods into hollow SnO_2 nanotubes. XRD and XPS were used to help confirm the changes in crystallinity and composition. Upon synthesis of the Sn nanorods, HR-TEM, SAED, XRD, and XPS provided evidence that the composition was mostly single crystalline tin. HR-TEM revealed a 3–5-nm layer of amorphous tin oxide due to exposure to air during synthesis and, presumably, post-synthetic application to the TEM grid. As the samples were allowed to age over several hours, the Kirkendall effect continued, and Sn atoms diffused outward as oxygen atoms diffused more slowly inward. The oxidation reaction resulted in nanotubes with a diameter 10–20 nm wider than the original Sn nanorods. HR-TEM and SAED along with XRD show that the SnO_2 generated was polycrystalline. The nanorods were not uniformly converted to perfectly hollow nanotube structures, however, as the TEM images of partly hollowed structures show in Fig. 5.5. The filled portions of the tubes were shown to be unoxidized tin, and the presence of partially hollow structures was

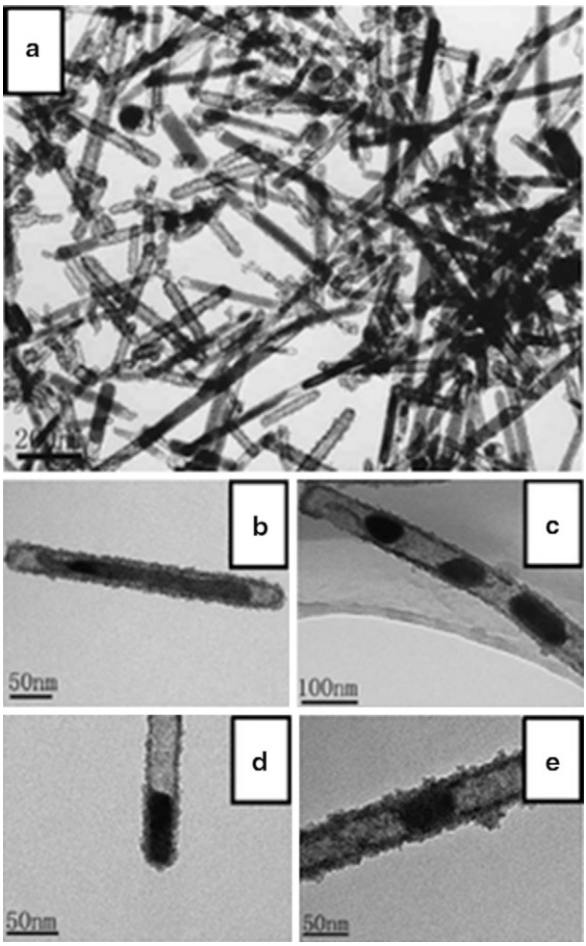


Fig. 5.5 TEM images of Sn-SnO_2 nanotubes partially hollowed by the Kirkendall effect. Several different cases of partial hollowing are shown. (Reproduced from *Chem Commun* 26: 3028–3030 with Permission of the Royal Society of Chemistry, 2008)

attributed to uneven flux of inner material diffusing outward. XPS analysis of the partially hollow structures confirmed the composition as being mostly SnO_2 with some presence of Sn metal [53].

Ceria nanotubes have been produced with a Kirkendall effect reaction and dubbed K-type CeO_2 by the authors [54]. The moniker is to differentiate the particular mechanisms of formation: other ceria types investigated by the authors include T-type, nanotubes formed by templating, and L-type, nanotubes formed by lamellar rolling of sheets. Analysis was performed with a similar approach as above with TEM, HR-TEM, XRD, and XPS. Precursor $Ce(OH)CO_3$ nanorods were allowed to react in aqueous solution with excess OH^-. Ce^{3+} available from the dissociation of $Ce(OH)CO_3$ at the nanorod surface reacted with OH^- to yield $Ce(OH)_3$, which was then converted to $Ce(OH)_4$ at the pH of the reaction mixture. Additional Ce^{3+} was able to diffuse from the interior of the nanorods more quickly than OH^- was able to diffuse inward, producing a shell of cerium (III/IV) hydroxide.

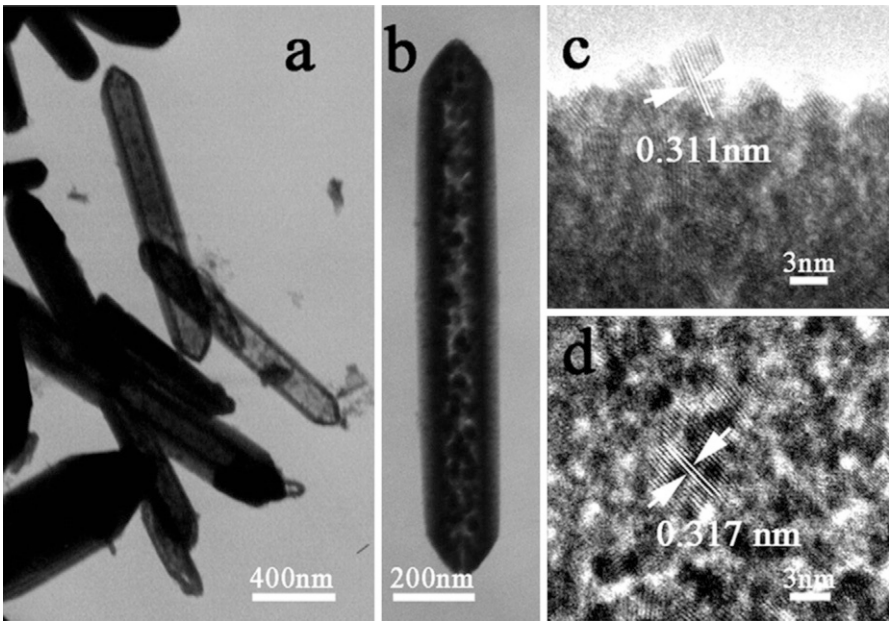


Fig. 5.6 (**a**) TEM and (**b–d**) HR-TEM images of CeO_2 nanotubes synthesized by the Kirkendall effect. High-resolution images of the shell and the interior are given in **c** and **d**, respectively. (Reprinted with permission from *Inorg Chem* 48(4):1334–1338. Copyright 2009, American Chemical Society)

The hydroxide shell was then converted to CeO_2 by calcining the solids in the air. When viewed under TEM, the interior of the nanotubes was seen to contain partial vacancies and some solids; however, unlike with the SnO_2 nanotubes described above [53], precursor material is not apparent in images of the ceria nanotubes (Fig. 5.6). The authors assert, however, that absence of precursor is likely due to the calcining step, which would decompose $Ce(OH)CO_3$ to CeO_2 [54].

An example of solution phase production of ternary oxide nanotubes via the Kirkendall effect is given by $Cr_2Te_4O_{11}$ [55]. In what is likely a coupled redox-Kirkendall mechanism, Te nanowires may be transformed into the ternary oxides, $Cr_2Te_4O_{11}$ and Mn_2TeO_6, by reaction with CrO_3 and $KMnO_4$, respectively. The reaction with potassium permanganate produced haphazardly layered, onion-like structures of Mn_2TeO_6. The precursor nanowires and oxide products were analyzed by TEM, HR-TEM, EDAX, XPS, and Raman spectroscopy. While the chemical changes can be monitored by the spectroscopies, the structural changes that could determine potential applications for the oxide nanomaterials could only be observed using the TEM techniques.

For the ternary oxide nanotube synthesis, precursor Te nanowires were synthesized by solution reduction of TeO_2 with hydrazine hydrate to produce single crystalline nanowires [55]. The TEM images show diameters of ~20 nm and lengths of 200–300 nm, and HR-TEM images reveal lattice planes that match the

growth planes of t-Te (trigonal tellurium) with no apparent structural or compositional defects. The ternary oxides were prepared by combining Te nanowires in solution with CrO_3 (or $KMnO_4$). The reaction mixtures were allowed to stir and were evaluated over the course of the reaction with the analysis techniques mentioned above. Over the course of 14 days, the previously colored solution (due to the nanowires and the chromium trioxide) became colorless. A similar color change was observed with the permanganate reaction mixture. In general, a loss of color indicates the occurrence of a reaction although it does not point to the specific changes related to nanostructure. TEM uncovered the structural changes that occurred over the reaction period. After 1 day, a thin shell was seen covering the nanowires, which was likely a result of a redox reaction between Te and CrO_3. This heterojunction gave rise to a Kirkendall effect that resulted in the formation of voids within the nanowire/nanotube structure that were observed after 5 days' reaction. The void spaces were irregular, and they continued to grow as Te diffused outward and was converted to $Cr_2Te_4O_{11}$ on the surface. HR-TEM images show traces of the Te lattice in the unreacted solids inside the forming nanotube (Fig. 5.7c). The shell, in contrast, shows no lattice features and is believed to be amorphous (Fig. 5.7d). By 10–14 days' reaction, the nanotubes were formed with no observable unreacted Te remaining. EDAX analyses of the intermediate and final structures indicate that the ternary oxide, which incorporates the Te starting material and the oxidizing agent into hollow nanotubes, is the final product [55].

Ternary oxide nanotubes formed with the Kirkendall effect may be crystalline rather than amorphous, as demonstrated with the growth of $ZnAl_2O_4$ spinel nanotubes [50, 56]. In a primarily TEM-based study, ZnO nanowires were grown according to a VLS mechanism from a catalyst nanoparticle (Au) [56]. A core-shell structure was then created by atomic layer deposition of Al_2O_3 over the entirety of the nanowires. The core-shell structures were transformed by the Kirkendall effect into crystalline, homogeneous spinel nanotubes. In this method, the crystalline ZnO VLS-grown core, the precisely controlled deposition of the alumina, and an annealing step (at 700 °C) resulted in a final nanotube structure that was single-crystalline, or at least largely so. Because of the VLS step and because no efforts were made to remove it, the Au nanoparticle catalyst remained in the final nanotube structures, as shown in Fig. 5.8a, b. The Au nanoparticle had been coated with the ALD alumina, and after nanotube formation, it was encased partly by the alumina, but also by $ZnAl_2O_4$. The mixed phase in this region makes sense because the Au nanoparticle sits in between the alumina and ZnO; however, the ZnO, as the more diffusive species, would be expected to diffuse into a region of lower concentration.

5.1.2 Using TEM to Find Structural Defects in Silicon Nanowires

The analysis of defects within VLS-grown Si nanowires has been performed with TEM and HR-TEM, often in conjunction with other techniques, such as XRD and Raman spectroscopy as well as computer simulations. The explanation of the origins of unusual electron diffraction patterns in particular, is a matter of ongoing research and debate within the literature [57–60]. Overlapping crystalline micro- and nanotwins [57, 58] and rare polytypes [59, 60] have been considered as

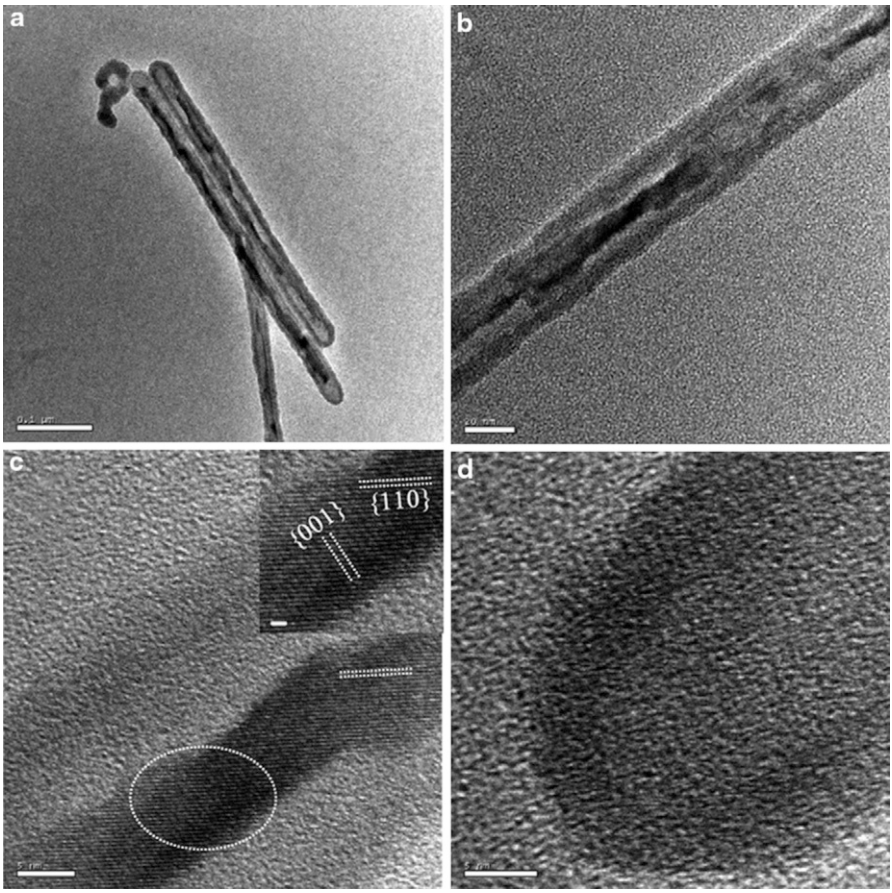


Fig. 5.7 Te nanowires reacting with CrO_3 after 5 days. Scale bars: (**a**) 100 nm, (**b**) 20 nm, (**c**) and (**d**) 5 nm. The *inset* (scale bar 2 nm) in (**c**) shows the lattice spacing for the circled structure. (Reprinted with permission from *J Phys Chem C* 115(33): 16524–16536. Copyright 2011, American Chemical Society)

explanations for the observed phenomena. The structures that are responsible for the electron diffraction patterns in question are certainly subtle regardless of their ultimate identity, and transmission electron microscopy techniques are central to their elucidation. The internal structure of the nanowires must be uncovered, imaged, and interpreted in the context of other available data. Using TEM and HR-TEM, multiple images and electron diffraction patterns may be obtained from single Si nanowires from various points of view (Fig. 5.9) [60]. By encapsulating the nanowire(s) of interest and then milling with focused ion beam (FIB), cross-sectional views of the nanowire(s) may be obtained. The cross-sectional, or end-on view, may be used in conjunction with the plan-view of the same nanowire in the same place (± 0.1 μm) to interpret electron diffraction patterns and Raman spectra



Fig. 5.8 TEM images of $ZnAl_2O_4$ nanotubes showing (**a**) the body and (**b**) the region near the tip, including the encased Au catatlyst particle. An enlarged view of the nanotube wall is shown in the *inset*. (Reprinted by permission from Macmillan Publishers Ltd: *Nat Mater* 5(8): 627–631, Copyright 2006)

obtained from the same. Further, when viewed in cross-section, the sample may be rotated about a given axis to reveal stacking disorder among the crystallographic planes [60]. HR-TEM images showing the end-on view and the side view are given in Fig. 5.9a, c, respectively.

When metal nanoparticles are used as the VLS catalyst, catalyst atoms can be drawn into the VLS-grown nanowires, particularly at defects [61–64]. Single Au atoms may be imaged within nanowires, and the three-dimensional distribution of the Au atoms may be reconstructed. By using high-angle annular dark-field (HAADF) STEM and collecting a series of images through the focal range of a Si

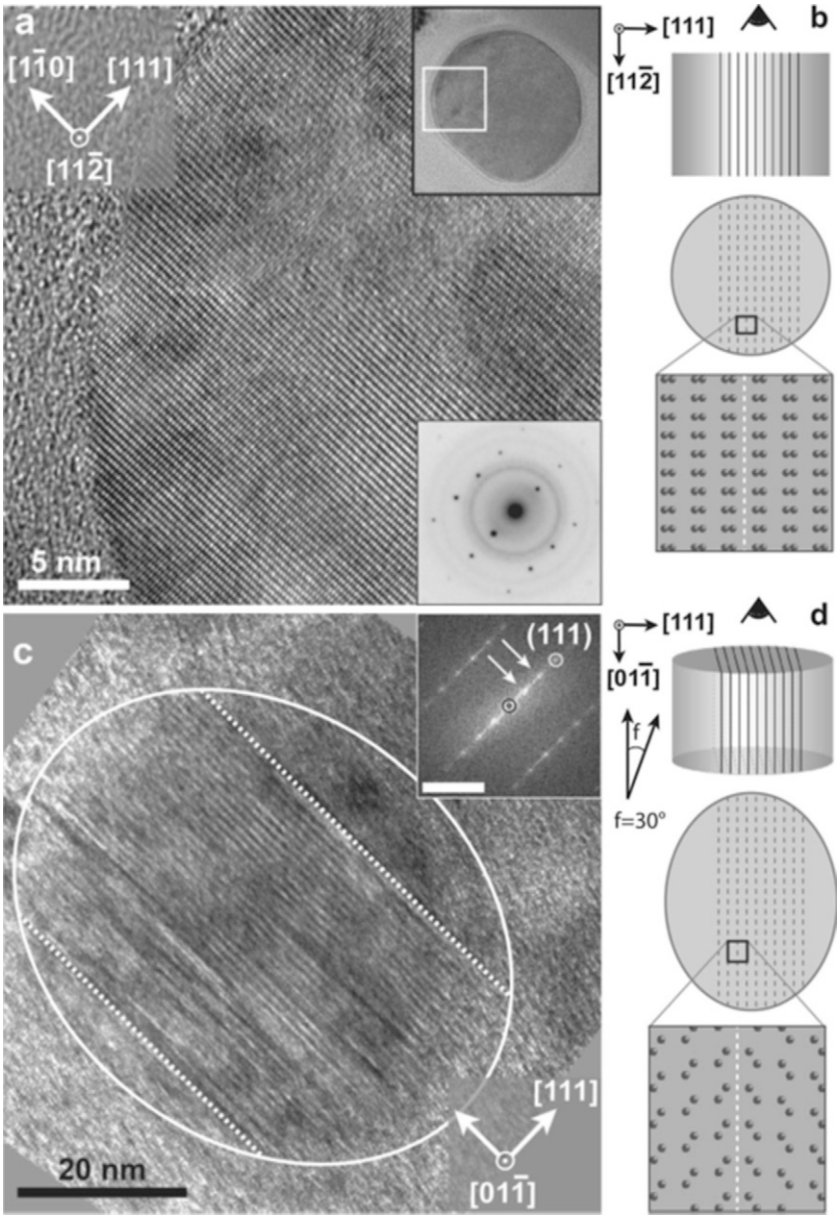


Fig. 5.9 TEM images of Si nanowire viewed in cross-section (**a**) and after tilting 30° about the [111] direction. Schematics in (**b**) and (**d**) show the orientations and viewing angles of (**a**) and (**c**), respectively. (Reprinted with permission from John Wiley & Sons Inc: *Small* 8(11): 1717–1724, Copyright 2012)

nanowire, the stacked or summed image can show single Au atoms trapped along defects [62]. The number of Au atoms observed exceeds that predicted by the estimated solubility of gold in silicon, and the authors have determined that the Au atoms observed do not diffuse into the Si structure after growth. An abrupt composition change between the Au catalyst nanoparticle and the Si wire is observed – as opposed to a concentration gradient of Au atom concentration that would indicate a diffusive process [62].

A series of HAADF-STEM images obtained at several angles and FIB cross-sectioning of the Au-catalyzed Si nanowires allows for enhanced viewing of the incorporated atoms and tomographic reconstruction of the catalyst-nanowire interface [64]. Angular imaging can be accomplished by rotating the nanowire sample along the direction of growth, similar to how nanocrystalline materials are imaged in three dimensions with TEM and image reconstruction [65]. The series of images comprises the three-dimensional structure of the nanowire along its growth axis [64]. Cross-sectional imaging of the same nanowire revealed the presence of grain boundaries within the nanowire and faceting at the catalyst-nanowire interface. The computer reconstruction of the nanowire and catalyst-nanowire interface and the incorporation of Au atoms along defects indicate that defects, and hence the Au incorporation along the defects, are favored when Si nanowires grow along [110] rather than [111]. Future work in this area concerning dopants smaller than Au should be considered [64].

5.1.3 Nanowire Growth by Oriented Attachment

Oriented attachment, also known as oriented aggregation, is a mechanism by which isolated nanoparticles attach to each other, often through aligned crystal lattices, to form a larger nanostructure. When the crystal lattice of an attaching particle is aligned to that of the growing assembly, the surface energy of the emerging structure is minimized. According to the growth mechanism, zero-dimensional nanostructures may be grown into one-dimensional nanowires or branched structures as more and more attaching particles join together [66]. This mechanism may be inferred by periodic sampling and (HR-)TEM analysis of reaction mixtures over time [67–74]. Careful observation of the superstructure lattice by HR-TEM can reveal defects generated during imperfect joining of two nanoparticles. Penn and Banfield have investigated the oriented attachment of TiO_2 nanoparticles and the presence of defects originating from the growth mechanism [75]. As evidenced by HR-TEM, the joining particles may not be perfectly matched or atomically flat at the attaching surfaces. Thermodynamics favors the full coordination of bonds by joining like particle surfaces, and a minor mismatch in surface structure is not enough to derail particle growth. If the interface is distorted, edge and screw dislocations result to varying degrees. Crystal steps on the adjoining nanocrystals and the relative rotation of the adjoining nanocrystals cause edge and screw dislocations, respectively. Slightly misoriented interfaces between nanocrystals form edge dislocations that can be imaged with HR-TEM. When the constituent nanoparticles are observed to be defect-free, the dislocations are therefore attributed to the oriented attachment mechanism of nanostructure growth [75].

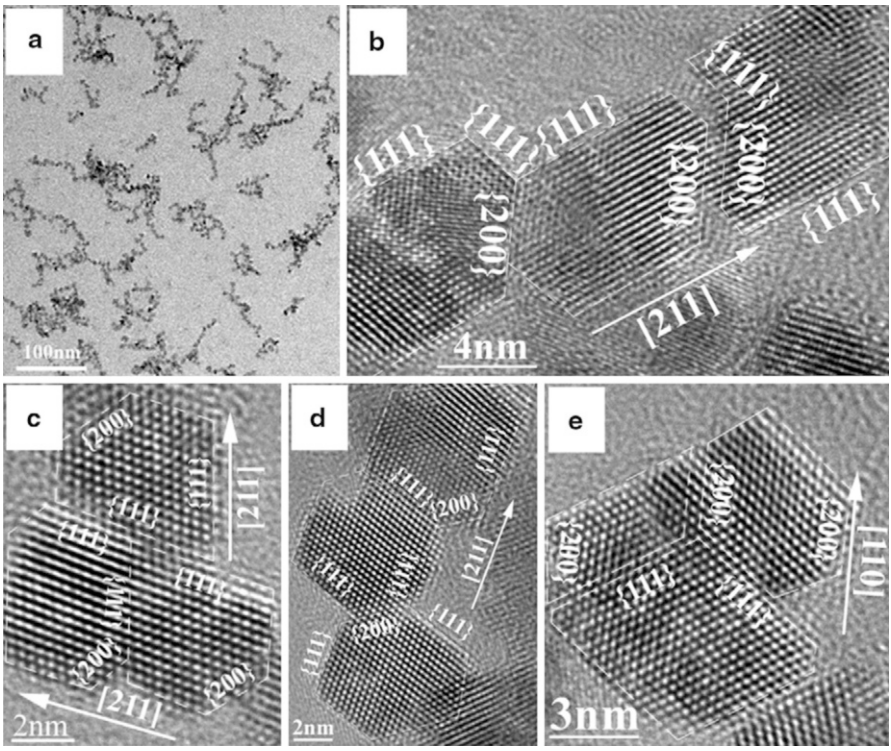


Fig. 5.10 TEM (**a**) and HR-TEM (**b**–**e**) images showing interparticle organization and the crystallographic orientation between/among nanoparticles. The structures shown are pearl-chain structures that formed via oriented attachment. (Reprinted with permission from *J Phys Chem C* 111(34): 12677–12680. Copyright 2007, American Chemical Society)

Hexagonal ceria nanocrystals have been shown to join via oriented attachment to ultimately form nanorods [76]. Intermediate structures formed by the linking of nanocrystals, referred to as "pearl chain" structures, are transformed by Ostwald ripening into smooth, rodlike nanoparticles. The nanorods have been shown to grow along the [211] or [110] direction, depending on which crystal faces, {111} or {200}, respectively, join during oriented attachment of the seed crystals. A thorough analysis of the structures with TEM and HR-TEM shows clear evidence of the oriented attachment growth mechanism and the two growth directions. For example, Fig. 5.10 shows how the hexagonal nanocrystals are aligned and joined in several of the preliminary "pearl chain" structures. XRD was also used to evaluate the structures. The "pearl chain" structures and nanorods were both indexed as cubic ceria; however, the diffraction peaks are narrower for the nanorods, indicating an increased crystallinity along with an increase in overall size [76].

Some of the most compelling examples of the oriented attachment/aggregation mechanism for nanorod/nanowire growth are when the aggregating species are rodlike nanoparticles [77, 78]. Structures formed from CdS and Ag_2S were observed

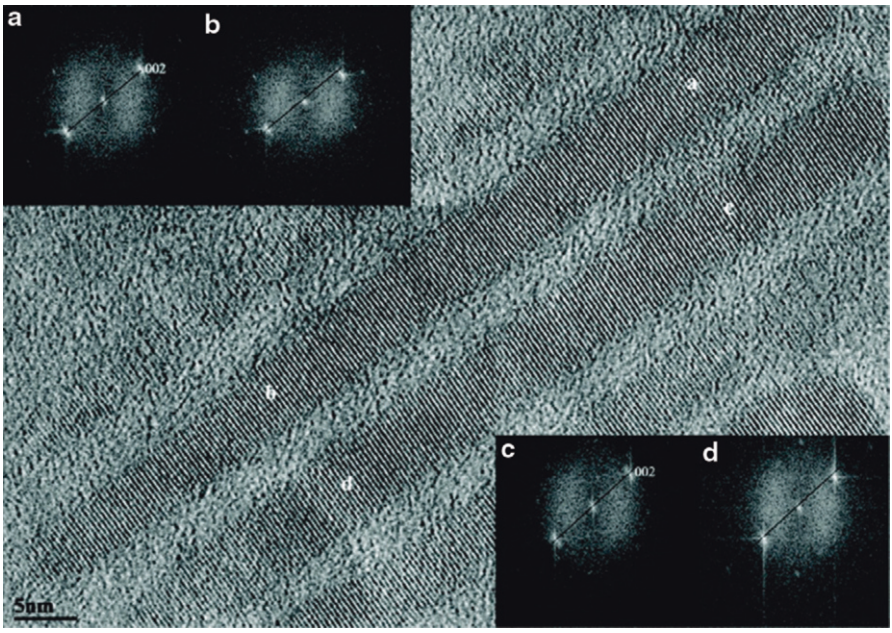


Fig. 5.11 HR-TEM image showing two CdS nanowires grown by one-dimensional oriented attachment. *Insets* are Fourier transforms of the corresponding areas of the nanowire images, **a**–**d**. Slight changes in lattice plane angles may be due to the oriented attachment of smaller nanorods to form longer nanowires. (Reprinted with permission from *J Am Chem Soc* 131(34): 12250–12257. Copyright 2009, American Chemical Society)

to grow by "integers" of the nanorods that comprise the final nanowire structures [77]. The CdS and Ag_2S structures doubled, tripled, and quadrupled in length between TEM analyses. The strongest evidence of interger growth was provided by the TEM images although UV–vis spectroscopy implied the aspect ratio changes. End-on growth was controlled by selectively depassivating the (001) facets of the nanowires, which were exposed at the nanorod tips, with the addition of amines to the reaction mixture. Amine-containing molecules, such as decylamine, hexylamine, diethylamine, trioctylamine, and several other amines that are liquid at room temperature are effective for the selective depassivation of (001) facets [77]. HR-TEM images of CdS nanowires produced with the one-dimensional oriented attachment of nanorods (Fig. 5.11) show a slight change in angle of the crystal lattice along the length of the nanowires. Image analysis with Fourier transform shows that the crystal direction of the (002) lattice plane changes by 1-2°, which may be an artifact of the oriented attachment growth mechanism. Polydispersity in nanorod diameter results in varying diameters of the nanowires. TEM and HR-TEM images in Fig. 5.11 shows the joining of polydisperse CdS nanorods to form nanowires with varying diameters.

Silver sulfide nanorods have been produced by adding Ag^+ ions to the CdS nanorod solutions [77]. Complete cation exchange was achieved by controlling the concentration of Ag^+ ions in solution. After cation exchange to form Ag_2S nanorods,

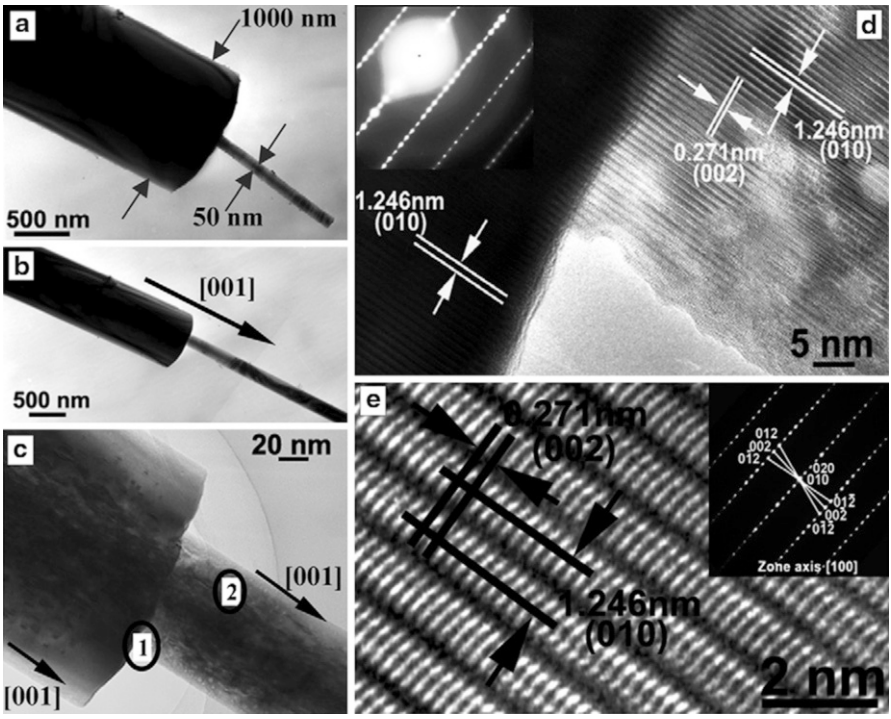


Fig. 5.12 TEM images of attachment region for Sb_2O_3 coaxial nanowires (**a**–**c**). Segment diameters (**a**) and growth directions (**b**, **c**) are noted on the images. Regions 1 and 2 of image **c** are shown with HR-TEM in **d** and **e**, respectively, to show lattice spacing and orientation. *Insets* in **d** and **e** are the corresponding SAED patterns for the high-resolution images. (Reprinted with permission from *J Phys Chem C* 111(14): 5325–5330. Copyright 2007, American Chemical Society)

nanowires were observed to form via the same mechanism of oriented attachment as CdS nanowires. Cation exchange to form Ag_2S was confirmed with XRD, and growth of nanorods to nanowires was evidenced by TEM. TEM revealed that cation exchange did not alter the dimensions of the original CdS nanorods. HR-TEM, however, was presented for neither the Ag_2S nanorods nor the nanowires [77].

While the reaction conditions allowed CdS and Ag_2S to grow only in length, Sb_2O_3 nanorods were observed to orient themselves end-to-end or side-by-side, thereby forming nanobelts with greater diameters and nanowires with longer lengths than the constituent nanorods [78]. Axial oriented attachment is readily apparent in the Sb_2O_3 system due to the polydispersity in the nanorod population. A variety of nanorod diameters were formed in the reaction mixture, and with time, multi-segmented nanowires were observable with TEM, as seen in Fig. 5.12. Nanowires hundreds of micrometers long can result from the oriented attachment of nanorods that range from 2 to 50 μm in length and 20–1,000 nm in diameter. The junctions of several Sb_2O_3 nanorods are apparent in Fig. 5.12 due to the various nanorod diameters in the sample. The corresponding high-resolution images show

the lattice spacing of two areas related to a junction. The lattice spacing measurements and the SAED patterns indicate a (nearly) single crystalline final product. Little to no misorientation of the constituent nanorod lattices is apparent. The coaxial alignment of multiple nanorods with atomic precision is indicated only through HR-TEM analysis of the resulting nanowires and the coaxial junctions. The side-by-side oriented attachment of Sb_2O_3 was observed during the direct air oxidation of Sb to its oxide at 80 °C. TEM shows the coexistence of aligned nanowires and nanobelts during the oxidation and oriented attachment process [78].

5.2 In Situ TEM Techniques for Analysis of Nanowires

5.2.1 Nanowire Syntheses In Situ for Observing or Determining Mechanisms of Growth

TEM techniques that allow for concurrent nanowire growth and imaging provide real-time evidence of growth mechanisms. In situ growth chambers include atmospheric (or environmental) chambers that allow for gas phase addition or production of nanowire precursor materials [79–83] and liquid chambers for solution-based mechanisms [9]. The advent of nanomaterial growth within TEM has allowed for continuous monitoring of individual particles, small groups of particles and other materials throughout the growth process [2, 4, 5]. Various growth mechanisms, including vapor–liquid–solid (VLS), vapor–solid–solid (VSS), and oriented attachment, have been investigated with in situ (HR-(S)) TEM imaging. Real-time growth and imaging allows researchers to "connect the dots" in time and among individual growing nanostructures. In situ growth provides a dynamic view of growing nanostructures that is unattainable by other methods. The object under observation may be monitored before, during, and after the reaction, and intermediate stages can be observed more directly thereby providing data that may be used for interpreting reaction mechanisms or kinetics. It is important, however, to consider the potential consequences of adding reactive materials to TEM sample chambers, as noted in a recent tutorial on the subject of in situ TEM of nanomaterials reactions [7]. The author of the tutorial cautions that reaction conditions and results should be consistent with analogous ex situ experiments and results so the in situ work may be meaningful.

In VLS and VSS growth mechanisms, a nanoparticle catalyst is typically the growth point for the emerging nanowires. In VLS, the liquid phase is the result of a eutectic formed between the catalyst nanoparticle and a dissolving species. Growth is initiated when supersaturation of the growth material and temperature of the system require the growth material to deposit as a solid. In situ TEM has allowed for analysis of the growth mechanism and has resulted in more complete observation and understanding of the process. In growing Ge nanowires from Au catalysts, the VLS process has been observed to occur at temperatures below the eutectic temperature of the Au–Ge system [79]. Additionally, nanowires have been observed to grow via a VSS process simultaneously with the VLS process. In situ growth and imaging show the phase transition of the catalyst nanoparticle owing to

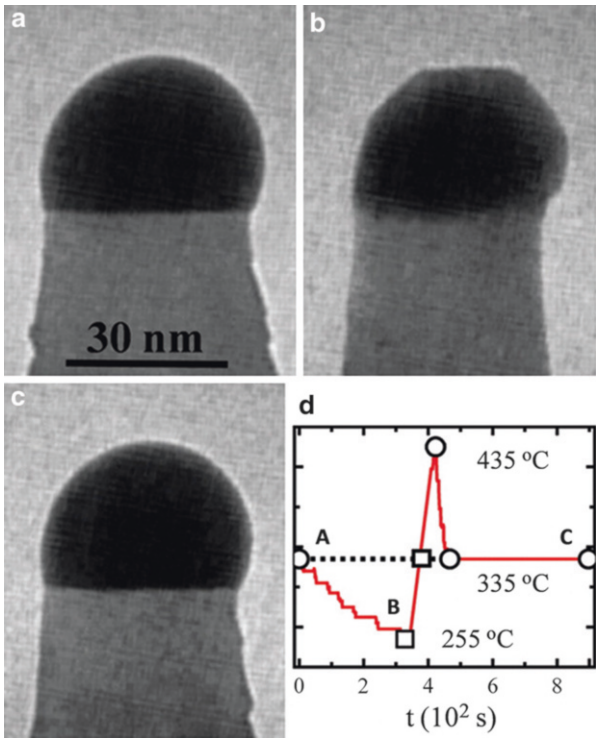


Fig. 5.13 In situ TEM images of the VLS/VSS growth of a Ge nanowire. The same nanowire is shown at three different temperatures (**a**–**c**), corresponding to the temperature-time plot in (**d**). In (**a**) and (**c**), the Au catalyst particle at the tip is liquid. In (**b**), the catalyst tip is solid, as is evidenced by the apparent facets on the tip. (From *Science* 2007 316(5825): 729–732. Reprinted with permission from AAAS)

the appearance and disappearance of facets with temperature changes (Fig. 5.13). Depending on the temperature and partial pressure of the gas phase growth material (Ge_2H_6), the catalyst may be liquid or solid. With the phase transition to solid, abrupt lengthening of the growing nanowire has been observed within a single video frame (30 frames/s). This sudden growth was attributed to the decreased solubility of Ge in the solid catalyst versus the liquid. VLS and VSS growth have been observed to occur simultaneously, under constant temperature and partial pressure of Ge_2H_6. Growth rates for individual nanowires were extracted from the video data with 9.9×10^{-2} nm/s and 1.3×10^{-2} nm/s as the growth rates for VLS and VSS, respectively. The series of images shown in Fig. 5.14 for the VLS- and VSS-grown nanowires display the distinguishing characteristics: smooth versus faceted catalyst, relatively wide versus relatively narrow diameters, constant diameter versus tapered diameter, respectively [79].

Video imaging of the catalyst droplet shape under varying partial pressures of Ge_2H_6 showed small but reproducible changes in height and diameter. When the partial pressure was increased from $\sim 2 \times 10^{-6}$ Torr to $\sim 8 \times 10^{-6}$ Torr, the diameter decreased by $\sim$5 nm and the height increased by $\sim$1.5 nm. When the partial pressure was decreased, the changes in diameter and height reverted. Ge nanowire growth was observed to occur with a liquid catalyst tip below the eutectic point of the Au–Ge phase diagram due to inhibition of Au nucleation by

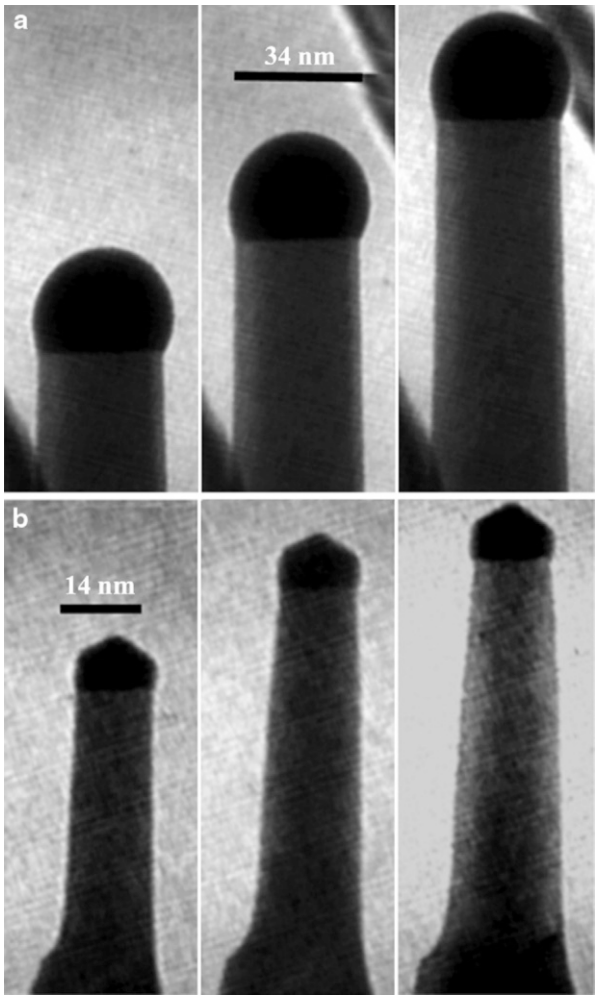


Fig. 5.14 In situ TEM images extracted from video recording of Ge nanowire growth. **a** shows VLS growth of a Ge nanowire, and **b** shows the VSS growth of a Ge nanowire. Images in (**a**) were recorded at 0, 309, and 618 s (*left to right*), and images in (**b**) were recorded at 0, 1,340, and 1,824 s (*left to right*). (From *Science* 2007 316(5825): 729–732. Reprinted with permission from AAAS)

supersaturation of Ge. The partial pressure of Ge_2H_6 and the diameter of the droplet influenced Au nucleation and growth rate of the nanowires. The observations made with in situ TEM have led to the assertion that source gas partial pressure, while not previously considered critical to nanowire growth, is quite important for the mode and the rate of nanowire growth [79]. This approach of varying the source gas pressure with real-time monitoring of the nanowire growth may be of interest in other VLS/VSS systems.

VLS/VSS growth systems can be controlled to produce nanowires with varied composition [80, 84–86]. In situ growth and TEM imaging provide a clear view of the growth process, and when the source gas is varied, concomitant imaging is important to the understanding of the growth. VLS growth is rapid when compared to VSS growth; however, under VSS conditions, the lower solubility of growth materials in

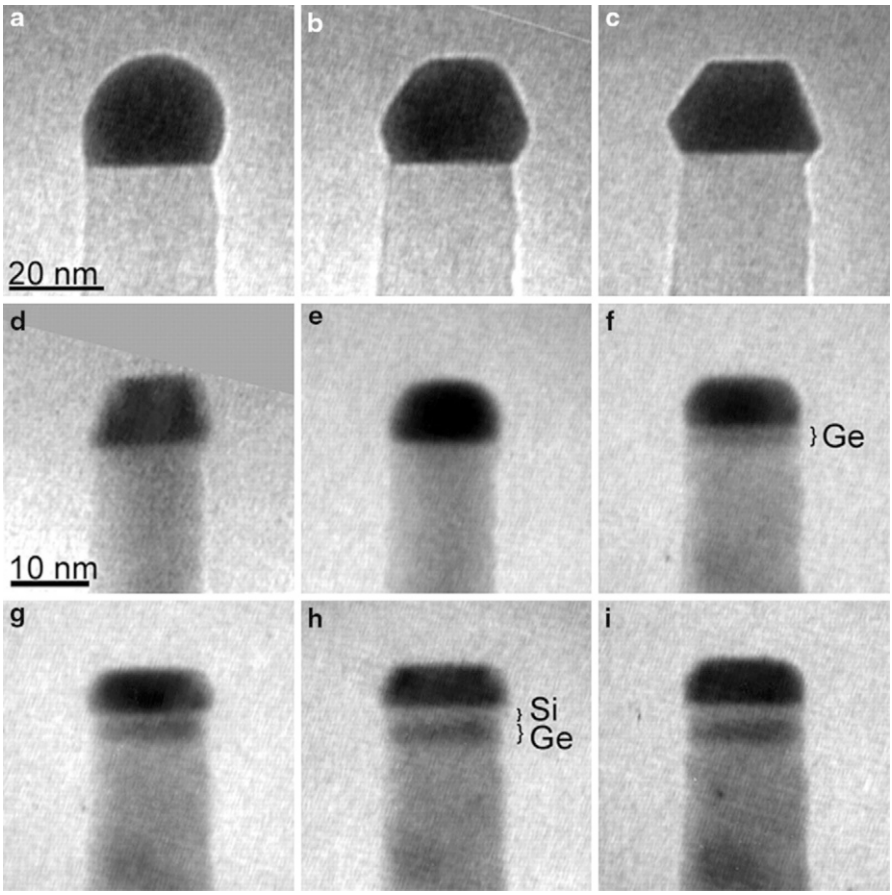


Fig. 5.15 Progress of growth of a Si nanowire when the temperature was reduced from 570 °C to 503 °C (**a**–**c**). The catalyst nanoparticle is liquid in (**a**), as noted by its rounded shape. The catalyst is just solidified in (**b**) and has been solid for several seconds in (**c**). Progress of growth of Ge heterojunction (**d**–**i**). The *darker stripe* in the nanowire is Ge. (From *Science* 2009 326(5957): 1247–1250. Reprinted with permission from AAAS)

the catalyst can provide for abrupt junctions of materials in the growing nanowire [80]. Incorporating multiple nanowire materials for VLS/VSS growth requires a catalyst that can solubilize the growth materials of interest. Eutectic points for the materials in the catalyst must also be similar. For nanowires composed of Si and Ge, $AlAu_2$ was found to be a more effective catalyst than Au. Two nanowire growth series are shown in Fig. 5.15. The initial growth of Si was accomplished via VLS in order to grow a relatively long wire quickly (Fig. 5.15a–c). The catalyst tip is shown before solidification (Fig. 5.15a), immediately after solidification (Fig. 5.15b), and several seconds after solidification (Fig. 5.15c). The faceting of the catalyst tip indicates the phase transition from liquid to solid. In another nanowire, the initial Si growth via VLS and subsequent solidification of the catalyst tip are shown

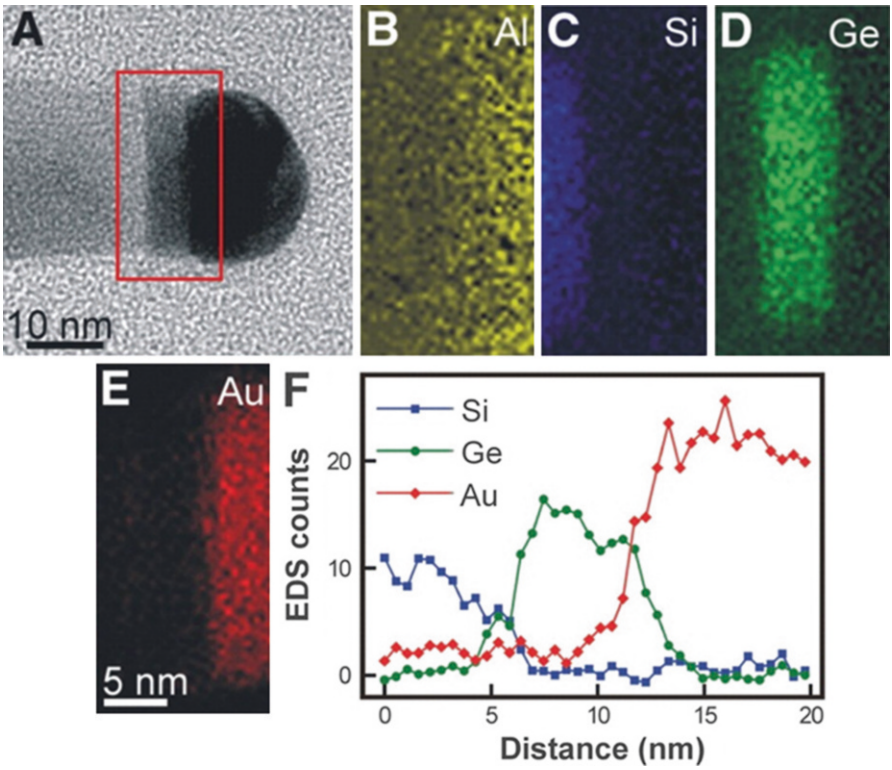


Fig. 5.16 Elemental analysis of a Si-Ge heterojunction nanowire. (**a**) The bright-field TEM image shows the area of analysis. It includes part of the Au catalyst nanoparticle, part of the Si nanowire body, and the Ge section. (**b–e**) The false color EDS elemental mapping of the section of the nanowire marked in (**a**). (**f**) The EDS line profile of Si, Ge, and Au shows the intensity averaged over a 3-nm-wide section along the axial midsection of the nanowire. (From *Science* 2009 326(5957): 1247–1250. Reprinted with permission from AAAS)

(Fig. 5.15d). The transition to Ge_2H_6 source gas is shown to alter the facets of the solid catalyst (Fig. 5.15e), and after several minutes of feeding Ge_2H_6, Ge became visible as a dark stripe in the growing wire (Fig. 5.15f). Switching the source gas back to Si_2H_6 under VSS conditions resumed production of Si and was shown to cause the catalyst tip to regain more defined facets (Fig. 5.15g–h). When the Ge source gas was reapplied, the faceting of the catalyst tip again softened (Fig. 5.15i). Analysis of similarly grown Si–Ge nanowires with HR-TEM and EDS after completed growth provides a higher-resolution view of the heterojunctions (Fig. 5.16). The high-resolution imaging shows crystalline heterojunctions, and EDS line analysis shows a transition region of <2 nm between Si and Ge. Further EDS analysis of the catalyst tip confirmed the low solubility of the source gas materials in the catalyst under VSS conditions, as shown in Fig. 5.16. The low solubility likely accounts for the sharpness of the junctions due to the lack of material reservoir effects. False color image

mapping for Al, Si, Ge, and Au shows sharp elemental placement along the nanowire and in the catalyst tip. EDS line analysis along the central portion of the nanowire shows clear transitions of the elements [80].

The nucleation and initial growth of nanowires may be directly observed with in situ TEM techniques [82, 83]. In VLS growth of GaN nanowires, Au nanoparticles were sputtercoated onto a silicon substrate present on the TEM grids to be used for the in situ growth [83]. The coated grids were heated to 480 °C within the environmental (S)TEM, and the organometallic gallium precursor, trimethylgallium, was introduced to the chamber. The precursor was thermally decomposed, Ga began to dissolve in the Au islands, and Ga–Au droplets formed. By monitoring the process with video, the shape and movement of the droplets were monitored in real time. As the droplets coalesced, ragged or uneven edges sometimes resulted. These edges were thinner than the main droplet, and the composition, as determined by in situ STEM-EDS, varied along the main droplet to the end of the thinned edge. The relative concentration of gallium was found to increase along the thinned edge of the droplet. When ammonia was introduced with the sample at 800 °C, the authors observed GaN nucleation only after the pressure of ammonia exceeded 0.93 Pa. The nucleation of GaN was also observed to occur in the thinned regions of the droplets, where Ga concentrations were relatively high. It is thought that higher concentrations of Ga leads to more GaN clusters that ultimately form the GaN nuclei. In situ EELS and SAED both showed the presence of GaN in the nuclei located at the thinned edges of the droplets. A similar process of observation of initiated growth has been shown with in situ VSS/VLS-grown Ge on gold catalyst nanoparticles [82]. With video image capture at 15 frames/s and image resolution of 0.134 nm, the initial phases of Ge nanowire growth can be analyzed. In the series of bright-field images shown in Fig. 5.17, the Au catalyst nanoparticle was solid before the addition of the germanium precursor, as indicated by the Fourier transform (FT) of the image (Fig. 5.17a and inset). The FT confirms the lattice spacing of [111] Au. As germanium precursor was added to the system, the nanoparticle surface liquefied while a solid Au core remained (Fig. 5.17b) until the entire particle liquefied (Fig. 5.17c) even though the system was kept below the eutectic temperature for Au–Ge. Solid Ge was shown to nucleate (Fig. 5.17d) on the liquid surface and then the system phase separated into two solids (Fig. 5.17e). The FT inset with Fig. 5.17e shows the reappearance of spacing consistent with the [111] lattice for solid Au. The Ge growth may then continue under a VSS mechanism, and, as observed by others [79], these authors have shown that both the VSS and VLS growth mechanisms can be observed to produce Ge nanowires [82].

TEM liquid cells allow for the direct observation of growing nanoparticles in solution [9]. The oriented attachment growth mechanism – often alongside monomer addition growth – for nanomaterials has been observed with liquid cells and in situ TEM. The direct observation of nanoparticles undergoing oriented attachment strengthens the inferred arguments made with ex situ imaging and broadens the understanding of nanoparticle growth processes [87]. The presence or absence of defects at attachment points, the reorienting of approaching nanoparticles, and the rate of the final approach before attachment have been observed and measured [88].

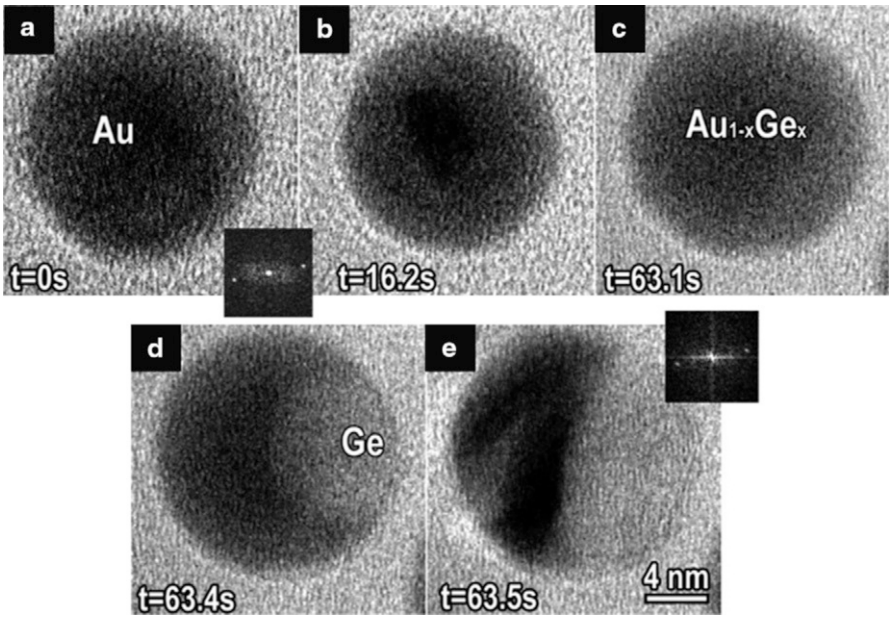


Fig. 5.17 Bright-field TEM images extracted from video of the Au catalyst nanoparticle during exposure to the Ge precursor gas in an environmental TEM. Over time, Ge nucleated for growth of a Ge nanowire. The *inset* Fourier transforms of (**a**) and (**e**) confirm that the Au nanoparticle in the image is in the solid state. (Reprinted with permission from *Nanolett* 10(8): 2972–2976. Copyright 2010, American Chemical Society)

The role of Ostwald ripening with oriented attachment growth has also directly been observed with liquid cells and in situ TEM [88–90]. Oriented attachment of TiO_2 nanoparticles to SnO_2 nanoparticles has been observed in situ to produce heterostructures [91]. With in situ liquid cell (HR-S)TEM, Pt_3Fe nanoparticles have been observed to aggregate into nanorods via oriented attachment [92]. The nanoparticles joined together as twisting polycrystalline nanoparticle chains and then straightened into single crystalline or polycrystalline nanorods, as seen in Fig. 5.18a. The four particles shown in Fig. 5.18a are examples of the structures observed in the in situ liquid cell, and the dark spots (indicated with arrows) are iron-rich regions common in this material [92]. In Fig. 5.18b, a sequence of images (I–IV) is shown of reorientation and straightening of a nanoparticle chain. The final structure shows the continuous orientation of the [111] growth direction. Through observations with in situ electron microscopy, the authors measured the velocity of nanoparticle approach as interparticle distance decreased. They found that beyond a critical interparticle distance, the motion of an approaching nanoparticle is random. Depending on the structure that the nanoparticle approaches, the critical distance changes: when it approaches another single nanoparticle, the critical distance is 3 nm, and when it approaches a chain of nanoparticles, the critical distance is ~6–8 nm. At the critical distance for the interaction, an approaching

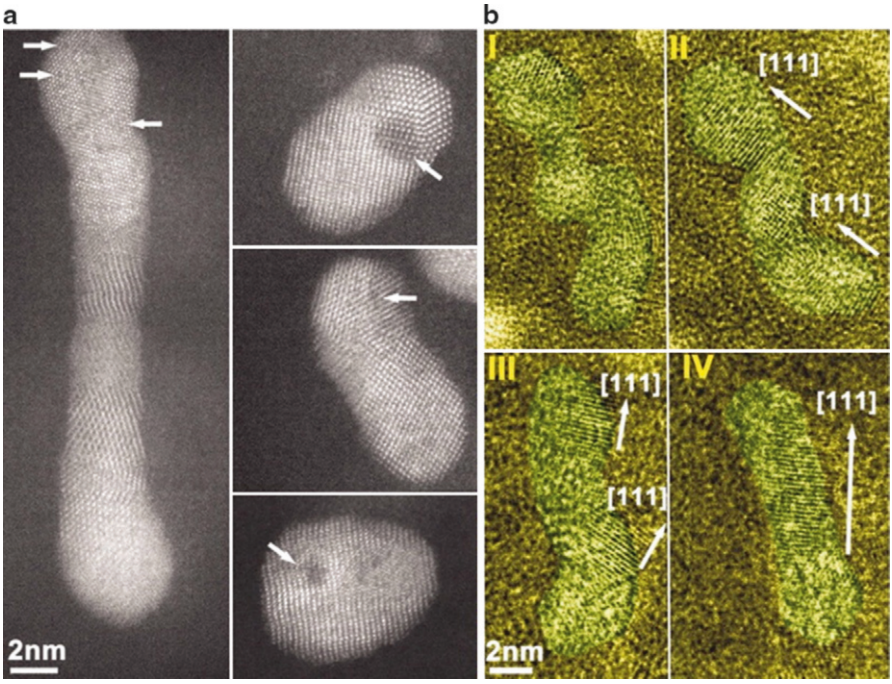


Fig. 5.18 HR-STEM images of Pt_3Fe nanorods undergoing dynamic reorientation within a liquid cell. (**a**) HAADF-TEM images of polycrystalline nanorods and particles. (**b**) Sequential (I–IV) HR-TEM images of a nanorod reorienting over time during oriented attachment. The final image shows the constituent nanoparticles aligned to form a continuous crystal lattice for the formed nanorods. (From *Science* 2012 336(6084): 1011–1014. Reprinted with permission from AAAS)

nanoparticle begins to drift toward the second particle or chain with increasing velocity [92].

Tungsten oxide nanowires have been grown via a vapor-solid mechanism and observed with in situ TEM [93]. The growth does not require environmental chamber or liquid cell since nanowire formation only requires heating of a tungsten filament and the residual oxygen present in the system. Temperature of the tungsten filament was controlled by Joule heating, and at ~873 K (and pressures lower than 10^{-6} Pa), tungsten oxide was observed to form on the filament surface. The nanowires, which grow from their bases at the filament-nanowire junction, do not seem to follow a VLS or VSS mechanism. There is no liquid or solid catalyst particle from which the wires grow. When viewed under HR-TEM, the $W_{18}O_{49}$ structure can be seen with the <010> direction apparent and no evidence catalytic particle on either end of the nanowire (Fig. 5.19). The $W_{18}O_{49}$ monoclinic structure is single crystalline, as is strikingly apparent with HR-TEM. Upon further heating to ~1,023 K and irradiation with the 200-keV electron beam, the $W_{18}O_{49}$ nanowires decomposed to bcc W and O_2 gas, as evidenced by electron diffraction and EDX [93].

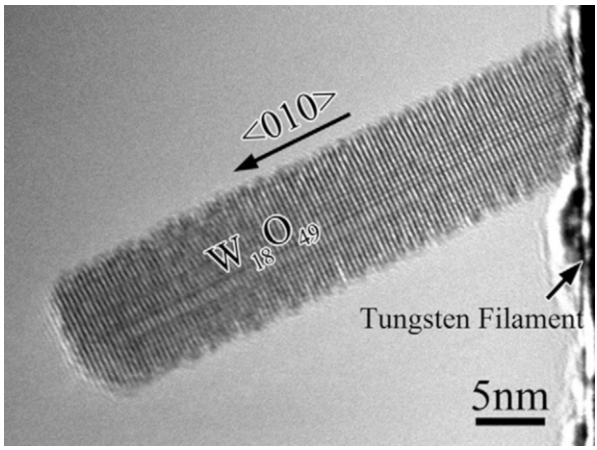


Fig. 5.19 High-resolution TEM shows that there is no liquid/solid catalyst nanoparticle present for the growth of a $W_{18}O_{49}$ nanowire. The single crystal growth direction away from the W filament is shown. (Reprinted with permission from *Nanotechnology* 20(28): 285604. Copyright 2009, IOP Publishing)

5.2.2 Heating Nanowires and In Situ TEM

Controlled heating of nanowires in situ may be accomplished by several means: heating with the electron beam [94, 95], Joule heating with a probe [96–99], by electrical pulsing of the nanowire [100], or by field emission [101] and using a heated stage [102, 103]. Structures under thermal stress may undergo structural changes [95, 96, 101], phase transformations [100, 102], dislocation or defect motion [100, 103], electrical changes [98, 100], and thermal breakdown of the structure beyond phase changes [97, 99]. Concurrent observation with in situ TEM provides a means to describe the effects of thermal strain on nanowires, providing necessary understanding about performance and stability of potential devices.

The electron beam in electron microscopy interacts with the sample being interrogated, and the beam can heat or otherwise damage samples. When ZnO-Al_2O_3 core-shell nanowires (synthesized ex situ) were heated to 600 °C in situ with the electron beam, the ZnO core melted, and the Al_2O_3 shell was crystallized but left behind [94]. Figure 5.20 shows several time-lapse images of the process (as well as a summary schematic of the melting). Over several minutes of heating, the ZnO core was disrupted, experienced phase transition, and was eliminated from the Al_2O_3 shell at an average rate of 4.2 nm/s. Additional analysis with HR-TEM and EDS showed that the Al_2O_3 shell was amorphous prior to heating, and it was crystalline after heating. According to EDS analyses, Zn was initially present in the core nanowire. After being heated and apparently draining from the shell, Zn was absent from the structure. The authors note that the Zn does not transfer into or through the Al_2O_3 shell via the Kirkendall effect because Zn was shown to be absent from the entire nanostructure [94].

Electrical pulsing of single crystalline VLS-grown $Ge_2Sb_2Te_5$ nanowires induces a change between a crystalline and amorphous state [100, 104]. The two states represent two different levels of resistivity in the material that can be used as nonvolatile memory. In the in situ electrical pulsing, the nanowires were assembled

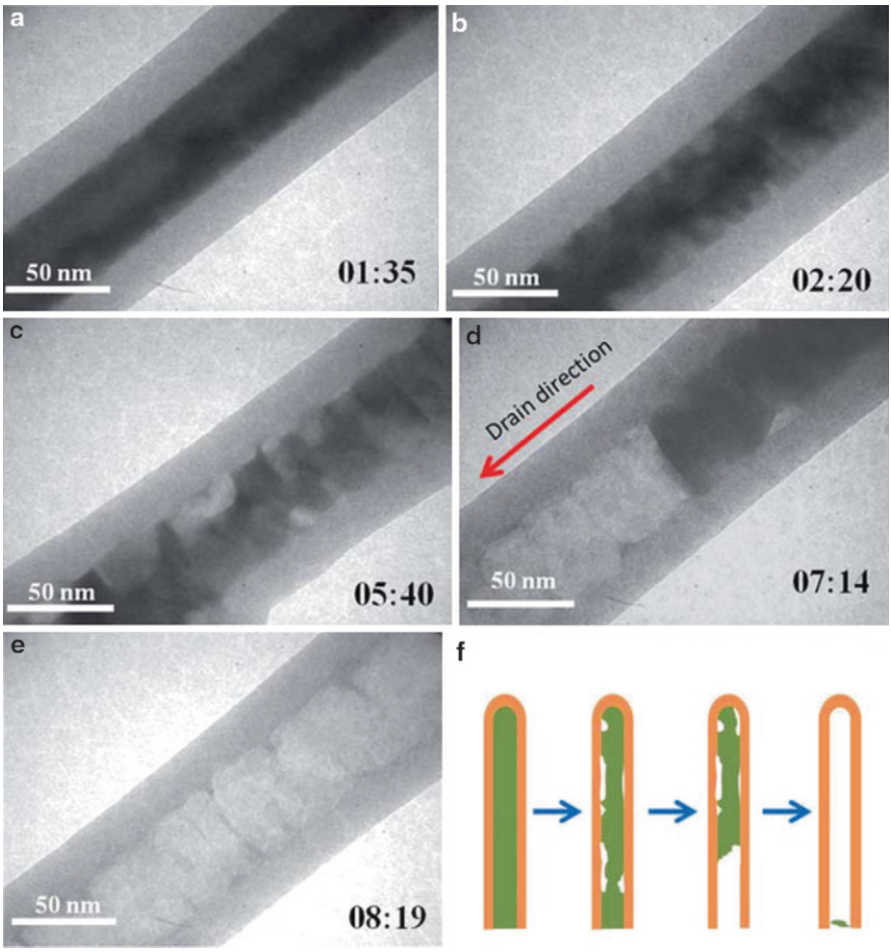


Fig. 5.20 A series of TEM images (extracted from video) of in situ heating of a ZnO-Al_2O_3 core-shell nanowire. The melting of ZnO occurred in images (**a**) through (**c**). The liquid ZnO drains from the nanotube in images (**d**) and (**e**), leaving a hollow Al_2O_3 nanotube. The schematic (**f**) summarizes the process. (Reproduced from *Nanoscale* 4(15): 4702–4706 with permission of The Royal Society of Chemistry, 2012)

to span 2-μm wide trenches on a silicon nitride membrane. The 100–1,000 ns pulses were increased in voltage with each pulse. The voltage pulses had an interval of ~0.5 s, and the resistance measurements were performed between each voltage pulse. The position of the structures in the TEM allowed for continuous plan view of the wire under interrogation. Because of the in situ TEM imaging, the resistance changes could be associated with changes in the crystalline state, the formation and movement of dislocations from the positive terminal to the negative terminal, the "jamming" or aggregation of dislocations, and the amorphization of the structure [100]. A relatively small decrease in resistance was measured prior to

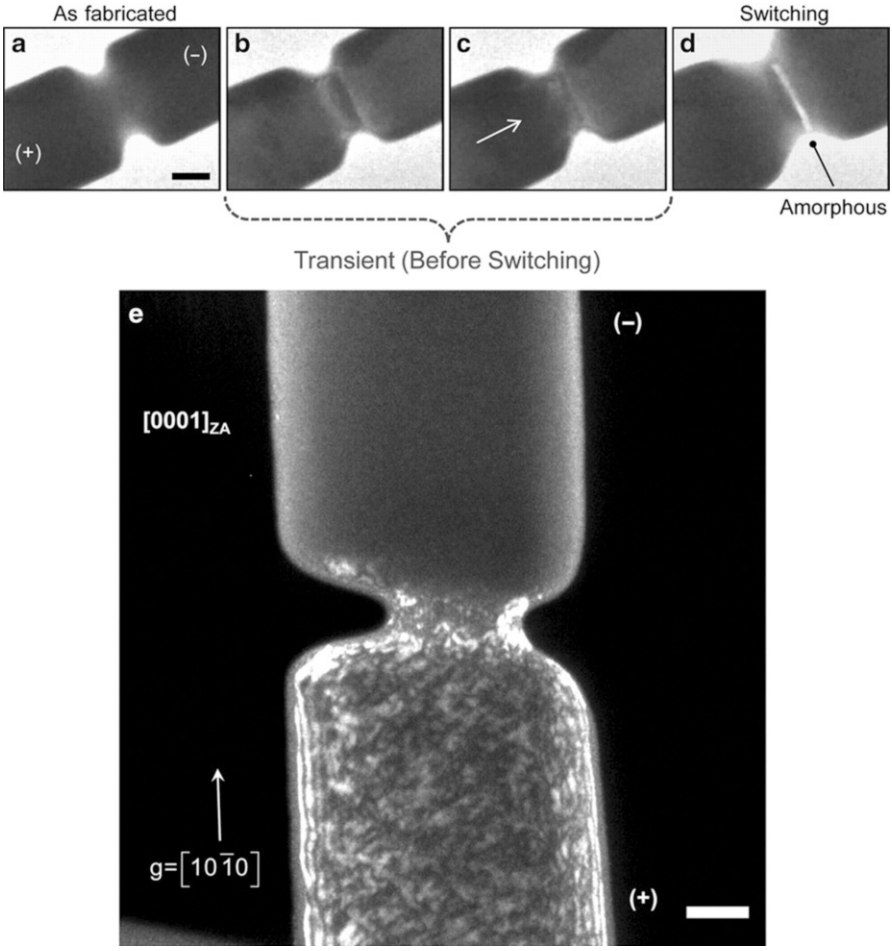


Fig. 5.21 TEM images of a notched $Ge_2Sb_2Te_5$ nanowire undergoing electrical switching in situ. Bright-field images (**a**–**d**, extracted from video) show the nanowire under applied bias. The *dark region* near the notch in (**b**) and (**c**) represent a region of strain. With continued application of voltage, the dark region switched (**d**) and became amorphous, as represented by the bright line near the notch. The dark-field image (**e**) shows the dislocation cloud present mostly at the (+) electrode side. Scale bars are 100 nm. (From *Science* 2012 336(6088): 1561–1566. Reprinted with permission from AAAS)

amorphization, whereupon device switching, a resistance increase of more than two orders of magnitude, was measured. In order to localize the phase change and to clearly image the switching, a notch was etched across the nanowire where it spanned the electrode gap [100, 104]. A thinned region of a nanowire bears increased current density and Joule heating during voltage pulses, and mobile dislocations cannot easily pass through the restricted geometry of the notch. As seen in Fig. 5.21, the notched nanowire is visually uniform in its as-fabricated state.

As the voltage pulses were applied, the strained region, seen as a darkening of the wire, appeared near the notch as dislocations were formed and flowed from the positive to the negative end of the wire. In the dark-field image acquired just before switching, the aggregation of most dislocations on the positive side of the notch is apparent from the mottled contrast of the nanowire. It should be noted that the notch is not necessary for this sequence of events to occur; it served to localize and highlight the changes. Device properties can be explored and explained with in situ TEM, and, as stated by the authors, other configurations, such as polycrystalline thin film devices, could operate in a similar fashion [100].

Joule heating has been performed in situ with an STM-TEM probe in which individual CdTe nanowires were attached to a gold nanowire on one end and to an STM tip on the other [96]. A completed circuit was formed because the Au nanowire, attached to a movable piezotube, could be moved to contact the CdTe nanowire to the STM tip. Voltage applied through the STM tip generated the Joule heating in the CdTe nanowire, and the TEM imaging was performed in real time to observe the nanowire's physical changes upon heating. The maximum temperature was likely to be at the STM tip-CdTe nanowire junction, and the authors estimate it to be 1,050 K when 15 V is applied for 15 min. The temperature experienced by the nanowire would decrease along the nanowire length, further from the STM tip. The structural changes are shown in Fig. 5.22. Before the bias was applied, the sides of the nanowires were smooth (Fig. 5.22a). After the bias was applied (15 V, 25 min), the nanowire developed bumps (Fig. 5.22b), and the portion of the nanowire closest to the STM tip was even more damaged (Fig. 5.22c). Approximately 400 nm away from the STM tip (Fig. 5.22b), the nanowire structure appears mostly intact despite the secondary structure formations on its surface. Closer to the nanowire tip, the secondary structures are more pronounced, and the overall nanowire diameter is inconsistent, narrowing considerably from its original diameter of 37 nm. For CdTe with larger initial diameters, superfine nanowires can form on the surface with Joule heating due to similar structural changes. With more narrow nanowires, like the one shown, the structural changes result in disintegration of the nanowire before the superfine structures are able to form [96].

5.2.3 Scanning Probe Techniques and In Situ TEM for Mechanical and Electrical Characterization of Nanowires and Nanorods

Crystalline-amorphous transitions [100], mechanical contact cold welding [105], structural deformations [11, 106, 107], and material failures [10, 107] can be observed with scanning probe techniques combined with TEM. With the in situ technique, displacement or transition forces may be measured as electrical measurements are made with concurrent TEM imaging of the nanowires. Alternatively, the electrical properties of individual nanowires may be measured as a function of nanowire properties, such as dimension [10] or crystal orientation at the contact point [108]. Just as thermal stress may cause changes in electrical properties of nanowires, so too may mechanical strain. The real-time application of force and TEM imaging provides a view of individual nanowires and may lead to additional understanding of the origins of the electronic and mechanical properties of

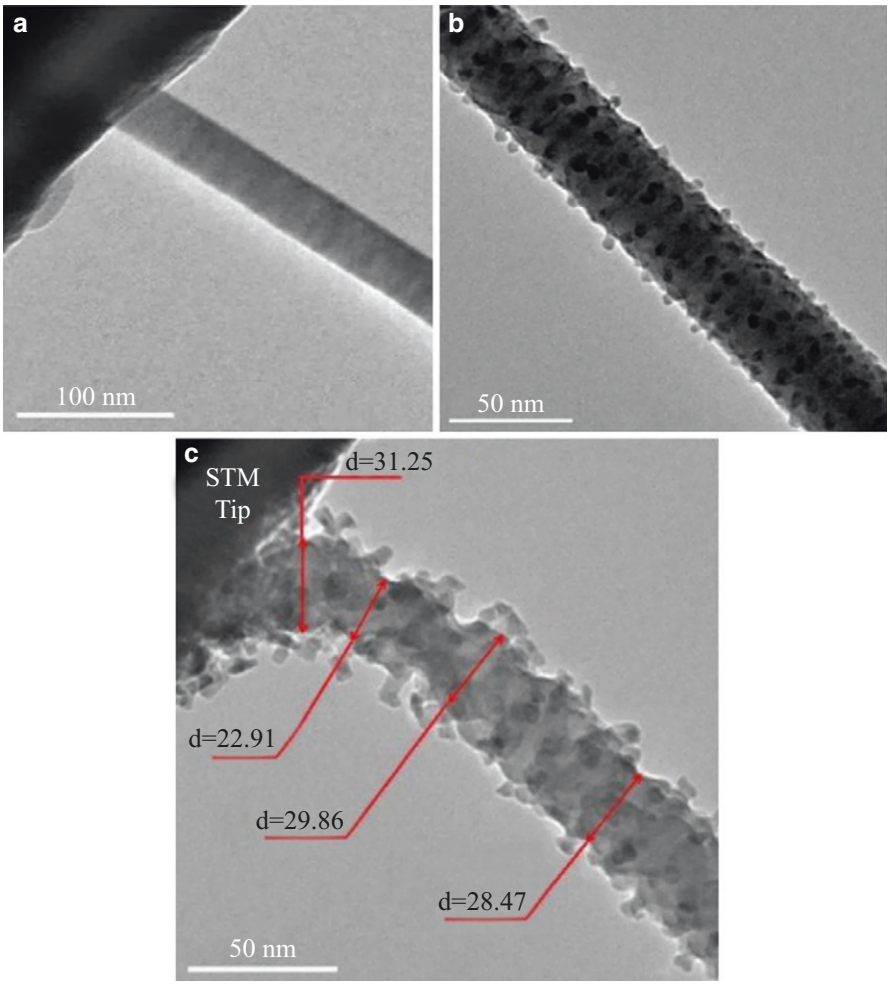


Fig. 5.22 In situ TEM images of a CdTe nanowire under an applied bias of 15 V. Before the bias was applied (**a**), the nanowire was smooth with a diameter of 37 nm. After 25 min of 15 V applied via the STM tip, damage was evident 400 nm away from the STM tip (b). Close to the STM tip, the damage was more severe (**c**, after 22 min of 15 V). (Reprinted with permission from *Nanotechnology* 22(43): 435204. Copyright 2011, IOP Publishing)

nanowires. In turn, this understanding could lead to more efficient design of nanowires for particular applications.

Zinc oxide is a semiconducting piezoelectric material that may be of use in applications related to sensors and transducers [109–111]. Because of properties that may make ZnO nanowires power sources or actuators for nanotechnology-based devices, the scaling of mechanical properties and the effect of loading-unloading cycles on the ZnO structure is of interest [107]. These properties have been investigated with in situ TEM outfitted with atomic force microscopy and nanoindentation

systems. With these combined techniques, the Young's modulus of various diameters of ZnO nanowires has been measured along with the changes in crystal structure resulting from the loading-unloading cycles. The authors determined a size dependence of Young's modulus for nanowires with diameters (d) 40 nm $\leq$ d $\leq$ 110 nm with the maximum value of ~249 GPa for the nanowires with the narrowest diameters. For nanowires in the range 200 nm $\leq$ d $\leq$ 400 nm, the above trend was not observed, and values similar to those of bulk ZnO were measured. In descriptive terms, nanowires with d $\geq$ 200 nm were brittle, and an example of a fractured 300-nm nanowire described with TEM images and force versus displacement measurements provided a critical force for fracture of ~250 μN. These properties along with the measured values for Young's modulus are due to effects of the surface relaxation and crystalline interactions within the nanowire material. Those with d $\leq$ 110 nm are flexible: a series of TEM images obtained during displacement shows a single crystalline 40-nm wire as it experiences bending due to force applied by an AFM tip. The bending generates distortion in the lattice which appears as changing contrast in the bright-field images. If the nanowire is released before it buckles, it is able to revert to a relaxed state. When the displacement on the nanowire generates a force of ~100 nN, a sharp drop in the measured force is observed due to buckling of the nanowire. A flexible nanowire that was subjected to several non-buckling loading-unloading cycles showed no changes in the internal crystalline structure when analyzed with HR-TEM. In a buckled flexible wire, the regions of compression (as noted by changes in contrast and the physical bending of the wire) show amorphization in HR-TEM (Fig. 5.23). The surrounding crystalline lattice is slightly distorted but intact [107].

When TEM is combined with STM, the spatial and mechanical control of the scanning probe is combined with electrical measurement capability [105, 108]. Cold welding, or the process by which solid material is joined together without the melting due to heat, can be performed to join together gold nanowires. Two types of anistropic gold have been cold-welded together: nanorods with dimensions ~5–10 nm by ~10–50 nm and ultrathin nanowires 3–9 nm by ~1 μm [105]. The nanorods, which were stationary, were approached by nanorods or nanowires either head-to-head or side-by-side with the STM piezoelectric controls. The two approach configurations are shown schematically in Fig. 5.24a, b, and a TEM image of the head-to-head approach is shown in Fig. 5.24c. With contact between nanowires, the surfaces were observed to bond together within ~1.5 s. Continuous observation with TEM showed the joined structure evolved for several seconds after cold welding, and the welding was most successful when the crystal orientations of the joining pieces matched (similar to the oriented attachment mechanism for nanowire growth described earlier). Increased contrast uniformity and surface smoothness suggest changes in the internal crystal structure of the joined nanowire. After the apparent stabilization of the joint, the STM tip could be withdrawn along the path of its approach, and the nanowire would remain as a free-standing structure, as shown in Fig. 5.25. When longer nanowires were used to approach nanorods, the longer structures often buckled although the cold welding aspect was found to be successful. The side-to-side approach required

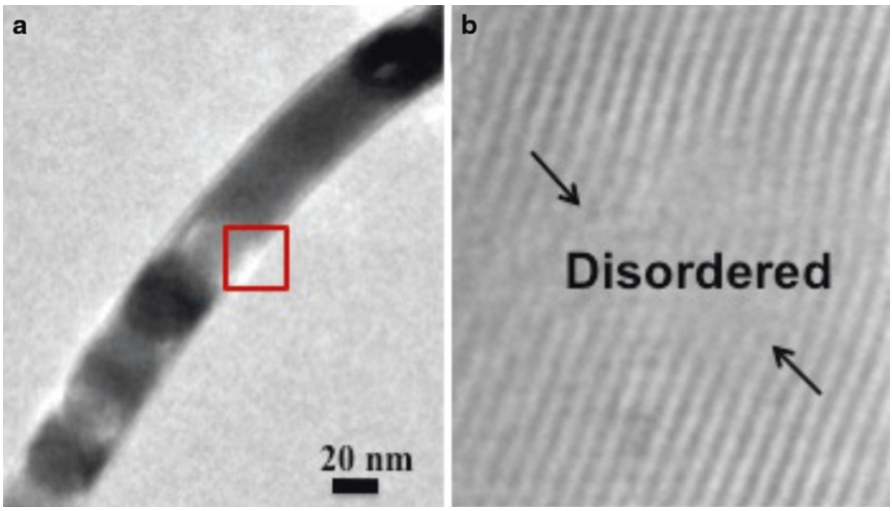


Fig. 5.23 In situ TEM (**a**) and HR-TEM (**b**) images of a ZnO nanowire experiencing physical bending stress in situ. The region *highlighted* in (**a**) is shown in high resolution in (**b**). The amorphous region was formed in response to the applied force and surrounded by slightly distorted lattice planes. (Reprinted with permission from *Nanotechnology* 22(26): 265712. Copyright 2011, IOP Publishing)

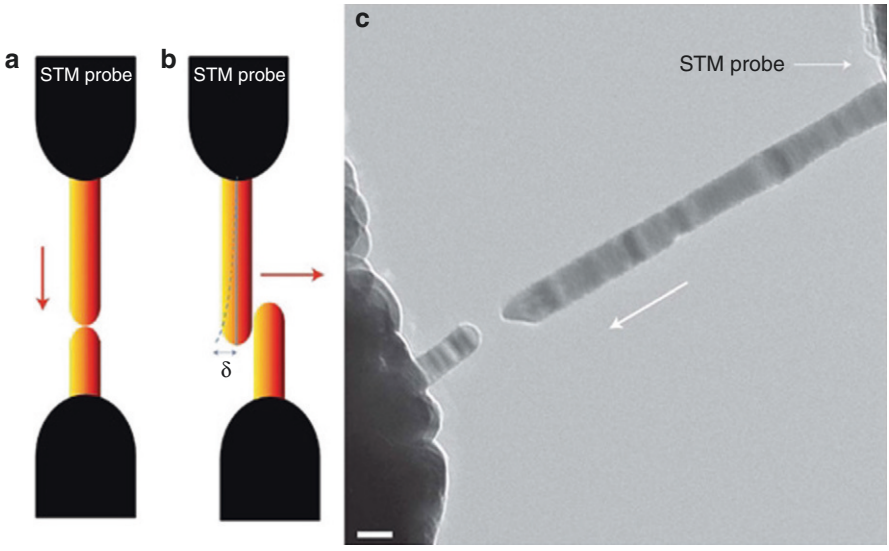


Fig. 5.24 In situ STM for contacting nanorods/nanowires for cold welding, nanowire breaking, and electrical measurements. The head-to-head and side-to-side approaches are shown schematically in (**a**) and (**b**), respectively. A bright-field TEM image of a gold nanowire approaching a gold nanorod is shown in (**c**). Scale bar = 10 nm. (Reprinted by permission from Macmillan Publishers Ltd: *Nat Nanotechnol* 5(3):218–224, Copyright 2010)

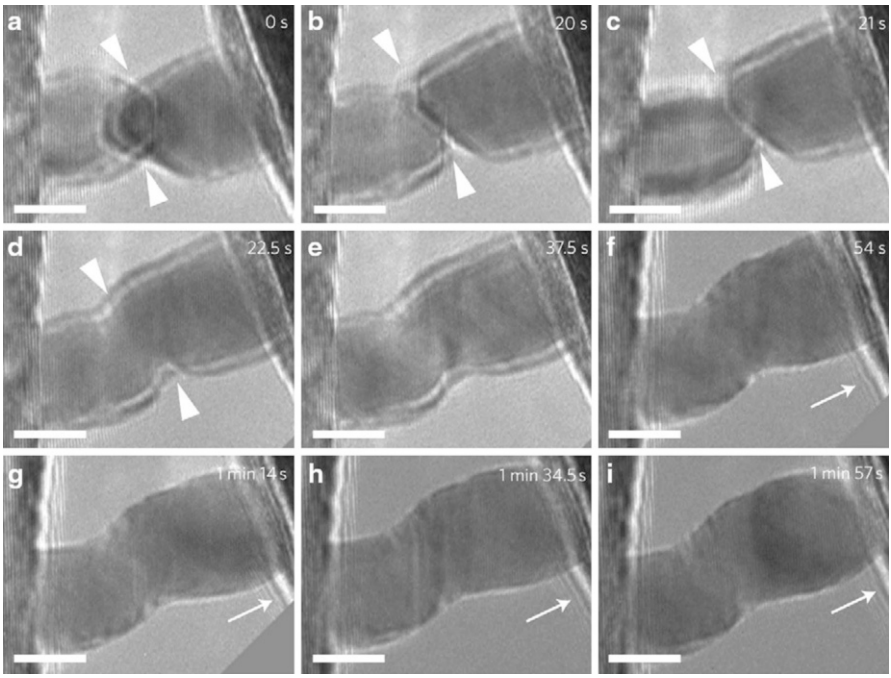


Fig. 5.25 A sequence of TEM images obtained during head-to-head cold welding of gold nanorods. The nanorod on the right is shown approaching the stationary nanorod on the left (**a**, **b**). Contact between the nanorods was maintained (**c**–**e**) with the arrow heads highlighting the contact region. Welding was completed in ~1.5 s (**c**, **d**), and the structure was allowed to relax for several seconds (**d**, **e**). The STM probe was withdrawn along the path of original approach, as indicated by the arrow (**f**–**i**). With the complete withdrawal of the STM probe, the welded nanorod was left as a free-standing structure. Scale bar = 5 nm. (Reprinted by permission from Macmillan Publishers Ltd: *Nat Nanotechnol* 5(3):218–224, Copyright 2010)

less precise alignment of the approaching nanostructures, and it was also successful in cold welding nanorods and nanowires. After welding in either configuration, the STM tip could be retracted to qualitatively test the strength of the weld, and the authors found that the welded wires would break in areas other than those recently joined [105].

With the control and electrical capabilities of the STM probe, the resistivities of the as-synthesized and broken-welded nanowires were measured [105]. The current–voltage response was tested for a nanowire (~7 × ~130 nm) with an applied bias of −1 to +1 mV. The average resistivity for nine measurements was 292.6 ± 5.8 Ω nm. The same nanowire was then subjected to several break-weld cycles with multiple resistivity measurements for each cycle. The nanowire broke in several different places and was welded back together in both head-on and side-on configurations. The average resistivity for the broken-welded nanowire was 298.1 ± 14.5 Ω nm, indicating that the quality of the weld (or several welds)

was electrically the same as the original nanowire. In addition, measurements of tensile strength were performed on the as-synthesized and welded nanowires by measuring the deflection of an AFM cantilever. Again, as-synthesized nanowires were tested against the same nanowires after they were welded back together. The tensile strength of the as-synthesized nanowires was found to be 600 ± 50 MPa. The side-to-side configuration was used for the tensile strength welding, and the breaking point was often found in an area other than the freshly welded region. The tensile strength for the welded wires was measured as 580 ± 40 MPa – again within measurement error of the as-synthesized nanowires [105]. The reliable electrical and mechanical properties of joined nanowires will certainly be important in developing technologies using nanostructures.

5.2.4 In Situ TEM Electrochemistry

As nanomaterials are integrated into batteries or other electrochemistry-based devices, the effects of charging-discharging on the nanomaterials will need to be understood. In situ observations of charging and discharging battery materials are necessary to explain how compositional and structural changes affect the performance of battery materials and to help design new generations of batteries [112]. Si nanomaterials [113], Si nanowires [114], and cobalt oxide nanowires [115] have been used as electrodes in lithium-ion batteries. While TEM analysis has been important for characterizing the nanomaterials, usually electrochemistry and electron microscopy have been performed separately. In situ TEM of electrochemical reactions of interest for applications in lithium ion batteries have been performed on individual nanowires, including those made of tin oxide [12, 112], silicon [13, 116], germanium [13], zinc oxide [13], and aluminum-aluminum oxide (core-shell) [13, 117]. In situ electrochemistry allows for the dynamic observation and characterization of electrode materials experiencing charging, and ex situ observations can be confirmed.

When tin oxide nanowires are used as the anode for a lithium ion battery, the tin oxide experiences lithation under charging [12, 112]. The chemical change is accompanied by striking structural changes as a "Medusa zone" of mobile dislocations lengthens, twists, and widens the nanowires [12]. As seen in Fig. 5.26, the progress of charging from 0 to 1860 s resulted in structural distortions of the original smooth, straight nanowire. As shown schematically in Fig. 5.26a, the ionic liquid electrolyte was contacted to the nanowire from the $LiCoO_2$ cathode side, and the ionic liquid is shown to wet the nanowire in the TEM images. An applied potential of −3.5 V (relative to the $LiCoO_2$ cathode) drove the electrochemical reaction, and it was shown to proceed from the cathode side to the anode side, as the nanowire was continuously distorted due to the lithation of the nanowire and the mobile zone of dislocations, as marked with a small *arrow* in several of the TEM images (Fig. 5.26e–s). After the entire nanowire was affected by the charging, the authors measured a 90 % lengthening and a diameter expansion of 35 %, giving a total volume increase of 250 % (original dimensions: 107 nm diameter, 14 μm length) [12]. Long-term exposure to the electron beam caused some of the ionic liquid electrolyte to gel on the nanowire, as seen in Fig. 5.26o in particular.

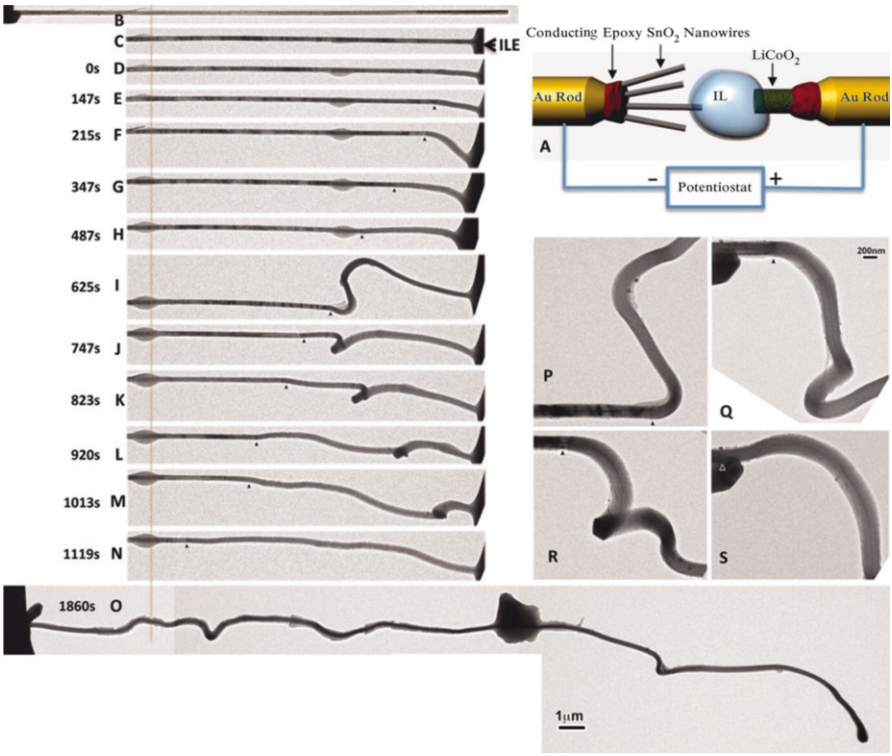


Fig. 5.26 A sequence of TEM images obtained during electrochemical lithation of a SnO_2 nanowire. The lithation grossly altered the original nanowire structure as the reaction progressed in time (**c**–**s**). A schematic of the in situ electrochemical cell is shown in (**a**) [12]

Further analysis of the crystallinity and the composition revealed that the originally crystalline SnO_2 nanowire was converted to Sn, Li, and Li_2O. With sufficient negative potential, the SnO_2 nanowire may be electrochemically reduced and converted to nanocrystalline Li_xSn and Sn particles scattered in amorphous Li_2O. The overall amorphous Li_2O matrix can be observed to travel along the wire as the dislocation cloud progresses. The presence of lithium may also be detected and quantified as the reaction proceeds along the nanowire length. Similar work with larger SnO_2 nanowires with ionic liquid electrolyte for in situ lithation reactions produced different structural changes under otherwise similar conditions [112]. After lithation, the SnO_2 was not detected, but nodules of Li_xSn_y were detected along with lithium oxide, as seen in Fig. 5.27. It should be expected that the much thinner nanowires described above (107 nm vs. >1 μm diameters) would experience more profound changes in overall structure due to amorphization and a progressing front of dislocations. Similar structural changes as well as analogous chemical changes have been seen with other nanowires tested in situ, including Si [13, 116], Ge [13], ZnO [13], and Al-Al_2O_3 [13, 117].

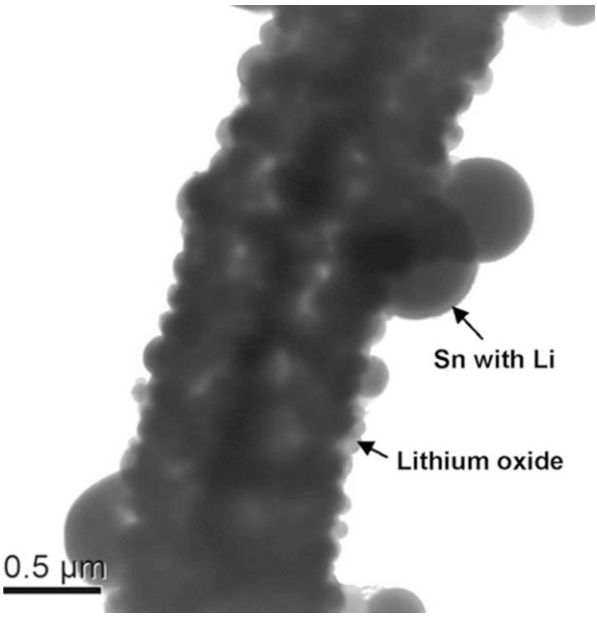


Fig. 5.27 A bright-field TEM image of a SnO_2 nanowire after lithation. Lithation produced structural and compositional changes, although not so pronounced as those in the previous case. (Reproduced with permission from *J Mater Res* 25(8): 1541–1547. Copyright 2010, Cambridge University Press)

6 Conclusions and Future Perspectives

As applications for nanowires (and other nanomaterials) are developed and as synthetic methods to obtain them are pursued, transmission electron microscopy and related in situ techniques will be developed to provide new information. Developing capabilities for analysis will certainly inspire researchers to ask new questions and then seek the answers. Contemporary limitations in in situ TEM analysis [7] can provide some insight into where additional work is required. When describing some of the current limitations of in situ TEM, Sharma mentions the rate of image acquisition (~1/30 s) and energy dispersive x-ray spectroscopy (~20 s) as restricting the reaction kinetics that may be evaluated with TEM and related in situ techniques [7]. Cameras and detectors that are more sensitive or have faster response rates may provide insight into processes or steps of processes that are currently unobservable with TEM-based techniques.

TEM imaging of nanomaterials undergoing electrochemical processes related to nanowires in miniaturized lithium-ion batteries seem to be focused on using ionic liquid electrolytes [112]. There are practical reasons for using the ionic liquid electrolytes – the high vapor pressure and likely the relative ease of manipulating the STM to contact a droplet. In situ TEM imaging through solid state or polymer gel electrolyte in nanowire-based lithium-ion batteries would likely provide relevant data to researchers in energy storage nanotechnology [112, 118, 119]. Indeed, it seems that other electrochemical reactions involving nanomaterials could be of

interest if in situ electrochemistry could be performed within a liquid cell or with solid state/gel electrolyte.

Liquid cells and TEM imaging will likely provide new arenas for investigation at the intersection of nanotechnology and biology, particularly with recent success in imaging live, hydrated yeast cells [120] and cells as they interacted with Au nanoparticles [121]. Nanowires and other nanomaterials interacting with living cells have possible uses in medical, environmental, and biotechnological applications. TEM coupled with electrochemical sensing or interaction with live cells may prove to be of interest as well.

Magnetic nanowires are of current interest for memory devices [122]. Lorentz transmission electron microscopy can be used to image magnetic domains and observe changes in magnetic state in situ as a function of temperature or applied magnetic field [123, 124]. Lorentz TEM in situ imaging has been used to characterize the magnetic behavior in "top down" patterned magnetic nanowires [125–130]. Nanowires, nanowire arrays, and other nanomaterials may be characterized by magnetic force microscopy, a scanning probe technique analogous to AFM and STM for the evaluation of nanomaterials and surfaces [131–133]. The resolution of Lorentz TEM has been limited to 5–10 nm [124], which may make it relatively unappealing, although work to improve resolution and develop techniques to allow for three-dimensional reconstruction of magnetic nanomaterials is ongoing [134, 135]. Perhaps with improved resolution, synthesized magnetic nanowires will join engineered nanowires as being characterized with Lorentz TEM.

Acknowledgments Sarah K. St. Angelo acknowledges support from the Dickinson College Research & Development Committee.

References

1. Nellist P, Chisholm M, Dellby N, Krivanek O, Murfitt M, Szilagyi Z, Lupini A, Borisevich A, Sides W, Pennycook S (2004) Direct sub-angstrom imaging of a crystal lattice. Science 305(5691):1741–1741
2. Stach EA (2008) Real-time observations with electron microscopy. Mater Today 11:50–58
3. Borisevich A, Lupini A, Pennycook S (2006) Depth sectioning with the aberration-corrected scanning transmission electron microscope. Proc Natl Acad Sci USA 103(9):3044–3048
4. Sharma R, Weiss K (1998) Development of a TEM to study in situ structural and chemical changes at an atomic level during gas-solid interactions at elevated temperatures. Microsc Res Tech 42(4):270–280
5. Sharma R (2005) An environmental transmission electron microscope for in situ synthesis and characterization of nanomaterials. J Mater Res 20(7):1695–1707
6. Sharma R (2009) Kinetic measurements from in situ TEM observations. Microsc Res Tech 72(3):144–152
7. Sharma R (2012) Experimental set up for in situ transmission electron microscopy observations of chemical processes. Micron 43(11):1147–1155
8. de Jonge N, Ross FM (2011) Electron microscopy of specimens in liquid. Nat Nanotechnol 6(11):695–704
9. Murray CB (2009) Watching nanocrystals grow. Science 324(5932):1276–1277

10. Erts D, Polyakov B, Lohmus A, Lohmus R, Olin H, Morris M, Holmes J (2003) Metallic and semiconducting nanowires studied by TEM-SPM. Phys Low-Dimens Struct 3–4:65–73
11. Pokropivny A, Erts D, Pokropivny V, Lohmus A, Lohmus R, Olin H (2004) Study of nanoscale contacts with the help of combined TEM-AFM technique and theoretical MD-TM calculations: in situ transformations of gold nanowires. Phys Low-Dimens Struct 1–2:83–90
12. Huang JY, Zhong L, Wang CM, Sullivan JP, Xu W, Zhang LQ, Mao SX, Hudak NS, Liu XH, Subramanian A, Fan H, Qi L, Kushima A, Li J (2010) In situ observation of the electrochemical lithiation of a single SnO_2 nanowire electrode. Science 330(6010):1515–1520
13. Liu XH, Liu Y, Kushima A, Zhang S, Zhu T, Li J, Huang JY (2012) In situ TEM experiments of electrochemical lithiation and delithiation of individual nanostructures. Adv Energy Mater 2(7):722–741
14. Wu Y, Yang P (2001) Direct observation of vapor-liquid-solid nanowire growth. J Am Chem Soc 123(13):3165–3166
15. Nichols PL, Sun M, Ning C (2011) Influence of supersaturation and spontaneous catalyst formation on the growth of PbS wires: toward a unified understanding of growth modes. ACS Nano 5(11):8730–8738
16. Morales A, Lieber C (1998) A laser ablation method for the synthesis of crystalline semiconductor nanowires. Science 279(5348):208–211
17. Morber JR, Ding Y, Haluska MS, Li Y, Liu P, Wang ZL, Snyder RL (2006) PLD-assisted VLS growth of aligned ferrite nanorods, nanowires, and nanobelts-synthesis, and properties. J Phys Chem B 110(43):21672–21679
18. Kast M, Schroeder P, Hyun YJ, Pongratz P, Brueckl H (2007) Synthesis of single-crystalline Zn metal nanowires utilizing cold-wall physical vapor deposition. Nano Lett 7(8):2540–2544
19. Xie X, Li Y, Liu Z, Haruta M, Shen W (2009) Low-temperature oxidation of CO catalysed by Co_3O_4 nanorods. Nature 458(7239):746–749
20. Chen Z, Waje M, Li W, Yan Y (2007) Supportless Pt and PtPd nanotubes as electrocatalysts for oxygen-reduction reactions. Angew Chem Int Ed 46(22):4060–4063
21. Zhang X, Li D, Dong D, Wang H, Webley PA (2010) One-step fabrication of ordered Pt-Cu alloy nanotube arrays for ethanol electrooxidation. Mater Lett 64(10):1169–1172
22. Alia SM, Zhang G, Kisailus D, Li D, Gu S, Jensen K, Yan Y (2010) Porous platinum nanotubes for oxygen reduction and methanol oxidation reactions. Adv Funct Mater 20(21):3742–3746
23. Guo S, Dong S, Wang E (2010) Pt/Pd bimetallic nanotubes with petal-like surfaces for enhanced catalytic activity and stability towards ethanol electrooxidation. Energy Environ Sci 3(9):1307–1310
24. Gu X, Cong X, Ding Y (2010) Platinum-decorated Au porous nanotubes as highly efficient catalysts for formic acid electro-oxidation. Chemphyschem 11(4):841–846
25. Cui C, Li H, Yu S (2011) Large scale restructuring of porous Pt-Ni nanoparticle tubes for methanol oxidation: a highly reactive, stable, and restorable fuel cell catalyst. Chem Sci 2(8):1611–1614
26. Ci S, Zou J, Zeng G, Luo S, Wen Z (2012) Single crystalline Pt nanotubes with superior electrocatalytic stability. J Mater Chem 22(33):16732–16737
27. Li H, Cui C, Zhao S, Yao H, Gao M, Fan F, Yu S (2012) Mixed-PtPd-shell PtPdCu nanoparticle nanotubes templated from copper nanowires as efficient and highly durable electrocatalysts. Adv Energy Mater 2(10):1182–1187
28. Alia SM, Jensen KO, Pivovar BS, Yan Y (2012) Platinum-coated palladium nanotubes as oxygen reduction reaction electrocatalysts. ACS Catal 2(5):858–863
29. Ding L, Wang A, Li G, Liu Z, Zhao W, Su C, Tong Y (2012) Porous Pt-Ni-P composite nanotube arrays: highly electroactive and durable catalysts for methanol electrooxidation. J Am Chem Soc 134(13):5730–5733
30. Choi B, Lee YW, Kang SW, Hong JW, Kim J, Park I, Han SW (2012) Multimetallic alloy nanotubes with nanoporous framework. ACS Nano 6(6):5659–5667

31. Lazar F, Morin A, Pauc N, Gentile P, Donet S, Guetaz L, Sicardy O (2012) Supported platinum nanotubes array as new fuel cell electrode architecture. Electrochim Acta 78:98–108
32. Meng F, Jin S (2012) The solution growth of copper nanowires and nanotubes is driven by screw dislocations. Nano Lett 12(1):234–239
33. Gorzny ML, Walton AS, Evans SD (2010) Synthesis of high-surface-area platinum nanotubes using a viral template. Adv Funct Mater 20(8):1295–1300
34. Mohl M, Dobo D, Kukovecz A, Konya Z, Kordas K, Wei J, Vajtai R, Ajayan PM (2011) Formation of CuPd and CuPt bimetallic nanotubes by galvanic replacement reaction. J Phys Chem C 115(19):9403–9409
35. Mor G, Shankar K, Paulose M, Varghese O, Grimes C (2006) Use of highly-ordered TiO_2 nanotube arrays in dye-sensitized solar cells. Nano Lett 6(2):215–218
36. Khan M, Jung H, Yang O (2006) Synthesis and characterization of ultrahigh crystalline TiO_2 nanotubes. J Phys Chem B 110(13):6626–6630
37. Jennings JR, Ghicov A, Peter LM, Schmuki P, Walker AB (2008) Dye-sensitized solar cells based on oriented TiO_2 nanotube arrays: transport, trapping, and transfer of electrons. J Am Chem Soc 130(40):13364–13372
38. Ratanatawanate C, Xiong C, Balkus KJ Jr (2008) Fabrication of PbS quantum dot doped TiO_2 nanotubes. ACS Nano 2(8):1682–1688
39. Guerrero S, Di Serio M, Li RF, Wolf EE (2009) Parallel reactor activity studies of the preferential oxidation of CO on transition metals supported on TiO_2 and TiO_2 nanotubes. Catal Lett 130(1–2):19–27
40. Goldberger J, He R, Zhang Y, Lee S, Yan H, Choi H, Yang P (2003) Single-crystal gallium nitride nanotubes. Nature 422(6932):599–602
41. Ai L, Jiang J (2012) Self-sacrificial templating synthesis of porous quaternary Cu-Fe-Sn-S semiconductor nanotubes via microwave irradiation. Nanotechnology 23(49):495601
42. Rao C, Govindaraj A, Deepak F, Gunari N, Nath M (2001) Surfactant-assisted synthesis of semiconductor nanotubes and nanowires. Appl Phys Lett 78(13):1853–1855
43. Wang X, Gao P, Li J, Summers C, Wang Z (2002) Rectangular porous ZnO-ZnS nanocables and ZnS nanotubes. Adv Mater 14(23):1732–+
44. Sun Y, Mayers B, Xia Y (2003) Metal nanostructures with hollow interiors. Adv Mater 15(7–8):641–646
45. Sun YG, Mayers B, Xia YN (2003) Transformation of silver nanospheres into nanobelts and triangular nanoplates through a thermal process. Nano Lett 3(5):675–679
46. Sun Y, Xia Y (2004) Mechanistic study on the replacement reaction between silver nanostructures and chloroauric acid in aqueous medium. J Am Chem Soc 126(12): 3892–3901
47. Sun Y, Wiley B, Li Z, Xia Y (2004) Synthesis and optical properties of nanorattles and multiple-walled nanoshells/nanotubes made of metal alloys. J Am Chem Soc 126(30):9399–9406
48. Dai G, Yu J, Liu G (2011) Synthesis and enhanced visible-light photoelectrocatalytic activity of p-n junction BiOI/TiO2 nanotube arrays. J Phys Chem C 115(15):7339–7346
49. Zeng H (2006) Synthetic architecture of interior space for inorganic nanostructures. J Mater Chem 16(7):649–662
50. Fan HJ, Goesele U, Zacharias M (2007) Formation of nanotubes and hollow nanoparticles based on Kirkendall and diffusion processes: a review. Small 3(10):1660–1671
51. Smigelskas AD, Kirkendall EO (1947) Zinc diffusion in alpha brass. Trans AIME 171:130–142
52. Yin Y, Rioux R, Erdonmez C, Hughes S, Somorjai G, Alivisatos A (2004) Formation of hollow nanocrystals through the nanoscale Kirkendall effect. Science 304(5671):711–714
53. Du N, Zhang H, Chen B, Ma X, Yang D (2008) One-pot, large-scale synthesis of SnO_2 nanotubes at room temperature. Chem Commun 26:3028–3030
54. Chen G, Sun S, Sun X, Fan W, You T (2009) Formation of CeO_2 nanotubes from Ce(OH) CO_3 nanorods through Kirkendall diffusion. Inorg Chem 48(4):1334–1338

55. Sreeprasad TS, Pradeep T (2011) Tubular nanostructures of $Cr_2Te_4O_{11}$ and Mn_2TeO_6 through room-temperature chemical transformations of tellurium nanowires. J Phys Chem C 115(33):16524–16536
56. Fan HJ, Knez M, Scholz R, Nielsch K, Pippel E, Hesse D, Zacharias M, Goesele U (2006) Monocrystalline spinel nanotube fabrication based on the Kirkendall effect. Nat Mater 5(8):627–631
57. Cayron C, Den Hertog M, Latu-Romain L, Mouchet C, Secouard C, Rouviere J, Rouviere E, Simonato J (2009) Odd electron diffraction patterns in silicon nanowires and silicon thin films explained by microtwins and nanotwins. J Appl Crystallogr 42:242–252
58. den Hertog MI, Cayron C, Gentile P, Dhalluin F, Oehler F, Baron T, Rouviere JL (2012) Hidden defects in silicon nanowires. Nanotechnology 23(2):025701
59. Lopez FJ, Givan U, Connell JG, Lauhon LJ (2011) Silicon nanowire polytypes: identification by Raman spectroscopy, generation mechanism, and misfit strain in homostructures. ACS Nano 5(11):8958–8966
60. Hemesath ER, Schreiber DK, Kisielowski CF, Petford-Long AK, Lauhon LJ (2012) Atomic structural analysis of nanowire defects and polytypes enabled through cross-sectional lattice imaging. Small 8(11):1717–1724
61. Koren E, Hyun JK, Givan U, Hemesath ER, Lauhon LJ, Rosenwaks Y (2011) Obtaining uniform dopant distributions in VLS-grown Si nanowires. Nano Lett 11(1):183–187
62. Allen JE, Hemesath ER, Perea DE, Lensch-Falk JL, Li ZY, Yin F, Gass MH, Wang P, Bleloch AL, Palmer RE, Lauhon LJ (2008) High-resolution detection of Au catalyst atoms in Si nanowires. Nat Nanotechnol 3(3):168–173
63. Perea DE, Hemesath ER, Schwalbach EJ, Lensch-Falk JL, Voorhees PW, Lauhon LJ (2009) Direct measurement of dopant distribution in an individual vapour-liquid-solid nanowire. Nat Nanotechnol 4(5):315–319
64. Hemesath ER, Schreiber DK, Gulsoy EB, Kisielowski CF, Petford-Long AK, Voorhees PW, Lauhon LJ (2012) Catalyst incorporation at defects during nanowire growth. Nano Lett 12(1):167–171
65. Liu HH, Schmidt S, Poulsen HF, Godfrey A, Liu ZQ, Sharon JA, Huang X (2011) Three-dimensional orientation mapping in the transmission electron microscope. Science 332(6031):833–834
66. Alivisatos A (2000) Biomineralization – naturally aligned nanocrystals. Science 289(5480):736–737
67. Pacholski C, Kornowski A, Weller H (2002) Self-assembly of ZnO: from nanodots, to nanorods. Angew Chem Int Ed 41(7):1188–1191
68. Halder A, Ravishankar N (2007) Ultrafine single-crystalline gold nanowire arrays by oriented attachment. Adv Mater 19(14):1854–1858
69. Yu J, Joo J, Park H, Baik S, Kim Y, Kim S, Hyeon T (2005) Synthesis of quantum-sized cubic ZnS nanorods by the oriented attachment mechanism. J Am Chem Soc 127(15):5662–5670
70. Cho K, Talapin D, Gaschler W, Murray C (2005) Designing PbSe nanowires and nanorings through oriented attachment of nanoparticles. J Am Chem Soc 127(19):7140–7147
71. Tang Z, Kotov N, Giersig M (2002) Spontaneous organization of single CdTe nanoparticles into luminescent nanowires. Science 297(5579):237–240
72. Polleux J, Pinna N, Antonietti M, Niederberger M (2004) Ligand-directed assembly of preformed titania nanocrystals into highly anisotropic nanostructures. Adv Mater 16(5):436–439
73. Shen S, Zhuang J, Xu X, Nisar A, Hu S, Wang X (2009) Size effects in the oriented-attachment growth process: the case of Cu nanoseeds. Inorg Chem 48(12):5117–5128
74. Lee E, Ribeiro C, Longo E, Leite E (2005) Oriented attachment: an effective mechanism in the formation of anisotropic nanocrystals. J Phys Chem B 109(44):20842–20846
75. Penn R, Banfield J (1998) Imperfect oriented attachment: dislocation generation in defect-free nanocrystals. Science 281(5379):969–971

76. Du N, Zhang H, Chen B, Ma X, Yang D (2007) Ligand-free self-assembly of ceria nanocrystals into nanorods by oriented attachment at low temperature. J Phys Chem C 111(34):12677–12680
77. O'Sullivan C, Gunning RD, Sanyal A, Barrett CA, Geaney H, Laffir FR, Ahmed S, Ryan KM (2009) Spontaneous room temperature elongation of CdS and Ag_2S nanorods via oriented attachment. J Am Chem Soc 131(34):12250–12257
78. Deng Z, Chen D, Tang F, Meng X, Ren J, Zhang L (2007) Orientated attachment assisted self-assembly of Sb_2O_3 nanorods and nanowires: end-to-end versus side-by-side. J Phys Chem C 111(14):5325–5330
79. Kodambaka S, Tersoff J, Reuter MC, Ross FM (2007) Germanium nanowire growth below the eutectic temperature. Science 316(5825):729–732
80. Wen C, Reuter MC, Bruley J, Tersoff J, Kodambaka S, Stach EA, Ross FM (2009) Formation of compositionally abrupt axial heterojunctions in silicon-germanium nanowires. Science 326(5957):1247–1250
81. Prikhodko SV, Sitzman S, Gambin V, Kodambaka S (2008) In situ electron backscattered diffraction of individual GaAs nanowires. Ultramicroscopy 109(1):133–138
82. Gamalski AD, Tersoff J, Sharma R, Ducati C, Hofmann S (2010) Formation of metastable liquid catalyst during subeutectic growth of germanium nanowires. Nano Lett 10(8):2972–2976
83. Diaz RE, Sharma R, Jarvis K, Zhang Q, Mahajan S (2012) Direct observation of nucleation and early stages of growth of GaN nanowires. J Crystal Growth 341(1):1–6
84. Bjork M, Ohlsson B, Sass T, Persson A, Thelander C, Magnusson M, Deppert K, Wallenberg L, Samuelson L (2002) One-dimensional steeplechase for electrons realized. Nano Lett 2(2):87–89
85. Schmid H, Bjoerk MT, Knoch J, Karg S, Riel H, Riess W (2009) Doping limits of grown in situ doped silicon nanowires using phosphine. Nano Lett 9(1):173–177
86. Clark TE, Nimmatoori P, Lew K, Pan L, Redwing JM, Dickey EC (2008) Diameter dependent growth rate and interfacial abruptness in vapor-liquid-solid $Si/Si_{(1-x)}Ge_{(x)}$ heterostructure nanowires. Nano Lett 8(4):1246–1252
87. Zheng H, Smith RK, Jun Y, Kisielowski C, Dahmen U, Alivisatos AP (2009) Observation of single colloidal platinum nanocrystal growth trajectories. Science 324(5932):1309–1312
88. Li D, Nielsen MH, Lee JRI, Frandsen C, Banfield JF, De Yoreo JJ (2012) Direction-Specific interactions control crystal growth by oriented attachment. Science 336(6084):1014–1018
89. Evans JE, Jungjohann KL, Browning ND, Arslan I (2011) Controlled growth of nanoparticles from solution with in situ liquid transmission electron microscopy. Nano Lett 11(7):2809–2813
90. Almeida TP, Fay MW, Zhu Y, Brown PD (2012) In situ TEM investigation of beta-FeOOH and alpha-Fe_2O_3 nanorods. Physica E 44(6):1058–1061
91. Ribeiro C, Longo E, Leite ER (2007) Tailoring of heterostructures in a SnO_2/TiO_2 system by the oriented attachment mechanism. Appl Phys Lett 91(10):103105
92. Liao H, Cui L, Whitelam S, Zheng H (2012) Real-time imaging of Pt_3Fe nanorod growth in solution. Science 336(6084):1011–1014
93. Chen CL, Mori H (2009) In situ TEM observation of the growth and decomposition of monoclinic $W_{18}O_{49}$ nanowires. Nanotechnology 20(28):285604
94. Huang C, Hsin C, Wang C, Chu F, Kao C, Chen J, Huang Y, Lu K, Wu W, Chen L (2012) Direct observation of melting behaviors at the nanoscale under electron beam and heat to form hollow nanostructures. Nanoscale 4(15):4702–4706
95. Zheng H, Rivest JB, Miller TA, Sadtler B, Lindenberg A, Toney MF, Wang L, Kisielowski C, Alivisatos AP (2011) Observation of transient structural-transformation dynamics in a Cu_2S nanorod. Science 333(6039):206–209
96. Davami K, Ghassemi HM, Sun X, Yassar RS, Lee J, Meyyappan M (2011) In situ observation of morphological change in CdTe nano- and submicron wires. Nanotechnology 22(43):435204

97. Davami K, Ghassemi HM, Yassar RS, Lee J, Meyyappan M (2012) Thermal breakdown of ZnTe nanowires. Chemphyschem 13(1):347–352
98. Kallesoe C, Wen C, Booth TJ, Hansen O, Boggild P, Ross FM, Molhave K (2012) In situ TEM creation and electrical characterization of nanowire devices. Nano Lett 12(6):2965–2970
99. Xu Z, Golberg D, Bando Y (2009) In situ TEM-STM recorded kinetics of boron nitride nanotube failure under current flow. Nano Lett 9(6):2251–2254
100. Nam S, Chung H, Lo YC, Qi L, Li J, Lu Y, Johnson ATC, Jung Y, Nukala P, Agarwal R (2012) Electrical wind force-driven and dislocation-templated amorphization in phase-change nanowires. Science 336(6088):1561–1566
101. Shen J, Vincent P, Blanchard NP, Nicolle J, Choueib M, Purcell ST, Poncharal P, Salles V, Brioude A (2012) Physical properties of individual anatase TiO_2 nanowires investigated by field emission in a transmission electron microscope. J Vac Sci Technol B 30(1):011801
102. Zheng H, Luo Z, Fang D, Phillips FR, Lagoudas DC (2012) Reversible phase transformations in a shape memory alloy In-T1 nanowires observed by in situ transmission electron microscopy. Mater Lett 70:109–112
103. Inkson B, Dehm G, Wagner T (2002) In situ TEM observation of dislocation motion in thermally strained Al nanowires. Acta Mater 50(20):5033–5047
104. Jung Y, Nam S, Agarwal R (2011) High-resolution transmission electron microscopy study of electrically-driven reversible phase change in $Ge_2Sb_2Te_5$ nanowires. Nano Lett 11(3):1364–1368
105. Lu Y, Huang JY, Wang C, Sun S, Lou J (2010) Cold welding of ultrathin gold nanowires. Nat Nanotechnol 5(3):218–224
106. Golberg D, Costa PMFJ, Lourie O, Mitome M, Bai X, Kurashima K, Zhi C, Tang C, Bando Y (2007) Direct force measurements and kinking under elastic deformation of individual multiwalled boron nitride nanotubes. Nano Lett 7(7):2146–2151
107. Asthana A, Momeni K, Prasad A, Yap YK, Yassar RS (2011) In situ observation of size-scale effects on the mechanical properties of ZnO nanowires. Nanotechnology 22(26):265712
108. Oshima Y (2012) Study of ballistic gold conductor using ultra-high-vacuum transmission electron microscopy. J Electron Microsc 61(3):133–144
109. Ozgur U, Alivov Y, Liu C, Teke A, Reshchikov M, Dogan S, Avrutin V, Cho S, Morkoc H (2005) A comprehensive review of ZnO materials and devices. J Appl Phys 98(4):041301
110. Wang X, Song J, Liu J, Wang ZL (2007) Direct-current nanogenerator driven by ultrasonic waves. Science 316(5821):102–105
111. Wang X, Zhou J, Song J, Liu J, Xu N, Wang ZL (2006) Piezoelectric field effect transistor and nanoforce sensor based on a single ZnO nanowire. Nano Lett 6(12):2768–2772
112. Wang CM, Xu W, Liu J, Choi DW, Arey B, Saraf LV, Zhang JG, Yang ZG, Thevuthasan S, Baer DR, Salmon N (2010) In situ transmission electron microscopy and spectroscopy studies of interfaces in Li ion batteries: Challenges and opportunities. J Mater Res 25(8):1541–1547
113. Magasinski A, Dixon P, Hertzberg B, Kvit A, Ayala J, Yushin G (2010) High-performance lithium-ion anodes using a hierarchical bottom-up approach. Nat Mater 9(4):353–358
114. Chan CK, Peng H, Liu G, McIlwrath K, Zhang XF, Huggins RA, Cui Y (2008) High-performance lithium battery anodes using silicon nanowires. Nat Nanotechnol 3(1):31–35
115. Nam K, Kim D, Yoo P, Chiang C, Meethong N, Hammond P, Chiang Y, Belcher A (2006) Virus-enabled synthesis and assembly of nanowires for lithium ion battery electrodes. Science 312(5775):885–888
116. Wang C, Li X, Wang Z, Xu W, Liu J, Gao F, Kovarik L, Zhang J, Howe J, Burton DJ, Liu Z, Xiao X, Thevuthasan S, Baer DR (2012) In situ TEM investigation of congruent phase transition and structural evolution of nanostructured silicon/carbon anode for lithium ion batteries. Nano Lett 12(3):1624–1632
117. Liu Y, Hudak NS, Huber DL, Limmer SJ, Sullivan JP, Huang JY (2011) In situ transmission electron microscopy observation of pulverization of aluminum nanowires and evolution of

the thin surface Al_2O_3 layers during lithiation-delithiation cycles. Nano Lett 11(10):4188–4194
118. Stephan A (2006) Review on gel polymer electrolytes for lithium batteries. Eur Polym J 42(1):21–42
119. Tarascon J, Armand M (2001) Issues and challenges facing rechargeable lithium batteries. Nature 414(6861):359–367
120. Peckys DB, Mazur P, Gould KL, de Jonge N (2011) Fully hydrated yeast cells imaged with electron microscopy. Biophys J 100(10):2522–2529
121. Peckys DB, de Jonge N (2011) Visualizing gold nanoparticle uptake in live cells with Liquid scanning transmission electron microscopy. Nano Lett 11(4):1733–1738
122. Parkin SSP, Hayashi M, Thomas L (2008) Magnetic domain-wall racetrack memory. Science 320(5873):190–194
123. Chapman J, Scheinfein M (1999) Transmission electron microscopies of magnetic microstructures. J Magn Magn Mater 200(1–3):729–740
124. Tanase M, Petford-Long AK (2009) In situ TEM observation of magnetic materials. Microsc Res Tech 72(3):187–196
125. Basith MA, McVitie S, McGrouther D, Chapman JN, Weaver JMR (2011) Direct comparison of domain wall behavior in permalloy nanowires patterned by electron beam lithography and focused ion beam milling. J Appl Phys 110(8):083904
126. Togawa Y, Kimura T, Harada K, Matsuda T, Tonomura A, Otani Y, Akashi T (2008) Current-excited magnetization reversal under in-plane magnetic field in a nanoscaled ferromagnetic wire. Appl Phys Lett 92(1):012505
127. Nagai T, Yamada H, Konoto M, Arima T, Kawasaki M, Kimoto K, Matsui Y, Tokura Y (2008) Direct observation of the spin structures of vortex domain walls in ferromagnetic nanowires. Phys Rev B 78(18):180414
128. O'Shea KJ, McVitie S, Chapman JN, Weaver JMR (2008) Direct observation of changes to domain wall structures in magnetic nanowires of varying width. Appl Phys Lett 93(20):202505
129. Rodriguez LA, Magen C, Snoeck E, Serrano-Ramon L, Gatel C, Cordoba R, Martinez-Vecino E, Torres L, De Teresa JM, Ibarra MR (2013) Optimized cobalt nanowires for domain wall manipulation imaged by in situ Lorentz microscopy. Appl Phys Lett 102(2):022418
130. Bruckner W, Thomas J, Hertel R, Schafer R, Schneider CM (2004) Magnetic domains in a textured Co nanowire. J Magn Magn Mater 283(1):82–88
131. Skomski R (2003) Nanomagnetics. J Phys Condens Matter 15(20):R841–R896
132. Martin Y, Wickramsinghe H (1987) Magnetic imaging by force microscopy with 1000-Å resolution. Appl Phys Lett 50(20):1455–1457
133. Nielsch K, Wehrspohn R, Barthel J, Kirschner J, Gosele U, Fischer S, Kronmuller H (2001) Hexagonally ordered 100 nm period nickel nanowire arrays. Appl Phys Lett 79(9):1360–1362
134. Phatak C, Beleggia M, De Graef M (2008) Vector field electron tomography of magnetic materials: theoretical development. Ultramicroscopy 108(6):503–513
135. Phatak C, Petford-Long AK, De Graef M (2010) Three-dimensional study of the vector potential of magnetic structures. Phys Rev Lett 104(25):253901

TEM for Characterization of Core-Shell Nanomaterials

6

Yiqian Wang and Chao Wang

Contents

1 Definition of the Topic 243
2 Overview 244
3 Introduction 244
4 Experimental and Instrumental Methodology 246
4.1 Synthesis of Core-Shell Nanomaterials 246
4.2 Transmission Electron Microscopy Techniques 247
5 Key Research Findings 248
5.1 Application of Diffraction Contrast Imaging in Nanomaterials 248
5.2 Application of High-Angle Annular Dark-Field Imaging in Nanoparticles 260
5.3 Application of High-Resolution Transmission Electron Microscopy Imaging in Nanoparticles 264
5.4 Application of Elemental Mapping in Nanowires 270
6 Conclusions and Future Perspective 275
References 276

1 Definition of the Topic

Transmission electron microscope is an essential tool for characterization of nanoscale materials and devices because it can shed light on the microstructure of nanomaterials. For core-shell nanostructured materials, transmission electron microscopy (TEM) can provide much more important information: overall particle size, core size, shell thickness, uniform or nonuniform shell coating, lattice fringe, elemental distribution, etc. In this chapter we will describe the application of TEM for characterization of core-shell nanomaterials.

Y. Wang (✉) • C. Wang
The Cultivation Base for State Key Laboratory, Qingdao University, Qingdao, People's Republic of China
e-mail: yqwang1013@yahoo.com.cn; yqwang@qdu.edu.cn

C.S.S.R. Kumar (ed.), *Transmission Electron Microscopy Characterization of Nanomaterials*, DOI 10.1007/978-3-642-38934-4_6,
© Springer-Verlag Berlin Heidelberg 2014

2 Overview

Nanomaterials have, by definition, at least one dimension in the range of 1–100 nm and subsequently show novel properties different from their bulk materials. The synthesis, characterization, and applications of nanomaterials are the most important parts among the wide range of nanotechnology areas falling under the general "nanotechnology" umbrella. In recent years, core-shell nanomaterials have attracted much attention for their excellent physical properties and chemical stability.

However, traditional characterization tools such as scanning electron microscope (SEM) and atomic force microscope (AFM) can only reflect the surface features of core-shell nanomaterials, lacking detailed information from the core. This is due to the fact that the core is embedded in the shell which is made up of complex materials such as metal, silica, and organics.

Here we describe how to employ TEM to investigate the interface between the core and shell, shape of the core and shell, uniform or nonuniform shell coating, formation of core-shell structure, etc.

3 Introduction

Nanostructured materials have drawn significant attention as potential building blocks for nanocomposites, nanoscale electronic devices, ultrahigh-density magnetic recording systems, and optical devices. The most important characteristics, among many others, on a nanoscale are as follows. First, the small size of nanomaterials leads to an increased surface area to volume ratio and as a result the quantum confinement effects dominate. Second, the increasing surface area to volume ratio leads to an increase in the dominance of the surface atoms over those in its interior.

Initially a lot of research work focused on single-phase nanoparticles because such nanomaterials had much better properties than bulk materials. In the late 1980s, it was found that heterogeneous composite or sandwich colloidal semiconductor nanoparticles had better efficiency than their corresponding single-phase particles; in some cases they even demonstrated some new properties [1–3]. More recently during the early 1990s, researchers synthesized concentric multilayered semiconductor nanoparticles with an aim to improving their properties. Hence, the terminology "core-shell" was subsequently adopted [4–6]. Furthermore, there has been a gradual increase in research activities because of tremendous need for more and more advanced materials fueled by modern technology. Simultaneously the advancement of characterization techniques has greatly helped to establish the structures of these different core-shell nanomaterials. A statistical data analysis is presented in Fig. 6.1 to show the increasing trend of published research papers in this area. These were collected in June 2012 from "SciFinder Scholar" using the keyword "core-shell nanoparticles."

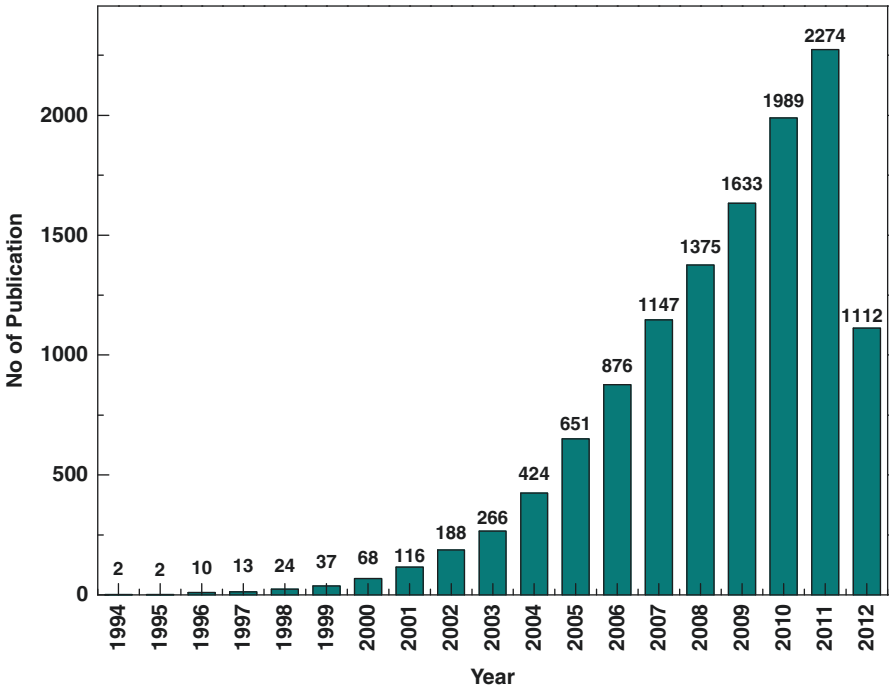


Fig. 6.1 Publications per year for core-shell nanoparticles during the period from 1994 to June 2012 (Data collected from SciFinder Scholar Database)

In recent years, the advances in new synthesis techniques have made it possible to fabricate not only the symmetrical (spherical) nanoparticles but also a variety of other shapes such as cube [7–14], prism [15, 16], hexagon [7, 8, 17–20], octahedron [11, 12], disk [21], wire [22–29], rod [22, 30–37], tube [22, 38–41], etc. Moreover, the structure and composition of core-shell nanomaterials also become more complicated. It means that core-shell nanomaterials are no longer simple spherical particles but are completely coated by a shell of different materials. The shell may have a complex multilayer structure [42–45], and the core may move freely instead of being fixed by the shell [46, 47]. Different classes of core-shell nanoparticles are shown schematically in Fig. 6.2. These core-shell nanomaterials have aroused immense interest because of their novel properties.

Current applications of different core-shell nanoparticles were summarized in a review article by Karele et al. [48] The individual report from different researchers also demonstrated the fact that core-shell nanoparticles are widely used in different applications such as biomedical [49–52] and pharmaceutical applications [53], catalysis [54, 55], electronics [4, 56, 57], enhancing photoluminescence [58–60], creating photonic crystals [61], etc. In particular, in the biomedical field, the majority of these particles were used for bioimaging [51, 62–68], controlled drug release [68, 69], targeted drug delivery [51, 65, 68–70], cell labeling [51, 71], and tissue engineering applications [69, 72].

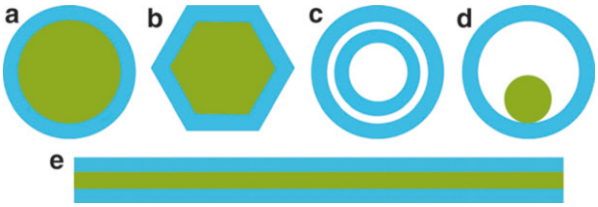


Fig. 6.2 Different kinds of core-shell nanomaterials: (**a**) Spherical core-shell nanoparticles. (**b**) Hexagonal core-shell nanoparticles. (**c**) Double shell core-shell nanoparticles. (**d**) Movable core with hollow shell nanoparticles. (**e**) Core-shell nanowires

Unfortunately, traditional characterization techniques are not good enough to demonstrate the growing complexity of core-shell nanomaterials. However, TEM is an effective method [73] to unlock the secret of the core due to its unique imaging procedure and various techniques.

At present, lots of books have focused on TEM techniques or applications, but few on TEM characterization of core-shell nanomaterials. This chapter is designed to illustrate some TEM techniques for characterizing the core-shell nanostructures, such as diffraction contrast imaging, high-resolution TEM (HRETM), high-angle annular dark-field (HAADF), and elemental mapping. We will take the TEM techniques as a clue to discuss the application of TEM for characterization of core-shell nanomaterials. The characteristic of each TEM technique will be explained and some up-to-date research work will be demonstrated.

4 Experimental and Instrumental Methodology

4.1 Synthesis of Core-Shell Nanomaterials

Approaches for the synthesis of nanomaterials can be broadly divided into two categories: "top-down" and "bottom-up." The "top-down" approach often adopts traditional workshop or microfabrication methods where externally controlled tools are used to cut, mill, and design materials into the desired shape and order. For example, the most common techniques are lithography techniques [74, 75], laser-beam processing [76], and mechanical techniques [77–79]. "Bottom-up" approach, on the other hand, exploits the chemical properties of the molecules to let them self-assemble into some useful conformations. The most common bottom-up approaches are chemical synthesis, chemical vapor deposition, laser-induced assembly, self-assembly, colloidal aggregation, film deposition and growth [80–82], etc. Currently it is hard to say which approach is superior because each has its advantages and disadvantages. However, the bottom-up approach can produce much smaller particles and has the potential to be more cost-effective in the future due to the advantages of absolute precision, complete control over the process, and minimum energy loss compared with that of a top-down approach. As far as the synthesis of core-shell nanomaterials is concerned, the bottom-up

approach has proven to be more suitable since the ultimate control is required for achieving a uniform coating of the shell materials during the particle formation. A combination of these two approaches can also be utilized. For example, core particles can be synthesized by a top-down approach and then coated by a shell fabricated by a bottom-up approach which could maintain uniform and precise shell thickness. To control the overall size and shell thickness precisely, a microemulsion instead of a bulk medium is preferable because water droplets can act as a nanoreactor template.

4.2 Transmission Electron Microscopy Techniques

TEM is a characterization technique whereby a beam of electrons transmits through an ultrathin specimen and interacts with the atoms or molecules in the specimen [73]. TEM is capable of imaging at a significantly higher resolution than light microscopes, owing to the small de Broglie wavelength of electrons. TEM has various imaging techniques, such as diffraction contrast imaging, high-resolution TEM, high-angle annular dark-field, and elemental mapping.

TEM bright field (BF) image is mainly caused by amplitude contrast. Amplitude contrast results from variations in mass or thickness or a combination of the two: the thickness variation can produce contrast because the electron interacts with more material (hence, more mass). Alternatively, diffraction can vary locally because the specimen is not a perfect, uniformly thin sheet. In order to translate the electron scatter into interpretable amplitude contrast, we use objective aperture which is placed in the back focal plane of the objective lens to select the direct beam in the selected area electron diffraction (SAED) to form BF images. Regions of no specimen show a bright background, and regions of the specimen that are thick or dense will present dark in the image.

The HAADF image is also called Z-contrast image. The HAADF image contrast is usually proportional to the Z^2 (Z is atomic number). Because of Bragg scattering, normal ADF detector is not suited for the study of crystalline specimens. But we can decrease the camera length with the post-specimen lenses to ensure that the Bragg electrons (including any HOLZ scattering) do not hit the detector. Thus, only the electrons scattered through very high angles contribute to the image. Bragg scattering effects are avoided if the HAADF detector only gathers electrons scattered through an angle larger than 50 mrad ($\sim 3^\circ$).

HRTEM is an important imaging technique in TEM, from which we can obtain the atomic structure information from a specimen. HRTEM image is mainly caused by phase contrast, and it is produced by interference of the transmitted beam with at least one diffracted beam. When performing HRTEM experiments, we should select a larger objective aperture and let through more beams carrying with their amplitudes and phases to produce a phase contrast image.

Elemental mapping is one important technique in energy-filtering transmission electron microscopy. Elemental maps extracted from ionization edges can obviously show the spatial distribution of elements in samples. Usually two methods,

two-window and three-window, are used to get this information. Two-window method is acquiring two images from electrons in selected energy windows, a pre-edge background image and a post-edge image, and then obtaining the ratio images of pre- and post-edge windows, which can give a qualitative elemental distribution. Three-window method is acquiring three images from electrons in selected energy windows: two pre-edge windows used to calculate the background fit and one post-edge window in which the extrapolated background is subtracted from the total intensity to leave the edge intensity. This method can give quantitative images of the distribution of specific elements.

Alternative operation modes of use allow for TEM to observe modulations in chemical composition, crystal orientation, and electronic structure.

5 Key Research Findings

5.1 Application of Diffraction Contrast Imaging in Nanomaterials

TEM image contrast arises because of the scattering of the incident beam by the specimen. For core-shell structure materials, the components of core and shell are different. As a result, it will produce a strong contrast in the BF image. Through the BF image, we can determine the formation of core-shell structure and measure the thickness of core and shell. In this section, we will discuss the application of TEM BF image for characterization of core-shell nanomaterials in detail.

5.1.1 Silica-Coated Core-Shell Nanomaterials

The silica coating has several advantages. The most basic advantages of the silica coating compared with other inorganic (metal or metal oxide) or organic coatings are as follows: It reduces the bulk conductivity and increases the suspension stability of the core particles. In addition, silica is the most chemically inert material available, and it can block the core surface without interfering the redox reaction at the core surface. Silica coatings can also be used to modulate the position and intensity of the surface plasmon absorbance band since silica is optically transparent. As a result, chemical reactions at the core surface can be studied spectroscopically. Therefore, researchers are more interested in the silica coatings on different inorganic core materials such as metals [83–94], binary inorganic composites [95–97], metal oxides [98–101], and metal salts [88, 102–106] than any other combination.

According to the literature, the shell thickness from 8 to 100 nm can be controlled by adjusting the experimental parameters such as coating time, concentration of reactants, catalyst, and other precursors [83, 84, 87]. Figure 6.3 shows $Au@SiO_2$ nanoparticles where the shells have different thicknesses [107]. These nanoparticles were prepared in the following steps. Gold colloids were homogeneously coated with silica using the silane coupling agent (3-aminopropyl)-trimethoxysilane as a primer to render the gold surface vitreophilic. After the formation of a thin silica layer in aqueous solution, the particles were transferred

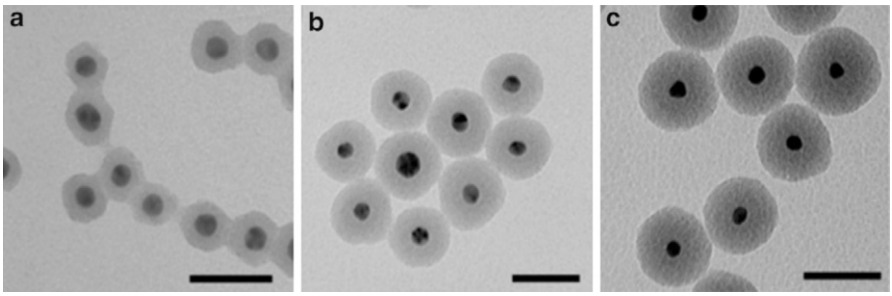


Fig. 6.3 TEM images of Au@SiO_2 nanoparticles. The core dimension is ~15 nm and the silica shells are around 8, 18, and 28 nm, respectively. Scale bars are 50 nm in all images [107] (Reprinted with permission from ref 107. Copyright 2002 Wiley-VCH)

into ethanol for further growth using the Stöber method [108]. From the BF image, we can find that the core is darker compared with the shell, mainly because the gold core has a stronger scattering ability than the silica shell. The image contrast is so clear that we can easily measure the size of core and shell through the image. The gold core is ~15 nm in diameter and a silica shell thickness ranges from 8 to 28 nm.

$CoFe_2O_4$ receives much attention in the biomedical field for its high magnetic anisotropy and saturation magnetization which give rise to suitable magnetic behavior at room temperature, but the presence of cobalt makes it potentially toxic [109, 110]. To protect magnetic nanoparticles, encapsulation both in polymeric and inorganic matrices has been proposed [111], while silica has been most often used [112]. Spherical nanoparticles of surfactant-coated $CoFe_2O_4$ (core) were prepared through thermal decomposition of metal acetylacetonates in the presence of a mixture of oleic acid and oleylamine and uniformly coated with silica shell by using tetraethyl orthosilicate and ammonia in a micellar solution (core/shell) [113]. TEM analysis of core-shell nanoparticles evidenced the high homogeneity of the coating process in producing single core-shell nanoparticle with a narrow size distribution. TEM images (Fig. 6.4a, b) in BF mode show the formation of spherical core-shell structures with an average overall size of 30 nm and a polydispersity of 5 % (Fig. 6.4c) with a single magnetic core in the center of the sphere. TEM image in dark-field mode (Fig. 6.4d) confirms the high degree of crystallinity of the core and the amorphous nature of the shell. The assembling of the nanoparticles appears to be in the form of hexagonal close packing. In some cases a deviation from spherical shape can be observed (Fig. 6.4b); this can be caused by a slight deformation of the particles along the close packing direction.

In some cases the density/concentration of one shell is different. Since the shells with different density/concentration own different scattering ability which will show different TEM image contrast, TEM BF imaging technique is also applied to characterize such kind of materials. Ge et al. [42] prepared nanoparticles in a facile and scalable way, and the procedure was outlined in Fig. 6.5. A monolayer of the metal nanocatalyst was first immobilized on the surface of silica colloids by using coupling agents. The core-satellite structures were then coated with another

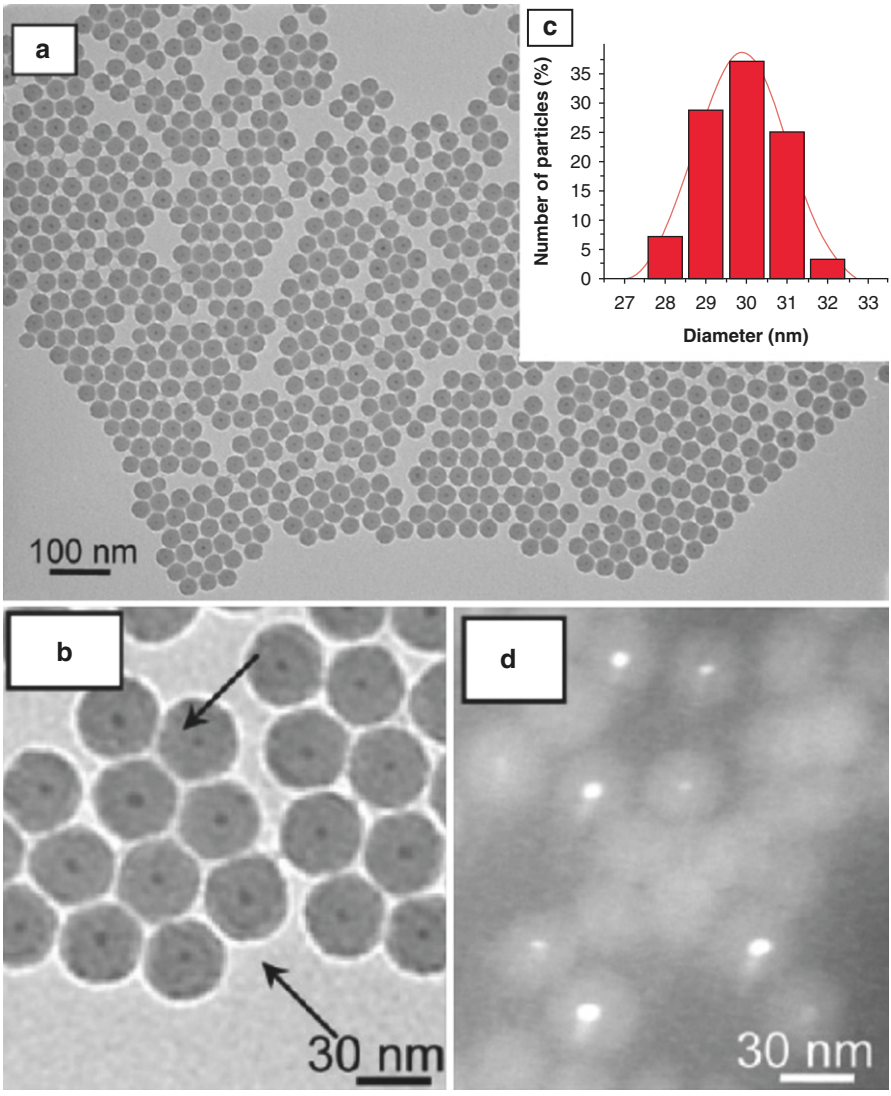


Fig. 6.4 TEM data of $CoFe_2O_4$-SiO_2 core-shell nanoparticles. (**a**) BF image at low magnification. (**b**) BF image at high magnification. (**c**) Particle size distribution. (**d**) Dark-field image [113] (Reprinted with permission from Ref. [113]. Copyright 2010 American Chemical Society)

layer of silica of the desired thickness to fix the position of metal nanoparticles. Finally, a "surface-protected etching" technique was applied to make the outer shell mesoporous, exposing the catalyst particles to outside chemical species [114]. To improve the recyclability, they also incorporated a superparamagnetic Fe_3O_4 core at the center of the initial silica colloids [115, 116]. The etching process can be well controlled by monitoring the transmittance of the colloidal solution. With an

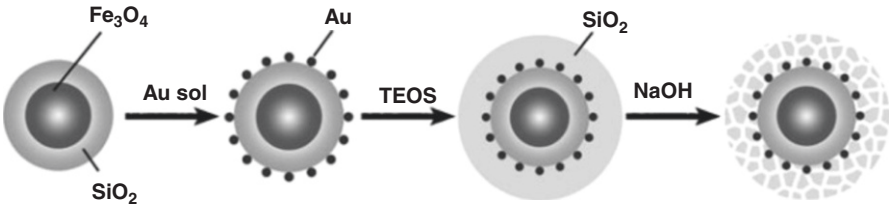


Fig. 6.5 Synthetic procedure of porous silica protected $Fe_3O_4/SiO_2/Au$ composite structures [42] (Reprinted with permission from Ref. [42]. Copyright 2008 Wiley-VCH)

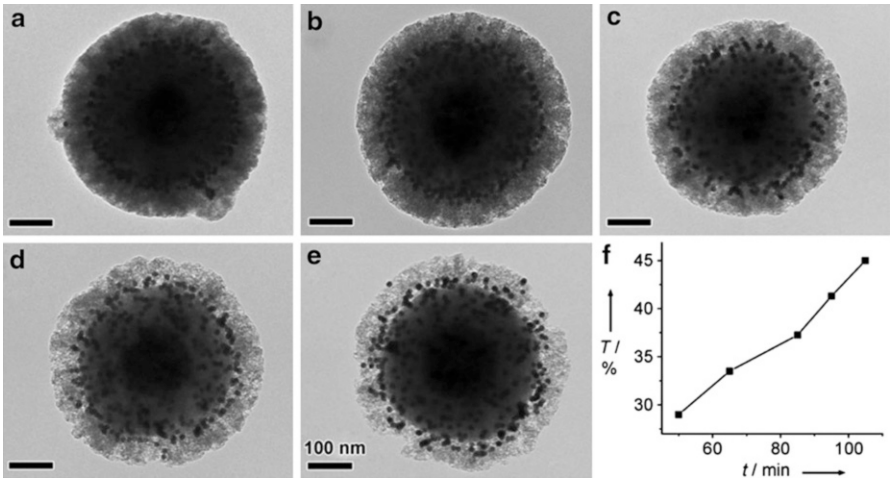


Fig. 6.6 (**a**–**e**) TEM BF images of $Fe_3O_4/SiO_2/Au/por\text{-}SiO_2$ composite colloids collected after different etching times: (**a**) 50, (**b**) 65, (**c**) 85, (**d**) 95, and (**e**) 105 min. (**f**) Changes in transmission intensity of the solution ($\lambda = 1{,}000$ nm) with etching time [42] (Reprinted with permission from Ref. [42]. Copyright 2008 Wiley-VCH)

increase of etching time, more silica materials dissolved in the form of soluble silicate oligomers, and accordingly the transmittance increased. Figure 6.6 shows typical TEM BF images of five $Fe_3O_4/SiO_2/Au/por\text{-}SiO_2$ composite colloids collected after 50, 65, 85, 95, and 105 min of etching [42]. It is clear that the thickness of shell shows no apparent change as time goes on, but the contrast between core and shell tends to be sharp. This is due to the fact that the shell is composed of a porous structure which has a weak scattering ability. Consistently, the transmittance of the solution increases from 29 % to 45 % with a near-linear dependence on the reaction time (Fig. 6.6f).

As an alloying electrode material, Si has attracted much attention because of its highest known theoretical charge capacity. One interesting behavior for an amorphous Si (a-Si) is that it reacts with lithium (Li) at slightly higher potential (~220 mV) [117, 118] than crystalline Si (c-Si) does (~120 mV) [119, 120], which leads to an idea of using c-a core-shell Si nanowires (NWs) as an anode

material. When limiting the charging potential, it should be possible to utilize only the amorphous shell material for Li storage while preserving the crystalline core as mechanical support and efficient electron transport pathways, as indicated in Fig. 6.7a. Figure 6.7 shows c-a core-shell Si NWs grown directly on stainless steel (SS) current collectors by a simple one-step synthesis. Cui et al. [121] found that large flow, high pressure, and high temperature promote the yield of c-a core-shell Si NWs on SS substrates. As shown in Fig. 6.7b, the thickness of amorphous shell increases linearly with growth time, while the core radius does not change. This suggests that c-Si cores grew first and a-Si was subsequently coated onto the cores from SiH_4 decomposition. Figure 6.7c–h shows the TEM images, selected SAED patterns, and HRTEM images of Si NWs grown at 485 °C for different growth times. After 10 min of growth, the NWs were mostly single crystalline (Fig. 6.7c, d) with little amorphous shell. After 20 min, a thick layer of amorphous shell was observed (Fig. 6.7e, f), which became even thicker after 40 min (Fig. 6.7g, h). Consistently, the SAED pattern in Fig. 6.7g shows amorphous diffraction ring which is not found in Fig. 6.7c.

5.1.2 Bimetallic Core-Shell Nanomaterials

Bimetallic core-shell and alloy nanoparticles have received intense attention, owing to their novel optical, electronic, magnetic, and catalytic properties different from those of individual metals [122–124]. Since these properties strongly depend on composition, shape, and size of the nanoparticles, extensive studies have been focused on the controlled synthesis of these nanoparticles with specific compositions and morphologies [125–140]. For the bimetallic core-shell nanostructures, a direct approach to determine their structure is TEM because a clear boundary between core and shell can be distinguished by bright or dark contrast in the TEM BF image. HAADF and HRTEM techniques can also be employed to characterize bimetallic core-shell structure. We will introduce them in detail in the following section.

Tsuji et al. [141, 142] synthesized shape-dependent Au@Ag core-shell nanocrystals successfully by using a two-step method. In order to understand growth mechanisms of these Au@Ag core-shell particles, they added Au seeds with different shapes into $AgNO_3$/DMF solution at $[AgNO_3]/[HAuCl_4]$ molar ratios of 1, 9, and 18, respectively. From the TEM BF images (Fig. 6.8), we can observe a mixture of Au@Ag core-shell nanocrystals with various shapes. Obviously, truncated-triangular and hexagonal plate-like Ag shells overgrew from triangular and hexagonal Au cores, respectively, whereas decahedral and octahedral Ag shells overgrew from the decahedral and octahedral Au cores, respectively. In addition, it can be clearly seen that the thickness of shell increased over $[AgNO_3]/[HAuCl_4]$ molar ratio. At low $[AgNO_3]/[HAuCl_4]$ molar ratio of 1, thin triangular and hexagonal shells are epitaxially formed over the triangular and hexagonal Au plate cores (Fig. 6.8a, b). With an increase of the $[AgNO_3]/[HAuCl_4]$ molar ratio, larger triangular, truncated-triangular, or hexagonal Ag shells are overgrown. The edge length of Ag shells enlarges with an increase of the molar ratio for the

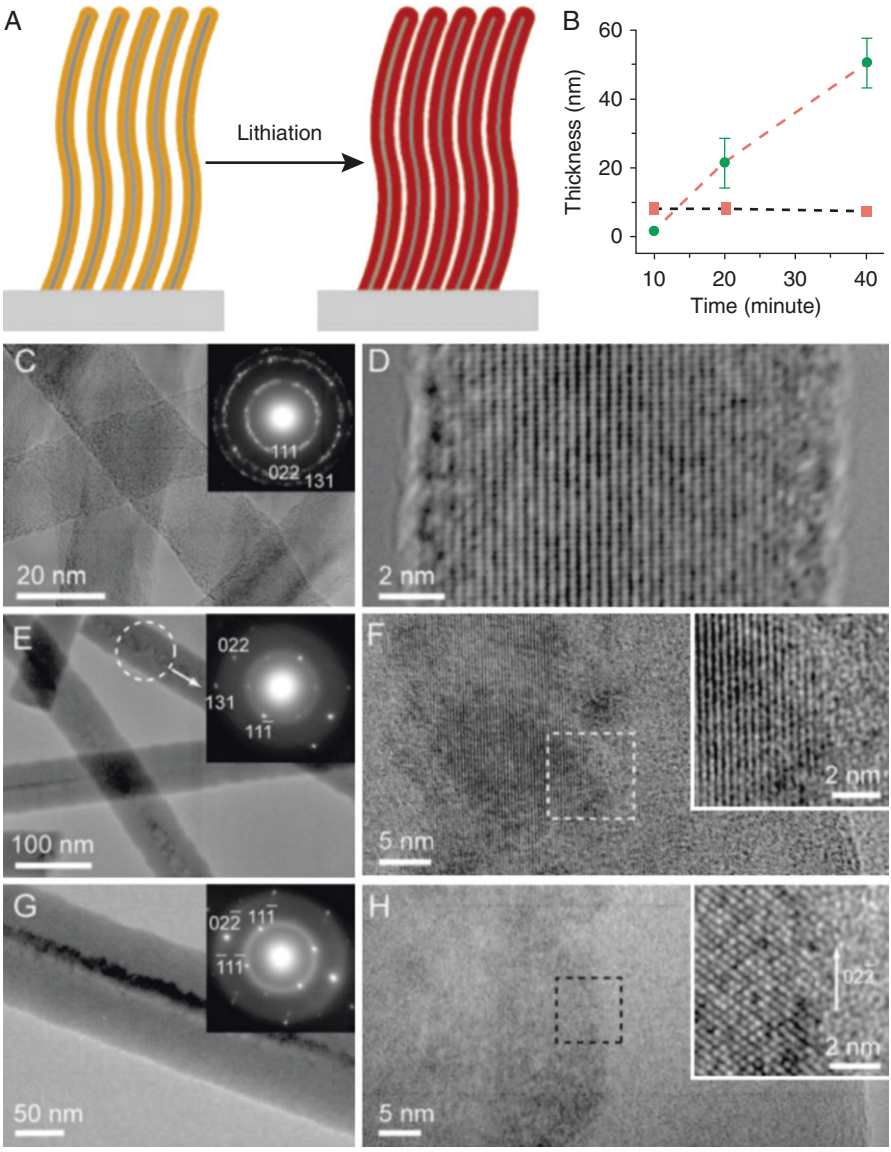


Fig. 6.7 (**a**) Schematic illustration of the lithiation of the c-a Si core-shell NWs grown on a stainless steel substrate. (**b**) Statistics of the core radius (*red*) and shell thickness (*green*) versus growth time. The growth temperature was 485 °C. (**c**) TEM and SAED images of NWs grown for 10 min. (**d**) HRTEM image of a nanowire grown for 10 min. (**e**) TEM and SAED images of NWs grown for 20 min. (**f**) HRTEM images of a nanowire grown for 20 min. (**g**) TEM and SAED images a nanowire grown for 40 min. (**h**) HRTEM images of a nanowire grown for 40 min [121] (Reprinted with permission from Ref. [121]. Copyright 2009 American Chemical Society)

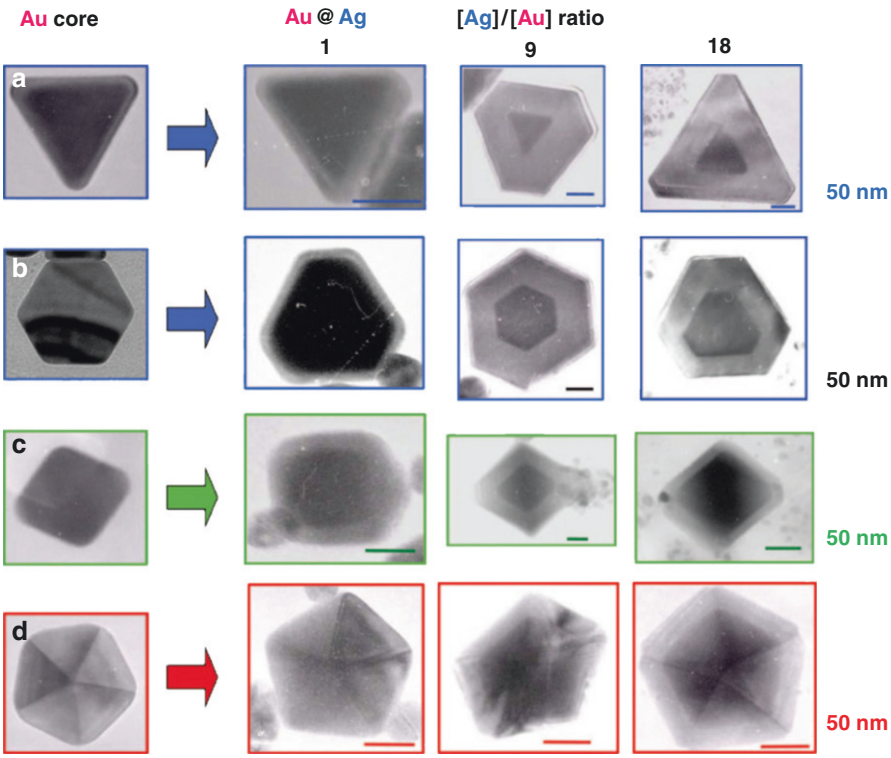


Fig. 6.8 TEM BF images of the Au cores synthesized by a microwave heating for 3 min and the Au@Ag nanocrystals prepared at different $[AgNO_3]/[H_2AuCl_4]$ molar ratios by an oil-bath heating [142] (Reprinted with permission from Ref. [142]. Copyright 2008 American Chemical Society)

$[AgNO_3]/[HAuCl_4]$. At the highest $[AgNO_3]/[HAuCl_4]$ molar ratio of 18, Ag shell edges can achieve about three times longer than those of plate-like Au cores, but Au cores are still observed easily in a constant contrast. This indicates that the Au@Ag core-shell particles have a plate-like shape. In order to further confirm the crystal structure of triangular and hexagonal particles, TEM imaging has been carried out from different view angles within $\pm 16^\circ$ (Fig. 6.9). No significant change can be found in the bright and dark contrast of these triangular and hexagonal particles.

5.1.3 Hollow Core-Shell Nanomaterials

As a unique class of structured materials, hollow colloidal particles have attracted growing research efforts owing to their technological importance in a wide range of applications [53, 143–148]. Templating against colloidal particles is probably the most effective and general method for preparation of hollow particles, especially for studies in which a narrow size distribution is required, i.e., self-assembly of photonic crystals. Monodisperse latex and silica spheres are commonly used as

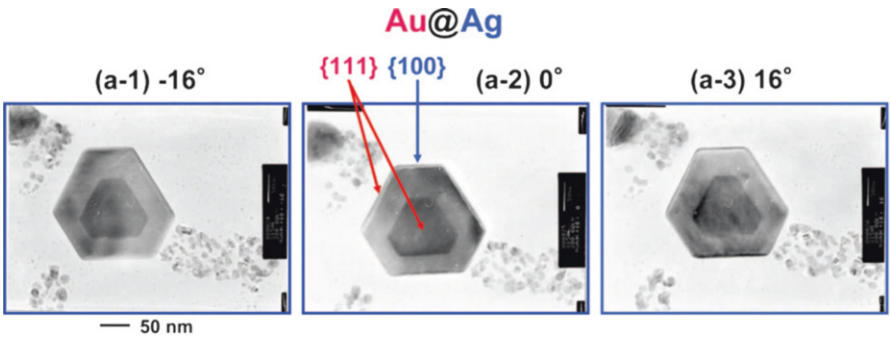


Fig. 6.9 TEM BF images of hexagonal Au@Ag nanocrystal observed from different view angles [142] (Reprinted with permission from Ref. [142]. Copyright 2009 American Chemical Society)

colloidal templates because they are readily available in a wide range of sizes [149–156]. In this section we will introduce some kinds of hollow core-shell nanomaterials which are characterized by TEM.

Figure 6.10 shows hollow core-shell nanoparticles which were designed for a double-electrode nanomaterial composed of a V_2O_5 matrix containing a low weight ratio of SnO_2 nanocrystals (10 % or 15 %) [45]. In this nanostructured composite electrode material, SnO_2 nanocrystals are homogenously distributed in a double-shelled V_2O_5 hollow nanocapsule. The V_2O_5-SnO_2 double-shelled nanocapsules were synthesized by a solvothermal treatment and final heat treatment in air. The SEM image (Fig. 6.10a) of the V_2O_5-SnO_2 nanocapsules indicates that these nanocomposites can be produced in large scale with an average diameter of 550 nm without aggregation. The inset of Fig. 6.10a shows a schematic structure of one individual double-shelled nanocomposite capsule. The red spheres represent SnO_2 nanocrystals, and the green double shells represent the V_2O_5 matrix. The microstructure and components of these nanocapsules were further studied by means of TEM and SAED. Figure 6.10b shows a TEM BF image of double-shelled V_2O_5-SnO_2 nanocapsules consisting of nanocrystals. A typical double-shelled nanocapsule is shown in Fig. 6.10c, which clearly confirms that these hollow nanocapsules have two thin shells. The diameter of the inner hollow nanocapsules is about 430 nm, and the inner cavity is around 250 nm. The thickness of the inner and outer walls can be determined to be ~90 nm through TEM BF image in Fig. 6.10d. To investigate the distribution of SnO_2 in the shell, HRTEM characterization was carried out. The micrographs in Fig. 6.10e and g are HRTEM images taken from the wall edge of the nanocapsules shown in Fig. 6.10d at different locations. Figure 6.10e shows a HRTEM image of a single nanocrystal that reveals the (310) lattice planes of V_2O_5. Figure 6.9f and g reveals the (110) and (101) lattice planes of SnO_2, respectively. These HRTEM images confirm that SnO_2 nanocrystals are homogeneously distributed in the V_2O_5 matrix (double shell). The polycrystalline nature of these nanocapsules was also confirmed by the SAED measurements (Fig. 6.10h). The formation mechanism of the

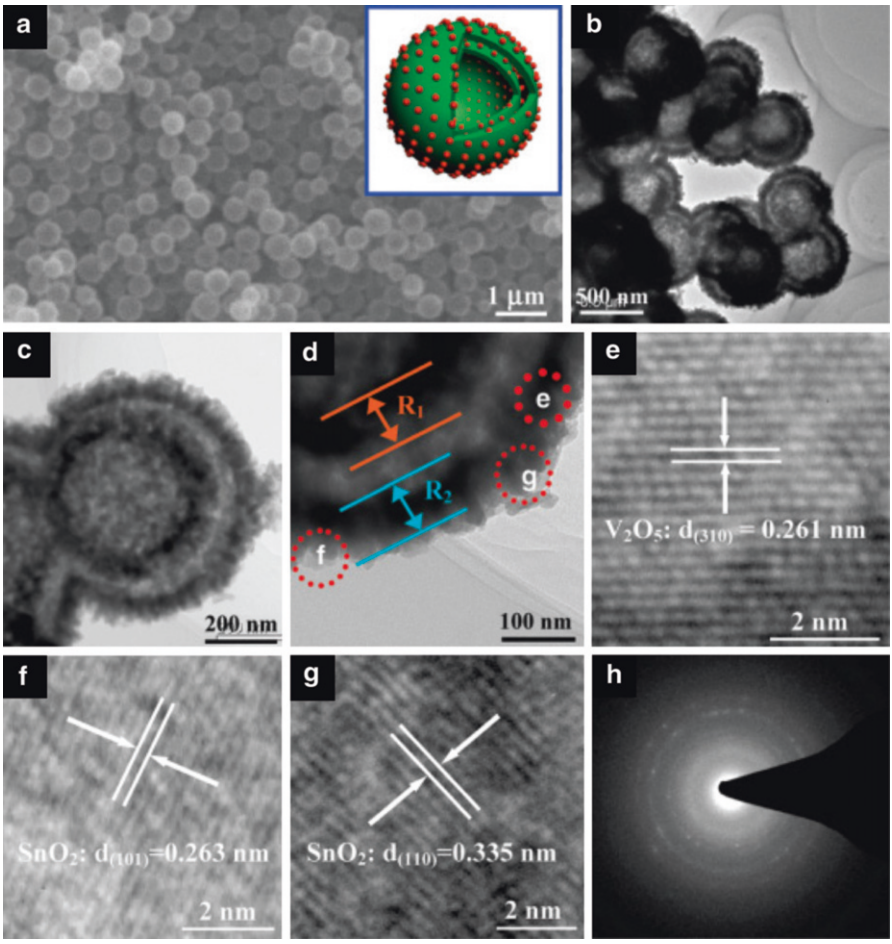


Fig. 6.10 (**a**) SEM image of V_2O_5-SnO_2 double-shelled nanocapsules. The *inset* shows a schematic structure of a double-shelled nanocapsule. The *red* spheres represent SnO_2 nanocrystals, and the *green* double shells represent the V_2O_5 matrix. (**b**) Low-magnification TEM image. (**c**, **d**) High-magnification TEM images showing that the porous shells consist of a great deal of nanocrystals and have thicknesses of R1 ≈ R2 90 nm. (**e**, **g**) HRTEM images revealing lattice planes of the V_2O_5 matrix and SnO_2 nanocrystals. (**h**) SAED pattern taken from individual nanocapsules, which shows that these nanocapsules are polycrystalline [45] (Reprinted with permission from Ref. [45]. Copyright 2009 American Chemical Society)

double-shelled hollow nanocapsules is a combination of two types of Ostwald ripening processes (both inward and outward ripening cases).

In order to understand the growth mechanism of double-shelled V_2O_5-SnO_2 hollow nanocapsules, Liu et al. [45] investigated the morphology evolution of the intermediates involved in the formation process. Two intermediates obtained at 5 and 10 h are shown in Fig. 6.11. With a short reaction time (5 h, Fig. 6.11a), the

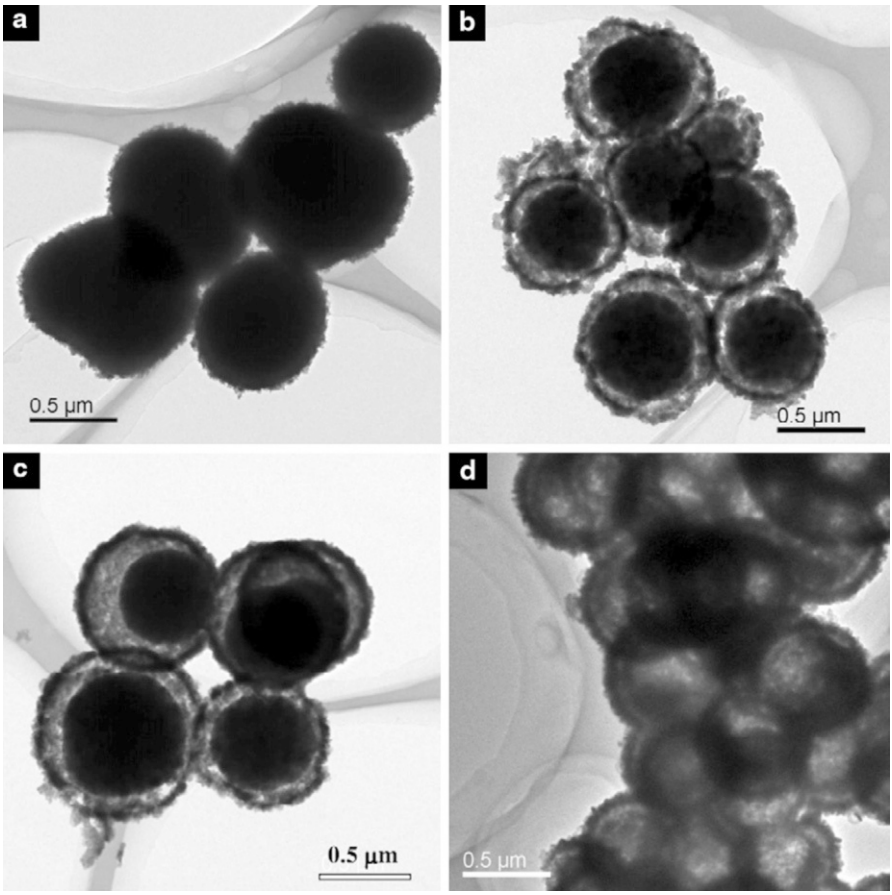


Fig. 6.11 TEM images show the formation process of V_2O_3-SnO_2 composite as double-shelled hollow nanocapsules. (**a**) 5 h, solid V_2O_3-SnO_2 composite nanospheres. (**b**, **c**) 10 h, core-shell intermediates. (**d**) 24 h, double-shelled V_2O_3-SnO_2 hollow nanocapsules [45] (Reprinted with permission from Ref. [45]. Copyright 2009 American Chemical Society)

crystallite aggregates gave a spherical morphology. When the reaction time was extended to 10 h, these solid spheres were converted into solid core-shell particles (Fig. 6.11b, c), and finally this solid core became hollow to form double-shelled hollow nanocapsules (Fig. 6.11d). They concluded that the formation mechanism of the double-shelled hollow nanocapsules is a combination of two types of Ostwald ripening processes (both inward and outward ripening cases). Ostwald ripening firstly took place at the surface of solid spheres, which differed from the previous simpler outward ripening process. Following this inward ripening process, the solid core of core-shell spheres ripened outward furthermore, and finally the double-shelled nanocapsules were achieved.

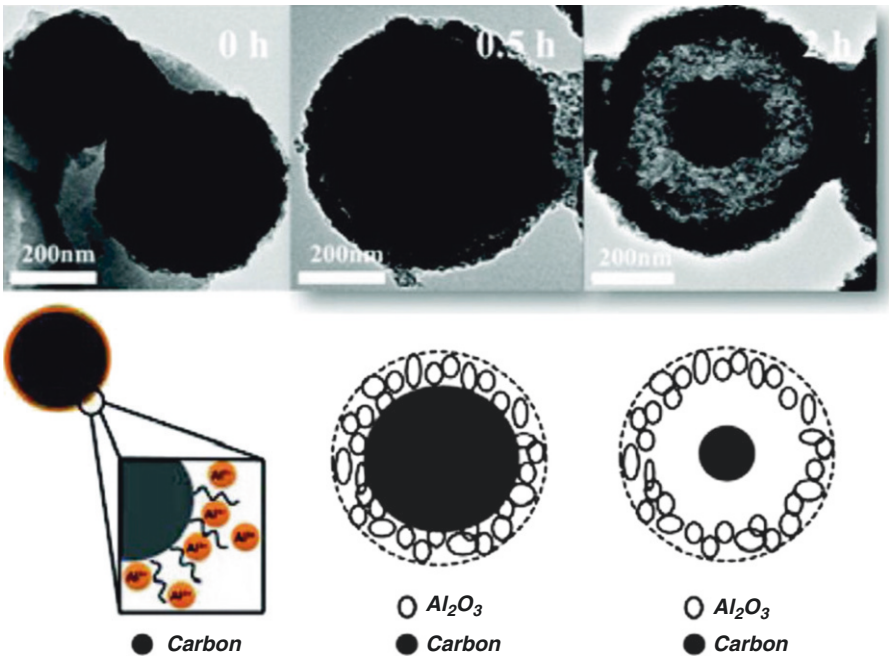


Fig. 6.12 Schematic illustration of the formation of rattle-type carbon-alumina particles; TEM images represent the samples obtained by calcination at 450 °C for 0, 0.5, and 2 h, respectively [159] (Reprinted with permission from Ref. [159]. Copyright 2012 American Chemical Society)

The rattle-type nanoarchitectures, a special class of core-shell particles, have been extensively studied because of their unique structural properties and potential applications. These architectures possess spherical shells and solid cores having a variable space between them. Some rattle-type particles such as Au-polymer, SiO_2-Fe_2O_3 nanoball, and Cu-silica have been synthesized [157, 158]. Zhou et al. [159] fabricated rattle-type carbon-alumina core-shell spheres with large cavities and proposed a formation mechanism for them.

The time-dependent evolution of morphology was elucidated by TEM and it is shown in Fig. 6.12. The alumina-carbon composite microspheres were obtained via hydrothermal treatment before calcination. After calcination at 450 °C, the carbon transforms into carbon dioxide, meanwhile the loosely adsorbed Al^{3+} ions turn into dense Al_2O_3 network forming the shells of the rattle-type spheres [160]. A closer observation of the TEM images reveals that small cavities exist between the carbon cores and alumina shells resulting from the shrinkage during the calcination process. The formation mechanism of the rattle-type carbon-alumina particles was described as a two-step process. First, the carbohydrate used as a carbon precursor is subjected to dehydration, condensation, polymerization, and aromatization [161] and finally carbon spheres are formed. The surface of these carbon spheres is hydrophilic because it contains a considerable amount of reactive

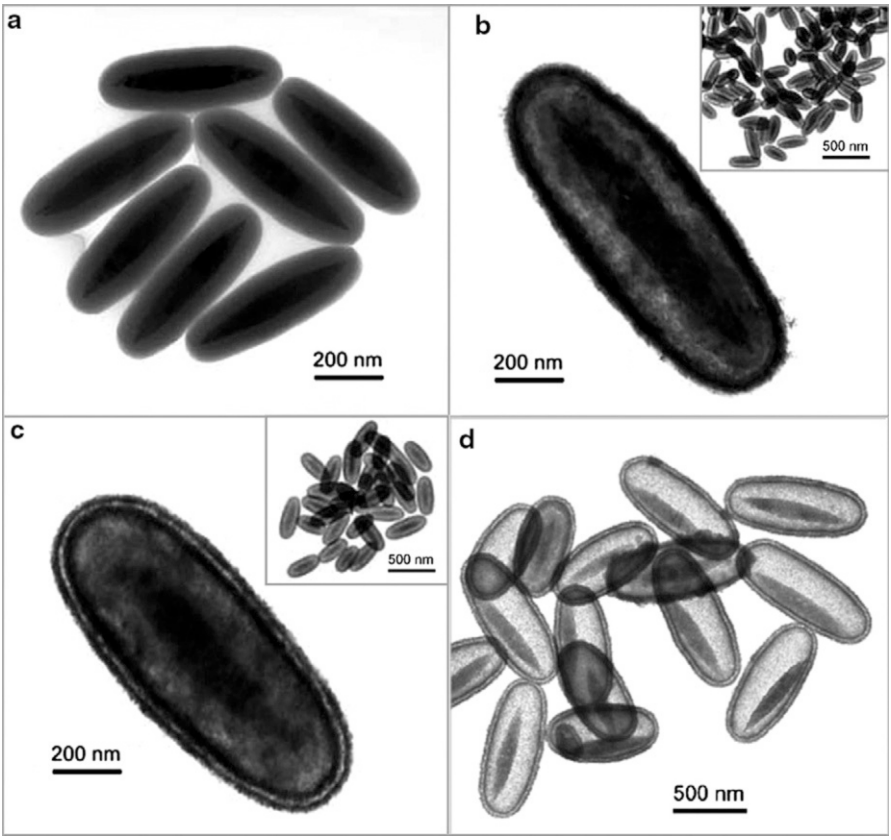


Fig. 6.13 TEM BF images of (**a**) α-Fe_2O_3/SiO_2 nanotemplates, (**b**) α-Fe_2O_3/SiO_2/SnO_2, (**c**) α-Fe_2O_3/SiO_2/$(SnO_2)_2$, (**d**) double-walled SnO_2 nano-cocoons with movable α-Fe_2O_3 spindles [46] (Reprinted with permission from Ref. [46]. Copyright 2007 Wiley-VCH)

oxygen-containing group. Therefore, Al^{3+} ions are easily attached to the surface of the carbon spheres. Second, 2 h calcinations result in the partial removal of carbon cores, and simultaneous densification and cross-linking of the incorporated aluminum ions in the shells, which leads to the formation of rattle-type structures.

Most work in this area was focused on spherical shape, and the resulting hollow spheres are generally single shelled. However, Lou et al. [46] reported a simple synthesis of double-walled SnO_2 ellipsoidal hollow nanoparticles with movable α-Fe_2O_3 cores. This method is based on hydrothermal shell-by-shell deposition of polycrystalline SnO_2 on ellipsoidal α-Fe_2O_3/SiO_2 nanotemplates. Firstly, α-Fe_2O_3 spindles were coated with a SiO_2 layer to produce ellipsoidal α-Fe_2O_3/SiO_2 core-shell particles (Fig. 6.13a). Then, two polycrystalline SnO_2 layers were deposited on the surface of the α-Fe_2O_3/SiO_2 core-shell particles through hydrothermal method. From Fig. 6.13c, a black core and double shell can be clearly distinguished. After annealing at 550 °C, the sandwiched silica layer is dissolved in sodium

hydroxide solution to produce double-walled SnO_2 nano-cocoons (Fig. 6.13d). As can be seen from the image, most nano-cocoons encapsulate only one α-Fe_2O_3 spindle which is usually not located in the center of the cocoon. It is therefore believed that the encapsulated α-Fe_2O_3 spindle is free to move within each cocoon at least when filled with liquid.

5.2 Application of High-Angle Annular Dark-Field Imaging in Nanoparticles

The HAADF approach can detect the variation in chemical composition of the multicomponent sample with an atom-level resolution due to the enhanced contrast difference of various elements (Z-contrast imaging). The contrast of HAADF images is strongly dependent on the average atomic number of the scatterer encountered by the incident probe, not strongly affected by dynamical diffraction effects and defocus. Spatial resolution is limited by the size of the focused incident probe. So HAADF is suitable for characterization of core-shell nanomaterials. In the following we will discuss the application of HAADF images for characterization of core-shell nanomaterials, especially core-shell structured bimetallic nanoparticles [43, 162–170].

5.2.1 Au@Cu_2O Nanoparticles

Figure 6.14a and b shows typical HAADF images of the Au/Cu_2O nanocube heterostructures formed after heating copper grid in ambient environment. TEM observations show that nearly all the gold nanoparticles (>95 %) near the bars of copper grid have transformed into core-shell heterostructures. It can be clearly seen from Fig. 6.14a, b that the core is much brighter than the shell, which indicates that the core has a higher atomic number than that of the shell. Combined with energy-dispersive X-ray spectroscopy (EDS), the chemical compositions of the core and shell are determined to be Au and Cu_2O, respectively. In addition, there are two kinds of morphologies: one being a nearly perfect core-shell nanocube heterostructure and the other being formed through coalescence of two or more small particles (examples of the latter are indicated by white arrows in Fig. 6.14a). These two morphologies have nearly equal volume fractions. The edge dimensions of these heterostructures range from 15 to 45 nm, and the sizes of the cores range from 3.2 to 7.5 nm. TEM examinations of more than 200 core-shell heterostructures show that the edge length of a nanocube is proportional to the diameter of the particles at the core. The linear relationship between the core size and the edge length of the nanocubes is plotted in Fig. 6.14c. The linear relationship indicates that the gold core controls the growth of Cu_2O shell, acting as a template and catalyst. Figure 6.14d shows the SAED patterns taken from the pure Cu_2O nanocubes (the left half) and the Au-Cu_2O core-shell nanocube heterostructures (the right half). Due to the lattice parameter difference between Cu_2O ($a = 4.269$ Å) and gold ($a = 4.09$ Å), it can be seen that some rings (i.e., 111) in the right half are a little broadened.

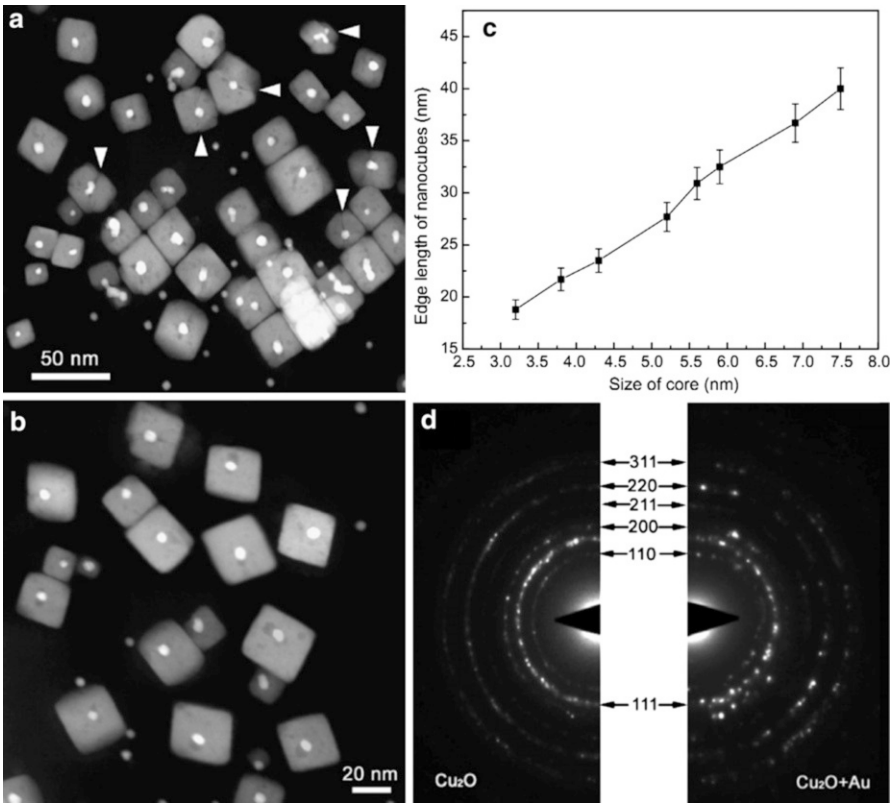


Fig. 6.14 (**a**, **b**) Typical HAADF images of core-shell nanocube heterostructures, showing two types of morphologies. (**c**) The relationship between the core sizes and the edge lengths of the nanocubes. (**d**) SAED patterns taken from the pure Cu_2O nanocubes and the Au-Cu_2O nanocube heterostructures [162] (Reprinted with permission from Ref. [162]. Copyright 2008 Elsevier Ltd.)

5.2.2 Metal@Metal Nanoparticles

Wu et al. [169] used HAADF techniques to observe the morphology of Au@Ag core-shell nanoparticles. As the atomic number difference between Ag(47) and Au (79) is sufficient, the Z-contrast imaging should be capable of distinguishing Au and Ag within the Au@Ag nanoparticles [171, 172]. The enlarged HAADF image in Fig. 6.15 shows that the Au core is brighter than Ag shell, and the Au@Ag core-shell nanoparticles could have various shapes such as cube, triangle, decahedron, and nanorod. Through careful analysis of Fig. 6.15, they found that the cubic Ag shells can form on Au cores with different shapes such as octahedral (Fig. 6.15a), truncated octahedral (Fig. 6.15b), and cubic (Fig. 6.15c). Single-twinned bi-triangular or bi-hexagonal Au cores predominated by {111}-type facets can epitaxially evolve into the single-twinned inverted bi-triangular Ag shells predominated by {100}-type facets (Fig. 6.15d, e). Decahedral Ag shells (Fig. 6.15f) are epitaxially overgrown from the decahedral Au cores and Ag shell

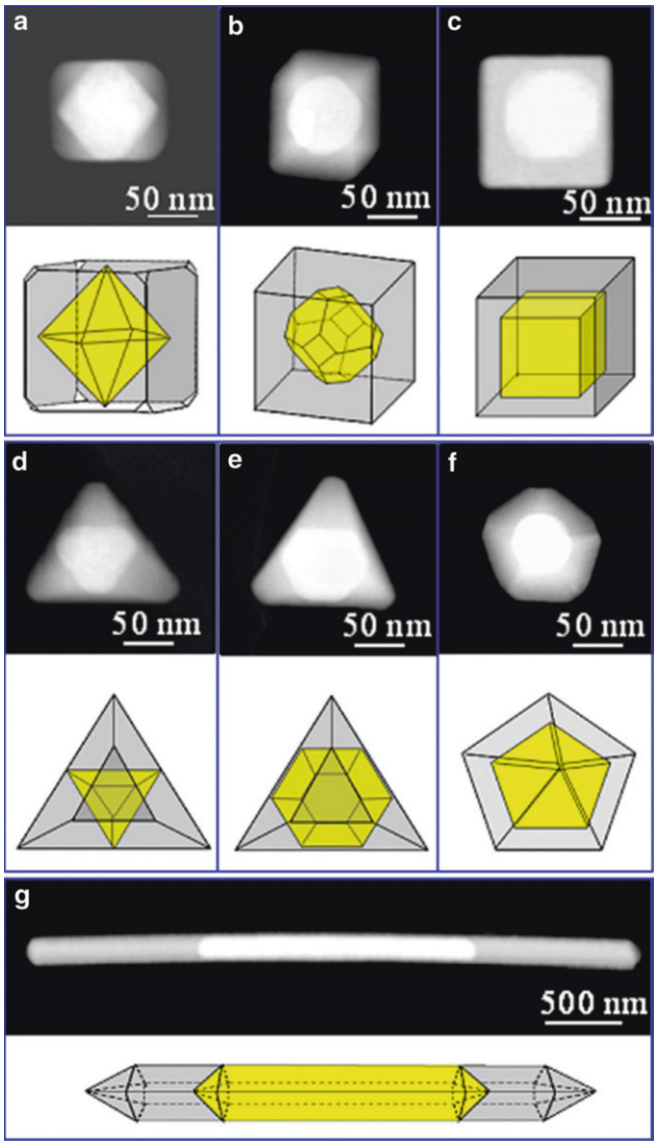


Fig. 6.15 The HAADF-STEM images of the individual Au@Ag nanoparticles with various shapes and their evolution models from different shaped Au core [169] (Reprinted with permission from Ref. [169]. Copyright 2009 IOP Publishing Ltd.)

nanorods (Fig. 6.15g) with a five-twinned cross section from the Au nanorod cores with the five-twinned cross section.

Serpell et al. [170] presented a new proof-of-concept method to synthesize core-shell nanoparticles in which ligand-based supramolecular forces are used to ensure

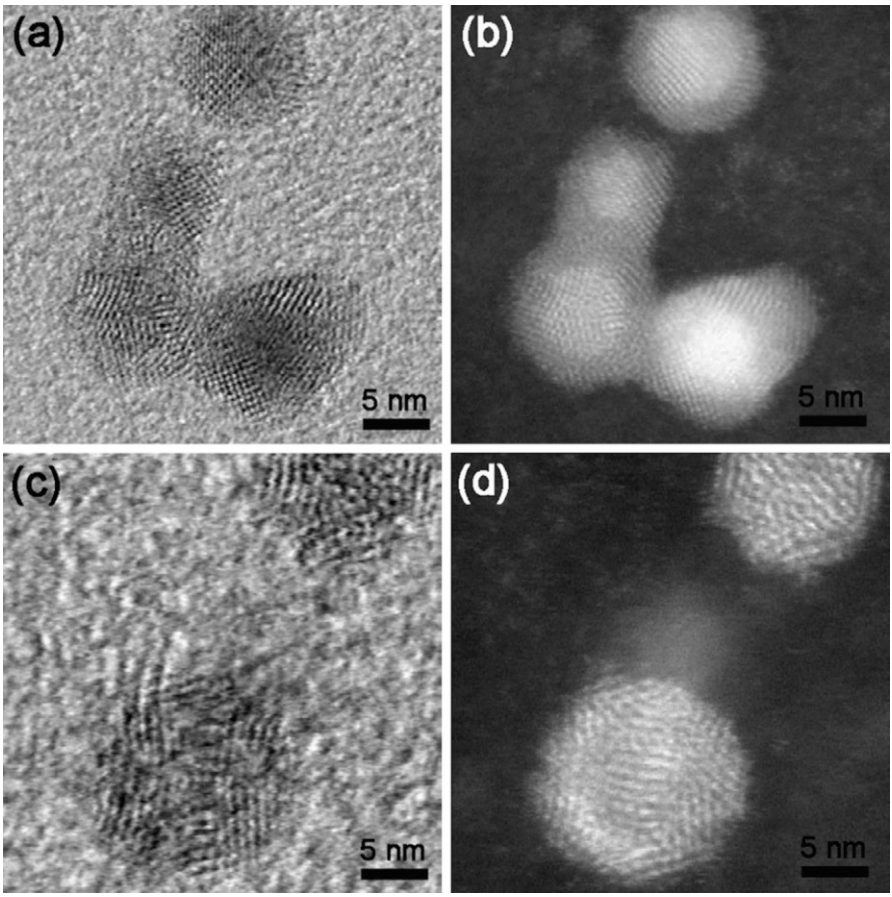


Fig. 6.16 HRTEM and aberration-corrected HAADF-STEM images of Au@Pd nanoparticles (**a**, **b**) and Pd@Au nanoparticles (**c**, **d**) [170] (Reprinted with permission from Ref. [170]. Copyright 2011 Nature Publishing Group)

surface segregation of the shell metal onto the preformed core before its reduction. They demonstrated the principle through the synthesis of Au@Pd, Pd@Au, Pt@Pd, and Pd@Pt nanoparticles using an anion coordination protocol. Conventional TEM instruments provide insufficient atomic number sensitivity for the determination of core-shell structure within the nanoparticles. Figure 6.16a, c is HRTEM images of Au@Pd and Pd@Au nanoparticles in which the lattice fringe images and the boundary between core and shell are not very clear. Therefore, aberration-corrected STEM with a HAADF detector was used to image the precise architectures of individual nanoparticles [173, 174]. The examination of Fig. 6.16b and d using a JEOL-2100F TEM/STEM with a probe correction and ~0.1 nm point resolution clearly reveals core-shell morphology. The intensity is directly related to the square of the atomic number of the elements, making Au atoms appear brighter

relative to Pd. The image of Fig. 6.16b strikingly shows the Au core surrounded by a Pd coating at atomic resolution, with a regular crystalline structure. The Pd@Au nanoparticles appear to have a less regular crystalline structure than the Au@Pd nanoparticles, suggesting a modestly defined core-shell structure for this sample (Fig. 6.16d). This clearly illustrates that the structure within the nanoparticles can be modified by varying the reaction conditions.

Using aberration-corrected scanning transmission electron microscopy (STEM) and electron energy-loss spectroscopy (EELS) line profiles with Ångstrom resolution, Lin et al. [175] studied the structural changes of individual nanoparticles. After electrochemical dealloying, all of the dealloyed Pt-Ni nanoparticles revealed Pt-rich shells surrounding Pt-Ni alloy cores, as shown in Fig. 6.17. The EELS data evidence a distinct difference in the Ni distribution across the alloy cores. Figure 6.17a–d shows a typical high-resolution HAADF-STEM image and line scan EELS spectra across several nanoparticles of the D-PtNi catalyst. The Ni composition shows a monotonic decrease from the particle center to the particle surface. Contrary to that, the D-$PtNi_3$ catalyst (Fig. 6.17e–h) revealed an unusual Ni composition profile across the core, showing a previously undiscovered spherical enrichment of Ni at the near surface. Figure 6.17f, g presents two perpendicular EELS line scan profiles across the nanoparticle shown in Fig. 6.17e. Two off-center maxima of Ni intensity are clearly discernible in both directions, which coincide with the inflection points in the Pt intensity profiles. In other words, a Ni-enriched inner shell is formed near the surface and sandwiched between a Ni-poorer core and a Pt outer shell. This Ni-enriched inner shell is found to be universal in the D-$PtNi_3$ catalyst (Fig. 6.17h). In D-$PtNi_5$ catalyst (Fig. 6.17i–l), it is interesting to note that the Ni-enriched inner shell is located closer to the surface compared with D-$PtNi_3$. Figure 6.17j, k again shows two perpendicular EELS line scans from the nanoparticle shown in Fig. 6.17i, which display the Ni compositional maxima located closer to the surface compared with D-$PtNi_3$ catalyst.

Kim et al. [176] also used HAADF-STEM and EELS line profiles to study the structural changes of individual core-shell nanoparticles. Figure 6.18 shows the HAADF-STEM images and the cross-sectional compositional line profiles measured at the central (left panels) and edge parts (right panels) of $Pt_{0.97}Ag_{0.03}$, $Pt_{0.95}Ag_{0.05}$, $Pt_{0.90}Ag_{0.10}$, $Pt_{0.70}Ag_{0.30}$, and $Pt_{0.0}Ag_{1.0}$ nanoparticles. It can be seen that all the Pt@Ag particles were composed of Pt and Ag atoms. A closer examination reveals that the line profiles for $Pt_{0.97}Ag_{0.03}$, $Pt_{0.95}Ag_{0.05}$, $Pt_{0.90}Ag_{0.10}$, and $Pt_{0.70}Ag_{0.30}$ particles (Fig. 6.18a–d) are of the Pt core-Pt/Ag alloy shell types, while that of $Pt_{0.00}Ag_{1.00}$ particles are of a Pt core-Ag shell type (Fig. 6.18e). It is obvious that not all, but a substantial amount of seed Pt, has taken part in the formation of Pt/Ag alloys, except in the case of $Pt_{0.00}Ag_{1.00}$ nanoparticles.

5.3 Application of High-Resolution Transmission Electron Microscopy Imaging in Nanoparticles

HRTEM could provide a lot of useful information about the sample, such as crystallographic orientation, defects, and interfaces at an atomic scale.

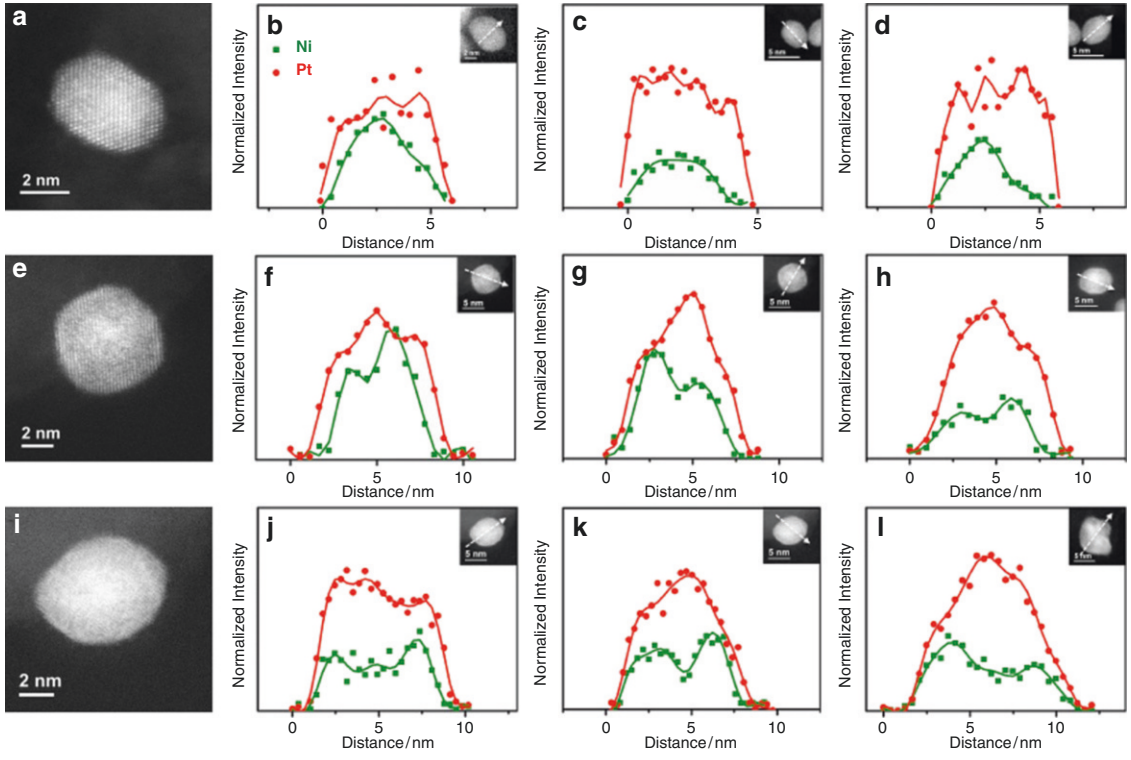


Fig. 6.17 High-resolution HAADF-STEM images and EELS compositional line profiles of individual D-PtNi (**a**–**d**), D-$PtNi_3$ (**e**–**h**), and D-$PtNi_5$ (**i**–**l**) nanoparticles. The directions of the line profiles were plotted as *dashed arrows* in the corresponding nanoparticles. The EELS profiles are normalized with the elemental scattering factors, and hence the intensity ratios represent thickness-projected compositions [175] (Reprinted with permission from Ref. [175]. Copyright 2012 American Chemical Society)

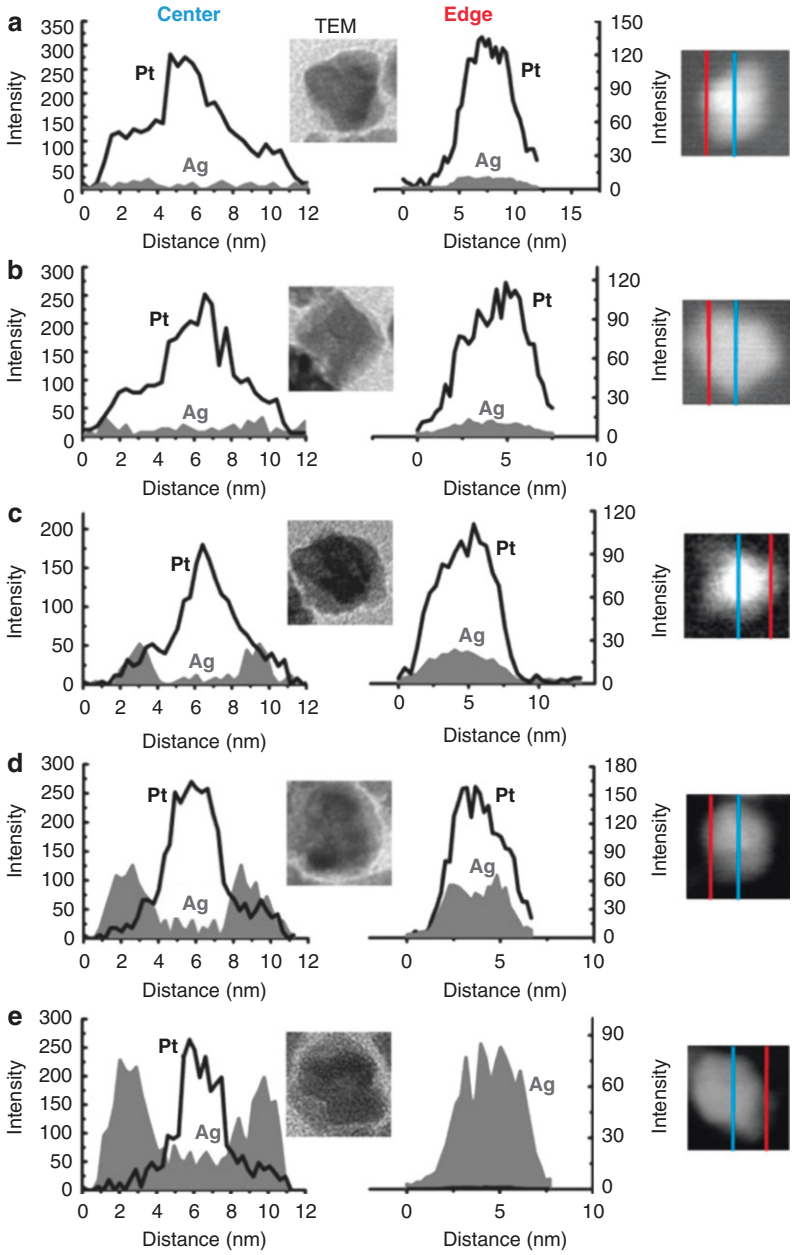


Fig. 6.18 HAADF-STEM images and cross-sectional compositional line profiles measured at the central (*left* panels) and edge parts (*right* panels) of (**a**) $Pt_{0.97}Ag_{0.03}$, (**b**) $Pt_{0.95}Ag_{0.05}$, (**c**) $Pt_{0.90}Ag_{0.10}$, (**d**) $Pt_{0.70}Ag_{0.30}$, and (**e**) $Pt_{0.0}Ag_{1.0}$ nanoparticles, each of which was grown on Pt seed particles [176] (Reprinted with permission from Ref. [176]. Copyright 2011 American Chemical Society)

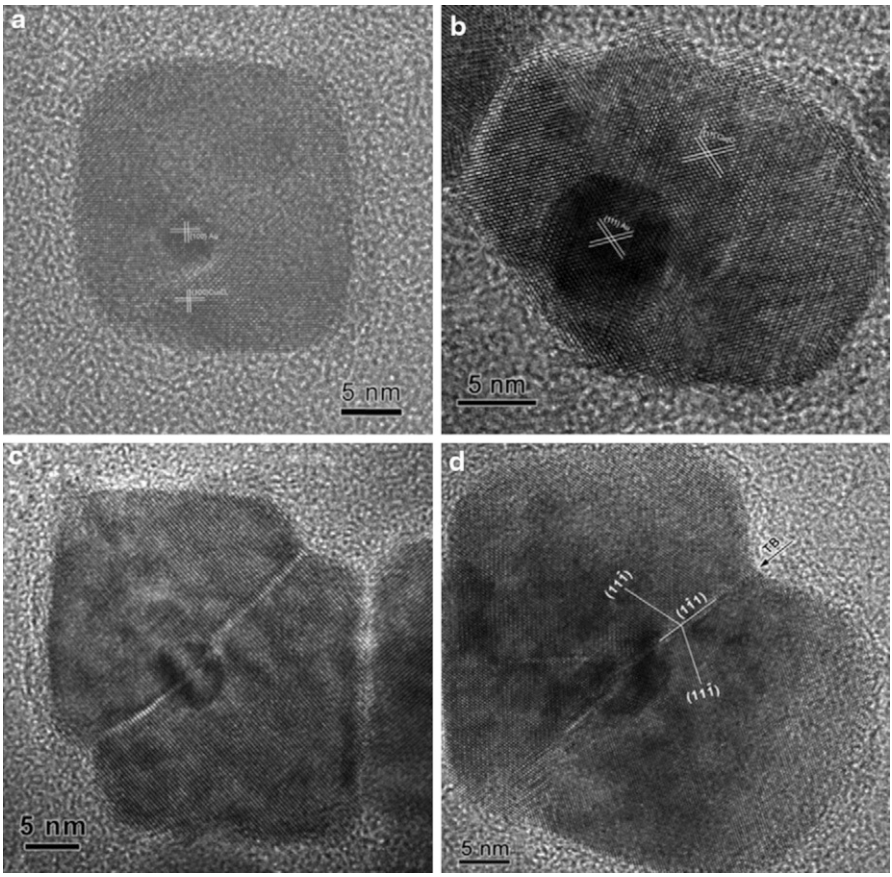


Fig. 6.19 (**a**) [001] zone-axis HRTEM image of a nearly perfect Au-Cu_2O nanocube heterostructure. (**b**) [011] zone-axis HRTEM image of a nearly perfect Au-Cu_2O nanocube heterostructure. (**c**) and (**d**) HRTEM images of coalesced Au-Cu_2O nanocube heterostructures [162] (Reprinted with permission from Ref. [162]. Copyright 2008 Elsevier Ltd.)

For core-shell structured nanomaterials, HRTEM images can illustrate the interface between core and shell. In the following, we will discuss the application of HRTEM image for characterization of core-shell nanomaterials [162, 177–184].

5.3.1 Au@Cu_2O Nanoparticles

In order to investigate the microstructure of Au@Cu_2O core-shell nanocubes, especially the interfaces between the gold nanoparticles and Cu_2O, Wang et al. [162] carried out systematic characterization of these nanoparticles by HRTEM. Most of the core-shell nanocube heterostructures demonstrate specific orientations of Au particle in Cu_2O cube. Figure 6.19 shows two major orientation relationships normally observed in these heterostructures: (a) [001]Au//[001]Cu_2O, {100}Au//{100}Cu_2O and (b) [011]Au//[011]Cu_2O, {111}Au//{111}Cu_2O. Contrary to the

HAADF images (Fig. 6. 14 in Sect. 5.2.1), the gold nanoparticle core has a dark contrast, while the Cu_2O shell has a light contrast. Figure 6.19a shows an example of a heterostructure in which gold nanoparticle and Cu_2O have an orientation relationship of [001]Au//[001]Cu_2O, {100}Au//{100}Cu_2O. However, the lattice is a little distorted around the interface due to the lattice misfit of about 4 % between Au and Cu_2O. Figure 6.19b shows an example of a heterostructure in which gold nanoparticle and Cu_2O have an orientation relationship of [011]Au//[011]Cu_2O, {111}Au//{111} Cu_2O. The {111} lattice misfit between Au and Cu_2O is about 2.3 %, which resulted in the lattice distortion around the interface. As mentioned earlier, some heterostructures are formed through coalescence of two or more small particles. Two examples are shown in Fig. 6.19c and d. Figure 6.19c shows an HRTEM image of a nanocube heterostructure formed through coalescence of two Cu_2O particles with a triangular shape. The boundary between two small particles is still evident. The final shape of this heterostructure is close to cubic. Figure 6.19d shows an HRTEM image of two coalesced particles with a trapezoid shape. The two particles coalesce through twinning, and the twinning configuration is indicated in Fig. 6.19d. Due to irregular shapes of the small particles, the final shape of the heterostructures is no longer cubic. The twinning configuration is thought to reduce the boundary energy and make the final structure more stable. It is believed that the presence of oxygen in the environment is crucial for the formation of Au-Cu_2O core-shell nanocube heterostructures since it can oxidize the copper into cuprous oxide at 300 °C.

5.3.2 PbTe/CdTe Core-Shell Nanoparticles

Core-shell quantum dots (QDs) are heterogeneous nanoparticles composed of an inorganic core enveloped by at least one inorganic shell of a second material. PbS/CdSe core-shell QDs can be prepared by cation exchange method [185]. Lambert et al. [183] demonstrated that the combination of the PbTe rock salt structure and the CdTe zinc blende structure allows for the direct observation of the core and the shell with HRTEM. This enables a direct visualization of the crystallographic properties of the PbTe/CdTe QDs and an evaluation of the cation exchange reaction. They observed a seamless match between the PbTe and CdTe crystal lattices and found that the formation of {111} terminated PbTe cores was favored. This intrinsic anisotropy of the exchange process leads to a strong increase in the heterogeneity of the cores formed, not only in terms of core size and shell thickness but also at the level of shape and position of the core.

Both PbTe and CdTe have a cubic structure [186] with almost no lattice mismatch (Fig. 6.20a, b). Since the appearance of the crystal lattice in HRTEM not only depends on the crystal orientation but also on the defocus, the same crystal plane may yield a different lattice image for both materials. Therefore, it is necessary to carry out a systematic HRTEM simulation. The simulated HRTEM images are shown in Fig. 6.20. When viewed along the <100> direction, PbTe and CdTe may yield two types of lattice images with a square symmetry (Fig. 6.20). The first has a lattice constant of 3.23 Å for PbTe (Fig. 6.20c) or 3.24 Å for CdTe (Fig. 6.20d); the second is tilted by 45° and has a lattice constant of 2.29 Å for both PbTe (Fig. 6.20e) and CdTe (Fig. 6.20f).

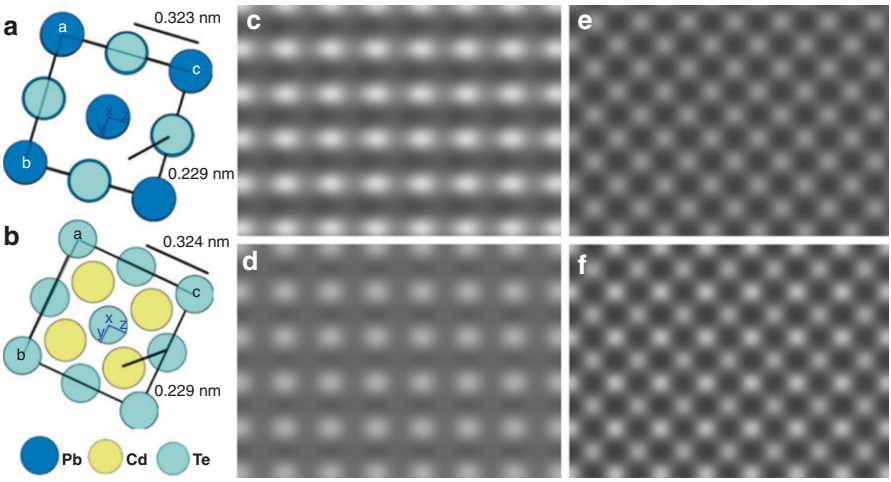


Fig. 6.20 Viewed along the <100> direction (**a**, **b**) structural models of PbTe and CdTe. (**c**, **e**) HRTEM simulation images of PbTe under different defocus. (**d**, **f**) HRTEM simulation images of CdTe under different defocus [183] (Reprinted with permission from Ref. [183]. Copyright 2009 American Chemical Society)

Figure 6.21 shows that resolved core-shell lattice images can be obtained in HRTEM for specific orientations of the particles. Viewed along the <100> direction, Fig. 6.21a represents an image where a core exhibits a 3.21 Å square pattern and a shell demonstrates a 2.34 Å square pattern. Both patterns are tilted by 45° and match seamlessly. By comparison with the simulated images, the core is determined to be PbTe and the shell is CdTe.

Along the <211> direction, PbTe and CdTe yield a rectangular lattice image with 2.29/1.94 Å and 3.89/2.29 Å unit cells, respectively. Figure 6.21b shows an image where both lattice images can be seen.

Along the <111> direction, the lattice images of both PbTe and CdTe show a hexagonal pattern with an almost identical lattice constant of 2.80 and 2.81 Å, respectively. Figure 6.21c gives an example of a PbTe/CdTe core-shell QD that exhibits this pattern. It appears as a simple, uniform particle with a continuously resolved lattice and no indication of any core-shell structure. This result is typical for all particles viewed along the <111> direction. It shows that the <111> axes of both core and shell point in the same direction, with a coherent alignment of {111} planes.

5.3.3 Zn/ZnO Core-Shell Nanobelts

ZnO nanomaterials can be used for fabricating nanolasers [187], field-effect transistors [188], gas sensors [189], nanocantilevers [190], and nanoresonators [191]. Wang et al. [184] synthesized heterostructured metal-semiconductor Zn-ZnO core-shell nanobelts successfully by a solid-vapor decomposition process [192]. The microstructure of epitaxial Zn-ZnO nanobelt has been studied by TEM.

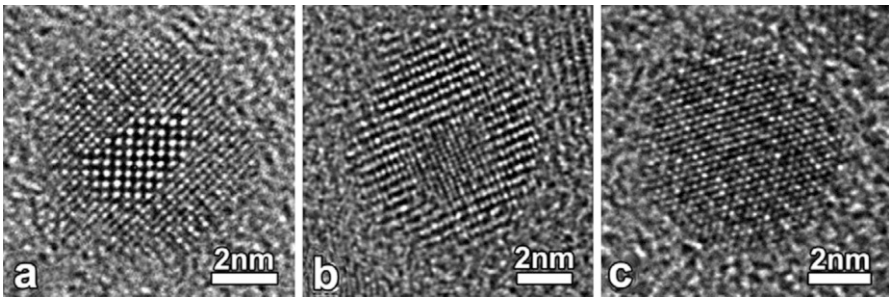


Fig. 6.21 HRTEM images of PbTe/CdTe core-shell particles in the (**a**) <100>, (**b**) <211>, and (**c**) <111> direction. A core-shell structure is observed only in the <100> and <211> direction [183] (Reprinted with permission from Ref. [183]. Copyright 2009 American Chemical Society)

Figure 6.22a is a low-magnification TEM image of the nanobelt, displaying a Zn-ZnO core-shell structure. The SAED pattern (Fig. 6.22c) indicates two sets of single-crystal diffraction spots, which are indexed to be [0001] Zn and [0001] ZnO with an epitaxial orientation. The weak reflection spots were produced by double diffractions from the core and the shell. Structurally, both Zn and ZnO have hexagonal crystal structure [193] with lattice constants of a = 2.665 Å, c = 4.947 Å and a = 3.249 Å, c = 5.206 Å, respectively, and the mismatch between the two in $(10\bar{1}0)$ is about 21.9 %. Therefore, the interference between the Bragg reflections from the two crystals produces Moiré fringes in the image, which are apparent in the HRTEM image in Fig. 6.22b at the region where the Zn core and the ZnO shell overlaps. However, in the region where there is only a ZnO shell, the HRTEM image shows clear lattice structure. The boundary between the Zn core and the ZnO shell is fairly sharp.

5.3.4 Pt@Pd Core-Shell Nanoparticles

Nguyen et al. [194] synthesized Pt@Pd core-shell nanoparticles and studied the structure of individual core-shell nanoparticles by HRTEM. Figure 6.23 shows the HRTEM images of Pt@Pd core-shell nanoparticles with the most characteristic polyhedral morphology and shape. The thin Pd shells grown over the Pt cores have led to form the core-shell configuration with the well-controlled size in the range of about 15–25 nm. The thickness of the coated shell was well controlled in the range of 1–3 nm. The Pt@Pd core-shell nanoparticles also show characteristic polyhedral morphology and shape, typically such as tetrahedral, octahedral, and cubes. Most of the Pt@Pd core-shell nanoparticles exhibit the low-index facets of {111}, {110}, and {100} planes.

5.4 Application of Elemental Mapping in Nanowires

Elemental mapping is based on inner-shell ionization of elements present in the sample giving rise to characteristic signals in well-defined energy-loss regions [195].

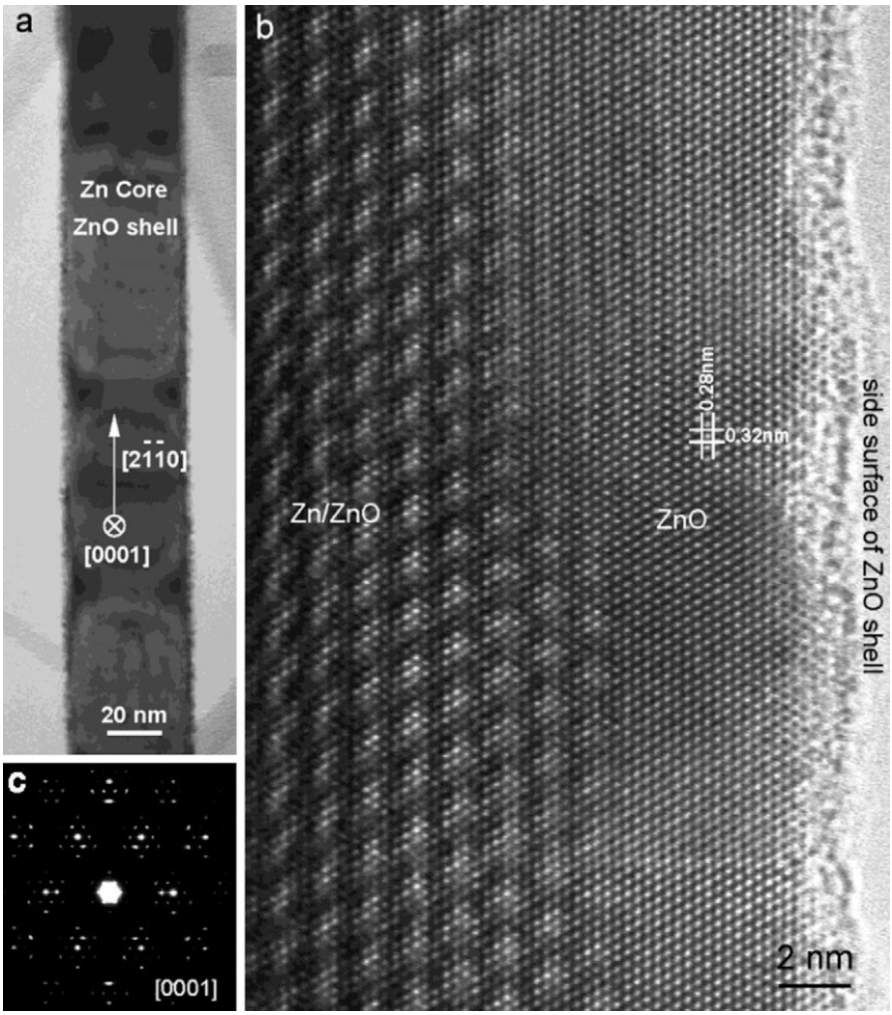


Fig. 6.22 (**a**) Low-magnification TEM image of a Zn-ZnO core-shell heteronanobelt. (**b**) [0001] HRTEM image recorded near the right-hand edge of a nanobelt, showing the Zn-ZnO overlapping region and the ZnO wall. (**c**) The corresponding SAED pattern [184] (Reprinted with permission from Ref. [184]. Copyright 2009 American Chemical Society)

It is a valuable tool for core-shell materials characterization. The applications of elemental mapping have spanned the range of research from biology to polymer materials [44, 196–199]. Elemental mapping, formed by imaging with electrons that have lost energies corresponding to inner-shell ionization edges for particular elements, can give the elemental distribution images in a relatively large area with high spatial resolution. In the following, we will discuss the application of elemental mapping for characterization of core-shell nanomaterials.

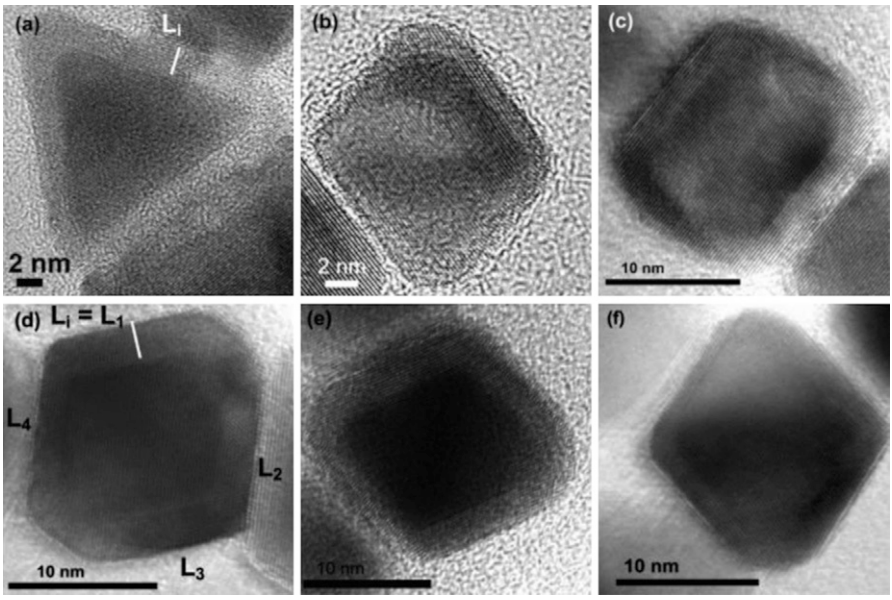


Fig. 6.23 (**a**–**e**) HRTEM images of Pt@Pd core-shell nanoparticles with the polyhedral morphology [194] (Reprinted with permission from Ref. [194]. Copyright 2009 American Chemical Society)

5.4.1 Boron@Boron Oxides Nanowires

It has been found that crystalline silicon [200] and germanium NWs [201] were sheathed with an amorphous oxide coating. Cao et al. [202] reported the successful synthesis of well-aligned straight amorphous boron NWs. From the HRTEM observation, it is difficult to detect whether there is an oxide coating layer of BO_x because the phase contrast of amorphous boron and amorphous BO_x coating cannot be easily distinguished. Therefore, it would be helpful to use the EFTEM. Wang et al. [197, 198] carried out a comprehensive characterization of boron NWs through EFTEM.

The aligned boron NWs were prepared by a radio-frequency magnetron sputtering method. A Philips CM200-FEG TEM equipped with a Gatan Imaging Filter (model 678) was used for elemental mapping and EELS examinations. A three-window method was used to study elemental distribution of boron and oxygen in order to clarify the existence of a boron oxide outer layer coating. The ionization edges selected for elemental mapping are listed as follows: B-K edge (188.5 eV) and O-K edge (532 eV). The exposure time for the elemental mapping of B and O was 10 and 20 s, and the width of the energy windows ΔE was set to be 10 and 20 eV, respectively. The EELS spectrum was acquired in the image mode with a half collection angle of $\sim$13 mrad.

The EELS spectrum of single boron NW is shown in Fig. 6.24, revealing the characteristic boron K-shell ionization edges ($\sim$188 eV). Careful examination of

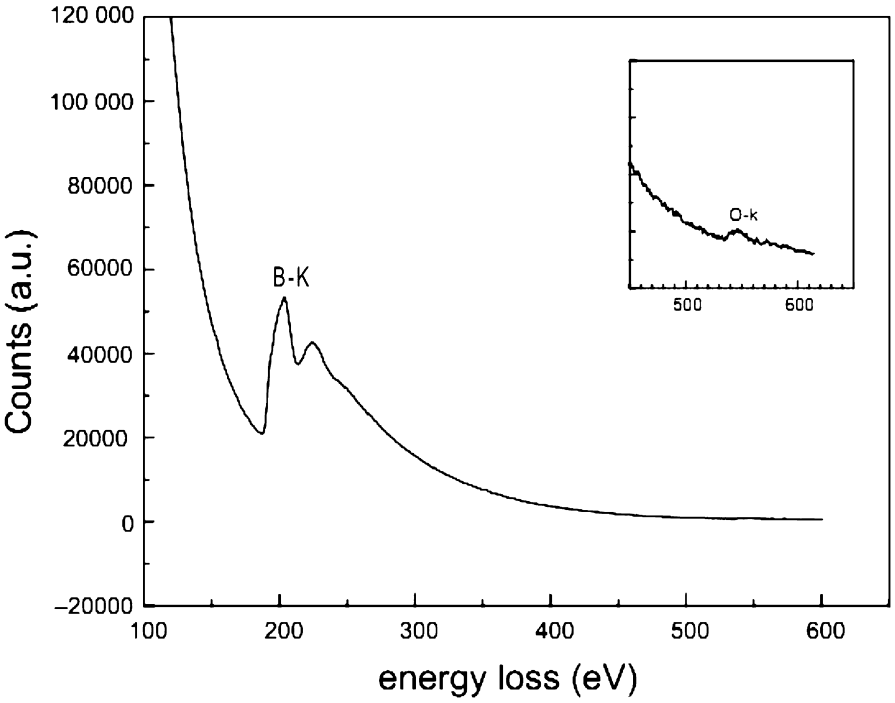


Fig. 6.24 EELS spectrum acquired from single boron nanowire (NW) showing strong boron K-shell peaks and a small peak at 532 eV corresponding to the oxygen K-edge [198] (Reprinted with permission from Ref. [198]. Copyright 2008 Elsevier Ltd.)

the EELS spectrum shows that a small peak is located at 532 eV, which corresponds to the K-shell excitation of oxygen. The magnified oxygen peak is shown in the inset of Fig. 6.24. This demonstrates that a small amount of oxygen exists in the boron NWs.

In order to further investigate the spatial distribution of boron and oxygen in the boron NWs, elemental mappings of boron and oxygen were achieved for the straight boron NWs (Fig. 6.25). It can be clearly seen that the boron is mainly distributed in the core (Fig. 6.25b), while oxygen is mainly located in the outer layer (Fig. 6.25c) of the boron NWs. The thickness of the outer oxidized layer is about 1–2 nm. The importance of oxide or oxygen for the both nucleation and growth of the boron NWs has been confirmed in an experiment (under the same conditions) using two targets (one is a mixture of B and B_2O_3, the other B only). The experiment showed that the quantity of NW stopped increasing after they switched the magnetron sputtering from the mixed target to the pure B target. Moreover, the diameter of the straight boron NWs (about 100 nm) using a pure B target is larger than that of the straight NWs (40–50 nm) using the mixed target.

In order to preclude the possibility of the oxidization layer after growth, some precautions were adopted. Before the boron NWs were put into TEM, they were

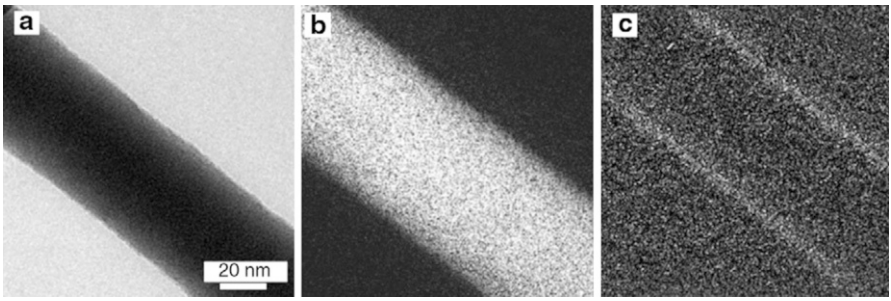


Fig. 6.25 (**a**) TEM image of single straight boron NW. (**b**) Elemental mapping of boron in the straight boron NW. (**c**) Elemental mapping of oxygen in the straight boron NW [198] (Reprinted with permission from Ref. [198]. Copyright 2008 Elsevier Ltd.)

kept in an argon atmosphere, not exposed to the air. The boron NWs were only exposed to air for several minutes during the TEM sample preparation. In addition, they carried out the oxygen mapping of the straight boron NWs (about 100 nm in diameter) produced by using a pure B target (without the oxygen source). The experimental results showed that there is no outer oxidized layer. So it is assured that the observed outer oxidized layer is not produced after growth. The oxide (B_2O_3) or oxygen is crucial for the nucleation and growth of the boron NWs.

5.4.2 Core-Multishell Semiconductor Nanowires

n-GaN/$In_xGa_{1-x}N$/GaN/*p*-AlGaN/*p*-GaN core-multishell NWs were synthesized by metal-organic chemical vapor deposition (MOCVD) [203], using a strategy involving axial elongation by nanocluster-catalyzed growth followed by controlled shell deposition onto the NW core [203]. To characterize the chemical composition and thickness of individual shells in the core-multishell heterostructures, Qian et al. [189] exploited cross-sectional imaging with the electron beam parallel (vs. perpendicular) to the NW axis since this allows for direct visualization of the spatial distribution of elements.

A cross-sectional BF TEM image (Fig. 6.26a) of a GaN/$In_xGa_{1-x}N$/GaN/AlGaN core-multishell NW taken along the $[11\bar{2}0]$ zone axis shows that the core-multishell wire has a triangular cross section with smooth facets. No dislocations or boundaries were observed in the NW, indicating an epitaxial deposition of the shells on the cores. Electron diffraction data (inset, Fig. 6.26a) further demonstrates that the core-multishell NW is single crystalline and that the three lateral facets can be indexed as (0001) and two $\{1\bar{1}0\bar{1}\}$ crystallographic planes. This result is consistent with the previous report on core/shell/shell NWs [203].

Additional analysis using STEM (Fig. 6.26b) revealed contrast indicative of variations in the radial chemical composition as expected for the core-multishell structure. STEM EDS mapping of the same NW region (Fig. 6.26c and e) confirmed the STEM results and defined clearly the spatial distributions of Ga, In, and Al in an individual shell that are consistent with targeted core-multishell structure. Interestingly, the thickness of InGaN shell was larger on the $(1\bar{1}0\bar{1})$

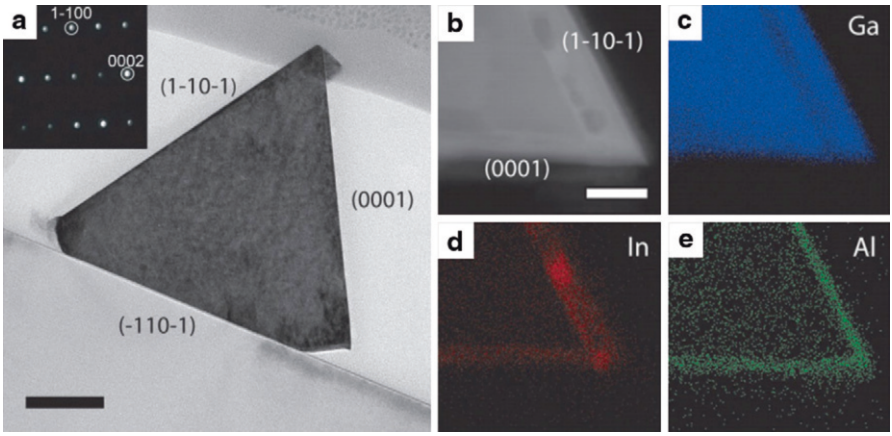


Fig. 6.26 TEM BF cross-section image of a GaN/In_xGa_{1-x}/GaN/AlGaN core-multishell NW. Scale bar is 100 nm. *Inset*: $[11\bar{2}0]$ zone-axis SAED pattern. (**b**) STEM image recorded at a NW corner with (0001) and $(1\bar{1}01)$ facets. Scale bar is 100 nm. (**c**–**e**) Elemental mapping of the same NW region, indicating spatial distribution of Ga (*blue*), In (*red*), and Al (*green*), respectively [44] (Reprinted with permission from Ref. [44]. Copyright 2008 American Chemical Society)

versus (0001) facet, indicating that shell deposition rate depends on the specific crystal planes. This can be understood in terms of different surface energies and polarities on nonequivalent facets [204] and suggests that these NWs could also serve as a model system to study growth kinetics. In addition, localized indium (In)-rich clusters on a scale of 10–50 nm were observed in the thicker InGaN layer grown on the $(1\bar{1}01)$ facet. However, In segregation was not observed in the thinner layer grown on the (0001) facet. Similar In inhomogeneity has been reported in InGaN-based planar structures and is dependent on several factors, including InGaN layer thickness [205].

6 Conclusions and Future Perspective

This chapter concentrates on the introduction of various TEM techniques for characterization of core-shell nanomaterials. The objective was to review the versatility of TEM and the complimentary applications of the techniques. We take the TEM techniques as the clue to discuss the application of TEM for characterization of core-shell nanomaterials.

For TEM BF images, mass-thickness and diffraction contrast contribute to image formation: thick and crystalline areas appear with dark contrast. Since core-shell nanomaterials usually consist of different components, TEM BF image is applicable to most of them. We focus on three kinds of core-shell nanomaterials: silica coating core-shell nanomaterials, bimetallic core-shell nanomaterials, and hollow core-shell nanostructure. HAADF image is strongly dependent on the atomic number of the scatterer encountered by the incident probe, not strongly

affected by dynamical diffraction effects or defocus conditions. So it has advantages in characterizing core-shell nanomaterials.

HRETM imaging process is very complicated and sensitive to the sample thickness and defocus conditions. HRTEM requires very thin TEM specimens free of preparation artifacts. Additionally, correct interpretation of HRTEM images requires systematic image simulations. Because of these limitations, only a small part of the core-shell nanomaterials can be characterized by HRTEM. But we can get lots of important information of core-shell nanomaterials through HRTEM image, such as orientation relationship and interface between the core and shell. So HRTEM is an effective characterization method, which cannot be ignored.

Elemental mapping combined with EELS can investigate the spatial distribution of elements in the nanomaterials. Especially when the core and shell has a same structure and similar atomic numbers, the three methods mentioned above cannot distinguish.

BF image, HADDF image, HRTEM image, and elemental mapping are the most popular and effective methods for the characterization of core-shell nanomaterials. In fact, other TEM techniques can also be used to investigate core-shell nanomaterials, such as TEM dark-field image and SAED. With the development of TEM techniques, the microstructure of core-shell nanomaterials can be studied in more detail.

Acknowledgment The authors would like to thank the financial support from the National Natural Science Foundation of China (Grant Nos. 10974105), the National Basic Research Program of China (Grant No. 2012CB722705), the Natural Science Foundation for Outstanding Young Scientists in Shandong Province (Grant No. JQ201002), the Project of Introducing Talents to Support Thousand Talents Programs (Grant No. P201101032), the Program of Science and Technology in Qingdao City (Grant No. 11-2-4-23-hz), and the Scientific Research Starting Foundation for the Introduced Talents at Qingdao University (Grant No. 06300701). Y. Q. Wang would also like to thank the financial support from the Taishan Outstanding Overseas Scholar Program in Shandong Province.

References

1. Henglein A (1989) Small-particle research: physicochemical properties of extremely small colloidal metal and semiconductor particles. Chem Rev 89(8):1861–1873
2. Spanhel L, Weller H, Henglein A (1987) Photochemistry of semiconductor colloids. 22. Electron ejection from illuminated cadmium sulfide into attached titanium and zinc oxide particles. J Am Chem Soc 109(22):6632–6635
3. Youn HC, Baral S, Fendler JH (1988) Dihexadecyl phosphate, vesicle-stabilized and in situ generated mixed cadmium sulfide and zinc sulfide semiconductor particles: preparation and utilization for photosensitized charge separation and hydrogen generation. J Phys Chem 92(22):6320–6327
4. Hoener CF, Allan KA, Bard AJ, Campion A et al (1992) Demonstration of a shell-core structure in layered cadmium selenide-zinc selenide small particles by x-ray photoelectron and Auger spectroscopies. J Phys Chem 96(9):3812–3817

5. Honma I, Sano T, Komiyama H (1993) Surface-enhanced Raman scattering (SERS) for semiconductor microcrystallites observed in silver-cadmium sulfide hybrid particles. J Phys Chem 97(25):6692–6695
6. Zhou HS, Sasahara H, Honma I, Komiyama H et al (1994) Coated semiconductor nanoparticles: the CdS/PbS system's photoluminescence properties. Chem Mater 6(9):1534–1541
7. Ahmed J, Sharma S, Ramanujachary KV, Lofland SE et al (2009) Microemulsion-mediated synthesis of cobalt (pure fcc and hexagonal phases) and cobalt-nickel alloy nanoparticles. J Colloid Interface Sci 336(2):814–819
8. El-Safty SA (2008) Synthesis, characterization and catalytic activity of highly ordered hexagonal and cubic composite monoliths. J Colloid Interface Sci 319(2):477–488
9. Song Q, Zhang ZJ (2004) Shape control and associated magnetic properties of spinel cobalt ferrite nanocrystals. J Am Chem Soc 126(19):6164–6168
10. Salazar-Alvarez G, Qin J, Sépelák V, Bergmann I et al (2008) Cubic versus spherical magnetic nanoparticles: the role of surface anisotropy. J Am Chem Soc 130(40):13234–13239
11. Schmidt E, Vargas A, Mallat T, Baiker A (2009) Shape-selective enantioselective hydrogenation on Pt nanoparticles. J Am Chem Soc 131(34):12358–12367
12. Wang ZL, Ahmad TS, El-Sayed MA (1997) Steps, ledges and kinks on the surfaces of platinum nanoparticles of different shapes. Surf Sci 380(2–3):302–310
13. Wei XW, Zhu GX, Liu YJ, Ni YH et al (2008) Large-scale controlled synthesis of FeCo nanocubes and microcages by wet chemistry. Chem Mater 20(19):6248–6253
14. Yamade M, Kon S, Miyake M (2005) Synthesis and size control of Pt nanocubes with high selectivity using the additive effect of NaI. Chem Lett 34(7):1050–1051
15. Hu JS, Guo YG, Liang HP, Wan LJ et al (2005) Three-dimensional self-organization of supramolecular self-assembled porphyrin hollow hexagonal nanoprisms. J Am Chem Soc 127(48):17090–17095
16. Jitianu M, Goia DV (2007) Zinc oxide colloids with controlled size, shape, and structure. J Colloid Interface Sci 309(1):78–85
17. Ren TZ, Yuan ZY, Hu WK, Zou XD (2008) Single crystal manganese oxide hexagonal plates with regulated mesoporous structures. Micropor Mesopor Mater 112(1–3):467–473
18. Ren XL, Han D, Chen D, Tang FQ (2007) Large-scale synthesis of hexagonal cone-shaped ZnO nanoparticles with a simple route and their application to photocatalytic degradation. Mater Res Bull 42(5):807–813
19. Suematsu NJ, Ogawa Y, Yamamoto Y, Yamaguchi T (2007) Dewetting self-assembly of nanoparticles into hexagonal array of nanorings. J Colloid Interface Sci 310(2):648–652
20. Wu L, Yu JC, Zhang LZ, Wang XC et al (2004) Selective self-propagating combustion synthesis of hexagonal and orthorhombic nanocrystalline yttrium iron oxide. J Solid State Chem 177(10):3666–3674
21. Qu XZ, Omar L, Le TBH, Tetley L et al (2008) Polymeric amphiphile branching leads to rare nanodisc shaped planar self-assemblies. Langmuir 24(18):9997–10004
22. Cao GZ, Liu DW (2008) Template-based synthesis of nanorod, nanowire, and nanotube arrays. Adv Colloids Interface Sci 136(1–2):45–64
23. Kline TR, Tian ML, Wang JG, Sen A et al (2006) Template-grown metal nanowires. Inorg Chem 45(19):7555–7565
24. Li MW, Mayer TS, Sioss JA, Keating CD et al (2007) Template-grown metal nanowires as resonators: performance and characterization of dissipative and elastic properties. Nano Lett 7(11):3218–3284
25. Liu Z, Elbert D, Chien CL, Searson PC (2008) FIB/TEM characterization of the composition and structure of core/shell Cu-Ni nanowires. Nano Lett 8(8):2166–2170
26. Peña DJ, Mbindyo JKN, Carado AJ, Mallouk TE et al (2002) Template growth of photoconductive metal-CdSe-metal nanowires. J Phys Chem B 106(30):7458–7462

27. Routkevitch D, Bigioni T, Moskovits M, Xu JM (1996) Electrochemical fabrication of CdS nanowire arrays in porous anodic aluminum oxide templates. J Phys Chem 100(33):14037–14047
28. Sioss JA, Keating CD (2005) Batch preparation of linear Au and Ag nanoparticle chains via wet chemistry. Nano Lett 5(9):1779–1783
29. Wu YY, Livneh T, Zhang YX, Cheng GS et al (2004) Templated synthesis of highly ordered mesostructured nanowires and nanowire arrays. Nano Lett 4(12):2337–2342
30. Bok HM, Kim S, Yoo SH, Kim SK et al (2008) Synthesis of perpendicular nanorod arrays with hierarchical architecture and water slipping superhydrophobic properties. Langmuir 24(8):4168–4173
31. Bok HM, Shuford KL, Kim S, Kim SK et al (2008) Multiple surface plasmon modes for a colloidal solution of nanoporous gold nanorods and their comparison to smooth gold nanorods. Nano Lett 8(8):2265–2270
32. Nicewarner-Peña SR, Freeman RG, Reiss BD, He L et al (2001) Submicrometer metallic barcodes. Science 294(5540):137–141
33. Park S, Chung SW, Mirkin CA (2004) Hybrid organic-inorganic, rod-shaped nanoresistors and diodes. J Am Chem Soc 126(38):11772–11773
34. Park S, Lim JH, Chung SW, Mirkim CA (2004) Self-assembly of mesoscopic metal-polymer amphiphiles. Science 303(5656):348–351
35. Paxton WF, Kistler KC, Olmeda CC, Sen A et al (2004) Catalytic nanomotors: autonomous movement of striped nanorods. J Am Chem Soc 126(41):13424–13431
36. Peng XG, Manna L, Yang WD, Wickham J et al (2000) Shape control of CdSe nanocrystals. Nature 404(6673):59–61
37. Yoo SH, Park S (2007) Platinum-coated, nanoporous gold nanorod arrays: synthesis and characterization. Adv Mater 19(12):1612–1615
38. Michailowski A, Almawlawi D, Cheng GS, Moskovits M (2001) Highly regular anatase nanotubule arrays fabricated in porous anodic templates. Chem Phys Lett 349(1–2):1–5
39. Shelimov KB, Moskovits M (2000) Composite nanostructures based on template-grown boron nitride nanotubules. Chem Mater 12(1):250–254
40. Shin TY, Yoo SH, Park S (2008) Gold nanotubes with a nanoporous wall: their ultrathin platinum coating and superior electrocatalytic activity toward methanol oxidation. Chem Mater 20(17):5682–5686
41. Xiao R, Cho SI, Liu R, Lee SB (2007) Controlled electrochemical synthesis of conductive polymer nanotube structures. J Am Chem Soc 129(14):4483–4489
42. Ge JP, Zhang Q, Zhang TR, Yin YD (2008) Core-satellite nanocomposite catalysts protected by a porous silica shell: controllable reactivity, high stability, and magnetic recyclability. Angew Chem Int Ed 120(47):8924–8928
43. Ferrer D, Torres-Castro A, Gao X, Sepúlveda-Guzmán S et al (2007) Three-layer core/shell structure in Au-Pd bimetallic nanoparticles. Nano Lett 7(6):1701–1705
44. Qian F, Gradečak S, Li Y, Wen CY et al (2005) Core/multishell nanowire heterostructures as multicolor, high-efficiency light-emitting diodes. Nano Lett 5(11):2287–2291
45. Liu J, Xia H, Xue DF, Lu L (2009) Double-shelled nanocapsules of V_2O_5-based composites as high-performance anode and cathode materials for Li ion batteries. J Am Chem Soc 131(34):12086–12087
46. Lou XW, Yuan C, Archer LA (2007) Double-walled SnO_2 nano-cocoons with movable magnetic cores. Adv Mater 19(20):3328–3332
47. Lee KT, Jung YS, Oh SM (2003) Synthesis of tin-encapsulated spherical hollow carbon for anode material in lithium secondary batteries. J Am Chem Soc 125(19):5652–5653
48. Kalele S, Gosavi SW, Urban J, Kulkami SK (2006) Nanoshell particles: synthesis, properties and applications. Curr Sci 91(8):1038–1052
49. Balakrishnan S, Bonder MJ, Hadjipanayis GC (2009) Particle size effect on phase and magnetic properties of polymer-coated magnetic nanoparticles. J Magn Magn Mater 321(2):117–122

50. Kim MJ, Choa YH, Kim DH, Kim KH (2009) Magnetic behaviors of surface modified superparamagnetic magnetite nanoparticles. IEEE Trans Magn 45(6):2446–2449
51. Laurent S, Forget D, Port M, Roch A et al (2008) Magnetic iron oxide nanoparticles: synthesis, stabilization, vectorization, physicochemical characterizations, and biological applications. Chem Rev 108(6):2064–2110
52. Salgueiriño-Maceira V, Correa-Duarte MA (2007) Increasing the complexity of magnetic core/shell structured nanocomposites for biological applications. Adv Mater 19(23):4131–4144
53. Caruso F (2001) Nanoengineering of particle surfaces. Adv Mater 13(1):11–22
54. Daniel MC, Astruc D (2004) Gold nanoparticles: assembly, supramolecular chemistry, quantum-size-related properties, and applications toward biology, catalysis, and nanotechnology. Chem Rev 104(1):293–346
55. Phadtare S, Kumar A, Vinod VP, Dash C et al (2003) Direct assembly of gold nanoparticle "shells" on polyurethane microsphere "cores" and their application as enzyme immobilization templates. Chem Mater 15(10):1944–1949
56. Kortan AR, Hull R, Opila RL, Bawendi MG et al (1990) Nucleation and growth of cadmium selenide on zinc sulfide quantum crystallite seeds, and vice versa, in inverse micelle media. J Am Chem Soc 112(4):1327–1332
57. Qi LM, Ma JM, Cheng HM, Zhao ZG (1996) Synthesis and characterization of mixed CdS-ZnS nanoparticles in reverse micelles. Colloids Surf A: Physicochem Eng Asp 111(3):195–202
58. Mews A, Eychmueller A, Giersig M, Schooss D et al (1994) Preparation, characterization, and photophysics of the quantum dot quantum well system cadmium sulfide/mercury sulfide/cadmium sulfide. J Phys Chem 98(3):934–941
59. Ma GH, He J, Rajiv K, Tang SH et al (2004) Observation of resonant energy transfer in Au: CdS nanocomposite. Appl Phys Lett 84(23):4684–4686
60. Kamat PV, Shanghavi B (1997) Interparticles electron transfer in metal/semiconductor composites. picosecond dynamics of CdS-capped gold nanoclusters. J Phys Chem B 101(39):7675–7679
61. Scodeller P, Flexer V, Szamocki R, Calvo EJ (2008) Wired-enzyme core-shell Au nanoparticle biosensor. J Am Chem Soc 130(38):12690–12697
62. Babes L, Denizot B, Tanguy G, Jacques J (1999) Synthesis of iron oxide nanoparticles used as MRI contrast agents: a parametric study. J Colloid Interface Sci 212(2):474–482
63. de Farias PMA, Santos BS, Menezes FD, Brasil AG Jr et al (2007) Highly fluorescent semiconductor core-shell CdTe-CdS nanocrystals for monitoring living yeast cells activity. Appl Phys Mater Sci Process 89(4):957–961
64. de Menezes FD, Brasil AG Jr, Moreira WL, Barbosa LC et al (2005) CdTe/CdS core shell quantum dots for photonic applications. Microelectron J 36(11):989–991
65. Gupta AK, Gupta M (2005) Synthesis and surface engineering of iron oxide nanoparticles for biomedical applications. Biomaterials 26(18):3995–4021
66. Schreder B, Schmidt T, Ptatschek V, Spanhel L (2000) Raman characterization of CdTe/CdS-"core-shell"-clusters in colloids and films. J Cryst Growth 214–215(2):782–786
67. Zimmer JP, Kim SW, Ohnishi S, Tanaka E et al (2006) Size series of small indium arsenide-zinc selenide core-shell nanocrystals and their application to in vivo imaging. J Am Chem Soc 128(8):2526–2527
68. Dresco PA, Zaitsev VS, Gambino RJ, Chu B (1999) Preparation and properties of magnetite and polymer magnetite nanoparticles. Langmuir 15(6):1945–1951
69. Sounderya N, Zhang Y (2010) Use of core/shell structured nanoparticles for biomedical applications. Recent Patents Biomed Eng 1(1):34–42
70. Yan E, Ding Y, Chen CJ, Li R et al (2009) Polymer/silica hybrid hollow nanospheres with pH-sensitive drug release in physiological and intracellular environments. Chem Commun 45(19):2718–2720
71. Michalet X, Pinaud FF, Bentolila LA, Tsay JM et al (2005) Quantum dots for live cells, in vivo imaging, and diagnostics. Science 307(5709):538–544

72. De M, Ghosh PS, Rotello VM (2008) Applications of nanoparticles in biology. Adv Mater 20(22):4225–4241
73. Williams DB, Carter CB (1996) Transmission electron microscopy. Springer, New York
74. Subramanian R, Denney PE, Singh J, Otooni M (1998) A novel technique for synthesis of silver nanoparticles by laser-liquid interaction. J Mater Sci 33(13):3471–3477
75. Kumar P, Kumar R, Kanjilal D, Knobel M et al (2008) Ion beam synthesis of Ni nanoparticles embedded in quartz. J Vac Sci Technol B 26(4):36–40
76. Li H, Vilar RM, Wang YM (1997) Laser beam processing of a SiC particulate reinforced 6061 aluminium metal matrix composite. J Mater Sci 32(20):5545–5550
77. Dodd AC (2009) A comparison of mechanochemical methods for the synthesis of nanoparticulate nickel oxide. Powder Technol 196(1):30–35
78. Deng WJ, Xia W, Li C, Tang Y (2009) Formation of ultra-fine grained materials by machining and the characteristics of the deformation fields. J Mater Process Technol 209(9):4521–4526
79. Sasikumar R, Arunachalam RM (2009) Synthesis of nanostructured aluminium matrix composite (AMC) through machining. Mater Lett 63(28):2426–2428
80. Sneh O, Clark-Phelps RB, Londergan AR, Winkler J et al (2002) Thin film atomic layer deposition equipment for semiconductor processing. Thin Solid Films 402(1–2):248–261
81. Wang YY, Cai KF, Yao X (2009) Facile synthesis of PbTe nanoparticles and thin films in alkaline aqueous solution at room temperature. J Solid State Chem 182(12):3383–3386
82. Yoo SH, Liu LC, Park S (2009) Nanoparticle films as a conducting layer for anodic aluminum oxide template-assisted nanorod synthesis. J Colloid Interface Sci 339(1):183–186
83. Ye J, de Broed BV, Palma RD, Libaers W et al (2008) Surface morphology changes on silica-coated gold colloids. Colloids Surf A: Physicochem Eng Asp 322(1–3):225–233
84. Qi YL, Chen M, Liang S, Yang W et al (2008) Micro-patterns of Au@SiO_2 core-shell nanoparticles formed by electrostatic interactions. Appl Surf Sci 254(6):1684–1690
85. Qi YL, Chen M, Liang S, Zhao J et al (2007) Hydrophobation and self-assembly of core-shell Au@SiO_2 nanoparticles. Colloids Surf A: Physicochem Eng Aspects 302(1–3):383–387
86. Poovarodom S, Bass JD, Hwang SJ, Katz A (2005) Investigation of the core-shell interface in gold@silica nanoparticles: a silica imprinting approach. Langmuir 21(26):12348–12356
87. Lu Y, Yin YD, Li ZY, Xia YN (2002) Synthesis and self-assembly of Au@SiO_2 core-shell colloids. Nano Lett 2(7):785–788
88. Alejandro-Arellano M, Ung T, Blanco Á, Mulvaney P (2000) Silica-coated metals and semiconductors. Stabilization and nanostructuring. Pure Appl Chem 72(1–2):257–268
89. Li T, Moon J, Morrone AA, Mecholsky JJ et al (1999) Preparation of Ag/SiO_2 nanosize composites by a reverse micelle and sol-gel technique. Langmuir 15(13):4328–4334
90. Fu WY, Yang HB, Chang LX, Li MH et al (2005) Preparation and characteristics of core-shell structure nickel/silica nanoparticles. Colloids Surf A: Physicochem Eng Aspects 262(1–3):71–75
91. Lu XG, Liang GY, Sun ZB, Zhang W (2005) Ferromagnetic Co/SiO_2 core/shell structured nanoparticles prepared by a novel aqueous solution method. Mater Sci Eng B 117(2):147–152
92. Cha HJ, Kim YH, Cha HG, Kang YS (2007) Preparation and characterization of Ag (core)/SiO_2 (shell) nanoparticles. Surf Rev Lett 14(4):693–696
93. Kanehara M, Watanabe Y, Teranishi T (2009) Thermally stable silica-coated hydrophobic gold nanoparticles. J Nanosci Nanotechnol 9(1):673–675
94. Ma ZY, Dosev D, Nichkova M, Dumas RK et al (2009) Synthesis and characterization of multifunctional silica core-shell nanocomposites with magnetic and fluorescent functionalities. J Magn Magn Mater 321(10):1368–1371
95. Mazaleyrat F, Ammar M, LoBue M, Bonnet JP et al (2009) Silica coated nanoparticles: synthesis, magnetic properties and spin structure. J Alloys Compd 483(1–2):473–478

96. Dong BH, Cao LX, Su G, Liu W et al (2009) Synthesis and characterization of the water-soluble silica-coated ZnS:Mn nanoparticles as fluorescent sensor for Cu^{2+} ions. J Colloid Interface Sci 339(1):78–82
97. Ammar M, Mazaleyrat F, Bonnet JP, Audebert P et al (2007) Synthesis and characterization of core-shell structure silica-coated Fe29.5Ni70.5 nanoparticles. Nanotechnology 18(28):285606
98. Lee J, Lee YJ, Youn JK, Na HB et al (2008) Simple synthesis of functionalized superparamagnetic magnetite/silica core/shell nanoparticles and their application as magnetically separable high-performance biocatalysts. Small 4(1):143–152
99. Aliev FG, Correa-Duarte MA, Mamedov A, Ostrander JW et al (1999) Layer-by-layer assembly of core-shell magnetite nanoparticles: effect of silica coating on interparticle interactions and magnetic properties. Adv Mater 11(12):1006–1010
100. Lien YH, Wu TM (2008) Preparation and characterization of thermosensitive polymers grafted onto silica-coated iron oxide nanoparticles. J Colloid Interf Sci 326(2):517–521
101. He R, You XG, Shao J, Gao F et al (2007) Core/shell fluorescent magnetic silica-coated composite nanoparticles for bioconjugation. Nanotechnology 18(31):315601
102. Correa-Duarte MA, Giersig M, Liz-Marzán LM (1998) Stabilization of CdS semiconductor nanoparticles against photodegradation by a silica coating procedure. Chem Phys Lett 286(5–6):497–501
103. Kobayashi Y, Shimizu N, Misawa K, Takeda M et al (2008) Preparation of amine free silica-coated AgI nanoparticles with modified Stöber method. Surf Eng 24(4):248–252
104. Rogach AL, Nagesha D, Ostrander JW, Giersig M et al (2000) "Raisin bun"-type composite spheres of silica and semiconductor nanocrystals. Chem Mater 12(9):2676–2685
105. Zhu MQ, Han JJ, Li ADQ (2007) CdSe/CdS/SiO_2 core/shell/shell nanoparticles. J Nanosci Nanotechnol 7(7):2343–2348
106. Zhang SC, Li XG (2004) Synthesis and characterization of $CaCO_3$@SiO_2 core-shell nanoparticles. Powder Technol 141(1–2):75–79
107. Wang D, Salaueiriño-Maceira V, Liz-Marzán LM, Caruso F (2002) Gold-silica inverse opals by colloidal crystal templating. Adv Mater 14(12):908–912
108. Liz-Marzán LM, Giersig M, Mulvaney P (1996) Synthesis of nanosized gold-silica core-shell particles. Langmuir 12(18):4329–4335
109. Kückelhaus S, Reis SC, Carneiro MF, Tedesco AC et al (2004) In vivo investigation of cobalt ferrite-based magnetic fluid and magnetoliposomes using morphological tests. J Magn Magn Mater 272:2402–2403
110. Baldi G, Bonacchi D, Innocenti C, Lorenzi G et al (2007) Cobalt ferrite nanoparticles: the control of the particle size and surface state and their effects on magnetic properties. J Magn Magn Mater 311(1):10–16
111. Tartaj P, del Puerto Morales M, Veintemillas-Verdaguer S, González-Carreño T et al (2003) The preparation of magnetic nanoparticles for applications in biomedicine. J Phys D Appl Phys 36(13):R182
112. Lin YS, Haynes CL (2009) Synthesis and characterization of biocompatible and size-tunable multifunctional porous silica nanoparticles. Chem Mater 21(17):3979–3986
113. Cannas C, Musinu A, Ardu A, Orrù F et al (2010) $CoFe_2O_4$ and $CoFe_2O_4$/SiO_2 core/shell nanoparticles: magnetic and spectroscopic study. Chem Mater 22(11):3353–3361
114. Hu YX, Ge JP, Sun YG, Zhang TR et al (2007) A self-templated approach to TiO_2 microcapsules. Nano Lett 7(6):1832–1836
115. Ge JP, Hu YX, Biasini M, Beyermann WP et al (2007) Superparamagnetic magnetite colloidal nanocrystal clusters. Angew Chem Int Ed 46(23):4342–4345
116. Ge JP, Huynh T, Hu YX, Yin YD (2008) Hierarchical magnetite/silica nanoassemblies as magnetically recoverable catalyst-supports. Nano Lett 8(3):931–934
117. Obrovac MN, Krause LJ (2007) Reversible cycling of crystalline silicon powder. J Electrochem Soc 154(2):A103–A108

118. Maranchi JP, Hepp AF, Kumta PN (2003) High capacity, reversible silicon thin-film anodes for lithium-ion batteries. Electrochem Solid-State Lett 6(9):A198–A201
119. Limthongkul P, Jiang YI, Dudney NJ, Chiang YM (2003) Electrochemically-driven solid-state amorphization in lithium-silicon alloys and implications for lithium storage. Acta Mater 51(4):1103–1113
120. Chan CK, Peng HL, Liu G, Mcllwrath K et al (2008) High-performance lithium battery anodes using silicon nanowires. Nat Nanotechnol 3(1):31–35
121. Cui LF, Ruffo R, Chan CK, Peng HL et al (2009) Crystalline-amorphous core-shell silicon nanowires for high capacity and high current battery electrodes. Nano Lett 9(1):491–495
122. Freeman RG, Hommer MB, Grabar KC, Jackson MA et al (1996) Ag-clad Au nanoparticles: novel aggregation, optical, and surface-enhanced Raman scattering properties. J Phys Chem 100(2):718–724
123. Toshima N, Yonezawa T (1998) Bimetallic nanoparticles-novel materials for chemical and physical application. New J Chem 22(11):1179–1201
124. Tomas JM, Johnson BFG, Raja R, Sankar G et al (2003) High-performance nanocatalysts for single-step hydrogenations. Acc Chem Res 36(1):20–30
125. Scott RWJ, Wilson OM, Crooks RM (2005) Synthesis, characterization, and application of dendrimer-encapsulated nanoparticles. J Phys Chem B 109(2):692–704
126. Link S, Wang ZL, El-Sayed MA (1999) Alloy formation of gold-silver nanoparticles and the dependence of the plasmon absorption on their composition. J Phys Chem B 103(18):3529–3533
127. Hodak JH, Henglein A, Giersig M, Hartland GV (2000) Laser-induced inter-diffusion in AuAg core-shell nanoparticles. J Phys Chem B 104(49):11708–11718
128. Mallik K, Mandal M, Pradhan N, Pal T (2001) Seed mediated formation of bimetallic nanoparticles by UV irradiation: a photochemical approach for the preparation of "core-shell" type structures. Nano Lett 1(6):319–322
129. Mallin MP, Murphy CJ (2002) Solution-phase synthesis of sub-10 nm Au-Ag alloy nanoparticles. Nano Lett 2(11):1235–1237
130. Shibata T, Bunker BA, Zhang ZY, Meisel D et al (2002) Size-dependent spontaneous alloying of Au-Ag nanoparticles. J Am Chem Soc 124(40):11989–11996
131. Chen DH, Chen CJ (2002) Formation and characterization of Au-Ag bimetallic nanoparticles in water-in-oil microemulsions. J Mater Chem 12(5):1557–1562
132. Liu MZ, Guyot-Sionnest P (2004) Synthesis and optical characterization of Au/Ag core/shell nanorods. J Phys Chem B 108(19):5882–5888
133. Shankar SS, Rai A, Ahmad A, Sastry M (2004) Rapid synthesis of Au, Ag, and bimetallic Au core-Ag shell nanoparticles using Neem (Azadirachta indica) leaf broth. J Colloid Interf Sci 275(2):496–502
134. Hang CC, Yang Z, Chang HT (2004) Synthesis of dumbbell-shaped Au-Ag core-shell nanorods by seed-mediated growth under alkaline conditions. Langmuir 20(15):6089–6092
135. Song JH, Kim FK, Kim D, Yang PD (2005) Crystal overgrowth on gold nanorods: tuning the shape, facet, aspect ratio, and composition of the nanorods. Chem Eur J 11(3):910–916
136. Liu FK, Huang PW, Chang YC, Ko FH et al (2005) Combining optical lithography with rapid microwave heating for the selective growth of Au/Ag bimetallic core/shell structures on patterned silicon wafers. Langmuir 21(6):2519–2525
137. Xu SP, Zhao B, Xu WQ, Fan YG (2005) Preparation of Au-Ag coreshell nanoparticles and application of bimetallic sandwich in surface-enhanced Raman scattering (SERS). Colloids Surf A: Physicochem Eng Aspects 257–258:313–317
138. Wilson OM, Scott RWJ, Garcia-Martinez JC, Crooks RM (2005) Synthesis, characterization, and structure-selective extraction of 1-3 nm diameter AuAg dendrimer-encapsulated bimetallic nanoparticles. J Am Chem Soc 127(3):1015–1024

139. Pedersen DB, Wang SL, Duncan EJS, Liang SH (2007) Adsorbate-induced diffusion of Ag and Au atoms out of the cores of Ag@Au, Au@Ag, and Ag@AgI core-shell nanoparticles. J Phys Chem C 111(37):13665–13672
140. Rai A, Chaudhary M, Ahmad A, Bhargava S et al (2007) Synthesis of triangular Au core-Ag shell nanoparticles. Mater Res Bull 42(7):1212–1220
141. Tusji M, Miyamae N, Lim S, Kimura K (2006) Crystal structures and growth mechanisms of Au@Ag core-shell nanoparticles prepared by the microwave-polyol method. Cryst Growth Des 6(8):1801–1807
142. Tsuji M, Matsuo R, Jiang P, Miyamae N (2008) Shape-dependent evolution of Au@Ag core-shell nanocrystals by PVP-assisted *N,N*-dimethylformamide reduction. Cryst Growth Des 8(7):2528–2536
143. Yin YD, Rioux RM, Erdonmez CK, Hughes S et al (2004) Formation of hollow nanocrystals through the nanoscale Kirkendall effect. Science 304(5671):711–714
144. Sun YG, Xia YN (2002) Shape-controlled synthesis of gold and silver nanoparticles. Science 298(5601):2176–2179
145. Wang Y, Cai L, Xia Y (2005) Monodisperse spherical colloids of Pb and their use as chemical templates to produce hollow particles. Adv Mater 17(4):473–477
146. Liang HP, Zhang HM, Hu JS, Guo YG et al (2004) Pt hollow nanospheres: facile synthesis and enhanced electrocatalysts. Angew Chem Int Ed 116(12):1566–1569
147. Lou XW, Wang Y, Yuan C, Lee JY et al (2006) Template-free synthesis of SnO_2 hollow nanostructure with high lithium storage capacity. Adv Mater 18(17):2325–2329
148. Zeng HC (2006) Synthetic architecture of interior space for inorganic nanostructure. J Mater Chem 16(7):649–662
149. Caruso F, Caruso RA, Möhwald H (1998) Nanoengineering of inorganic and hybrid hollow spheres by colloidal templating. Science 282(5391):1111–1114
150. Yang ZZ, Niu ZW, Lu YF, Hu ZB et al (2003) Templated synthesis of inorganic hollow spheres with a tunable cavity size onto core-shell gel particles. Angew Chem Int Ed 42(17):1943–1945
151. Chen M, Wu L, Zhou S, You B (2006) A method for the fabrication of monodisperse hollow silica spheres. Adv Mater 18(6):801–806
152. Lou XW, Yuan CL, Archer LA (2007) Shell-by-shell synthesis of tin oxide hollow colloids with nanoarchitectured walls: cavity size tuning and functionalization. Small 3(2):261–265
153. Lou XW, Yuan C, Rhoades E, Zhang Q et al (2006) Encapsulation and Ostwald ripening of Au and Au-Cl complex nanostructures in silica shells. Adv Funct Mater 16(13):1679–1684
154. Kim SW, Kim M, Lee WY, Hyeon T (2002) Fabrication of hollow palladium spheres and their successful application to the recyclable heterogeneous catalyst for Suzuki coupling reactions. J Am Chem Soc 124(26):7642–7643
155. Dhas NA, Suslick KS (2005) Sonochemical preparation of hollow nanospheres and hollow nanocrystals. J Am Chem Soc 127(8):2368–2369
156. Zhou J, Liu J, Yang R, Lao CS et al (2006) SiC-shell nanostructures fabricated by replicating ZnO nano-objects: a technique for producing hollow nanostructures of desired shape. Small 2(11):1344–1347
157. Kamata K, Lu Y, Xia YN (2003) Synthesis and characterization of monodispersed core-shell spherical colloids with movable cores. J Am Chem Soc 125(9):2384–2385
158. Zhu YF, Kockrick E, Ikoma T, Hanagata N (2009) An efficient route to rattle-type Fe_3O_4@SiO_2 hollow mesoporous spheres using colloidal carbon spheres templates. Chem Mater 21(12):2547–2553
159. Zhou JB, Tang C, Cheng B, Yu JG et al (2012) Rattle-type carbon-alumina core-shell spheres: synthesis and application for adsorption of organic dyes. ACS Appl Mater Interfaces 4(4):2174–2179
160. Yu JG, Yu XX (2008) Hydrothermal synthesis and photocatalytic activity of zinc oxide hollow spheres. Environ Sci Technol 42(13):4902–4907

161. Sevilla M, Fuertes AB (2009) Chemical and structural properties of carbonaceous products obtained by hydrothermal carbonization of saccharides. Chem Eur J 15(16):4195–4203
162. Wang YQ, Nikitin K, McComb DW (2008) Fabrication of Au-Cu_2O core-shell nanocube heterostructures. Chem Phys Lett 456(4–6):202–205
163. Wagner JB, Sköld N, Wallenberg LR, Samuelson L (2010) Growth and segregation of Ga-As-$Al_xIn_{1-x}P$ core-shell nanowires. J Cryst Growth 312(10):1755–1760
164. Garcia-Gutierrez D, Gutierrez-Wing C, Miki-Yoshida M, Jose-Yacaman M (2004) HAADF study of Au-Pt core-shell bimetallic nanoparticles. Appl Phys Mater Sci Process 79(3):481–487
165. Ren F, Jiang CZ, Wang YH, Wang QQ et al (2006) The problem of core/shell nanoclusters formation during ion implantation. Nucl Instrum Methods Phys Res B 245(2):427–430
166. Wang JX, Inada H, Wu LJ, Zhu YM et al (2009) Oxygen reduction on well-defined core-shell nanocatalysts: particle size, facet, and Pt shell thickness effects. J Am Chem Soc 131(47):17298–17302
167. Tak Y, Hong SJ, Lee JS, Yong K (2009) Fabrication of ZnO/CdS core/shell nanowire arrays for efficient solar energy conversion. J Mater Chem 19(33):5945–5951
168. Strasser P, Koh S, Anniyev T, Greeley J et al (2010) Lattice-strain control of the activity in dealloyed core-shell fuel cell catalysts. Nat Chem 2(6):454–460
169. Wu Y, Jiang P, Jiang M, Wang TW et al (2009) The shape evolution of gold seeds and gold@silver core-shell nanostructures. Nanotechnology 20(30):305602
170. Serpell CJ, Cookson J, Ozkaya D, Beer PD (2011) Core@shell bimetallic nanoparticle synthesis via anion coordination. Nat Chem 3(6):478–482
171. Li ZY, Yuan J, Chen Y, Palmer RE et al (2005) Direct imaging of core-shell structure in silver-gold bimetallic nanoparticles. Appl Phys Lett 87(24):243103
172. Habas SE, Lee H, Radmilovic V, Somorjai GA et al (2007) Shaping binary metal nanocrystals through epitaxial seeded growth. Nat Mater 6(9):692–697
173. Sanchez SI, Small MW, Zuo JM, Nuzzo RG (2009) Structure characterization of Pt-Pd core-shell nanoclusters at atomic resolution. J Am Chem Soc 131(24):8683–8689
174. Lim B, Jiang MJ, Camargo PHC, Cho EC (2009) Pd-Pt bimetallic nanodendrites with high activity for oxygen reduction. Science 324(5932):1302–1305
175. Lin G, Heggen M, Rudi S, Strasser P (2012) Core-shell compositional fine structures of dealloyed Pt_xNi_{1-x} nanoparticles and their impact on oxygen reduction catalysis. Nano Lett 12(10):5423–5430
176. Kim K, Kim KL, Shin KS (2011) Coreduced Pt/Ag alloy nanoparticles: surface-enhanced raman scattering and electrocatalytic activity. J Phys Chem C 115(47):23374–23380
177. Greene LE, Law M, Yuhas BD, Yang PD (2007) ZnO-TiO_2 core-shell nanorod/P3HT solar cells. J Phys Chem C 111(50):18451–18456
178. Lin HM, Chen YL, Yang J, Liu YC et al (2003) Synthesis and characterization of core-shell CaP@GaN and GaN@GaP nanowires. Nano Lett 3(4):537–541
179. Law M, Greene LE, Radenovic A, Kuykendall T et al (2006) ZnO-Al_2O_3 and ZnO-TiO_2 core-shell nanowire dye-sensitized solar cells. J Phys Chem B 110(45):22652–22663
180. Lauhon LJ, Gudiksen MS, Wang DL, Lieber CM (2002) Epitaxial core-shell and core-multishell nanowire heterostructures. Nature 420(6911):57–61
181. Algra RE, Hocevar M, Verheijen MA, Zardo I et al (2011) Crystal structure transfer in core/shell nanowires. Nano Lett 11(4):1690–1694
182. Kim H, Achermann M, Balet LP, Hollingsworth JA et al (2005) Synthesis and characterization of Co/CdSe core/shell nanocomposites: bifunctional magnetic-optical nanocrystals. J Am Chem Soc 127(2):544–546
183. Lambert K, Geyter BD, Moreels I, Hens Z (2009) PbTe|CdTe core|shell particles by cation exchange, a HR-TEM study. Chem Mater 21(5):778–780
184. Kong XY, Ding Y, Wang ZL (2004) Metal-semiconductor Zn-ZnO core-shell nanobelts and nanotubes. J Phys Chem B 108(2):570–574

185. Pietryga JM, Werder DJ, Williams DJ, Casson JL (2008) Utilizing the lability of lead selenide to produce heterostructured nanocrystals with bright, stable infrared emission. J Am Chem Soc 130(14):4879–4885
186. Koike K, Honden T, Makabe I, Yan FP et al (2003) PbTe/CdTe single quantum wells grown on GaAs (100) substrates by molecular beam epitaxy. J Cryst Growth 257(1–2): 212–217
187. Huang MH, Mao S, Feick H, Yan HQ et al (2001) Room-temperature ultraviolet nanowire nanolasers. Science 292(5523):1897
188. Arnold MS, Avouris P, Pan ZW, Wang ZL (2003) Field-effect transistors based on single semiconducting oxide nanobelts. J Phys Chem B 107(3):659
189. Comini E, Faglia G, Sberveglieri G, Pan ZW et al (2002) Stable and highly sensitive gas sensors based on semiconducting oxide nanobelts. Appl Phys Lett 81(10):1869
190. Hughes WL, Wang ZL (2003) Nanobelts as nanocantilevers. Appl Phys Lett 82(17):2886
191. Bai XD, Gao PX, Wang ZL, Wang EG (2003) Dual-mode mechanical resonance of individual ZnO nanobelts. Appl Phys Lett 82(26):4806
192. Pan ZW, Dai ZR, Wang ZL (2001) Nanobelts of semiconducting oxides. Science 291(5510):1947
193. Gallaso F (1970) Structure and properties of inorganic solids. Pergamon, Oxford
194. Nguyen VL, Ohtaki M, Matsubara T, Cao MT et al (2012) New experimental evidences of Pt-Pd bimetallic nanoparticles with core-shell configuration and highly fine-ordered nanostructures by high-resolution electron transmission microscopy. J Phys Chem C 116(22):12265–12274
195. Schlötzer-Schrehardt U, Körtje KH, Erb C (2001) Energy-filtering transmission electron microscopy (EFTEM) in the elemental analysis of pseudoexfoliative material. Curr Eye Res 22(2):154–162
196. Leapman RD, Kocsis E, Zhang G, Talbot TL et al (2004) Three-dimensional distributions of elements in biological samples by energy-filtered electron tomography. Ultramicroscopy 100(1–2):115–125
197. Wang YQ, Duan XF, Cao LM, Wang WK (2002) One-dimensional growth mechanism of amorphous boron nanowires. Chem Phys Lett 359(3–4):273–277
198. Wang YQ, Duan XF, Cao LM, Li G et al (2002) Application of energy-filtering transmission electron microscopy to characterize amorphous boron nanowires. J Cryst Growth 244(1):123–128
199. Tambe MJ, Lim SK, Smith MJ, Allard LF et al (2008) Realization of defect-free epitaxial core-shell GaAs/AlGaAs nanowire heterostructures. Appl Phys Lett 93(15):151917
200. Morales AM, Lieber CM (1998) A laser ablation method for the synthesis of crystalline semiconductor nanowires. Science 279(5348):208–211
201. Zhang YF, Tang YH, Wang N, Lee CS (2000) Germanium nanowires sheathed with an oxide layer. Phys Rev B 61(7):4518–4521
202. Cao LM, Zhang Z, Sun LL, Gao CX et al (2001) Well-aligned boron nanowire arrays. Adv Mater 13(22):1701–1704
203. Qian F, Li Y, Gradečak S, Wang DL et al (2004) Gallium nitride-based nanowire radial heterostructures. Nano Lett 4(10):1975–1979
204. Hiramatsu K, Nishiyama K, Motogaito A, Miyake H et al (1999) Recent progress in selective area growth and epitaxial lateral overgrowth of III-nitrides: effects of reactor pressure in MOVPE growth. Appl Mater Sci 176(1):535–543
205. Gerthsen D, Hahn E, Neubauer B, Potin V et al (2003) Indium distribution in epitaxially grown InGaN layers analyzed by transmission electron microscopy. Phys Status Solidi C 0(6):1668–1683

Valence Electron Spectroscopy for Transmission Electron Microscopy

7

Masami Terauchi

Contents

1 Definition of the Topic 287
2 Overview 288
3 Introduction 288
4 Experimental and Instrumental Methodology 291
5 Valence Electron Spectroscopy by TEM 294
5.1 Ultrasoft-X-Ray Emission Spectra of Simple Metals 294
5.2 Al-L and Si-L Emission Spectra of Compounds 298
5.3 Boron K-Emission Spectra 301
5.4 Carbon K-Emission Spectra 306
5.5 L-Emissions of a Few Transition Metal Elements 310
6 M-Emission Intensity and 4*f*-Electron Numbers of Lanthanide Atoms 314
7 Anisotropic Soft-X-Ray Emission 317
8 Total Electronic Structure Analyses 320
9 Extension for Much Higher-Energy Region 324
10 Conclusions and Future Prospective 327
References 328

1 Definition of the Topic

Soft-X-ray emission spectroscopy (SXES) based on transmission electron microscopy can give us information of energy state of valence electrons (bonding electrons) from small specimen areas examined by microscopy, electron diffraction, and elemental analysis. The information of valence electrons cannot be directly obtained by electron energy-loss spectroscopy (EELS) widely used nowadays.

M. Terauchi
Institute of Multidisciplinary Research for Advanced Materials, Tohoku University, Aoba-ku, Sendai, Japan
e-mail: terauchi@tagen.tohoku.ac.jp

C.S.S.R. Kumar (ed.), *Transmission Electron Microscopy Characterization of Nanomaterials*, DOI 10.1007/978-3-642-38934-4_7,
© Springer-Verlag Berlin Heidelberg 2014

In this chapter, developments of SXES instruments for conventional transmission electron microscopes (TEMs) and those results applied to materials to obtain information of valence electrons are described.

2 Overview

We constructed grazing-incidence soft-X-ray spectrometers for transmission electron microscopes. The spectrometers were composed of varied-line-spacing (aberration-corrected) gratings and charge-coupled device (CCD) or multichannel plate (MCP) detectors. Those instruments have been applied to obtain the density of states (DOS) of valence bands (VB) by analyzing photon energies of K-emissions of Li, Be, B, and C and L-emissions of Mg, Al, and Si. L-emissions of some transition metal elements were also measured. Characteristic intensity distributions (DOS) of corresponding materials were obtained from identified specimen areas. M-emission intensities of lanthanide atoms of those oxides were measured and related to the number of 4*f* electrons. As SXES spectrum can be obtained from a single-crystalline area of a well-defined crystal orientation, the instruments were also applied to detect anisotropic soft-X-ray emission intensity, which reflects an anisotropic spatial distribution of valence electrons, of graphite and hexagonal BN. As a goal of electronic structure analysis based on transmission electron microscopy, combined analyses of SXES (DOS of VB) and inner-shell excitation EELS (DOS of conduction bands, CB) and a result of Kramers-Kronig analysis of valence excitation EELS (joint DOS of VB and CB) are presented. Finally, further development and future prospects are described.

3 Introduction

Transmission electron microscope (TEM) is a powerful and widely used tool for analyzing the crystalline order and orientation by electron diffraction patterns, lattice defects by Bragg contrast imaging, atomic arrangements by phase-contrast and/or annular high-angle dark-field contrast imagings, and the composition by X-ray emission spectroscopy (energy-dispersive spectroscopy, EDS) of nm-scale specimen areas. Those capabilities of TEM have been applied to improve LSI devices by miniaturizing gate transistors and develop new functional materials composed of nanometer-scale objects. In those applications, it has been requested not only the analyses of the structure and the composition but also the evaluation of physical properties with a nanometer-scale spatial resolution.

High energy-resolution electron energy-loss spectroscopy (EELS) with energy resolutions of 0.1–0.2 eV based on TEM is a powerful method for investigating physical properties from identified small specimen areas. Figure 7.1 shows a schematic drawing of electronic transitions among conduction bands (CB), valence bands (VB), and inner-shell levels. Valence electron excitation EELS spectra (process **a**) include information of a bandgap energy, interband transition energies,

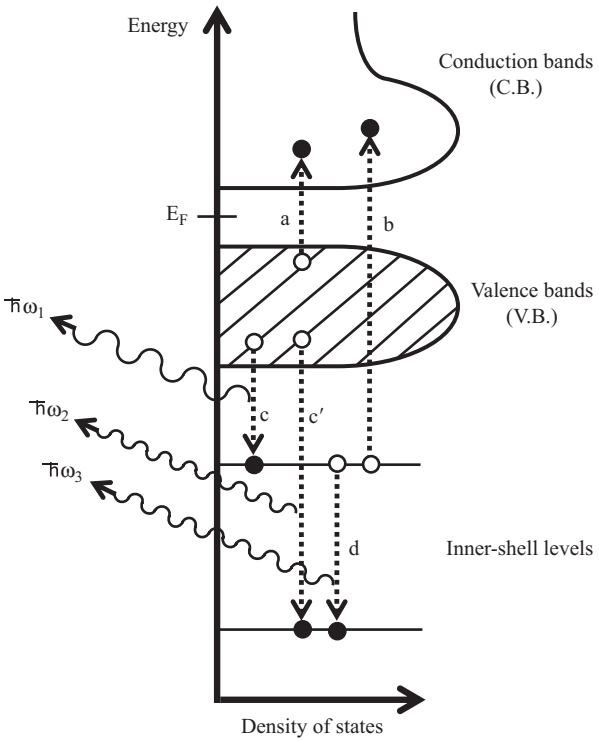


Fig. 7.1 Schematic diagram of electronic structure and electronic transitions related to EELS (*a* and *b*) and XES (*c*, *c*', and *d*)

and refractive indices. The information is obtained as a dielectric function, which is derived from an experimentally determined loss function by using Kramers-Kronig analysis. Thus, this process, experiment and analysis, corresponds to optical experiments continuously conducted in a wide energy range from the near-infrared to the extreme ultraviolet or soft X-ray. Inner-shell electron excitation EELS spectra (process **b**) give us information of the density of states (DOS) of the CB, unoccupied states. This spectroscopy corresponds to X-ray absorption experiments. This experiment with TEM is usually conducted under the dipole-transition condition, which means that the difference between the angular-momentum quantum numbers of initial and final states, Δl, should be ± 1. As the symmetry of the initial states, inner-shell orbitals, are well defined, the symmetry of the final states are restricted. For example, a K-shell electron ($l = 0$) has to go into the *p*-symmetry states ($l = 1$) of CB. Thus, an intensity distribution of inner-shell excitation spectrum corresponds to a partial DOS of CB with a specific symmetry. Together with the DOS of the conduction bands, the DOS of the valence bands (occupied states) is necessary to understand the whole electronic structure of a material. This is important because the origin of stabilizing a material is the energy states of valence electrons (bonding electrons). This information is included in the joint DOS of CV and VB (the imaginary part of ε, ε_2), which can be obtained from valence electron

excitation EELS experiments. However, it is usually not possible to deduce the valence DOS from ε_2 and the DOS of CB, because the information of energy dispersion is included in ε_2 but lost in the DOS of CB.

Photoelectron emission spectroscopy (PES) gives us the total DOS (without symmetry selection) of VB of a material. Furthermore, the energy dispersion of electronic states can be obtained by angle-resolved PES experiments. On the other hand, PES experiment needs clean surface under an ultrahigh-vacuum condition, because the escape depth of photoelectrons is smaller than one nm. Thus, this method is usually unsuited to combine with a conventional TEM. X-ray emissions caused by electronic transitions from valence bands to inner-shell core-hole states (process **c** and **c**′ in Fig. 7.1) also include the information of the energy states of the valence electrons. Since the symmetry of the inner-shell states is well defined, the emission intensity includes the information of a partial DOS of VB with a specific symmetry. Furthermore, X-ray emission spectra of different atoms of a compound show us the component of different atoms of the valence DOS. X-ray emission caused by the electronic transition **d**, which is between inner-shell levels, does not contain the information of valence electrons. However, this transition energy can be affected by an amount of valence charge via chemical shifts of the two inner-shell levels. Those emission energies range in the soft-X-ray energy region from 15 to 6,000 eV [1]. Since there are many atomic resonances in this energy region, soft-X-ray emission spectroscopy (SXES) provides not only the probing method for the energy states of VB but also a sensitive tool for elemental and chemical identification, which can make many application opportunities. Thus, SXES is a one candidate for valence electron spectroscopy by TEM. This method does not need an ultrahigh-vacuum condition, because the absorption length of soft X-rays is larger than surface thickness of a few tens of nanometers [2]. Then, it can be combined with a conventional TEM. Another advantage of SXES is that a charging problem of a specimen in PES, which causes an ambiguity in energy determination, does not come out because soft-X-ray emissions originate from electronic transitions inside a material. One drawback of this method is the low emission efficiency. For example, the yield of X-ray emission of carbon 1*s* core-hole state is 2.8×10^{-3} [3]. Thus, a longer acquisition time is necessary compared to those of EELS experiments. An energy resolution of SXES instrument for obtaining fine structures of the DOS of VB should be better than 1 eV, because the energy spread of the valence band is usually from 5 to 10 eV. This energy resolution is comparable to those of conventional X-ray photoelectron spectroscopy (XPS) or electron spectroscopy for chemical analysis (ESCA) instruments.

Another point should be taken into account for obtaining the energy resolution of better than 1 eV is a natural width, lifetime broadening, of inner-shell levels [4]. This natural broadening is directly related to the fluorescent yield of each transition. The initial state for emission, a highly excited state with an inner-shell core-hole, can decay to the lower excited states or the ground state by X-ray emission, Auger electron emission, and a creation of another core-hole state via Coster-Kronig process. A high yield for X-ray emission, a short lifetime, causes a larger natural width. For example, the emission yield and the

natural width of Cu-L_3 level are 6×10^{-3} and 0.56 eV, respectively. Then, an instrumental energy resolution of 0.8 eV is necessary for realizing 1 eV resolution for Cu-Lα emission ($3d \rightarrow L_3$; 930 eV). Other origins for level broadenings can be a multiple splitting of inner-shell level and a multiple ionization of atom.

After the pioneering work of an electron-beam-induced X-ray emission analysis of Al–Cu alloys by Castaing [5], the method has been widely used for phase identifications and/or elemental analyses of materials as wavelength-dispersive X-ray spectroscopy (WDS) and energy-dispersive X-ray spectroscopy (EDS). WDS devices are usually based on Rowland mounting optics, which needs a moving mechanism for obtaining a spectrum in a certain energy range. Although a usual WDS device has a better energy resolution of about 10 eV than that of EDS, it has not been applied for a TEM, because a moving mechanism can be an origin of a mechanical noise. A conventional EDS, Si(Li) or silicon-drift detector, attached to a TEM, has energy resolutions of 120–130 eV without any moving mechanism. This energy resolution is limited by the statistical nature of electron-hole creation and the electron-hole formation energy. A new microcalorimeter EDS device [6, 7] has an energy resolution of about 10 eV. As this new EDS works under a cryogenic temperature of about 0.1 K, the reductions of size and mechanical noise of refrigerator are important issues at present. Those energy resolutions of WDS and EDS are useful for elemental analyses but not enough for obtaining the DOS of VB. High-energy-resolution WDS systems with energy resolutions of about 0.1 eV have been constructed for synchrotron orbital-radiation (SOR) facilities. Although the WDS systems of SOR can obtain the DOS of the valence band, those instruments cannot be introduced to a TEM because they have a few or several meters in those lengths. For an SXES instrument for a TEM, a size of smaller than about 1 m without a moving mechanism is necessary. At the same time, the energy resolution should be better than 1 eV for obtaining fine structures of the DOS of VB. For that purpose, compact SXES spectrometers have been designed, manufactured, and tested by attaching to a conventional TEM [8–12].

In the following sentences, optics and instrumentations of the spectrometers, application results showing DOS of characteristic electronic states of metal and semiconductors, the relation between emission intensity and 4*f*-electron numbers of lanthanum atoms, anisotropic emission intensities due to anisotropic valence charge distribution in real space, total electronic structure analysis by combining EELS and SXES, and possibility of a further development are described.

4 Experimental and Instrumental Methodology

We have developed six SXES instruments without a moving mechanism for conventional TEMs [7–11]. Those spectrometers are wavelength-dispersive type and based on not Rowland mounting optics but the flat-field grazing-incidence optics

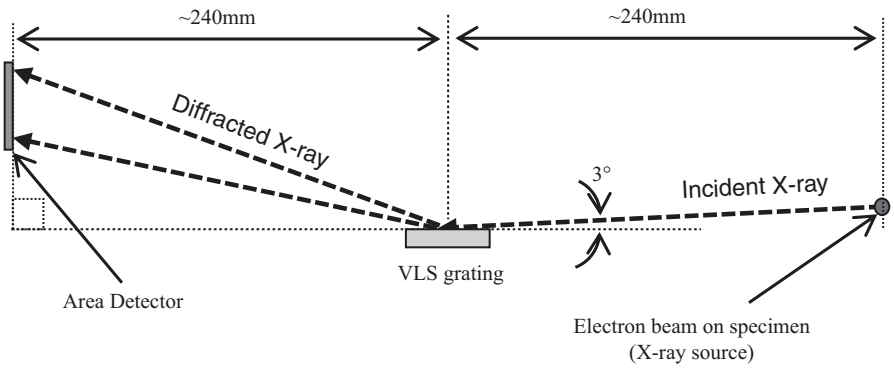


Fig. 7.2 Schematic figure of the optics of a grazing-incidence soft-X-ray spectrometer by using a varied-line-spacing (aberration-corrected) grating

by using varied-line-spacing (VLS) gratings [13, 14]. The grazing-incidence optics is for improving the reflection efficiency of the grating. The systematic change of the groove spacing of the gratings has been designed for reducing the aberration. Figure 7.2 shows a schematic figure of the optics of a spectrometer. The grating works for a fixed grazing incidence angle, which ranges from 1.4° to 4°, depending on the design of the acceptance energy range of the grating. This small grazing incidence angle causes a small solid angle for detection. For improving detection efficiency, X-ray correction mirrors have been designed and fabricated to increase the detection solid angle of SXES instruments by a factor of 2–3. The detection efficiency was also improved by adopting an area detector, a parallel detection. On the other hand, this small collection angle enables us to integrate the spectrometer into a conventional electron microscope without any change in electron optics of the microscope. The distance from the electron-probe position on a specimen (a source of X-ray emission) to the spectrum plane (detector plane) is about 50 cm. This compact size means smaller energy dispersion on the spectrum plane. Then, a smaller pixel-sized detector for soft X-ray is necessary for obtaining a reasonable energy resolution.

The first spectrometer (ver.1) was composed of a VLS grating with an average groove density of 1,200 lines/mm and a back-thin-type charge-coupled device (CCD) detector of 26.4 × 7.9 mm^2 (1,100 × 330 channels) [7]. This spectrometer worked for 60–300 eV. Figure 7.3 shows a photo of ver.1 attached to a conventional TEM. The spectrometer successfully gave us SXES spectra of *h*-BN, whose intensity profile showed the characteristics of the DOS of the material. Unfortunately, the specimen had to be tilted more than 20° for the emitted soft X-rays to go into the spectrometer. After that, some SXES instruments had been constructed with different specifications in acceptable energy range and energy resolution.

The latest spectrometer (ver.6) was designed to cover from 50 to 3,800 eV by using four VLS gratings, whose optics also adopted the flat-field grazing-incidence [10, 11]. Figure 7.4 shows a photo of ver.6 spectrometer attached to a conventional TEM. The most different point in spectrometer design from that of ver.1 (Fig. 7.3) is the direction of soft X-ray to analyze. The elevation angle from the lateral

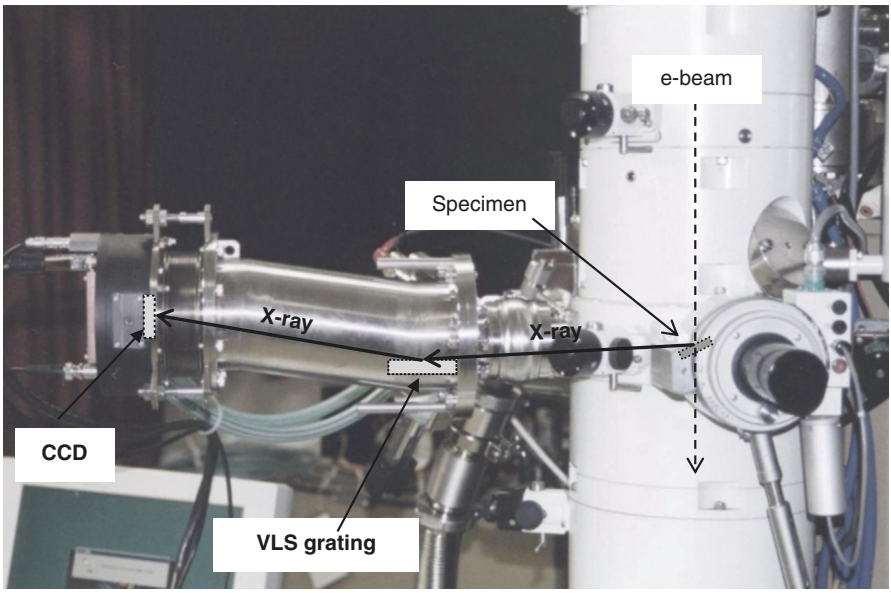


Fig. 7.3 Photo of SXES spectrometer ver.1 attached to a conventional TEM. Specimen had to be tilted more than 20° for the emitted soft X-rays to go into the spectrometer

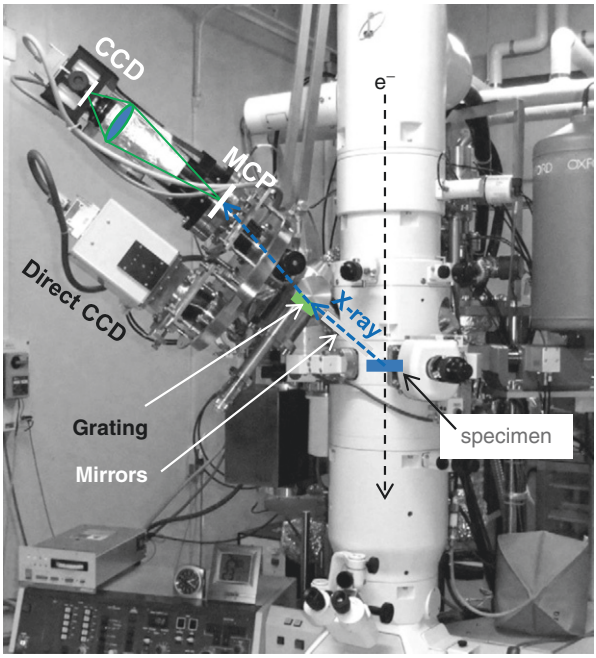


Fig. 7.4 Photo of ver.6 spectrometer attached to a conventional TEM. The elevation angle of X-rays to analyze from the lateral direction is about 35°, which enables us to analyze emitted X-rays under a usual TEM experimental condition without a special specimen tilt as in the case of early instruments

direction is about 35°, which enables us to analyze emitted X-rays under a usual TEM experimental condition without a special specimen tilt as in the case of early instruments. This spectrometer is composed of a pair of X-ray reflection mirrors, VLS gratings, and detectors. The X-ray reflection mirrors have gold surface and a length of 14 cm along incoming X-ray path. Two types of detectors are attached. Upper detector in Fig. 7.4 is for lower-energy region. It is a multichannel plate (MCP) optically coupled with a conventional CCD camera (1,344 × 1,024 channels). This detector was operated in photon-counting mode to obtain the following SXES spectra. The MCP + CCD detector has an effective pixel size of 24 μm on the MCP plane, which is larger than that of the CCD detector of 13.5 μm used in the previous version. However, it does not cause a serious drawback because large energy dispersion is expected in a low-energy region (long-wavelength region). Another detector (lower one) is a back-thin-type CCD (2,048 × 506 channels) with a pixel size of 12 μm. This smaller pixel-sized CCD is mainly applied for higher-energy region, where the energy dispersion is smaller than the lower-energy region due to a shorter X-ray wavelength. Those two detectors can be interchanged keeping a high-vacuum condition of the spectrometer and the TEM.

In the following experiments, an accelerating voltage of the TEM was 100 kV. Examined specimen areas and illumination beam current were 0.5–3 μm and 4–20 nA, respectively, which were selected to escape from irradiation beam damage of specimens. Acquisition times were ranged from 5 min to 1 h because the emission yield is very small. The emission yield for soft-X-ray energy lower than 1 keV ranges from 10^{-5} to 10^{-2}. The energy scale of emission spectra was calibrated by using emission energies of elemental materials already known.

5 Valence Electron Spectroscopy by TEM

5.1 Ultrasoft-X-Ray Emission Spectra of Simple Metals

For simple metals, it is expected that the free electron model can be applied. Thus, K-emissions of metal-Li and metal-Be, L-emissions of metal-Mg and metal-Al, and M-emission of metal-Cu were measured.

Figure 7.5a shows a Li K-emission spectrum (VB → K-shell) of metal-Li. A piece of metal-Li specimen was prepared and transferred to a conventional TEM, as shown in Fig. 7.4, under an Argon atmospheric condition, since metal-Li is easily oxidized and/or nitrized in the air. This spectrum shows a clear Fermi edge at the right-hand-side end of the intensity distribution. A lateral thin arrow indicates the assigned top position of the Fermi edge. Fermi energy position (E_F), marked by x at the middle of Fermi edge, corresponds to the top of the occupied energy level of metal-Li. A small hump at 49.5 eV indicates that the surface of the specimen was oxidized a little. This soft-X-ray emission is due to transitions of valence electrons to 1*s* core-hole state. In case of isolated Li atoms, this transition is forbidden under the dipole-transition condition because the valence electrons have the character of 2*s* orbital. However, valence 2*s* electrons of Li atoms of

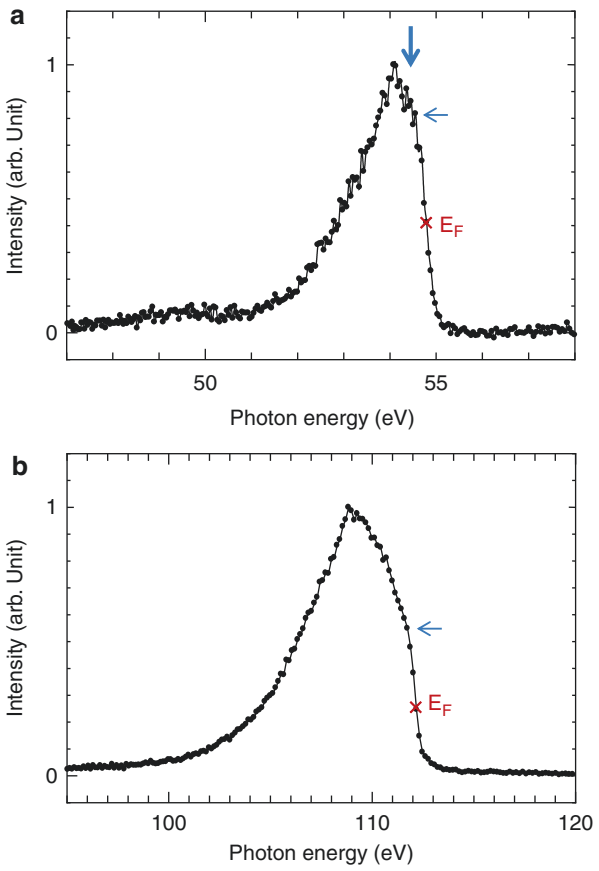


Fig. 7.5 (**a**) Li K-emission spectrum (VB → K-shell) of metal-Li. This spectrum shows a clear Fermi edge at the right-hand-side end of the intensity distribution. Fermi energy position (E_F), marked by x at the middle of Fermi edge, corresponds to the top of the occupied energy level of metal-Li. The suppressed intensity just below E_F, indicated by a vertical thick arrow, is due to the effect of 1*s* core-hole. (**b**) Be K-emission (VB → K-shell) spectrum of metal-Be. A Fermi energy position is marked by x at the middle of the Fermi edge. The delayed peak structure is well similar to a calculated density of states

bulk metal-Li form a free-electron-like band well described by plane waves. Then, dipole selection rule cannot be applied to metal-Li. Since Li atom has one valence electron (2*s* electron) per atom, the free electron Fermi sphere is well inside Brillouin zone and may not be affected from Brillouin zone boundary (BZB), where the band dispersion is modified. Then, the intensity distributions $I(E)$ of the lower part (apart from E_F) of the spectrum are expected to be written as $I(E')_K \propto E'^{3/2}$ (density of states of *p*-symmetry) due to the dipole selection rule (the effect of transition matrix) [1]. E' is an energy measured from the bottom of VB. For an accurate comparison between $I(E')$ and calculated DOS of VB, an energy dependence of transition matrix elements, E^3 (E: emitted photon energy), has to be taken into account. It can be now omitted because an interested energy region is limited. Experimental intensity distributions seem like those ways, indicating that the free electron model is appropriate for metal-Li. However, it is clearly seen that the intensity just below E_F is apparently suppressed, indicated by a vertical thick arrow, apart from $E'^{3/2}$. This discrepancy in Li K-emission has been explained

by the effect of 1*s* core-hole, which exists before an electronic transition from VB [15, 16]. It should be mentioned that Li K-emission intensity from Li-included compounds is very small compared with that of metal-Li. It reflects that Li atoms in compounds usually exist as Li^+ ions, which do not have 2*s* valence electrons, and little partial DOS of Li-2*s* component in VB. Weak intensity of Li K-emission of Li-contained materials can be observed in a little lower energy than that of metal-Li, because of a lower-energy position of VB of those materials as reported for LiF [17, 18]. In other words, an apparent Li K-emission intensity in Li compounds suggests a presence of a metal-Li particle due to a segregation of the compound.

Figure 7.5b shows a Be K-emission (VB → K-shell) spectrum of metal-Be. This spectrum shows a clear Fermi edge at the right-hand-side end of the intensity distribution. A lateral thin arrow indicates the assigned top position of the Fermi edge. A Fermi energy position, marked by x at the middle of the Fermi edge, corresponds to the top of the occupied energy level of the metal. Beryllium has two valence electrons (2*s* electrons) per atom. Then, it can be affected form BZB because of a larger free electron Fermi sphere than that of metal-Li. Thus, intensity distribution is obeyed to $I(E') \propto E'^{3/2}$ in the lower part of VB as in the case of Li K-emission and is strongly affected from BZB in the upper part of VB. The delayed peak structure is well similar to a calculated density of states [19]. The larger width of Be K-emission than that of Li-K may be due to the larger number of valence electrons per atom, two for Be and one for Li. Present separate observation of Fermi edge and the DOS profile of VB from an identified single-crystalline area show a high performance of the SXES instrument (ver.6) attached to a conventional TEM for valence electron spectroscopy.

Figure 7.6 shows L-emission (VB → $L_{2,3}$-shell) spectra of (a) metal-Mg and (b) metal-Al. The lower end of Mg L-emission was not observed due to the lower detection limit of the spectrometer ver.6. Each spectrum shows a sharp Fermi edge at the right-hand-side end. This sharp-edge position corresponds to transitions from Fermi energy (E_F) level, the highest occupied state. From the width of Fermi edge of Mg-L, an energy resolution was evaluated to be 0.15 eV. It can be seen that each Fermi edge shows a small shoulder at the bottom region as indicated by an arrow. This shoulder structure can be attributed to the electronic transitions from Fermi level to L_2-shell level. The remaining dominant intensity increase in each Fermi edge corresponds to transitions from E_F to L_3-shell level. The intensity ratio L_2/L_3 in each spectrum is about 1/8, which is similar to those already reported [20]. This value is much smaller than that of L-shell absorption spectrum of EELS, in which L_2/L_3 is about 1/2. This small L_2/L_3 value for X-ray emission is due to a redistribution process (Coster-Kronig (CK) transition) of core-hole states between subshells before radiative decay of core-hole states. By this process, an initial L_2-hole moves to L_3-level. This causes a decrease of L_2-emission and an increase of L_3-emission intensities. When taking into account the occupancies of L_2 and L_3 subshells, the CK probability from L_2 to L_3 is calculated to be 0.7 for $L_2/L_3 = 1/8$. This means that the 70 % of L_2-hole states transit to L_3-shell before making a radiative decay in metal-Mg and metal-Al. For more precise analysis, cross sections of L*i* ($i = 1, 2, 3$) subshells and CK transition from L_1-shell to $L_{2,3}$-shells have to be taken into account.

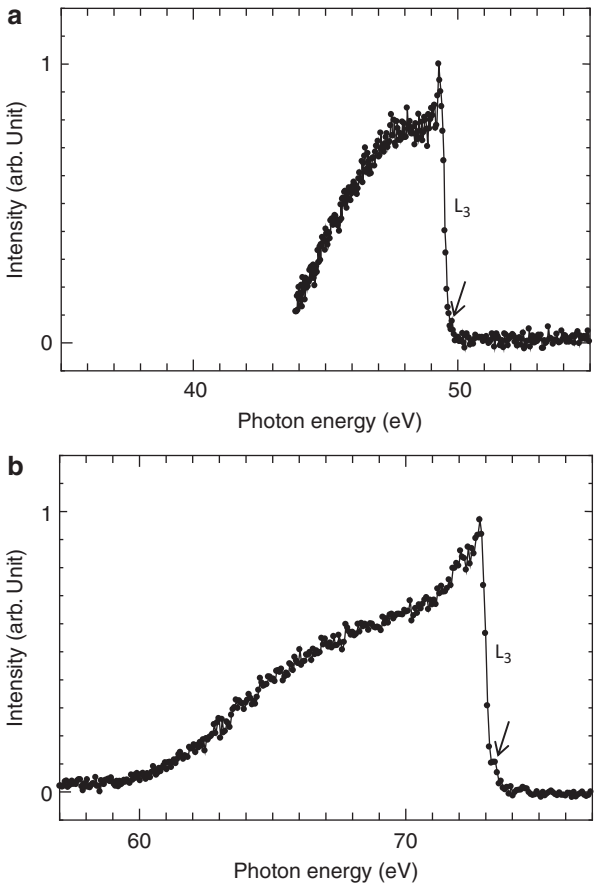


Fig. 7.6 L-emission (VB → $L_{2,3}$-shell) spectra of (**a**) metal-Mg and (**b**) metal-Al. From the width of Fermi edge of Mg-L, an energy resolution is evaluated to be 0.15 eV. Small shoulder structure indicated by arrows can be attributed to the electronic transitions from Fermi level to L_2-shell level

Since the valence electron states of metal-Mg and meta-Al can be described by a free electron model, the intensity distributions $I(E)$ of the lower part (apart from Fermi edge) of those L-emission spectra are expected to be written as $I(E')_{\mathrm{L}} \propto E'^{1/2}$ (density of states of *s*-symmetry) [1]. E' is an energy measured from the bottom of VB. Experimental intensity distributions seem like those ways except the top and the bottom regions, indicating that the free electron model is appropriate for those metals. It can be seen a characteristic sharp narrow peak just below Fermi edge in each spectrum. There has been a discussion about a role of *d*-like state just below E_F in Mg-based alloys [21, 22]. It has been concluded that the sharp narrow peak, in case of pure metals of Mg and Al, is mainly due to many-electron effect in the emission process than the contribution of *d*-like states. The intensity profile of the bottom part of Al-L emission seems different from $E'^{1/2}$. This tailing intensity was discussed as multi-electron or many-body effects [23]. The energy spread of valence electrons in metal-Al is about two times larger than that of metal-Mg. This suggests a larger energy dispersion of electron bands in metal-Al than that in metal-Mg.

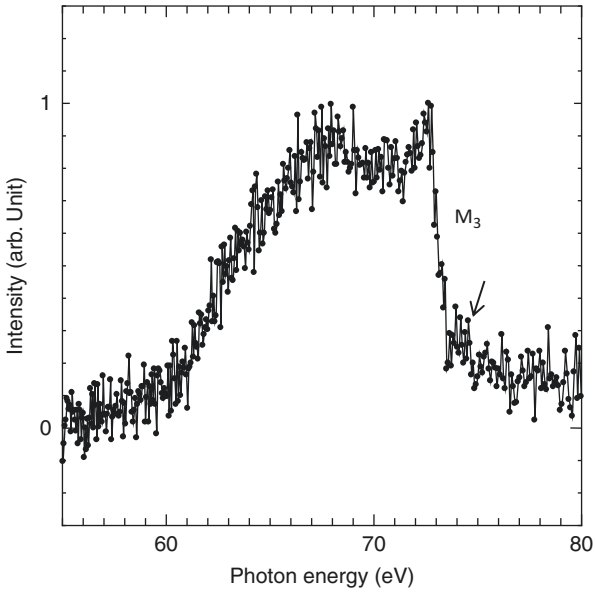


Fig. 7.7 $M_{2,3}$-emission (VB → $M_{2,3}$-shell) spectrum of metal-Cu

Figure 7.7 shows an $M_{2,3}$-emission (VB → $M_{2,3}$-shell) spectrum of metal-Cu. Since $M_{2,3}$-shell level has *p*-character, this spectrum intensity corresponds to *s*- and *d*-symmetry part of VB of metal-Cu. The *s*-character of VB, 4*s* band, spreads in energy and accommodated only one electron per atom. On the other side, the *d*-character, 3*d* bands, has a smaller spread in energy and accommodated ten electrons per atom. Thus, the observed intensity should be dominated from electronic transitions from 3*d* to M_3-shell by taking into account CK transition stated above. Fermi energy of metal-Cu is placed in the dispersive 4*s* band, where it is about 2 eV higher than the top of the 3*d* bands. At the position 2 eV higher than the onset of M_3-emission intensity, there can be seen a small onset intensity indicated by an arrow, where is also expected to appear the M_2-emission intensity. Thus, the onset intensity should be assigned to transitions from 3*d* to M_2-shell, because the DOS of 4*s* component at E_F may be much smaller compared to that of M_3-emission intensity [24].

5.2 Al-L and Si-L Emission Spectra of Compounds

Figure 7.8a shows Al-L emission (VB → L-shell) spectra of Al, AlN, and $MgAl_2O_4$. Those spectra were measured to have a similar signal to noise ratio. The probe current was almost the same for the spectra, but acquisition times were different as written beside each spectrum. The longer acquisition time for AlN and $MgAl_2O_4$ than that of Al reflects the smaller Al-3*s* component in VB of those materials. The top of the valence bands of insulators AlN and $MgAl_2O_4$ is indicated by vertical lines, where spectral intensity increased larger than the noise level of the background. The top of the valence bands (occupied states) of metal-Al is Fermi

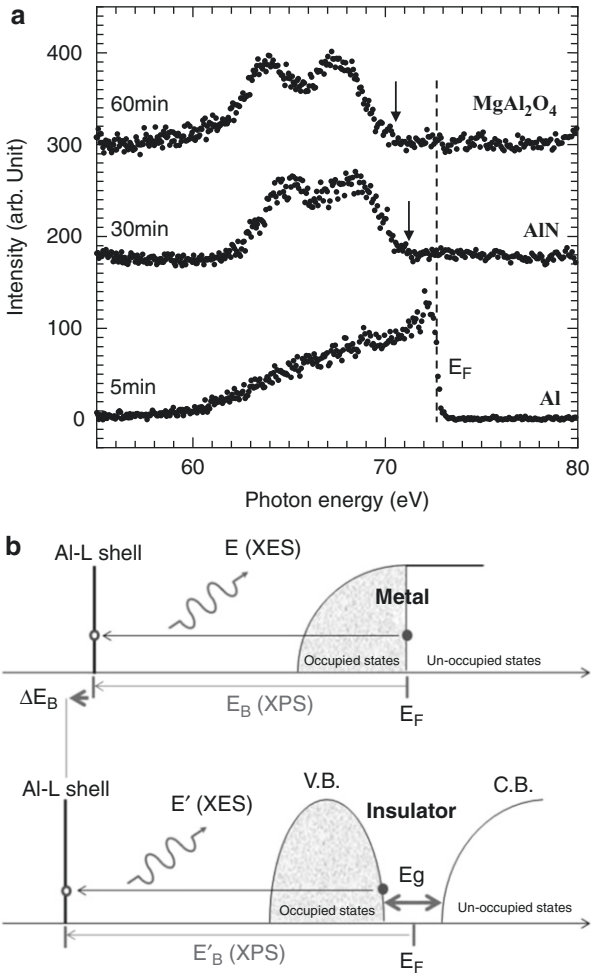


Fig. 7.8 (**a**) Al L-emission (VB → L-shell) spectra of Al, AlN, and $MgAl_2O_4$. Al-L emission spectra of AlN and $MgAl_2O_4$ are apparently different in those intensity distributions and energy positions from that of meta-Al. Those differences present us different chemical states of Al atoms in those materials from that of metal-Al. (**b**) A radiative electronic transition, corresponding to E_F position of the spectrum of metal-Al, is schematically shown in the upper part. The lower part schematically shows a radiative electronic transition from the top of the valence bands to an Al L-shell hole state, corresponding to AlN and $MgAl_2O_4$ (insulators) [11]

energy (E_F), indicated by a vertical dotted line. It is seen that Al L-emission spectra of AlN and $MgAl_2O_4$ are apparently different in those intensity distributions and energy positions from those of meta-Al. Those differences present us different chemical states of Al atoms in those materials from that of metal-Al. Intensity profiles of AlN and $MgAl_2O_4$ should be compared with Al *s*-symmetry components of the DOS of VB. The difference in energy positions of the top of the valence bands (indicated by vertical arrows) has to be considered by taking into account a chemical shift of Al L-shell, where a valence electron falls into, and an energy gap of the materials. A radiative electronic transition, which corresponds to Fermi edge intensity of the spectrum of metal-Al, is schematically shown in the upper part of Fig. 7.8b. The lower part schematically shows a radiative electronic transition from the top of the valence bands to an Al L-shell hole state, which corresponds to the right-hand-side ends of the intensity distributions of AlN and $MgAl_2O_4$ (insulators).

A decrease of valence electron causes a change of core-electron binding energy $\Delta E_B > 0$ (chemical shift). A positive chemical shift $\Delta E_B > 0$ causes an increase of emission energy. A presence of the bandgap energy (E_g) causes a decrease of emission energy by an amount of $\Delta E_B/2$. By comparing the two schematic figures, a relation of $E' = E + \Delta E_B - E_g/2$ in the energies of two emitting photons is obtained. A chemical shift of Al-L level and a bandgap energy are reported as 1.6 eV [25] and 6 eV [26] for AlN, and 1.9 eV [27] and 7.8 eV [28] for $MgAl_2O_4$, respectively. Then, shifts of spectral onset in higher-energy side of AlN and $MgAl_2O_4$ compared to that of Al metal, E′–E, are expected to be −1.4 and −2.0 eV, respectively. Those values are almost agreeable with those observed in corresponding spectra in Fig. 7.8a. The accuracy of this discussion may be 0.1–0.3 eV due to a variation of reported ΔE_B values by XPS experiments. It seems that this simple explanation based on the schematic picture of Fig. 7.8b works well. It may be due to the fact that the present and usual electron-beam-induced X-ray emission spectroscopy experiments give spectra corresponding to off-resonant condition and there is no significant core-hole effect, which is always a problem in interpretation of electron energy-loss near-edge fine structure (ELNES). SXES on resonant condition has been widely investigated by using synchrotron orbital-radiation facilities [29].

Figure 7.9a shows Si L-emission (VB → L-shell) spectra of Si, 3C-SiC, and SiO_2 (quartz). As in the case of aluminum oxides, the spectrum of SiO_2 (quarts) takes three times longer acquisition time than that of pure Si, even though the signal to noise ratio is lesser than the spectrum of pure Si. It may be not only due to a small amount of valence charge at Si atom sites in SiO_2 but also due to a relatively large absorption coefficient of oxygen atoms [30]. Four labels of $L_{2'}$, L_1, X_4, and $L_{3'}$ on the spectrum of crystalline Si are assignments in the band diagram [31]. The intensity distribution of spectra of 3C-SiC and SiO_2 is considerably different from that of Si, showing different chemical environments of Si atoms in those materials. The discussion on energy positions of the top of the valence bands for Fig. 7.8b has to be modified a little, because the top of the Si spectrum corresponds to an energy position below E_F by $E_g/2 = 0.6$ eV. Then, ΔE_B should be replaced by $\Delta E_B - 0.6$. A chemical shift of Si-L level and a bandgap energy are reported as 1.6 and 2.2 eV [32] for 3C-SiC and 4.1 eV [33, 34] and 9.6 eV [35] for SiO_2 (quartz), respectively. Then, shifts of spectral onset in higher-energy side of 3C-SiC and SiO_2 (quartz) compared to that of Si crystal, E'-E, are expected to be −0.1 eV and −1.3 eV, respectively. Those values almost agree with those shifts observed in Fig. 7.9a (indicated by vertical arrows).

Figure 7.9b shows Si L-emission spectra (VB → L-shell) of $TiSi_2$. An L-emission spectrum of bulk Si is also shown for comparison. $TiSi_2$ has been an interested conducting material in large-scale integrated circuit technology and a field-emission property of nanowires. Width of VB of $TiSi_2$ is almost the same with that of Si. The closely placed two-peak structures in the lower part of VB in $TiSi_2$, indicated by vertical lines, may correspond to two peaks labeled $L_{2'}$ and L_1 of Si. It is noted that the relative intensity in the upper part of VB (indicated by an arrow) is increased in $TiSi_2$ compared to that of Si. This intensity increase is reported to be a contribution of *d*-symmetry of Si, which interacts with 3*d* orbitals

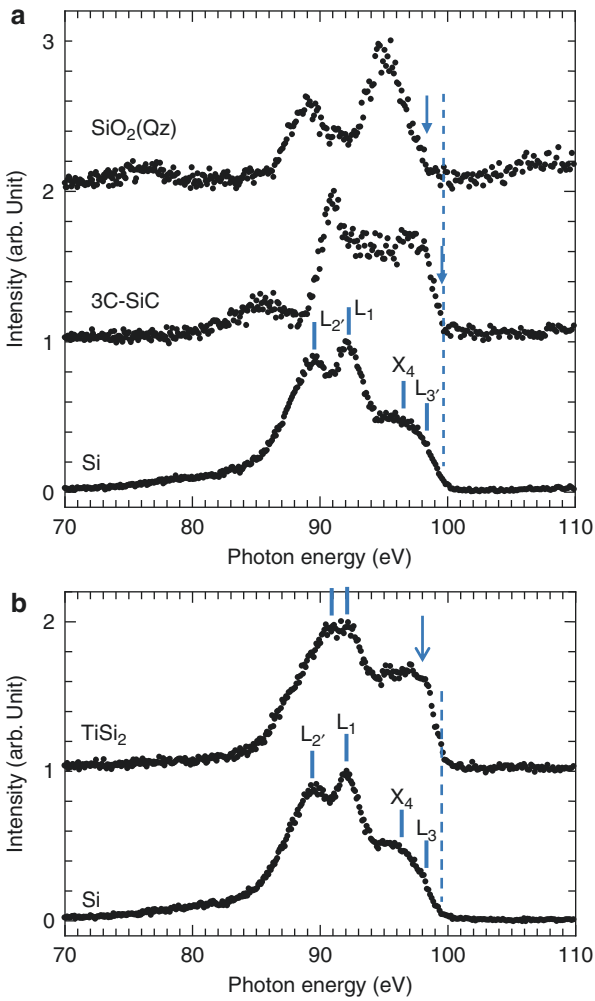


Fig. 7.9 (**a**) Si L-emission (VB → L-shell) spectra of Si, 3C-SiC, and SiO_2 (quartz). Four labels of $L_{2'}$, L_1, X_4, and $L_{3'}$ on the spectrum of crystalline Si are assignments in the band diagram. (**b**) Si L-emissiom spectra (VB → L-shell) of $TiSi_2$. The relatively large intensity in the upper part of VB (indicated by an *arrow*) in $TiSi_2$ is reported to be a contribution of *d*-symmetry of Si, which interacts with 3*d* orbitals of Ti

of Ti, based on a theoretical calculation [36]. The relative energy shift of $TiSi_2$ compared to Si should be evaluated by $\Delta E_B - E_g/2$, where ΔE_B is a chemical shift value of Si-L level in $TiSi_2$ and E_g is an energy gap of 1.2 eV for Si. ΔE_B is reported to be about 0.5 eV [37]. Then, $\Delta E_B - E_g/2$ is calculated to be −0.1 eV, which is consistent with present experimental results within the accuracy.

5.3 Boron K-Emission Spectra

Boron forms four allotropes: α-rhombohedral boron (α-r-B), α-tetragonal boron, β-rhombohedral boron (β-r-B), and β-tetragonal boron. Those allotropes and amorphous boron (am-B) are constructed by B_{12} icosahedral clusters [38, 39].

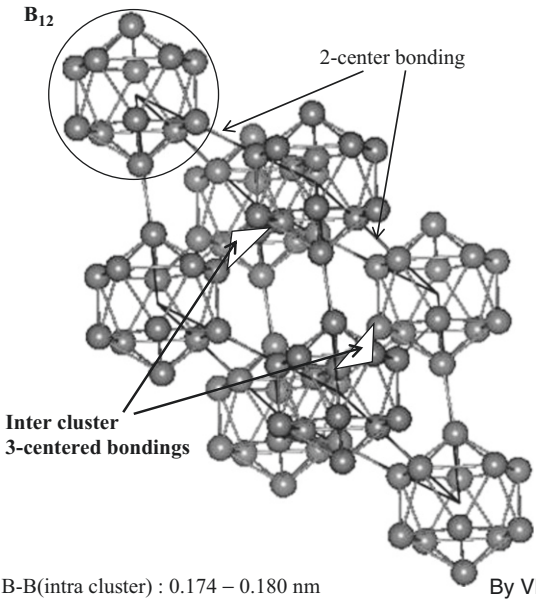


Fig. 7.10 Crystal structure of α-r-B. B_{12} clusters are placed at the corners of the rhombohedral unit cell. One characteristic of this structure is a presence of three-centered bonding between B_{12} clusters as presented by triangles

The crystal structure of α-r-B is the simplest among them, in which B_{12} clusters are placed at the corners of the rhombohedral unit cell as shown in Fig. 7.10. One characteristic of this structure is a presence of three-centered bonding between B_{12} clusters as indicated by two triangles in the figure. α-r-B is a semiconductor with bandgap energy of 2 eV [40]. Theoretical calculations of the electronic structure of α-r-B suggested a possibility of superconductor by Li doping [41]. In recently, a superconductivity of Li-doped α-r-B (Li_xB_{12}: $x = 1$–2.5) with $T_c = 3.2$–7 K was reported [42]. Unfortunately, DOS of VB of α-r-B had not been extensively examined by experiments, because a production of a large single crystal is difficult. Recent powder X-ray diffraction experiment by using maximum-entropy analysis combined with Rietveld structure refinement visualized the spatial distribution of the three-centered bonding of intra- and interclusters [43].

Figure 7.11a shows B K-emission (VB → K-shell) spectrum of α-r-B obtained from a single-crystalline area of about 500 nm in diameter. K-emission spectra of β-r-B and am-B are also shown for comparison. These spectra were obtained by using the high-dispersion-type spectrometer ver.4 [10]. Due to the dipole-transition condition for soft-X-ray emissions, each intensity distribution corresponds to the partial DOS of the VB with *p*-symmetry of each material. The intensity maximum of each spectrum indicated by a dotted vertical line places almost the same energy position, except a fine structure of α-r-B. In the lower-energy side of the peak, there can be seen a structure, as indicated by thin lines, almost the same energy position for the materials. It can be seen that the width of the main peak of β-r-B is smallest

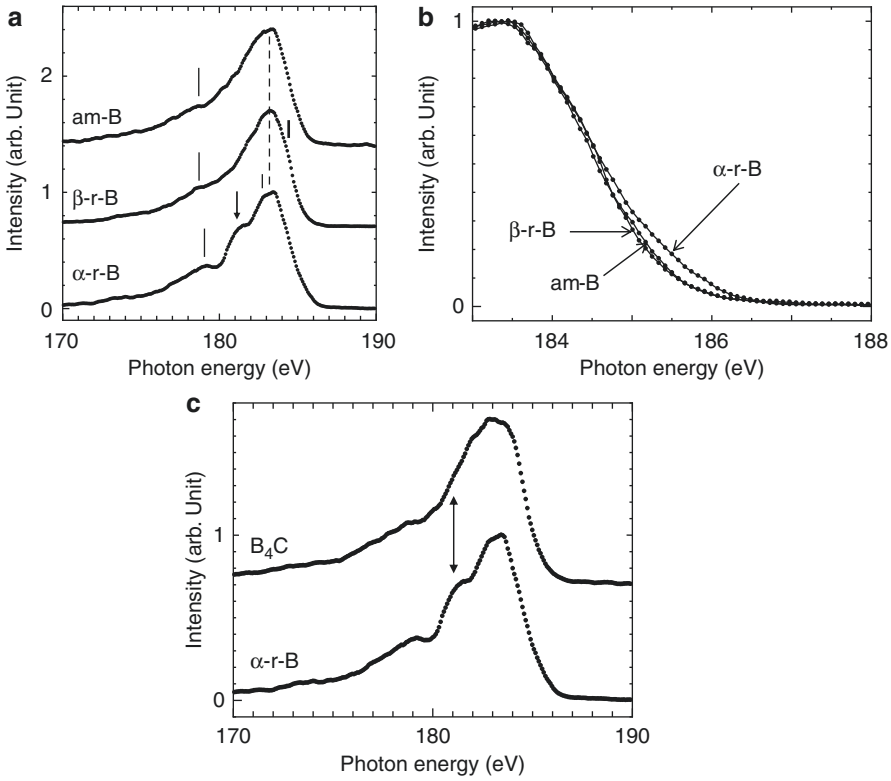


Fig. 7.11 (**a**) B K-emission (VB → K-shell) spectrum of α-r-B obtained from a single-crystalline area of about 500 nm in diameter. K-emission spectra of β-r-B and am-B are also shown for comparison. α-r-B has an additional shoulder structure as indicated by a vertical *arrow*. (**b**) A comparison of the intensity profiles of α-r-B, β-r-B, and am-B at the top of the VB region. (**c**) B-K emission spectrum of B_4C, in which the structure is similar to that of α-r-B except three-center bonding between B_{12} clusters

among the three spectra. Small shoulder intensity may exist at the higher-energy side of the main peak as indicated by a thin line. This intensity is much weaker for α-r-B. It should be noted that α-r-B has an apparent shoulder structure as indicated by a vertical arrow compared with those of β-r-B and am-B. Top part of the main peak also shows a fine structure compared to that of β-r-B. Furthermore, the intensity profile at the top of the VB of α-r-B shows a little additional intensity compared to those of other two materials as shown in Fig. 7.11b. Those differences in the DOS of VB of the three boron allotropes were successfully identified for the first time by using the high-dispersion-type spectrometer ver.4 [10, 44]. For confirming the possible origin of the arrowed shoulder structure of α-r-B, B K-emission spectrum of B_4C was measured as shown in Fig. 7.11c. B_4C has the same arrangement of B_{12} clusters with that of α-r-B, but does not have the intercluster three-center bonding shown as triangles in Fig. 7.10 due to the presence

of diagonal carbon chain. In recent analysis, this diagonal chain structure is recognized as not CCC:B_{12} but CBC:$B_{11}C$ [45]. In anyway, it is clearly seen that the spectrum of B_4C does not show shoulder structures as seen in that of α-r-B. This shows that the origin of the shoulder structure of the DOS of α-r-B can be the intercluster three-center bonding, which is a characteristic electronic state of α-r-B.

Figure 7.12 shows (a) calculated partial DOS with 2*p*-symmetry of α-r-B and (b)–(e) distributions of valence charge of selected energy ranges indicated in (a). This calculation was done by using Wien2k code. From the comparison between (a) and the spectrum in Fig. 7.11a, the energy windows b–e shown in (a) correspond to the top of the VB, the main peak, the shoulder structure indicated by an arrow, and the structure indicated by a vertical line, respectively. Positions of B_{12} clusters are drawn by circles in (b)–(e). Areas of intercluster three-center bonding are indicated by dotted ellipses. It can be recognized that valence charges of energy regions of b–e mainly correspond to intercluster two-center bond of B_{12}-B_{12}, intracluster bond of B_{12}, intercluster two- and three-center bonds, and intercluster three-center bond, respectively. Since the intercluster three-center bonding exists only for α-r-B, the shoulder structure observed for α-r-B indicated by an arrow should be formed by the bonding state of the intercluster three-center bond in α-r-B. The additional intensity at the top of the VB of α-r-B may be attributed to intercluster two-center bonding. This energy position suggests that this intercluster two-center bonding may be weak, which is suggested from the charge density analysis [43].

Other boron material familiar to electron microscopists is LaB_6, which is a cathode material for a thermal electron gun. This material belongs to metal hexaboride MB_6. The crystal structure of this material is based on a network of B_6 clusters located on each corner of cubic unit cell as shown in Fig. 7.13. M atom occupies at the body-centered position of the unit cell. When an M atom can supply two electrons to B_6 network, the VB of this material is fully occupied and becomes a semiconductor. Since La atom can transfer three electrons to B_6 network, LaB_6 becomes a metal due to an occupation of conduction bands by the transferred one electron. Lattice constants and distances between B atoms of intra- and intercluster of MB_6 (M = Ba, La, Ca) are listed in the figure [46]. MB_6 materials have been investigated as a candidate for a thermoelectric-power material [47]. Then, valence electron spectroscopy method based on microscopy is important.

Figure 7.14 shows B K-emission (VB → K-shell) spectra of BaB_6 (semiconductor), LaB_6 (metal), and CaB_6 (semiconductor). Due to the dipole selection rule, K-emission intensity corresponds to *p*-symmetry component of VB. By referring to a theoretical band calculation [48], the main peak in each spectrum corresponds to B-B bonding states of B_6 cluster (intra-cluster), which is located at each corner of a cubic unit cell. The energy positions of the shoulder structures, indicated by vertical lines, are apparently different for the three materials. It may be due to a difference in the intra-cluster B-B bonding length of those materials. It should be mentioned that the width of the main peak increases with a decrease of lattice constant and/or intra-cluster B-B distance. This tendency can be explained by an increase of band dispersion. The lower part of VB is assigned to intercluster bonding states labeled as B_6-B_6 [49]. CaB_6 shows a longer tail of B_6-B_6 intensity

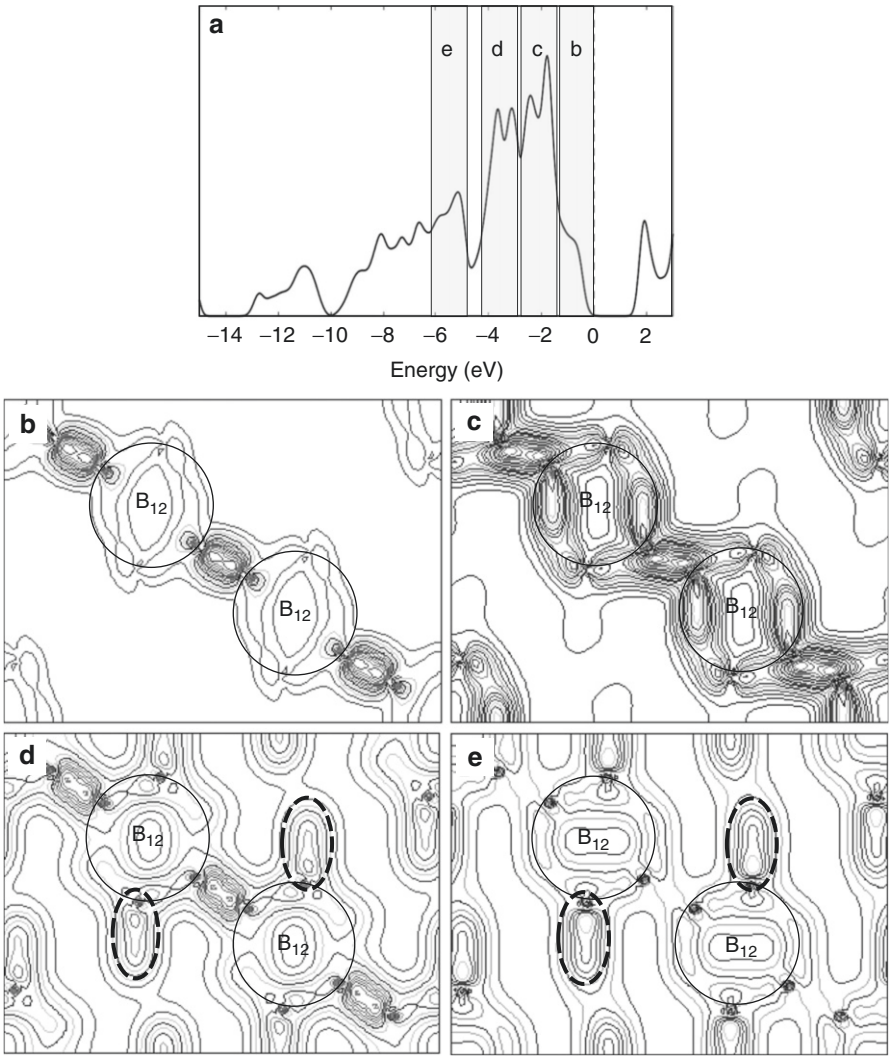
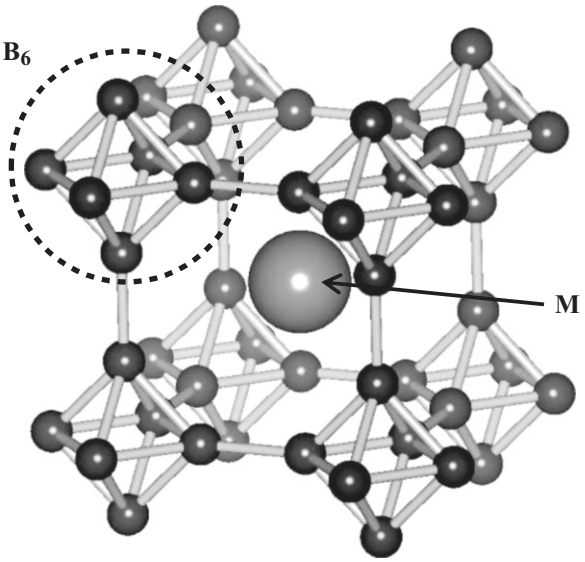


Fig. 7.12 (**a**) Calculated partial DOS with 2*p*-symmetry of α-r-B and (**b**–**e**) distributions of valence charge of selected energy ranges indicated in (**a**). It can be seen that energy ranges of (**b**–**e**) of the DOS correspond to charge distributions of (**b**) intercluster two-center bond of B_{12}-B_{12}, (**c**) intra-cluster bond of B_{12}, (**d**) intercluster two- and three-center bonds, and (**e**) intercluster three-center bond, respectively

than that of BaB_6. It may be due to shorter intercluster distances, which causes a larger energy dispersion for intercluster bonding bands. The most dominant difference among the three spectra is seen in the top part of VB of LaB_6. As mentioned above, La atom can transfer three electrons to B_6-cluster network. Then, higher energy levels should be occupied by electrons in LaB_6 than those in



	Property	Lattice constant (nm)	Intra-cluster B-B (nm)	Inter-cluster B-B (nm)
BaB_6	Semiconductor	0.4269	0.1780	0.1752
LaB_6	Metal	0.4154	0.1764	0.1659
CaB_6	Semiconductor	0.4146	0.1752	0.1667

Fig. 7.13 Structure of metal hexaboride MB_6 (by VESTA). The this material is based on a network of B_6 clusters located on each corner of cubic unit cell

BaB_6 and CaB_6. The spectrum of LaB_6 clearly shows an additional intensity at the right-hand side of the dominant B-B peak compared to those of BaB_6 and CaB_6. It should be noted that a clear Fermi edge is seen corresponding to a metal nature of this material. The energy resolution at E_F was evaluated to be 0.4 eV. The Fermi level exists in a hybridized band of B-2*p* and La-5*d* orbitals [49]. Since MB_6 is a candidate for a thermoelectric-power material, the top of VB should be investigated with higher energy resolution of about 0.1 eV for an identified (composition, crystalline quality) specimen area. Thus, much more improvement in energy resolution for SXES-TEM instrument is necessary.

5.4 Carbon K-Emission Spectra

Carbon atoms form different types of structures depending on bonding nature of valence electrons (2*s* and 2*p*). Diamond has a three-dimensional σ-bond network by

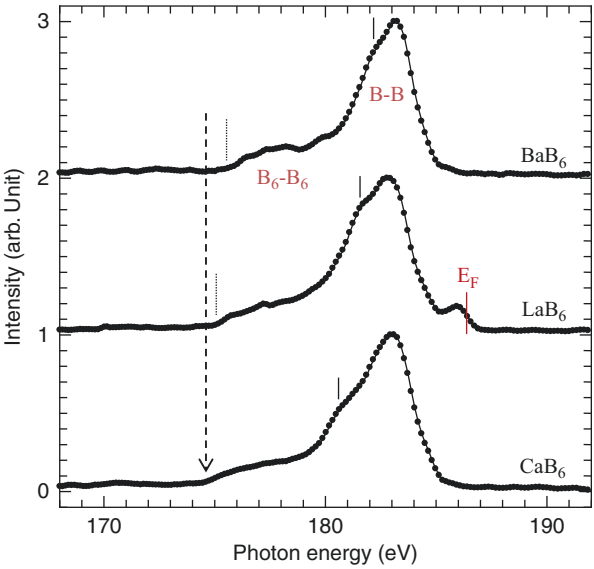


Fig. 7.14 B K-emission (VB → K-shell) spectra of BaB_6 (semiconductor), LaB_6 (metal), and CaB_6 (semiconductor). The main peak in each spectrum is due to B-B bonding of B_6 cluster (intra-cluster). The width of the main peak increases with a decrease of lattice constant and/or intra-cluster B-B distance. The spectrum of LaB_6 clearly shows an additional intensity at the right-hand side of the dominant B-B peak, showing Fermi edge corresponding to a metal nature of this material

four sp^3 orbitals/atom. Graphite has a two-dimensional network composed of the σ-bond by three sp^2 orbitals/atom and the π-bond by one p orbital/atom. Fullerene cluster C_{60} can be thought as a curved graphene sheet. Thus, it is interesting to know the energy distribution of valence electrons to characterize carbon materials. Furthermore, it is reported that a high temperature and pressure treatment of monomer-C_{60} crystal causes a polymerization of C_{60} clusters [50, 51]. Since carbon materials are rather sensitive for electron-beam irradiation, electron-beam density was lowered compared to those of other SXES experiments. Then, total acquisition time was needed to be an order of 1 h.

Figure 7.15 shows carbon K-emission (VB → K-shell) spectra of single-crystalline diamond, graphite, and face-centered cubic (FCC) monomer-C_{60}. Crystal structures of those materials are also shown in the figure. The right-hand-side end of each spectrum intensity distribution corresponds to the top of the VB. Dominant peaks of diamond and graphite indicated by vertical lines are assigned to σ-bonding states. Even if taking account the larger binding energy of 1*s* level of diamond (sp^3) by about 1 eV than that of graphite (sp^2) [52], the peak top of graphite is located in a larger binding energy side than that of diamond. This tendency is reasonable because σ-bonding states of graphite, which have a shorter σ-bonding length (0.142 nm) than that of diamond (0.155 nm), should have an intensity maximum in larger binding energy side than that of diamond. The spectrum of monomer-C_{60} crystal shows four peaks as indicated by vertical lines. The left two peaks correspond to the σ-bonding states. The left side peak of the two is placed almost the same energy position with that of graphite. The remaining two peaks correspond to π-bonding states indicated by vertical dotted lines. These two π-bonding peaks are assigned to h_u (right-hand side) and $h_g + g_g$ (left-hand

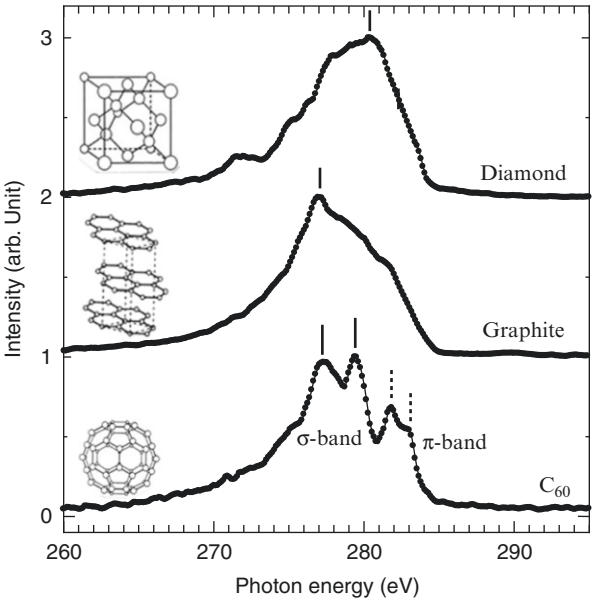


Fig. 7.15 Carbon K-emission (VB → K-shell) spectra of single-crystalline diamond, graphite, and face-centered cubic (FCC) monomer-C_{60}. Crystal structures of those materials are also shown. A characteristic dip structure between the π-bonding and the σ-bonding states is seen for C_{60} monomer crystal

side) states of the band diagram of C_{60} monomer crystal [53]. It can be seen as a characteristic dip structure between the π-bonding and the σ-bonding states. This dip structure is due to the separation of σ- and π-bonding states of C_{60} monomer crystal. In graphite, σ- and π-bonding states are energetically overlapped around the Brillouin zone center (Γ point). Thus, there is no dip structure in the spectrum of graphite. Those fine structure observations indicate hopeful application fields of a SXES instrument based on TEM in grapheme and polymerization of carbon-network materials.

Figure 7.16 shows carbon K-emission (VB → K-shell) spectra of (a) one-dimensional (1D-C_{60}, *I*mmm) and two-dimensional (2D-C_{60}, *R*-3m) and (b) two three-dimensional (3D-C_{60}, *I*mmm and *F*m-3) polymerized-C_{60} crystals produced by a high temperature and pressure treatment of monomer-C_{60} crystal. Each structure unit is shown as an inset, drawn by VESTA [54]. In each figure, a spectrum of monomer-C_{60} (C_{60}) crystal was also shown for comparison. It can be notified that the energy resolution of this experiment is a little higher than that of Fig. 7.15 from the separation of π-peaks of monomer-C_{60} crystal. A piece of polymerized C_{60} material produced was 0.1–0.3 mm in diameter. The specimen was crushed in a crucible and mounted on a supporting grid for TEM experiments under an optical microscope observation. SXES spectra were obtained from specimen areas of single crystalline and no impurities checked by electron diffraction patterns and EDS, respectively.

From X-ray diffraction study on crystal structures of polymerized-C_{60} crystals, C_{60} unit is deformed with an increase of covalent bonding between the units [50, 51]. The number of covalently connected nearest-neighbor C_{60} units for those materials are two for 1D-C_{60}, six for 2D-C_{60}, eight for 3D-C_{60} (*I*mmm),

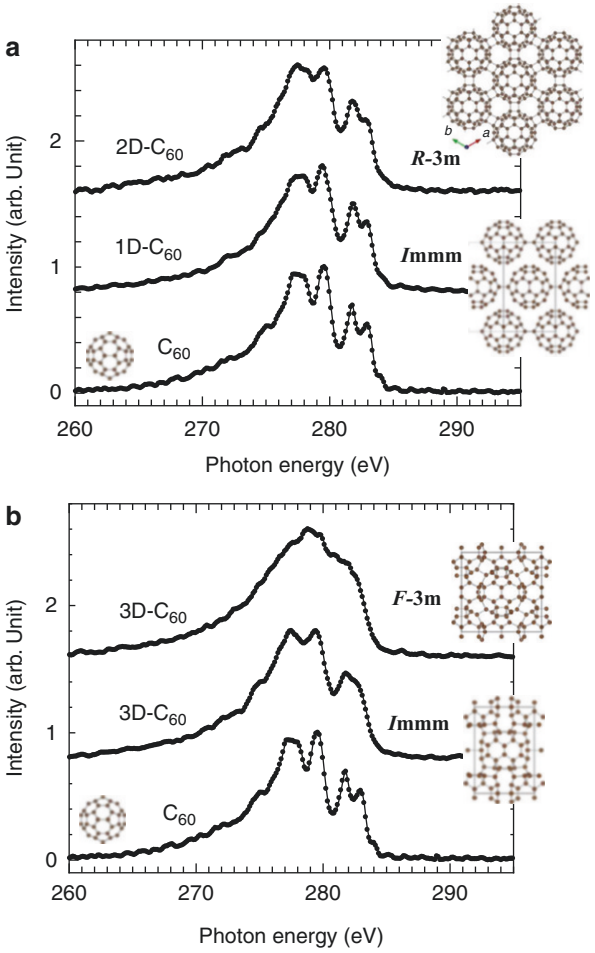


Fig. 7.16 Carbon K-emission (VB → K-shell) spectra of (**a**) one-dimensional (1D-C_{60}, *I*mmm) and two-dimensional (2D-C_{60}, *R*-3 m) and (**b**) two three-dimensional (3D-C_{60}, *I*mmm and *F*m-3) polymerized-C_{60} crystals produced by a high temperature and pressure treatment of C_{60} crystal. The characteristic dip structure between the π-bonding and the σ-bonding states in monomer-C_{60} disappeared for the most polymerized C_{60} crystal, 3D-C_{60} (*F*m-3)

and twelve for 3D-C_{60} (*F*m-3). Thus, 3D-C_{60} (*F*m-3) should be composed of the most deformed C_{60} unit. Peak structures observed in the spectrum of monomer-C_{60} crystal become broad in polymerized-C_{60} materials without an apparent change of those energy positions. It can be seen from (a) that the spectrum of 2D-C_{60} crystal is much broader than that of 1D-C_{60} one. This may reflect that the deformation of C_{60} cage in 2D-C_{60} crystal is larger than that of 1D-C_{60} crystal, because a larger deformation can cause a removal of degeneracy of energy bands and also a broadening of a profile of DOS of VB. However, the change of intensity distribution of 1D- and 2D-C_{60} crystals is smaller compared to those observed in 3D-C_{60} crystals in (b). High-energy-resolution EELS experiments on 1D- and 2D-C_{60} crystals also reported that there were changes in valence excitation and core-electron excitation spectra but not so drastically changed [55]. On the other hand, the C-K emission spectra of 3D-C_{60} crystals in (b) show rather drastic change

in those intensity distributions compared to those of monomer-C_{60} and also 1D- and 2D-C_{60} crystals. Especially, the characteristic dip structure between the π-bonding and the σ-bonding states in monomer-C_{60} disappeared for the most polymerized C_{60} crystal, 3D-C_{60} (*F*m-3). It should be noted that the intensity maximum of the spectrum of *F*m-3 crystal positions in between two σ-bonding peaks of monomer-C_{60} crystal. This peak position is between those of graphite and diamond. Thus, this most polymerized C_{60} crystal of *F*m-3 loses a character of C_{60} molecule and may be formed by sp^2 and sp^3 bondings. A theoretical calculation pointed out a possibility of a metallic nature of this material. Unfortunately, the energy resolution of the present experiments is not enough for this investigation of metallic nature, Fermi edge. Thus, high-energy-resolution EELS is now applying to this material and will be reported.

Finally, it should be commented on a small shoulder structure that appeared at the right-hand-side end (top of VB) of the spectra of monomer-C_{60} in Fig. 7.16. This intensity is also seen as a broader tailing intensity in Fig. 7.15 due to the lower energy resolution. The similar tailing is also seen in the reported C K-emission spectrum of monomer-C_{60} obtained at a SOR facility [56]. The apparent shoulder as seen in Fig. 7.16 is not expected from the theoretical calculation [53] and not observed in a photoelectron emission spectrum [57]. One possible origin of this structure is the elastic peak intensity, which is usually observed in resonant excitation X-ray emission experiments. An intense elastic peak that appeared almost the same energy with that of Fig. 7.16 was reported in the C K-emission spectra of monomer-C_{60} at the π*-resonance excitation condition [58]. It is known that an intense π*-absorption peak, which corresponds to π*-resonance excitation, appears in C K-absorption spectrum of monomer-C_{60}. Then, it is reasonable that the present C K-emission spectrum produced by high-energy electron excitation has a character of π*-resonance excitation. Thus, the shoulder and/or the tailing intensity at the top of the C K-emission spectra of polymerized C_{60} also attributed to the elastic intensity. The broadening of the intensity in highly polymerized material may reflect a decrease of the resonance effect.

5.5 L-Emissions of a Few Transition Metal Elements

Physical properties of 3*d* transition metal elements are related to the occupation and spin state of 3*d* electrons. Thus, it is necessary to investigate L-emissions (VB (3*d*) → 2*p*) for probing the electronic state of 3*d* electron orbitals. Those emission energies of 3*d* elements range from about 400 eV for Sc to about 930 eV for Cu. This energy range is higher than those presented in the previous sections. This means the obtainable energy dispersion by a grating is smaller due to a shorter wavelength, causing a lower energy resolution. Then, the combination of a VLS grating with a higher groove density of 2,400 lines/mm and the CCD detector with a pixel size of 12 μm was used. However, a discussion on Fermi edge as for Al-L emission is hopeless at present. Peak shifts depending on charge states (chemical shifts) and a rough profile of DOS of VB may be obtainable.

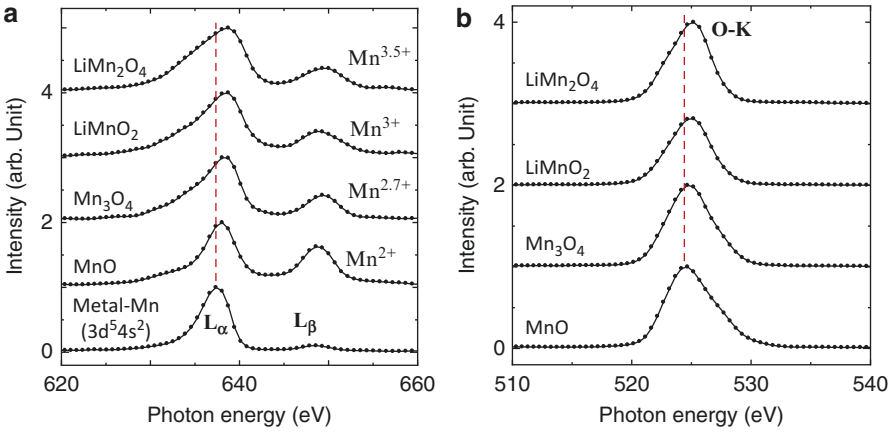


Fig. 7.17 (**a**) Mn $L_{\alpha,\beta}$-emissions (L_α:$3d_{5/2,3/2} \rightarrow 2p_{3/2}$, L_β:$3d_{3/2} \rightarrow 2p_{1/2}$) of metal-Mn (Mn; [Ar] $3d^5 4s^2$), MnO (Mn^{2+}), Mn_3O_4 ($Mn^{2.7+}$), $LiMnO_2$ (Mn^{3+}), and $LiMn_2O_4$ ($n^{3.5+}$). Mn L_α-emissions of compounds systematically shift to higher-energy side with a decrease of formal valence charge of Mn atom (chemical shift). (**b**) O K-emissions of those materials showing a systematic shift to higher-energy side, indicating a decrease of valence charge to form a covalent bonding

Figure 7.17a shows Mn $L_{\alpha,\beta}$-emissions (L_α:$3d_{5/2,3/2} \rightarrow 2p_{3/2}$, L_β:$3d_{3/2} \rightarrow 2p_{1/2}$) of metal-Mn (Mn; [Ar]$3d^5 4s^2$), MnO ($Mn^{2+}$), Mn_3O_4 ($Mn^{2.7+}$), $LiMnO_2$ (Mn^{3+}), and $LiMn_2O_4$ ($n^{3.5+}$). The electron configuration and the formal valence of Mn atom of each material are shown in the bracket. Radiative electronic transitions from $4s$ to $2p$ are allowed but the intensity is dispersed and small to recognize in those spectra. A small intensity ratio of L_β/L_α of metal-Mn compared to those of other materials is due to L_2L_3V Coster-Kronig decay of initial L_2-hole states, which is suppressed in materials with bandgaps [59], and self absorption. It can be seen that the Mn L_α-emissions of compounds systematically shift to higher-energy side with a decrease of formal valence charge of Mn atom (chemical shift). L_β-emissions also show a similar systematic shift except that of Mn_3O_4. However, the shift amounts compared to metal-Mn do not linearly change with the formal valence. This suggests that the solid-state effect (band structure, bandgap) has to be taken into account for quantitative discussion on the shift amount. It can be seen that the enhancement of the asymmetric intensity profiles of L_α lines for highly oxidized Mn atoms. The tail intensity in the lower-energy side of L_α line is attributed to form a covalent bonding between Mn and surrounding O atoms [60]. Actually, O K-emissions of those materials in Fig. 7.17b show a systematic shift to higher-energy side, indicating a decrease of valence charge to form a covalent bonding. It should be mentioned that intensity distributions are not symmetric indicating a presence of the band structure effect. The intensity profile of MnO shows an apparent shoulder or tail intensity in the higher-energy side.

Figure 7.18a shows Co $L_{\alpha,\beta}$-emissions (L_α:$3d_{5/2,3/2} \rightarrow 2p_{3/2}$, L_β:$3d_{3/2} \rightarrow 2p_{1/2}$) of metal-Co (Co: [Ar]$3d^7 4s^2$), CoO ($Co^{2+}$), and $LiCoO_2$ (Co^{3+}). As in the case of

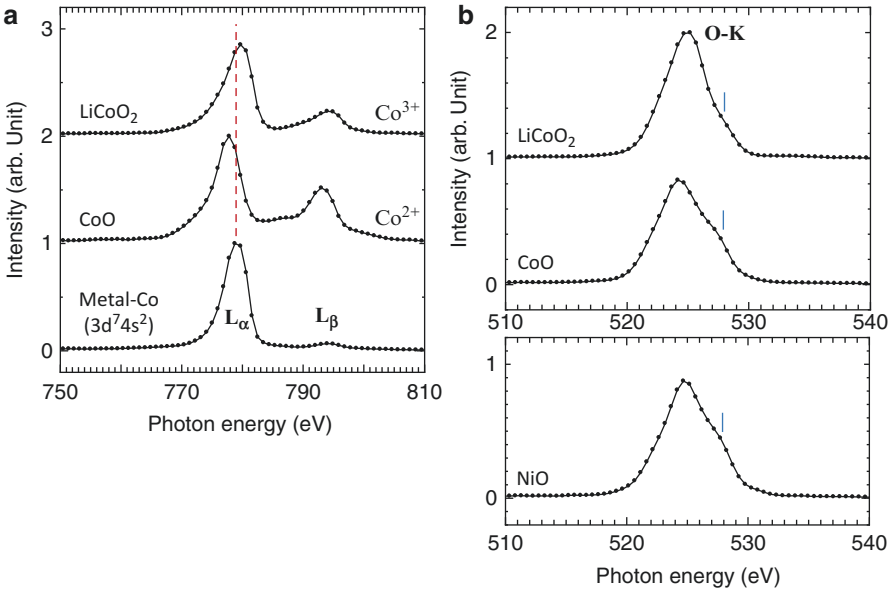


Fig. 7.18 (**a**) Co $L_{\alpha,\beta}$-emissions (L_α:$3d_{5/2,3/2} \rightarrow 2p_{3/2}$, L_β:$3d_{3/2} \rightarrow 2p_{1/2}$) of metal-Co (Co: [Ar] $3d^7 4s^2$), CoO (Co^{2+}), and $LiCoO_2$ (Co^{3+}). (**b**) O K-emissions of CoO (Co^{2+}), $LiCoO_2$ (Co^{3+}), and NiO

Mn L-emissions, the peak position of Co Lα-emission of metal-Co, CoO (Co^{2+}), and $LiCoO_2$ (Co^{3+}) does not show a systematic shift with the valence. Then, it needs to include the solid-state effect to discuss the shift amount. Furthermore, a consideration of 3*d* spin state may be necessary because Co^{2+} of CoO and Co^{3+} of $LiCoO_2$ possess high-spin and low-spin states, respectively [61]. O K-emissions of CoO (Co^{2+}) and $LiCoO_2$ (Co^{3+}) are shown in the upper part of Fig. 7.18b. It can be seen that those intensity profiles are not symmetric. The profile of CoO apparently shows a shoulder structure indicated by a vertical line. $LiCoO_2$ shows a smaller shoulder structure. Similar apparent shoulder structure is also observed for O K-emission of NiO as shown in the lower part of Fig. 7.18b. Those apparent shoulder structures of CoO and NiO were reported to be due to strong 2*p*–3*d* hybridization by comparing XES spectra obtained by SOR and theoretical calculations for strongly correlated oxides [62]. This report also pointed that the asymmetry of O K-emission profile of MnO stated above is also due to the same origin.

Figure 7.19 shows Ti $L_{\alpha,\beta}$- emission (L_α:$3d_{5/2,3/2} \rightarrow 2p_{3/2}$, L_β:$3d_{3/2} \rightarrow 2p_{1/2}$) and O K-emission energy region of metal-Ti (Ti; [Ar]$3d^2 4s^2$), Ti_3O_5 ($Ti^{3.3+}$; [Ar] $3d^{0.7} 4s^0$), and TiO_2 (rutile, Ti^{4+}; [Ar]$3d^0 4s^0$). Assigned structures at 465 eV and 475 eV are second-order diffracted ray of Cu-$L_{\alpha,\beta}$, which originates from the supporting Cu-grid of the specimens. The electron configuration and formal valence charge of Ti atom of each material are shown in the bracket. O K-emission intensity of metal-Ti is due to an oxidation of specimen surface. Ti-$L_{\alpha,\beta}$ spectra of

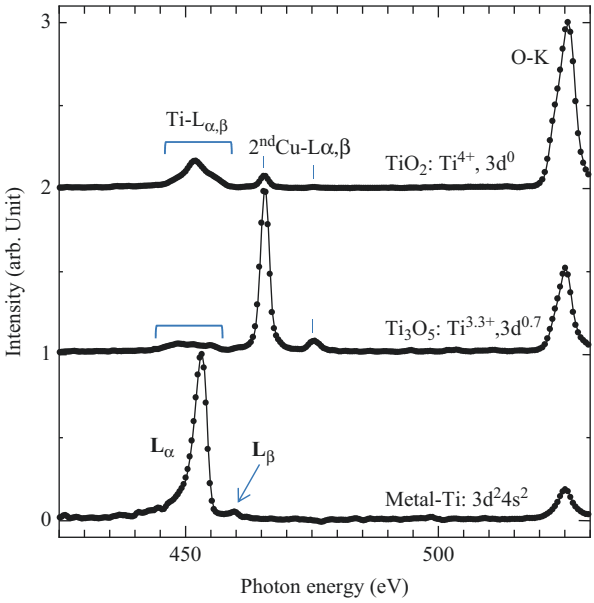


Fig. 7.19 Ti $L_{\alpha,\beta}$-emission (L_α:$3d_{5/2,3/2} \rightarrow 2p_{3/2}$, L_β:$3d_{3/2} \rightarrow 2p_{1/2}$) and O K-emission energy region of metal-Ti (Ti; [Ar]$3d^2 4s^2$), Ti_3O_5 ($Ti^{3.3+}$; [Ar]$3d^{0.7}4s^0$), and TiO_2 (rutile, Ti^{4+}; [Ar]$3d^0 4s^0$). Ti-$L_{\alpha,\beta}$ spectra of those materials show a variety in those intensity distributions and energy positions, which suggest a simple explanation by a chemical shift and a formal valency cannot be applied. O-K emission intensity of metal-Ti is due to an oxidation of specimen surface

those materials show a variety in those intensity distributions and energy positions, which suggest a simple explanation by a chemical shift and a formal valence charge cannot be applied. In other words, those include fruitful solid-state information. The Ti-$L_{\alpha,\beta}$ spectrum of metal-Ti shows the intense L_α peak with an apparent asymmetric intensity profile, which related to the partial DOS of 3*d* electrons of VB. As Fermi level of metal-Ti exists in the 3*d* bands, the sharp edge in the right-hand side of the peak may correspond to Fermi edge. The suppressed L_β intensity should be due to L_2L_3V Coster-Kronig decay process and self absorption as already observed for metal-Mn and metal-Co. Ti atom in TiO_2 (rutile) does not have a 3*d* electron formally. However, there is a small but apparent L-emission intensity with a characteristic intensity distribution. It is composed of a rather broad intensity from 445 to 460 eV. The broad intensity should be assigned to the emission intensity from the 3*d* component of the VB, which is the bonding state (mainly composed of O 2*p* orbitals) between Ti and octahedrally surrounding O atoms. A little intensity due to transitions from the conduction band to L_3 ($2p_{3/2}$) core level can be expected [34]. It is related to a decay process of excited electrons from the core level, produced in the excitation process prior to the emission. However, it cannot be observed due to the overlapping of Cu-L_α intensity. The spectrum of Ti_3O_5 shows a broad intensity due to emissions from 3d component of VB, which show a different intensity distribution from that of TiO_2 Some intensity due to transitions from CV could be overlapped on the Cu-L_α intensity, because of a presence of 3*d* electron for Ti_3O_5 ($Ti^{3.3+}$; $3d^{0.7}4s^0$).

6 M-Emission Intensity and 4*f*-Electron Numbers of Lanthanide Atoms

Most of the physical properties of lanthanide atoms are related to the presence of the 4*f* electronic subshell, which fills up progressively along the series. Thus, it is important to know the number of 4*f* electrons for evaluating the physical properties of lanthanide materials. EELS studies on lanthanide oxides reported that $M_{4,5}$-absorption ($3d \rightarrow 4f$) white-line intensity ratio of M_5/M_4 changes systematically as a function of 4*f*-electron number [63, 64]. One problem is that $M_{4,5}$ white-line intensity becomes smaller and has a low S/N with an increase of 4*f*-electron number due to a decrease of unoccupied 4*f* states. On the other hand, emission intensity due to transitions of 4*f* electrons to 3*d* core-hole levels should increase with an increase of 4*f* electrons and can obtain a better S/N in X-ray emission spectroscopy than EELS. Then, $M_{\alpha,\beta}$-emission ($4f \rightarrow 3d$) of lanthanide oxides, La_2O_3 ($4f^{\sim 0}$), CeO_2 ($4f^{0\sim 1}$), Pr_2O_3 ($4f^2$), Nd_2O_3 ($4f^3$), Sm_2O_3 ($4f^5$), Eu_2O_3 ($4f^6$), Gd_2O_3 ($4f^7$), Tb_4O_7 ($4f^8$), Dy_2O_3 ($4f^9$), Ho_2O_3 ($4f^{10}$), Er_2O_3 ($4f^{11}$), Tm_2O_3 ($4f^{12}$), and Yb_2O_3 ($4f^{13}$), was measured for investigating a relation between M-emission intensity and 4*f*-electron number. The subscript number n of $4f^n$ means an expected number of 4*f* electrons for each oxide. Those $M_{\alpha,\beta}$-emission energies of lanthanide atoms range from 800 to 1,600 eV. In this energy region (shorter wavelength), our compact SXES spectrometer cannot present intensity profiles of the DOS. Then, only the integrated peak intensity can be used for evaluation. All specimen areas used for SXES measurements confirmed those compositions by EDS and the crystalline quality by electron diffraction patterns.

Figure 7.20a shows emission spectra of La_2O_3 ($4f^{\sim 0}$), CeO_2 ($4f^{0\sim 1}$), Pr_2O_3 ($4f^2$), Nd_2O_3 ($4f^3$), Sm_2O_3 ($4f^5$), and Eu_2O_3 ($4f^6$) in an energy region from 600 to 1,600 eV. It can be seen that the $M_{\alpha,\beta}$-emission (M_α, $4f_{7/2,5/2} \rightarrow 3d_{5/2}$; M_β, $4f_{5/2} \rightarrow 3d_{3/2}$) intensity distributions show fine structures due to the self-absorption effect ($M_{4,5}$ absorption) [65]. Other than $M_{\alpha,\beta}$-emission intensity, $M_\zeta(4p_{3/2} \rightarrow 3d_{5/2})$, $M_5O_{2,3}(5p_{3/2,1/2} \rightarrow 3d_{5/2})$, and $M_\gamma(4d_{3/2,5/2} \rightarrow 3p_{3/2})$ intensities are also seen. Intensity of Cu-L emission is due to Cu mesh of specimen-supporting grid. For clarifying the fine structure due to self-absorption, an enlarged $M_{\alpha,\beta}$-emission spectrum of Pr_2O_3 is shown in Fig. 7.20b. By consulting the report on self-absorption effect in lanthanide M-emissions [63], this intensity profile should be explained as $M_{\alpha-}$ and M_β-emission intensities with dip structures due to strong absorptions by M_5 for M_α and M_4 for M_β absorptions of Pr, as indicated by vertical lines. Figure 7.21 shows spectra of Gd_2O_3 ($4f^7$), Tb_4O_7 ($4f^8$), Dy_2O_3 ($4f^9$), Ho_2O_3 ($4f^{10}$), Er_2O_3 ($4f^{11}$), Tm_2O_3 ($4f^{12}$), and Yb_2O_3 ($4f^{13}$) in an energy region from 600 to 1,600 eV. It is seen that the $M_{\alpha,\beta}$ intensity distributions of Gd_2O_3, Tb_2O_3 and Dy_2O_3 show fine structures due to the self-absorption effect ($M_{4,5}$ absorption). The other materials do not show an apparent effect of the self-absorption. It may be due to a small number of unoccupied 4*f* states for Ho, Er, Tm, and Yb. As high-energy incident electrons are used in TEM experiments, emission intensity can come out from well below the surface. Then, the self-absorption effect cannot

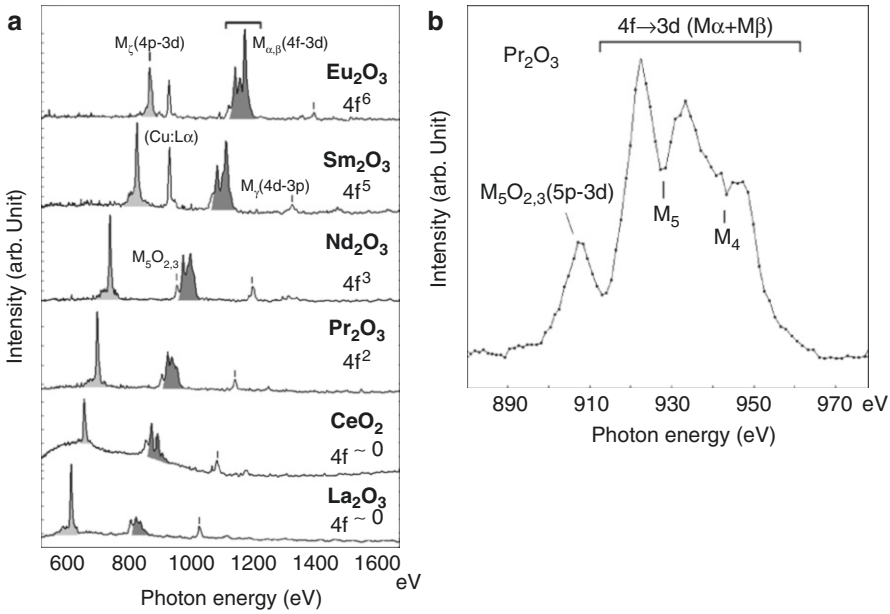


Fig. 7.20 (**a**) M-emission spectra of lanthanum atoms of La_2O_3 ($4f^{\sim 0}$), CeO_2 ($4f^{0\sim 1}$), Pr_2O_3 ($4f^2$), Nd_2O_3 ($4f^3$), Sm_2O_3 ($4f^5$), and Eu_2O_3 ($4f^6$). $M_{\alpha,\beta}$ emission (M_α, $4f_{7/2,5/2} \rightarrow 3d_{5/2}$; M_β, $4f_{5/2} \rightarrow 3d_{3/2}$) intensity distributions show fine structures due to the self-absorption effect ($M_{4,5}$ absorption). $M_\zeta(4p_{3/2} \rightarrow 3d_{5/2})$, $M_5O_{2,3}(5p_{3/2,1/2} \rightarrow 3d_{5/2})$, and $M_\gamma(4d_{3/2,5/2} \rightarrow 3p_{3/2})$ intensities are also seen. Intensity of Cu-L emission is due to Cu mesh of specimen-supporting grid. (**b**) An enlargement of $M_{\alpha,\beta}$-emission intensity of Pr_2O_3

be avoided in TEM experiment. Thus, a systematic evaluation of 4*f*-electron numbers of lanthanum atoms only from M_α/M_β may be not easy.

When thinking about the initial state of M-emission, lanthanum atoms are in excited states with a 3*d* core-hole. Those excited atoms go back to ground states via radiative decay of X-ray emission or non-radiative decay of electron emission. Figure 7.22 shows a schematic level drawing with decay processes of the 3*d* core-hole, which are assigned in the present experiment. $M_4O_{2,3}$ decay process is also possible. However, it could not be assigned in the spectra due to the overlapping with the large $M_{\alpha,\beta}$ intensity. In Figs. 7.20a and 7.21, not only $M_{\alpha,\beta}$-emission (M_α, $4f_{7/2,5/2} \rightarrow 3d_{5/2}$; M_β, $4f_{5/2} \rightarrow 3d_{3/2}$) intensities but also M_ζ ($4p_{3/2} \rightarrow 3d_{5/2}$)- and $M_5O_{2,3}$ ($5p_{3/2,1/2} \rightarrow 3d_{5/2}$)-emission intensities have been assigned. It is also noticed that the intensity of $M_{\alpha,\beta}$ emission compared to those of M_ζ emission seems to increase with an increase of 4*f*-electron number. This shows an increase the radiative decay rate of the 3*d* core-hole by transitions from 4*p* electron with an increase 4*f*-electron number. Since 4*p* and 5*p* states are fully occupied, the possibility for M_ζ and $M_5O_{2,3}$ is constant for all lanthanide atoms. On the other hand, the possibility of $M_{\alpha,\beta}$ increases with an increase of 4*f*-electron number. Then, the integrated intensity ratio of $M_{\alpha,\beta}/(M_{\alpha,\beta}+M_\zeta+M_5O_{2,3})$ can be a candidate for evaluating a change of intensity distribution of lanthanum atoms with a change

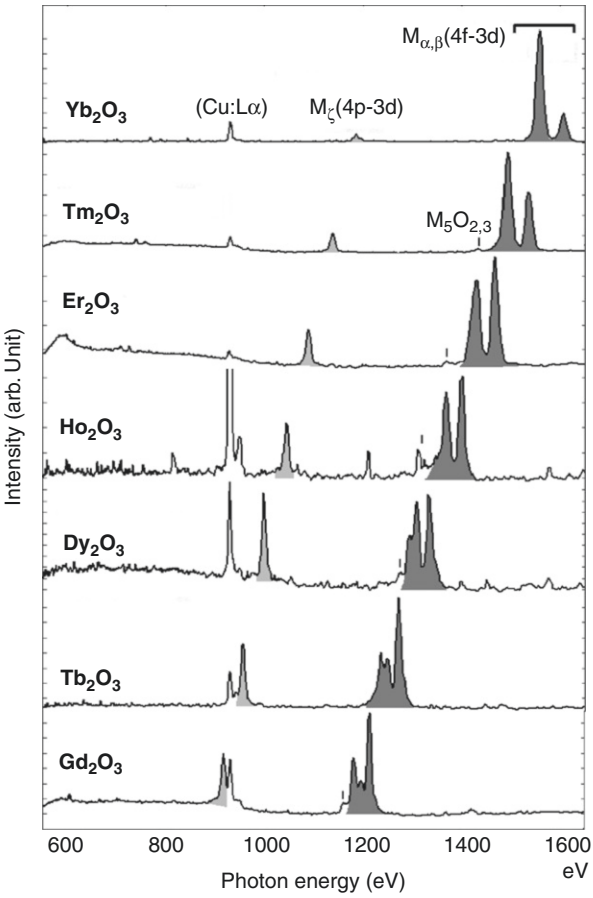


Fig. 7.21 M-emission spectra of lanthanum atoms of Gd_2O_3 ($4f^7$), Tb_4O_7 ($4f^8$), Dy_2O_3 ($4f^9$), Ho_2O_3 ($4f^{10}$), Er_2O_3 ($4f^{11}$), Tm_2O_3 ($4f^{12}$), and Yb_2O_3 ($4f^{13}$)

of 4*f*-electron number. The evaluated values from the raw data are plotted as a function 4*f*-electron number in Fig. 7.23a. This shows that the integrated intensity ratio of $M_{\alpha,\beta}/(M_{\alpha,\beta}+M_\zeta+M_5O_{2,3})$ shows rather monotonic increase as a function of 4*f*-electron number. This can be used as a measure of the number of 4*f* electrons. It should be mentioned that this relation is obtained from the M-emission with an apparent self-absorption effect, which is important for a practical use. However, $M_{\alpha,\beta}/(M_{\alpha,\beta}+M_\zeta+M_5O_{2,3})$ values of Sm_2O_3, and Dy_2O_3 are apparently deviated from the linearity. Thus, SXES measurement under a smaller self-absorption effect on $M_{\alpha,\beta}$-emission intensity is better. Then, the intensity distribution of $M_{\alpha,\beta} + M_5O_{2,3}$ was fitted by including the self-absorption effect as shown for Pr_2O_3 in Fig. 7.23b. The linearity of $M_{\alpha,\beta}/(M_{\alpha,\beta}+M_\zeta+M_5O_{2,3})$ versus 4*f*-electron number is improved with a drawback of an increase of ambiguity due to the ambiguity of the fitting. This study presents that the evaluation of 4*f*-electron number of lanthanides is practicable by using TEM-SXES instrument. This also shows an importance of the extension of an energy range of TEM-SXES instrument for higher-energy region.

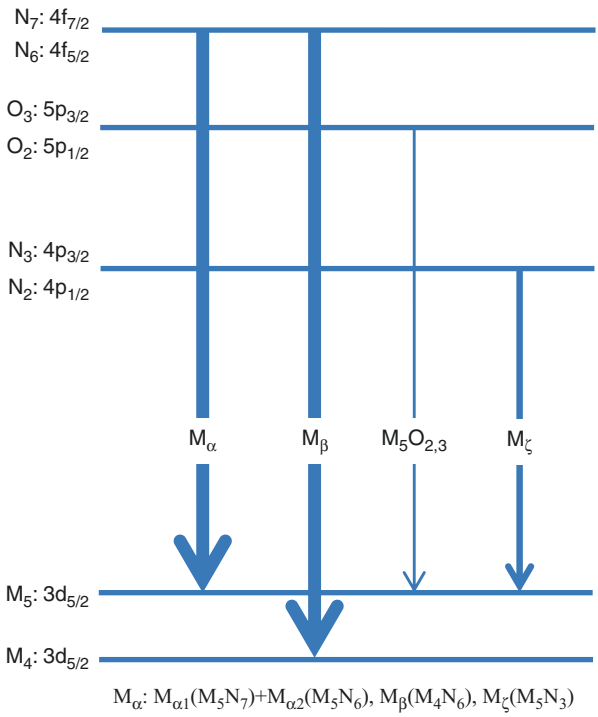


Fig. 7.22 Schematic level drawing and the assigned radiative decay processes of 3*d* core-hole

7 Anisotropic Soft-X-Ray Emission

The emission intensity due to transitions of valence electrons to inner-shell levels is proportional to $\sin^2\theta$, where θ is an angle between the emission (detection) direction and the position vector of an electron related to the nucleus as shown in Fig. 7.24 [66]. This means that angle-resolved measurements of soft-X-ray emission intensity due to those transitions give us information about the anisotropic distribution of bonding electrons. Furthermore, soft-X-ray emission spectra of different atoms of a compound show us the component of different atoms of the DOS of VB. Especially, SXES measurements based on TEM can be obtained from a single-crystalline area with a definite crystal orientation. Then, this angle-resolved SXES-TEM experiment has a great potential on research on charge distributions. Unfortunately, this experiment is limited by a poor controllable angle range of specimen stage for TEM at present.

Graphite and hexagonal BN are typical examples having anisotropic crystal and electronic structures. Angle-resolved SXES experiments of those materials had been reported [67, 68]. Those experiments were conducted for polycrystalline specimens with mm-scale spatial resolution by using SOR facility. In this experiment, specimen area was confirmed that there is no stacking fault, perfect crystal,

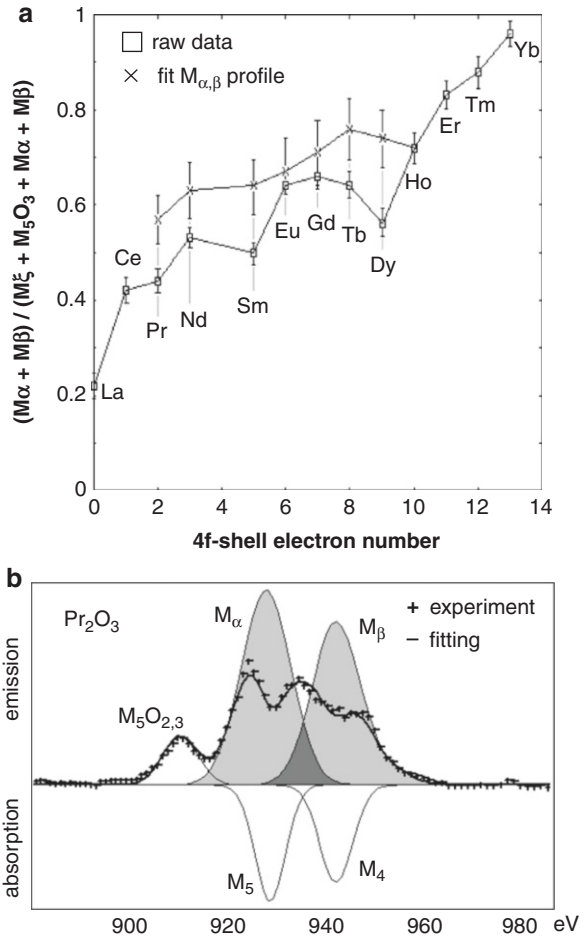


Fig. 7.23 (**a**) Integrated intensity ratio of $M_{\alpha,\beta}/(M_{\alpha,\beta}+M_{\zeta}+M_5O_{2,3})$ of the experimental data plotted as a function 4*f*-electron number, showing a rather monotonic increase as a function of 4*f*-electron number. (**b**) Intensity distribution of $M_{\alpha,\beta} + M_5O_{2,3}$ fitted by M_α, M_β, $M_5O_{2,3}$, and two self-absorptions of M_4 and M_5 for Pr_2O_3

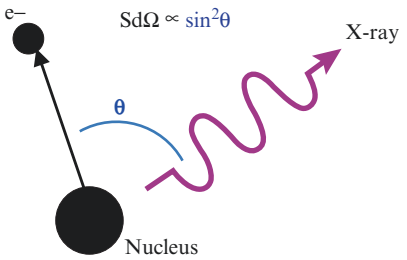


Fig. 7.24 Schematic figure of emission intensity proportional to $\sin^2\theta$, where θ is an angle between the emission (detection) direction and the position vector of an electron related to the nucleus

by using convergent-beam electron diffraction before SXES measurements. Figure 7.25 shows carbon K-emission spectra of single-crystalline graphite obtained at take-off angles of 60° and 15°, which are angles between emission directions and (0001) plane of graphite as shown as an inset. Both spectra are

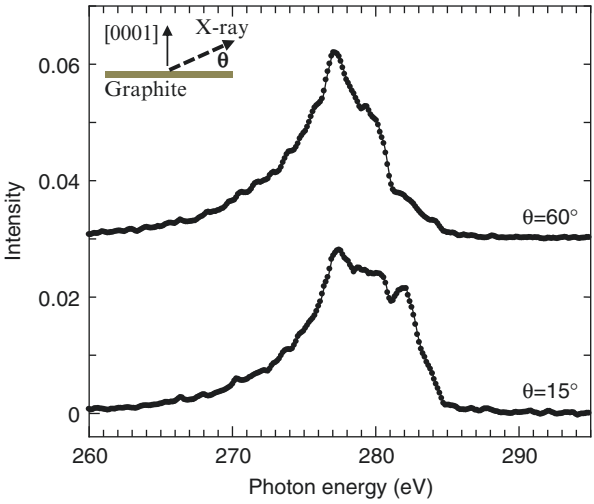


Fig. 7.25 Carbon K-emission spectra of single-crystalline graphite obtained at take-off angles of 60° and 15°, which are angles between emission directions, and (0001) plane of graphite as shown as an *inset*. Both spectral areas were normalized prior to the next analysis

presented by normalizing the area, which is necessary for the next analysis. It is clearly seen that the two spectra show a different intensity distribution especially in the right-hand side of those intensity distributions, where it corresponds to the top part of valence bands, π-bonding bands. The top part of valence bands shows a larger intensity for $\theta = 15°$ than that for $\theta = 60°$. This means that π-bonding orbital distributes in the direction perpendicular to (0001) plane of graphite.

Emission intensity $I(\theta)$ at a take-off angle θ is written as $I(\theta) = \cos^2\theta \cdot I_\pi + 1/2(1 + \sin^2\theta) \cdot I_\sigma$, where I_π and I_σ are emission intensities from π- and σ-bonding states, respectively [68]. Thus, an algebraic equation can be written for each spectrum. Figure 7.26 shows intensity distributions of I_π and I_σ derived from the two experimental data in Fig. 7.25 by using the equations. It is clearly seen that the lower spectrum intensity distributes in the upper part of VB, which should be assigned to DOS of the π-bonding states. The other one should correspond to the DOS of σ-bonding states. The right-hand-side end and a peak indicated by vertical lines of π-bonding states correspond to electronic states on Brillouin zone boundary at P and Q, respectively [69]. It can be seen that those electronic states are placed at higher energy than σ-bonding states. The peak of σ-bonding states indicated by a vertical line corresponds also to electronic states on Brillouin zone boundary, Q. This indicates that electronic states corresponding to the maximum DOS of π- and σ-bands have the same wave vector, Q point, but different energy. The overlapped region of π- and σ-bands corresponds to around Brillouin zone center (Γ). As π- and σ-bands are not overlapped around the zone center in the case of crystalline monomer-C_{60}, C K-emission intensity shows a dip structure as already shown in Fig. 7.15. The total width of the valence band, π + σ, is also consistent with the theoretical calculation. Those results show that anisotropic SXES gives us not only the DOS of VB but also the information on spatial distribution of valence electrons (bonding electrons).

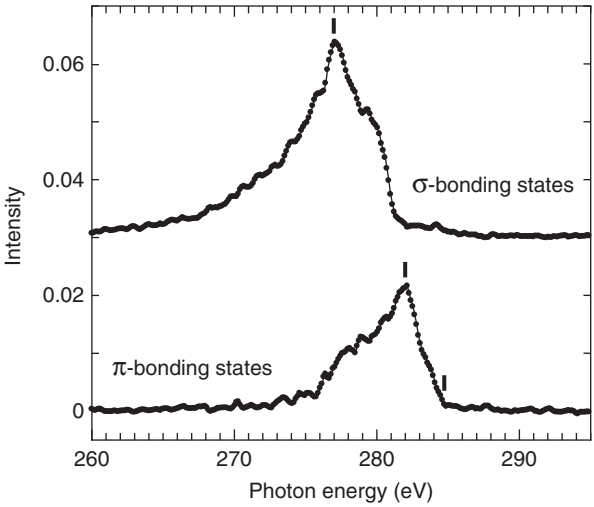


Fig. 7.26 Intensity distributions of I_π and I_σ derived from the two experimental data in Fig. 7.25 by using the equation of $I(\theta) = \cos^2\theta \cdot I_\pi + 1/2(1 + \sin^2\theta) \cdot I_\sigma$. The lower spectrum intensity distributes in the upper part of VB, which should be assigned to DOS of the π-bonding states. The other one should correspond to the DOS of σ-bonding states

Figure 7.27a shows N K-emission spectra of *h*-BN obtained at take-off angles of 15° and 60°. obtained from a single-crystalline area. Those intensity distributions correspond to DOS of N-2*p* component of the valence bands. The right-hand-side end indicated by a vertical arrow corresponds to the top of the VB. Both spectra show four structures indicated by vertical lines but those relative intensities are different due to anisotropic special distributions of π- and σ-bonding orbitals. This intensity change in N K-emission is larger than those of B K-emission [9]. It reflects that the VB is dominated by nitrogen orbitals due to the lower orbital energy of nitrogen 2*p* than that of boron 2*p*. By the same algebraic process done for graphite of Fig. 7.25, I_π and I_σ distributions derived are shown in Fig. 7.27b. As for graphite, it is apparently seen that π- and σ-orbitals are located at the upper and the lower part of VB, respectively. The distribution of π-bands is apparently sharper in energy than that of graphite. This sharp DOS corresponds to π-bonding states with less dispersion at Brillouin zone boundary (K-H/M-L) [70]. The small intensity indicated by a vertical line corresponds to around Brillouin zone center (Γ). Around the Γ point, π− and σ-bands are overlapped in energy. There can be seen three structures in the DOS of σ-bonding states. Structures a, b, and c correspond to the almost flat band A-Γ, the zone boundary M-L, and K-H/M-L, respectively, by referring to a theoretical calculation [70].

8 Total Electronic Structure Analyses

As stated and presented above, SXES can give us information of DOS of valence bands. TEM can also give us information of DOS of conduction bands by using EELS. Furthermore, the excitation spectrum of valence electrons, the imaginary part of dielectric function, can be derived from the valence excitation EELS spectrum by using Kramers-Kronig analysis. Thus, there is a possibility

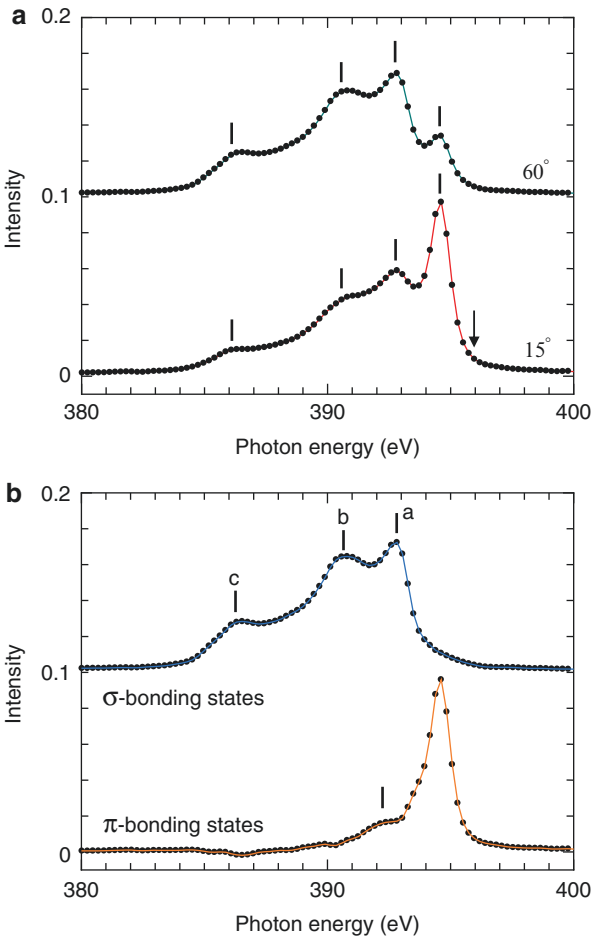


Fig. 7.27 (**a**) N K-emission spectra of *h*-BN obtained at take-off angles of 15° and 60° obtained from a single-crystalline area. (**b**) I_π and I_σ distributions obtained from (**a**). Sharp DOS corresponds to π-bonding states with less dispersion at Brillouin zone boundary (K-H/M-L). Three structures *a*, *b*, and *c* in the DOS of σ-bonding states correspond to the almost flat band A-Γ, the zone boundary M-L, and K-H/M-L, respectively

of a total electronic structure analysis of an identified small specimen area by a combined analysis of SXES and EELS based on transmission electron microscopy.

Figure 7.28 shows the combination of an Mg L-edge EELS spectrum (L-shell ($2p$) → CB ($3s$,$3d$)) and an Mg-L SXES spectrum (VB ($3s$,$3d$) → L-shell ($2p$)) of metal-Mg. EELS data was obtained with an energy resolution of 0.09 eV by using a monochromator TEM [71]. Two spectra are placed according to the experimentally determined energy. As two spectra were joined at the middle of the Fermi edge, which corresponds to the Fermi energy, it can be said that there is no core-hole effect for Mg L-edge (absorption spectrum), which is expected for metal. The relative intensity was adjusted by consulting the total height of Fermi edge, which means the sum of L_2 and L_3 edges. It should be mentioned on a dip appeared just above E_F as indicated by an arrow. The dip is formed by a presence of apparent

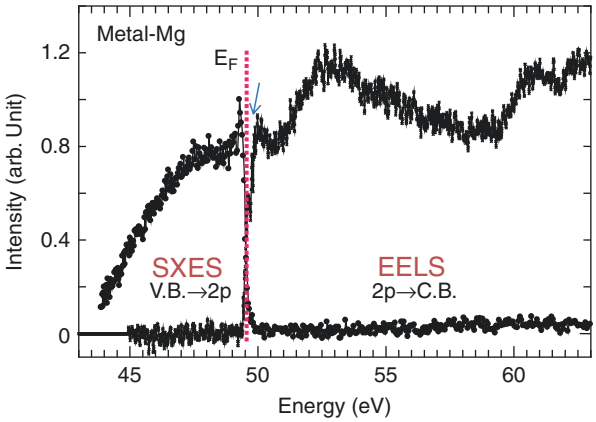


Fig. 7.28 Combination of an Mg L-edge EELS spectrum (L-shell ($2p$) → CB ($3s$, $3d$)) and an Mg L-emission SXES spectrum (VB ($3s$, $3d$) → L-shell ($2p$)) of metal-Mg. The relative intensity was adjusted by consulting the total height of Fermi edge, which means the sum of L_2 and L_3 edges. The dip indicated by an *arrow* is formed by a presence of apparent height of L_2-edge (L_2-shell → CB), which is suppressed in the emission spectrum due to CK transition process stated in Sect. 5.1 of this chapter

height of L_2-edge (L_2-shell → CB), which is suppressed in the emission spectrum due to CK transition process stated in Sect. 5.1.

Figure 7.29 shows the combination of an Al L-edge EELS spectrum (Al L-shell ($2p$) → CB ($3s$,$3d$)) and an Al-L SXES spectrum (VB ($3s$,$3d$) → Al L-shell ($2p$)) of metal-Al. EELS data was obtained by another monochromator TEM [72]. The two spectra were joined at the middle of the Fermi edge, which corresponds to the Fermi energy. The relative intensity was adjusted by consulting the total height of the Fermi edge. It is also seen a dip just above E_F as that of Mg-L. Figure 7.29b shows the combination of an Al L-edge spectrum and an Al L-emission spectrum of Al-based decagonal quasicrystals, Al-Ni-Co. This combination clearly shows a decrease of DOS around Fermi energy (called a pseudogap) compared to that of Fig. 7.29a. This pseudogap structure is believed to be an origin of the stability of the quasiperiodic structure and also characteristic high resistivities of quasicrystals. This is the first experimental presentation of the whole shape of a pseudogap structure of quasicrystals [9, 73].

Figure 7.30 shows the combination of a B K-edge EELS spectrum (K-shell ($1s$) → CB ($2p$)) and a B K-emission spectrum (VB ($2p$) → K-shell ($1s$)) of c-BN [9]. Two spectra are placed according to the experimentally determined energy. Calculated energy-band diagrams are also shown for comparison [70]. Dotted vertical lines show good correspondence between the peak and/or shoulder structures of the experimental data and special symmetry points of the calculated band diagram. It should be noted that an additional separation of 2 eV between the valence and the conduction bands was needed to obtain the good agreement between the experiments and the calculation. It indicates that the calculation, which was conducted under a local density approximation, evaluated the bandgap energy of c-BN smaller than that of real

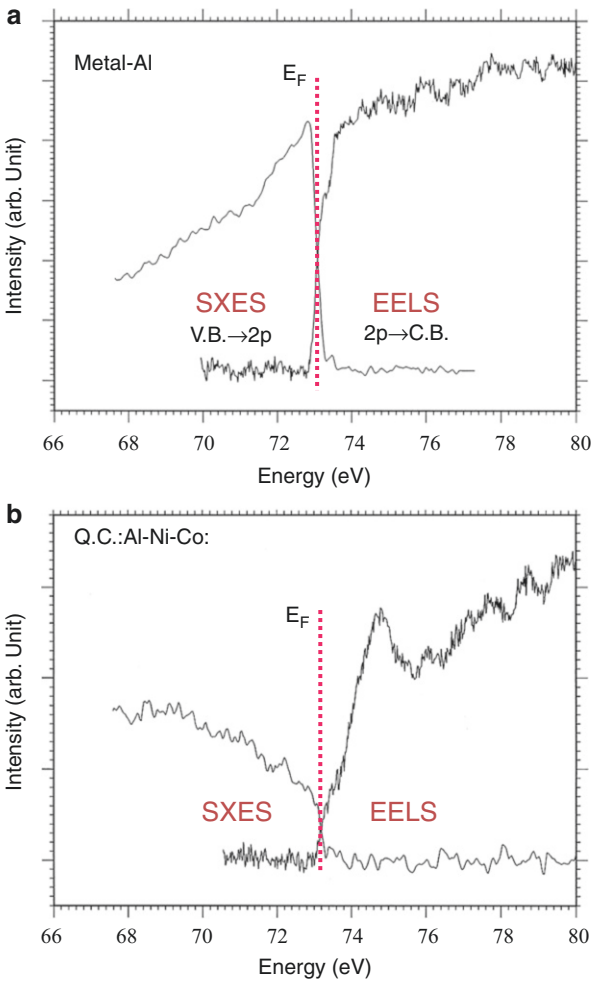


Fig. 7.29 (**a**) Combination of an Al L-edge EELS spectrum (Al L-shell ($2p$) → CB ($3s$, $3d$)) and an Al L-emission SXES spectrum (VB ($3s$, $3d$) → Al L-shell ($2p$)) of metal-Al. (**b**) Combination of an Al L-edge spectrum and an Al L-emission spectrum of Al-based decagonal quasicrystals, Al-Ni-Co. This clearly shows a decrease of DOS around Fermi energy (called a pseudogap) compared to that of (**a**)

material by an amount of 2 eV. The imaginary part of the dielectric function ε_2 of c-BN derived from a valence electron excitation spectrum obtained by using Kramers-Kronig analysis is also shown as an inset. Peak structures of A, B, and C correspond to electronic transitions from the valence bands to the conduction bands. From a comparison with the EELS/SXES spectrum and the ε_2, interband transitions labeled A, B, and C in ε_2 were assigned as lateral arrows shown in the band diagram. The peak A in ε_2 was assigned to transitions around Brillouin zone center (Γ point). The structure B may be assigned to transitions around L and X points. The peak C may be transitions around X and/or K points. Another example of the total electronic structure analysis for h-BN by EELS/SXES (not shown here) successfully assigned two $\pi \rightarrow \pi^*$ and one $\sigma \rightarrow \sigma^*$ transitions in the band diagram [74].

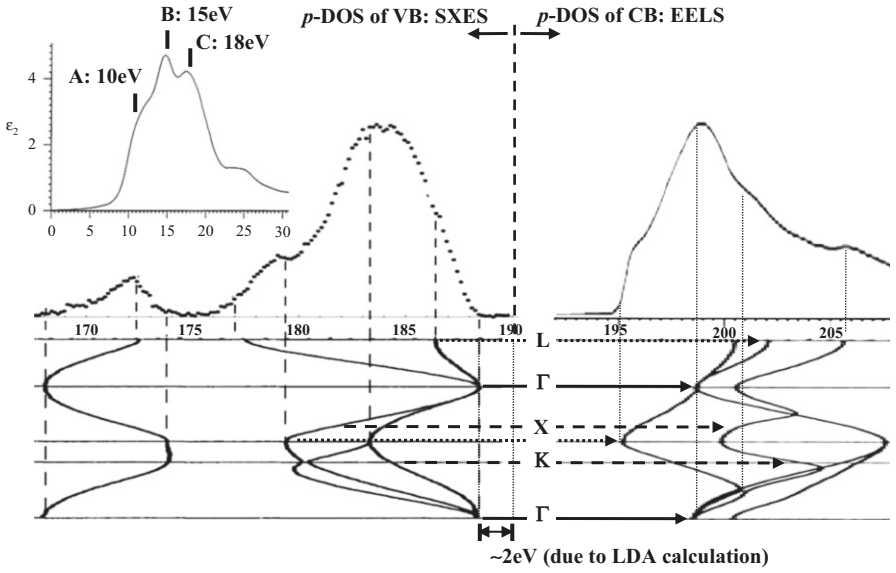


Fig. 7.30 Combination of a B K-edge EELS spectrum (K-shell (1*s*) → CB (2*p*)) and a B K-emission spectrum (VB (2*p*) → K-shell (1*s*)) of *c*-BN. Calculated energy-band diagrams are also shown for comparison. *Dotted vertical lines* show correspondence between the peak and/or shoulder structures of the experimental data and special symmetry points of the calculated band diagram. The imaginary part of the dielectric function ε_2 derived from a valence electron excitation spectrum is shown as an *inset*

Experimentally obtained B K-shell excitation spectrum (a partial DOS of CB), B K-emission spectrum (a partial DOS of VB), and ε_2 (a joint DOS of CB and VB) of *c*-BN were linked consistently with the help of the theoretical calculation. It should be noted that all data were obtained from assigned small specimen areas based on transmission electron microscopy. This success demonstrates a possibility of the analysis of a whole electronic structure of small specimen areas or small-volume materials by linking spectroscopy methods based on transmission electron microscopy.

9 Extension for Much Higher-Energy Region

The highest energy presented above is just below 2 keV for lanthanum M-emissions. The energy dispersion at 2 keV of our instrument is about 4 eV per detector channel. For much higher-energy X-rays more than 2 kV, the shorter wavelength causes a smaller energy dispersiton and a lower energy resolution. Thus, the observation of DOS by SXES cannot be hoped by using our compact spectrometer. For obtaining DOS information by high-energy X-ray emission, it is necessary to measure a low-yield emission (a smaller natural width of inner-shell

level) due to the transition process c′ shown in Fig. 7.1 by using a large-size spectrometer (a high instrumental resolution), SOR facility. Even though the resolution is low compared to SOR, SXES-TEM is useful for obtaining some information of valence electron, presented for the case of lanthanum M-emissions. As the energy resolution of present spectrometer is better than Si(Li)-based EDS, SXES-TEM method is useful for resolving closely placed emission lines, which are usually overlapped in conventional EDS spectra.

The bottleneck of our grating spectrometer for extending to higher-energy region is to prepare a grating with an effective reflectance for high-energy X-rays more than about 2 keV, because the reflectivity of gold (Au), usual surface material of grating, suddenly drops above Au-M absorption energy of 2.2 keV. Thus, much effort has been spent to manufacture multilayer coatings on gratings for improving the reflectivity in that higher-energy region [75]. The usual multilayer coatings for soft-X-rays have a mutual stacking structure of two materials, which have different refractive indices and works to enhance the reflectivity of X-ray owing to interferences among weak reflected X-rays from periodically arranged interfaces of the multilayer coating. The coating functions in a narrow energy range as a band-pass filter due to a periodic array of interfaces. A Mo/C multilayer-coated (MLC) grating for SXES for a TEM (ver.4) has tested for obtaining Pt M-emission of Pt catalysis [10]. It performs at high reflectivity in a narrow energy range of about 100 eV. On the other hand, a wide-band multilayer-coated grating for microscopy-based SXES is very important to apply to this method for a wide variety of materials. Recently, a simple design of wide-band multilayer structure for 2–4 keV has been reported for aiming microscopy-based SXES [76]. Although the effective wide energy range causes smaller reflectivity, the reflectivity is still higher than that of Au coating. This minor drawback can be easily overcome by making a combination of this grating and parallel detection optics (flat-field optics with a two-dimensional detector).

Figure 7.31 shows soft-X-ray emission spectra of $KNbO_3$ measured by using the new MLC-VLS grating (upper) and an Au-coated VLS grating (lower). Those gratings have the same groove structure. It can be noted that the lower spectrum shows a smaller Nb-$L_{\beta 1}$ and no K-$L_{\alpha,\beta}$ intensities, when compared with those of the upper spectrum. This comparison clearly presents that the new MLC-VLS grating can work continuously from below to above Au-M absorption energy of 2.2 keV, as indicated by a vertical dotted line. The acceptable energy range of the new grating was confirmed from 1.5 to 4.2 keV [12].

Figure 7.32 shows the emission spectra obtained from an indium-tin-oxide $(InO_3)_{1-x}(SnO_2)_x$ ($x = 0.05 \sim 0.1$) particle by using the present MLC-grating system (solid line) and a conventional EDS (dotted line). This material is widely used for transparent electrode films. Thus, the analysis of this material is very important. As In ($Z = 49$) and Sn ($Z = 50$) are neighbors in the periodic table, L-emission energies of the elements are very close. As a result, it is impossible to resolve Sn-L_α and In-$L_{\beta 1}$ by a conventional EDS, as shown by a dotted blue line. On the other hand, it is clearly seen that Sn-L_α ($M_{4,5} \rightarrow L_3$; 3,444 eV) and In-$L_{\beta 1}$ ($M_4 \rightarrow L_2$; 3,487 eV) emission lines are resolved by using the present MLC grating

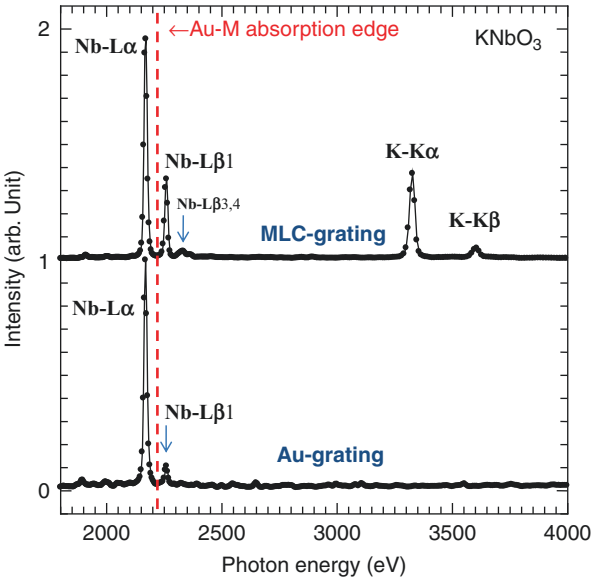


Fig. 7.31 Soft-X-ray emission spectra of $KNbO_3$ obtained by using a new wide-band multilayer-coated grating. Upper and lower spectra were obtained by using the new multilayer-coated grating and a conventional Au-coated grating, respectively

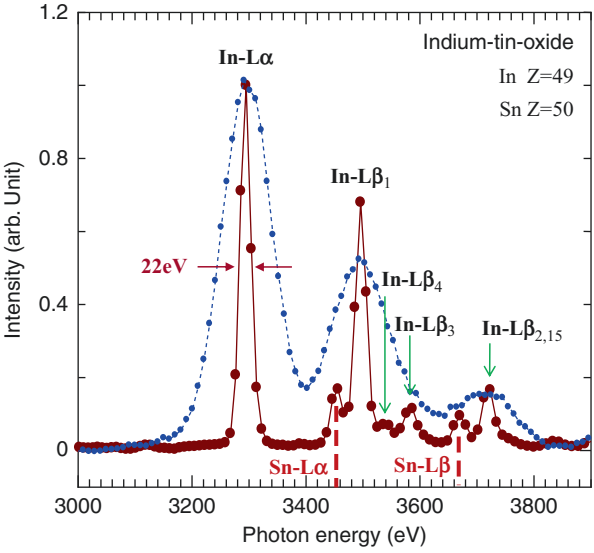


Fig. 7.32 Emission spectra obtained from a $(InO_3)_{1-x}(SnO_2)_x$ ($x = 0.05 \sim 0.1$) particle by using the new MLC-grating system (*dots with a solid line*) and a conventional EDS (*dots with a dotted line*). It is clearly seen that Sn-L_α ($M_{4,5} \rightarrow L_3$; 3,444 eV) and In-$L_{\beta 1}$ ($M_4 \rightarrow L_2$; 3,487 eV) emission lines are resolved by using the present MLC grating [12]

(red line). The energy resolution evaluated by the FWHM of In-Lα line is 22 eV, which is lower than the energy gap of Sn-L_α and In-$L_{\beta 1}$ lines of 43 eV. Furthermore, weak intensity lines of In-$L_{\beta 2,15}$, $L_{\beta 3}$, $L_{\beta 4}$ and Sn-L_β, as indicated by arrows, can also be observed.

When this new MCL spectrometer was applied to electron-probe microanalyzer (EPMA), probe current of 1 μA is usable, which is about 100 times higher than that

employed in the present experiment. One drawback of this experimental condition is to lower the spatial resolution for analysis. However, a two-order short detection time of about 10 s can be expected for this spectrum and also for previously presented all soft-X-ray spectra. It develops a potential of new evaluation method by spectral and/or state mappings.

10 Conclusions and Future Prospective

High-energy-resolution EELS based on transmission electron microscopy is a powerful method to obtain the density of states of the conduction band as well as the dielectric properties from a specified small specimen area. Since EELS cannot give us the DOS of the valence bands, soft-X-ray emission spectroscopy was introduced to transmission electron microscopy. For keeping the performance of a TEM, compact spectrometers of grazing-incidence flat-field optics have been designed and constructed. The spectrometers were composed of varied-line-spacing (aberration-corrected) gratings and charge-coupled device (CCD) or multichannel plate (MCP) detectors. Those instruments clearly presented us the DOS of VB from identified specimen areas by TEM. It should be reminded that the different intensity distribution of the DOS of VB and Fermi edge was clearly observed for simple metals, K-emissions of Li, Be, B, and C, and L-emissions of Mg and Al. A characteristic change of the DOS of VB due to a change of bonding states was observed for emissions of Al, Si, B, and C. L-emissions of transition elements showed that the expected chemical shifts are affected by the band structure effects. M-emissions of lanthanide atoms showed a relation to the number of 4*f* electrons. Angle-resolved SXES experiments presented a possibility to probe an anisotropic charge distribution of valence electrons. As a goal of electronic structure analysis based on transmission electron microscopy, combined analyses of SXES (DOS of VB) and inner-shell excitation EELS (DOS of CB) and a result of Kramers-Kronig analysis of valence excitation EELS (joint DOS of VB and CB) were also presented. Finally, further development and future prospects are described. Those presented results clearly showed an importance of SXES in TEM. One drawback is the long acquisition time from 10 min to 1 hour, which is owing to a low emission efficiency of soft X-ray and a small solid angle of the spectrometers. Since EPMA can use a two-order larger probe current than that of TEM, SXES-EPMA is the first candidate to apply the SXES spectrometer for material science. This SXES electron microscopy will give not only the elemental maps but also a chemical state and/or a specific bond mapping method. However, the spatial resolution may be about 1 μm. On the other hand, TEM will be necessary for a higher spatial resolution SXES and an angle-resolved SXES measurements despite of a longer acquisition time. Furthermore, this SXES electron microscopy provides a new valence electron spectroscopy method for chemical analyses not only for a wide variety of new functional materials developments of battery materials, thermo-electric materials, and catalytic material, but also for basic research of orbital-ordering states of transition-metal oxides, charge-states analyses, and partial DOSs of compounds.

Acknowledgments The author thanks the technical staffs of Institute of Multidisciplinary Research for Advanced Materials, Tohoku University, for their skillful technical assistance. The author also thanks Prof. S. Yamanaka of Hiroshima University for supplying monomer-C_{60} and polymerized-C_{60} crystals; Prof. K. Kimura of University of Tokyo and Associate Prof. M. Takeda of Nagaoka University of Technology for supplying boron materials; Dr. M. Koike and Dr. T. Imazono of Quantum Beam Science Directorate, Japan Atomic Energy Agency, for designing new VLS gratings and multilayer structures; and Dr. Y. Sato of Tohoku University for calculating electronic structure of α-rhombohedral boron. Thank is also for Mr. Y. Yoneda for his efforts on experiments of lanthanum oxides.
Fundings: Those developments and applications of spectrometers were supported by Grant-in-Aid for Scientific Researches (No.12440079, No.13554010), a leading project "Development of an EELS/XES electron microscope for electronic structure analyses," a Grant-in-Aid for Scientific Research on Priority Areas "New Materials Science Using Regulated Nano Spaces − Strategy in Ubiquitous Elements" of the Ministry of Education, Culture, Sports, Science and Technology of Japan (No.19051002), and a project of Collaborative Development of Innovative Seeds (Practicability verification stage) of Japan Science and Technology Agency.

References

1. Fabian DJ, Watson LM, Marshall CAW (1972) Soft x ray spectroscopy and the electronic structure of solids. Rep Prog Phys 34:601–696
2. Attwood D (2000) Soft x-rays and extreme ultraviolet radiation. New York: Cambridge University Press
3. Krause MO (1979) Atomic radiative and radiationless yields for K and L shells. J Phys Chem Ref Data 8(2):307–327
4. Krause MO, Oliver JH (1979) Natural widths of atomic K and L levels, Kα X-Ray lines and several KLL auger lines. J Phys Chem Ref Data 8(2):329–338
5. Castaing R, Guinier A (1950) Application des sondes electroniques a l'analyse metallographique. Proceedings of the 1st international conference on electron microscopy, p 60
6. Wollman DA, Irwin KD, Hilton GC (1997) High-resolution energy-dispersive microcalorimeter spectrometer for X-ray microanalysis. J Microsc 188(3):196–223
7. Hara T, Tanaka K, Maehata K, Mitsuda K et al (2010) Microcalorimeter-type energy dispersive X-ray spectrometer for a transition electron microscope. J Electron Microsc 59(1):17–26
8. Terauchi M, Yamamoto H, Tanaka M (2001) Development of a sub-eV resolution soft-X-ray spectrometer for a transmission electron microscope. J Electron Microsc 50(2):101–104
9. Terauchi M, Kawana M (2006) Soft-X-ray emission spectroscopy based on TEM –toward a total electronic structure analysis. Ultramicroscopy 106(11/12):1069–1075
10. Terauchi M, Koike M, Fukushima K, Kimura A (2010) Developments of wavelength-dispersive soft-X-ray emission spectrometers for transmission electron microscopes – an introduction of valence-electron spectroscopy for transmission electron microscopy. J Electron Microsc 59(4):251–261
11. Terauchi M, Takahashi H, Handa N, Murano T et al (2012) Ultrasoft-X-ray emission spectroscopy by using a newly designed WDS spectrometer attached to a transmission electron microscope. J Electron Microsc 61(1):1–8
12. Terauchi M, Takahashi H, Handa N, Murano T et al (2013) A new grating X-ray spectrometer for 2–4 keV enabling a separate observation of In-Lβ and Sn-Lα emissions of indium-tin-oxide. Microsc 62(3):391–395
13. Harada T, Kita T (1980) Mechanically ruled aberration-corrected concave gratings. Appl Opt 19(23):3987–3993

14. Koike M, Yamazaki T, Harada Y (1999) Design of holographic gratings recorded with aspheric wave-front recording optics for soft X-ray flat-field spectrographs. J Electron Spectrosc Relat Phenom 101–103:913–918
15. Allotey FK (1967) Effect of electron–hole scattering resonance on X-ray emission spectrum. Phys Rev 157(3):467–479
16. Mizuno Y, Ishikawa K (1968) Anomalies in edges of soft X-ray emission spectra of metals. J Phys Soc Jpn 25:627–628
17. Arakawa ET, Williams MW (1976) Radiative decay of core excitons in alkali halides. Phys Rev Lett 36(6):333–336
18. Tsang KL, Zhang CH, Callcott TA, Arakawa ET et al (1987) Fluorescent emission spectra of lithium fluoride with use of synchrotron radiation. Phys Rev B 35(16):8374–8377
19. Inoue ST, Yamashita J (1973) Electronic structure of metallic beryllium. J Phys Soc Jpn 35(3):677–683
20. Neddermeyer H (1976) X-ray emission and absorption edges of magnesium and aluminum. Phys Rev B 13(6):2411–2417
21. Nozieres P, De Dominicis CT (1969) Singularities in the X-ray absorption and emission of metals III. One-body theory exact solution. Phys Rev 178(3):1097–1107
22. Belin-Ferre E, Dubois JM (2008) Experimental evidence of the formation d-like states near the Fermi energy in complex metallic alloys. Philos Mag 88(13–15):2163–2170
23. Livins P, Schnatterly SE (1988) Shakeup in soft-x-ray emission. I. The low-energy tail. Phys Rev B 37(12):6731–6741
24. Courths R, Hufner S, Schulz H (1978) High-resolution normal emission UV-photoelectron spectra and band structure of Cu. Z Phys B 35:107–117
25. Schoser S, Brauchle G, Forgt J, Kohlhof K et al (1998) XPS investigation of AlN formation in aluminum alloys using plasma source ion plantation. Surf Coat Technol 103–104:222–226
26. Li J, Nam KB, Nakarmi ML, Lin JY et al (2003) Band structure and fundamental optical transitions in wurtzite AlN. Appl Phys Lett 83(25):5163–5165
27. Mattogno G, Righini G, Montesperelli G, Traversa E (1994) X-ray photoelectron spectroscopy investigation of $MgAl_2O_4$ thin films for humidity sensors. J Mater Res 9(6):1426–1433
28. Bortz ML, French RH, Jones DJ, Kasowski RV et al (1990) Temperature dependence of the electronic structure of oxides: MgO, $MgAl_2O_4$ and Al_2O_3. Phys Scripta 41:537–541
29. Kotani A, Shin S (2001) Resonant inelastic x-ray scattering spectra for electrons in solids. Rev Mod Phys 73(1):203–246
30. Henke BL, Gullikson EM, Davis JC (1993) X-ray interactions: photoabsorption, scattering, transmission and reflection at E = 50-30000 eV, Z = 1-92. At Data Nucl Data Tables 54(2):181–342
31. Shin S, Agui A, Watanabe M, Fujisawa M et al (1996) Observation of resonant Raman scattering at the Si $L_{2,3}$ core exciton. Phys Rev B 53(23):15660–15666
32. Boo LH, Lee SB, Yu KS, Sung MM et al (2000) High vacuum chemical vapor deposition of cubic SiC thin films on Si(001) substrates using single source precursor. Surf Coat Technol 131:147–152
33. Barr TL (1983) An XPS study of Si as it occurs in adsorbents, catalysts, and thin films. Appl Surf Sci 15:1–35
34. Nithianandam VJ, Schnatterly SE (1988) Soft-x-ray emission and inelastic electron-scattering study of the excitations in amorphous and crystalline silicon dioxide. Phys Rev B 38(8): 5547–5553
35. Okada K, Kameshima Y, Yasumori A (1998) Chemical shifts of silicon X-ray photoelectron spectra by polymerization structure of silicates. J Am Ceram Soc 81(7):1970–1972
36. Weijs PJW, van Leuken H, de Groot RA, Fuggle JC (1991) X-ray-emission studies of chemical bonding in transition-metal silicides. Phys Rev B 44(15):8195–8203
37. Yamauchi Y, Yoshitake M, SERD project group of SASJ (2002) Chemical shift at interface for silicides. J Surf Anal 9(3):432435

38. Golicova OA (1987) Semiconductors with complex lattice and the amorphization problem. Phys Stat Sol 101:277–314
39. Katada K (1966) An electron diffraction study of evaporated boron films. Jpn J Appl Phys 5(7):582–587
40. Horn FH (1959) Some electrical and optical properties of simple rhombohedral boron. J Appl Phys 30(10):1611–1612
41. Gunji S, (1996) Kamimura H First-principles study on metal-doped icosahedral B_{12} solids. Phys Rev B 54(19):13665–13673
42. Nagatochi T, Hyodo H, Sumiyoshi A, Soga K et al (2011) Superconductivity in Li-doped α-rhombohedral boron. Phys Rev B 83:184507–1-184507–5
43. Fujimori M, Nakata T, Nakayama T, Nishibori E et al (1999) Peculiar covalent bonds in α-rhombohedral boron. Phys Rev Lett 82(22):4452–4455
44. Terauchi M, Satoh Y, Kimura K (2009) Soft-X-ray emission spectroscopy study of the valence electron states of α-rhombohedral boron. J Phys Conf Series 176:012025-1-6
45. Bylander DM, Kleinman L, Lee S (1990) Self-consistent calculations of the energy bands and bonding properties of $B_{12}C_3$. Phys Rev B 42(2):1394–1403
46. Takeda M, Terui M, Takahashi N, Ueda N (2006) Improvement of thermoelectric properties of alkaline-earth hexaborides. J Solid State Chem 179:2823–2826
47. Muetterties EL (ed) (1967) The chemistry of boron and its compounds. New York: Wiley
48. Schmitt K, Stuckl C, Ripplinger H, Albert B (2001) Crystal and electronic structure of BaB_6 in comparison with CaB_6 and molecular $[B_6H_6]^{2-}$. Solid State Sci 3:321–327
49. Hasegawa A, Yanase A (1977) Energy bandstructure and Fermi surface of LaB_6 by a self-consistent APW method. J Phys F Metal Phys 7(7):1245–1260
50. Yamanaka S, Kubo A, Inumaru K, Komaguchi K (2006) Electron conductive three-dimensional polymer of cuboidal C_{60}. Phys Rev Lett 96:076602-1-4
51. Yamanaka S, Kini NS, Kubo A, Jida S et al (2008) Topochemical 3D polymerization of C_{60} under high pressure at elevated temperatures. J Am Chem Soc 130(13):4303–4309
52. Jackson ST, Nuzzo RG (1995) Determining hybridization differences for amorphous carbon from the XPS C 1 s envelope. Appl Surf Sci 90(2):195–203
53. Saito S, Oshiyama A (1991) Cohesive mechanism and energy bands of solid C_{60}. Phys Rev Lett 66(20):2637–2640
54. Momma K, Izumi F (2011) VESTA 3 for three-dimensional visualization of crystal, volumetric and morphology data. J Appl Crystallogr 44(6):1272–1276. doi:10.1107/S0021889811038970
55. Terauchi M, Nishimura S, Iwasa Y (2005) High energy-resolution electron energy-loss spectroscopy study of the electronic structure of C_{60} polymer crystals. J Electron Spectrosc Relat Phenom 143(2–3):169–174
56. Muramatsu Y, Hirono S, Umemura S, Ueno Y et al (2001) Soft X-ray emission and absorption spectra in the C K region of sputtered amorphous carbon films. Carbon 39:1403–1407
57. Merkel M, Knupfer M, Golden MS, Fink J et al (1993) Photoemission study of the electronic structure of C_{60} and K_xC_{60}. Phys Rev B 47(17):11470–11478
58. Guo JH, Glans P, Skytt P, Wassdahl N et al (1995) Resonant excitation x-ray fluorescence from C_{60}. Phys Rev B 52(15):10681–10684
59. Matthew JAD, Nuttall JD, Gallon TE (1976) Enhancement of coster-kronig rates in solid-state environments. J Phys C Sollid State Phys 9:883–888
60. Grush MM, Horne CR, Perera RCC, Ederer DL et al (2000) Correlating electronic structure with cycling performance of substituted $LiMn_2O_4$ electrode materials: a study using the techniques of soft X-ray absorption and emission. Chem Mater 12(3):659–664
61. van Elp J, Wieland JL, Eskes H, Kuiper P (1991) Electronic structure of CoO, Li-doped CoO, and $LiCoO_2$. Phys Rev B 44(12):6090–6103
62. Kurmaev EZ, Wilks RG, Moewes A, Finkelstein LD (2008) Oxygen x-ray emission and absorption spectra as a probe of the electronic structure of strongly correlated oxides. Phys Rev B 77:1651271-1-5

63. Manoubi T, Colliex C, Rez P (1990) Quantitative electron energy loss spectroscopy on M45 edges in rare earth oxides. J Electron Spectrosc Rel Phenom 50(1):1–18
64. Egerton RF (1996) Electron energy-loss spectroscopy in the electron microscope. New York: Plenum
65. Fischer DW, Baun WL (1967) Self-absorption effects in the soft X-ray M_α and M_β emission spectra of the rare earth elements. J Appl Phys 38(12):4830–4836
66. Heitler W (1954) The quantum theory of radiation. New York: Oxford University Press
67. Kieser J (1977) On the electronic structure of graphite. Z Phys B 26:1–10
68. Tegeler E, Kosuch N, Wiech G, Faessler A (1977) Anisotropic emission of the X-Ray K-emission band of nitrogen in hexagonal boron nitride. Phys Stat Sol 84:561–567
69. McFeely FR, Kowalczyk SP, Ley L, Gavell RG et al (1974) X-ray photoemission studies of diamond, graphite, and glassy carbon balance bands. Phys Rev B 9(12):5268–5278
70. Xu YN, Ching WY (1991) Calculation of ground-state and optical properties of boron nitrides in the hexagonal, cubic, and wurtzite structures. Phys Rev B 44(15):7787–7798
71. Sato Y, Terauchi M, Mukai M, Kaneyama T et al (2011) High energy-resolution electron energy-loss spectroscopy study of the dielectric properties of bulk and nanoparticle LaB_6 in the near-infrared region. Ultramicroscopy 111:1381–1387
72. Terauchi M, Tanaka M, Tsuno K, Ishida M (1999) Development of a high energy resolution electron energy-loss spectroscopy microscope. J Microscopy 194(1):203–209
73. Terauchi M, Uemichi Y, Ueda H, Tsai AP et al (2007) TEM spectroscopy study of electronic structure of quasicrystals and approximants. Philos Mag 87(18–21):2947–2955
74. Terauchi M (2006) Electronic structure analyses of BN network materials using high energy-resolution spectroscopy methods based on transmission electron microscopy. Microsc Res Tech 69:531–537
75. Spiller E (2000) Reflection optics: multilayers. In: Samson JA, Ederer DL (eds) Vacuum ultraviolet spectroscopy. Academic, San Diego
76. Imazono T, Koike M, Koeda M, Nagano T et al (2012) A multilayer grating with a novel layer structure for a flat-field spectrograph attached to transmission electron microscopes in energy region of 2–4 keV. AIP Conf Proc 1465:33–37

TEM Characterization of Nanocomposite Materials

8

Kenji Kaneko, Yoshio Sakka, and Yoshizumi Ishikawa

Contents

1 Definition of the Topic 333
2 Overview 334
3 Introduction 334
4 Experimental Methodology 336
4.1 Imaging Mode 338
4.2 Diffraction Mode 338
4.3 Scanning Mode 339
4.4 Analytical Mode 339
4.5 Tomographic Mode 342
5 Key Research Findings 348
5.1 TEM for Characterization of Ceramic Matrix Nanocomposites 348
5.2 TEM for Characterization of Polymer Matrix Nanocomposites 355
6 Conclusions and Future Prospective 363
References 364

1 Definition of the Topic

In this chapter, we describe the introduction and application of 2-dimensional (2D) and 3-dimensional (3D) characterization by transmission electron microscopy (TEM) of two types of nanocomposite materials, ceramic matrix nanocomposites (CMNC),

K. Kaneko (✉)
Department of Materials Science and Engineering, Kyushu University, Fukuoka, Japan
e-mail: kaneko@zaiko.kyushu-u.ac.jp

Y. Sakka
Advanced Ceramics Group, Materials Processing Unit, National Institute for Materials Science, Tsukuba, Japan

Y. Ishikawa
Advanced Materials Research Group, New Technology Research Laboratory, Sumitomo Osaka Cement Co., LTD, Chiba, Japan

C.S.S.R. Kumar (ed.), *Transmission Electron Microscopy Characterization of Nanomaterials*, DOI 10.1007/978-3-642-38934-4_8,
© Springer-Verlag Berlin Heidelberg 2014

and polymer matrix nanocomposites (PMNCs), in particular. For the case of CMNC, structural and morphological characterizations of matrix and nanostructure phases were carried out, and for the case of PMNC, dispersion and distribution of nanoparticles as well as interparticle distances between them were investigated.

2 Overview

Nanoscale characterization by transmission electron microscopy (TEM) and/or scanning transmission electron microscopy (STEM) plays an essential role in design, process, and property of nanocomposites used in nanoscience and nanotechnology. Large numbers of researches have been made concerning nanocomposites based on 2D TEM images of them, which would not reflect the true 3D nature, and researchers had to correlate 2D images with 3D physical properties of nanocomposites.

Here we describe the importance of TEM characterizations to acquire both 2D information and 3D information of nanocomposites.

3 Introduction

In recent years, nanoscale materials, which display properties very different from those of conventionally prepared bulk materials, have received special attention as they are the key materials of nanoscience and nanotechnology. Among those nanoscale materials, researches on nanocomposite materials, combinations of bulk matrix and nanostructured phases, have been progressing rapidly to achieve desired properties and to overcome limitations of bulk matrix by integrating nanostructured phases.

In general, the nanostructured phases are either adhered or incorporated into the matrix so that the significant improvements in their physical and/or chemical properties are expected. In fact, the integration of nanostructured phases into the matrix results in the combination and enhancement of their properties, as well as the generation of unique and advanced properties. The properties of nanocomposites are therefore not only the simple sum but also the hybrid of the properties of the individual component. Consequently, nanocomposites have been acknowledged as the materials of next generation due to its unique and advanced properties with comparison to the conventional materials, and the development of nanocomposites has emerged as an important step in creating a new generation of materials. In addition, the large surface area to volume ratio characteristics of the nanostructured phases in the nanocomposites makes them very attractive since only a small portion of them is required to achieve for a variety of applications.

There are several matters associated with nanocomposites, in particular the dispersion of nanostructured phases, as shown in Fig. 8.1. Nanostructured phases should be dispersed homogeneously within the matrix to maintain the even and uniform properties; however, they have tendencies to aggregate and form larger agglomerates, due to their large specific surface energy, resulting in homogeneous

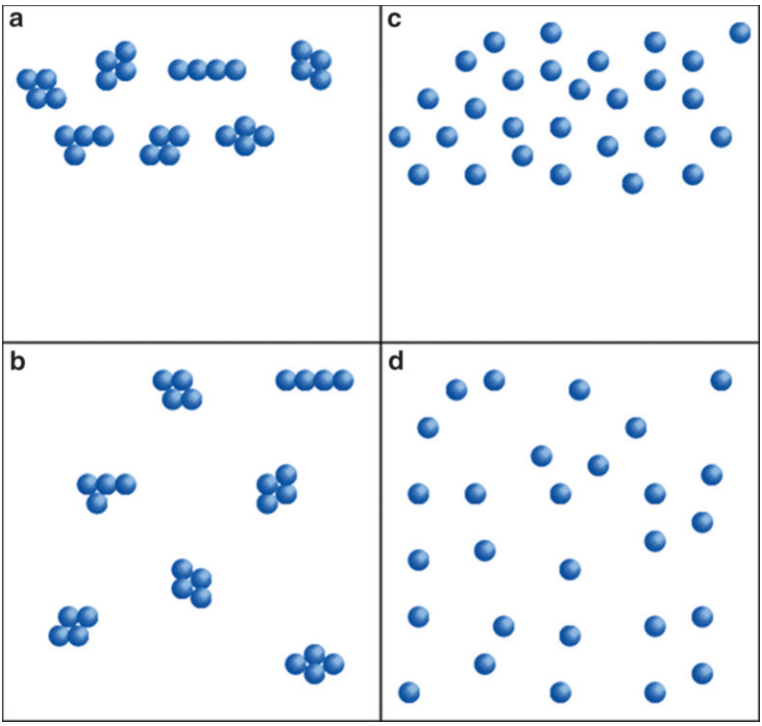


Fig. 8.1 A schematic diagram of the relationship between the distribution and the dispersion, (**a**) poor distribution and poor dispersion, (**b**) poor distribution and good dispersion, (**c**) good distribution and poor dispersion, and (**d**) good distribution and good dispersion

dispersion of them within the matrix, and degrade the properties associated with their nanoscale. Several fabrication methods have thus been challenged to achieve homogeneous dispersion of nanostructured phases by modifying the surface of them. In addition to the way nanostructured phases are being dispersed, other factors, such as the volume fraction, the structure, the grain size, the morphologies and others, also play important roles on nanocomposite materials. It is therefore that there have been large attentions on design, processing, characterization, and evaluation of nanocomposite materials.

In general, nanocomposite materials are classified into three different categories according to their matrix materials, CMNC, metal matrix nanocomposites (MMNC), and PMNC. Among these nanocomposites, CMNC as ceramic matrix with nanostructured metal in particular has been employed as versatile tools for various industrial applications. The potential of CMNC was firstly revealed by the pioneering work of Niihara [1] by incorporating the nanoscale particles into the ceramic matrix which could improve properties dramatically. Most studies reported so far have confirmed the great improvements of mechanical properties of the ceramic matrix after an addition of a small (i.e., $\sim$10 %) volume fraction of

nanostructured phases. MMNC refer to materials consisting of a ductile metal or alloy matrix in which some nanosized reinforcement material is implanted. These materials combine metal and ceramic features, i.e., ductility and toughness with high strength and modulus. Thus, MMNCs are suitable for production of materials with high strength in shear/compression processes and high service temperature capabilities. They show an extraordinary potential for application in many areas, such as aerospace and automotive industries, and development of structural materials. PMNC refers to polymer-based inorganic nanoparticle composites, which have attracted increasing attention due to their unique properties from the combination of organic and inorganic components. The properties of the PMNCs are obviously dependent on the properties of constituents, the volume fraction of components, the morphology, the size and the arrangement of inorganic materials, and the interfacial interaction between matrix and inorganic materials.

4 Experimental Methodology

TEM has been playing important roles for thorough characterizations and advancement of materials and has become a most essential tool for materials research, as schematically drawn in Fig. 8.2. Various imaging methods including bright-field (BF) and dark-field (DF) imaging as well as selected-area electron diffraction pattern (SADP) methods for structural and crystallographic measurement have widely been acknowledged as one of the most standard procedures to characterize materials. In addition, local atomic arrangements can be recognized from images obtained at high magnification and high resolution. The availabilities of spectroscopic techniques, including electron energy-loss spectroscopy (EELS) and energy dispersive X-ray spectroscopy (EDXS), lead to both quantitative and qualitative compositional analysis close to the single-atom level. Furthermore, 3D material characterization with spatial resolution at about 1 nm is now available by 3D electron tomography (3D-ET), the combination of TEM and computed tomography (CT). In fact, when there is a keyword “nanoscale” or “atomic-scale” for microscopic and spectroscopic characterizations, there always is the need of TEM.

In addition to these TEM techniques, combination of “scanning method” and TEM, scanning transmission electron microscopy (STEM), has become very popular and effective method to characterize materials. When a finely focused electron probe is scanned across a defined region of specimen, signals generated by the interaction between the incident electron beam and the specimen will vary according to the specimen characteristics such as composition, structure, and orientation. As a result, STEM with compositional analysis leads to the 2D elemental distribution. Furthermore, STEM with high-angle annular dark-field (HAADF) detector collecting electrons that undergo high-angle scattering leads to the atomic number contrast, Z-contrast, image due to the signals being approximately proportional to the mean square atomic number, Z^2 [2]. The Z-contrast

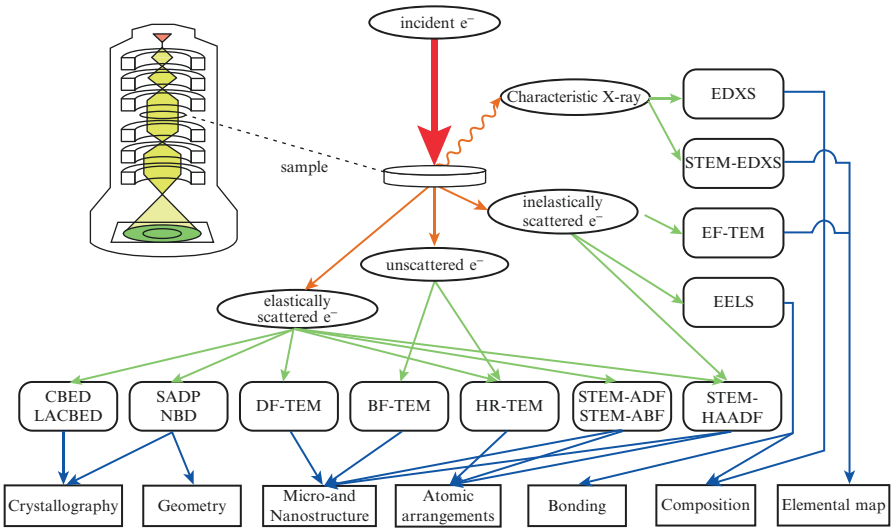


Fig. 8.2 A schematic diagram of the information achieved by TEM/STEM methods

Table 8.1 The nonrelativistic and relativistic wavelength of electron microscopes

Accelerating voltage (kV)	Nonrelativistic wavelength (nm)	Relativistic wavelength (nm)	Velocity (10^8 m/s)
100	0.00386	0.00370	1.644
200	0.00273	0.00251	1.759
300	0.00223	0.00197	2.330
400	0.00193	0.00164	2.484
1000	0.00122	0.00087	2.823

imaging performed in STEM is almost perfectly incoherent, whereas the conventional imaging in TEM is almost perfectly coherent.

The wavelength of the beam of electrons is a function of the accelerating voltage in an electron gun. According to de Broglie's hypothesis of the wave-particle durability [3], there should be a correlation between particle momentum p and its wavelength λ through Planck's constant h $(= 6.626 \times 10^{-34}(\mathrm{Js}))$, and the relativistic wavelength of the accelerated electron can be obtained [4] (Table 8.1):

$$\lambda = \frac{h}{p} = \frac{h}{mv} = 2.426 \times \left(\frac{\sqrt{1 - \frac{v^2}{c^2}}}{\sqrt{1 - \left(\sqrt{1 - \frac{v^2}{c^2}}\right)^2}} \right) \tag{8.1}$$

4.1 Imaging Mode

In general, the changes in the amplitude and phase of the electron wave in the specimen contribute to the formation of image contrast, due to the scattering processes during the interaction. The difference between the amplitude contrast and the phase contrast is based on the thickness of the specimen and the size of the objective apertures. The phase contrast image in the image plane, namely, the interference pattern of electron waves, is formed by a small phase shift while travelling through the specimen, which is sensitive to the atom distribution in the specimen and the fundamental of high-resolution (HR) TEM. The amplitude contrast image is formed by selecting a single electron beam of the unscattered or elastically scattered electrons using a small objective aperture. Whether the unscattered electron beam or the scattered electron beams in the diffraction pattern have been selected, it results either a BF- or a DF-TEM image. The contrast in BF- and DF-TEM images is attributed to the change of the amplitude of either the unscattered beam or diffracted beam due to absorption and dynamic scattering in the specimens. BF-TEM imaging technique using unscattered electron beam is most commonly used imaging method by TEM. The size of the objective aperture should be small enough to remove unwanted diffracted electron beams caused by the lattices of the crystal. DF-TEM images are formed when one or more specific diffracted electron beams are selected by the objective aperture by tilting the incident electron beam. In this case, the unscattered electron beam should be blocked by the objective aperture. The advantage of the DF-TEM imaging method is its high amplitude contrast and usually used for observing grain-size distribution, different phases, precipitates, and dislocations.

On the other hand, image formation by a phase contrast requires the selection of a large objective aperture for selecting more than two beams on the back focal plane and transmitted beams in order to achieve a maximum resolution in the resulting interference pattern on the fluorescent screen or CCD. The wave function suffers a phase change proportional to the potential of the specimen projected along the incident beam direction.

The cross section for Rutherford scattering is strongly dependent on the mass or density ρ and the thickness t of the specimen, which causes the mass-thickness contrast [5]. Interaction of incident electrons with heavy atoms is stronger than that with light atoms. If the thickness is homogeneous, areas concentrated with heavy atoms or with high densities appear with darker contrast than that with light atoms or with low densities (mass contrast). More electrons are scattered in thick areas than in thin areas so that thick areas also appear dark (thickness contrast). It is usually necessary to consider carefully when there are the similar contrast regions, either at thick specimen area with light elements or at thin specimen area with heavier atoms.

4.2 Diffraction Mode

The diffracted electrons are focused into a regular arrangement of diffraction spots which are projected and recorded as the electron diffraction pattern.

Diffracted waves scattered by the atomic potential form diffraction spots on the back focal plane after being focused with the objective lens. The space where the diffraction pattern forms is called "reciprocal space," while the space at the image plane or at a specimen is called "real space," and the transformation from the real space to the reciprocal space is mathematically given by the Fourier transform. The electron diffraction pattern consists of spots or rings very similar to X-ray diffraction pattern, and crystal symmetry can be extracted via the extinction rule. Interplanar spacing can also be calculated from electron diffraction patterns. Incident electrons can be converged on a specimen to obtain a diffraction pattern from an area only a few nm in diameter, known as nanobeam diffraction (NBD) method. Convergent beam electron diffraction (CBED) uses a large probe with small convergence angles to produce diffraction disks, which contains the information of structure, symmetry details, and atom positions.

4.3 Scanning Mode

TEM and STEM are related techniques that use an electron beam to image a sample. In the case of TEM, the whole imaged area is illuminated simultaneously, but the specimen is scanned in a raster point by point with a focused electron probe in the STEM. STEM with annular dark-field (ADF) is also a powerful technique for acquiring high-resolution images of materials, as demonstrated by Crewe and co-workers [6]. When a finely focused electron probe is scanned across a defined region of specimen, signals generated by the interaction between the incident electron beam and the specimen will vary according to specimen characteristics such as composition, structure, and orientation, as in the case of TEM. In particular, when an energetic electron beam passes near the nucleus of an atom, the electron can be scattered elastically by the Coulombic field of nucleus, known as Rutherford scattering [5].

By using an ADF detector with a large inner radius, electrons are collected which are not Bragg scattered [2]. In particular, Z-contrast imaging can be achieved with HAADF detector proposed by Howie [7] by suppressing the amplitude contrast effects in ADF images due to the dominated effect of thermal diffuse scattering since the high-angle scattered electrons are basically incoherent [8]. As such HAADF images show little or no Bragg scattered events, and their intensity is approximately proportional to the square of the atomic number, Z^2. In addition, STEM is a powerful tool to carry out the spectroscopic analysis at near atomic resolution. Atomically resolved EDXS and EELS measurements of local compositions and electronic structures can be achieved from an individual atomic column [9].

4.4 Analytical Mode

4.4.1 EDXS

EDXS is a method for both qualitative and quantitative elemental analysis using the characteristic X-rays, which have unique energies from each element.

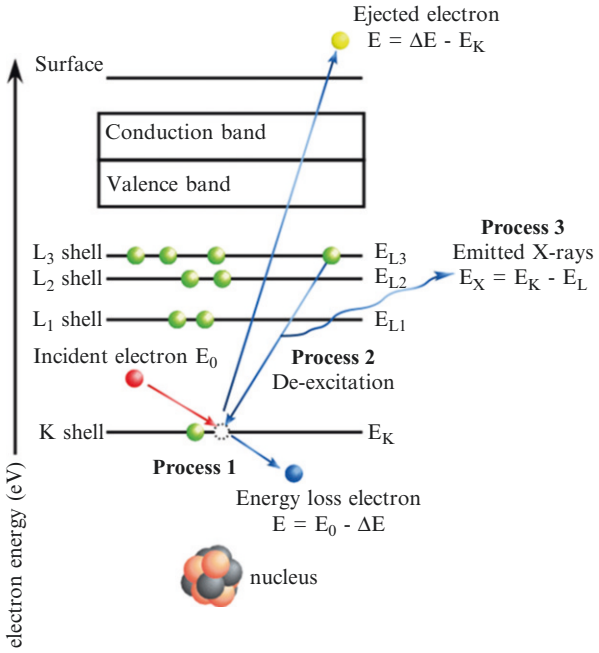


Fig. 8.3 Interaction between the incident electron and the sample

The characteristic X-ray spectrum is caused by the de-energization of atom after inelastically scattered process is taken place between incidental electron and the sample, as schematically drawn in Fig. 8.3. A lower-shell electron is emitted from the atom during **process 1** and there will be a vacancy at the lower shell. A higher-shell electron can fall into the lower shell and fill the vacancy (**process 2**). The characteristic X-ray energy corresponds to a difference between two energy levels of the electron cloud of an atom. Since these energy levels are quantified, the X-ray energy spectrum represents the signature of the atom. As the electron falls into the lower shell, it emits X-rays to balance the total energy of the atom (**process 3**). Then the X-rays are detected by a semiconductor and processed by a detector. An EDXS spectrum is constituted by a background produced by the Bremsstrahlung X-rays and by peak characteristic to the chemical elements of the material [10].

There is a correlation between the intensity of the integrated intensities of elements and the weight fraction of elements, known as the standard relationship, Eq. 8.2 [11]:

$$\frac{C_A}{C_B} = K_{AB}\frac{I_A}{I_B} \tag{8.2}$$

where C_A and C_B are the weight fractions of elements, I_A and I_B are the characteristic X-ray intensities, of elements A and B, respectively, and k_{AB} is the Cliff-Lorimer factor which is independent of composition and also of thickness.

In addition, the characteristic X-ray intensity is given by Eq. 8.3 in the case of very thin specimen:

$$I_A \propto N_0 \left(\frac{Q\omega a}{A} \right)_A \rho t \tag{8.3}$$

where I_A is the characteristic X-ray intensity of element A, N_0 is the Avogadro number, Q is the ionization cross section, ω is the fluorescent yield, a is intensity ratio, A is the atomic weight, ρ is the density, and t is the specimen thickness.

Furthermore, EDXS can be combined with STEM, and line profiles or elemental maps can be obtained from a defined line or a region of the specimen.

4.4.2 EELS

Collisions of an incident electron with the sample can be elastic or inelastic. When an incident electron suffers collisions resulting in energy transfer, the energy transferred to the sample can be used for obtaining analytical information of the specimen. A simple way to analyze the energy transfer of the electrons is to analyze the bending of electron trajectory depending on the velocity of an electron in magnetic field by magnetic-prism spectrometer. In practice, the trajectories of electrons which interacted with the sample inelastically are bent more than those which interacted with the sample elastically.

For the case of elastic collisions, the prominent peak appearing at 0 eV is called zero-loss peak since there is no loss of energy. The inelastic interaction can be classified by the type of interaction an electron suffered. Inelastic scattering by outer-shell (valence) electrons leads to the plasmon oscillations in the material generally appears in the range 10–30 eV. The information on those oscillations is in the low-loss part of a spectrum, known as the plasmon loss. The interaction of incident electrons with core-level electrons results in higher energy losses, above about 50 eV, known as the core loss. The threshold energy of core-loss edge is the binding energy of the corresponding atomic shell, allowing elements to be identified in the sample. The shape of such a core-loss edge can provide information on chemical state of the atoms involved in the interaction and often called as energy-loss near-edge structure (ELNES). Additional information on the local geometry as distance of nearest-neighbor atoms can be retrieved from extended energy-loss fine structure (EXELFS) of core-loss ionization edges, an intensity modulation starting at 50 eV or more from the ionization edge. The intensities of such core-loss edges can be used to obtain information on areal density of given type of atom.

Similar to the case of EDXS method as presented in Eq. 8.3, the number of atoms, N_A, of the element analyzed can be quantified by Eq. 8.4 using EELS signal [12]:

$$N_A = \frac{I_A(\beta, \Delta E, E_0)}{I_t} \cdot \frac{1}{t\sigma_A(\beta, \Delta E, E_0)} \tag{8.4}$$

where I_t is the incident electron intensity, I_A is the number of electron having excited a kth inner shell from element A, t is the specimen thickness, β is the collection angle, ΔE is the energy slit width, E_0 is the energy of entering electron, and $\sigma_A(\beta, \Delta E, E_0)$ is the ionization cross section for the kth shell of element A. Furthermore, the ratio of elements can be quantified by modifying Eqs. 8.4, and 8.5:

$$\frac{N_A}{N_B} = \frac{I_A(\beta, \Delta E, E_0)}{I_B(\beta, \Delta E, E_0)} \cdot \frac{\sigma_B(\beta, \Delta E, E_0)}{\sigma_A(\beta, \Delta E, E_0)} \tag{8.5}$$

In the case of conventional TEM, the electrons for imaging are selected using an objective aperture according to their scattering angles. In the case of energy-filtering (EF) TEM, the element sensitive contrast is optimized by EF method either by filtering out the contrast-reducing electrons from the spectrum of transmitted electrons or by selecting electrons containing specific energy. The contribution of inelastically scattered electrons to an image or a diffraction pattern leads to blurring due to chromatic aberration. Zero-loss filtering removes the contribution of such inelastically scattered electrons to both images and diffraction patterns to improve signal to noise ratio, specially for the thick specimens. The most common usage of EF-TEM is the elemental mapping which is a method of achieving a 2D distribution of a specific element by selecting core-loss peak at specific energy.

4.5 Tomographic Mode

Physical and chemical properties of materials are dependent on their structures, compositions, morphologies, and distributions. Materials usually have volume and should be dealt in 3D, but micro- and nanoscopic images obtained by electron microscopes are typically in 2D and the information of the depth is usually disregarded [13].

In a classical approach the stereo-pair method has been used to extract depth information from two projected micrographs of a specimen that is tilted [14, 15]. On the other hand, a complete 3D view of the actual structures of specimen can be obtained through a method known as 3D-ET, a combination of TEM/STEM and CT [16]. The mathematical principle of 3D-ET was firstly proposed by Radon in 1917 [17], but the first example of tomographic imaging in an electron microscope was reported almost a half century later [18–20]. At that time, irradiation damage during manual recording of images, insufficient memory and speed of computers, and angular range and manual tilts of the specimen holders were the source of artifacts for achieving 3D-ET. In addition, goniometer was imperfect mechanically and samples were not exactly at the eucentric height, so that it moved both laterally and vertically when the sample was tilted within.

Recently, 3D-ET method has widely been accepted in the materials science as one of the characterization methods for achieving 3D information from nanoscale

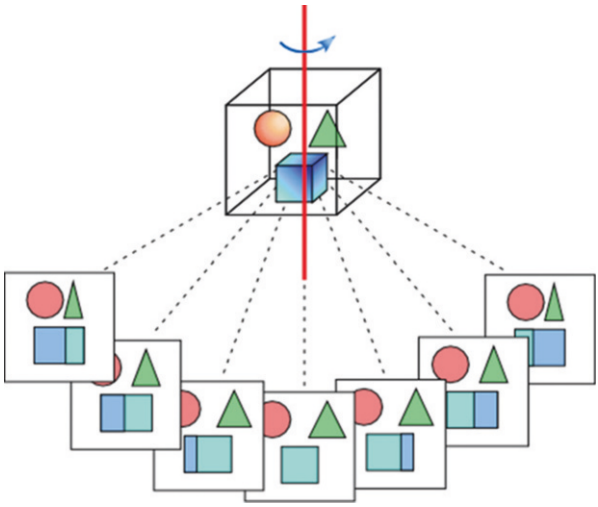


Fig. 8.4 A schematic diagram of acquiring 2D projections and achieving 3D reconstructed volume, sphere, triangular plate, and cubic which are present in the field

materials [21–23]. For the case of crystalline materials research, combination with STEM has become a more standard procedure than that with TEM for achieving 3D information needed to characterize nanostructured phases such as the volume fraction, the morphologies, and the spatial distribution of them ([24–26], [27, 28]) to minimize the effect of amplitude contrast.

In the case of 3D-ET, many of TEM parameters were controlled digitally during the acquisition of the tilt series of projections: the defocus, the beam shift, the beam tilt, the image shift, the specimen tilt, and the specimen height, therefore a fully automated and fully digitized TEM with an accurate tilt stage and a especially designed high-tilt specimen holder is necessary.

Imaging from various tilt angles provides information of depth which enables distinction of overlapped structure. As can be seen in Fig. 8.4, even if the model particles are observed as almost overlapping each other within the same field of view from one direction, it can be seen separated from another direction. In addition, the morphologies of particles are seen dissimilar from different orientations.

The spatial resolution and the quality of reconstructed volume are strongly dependent on that of original image, on the angular range and on the angular increment. The total angular range determines the amount of 3D data seen over all tilt angles. The larger the total tilt angle, the more qualitative data can be obtained in the reconstructed volume [29]. In addition, the smaller the tilt increment, the better quality can be achieved in the reconstructed volume [30].

The resolution, R, of a reconstructed tomogram is determined by the angular range and increment and can be approximated with Eq. 8.6:

$$R = \frac{\pi D}{N} \tag{8.6}$$

Table 8.2 Calculated elongation factor, e, for different maximum angular ranges [34]

Angular range (°)	±90	±80	±70	±60	±50	±40
Elongation factor	1.00	1.13	1.31	1.55	1.89	2.41

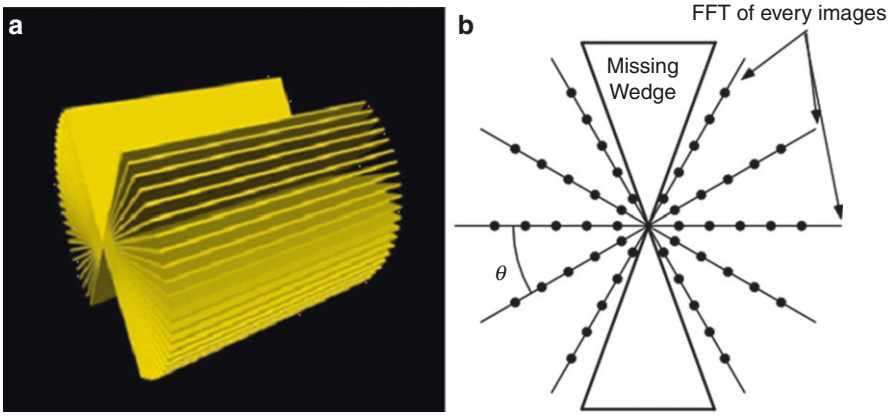


Fig. 8.5 Schematic diagrams of (**a**) the absence of the images at higher tilt angle and (**b**) missing wedge

where D is the diameter of the object and N is the number of tilt projections [31]. An additional factor that adversely affects the resolution in single-axis tilt tomography is the presence of a "missing wedge" due to the limited angular range available in a TEM. This arises either due to blocking of the electron beam by the specimen holder, TEM grid or other parts of the specimen, or because the projected specimen thickness to be penetrated by the beam becomes too great at high tilt angles [32]. The missing wedge problem can lead to artifacts and anisotropy in the spatial resolution [24]. Further limitations on the reconstruction quality come from nonlinear relationships between the transmission intensity and sample properties, such as local mass thickness [33]. This missing information leads to the lowering of the spatial resolution in the direction parallel to the optic axis by an "elongation factor," e, by Eq. 8.7 [34] (Table 8.2):

$$e = \sqrt{\frac{\alpha_{\max} + \cos\alpha_{\max}\sin\alpha_{\max}}{\alpha_{\max} - \cos\alpha_{\max}\sin\alpha_{\max}}} \tag{8.7}$$

In general, the spatial resolution of the reconstruction is anisotropic for the single-axis tilt geometry. In practice, the limited space between the objective lens pole pieces and the finite thickness of the specimen holder limits the angular range, giving rise to the missing wedge of information, as schematically shown in Fig. 8.5.

The improvements of spatial resolution and the image quality of the reconstructed image require large numbers of tilted images from high angles, as schematically drawn in Figs. 8.6 and 8.7, which suggest that the total amount of

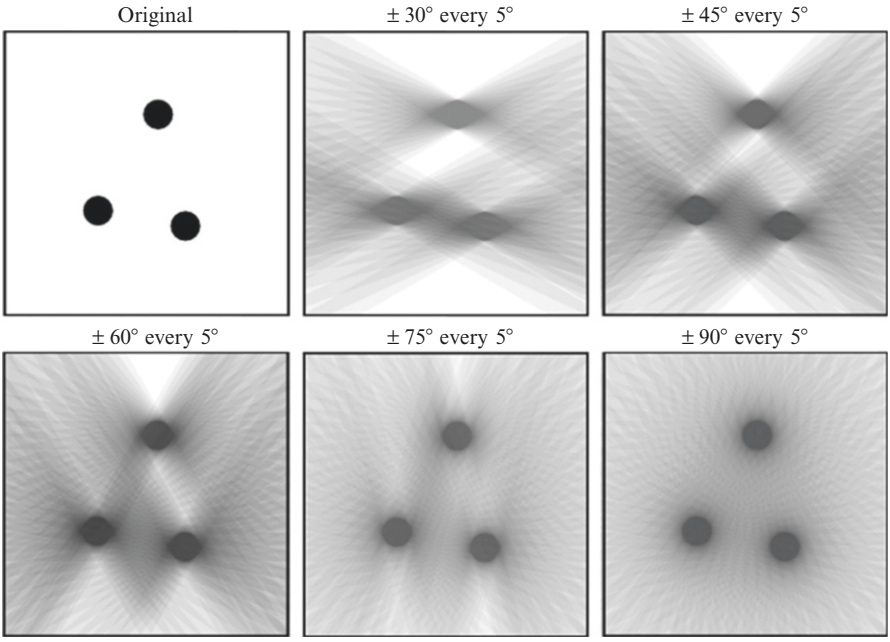


Fig. 8.6 The relationship between the angular range and the quality of image, with the same tilt increment. With the same tilt increment, the higher the angular range, the better quality can be achieved in the reconstruction via back projection

time required for achieving tilt series is the multiplication of the time taken to obtain one image and the number of images required from the same field of view. This may result the irradiation damage and the contamination over the field of view. Furthermore, acquisition of large numbers of tilted images with large size means an enormous amount of processing time and memories.

In addition to these angular matters, it is necessary to consider the increase of thickness during the tilts, i.e., the path length of the electron beam through the specimen becomes twice the specimen thickness at 60° and approximately three times at 70°, as schematically drawn in Fig. 8.8. The quality of the reconstructed volume decreases by the increase of thickness, namely, the increase of inelastic scattering electron, due to the relative specimen thickness increase by tilting the specimen at higher degrees, as

$$t = \frac{t_0}{\cos\theta} \tag{8.8}$$

where t is the relative specimen thickness and t_0 is the original specimen thickness as can be seen in Fig. 8.8. For this case, EF-TEM method should be applied to remove the inelastically scattered electrons to improve the image quality. In addition, it is possible to acquire the reconstructed 3D volume from the plasmon-loss images and core-loss images [24, 35].

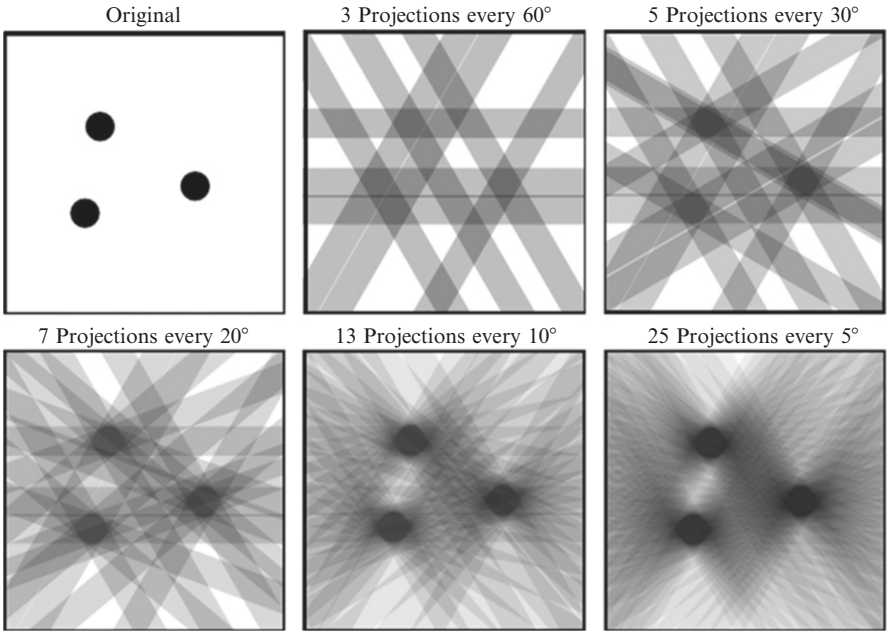


Fig. 8.7 The relationship between the number of projections and the quality of image, with the same angular range, from −60° to 60°. With the same angular range, the higher the number of projections so that the smaller the tilt increment, the better quality can be achieved in the reconstruction via back projection

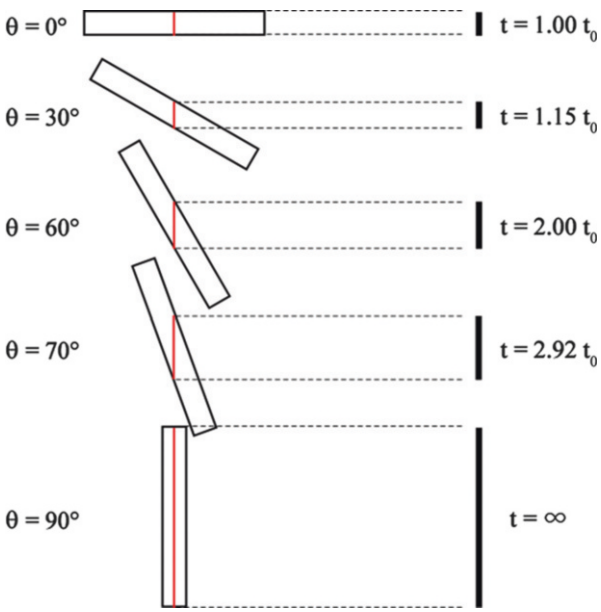


Fig. 8.8 In the case of thin specimen, the relative specimen thickness, t, increases with the function of angle θ, as $t_0/\cos\theta$

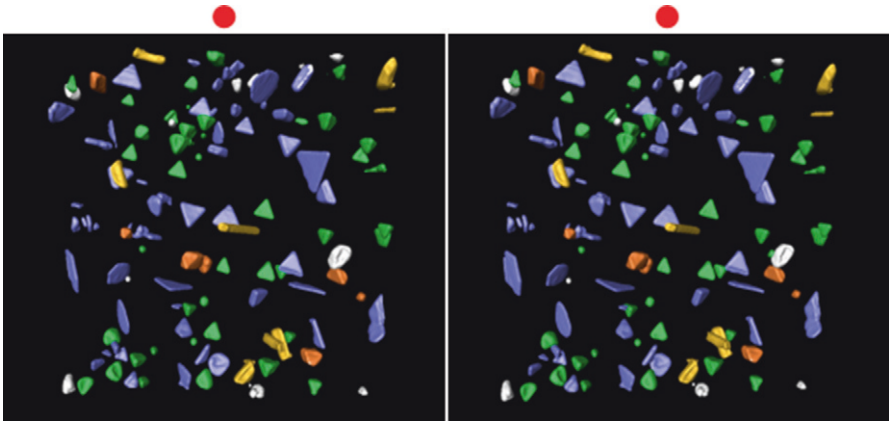


Fig. 8.9 A typical stereo-pair image contains two views of a precipitate in Al alloy, as an example. *Left image* is intended to be seen by the left eye and the other by the right eye. The image is viewed by deliberately diverging one's eyes until the two images come together

Furthermore, 3D-ET method is not suitable for crystalline materials due to the presences of amplitude contrast at specific angles so that the relationship between the contrast of TEM images and the tilt angles becomes not monotonous. It is therefore that the Z-contrast imaging method is very useful in the study of (poly-) crystalline materials to minimize the coherent amplitude contrast, which is unwanted for the tomographic reconstructions.

Nevertheless, the quality of reconstruction results in 3D-ET has been steadily improving in recent years for several reasons. First, new computational algorithms have been developed, weighted back projection (WBP) methods [36], algebraic reconstruction techniques (ART) [37], simultaneous iterative reconstruction technique (SIRT) [38], and discrete algebraic reconstruction technique (DART) [39]. Second, innovative specimen holders have commercially been developed for 3D-ET, capable of tilting at high angles so that the effect of the missing wedge could be minimized or almost eliminated (Gatan, Melbuild, Fischione). Recently, a specimen preparation method is proposed to avoid missing edges via focused ion beam (FIB) method, and one can now fabricate pillar-shaped specimens that can take advantage of the full angular range [32]. Third, more recently widespread imaging methods in electron microscopy, such as Z-contrast and EF-TEM tomography, also minimize the effect of multiple electron scattering and reduce non-linearities between image intensity and projected (mass) thickness, as compared to more standard BF-TEM tomography [24]. Furthermore, it is possible to reduce the effect of Bragg scattering by using STEM-HAADF imaging method to achieve final reconstructed images. A typical example of 3D reconstructed volume of Al alloys is shown in Fig. 8.9.

As long as there are contrasts reflecting the information of materials within 2D tilted series, it would be possible to obtain 3D reconstructed volume reflecting the information of materials.

5 Key Research Findings

Both 2D and 3D TEM methods were applied for characterizing CMNC and PMNC, and then their microstructures were correlated with physical properties. In the case of CMNC, growth mechanisms at extreme condition were deduced. In the case of PMNC, the optical properties were explained by the dispersion and distribution of nanostructured phases.

5.1 TEM for Characterization of Ceramic Matrix Nanocomposites

CMNC can exhibit large improvements in physical and chemical properties in various technological applications, in which metallic clusters or crystals of nanometer scale embedded within or adhered on ceramics. It is therefore that the development of CMNCs has emerged to develop highly functional ceramics with additional properties by incorporating the small amount of metallic nanoparticles in creating a new generation of materials.

Metallic nanoparticles ranging from 1 to 100 nm in size have shown different physical and chemical properties from their bulk, which can be attributed to the large portion of surface atoms and quantum size effect.

5.1.1 Titanium Nitride (TiN)

Recently, non-oxide advanced ceramics with special properties has received a large attention in the world, such as carbides, nitrides, borides, and sulfides. Among transition metal nitrides, the most attention has been paid to titanium nitride (TiN), since it has a simple NaCl-type face-centered cubic structure (lattice constant $a = 4.24$ Å) [40] with many desirable properties. In fact, TiN exhibits an exceptional combination of chemical, physical, mechanical, and electrical properties such as good corrosion resistance, heat resistance, chemical stability, chemical inertness, wear resistance [41–43], exceptionally high hardness (≈20 GPa) which results from the high degree of metallic and covalent bonding [44–46], low friction coefficient against dry steel (≈0.4) [47–50], good electrical conductivity ($\rho = 21.7$ mΩ cm) [51], high thermal conductivity [52], high melting temperature (2,927 °C) [53], high reflectance in the IR region [54], a metallic luster with a beautiful golden color [55], biocompatibility [56], good chemical/thermal stability [45, 46, 57], good adhesion, and good corrosion resistance [58] and barrier properties [47, 59]. The strength of TiN is from the small separation of atoms, large surface energy, and high elastic modulus (320 GPa) [60], high yield stress (14 GPa), and high specific gravity (5.4 g/cm^3) [61–72]. Reported work functions of TiN vary between 3.5 and 4.5 eV [73–75].

Comparing to the conventional bulk material, TiN in nanoscale has high surface area, which makes it an attractive candidate for improving its physical and chemical properties. For example, TiN nanomaterial is a favored choice for supercapacitors [76] and an excellent catalyst [77]. Furthermore, many advanced functional materials can be made from TiN nanocomposites to achieve enhanced

conductivity [78], superhardness [79], excellent toughness, and good sinterability at lower temperatures [80].

In addition, TiN properties generally depend on the stoichiometry (Ti/N ratio) [63], the impurity content, and the microstructure, which can be controlled by changing deposition technique and process parameters [81, 82].

5.1.2 Application of TiN

Due to these outstanding properties, TiN has been widely used in a variety of applications in many fields. For example, thin TiN films are thermally stable at high temperature and have found application in microelectronics as a diffusion barrier between metal and semiconductor to prevent interdiffusion of metals, such as Cu and Ag, in integrated circuits and low barrier metal in Schottky diodes [68, 83–92].

The use of TiN as a coating material for high-speed steel cutting tools has been available for several decades [43, 93–96]. TiN thin films have also been regarded as a potential candidate for biocompatible applications such as dental prosthesis, materials for hip joint replacement and heart valve replacement, and microelectrode materials for biosensors [97–103]. TiN has also been used as the sensitive material in all solid-state potentiometric pH electrodes [104, 105].

Furthermore, TiN has been applied in other applications such as decorative coatings [106], heat mirrors in high temperature regions [88, 107–109], semiconductors and microelectronic instrumentations [74, 83, 110], high-temperature heterogeneous catalysis [77, 111], and solar cell applications [112, 113].

TiN nanoparticles present advantages such as improved sinterability and catalytic effects with comparison to TiN bulk materials [77, 82, 111, 114–116], and TiN nanoparticles are found to be a promising catalyst support and active catalyst in hydrogen storage applications [117].

5.1.3 Fabrication of TiN

TiN has been prepared by a variety of fabrication processes, so far. Conventionally, bulk TiN is synthesized by directly reacting metallic Ti with N_2 gas or NH_3 at temperatures near 1,200 °C or by self-propagating high temperature synthesis (SHS), through heating or igniting fine titanium powders in nitrogen [118].

Many studies have focused on the fabrication of nanoparticles with high purity, submicrometer particle size, narrow particle-size distribution, and minimum agglomeration. In general, TiN particles can conventionally be prepared in several ways [119], for example:

(i) Nitridation of Ti metal or TiH powders:

$$\mathrm{Ti_{(S)}} + \frac{1}{2}\mathrm{N_{2(g)}} = \mathrm{TiN_{(S)}} \tag{8.9}$$

$$\mathrm{TiH_{(S)}} + \frac{1}{2}\mathrm{N_{2(g)}} = \mathrm{TiN_{(S)}} + \frac{1}{2}\mathrm{H_{2(g)}} \tag{8.10}$$

(ii) Vapor-phase reaction between $TiCl_4$ vapor and NH_3 [82, 120]

$$TiCl_{4(g)} + \frac{4}{3}NH_{3(g)} = TiN_{(S)} + \frac{1}{6}N_{2(g)} + 4HCl_{(g)} \tag{8.11}$$

Industrial TiN is normally prepared by nitriding TiO_2 in the presence of C, carbothermal nitridation [121], which has the advantage that it uses readily available and inexpensive raw materials, a comparably simple reaction environment, and has the potential for large-scale production, but it does not produce a highly pure product:

$$TiO_{2(S)} + 2C_{(S)} + \frac{1}{2}N_{2(g)} = TiN_{(S)} + 2CO_{(g)} \tag{8.12}$$

with standard Gibbs functions at 1,327 °C.

In addition to these conventional fabrication methods, unconventional methods, such as electrochemical synthesis [122], solid-state metathesis (SSM) [123] with $TiCl_4$ or $TiCl_3$ using various solid nitrogen sources as [124–130] microwave plasma heating producing a large quantity of nanopowder in a short period of time [131], self-propagating high temperature synthesis (SHS) [115, 132] and plasma nitridation of metal oxides [133], pulsed laser deposition [58, 70], and dc arc-plasma synthesis [134, 135], are also employed to prepare TiN powders. In the case of 2-step synthesis, TiN nanoparticles were obtained from heat treatment of a precursor obtained by reacting liquid $TiCl_4$ with NH_3 in anhydrous organic liquids [111, 136].

Crystalline TiN can also be formed in situ during high-energy milling process with long milling period. During the ball-milling process, solid Ti metal and gaseous N_2 molecules are reacted to form TiN. Mechanical alloying by high-energy "dry" ball milling of Ti metals under a flow of N_2 has been developed for aiming at mass production of industrial TiN under a flow of N_2 [114, 137–142] or NH_3 [142–144]. Mechanochemical route to synthesize TiN has also been reported by "wet" ball-milling Ti metal powder with ring-type organic compound pyrazine in a benzene solution for a certain period of time [121, 145].

The properties of TiN coating films highly depend on its microstructures often dominated by the coating process, so that it is necessary to apply suitable process for the wide range of applications. Currently, TiN coatings are applied by the following representative methods, including chemical vapor deposition (CVD) [146], physical vapor deposition (PVD) [147], ion implantation [58], ion plating [148], sputtering [57, 101, 149, 150], plasma reactive spraying [41, 151], atomic layer deposition [76], and ion beam assisted deposition [152].

Since the addition of TiN to the matrix material was reported to increase some mechanical properties, and to lower the electrical resistivity of the ceramic composites, the properties of TiN particles reinforced Al_2O_3 or Si_3N_4 composites were widely studied. Furthermore, many advanced functional materials have been reported by combining TiN and nanoparticles, namely, "TiN nanocomposites," to

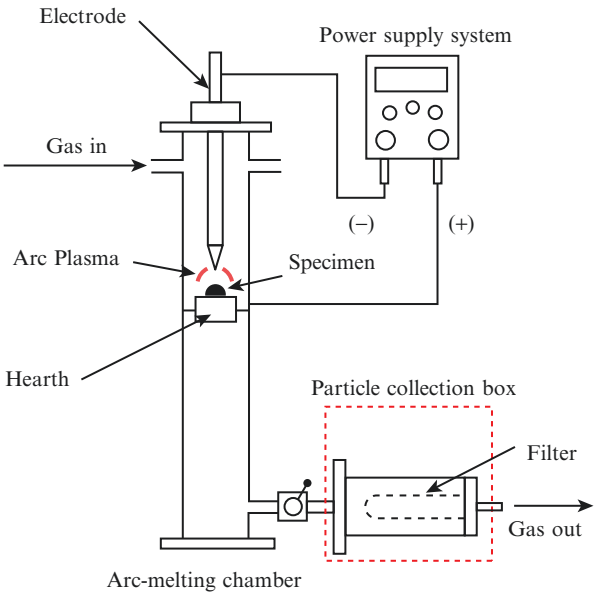


Fig. 8.10 A schematic diagram of apparatus for producing nanocomposites by means of an active plasma–metal reaction method

achieve synergetic effects, such as enhanced conductivity [78], superhardness [79], excellent toughness, and good sinterability at lower temperatures [80], and catalytic activities ([134, 135], Kitawwaki 2008).

5.1.4 TiN–Ag

TiN–Ag (63.98wt%TiN–36.02wt%Ag) nanocomposites were synthesized by dc arc-plasma method, schematically drawn in Fig. 8.10, which composed of an arc-melting chamber, a particle transport system, particle collection box, a gas circulation system, a vacuum system, and power supply system [135, 205, 28].

Nanocomposites generated in the arc chamber were transported by a carrier gas to collection filter. The electric DC power supply equipment (Sanshadenki Co. Ltd., Osaka, Japan) was employed that could produce stable arc states up to 70 V even when the hydrogen or nitrogen concentration increased. The bulk ingots of Ti–Ag as parent alloys (63.98wt%Ti–36.02wt%Ag) were prepared from pure metals of 99.99%Ti and 99.99%Ag by arc melting in an argon atmosphere. When the arc-flame of nitrogen or hydrogen strikes the metal, nanoparticles are subsequently generated around the arc spot area of the molten droplet. TiN–Ag nanocomposites were then synthesized by arc melting of each parent alloy under the following conditions: atmosphere 7 %N_2–46 %H_2-Ar, total pressure 0.1 MPa, gas flow rate 5×10^{-4} m^3/s, arc current 150 A, arc voltage 35–45 V, reaction time 240–600 s, and are gathered on a filter. The TiN–Ag nanocomposites were treated in a collection box or under a flowing nitrogen atmosphere to avoid an oxidation reaction. Before exposure to air, a slow oxidation treatment, where formation of the surface oxide layer was performed in a 99%Ar–1%O_2 atmosphere at room temperature for 12 h, was applied to the nanoparticles to prevent a rapid spontaneous

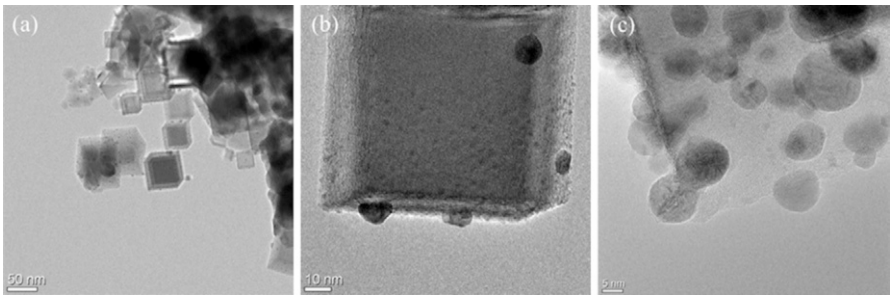


Fig. 8.11 (**a**–**c**) A set of BF-TEM images

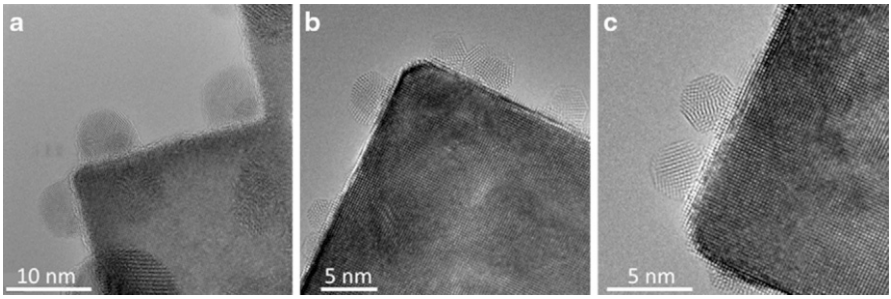


Fig. 8.12 (**a**–**c**) A set of HRTEM images

combustion. Then the TiN–Ag nanocomposite particles were ultrasonically dispersed in alcohol and mounted on an amorphous carbon-coated Cu grids.

Structural characterizations of the TiN–Ag nanocomposites were carried out in TEM and STEM. Figure 8.11a–c displays a typical set of bright-field TEM images at various magnifications of TiN–Ag nanocomposites. A low-magnified image, Fig. 8.11a, shows a number of nanocomposites showing cubic morphologies with an average grain size about 50 nm, which are occasionally aggregated to form agglomerates, where both mass–thickness and amplitude contrasts are present within the field of view. In addition, almost evenly distributed fine and coarse dark particles with the size ranging from about a few nm are visible on the surface, as shown in Fig. 8.11b. Occasionally, relatively large Ag particles, 10–20 nm diameter, were seen adhered on the surface of cubic TiN, as shown in Fig. 8.11c.

Figure 8.12a–c shows a set of HRTEM images obtained from the similar field of view to identify the orientation and bonding relationship between the second phase and the matrix. The lattice spacing of the cubic TiN particle is measured as 0.21 nm, which corresponds to that of the $(200)_{TiN}$. As can be seen from these HRTEM images that almost all nanoparticles are found randomly oriented with respect to TiN, there might be direct bonding and atomic rearrangements of Ag particles to relax on the surface of TiN.

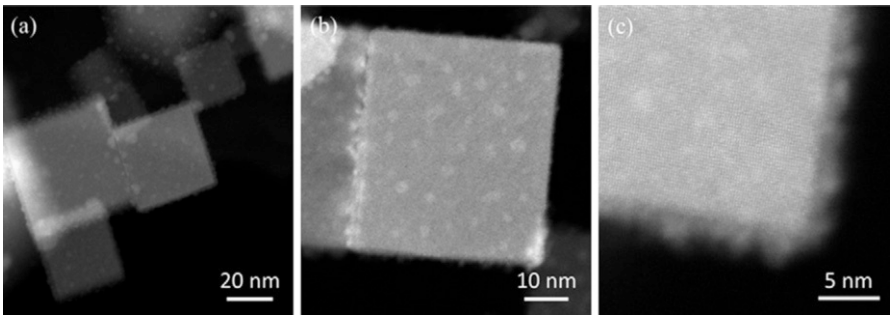


Fig. 8.13 (**a**–**c**) A typical set of STEM-HAADF images

The STEM-HAADF images, shown in Fig. 8.13a–c, indicate the presences of Ag nanoparticles including relatively large particles and small Ag particles on the surface of cubical TiN nanoparticles. Since the intensity of STEM-HAADF image strongly reflects the atomic number, highly dispersed Ag nanoparticles of irregular-morphology on cubical TiN nanoparticles can be confirmed.

Although the conventional TEM method provides information with regard to the 2D distribution of Ag and microstructure of TiN–Ag nanocomposite, in-depth information and their 3D dispersion of Ag is unable to be observed. Therefore, 3D-ET was carried out to enable further investigation of the 3D characterization of Ag nanoparticles. A tilt series of STEM-HAADF images was acquired from −78° to 70° with an image taken every 2° increment with especially designed high-tilt holders (a part of the series is shown in Fig. 8.14). Once the acquisition of the tilt series was completed, images were spatially aligned by a cross-correlation algorithm using Inspect3D software (FEI, the Netherlands), and 3D reconstructions were achieved using a simultaneous iterative reconstruction algorithm (SIRT). Visualization was performed using Avizo 7.0 (Visualization Sciences Group).

During the acquisition of tilt series, there were occasional appearances of strong amplitude contrast corresponding to the convergent angle of STEM-HAADF detector, and TiN nanocrystallines appear brighter than TiN nanocrystallines at other tilt angles.

Reconstructed volume, Fig. 8.15a–b, also confirms the formation of cubic TiN–Ag nanocomposites with some Ag nanoparticles on the surface. Dispersions of fine Ag nanoparticles were not observed due to the spatial resolution; however, large Ag nanoparticles were easily seen on the surface of TiN–Ag nanocomposite, as fake colored in red in Fig. 8.15a.

The formation mechanism of the nanocomposite particle is then considered as shown in Fig. 8.16: (i) vaporization of Ti and Ag into the nitrogen atmosphere, (ii) nucleation of TiN owing to the higher reactivity with nitrogen of Ti vapor than that of Ag vapor, (iii) crystallization and growth of TiN nanocrystallines, and (iv) solidification of vaporized Ag on the surface of TiN nanocrystallines as Ag nanoparticles at the region of lower temperature and their Ostwald ripening. Some of the vaporized Ag may remain within the chamber with its condensations.

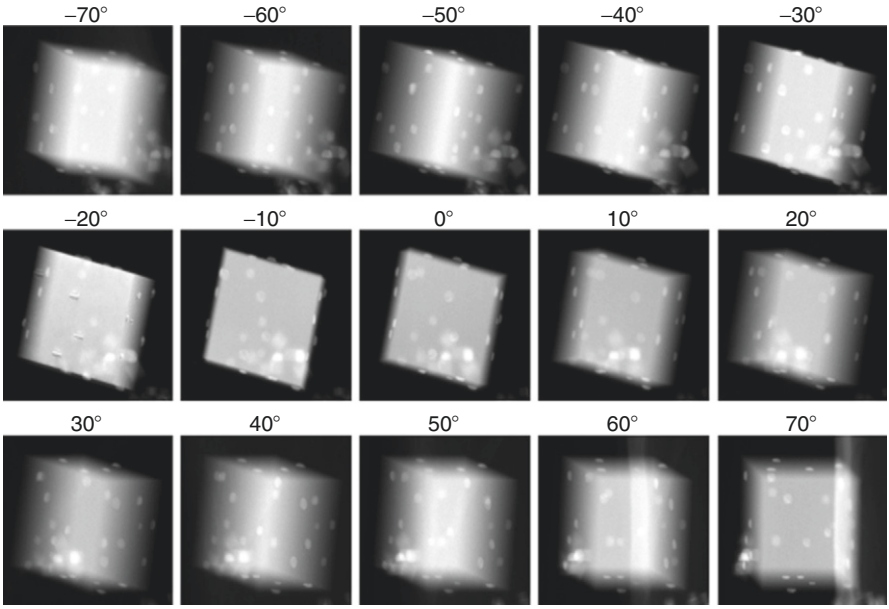


Fig. 8.14 Representative STEM-HAADF images from a tilt series from −70° to 70°

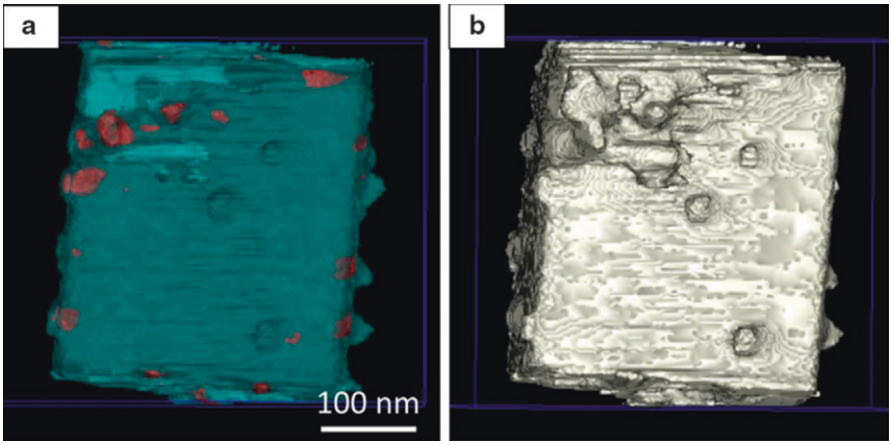


Fig. 8.15 (**a**) A semitransparent reconstructed volume of TiN–Ag nanocomposite with intentional coloration of Ag as *red* and TiN as *dark green*. (**b**) A surface-rendered image of the same nanocomposite from the same field of view

Those relatively large condensed Ag nanoparticles may also be mounted on the surface of TiN.

Ag nanoparticles with irregular morphology seemed to be randomly oriented with respect to the TiN nanocrystallines, so that there would not be a clear

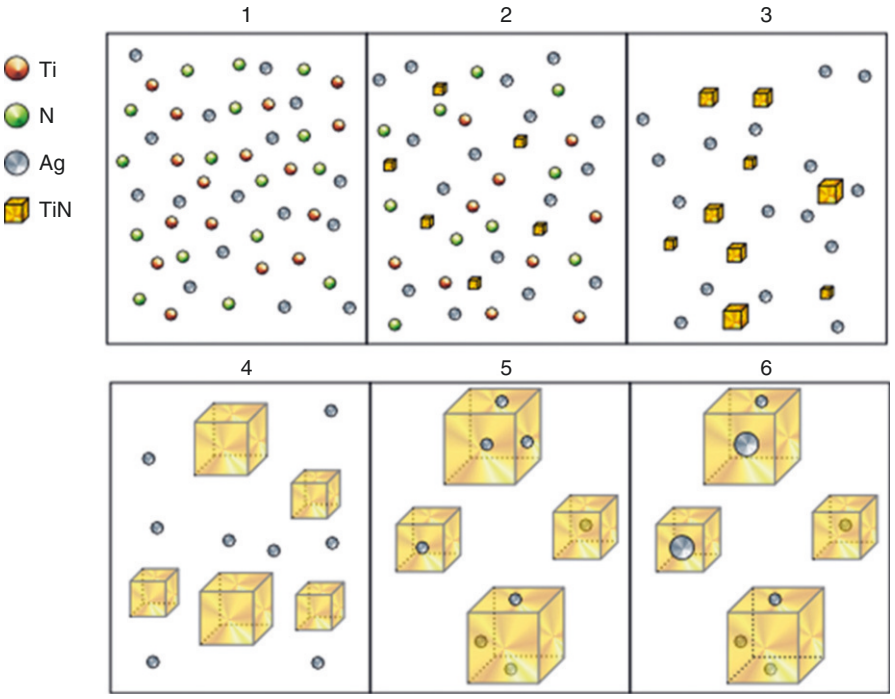


Fig. 8.16 A schematic diagram of formation mechanism of the TiN–Ag nanocomposite

orientation relationship between the TiN nanocrystallines and Ag nanoparticles. This phenomenon strongly suggests that Ag nanoparticles are not chemically bonded on the surface of TiN nanocrystallines, such as metallic Ag–Ti or local nitridation of Ag. It is still necessary to confirm if the surface of TiN nanocrystallines terminates with Ti or N atom, so that if there is either Ti–Ag metal–metal bonding, N–Ag bonding, or Ag being simply caught on the rough surface of TiN nanocrystallines.

In summary, TiN–Ag nanocomposites were synthesized by dc arc-plasma method and consist of cubical TiN nanocrystallines with their surface being covered by Ag nanoparticles. Structural and morphological information was achieved by TEM and STEM-CT. Their formation mechanisms were also predicted. The microwave plasma generated from the injection of N_2 gas provides nitrogen-rich radicals and ions to enhance the reaction between Ti and N, but not between Ag and N due to their formation enthalpies.

5.2 TEM for Characterization of Polymer Matrix Nanocomposites

In recent years, PMNC materials have received a large attention upon the significant development of nanoscience and nanotechnology for producing advanced

materials, due to their fascinating properties arisen from the introduction of nanostructured inorganic nanomaterials into organic polymers. PMNC materials have generated a unique combination of synergetic physical and chemical properties by maximizing the properties of both organic polymers and inorganic nanomaterials, not accessible with bulk composites.

PMNC materials containing small amounts of various inorganic nanomaterials with the size typically in the range of 1–10 nm offer a number of desirable characteristics in a number of applications, such as magnetics, electronics, and optics. It is noteworthy that optimal combinations of organic polymer matrix and inorganic nanomaterials (nanofiller) would lead further to PMNC with novel polymer structures and enhanced thermal, mechanical, and electrical properties. The incorporation of inorganic nanoparticles into the flexible lightweight polymer matrix can provide highly performing inexpensive materials for many industrial applications. For example, PMNCs have their potential use in a wide range of optoelectronic devices such as high refractive index materials, waveguide materials, nonlinear optical materials, and photochromic materials due to their transparent and high refractive index. In fact, it has been known that the agglomerated particles would cause significant scattering and deteriorate the transparency of nanocomposites, so that PMNCs become opaque [153]. It is therefore that the homogeneous dispersion of incorporated inorganic nanoparticles within the matrix has long been desired. Furthermore, extremely low solid content of inorganic particle can also be considered as a limitation to the application of optical devices using the PMNC.

According to Caseri [154], a polymer–Au nanocomposite was probably the first reported PMNC in the literature by Lüdersdorff [155]. An Au salt was reduced in the presence of gum arabic, and a purple solid nanocomposite was formed by co-precipitation. After Au was first used as inorganic nanofiller in PMNC for optical applications [156], other metals such as Ag [157], Pt [158] were used for similar optical applications [154].

5.2.1 Application

Popular applications of PMNCs include optical, magnetic, mechanical, catalytic, electrochemical, electrical, thermal, and biomedical applications. Among these applications, optical and magnetic applications are two of the most important application aspects. For optical applications, inorganic nanoparticles of metals such as Au [156] or Ag [157, 159, 160] and semiconductors such as TiO_2 [161], ZnO [162], CdTe [163], or PbS [164] have been added as "optically effective additives," while transparent polymers are used as polymer matrix, and flexible films with transparency and high refractive indices can be obtained. For magnetic applications, metals and metal alloys such as Fe [165] or CoPt [166], oxides such as Fe oxide [167], and ferrite [168] are always used as inorganic nanofillers. In addition to these two main use of PMNC, mechanical application is also important application area of PMNCs where industrial plastics have always been selected as the polymer matrix and clay minerals are the nanofillers [169]. Catalytic and electrochemical applications, such as sensors, are other applications of PMNCs

where inclusion of metallic Au [170], Pd [171], Cu [172], and Pt [173] and that of oxides SiO_2 [174], TiO_2 [175] and ZrO_2 [176] is the choice as inorganic nanofillers. While Au and Fe-oxide nanoparticles were frequently used in biomedical applications [177, 178], their polymeric nanocomposites have also recently been used as an intelligent system [206] and bioimaging agents [179].

5.2.2 Synthesis

Because of the huge difference between the polymer and inorganic nanomaterials in their properties, nanoparticles typically aggregate and cancel out their benefits associated with the size [180]. In addition, it is usually necessary to add inorganic nanomaterials at high concentrations to achieve desired physical and chemical properties. It is therefore that the particles should be isolated and well dispersed in the matrix.

So far, there have been several attempts for the synthesis of PMNCs and they can be classified into two major categories: as physical and chemical methods. Physical methods include solvent processing, melt processing, and polymer melt intercalation, whereas chemical methods are in situ processes [181]. The most commonly used preparation technologies for the fabrication of nanocomposite can be technically divided into three methods: (i) a melt mixing [182], (ii) a solution blending [183], and (iii) in situ polymerization [184].

Physical methods for PMNCs are based on liquid particle dispersions, but differ in the type of the continuous phase. In melt processing, particles are dispersed into a polymer melt and then PMNCs are obtained by extrusion. Direct melt mixing of particles with polymers often leads to the gradients of the incorporated fillers in the matrix and to the agglomeration of the nanoparticles.

Solution blending is a simple way to fabricate polymer–inorganic nanocomposites. A polymer is first dissolved in a solvent to form a solution, and then inorganic nanoparticles are added into the solution and dispersed by stirring. Although the solution blending method is easy to operate and suitable for all kinds of inorganic materials, the concentrations of the polymer and inorganic components are easy to control [185], and the inorganic ingredients tend to aggregate in the nanocomposites [186].

In sol–gel method, organic monomers, oligomers, or polymers and inorganic nanoparticle precursors are mixed together in the solution. The inorganic precursors then hydrolyze and condense into well-dispersed nanoparticles in the polymer matrix. The advantage of this method is that the reaction conditions are moderate – usually room temperature and ambient pressure – and the concentrations of organic and inorganic components are easy to control in the solution. In addition, the organic and inorganic ingredients are dispersed at the molecular or nanometer level and thus become homogeneous [187, 188].

Chemical methods based on the in situ sol–gel polymerization method allow single-step synthesis of PMNCs in the presence of polymer or monomer [189]. This method is capable of manipulating the organic/inorganic interfacial interactions at various molecular and nanometer length scales, resulting in homogeneous PMNC structures [190]. The procedure of in situ polymerization involves dispersing the

Table 8.3 Description of samples

Sample	Average particle diameter	ZrO_2 content	Surface modification
#1	3 nm	10 wt%	Silane-containing methacrylate group
#2	3 nm	30 wt%	Silane-containing methacrylate group
#3	5 nm	30 wt%	Silane-containing methacrylate group

inorganic nanoparticles directly in the monomer solution prior to a polymerization process. Inorganic particles tend to phase separate and sediment quickly from the organic polymer. In the in situ polymerization method, inorganic nanoparticles with functional groups can be connected with polymer chains by covalent bonds. This is usually achieved by reducing a metal salt already present in the matrix or by evaporating the metal at the heated surface of the matrix.

5.2.3 ZrO_2 Dispersed PMNC

Transparent thin films with high refractive index are very attractive due to their potential applications in photonic crystal films, optical waveguide, antireflection films, and others. As the nanofiller of PMNC, ZrO_2 nanoparticles have received a large attention to fabricate nanocomposite coatings since ZrO_2 has advantages of chemical inertness, excellent thermal stability, high refractive index 2.1–2.3 [191–193], high hardness [194], and improved scratch resistance [195]. In addition to these physical and chemical properties, colloidal ZrO_2 sols prepared from reverse emulsion technique were found to increase the dielectric permittivity of conductive polymer [196].

There have been several attempts to fabricate thin films, including filtered cathodic vacuum arc [197], ion beam-induced chemical vapor deposition [198], sputtering [199], blending [193], and sol–gel process using ZrO_2 alkoxide [191, 192, 200, 201]. Although annealing at high temperature is usually employed to dense and to crystallize the ZrO_2 nanoparticles during the process, which limits their application on plastic substrate, sol–gel process is probably a best choice among them because it does not require high vacuum and/or expensive equipment, and it is easy to scale up for industrial applications. Obtained PMNC film can be applied large scale on various substrates. The weakness of blending method lies in its difficulty to achieve homogeneous dispersion of ZrO_2 nanoparticles in the PMNC film due to the phase separation or agglomeration of ZrO_2 nanoparticles which degrades the transparency of the PMNC film.

As PMNC, three different ZrO_2 nanoparticle-dispersed epoxies were fabricated by in situ polymerization method for comparison, as listed in Table 8.3. The surface of ZrO_2 nanoparticles was intentionally modified by organoalkoxysilane to increase the chemical compatibility between ZrO_2 nanoparticle surface and epoxy matrix, aimed for homogeneously distributed ZrO_2 nanoparticles in the epoxy matrix without agglomeration (Ishikawa Y, private communication, 2012).

It is obvious that the optical properties of PMNCs are strongly influenced by the dispersion characteristics, the volume ratio, and the interparticle distances of nanoparticles, and different types of transmittance and transparencies were

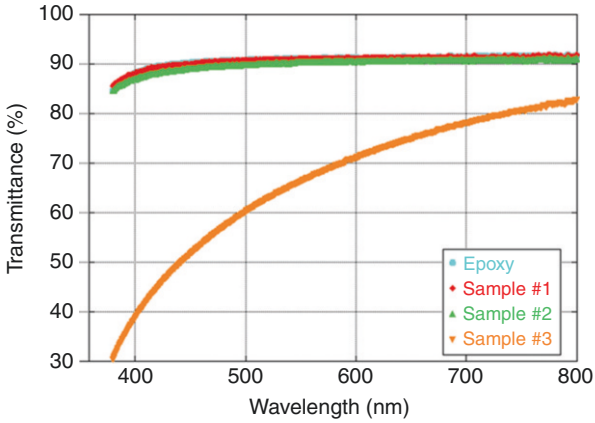


Fig. 8.17 Transmittance spectra of nanocomposite versus wavelength on different samples



Fig. 8.18 (**a–c**) Different transparencies from 25 mm and 1 mm thick samples of samples #1–#3, respectively. Slight opaqueness can be recognized from sample #3

recognized from these samples, as shown in Figs. 8.17 and 8.18. Pure epoxy has a transmittance of ~90 %. The loss of 10 % is possibly caused by the reflection on surfaces of bulk PMNC with 1 mm thickness. Since the average diameter of incorporated ZrO_2 nanoparticles is 3.0 nm and rarely agglomerated in the composite, the transmittance of the final PMNC is found very high for the case of samples #1 and #2. Larger ZrO_2 nanoparticles with average diameter 5.0 nm would give rise to a significant reduction of the transmittance as seen in the case of sample #3.

Pillar-shaped TEM specimens were fabricated by FIB method and then characterized by the combination of TEM, STEM, and 3D-ET. After the acquisition of tilt series from −70° to +70° with 2° steps, they were aligned spatially and rotationally, and then the volume of interest was reconstructed, as schematically drawn in Fig. 8.19.

In the STEM-HAADF images of pillar-shaped specimens shown in Fig. 8.20a–c, the ZrO_2 nanoparticles appeared as white inclusions slightly larger than the primary nanoparticle size, 3.0 nm, for samples #1 and #2, and 5.0 nm for sample #3. Low degrees of agglomeration were detected in the case of samples #1 and #2, and a moderate degree of agglomeration was detected in the case of sample #3.

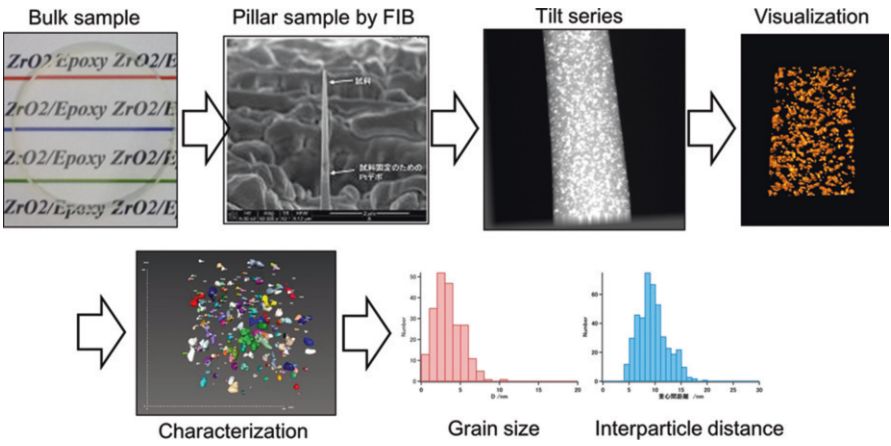


Fig. 8.19 A schematic diagram of the way 3D information is achieved

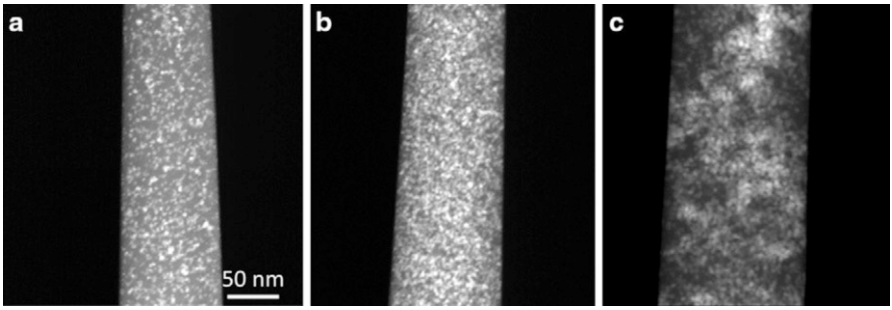


Fig. 8.20 (**a**–**c**) STEM-HAADF images of sample #1, sample #2, and sample #3, respectively. Scale bars are indicating 50 nm

The degree of homogeneity in sample #3 was apparently lower than that of samples #1 and #2, which probably caused the lower transmittance and opaqueness of bulk, as shown in Fig. 8.18c.

Various distributions and dispersions individual ZrO_2 nanoparticle within the matrix can easily be identified from the segmented and fake-colored reconstructed 3D volumes, shown in Fig. 8.21a–c, which show intentionally colored ZrO_2 nanoparticles for quantification measurements, such as volumes and interparticle distances in particular. Although Fig. 8.21c shows good distribution and poor dispersion of ZrO_2 nanoparticles in which localized ZrO_2 nanoparticles were seen, Fig. 8.21a, b show good dispersion and good distribution of ZrO_2 nanoparticles.

The presences of aggregated particles were occasionally seen in Fig. 8.21; in particular, some of them were found larger than 20 nm and more in the case of semitransparent sample #3. As agglomerated particles larger than 30 nm would

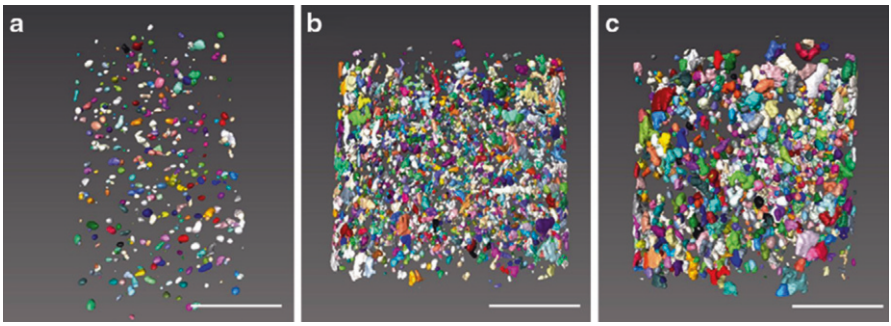


Fig. 8.21 3D reconstructed volume of ZrO_2 nanoparticle dispersed hybridized samples, (**a**) sample #1, (**b**) sample #2, and (**c**) sample #3. The *white* scale bars in all figures are representing 50 nm

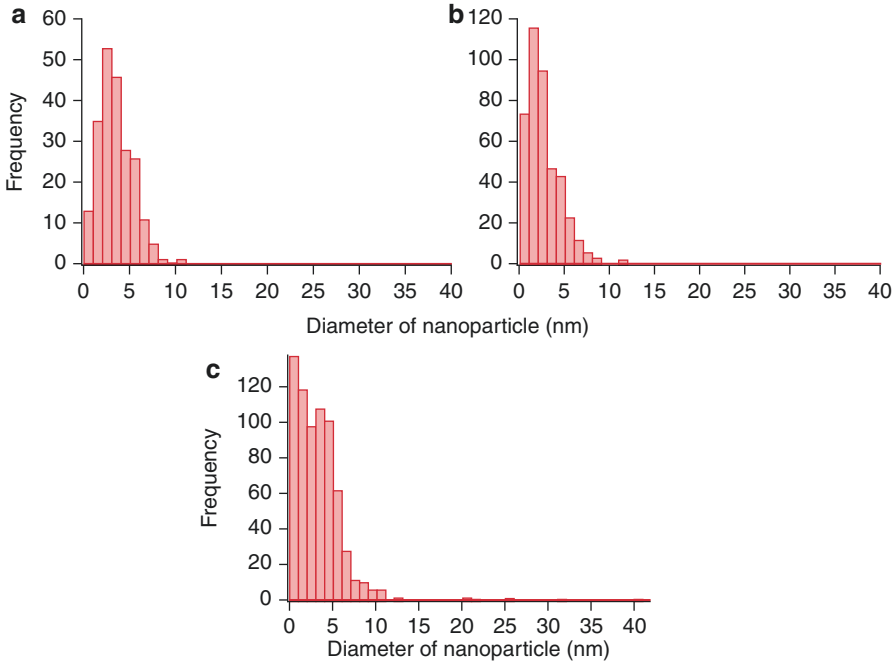


Fig. 8.22 Histograms of grain diameters measured from the volume of aggregated ZrO_2 nanoparticle of sample #1 (**a**), sample #2 (**b**), and sample #3 (**c**). Frequency is the number of incidence

cause significant scattering [153], these large agglomerates found in sample #3 would be the cause of opaqueness.

After this identification of individual ZrO_2 nanoparticles, quantification was carried out further using Avizo 7.0, for measuring the particle diameter from the volume of these dispersed ZrO_2 nanoparticles, as shown in Fig. 8.22.

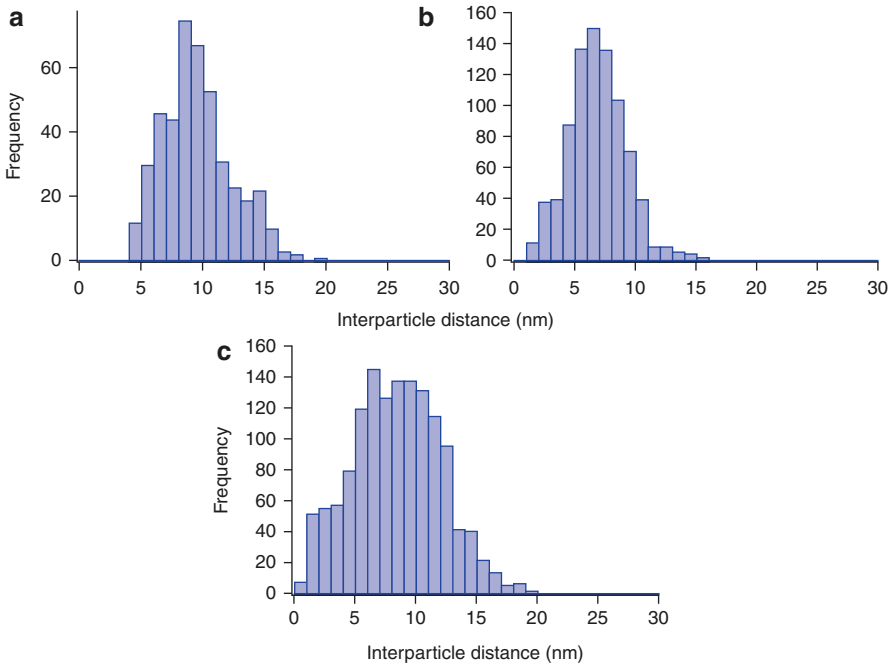


Fig. 8.23 Histograms of interparticle distances measured of the individual ZrO_2 nanoparticles of sample #1 (**a**), sample #2 (**b**), and sample #3 (**c**). Frequency is the number of incidence

In addition to these grain-size distributions, interparticle distances, distances between the center of gravity to the nearest particle, were also measured, where a large spread of the distances was found from #3 sample (c) with comparison to samples #1 (a) and #2 (b), as shown in Fig. 8.23. In addition, both Fig. 8.23a, b show good Gaussian distributions where the average closest interparticle distances from the center of gravity are found 8.02 nm and 5.13 nm, respectively. On the other hand, relatively small with broad interparticle distances was found in the case of semitransparent sample #3 shown in Fig. 8.23c.

Light scattering of nanoparticles is believed to be responsible for the reduction of transparency or opaque appearance of PMNCs, caused by agglomerated particles and refractive index mismatch between the nanoparticle and the matrix. The transparency, T, of the PMNCs is the subtraction of the light scattering, S, caused by randomly dispersed spherical particles with radius, r_P, and volume fraction, Φ_P, described by the Rayleigh scattering formula [202]:

$$T = 1 - S = \frac{I_T}{I_0} = \exp\left\{ -\frac{32\pi^4 \Phi_P x r_P^3 n_m^4}{\lambda^4} \left[\frac{\left(\frac{n_P}{n_m}\right)^2 - 1}{\left(\frac{n_P}{n_m}\right)^2 + 2} \right]^2 \right\} \tag{8.13}$$

where I_T and I_0 are the intensities of the transmitted and incident light respectively, λ is the wavelength of light, x is the optical path length, and n_P and n_m are the refractive indexes of the particles and the matrix, respectively. As can be deduced from Eq. 8.13, there are several ways to minimize the scattering losses and improve the transparency of nanocomposites at a given wavelength. One is to minimize the differences in refractive indexes between the particle and the matrix, namely, $n_p \approx n_m$, another one is to minimize the size or volume fraction of nanoparticles, and the other one is to reduce the thickness of PMNCs. It has been shown that the portion of light scattering can be reduced when the inorganic domain size is less than one-tenth of the visible light wavelength (380–760 nm) [202]. The mismatch of refractive index between nanoparticle and matrix should be compensated by small particle size in order to suppress the losses by light scattering for the design of PMNCs with high refractive index and high particle weight fraction. Ideally, the inorganic particles should have a diameter below 10 nm because the presence of even a small percentage of particles or aggregates larger than 100 nm results in strong light scattering in the visible region for fabricating high refractive index PMNCs [153, 203].

In summary, epoxy-ZrO_2 nanocomposite samples prepared by in situ polymerization method were characterized by STEM and STEM-CT and compared with their optical properties. After these quantifications, the correlation between the transparency and the microstructures of the sample was fully characterized. Although the small thickness of the film would probably result high transmittance in the case of thin PMNC films ($t = 1$ mm), agglomeration of nanoparticles may lead to a severe loss of the transmittance in the case of thick PMNC films ($t > 5$ mm). It is therefore that the small particle diameter and narrow particle size distribution without agglomeration inside the polymer matrix are essential for the development of highly transparent bulk PMNC nanocomposites. Furthermore, a stable homogeneous dispersion of the nanoparticles within the PMNC films is obviously the key to the highly transparent PMNC films so that the interparticle distances are also significant.

Furthermore, it was difficult to differentiate individual ZrO_2 nanoparticles in PMNCs from 2D STEM images due to their nature of projection and almost impossible to determine the interparticle distances due to the lack of information of depth, the 3rd dimention. After the reconstruction of 3D volumes from tilt series, it was capable of determining the true interparticle distances successfully.

6 Conclusions and Future Prospective

This chapter was concentrated on the introduction of 2D and 3D characterization by TEM of two types of nanocomposite materials, CMNC and PMNC, in particular. For the case of CMNC, structural and morphological characterizations of matrix and nanostructure phases were carried out to examine the growth mechanisms. For the case of PMNC, dispersion and distribution of nanoparticles as well as interparticle distances between them were investigated and correlated with optical properties.

Nanoscale characterization by TEM/STEM plays a vital role in both the design and property of nanocomposites used in nanoscience and nanotechnology. So far, large numbers of publications have been made concerning nanocomposites based on 2D TEM images, which would not reflect the true 3D nature of nanocomposites, and authors had to correlate those results with 3D physical properties of them. It has to be undoubtedly emphasized that both 2D information and 3D information are vital to characterize 3D nanocomposites.

References

1. Niihara K (1991) New design concept of structural ceramics. Ceramic nanocomposites. J Ceram Soc Jpn 99:974–982
2. Pennycook SJ (1989) Z-contrast stem for materials science. Ultramicroscopy 30:58–69
3. De Broglie L (1923) Radiations. Ondes et quanta. C R Acad Sci 177:507–510
4. Williams DB, Carter CB (1996) Transmission electron microscopy. Plenum, New York
5. Rutherford E (1911) The scattering of α and β particles by matter and the structure of the atom. Philos Mag 21:669–688
6. Crewe AV, Wall J, Welter LM (1968) A high-resolution scanning transmission electron microscope. J Appl Phys 39:5861–5868
7. Howie A (1979) Image contrast and localized signal selection techniques. J Microsc 117:11–23
8. Pennycook SJ, Jesson DE (1992) Atomic resolution Z-contrast imaging of interfaces. Acta Metallurg Mater 40:S149–S159
9. Pennycook SJ, Nellist PD (1999) Impact of electron and scanning probe microscopy on materials research. Kluwer, The Netherlands, pp 161–207
10. Joy DC, Romig Jr AD, Goldstein JI (1989) Principles of analytical electron microscopy. Plenum, New York
11. Cliff G, Lorimer GW (1975) The quantitative analysis of thin specimens. J Microsc 103:203–207
12. Egerton RF (1996) Electron energy-loss spectroscopy in the electron microscope. Plenum, New York
13. Frank J (2006) Three-dimensional electron microscopy of macromolecular assemblies. Academic, San Diego
14. Modéer B (1974) Dislocation link length distributions studied by stereo electron microscopy. Scripta Metallurg 8:1145–1152
15. Hare TM, Russ JC, Lane JE (1988) Volume determination of TEM specimens containing particles of precipitates. J Electron Microsc Tech 10:1–6
16. Frank J (1996) Electron tomography: three-dimensional imaging with the transmission electron microscope. Academic, San Diego
17. Radon J (1917) Über die bestimmung von funktionen durch ihre integralwerte längs gewisser mannigfaltigkeiten. Akad Wiss Leipzig Math-Phys Klasse 69:262–277
18. De Rosier DJ, Klug A (1968) Reconstruction of three dimensional structures from electron micrographs. Nature 217:130–134
19. Hoppe W, Langer R, Knesch G, Poppe C (1968) Protein-kristallstrukturanalyse mit elektronenstrahlen. Naturwissenschaften 55:333–336
20. Hart RG (1968) Electron microscopy of unstained biological material: the polytropic montage. Science 159:1464–1467
21. Midgley PA, Dunin-Borkowski RE (2009) Electron tomography and holography in materials science. Nat Mater 8:271–280
22. Midgley PA, Ward EPW, Hungría AB, Thomas JM (2007) Nanotomography in the chemical, biological and materials sciences. Chem Soc Rev 36:1477–1494

23. Weyland M, Midgley PA (2004) Electron tomography. Materials Today 7:32–40
24. Midgley PA, Weyland M (2003) 3D Electron microscopy in the physical sciences: the development of Z-contrast and EFTEM tomography. Ultramicroscopy 96:413–431
25. Kaneko K, Inoke K, Freitag B, Hungria AB, Midgley PA, Hansen TW, Zhang J, Ohara S, Adschiri T (2007) Structural and morphological characterization of cerium oxide nanocrystals prepared by hydrothermal synthesis. Nano Lett 7:421–425
26. Kaneko K, Inoke K, Sato K, Kitawaki K, Higashida H, Arslan I, Midgley PA (2008) TEM characterization of Ge precipitates in an Al–1.6 at% Ge alloy. Ultramicroscopy 108:210–220
27. Kaneko K, Furuya K, Yamada K, Sadayama S, Barnard JS, Midgley PA, Kato T, Hirayama T, Kiuchi M, Matsushita T, Ibi A, Yamada Y, Izumi T, Shiohara Y (2010) Three-dimensional analysis of $BaZrO_3$ pinning centers gives isotropic superconductivity in $GdBa_2Cu_3O_{7-\delta}$. J Appl Phys 108:063901
28. Kaneko K, Kitawaki K, Sadayama S, Razavi H, Hernandez-Garrido JC, Midgley PA, Okuyama H, Uda M, Sakka Y (2010) Fabrication and characterization of TiN nanocomposite powders fabricated by DC arc-plasma method. J Alloys Compd 492:685–690
29. Tong J, Arslan I, Midgley PA (2006) A novel dual-axis iterative algorithm for electron tomography. J Struct Biol 153:55–63
30. Baumeister W, Grimm R, Walz J (1999) Electron tomography of molecules and cells. Trends Cell Biol 9:81–85
31. Crowther RA, de Rosier DJ, Klug A (1970) The reconstruction of a three-dimensional structure from projections and its application to electron microscopy. Proc R Soc Lond Ser A 317:319–340
32. Kawase N, Kato M, Nishioka H, Jinnai H (2007) Transmission electron microtomography without the "missing wedge" for quantitative structural analysis. Ultramicroscopy 107:8–15
33. Kaneko T, Nishioka H, Nishi T, Jinnai H (2005) Reduction of anisotropic image resolution in transmission electron microtomography by use of quadrangular prism-shaped section. J Electron Microsc 54:437–444
34. Radermacher M (1988) Three-dimensional reconstruction of single particles from random and nonrandom tilt series. J Electron Microsc Tech 9:359–394
35. Jin-Phillipp NY, Koch CT, van Aken PA (2011) Toward quantitative core-loss EFTEM tomography. Ultramicroscopy 111:1255–1261
36. Radermacher M (2006) Weighted back-projection methods. In: Frank J (ed) Electron tomography: methods for three-dimensional visualization of structures in the cell, 2nd edn. Springer, New York, pp 245–273
37. Marabini R, Rietzel E, Schroeder R, Herman GT, Carazo JM (1997) Three-dimensional reconstruction from reduced sets of very noisy images acquired following a single-axis tilt schema: application of a new three-dimensional reconstruction algorithm and objective comparison with weighted backprojection. J Struct Biol 120:363–371
38. Sorzano COS, Marabini R, Boisset N, Rietzel E, Schröder R, Herman GT, Carazo JM (2001) The effect of overabundant projection directions on 3D reconstruction algorithms. J Struct Biol 133:108–118
39. Batenburg KJ, Bals S, Sijbers J, Kübel C, Midgley PA, Hernandez JC, Kaiser U, Encina ER, Coronado EA, Van Tendeloo G (2009) 3D Imaging of nanomaterials by discrete tomography. Ultramicroscopy 109:730–740
40. Wong-Ng W, McMurdie HF, Partezkin B, Hubbard CR, Dragoo AL, Stewart JM (1987) Standard X-ray diffraction powder patterns of fifteen ceramic phases. Powder Diffr 2:200
41. Kobayashi A (2000) Formation of TiN coatings by gas tunnel type plasma reactive spraying. Surf Coat Technol 132:152–157
42. Bacci T, Bertamini L, Ferrari F, Galliano FP, Galvanetto E (2000) Reactive plasma spraying of titanium in nitrogen containing plasma gas. Mater Sci Eng A 283:189–195
43. Shieu FS, Cheng LH, Sung YC, Huang JH, Yu GP (1998) Microstructure and coating properties of ion-plated TiN on type 304 stainless steel. Thin Solid Films 334:125–132

44. Didziulis SV, Lince JR, Stewart TB, Eklund EA (1994) Photoelectron spectroscopic studies of the electronic structure and bonding in TiC and TiN. Inorg Chem 33:1979–1991
45. Dunand A, Flack H, Yvon K (1985) Bonding study of TiC and TiN. I. High-precision x-ray-diffraction determination of the valence-electron density distribution, Debye-Waller temperature factors, and atomic static displacements in $TiC_{0.94}$ and $TiN_{0.99}$. Phys Rev B 31:2299–2315
46. Blaha P, Redinger J, Schwarz K (1985) Bonding study of TiC and TiN. II. Theory. Phys Rev B 31:2316–2325
47. Tu JP, Zhu LP, Zhao HX (1999) Slurry erosion characteristics of TiN coatings on α-Ti and plasma-nitrided Ti alloy substrates. Surf Coat Technol 122:176–182
48. Bull SJ, Sharkeev YP, Fortuna SV, Shulepov LA, Perry AJ (2001) Mechanism of improvement of TiN-coated tool life by nitrogen implantation. J Mater Res 16:3293–3303
49. Monaghan DP, Laing KC, Logan PA, Teer DG (1993) Advanced hard and soft coatings for high performance machining and forming. Finishing 17:1–6
50. Wei C, Lin JF, Jiang T-H, Ai C-F (2001) Tribological characteristics of titanium nitride and titanium carbonitride multilayer films part II. The effect of coating sequence on tribological properties. Thin Solid Films 381:104–118
51. Marin-Ayral RM, Pascal C, Martinez F, Tedenac JC (2000) Simultaneous synthesis and densification of titanium nitride by high pressure combustion synthesis. J Eur Ceram Soc 2:2679–2684
52. Martan J, Beneš P (2012) Thermal properties of cutting tool coatings at high temperatures. Thermoch Acta 539:51–55
53. Huang Y, Gu Y, Zheng M, Xu Z, Zeng W, Liu Y (2007) Synthesis of nanocrystalline titanium nitride by reacting titanium dioxide with sodium amide. Mater Lett 61: 1056–1059
54. Andersson KE, Wahlström MK, Roos A (1992) High stability titanium nitride based solar control films. Thin Solid Films 214:213–218
55. Borah SM, Bailung H, Chutia J (2010) Decorative titanium nitride colored coatings on bell-metal by reactive cylindrical magnetron sputtering, progress in color. Colorants Coat 3:74–80
56. Mumtaz A, Class WH (1982) Color of titanium nitride prepared by reactive dc magnetron sputtering. J Vac Sci Technol 20:345–348
57. Sundgren JE (1985) Structure and properties of TiN coatings. Thin Solid Films 128:21–44
58. Heide N, Schultze J (1993) Corrosion stability of TiN prepared by ion implantation and PVD. Nucl Inst Methods Phys Res B 80(81):467–471
59. Tu JP (2000) The effect of TiN coating on erosion-corrosion resistance of α-Ti alloy in saline slurry. Corros Sci 42:147–163
60. Patsalas P, Charitidis C, Logothetidis S (2000) The effect of substrate temperature and biasing on the mechanical properties and structure of sputtered titanium nitride thin films. Surf Coat Technol 125:335–340
61. Cheng ZY, Zhu J, Liu XH, Wang X, Yang GQ (1995) Thermal stability of Cu/TiN and Cu/Ti/TiN metallizations on silicon. J Mater Res 10:995–999
62. Ensinger W, Rauschenbach B (1993) Microstructural investigations on titanium nitride films formed by medium energy ion beam assisted deposition. Nucl Instr Meth Phys Res B 80(81):1409–1414
63. Igasaki Y, Mitsuhashi H (1980) Effects of substrate bias on the structural and electrical properties of TiN films prepared by reactive R. F. Sputtering. Thin Solid Films 70:17–25
64. Sinke W, Frijlink G, Saris F (1985) Oxygen in titanium nitride diffusion barriers. Appl Phys Lett 47:471–473
65. Schiller S, Beister G, Sieber W (1984) Reactive high rate D.C. Sputtering: deposition rate, stoichiometry and features of TiO_x and TiN_x films with respect to the target mode. Thin Solid Films 111:259–268

66. Poitevin JM, Lemperiere G, Tardy J (1982) Influence of substrate bias on the composition, structure and electrical properties of reactively d.c.-sputtered TiN films. Thin Solid Films 97:69–77
67. Ahn KY, Wittmer M, Ting CY (1983) Investigation of TiN films reactively sputtered using a sputter gun. Thin Solid Films 107:45–54
68. Kanamori S (1986) Investigation of reactively sputtered TiN films for diffusion barriers. Thin Solid Films 136:215–227
69. Johansen O, Dontje J, Zenner R (1987) Reactive arc vapor ion deposition of TiN, ZrN and HfN. Thin Solid Films 153:75–82
70. Chowdhury R, Vispute RD, Jagannadham K, Narayan J (1996) Characteristics of titanium nitride films grown by pulsed laser deposition. J Mater Res 11:1458–1469
71. Wakabayashi T, Williams J, Hutchings I (1993) The action of gaseous lubricants in the orthogonal machining of an aluminium alloy by titanium nitride coated tools. Surf Coat Technol 57:183–189
72. Jaschek R, Russel C (1991) Titanium nitride and titanium aluminum nitride coatings on silica glass, prepared by pyrolysis of a polymeric precursor film. J Non-Cryst Solids 135:236–242
73. Lima LPB, Diniz JA, Doi I, Godoy Fo J (2012) Alternative extraction method of titanium nitride work function. Microelectron Eng 92:86–90
74. Fillot F, Morel T, Minoret S, Matko I, Maîtrejean S, Guillaumot B, Chenevier B, Billon T (2005) Investigations of titanium nitride as metal gate material, elaborated by metal organic atomic layer deposition using TDMAT and NH_3. Microelectron Eng 82:248–253
75. Yokota K, Nakamura K, Kasuya T, Ohnishi M (2003) Phase composition and crystalline structure of titanium nitride deposited on silicon by an ion-beam assisted deposition technique. J Nucl Instrum Methods Phys Res B 206:386–389
76. Lee YJ (2005) Low-impurity, highly conformal atomic layer deposition of titanium nitride using NH_3–Ar–H_2 plasma treatment for capacitor electrodes. Mater Lett 59:615–617
77. Kaskel S, Schlichte K, Kratzke T (2004) Catalytic properties of high surface area titanium nitride materials. J Mol Catal A Chem 208:291–298
78. Qiu Y, Gao L (2005) Novel polyaniline/titanium nitride nanocomposite: controllable structures and electrical/electrochemical properties. J Phys Chem B 109:19732–19740
79. Musil J (2000) Hard and superhard nanocomposite coatings. Surf Coat Technol 125:322–330
80. Jin X, Gao L, Li J, Zheng S (2004) Influence of microstructure evolution on the electroconducting behavior of intragranular TiN/ZTM nanocomposites. J Am Ceram Soc 87:162–165
81. Rocha LA, Ariza E, Ferreira J, Vaz F, Ribeiro E, Rebouta L, Alves E, Ramos AR, Goudeau P, Rivière JP (2004) Structural and corrosion behaviour of stoichiometric and substoichiometric TiN thin films. Surf Coat Technol 180-181:158–163
82. Ramanuja N, Levy RA, Dharmadhikari SN, Ramos E, Pearce CW, Menasian SC, Schamberger PC, Collins CC (2002) Synthesis and characterization of low pressure chemically vapor deposited titanium nitride films using $TiCl_4$ and NH_3. Mater Lett 57:261–269
83. Gao L, Gstöttner J, Emling R, Balden M, Linsmeier C, Wiltner A, Hansch W, Schmitt-Landsiedel D (2004) Thermal stability of titanium nitride diffusion barrier films for advanced silver interconnects. Microelectron Eng 76:76–81
84. Chen JS, Lu K-Y (2001) Thermal stability of Cu/TiN and Cu/Ti/TiN metallizations on silicon. Thin Solid Films 396:204–208
85. Kwak MY, Shin DH, Kang TW, Kim KN (1999) Characteristics of TiN barrier layer against Cu diffusion. Thin Solid Films 339:290–293
86. Moriyama M, Kawazoe T, Tanaka M, Murakami M (2002) Correlation between microstructure and barrier properties of TiN thin films used Cu interconnects. Thin Solid Films 416:136–144
87. Wang SQ, Raaijmakers IJ, Burrow BJ, Suthar S, Redkar S, Kim KB (1990) Reactively sputtered TiN as a diffusion barrier between Cu and Si. J Appl Phys 68:5176–5187

88. Sherman A (1990) Growth and properties of LPCVD titanium nitride as a diffusion barrier for silicon device technology. J Electrochem Soc 137:1892–1897
89. Mårtensson P, Juppo M, Ritala M, Leskelä M, Carlsson JO (1999) Use of atomic layer epitaxy for fabrication of Si/TiN/Cu structures. J Vac Sci Technol B 17:2122–2128
90. Smith S, Li W-M, Elers K-E, Pfeifer K (2002) Physical and electrical characterization of ALCVD™ TiN and WN_xC_y used as a copper diffusion barrier in dual damascene backend structures (08.2). Microelectron Eng 64:247–253
91. Kim D-J, Jung Y-B, Lee M-B, Lee Y-H, Lee J-H, Lee J-H (2000) Applicability of ALE TiN films as Cu/Si diffusion barriers. Thin Solid Films 372:276–283
92. Savvides N, Window B (1988) Electrical transport, optical properties, and structure of TiN films synthesized by low-energy ion assisted deposition. J Appl Phys 64:225–234
93. Takahashi T, Itoh H (1977) Chemical vapor deposition of titanium nitride on iron in an ultrasonic field. J Electrochem Soc 124:797–802
94. Arai T, Fujita H, Oguri K (1988) Plasma-assisted chemical vapour deposition of TiN and TiC on steel: properties of coatings. Thin Solid Films 165:139–148
95. Tian XB, Zeng ZM, Tang BY, Fu KY, Kwok DTK, Chu PK (2000) Properties of titanium nitride fabricated on stainless steel by plasma-based ion implantation/deposition. Mater Sci Eng A282:164–169
96. Omrani M, Habibi M, Amrollahi R (2012) Coating of titanium nitride on stainless steel targets by a 4 kJ plasma focus device. J Fusion Energ 31:401–404
97. Kola PV, Daniels S, Cameron DC, Hashmi MSJ (1996) Magnetron sputtering of TiN protective coatings for medical applications. J Mater Process Technol 56:422–430
98. Mezger PR, Creugers NHJ (1992) Titanium nitride coatings in clinical dentistry. J Dent 20:342–344
99. Mändl S, Rauschenbach B (2002) Improving the biocompatibility of medical implants with plasma immersion ion implantation. Surf Coat Technol 156:276–283
100. Dion I, Roques X, More N, Labrousse L, Caix J, Lefebvre F, Rouais F, Gautreau J, Baquey C (1993) Ex vivo leucocyte adhesion and protein adsorption on TiN. Biomaterials 14:712–719
101. Cyster LA, Grant DM, Parker KG, Parker TL (2002) The effect of surface chemistry and structure of titanium nitride (TiN) films on primary Hippocampal cells. Biomol Eng 19:171–175
102. Cyster LA, Parker KG, Parker TL, Grant DM (2003) The effect of surface chemistry and nanotopography of titanium nitride (TiN) films on 3 T3-L1 fibroblasts. J Biomed Mater Res A 67A:138–147
103. Cyster LA, Parker KG, Parker TL, Grant DM (2004) The effect of surface chemistry and nanotopography of titanium nitride (TiN) films on primary hippocampal neurons. Biomaterial 25:97–107
104. Kirchner CN, Hallmeier KH, Szargan R, Raschke T, Radehaus C, Wittstock G (2007) Evaluation of thin film titanium nitride electrodes for electroanalytical applications. Electroanalysis 19:1023–1031
105. Wang Y, Yuan H, Lu X, Zhou Z, Xiao D (2006) All solid-state pH electrode based on titanium nitride sensitive film. Electroanalysis 18:1493–1498
106. Musher JN, Gordon RG (1996) Atmospheric pressure chemical vapor deposition of titanium nitride from tetrakis (diethylamido) titanium and ammonia. J Electrochem Soc 143:736–744
107. Muratore C, Hu JJ, Voevodin AA (2007) Adaptive nanocomposite coatings with a titanium nitride diffusion barrier mask for high-temperature tribological applications. Thin Solid Films 515:3638–3643
108. Subramanian C, Cavallaro G, Winkelman G (2000) Wear maps for titanium nitride coatings deposited on copper and brass with electroless nickel interlayers. Wear 241:228–233
109. Gong C, Zhang J, Yan C, Cheng X, Zhang J, Yu L, Jin Z, Zhang Z (2012) Synthesis and microwave electromagnetic properties of nanosized titanium nitride. J Mater Chem 22:3370–3376

110. Park D-G, Lim K-Y, Cho H-J, Cha T-H, Yeo I-S, Roh J-S, Park JW (2002) Impact of atomic-layer-deposited TiN on the gate oxide quality of W/TiN/SiO_2/Si metal-oxide-semiconductor structures. Appl Phys Lett 80:2514–2516
111. Kaskel S, Schlichte K, Chaplais G, Khanna M (2003) Synthesis and characterisation of titanium nitride based nanoparticles. J Mater Chem 13:1496–1499
112. Von Seefeld H, Cheung NW, Maenpaa M, Nicolet M-A (1980) Investigation of titanium – nitride layers for solar-cell contacts. IEEE Trans Electron Devices 27:873–876
113. Cheung NW, von Seefeld H, Nicolet M-A, Ho F, Iles P (1981) Thermal stability of titanium nitride for shallow junction solar cell contacts. J Appl Phys 52:4297–4299
114. Ding ZH, Yao B, Qiu LX, Bai SZ, Guo XY, Xue YF, Wang WR, Zhou XD, Su WH (2005) Formation of titanium nitride by mechanical milling and isothermal annealing of titanium and boron nitride. J Alloys Compd 391:77–81
115. Russias J, Cardinal S, Fontaine J, Fantozzi G, Esnouf C, Bienvenu K (2005) Bulk titanium nitride material obtained from SHS starting powder: densification, mechanical characterization and tribological approach. Int J Refract Metals Hard Mater 23:344–349
116. Kim JW, Shim J-H, Kim SC, Remhof A, Borgschulte A, Friedrichs O, Gremaud R, Pendolino F, Züttel A, Cho YW, Oh KH (2009) Catalytic effect of titanium nitride nanopowder on hydrogen desorption properties of $NaAlH_4$ and its stability in $NaAlH_4$. J Power Sources 192:582–587
117. Kakati M, Bora B, Sarma S, Saikia BJ, Shripathi T, Deshpande U, Dubey A, Ghosh G, Das AK (2008) Synthesis of titanium oxide and titanium nitride nano-particles with narrow size distribution by supersonic thermal plasma expansion. Vacuum 82:833–841
118. Lee K-O, Cohen JJ, Brezinsky K (2000) Fluidized-bed combustion synthesis of titanium nitride. Proc Combust Inst 28:1373–1379
119. Li W-Y, Riley FL (1991) The production of titanium nitride by the carbothermal nitridation of titanium dioxide powder. J Eur Ceram Soc 8:345–354
120. Duan G, Zhao G, Wu L, Lin X, Han G (2011) Structure, electrical and optical properties of TiN_x films by atmospheric pressure chemical vapor deposition. Appl Surf Sci 257: 2428–2431
121. Vaidhyanathan B, Rao KJ (1997) Synthesis of Ti, Ga, and V nitrides: microwave-assisted carbothermal reduction and nitridation. Chem Mater 9:1196–1200
122. Griffiths LE, Lee MR, Mount AR, Kondoh H, Ohta T, Pulham CR (2001) Low temperature electrochemical synthesis of titanium nitride. Chem Commun 579–580
123. Parkin IP (2002) Solvent free reactions in the solid state: solid state metathesis. Transit Met Chem 27:569–573
124. Gillan EG, Kaner RB (1994) Rapid solid-state synthesis of refractory nitrides. Inorg Chem 33:5693–5700
125. Joshi UA, Chung SH, Lee JS (2005) Low-temperature, solvent-free solid-state synthesis of single-crystalline titanium nitride nanorods with different aspect ratios. J Solid State Chem 178:755–760
126. Chen B, Evans JRG (2004) Preferential intercalation in polymer-clay nanocomposites. J Phys Chem B 108:14986–14990
127. Guo Q, Xie Y, Wang X, Lv S, Hou T, Bai C (2005) Synthesis of uniform titanium nitride nanocrystalline powders via a reduction-hydrogenation-dehydrogenation-nitridation route. J Am Ceram Soc 88:249–251
128. Feng X, Bai Y-J, Lu B, Wang C-G, Qi Y-X, Liu Y-X, Geng G-L, Li L (2004) Low temperature induced synthesis of TiN nanocrystals. Inorg Chem 43:3558–3560
129. Janes RA, Aldissi M, Kaner RB (2003) Controlling surface area of titanium nitride using metathesis reactions. Chem Mater 15:4431–4435
130. Yang X, Li C, Yang L, Yan Y, Qian Y (2003) Reduction-nitridation synthesis of titanium nitride nanocrystals. J Am Ceram Soc 86:206–208
131. Chau JLH, Kao CC (2007) Microwave plasma synthesis of TiN and ZrN nanopowders. Mater Lett 61:1583–1587

132. Yi HC, Moore JJ (1990) Self-propagating high-temperature (combustion) synthesis (SHS) of powder-compacted materials. J Mater Chem 25:1159–1168
133. Van Stappen M, Malliet B, Stals L, De Schepper L, Roos JR, Celis JP (1991) Characterization of TiN coatings deposited on plasma nitrided tool steel surfaces. Mater Sci Eng A 140:554–562
134. Sakka Y, Ohno S (1996) Hydrogen sorption-desorption characteristics of mixed and composite Ni–TiN nanoparticles. Nanostruct Mater 7:341–353
135. Sakka Y, Okuyama H, Uchikoshi T, Ohno S (1997) Morphology and hydrogen desorption characteristic of Ni-TiN nanocomposite particle prepared by RF plasma. Nanostruct Mater 8:465–475
136. Choi DW, Kumta PN (2005) Synthesis of nanostructured TiN using a two-step transition metal halide approach. J Am Ceram Soc 88:2030–2035
137. Benjamin JS (1970) Dispersion strengthened superalloys by mechanical alloying. Metall Trans A, Phys Metall Mater Sci 1:2943–2951
138. El-Eskandarany MS, Sumiyama K, Aoki K, Suzuki K (1992) Morphological and structural evolutions of nonequilibrium titanium-nitride alloy powders produced by reactive ball milling. J Mater Res 7:888–893
139. Chin Z-H, Perng T-P (1997) In situ observation of combustion to form TiN during ball milling Ti in nitrogen. Appl Phys Lett 70:2380–2382
140. El-Eskandarany MS, Omori M, Konno TJ, Sumiyama K, Hirai T, Suzuki K (1998) Syntheses of full-density nanocrystalline titanium nitride compacts by plasma-activated sintering of mechanically reacted powder. Metall Mater Trans A Phys Metall Mater Sci 29:1973–1981
141. Ogino Y, Yamasaki T, Miki M, Atsumi N, Yoshioka K (1993) Synthesis of TiN and (Ti, Al) N powders by mechanical alloying in nitrogen gas. Scripta Metallurgica et Materiala 28:967–971
142. Campbell SJ, Hofmann M, Calka A (2000) The synthesis of TiN by ball-milling – a neutron diffraction study. Physica B 276–278:899–900
143. Chen Y, Li ZL, Williams JS (1995) The evolution of hydriding and nitriding reactions during ball milling of titanium in ammonia. J Mater Sci Lett 14:542–544
144. Wexler D, Calka A, Mosbah Y (2000) Ti–TiN hardmetals prepared by in situ formation of TiN during reactive ball milling of Ti in ammonia. J Alloys Compd 309:201–207
145. Zhang F, Kaczmarek WA, Lu L, Lai MO (2000) Formation of titanium nitrides via wet reaction ball milling. J Alloys Compd 307:249–253
146. Sandhu GS, Meikle SG, Doan TT (1993) Metalorganic chemical vapor deposition of TiN films for advanced metallization. Appl Phys Lett 63:240–242
147. Dixit GA, Wei CC, Liou FT, Zhang H (1993) Reactively sputtered titanium nitride films for submicron contact barrier metallization. Appl Phys Lett 62:357–359
148. Mader W, Fischmeister HF, Bergmann E (1989) Defect structure of ion-plated titanium nitride coatings. Thin Solid Films 182:141–152
149. Archer NJ (1981) The plasma-assisted chemical vapour deposition of TiC, TiN and TiC_xN_{1-x}. Thin Solid Films 80:221–225
150. Roth R, Schubert J, Martin M, Fromm E (1995) Effect of process parameter changes on the composition of magnetron sputtered and evaporated TiN and AlN films measured by UHV in-situ techniques. Thin Solid Films 270:320–324
151. Kobayashi A (1996) Surface nitridation of titanium metal by means of a gas tunnel type plasma jet. J Mater Eng Perform 5:373–380
152. Nakagawa Y, Ohtani S, Nakata T, Mikoda M, Takagi T (1993) Titanium nitride film formation by the dynamic ion beam mixing method. Nucl Instrum Meth Phys Res B 80(81):1402–1405
153. Althues H, Palkovits R, Rumplecker A, Simon P, Sigle W, Bredol M, Kynast U, Kaskel S (2006) Synthesis and characterization of transparent luminescent ZnS:Mn/PMMA nanocomposites. Chem Mater 18:1068–1072
154. Caseri W (2009) Inorganic nanoparticles as optically effective additives for polymers. Chem Engi Commun 196:549–572

155. Lüdersdorff FW (1833) Verh. Verein. Beförderung Gewerbefleiss. Preussen 12:224
156. Corbierre MK, Cameron NS, Sutton M, Mochrie SGJ, Lurio LB, Rühm A, Lennox RB (2001) Polymer-stabilized gold nanoparticles and their incorporation into polymer matrices. J Am Chem Soc 123:10411–10412
157. Kang SW, Kim JH, Char K, Won J, Kang YS (2006) Nanocomposite silver polymer electrolytes as facilitated olefin transport membranes. J Membr Sci 285:102–107
158. Karthikeyan B, Anija M, Venkatesan P, Suchand Sandeep CS, Philip R (2007) Ultrafast optical power limiting in free-standing Pt-polyvinyl alcohol nanocomposite films synthesized in situ. Opt Commun 280:482–486
159. Takele H, Greve H, Pochstein C, Zaporojtchenko V, Faupel F (2006) Plasmonic properties of Ag nanoclusters in various polymer matrices. Nanotechnology 17:3499–3505
160. Schürmann U, Hartung W, Takele H, Zaporojtchenko V, Faupel F (2005) Controlled syntheses of Ag-polytetrafluoroethylene nanocomposite thin films by co-sputtering from two magnetron sources. Nanotechnology 16:1078–1082
161. Baraton M-I, Merhari L, Wang J, Gonsalves KE (1998) Investigation of the TiO_2/PPV nanocomposite for gas sensing applications. Nanotechnology 9:356–359
162. Zhang X, Shao C, Zhang Z, Li J, Zhang P, Zhang M, Mu J, Guo Z, Liang P, Liu Y (2012) In situ generation of well-dispersed ZnO quantum dots on electrospun silica nanotubes with high photocatalytic activity. ACS Appl Mater Interfaces 4:785–790
163. Li X, Ni X, Liang Z, Shen Z (2012) Synthesis of imidazolium-functionalized ionic polyurethane and formation of CdTe quantum dot-polyurethane nanocomposites. J Polym Sci A Polym Chem 50:509–516
164. Mcdonald SA, Konstantatos G, Zhang S, Cyr PW, Klem EJD, Levina L, Sargent EH (2005) Solution-processed PbS quantum dot infrared photodetectors and photovoltaics. Nat Mater 4:138–142
165. Wilson JL, Poddar P, Frey NA, Srikanth H, Mohomed K, Harmon JP, Kotha S, Wachsmuth J (2004) Synthesis and magnetic properties of polymer nanocomposites with embedded iron nanoparticles. J Appl Phys 95:1439–1443
166. Fang J, Tung LD, Stokes KL, He J, Caruntu D, Zhou WL, O'Connor CJ (2002) Synthesis and magnetic properties of CoPt-poly(methylmethacrylate) nanostructured composite material. J Appl Phys 91:8816–8818
167. Gass J, Poddar P, Almand J, Srinath S, Srikanth H (2006) Superparamagnetic polymer nanocomposites with uniform Fe_3O_4 nanoparticle dispersions. Adv Funct Mater 16: 71–75
168. Prabhakaran T, Hemalatha J (2008) Synthesis and characterization of magnetoelectric polymer nanocomposites. J Polym Sci, Part B: Polym Phys 46:2418–2422
169. Liu L, Qi Z, Zhu X (1999) Studies on nylon 6/clay nanocomposites by melt-intercalation process. J Appl Polym Sci 71:1133–1138
170. Smith JA, Josowicz M, Janata J (2003) Polyaniline-gold nanocomposite system. J Electrochem Soc 150:E384–E388
171. Harish S, Mathiyarasu J, Phani KLN, Yegnaraman V (2009) Synthesis of conducting polymer supported Pd nanoparticles in aqueous medium and catalytic activity towards 4-nitrophenol reduction. Catal Lett 128:197–202
172. Athawale AA, Bhagwat SV (2003) Synthesis and characterization of novel copper/polyaniline nanocomposite and application as a catalyst in the Wacker oxidation reaction. J Appl Polym Sci 89:2412–2417
173. Macanas J, Parrondo J, Munoz M, Alegret S, Mijangos F, Muraviev DN (2007) Preparation and characterisation of metal–polymer nanocomposite membranes for electrochemical applications. Phys Status Solidi (a) 204:1699–1705
174. Harmer MA, Farneth WE, Sun Q (1996) High surface area nafion resin/silica nanocomposites: a new class of solid acid catalyst. J Am Chem Soc 118:7708–7715
175. Ganesan R, Gedanken A (2008) Organic-inorganic hybrid materials based on polyaniline/TiO_2 nanocomposites for ascorbic acid fuel cell systems. Nanotechnology 19:435709

176. Ahmad S, Agnihotry SA, Ahmad S (2008) Nanocomposite polymer electrolytes by in situ polymerization of methyl methacrylate: for electrochemical applications. J Appl Polym Sci 107:3042–3048
177. Lévy R, Shaheen U, Cesbron Y, Sée V (2010) Gold nanoparticles delivery in mammalian live cells: a critical review. Nano Rev 1:4889
178. Lin MM, Kim HH, Kim H, Muhammed M, Kim DK (2010) Iron oxide-based nanomagnets in nanomedicine: fabrication and applications. Nano Rev 1:4883
179. Kim JH, Park K, Kwon IC, Nam HY, Lee S, Kim K (2007) Polymers for bioimaging. Prog Polym Sci 32:1031–1053
180. Balazs AC, Emrick T, Russell TP (2006) Nanoparticle polymer composites: where two small worlds meet. Science 314:1107–1110
181. Chen L, Gu Y, Shi L, Ma J, Yang Z, Qian Y (2004) A room-temperature synthesis of titanium nitride hollow spheres. J Nanosci Nanotechnol 4:896–898
182. Verbeek CJR (2002) Highly filled polyethylenerphlogopite composites. Mater Lett 52:453–457
183. Rossi GB, Beaucage G, Dang TD, Vaia RA (2002) Bottom-Up synthesis of polymer nanocomposites and molecular composites: ionic exchange with PMMA latex. Nano Lett 2:319–323
184. Mandal TK, Fleming MS, Walt DR (2002) Preparation of polymer coated gold nanoparticles by surface-confined living radical polymerization at ambient temperature. Nano Lett 2:3–7
185. Stephen R, Ranganathaiah C, Varghese S, Joseph K, Thomas S (2006) Gas transport through nano and micro composites of natural rubber (NR) and their blends with carboxylated styrene butadiene rubber (XSBR) latex membranes. Polymer 47:858–870
186. Mascia L, Zhang Z, Shaw SJ (1996) Carbon fibre composites based on polyimide/silica ceramers: aspects of structure–properties relationship. Composites A 27:1211–1221
187. Livage J, Sanchez C (1992) Sol–gel chemistry. J Non-Cryst Solids 145:11–19
188. Smaihi M, Jermoumi T, Marignan J, Noble RD (1996) Organic–inorganic gas separation membranes: preparation and characterization. J Membr Sci 116:211–220
189. Yuwono AH, Liu B, Xue J, Wang J, Elim HI, Ji W, Li Y, White TJ (2004) Controlling the crystallinity and nonlinear optical properties of transparent TiO_2-PMMA nanohybrids. J Mater Chem 14:2978–2987
190. Hench LL, West JK (1990) The sol–gel process. Chem Rev 90:33–72
191. Molina C, Moreira PJ, Gonçalves RR, Ferreira RAS, Messaddeq Y, Ribeiro SJL, Soppera O, Leite AP, Marques PVS, De Zea BV, Carlos LD (2005) Planar and UV written channel optical waveguides prepared with siloxane-poly(oxyethylene)-zirconia organic-inorganic hybrids. Structure and optical properties. J Mater Chem 15:3937–3945
192. Sangermano M, Voit B, Sordo F, Eichhorn K-J, Rizza G (2008) High refractive index transparent coatings obtained via UV/thermal dual-cure process. Polymer 49:2018–2022
193. Lee S, Shin H-J, Yoon S-M, Yi DK, Choi J-Y, Paik U (2008) Refractive index engineering of transparent ZrO_2-polydimethylsiloxane nanocomposites. J Mater Chem 18:1751–1755
194. Rosidian A, Liu Y, Claus RO (1998) Ionic self-assembly of ultrahard ZrO_2/polymer nanocomposite thin films. Adv Mater 10:1087–1091
195. Zhou S, Wu L (2008) Phase separation and properties of UV-curable polyurethane/zirconia nanocomposite coatings. Macromol Chem Phys 209:1170–1181
196. Dey A, De SK (2007) Conductivity relaxation in zirconia nanoparticles dispersed in conducting polymer. J Appl Polym Sci 105:2225–2235
197. Zhao ZW, Tay BK, Huang L, Yu GQ (2004) Study of the structure and optical properties of nanocrystalline zirconium oxide thin films deposited at low temperatures. J Phys D: Appl Phys 37:1701–1705
198. Ferrer FJ, Frutos F, García-López J, González-Elipe AR, Yubero F (2007) Optical refractive index and static permittivity of mixed Zr-Si oxide thin films prepared by ion beam induced CVD. Thin Solid Films 516:481–485

199. Zhao S, Ma F, Song Z, Xu K (2008) Thickness-dependent structural and optical properties of sputter deposited ZrO_2 films. Opt Mater 30:910–915
200. Liu W-C, Wu D, Li A-D, Ling H-Q, Tang Y-F, Ming N-B (2002) Annealing and doping effects on structure and optical properties of sol-gel derived ZrO_2 thin films. Appl Surf Sci 191:181–187
201. Ehrhart G, Capoen B, Robbe O, Boy P, Turrell S, Bouazaoui M (2006) Structural and optical properties of n-propoxide sol–gel derived ZrO_2 thin films. Thin Solid Films 496:227–233
202. Lü C, Yang B (2009) High refractive index organic–inorganic nanocomposites: design, synthesis and application. J Mater Chem 19:2884–2901
203. Ramaswami R, Sivarajan K (2001) Optical networks: a practical perspective. Morgan Kaufmann, San Francisco
204. Baumeister W, Steven AC (2000) Macromolecular electron microscopy in the era of structural genomics. Trends Biochem Sci 25:624–631
205. Kitawaki K, Kaneko K, Inoke K, Hernandez-Garrido JC, Midgley PA, Okuyama H, Uda M, Sakka Y (2009) Fabrication and characterization of TiN-Ag nano-dice. Micron 40:308–312
206. Owens DE, Eby JK, Jian Y, Peppas NA (2007) Temperature responsive polymer-gold nanocomposites as intelligent therapeutic systems. J Biomed Mater Res 3:692–695

High Resolution in STEM Mode: Individual Atom Analysis in Semiconductor Nanowires

9

María de la Mata and Jordi Arbiol

Contents

1 Definition of the Topic 375
2 Overview 376
3 Introduction 376
4 Experimental and Instrumental Methodologies 380
4.1 Resolution Improvement: Aberration Correctors 380
4.2 Scanning Transmission Electron Microscopy Special Modes 383
4.3 EELS at Atomic Resolution More Than Just Chemical Analysis 392
5 Key Research Findings 399
5.1 Mapping of Individual Atoms 399
5.2 Dumbbell Identification: Direct Polarity Assignment in Semiconductor NWs 402
6 Conclusions and Future Perspective 419
References 419

1 Definition of the Topic

Aberration-corrected scanning transmission electron microscopy (STEM) in its different advanced modes such as high-angle annular dark field (HAADF), annular bright field (ABF), and middle-angle bright field (MABF) coupled to electron energy-loss spectroscopy (EELS) allows for high-resolution analysis of nanomaterials and can identify their properties at atomic scale, even on individual

M. de la Mata
Institut de Ciència de Materials de Barcelona, ICMAB-CSIC, Campus de la UAB, Bellaterra, CAT, Spain

J. Arbiol (✉)
Institut de Ciència de Materials de Barcelona, ICMAB-CSIC, Campus de la UAB, Bellaterra, CAT, Spain

Institució Catalana de Recerca i Estudis Avançats (ICREA), Barcelona, CAT, Spain
e-mail: arbiol@icrea.cat

C.S.S.R. Kumar (ed.), *Transmission Electron Microscopy Characterization of Nanomaterials*, DOI 10.1007/978-3-642-38934-4_9,
© Springer-Verlag Berlin Heidelberg 2014

atoms. Among those properties, not only the atomic chemical composition but also their chemical state (oxidation, valence states or even coordination states) or localized physical properties, as their associated band gap, can be obtained on individual atomic columns or individual atoms. In this chapter we describe the application of aberration-corrected STEM in its different application modes and related spectroscopies (such as EELS and EDX) in order to correlate the structure and chemical composition at the atomic scale with the growth mechanisms and physical properties of semiconductor nanowires (NWs).

2 Overview

The resolution improvement and the enhancement of the intensity beam due to the development of aberration correctors have involved a huge step toward individual atoms visualization. Its implementation to operate a TEM in scanning (STEM) mode allows resolving atomic distances through different techniques depending on the scattered electrons collected. For instance, the collection of high-angle scattered electrons with an annular detector leads to Z-contrast or High-Angle Annular Dark-Field (HAADF) images, which main advantage is its chemical contrast, as will be shown along this chapter. Instead, the collection of the elastically scattered electrons, also employing an annular detector, gives raise to the recently develop Annular Bright Field (ABF) imaging that permits imaging light and heavy atoms at the same time, as it will be seen, too. Finally, newly developed techniques, such as Middle-Angle Bright Field (MABF), allow visualization only of the light atoms, masking the heavier ones.

Concerning the Electron Energy-Loss Spectroscopy (EELS) signal, since remarkable enhancement of the signal-to-noise ratio has been provided by the aberration correctors, atomic resolution EELS is possible, even to map some related properties (e.g., oxidation state). The exact location of atomic columns within a material represents a breakthrough in many different applications such as the study of coherent interfaces, the atomic chemical mapping, or the direct polarity assignment. These capabilities are especially important when dealing with nanostructed materials, which nowadays are attracting great interest in materials science. In this chapter, particular attention will be paid to the polarity determination in semiconductor nanowires through direct dumbbell resolution, showing its importance in understanding the growth mechanism and the related physical properties.

3 Introduction

Parallelly to the fast development and advancement of Nanoscience and Nanotechnology, there has been an increasing necessity for the detailed analysis of the newly created nanostructures. The new technologies and devices require very specific properties on the synthesized materials devoted to advanced applications. Thus, a deep knowledge of the material is essential to understand the underlying

physical and chemical properties and to be able to tune them in the desirable applicability range.

Many of the new application fields can be achieved thanks to the material miniaturization at the nanometric scale, where analyzing the material is not straightforward. Moreover, these nanostructures have shown not to share the bulk physical properties, but presenting some modified ones as a consequence of their size. In some extreme cases, even the classic physical laws cannot be applied to understand these properties, and new theories based on quantum mechanics must be taken into account. As the material final properties are dependent on its nanostructure, an insight at the nanoobjects at atomic scale is highly desirable to describe the characteristics of the materials. This is a matter of especial relevance when dealing with small collections of atoms, as is the case of nanostructures where the presence of crystalline defects might have detrimental effects on the final material properties. Otherwise, structural defects can be intentionally caused with different purposes as the creation of quantum wells or polytypic modulations that can dramatically modify the physical properties of the material such as the electronic band structure, responsible of the optical emission [1–8]. Along the present chapter, from all the possible nanostructured morphologies, especial emphasis will be taken into nanowires (NWs), and more concretely into semiconductor ones.

Semiconductor materials present very interesting properties for functional applications related with their electronic and optoelectronic [9–18], sensing [19, 20], specially biosensing [21–23], and gas sensing [24–27] properties. For example, from the optical point of view, the presence of a band gap in this kind of materials and its possible modulation through nanostructuration [2, 28–32] are the basis to develop related optoelectronic devices [33]. As a consequence of reducing the structures size to scales in the range of the Bohr exciton diameter, the spatial confinement of the charges takes place leading to the quantum confinement [34]. This results in quantitative shifts of the absorption/emission edges toward higher energies, depending on the structure dimensions [35] and the material composition [36].

Techniques as Scanning Tunnel Microscopy (STM) [37, 38] have been used during the past decade to perform suitable analysis at atomic scale containing compositional information. STM can be used to extract relevant compositional and structural information from the sample surface. So, it usually requires treating the sample before performing the analyses in order to remove the surrounding oxide. If samples are properly cleaved, further information from the inside of the structure can be obtained, as shown in Ref. [39]. The chapter shows the atomic structure inside a GaAs NW through STM measurements after embedding the NW and clearing it to expose the growth plane perpendicular to the STM observation direction. This procedure is known as cross-sectional STM (XSTM) and allows providing direct atomic scale information of the embedded structures. In Fig. 9.1 there are presented both low-magnification (Fig. 9.1b) and high-magnification (Fig. 9.1c) STM images of the NW studied. A model of the NW on the substrate is included in the figure (Fig. 9.1a), pointing to the analyzed area in Fig. 9.1b. The high-resolution STM image in Fig. 9.1c shows the As lattice revealing that the NW grown in the zinc-blende crystalline structure. Different single defects can be

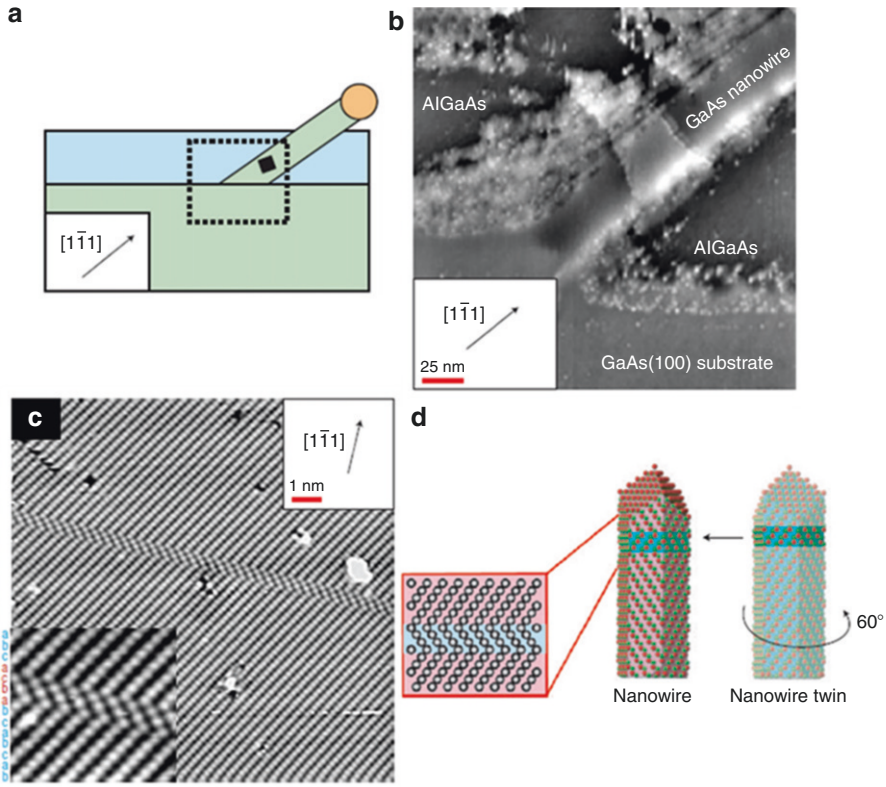


Fig. 9.1 (**a**) Sketch of the studied GaAs NW grown along the [1–11] direction. (**b**) Low-magnification STM image of one of the NW near the interface pointed in a). (**c**) High-resolution XSTM image of the As lattice. The NW presents zinc-blende structure with some atomic impurities (bright spots) and a twin boundary crossing the NW, magnified in the *inset*. (**d**) Model explaining how the twin is accommodated to the NW (Reprinted with permission from Ref. [39], Copyright 2004)

identified easily, as the dark spots correlated with As vacancies may be promoted by the STM measurements. Other defects are intrinsic of the material, as the brighter spots that correspond with the presence of individual atom impurities. However, the most remarkable feature is the four atoms planar defect that crosses the whole NW (see Fig. 9.1c, d) and that can be explained by the presence of a twin boundary which changes the atomic stacking sequence through a lattice rotation (see Sect. 5.2 of the present chapter for further explanation).

Depending on the results expected, the best solution for a complete characterization is the combined use of different techniques, as shown by Xu et al. in a recent paper [40] (see also Fig. 9.2). In the latter mentioned work, the analysis is performed employing imaging and spectroscopy experiments, by combining TEM, SEM, and STM, as well as derived TEM spectroscopies, such as Energy-Dispersive X-ray Spectroscopy (EDS). All these combined techniques are used to

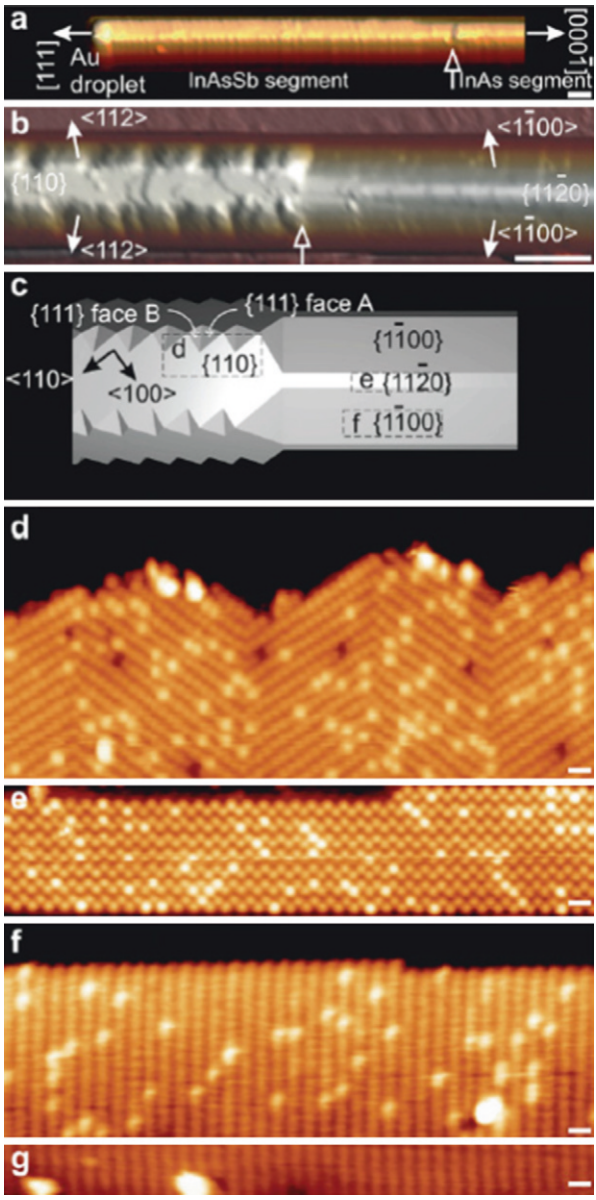


Fig. 9.2 (**a**) STM image of an entire [0001]/[-1-1-1]B InAs/$InAs_{1-x}Sb_x$ NW. (**b**) Zoom in image of the heterojunction in (**a**), where the sidewalls directions are indicated. (**c**) 3D model of the region in (**b**) showing the regions corresponding to the different sidewalls of the NW analyzed under high-resolution STM in (**d**–**f**). (**d**) and (**f**) are images of an NW with x = 0.05 while (**e**) was taken in a x = 0.10 NW. (**g**) High-resolution STM image of the {1-100} sidewall of a pure In As NW. Scale bars in (**a**) and (**b**) are 80 nm and 1 nm in (**d**–**g**) (Adapted with permission of Nanotechnology, from Ref. [40]. Copyright 2012)

obtain the accurate composition, which varies along the studied NWs, and correlate it, for instance, with the nanofaceting observed. Concretely, the sidewalls of the InAs NWs, presenting certain Sb-doped segments (analyzed by EDX), were studied under STM to reveal the morphology, structure, and surface composition, as well as to localize the individual Sb atoms (Fig. 9.2) at the oxide-free sidewalls of the NWs. It was found that the pure wurtzite structure of the InAs NWs becomes pure

zinc-blende when adding Sb and, moreover, it causes lateral growth leading to core-shell InAs/$InAs_{1-x}Sb_x$ heterostructures.

Despite of achieving atomic resolution, STM is only useful for extracting surface information, and its applicability is restricted to certain samples. Furthermore, the lightest elements are not visible by STM.

In this way, in the context of individual atom/column visualization, Transmission Electron Microscope (TEM) is one of the most powerful instruments allowing the observation of atomic sites through a variety of modes, even combining them to extract deeper information. The latest instrumental improvements on TEM ensure a resolution limit below 0.5 Å [41], not only operating with parallel illumination but also working in scanning (STEM) mode. Remarkable advances have been made evolving atomic visualization since even the lightest elements are now detected. Some of the most useful STEM techniques and its combination with EELS employed for single atom visualization are briefly explained along this chapter, including their theoretical basis and some related examples. Later along the chapter, we will depict some key research findings were mapping of individual atoms can help to determine the growth mechanisms and physical properties of our nanostructures, in this case semiconductor nanowires.

4 Experimental and Instrumental Methodologies

4.1 Resolution Improvement: Aberration Correctors

Neglecting the lenses aberrations, the microscope resolution is limited by diffraction, so considering a perfect imaging system, the microscope resolution is given by the information limit of the instrument. However, electromagnetic lenses are not perfect and are affected by the lenses aberrations reducing the microscope resolution power. As Scherzer established, the microscope resolution is given by

$$d_s = 0.67 C_s^{1/4} \lambda^{3/4} \tag{9.1}$$

being C_s the spherical aberration and λ the wavelength of the incident electrons. Thus, the main limitation to the microscope resolution becomes from the spherical aberration (C_s) which converts a point object into a disk, of radius r_{sph},

$$r_{sph} = C_s \beta^3 \tag{9.2}$$

where β is the objective lens collection angle.

C_s appears because those rays passing the objective lens far away from the optical axis experiment a greater bending than those which cross the lens close to the axis (see Fig. 9.3). Nevertheless, nowadays this effect can be compensated to a great extend by the use of combinations of multipoles and lenses developed by Haider et al. [42], basing on the earlier Rose's ideas [43]. In addition, the use of

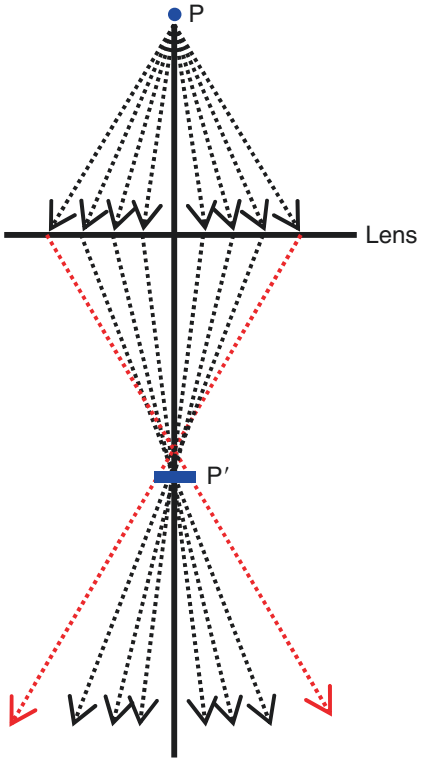


Fig. 9.3 The punctual object, P, is converted into a disk, P', when the electron rays go through the lens as a consequence of the spherical aberration. The rays crossing the lens far away from the optical axis experiment higher bending (shown in *red*)

C_s-correctors allows measuring the higher order aberration coefficients such as coma, two- and threefold astigmatisms and making them negligible. Avoiding the spherical aberration not only extends the point resolution to the information limit but also maximizes the phase contrast while minimizes the contrast delocalization [44]. So, improving the resolution in a C_s-corrected system implies the improvement of the information limit [45].

Once the spherical aberration has been compensated, the presence of the chromatic aberration becomes increasingly important. The chromatic aberration (C_c) appears as a consequence of the different wavelengths of the electrons emerging from the sample. When these electrons cross the objective lens, they are bent differently depending on their energies: the lower energy electrons are more bent than the higher energy ones and, as in the case of spherical aberration, a point is converted into a disk of radius r_{chr}

$$r_{chr} = C_c \frac{\Delta E}{E_0} \beta \tag{9.3}$$

In Eq. 9.3, ΔE is the energy lost by the electrons and E_0 is the initial energy of the electron beam. In these cases where the spherical aberration has been

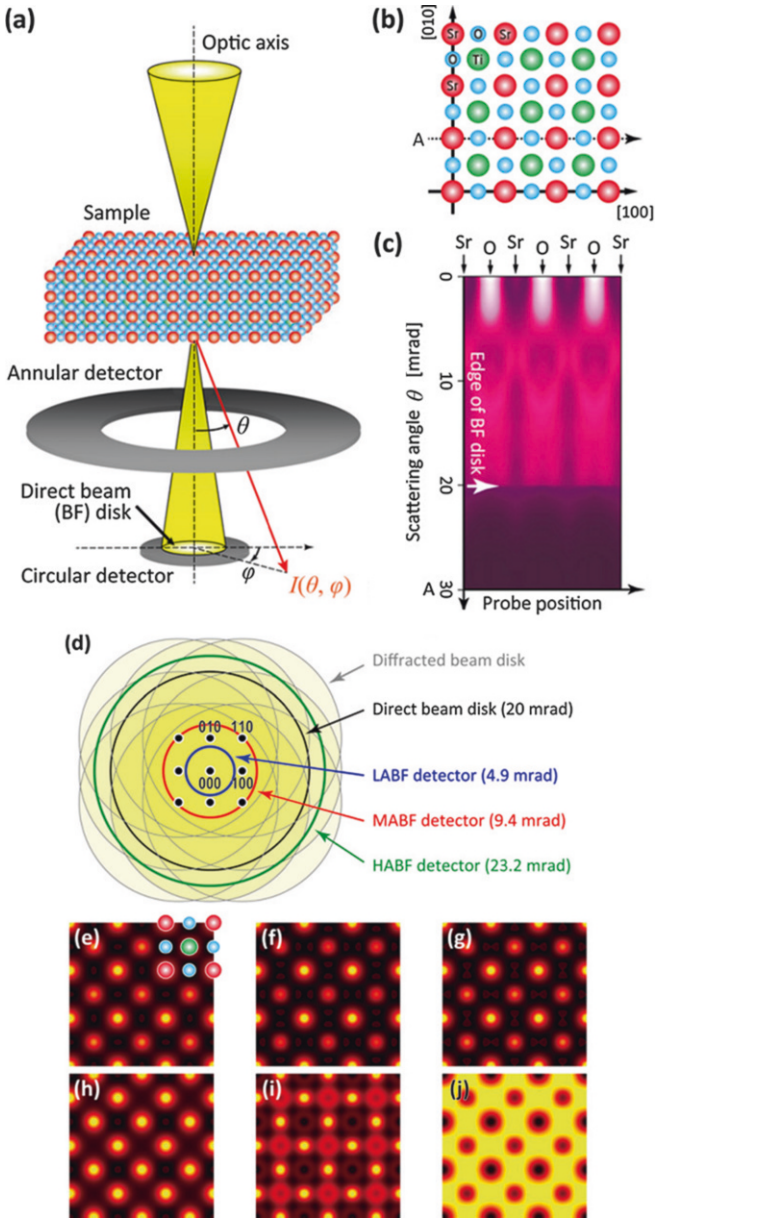


Fig. 9.4 (**a**) Schematic diagram of STEM instrument. (**b**) Schematic diagram of atomic column positions of [001]-oriented $SrTiO_3$ single crystal. (**c**) Calculated radially averaged angular distribution of electron intensities on the detector plane; corresponding probe positions are indicated in (**a**) as *dashed line* A–A0 for various scattering angles. (**d**) Schematic configurations of circular BF detectors under LA, MA, and HA conditions, respectively. *Black* spots are schematic diffraction spots of [001]-oriented $SrTiO_3$ single crystal for a plane-wave illumination.

compensated ($C_s = 0$), the microscope resolution is proportional to the C_c and can be written as

$$d_{Cs=0} = \sqrt{\frac{\Delta E}{E_0}\lambda C_c} \tag{9.4}$$

4.2 Scanning Transmission Electron Microscopy Special Modes

Depending on the detector we use (annular or circular), its position on the microscope and the imaging conditions (such as camera length, sample thickness, and focus), we can obtain different imaging conditions in STEM. As an example, in Fig. 9.4, we show how HAADF can image the heavy elements while simultaneously MABF can image the light ones [46]. In the following we will describe those modes that are the most interesting for individual atom visualization.

4.2.1 High-Angle Annular Dark Field (HAADF)

Different interactions take place when electrons go through the sample, and depending on the collected electrons, a variety of techniques have been developed. While performing conventional transmission electron microscopy, the image is formed as a result of the coherent phase interference of the elastically scattered electrons, operating in scanning mode (Scanning Transmission Electron Microscopy, STEM), and collecting the scattered electrons at high angles produces amplitude images. These latter electrons interfere incoherently mainly through interactions with phonons (Thermal Diffusive Scattering, TDS) providing Z-contrast images. Thus, the contrast at the image is scaled with the atomic number of the observed atomic column at the image, being the process similar to the Rutherford scattering. For this purpose, annular detectors with large collection angles are employed in the dark-field region defining these techniques, so-called high-angle annular dark field or HAADF. A sketch of the HAADF set up can be seen in Fig. 9.5a.

Operating in STEM mode, the probe brightness and dimension plays a determining role in the resulting image. This is why the development of aberration correctors has great benefits in STEM mode, not only reducing the probe diameter but also allowing higher probe currents which enhance the signal-to-noise ratio. Before the development of aberration correctors, the resolution limit for the annular dark-field experiments was 0.13 nm, while using them the probe could be converged until a probe size of about 60 pm. As a comparative example between

Fig. 9.4 (continued) (**e**–**g**) ADF-STEM images calculated under LA, MA and HA conditions, respectively. (**h**–**j**) Simulated BF-STEM images corresponding to same camera length conditions as ADF-STEM images in (**e**–**g**), respectively. Simulations in this figure assumed that the probe-forming lens defocus is zero (Reprinted from Ref. [46]. Copyright 2012, with permission from Elsevier)

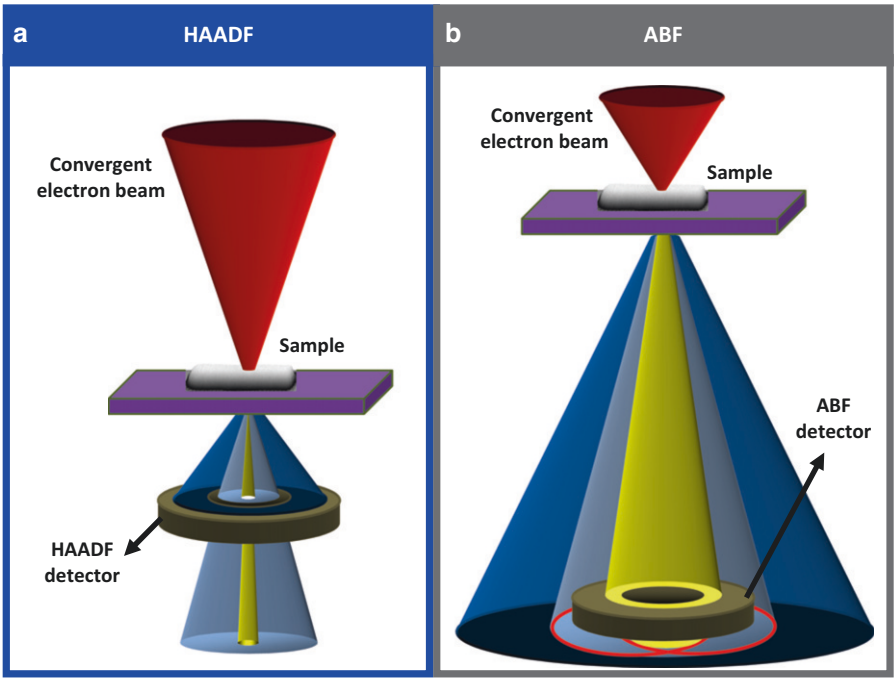


Fig. 9.5 Experimental set ups used in (**a**) HAADF and (**b**) ABF. Both techniques scan the convergent electron beam over the sample collecting: (**a**) the elastically scattered electrons at high angles to form incoherent Z-contrast images and (**b**) the coherent elastically scattered electrons in the bright-field region (Reprinted with permission from Ref. [116]. Copyright 2012, American Chemical Society)

uncorrected and aberration-corrected systems, see Fig. 9.6. There, Batson et al. [47] have shown differences between the Ronchygram, the image obtained and the FFT when working with an uncorrected probe and a corrected one (probe sizes 1.9 Å and 0.75 Å, respectively). The sample studied was $Ge_{30}Si_{70}$ along the [112] and information collected has covered the range until the {551} planes (notice that those reflections appear at distances just 0.76 Å apart, see Fig. 9.6e). A couple of years later, it has already been possible to perform HAADF with sub-Ångstrom resolution as Nellist et al. have already shown [48] solving the silicon dumbbell along the [114] axis, where the atoms in the dumbbell are 78 pm apart, and even obtaining lattice information at 61 pm.

A particular lack in the structures understanding emerges from the incapability to resolve the matching between structures. The defects present at interfaces caused by their mismatch, the flatness of an interface, or the possible interdiffusion of one material into the other are only few examples of the interfacial study relevance. Some studies on heterostructure interfaces in NWs have been performed recently, for example, by using uncorrected TEM combined with chemical characterizations such as Energy-Dispersive X-Ray spectroscopy (EDX) [49], while other

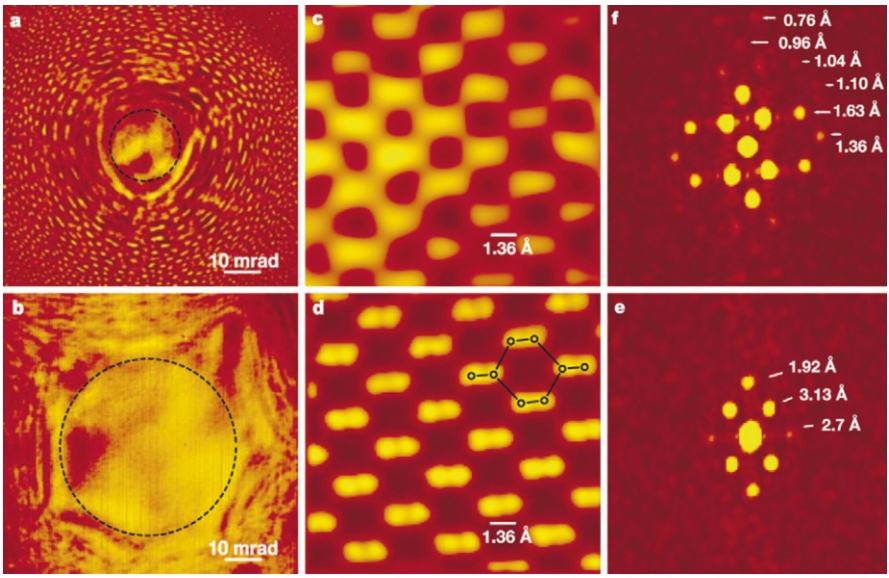


Fig. 9.6 Visualization of the ronchigram for the uncorrected (**a**) and corrected probes (**b**). $Ge_{30}Si_{70}$ visualized along the [112] using (**a**) and (**b**) conditions, respectively, in (**c**) and (**d**). The FFTs included in (**f**) and (**e**) are also correlated with the (**a**) and (**b**) conditions. Notice the further information when employing corrected imaging systems (Reprinted with permission from Ref. [47], Copyright 2002)

experiments were performed by means of STM data analysis [40, 50, 51]. For example, in the case of InAs/GaAs NW heterostructures, Dick and co-workers [52] recently showed the presence of a quite abrupt interface in the heterojunction region between both materials, which extended over a length of less than 10 nm. By combining HRTEM (filtering the suitable frequencies in the corresponding FFT) with STEM analysis (in HAADF imaging mode) and EDS measurements, it was possible to obtain these results, which are summarized in Fig. 9.7.

Moreover, the use of annular detectors allows the simultaneous collection of electrons belonging to the bright-field region through spectra (i.e., recording the electron energy-loss (EEL) spectrum) or imaging acquisition. On this way, there is much more sample information with the same time cost, as we will see in Sect. 4.3.

Regarding the technique drawbacks, the main limitation is found when trying to visualize light elements, especially in the case of structures involving also heavy atoms. Due to the dependence of the scattering power with the atomic number, atomic columns containing light elements are not visualized by HAADF in presence of heavier ones. Actually, this fact limits the understanding of very common functional materials which usually content light elements as, for instance, oxides or nitrides where neither the O nor N atomic columns are detectable within the

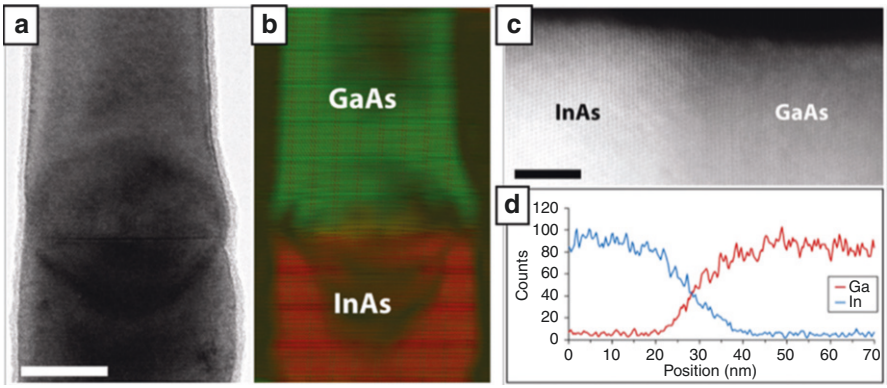


Fig. 9.7 (**a**) HRTEM image of the InA/GaAs interface in an NW seen from the [112] direction. (**b**) Reconstructed image from filtering the suitable frequencies corresponding to each phase, to show an abrupt interface extended over less than 10 nm. (**c**) High-resolution HAADF the heterojunction. (**d**) EDX profile across the interface with a gradient length of about 15 nm, in agreement with the contrast shown in (**c**) (Adapted with permission from Ref. [52]. Copyright 2012, American Chemical Society)

compound. However, as shown in the next sections, this is not a limitation anymore thanks to the recently developed annular bright-field (ABF) and middle-angle bright-field (MABF) techniques.

4.2.2 Annular Bright Field (ABF)

The availability of aberration-corrected microscopes operated in STEM mode results in high-resolution Z-contrast images. As mentioned in the previous section, light atoms are excluded of these images, especially when they are combined with heavy ones. To overcome this limitation, E. Okunishi and coauthors [53] have studied the annular bright-field configuration as an equivalent set up for obtaining a TEM hollow cone illumination. Such an illumination has been reported to provide better resolution than the BF-STEM and non-oscillating contrast transfer, making images easily interpretable and allowing the visualization of both, light and heavy, elements at once [54].

The set up employed for this purpose consists on a bright-field detector with its central area blocked by a beam stopper or, equivalently, an annular detector placed in the bright-field region (see Fig. 9.5b). For this reason, this new technique is called Annular Bright Field (ABF). This configuration ensures the collection of elastically scattered electrons with a negligible contribution of the thermal diffusive scattering, especially in the case of light elements. The coherent interference of such electrons results in a phase image presenting inverted contrast with respect to the HAADF image.

The first ABF experiment showing oxygen atomic columns was performed by Okunishi et al. [53] in 2009 applying the hollow cone illumination to irradiate a $SrTiO_3$ sample as shown Fig. 9.8. They have also extended the study to other materials such as Fe_3O_4 and Si_3N_4 being able to observe both O and N columns.

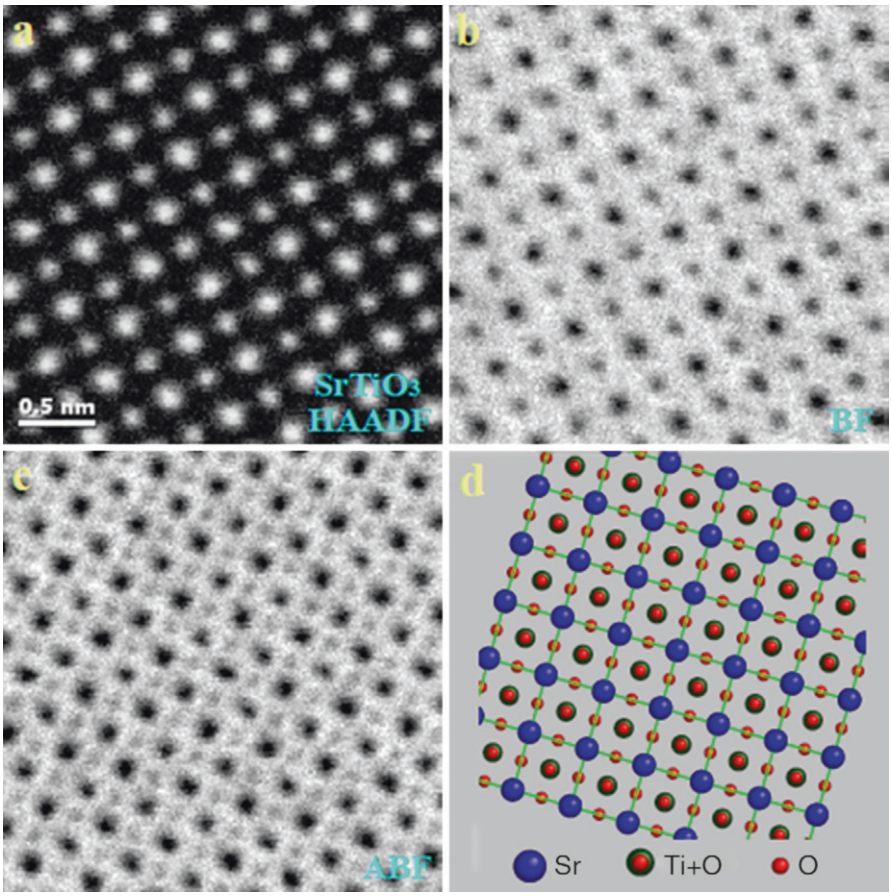


Fig. 9.8 (**a**) HAADF image of $SrTiO_3$, where Sr (brighter) and Ti (dimmer) are visualized. (**b**) BF image of the same region, showing the same atomic columns. (**c**) ABF image of the $SrTiO_3$ sample showing the O atomic columns. (**d**) Model of the $SrTiO_3$ crystalline structure view from the same axis than the experimental images, [001] (Reprinted with permission from Ref. [53]. Copyright 2009)

A deep study about the technique dynamics was made by Findlay et al. [55], accompanying their theoretical inspections with simulated images. The ABF technique was shown to be quite insensitive to the sample thickness for suitable defocus values as it is also the HAADF. However, it presents a restricted defocus range of operability, extending from −40 Å to +40 Å, and the image contrast cannot be directly correlated with the atomic column composition in an as reliable way as HAADF, as a consequence of the incomplete suppression of coherence effects. An extensive simulation study of the ABF technique regarding the influence of many parameters was recently performed by X. He et al. [56], basing their study on $LiFePO_4$ NWs, where they experimentally observed the Li and O constituents.

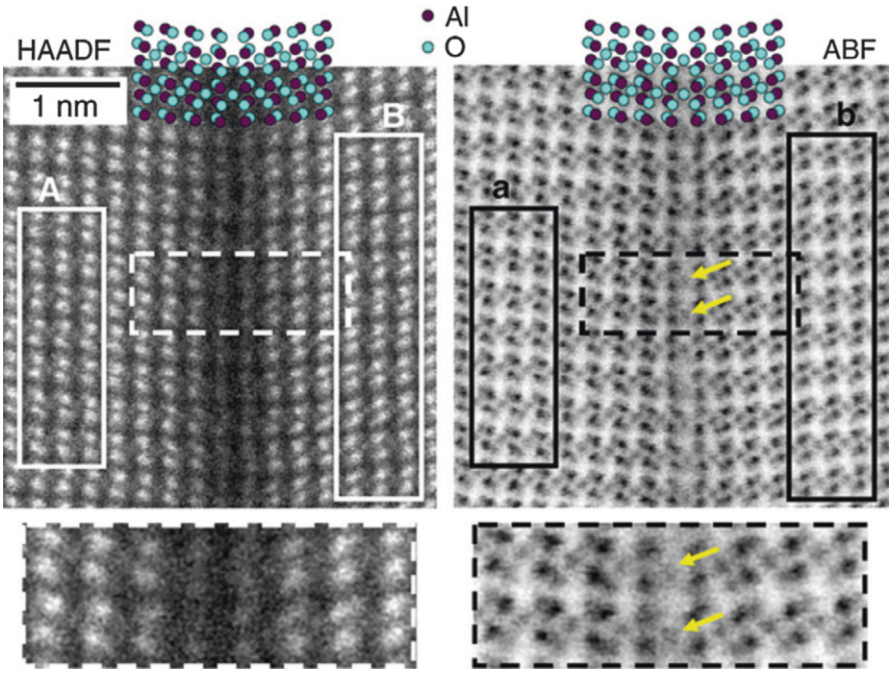


Fig. 9.9 Grain boundary images in the α-Al_2O_3 along the [1-210] obtained by HAADF and ABF, from left to right. *Dashed rectangles* point the region magnified below. The *yellow arrows* in the ABF image highlight the oxygen columns at the defect, which are undetectable in the HAADF (Reprinted from Ref. [57]. Copyright 2011, with permission from Elsevier)

Once tested the applicability of the technique, structural studies allowing O columns to be imagined could be performed, for instance, in distorted lattices. As an example, S. D. Findlay et al. [57] showed the O network in a grain boundary and its vicinity in α-Al_2O_3. They discussed the techniques applicability in structural defects, concluding that while ABF is more robust leading to a better atomic column location within the defects, the HAADF technique is more sensitive to the presence of structural defects. Bottom images in Fig. 9.9 show the HAADF and ABF images of the grain boundary regions obtained in the mentioned study.

Going further, ABF allows even imaging the lightest element, H, within crystalline hydrides, as shown Findlay et al. [58] in the case of VH_2 and Ishikawa et al. [59] in YH_2. In Fig. 9.10 we show the YH_2 structure along the [010] in different STEM images, being Fig. 9.10b, d the ABF and ADF images simultaneously acquired and Fig. 9.10c the BF one, taken from Ref. [59]. Note that the presence of H sites is only detected by the ABF, even in the simulated insets. A model of the crystallographic phase of the YH_2 is included in the panel 10a, and the projected crystalline structure is superposed in the ABF image.

Once the present state of the art in scanning transmission electron microscopy has been achieved, a huge range of applications in the field of materials science has

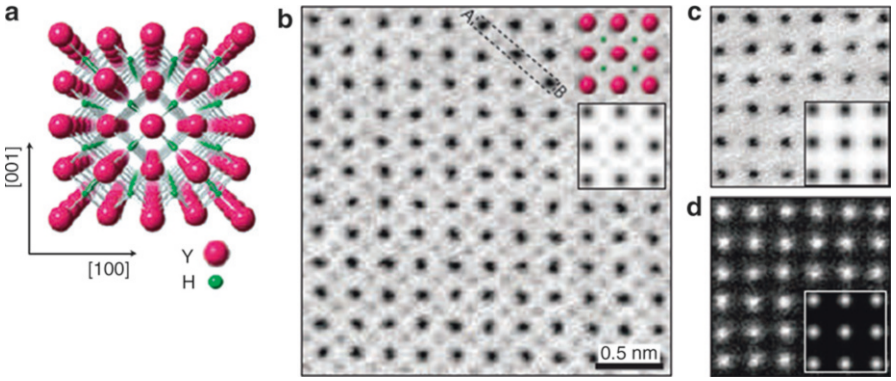


Fig. 9.10 Different images of the projected YH_2 structure along the [010] axis. (**a**) Structural model of the YH_2 phase and (**b**) ABF image showing the H atomic columns. The projected structure is superimposed in the *upper right corner* of the image; (**c**) Bright-field image and (**d**) ADF image. Every image includes an *inset* with the simulated structure under the considered technique (Reprinted with permission from Macmillan Publishers Ltd: Nature Materials; Ref. [59]. Copyright 2011)

been opened. There are many functional materials containing light elements where a full comprehension of the material properties involves a complete microstructural characterization. That is the case of, for instance, ceramic oxides where structural analyses of the interfaces and surfaces, as well as the study of structural defects, play an essential role in the material properties. Concerning these materials, we show here an example of a multilayer system composed by $SrTiO_3(100)$/$BaTiO_3(100)$ (ABO_3 structures or perovskites) presenting a mismatch of 3.0 %. Such a mismatch induced certain strain to the system, which was released by structural defects allowing the accommodation between both structures. The HAADF-ABF study shows abrupt interfaces without intermixing of atoms at A sites (Sr and Ba) in a highly epitaxial cube-on-cube system. The presence of interfacial misfit dislocations (showing [102] Burgers vector) relaxes the system strain and distorts the lattice as shown in Fig. 9.11 [60].

4.2.3 Middle-Angle Bright Field (MABF)

As it was said at the beginning of this Sect. 4.2, playing with different detector geometries leads to the development of different STEM-related techniques. Until now, in Sects. 4.2.1 and 4.2.2, we were considering annular detectors placed in such a way that different kind of scattered electrons were collected to create different types of images. Despite the relative novelty of the ABF technique, the most recent advances in STEM are connected with the use of the circular bright-field (BF) detectors instead of annular ones but located to have intermediate collection angles by adjusting the camera length [46, 61]. Based on previous theoretical studies developed, the starting point is that restricting the collection angle of the BF detector to very small values (on-axis detector) gives a tool highly sensitive to

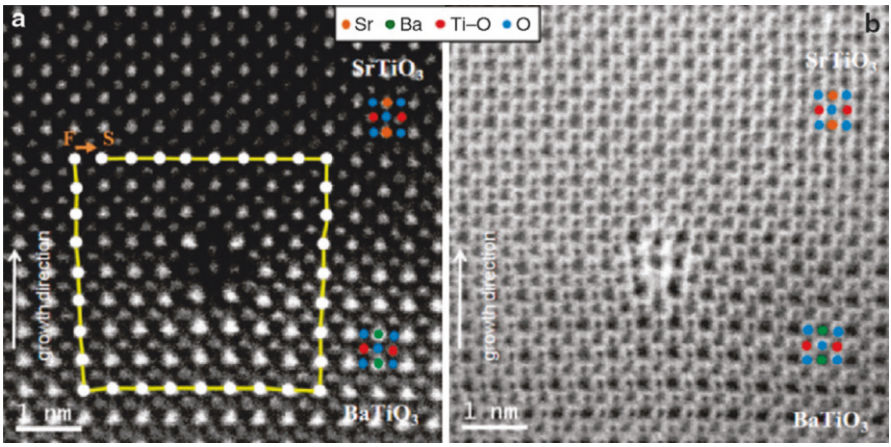


Fig. 9.11 HAADF (**a**) and ABF (**b**) images of the $SrTiO_3(100)/BaTiO_3(100)$ system along the [001] zone axis. Atomic models for both structures are superimposed to the images (Reprinted with permission from Ref. [60]. Copyright 2011, American Chemical Society)

the light atomic columns, while large collection angles of the BF detector lead to images sensitive to the heavier elements. Thus, it might be an optimum collection angle capable of being sensitive to both light and heavy atoms (see Fig. 9.4a, d). This angle has been previously calculated and, then, implemented in a [001] $SrTiO_3$ crystal. Calculated images of a postulated specimen of $SrTiO_3$ along the [001] with different collection angles (low, L; medium, M; and high, H) in dark-field and bright-field modes are included in Fig. 9.4. On one hand, Fig. 9.4h is the low-angle BF (LABF) calculated image considering a 4.9 mrad collection angle, only showing the location of the O atomic column. On the other hand, Fig. 9.4j shows the high-angle BF (HABF) calculated image where the collection angle was fixed to a value of 23.2 mrad, and the visible atomic sites are the ones corresponding to the heavier columns. In between, there is the calculated image of considering an intermediate collection angle (9.4 mrad), and, as can be seen in Fig. 9.4i, both light and heavy atoms are simultaneously imagined, having the former bright contrast and the latter appear as dark spots with bright surrounding rings. Moving to a real $SrTiO_3$ sample viewed along the same direction, results are in agreement with theoretical predictions as shown in Fig. 9.12 (Fig. 9.12a displays the ADF image and Fig. 9.12b the BF image). The ADF image taken under a collection angle of 40–160 mrad dictated by the camera length imposed for getting the MABF condition is presented in Fig. 9.12a. The back images are the raw data, the overlapping layers correspond to the processed data (with the atomic sites of the structure pointed in different colors), and the upper smaller layer is the simulated structure in both modes.

4.2.4 STEM Image Simulation

As we have seen in the previous sections, whenever a STEM result is presented, it must always be accompanied by a simulation in order to assure its interpretation at

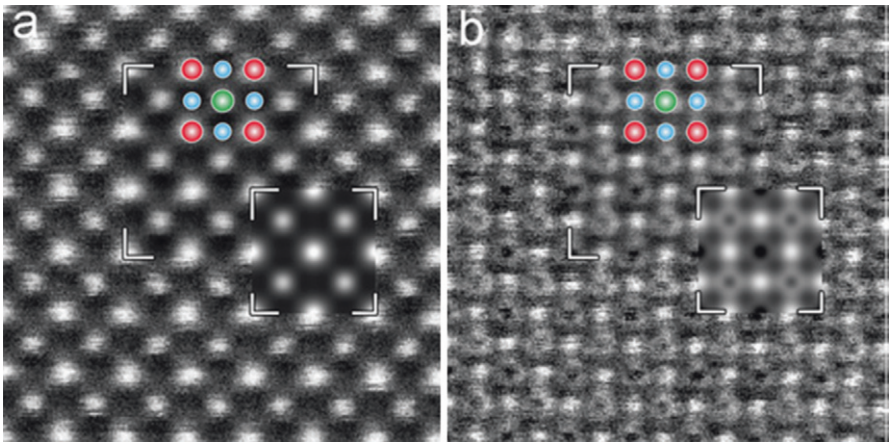


Fig. 9.12 (**a**, **b**) Raw ADF/MABF image of a $SrTiO_3$ sample oriented along the [001] axis, where the *color inset* is the processed image and the upper and smaller enclosed layer is the simulated structure under the experimental conditions (Reprinted from Ref. [46]. Copyright 2012, with permission from Elsevier)

atomic scale. In this way, many strategies and algorithms have been conceived to obtain a proper simulation of the experimental STEM images on the different modes. Some of these procedures were firstly developed for the case of HRTEM images, giving rise to software packages as, for instance, EMS [62]. Based on the same principles than the simulation of HRTEM images, the methods developed for simulating the STEM images follow either the multislice algorithms or the Bloch wave technique. The former approximation involves mathematically slicing the specimen and taking into account the successive interactions with the incident electrons at each slice. The later consider the total intensity as the sum of the different contributions of the electronic probe at each atomic column which is approximated as the 1 s state [63]. The first published ADF-STEM simulation was performed by Kirkland et al. [64] considering the elastic scattered electrons but neglecting the interaction with phonons and applying the multislice algorithm. Nevertheless, the contrast in HAADF images is mainly due to the interactions with phonons so, since then, different approaches have been developed to take into account the thermal diffuse scattering (TDS) and providing more realistic simulations [65–70]. The amazingly large computer time and power needed for this kind of simulations has made the researchers to think about algorithm approximations that reduce the computer time and may lead to easily resolve even large atomic cells.

The incoherent nature of Z-contrast has many effects: contrarily to diffraction contrast intensity, the Z-contrast intensity is less affected by small distortions of the crystal lattice [71].

At first approximation, HAADF contrast can be assumed as an ideal mass-thickness mapping of specimens, being then a very useful technique to characterize

interfaces and compositional variation in nanostructures. However, a more detailed description of the image formation is required if a quantitative analysis of the composition is needed and also to understand contrast features that originate in strongly deformed crystals.

As a matter of fact, when a crystalline material is aligned in a low index zone axis direction, the intensity is strongly influenced by the channeling effects: the propagation of the beam is indeed strongly influenced by the in-plane bound states that attract the electron in ion positions.

In particular, the coupling between the probe and the 1 s state is most effective as their shape are quite similar. The effect of the channeling can be understood after Eq. 9.5 is made more general, by assuming that the probe intensity may vary during the propagation through the sample, which is more realistic.

The probe density can be therefore named $J(r,z)$ with $J(r,0)$ equal to the impinging probe P^2. In this case the total intensity for a t thick sample is just (in the incoherent approximation) [71]

$$I = J(r,z_1) \otimes 0 + J(r,z_2) \otimes 0 + \ldots + J(r,t) \otimes 0 = \int_0^t J(r,z) \otimes 0 dz \qquad (9.5)$$

The term j is therefore proportional to the derivative of the intensity with thickness and contains the effect of channeling.

Grillo has, for example, recently introduced a system of equation that permits to describe in approximate way the propagation of J in presence of a crystal deformation.

The Grillo's equation in particular predicts that probe density decreases as the square of the local curvature of the atomic column and that its initial value depends on the local tilt of the lattice plane at surface. In a differential forms, the evolution of j with thickness z can be found by solving [72]

$$\frac{d^2 j(z)}{dz^2} = \left[-2\mu_{1s} \frac{dj(z)}{dz} - \Gamma^2 j(z) \right] \qquad (9.6)$$

where μ_{1s} is the absorption coefficient of the 1 s state and $\Gamma = \frac{\partial^2 \mathbf{u}||}{\partial z^2}$ is the column curvature expressed in terms of the displacement vector in the x,y plane orthogonal to the propagation direction.

This simple formula along with Eq. 9.5 and boundary conditions permits to describe important strain features that could be erroneously interpreted as strain effects. The application to dislocation, surface strain relaxation in quantum dots and quantum wells, and core-shell nanowires has been already successfully demonstrated [73].

4.3 EELS at Atomic Resolution More Than Just Chemical Analysis

The Electron Energy-Loss Spectroscopy (EELS) consists on recording the loss of energy suffered by the electrons when they cross the sample. The incoming electrons have all the same energy but their interactions with the sample promote

an energy transfer which will be dependent on the sample composition. To obtain such information, the elastically scattered electrons are split in different channels according to their kinetic energy before they arrive to the detector and, then, are recorded. One of the main advantages presented by the technique is that simultaneous HAADF signal acquisition is possible so that a spatial correlation with the spectra can be obtained.

4.3.1 Chemical Analysis at Atomic Scale

The development of aberration correctors has had great impact not only in the imaging related techniques but also in the spectroscopic ones. As well as allowing the formation of smaller electron probes, the aberration compensation enhances the brightness for the same probe size. So, the use of aberration correctors increases the beam current and provides the chance to get greater collection angles, leading to better signal-to-noise ratio. Moreover, there is also a remarkable drop in the acquisition time which minimizes the spatial drift during the data recording. As a consequence, 2D chemical mapping with atomic resolution is now possible. Regarding the signal fine structure, much more details can be distinguished when employing Cs-correctors, and other electronic-state-related properties (e.g., oxidation stated, bonding) can be mapped. As an example, Bosman et al. have reported the structural and chemical characterizations, simultaneously acquired working in STEM mode [74]. The characterization was made on a $Bi_{0.5}Sr_{0.5}MnO_3$ sample, accompanying the experimental data with simulations to confirm the results as shown Fig. 9.13.

This gain in resolution in chemical mapping is very useful, for example, to study interfaces, particularly to see if interdiffusion takes place. Figure 9.14 shows the results obtained by Kourkoutis and co-workers [75] when analyzing the interfaces in a $SrTiO_3/LaVO_3$ multilayer system. In Fig. 9.14b, an abrupt upper interface can be observed for the La lattice, while combining the Ti map from the $SrTiO_3$ (red) and the V from $LaVO_3$ (blue), the purple areas between the different layers (seen Fig. 9.14c) demonstrate the presence of Ti/V intermixing.

The EELS technique can be especially useful when studying the dopant distribution within a structure. Doping materials is an extended procedure to tailor their properties, but the success of the doping process will depend on the material final homogeneity. When dealing with nanostructures, obtaining such information requires the use of high spatial resolution techniques, as EELS has become. In this direction, Rosell and coauthors [76] have investigated the Ba distribution in $SrTiO_3$ nanoparticles to conclude the existence of Ba clustering giving an explanation for the previously detected polar nanoregions. Figure 9.15 shows the different cations distribution in a region of the $Ba_{0.03}Sr_{0.97}TiO_3$ nanoparticle. The Ba signal presence is restricted to smaller regions where the total of the Ba atoms are clustered.

When dealing with carbon-derived nanostructures as fullerenes or carbon nanotubes, which are easily damaged under the electron beam, especial care has to be taken (e.g., working at low voltages). In this way, Suenega and coworkers could achieve individual metallic dopant identification within

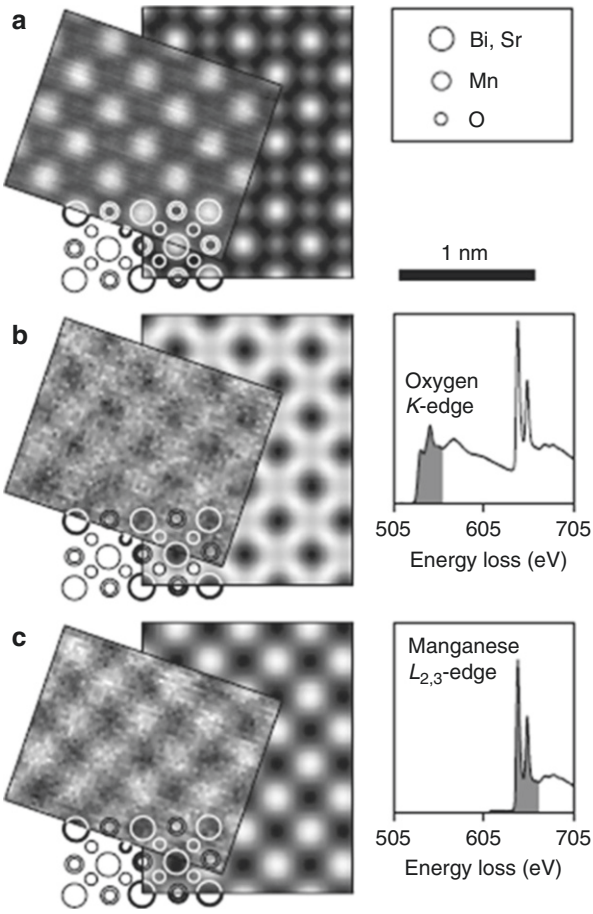


Fig. 9.13 The tilted pictures correspond with experimental data while the ones on the back are simulations of the $Bi_{0.5}Sr_{0.5}MnO_3$ structure view along the [001] axis being: (**a**) the HAADF image, (**b**) the oxygen k-edge and (**c**) the manganese L-edge. Examples of both O and Mn spectra are included at the right side of the images (Reprinted with permission from Ref. [72]. Copyright 2007)

carbon-based nanostructures [77]. Among their goals, Fig. 9.16 collects the EELS results of analyzing carbon nanotubes with atomic inclusions of lanthanum and erbium. They also aimed to identify for the first time a single calcium atom by means of EELS within a peapod (single-wall nanotube with carbon fullerenes embedded in it).

4.3.2 Advanced Atomic Analyses at Atomic Scale: Oxidation, Bonding, and Coordination States

As the measured signal in an EELS experiment is the kinetic energy lost by the electrons when crossing a specimen, it reflects not only the chemical composition of the material but also the surrounding environment of each constituent if employing the suitable resolution. Thus, proceeding properly, useful information about the oxidation and coordination states can be extracted to complete the material characterization.

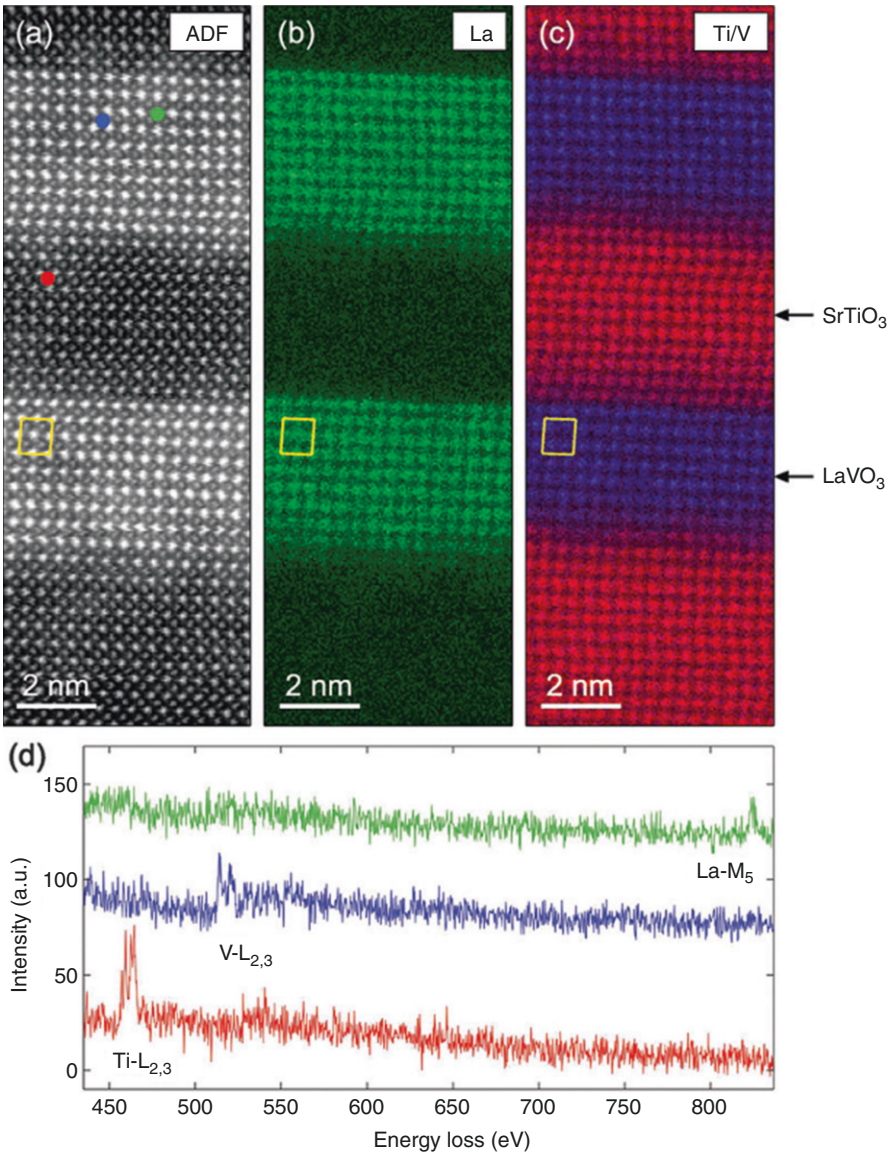


Fig. 9.14 (**a**) ADF image simultaneously acquired with the EELS spectra of a certain region of a $SrTiO_3/LaVO_3$ multilayer sample. (**b**) La extracted signal showing individually resolved La atomic columns. The upper interface is atomically abrupt. (**c**) Combination of the Ti (*red*) and V (*blue*) maps, showing a clear intermixing area which appear in *violet*. (**d**) EELS signal corresponding to the different color spots in (**a**). Figure Ref. [75] (Reprinted with permission of the publisher Taylor & Francis Ltd, http://www.tandf.co.uk/journals)

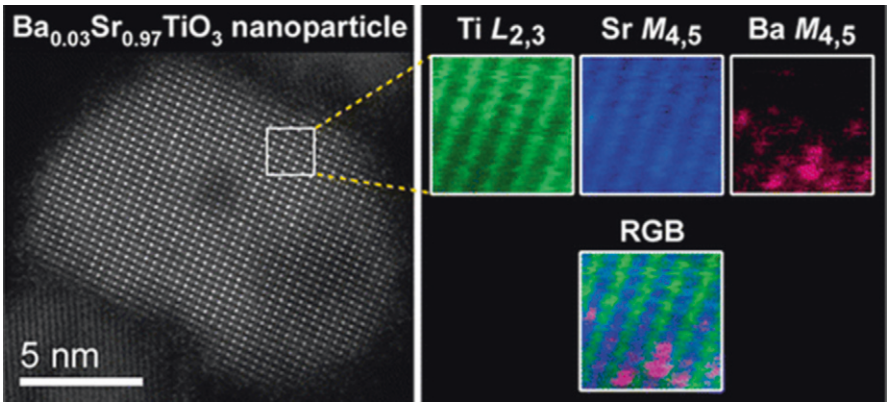


Fig. 9.15 HAADF of the studied $Ba_{0.03}Sr_{0.97}TiO_3$ nanoparticle. At *right side*, the elemental 2D maps of the cations in the *white squared region* of the image are included. Ti is represented in *green*, Sr in *blue*, and Ba in *pink*. The sum of these three maps results in the RGB image also enclosed, showing Ba clustering (Reprinted with permission from Ref. [76]. Copyright 2012, American Chemical Society)

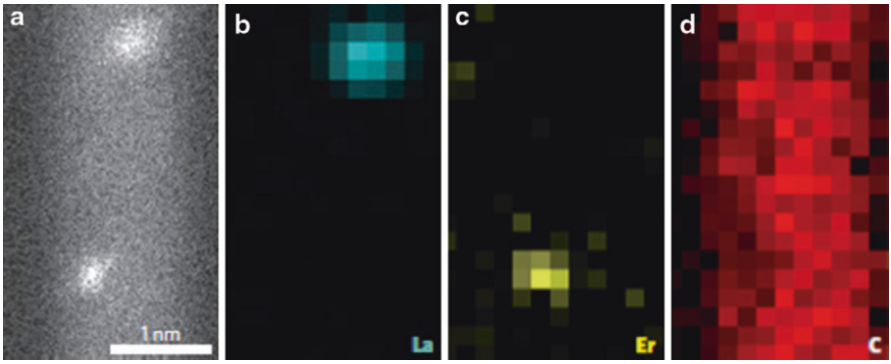


Fig. 9.16 (**a**) ADF image of a peapod doped with La@C_{82} and Er@C_{82} where the presence of the two heavier atoms is clear but not their identification. (**b**) La EELS map. (**c**) Er EELS map. (**d**) C EELS map (Reprinted with permission from Macmillan Publishers Ltd: Nature Chemistry; Ref. [77]. Copyright 2009)

One possible application of the careful inspection of an EELS spectrum is getting the bonding map of the material as reported in Ref. [78], where it obtained the Ti bonding mapping for a $La_{0.7}Sr_{0.3}MnO_3/SrTiO_3$ (LSMO/STO) multilayer system. The Ti signal is characteristic at each material, and the crystal-field splitting in both L_3 and L_2, in the t_{2g} and e_g orbitals, can be observed. For treating these data it is needed to perform a component analysis to decompose the spectra in their weighted components. Then, differences in the ELNES of the peaks allow the determination, for instance, of the graphite sheet orientation in a multiwalled

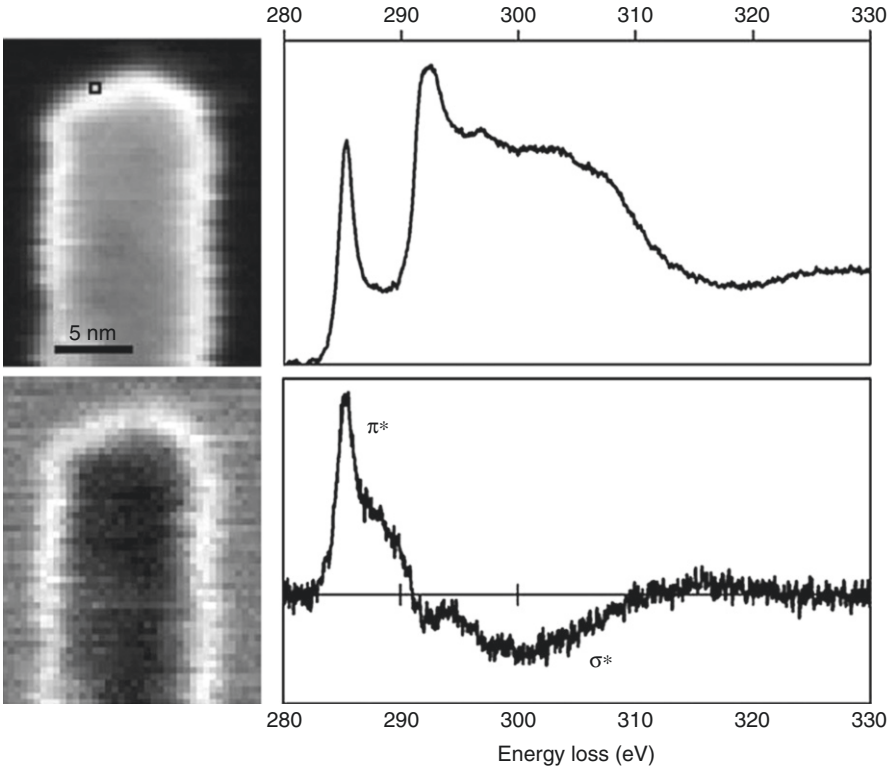


Fig. 9.17 First two components extracted with from the spectrum imaging performed in a multiwalled carbon nanotube (Reprinted from Ref. [79]. Copyright 2006, with permission from Elsevier)

carbon nanotube as shown Fig. 9.17 from Ref. [79]. Notice how at the nanotube edges the π* signal increases as the sheets are parallel to the electron beam, while at the center they are perpendicular to the probe.

Paying attention to the near-edge structure of the energy loss, differences can be found for the same elemental constituent under different valence states, leading to the determination of the oxidation state. By comparison of the edge shape with standards or simulated spectra, the atomic assignment of the oxidation state is nowadays possible, as reported in ref. [80] for a mixed valence oxide, Mn_3O_4. In the chapter, authors fitted the $L_{2,3}$-edge of the Mn to find different ordering for the Mn^{2+} and Mn^{3+} within the structure, as shown Fig. 9.18 (in a) as raw data, (in b) filtered maps, and (in c) simulated maps.

As shown in the previous example, some oxidation states are related with a characteristic coordination state within the compound. Nevertheless, in some other cases, different positions within the lattice are allowed for a certain valence state, as is the case of Ca_2FeCoO_5, where Fe and Co can be placed in both, the octahedral and tetrahedral positions. Through the analysis of the near-edge

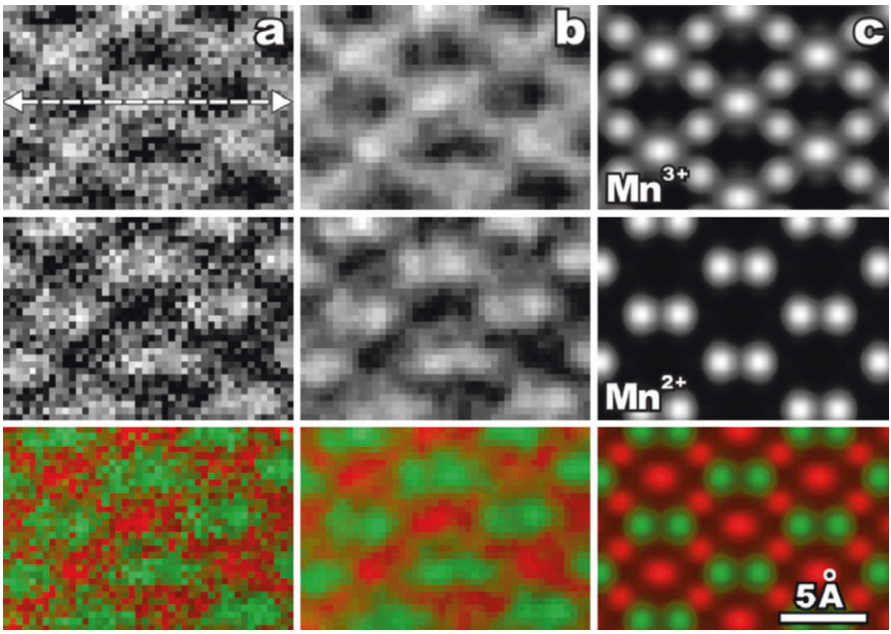


Fig. 9.18 EELS analysis of the oxidation state in Mn_3O_4, view along the [102]. The *upper row* shows the Mn^{3+} maps and the *middle row* contains the Mn^{2+} maps, while in the *last row* are the color maps of both signals. Column (**a**) includes the raw data, in column (**b**) are the low-pass filtering maps, and in (**c**) are the simulated maps (Reprinted with permission from Ref. [80]. Copyright 2011)

energy-loss spectrum (ELNES) with the suitable spatial and energy resolutions, even the coordination state of this kind of structures can be obtained. Focusing in the Ca_2FeCoO_5 case, Turner and co-workers were able to map the octahedral and tetrahedral positions of the structure [81], which are displayed in alternated layers when looking at the structure along the [102] (see Fig. 9.19a, showing the recorded spectrum image and Fig. 9.19d, which is the model of the lattice along the [102] direction). The different shape in both signals, Fe and Co, under the different lattice positions (octahedral in red and tetrahedral in blue) can be seen in Fig. 9.19e, f. Due to these spectral differences, it is possible to assign the coordination state, as shown Fig. 9.19b, c.

Before concluding the techniques section, it is worth to mention a few words about the other spectroscopic technique accessible from the STEM and the Energy-Dispersive X-ray Spectroscopy (EDS or EDX). By EDX, the X-rays emitted by the sample when irradiated with the electron probe are recorded giving incoherent images directly interpretable, as in the case of HAADF. That represents a great advantage over the EELS, which requires exhaustive data processing. So, the instrumental improvements achieved in the last years allow 2D atomically resolved chemical maps obtained from the X-ray spectroscopy [82, 83].

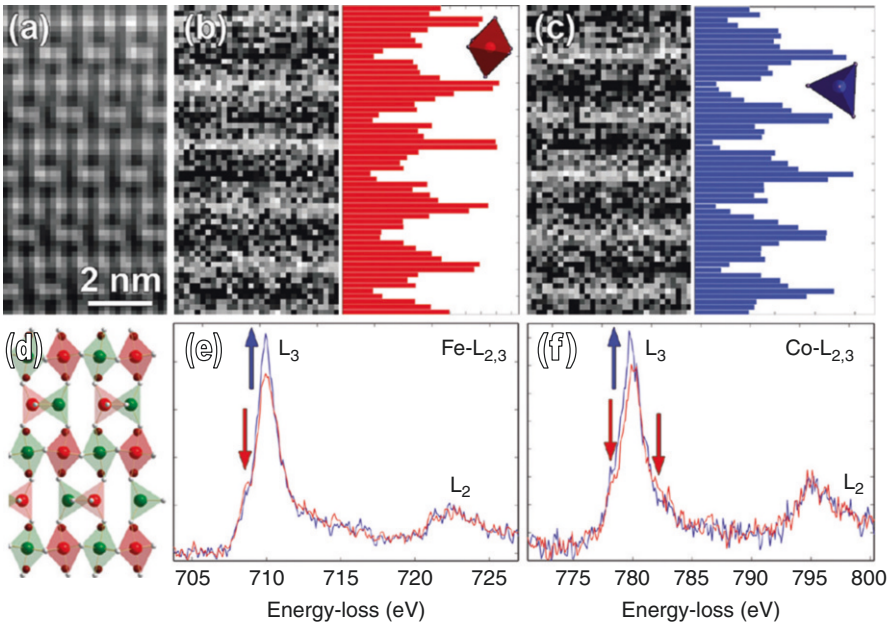


Fig. 9.19 (**a**) EELS spectrum image of a Ca_2FeCoO_5 specimen along the [102], modeled in (**d**), where the structure can be understood as an alternation of the octahedral and tetrahedral layers. (**b**) and (**c**) shown the octahedral and tetrahedral coordination maps, respectively, obtained from the spectral differences between the Fe and Co signals in the different places. (**e**) and (**f**) include both signals (*red* for the octahedral and *blue* for the tetrahedral) for Fe and Co (Adapted with permission from Ref. [81]. Copyright 2012, American Chemical Society)

5 Key Research Findings

5.1 Mapping of Individual Atoms

5.1.1 Au Distribution in Si and GaAs NWs

With such a resolution it is possible to apply the STEM techniques to the study of atomic defects, as is the case reported by S. H. Oh et al. [84]. It is widely known that the incorporation of catalytic atoms while growing semiconductor materials has a detrimental effect in their electronic properties, as they may decrease the electron mean free path. In this sense, Oh et al. analyzed Si nanowires grown with a gold droplet as catalytic agent and focused the study in the diffusion of individual Au atoms within the Si structure of the nanowire (Fig. 9.20a–d). They could classify the defects as substitutional or interstitial in three different environments (tetrahedral, hexagonal, and bucked Si-Au-Si chains) shown all of them in Fig. 9.20e–h. In addition, they also found a predictable experimental defect distribution based on DFT calculations of the defect formation energies.

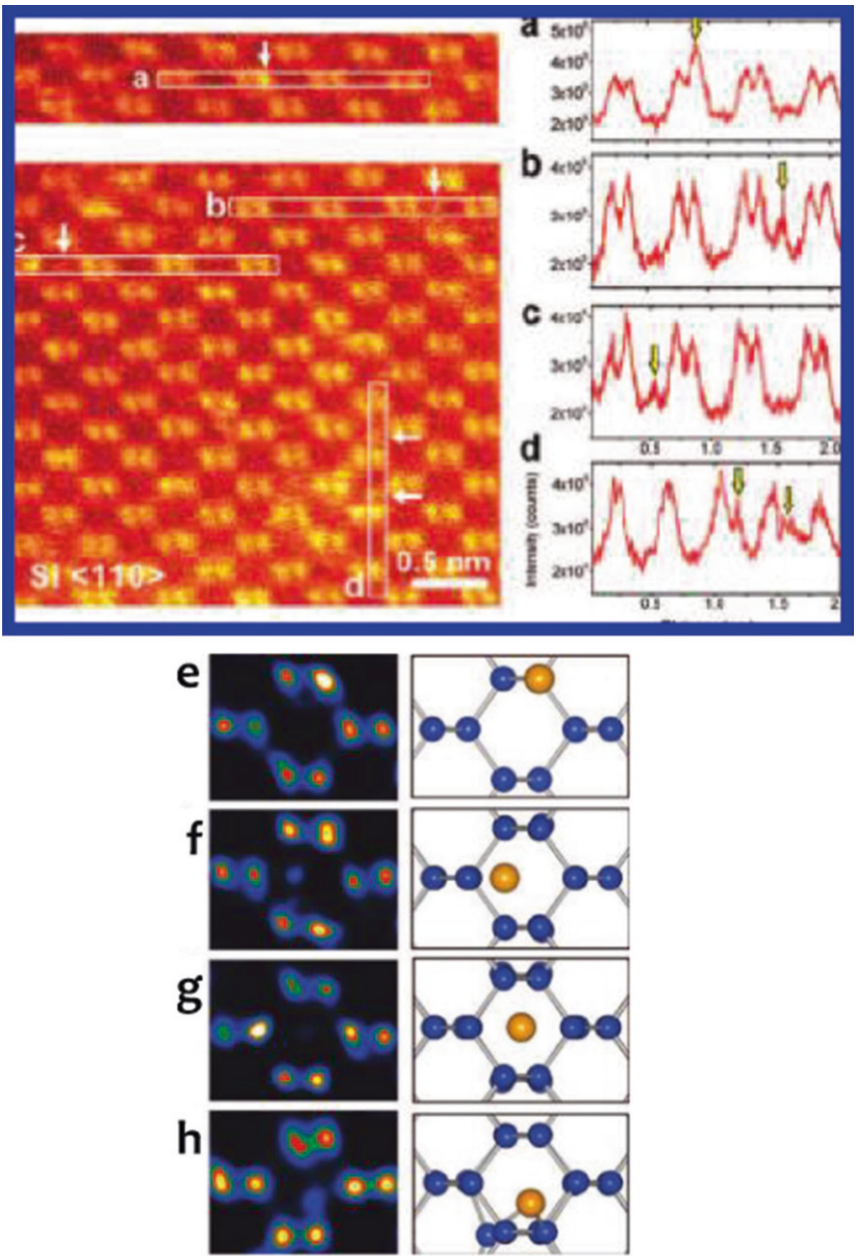


Fig. 9.20 HAADF images of a Si NW along the [112] direction, with different region of interest squared where intensity profiles were taken and displayed in (**a**–**d**). The punctual defects are emphasized by *white arrows* in the images. (**f**–**h**) are the different defects shown as HAADF images processed by maximum entropy image deconvolution (*left side*) and the atomic models

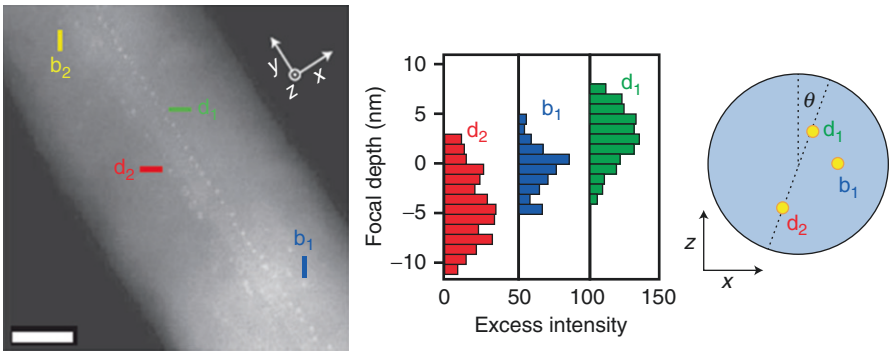


Fig. 9.21 Sum of seven aligned HAADF images of a longitudinally twinned Si NW containing Au impurities. The bar scale is 5 nm. The brighter features are related with the presence of Au impurities. The plot shows that b1 is contained in the NW since *d1* and *d2* are within the wire; *b1* must also be. The sketch at *right side* represents the transversal section of the NW, where the *dashed line* crossing the *circle* is the (111) twin boundary (Reprinted with permission from Macmillan Publishers Ltd: Nature Nanotechnology; Ref. [85]. Copyright 2008)

Working with the same materials, Allen and coauthors [85] also reported the implantation of Au atoms within the Si structure in nanowires when a gold catalytic nanoparticle is employed. In that case, Au atoms were trapped along a twin boundary extended through the growth direction (d_1 and d_2 in Fig. 9.21) and in the bulk of the NW (b_1 and b_2 in the figure). To perform the study of the 3D distribution of the Au impurities, a focal series of the NW was taken. Figure 9.21 shows the sum of seven aligned HAADF images, where the Au atoms are labeled as d (trapped in the twin) or b (atoms present in the bulk). The figure includes profiles taken into account the focal depth to distinguish if the brighter spots correspond to the presence of Au impurities in the wire and a sketch of the transversal section of the NW. As the twin boundary was contained in the NW and the feature b_1 was comprised between them, it was assumed that b_1 was a Au atom within the bulk of the wire. The final conclusions show that surface recombination controlled minority carrier transport, being negligible the Au impurities effect.

As the vapor-liquid–solid (VLS) method is very used in the synthesis of semiconductor NWs, there are lots of studies related with the catalytic contamination during the growth process [86, 87]. For instance, working with binary semiconductors, Bar-Sadan et al. [88] have applied similar procedures to those above mentioned, based on the acquisition focal series of HAADF images to found individual Au atoms confined in GaAs NWs.

Fig. 9.20 (continued) calculated by DFT (*right side*). In (**a**, **e**), a substitutional defect is shown, while the rest are interstitial defects. (**b**, **f**) show the tetrahedral configuration, (**c**, **g**) the hexagonal, and (**d**, **h**) the buckled Si–Au–Si chain (Adapted with permission from Ref. [84]. Copyright 2008, American Chemical Society)

5.1.2 Ga in AlN Barriers on Core-Shell NWs

Different materials grown one over the other lead to heterogeneous systems, as it is the case of the core-shell structures. The interfaces generated when putting together both phases used to present modified properties from the one expected for the isolated materials, especially when dealing with low-dimensional structures, as it was said in the introduction section. That is the case found by the authors in [89], where it is reported how the stepped growth of GaN/AlN core-shell NWs employing plasma-assisted molecular beam epitaxy (PAMBE) leads to the generation of self-assembled quantum wires (QWRs). The NW growth starts with the formation of the GaN core, followed by an AlN deposition, to finish with another GaN deposition (some samples included a final AlN covering to protect the quantum system). Using the Z-contrast technique, quick differentiation between GaN and AlN is possible, revealing the presence of GaN QWRs along the [11–22] direction of the AlN shell, where takes place the intersection of two of the (1–100) lateral facets of the NW. Some of these QWRs, as the ones shown in Fig. 9.22, are as thin as one monolayer (ML), which can be distinguished in the HAADF images because of the presence of Ga atomic sites in the lighter AlN matrix (see Fig. 9.22c, d).

Further time-resolved photoluminescence (TRPL) analyses were performed on the NW arrays and micro-photoluminescence (μ-PL) studies of individual NWs, demonstrating the 2D quantum confinement. Figure 9.22a includes a low-magnification image of a couple of NWs where QWRs are indicated with red arrows in one of them. The squared region in Fig. 9.22a is analyzed at higher magnification in Fig. 9.22b through the HAADF technique, revealing the atomic position of the single Ga atoms placed along the vertex direction. The figure also includes an inset showing a model of the structure.

5.2 Dumbbell Identification: Direct Polarity Assignment in Semiconductor NWs

In ionic crystals there is a charge transfer between the constituent elements, leading to the generation of atomic pairs with opposite partial charge called dumbbells, where the chemical bonding are partially ionized. The polarity in compound semiconductors emerges as a consequence of this partial iconicity of the chemical bonds. Relevant implications are related with polarity as the growth mechanism or the final optoelectronic properties of semiconductor materials. Thus, it is a matter of great importance determining the polarity for getting a deeper understanding of such materials. Moreover, changes in the polarity within a structure spoil its ultimate properties being crucial with the ability to confirm the polarity preservation. Especial attention must be paid in structures crystallized in the zinc-blende (ZB) phase, consisting in an ABC stacking sequence, where the presence of twin boundaries is quite frequent. The twin presence in the ZB structure generates a monolayer of the wurtzite (WZ) phase of the material (stacking sequence AB, see Fig. 9.23). So, both polymorphs are related by the presence of twin boundaries when they are along the [113] direction for the ZB and [0001] for the WZ [2, 6].

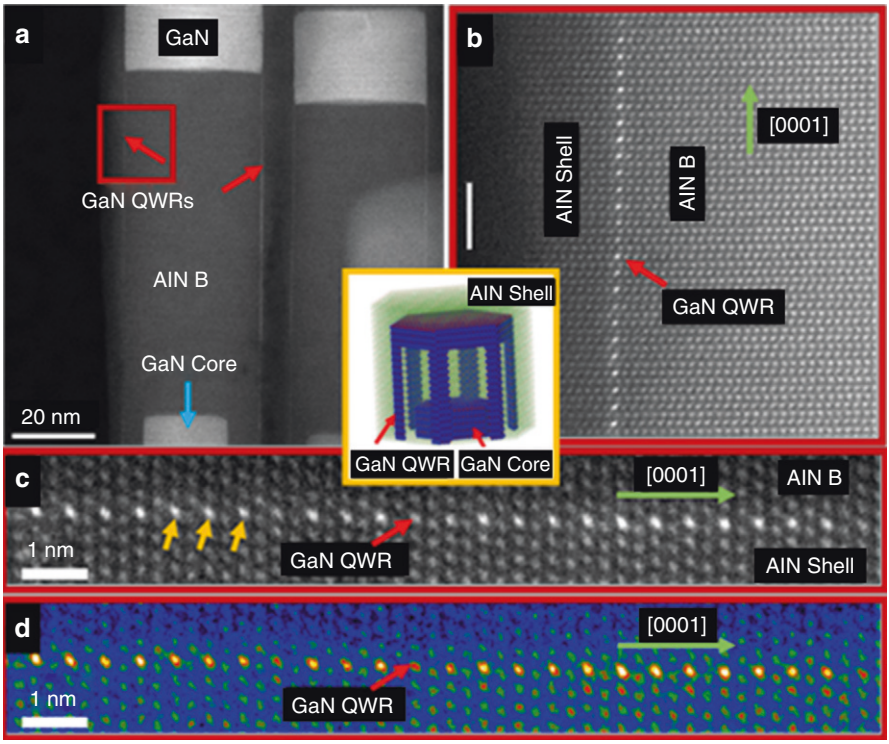


Fig. 9.22 (**a**) Low-magnification HAADF image of a couple of GaN/AlN core-shell NWs, showing QWs at the NW facets intersections (vertex). (**b**) High-resolution HAADF image of the region *squared* in (**a**) where the scale bar represents 2 nm. Ga sites are individually seen as brighter features, due to its higher atomic number. (**c**) and (**d**) are zoom in details of the QWs displayed as grey contrast in (**c**) and temperature color in (**d**). The *inset* shows a model of the structure of the NWs, pointing the core, the shell, and one of the QWs (Reprinted with permission from Ref. [89]. Copyright 2012. See also the following link for the corresponding animated 3D atomic models: http://www.icmab.cat/gaen/research/165)

Depending on the twin periodicity, different polytypes would appear in the structures ranging between the non-twinned case (ZB) and the completely twinned (WZ), some of which have been reported [90]. The structural differences between the polytypes give rise to variations in the electronic band alignment and, thus, in their optical properties [34, 91, 92]. Lots of binary semiconductors crystallized in one, another, or both phases, being their relative stabilities dependent on many factors [93, 94]. In addition, the presence of twin boundaries conditions the final morphology [8, 95, 96] and size [97] of the nanostructure. Anyway, these defects imply a 180° rotation of the structure around one of the [113] axes which can preserve (orthotwins) or invert (paratwins) [98] the polarity.

Until now, different microscopy-related techniques have been used to determine the polarity as convergent beam electron diffraction (CBED) [98–101], high-resolution transmission microscopy (HRTEM) [102–105], spectrum imaging (SI)

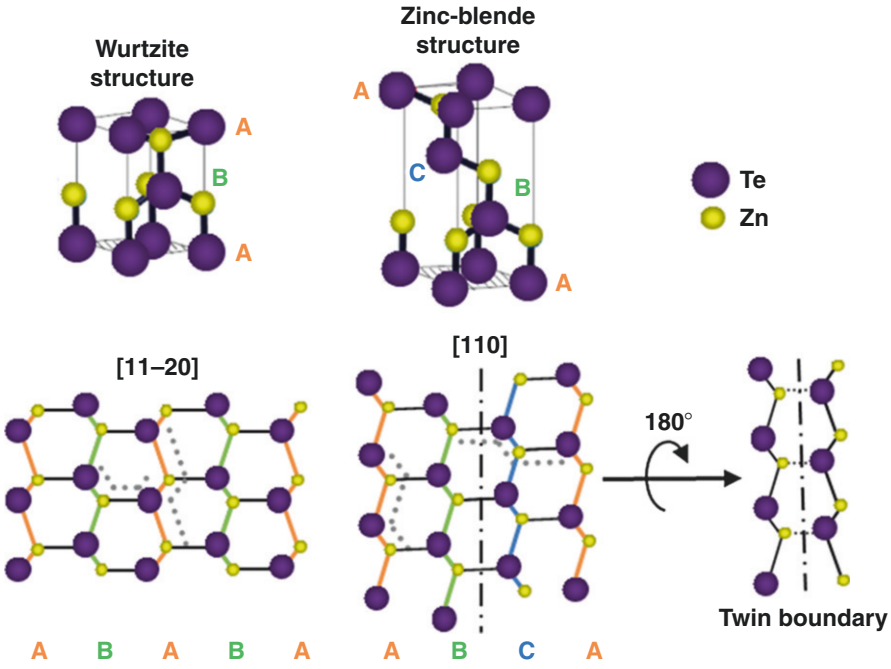


Fig. 9.23 WZ and ZB unit cell structures (*top row*) and their projections along the [11–22] and [112], respectively (*bottom row*). The WZ shows alternating dumbbell orientation while in the ZB keeps the orientation in the entire structure. The presence of twin boundaries along one {111} direction modifies the stacking sequence allowing the conversion from one structure to another or, depending in the twin periodicity, generating other polytypes

by means of electron energy-loss spectroscopy (EELS) [106–108] or dispersive X-ray spectroscopy (EDX) [109, 110], or scanning tunnel microscopy (STM) [111]. There is another easier procedure, consisting on assuming that the system is homoepitaxial and that the substrate polarity dictates the nanostructure polarity [112–115]. This method cannot be applied in nonpolar or amorphous substrates and does not consider possible polarity inversion at the interface. But every mentioned procedure has its own drawbacks and none of them allows direct atomic polarity assignment. For instance, to get an accurate diffraction pattern, it is needed a considerable sample volume. That excludes the smaller objects as nanostructures for the analysis, limiting the CBED applicability. Moreover, the lack of spatial resolution in CBED does not allow the detection of possible polarity changes at interfaces as antiphase boundaries. In the case of HRTEM, its high spatial resolution achieves the dumbbell visualization in suitable samples, being these nanostructured systems as thin and flat as possible. Nevertheless, to ensure the image interpretation, a complete analysis requires computer simulations complicating the study. Regarding the related EELS or EDX methods, they consume long time at each analysis and required intense electron beams,

conditions that often damage the material. The STM is not a universal method requiring previous sample treatment before the analysis. Thus, the polarity study in NWs can only be performed if they are located in conductive substrates or in the case they are embedded in a matrix and cleaving the substrate in situ. In addition, the technique not always can resolve the dumbbells and the lightest elements are not visible by STM.

As seen in the previous sections, HAADF and ABF can be used together as a powerful tool for obtaining atomic resolution images with almost direct contrast interpretation. So, analyzing semiconductor nanostructures under both techniques simultaneously in aberration-corrected microscopes allows direct atomic identification and thus polarity assignment. This "tandem" technique is especially interesting in two extreme cases: when dumbbells are formed by at least one light element and dealing with materials composed by similar atomic number elements.

5.2.1 Mapping Dumbbells with Medium and High Atomic Number Atoms

Whenever we want to measure the polarity on dumbbells composed of atoms with high and medium atomic number, the procedure can be as follows. As an example, the material selected in this case is ZnTe. As a consequence of their atomic numbers (30 and 52 for Zn and Te, respectively), both constituents can be imagined under HAADF conditions and they are different enough to allow direct identification by eye from the image contrast. Fig. 9.24a [116] shows a high-resolution HAADF image of the ZnTe structure along the [112] axis where the assignment of the atomic columns is straightforward with the Te (heavier and, thus, brighter) pointing to the growth direction. There are two dumbbell orientations which have been colored differently in the image and which are related by 180° rotations as correspond to the presence of twin boundaries (yellow dashed lines).

However, it is clear that the twins preserve the polarity and Te is always above Zn in the material dumbbells (orthotwins). The left upper inset of the figure shows the whole nanowire (NW) analyzed and the right one, the HAADF set up, employed. There is also enclosed a magnified detail of two dumbbells related by a twin, in grey scale and temperature colored. The red-squared dumbbell is used to obtain the intensity profile included in Fig. 9.24b, which unmistakably shows the higher Te intensity.

In order to compare HAADF and ABF, both techniques were applied to this material although, as it has just been shown, HAADF enables to solve the polarity in this material. The resulting ABF image can be seen in Fig. 9.24c. The inversion of contrast with respect to the HAADF is obvious. The left bottom inset, corresponding again to a magnified detail of two couples of dumbbells related by a twin, has been displayed in temperature color, showing darker contrast for the heavier element. The d) section of the figure shows the intensity profile along one dumbbell. As it was expected, both techniques are in agreement, providing two different tools for the polarity assignment when dealing with medium/heavy elements with the appropriated mass difference between constituents.

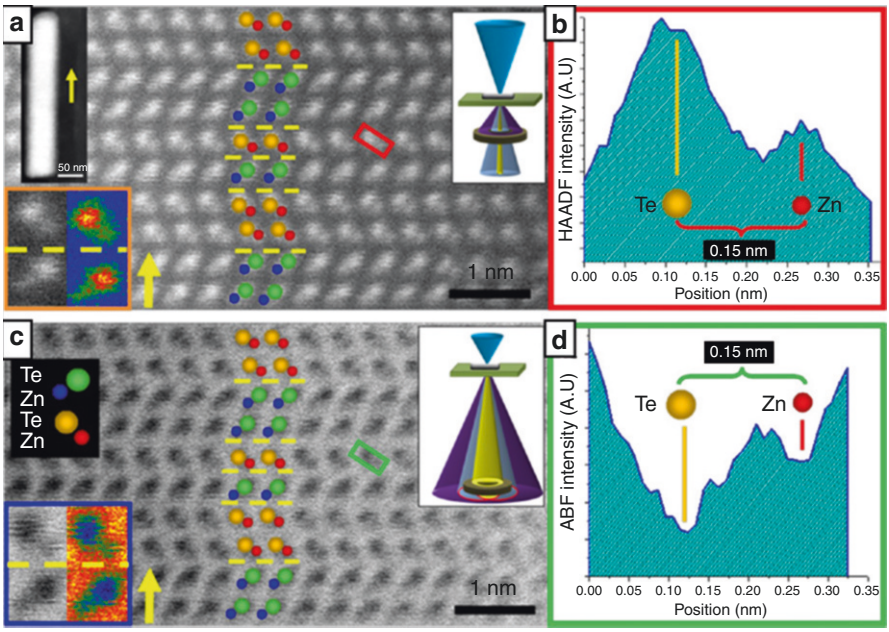


Fig. 9.24 (**a**, **c**) HAADF and ABF STEM images, respectively, of the ZnTe structure showing some of the dumbbells colored to differentiate the two orientations connected by twin boundaries (*yellow dashed lines*) and better distinguishable in the *bottom left* detail displayed as raw and as temperature color images. The *right inset* represents the used set up. The *left upper inset* in (**a**) shows the analyzed NW, including a *yellow arrow* pointing to the growth direction (the same as in the high-resolution images). (**b**, **d**) Intensity profiles along the *red* and *green squared* dumbbell in (**a**) and (**c**) (Reprinted with permission from Ref. [116]. Copyright 2012, American Chemical Society)

5.2.2 Mapping Dumbbells Including Light Atoms (e.g., N and O)

Following with the polarity study in the different semiconductor NWs, it is time to deal with light elements. Let's see what happen when applying the ABF technique to localize oxygen atomic sites in a ZnO NW [117]. Studying the NW shown in Fig. 9.25a under ABF conditions (Fig. 9.25b), the resulting image clearly shows the two different atomic columns, corresponding to Zn and O, where the O sites have always been found below the Zn atoms within the dumbbell. The perfect dumbbell zigzag along the entire NW ensures that no other polytypes are present but only the pure WZ crystalline phase. In the down panel (Fig. 9.25d) is represented the intensity profile taken along the arrow in Fig. 9.25c, which removes any assignment doubt, despite that atoms forming the dumbbell are only 1.2 Å apart.

Once established that NWs are Zn-polarized in the [0001] vertical growth direction, it is assumable that the wires should start growing from an (000–1) O-plane at the base, which is in contact with the substrate. In this research, the substrate is a certain kind of mica known as muscovite, which presents layered structure easily cleavable along the (001) planes (K^+-terminated), for obtaining clean surfaces devoid of adatoms. The goal of employing the mica substrate is to

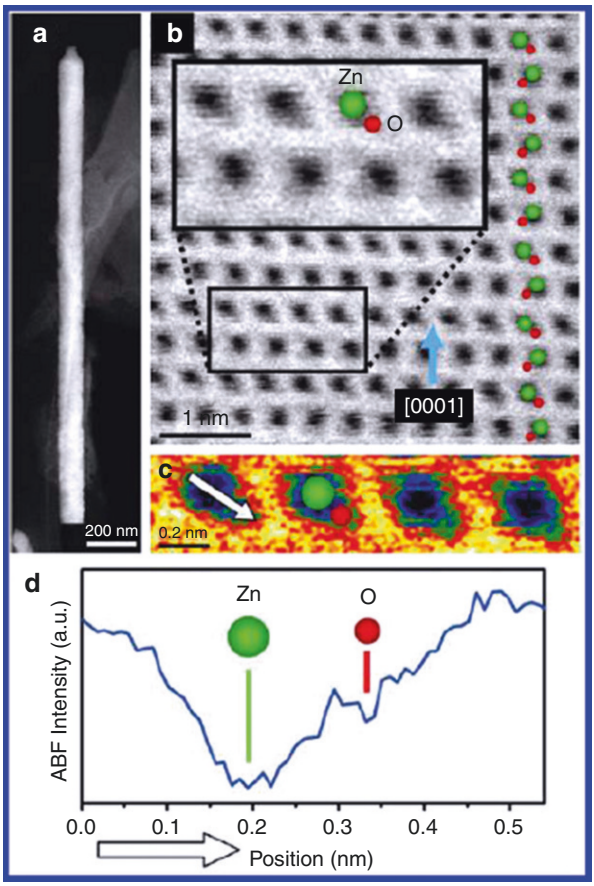


Fig. 9.25 (**a**) HAADF low-magnification micrograph of the entire ZnO NW analyzed. (**b**) ABF image of the ZnO structure. In the magnified detail in (**c**), taken from (**b**), one of the atomic stacking planes is shown in temperature color. Although in (**b**) and (**c**) the polarity assignment is straight forward, the study has been completed with the intensity profile displayed in (**d**) and performed along the *white arrow* in (**c**). The final conclusion is that the NWs show Zn polarity (Reprinted with permission from Ref. [117]. Copyright 2012, American Chemical Society)

attempt the growth of structures via the so-called Van der Waals epitaxy. After the structural analysis, it was seen that, despite the huge mismatch between the ZnO and muscovite phases (−8.36 % in the $[1\text{–}100]_{ZnO} \parallel [200]_{mica}$; and 64.0 % considering the $[11\text{–}20]_{ZnO} \parallel [020]_{mica}$), the NWs were allowed to grow and, moreover, there was an epitaxial relationship. Periodic misfit dislocations were found every 11 ZnO (1–120) planes and four muscovite (020) planes (corresponding to the 64.0 % mismatch direction) and every 12 (1–100) ZnO planes and 13 (100) mica ones (in the case of the −8.36 % of mismatch). These findings were employed to create the model included in Fig. 9.26, where the incommensurate Van der Waals epitaxy of the high quality ZnO arrays of NWs on the mica surface could be corroborated, concluding an epitaxial relationship as follow: $[0001]_{ZnO} \parallel [001]_{mica}$ [117].

In the context of working with less common substrates, we show the results obtained by Schuster et al. [118] using diamond as substrate to grow GaN NWs without neither catalyst nor buffer layer through the PAMBE synthesis procedure. They probed the high optical quality of the wires by photoluminescence

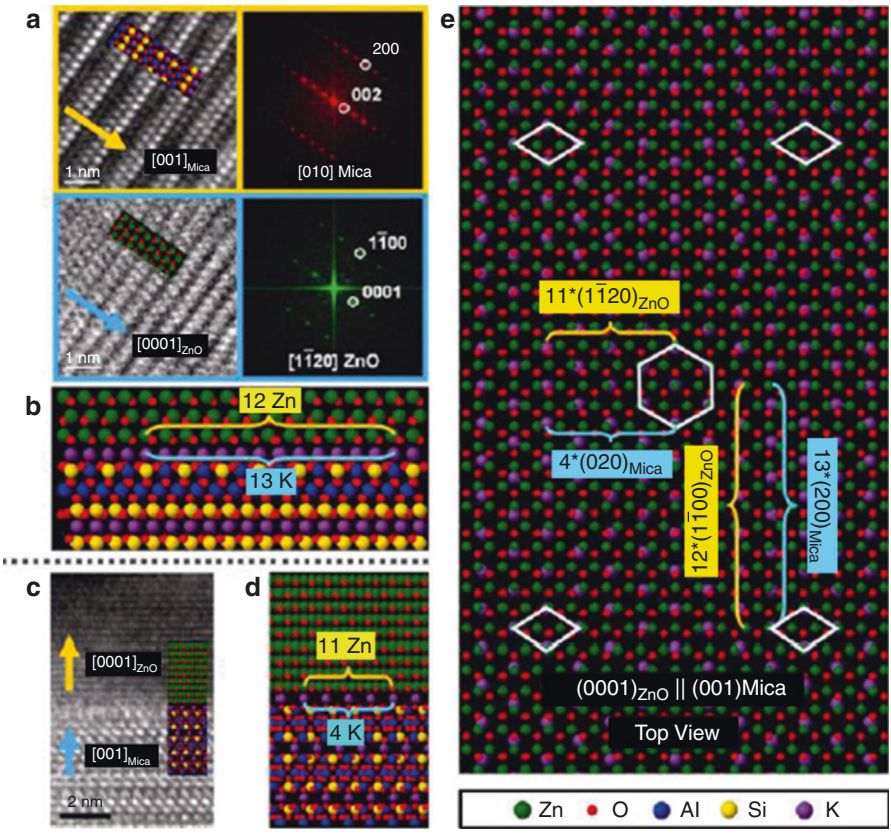


Fig. 9.26 (**a**) HRTEM images of the mica substrate (*yellow squared*) and ZnO structures (*blue squared*) within their FFTs and pointing the growth direction and (**b**) atomic model of both phases seen from the same axes as in the HRTEM image. (**c**) Shows a HRTEM image of the interface where the structural models are overlapped, while (**d**) is the model created of the same region. In (**e**) the structural model is seen along the growth direction where the misfit dislocation pattern can be seen (Reprinted with permission from Ref. [117]. Copyright 2012, American Chemical Society)

measurements, highlighting the method efficiency for obtaining promising semiconductor heterostructures for optoelectronic applications. Though high-resolution X-ray diffraction (HRXRD) analysis, they confirmed single domain growth and found the $[10–10]_{GaN} \parallel [01–1]_{Diamond}$ relationship between both crystallographic phases. Further studies on the system polarity were performed by means of ABF, showing N-polarized NWs along the growth direction (see Fig. 9.27b–c) indicating that the nucleation process took place by the biding of the Ga atoms to the O-terminated diamond surface. The HRTEM study is in accordance with the HRXRD results showing an abrupt interface (Fig. 9.27d, e) studied also under EELS conditions (Fig. 9.27f) to reject the possible interdiffusion.

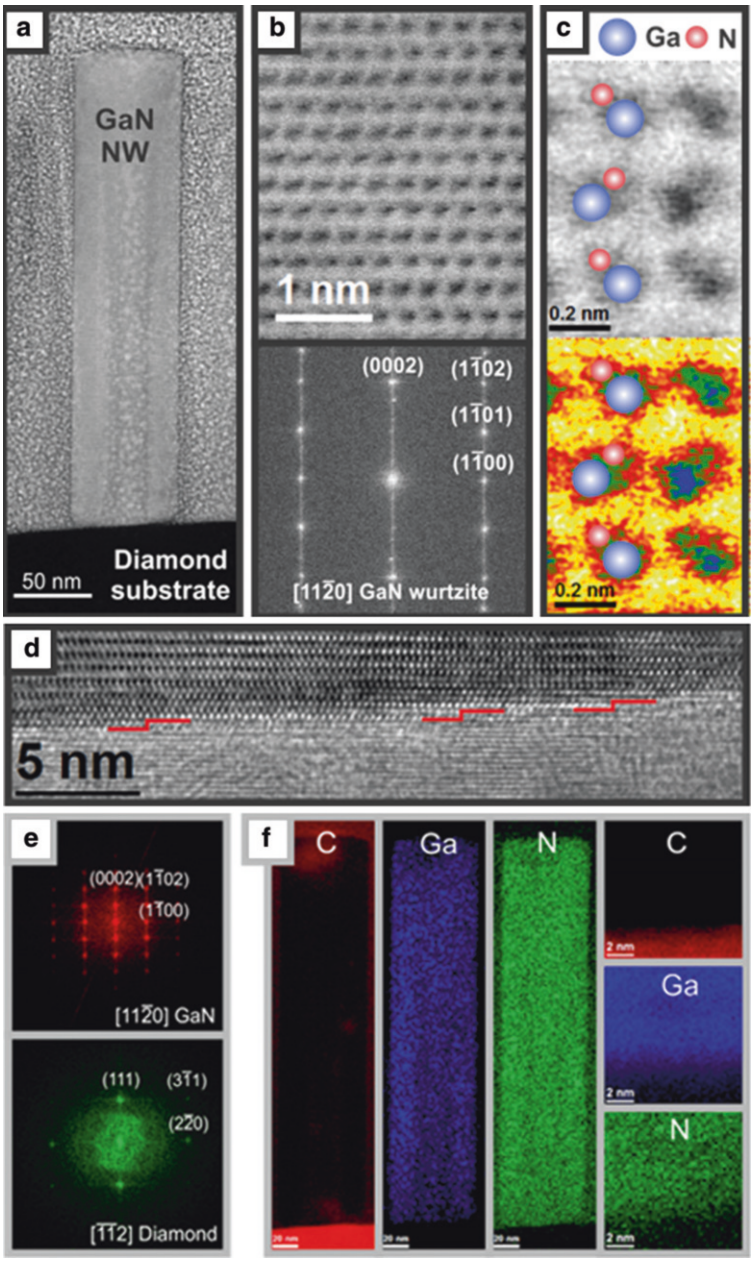


Fig. 9.27 (**a**) HAADF image of one studied GaN NW grown on diamond. In (**b**) there are the high-resolution ABF image and its FFT leading to assign the growth direction as the [0001]. The magnified details in (**c**) are used to establish the NW polarity as N. The high-resolution image in (**d**) highlight the abruptness of the interface, which was corroborated with the EELS maps displayed in (**f**) (Reprinted with permission from Ref. [118]. Copyright 2011, American Chemical Society)

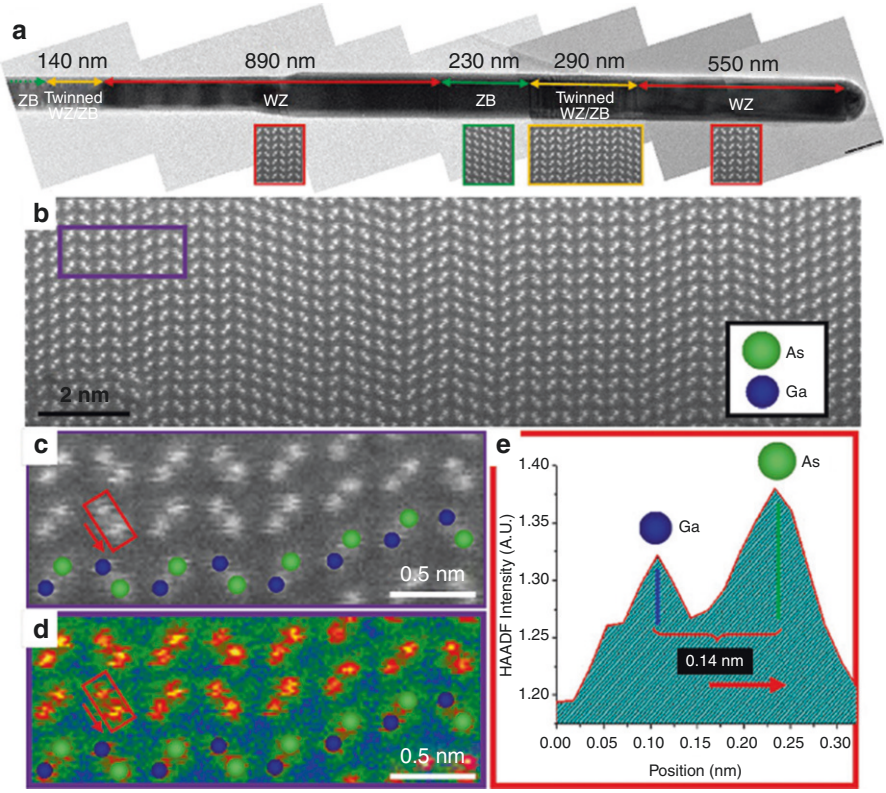


Fig. 9.28 (**a**) Low-magnification image of one GaAs NW studied showing modulated polytypic segments, including ZB and WZ. (**b**) GaAs structure Z-contrast image presenting different twin density in different regions. (**c**, **d**) Zoom in details displayed as raw and in temperature color, respectively, where the selected dumbbell for performing the intensity profile in (**e**) is *red squared*, as is found to be the favorite driving the growth (Reprinted with permission from Ref. [116]. Copyright 2012, American Chemical Society)

5.2.3 Polarity Influence on the Growth Mechanisms

Multiple Order Twinning Polarity Driven Growth in GaAs NWs on Si Substrates

In the case of materials where the dumbbells are constituted by similar atomic mass elements, as it is the case of GaAs NWs ($Z_{Ga} = 31$; $Z_{As} = 33$) (Fig. 9.28a), it is sometimes difficult to distinguish both elements. The sample shown here was grown by molecular beam epitaxy (MBE) with a great control of the growth parameters allowing the modulation of the structure [116]. So, the NW presents regions of pure ZB (marked in green), others with pure WZ (pointed in red), and zones with different polytypic mixtures (indicated in yellow). In the high-resolution HAADF image (Fig. 9.28b), the dumbbells are resolved but, although the atomic sites are properly separated, the observed intensity seems very similar even displaying the image in temperature color (see Fig. 9.28d). Nevertheless, taking

an intensity profile along one dumbbell the identification is unequivocal and the NWs have shown As polarity.

This polarity is in agreement with the one found in other studies performed in the same material and plays a key role in the understanding of the growth of the NWs on nonpolar substrates (such as Si) [119]. An explanation for the undesirable non-vertically growth of GaAs NWs, on Si substrates, pointing at different angles has been reported. In such case, the NWs were grown by the gallium-assisted method in a self-catalyzed process, [115] initiated, in the simpler case, with a monocrystalline octahedral seed faceted by {111} planes, half of which are Ga-polarized, called {111}A, while the other half are As-polarized or {111}B facets [119]. From the theoretical point of view, only {111}B facets allow the NW growth, which leads to two possibilities: (i) octahedral seed showing As-terminated surface allowing the perpendicular growth of the NW and (ii) octahedral seed with Ga-terminated surface, with three adjacent As-terminated facets at 19.47° allowing the growth along these directions. Nevertheless, the 41 % of the NWs grew at different angles, e.g., 34° or 51°, which cannot be explained with the single crystalline nucleation seed model.

Through high-resolution STEM analysis of the initial growth state performed in one branched seed, it was revealed that the presence of different octahedral grains in the seed (second and third order seeds, labeled in Fig. 9.29 as α and γ, respectively) related by twins and resulting in {111}B facets along the found angles of 34° and 51°. This mechanism is summarized in Fig. 9.29, which includes a low-magnification image of the seed studied (Fig. 9.29b) within a magnified detail of the region in direct contact with the Si substrate (Fig. 9.29a) and the resulting image from filtering the frequencies corresponding to the different grains (Fig. 9.29c) in the colors corresponding with their FFTs. Finally, the last panel (Fig. 9.29e) of the figure shows the proposed model for the nucleation seed within high-resolution HAADF details of the regions near the twins, which are all of them orthotwins. Finally, and thanks to the understanding of the growth mechanism by the precise polarity study, the 100 % growth of vertical GaAs NWs on Si substrates could be achieved [120].

Formation of Single ZnTe Nanowires, -Tripods, and -Tetrapods

The technological demand of nanometric devices has focused several investigations in the growth methods for obtaining such nanostructures. Several approaches, based on physical and chemical procedures, have been tested where a full comprehension of the growth process is desirable for its optimization. As an illustrative example, Utama et al. [121] have studied the genesis of ZnTe nanorods, tripods, and tetrapods by self-catalyzed methods using a free-adatom substrate (muscovite). With this kind of surface, the growing structure is pinned to the substrate via van der Waals forces, allowing any atomic plane to be in contact with the cleaved mica, meaning that both polarities can be expected. Thereby, the nanostructures start growing from an epitaxial nucleation seed attached to the substrate which, depending on the polarity seed, give rise to two types of architectures: (i) unidirectional growing structures or nanorods (from the Te-polarized seed) and (ii) branched structures as

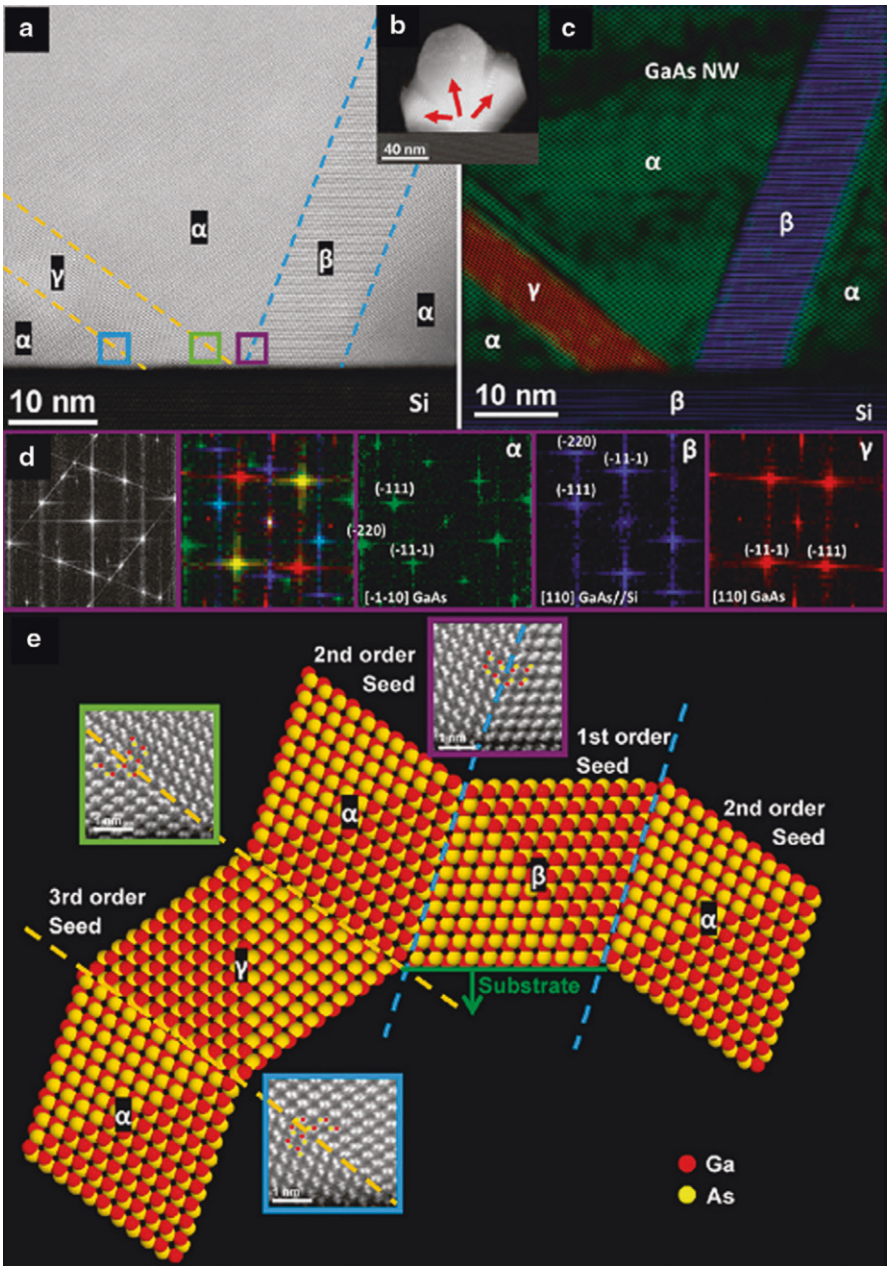


Fig. 9.29 (**a**) HAADF image of the interfacial region of the branched seed in (**b**), showing the presence of four twin boundaries that generate the higher order seeds, labeled as α and γ for the second and third order, respectively. The grain in intimate contact with the substrate is considered the first-order seed. Panel (**c**) was obtained by reconstructing the image from the filtrated frequencies of the different grains. The frequencies are extracted from the FFTs shown in (**d**),

tripods and tetrapods (if the growth starts with a Zn-polarized seed). In the above work, the authors can select the formation of those nanostructures by controlling the growth parameters.

Focusing on the nanorods, three different types could be distinguished attending to their morphology: nanorods presenting cylindrical cross-section, those with hexagonal one, and a third type with cylindrical base and faceted hexagonal tip. A careful inspection of the hybrid nanorods gave the authors the chance to compare the structural differences of the differentiated sections and relate them with the ultimate morphology of the rods. Compositional analyses were also performed checking that the cylindrical and faceted sections share composition and rejecting compositional changes as cause for the morphological transition. Nevertheless, the high-resolution analyses revealed the presence of many twin boundaries, and, more interestingly, changes in the defect densities were found in the different regions. Figure 9.30 shows a hybrid nanorod, where the different sections can be distinguished. From the selected area electron diffraction (SAED) patterns and the high-resolution images (performed in TEM, in the middle column and in HAADF in the right column), the structural differences are highlighted. At the tip of the nanorod (Fig. 9.30b–h, first row), we find the zinc-blende structure with some sparse twin boundaries that result in the presence of wide fringes of different contrast at the HRTEM image (Fig. 9.30e) and which is consistent with the spot duplicity (related by 180° rotations) seen at the SAED pattern.

Moving to the transitional section (Fig. 9.30c–i), there is an increase of the twin density which is more remarkable at the base of the nanorod (Fig. 9.30d–j). The random distribution of the twins prevents any periodicity and results in a variety of mixed polytypes, as reflects the high spot multiplicity at the SAED patterns. The HAADF images revealed that the structure is Te-polarized along the [-1-1-1] growth direction and that this polarity is preserved along the entire rod despite the defects (orthotwins). Anyway, with the lower defect concentration, the atomic stacking sequence (ABC, for the zinc-blende structure) can be completed allowing the faceted growth of the rods. However, when twin boundaries appear every few atomic planes, they restrict the formation of short truncated faceted segments with different shapes that pill up rotated (as a consequence of the twins) consecutively, resulting in cylindrical sections. Moreover, the different twin distribution is related with growth parameters, getting that the higher growth temperature favors the twin boundary formation obtaining cylindrical nanorods, while lower growth temperature allows the atomic sequence to be completed in a greater extension and forming the nanowire facets.

From the full characterization of the ZnTe nanorods, tripods, and tetrapods, it was possible to depict the underlying growth mechanism of the different structures. As it was mentioned above, the nanorods are always Te-polarized along the growth

Fig. 9.29 (continued) colored with the same code. (**e**) Model of the 3D twinning seed formulated to understand the different growing directions of the NWs found in the sample. *Insets* show the twins with atomic resolution (Adapted with permission from Ref. [119]. Copyright 2011, American Chemical Society. See also the following link for the corresponding animated 3D atomic models: http://www.icmab.cat/gaen/research/160)

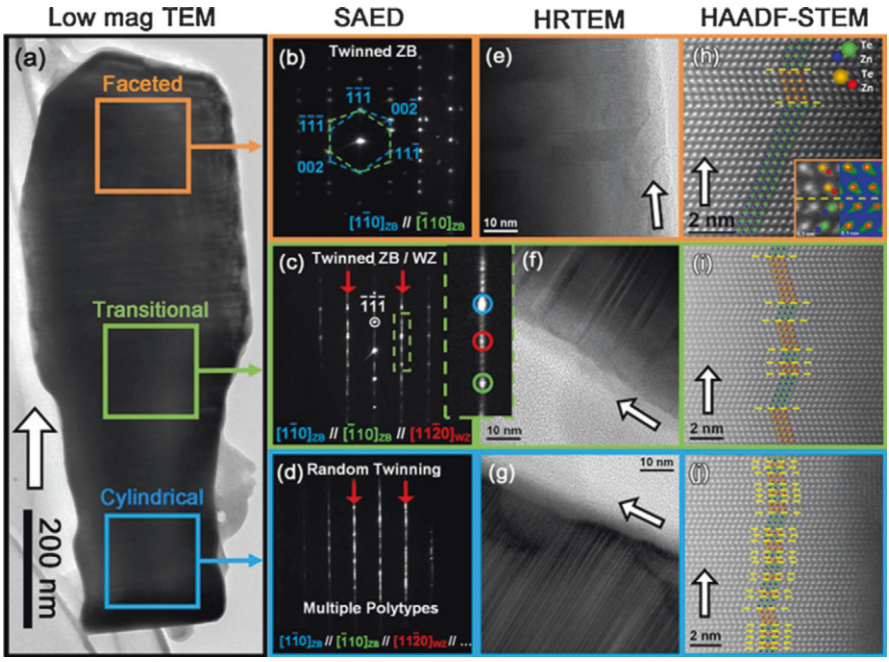


Fig. 9.30 (**a**) Low-magnification image of an entire hybrid nanorod. *Squared* in *orange*/*green*/*blue* are results presented from the faceted tip/transitional section/base: (**b**–**d**) SED patterns, (**e**–**g**) HRTEM image, and (**h**–**j**) high-resolution HAADF image (Reprinted with permission from Ref. [119]. Copyright 2012)

direction (see Fig. 9.30h–j), being the fast growth plane of the material. Thus, when the growth starts with the formation of a flat Te-polarized nucleation seed (see Fig. 9.31a), it would take place the unidirectional growth of the nanorod perpendicular to the substrate ($[\text{-}1\text{-}1\text{-}1]_{ZB}$ or $[000\text{-}1]_{WZ}$ direction). Regarding the tripods and tetrapods, it was also found that the legs of those architectures shared the nanorods polarization, and the presence of same kind of structural defects (orthotwin boundaries) could be noticed. The body (or central region) of these branched structures showed pure ZB structure. A tripod top view shows non-coplanar legs, 120° apart (see Fig. 9.31a). From the lateral view (modeled in Fig. 9.32b), we can observe the 19.5° angle between the substrate and the legs growth direction that is explained through the formation of an initial octahedral nucleation seed.

Considering an initial growth state started by the formation of an octahedral ZnTe seed, it must present four Zn-polarized surfaces and other four Te-polarized ones. If the seed grows with one Te-polarized facet in contact with the substrate, other three fast growth Te-polarized surfaces allow the growth of three legs (120° apart in projection) from the initial octahedron, creating a tripod (see Fig. 9.32b). If, instead, the seed is Te-polarized (Zn-surface touching the substrate), it shows four Te surfaces that result in the tetrapod formation through a more complex process involving second-order twining seeds (Fig. 9.32c, d). From an initial

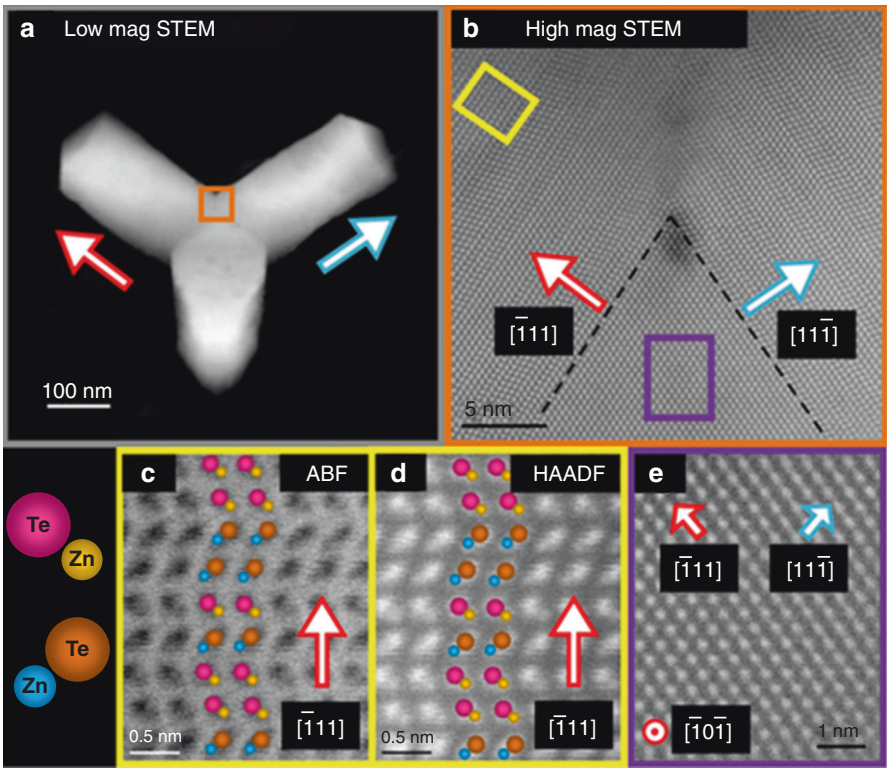


Fig. 9.31 (**a**) Low-magnification HAADF image of one ZnTe tripod pointing the region of interest magnified in (**b**), where it is presented a high-resolution HAADF image. In (**c**) and (**d**) the ABF and HAADF images of one tripod leg showing the Te polarity along the growth direction are displayed, while in (**e**) the high-resolution HAADF image of the tripod body is shown (Reprinted with permission from Ref. [121]. Copyright 2012)

octahedral truncated nucleation seed (interfered with the substrate), a twin boundary occurs in one of the fast growth directions, to get the second-order seed with octahedral morphology which is proposed as the nucleating agent for the tetrapod growth. At that point, the growth goes on following the fast growth directions to generate the tetrapods. There are two possibilities for the first-order seed truncation as it interferes with the substrate: (i) when the seeds are truncated by the (101) planes, leading to tetrapods with one shorter leg (type 1, Fig. 9.32c) and (ii) seeds supported on the (121) planes, result in tetrapods with two shorter legs (two legs growth directed to the substrate, type 2, Fig. 9.32d).

5.2.4 Polarity Influence on the Electronic and Optoelectronic Properties in NWs

As we comment along this section, polarity is not only relevant for getting deeper insights about the growth mechanisms but also its preservation has great impact in the

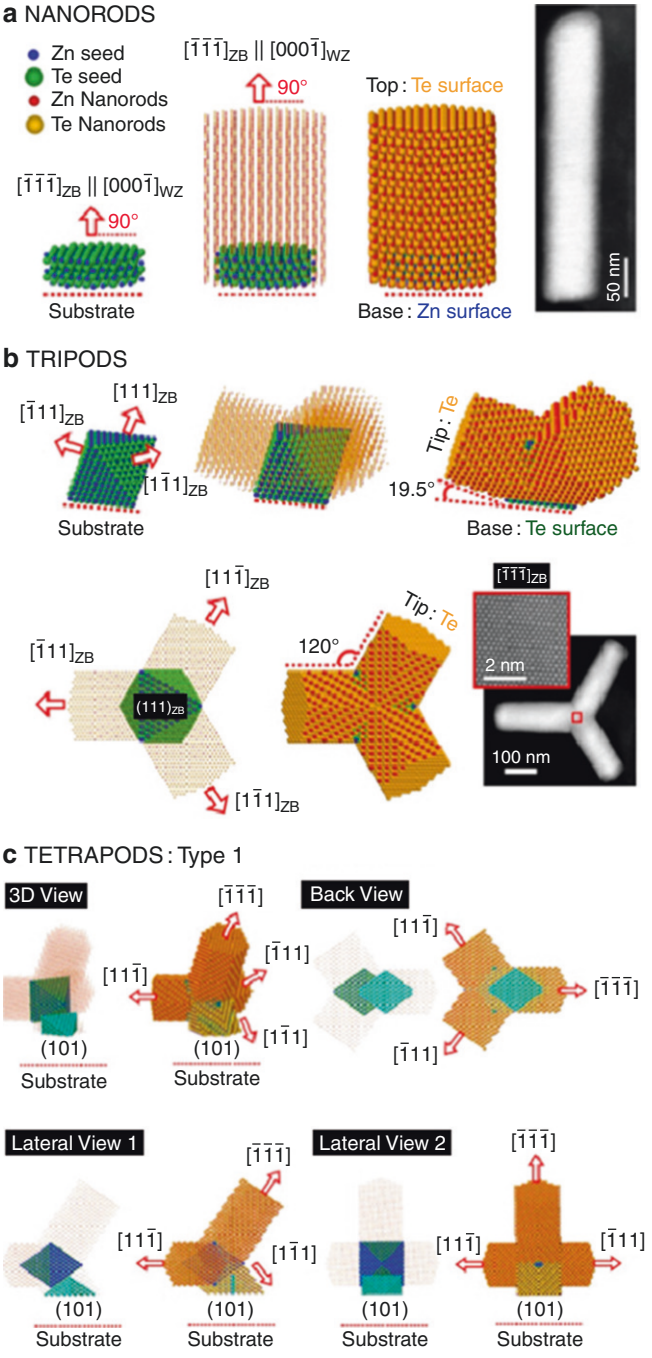


Fig. 9.32 (continued)

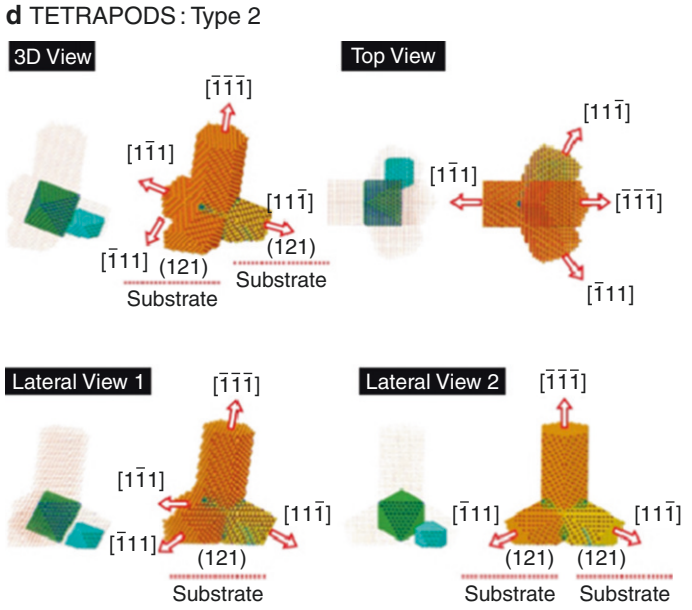


Fig. 9.32 Proposed growth mechanism models for ZnTe (**a**) nanorods, (**b**) tripods (**c**), and (**d**) tetrapods. (**a**) The seed shows Zn-terminated surface in direct contact with the substrate allowing the Te-driving growth. Inversely, (**b**) when an octahedral seed is located with Te pointing to the substrate, there are three more seed facets Te-polarized equivalent, which leads to the tripod formation. An initial-twinned octahedral seed interfering a (101) plane with the substrate, type 1 in (**c**), or (121), type 2 in (**d**), results in a tetrapod with one (**c**) or two (**d**) shorter legs (Reprinted with permission from Ref. [121]. Copyright 2012. See also the following link for the corresponding animated 3D atomic models: http://www.icmab.cat/gaen/research/179)

final material properties. To illustrate the detrimental effect of a polarity inversion within a material, de la Mata et al. simulated the conductance variation as a consequence of the presence of twin boundaries in the case of the GaAs [116]. Figure 9.33 comprises the three different models of the structures emerging from the presence of a twin boundary: the case of a nonpolar twin or orthotwin (Fig. 9.33a) and the two possibilities in the case of a polar one or paratwin (differentiating between the Ga–Ga facing, shown in Fig. 9.33b, and the As–As, in Fig. 9.33c).

Through density functional theory (DFT) calculations using the Siesta code [122], the conductance is analyzed following the Landauer formalism [123] (Fig. 9.33d) in three cases: pristine GaAs, twinned GaAs with polarity preservation, and GaAs with polarity inversion. The better conductivity is found for the defect-free material. Nevertheless, it can be seen that the presence of nonpolar defects have a minor detrimental effect in the conductivity, especially at the valence band where it is almost completely preserved, while the polar inversion in the paratwins spoils the final GaAs conductivity. Furthermore, the electrostatic potential plot also included in Fig. 9.33e evidences the difference not only between polar

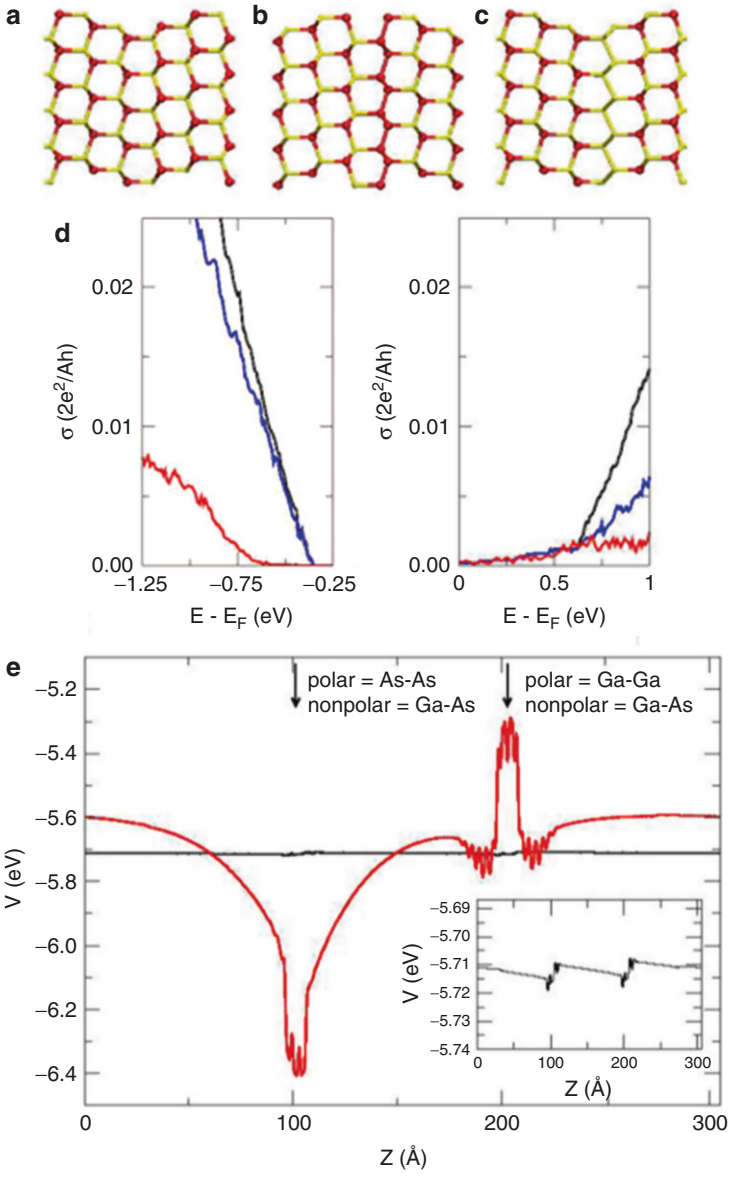


Fig. 9.33 Atomic models of the GaAs structure presenting one nonpolar twin (**a**), one As–As polar twin (**b**), and one Ga–Ga polar twin (**c**). (**d**) Conductivity plot at the valence and conduction bands for the case of pristine GaAs (*black curve*), GaAs twinned by nonpolar defects (*blue*), and GaAs presenting polar twins (*red*). (**e**) The simulated electrostatic potential (V) of GaAs preserving the polarity is shown in *black*, while the *red curve* represents V when polarity inversion takes place. As–As twins act as hole scattering centers ($z \sim 100$ Å) and Ga–Ga twins act as electron scattering centers ($z \sim 200$ Å) (Reprinted with permission from Ref. [116]. Copyright 2012, American Chemical Society)

(red curve) and nonpolar (black) twins but also between the two possible polar twins. It was found that the Ga–Ga paratwins type act as an electron scattering center while the As–As type is a hole scattering center.

6 Conclusions and Future Perspective

Along this chapter we have reviewed some of the last advances in STEM concerning the direct visualization of atomic columns and even isolated atoms, centering our review on results obtained in semiconductor nanowires. The magnetic lenses correctors for the spherical aberration and the monochromators development are the most relevant instrumental improvements of the last decade in the field of electron microscopy. Their implementation in transmission electron microscopes enhances the spatial resolution, resulting in resolution limits below 0.5 Å. One of the major advantages introduced is the possibility of forming smaller electron probes with higher currents, which makes spectrometry analysis much faster, minimizing beam-induced damage and the spatial drift.

With the benefits introduced by the instrumental novelties, more sophisticated techniques can be developed. Playing with different detector geometries and their location, different signals can be collected. In this context, the employment of annular detectors at different collection angles have been the key points allowing the formation of Z-contrast images if the collection angle is high enough (HAADF). If not, low collection angles neglecting the transmitted beam (ABF) give rise to phase images sensitive to the presence of light elements, otherwise very hard to obtain. Even collecting the signal in the bright-field region for middle angles (MABF) can be useful to detect heavy and light elements with opposite contrast.

Several examples regarding the technological and methodological advances in the transmission electron microscopy and related techniques are included, especially focused on nanowires characterizations. Nanostructures as nanowires are typical cases of study, where a full structure characterization can be needed even at the atomic scale. The atomic polarity study shown here gives the chance to discuss very frequent features in these materials as the presence of twin boundaries, presence of different polytypes, or deduced growth mechanisms. In the near future, improvement of the resolution in the STEM techniques by including, for example, the chromatic aberration correction, may lead to new and deeper analyses, identifying individual atoms such as dopants within the same nanowire heterostructures. Further improvements in this way may lead to a complete understanding of the growth mechanisms and physical properties of future-designed nanodevices.

References

1. Spirkoska D, Arbiol J, Gustafsson A, Conesa-Boj S et al (2009) Structural and optical properties of high quality zinc-blende/wurtzite GaAs nanowire heterostructures. Phys Rev B 80(24):245325

2. Arbiol J, Estrade S, Prades JD, Cirera A et al (2009) Triple-twin domains in Mg doped GaN wurtzite nanowires: structural and electronic properties of this zinc-blende-like stacking. Nanotechnology 20(14):145704
3. Ketterer B, Heiss M, Uccelli E, Arbiol J, I Morral AF (2011) Untangling the electronic band structure of wurtzite GaAs nanowires by resonant raman spectroscopy. ACS Nano 5(9):7585–7592
4. Heiss M, Conesa-Boj S, Ren J, Tseng H-H et al (2011) Direct correlation of crystal structure and optical properties in wurtzite/zinc-blende GaAs nanowire heterostructures. Phys Rev B 83(4):045303
5. Zardo I, Conesa-Boj S, Peiro F, Morante JR et al (2009) Raman spectroscopy of wurtzite and zinc-blende GaAs nanowires: polarization dependence, selection rules, and strain effects. Phys Rev B 80(24):245324
6. Arbiol J, I Morral AF, Estrade S, Peiro F et al (2008) Influence of the (111) twinning on the formation of diamond cubic/diamond hexagonal heterostructures in Cu-catalyzed Si nanowires. J Appl Phys 104(6):064312
7. Lopez FJ, Hemesath ER, Lauhon LJ (2009) Ordered stacking fault arrays in silicon nanowires. Nano Lett 9(7):2774–2779
8. Algra RE, Verheijen MA, Borgstrom MT, Feiner L-F et al (2008) Twinning superlattices in indium phosphide nanowires. Nature 456(7220):369–372
9. Hernandez-Ramirez F, Prades JD, Tarancon A, Barth S et al (2007) Portable microsensors based on individual SnO_2 nanowires. Nanotechnology 18(49):495501
10. Duan X, Huang Y, Agarwal R, Lieber CM (2003) Single-nanowire electrically driven laser. Nature 421:241–245
11. Gudiksen MS, Lauhon LJ, Wang J, Smith DC, Lieber CM (2002) Growth of nanowire superlattice for nanoscale photonics and electronics. Nature 415:617–620
12. Huang MH, Mao S, Feick H, Yan H et al (2001) Room-temperature ultraviolet nanowire nanolasers. Science 292(5523):1897–1899
13. Moore D, Morber JR, Snyder RL, Wang ZL (2008) Growth of ultralong ZnS/SiO_2 core-shell nanowires by volume and surface diffusion VLS process. J Phys Chem C 112:2895–2903
14. Moore DF, Ding Y, Wang ZL (2004) Crystal orientation-ordered ZnS nanowire bundles. J Am Chem Soc 126(14372):2895–2903
15. Chueh Y-L, Hsieh C-H, Chang M-T, Chou L-J et al (2007) RuO_2 nanowires and RuO_2/TiO_2 core/shell nanowires: form synthesis to mechanical, optical, electrical, and photoconductive properties. Adv Mater 19(1):143–149
16. Lao CS, Gao PX, Zhang L, Davidovic D et al (2006) ZnO nanobelt/nanowire schottky diodes formed by dielectrophoresis alignment across Au electrodes. Nano Lett 6(2):263–266
17. Zhou J, Deng SZ, Gong L, Ding Y et al (2006) Growth of large-area aligned molybdenum nanowires by high temperature chemical vapor deposition: synthesis, growth mechanism, and device application. J Phys Chem B 110:102–196
18. Ponzoni A, Comini E, Sberveglieri G, Zhou J et al (2006) Ultrasensitive and highly selective gas sensors using three-dimensional tungsten oxide nanowire networks. Appl Phys Lett 88:203101
19. Wang X, Zhou J, Song J, Liu J et al (2006) Piezoelectric field effect transistor and nanoforce sensor based on a single ZnO nanowire. Nano Lett 6(12):2768–2772
20. Zhou J, Fei P, Gao Y, Gu Y et al (2008) Mechanical–electrical triggers and sensors using piezoelectric micowires/nanowires. Nano Lett 8(9):2725–2730
21. Liu A (2008) Towards development of chemosensors and biosensors with metal-oxide-based nanowires or nanotubes. Biosens Bioelectron 24(2):167–177
22. Cui Y, Wei Q, Park H, Lieber CM (2001) Nanowire nanosensors for highly sensitive and selective detection of biological and chemical species. Science 293(5533):1289–1292
23. Patolsky F, Timko BP, Yu G, Fang Y et al (2006) Detection, stimulation, and inhibition of neuronal signals with high-density nanowire transistor arrays. Science 313(5790): 1100–1104

24. Liu J, Wang X, Peng Q, Li Y (2006) Preparation and gas sensing properties of vanadium oxide nanobelts coated with semiconductor oxides. Sensors and Actuators B 115:481–487
25. Comini E, Faglia G, Ferroni M, Ponzoni A et al (2009) Metal oxide nanowire: preparation and application in gas sensing. J Mol Catal A: Chem 305:170–177
26. Arbiol J, Cirera A, Peiro F, Cornet A et al (2002) Optimization of tin dioxide nanosticks faceting for the improvement of palladium nanocluster epitaxy. Applied Physics Letters 80(2):329–331
27. Hernandez-Ramirez F, Tarancon A, Casals O, Arbiol J et al (2007) High response and stability in CO and humidity measures using a single SnO_2 nanowire. Sensors Actuators B 121:3–17
28. Ketterer B, Arbiol J, i. Morral AF (2011) Phonon confinement and plasmon-phonon interaction in nanowire-based quantum wells. Phys Rev B 83(24):245327
29. Heiss M, Ketterer B, Uccelli E, Morante JR, Arbiol J et al (2011) In(Ga)As quantum dot formation on group-III assisted catalyst-free InGaAs nanowires. Nanotechnology 22(19):195601
30. Uccelli E, Arbiol J, Morante JR, Fontcuberta A, Morral I (2010) InAs quantum dot arrays decorating the facets of GaAs nanowires. ACS Nano 4(10):5985–5993
31. Heigoldt M, Arbiol J, Spirkoska D, Rebled JM et al (2009) Long range epitaxial growth of prismatic heterostructures on the facets of catalyst-free GaAs nanowires. J Mater Chem 19(7):840–848
32. Morral AF, Spirkoska D, Arbiol J, I Heigoldt M et al (2008) Prismatic quantum heterostructures synthesized on molecular-beam epitaxy GaAs nanowires. Small 4(7):899–903
33. Qian F, Li Y, Gradeak S, Park H-G et al (2008) Multi-quantum-well nanowire heterostructures for wavelength-controlled lasers. Nat Mater 7:701–706
34. Zhang L, Luo JW, Zunger A, Akopian N et al (2010) Wide InP nanowires with wurtzite/zincblende superlattice segments are type-II whereas narrower nanowires become type-I: an atomistic pseudopotential calculation. Nano Lett 10(10):4055–4060
35. Henglein A (1989) Small-particle research: physicochemical properties of extremely small colloidal metal and semiconductor particles. Chem Rev 89(8):1861–1873
36. Yang J-H, Chen S, Yin W-J, Gong XG (2009) Electronic structure and phase stability of MgTe, ZnTe, CdTe, and their alloys in the B3, B4, and B8 structures. Phys Rev B 79(24):245202
37. Wang J, Li M, Altman EI (2004) Scanning tunneling microscopy study of self-organized Au atomic chain growth on Ge(001). Phys Rev B 70(23):233312
38. Ma DDD, Lee CS, Au FCK, Tong SY, Lee ST (2003) Small-diameter silicon nanowire surfaces. Science 299:1874–1877
39. Mikkelsen A, Sköld N, Ouattara L, Borgström M et al (2004) Direct imaging of the atomic structure inside a nanowire by scanning tunnelling microscopy. Nature 3:519–523
40. Xu T, Dick KA, Plissard S, Nguyen TH et al (2012) Faceting, composition and crystal phase evolution in III–V antimonide nanowire heterostructures revealed by combining microscopy techniques. Nanotechnology 23(9):095702
41. Kisielowski C, Freitag BB, Bischoff M, van Lin H et al (2008) Detection of single atoms and buried defects in three dimensions by aberration corrected electron microscope with 0.5Å Information limit. Microsc Microanal 14(5):467–477
42. Haider M, Uhlemann S, Schwan E, Rose H et al (1998) Electron microscopy image enhanced. Nature 392:768–769
43. Rose H (1990) Outline of a spherically corrected semiaplanatic medium-voltage transmission electron-microscope. Optik 85(1):19–24
44. Letzen M, Jahnen B, Jia CL, Thust A et al (2002) High-resolution imaging with an aberration-corrected transmission electron microscope. Ultramicroscopy 92:233–242
45. O'Keefe MA (2008) Seeing atoms with aberration-corrected sub-ångström electron microscopy. Ultramicroscopy 108:196–209
46. Ohtsuka M, Yamazaki T, Kotaka Y, Hashimoto I, Watanabe K (2012) Imaging of light and heavy atomic columns by spherical aberration corrected middle-angle bright-field STEM. Ultramicroscopy 120:48–55

47. Batson PE, Delby N, Krivanek OL (2002) Sub-ångstrom resolution using aberration corrected electron optics. Nature 418:617–620
48. Nellist PD, Chisholm MF, Dellby N, Krivanek OL et al (2004) Direct sub-angstrom imaging of a crystal lattice. Science 305(5691):1741
49. Caroff P, Wagner JB, Dick KA, Henrik HA et al (2008) High quality InAs/InSb nanowire heterostructrues grown by metalorganic vapour phase epitaxy. Small 4(7):878–882
50. Ouattara L, Mikkelsen A, Sköld N, Knaapen T et al (2007) GaAs/AlGaAs nanowire heterostructures studied by scanning tunneling microscopy. Nano Lett 7(9):2859–2864
51. Hilner E, HåKanson U, Fröberg LE, Karlsson M et al (2008) Direct atomic scale imaging of III-V nanowire surfaces. Nano Lett 8(11):3978–3982
52. Dick KA, Bolinsson J, Borg BM, Johanson J (2012) Controlling the abrupness of axial heterojunctions in III-V nanowires: beyond the reservoir effect. Nano Lett 12(6):3200–3206
53. Okunishi E, Ishikawa I, Sawada H, Hosokawa F et al (2009) Visualization of light elements at ultrahigh resolution by STEM annular bright field microscopy. Microsc Microanal 15(Suppl 2):164–165
54. Saxton WO, Jenkins WK, Freeman LA, Smith DJ (1978) TEM observations using bright field hollow cone illumination. Optik 49:505–510
55. Findlay SD, Shibata N, Sawada H, Okunishi E et al (2010) Dynamics of anular bright field imaging in scanning transmission electron microscopy. Ultramicroscopy 110(7):903–923
56. He X, Gu L, Zhu C, Yu Y et al (2011) Direct imaging of lithium ions using aberration-corrected annular-bright-field scanning transmission electron microscopy and associated contrast mechanisms. Mat Express 1(1):43–50
57. Findlay SD, Azuma S, Shibata N, Okunishi E, Ikuhara Y (2011) Direct oxygen imaging within a ceramic interface, with some observations upon the dark contrast at the grain boundary. Ultramicroscopy 111:285–289
58. Findlay SD, Saito T, Shibata N, Sato Y et al (2010) Direct imaging of hydrogen within a crystalline enviroment. Appl Phys Express 3:116603
59. Ishikawa R, Okunishi E, Sawada H, Kondo Y et al (2011) Direct imaging of hydrogen-atom columns in a crystal by annular bright-field electron microscopy. Nat Mater 10(4):278–281
60. Hosokura T, Iwaji N, Nakagawa T, Ando A et al (2011) (100)-Oriented $SrTiO_3$/$BaTiO_3$ artificial superlattices fabricated by chemical solution deposition. Cryst Growth Des 11(10):4253–4256
61. Kotaka Y (2012) Direct visualization method of the atomic structure of light and heavy atoms with double-detector Cs corrected scanning transmission electron microscopy. Appl Phys Letters 101:133107
62. Stadelmann PA (1987) EMS-A software package for electron diffraction analysis and HREM image simulationin material science. Ultramicroscopy 21(2):131–146
63. Amali A, Rez P (1997) Theory of lattice resolution in high-angle annular dark-field images. Microsc Microanal 3:28–46
64. Kirkland EJ, Loane RF, Silcox J (1987) Simulation of annular dark field STEM images using a modified multislice method. Ultramicorscopy 23:77–96
65. Ishizuka K (2002) A practical approach for STEM image simulation based on the FFT multislice method. Ultramicroscopy 90(2–3):71–83
66. Pennycook SJ, Jesson DE (1988) High-resolution Z-contrast imaging of crystals. Ultramicroscopy 37(1–4):14–38
67. Wang ZL, Cowley JM (1989) Simulating high-angle annular dark-field STEM images including inelastic thermal diffuse scattering. Ultramicroscopy 31(4):437–454
68. Dinges C, Berger A, Rose H (1995) Simulation of TEM images considering phonon and electronic excitations. Ultramicroscopy 60(1):49–70
69. Hartel P, Rose H, Dinges C (1996) Conditions and reasons for incoherent imaging in STEM. Ultramicroscopy 63(2):93–114

70. Nakamura K, Kakibayashi H, Kanehori K, Tanaka N (1997) Position dependence of the visibility of a single gold atom in silicon crystals in HAADF-STEM image simulation. J Electron Microsc 46(2):119–127
71. Voyles PM, Grazul JL, Muller DA (2003) Imaging individual atoms inside crystals with ADF-STEM. Ultramicroscopy 96(3–4):251–273
72. Grillo V (2009) The effect of surface strain relaxation on HAADF imaging. Ultramicroscopy 109(12):1453–1464
73. Grillo V, Rossi F (2011) A new insight on crystalline strain and defect features by STEM-ADF imaging. J Cryst Growth 318:1151
74. Bosman M, Keast VJ, García-Muñoz JL, D'Alfonso AJ et al (2007) Two-dimensional mapping of chemical information at atomic resolution. Phys Rev Lett 99(8):086102
75. Kourkoutis LF, Xin HL, Higuchi T, Hotta Y et al (2010) Atomic-resolution spectroscopic imaging oxide interfaces. Phil Mag 90(35–36):4731–4749
76. Rossell MD, Ramasse QM, Findlay SD, Rechberger F et al (2012) Direct imaging of dopant clustering in metal oxide nanoparticles. ACS Nano 6(8):7077–7083
77. Suenaga K, Sato Y, Liu Z, Kataura H et al (2009) Visualizing and identifying single atoms using electron energy-loss spectroscopy with low accelerating voltage. Nat Chem 1:415–418
78. Muller DA, Kourkoutis LF, Murfitt M, Song JH et al (2008) Atomic-scale chemical imaging of composition and bonding by aberration-corrected microscopy. Science 319:1073
79. Bosman M, Watanabe M, Alexander DTL, Keast VJ (2006) Mapping chemical and bonding information using multivariate analysis of electron energy-loss spectroscopy. Ultramicroscopy 106(11–12):1024–1032
80. Tan H, Turner S, Yücelen E, Verbeeck J, Van Tendeloo G (2011) 2D Atomic mapping of oxidation states in transition metal oxides by scanning transmission electron microscopy and electron energy-loss spectroscopy. Phys Rev Lett 107:107602
81. Turner S, Verbeeck J, Ramezanipour F, Greedan JE et al (2012) Atomic resolution coordination mapping in Ca_2FeCoO_5 brownmillerite by spatially resolved electron energy-loss spectroscopy. Chem Mater 24:1904–1909
82. D'Afonso AJ, Freitag B, Klenov D, Allen LJ (2010) Atomic-resolution chemical mapping using energy-dispersive x-ray spectroscopy. Phys Rev B 81:100101
83. Allen LJ, D'Alfonso AJ, Freitag B, Klenov DO (2012) Chemical mapping at atomic resolution using energy-dispersive x-ray spectroscopy. MRS Bull 37:47–52
84. Oh SH, van Benthem K, Molina SI, Borisevich AY et al (2008) Point defect configurations of supersaturated Au atoms inside Si nanowires. Nano Lett 8(4):1016–1019
85. Allen JE, Hemesath ER, Perea DE, Lensch-Falk JL et al (2008) High-resolution detection of Au catalyst atoms in Si nanowires. Nat Nanotechnol 3:168–173
86. Dick KA, Deppert K, Larlsson LS, Wallenberg LR et al (2005) A new understanding of Au-assisted growth of III-V semiconductor nanowires. Adv Funct Mater 15(10):1603–1610
87. Hao Y, Meng G, Wang ZL, Ye C, Zhang L (2006) Periodically twinned nanowires and polytypic nanobelts of ZnS: the role of mass diffusion in vapor-liquid–solid growth. Nano Lett 6(8):1650–1655
88. Bar-Sadan M, Barthel J, Shtrikman H, Houben L (2012) Direct imaging of single Au atoms within GaAs nanowires. Nano Lett 12(5):2352–2356
89. Arbiol J, Magen C, Becker P, Jacopin G et al (2012) Self-assembled GaN quantum wires on GaN/AlN nanowire templates. Nanoscale 4(23):7517–7524
90. Ramsdell LS (1947) Studies on silicon carbide. Am Mineral 32:64–82
91. Lopez FJ, Hemesath ER, Lauhon LJ (2009) Ordered stacking fault arrays in silicon nanowires. Nano Lett 9(7):2774–2779. doi:10.1021/nl901315s
92. Bao J, Bell DC, Capasso F (2008) Optical properties of rotationally twinned InP nanowire heterostructures. Nano Lett 8(3):836–841
93. Caroff P, Bolinsson J, Johansson J (2011) Crystal phases in III-V nanowires: from random toward engineered polytypism. IEEE J Sel Top Quantum Elecron 17(4):829–846

94. Dubrovskii VG, Sibirev NV (2008) Growth thermodynamics of nanowires and its application to polytypism of zinc blende III-V nanowires. Phys Rev B 77(3):035414
95. Kitauchi Y, Kobayashi Y, Tomioka K, Hara S et al (2010) Structural transition in indium phosphide nanowires. Nano Lett 10(5):1699–1703
96. Algra RE, Verheijen MA, Feiner L-F, Immink GGW et al (2010) Paired twins and 11–2 morphology in GaP nanowires. Nano Lett 10(7):2349–2356
97. Li Q, Wang C, Wang J, Ip K, Hark S (2004) Size-dependent periodically twinned ZnSe nanowires. Adv Mater 16(16):1436–1440
98. Cohen D, McKernan S, Carter CB (1999) Characterization of the absolute crystal polarity across twin boundaries in gallium phosphide using convergent-beam electron diffraction. Microsc Microanal 5(3):173–186
99. Jin L, Wang J, Jia S, Jiang Q et al (2010) ZnSe heterocrystalline junctions based on zinc blende-wurtzite polytypism. J Phys Chem C 114(3):1411–1415
100. Furtmayr F, Vielemeyer M, Stutzmann M, Arbiol J et al (2008) Nucleation and growth of GaN nanorods on Si (111) surfaces by plasma-assisted molecular beam epitaxy – The influence of Si- and Mg-doping. J Appl Phys 104:034309
101. Baxter JB, Wu F, Aydil ES (2003) Growth mechanism and characterization of zinc oxide hexagonal columns. Appl Phys Lett 83:3797
102. Kisielowski C, Hetherington CJ, Wang YC, Kilaas R et al (2001) Imaging columns of the light elements carbón, nitrogen and oxygen with sub angstrom resikution. Ultramicroscopy 89(4):243–263
103. Wagner MR, Bartel TP, Kirste R, Hoffmann A (2009) Influence of substrates surface polarity on homoepitaxial growth of ZnO layers by chemical vapor deposition. Phys Rev B 79:035307
104. Alem N, Erni R, Kisielowski C, Rossell MD et al (2009) Atomically thin hexagonal boron nitride probed by ultrahigh-resolution transmission electron microscopy. Phys Rev B 80:155425
105. Polking MJ, Urban JJ, Milliron DJ, Zheng H et al (2011) Size-dependent polar ordering in colloidal GeTe nanocrystals. Nano Lett 11(3):1147
106. Browning ND, Chisholm MF, Pennycook SJ (1993) Atomic-resolution chemical analysis using a scanning transmission electron microscope. Nature 366:143–146
107. Shavel A, Arbiol J, Cabot A (2010) Synthesis of quaternary chalcogenide nanocrystals: stannite $Cu_2Zn_xSn_ySe_{1+x+2y}$. J Am Chem Soc 132(13):4514–4515
108. Carretero-Genevrier A, Gazquez J, Idrobo JC, Arbiol J et al (2011) Single crystalline $La_{0.7}Sr_{0.3}MnO_3$ Molecular sieve nanowires with high temperature ferromagnetism. J Am Chem Soc 133(11):4053–4061
109. D'Alfonso AJ, Freitag B, Klenov D, Allen LJ (2010) Atomic-resolution chemical mapping using energy-dispersive x-ray spectroscopy. Phys Rev B 81:100101
110. Gonzalez E, Arbiol J, Puntes VF (2011) Carving at the nanoscale: sequential galvanic exchange and kirkendall growth at room temperature. Science 334:1377–1380
111. Binning G, Roher H, Gerber C, Weibel E (1982) Surface studies by scanning tunneling microscopy. Phys Rev Lett 49(1):57–61
112. Karlsson LS, Dick KA, Wagner JB, Malm J-O et al (2007) Understanding the 3D structure of GaAs [111]B nanowires. Nanotechnology 18:485717
113. Krishnamachari U, Borgstrom M, Ohlsson BJ, Panev N et al (2004) Defect-free InP nanowires grown in [001] direction on InP (001). Appl Phys Lett 85(11):2077–2079
114. Colombo C, Spirkoska D, Frimmer M, Abstreiter G, Morral AFI (2008) Ga-assisted catalyst-free growth mechanism of GaAs nanowires by molecular beam epitaxy. Phys Rev B 77:155326
115. I Morral AF, Colombo C, Abstreiter G, Arbiol J, Morante JR (2008) Nucleation mechanism of gallium-assisted molecular beam epitaxy growth of gallium arsenide nanowires. Appl Phys Lett 92:063112
116. de la Mata M, Magen C, Gazquez J, Utama MIB et al (2012) Polarity assignment in ZnTe, GaAs, ZnO and GaN-AlN nanowires from direct dumbbell analysis. Nano Lett 12(5):2579–2586

117. Utama MIB, Belarre FJ, Magen C, Peng B et al (2012) Incommensurate van der Waals epitaxy of nanowire arrays: a case study with ZnO on muscovite mica substrates. Nano Lett 12(4):2146–2152
118. Schuster F, Furtmayr F, Zamani R, Magen C et al (2011) Self-assembled GaN nanowires on diamond. Nano Lett 12(5):2199–2204
119. Uccelli E, Arbiol J, Magen C, Krogstrup P et al (2011) Three-dimensional multiple-order twinning of self-catalyzed GaAs nanowires on Si substrates. Nano Lett 11(9):3827–3832
120. Russo-Averchi E, Heiss M, Michelet L, Krogstrup P et al (2012) Suppression of three dimensional twinning for a 100% yield of vertical GaAs nanowires on silicon. Nanoscale 4(5):1486–1490
121. Utama MIB, de la Mata M, Magen C, Arbiol J, Xiong Q (2013) Twinning-, polytypism-, and polarity-induced morphological modulation in nonplanar nanostructures with van der Waals epitaxy. Adv Func Mat 23(13):1636–1646
122. Soler JM, Artacho E, Gale JD, García A et al (2002) The SIESTA method for ab initio order-N materials simulation. J Phys Condens Matter 14(11):2745–2779
123. Brandbyge M, Mozos JL, Ordejón P, Taylor J et al (2002) Density-functional method for nonequilibrium electron transport. Phys Rev B 65(16):165401

Electron Microscopy for Characterization of Thermoelectric Nanomaterials

10

Haijun Wu and Jiaqing He

Contents

1 Definition of the Topic 428
2 Overview 428
3 Introduction 428
3.1 Overview of Special Transmission Electron Microscope (TEM) Techniques 428
3.2 Overview of TE Material 433
4 Experimental and Instrumental Methodology 443
4.1 Synthesis 443
4.2 X-Ray Diffraction 443
4.3 Electrical Conductivity/Seebeck Coefficient Measurements 443
4.4 Thermal Conductivity 444
4.5 SEM 444
4.6 TEM 444
4.7 APT 445
5 Key Research Findings 445
5.1 Doped PbTe 445
5.2 PbTe + XTe (X = Mg, Ca, Sr, Ba, Cd) 448
5.3 PbTe + PbX (X = S, SnS_2) 468
5.4 PbTe + X (X = Pb, Sb, Bi, Si/Ge) 487
5.5 TAGS 497
5.6 LAST(T) 501
5.7 SALT 512
5.8 PbTe-Sb_2Te_3TE Compounds 523
6 Conclusions and Future Perspective 530
References 531

H. Wu • J. He (✉)
Department of Physics, South University of Science and Technology of China, Shenzhen, People's Republic of China
e-mail: he.jq@sustc.edu.cn

C.S.S.R. Kumar (ed.), *Transmission Electron Microscopy Characterization of Nanomaterials*, DOI 10.1007/978-3-642-38934-4_10,
© Springer-Verlag Berlin Heidelberg 2014

1 Definition of the Topic

Over the last decade, electron microscopy has evolved into a powerful analytical tool to provide micro-/nano-/atomic-scale information of materials. The microstructural base of thermoelectric (TE) materials, which can be capable of directly converting heat into electricity, is essential for understanding the mechanism and also a powerful guide to exploit new TE materials with higher performance and lower cost. The idea of this chapter is to review well-used tools of advanced electron microscopy to various TE materials.

2 Overview

Nowadays, the scale of materials' structures required for technology is shrinking at a fast speed, and electron microscopy is a primary characterization tool for exploring this nanoworld. In this chapter, we will first give a brief background of newly developed electron microscopy techniques, geometric phase analysis (GPA), and atom probe tomography (APT).

TE power generation represents a field of energy conversion technology, showing notable advantages to harvest the widely distributed waste heat into electricity. Various TE materials are then reviewed. The efficiency of TE materials is determined by a dimensionless figure of merit (ZT), defined as $ZT = (S^2\sigma/\kappa)T$, where S is the thermopower, σ the electronic conductivity, κ the thermal conductivity, and T the temperature. In the past decade, persistent efforts have been made to enhance ZT through either lowering κ or boosting power factor ($S^2\sigma$). Several innovative strategies introduced to increase the ZT value of various TE materials will be summarized.

Most state-of-the-art TE materials are characterized with various microstructural features from fine grains, dispersed nanoprecipitates, to atomic-scale lattice disorder, accompanying strains around above various defects. Thus the main body of this chapter will be to review the application of advanced electron microscopy in PbTe-based TE materials.

3 Introduction

3.1 Overview of Special Transmission Electron Microscope (TEM) Techniques

3.1.1 Image Processing, Especially Geometric Phase Analysis (GPA)

High resolution TEM (HRTEM) is a likely candidate for atomic-scale strain mapping, as lattice fringes in HRTEM images can depict the atomic lattice. Ideally, therefore, local deformation and its accompanying strain can be identified directly by measuring the displacement of the lattice fringes in the image. However, there are

several difficulties that have to be considered before this can be achieved with sufficient reliability. Firstly, the displacement of lattice fringes in an HRTEM image is not necessarily corresponding to those of the atomic lattice. Secondly, in order to obtain images with sufficiently high signal/noise ratios without undue strain relaxation and buckling, specimen preparation has to be optimized. Finally, to extract the information from images exactly, computational methods have had to be developed to eliminate the optical distortions introduced by the microscope itself [1].

Image processing is essentially manipulating images. The basic idea of image processing is changing images into numbers and manipulating the numbers. HRTEM images need be processed primarily for two reasons: (1) to improve the appearance of an image, make it look sharper, move even in contrast or higher contrast, etc., and (2) to quantify the information contained in the image. Here, we mainly introduce two image-processing methods which our group applies a lot: fast Fourier transformation (FFT) and GPA.

The principle involved in filtering is that a mask is used to remove unwanted information from an image in order to emphasize interested information. We want to vary the size of apertures and the sharpness of their edges. However, this is not possible in a modern TEM with normal fixed-diameter objective apertures. What the FFT does is to allow you to do microscopy in the computer, by regarding image as the specimen. We can process the image as follows, e.g., FFT of an HRTEM image, then apply a mask and then reverse the processing. You form the diffraction pattern, and then you can use "apertures" to select one or more beams to form the image; these "apertures" are actually the computer version of the objective aperture. Small aperture limits resolution as in the real "TEM" because the information about anything other than the perfect lattice is carried between the reciprocal lattice points.

HRTEM lattice image of crystalline materials and the specimen lattice have the related periodicity, which allows the use of image processing techniques based on reciprocal space. For filtering and quantification of HRTEM images, Fourier techniques in reciprocal space have distinct advantages over real space techniques, although both of them have the potential for creation of processing artifacts. Traditionally, these techniques have been regarded only as a qualitative way to improve the image. Image analysis quantitatively, for example, the measurement of lattice distortion and surrounding strains, has been the forte of real space techniques, usually involving superimposition of reference lattices. In order to apply HRTEM as a metrological tool for strain analysis qualitatively and quantitatively at the atomic level, it is therefore essential to determine the displacement field for a known object and to compare the results directly with theory. Hÿtch proposed a method for measuring continuous displacement fields around defects using the geometric phase technique [2].

The geometric phase approach is based on combining real-space and reciprocal-space information. Displacements are measured by calculating the "local" Fourier components of the lattice fringes in an image [3]. The intensity in an image, $I(r)$, is written as

$$I(r) = \sum_g I_g(r) e^{2\pi i g \cdot r} \tag{10.1}$$

where g is the reciprocal lattice vector describing the undistorted lattice. The local Fourier components are obtained by filtering in Fourier space and have an amplitude and phase:

$$I_g(r) = A_g(r) e^{iPg(r)} \tag{10.2}$$

where the amplitude, $A_g(r)$, describes the local contrast of the fringes and the phase, $P_g(r)$, their position. The phase is related simply to the displacement field $u(r)$ by the following relation:

$$P_g(r) = -2\pi g \cdot u(r) \tag{10.3}$$

and by measuring two phase images, $P_{g1}(r)$ and $P_{g2}(r)$, the two-dimensional displacement field can be determined:

$$u(r) = -\frac{1}{2\pi}\left[P_{g1}(r)a_1 + P_{g2}(r)a_2\right] \tag{10.4}$$

here a_1 and a_2 are the basis vectors for the lattice in real space corresponding to the reciprocal lattice defined by g_1 and g_2.

Based on Eq. 10.4, phase gradient and reciprocal lattice deviation can be expressed as

$$\nabla P_g(r) = 2\pi \Delta g(r) \tag{10.5}$$

Strain tensor for small deformation can be expressed as

$$\varepsilon_{ij} = \frac{1}{2}\left(\frac{\partial u_i}{\partial x_j} + \frac{\partial u_j}{\partial x_i}\right) \qquad \text{i.e.,}\ \varepsilon_{xx} = \frac{\partial u_x}{\partial x},\ \varepsilon_{yy} = \frac{\partial u_y}{\partial y},\quad \varepsilon_{xy} = \frac{1}{2}\left(\frac{\partial u_x}{\partial y} + \frac{\partial u_y}{\partial x}\right) \tag{10.6}$$

Mean dilatation can be expressed as

$$\Delta_{ij} = \frac{1}{2}\left(\frac{\partial u_i}{\partial x_i} + \frac{\partial u_j}{\partial x_j}\right), \quad \text{i.e.,}\ \Delta_{xy} = \frac{1}{2}\left(\varepsilon_{xx} + \varepsilon_{yy}\right) \tag{10.7}$$

Rotation (in radians and anticlockwise positive) can be expressed as

$$\omega_{ij} = \frac{1}{2}\left(\frac{\partial u_j}{\partial x_i} - \frac{\partial u_i}{\partial x_j}\right), \quad \text{i.e.,}\ \omega_{xy} = \frac{1}{2}\left(\frac{\partial u_y}{\partial x} - \frac{\partial u_x}{\partial y}\right) \tag{10.8}$$

Strong Bragg peaks are characteristics of HRTEM lattices from crystalline materials. A Bragg peak corresponds to the periodicity and orientation of the fringes in the image, while the phase of the peak corresponds to the location of the fringes in the image. Selection of an asymmetric region of the reciprocal (FFT) image can give directional information. If the lattice is free of any distortions, the phase corresponding to the reciprocal lattice vector g will be constant across the image. Shifts of the fringes can thus be described as changes in the phase image. Sensitivity of the technique to lattice distortions depends on the resolution of the calculated phase image. The phase obtained thus corresponds to a geometric phase related to the fringe positions in the image. The specific steps are as follows: (1) Calculate the full-plane FFT of HRTEM image with high quality, (2) select the region around the particular reciprocal lattice vector of interest in the FFT, (3) inverse transform the filtered Fourier spectrum to obtain a complex image, and (4) subtract from this raw phase image to get a phase ramp image relating to the selected g vector. The resulting phase image is a map of the deviations from regular periodicity in the image and thus can be used to obtain a strain map after suitable scaling.

GPA as a powerful quantitative method of deformation and strain field for high-quality HRTEM images has been already applied to the measurement of localized displacements and strain of various materials. Hÿtch reported the measurement of displacements around an edge dislocation in Si [1]. Johnson presented a detailed analysis of the internal structure of a decahedral Au nanoparticle using Cs-corrected HRTEM and strain mapping [4]. Johnson also reported lattice rotation across a low-angle grain boundaries in $Mg_{1.8}Fe_{0.2}SiO_4$ measured at the nanometer scale by using quantitative HRTEM and strain analysis [5]. Cs-corrected HRTEM is used to measure strain in a strained Si metal–oxide–semiconductor field-effect transistor, and the strain components parallel and perpendicular to the gate are determined directly from the HRTEM image by GPA [6]. Recently, our group applied GPA as a semiquantitative lattice image-processing approach for revealing spatially distributed strain fields around nanoscale precipitate (to be discussed in detailed in the Sect. 5, “Key Research Findings”).

3.1.2 Atom Probe Tomography (APT)

The atom probe is a microscope used in material science invented in 1967 by Erwin Wilhelm Müller [7], which is closely related to the method of field ion microscopy (FIM) [8]. Atom probes are unlike conventional optical or electron microscopes, in which the magnification effect is provided by a highly curved electric field, rather than by the manipulation of radiation paths. Technically, the method is destructive in nature because ions need to be removed from a sample surface to be imaged and identified, generating sufficiently high magnifications to observe individual atoms. Through coupling of this magnification method with time of flight mass (TOF) spectrometry, ions evaporated by application of electric pulses can have their mass/charge ratio computed.

Atom probe tomography (APT or 3D atom probe) is the only material analysis technique offering extensive abilities for both 3D imaging and chemical

composition measurements at the atomic scale (around 0.1–0.3 nm resolution in depth and 0.3–0.5 nm laterally). The sample needs to be prepared in the form of a sharp tip. The cooled tip is biased at high dc voltage (5–20 kV). The highly small radius of the tip and the high voltage will induce a high electrostatic field (tens V nm^{-1}) at the tip surface, just below the point of atom evaporation. Under laser or high-voltage pulsing, a few atoms are evaporated from the surface by field effect (near 100 % ionization) and then projected onto a position sensitive detector (PSD) with an extremely high detection efficiency.

The detector can measure simultaneously as follows: (1) In the TOF of the ions, measuring the time between the laser flash and the arrival on the PSD allows to determine the mass-over-charge ratio (m/q); (2) in the (X,Y) position of the ion impact on the detector, measuring the X-Y position and the order of arrival of the ions on the PSD allows to reconstruct the original position of the atoms on the tip. By repeating this sequence, the atoms are progressively removed from the tip, and a 3D image of the material can be reconstructed at the atomic scale. The detailed measurement process can be seen in Fig. 10.1, which is a schematic of a local-electrode atom-probe (LEAP) tomograph operating in the scanning mode. An array of microtip specimens sits on a conducting substrate at V_{dc}. In order to field-evaporate atoms as ions, the local electrode is pulsed with a negative potential, V_{pulse}, which increases the local E-field at a microtip to the required value. The PSD consists of 80-mm-diameter multichannel plates (MCP) in series with a delay-line detector at a variable distance of between 90 and 120 mm from the microtip. Thereby the researcher can vary the magnification of a FIM image and/or the TOF distance. The MCP plus the delay-line detector measure an ion's TOF and its position within an atomic plane: The spatial accuracy of the delay-line detector is <0.2 mm, with a timing accuracy of 50 ps and a multihit resolution of 1.5 ns. Employing electrical pulses, the repetition rate is variable in discrete steps from 1 to 250 kHz, and a detection rate of up to 2×10^6 ion/min can be achieved. The full width at half maximum (FWHM) value of the mass resolving power ($m/\Delta m$) is 500 for Al^+, and the full width at tenth maximum (FWTM) $m/\Delta m$ value is 180, with the microtip at 120 mm from the composite PSD: Δm is typically measured either at FWHM or FWTM of a peak in the mass spectrum.

An APT setup involves a FIM coupled directly to a special TOF mass spectrometer that permits one to determine the mass/charge states of individual field-evaporated ions plus their x-, y-, and z-coordinates in a specimen in direct space with subnanoscale resolution. APT allows 3D analysis of a material at the atomic scale [9, 10]. The 3D data sets acquired are analyzed using increasingly sophisticated software programs that utilize high-end workstations, which permit the researcher to handle continuously increasing large data sets.

Dual-beam focused ion beam (FIB) microscopy and its application to the fabrication of APT microtip specimens has dramatically improved the ability to prepare microtips of different materials in different configurations, especially for multilayer films and semiconductor devices. Producing site-specific specimens greatly extends the capabilities of APT to a wider range of scientific and

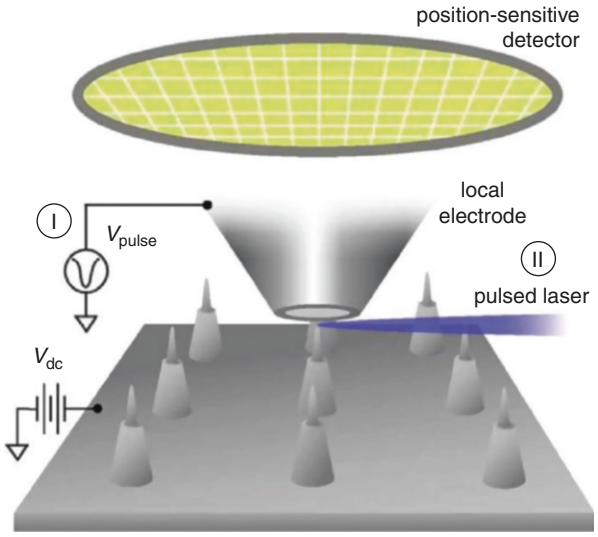


Fig. 10.1 Schematic drawing of a LEAP tomograph employing either voltage I or laser pulses II. The substrate containing an array of microtip specimens is maintained at a positive potential V_{dc}. The local electrode is pulsed with a negative voltage V_{pulse}, to increase the E-field at a microtip specimen to the required value for field evaporating atoms as ions. Alternatively, a specimen is pulsed with laser pulses at a high repetition rate. The multichannel plate is used to obtain a FIM image of the atoms on the surface of a microtip employing He or Ne as an imaging gas [9]

engineering problems for a wide range of materials: metallic materials [11], semiconductors [12] (including TE materials [13]), ceramics, biominerals, and organic materials [9]. Figure 10.2 is an example of the use of the lift-out technique to prepare a microtip for APT from a Si wafer containing a device.

3.2 Overview of TE Material

3.2.1 Energy Crisis and Energy Conversion Efficiency

Abundant and economical energy is the life blood of modern civilizations. Oil, coal, and natural gas together supplied 85 % of the world's energy supply in 2008 [14]. If oil production remains constant until it's gone, there is enough to last 42 years. However, oil wells produce less as they become depleted which will make it impossible to keep production constant. Similarly, there is enough natural gas to last 61 years and there is enough coal to last 133 years. Nearly everyone realizes oil and gas will become scarce and expensive within the life times of living humans.

What's worse, the energy conversion efficiency of these scarce energy sources is quite low; at least 50 % of all used energy in general was injected as waste heat. Table 10.1 summarizes some examples of energy conversion efficiency. Waste heat, sometimes called secondary heat or low-grade heat, refers to heat produced by machines, electrical equipment, and industrial processes for which no useful

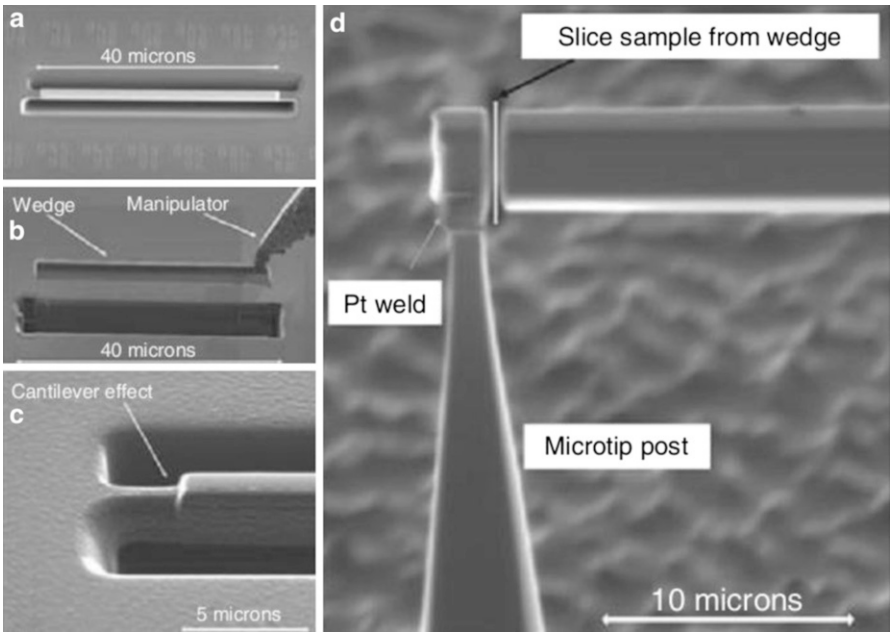


Fig. 10.2 Preparation of a microtip from a Si wafer. (**a**) Initial mill cuts for wedge lift-out from a Si wafer containing a device. (**b**) Close-up image showing the wedge still attached to the Si wafer. The long wedge forms a cantilever-type structure. (**c**) Wedge extracted from the wafer. (**d**) Sample wedge mounted to a microtip structure using a micromanipulator and then sliced free from the remaining wedge employing a low-energy Ga^+ ion beam [9]

application is found. Energy is often produced by a heat engine, running on a source of high-temperature heat. A heat engine can never have perfect efficiency, according to the second law of thermodynamics; waste heat is regarded as a waste by-product of this process. When produced by humans, or by human activities, it is a component of anthropogenic heat, which additionally includes unintentional heat leakage, such as from space heating. Waste heat is thought by some to contribute to the urban heat island effect. The biggest point sources of waste heat originate from machines such as electrical generators or industrial processes, such as steel or glass production. The burning of transport fuels is a major contribution to waste heat.

Therefore, the significance and scale of the energy crisis around the world necessitate consideration of all options for renewable energy and even nuclear energy, the enhancement of energy conversion efficiency, and the recycle of the lost waste heat.

Renewable energy is derived from natural processes that are replenished constantly. In its various forms, it derives directly from the sun or from heat generated deep within the earth. Included in the definition is electricity and heat generated from solar, wind, ocean, hydropower, biomass, geothermal resources, and biofuels and hydrogen derived from renewable resources. About 15 % of global final energy

Table 10.1 Example of energy conversion efficiency [15]

Conversion process	Energy efficiency
Electricity generation	
Gas turbine	Up to 40 %
Gas turbine plus steam turbine (combined cycle)	Up to 60 %
Water turbine	Up to 90 % (practically achieved)
Wind turbine	Up to 59 % (theoretical limit)
Solar cell	6–40 % technology dependent, 15 % most often, 85–90 % theoretical limit
Fuel cell	Up to 85 %
World electricity generation 2008	Gross output 39 %, net output 33 %
Engine/motor	
Combustion engine	10–50 %
Electric motors	70–99.99 % (above 200 W), 50–90 % (between 10 and 200 W), 30–60 % (small ones < 10 W)
Natural process	
Photosynthesis	Up to 6 %
Muscle	14–27 %
Appliance	
Household refrigerators	Low-end systems $\sim$ 20 %; high-end systems $\sim$ 40–50 %
Incandescent light bulb	0.7–5.1 %, 5–10 %
Light-emitting diode (LED)	4.2–14.9 %, up to 35 %
Fluorescent lamps	8.0–15.6 %, 28 %
Low-pressure sodium lamps	15.0–29.0 %, 40.5 %
Metal halide lamps	9.5–17.0 %, 24 %
Switched-mode power supply	Currently up to 95 % practically
Electric shower	90–95 % (overall it would be more efficient to use a heat pump, requiring less electric energy)
Electric heaters	$\sim$100 % (essentially all energy is converted into heat)
Others	
Firearm	$\sim$30 % (.300 Hawk ammunition)
Electrolysis of water	50–70 % (80–94 % theoretical maximum)

consumption comes from renewables. In fact, they have some common disadvantages of renewable energy. One is that the density of energy gathered in these technologies is dramatically less than a power plant, which means we need many square miles, extremely larger area than you think of as a normal energy plant. Also, these are intermittent sources. The sun doesn't shine all day, it doesn't shine every day, and likewise, the wind doesn't blow all the time. And so, if you depend on these sources, you have to have some way of getting the energy during those time periods that it's not available. The final is transmission challenges. For example, say this energy source is outside your country, you not only need the technology, but you have to deal with the risk of the energy coming from elsewhere.

Nuclear energy, which is regarded as the most powerful and efficient sustainable energy source, has also its own obvious problems. Cost, particularly in highly regulated countries, is high. From the outset, there has been a strong awareness of the potential hazard of both nuclear criticality and release of radioactive materials from generating electricity with nuclear power. As in other industries, the design and operation of nuclear power plants aims to minimize the likelihood of accidents and avoid major human consequences when they occur.

Since humans have tried their best to enhance energy conversion efficiency in various areas for long time, it seems that this approach gets to the end. The recycle of the lost waste heat seems to be the most hopeful approach, one of which (TE material) we will discuss in detailed in the following sections, since any heat-generating process can be made more efficient by recouping lost waste heat.

3.2.2 TE Materials

TE materials, directly converting heat into electricity, are particularly promising in heat-producing processes, such as the combustion of fossil fuel in power plants or commercial vehicles, specially, may become more efficient if wasted heat may be recouped as electricity.

TE materials can be classified roughly on the basis of their applicable temperature range. For near-room temperature applications up to 500 K, Bi_2Te_3/Sb_2Te_3 alloys currently possess the highest ZT for both n-type [16] and p-type [17, 18] systems. For mid-temperature (500–900 K) TE materials, Te-based alloys are widely used. High-temperature (>900 K) TE generators have typically used SiGe alloys for both n-type [19] and p-type [20] legs.

For near-room temperature applications, such as refrigeration and waste heat recovery up to 200 °C, Bi_2Te_3/Sb_2Te_3 alloys have been proved to possess the highest ZT for both n- and p-type TE systems [16, 17]. Bi_2Te_3 was first investigated as a great TE material in the 1950s [21]. It was quickly realized that compounds of Sb_2Te_3 and Bi_2Te_3could allow for the fine-tuning of the carrier concentration alongside a reduction in lattice thermal conductivity (k_{lat}). The most commonly investigated p-type compositions are near $(Sb_{0.8}Bi_{0.2})_2Te_3$, whereas n-type compositions are close to $Bi_2(Te_{0.8}Se_{0.2})_3$. The electronic transport properties and detailed defect chemistry of these alloys are now well understood thanks to extensive studies of single crystal and polycrystalline material. Peak ZT values for these materials are typically in the range of 0.8–1.1 with p-type materials. By adjusting the carrier concentration, ZT can be optimized to peak at different temperatures, enabling the tuning of the materials for specific applications such as cooling or power generation [22].

SiGe alloys are suitable candidates for high-temperature TE applications because of their acceptable good TE properties and superior long-term reliability at high temperatures. Consequently, SiGe TE modules with a ZT value of 0.5 (p-type) and 0.9 (n-type) have been used in space radioisotope TE generators (RTGs) by United States NASA since 1976 [23]. New applications, especially heat conversion at high temperatures, demand higher ZTs for such material applications. Recently, a good enhancement in ZT values has been demonstrated for both n- and p-type SiGe alloys by using a nanocomposite approach. The high

density of grain boundaries of the numerous nanograins can effectively scatter long-wavelength phonons; thus the k_{lat} of the nanocomposite samples is much lower compared to that of their equivalent large crystalline bulk materials. The peak ZT value of p-type nanostructured $Si_{80}Ge_{20}B_5$ samples was improved from 0.5 to 0.95 [20] and that of n-type $Si_{80}Ge_{20}P_2$ from 0.93 to around 1.3 [19]. However, these materials contain a fairly high concentration of Ge that is about a 100 times more expensive than Si. In 2009, Zhu et al. reported [24] that by using similar nanocomposite approach, excitingly only a 5 % Ge replacement of Si is sufficient to further reduce the κ of n-type nano-Si by a factor of 2, resulting in a ZT peak value of 0.94 in $Si_{95}Ge_5$ doped with GaP and P at ~900 °C, which is significant since a much smaller amount of expensive Ge is used. Recently, Yu reported an interesting material design, using alloy $Si_{70}Ge_{30}$ instead of Si as the nanoparticles and $Si_{95}Ge_5$ as the matrix, to increase the $S^2\sigma$ but not the κ, leading to a ZT of 1.3 ± 0.1 at 900 °C [25]. Furthermore, if Ge is entirely eliminated, the ZT peak of pure nano-Si would drop to about 0.7 at around 1,000 °C [26]. Clearly there is a trade-off between the cost and the performance of $Si_{1-x}Ge_x$ alloys.

For mid-temperature power generation (500–900 K), Te-based materials, such as PbTe, GeTe, or SnTe, are typically used [27]. Most of the compounds are environmentally stable with high melting points. They combine a set of properties that make them suitable for practical TE applications, because of the versatility in the element choice and the suitable electronegativity of the chalcogen elements. The peak ZT in optimized n-type PbTe material is about 0.8, and a tuning of the carrier concentration will alter the temperature where ZT peaks. Alloys, particularly with $AgSbTe_2$, have led to several reports of ZT > 1 for both n-type and p-type materials [28–30]. The p-type alloy $(GeTe)_{0.85}(AgSbTe_2)_{0.15}$(TAGS), with a maximum ZT greater than 1.2, has been successfully used in long-life TE generators [23]. With the advent of modern microstructural and chemical analysis techniques, Te-based materials are being reinvestigated with great promise. The biggest advances in this field have been achieved in nanostructured PbTe-based materials in which very low κ can be obtained, resulting in the highest ZT values among all TEs. To date, both n-type (e.g., $AgPb_mSbTe_{m+2}$ (LAST) [28, 30], $Pb_{1-x}Sn_xTe$-PbS [31], PbTe-CdTe [32], PbTe-PbS [33], PbTe-Ge/GeSi/Si [34, 35], and PbTe-Ag_2Te [36]) and p-type (e.g., $AgPb_mSn_nSbTe_{m+n+2}$ (LASTT) [29, 37], $PbTe_{1-x}Se_x$ [38], $NaPb_mSbTe_{m+2}$ (SALT) [39], PbTe-XTe (X = Mg [40], Ca [41], Sr [42, 43], Ba [41, 44]), PbTe-PbS [45–47], and PbTe-$PbSnS_2$ [48, 49]) materials have been developed.

These materials above, the leading commercialized TE materials as well as those poised for commercialization in the near future, however, all contain a significant amount of Te or Ge, which is scarce in the earth's crust. To allow for widespread use of TEs in a variety of applications, inexpensive alternatives are needed. Attention is now turning to materials such as PbSe and PbS [50, 51].

PbSe can potentially play a significant role in the advancement of TEs at temperatures above 800 K for several reasons. (1) PbSe has a higher melting point (1,355 K) than PbTe (1,253 K); it thus can in principle sustain higher

Table 10.2 Some physical properties for Pb-based chalcogenides and the maximum ZT values reported so far [59]

PbQ, Q = Te, Se, S	Melting point (K)	Band gap (eV)	Earth abundance *Q* [60], (ppm)	ZT, n-type	ZT, p-type
PbTe	1,197	0.31	0.001	$AgPb_{18}SbTe_{20}$ [29], 1.8 at 800 K	PbTe + 4 % SrTe + 2 % Na [42], 2.2 at 915 K
PbSe	1,352	0.28	0.05	PbSe + 12 % PbS + 0.3 % $PbCl_2$ [50], 1.3 at 900 K	$Pb_{0.993}Na_{0.007}Se$ [51], 1.2 at 850 K
PbS	~1,391	0.41	~420	PbS + 1 % Bi_2S_3 + 1 % $PbCl_2$ [58], 1.1 at 923 K	PbS + 3 % CdS + 2.5 % Na [59, 61], 1.3 at 923 K

operation temperatures up to 1,000 K. Therefore, very high-temperature applications (e.g., >800 K), including solar thermal energy conversion, could benefit from the development of PbSe-based thermoelectric generators [52]. (2) PbSe exhibits a monotonically increasing S even up to at least 1,000 K with a favorable electronic structure similar to that of PbTe and has a lower k_{lat} at room temperature compared to PbTe [53]. (3) More importantly, Se is less expensive and ~50 times more abundant than Te in the Earth's crust [54]. The aforementioned attractive combination of properties has prompted us to study in detail the TE behavior of PbSe at high temperatures.

Another possibility is PbS, which is isostructural to PbTe adopting the rock salt structure with lattice parameters of 5.94 Å [55]. The electronic properties of the compounds are very similar. PbS has its special advantages compared with PbTe. (1) PbS has a reported larger room temperature band gap of 0.41 eV than that of PbTe (0.32 eV) [56], which suggests PbS will show a maximum TEZT at higher temperatures than PbTe, following 10 k_BT rule [57]. (2) Coupled with the significantly higher melting point of PbS (1391 K) in comparison with PbTe (1,197 K), PbS-based TE materials have the potential to be used at higher temperatures. (3) The room temperature effective mass of the conduction band is slightly higher in PbS than in PbTe. Consequently, the reported electron mobilities are smaller in PbS, whereas the reported room temperature S for n-type PbS is higher at similar charge-carrier concentration than in n-type PbTe. (4) Still quite importantly, PbS is an ideal candidate because S is more abundant and less expensive than both Se and Te. Recently, we investigated the TE properties of compositions lying on the PbS-rich side of the PbS–PbTe phase diagram and reported that significant TE enhancements for n-type samples can be achieved [51]. This motivated us to expand our investigations to Te-free PbS-based systems by utilizing many of the new concepts and ideas developed for PbTe. Indeed, for n-type PbS we showed dramatic improvements in ZT from 0.4 to 1.1 at 923 K by combining nanoprecipitates of Bi_2S_3 and Sb_2S_3 s phases with heavy $PbCl_2$ doping [58]. A comparison of some physical properties for optimized, high-performance n- and p-type Pb-based chalcogenide TE materials is listed in Table 10.2.

At the same time, complex bulk materials [22] (such as skutterudites [62], half-Heusler [63], Stannite [64], Zintl phases [65]) have been explored and found

that high efficiencies could indeed be obtained. Many of the recent high-ZTTE materials similarly achieve a reduced k_{lat} through disordering the unit cell. This disorder is achieved through interstitial sites, partial occupancies, or rattling atoms in addition to the disorder inherent in the alloying used in the state-of-the-art materials. Thus, the promising potential to reduce κ through disorder within the unit cell is particularly extremely large in structures inherently containing void spaces. One class of such materials is skutterudites [62], which contain corner-sharing $CoSb_6$ octahedra, and can be viewed as a distorted variant of the ReO_3 structure. These tilted octahedra create void spaces that may be filled with rattling atoms. For skutterudites containing elements with low electronegativity differences such as $CoSb_3$ and $IrSb_3$, there is a high degree of covalent bonding, enabling high carrier mobilities and therefore good electron-crystal properties. Thus, this combination of properties qualifies these complex bulk materials as a potentially outstanding TE material.

Furthermore, the above widely studied TE materials, especially for alloys of Bi_2Te_3, PbTe, and SiGe, which are often with poor temperature durability and poor chemical stabilities, are also harmful or scarce and have costly constituting elements. Oxides, owing to their natural merits of low κ and high resistance of oxidation at high temperature, have recently been exploited as alternative TE materials. Therefore, TE oxides are expected to play an important role in extensive applications for waste heat recovery, on the basis of their potential advantage over heavy metallic alloys of chemical and thermal robustness [66]. Typical TE oxides include $Ca_3Co_4O_9$ based [67, 68], $CaMnO_3$ based [69], In O_3 based [70], LnCuChO based [66, 71–73], $SrTiO_3$ based [74], and ZnO based [75].

3.2.3 ZT of TE Material

The TE effects can be regarded as charge carriers in metals, and semiconductors are free to move much like gas molecules, while carrying charge as well as heat. When a temperature gradient (ΔT) is applied to a TE material, the mobile charge carriers at the hot end are induced to diffuse to the cold end. The buildup of charge carriers results in a net charge (negative for electrons, e^-, positive for holes, h^+) at the cold end, producing an electrostatic potential (voltage). An equilibrium is thus expected between the chemical potential for charge-carrier diffusion and the electrostatic repulsion due to the buildup of charge. This property, known as the Seebeck effect [76] is the basis of TE power generation.

TE devices contain many TE couples (Fig. 10.3, bottom) composing n-type (containing free electrons) and p-type (containing free holes) TE elements wired electrically in series and thermally in parallel (Fig. 10.3, top). A TE generator induces heat flow across a temperature gradient to power an electric load through the external circuit. The temperature difference provides the voltage ($V = S\Delta T$) based on the S, while the heat flow drives the electrical current, which therefore determines the power output. In a Peltier cooler the external circuit is a dc power supply, which drives the electric current (I) and heat flow (Q), thereby cooling the top surface due to the Peltier effect ($Q = STI$) [77]. In both devices the heat rejected must be removed through a heat sink.

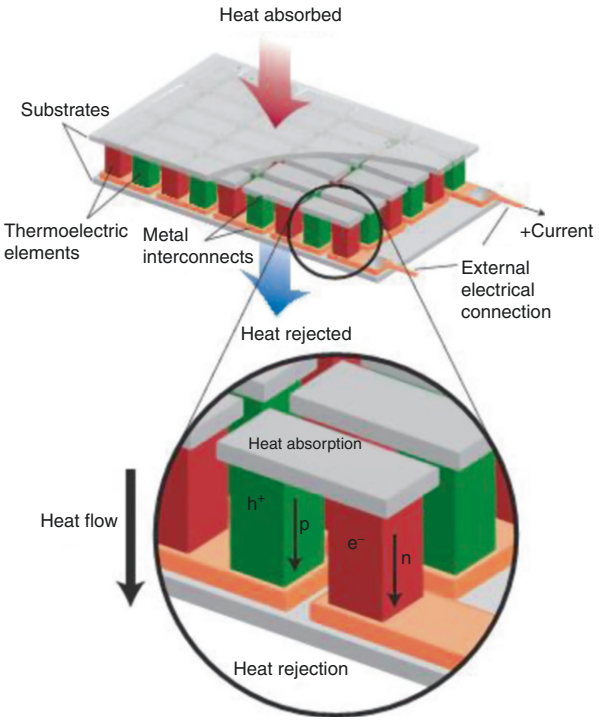


Fig. 10.3 TE module showing the direction of charge flow on both cooling and power generation [22]

In practical applications, the efficiency of TE devices is determined by the materials used in making the device, and thus the main focus of research has been the search for better materials. The efficiency of TE materials is determined by the ZT:

$$ZT = \frac{S^2\sigma}{\kappa}T \tag{10.9}$$

where σ is the electrical conductivity, S is the thermopower, κ is the thermal conductivity, and T is the temperature. The numerator ($S^2\sigma$) is called the power factor. The quantities are determined by the electronic structure and scattering of charge carriers and thus are not independently controllable parameters.

The overall efficiency η of a TE engine depends not only on ZT but also on the temperature difference of operation. This is quantified by the relation:

$$\eta = \frac{T_H - T_C}{T_H}\frac{\sqrt{1+ZT}-1}{\sqrt{1+ZT}+\frac{T_C}{T_H}} \tag{10.10}$$

where T_H and T_C are the high and low temperatures of operation of the TE engine, respectively (the first fraction is the Carnot efficiency). It is evident that η can be increased by application of higher-temperature gradients.

Therefore, high-performance TE materials require a perfect combination of high $S^2\sigma$ and low κ. However, it is very difficult to control the above three parameters independently, which often counter each other, and all of them are restricted by the carrier concentration. The S is inversely related to the σ according to the Boltzmann transport equation, and as a result, increasing σ usually results in a decrease in the S. In addition, the reduction of κ often leads to a decrease of σ. Therefore, the main purposes of the research on TE materials are to increase electrical transport properties but decrease κ [23, 30].

3.2.4 Methods to Enhance ZT

The interdependence of S, σ and κ, complicates efforts in designing strategies to improve a material's ZT above 2. In the past decade, persistent efforts have been made to enhance ZT through either lowering κ or boosting $S^2\sigma$. Several innovative strategies have recently been introduced to increase the ZT value of various TE materials.

Lowering κ

1. Nanostructuring

   The most successful route is reducing the κ particularly through nanostructuring. Typical examples are embedding nanoscale precipitates in bulk materials that scatter heat-carrying phonons, e.g., PbTe–SrTe [42, 43], $AgPb_mSbTe_{m+2}$ [28–30], $AgPb_mSn_nSbTe_{2+m+n}$ [29, 37], $NaPb_mSbTe_{2+m}$ [39], PbTe–PbS [47], PbTe–CdTe [32], PbSe–PbS [50], PbS–PbTe [51], PbS–Bi_2S_3/Sb_2S_3 [58], PbS–SrS/CaS [59], and PbS–ZnS/CdS [61].

   One typical sample is PbTe with nanostructuring XTe (X = MgTe, CaTe, SrTe, and BaTe). These nanostructural precipitates arouse broad phonon scattering meanwhile allow carrier transport between endotaxially aligned components and thus minimize significant deterioration of the hole mobility and σ [42–44, 78–80].

   Recently, Biswas experimentally achieved concurrent phonon blocking and charge transmitting via the endotaxial placement of nanoscaled precipitates SrTe in a PbTe TE material host with p-type Na_2Te dopant. This effectively inhibits the heat flow in the system but does not affect the hole mobility. The crystallographic alignment of SrTe and PbTe lattices decouples phonon and electron transport and allows the system to reach a TEZT of 1.7 at ~800 K [43]. Nanostructures in bulk TEs allow effective phonon scattering of a significant portion of the phonon spectrum, but phonons with long mean free paths remain largely unaffected. Heat-carrying phonons with long mean free paths can be scattered by fine-tuning the mesoscale architecture of nanostructured TE materials. Thus, by a combined method from atomic-scale lattice disorder and nanoscale endotaxial precipitates to mesoscale grain boundaries, Biswas further achieved the maximum reduction in k_{lat} and a largest enhancement in the ZT value of ~2.2 at 915 K still in a more concentration of SrTe doped PbTe TE bulk material after powder processing and spark plasma sintering (SPS) [42]. With considering nanostructuring and band structure tailoring, very recently,

we reported heavily Na doped PbTe with MgTe fractions up to 8 % with extremely low k_{lat} and enhanced S; thus pushing ZT to ~2.0 at 923 K. S can be enhanced by lowering energy offsets of valence bands (L and Σ bands) and push two-band convergence shifting to lower temperature through Mg alloying in the PbTe; meanwhile, a low k_{lat} has been realized through nanostructuring by the multiscale hierarchical architecture, similar with that of PbTe–SrTe system. Results indicated that band engineering to enhance the S is independent of thermal transport properties, implying that improvements in ZT induced by reducing the k_{lat} can work in synergy with the band engineering mechanism [80].

2. Superlattice structure
   Epitaxial superlattice Bi_2Te_3/Sb_2Te_3 thin films exhibit a very high ZT of about 2.4 at room temperature, compared to state-of-the-art bulk Bi_2Te_3 alloys [18]. The enhancement is achieved by controlling the transport of phonons and electrons in the superlattices, using the acoustic mismatch between the superlattice components to reduce the k_{lat}, rather than using alloy scattering of carriers. At the same time, band offsets in the superlattices are chosen to allow carrier transmission.

Boosting $S^2\sigma$

1. Through multiple valence bands:
   P-type PbTe–PbSe has excellent TE properties, arising from its special multiple valence bands [38]. It is well known that a high valley degeneracy in the electronic bands is conducive to high ZT, which stimulates attempts to design such degeneracy by adopting low-dimensional nanostructures. Pei proposed to direct the convergence of many valleys in a bulk material by tuning the doping. By this route, the author achieved a convergence of valleys in doped PbTe–PbSe alloys, leading to a ZT value of 1.8 at 850 K. Band engineering to converge the valence (or conduction) bands to achieve high valley degeneracy should be a general strategy to obtain a high S and high σ [38].
2. Through modifying band structure by density-of-states distortion in the valence band:
   Tl–PbTe [28] also has excellent TE properties by the introduction of a density-of-states distortion in the valence band. Heremans explored enhancing the S through a distortion of the electronic density of states and reported a successful implementation through doping the Tl impurity levels in PbTe. Such band structure engineering results in a doubling of ZT in p-type PbTe to above 1.5 at 773 K. Use of this new physical principle in conjunction with nanostructuring to lower the κ could further enhance ZT and enable more widespread use of TE systems [28].
3. Through electron energy barrier filtering:
   Heremans demonstrated an enhancement in the $S^2\sigma$ of PbTe nanostructures with grain sizes on the order of 30–50 nm. Based on measurements of the transverse Nernst effect, the author proved that the enhancement has its origin in electron energy filtering induced by an alteration of the scattering mechanism [81].

Other Method to Enhance ZT

Bulk materials with complex structure (such as skutterudites [62], half-Heusler [63], Stannite [64], Zintl phases [65]) are promising approach to obtain high TE performance because of their intrinsic special structures [22]. Here, we can take skutterudite structure, for example. Bulk $Ba_uLa_vYb_wCo_4Sb_{12}$ multiple-filled skutterudites exhibit high TEZT of 1.7 at 850 K. HRSTEM and EDS analyses confirm that multiple guest fillers occupy the nanoscale cages in the skutterudites. The results firmly showed that high $S^2\sigma$ can be achieved by modifying the fraction of fillers with different charge states to reach the optimum carrier density. At the same time, k_{lat} can also be significantly reduced to values near the glass limit of these materials, through combining filler species of different rattling frequencies to achieve broad-frequency phonon scattering. The idea of combining multiple fillers with different charge states and rattling frequencies for performance optimization is also expected to be valid for other caged TE compounds [82].

4 Experimental and Instrumental Methodology

4.1 Synthesis

Detailed sample preparation of doped PbTe [83, 84], PbTe + XTe (X = Mg, Ca, Sr, Ba, Cd) [32, 40–44], PbTe + PbS [33, 45–47], PbTe + $PbSnS_2$ [48, 49], PbTe + X (X = Pb, Sb, Bi, Si/Ge) [34, 35, 85, 86], TAGS [87], LAST(T) [88], SALT [89, 90], and PbTe-Sb_2Te_3 [91] can be found in corresponding literatures, which will be discussed in the following sections.

4.2 X-Ray Diffraction

Finely ground samples were placed in an Inel CPS-120 X-ray powder diffractometer using Ni-filtered Cu K_α radiation (λ = 1.54056 Å) in reflection geometry, equipped with a position sensitive detector and operating at 40 kV and 20 mA.

4.3 Electrical Conductivity/Seebeck Coefficient Measurements

σ and S were measured on polished parallelepipeds approximately 2 × 2 × 8 mm or 18 × 3 × 3 mm in a ULVAC ZEM-3 system. Samples were sandwiched between two Ni electrodes with two probe thermocouples providing forced contacts on one side. The samples were coated with a thin layer of BN to protect the instruments. The sample chamber was evacuated and back-filled with He and heated from room temperature to 900 K using an IR furnace. σ is measured using standard four-point probe technique [92]. The S is calculated by measuring average induced voltage resulting from temperature gradients provided by resistive Pt coils located beneath

one electrode. Heating and cooling cycles gave repeatable electrical properties to verify the thermal stability. Electrical properties obtained from different slices cut from the same pellets were similar, attesting to the homogeneity of the samples. The uncertainty of the S and σ measurements is 5–10 %.

4.4 Thermal Conductivity

Thermal diffusivity and specific heat of samples were measured. Coins measuring approximately 8 mm in diameter by 2 mm in thickness were heated from room temperature to 900 K. The samples were coated with a thin layer of graphite to minimize errors from the emissivity of the material. Total thermal conductivity (k_{total}) was calculated using the equation:

$$\kappa_{\text{total}} = \alpha C_P \rho \tag{10.11}$$

where α is thermal diffusivity, C_P is specific heat, and ρ is density. The α was measured using the laser flash diffusivity method in a Netzsch LFA 427 (Germany), and the thermal diffusivity data were analyzed using a Cowan model with pulse correction. The C_P was determined by differential scanning calorimetry (NETZSCH DSC 404C, Germany). The ρ was determined using the Archimedes method. The uncertainty of the κ is estimated to be within 10 %, considering the uncertainties for α, C_P, and ρ.

4.5 SEM

The microstructure of finely polished sample surfaces were observed and identified using a Hitachi S3400 SEM equipped with a back-scattered electron detector operating at 20 kV voltage and 15 mA current at a working distance of 10 mm. Differences in phase composition were successfully identified using EDS analysis using the program Inca. The samples used for SEM and EDS were the same coins used for thermal diffusivity measurements, and they were polished using a suspension of 50 nm Al_2O_3 particles. High-resolution images were observed using a FEI Helios Nanolab FIB/SEM. Areas of the sample were bombarded with Ga^+ ions, resulting in preferential etching of the sample along grain boundaries and differing phases. The resulting image provides a more clear representation of the microstructure, with minimized appearance of surface defects and scratches.

4.6 TEM

TEM investigations were carried out using a JEOL 2100F microscope operated at 200 kV using a double-tilt holder. The thin TEM specimens were prepared by

conventional standard methods. The samples were cut into 3-mm-diameter disks by disk cutter, and then ground, dimpled, polished, and subsequently Ar-ion-milled on a stage cooled with liquid nitrogen. The in situ TEM experiments were carried out in a JEOL 2100F microscope equipped with a heating stage (Gatan Corporation).

Image processing and simulation are not only becoming more common but are also finding new application in many fields. Faster, more powerful computers and increased memory storage are making tasks possible which could not previously have been considered. As a result of this increasing user base, there are now many software packages available which can be used in microscopy. We choose DigitalMicrograph (Gatan package) for image processing, GPA software (HRTEM Research Inc.) for strain analysis of HRTEM images, CrystalKit software (Total Resolution LLC) for defect and interface modeling, and MacTempas (Total Resolution LLC) software for image simulation. High-resolution images were simulated with the MacTempas program code with the following parameters as input: spherical aberration of 1 mm, defocus spread of 8 nm, semiconvergence angle of illumination of 0.55 mrad, and a 7 nm^{-1} diameter of the objective lens' aperture.

4.7 APT

Samples were prepared for APT analyses using dual-beam FIB microscopy [42, 84]. The APT analyses were performed using a LEAP tomograph (Cameca LEAP-4000X Si, Madison, WI), equipped with a picosecond ultraviolet laser (wavelength = 355 nm). During the analysis, the sample was maintained at 32.4 K. Samples were also analyzed using voltage pulsing, with an evaporation rate of 0.005 atom $pulse^{-1}$, a pulse fraction (pulse voltage/steady-state dc voltage) of 15 %, and a pulse repetition rate of 200 kHz. Individual ions were detected using a two-dimensional micro-channel plate detector with detection efficiency of about 50 %. The data were analyzed using the program IVAS v 3.4.3 (Cameca, Madison, WI). During the APT analyses, low-density hkl poles and zone lines were observed, giving information about the crystallographic orientation of the sample. The contribution of each ion to the overall composition was measured by deconvolution of the corresponding peaks using a fitting procedure.

5 Key Research Findings

5.1 Doped PbTe

PbTe can be adjusted as p-type by monovalent cation (Li^+, Na^+, K^+, Rb^+, Cs^+, Ag^+, and Tl^+) substitutions on the Pb^{2+} sublattice. R band Cs with too large atomic radius are due to steric interactions. Since Tl is extremely toxic and expensive, while Ag exhibits mobility due to ionic conductivity in PbTe, they are less attractive. Thus,

one is left with relatively few choices for p-type doping out of which Na (and to a certain extend K) have been the most effective. Na/K doped p-type PbTe is a canonical TE material studied extensively. We employ advanced TEM to explore its microstructural base of unexpected weak phonon scattering from nanostructures in Na/K doped p-type PbTe, as Fig. 10.4 shows.

TEM investigation of Na/K single or codoped samples shows high density of nanoscale precipitates in heavily doped samples. Analyses along different crystallographic directions are used to obtain information about the precipitates' morphology and distribution. When the electron beam is along <110> or <111> zone axis, precipitates with quasi-circular shape appear, while along the <100> zone axis, precipitates are platelet-like dark lines of a few nanometers in length. Figure 10.4a–d shows typical low-magnification TEM images of the samples with different directions indexed by the inset DPs. Figure 10.4f shows the size distribution histogram of precipitates in different samples using the same TEM observation volume. It is clear that most of codoped samples have about twice higher density of precipitates (0.5–2 nm) than single doped samples. Elemental analysis of the precipitates was performed by means of EDS in the STEM mode using a 1-nm probe size. Although it is difficult to quantitatively determine the compositions of the individual nanoscaled precipitates owing to their overlap with the surrounding matrix and beam-induced evaporation typical of alkaline species, EDS data of Na doped PbTe samples shows Na signal besides Pb and Te in precipitates, compared to PbTe matrix regions, just as EDS spectrum in Fig. 10.4c. This observation provides evidence that the sample contains precipitates that are richer than the matrix in Na, which is also confirmed by APT analysis of the sample [42].

The microstructural features of the nanoscale precipitates and the strain distribution at the boundaries between the precipitates and the PbTe matrix should be explored by HRTEM. Figure 10.5a is a representative HRTEM image of platelet-like precipitates in sample Na/K codoped PbTe, obtained along [001] zone axis. Two precipitates appear as two perpendicular dark lines. The inset image in Fig. 10.5a taken along the [010] direction shows elliptical-shape precipitate. Furthermore, Fig. 10.5b, c shows typical HRTEM images along [011] and [111] directions, respectively. Figure 10.5d is a schematic of a platelet-like precipitate (black) which is parallel to the (010) plane. Its projections along the <100>, <110>, and <111> directions are shown in red, green, and blue, respectively. It is clear that the precipitates can appear both as dark lines and circles only if analyzed along the <100> direction, while it will appear as an ellipsoid if observed from any other direction.

Further HRTEM studies revealed that all the precipitates have similar crystal structural features as PbTe, showing crystallographic coherent relationship. A high-magnification HRTEM lattice image of a platelet-like precipitate is shown in Fig. 10.5e. Figure 10.5f (up) shows the corresponding measured line-scanning profile. The simulated HRTEM of platelet-like precipitate in Na/K codoped PbTe was proceeded as follows: (1) Assume K/Na ratio in the precipitates equal to the nominal K-Na ratio in the prepared sample and both atoms occupying Pb sites, the

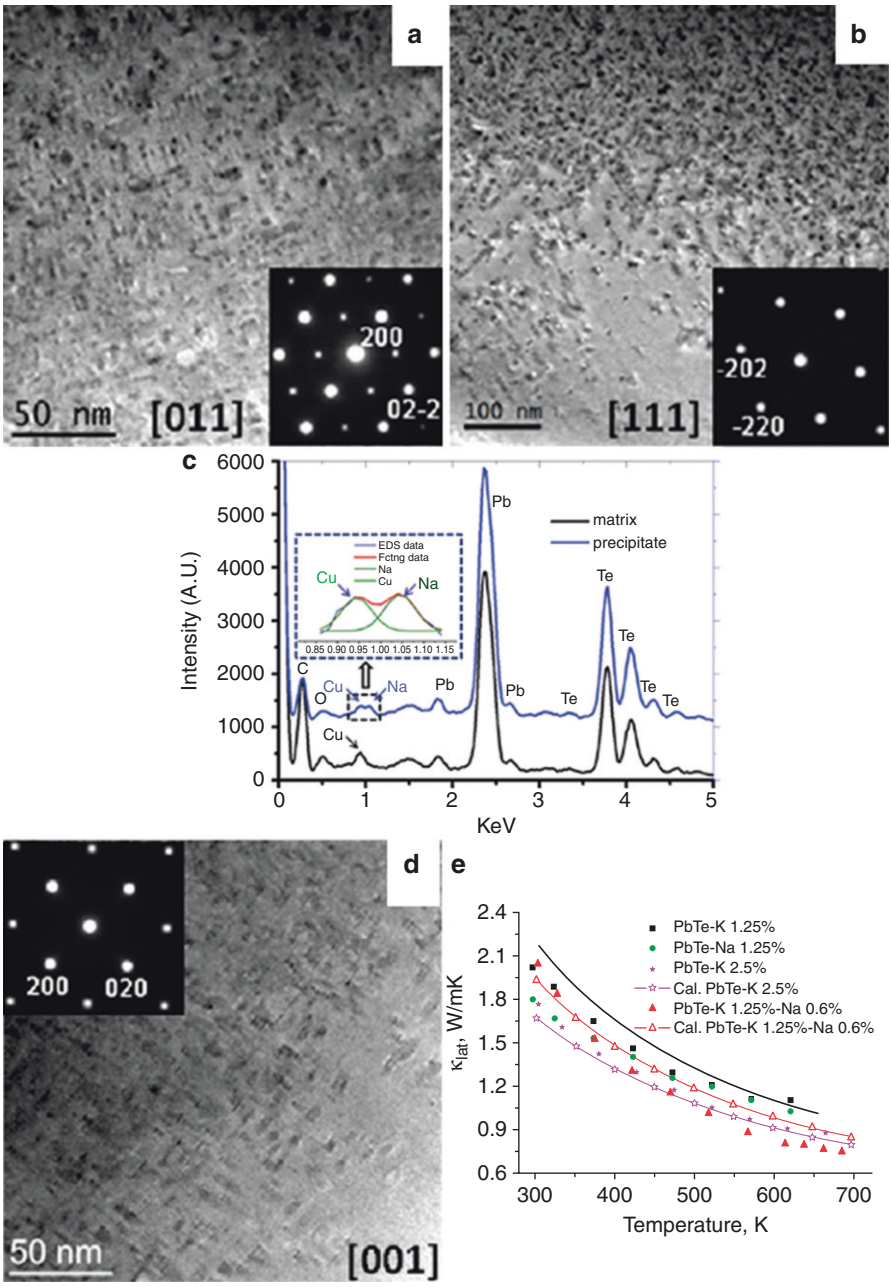


Fig. 10.4 (continued)

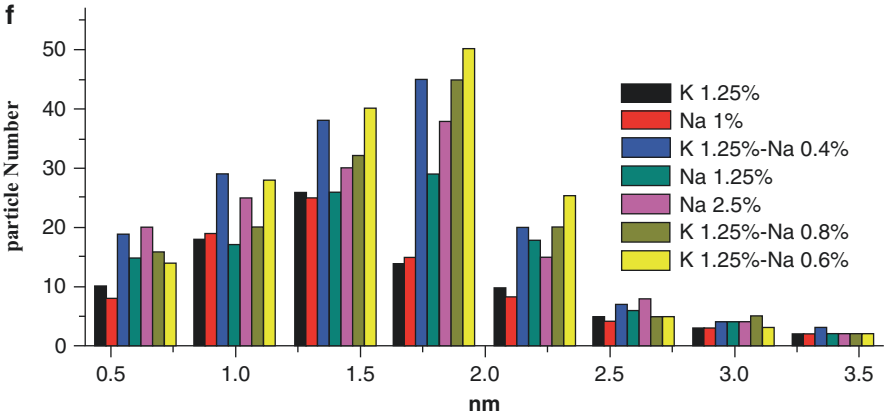


Fig. 10.4 Typical low-magnification TEM images of three samples: (**a**) [11] Na doped PbTe, (**b**) [111] Na/K codoped PbTe, (**c**) EDS analysis between the matrix and precipitate, and (**d**) [1] K doped PbTe. (**e**) Temperature dependence of *k*lat of three typical Na/K single or codoped PbTe samples plus pure PbTe; the open symbols are from the theoretical calculations based on TEM observations. (**f**) Histogram of nanoscale precipitates in the studied samples [83]

composition of precipitates is of $Pb_{1-x}(K_{0.6}Na_{0.4})_xTe$. (2) Adjust the x value to obtain the best match with the measured profiles. The best consistency with the measured image was obtained for $x \approx 0.15$ (inset in Fig. 10.5e), and similar contrast is also observed for the line-scanning profiles (Fig. 10.5f) for the measured (up) and simulated (down) profiles. To analyze the possible strain at or close to the precipitate/matrix interface, some regular circular-shaped precipitates were studied by GPA [2]. Figure 10.5g, h shows GPA analysis results, namely, strain maps along ε_{xx} and ε_{yy} directions, respectively. The line-scanning profile crossing both the matrix and the precipitate (inset Fig. 10.5g, h) shows that the lattice parameter difference is ~6 % (that of precipitate is larger), which is mainly due to the (Na, K) partially replacing Pb atoms, while there is little lattice parameter difference in the y direction. These results show that the lattice parameters of the precipitates change only along the *x* direction and remain constant along *y* and *z* directions compared to the matrix.

The above findings are meaningful in the understanding of alkali metals as carriers in p-type PbTe. These results also underscore that not all nanostructures favorably scatter phonons in a matrix, an insight that may help in further improvements of the $S^2\sigma$ and the overall ZT.

5.2 PbTe + XTe (X = Mg, Ca, Sr, Ba, Cd)

Recently, we have experimentally achieved concurrent phonon blocking and charge transmitting via the endotaxial placement of nanocrystals XTe (X = Mg, Ca, Sr, Ba, Cd) in a TE material PbTe host. Endotaxially arranged XTe nanocrystals at low

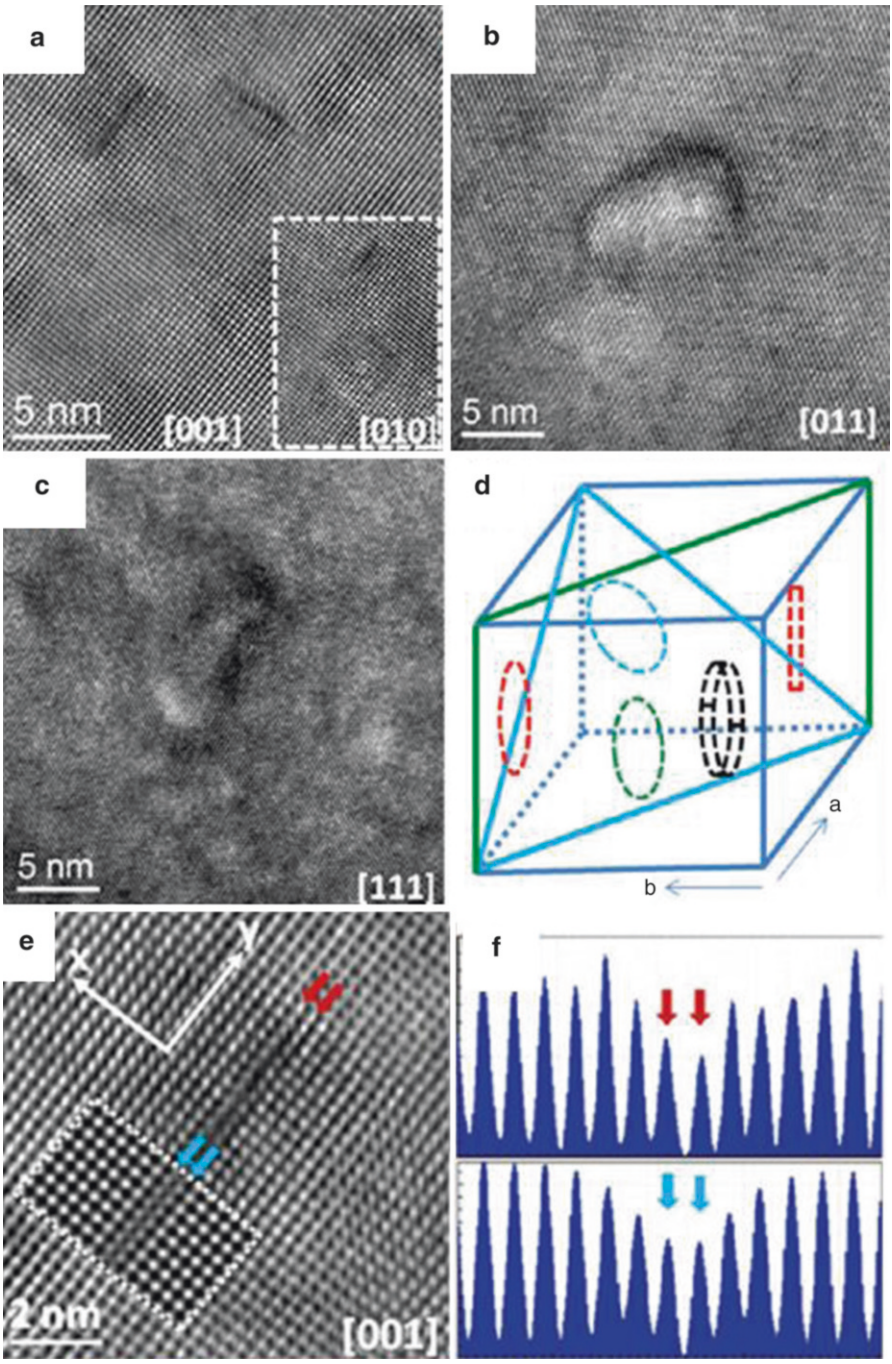


Fig. 10.5 (continued)

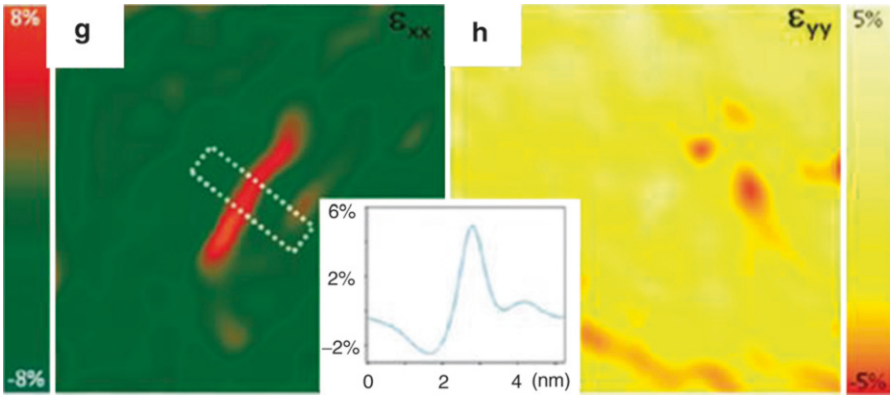


Fig. 10.5 (**a**) HRTEM lattice image of [001] Na/K codoped PbTe depicting two platelet-like precipitates. The inset along the [010] direction shows an elliptical-shape precipitate. (**b**, **c**) Random-shaped precipitates along the [011] direction and the [111] direction, respectively. (**d**) Schematic diagram describing the observed shape of a platelet-like precipitate as projected along the <100> (*red*), <110> (*green*), and <111> (*blue*) directions. (**e**) HRTEM lattice image along [001] direction of platelet-like precipitate. Inset simulated lattice image based on the platelike precipitate with $Pb_{0.85}(K_{0.6}Na_{0.4})_{0.15}Te$. (**f**) Line-scanning profiles of experimental image (*up*) and simulated image (*down*). (**g**, **h**) The ε_{xx} and ε_{yy} strain distribution of the platelet-like precipitate [83]

concentrations were incorporated in a PbTe matrix doped with Na_2Te, which effectively inhibits the heat flow in the system but does not affect the hole mobility, allowing a large $S^2\sigma$ to be achieved.

Figure 10.6a, b shows temperature-dependence σ and S of PbTe–SrTe (1 %) Na_2Te samples. There is very little effect on S with the change of SrTe concentration. Figure 10.6c gives a schematic representation of the alignment of the valence band and conduction band energies of SrTe precipitates in the PbTe matrix at $T > 300$ K; thus the insertion of endotaxial SrTe nanocrystals in the PbTe matrix does not affect the hole scattering. The lowest room temperature k_{total} and k_{lat} of about 3 W/(mK) and 1.2 W/(mK) was observed for samples containing 2 % SrTe which decreased to 0.9 W/(mK) and 0.45 W/(mK) at 800 K, respectively (Fig. 10.6d, e). It is clear that a large decrease (55 %) in k_{lat} occurs with insertion of SrTe in PbTe. Figure 10.6f presents the ZT values as a function of temperature for different PbTe–SrTe samples doped with 1 % Na_2Te. The highest ZT achieved was 1.7 at 815 K for a 2 % SrTe sample.

TEM investigations of the PbTe–SrTe (1 %) Na_2Te samples were presented to explore its microstructural base. In Fig. 10.7a, b, typical low-magnification TEM images of the 1 % and 2 % SrTe-containing samples show numerous spherical or ellipsoidal precipitates with dark (diffraction) contrast in the range of 5–15 nm. DP (Fig. 10.7b) shows an endotaxial relation between PbTe matrix and SrTe precipitates: Similar symmetry, structure, and lattice parameters and corresponding crystallographic planes and directions are completely aligned in three dimensions. Indeed, PbTe and SrTe have similar bulk lattice parameters of 6.453 and 6.660 Å, respectively. Figure 10.7c shows the size distribution histogram of SrTe nanocrystals for samples containing 1 % and 2 % SrTe under the same TEM

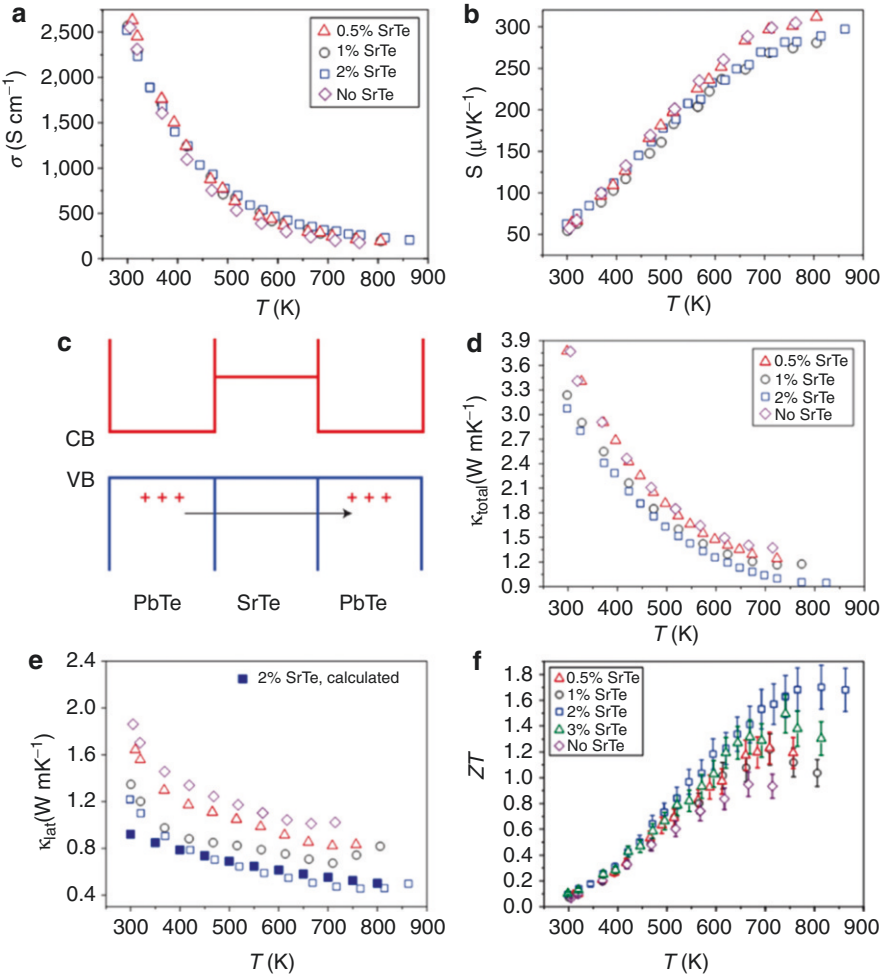


Fig. 10.6 (**a**) Temperature dependence of σ of different PbTe-2 % SrTe-1 % Na_2Te samples and a control sample containing no SrTe. (**b**) Temperature-dependent S. (**c**) Schematic representation of the alignment of the valence band and conduction band energies of SrTe precipitates in the PbTe matrix at T > 300 K. Temperature dependence of k_{total} (**d**) and k_{lat} (**e**). The *solid blue squares* in (**e**) show the temperature-dependent k_{lat} calculated with the Callaway model and input parameters obtained from TEM investigation of PbTe (2 %) SrTe (1 %) Na_2Te [43]

observation condition. It is clear that the 2 % SrTe sample has approximately doubled the precipitate density of the 1 % SrTe sample. On average, the precipitate number density can be estimated as $\sim 1.5 \times 10^{12}$ cm^{-2} for PbTe (2 %) SrTe (1 %) Na_2Te. Figure 10.7d shows an HRTEM phase-contrast image containing lattice fringes of several 2–4-nm precipitates with a typical interfacial boundary (~1 nm dark contrast) between the matrix and the precipitate. Figure 10.7e is the enlarged HRTEM image of precipitate, which clearly shows no dislocations at the boundary

marked by a dotted line. In Fig. 10.7f, the inverse first Fourier transform (IFFT) image of the precipitate depicts a coherent (elastically strained) interface between the precipitate and matrix. To analyze the presence of elastic and plastic strain, the image in Fig. 10.7d was subjected to GPA. Figure 10.7g shows the shear strain map

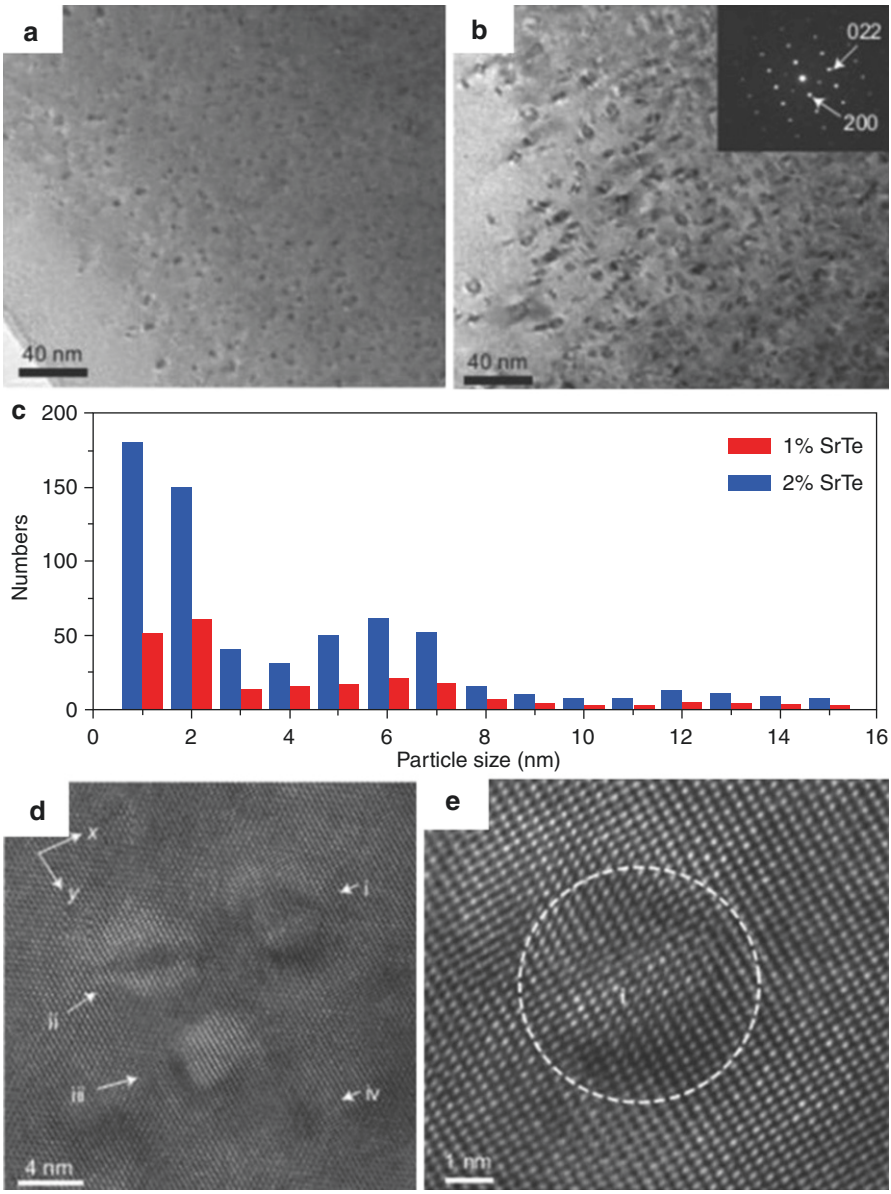


Fig. 10.7 (continued)

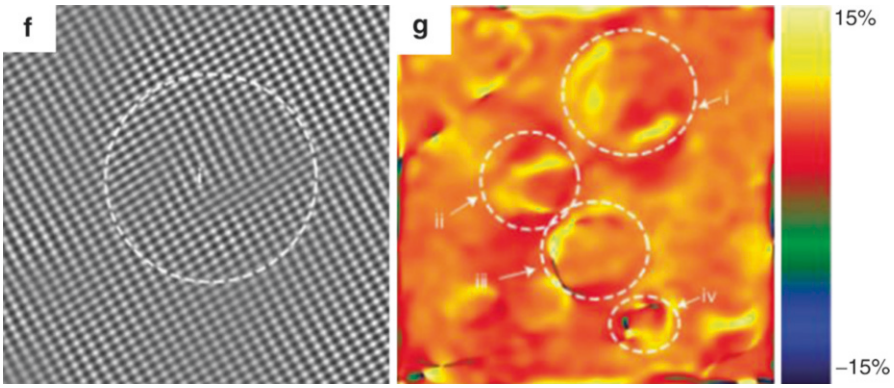


Fig. 10.7 Low-magnification TEM images of PbTe containing 1 % SrTe (**a**) and 2 % SrTe (**b**) (both doped with 1 % Na_2Te). The *inset* in (**b**) shows the corresponding DP. (**c**) SrTe nanocrystal size distribution histogram. (**d**) High-resolution TEM phase-contrast image of several endotaxial nanocrystals of SrTe in the PbTe matrix. (**e**) Enlarged image of particle in (**d**). (**f**) IFFT image showing the coherent interface with no misfit dislocations. (**g**) The shear strain distribution of the nanoscale inclusions [43]

profiles (σ_{xy}) of the precipitates, in which elastic strain is in and around all precipitates, although there is additional plastic strain around the dislocation cores.

Nanostructures in bulk TEs allow effective phonon scattering of a significant portion of the phonon spectrum, but phonons with long mean free paths remain largely unaffected. Recently we showed that heat-carrying phonons with long mean free paths can be scattered by fine-tuning the mesoscale architecture of nanostructured TE materials—we can achieve a record-high ZT value of ~2.2 at 915 K in the same SrTe-doped PbTe system as mentioned above, but with more SrTe and Na_2Te doping, as Fig. 10.8b shows [42].

Optimized atomic-scale doping/substitution (Fig. 10.8a) in the PbTe structure can lead to a ZT value of ~1.1 at 775 K (Fig. 10.8b) in the case of a PbTe bulk ingot sample doped with 2 % Na_2Te. The maximum ZT value increases to ~1.7 at 800 K (Fig. 10.8b) on the introduction of 2–10 nm endotaxial SrTe nanocrystals (Fig. 10.8a) into the Na-doped PbTe matrix [43]. Nanostructuring itself, however, scatters phonons with short and medium mean free paths (<100 nm), thus rendering only phonons with longer mean free paths unaffected. An additional and significant reduction in κ_{lat} may be achieved by further scattering of the phonons with longer mean free paths (>100 nm, i.e., mesoscale; Fig. 10.8a), on which scale additional mechanisms of grain-boundary phonon scattering can be exploited. The σ values of the SPS samples are higher at high temperatures and effectively reach a plateau from 600 to 850 K (Fig. 10.8c). The high values of S at high temperature arise from the well-known contribution of the two valence bands in PbTe [43, 93]. The coupling of high σ and S values results in $S^2\sigma$ remaining high at higher temperatures (Fig. 10.8e). A typical room temperature value of $\kappa_{total} \approx 2.85$ W/(mK) was

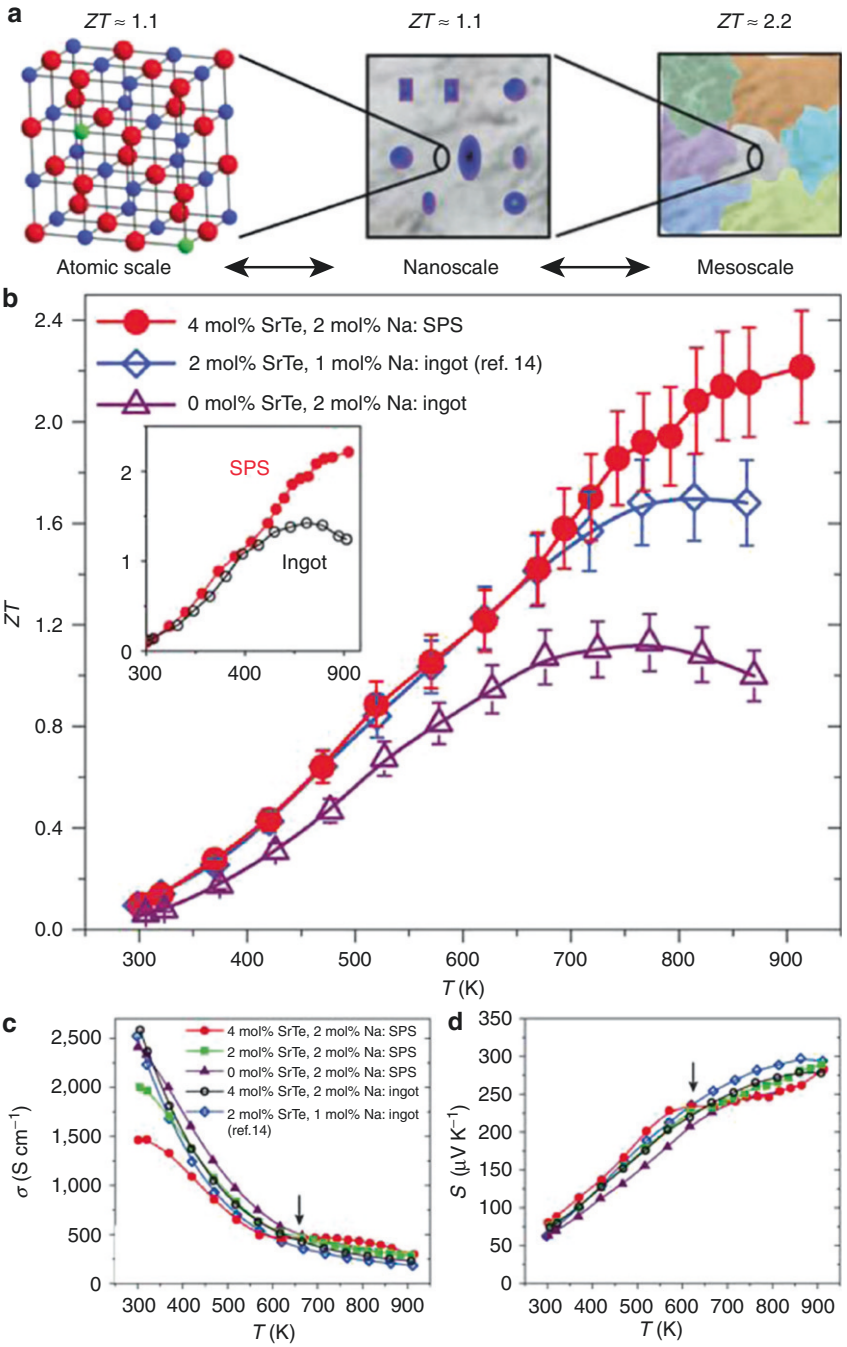


Fig. 10.8 (continued)

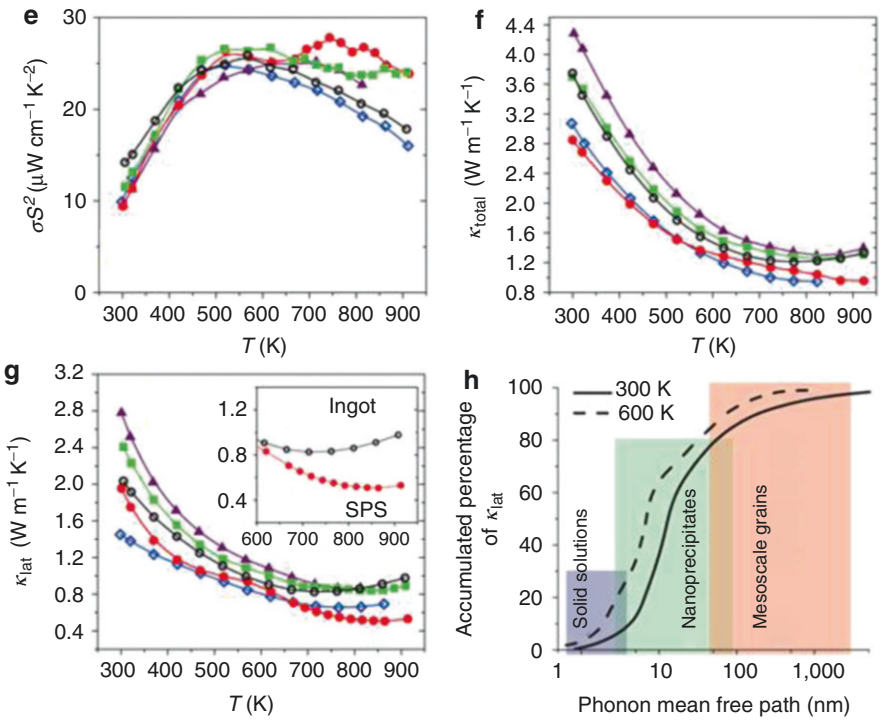


Fig. 10.8 (**a**) Maximum achievable ZT values for the respective length scales: the atomic scale (alloy scattering: *red*, Te; *blue*, Pb; *green*, dopant) and the nanoscale (PbTe matrix, *gray*; SrTe nanocrystals, *blue*) to the mesoscale (grain-boundary scattering). (**b**) ZT as a function of temperature for an ingot of PbTe (2 %) Na_2Te, PbTe (2 %) SrTe (1 %) Na_2Te [43]; atomic plus nanoscale) and SPS PbTe (4 %) SrTe (2 %) Na_2Te (atomic- plus nano- plus mesoscale). (**c**) Temperature-dependent σ. The temperature-dependent transport data for the bulk ingot of PbTe (2 %) SrTe (1 %) Na_2Te is shown for comparison. (**d**–**g**) Temperature-dependent S (**d**), $S^2\sigma$ (**e**), k_{total} (**f**), and k_{lat} (**g**). *Inset* in (**e**) comparison of κ_{lat} in SPS and ingot samples with the same composition. (**i**) Contributions of phonons with different mean free paths to the cumulative κ_{lat} value for PbTe [42]

observed for PbTe (4 %) SrTe (2 %) Na_2Te, which decreased to ~0.96 W/(mK) (Fig. 10.8f). We observe that the κ_{lat} values of the SPS samples are lower than those of the same composition ingots and, more importantly, that the difference increases as the temperature is increased (Fig. 10.8g, inset). The upturn in the plot of κ_{lat} as a function of T at high temperature for the ingot sample is due to the bipolar contribution to the κ by thermally generated electrons and holes [94]. In contrast, in the SPS samples the bipolar contribution is negligible, and there is no upturn because of the existence of an interfacial potential at grain boundaries that scatters more electrons than holes [17].

The SPS PbTe (4 %) SrTe (2 %) Na_2Te contains nanoscale precipitates and mesoscale grains, which are clearly evident in TEM and APT studies (Fig. 10.9).

The presence of mesoscale grains 0.1–1.7 μm (0.8 μm in average) in size (Fig. 10.9a, c) and nanoscale precipitates with dark contrasts in the range of 1–17 nm (2.8 nm in average) (Fig. 10.9b, d) is evident in these images. The small precipitates (∼1–6 nm) with a platelet-like morphology are coherently strained, while the larger precipitates (∼10–17 nm) have spherical or ellipsoidal shapes along with interfacial misfit dislocations. Figure 10.9e shows a representative HRTEM image of platelet-like precipitates obtained along [001] zone axis. All platelet-like precipitates are organized perpendicular or parallel to each other, consistent with two of three possible crystallographic variants. The inset image shows a spherical precipitate with a coherent (elastically strained) interface with the matrix, without any interfacial dislocations. Figure 10.9f shows the image and the results of the GPA, namely, the components ε_{xx} and ε_{yy} of the strain. The image showing two perpendicular platelet-like precipitates enclosed by dotted lines indicates that there is elastic strain only along the x direction for the upper precipitate and only along the y direction for the lower. Thus, the strain distribution in platelet-like precipitates is anisotropic compared with spherical precipitates, which have uniform omnidirectional strain distributions. STEM investigations (Fig. 10.9g) show the presence of some medium-size (20–50 nm) precipitates, in addition to smaller ones (1–15 nm). EDS indicates a large increase in the Sr signal from the precipitates compared to the matrix regions (Fig. 10.9g), suggesting that precipitates are mainly SrTe. The segregation of Na at grain boundaries, precipitate-matrix interfaces, and dislocations was confirmed by 3D APT [11]. The 3D reconstruction of the volume of PbTe (4 %) SrTe (2 %) Na_2Te analyzed by APT is given in Fig. 10.9h. The compositions of the matrix and the precipitates correspond to SrTe and PbTe, respectively. The composition profile across the interface of the large precipitate is measured using a proximity histogram (Fig. 10.9i), which shows ∼1.6 at.% Na accumulation at the interface. Na also accumulates at the core of a dislocation core and at grain boundaries (Fig. 10.9j). We believe that the Na which is confined to grain boundaries (and other defect sites) at low temperature goes back into solid solution with the PbTe matrix at elevated temperatures, thus increasing the p-type charge-carrier density. This provides a viable explanation for the enhanced σ and S of SPS samples at high temperature as discussed above (Fig. 10.8c).

TEM studies show that a PbTe–BaTe bulk TE system represents the coexistence of solid solution and nanoscale BaTe precipitates, which collectively provide scatter phonons [44]. Figure 10.10a, b reveals high number density nanostructures in the sample. Statistical analysis (inset Fig. 10.10a, b) of PbTe (3 %) BaTe sample has higher number density than that of 1 % BaTe sample. Many dark-contrast spherical precipitates (<20 nm) are observed. Corresponding DP along [011] zone axis (inset) with an aperture including matrix and several precipitates shows only one set of Bragg reflections, which means endotaxial relation between the matrix and precipitates. EELS (Fig. 10.10c) and EDS (Fig. 10.10d) measurements were conducted to confirm the existence of Ba and Te in the large precipitates. In the EELS patterns, the Ba M4 and M5 edges are clearly seen at the spot 2 (precipitate), while there is no Ba signal at the spot 1 (matrix). In order to enhance the visibility of

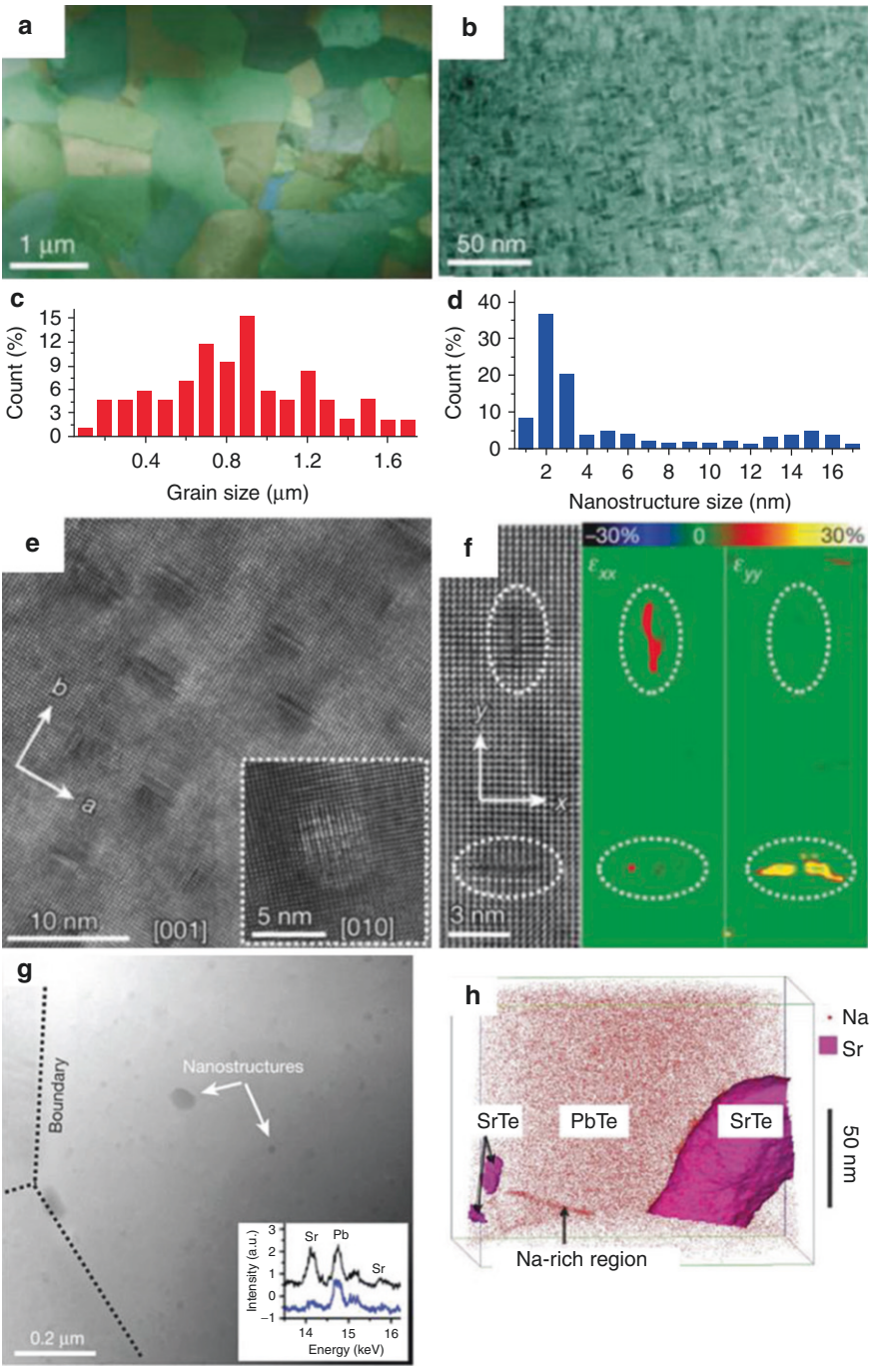


Fig. 10.9 (continued)

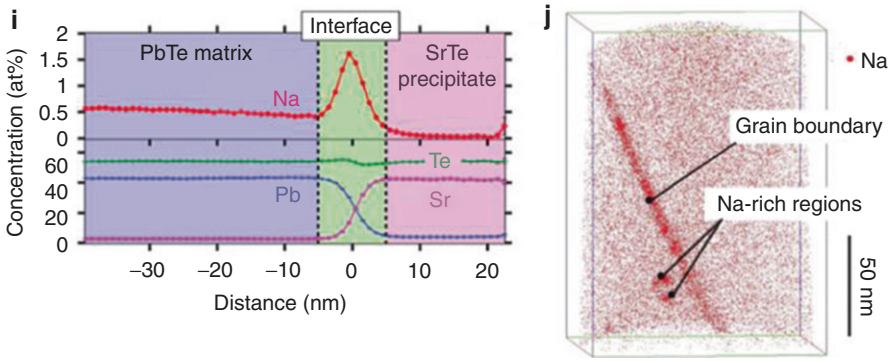


Fig. 10.9 (**a**) Low-magnification TEM image showing mesoscale grains in the sample. (**b**) Medium-magnification TEM image revealing presence of platelet-like and spherical/ellipsoidal nanoscale precipitates. (**c**) Grain size distribution histogram. (**d**) Size distribution histogram of SrTe nanoparticles. (**e**) HRTEM lattice image depicting some perpendicular or parallel platelet-like precipitates. Inset is a small spherical precipitate with a coherent interface with the matrix. (**f**) Lattice image and strain maps showing elastic strain. (**g**) STEM image showing the presence of SrTe nanostructures in the PbTe matrix. *Inset* is EDS (*black*, precipitate; *blue*, matrix). (**h**) 3D reconstruction of the volume analyzed by APT. (**i**) Proximity histogram showing the concentration profiles of Pb, Te, Sr, and Na across the interface of the large SrTe precipitate. (**j**) 3D reconstruction of a volume analyzed by APT, containing a grain boundary [42]

the core-loss edges of Ba, the background signals originated from multiple scattering need to be subtracted. The similar backgrounds shown in Fig. 10.10d indicate that these two spots have comparable thickness.

HRTEM images of Fig. 10.10e, f show endotaxial precipitates in the matrix with coherent interface. The line with no contrast marked by arrows corresponds to the plane that is not distorted by the strain field of the precipitates. Assuming the full strained and high coherence between PbTe and BaTe, the simplified atomic model and simulated images of the precipitate and the matrix are illustrated in Fig. 10.10h, and the corresponding high-resolution image is shown in Fig. 10.10g. In some areas, Moiré fringes can be found around the precipitate. It is well known that Moiré fringes are formed by the interference between two sets of planes with nearly common periodicity and small relative rotation angle. The correlation between two interfaces can be determined by measuring the lattice spacing of the three sets of planes as indicated in Fig. 10.10g. The general Moiré fringe relationship [95] is given by

$$d_{gm} = \frac{d_1 d_2}{\sqrt{(d_1 - d_2)^2 + d_1 d_2 \beta^2}} \tag{10.12}$$

where d_{gm} (~1.49 nm) is the spacing of the fringes, d_1 (~0.34 nm) and d_2 (~0.28 nm) are the lattice spacing of the matrix and the precipitate along

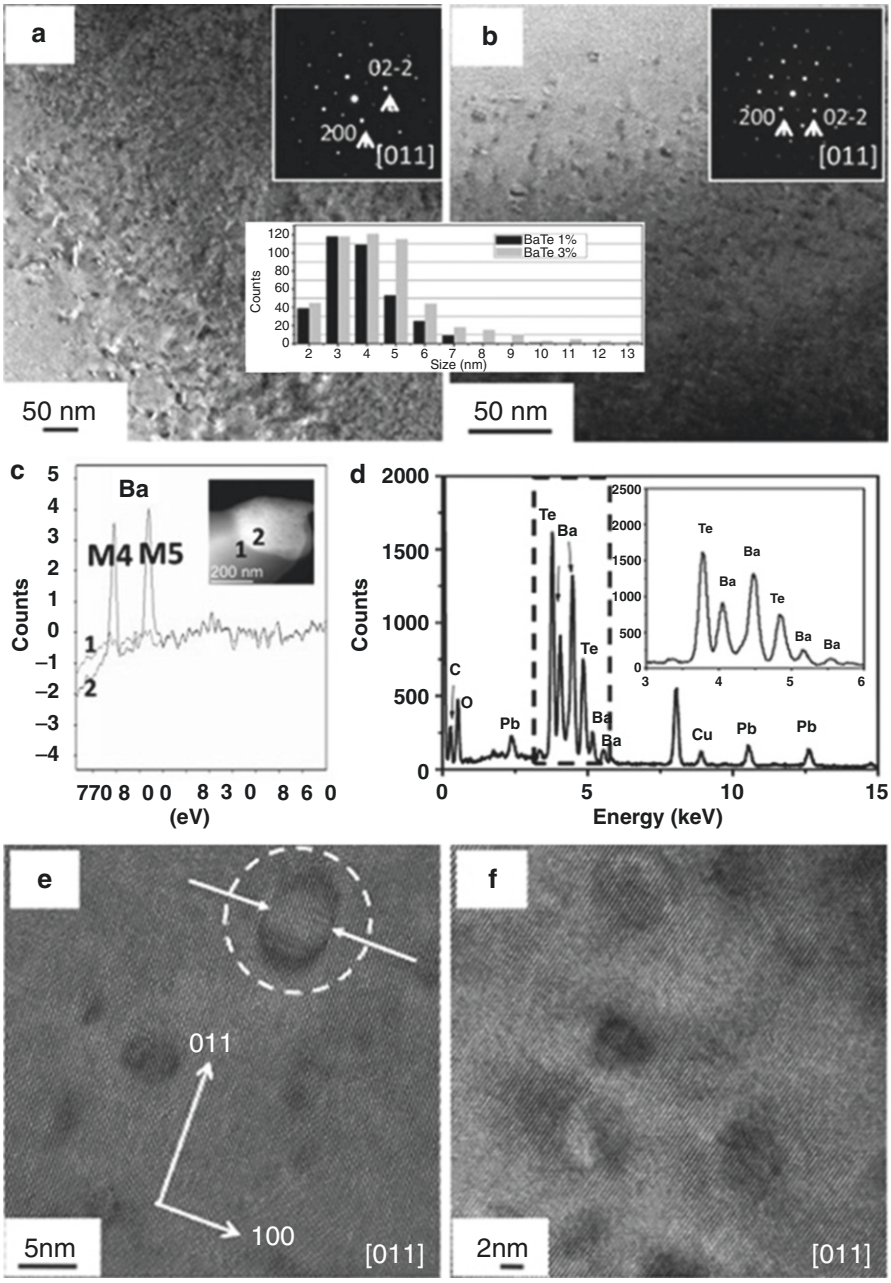


Fig. 10.10 (continued)

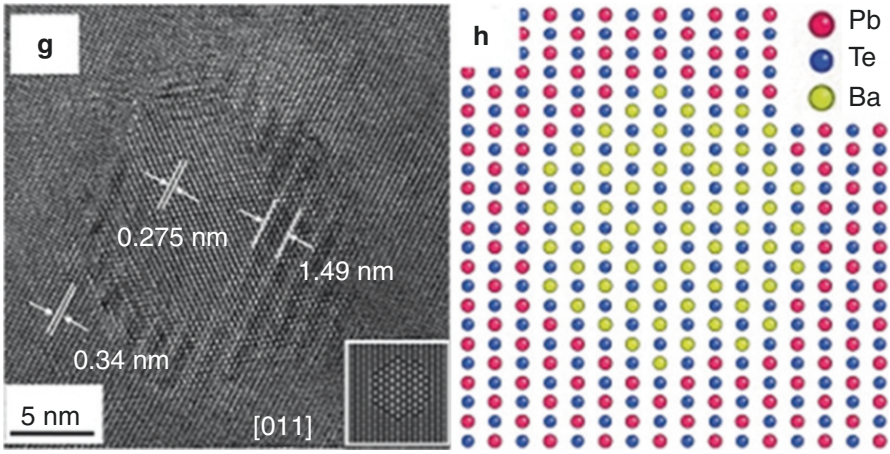


Fig. 10.10 TEM analysis of PbTe–BaTe (1 %) Na_2Te. Low-magnification TEM images of PbTe containing 3 % (**a**) and 1 % of BaTe (**b**). The insets in the (**a**) and (**b**) show the corresponding DPs and their histogram of BaTe nanoscale precipitate size distribution. (**c**, **d**) EELS and EDS spectra confirming the element Ba. HRTEM phase-contrast images of the precipitates for 3 mol% BaTe (**e**) and 1 mol% BaTe (**f**). Enlarged HRTEM phase-contrast image of precipitate with modulation (**g**) and, correspondingly, the simulated image in the inset and the atomic model (**h**) [44]

[100], respectively, and β is the relative rotation angle. The small rotation angle between PbTe matrix and BaTe precipitate can be cross-checked as about 1.26°.

Detailed analysis of the boundaries between the precipitates and matrix is shown in Fig. 10.11. The misfit dislocation is observed at the interface in the HRTEM phase contrast (Fig. 10.11a). The extra lattice plane is located at the side of PbTe, which has smaller lattice parameter ($a = 6.46$ Å) than that of BaTe ($a = 7.001$ Å). Figure 10.11b, c represents the simulated image along [110] zone axis and the modeling of the misfit dislocation. This model demonstrates the measured displacement vector of $a/2$ [100]. The HRTEM lattice image with several precipitates is shown in Fig. 10.11d. Comparing this diffractogram obtained by FFT (inset in Fig. 10.11d) with the DP shown in Fig. 10.10a, b, two sets of superimposed DPs can be obtained: One set is exactly the same as the DP along [110] zone axis (insets in Fig. 10.10a, b), and the other set is the diffuse spot indicated by white triangles. These superlattice-like spots due to the multiple scattering were selected to reconstruct the IFFT image as depicted in Fig. 10.11e. The stacking faults due to crystal defect and overlapping patterns can be clearly seen. Figure 10.11f, g shows the tensile in-plane strain field ε_{xx} and ε_{yy}, in which the elastic as well as plastic strains are observed.

Phonons can also be strongly scattered with little effect on the $S^2\sigma$ in endotaxially embedding nanocrystals of CaTe in PbTe. The highest TEZT value achieved is ~1.5 at 765 K for 6 % CaTe containing sample. TEM of 2 % CaTe sample and STEM of 5 % CaTe sample (Fig. 10.12a, b) demonstrate the presence of endotaxially nanostructures (1–7 nm). EELS confirms the presence of Ca in the

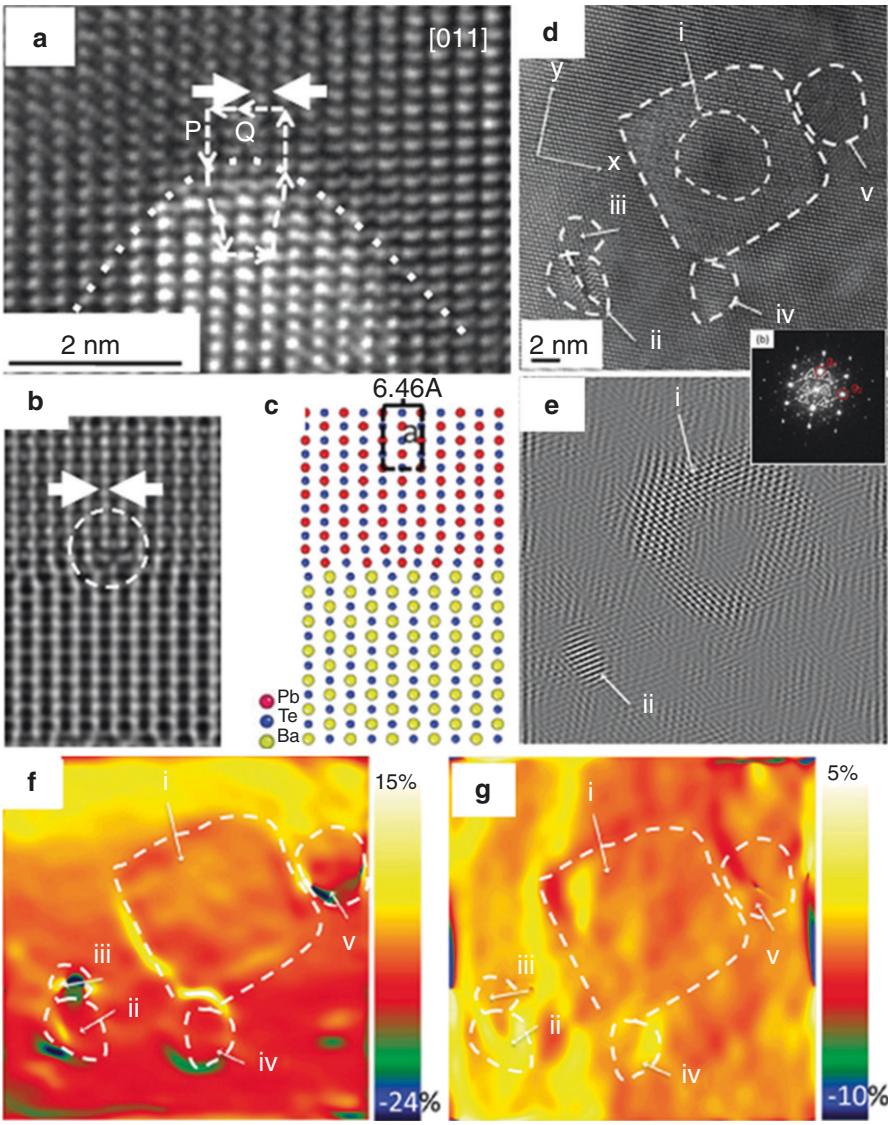


Fig. 10.11 (**a**) The HRTEM image of the misfit dislocation on the boundary between the matrix and the precipitate. The dislocation is circled in the simulated image as (**b**) and the extra plane is indicated by *arrows*. (**c**) The corresponding atomic structural model of the boundary and the misfit dislocation. (**d**) HRTEM phase-contrast image of nanoscale precipitates and stacking faults. (**e**) IFFT image. The *inset* in (**d**) and (**e**) is the corresponding power spectrum. (**f**, **g**) The shear strain distribution of the nanoscale precipitates along y and x directions [44]

nanoprecipitates (Ca-$L_{2,3}$ edge in Fig. 10.12c). Figure 10.12e shows the size distribution histogram of the 2 % and 5 % CaTe (higher density) containing samples. Figure 10.12f, g shows a typical HRTEM lattice image with nanoscaled precipitates. Figure 10.12h, i is the ε_{xx} and ε_{yy} strain map profiles of the precipitates in Fig. 10.12g, respectively. It appears that elastic strain is pervasive in and around

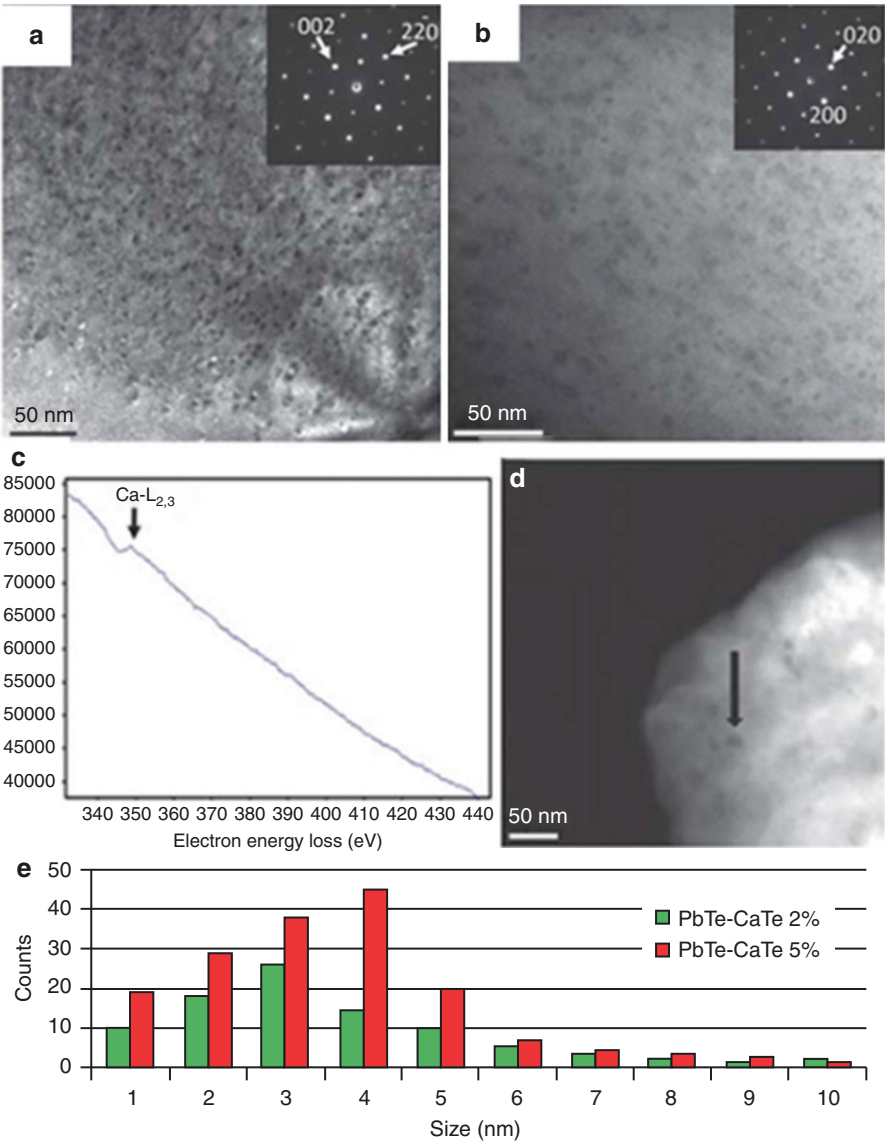


Fig. 10.12 (continued)

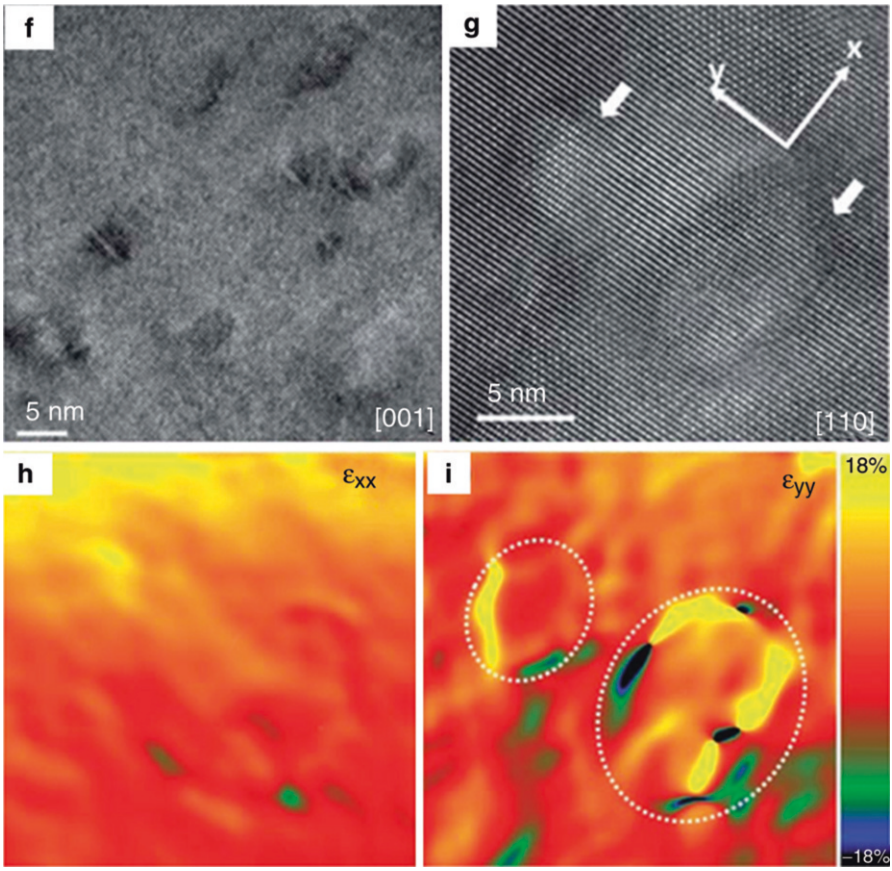


Fig. 10.12 Low-magnification (**a**) TEM image of PbTe (2 %) CaTe (1 %) Na_2Te and (**b**) STEM image of PbTe (5 %) CaTe (1 %) Na_2Te. *Insets* show the DPs and the corresponding directions of each image. (**c**) EELS spectra of the PbTe (5 %) CaTe obtained from the nanoprecipitate indicated by the *arrow mark* in the STEM image shown in (**d**). (**e**) CaTe nanocrystal size distribution histogram. Different magnified HRTEM images (**f**) and (**g**) of PbTe (5 %) CaTe (1 %) Na_2Te. (**h**) and (**i**) are the ε_{xx} and ε_{yy} strain maps of the image in (**g**), respectively [41]

the small precipitate with the absence of dislocations. For larger precipitates, plastic strain around the dislocation cores in addition to the elastic strain at the boundary is observed.

MgTe in PbTe has also a large effect on thermal transport (Fig. 10.13a), while only a small effect on the electrical transport properties. A ZT of 1.6 at 780 K can be achieved for the PbTe (2 %) MgTe (2 %) Na_2Te (Fig. 10.13b). Figure 10.13c shows a typical low-magnification TEM image showing nanoscale precipitates as dark contrast embedded in the matrix. The DP along [011] zone axis indicates the complete alignment of the nanoprecipitate/matrix lattices (endotaxy). HRTEM image of nanoscale precipitates (2–15 nm) with elliptical shape is presented in Fig. 10.13d.

The full endotaxy is believed to be important in achieving the high carrier mobilities in these samples; EDS elemental mapping (Fig. 10.13e) and microprobe spectroscopy (Fig. 10.13f) on a comparatively bigger precipitate in PbTe (10 %) MgTe sample show the clear presence of Mg in the nanoprecipitate but not in the matrix.

We also explored the effect of Cd substitution on the TE properties of PbTe. Cd atoms on Pb sites of the rock salt lattice can increase the S via the formation of a resonance level in the density of states near the Fermi energy. A maximum ZT of ~1.2 at 720 K was achieved for the PbTe (1 %) CdTe (0.055 %) PbI_2 sample arising from a high $S^2\sigma$ of ~17 μW/(cmK^2) and a very low k_{lat} of ~0.5 W/(mK) at 720 K, just as Fig. 10.14a–c shows. The significant reduction of k_{lat} in the PbTe − CdTe system should be due to the endotaxially formed CdTe

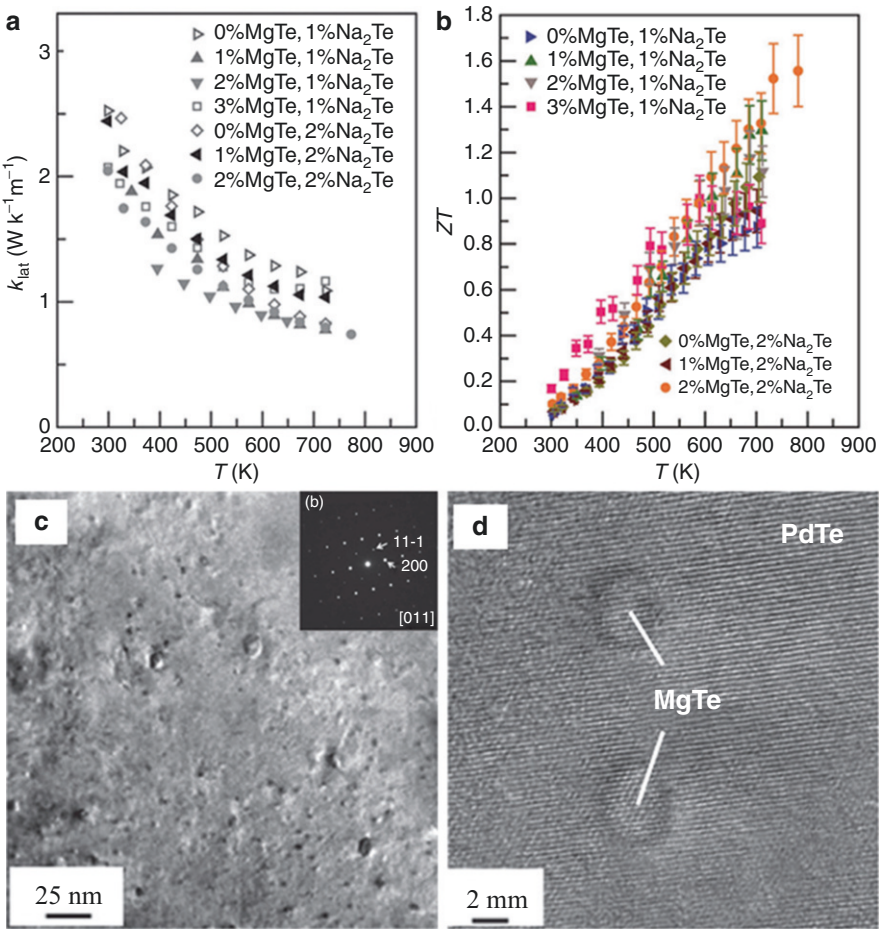


Fig. 10.13 (continued)

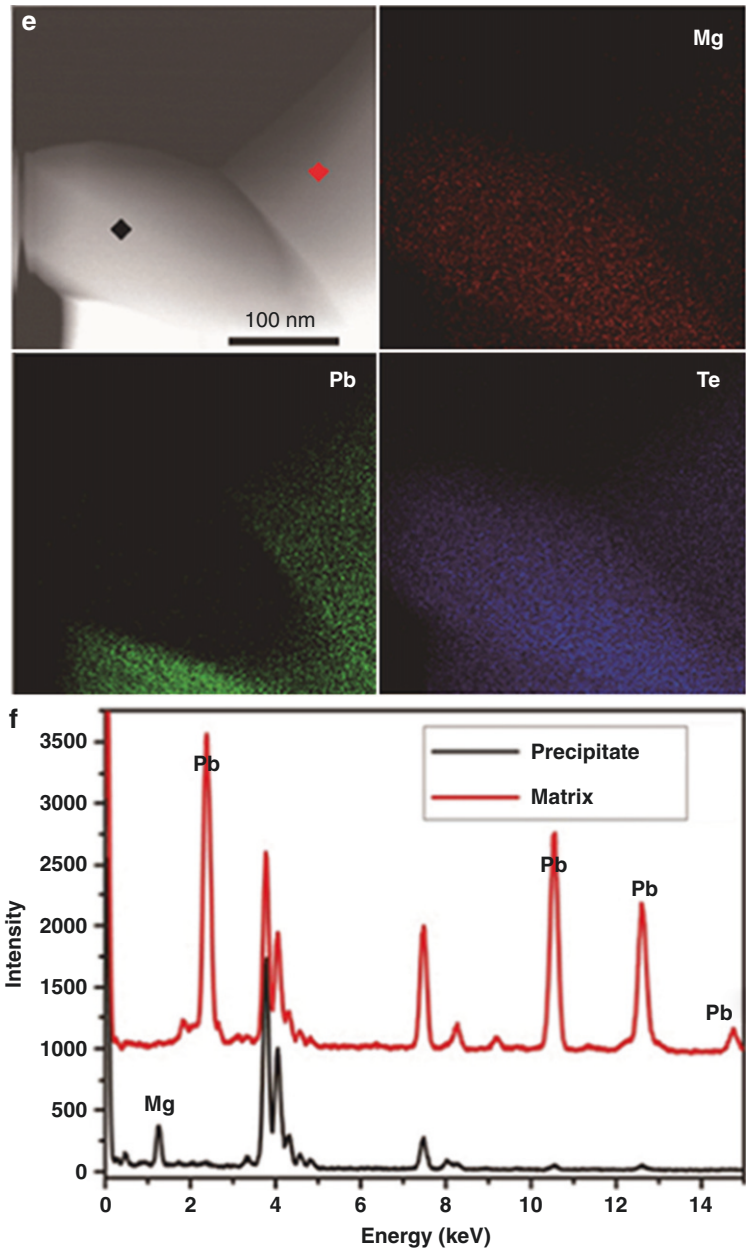


Fig. 10.13 Temperature dependences of the k_{lat} (**a**), ZT (**b**) of PbTe-*x*MgTe (x = 0–3 %) doped with Na_2Te (1–2 %). (**c**) Low-magnification TEM image of PbTe (2 %) MgTe (2 %) Na_2Te. *Inset* DP along [011] zone axis. (**d**) HRTEM image. (**e**) EDS elemental mapping on comparatively bigger MgTe nanoprecipitate of PbTe (10 %) MgTe and (**f**) the corresponding spectrum [40]

nanoparticles inside the PbTe matrix. Figure 10.14d shows a typical low-magnification TEM image of the PbTe (1 %) CdTe sample, which depicts some nanoparticles (2–8 nm) in the matrix. Figure 10.14e is an HRTEM lattice image with two precipitates with clear coherent interface. These results suggest that the 3 % solubility limit of CdTe in PbTe reported in the phase diagram is overestimated, and the true limit is less than 1 %, which highlights the dangers

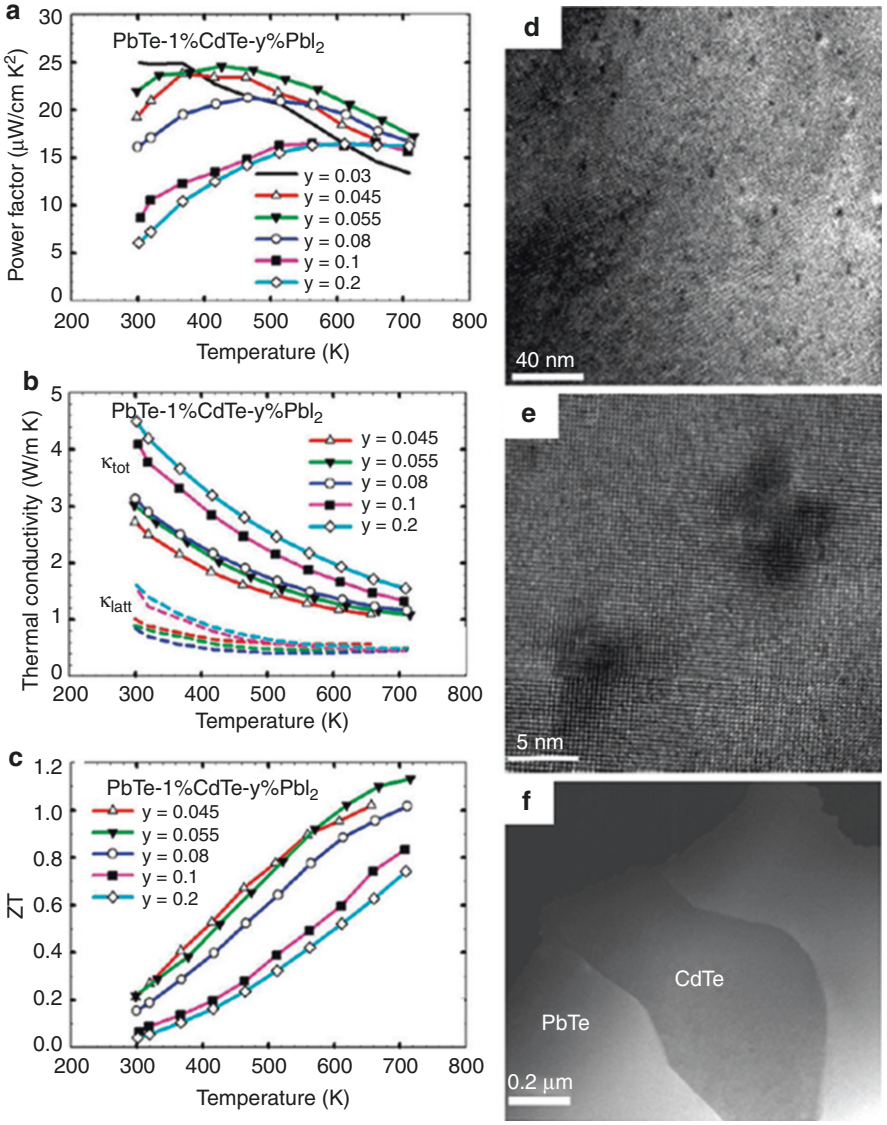


Fig. 10.14 (continued)

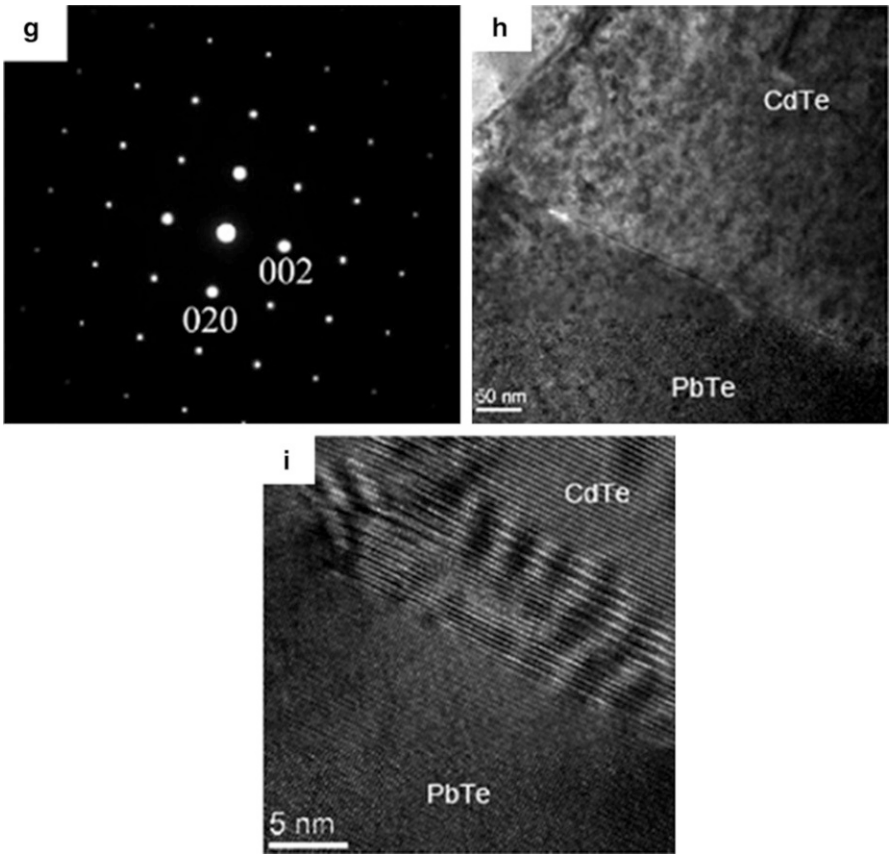


Fig. 10.14 (**a**) Temperature dependence of (**a**) $S^2\sigma$, (**b**) the κ_{total} (*solid line*) and κ_{latt} (*dash line*), and (**c**) the TEZT of samples of PbTe (1 %) CdTe (*y*%) PbI_2 ($y = 0.03, 0.045, 0.055, 0.08, 0.1, 0.2$). (**d**) Low-magnification TEM image and (**e**) HRTEM lattice image of PbTe (1 %) CdTe. (**f**) STEM image. (**g**) DP including the large precipitate and matrix. (**h**) Low-magnification TEM image of PbTe (10 %) CdTe sample. (**i**) HRTEM lattice image of boundary between the PbTe matrix and large CdTe precipitate [32]

of using XRD studies to determine solubility limits. Figure 10.14f is a STEM image of the PbTe (10 %) CdTe sample depicting a large dark CdTe precipitate in the PbTe matrix, while the nanoscale precipitates at this magnification cannot be seen. DP (Fig. 10.14g) shows coherent relation between precipitates and matrix. Two types of CdTe precipitates (nanoscale and microscale) are clearly shown in a low-magnification TEM image (Fig. 10.14h). In Fig. 10.14i the HRTEM lattice image shows boundaries between the PbTe matrix and large CdTe precipitates, in which modulated regions arised simply from the overlap between the PbTe and CdTe lattices along the electron beam direction can be seen.

5.3 PbTe + PbX (X = S, SnS_2)

Besides varying A-site substitution of PbTe (i.e., XTe (X = Mg, Ca, Sr, Ba, Cd)), we also found B-site substitution of PbTe, i.e., PbX (X = S, SnS_2), as effective way to enhance TE performances. In this section, we mainly focus on the peculiar microstructural features in PbTe–PbX systems, which have influence on the TE properties.

We reported a TE material system PbTe (12 %) PbS (2 %) Na_2Te with a maximum ZT of 1.8 at 800 K (Fig. 10.15f), whereby we can control nanostructure formations to effectively reduce κ, while concurrently modifying the electronic structure to significantly enhance $TES^2\sigma$ (Fig. 10.15c) [47]. The peculiar enhance TE electron transport (Fig. 10.15a–c) phenomenon can be described as the schematic figure in Fig. 10.15d. As PbS is dissolved in the PbTe matrix, the light hole valence band of PbTe is lowered in energy (increased in band gap E_g), decreasing the difference in energy between the light and heavy hole bands. At elevated temperatures, thermally excited carriers traverse from the heavy to light hole bands, increasing the population of heavy holes and enhancing thermopower at elevated temperatures. The introduction of nanostructures in PbTe (12 %) PbS reduces the k_{lat} by 50 % relative to pure PbTe at 800 K (Fig. 10.15e).

Figure 10.15g, h shows low-magnification TEM images of PbTe (8 %) PbS (2 %) Na_2Te and PbTe (12 %) PbS (2 %) Na_2Te, respectively. The inset in Fig. 10.15g shows a typical magnified TEM image with regular rectangular-shaped nanoparticles with the precipitate and matrix interfaces along the [100] or [010] directions, which is the projection of the nanocube along [001] axis as pointed by the arrowhead. The DP in the inset of Fig. 10.15h confirms the two separate phases (i.e., matrix and cubic precipitate) and their excellent endotaxial crystallographic alignment. The inset of Fig. 10.15h is a typical HRTEM image of a small irregularly shaped precipitate. In Fig. 10.15i, the low-magnification TEM image of PbTe (12 %) PbS (1 %) Na_2Te (with lower Na dopant) also shows truncated nanocubes in addition to the nanocubes. The inset is a projection of a truncated nanocube, which clearly shows the [100] and [111] planes. Figure 10.15j and inset show randomly shaped precipitates in PbTe (12 %) PbS (0.5 %) Na_2Te. Thus the shape control of PbS nanocrystals by tuning the Na concentration can be realized.

Recently, we found an interesting phenomenon: in situ nanostructure formation in PbTe–PbS system. Solid solution alloys of PbTe − PbS can be synthesized through rapid cooling and subsequent high-temperature activation that induces a spontaneous nucleation and growth of PbS nanocrystals. HRTEM lattice image in Fig. 10.16a shows homogeneous microstructure for rapidly cooled samples. DP of PbTe (8 %) PbS samples confirm a single-phase material (Fig. 10.16a, inset). SEM analysis of PbTe (8 %) PbS after annealing (Fig. 10.16b) shows the average size of precipitated particles is generally 100 nm in diameter. EDS line-scanning analysis of the precipitates confirms precipitate composition to be PbS (Fig. 10.16c). STEM of the annealed sample reveals even smaller particles 2–10 nm in diameter in addition to the larger PbS precipitates (Fig. 10.16d). A DP from the PbTe matrix/PbS particle interface is shown in inset Fig. 10.16e.

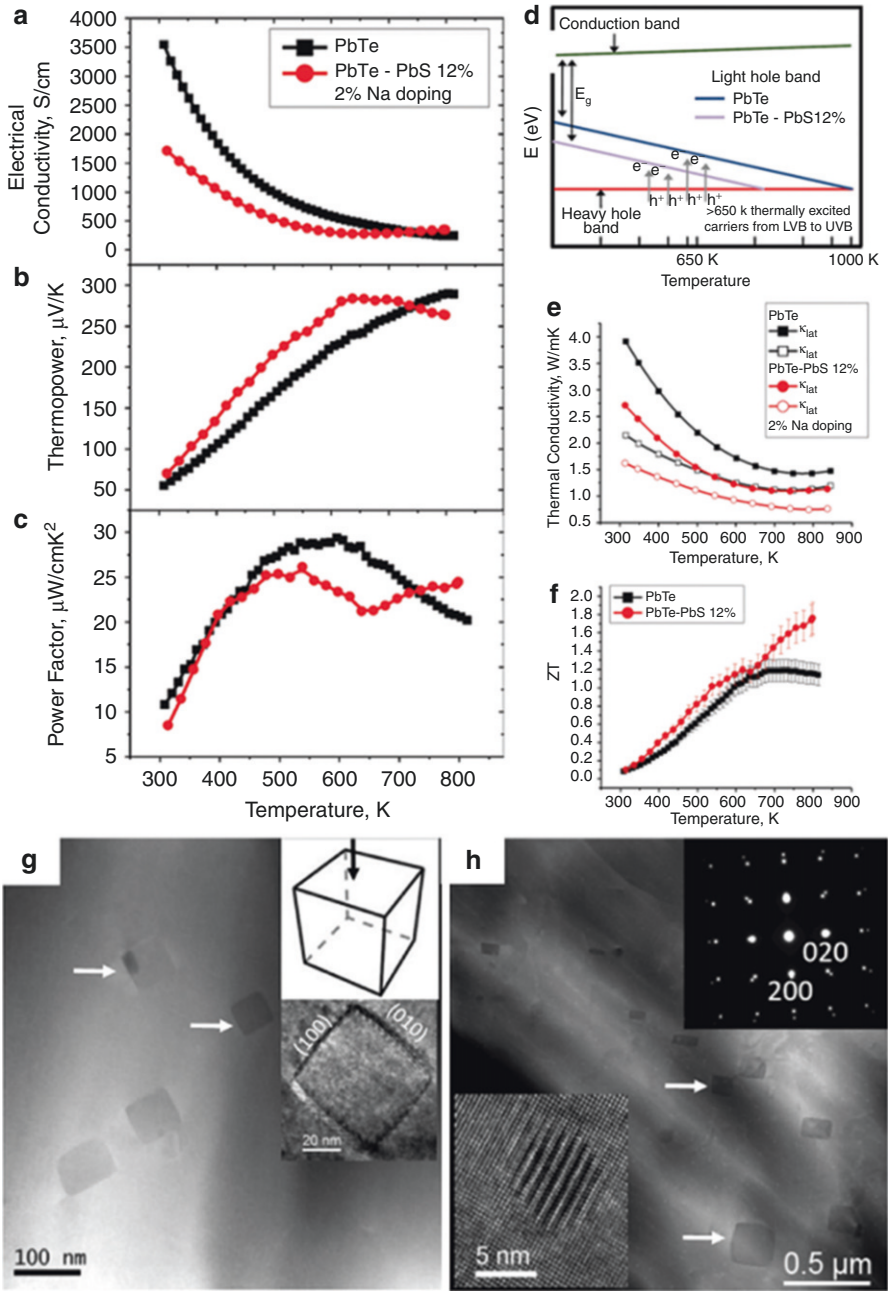


Fig. 10.15 (continued)

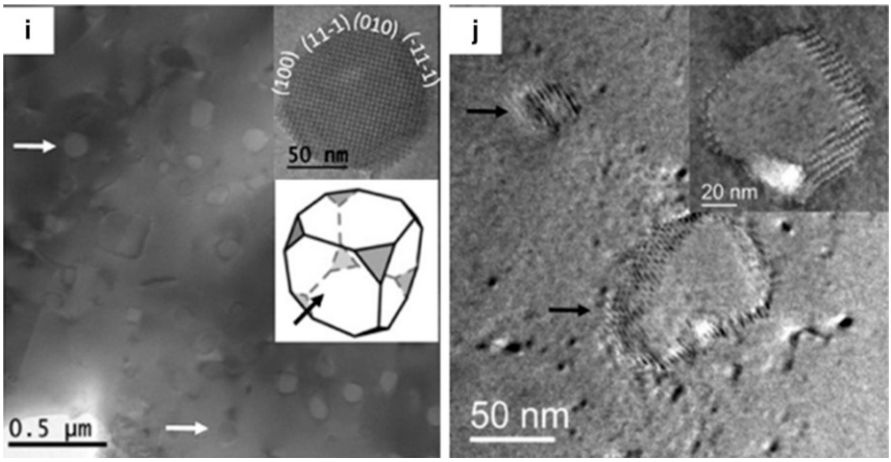


Fig. 10.15 High-temperature (**a**) σ, (**b**) thermopower, and (**c**) $S^2\sigma$ of PbTe (12 %) PbS (2 %) Na_2Te. (**d**) Schematic showing shift of valence band extreme of PbTe and PbTe (12 %) PbS with temperature. High-temperature (**e**) k_{total} and k_{lat} and (**f**) ZT of PbTe (12 %) PbS (2 %) Na_2Te. S/TEM images of (**g**) PbTe (8 %) PbS (2 %) Na_2Te and (**h**) PbTe (12 %) PbS (2 %) Na_2Te. (**i**) As the Na concentration is reduced to PbTe (12 %) PbS (1 %) Na_2Te, truncated cubes are formed with additional facets along the [111] crystallographic planes. (**j**) As the Na doping is further reduced to PbTe (12 %) PbS (0.5 %) Na_2Te, randomly shaped PbS precipitates are observed [47]

Each diffracted spot is clearly split along all directions, indicating the cubic PbS second phase is oriented in the same crystallographic direction as the PbTe matrix. From the DP, an accurate image calibration employing digital micrograph processing software (assuming the cubic PbTe lattice parameter $a_{PbTe} = 6.460$ Å as a calibration standard) [23] allowed us to determine the lattice parameters of PbS ($a_{PbS} = 5.93$ Å), which closely agrees with the bulk lattice parameter ($a_{PbS} = 5.936$ Å). In Fig. 10.16f, an HRTEM lattice image of the semi-coherent boundary between the PbS particle and PbTe matrix reveals a regular series of misfit dislocation cores, confirming the strain should be relaxed at the interfaces. HRTEM images in Fig. 10.16g, h show PbS nanoparticles within the PbTe matrix and PbTe nanoprecipitates within the larger PbS particles, respectively. The size of these small fully coherent particles generally ranges between 2 and 10 nm. On average, the estimate of the distribution density of the smaller nanoparticles (6 nm) is $\sim 1 \times 10\ cm^{-2}$, while for the larger precipitates (100 nm) is $\sim 1 \times 10\ cm^{-2}$. The fully coherent smaller particles are effective at scattering acoustic phonons at high temperature due to their small size, while the misfit dislocations at the boundaries of the larger particles and the resultant plastic strain situated with them will also disrupt phonon transport.

Another interesting phenomenon, spinodal decomposition, was found in PbTe with more alloying PbS, PbTe (30 %) PbS. The nominal PbTe (30 %) PbS composition spinodally decomposes into two phases: PbTe and PbS. Regularly shaped nanometer-scale precipitates, orderly misfit dislocations, incomplete

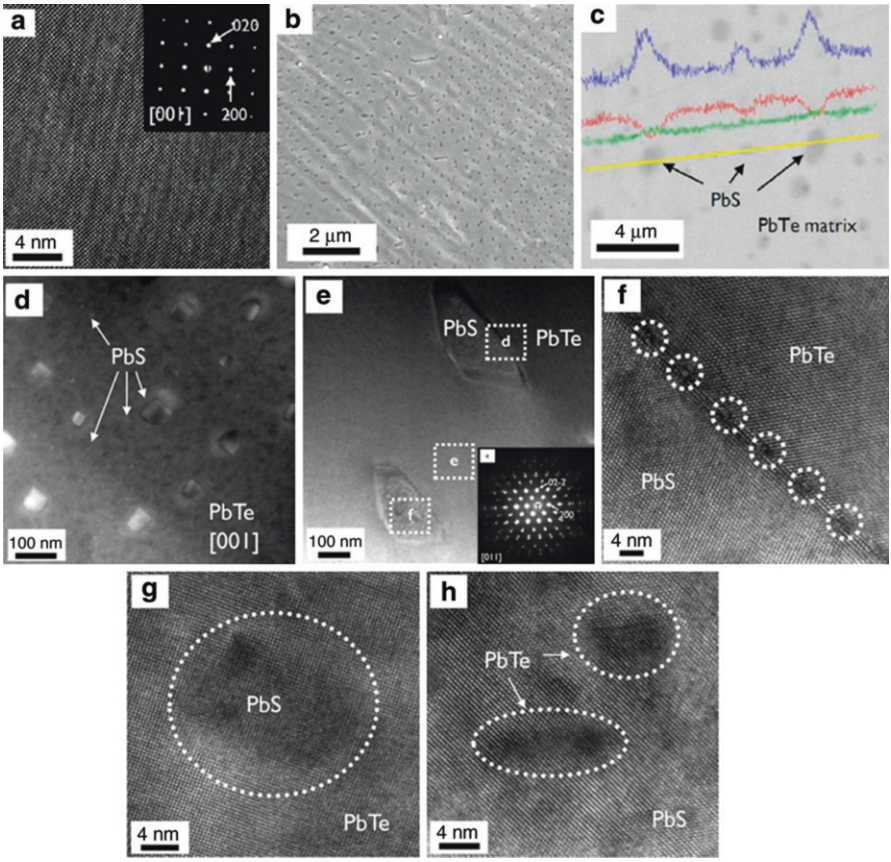


Fig. 10.16 (**a**) HRTEM image of solid solution PbTe (8 %) PbS with an *inset* DP along [001] zone axis. (**b**) SEM image of an annealed sample. (**c**) Typical EDS line-scanning profiles reveal the darker particles show increased counts for S and decreased Te. (**d**) STEM image of PbTe (8 %) PbS. (**e**) TEM image of PbS particles showing nanoscale inhomogeneities within the PbS particle. *Inset* DP shows coherent relation. (**f**) HRTEM image of the semi-coherent interface of a PbS nanoparticle and the PbTe matrix with a series of regularly spaced misfit dislocations along the boundary. (**g**, **h**) HRTEM image of nanoscale precipitates located within the PbTe matrix and larger PbS particle [33]

relaxed strain, and structure-modulated contrast rather than composition-modulated contrast are observed at the boundaries between the two phases. It is shown that phase boundaries, interfacial dislocations, and nanometer-scale precipitates play an important role in enhancing phonon scattering and, therefore, in reducing the k_{lat}.

A low-magnification TEM image (Fig. 10.17a) and its inset DP of solid solution sample reveal a relatively homogenous contrast, except for some dark line-like features due to stacking fault defects. However, in Fig. 10.17b the corresponding HRTEM image depicts many particles with weak contrast with a size of ~1 nm,

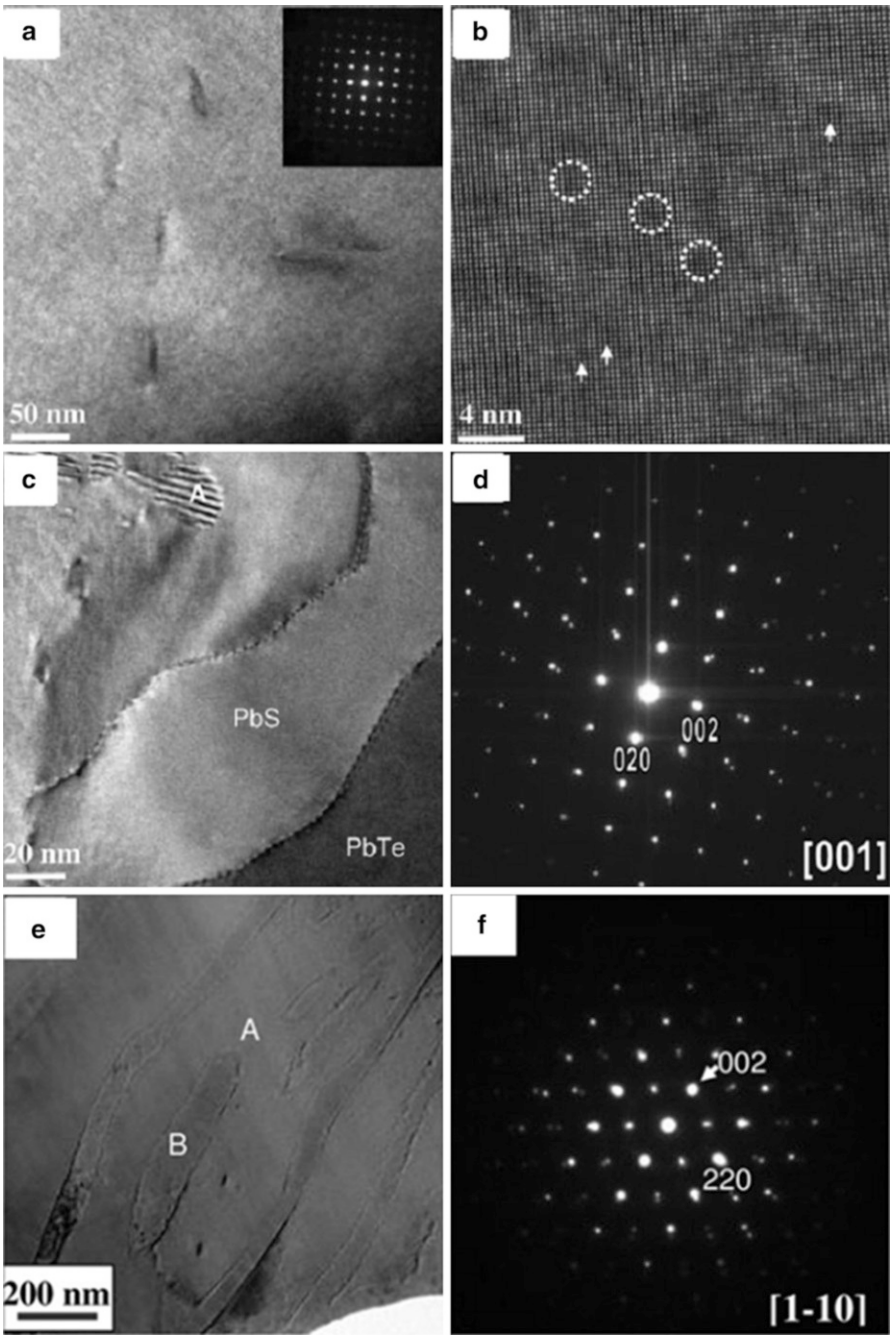


Fig. 10.17 (continued)

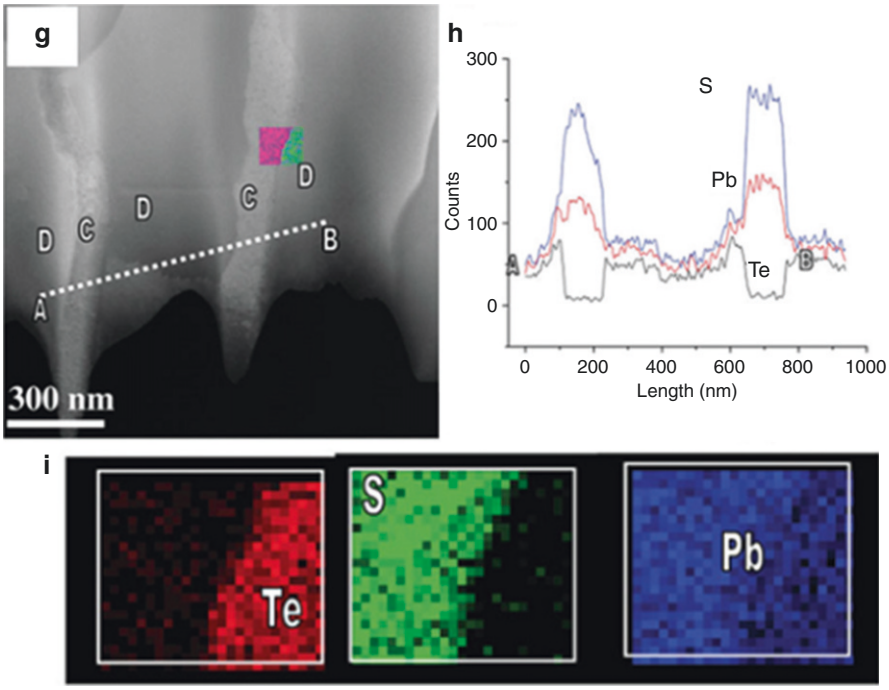


Fig. 10.17 Microstructure of solid solution PbTe (30 %) PbS. (**a**) Low-magnification TEM image with *inset* DP. (**b**) The HRTEM lattice image of solid solution PbTe (30 %) PbS. (**c**) Low-magnification TEM image after in situ heated to 500 °C. (**d**) DP with the aperture including the two different regions of contrast. (**e**) Low-magnification TEM image showing two contrasting areas, marked *A* and *B*. (**f**) DP taken from the A/B boundary. (**g**) Low-magnification STEM image showing regions of PbS (*labeled C*) and PbTe (*labeled D*). (**h**) EDS line-scanning profiles from A to B in (**g**). (**i**) EDS spectrum imaging [45]

which is indicative of a possible nanostructured pseudo-solid solution or the early stage of spinodal decomposition. To verify the spinodal decomposition, the sample was in situ heated to 600 °C, at rate of 10 °C min^{-1}. Figure 10.17c is a TEM image of the sample at 500 °C depicting decomposited PbTe and PbS regions. The DP (Fig. 10.17d) covering the two areas shows two distinct sets of diffraction patterns. Figure 10.17e is the low-magnification TEM image showing two types of contrast, marked as A and B. DP (Fig. 10.17f) taken from the A/B boundary shows the coherency between PbTe and PbS with an orientation relationship of $(001)_{PbTe}||(001)_{PbS}$. Elemental maps were collected using EDS in the STEM mode using a ~1 nm probe size to further confirm the composition of the two phases. The low-magnification HADDF STEM image (Fig. 10.17g) clearly shows the different contrast of the two phases. The compositional line-scanning profile from A to B (Fig. 10.17g) is plotted in Fig. 10.17h. The relative counts of S are higher in the C region than in the D region, while the reverse is the case for Te.

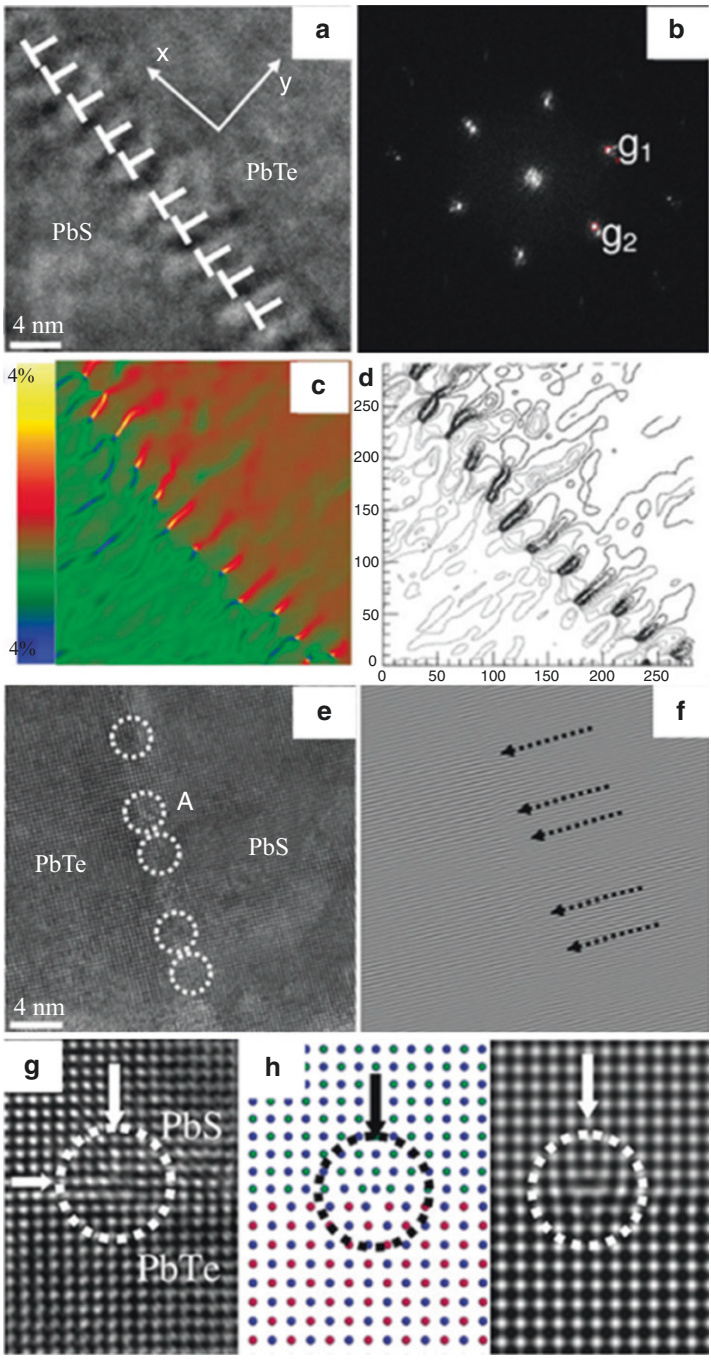


Fig. 10.18 (continued)

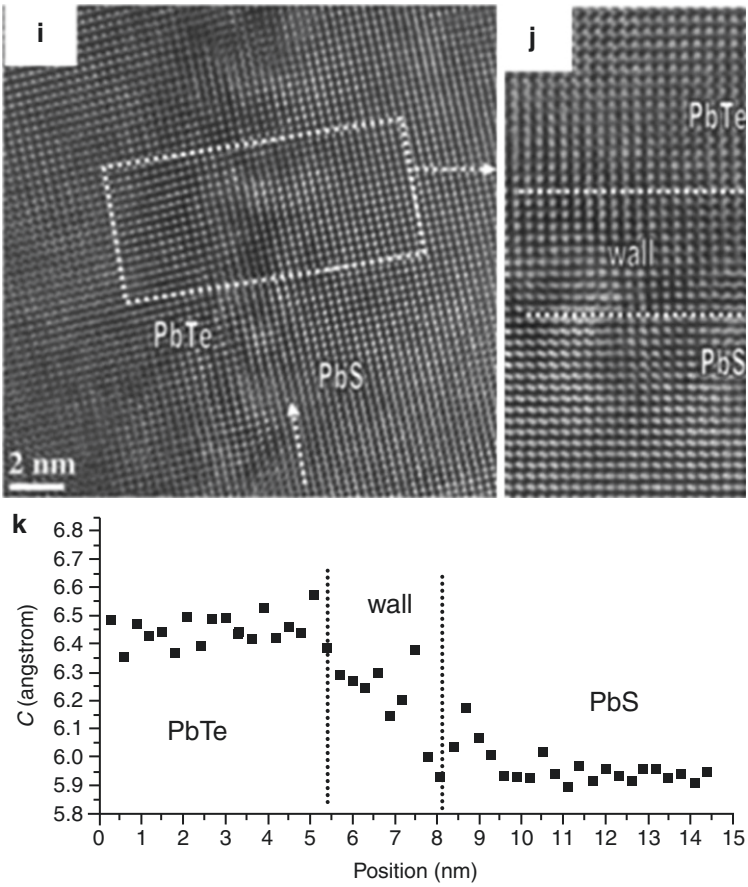


Fig. 10.18 (**a**) The HRTEM image of the PbTe/PbS boundary with Moiré fringes. (**b**) Power spectrum plot of image (**a**), the two vectors g_1 and g_2 were selected for image processing. (**c**) Strain mapping of image (**a**). (**d**) The magnitude of the displacement depicted as a contour map. (**e**) The HRTEM lattice image of the PbTe/PbS boundary in the very thin regions shows some dislocations encircled in white. (**f**) The IFFT image depicts the additional semi-atomic planes (pointed by *arrows*) at the dislocation core of the PbS side. (**g**) HRTEM image from region *A* in image (**e**) includes one clear dislocation core. (**h**) The atomic model of this dislocation and its simulation lattice image. (**i**) Atomic resolution image" of the near-PbTe/PbS interface region. The white arrow points to the interface. (**j**) The digital region from the boxed area of the image in (**i**). (**k**) Evolution of the out-of-the-plane lattice parameters with depth along the out-of-the-plane direction, revealing that the boundary about 2.5 nm is strained [45]

Spectrum imaging in Fig. 10.17i confirmed these results. Thus, comparison of these data with the DP in Fig. 10.17f confirms the identity of PbS and PbTe in region C and D, respectively.

Because of the large lattice mismatch of about 6 % between PbTe and PbS, there is considerable expected lattice strain at the PbTe/PbS boundaries.

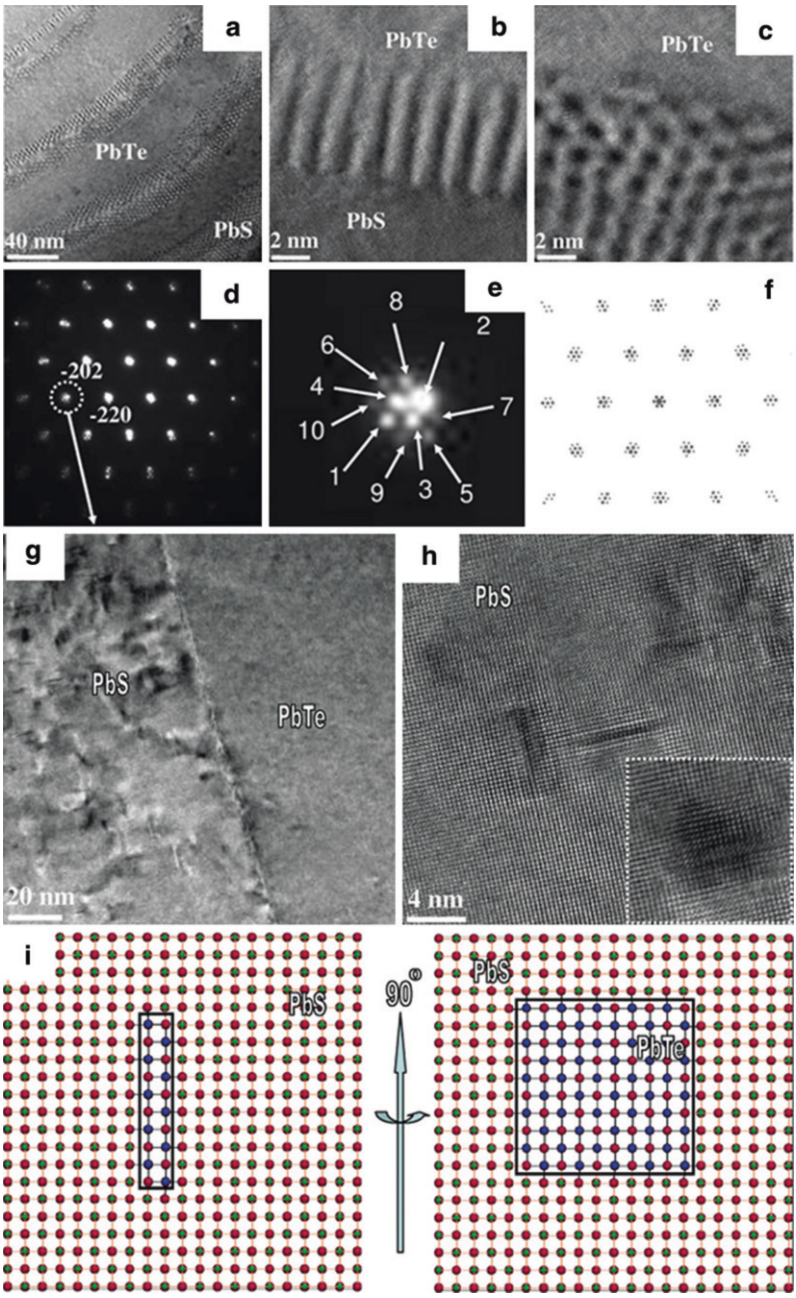


Fig. 10.19 (**a**) The low-magnification HRTEM image of PbTe/PbS boundaries showing two types of modulated structures: (**b**) unidirectional modulated structure and (**c**) modulation along three directions. (**d**) DP generated by one select area aperture including PbTe, PbS, and the modulated structure boundary shows that all the spots are split. (**e**) The enlarged split spot marked

The TEM observations reveal the presence of regular misfit dislocations (Fig. 10.18a–h), a small distorted region (Fig. 10.19i–k), and structural modulations (Fig. 10.20a–f). Besides the dislocations and small remaining strain at the PbTe/PbS boundary, many nanometer-scale sphere and platelike precipitates were detected in most PbS features and in some regions of the PbTe matrix (Fig. 10.20g–i). Then we can describe these microstructural features extensively one by one.

Figure 10.18a is an HRTEM image with Moiré fringes of the PbTe/PbS boundary with a series of misfit dislocation cores. In order to investigate the strain variation of dislocation cores at/around this boundary in the image, the profile of the strain map along the in-plane direction (ε_{xx}) is given in Fig. 10.18c, which displays orderly dislocation cores and about a 6 % displacement from PbTe to PbS. In an alternative depiction in Fig. 10.18d, the magnitude of the displacement is represented by a contour map that unambiguously confirms the difference between the two phases and dislocation cores at the boundary. There is a regular spacing of about 2 nm among the dislocation cores (the density of dislocation in the sample is $\sim 2.5 \times 10^{12}$ cm^{-2}). Figure 10.18e is an HRTEM image of the PbTe/PbS boundary close to the edge of the sample hole, in which the circles highlight the dislocation cores. Its IFFT in Fig. 10.18f clearly indexes the positions of the dislocation cores. Figure 10.18g is the enlarged part of dislocation core, and the Burger's circuit around the dislocation core yields a closure failure with a projected vector $1/2a$ [100]. This finding means that the misfit dislocation a [100] usually has dissociated into two partial ones with Burger's vectors $1/2a$ [100] and that the two partials are related by a stacking fault or an antiphase boundary between them. Figure 10.18h illustrates the results of modeling and simulation of this type of edge dislocation, in which the arrowheads point to the extra semi-atomic plane. The atomic resolution image of another PbTe/PbS boundary is depicted in Fig. 10.18i. The misfit dislocations are still apparent; however, the spacing between them is slightly larger because of the incomplete relaxation of the strain. A numerical center-of-mass approach (the crosses marking location of atoms in Fig. 10.18j) was applied, taking the out-of-plane PbS lattice parameters as the calibration standard. The results of this analysis (Fig. 10.18k) reveal that the lattice parameter of PbTe is around 6.4 Å, while in the boundary region (within about 2.5 nm), the lattice parameters continuously fall from 6.4 to 5.9 Å. These observations suggest that some strain at the boundary is not completely relaxed.

Figure 10.19a is a low-magnification HRTEM image of the PbTe/PbS boundaries with two types of modulated structures: one with unidirectional modulation shown in Fig. 10.19b and the other one with 3D modulation shown in Fig. 10.19c. A complex DP with all the spots splitting (Fig. 10.19d) is from PbTe, PbS, and the secondary modulated structure boundary. Interestingly, these spots cannot be

Fig. 10.19 (continued) by a *circle* in (**d**). (**f**) The simulated DP of PbTe and PbS including double diffraction. (**g**) Low-magnification TEM image showing nanometer-scale precipitates in PbS area. (**h**) The high-magnification images show the straight-line and square-like (*inset*) contrasts. (**i**) The modeling of the nanometer-scale straight-line-like precipitates; their appearance in one direction is line-like, but after a 90° rotation, a square emerges [45]

obtained by simply superimposing the DPs of PbTe and PbS zones, but can be due to double diffraction of the PbTe [111] and PbS [111] zones. Figure 10.19e is the enlarged split-spot indexed as (−422) in Fig. 10.19 (d). The reciprocal lattice vector g_{hlkuvw} of such a diffraction spot is expressed by

$$g_{hkluvw} = ha^*_{\mathrm{PbTe}} + kb^*_{\mathrm{PbTe}} + lc^*_{\mathrm{PbTe}} + ua^*_{\mathrm{PbS}} + vb^*_{\mathrm{PbS}} + wc^*_{\mathrm{PbS}} \tag{10.13}$$

where h, k, l, u, v, and w are all integers; $a_{\mathrm{PbTe}}{}^*$, $b_{\mathrm{PbTe}}{}^*$, and $c_{\mathrm{PbTe}}{}^*$ are unit vectors of PbTe in the reciprocal space; and $a_{\mathrm{PbS}}{}^*$, $b_{\mathrm{PbS}}{}^*$, and $c_{\mathrm{PbS}}{}^*$ correspond to the reciprocal unit vectors of PbS. We can then index the diffraction spots in Fig. 10.19e using six indices (*hkluvw*). The diffraction spots with (*hkl*000) indices correspond to PbTe, while those with (000*uvw*) correspond to PbS. The diffraction spots with (*hkluvw*) (h, k, l, u, v, and w are nonzero integers) correspond to the double-diffraction spots. Figure 10.19f is the simulated electron diffraction pattern based on PbTe and PbS with a double-diffraction effect, which is quite similar to the experimental DP in Fig. 10.19d. Figure 10.19g is a typical low-magnification TEM image that has several precipitates in the PbS area. Figure 10.19h shows several nanoscaled platelike precipitates with straight-line-like contrast, while a square contrast in the orthogonal direction can be seen in the inset. Simulated images in Fig. 10.19i schematically represent the nanocrystals of the platelike precipitates. The two images in Fig. 10.19h correspond to the two orthogonal directional views of Fig. 10.19i. The estimates of the distribution density and average size of all types of nanometer-scale precipitates are 1×10^{12} cm^{-2} and 3 nm, respectively.

Recently, we further present experimental evidence for the role of p-type dopant element Na in controlling the morphology of nanoscale PbS crystals nucleating in a PbTe matrix. Doping Na (1–2 mol %) can alter dramatically the morphology of the PbS precipitates, because the segregation of Na at PbTe/PbS interfaces results in cuboidal and truncated cuboidal morphologies for PbS [46]. Figure 10.20a–e displays low-magnification STEM images of PbTe (x)_PbS (2 %) Na_2Te ($x = 0.30$, 0.16, 0.12, 0.08, and 0.04, respectively). A combination of DPs (Fig. 10.20f) and APT studies (described below) demonstrates that the different precipitates all have the PbS structure, except for those in Fig. 10.20e, which represent a rock salt structured phase composed of all three elements Na, Pb, and S, rather than pure PbS or Na_2S. Figure 10.20a–e reveals changes in precipitate morphology with decreasing PbS concentration. A hexagonal morphology is observed for $x = 0.30$ and 0.16 (Fig. 10.20a, b), while perfect square and rectangular morphologies are observed for $x = 0.12$ and 0.08 (Fig. 10.20c, d), and an irregular morphology is observed for $x = 0.04$ (Fig. 10.20e). The number density of precipitates decreases as the concentration of PbS decreases. These observations indicate that the precipitate morphology can be controlled by the ratio PbS/Na. In general, almost all of the precipitates exhibit rectangular and square morphologies when the PbS/Na ratio is 4–6. When the PbS/Na ratio is greater than 6 or smaller than 4, more truncated square or hexagonal precipitates are observed. The TEM observations show that the rectangular precipitates form facets parallel to the {100} planes, while the hexagonal precipitates exhibit facets parallel to the {111} (or very few {110}) planes in

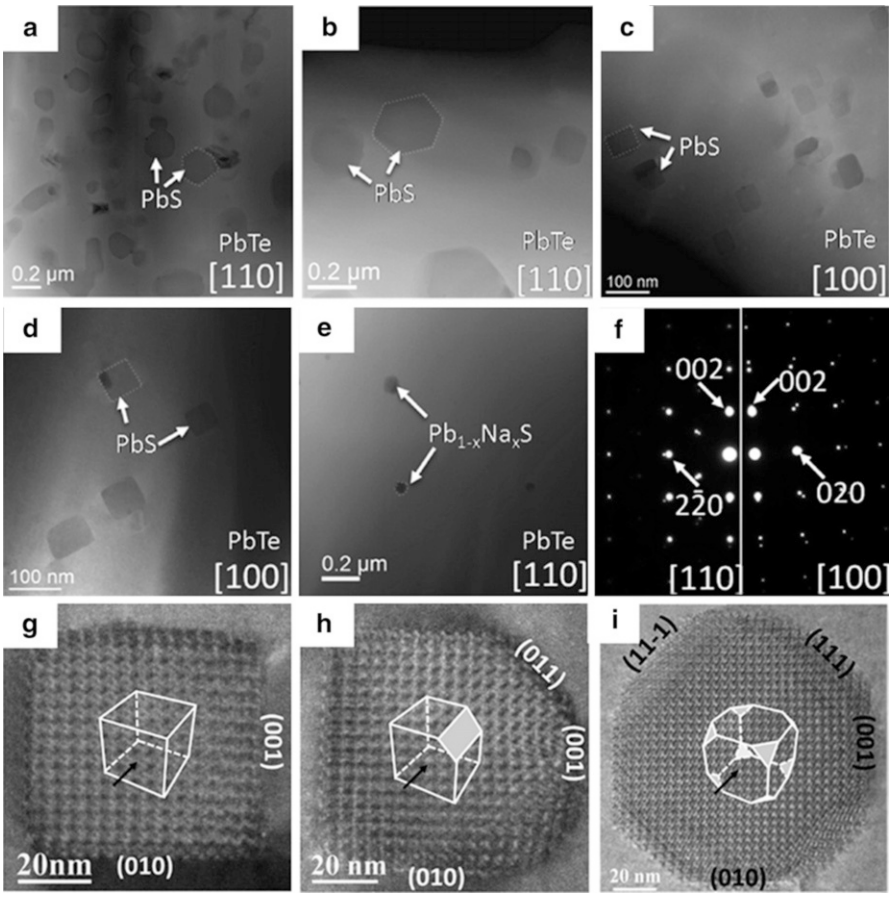


Fig. 10.20 (**a**–**e**) Low-magnification TEM images of PbTe (x) PbS (2 %) Na_2Te samples exhibiting morphological changes of precipitates with different X values: (**a**) $x = 0.3$, (**b**) $x = 0.16$, (**c**) $x = 0.12$, (**d**) $x = 0.08$, (**e**) $x = 0.04$. (**f**) DPs with an aperture including matrix and precipitate: *left* for (**a**) and (**b**) and *right* for (**c**) and (**d**). (**g**–**i**) Middle-magnification TEM images of a PbTe (12 %) PbS (1 %) Na_2Te displaying three typical projections of PbS precipitates. A schematic of the corresponding precipitate morphology in 3D space is inserted; the *black arrowheads* indicate the directions of the TEM observations [46]

addition to the {100} planes, as Fig. 10.20g–i shows. Figure 10.20g shows a square precipitate projected along the [100] direction with all edges along [001] and [010] directions. The Moiré fringes in the precipitate are due to the matrix/precipitate overlap along the viewing direction. One corner of the precipitate, in Fig. 10.20h, appears cut along the [011] direction, and the same feature is observed for the four corners of the rectangular precipitate displayed in Fig. 10.20i. The schematic diagrams of 3D precipitates exhibiting three different morphologies, a cube, a partially truncated cube, and a fully truncated cube, are inserted into the respective images, and each image was obtained along the respective black arrow direction of the 3D precipitates.

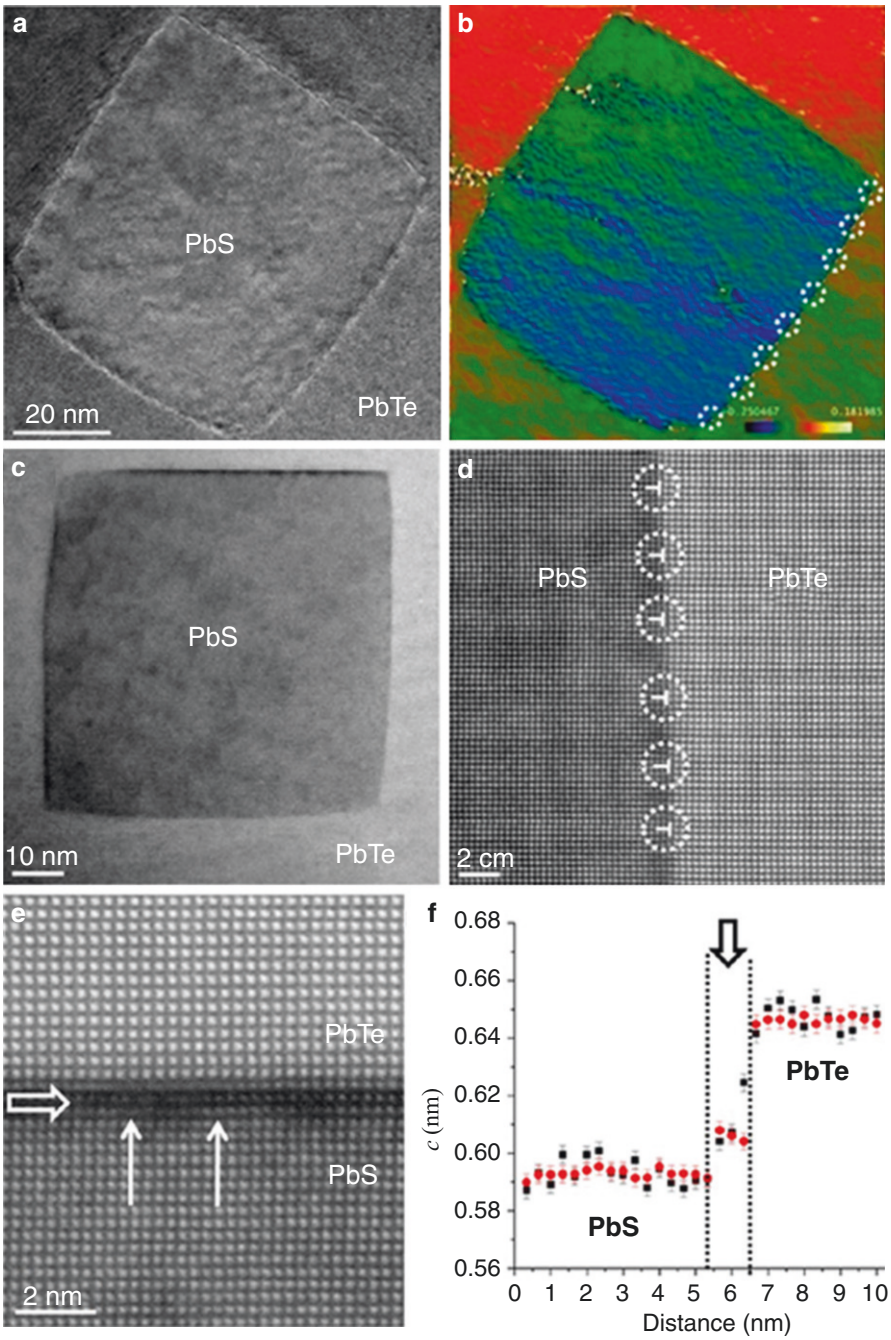


Fig. 10.21 (**a**) HRTEM image of one PbS precipitate in a PbTe (8 %) PbS (2 %) Na_2Te sample, (**b**) GPA analysis of (**a**), (**c**) STEM image of the precipitate in a PbTe (12 %) PbS (2 %) Na_2Te

Figure 10.21a is an HRTEM image of one PbS cube taken close to the edge of PbTe (x) PbS (2 %) Na_2Te. GPA analysis (Fig. 10.21b) confirms the presence of regularly distributed misfit dislocations with the Burger vector 1/2*a* [101], with ~4 nm spacing, at or close to the PbTe/PbS interface. The interfacial contrast is unclear due to the large delocalization of the JEOL-2100F TEM. To mitigate this imaging artifact, we studied a similar cubic PbS precipitate in another sample using a C_s(probe) corrected JEOL ARM200F microscope in the STEM mode. Figure 10.21c is an HAADF image of the cube precipitate in a PbTe (x) PbS (2 %) Na_2Te sample. The image is of higher quality than the image presented in Fig. 10.21a due to the STEM corrected for spherical aberration. The STEM image exhibits wide dark contrast at the left and top PbTe/PbS interfaces, darker than either the PbTe matrix or the PbS nanostructures. The right and bottom interfaces exhibit clear interfacial contrast and misfit edge dislocations, which are observed in the enlarged image (Fig. 10.21d). This demonstrates that the PbTe/PbS interfacial region is different among the four interfaces. The higher-magnification STEM image (Fig. 10.21e) shows that the interfacial region has a transition width of three atomic planes. The lattice parameters of the three layers are shown in Fig. 10.21f, and the lattice parameters of the interfacial region are slightly (1.5 %) larger than those of PbS.

Then APT was utilized for quantitative composition analyses of the interfacial region. Analyses of the PbTe (12 %) PbS (1 %) Na_2Te sample by APT indicate the presence of an S-rich precipitate (Fig. 10.22a). Figure 10.22a shows the isoconcentration surface of the same precipitate, as observed from a [100] direction. These two images of the precipitate demonstrate that its morphology is consistent with a truncated cube. The large facets are parallel to the {100} planes, while the smaller facets are parallel to the {111} planes, confirming the general observations made by TEM for this composition. The measured compositions are consistent with the compositions PbTe and PbS for the matrix and the precipitate, respectively. The Na concentration is 3.49 at. % in the precipitate, while it is only 0.33 at.% in the matrix, yielding a partitioning coefficient of $Na^{PbS}/Na^{PbTe} = 10.6$. Concentration profiles were measured perpendicular to two interfaces: parallel to the (100) plane (Fig. 10.22b) and to the (111) plane (Fig. 10.22c). In the case of the (100) interface, Na segregates to a maximum concentration of 5 at. %.

For PbTe–$PbSnS_2$, displacement layers instead of nanostructures in PbTe–PbS system are formed, which can allow effectively phonon scattering. We find that the incorporation of $PbSnS_2$ in PbTe results in a significant reduction in k_{lat}. The presence of phase boundaries, misfit dislocations, and displacement layers was confirmed by TEM. However, displacement layers are more responsible for strong scattering of heat-carrying phonons in this system. This is an excellent example of a bulk PbTe TE system without nanostructures that can still largely enhance phonon scattering and provide a very low κ [49].

Fig. 10.21 (continued) sample, (**d**, **e**) are magnified Z-contrast images of the left vertical interface and highest horizontal interface, respectively. (**f**) Evolution of the in-plane (*red circles*) and out-of-plane (*black squares*) lattice parameters, with depth along the out-of-plane direction [46]

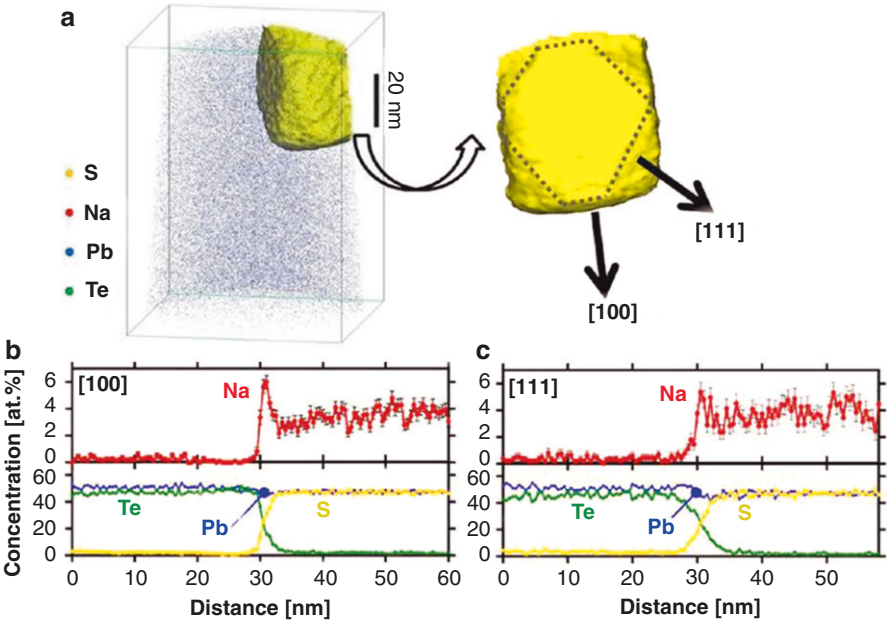


Fig. 10.22 Composition analyzed by APT. (**a**) 3D reconstruction of a volume. Only 3 % of the detected Pb atoms are displayed (*blue dots*) for clarity. The yellow isoconcentration surface corresponds to 20 at.% S and highlights the precipitates' interfaces. (**b**) Atomic concentration profiles of Na (*red*), S (*yellow*), Pb (*blue*), and Te (*green*) across the (100) and (111) interfaces [46]

PbTe has cubic rock salt structure (Fig. 10.23a) with a lattice parameter $a = 6.464$ Å. $PbSnS_2$ has orthorhombic structure (Fig. 10.23b) with space group *Pnma* and lattice parameters $a = 11.166$ Å, $b = 3.999$ Å, and $c = 4.210$ Å [96]. The crystal structure of $PbSnS_2$ exhibits Pb–Sn bilayers, which form a superstructure along the a axis.

The incorporation of $PbSnS_2$ in PbTe results in significant reduction in k_{lat} to 0.4–0.65 W/(mK) over the temperature range 300–700 K, a reduction of 50–70 % over bulk PbTe (Fig. 10.24a). As a result, a maximum ZT of 1.1 is obtained for ingot samples of the PbTe (6 %) $PbSnS_2$ composition (Fig. 10.24b). TEM reveals the $PbSnS_2$ segregates into coherent lamellar structures 50–100 nm in width and 100 nm to 15 μm in length. There exists a large range of particle sizes, depending on the concentration of $PbSnS_2$ added. Figure 10.24c, d shows immiscibility in PbTe (6 %) $PbSnS_2$. The smallest $PbSnS_2$ regions are 50–100 nm in width (Fig. 10.24c), extending microns in length (Fig. 10.24d). Figure 10.24e shows a low-magnification SEM micrograph of PbTe (25 %) $PbSnS_2$. Because of the larger size and dispersity of $PbSnS_2$ throughout the sample, the interconnected network of $PbSnS_2$ is clearly observed at the macroscale in Fig. 10.24e. At concentrations of $PbSnS_2$ larger than 6 %, a significant increased density of large macroscale $PbSnS_2$ particles (1–10 μm) was observed (Fig. 10.24e, f). However, these large particles are detrimental to the TE transport by reducing the electron mobility.

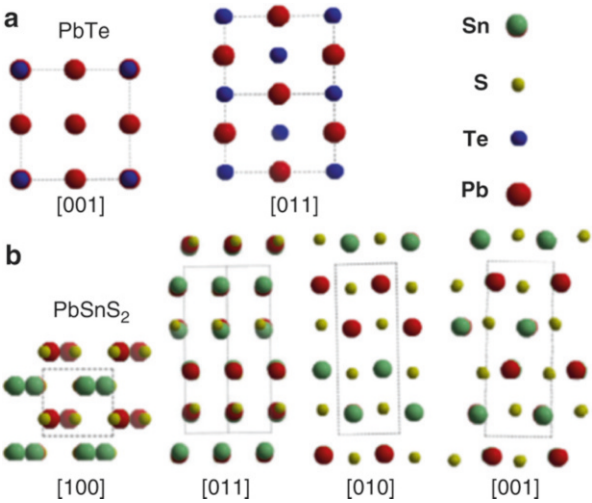


Fig. 10.23 (**a**) Cubic structure of rock salt PbTe in the projections along the crystallographic [001] and [011] direction. (**b**) Orthorhombic $PbSnS_2$ in the projections along [100], [011], [010], and [001] directions. The unit cells are line out [48]

Thus, a balance between the $PbSnS_2$ particle size and volume density must be achieved to maximize reduced lattice thermal conductivities while not severely limiting electron mobility. Then the PbTe (11 %) $PbSnS_2$ sample was analyzed with HRTEM because of the relatively high volume density of $PbSnS_2$ particles. The results, shown in Fig. 10.24i–m, reveal the extended lamellar character of the $PbSnS_2$ phase and its plate morphology. Figure 10.24i shows the $PbSnS_2$ phase self-assembled into rodlike lamellae 50–100 nm in width spaced 100–200 nm apart in the PbTe matrix. Figure 10.24j shows DPs with an aperture including the matrix and lamellae along $[001]_{PbTe}$ (left) and $[-110]_{PbTe}$ (right) directions, showing excellent crystallographic alignment between matrix PbTe and $PbSnS_2$ lamellae. The HRTEM image in Fig. 10.24k, l further confirms semi-coherent PbTe–$PbSnS_2$ interface and also clearly shows the extended layered structure of the Pb–Sn bilayers throughout the lamellae. There exists a superstructure along the [010] direction, corresponding to the bilayers oriented along the *a* axis in the *Pnma* crystal structure of $PbSnS_2$, shown in Fig. 10.24m. In fact, the $PbSnS_2$ regions are naturally nanostructured owing to their unique crystalline structure to produce the Pb–Sn bilayers.

Further, TEM investigation of the three samples of PbTe (x %) $PbSnS_2$ (x = 11, 14, 25) is performed to explore the microstructural details. A low-magnification TEM image (Fig. 10.25a) of PbTe (14 %) $PbSnS_2$ sample shows lamellar microstructure with two types of contrast. EDS (inset in Fig. 10.25a) together with DP (Fig. 10.25b) confirmed the dark-contrast phase as $PbSnS_2$ and bright-contrast one as PbTe. The $PbSnS_2$ nanorods (50–100 nm in width and 0.4–1 μm in length) are spaced 100–200 nm apart in the PbTe matrix. Because of the large lattice mismatch between PbTe and $PbSnS_2$, there are considerable expected misfit dislocations and/or lattice strain at and around the PbTe/$PbSnS_2$ boundaries. Figure 10.25c is an HRTEM image of an edge on PbTe/$PbSnS_2$ boundary along $[001]_{PbTe}$ direction. The circles highlight the dislocation cores at or close to the boundary. Figure 10.25d

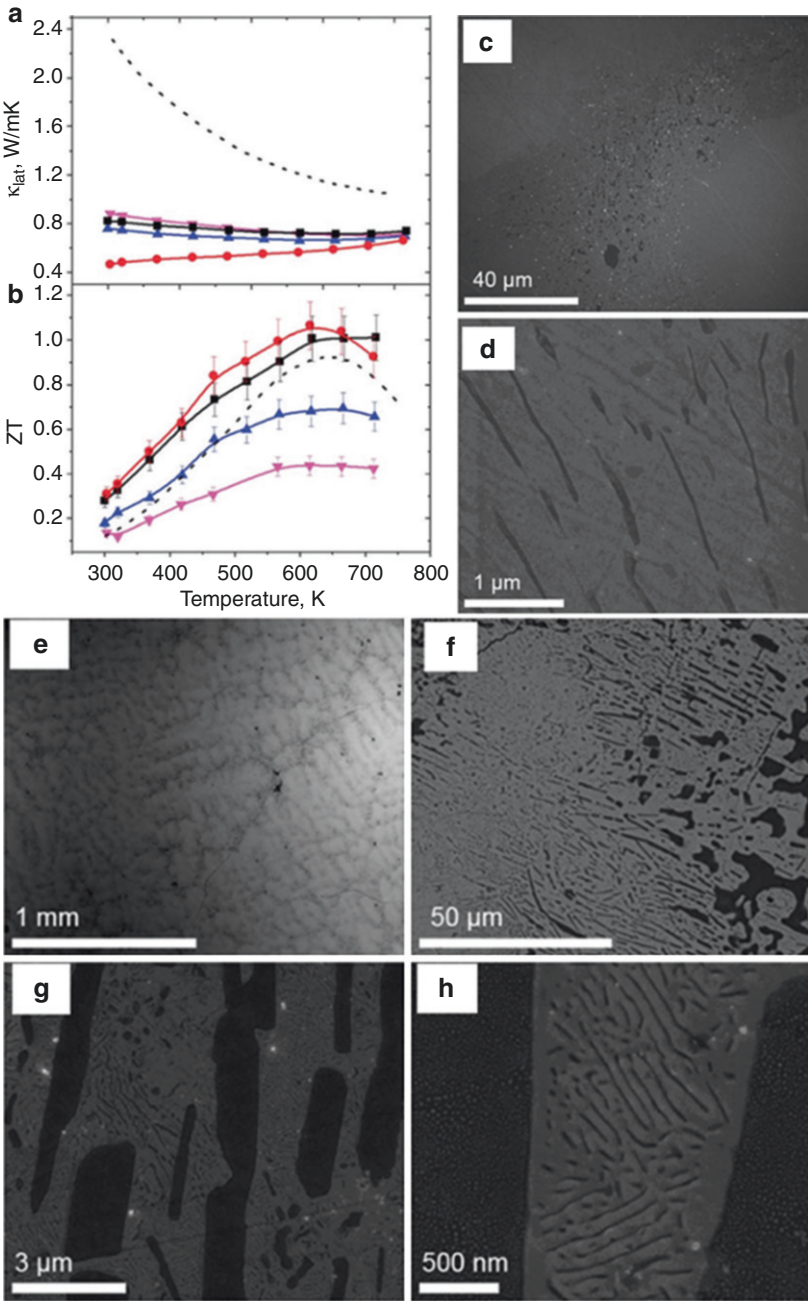


Fig. 10.24 (continued)

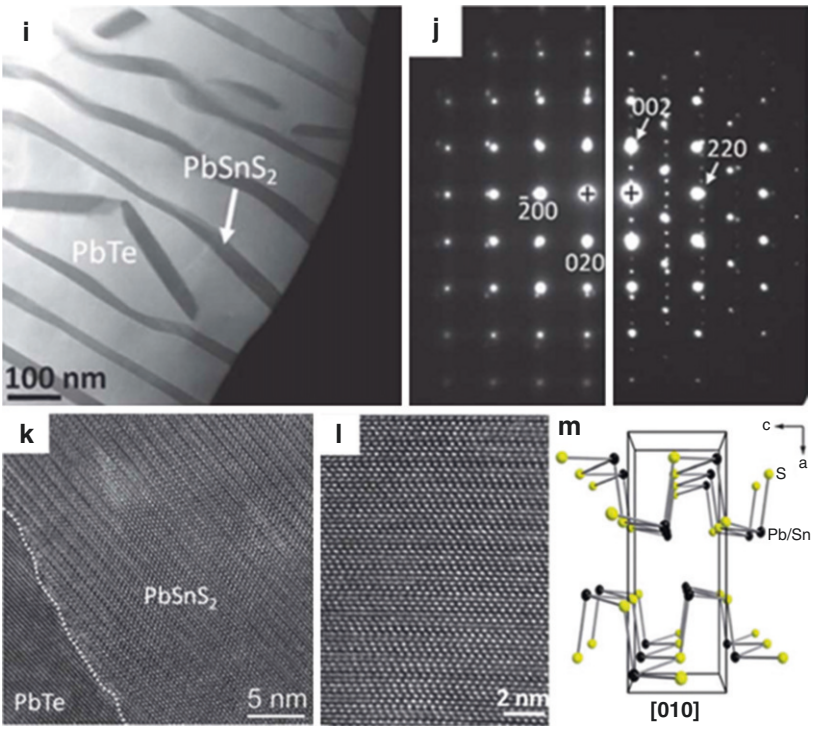


Fig. 10.24 (**a**) k_{lat}, and (**b**) ZT of PbTe–$PbSnS_2$ materials. SEM images of PbTe (6 %) $PbSnS_2$ (**c**, **d**). PbTe (25 %) $PbSnS_2$ (**e**, **f**). (**g**, **h**) Coexistence of large (>1 μm) and small (<100 nm) lamellar structures of $PbSnS_2$. (**i**) Low-magnification STEM image of PbTe (11 %) $PbSnS_2$. (**j**) DP showing characteristic diffraction along [001] (*left*) and [110] (*right*) crystallographic planes of PbTe. (**k**) HRTEM lattice image along $[-110]_{PbTe}$ direction showing the PbTe–$PbSnS_2$ interface. (**l**) Enlarged image from (**k**) showing the natural $PbSnS_2$layered structure along [010] direction. (**m**) $PbSnS_2$ crystal structure along [010] for comparison [49]

is the enlarged part of region A of Fig. 10.25c where the Burger's circuit around the dislocation core yields a closure failure with a projected vector *a*/2 [110]. The regular spacing of about 4 nm was measured among the dislocation cores at the phase boundaries (the number density of misfit dislocation in the sample is calculated to be $\sim 4 \times 10^{11}$ cm^{-2}). Figure 10.25e is an HRTEM image along $[110]_{PbTe}$ direction, showing one typical feature in $PbSnS_2$ as pointed by a vertical arrowhead. The dotted boxed area is shown in Fig. 10.25f, which reveals three parts ([001] direction for left and right parts, [010] direction for middle one). The image simulation based on further analysis inserted in the boxed area in Fig. 10.25f well matches the experimental image. The mismatch between the 001 direction and 010 direction of $PbSnS_2$ is around 5 %, which also can release the strain by formations of some dislocations in $PbSnS_2$.

Besides the phase boundaries and dislocations above, high-density stacking faults and displacement layers can also be found. Figure 10.25g–i clearly show two types of

stacking faults as marked by arrowheads: One (Fig. 10.25h) shows the two variants' 1/2 unit cell shifts along 001 direction, and the other (Fig. 10.25i) shows 1/2 unit cell shift along 001 direction and 1/4 unit cell shift along 100 direction as well. The density of the stacking faults is estimated as 9×10^5 cm^{-2}. Figure 10.25j is an atomic resolution image along [011] zone axis recording using a value of underfocus close to Scherzer's conditions, which distinctly shows displacement layers with regular bright contrast. The application of Scherzer's imaging conditions represents a classical

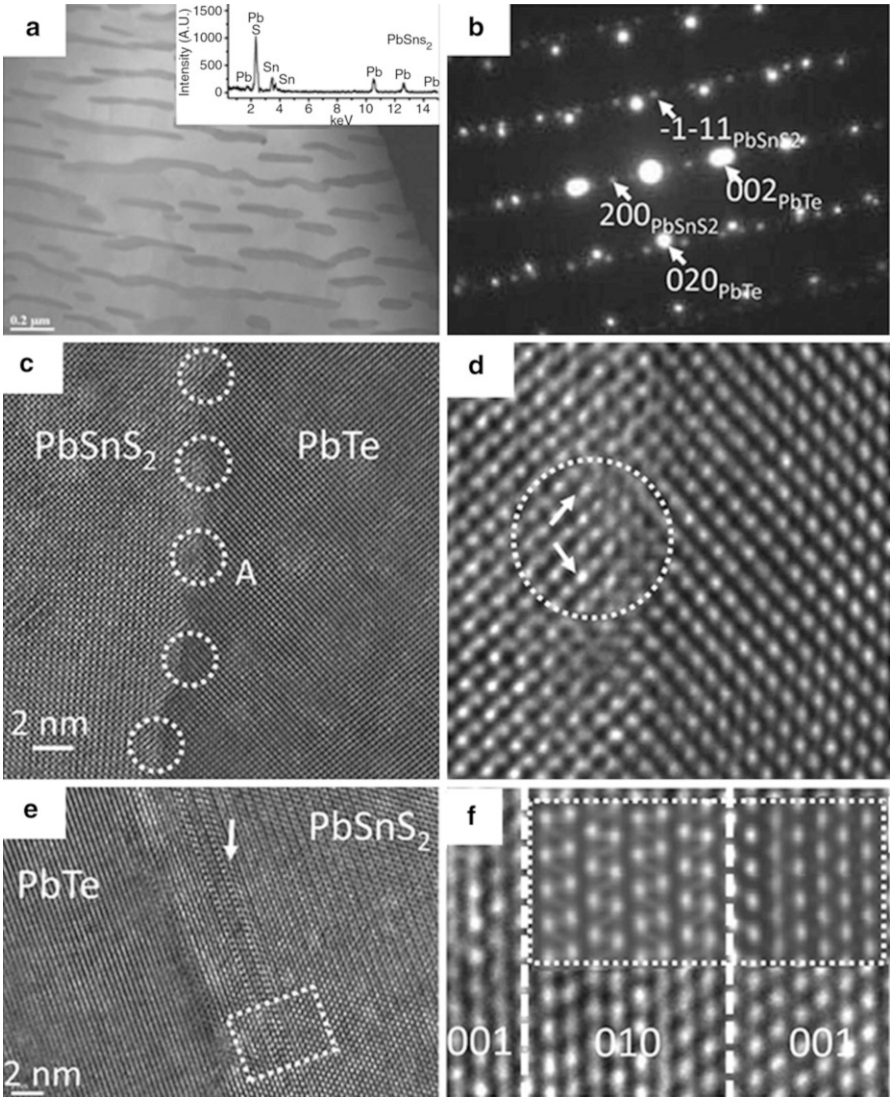


Fig. 10.25 (continued)

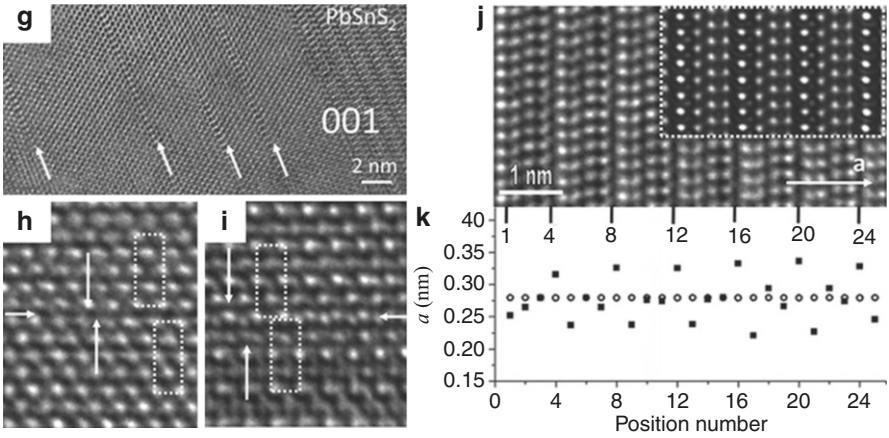


Fig. 10.25 (**a**) Low-magnification STEM image showing $PbSnS_2$ networks (*dark regions*) extending primarily at grain boundaries of PbTe in PbTe (14 %) $PbSnS_2$. (**b**) DP with a selected area aperture including PbTe and $PbSnS_2$. (**c**) Typical HRTEM image of the PbTe/$PbSnS_2$ boundary along $[001]_{PbTe}$ direction showing regular dislocations encircled in *white*. (**d**) Magnified image from region *A* in image (**c**). (**e**) One lattice image of the PbTe/$PbSnS_2$ boundary along $[011]_{PbTe}$. (**f**) Enlarged image in *highlighted region* of image (**e**). A simulation image with one 010/001 interface [48]

technique in HRTEM [95]. However, to precisely measure atom positions, lens aberrations, which may affect the atomic resolution images, have to be considered. Therefore, simulated HRTEM images were employed [45]. In order to illustrate the variation of subunit cells along *a* direction of the $PbSnS_2$ in Fig. 10.25j, the spacing between cation positions was calculated by peak finder method on the image. The results (Fig. 10.25k) reveal a very large fluctuation in the spacing of each layer in $PbSnS_2$, which suggests highly distorted layers in the $PbSnS_2$ phase. Comparing the HRTEM simulation image based on Pb-rich in these superlayers with experimental image (inset in Fig. 10.25k), these displacement layers may originate from Pb-rich in these layers which come from extra amount of PbS in the sample. The number density of the displacement layers is around 2×10^6 cm^{-1} in the sample. Such a superstructure with bilayers size of ~0.6 nm is particularly well suited to scatter high-energy acoustic phonons, whose wavelengths are generally around 1–2 nm in the temperature range 300–700 K.

5.4 PbTe + X (X = Pb, Sb, Bi, Si/Ge)

Recent years, we have investigated the possible mechanisms of phonon scattering by defects, interfaces, and nanostructures in PbTe-X (Pb, Sb, Bi, Si/Ge) TE material systems. Figure 10.26 shows a schematic representation of three types of precipitate − matrix interfaces: coherent (with possible elastic strain), incoherent (with minimal interactions between the phases), and semi-coherent (misfit dislocations separated by elastic strain), all of which embody different atomic

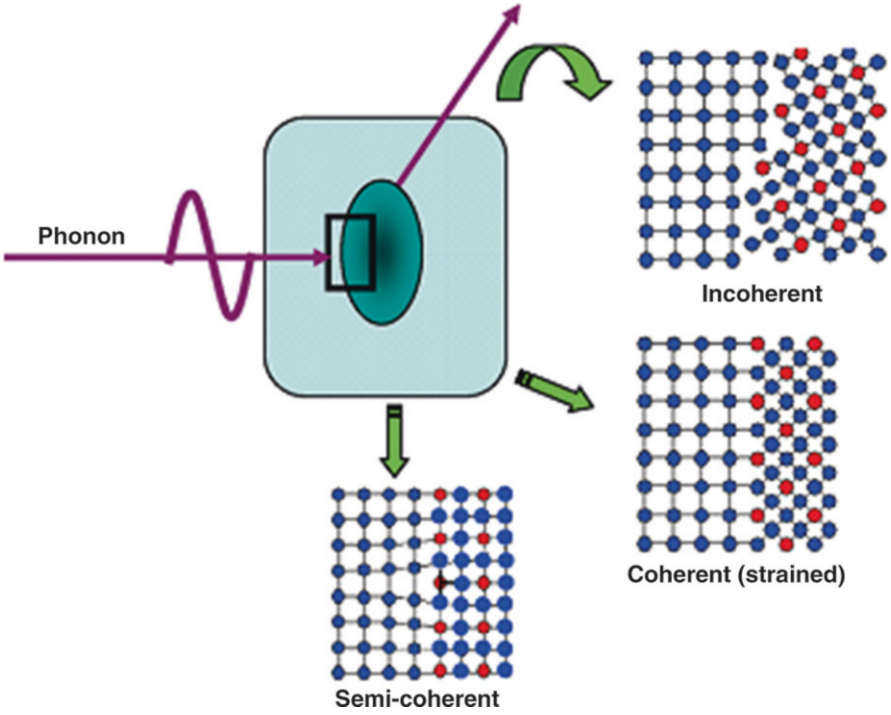


Fig. 10.26 Schematic of phonons scattered by three possible types of boundaries between matrix and nanoparticles [86]

configurations and associated local interfacial relaxation mechanisms. The nature of precipitate − matrix interfaces has notable influence on phonon scattering at and across such interfaces. Thus, over and above the control of the size and morphology of nanoscale particles, control of interfacial characteristics is likely to be important in developing TE materials with a higher ZT [37].

Among PbTe-X (X = 2 % Pb, Sb, Bi) systems, PbTe (2 %) Sb has the lowest k_{lat} and exhibits a largest strain and notably most misfit dislocations at the precipitate/PbTe interfaces; PbTe–Pb 2 % exhibits pure Pb nanoparticles and nanostructures with Te vacancies; PbTe–Bi 2 % sample shows weakest phonon scattering with BiTe precipitates and Bi nanostructures.

In Fig. 10.27 (a), both weak contrast spherical- and platelet-like nanoscale precipitates were observed in the PbTe (2 %) Pb sample. The spherical-like precipitates show a twofold larger in density distribution than that of the platelet-like precipitates. Representative HRTEM image of spherical-like precipitates (Fig. 10.27b) along [001] direction and platelet-like precipitates (Fig. 10.27c) along [010] direction shows coherent interfaces with the matrix. The precipitates can be likely comprised of Te vacancies (Fig. 10.27b–d) or Pb-rich (e–f) within the PbTe region. Figure 10.27d shows a model of a Te-deficient PbTe precipitate in the nominally stoichiometric PbTe matrix, based on which the simulated image (inset

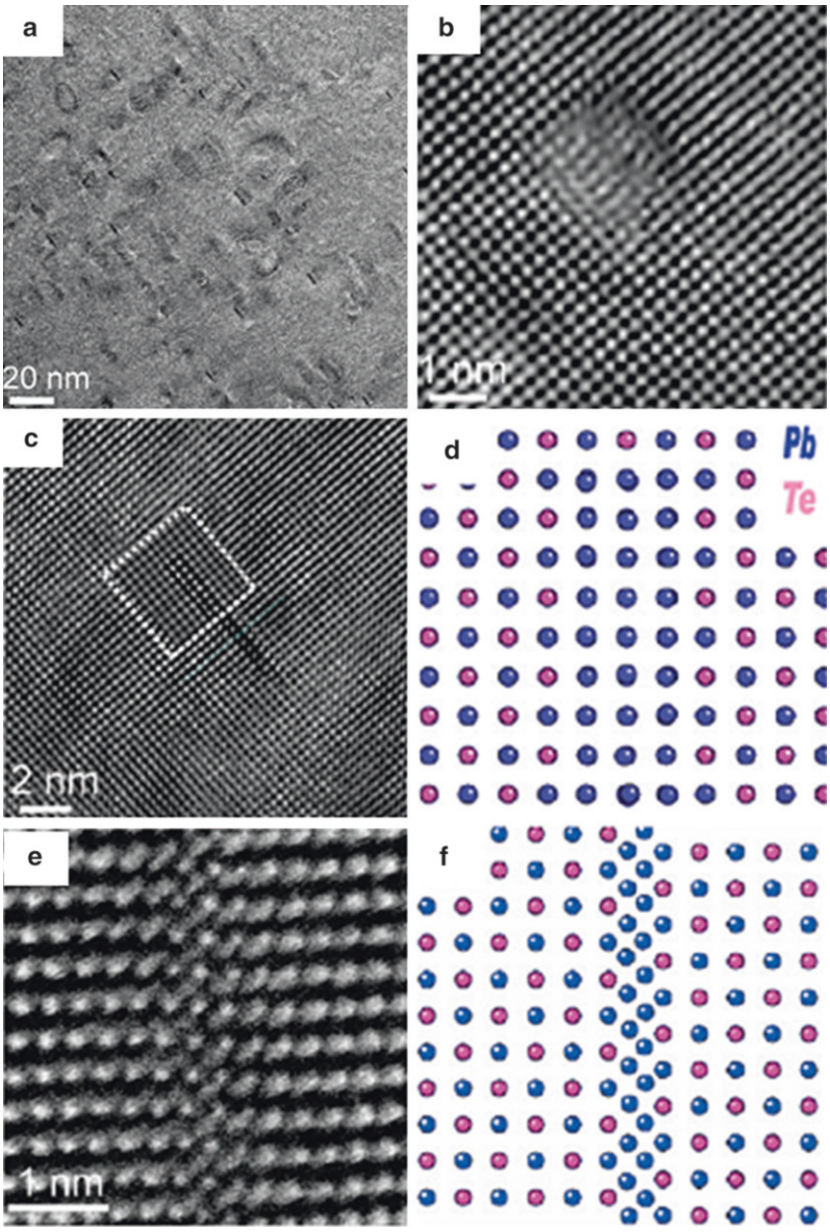


Fig. 10.27 (**a**) TEM image of PbTe (2 %) Pb shows two types of nanoscale precipitates with a regular spherical-like shape and a platelet-like shape. (**b**) HRTEM image along [001] direction of one typical precipitate. (**c**) HRTEM image along [010] direction. (**d**) The structure modeling of platelet-like precipitate with Te vacancy, the corresponding simulated image *inset* in (**c**). (**e**) The enlarged STEM image depicts another type of platelet-like nanoscale precipitate. (**f**) is the structure model of the precipitate and matrix [86]

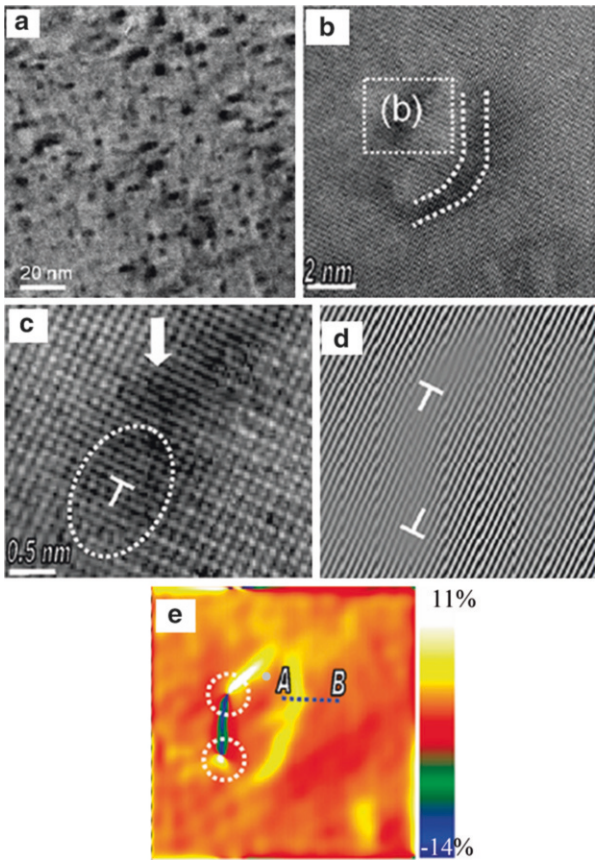


Fig. 10.28 (**a**) Typical image of PbTe (2 %) Sb shows nanoscaled precipitate. (**b**) HRTEM lattice image depicts clearly the boundary between precipitate and matrix. (**c**) Enlarged image of *box* in (**a**). (**d**) IFFT image of (**c**). (**e**) The strain distribution of the nanoscale inclusions [86]

in Fig. 10.27c agrees well with the experimental result. Figure 10.27e is enlarged image of a STEM of another type of platelet-like precipitate. The platelet-like Pb precipitate links the antiphase domains of PbTe separated by a pair of partial dislocations with a Burger vector of 1/2*a* [100]. Figure 10.27f is the atomic level model, which illustrates the likely atomic structure of the Pb (-rich) precipitate.

In Fig. 10.28a, TEM image of PbTe (2 %) Sb depicts higher-density nanoscale Sb-rich precipitates with a size distribution of 1–10 nm. HRTEM image (Fig. 10.28b) of a precipitate shows one interfacial boundary (~1 nm dark contrast) between the matrix and precipitate. The enlarged lattice image of the boxed area clearly shows a dislocation at the boundary marked by an oval dotted line in Fig. 10.28c, and the dislocation cores at the boundary can be seen in its IFFT image (Fig. 10.28d). Burger's circuit around the dislocation core in Fig. 10.28c yields a closure failure with a projected vector of 1/2*a* [010]. Figure 10.28e is the strain map profile along the 001 direction (ε_{yy}) showing two highly strained dislocation cores, with yellow indicating expansion and blue compression

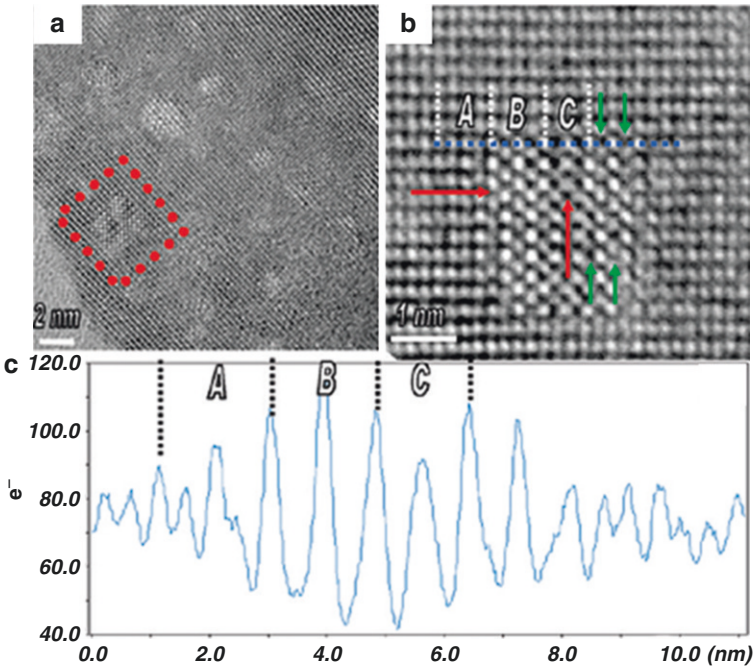


Fig. 10.29 (**a**) HRTEM image of sample PbTe-2 % Bi shows some precipitates. (**b**) The enlarged image *boxed* in (**a**). (**c**) Line-scanning profile *blue line* in (**b**) [86]

(see the color scale). From the strain map distribution of this image, it is clear the arrowhead-indicated precipitate/matrix boundary is highly strained.

In a representative Fig. 10.29a, the PbTe (2 %) Bi sample shows precipitates of a 2–4 nm size distribution. Most of the precipitates are detected as Bi, while a few precipitates, for example, in Fig. 10.29b which is an enlarged part from Fig. 10.29a, clearly show different structures from Bi precipitates. Two types of antiphase boundaries are seen in/around this precipitate: a conservative one (horizontal red arrowhead) with a one-half unit cell shift (marked by green arrowheads) and a nonconservative one (perpendicular red arrowhead) depicting one missing lattice plane, similar to the observations in Ref. [97]. A line-scanning profile across the latter one (blue line in Fig. 10.29b) is shown in Fig. 10.29c. If we use the lattice parameter of PbTe (marked *A* in Fig. 10.29b, c) as a reference, the *B* and *C* distances are 0.88 and 0.78 nm, respectively. The lattice parameters of this precipitate are determined to a likely BiTe phase which is also cubic with a lattice parameter of 6.47 Å.

From such above-detailed TEM observations of PbTe-X (X = 2 % Pb, Sb, Bi) respectively, it is obvious that all three compositions have variable strain at the precipitate/matrix boundaries. After the processing and analysis of more than ten precipitates, Fig. 10.30a shows typical line-scanning profiles of the boundaries between the matrix and precipitate for all three samples. The misfit strain across boundaries in PbTe (2 %) Sb is ~8 %, and for PbTe (2 %) Bi it is ~4 %, while for

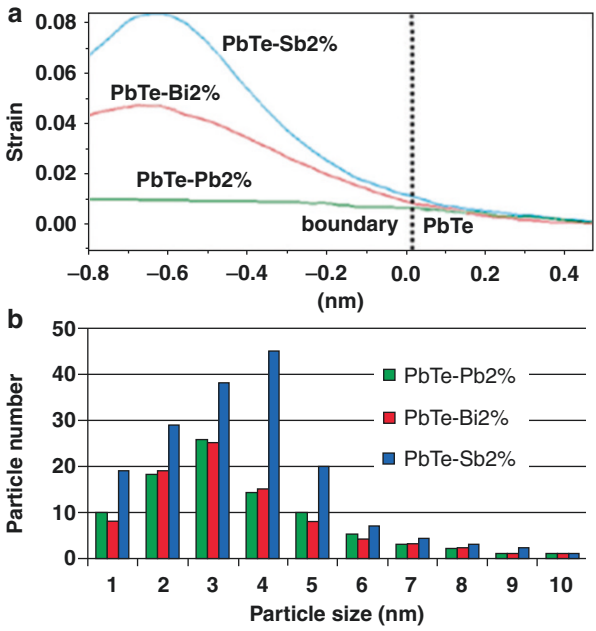


Fig. 10.30 (**a**) Average strain distributions of boundaries between nanoscale inclusions and matrixes in PbTe (2 %) Sb, PbTe (2 %) Bi, and PbTe (2 %) Pb. (**b**) Under the same volume, histograms of nanoscale precipitates in three systems [86]

PbTe-2 % Pb it is only 1 % or less. Figure 10.30b shows the size distribution for all three samples under the same TEM observation volume. It is clear that the PbTe (2 %) Sb has the highest density of precipitates, approximately two times more than the PbTe (2 %) Pb (2 %) or PbTe (2 %) Bi. However, all samples have an average particle size of 2–4 nm. On average, the estimates of the distribution density of all types of nanoscale precipitates are as follows: 1×10^{12} cm^{-2} for PbTe (2 %) Sb and 3×10^{11} cm^{-2} for PbTe (2 %) Pb and PbTe (2 %) Bi. Many misfit dislocations appear in almost every precipitate are observed at the precipitate/matrix boundary in PbTe (2 %) Sb, which means that the density of dislocations is similar to that of precipitates.

Different from Pb or Sb single doped PbTe, the Pb/Sb codoped system exhibits dual nanostructures, which is corresponding to an anomalous electronic transport behavior wherein the carrier mobility first increases and then decreases with increase in temperature, as shown in Fig. 10.31a. Such slow rate of decrease in σ in the dual-nanostructured PbTe samples gives rise to a much higher $S^2\sigma$ at elevated temperatures (Fig. 10.31b). The plots of the k_{total} (Fig. 10.31c) show the dual-nanostructured samples have trends similar to those of PbTe-Sb. The measured ZT values in Fig. 10.31d represent a notable and significant increase, and the enhancement comes from the $S^2\sigma$.

In order to investigate the microstructural basis for the $S^2\sigma$ enhancement in Pb/Sb codoped PbTe system, TEM measurements were conducted to assess the presence and extent of nanostructures. The TEM results show nanoscale with higher density of 2×10^{12} cm^{-2} and microscale precipitates with only

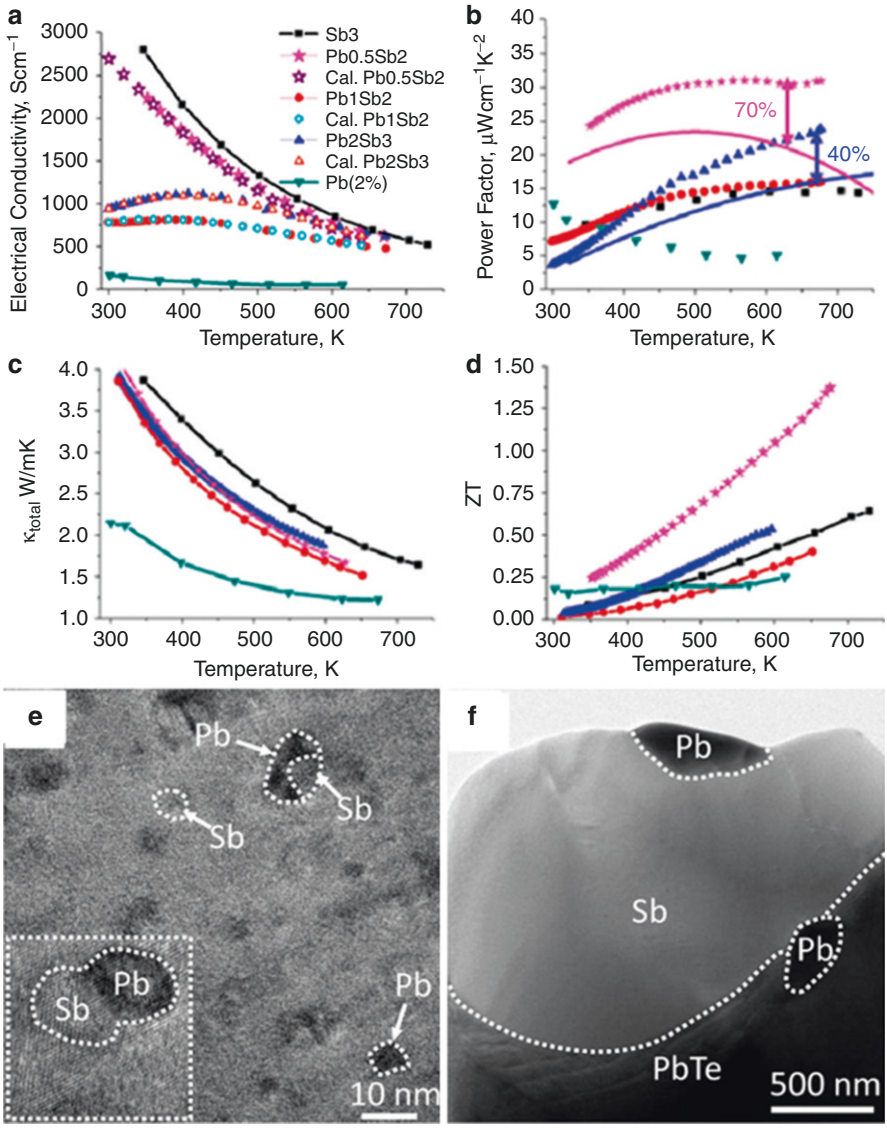


Fig. 10.31 Temperature-dependent measurements and corresponding calculations of σ (**a**), $S^2\sigma$ (**b**), κ_{total} (**c**), and ZT (**d**) for five samples PbTe (2 %) Pb, (−3 %) Sb, (0.5 %) Pb (2 %) Sb, (1 %) Pb (2 %) Sb, and (2 %) Pb (3 %) Sb. Typical TEM images of PbTe (1 %) Pb (2 %) Sb show two types of precipitates: (**e**) nanoscale regime and (**f**) microscale regime [85]

4×10^2 cm^{-2} density. The typical low-magnification TEM images in Fig. 10.31e, f show most precipitates have a regular spherical morphology. In Fig. 10.31e precipitates with three types of contrast levels, mostly dark, gray, and dual dark/gray contrast, are obvious, although generally the number density of the first two types is

higher than that of the third type. A combination of HRTEM and EDS reveals that the dark- and gray-contrast precipitates are rich in Pb and Sb, respectively. Figure 10.31f is a typical image of one single precipitate with coexisted Pb and Sb as labeled in Fig. 10.31f.

In order to determine the stability of the Pb and Sb dual precipitates at high temperature, in situ TEM was performed using a heating stage. A constant heating rate of 10 deg min^{-1} was used, and TEM images were collected from room temperature to 678 K (Fig. 10.32a–g). A reference hole was created by electron beam in the sample to accurately determine the location of the sample (bright spot in images). Initially, at room temperature a large number of precipitates are clearly observed. With temperature increase, the Pb-rich precipitates begin to melt and evaporate at approximately 398–448 K and start to dissolve and eventually completely disappear at 678 K. The disappearance of small precipitates occurs due to the thin-foil nature of TEM samples and the presence of high vacuum and high vapor pressures of constituent elements in the TEM, while these precipitates should be stable at room atmosphere and bulk condition. When the high-temperature specimen was cooled down to room temperature, some precipitates reappeared, as in Fig. 10.32h. Compared with the precipitates before heating, their number density and size are reduced because of loss of mobile Pb/Sb atoms to the atmosphere during the experiment. The reappearance of the particles offers evidence that during the heating experiment a portion of precipitates has dissolved into the PbTe matrix because of high solubility of dopant at high temperature. Figure 10.32i–m shows STEM images in the heating sequence repeated on a larger precipitate. Figure 10.32i is an image taken at 573 K, which appears similar to that at room temperature. When the temperature is increased from 573 to 723 K (Fig. 10.32j–m), the dark-contrast region (defined as Sb) changes to lighter contrast starting from the Pb region, and finally the big precipitate becomes entirely of white contrast. This suggests that Pb begins to diffuse into Sb and also the whole Sb particle. As shown in Fig. 10.32n, after the sample is cooled to 573 K, the Pb particles reappear. While one precipitate is at its original position, the other has diffused through the Sb particle to get to the interface between the Sb particle and PbTe matrix. EDS showed that the part labeled as "A" is still predominantly Sb-rich and the brighter region is predominantly Pb-rich. These observations corroborate with expectation that liquid Pb can readily diffuse into solid or liquid Sb, but has difficulty diffusing into the PbTe matrix.

Figure 10.32o–p show the schematic illustration of the above experiment. A small shrinkage associated with Pb- and Sb-rich precipitates during heating above 450 K is due to interdiffusion in the PbTe matrix; the dotted lines outline the particle size before heating (Fig. 10.32p). For precipitates containing both Sb and Pb, Pb appreciably diffuses into Sb at high temperature due to its higher diffusivity, which leads to conversion of PbTe–Pb interfaces to PbTe–Sb. Therefore, nominally Pb-rich precipitates become Sb-rich precipitates at the higher temperature.

Si or Ge is recently reported to effectively enhance the mechanical strength of PbTe. We reported the microstructure of composite PbTe-Si/Ge TE materials based

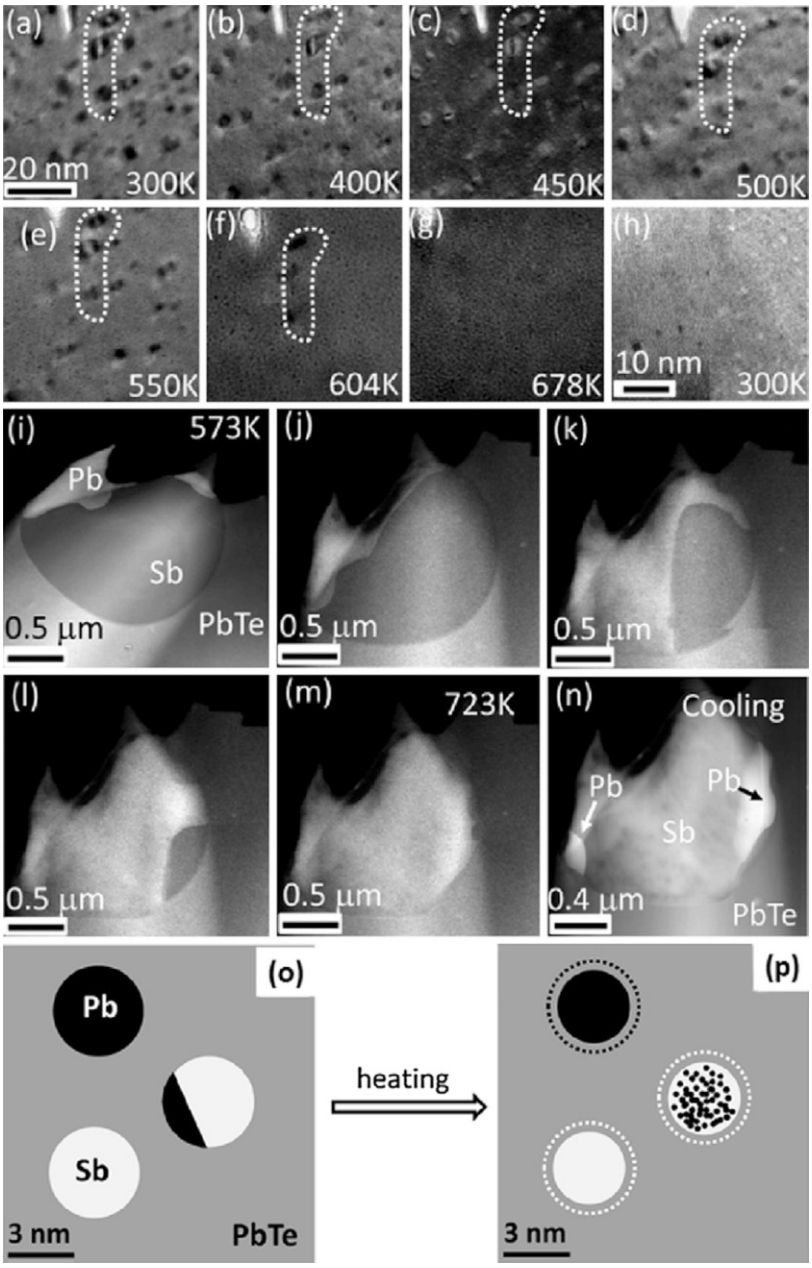


Fig. 10.32 In situ TEM/STEM images of PbTe (1 %) Pb (2 %) Sb. (**a**–**g**) Focus on small precipitates with the same magnification, while (**i**–**n**) concentrate on one large precipitate with Sb and Pb, which show the Pb melting and diffusing into Sb precipitate. (**h**, **n**) Image after cooling to room temperature. (**o**, **p**) Schematic diagram of Pb and Sb nanoscale precipitates in the PbTe at room temperature and higher temperature [85]

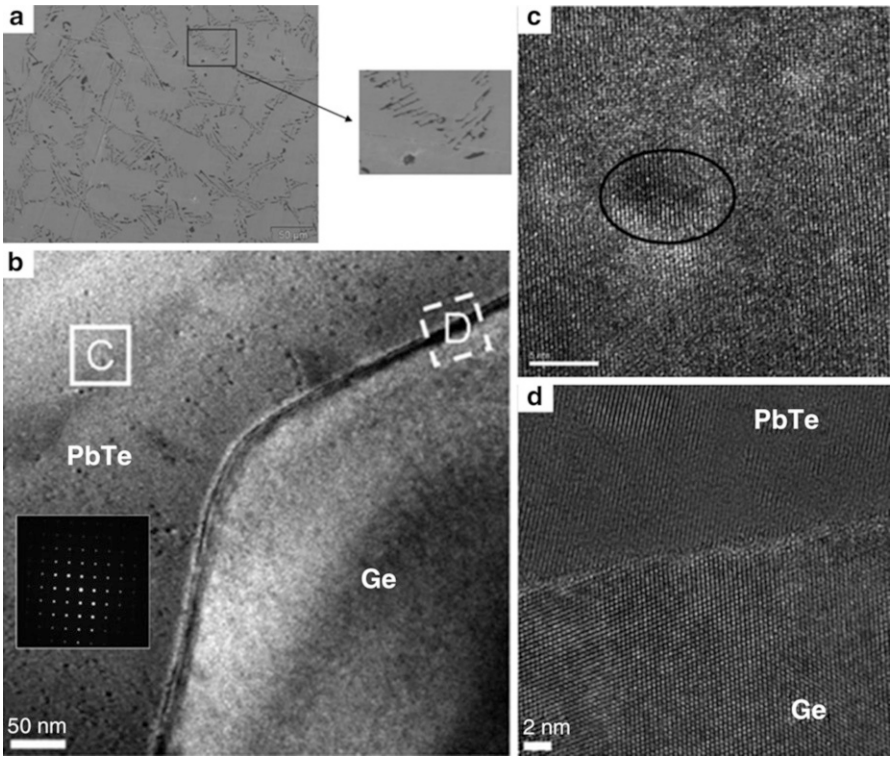


Fig. 10.33 (**a**) SEM image of the PbTe (20 %) Ge eutectic showing the rodlike microstructure of Ge (*darker*) in the PbTe matrix (*light gray*). (**b**) TEM image showing a Ge domain next to a PbTe domain. *Inset* is the DP of the matrix was indexed as PbTe. (**c**) One typical nanoscale precipitate in PbTe and (**d**) the incoherent boundary between the Ge precipitate and PbTe matrix without any precipitate [35]

on the eutectic phase transformation. These eutectic mixtures after quenched exhibit considerably stronger mechanical strength and reduced brittleness compared to PbTe itself while at the same time they possess lower k_{lat}. ZT values approaching 1.3 at 778 K for PbTe (5 %) $Ge_{0.8}Si_{0.2}$ and 0.9 at 675 K for PbTe (8 %) Si can be obtained [34, 35].

SEM reveals that the PbTe–Ge eutectic composition results in a rodlike microstructure. The rods of Ge formed through the rapidly solidified eutectic were 10–50 μm in length and 0.5–1 μm in diameter randomly oriented in the PbTe matrix (Fig. 10.33a). TEM investigation (Fig. 10.33b–d) shows three regions of interest: the large Ge precipitates, the boundary between Ge and PbTe, and nanoscaled Ge precipitates within the PbTe region itself (Fig. 10.33b). DP (inset of Fig. 10.33b) shows that regions within the PbTe domains are often pure without additional reflections. Nanoscaled precipitates (2–5 nm) can be observed, as shown in Fig. 10.33c. Figure 10.33d shows that the boundary between PbTe and Ge is not

coherent and the Ge domains do not have a preferred orientation with the PbTe domains. The micro- and nanostructure of the composite has important implications in the electrical and thermal transport properties.

SEM was used to analyze the microstructure of the eutectic compound PbTe (8 %) Si. Rodlike Si precipitates with 40–250 nm in diameter and several micrometers in length, generally smaller than those observed in the PbTe-Ge [35], were observed throughout regions of PbTe (Fig. 10.34a, b). The crystallization of the PbTe–Si eutectic during quenching occurs fast and does not allow Si to migrate through the sample to form large precipitates. TEM images revealed several regions exist including the PbTe matrix with Si precipitates (Fig. 10.34c), PbTe matrix with Pb nanoprecipitates (Fig. 10.34d, e), and a boundary layer between the matrix and Si. The Si precipitates exhibit as light-colored regions (80–150 nm) in the TEM image due to their significantly lower atomic number compared to PbTe. The Pb nanoprecipitates (2–20 nm) have a darker contrast than the matrix PbTe. In contrast to the PbTe–Ge system, where a stable $Pb_{1-x}Ge_xTe$ solid solution is formed, there is little solubility of Si in PbTe and the resulting Si–Te phase is trapped at interparticle boundaries. This boundary phase may decompose upon exposure to water during sample preparation and appear as a glassy interfacial film at the surface of Si precipitates embedded in the PbTe matrix. One representative precipitate is shown in Fig. 10.34g along with an HRTEM image of the boundary (Fig. 10.34h). At the surface of the Si precipitates, the crystalline Si_2Te_3 was readily hydrolyzed upon exposure to water during sample preparation forming glassy SiO_x and H_2Te. The presence of oxygen at this amorphous boundary was confirmed using EELS measurements (Fig. 10.34i). The EELS calculation, curve 4 in Fig. 10.34i, confirms the two oxygen peaks both come from SiO_x. It is likely that this Si_2Te_3, when embedded in the bulk material, is stable and may act as an interface to allow charge transport between the PbTe and Si.

5.5 TAGS

$(GeTe)_x(AgSbTe_2)_{100-x}$ (TAGS-x) alloys, which have been studied for many years and used in radioisotope TE generators, have chemical similarity to LAST [28–30, 98] (to be discussed later) and $AgSbTe_2$–SnTe [99] compounds. The ZT of TAGS-85 and TAGS-80 alloys can reach 1.4 [100] and 1.9 [101], respectively, at 800 K. Note that the LAST compounds are n-type, while most TAGS alloys are p-type; thus we can use them as the n- and p-type legs in a high-efficiency TE device. The most important characteristic contributing to the high TE performance of TAGS-x is its exceptionally low k_{lat}.

Yang [87] studied the nanoscale microstructures of TAGS alloys using TEM associated with TE property measurement. The results show the existence of nanodomains, which should contribute to the low k_{lat} in TAGS materials. The TE properties of TAGS-x compounds ($x = 75, 80, 85$ and 90) have been studied. At 720 K the ZT (Fig. 10.35c) reaches 1.53 for TAGS-75 and 1.50 for TAGS-80 and TAGS-85 samples due to the low κ (Fig. 10.35b) and good electrical properties (Fig. 10.35a),

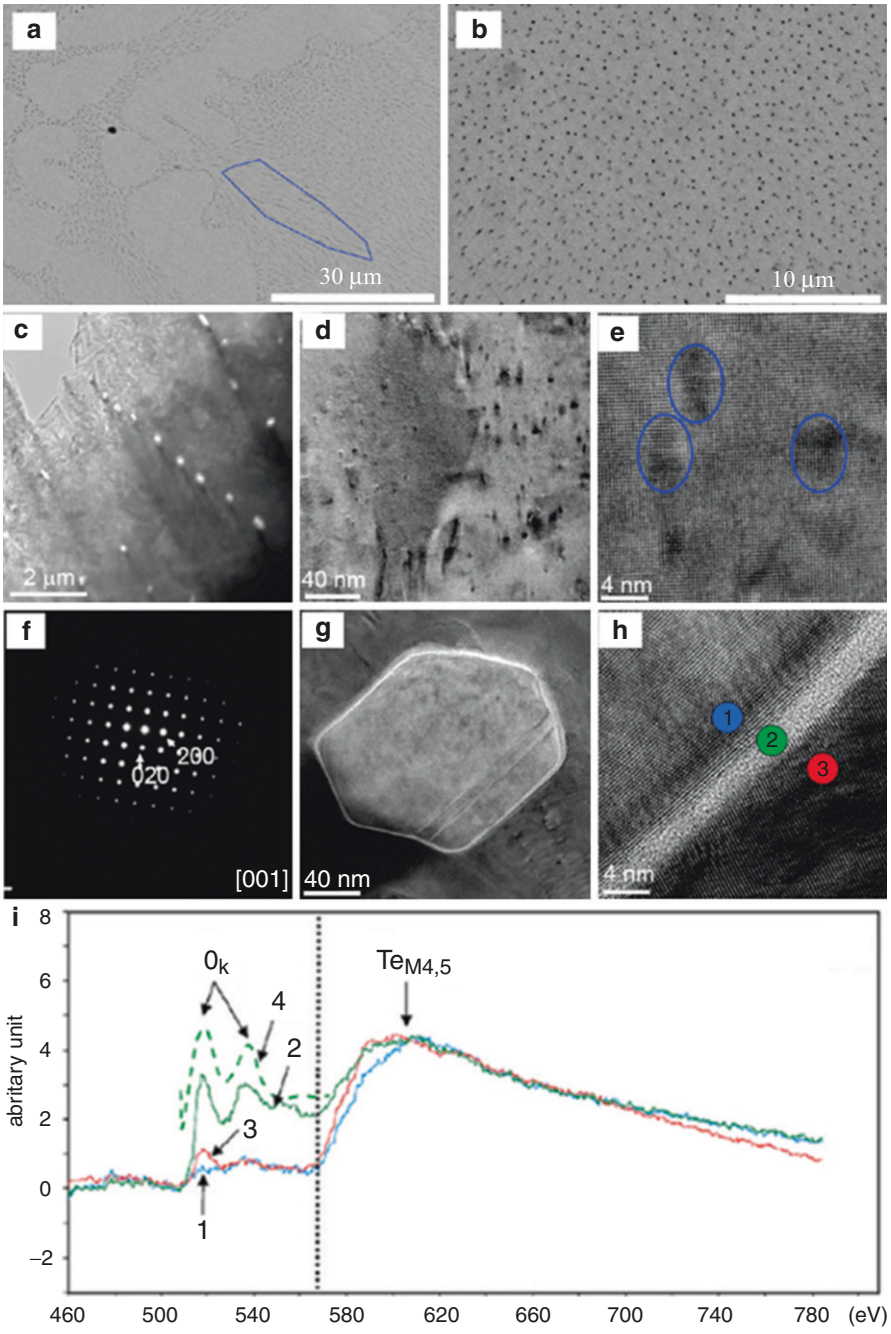


Fig. 10.34 SEMs of PbTe (8 %) Si indicating (**a**) the rodlike morphology of the Si precipitates, (**b**) the relatively narrow size distribution of the diameter of the Si precipitates. (**c**) Low-magnification TEM image showing Si precipitates (*white spots*) embedded in the PbTe matrix.

respectively. Figure 10.35d–h shows the TEM, HRTEM images, and inset SAED patterns for TAGS-80. Figure 10.35d shows the presence of nanoscale particles and inhomogeneities embedded in the compound varying from tens of nanometers to several micrometers. Figure 10.35e presents an HRTEM image of a homogeneous region. The electron diffraction spots and a magnified HRTEM image exhibited on the right-hand side indicate the feature of a perfect crystal. The DP can be indexed as the rhombohedral phase on [110] zone axis. The HRTEM image in Fig. 10.35f clearly displays the in situ formed nanoparticles with different crystal orientations in the sample and reveals the inhomogeneities at a nanoscopic level. The inset DP with more than one set of electron diffraction spots confirms the inhomogeneity of this region. Those nanodomains (about 10 nm) with different atomic spacings and crystalline orientations may have different compositions or fluctuation in components. They can be as potential barriers for intermediate-frequency phonons. The magnified images in Fig. 10.35g, h, from the regions A and B in Fig. 10.35f, show the joint regions of nanodomains with different orientations and atomic spacings. The high density of domain interfaces could provide a barrier for transmitting phonons in bulk samples. The nanodomains of size ~10 nm and the interfaces between them should have a strong scattering effect on the intermediate-frequency phonons which carry lots of heat, partially contributing to the low κ in TAGS alloys. These nanostructures in TAGS alloys are quite similar to those observed in LAST [30, 98] and $AgSbTe_2$–SnTe [99], which mainly contribute to the low k_{lat} of those compounds [10–12].

The nature of the crystallographic transformation in TAGS-x and its effect on electrical transport need to be established. It has been widely recognized that TAGS-x undergoes a polymorphic transformation above 300 K, from a low-temperature rhombohedral (R-3m) to a high-temperature cubic (Fm-3m) structure, the transition temperature depending primarily on the ratio of $GeTe/AgSbTe_2$ and also on the ratio of Sb/Ag. In the high-temperature NaCl polymorph, the Ge and Te atoms occupy the 4a Wyckoff position, with Te at the (0,0,0) and Ge at the (½, ½, ½) positions. In the TAGS composition, Ag and Sb substitute for Ge, on the (½, ½, ½) positions. As the material is cooled through the transformation temperature, thermal strain in the NaCl-type lattice is accommodated by a slight shift in the position of the Ge and Te atoms within the (220) planes. The shift manifests itself as a distortion along the [111] direction in the unit cell, producing the rhombohedral R-3m structure. As a consequence of the degeneracy due to the rhombohedral distortion, the {110} mirror planes within the cubic system are now potential twin planes [9].

Fig. 10.34 (continued) (**d**) TEM image showing the matrix PbTe material containing Pb nanoprecipitates. (**e**) HRTEM image and DP of (**d**). (**g**) Medium-magnification TEM image containing one Si precipitate. (**h**) HRTEM image of the amorphous glassy SiO_x interface phase between the PbTe and Si precipitate (region *1* is the Si, region *2* the boundary, and region *3* the PbTe). (**i**) EELS spectrum showing the presence of oxygen in the glassy SiO_x interface. The number labels in the spectrum correlate to those shown in (**b**). EELS spectrum (*line 4*) is from multiple-scattering calculation of oxygen K edge in SiO_2 [34]

The room temperature and 600 KXRD patterns for as-solidified TAGS-85 are shown in Fig. 10.36a, b, which were indexed as the low-temperature rhombohedral and high-temperature cubic polymorph, respectively. The characteristic splitting of the (220) Bragg reflection of the R-3m phase can be seen in the room temperature pattern. Two beam conditions were used to characterize the twinning along the {220} planes, associated with the room temperature rhombohedral polymorph, as shown in Fig. 10.36c. The twins possess a characteristic spacing ranging from 450 to 500 nm, as expected as a consequence of the inherent formation mechanism associated with the crystallographic distortion. Most twins were found to terminate

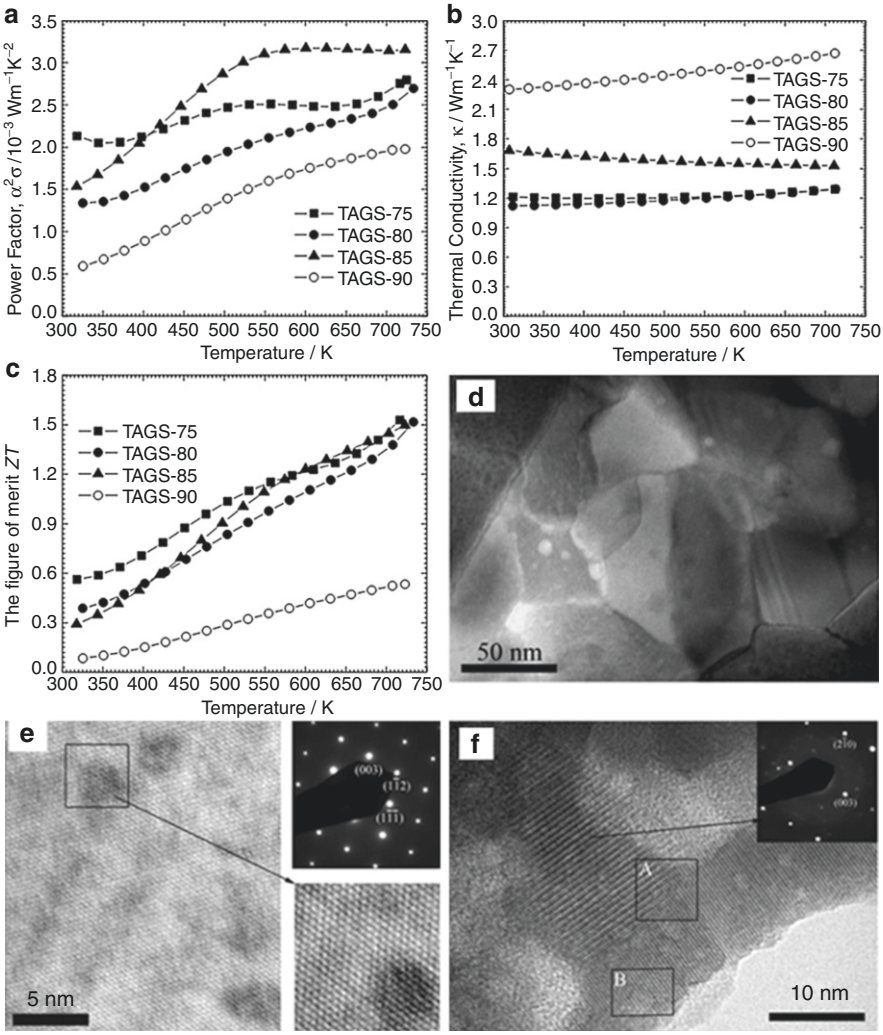


Fig. 10.35 (continued)

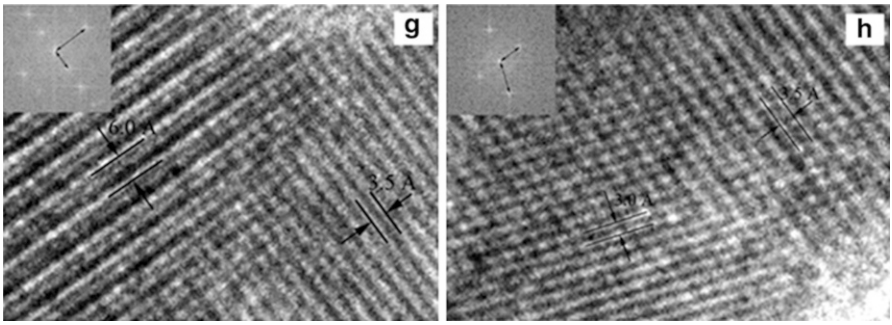


Fig. 10.35 Temperature dependences of (**a**) $S^2\sigma$, (**b**) κ, and (**c**) the dimensionless ZT of TAGS alloys. The microstructures of TAGS-80: (**d**) nanoscale particles and inhomogeneities in the hot-pressed sample. (**e**) Typical HRTEM images and SAED pattern. (**f**) Nanodomains of about 10 nm with different crystal orientation and atomic spacing. Regions *A* and *B* are the joint areas of different domains. The *inset* DP in (**f**) indicates there are several sets of electron diffraction spots. (**g**, **h**) Magnified regions of *A* and *B* in (**f**), and the *insets* are the FFT of such zones [87]

on grain boundaries or form as clusters of interpenetrating polysynthetic twins. While the twins are purely structural modulations, numerous antiphase domains are also observed throughout the material (Fig. 10.36d), which correspond to compositional fluctuations. The antiphase domains are typically elongated with dimensions of ~250 × 100 nm with an average separation of ~1 μm. The corresponding DP along the [001] zone axis is shown in inset of Fig. 10.36c, d.

As the sample was heated using an in situ hot stage, the microstructure changed appreciably as the phase contrast of the twins disappeared, as shown in Fig. 10.36e, f. Attempts to follow the rhombohedral to cubic transformation using an in situ heating stage revealed preferential loss of volatile material from the high surface to volume ratio foils, leading to irreversible compositional modulations.

5.6 LAST(T)

Hsu [29] reported a cubic $AgPb_mSbTe_{m+2}$(LAST-m) bulk TE materials with high ZT. The ZT value of ingots with the composition LAST-12 is about 1 at 700 K (Fig. 10.37a). However, the ZT of LAST-18 can reach a value of 2.1 at 800 K (Fig. 10.37b).

The reason of the above-enhanced TE properties of LAST-m systems may lie in the microstructural base of these materials at the atomic scale. The LAST-m materials are derived by isoelectronic substitution of Pb^{2+} ions for Ag^{+} and Sb^{3+} in the lattice. This generates local structural and electronic distortions, which are critical in determining the properties of LAST-m. The controversy is whether the Ag^{+} and Sb^{3+} ions are distributed in the structure homogeneously or inhomogeneously. Arguably, someone proposed an inhomogeneous distribution considering the different formal charges of +1/+3 versus +2 arising from

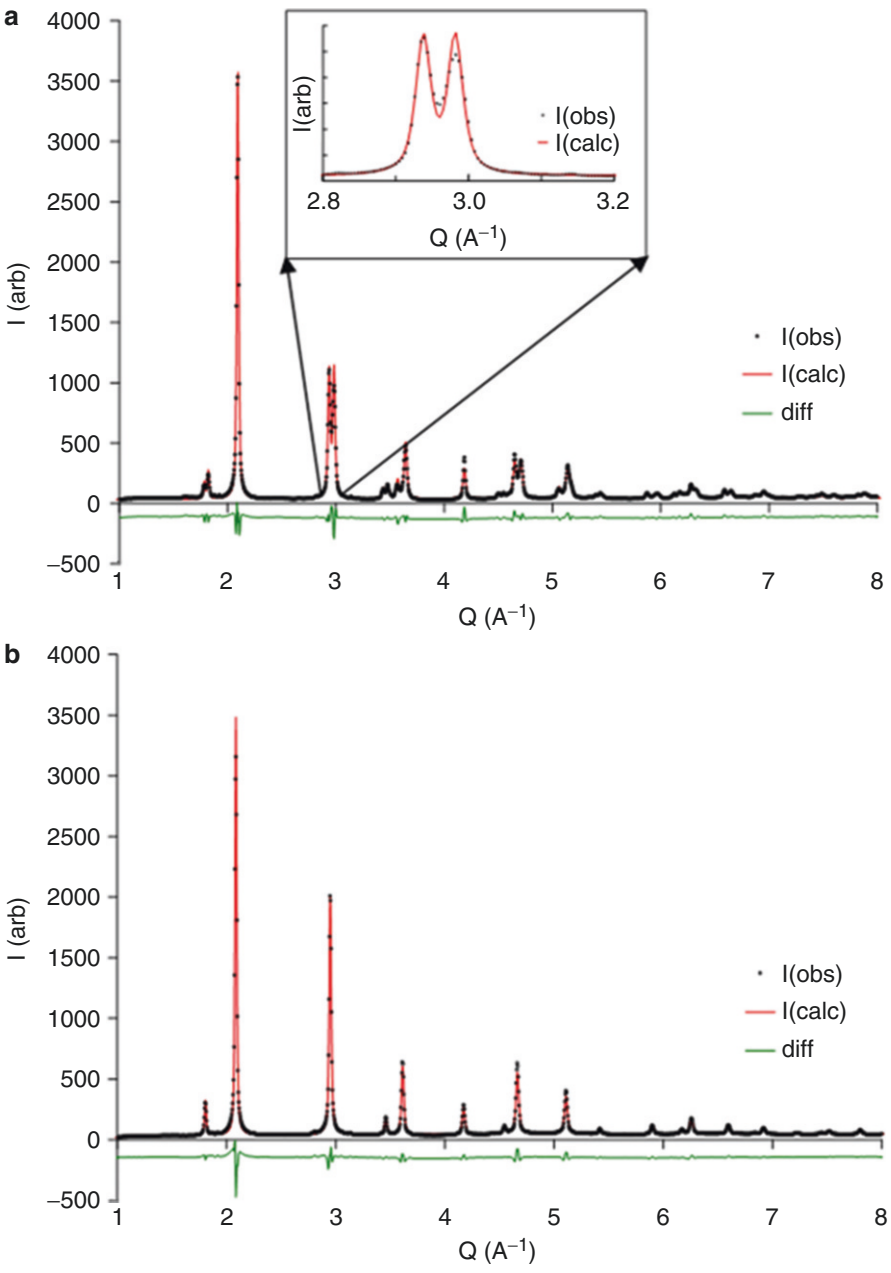


Fig. 10.36 (continued)

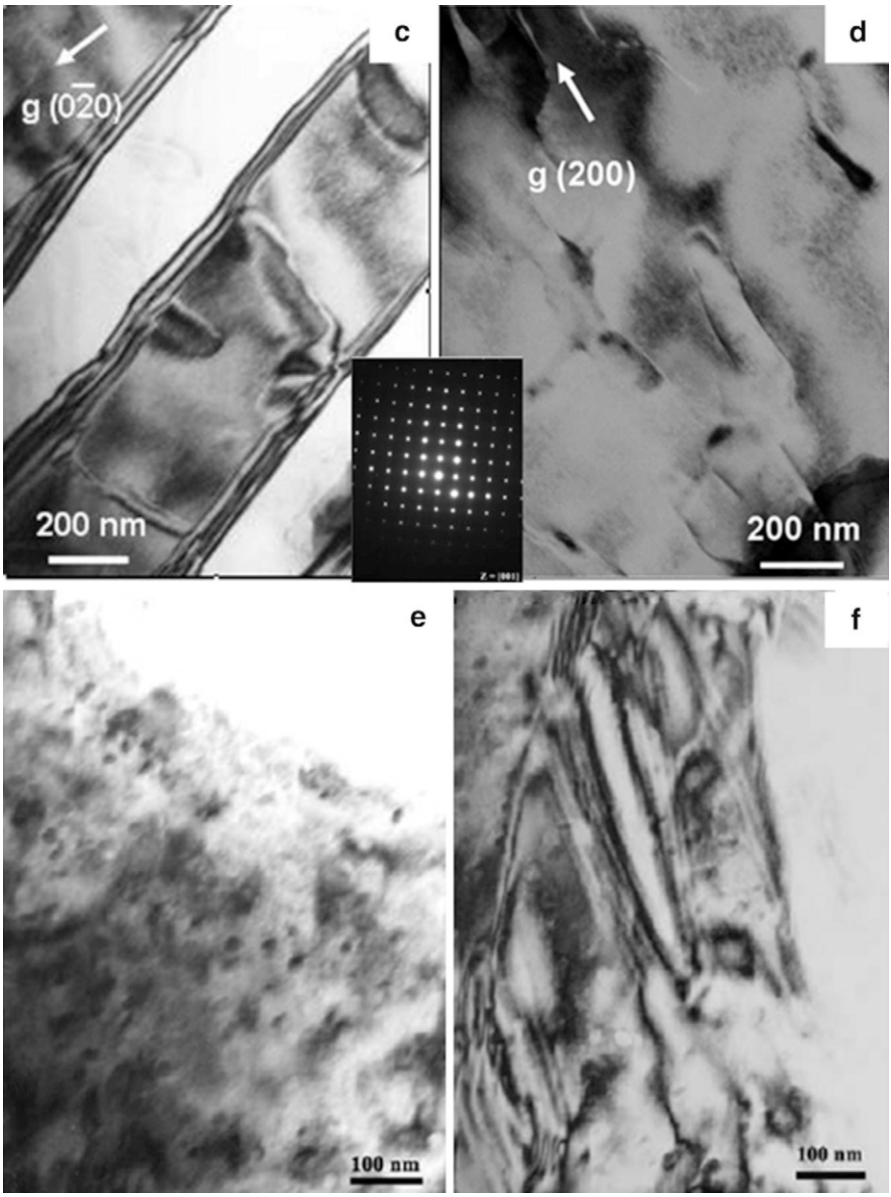


Fig. 10.36 XRD patterns and their Rietveld refinement of as-solidified TAGS-85: (**a**) 320 K and (**b**) 600 K. Note the presence of the {220} doublet associated with the low-temperature polymorph (shown in the *inset* of (**a**)). (**c**) TEM image of twin structures associated with the rhombohedral polymorph of TAGS-85. (**d**) Antiphase domains are seen as continuous across twin boundaries by tilting the sample stage, which brings the twins out of contrast. The inset DP in (**c**) and (**d**) shows the rhombohedral polymorph of TAGS-85 on [001] zone. (**e**) Point defects in TAGS-85 TEM foil at 433 K. (**f**) TEM image of TAGS-85 at room temperature following in situ heating to 436 K. Note the retained point defects after thermal cycling [102, 103]

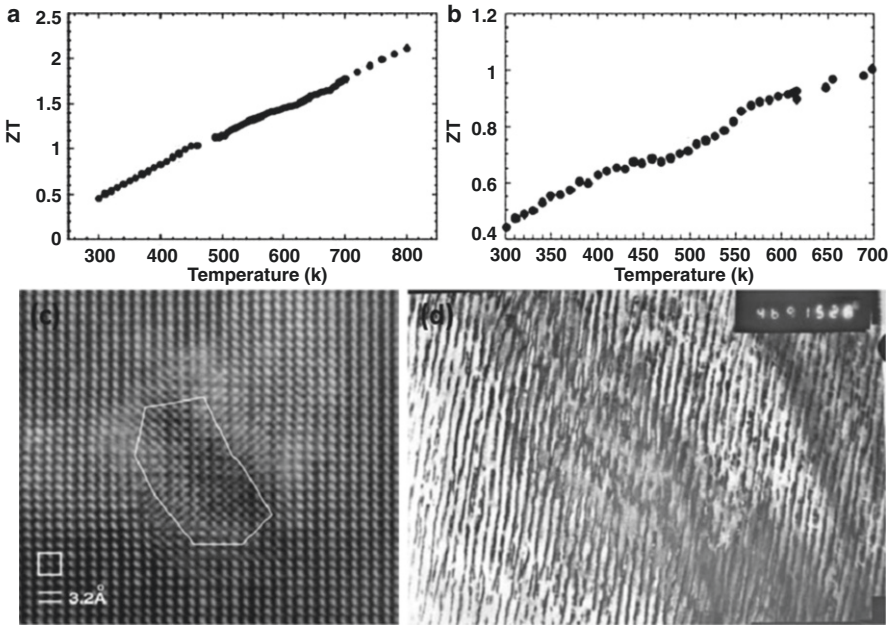


Fig. 10.37 (**a**) ZT as a function of temperature of (**a**) LAST-18 and (**b**) LAST-10. (**c**) TEM image of a LAST-18 sample showing a nano-sized region of Ag–Sb-rich in composition. The surrounding structure is close to that of PbTe. (**d**) Compositional modulations over an extended region of a LAST-10 specimen [29]

Coulombic interactions. On the other hand, a completely homogeneous Ag^{+} and Sb^{3+} dispersion in the Fm-3m lattice would require the complete separation of the Ag^{+} and Sb^{3+} pair in long-range order, which could create charge imbalances in the vicinity of these atoms. Given the relatively high concentrations of Ag^{+}–Sb^{3+} in the LAST-18, these essentially Coulombic factors could act to favor compositional modulations in the crystal which will result in separated regions of high Ag/Sb and high Pb concentration. Preliminary evidence for this comes from HRTEM images that indicate inhomogeneities in the microstructure of these materials, showing nanoscaled precipitates of an Ag–Sb-rich phase embedded in a PbTe matrix (Fig. 10.37c). For LAST-10, different compositional modulations were observed (Fig. 10.37d) [29].

The detailed microstructure nature of the TE materials LAST-m at the atomic as well as nanoscale was studied with powder XRD, electron diffraction, and HRTEM, which followed the above work [29]. XRD patterns of different members ($m = 0, 6, 12, 18, \infty$) (not shown here) are consistent with pure phases crystallizing in the NaCl-structure-type (Fm-3m), which means that the LAST family behaved as solid solutions between the PbTe and $AgSbTe_2$ compounds. However, electron diffraction and HRTEM studies suggest the LAST phases are inhomogeneous in local with at least two coexisting phases, compared with its homogeneity in average. The precipitated phase which is richer in Ag/Sb is on

the nanoscale, and it is endotaxially embedded in the matrix phase which is poorer in Ag and Sb. Moreover, within each nanodomain extensive long-range ordering of Ag, Pb, and Sb atoms can be observed. Indeed, data collections were successfully refined in space groups of lower symmetry than Fm-3m including P4/mmm and R-3m.

DP was performed on samples of LAST-15. Different areas exhibiting varying structural features on the LAST-15 sample were analyzed (Fig. 10.38). This indicated phase inhomogeneity at the nanoscopic level (Table 10.3).

One model showing the Ag–Sb-rich chains is shown in Fig. 10.38d. The nearby calculated DPs present two examples of orientations [001] and [012] in orthorhombic axes deduced from this model, and the simulated patterns can be in good agreement with the experimental ones. The electron diffraction studies clearly show the LAST-m samples possessing different domains exhibiting nanostructures [98].

Finally, HRTEM performed on samples of LAST-18 clearly presents inhomogeneities at the nanoscale. Endotaxially embedded nanocrystals of varying sizes and shapes can be found in the samples. Two types of coherent nanodomains, with different atomic spacings, can be observed in Fig. 10.39a magnified in Fig. 10.39 (b1), (c1). Some domains show a doubling of the periodicity, and their FFT yields a doubling of the lattice parameter (Fig. 10.39(c2)). Some neighboring domains show normal F symmetry (Fig. 10.39(b2)). The observed structural differences are the result of coexisted regions: rich in Ag–Sb and Pb, which leads to a situation that produces Ag–Sb-rich nanoprecipitates embedded in a PbTe matrix. The endotaxial nature of these nanoprecipitates with the surrounding matrix is an important feature, as HRTEM images clearly reveal (Fig. 10.39d). Dislocations are observed at the nanoprecipitates/matrix interface. This endotaxy occurring in these materials could be highly conducive to facilitate carrier transport throughout the sample. At the same time the very high density of nanoprecipitates/matrix interfaces could provide a formidable barrier to phonon transmission in the bulk sample, thereby setting the combining foundation for a marked enhancement in ZT relative to that of the classical solid solution system. In the case of LAST-18 member, HRTEM images were able to clarify the endotaxial-nature grown nanoprecipitates. In Fig. 10.39(e1), an HRTEM image is presented showing a nanoprecipitate in the matrix. Figure 10.39 (e2), (e3) shows the corresponding FFTs of the left and the right side of the image. It is clear that the left one corresponds to a cubic structure, while the right one (due to the presence of extra spots along the one of the [100] axes) to a noncubic phase (possibly tetragonal or orthorhombic). The nanoprecipitate shown in Fig. 10.39(f1) appears with different features than the previous one (Fig. 10.39(e1–e3)). As it can be seen also from the corresponding FFT (Fig. 10.39(f2)), extra spots appear along the {110}. It is probably the cubic phase with P symmetry described above [98].

Beside LAST-m TE materials, other related LAST compounds with high thermoelectric performance have also been reported. The nanostructured $Ag_{0.8}Pb_{22.5}SbTe_{20}$ compounds were fabricated by mechanical alloying and SPS method. The electrical resistivity of all the annealed samples increases with temperature and then decreases when the temperature is over 400 K, showing a semimetallic to semiconducting transforming behavior at 400 K (Fig. 10.40a).

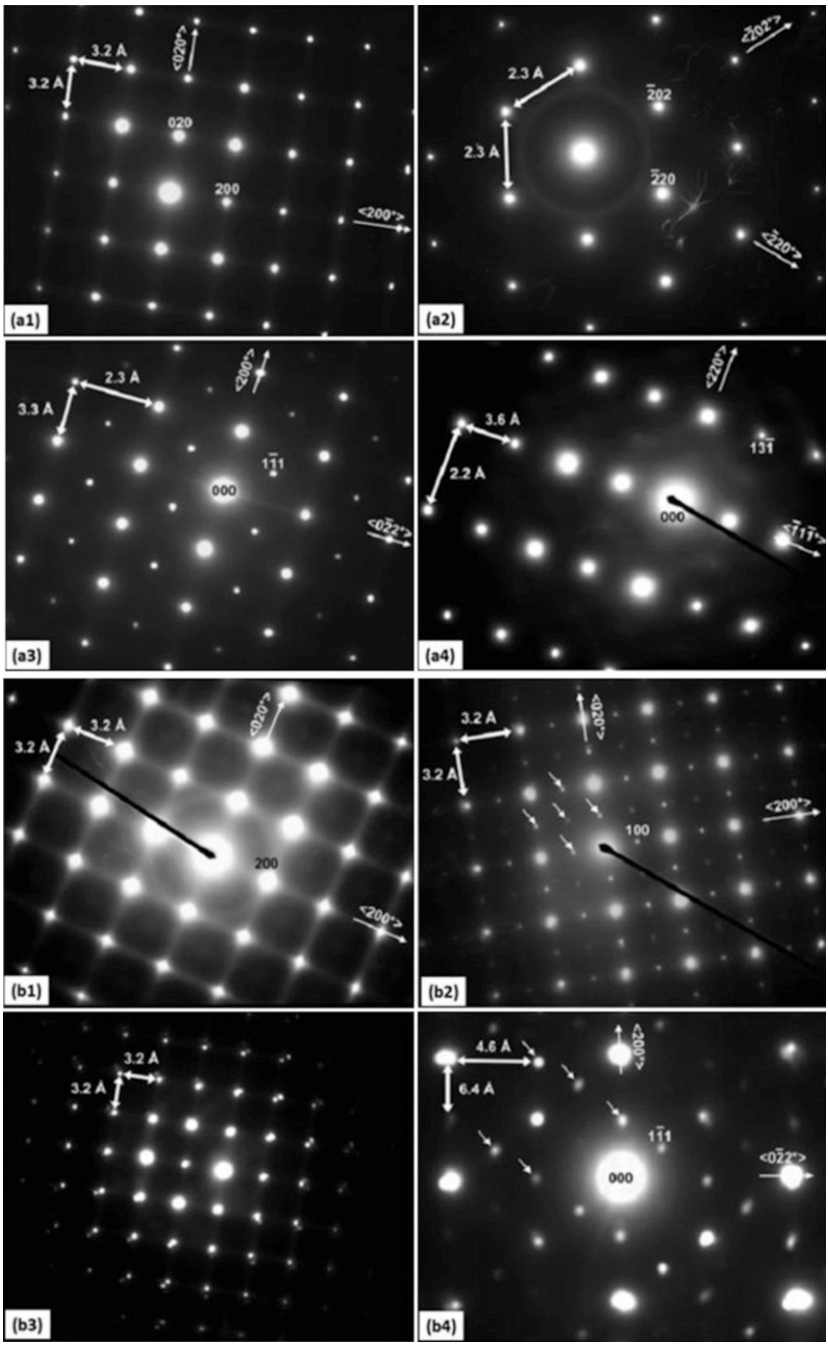


Fig. 10.38 (continued)

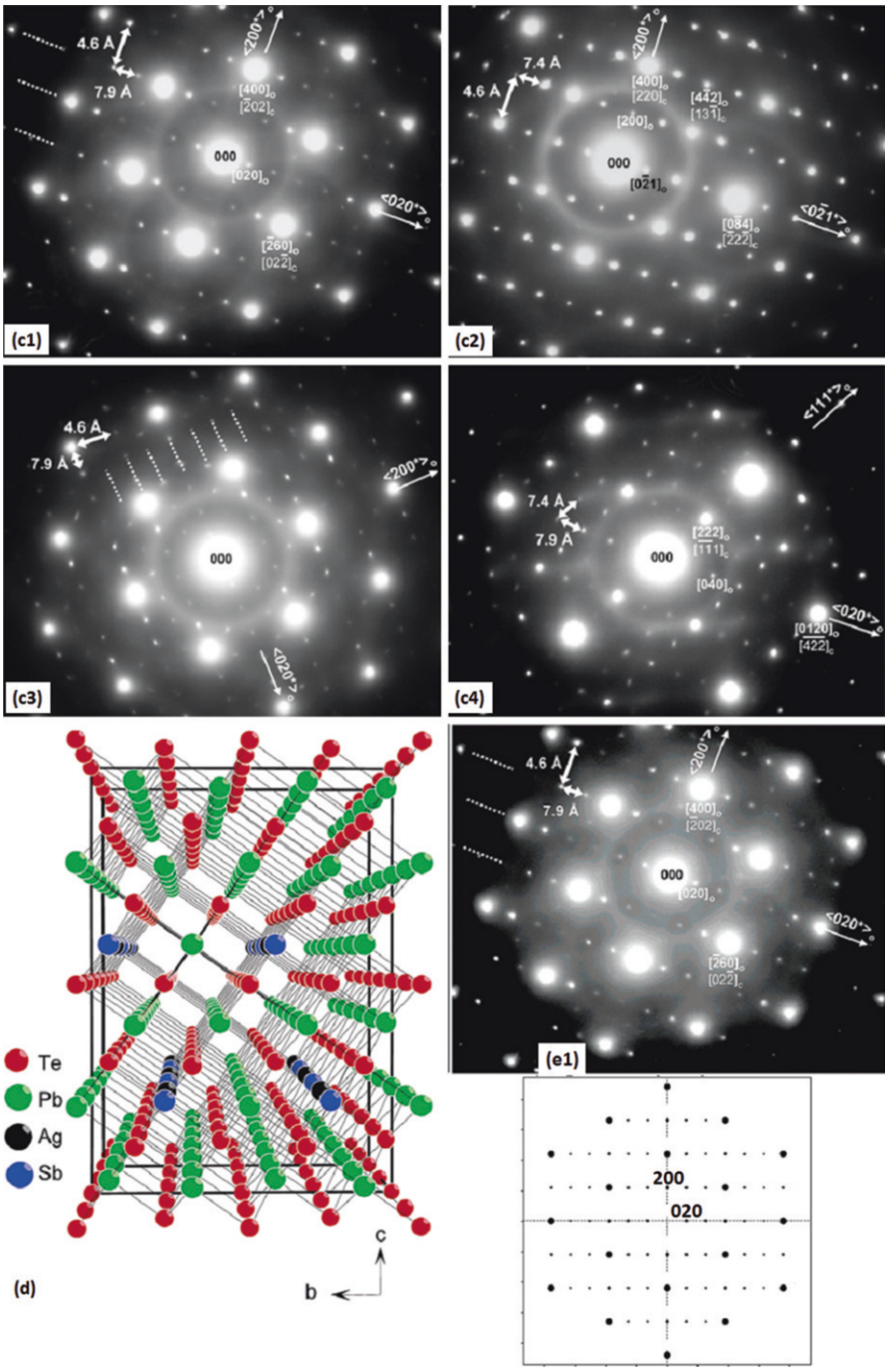


Fig. 10.38 (continued)

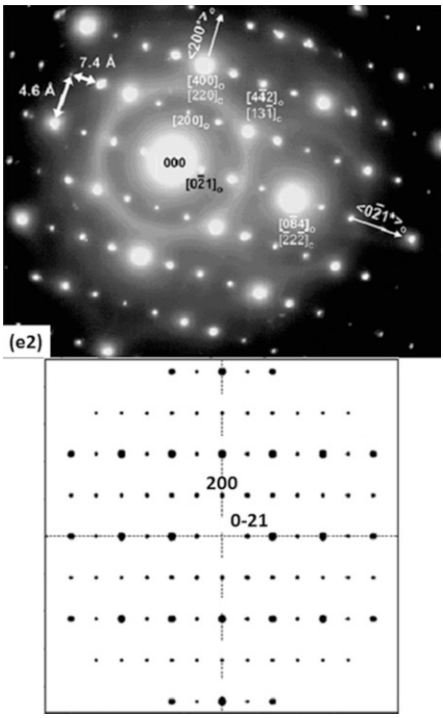


Fig. 10.38 (**a1**)–(**a4**) DP revealing a cubic F lattice viewed along four distinct crystallographic directions: (**a1**) [001], (**a2**) [111], (**a3**) [011], and (**a4**) [1–12]. (**b1**)–(**b4**) Examples of DPs exhibiting F-centered lattice with additional features: (**b1**) diffuse streaks on [001] zone axis, (**b2**) supplementary spots (*white arrows*) on [001] zone axis, (**b3**) splitting spots on [001] zone axis, and (**b4**) extra spots (*white arrows*) on [011] zone axis leading doubling of the a cubic cell parameter. (**c1**)–(**c4**) DPs showing a lowering of the crystal symmetry from cubic to orthorhombic. They correspond to (**c1**, **c3**) $[111]_c$, (**c2**) $[1–12]_c$, and (**c4**) $[2–31]_c$ zone axis in F symmetry. The corresponding zone axes are (**c1**, **c2**) $[001]_o$, (**c3**) $[012]_o$, and (**c4**) $[1]_o$. (**d**) Example of structural model highlighting the isolated parallel Ag–Sb chains within the structure. (**e1**)–(**e2**) The experimental and nearby calculated DPs present two examples of orientations $[001]_o$ (**e1**) and $[012]_o$ (**e2**) deduced from the model in (**d**) [98]

As a potential TE material, $Ag_{0.8}Pb_{22.5}SbTe_{20}$ has a high $S^2\sigma$ (Fig. 10.40b) and low κ at high temperature (Fig. 10.40c). The TE properties of these compounds can be enhanced by annealing treatment. The κ is greatly reduced with annealing time, and a minimum κ value of 0.89 W/(mK) is obtained at 700 K for the sample annealed for 30 days (Fig. 10.40c). It is very interesting that the $S^2\sigma$ does not decrease but increases with annealing time over the measured temperature range (Fig. 10.40b). As a result, a large ZT value of 1.5 has been obtained for the sample annealed for 30 days at 700 K [30].

The lowering of κ can be mainly due to the significant reduction of k_{lat} caused by the enhanced point defects scattering with annealing time. Actually, besides point

Table 10.3 Five different types of structural features were observed by DP on samples of LAST-15

Index	Figure	Pattern description	Structural features
1	Fig. 10.38 (a1)–(a4)	A perfect cubic F lattice with cell parameter $a \approx 6.4$ Å	Ag, Sb, and Pb atoms are tending to order but still are randomly arranged within the structure
	Fig. 10.38 (b1)	Accompanied with diffuse streaks	
2	Fig. 10.38 (b2)	Extra spots	The extra spots, highlighted by small white arrows, can be indexed to a cubic P unit cell with $a \approx 6.4$ Å
3	Fig. 10.38 (b3)	Spots splitting	This feature is evidence of the coexistence of two phases with similar lattice parameters and endotaxial crystallographic orientation
			The phase with the slightly smaller lattice parameter is corresponding to precipitates with a richer Ag/Sb, whereas the phase with the longer lattice parameter is correspondingly more rich in Pb
			This observation strongly implies a well-defined compositional fluctuation in the material
4	Fig. 10.38 (b4)	Supercell reflections characteristic of a doubling of the cubic unit cell at least along one crystallographic direction	The [11] zone axis exhibits extra diffraction spots indicated by the small white arrows and indexed to a possible F supercell of $a \approx 12.8$ Å, which is a doubling of the cubic F unit cell
5	Fig. 10.38 (c1)–(c4)	Extra spots involving modification of the unit cell	An orthorhombic unit cell, with lattice parameters $a_O \approx 9.1$ Å, $b_O \approx 15.8$ Å, and $c_O \approx 22.3$ can be identified

defect, the author observed a lot of nanoprecipitates embedded in the PbTe-rich matrix in the TEM images for the samples before and after annealing treatment, as shown Fig. 10.40e, f. Obviously, the density and size of these nanoscopic regions increase with annealing time. The HRTEM images of the unannealed sample revealed the existence of nanoscale features. As shown in Fig. 10.40g, a certain amount of localized wavy pattern with a size of about 5–10 nm presents inside of all the crystal grains. These nanostructures are endotaxial with their surrounding matrix, which should be related to compositional fluctuations between Ag, Sb, and Pb: Ag-/Sb-rich regions are formed as precipitates and embedded in the surrounding matrix endotaxially without disturbing the electronic flow. The HRTEM images of annealed samples displayed larger nanoscopic regions with a size of 10–50 nm, as shown in Fig. 10.40h. It was also found that the number of this kind of nanoscopic regions greatly increased compared to the unannealed sample. The increased density of these nanoscopic regions and surrounding nanointerfaces are thought to effectively scatter phonons, especially

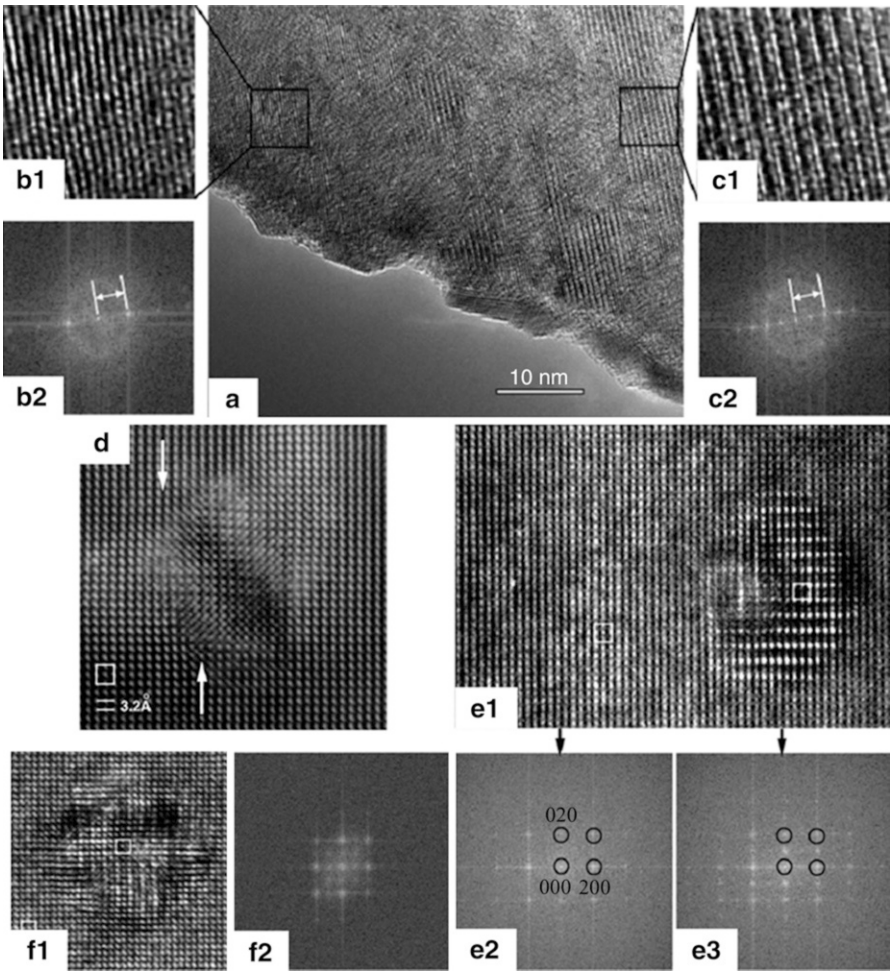


Fig. 10.39 Microstructurs on LAST-18 sample. (**a**) HRTEM showing the coexistence at the nanoscale of two kinds of domains with magnified images in (**b1**) and (**c1**). The FFTs of such zones (**b2** and **c2**, respectively) show that the lattice parameter of domain c is double than that of domain b. (**d**) HRTEM image showing the endotaxial growth of a nanoprecipitates in the matrix. The presence of dislocations at the nanoprecipitate/matrix interface is indicated by arrows. HRTEM image (**e1**) and the FFTs from the matrix (**e2**) and the nanoprecipitate (**e3**) along [100] zone axis. HRTEM image (**f1**) and the corresponding FFTs from nanoprecipitate (**f2**) along [100] zone axis. The HRTEM image and the FFT have different features compared with the previous one (**e**)–(**e2**) [98]

the intermediate-frequency heat-carrying phonons. As a result, the κ of the annealed samples dropped compared to the unannealed sample [30].

Androulakis reported on the $Ag(Pb_{1-y}Sn_y)_mSbTe_{2+m}$(LASTT-$m$) series and showed that certain compositions exhibit high-performance p-type TE properties (e.g., ZT∼1.45 at 630 K) as a result of their very low κ. The k_{lat} of the LASTT system at all temperature is quite small compared with PbTe just as Fig. 10.41a

shows. These exceptional properties (Fig. 10.41b) outperform the standard state-of-the-art p-type systems previously reported like TAGS (ZT∼1.2 at 720 K [104]) and Zn_4Sb_3 (ZT∼1.3 at 670 K [65]). An HRTEM investigation of several LASTT samples revealed striking structural nanoscopic and coherent inhomogeneities (Fig. 10.41c–f). The localized wavy pattern shown in Fig. 10.41c–f with a length scale of ∼3 nm appears unambiguously in all the investigated samples.

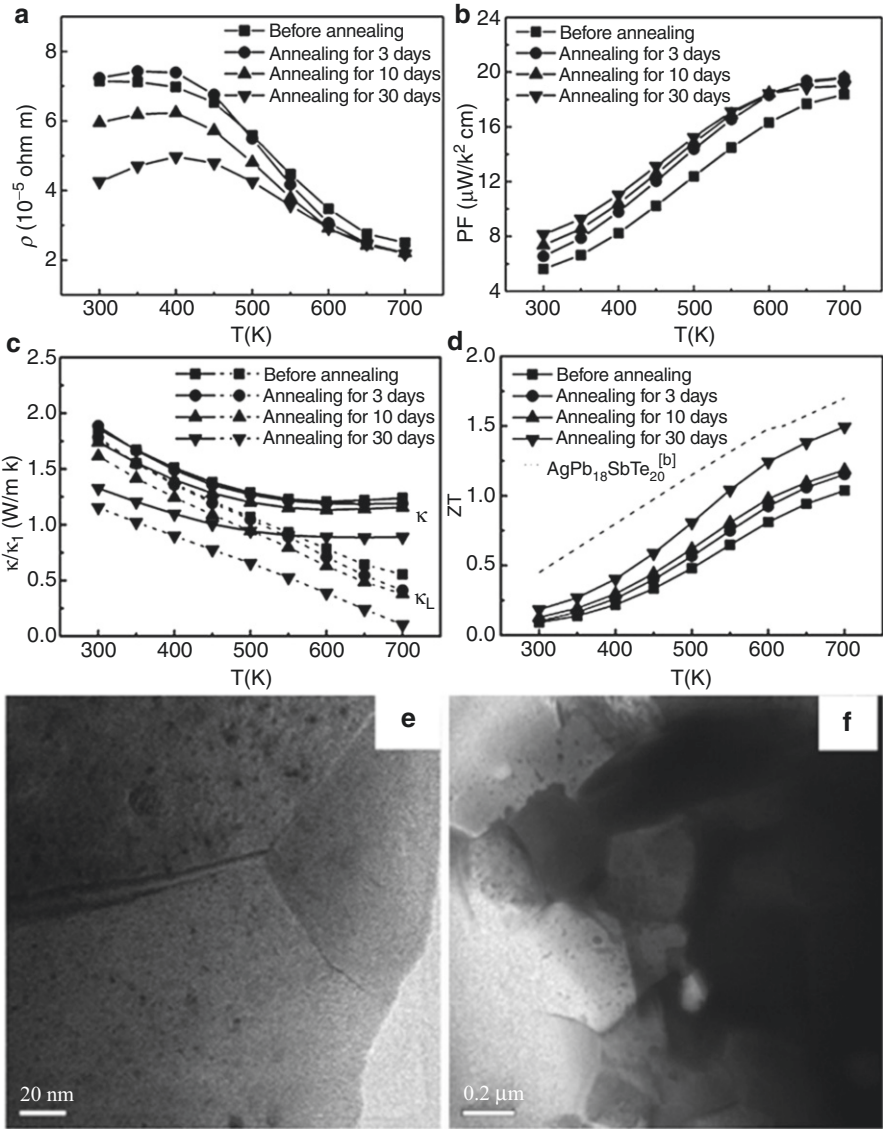


Fig. 10.40 (continued)

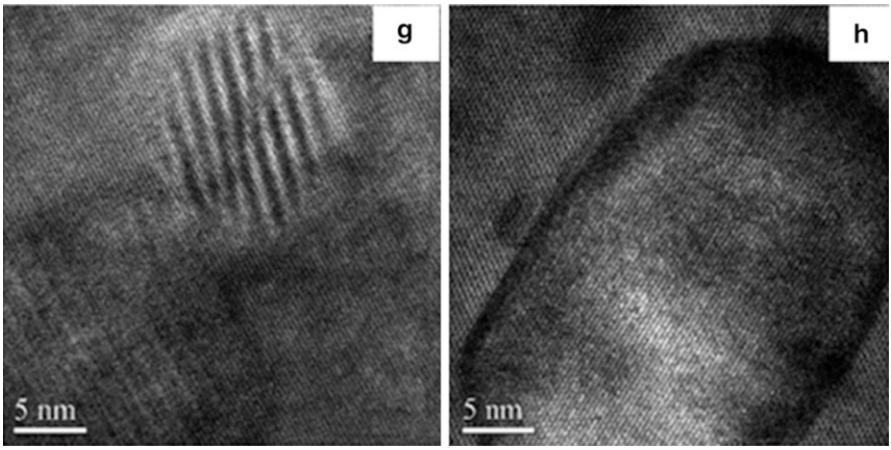


Fig. 10.40 Temperature dependence of (**a**) electrical resistivity, (**b**) $S^2\sigma$ value, (**c**) κ, and (**d**) ZT value for $Ag_{0.8}Pb_{22.5}SbTe_{20}$ bulks before and after annealing for different times. Low-magnification TEM images of (**e**) unannealed sample and (**f**) the sample annealed for 30 days. HRTEM images of (**g**) unannealed sample and (**h**) the sample annealed for 30 days [30]

The nanostructure is endotaxial with its surrounding matrix and is related to compositional fluctuations between Ag, Sb, and Pb/Sn. In other words, Pb-/Sn-poor regions (nanoprecipitates) are formed that disperse in the surrounding matrix endotaxially without disturbing the electronic flow. Other types of nanometer-scale inhomogeneities are observed as well, such as distinct nanoprecipitates 5–20 nm in size; see Fig. 10.41d. It is believed that strong suppression of the intermediate-frequency heat-carrying phonons is achieved via nanostructuring [37].

5.7 SALT

Poudeu reported that the Ag-free system $Na_{1-x}Pb_mSb_yTe_{m+2}$ (SALT), with appropriate combinations of m, y, and x, achieved record-high ZT values for a p-type bulk TE material. The high performance of these materials results mainly from a low κ. HRTEM demonstrates pervasive nanostructuring in SALT, which may be the root cause for the remarkably low κ [39].

For samples of composition $Na_{0.95}Pb_{20}SbTe_{22}$ ($m = 20$, $x = 0.05$, $y = 1$), a relatively high σ of 1541 S cm^{-1} and a thermopower of $S = 96$ μV K^{-1} can be obtained, just as Fig. 10.42a shows. The temperature dependence of the κ of $Na_{0.95}Pb_{20}SbTe_{22}$, along with the lattice and carrier contributions to the κ, is plotted in Fig. 10.42b. At room temperature, the k_{total} of the sample is $\kappa = 1.8$ W/(mK), which is approximately 22 % lower than the typical value of $\kappa = 2.3$ W/(mK) reported for p-type PbTe [105]. The value of $\kappa_{latt} = 0.74$ W/(mK) at 300 K is only one third of that of PbTe ($\kappa_{latt} = 2.2$ W/(mK)) [106]. Below 500 K, the κ is mostly due to the electronic contribution, whereas above 500 K, the lattice contribution

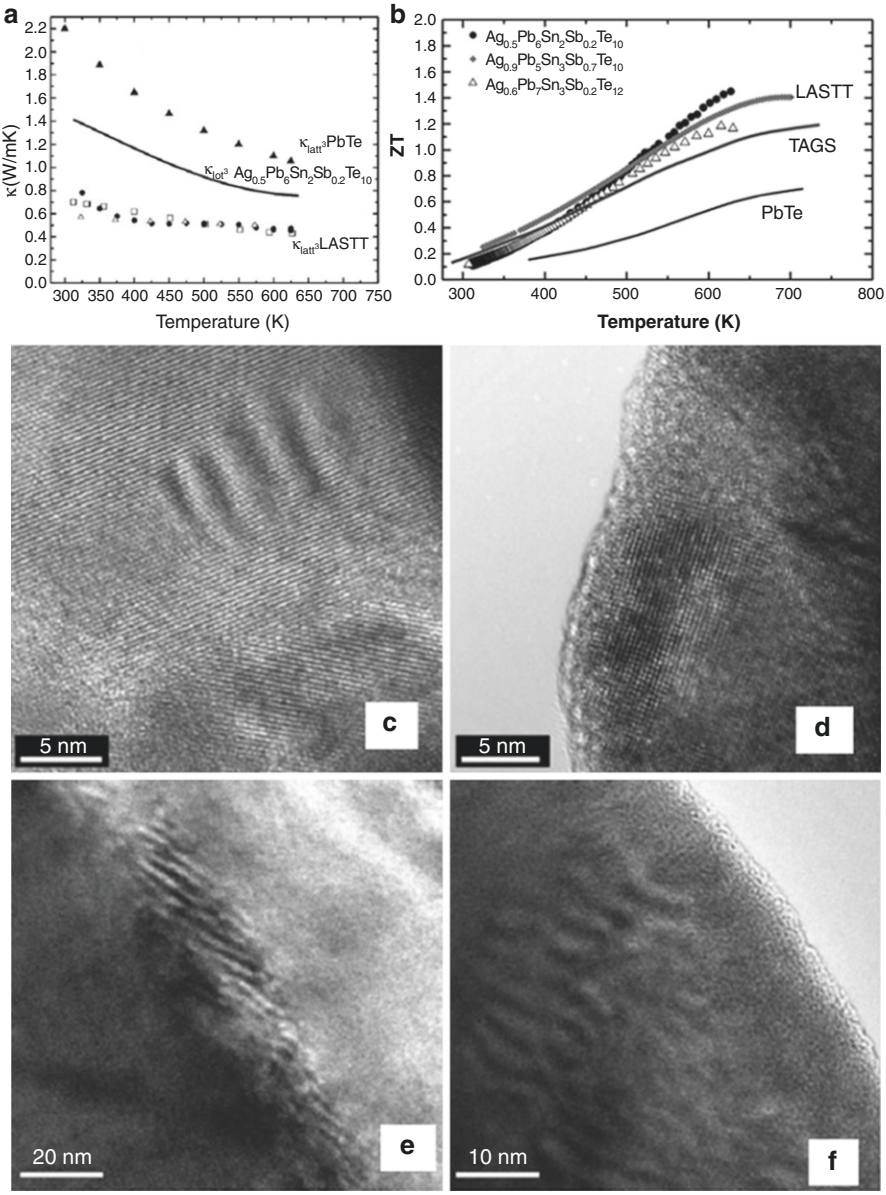


Fig. 10.41 (**a**) k_{lat} for three compounds of the LASTT series in comparison to that of PbTe. (**b**) Comparison of the ZT as a function of temperature for some of the best LASTT samples (indicated on the graph), with two of the state-of-the-art p-type TEs, TAGS and PbTe. (**c**) HRTEM image of $Ag_{0.5}Pb_6Sn_2Sb_{0.2}Te_{10}$ showing a wave pattern that is rich in Ag and Sb. (**d**) Characteristic inhomogeneity observed as an embedded nanoprecipitate 5 × 20 nm in size in $Ag_{0.5}Pb_6Sn_2Sb_{0.2}Te_{10}$. (**e**) HRTEM image of $Ag_{0.9}Pb_5Sn_3Sb_{0.7}Te_{12}$. (**f**) The same as (**c**), but showing compositional waves over an extended region [37]

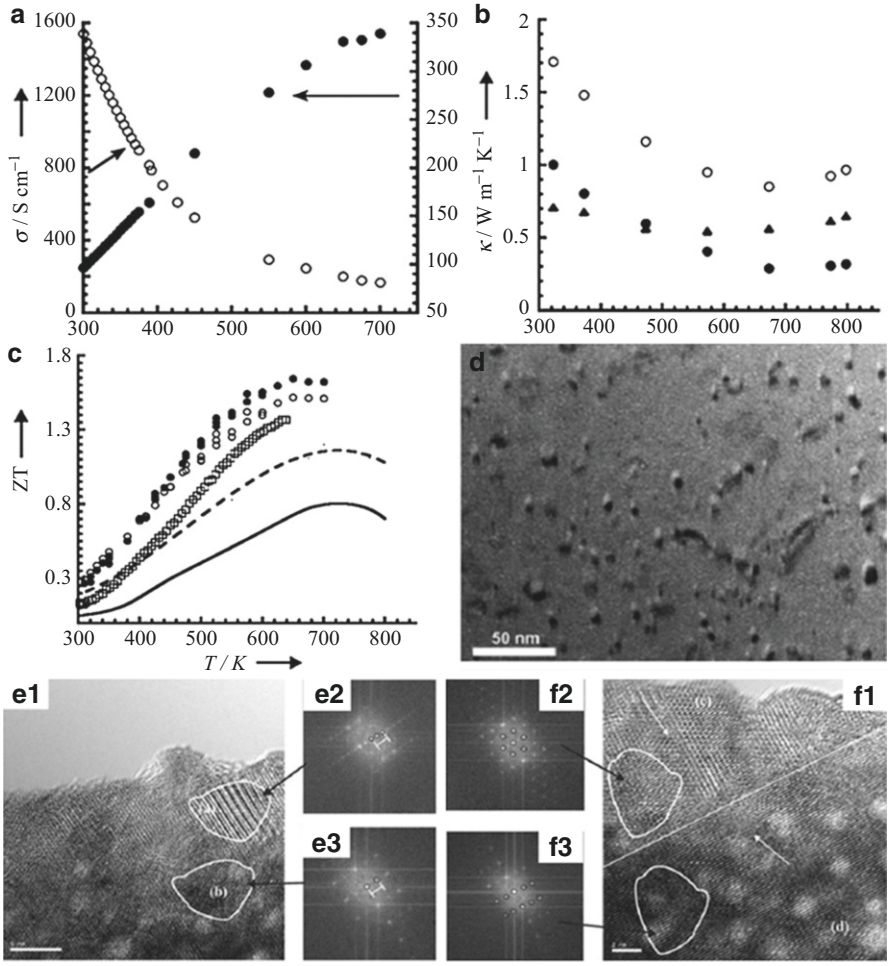


Fig. 10.42 Temperature dependence of (**a**) the σ (◦) and the S (•) for $Na_{0.95}Pb_{20}SbTe_{22}$, (**b**) the κ of $Na_{0.95}Pb_{20}SbTe_{22}$ (◦), showing the lattice κ_{latt} (▲) and carrier κ_{el} (•) contributions, and (**c**) the TEZT for $Na_{0.95}Pb_{20}SbTe_{22}$ (•), $Na_{0.95}Pb_{19}SbTe_{21}$ (◦), and $Na_{0.8}Pb_{20}Sb_{0.6}Te_{22}$ (□), compared to those of the p-type PbTe (*solid line*) and TAGS (*dashed line*). (**d**) A low-magnification TEM image of a $Na_{0.95}Pb_{20}SbTe_{22}$ sample. (**e1**) HRTEM image of $Na_{0.95}Pb_{20}SbTe_{22}$ and its corresponding FFTs (**e2**) and (**e3**) (*right*). (**f1**) HRTEM image of $Na_{0.95}Pb_{20}SbTe_{22}$ and its corresponding FFTs (**f2**) and (**f3**) (*left*). The *white arrows* in the HRTEM image indicate crystal boundaries between domains of similar orientation. The *white line* across the HRTEM image, which divides the two areas, is drawn over one atomic row and traverses domains of type (**c**) and (**d**), without a shift in atomic row [39]

dominates. In Fig. 10.42d, the ZT for the SALT samples is compared to those of the p-type TAGS and PbTe-based materials. The exceptionally high ZT of SALT, which exceeds those of the state-of-the-art materials PbTe and TAGS, derives from their very low lattice thermal conductivities.

The κ of a material is typically reduced by large mass-fluctuation disorder in one atomic position of its crystal structure (random alloy disorder, point defects, nanoscaled precipitates and grain boundaries, and so on). Nanostructuring in bulk samples could produce strong phonon scattering, and the presence of nanostructuring can only be probed through a detailed examination of the structure at the atomic scale. The abundance of nanoscaled precipitates, which are favorable for phonon scattering, is apparent in the large-area view shown in Fig. 10.42d. In Fig. 10.42(e1), two distinct domains with obviously different atomic spacings, which have cocrystallized at the nanoscale, can be seen. The corresponding FFTs of the two domains in the HRTEM image reveal a doubling of the periodicity in one direction for precipitated nanodomain (a) with respect to the cubic spacing of matrix domain (b). The nanocrystal domains of type (a) have compositions rich in Na and Sb ($NaSbTe_2$). Figure 10.42(f1) shows two areas (c) and (d) with different orientations, [111] and [011], as revealed by the corresponding FFTs. The arrows indicate crystal boundaries between domains of similar orientation. Both domains are coherently grown, which is called endotaxy and is important in allowing facile charge transport through the sample, owing to reduced electronic scattering [98]. The matrix (Pb-rich regions) are indicated by the slightly larger lattice spacing evident in the images (PbTe (NaCl-type, Fm-3m) has a larger lattice spacing than precipitated phase $NaSbTe_2$) [39].

Recently, we also applied various of advanced TEM techniques including HRTEM, HAADDF, and EDS on several members of the $NaPb_{18-x}Sn_xBiTe_{20}$ (x = 5, 8) series and found that they are inhomogeneous on the nanoscale with widely dispersed nanocrystals embedded in a $Pb_{1-y}Sn_yTe$ matrix. Lamellar features in these materials associated with compositional fluctuations and significant strain at the nanocrystal/matrix interface are also observed.

To gain information about the local lattice distortion around the nanostructures, we studied the sample $NaPb_{13}Sn_5BiTe_{20}$ with HAADF (Fig. 10.43a, b). The line profile across a selected array in Fig. 10.43c indicates the sequence of major heavy elements (Pb/Te) in the structure. However, such periodic uniform sequence is clearly perturbed by the presence of nanostructures, which is indicated in Fig. 10.43d–g. HRTEM studies indicate the nominal lattice parameter of the precipitate to be twice of that of the matrix (Fig. 10.43d, e). FFTs of the two regions are shown in Fig. 10.43f, g, which indicate the apparent doubling of the unit cell of nanostructure compared to the matrix.

In addition to discrete nanoscale precipitates, nanoscale lamellar features are also observed in $NaPb_{13}Sn_5BiTe_{20}$ (Fig. 10.44a) system. GPA was used to investigate the variation in lattice parameters, thus the elastic strain, at/around these layers. Figure 10.44b shows the power spectrum (from FFT) of the image in Fig. 10.44a with $g_1 = 002$ and $g_2 = 220$ chosen as the Fourier vectors. The strain map profiles along the 001 direction (ε_{yy}) and the shear direction (ε_{xy}) are shown in Fig. 10.44c, d. There is about 6 % difference between lamella A and B. It is possible that the lamellar features may be due to local ordering between PbTe and SnTe phases. Another type of lamellar feature with sawtooth shaped (Fig. 10.44e–h) is formed at the edge of the sample during ion beam thinning, indicating clear difference in thinning rate, thus the

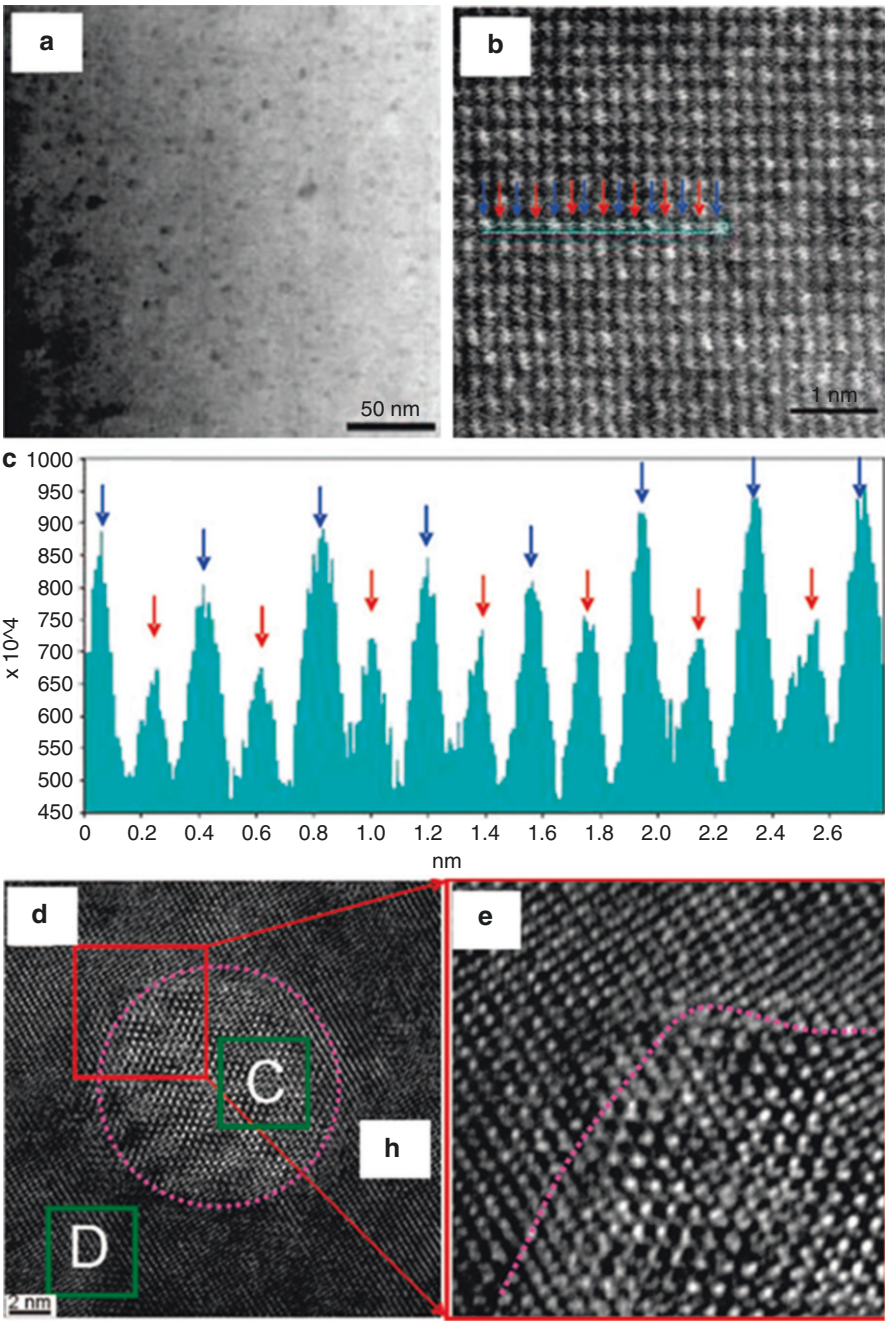


Fig. 10.43 (continued)

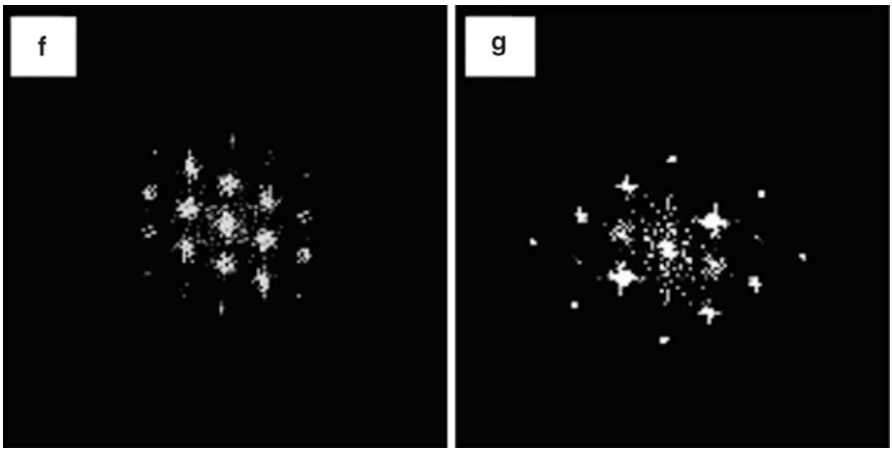


Fig. 10.43 Disperse precipitates observed in (**a**) low- and (**b**) high-magnification HADDF image for $NaPb_{13}Sn_5BiTe_{20}$. (**c**) Line-scanning profile of the selected atomic array in (**b**); the positions that the red arrows point out are Te, and those marked by blue arrows mainly come from Pb. (**d**) HRTEM image and (**e**) enlarged part showing the lattice parameters of the precipitate and that of the matrix are different. (**f**, **g**) FFT images of the two regions *C* and *D* in (**a**) [89]

atomic bonding (the Pb–Te bond is stronger than the Sn–Te bond). This may also be the result of local ordering between PbTe and SnTe phases. Hence during sample milling, the SnTe layer may be more easily removed than the PbTe layer. Such nanostructure and interface-induced matrix elastic perturbations can play a decisive role in mediating the phonon propagation pathway and thus contribute to enhanced phonon scattering resulting in reduced κ in these systems.

We also compared the electrical transport properties of $NaPb_{18-x}Sn_xBiTe_{20}$ ($x = 5, 9$) sample with its basic parent PbTe, SnTe, and $Pb_{0.6}Sn_{0.4}Te$ compounds, as shown in Fig. 10.45a–c. SnTe has invariably higher σ, lower S, and higher k_{lat}, which can be explained by the high amount of naturally occurring vacancies in the Sn sublattice that greatly increases the carrier concentration to nearly metallic levels. On the contrast, $NaPb_{13}Sn_5BiTe_{20}$ has the lowest k_{lat} value (Fig. 10.45c).

To clarify the underlying mechanism of differences in these systems, we undertook a TEM investigation of the internal microstructure of these samples. Figure 10.45d, e, h shows the low-magnification images of PbTe (homogeneous), $Pb_{0.6}Sn_{0.4}Te$ (nonuniform due to point defects and grain boundaries), and $NaPb_9Sn_9BiTe_{20}$ (nanoscaled precipitates), respectively. EDS data (inset in Fig. 10.45e) of different positions shows uniform composition of $Pb_{0.6}Sn_{0.4}Te$ sample. In Fig. 10.45f, a DP of $Pb_{0.65}Sn_{0.35}Te$ with an aperture including a large number of crystal grains does not show extra diffraction spots. Only some high-order spots are elongated due to a small fraction of in-plane misaligned grains. In contrast to the basic parent materials PbTe, PbSn, and $Pb_{0.6}Sn_{0.4}Te$ above, a representative TEM image (Fig. 10.45h) of the $NaPb_9Sn_9BiTe_{20}$ sample shows two typical features: One close to the edge of the image displays very uniform contrast due to beam

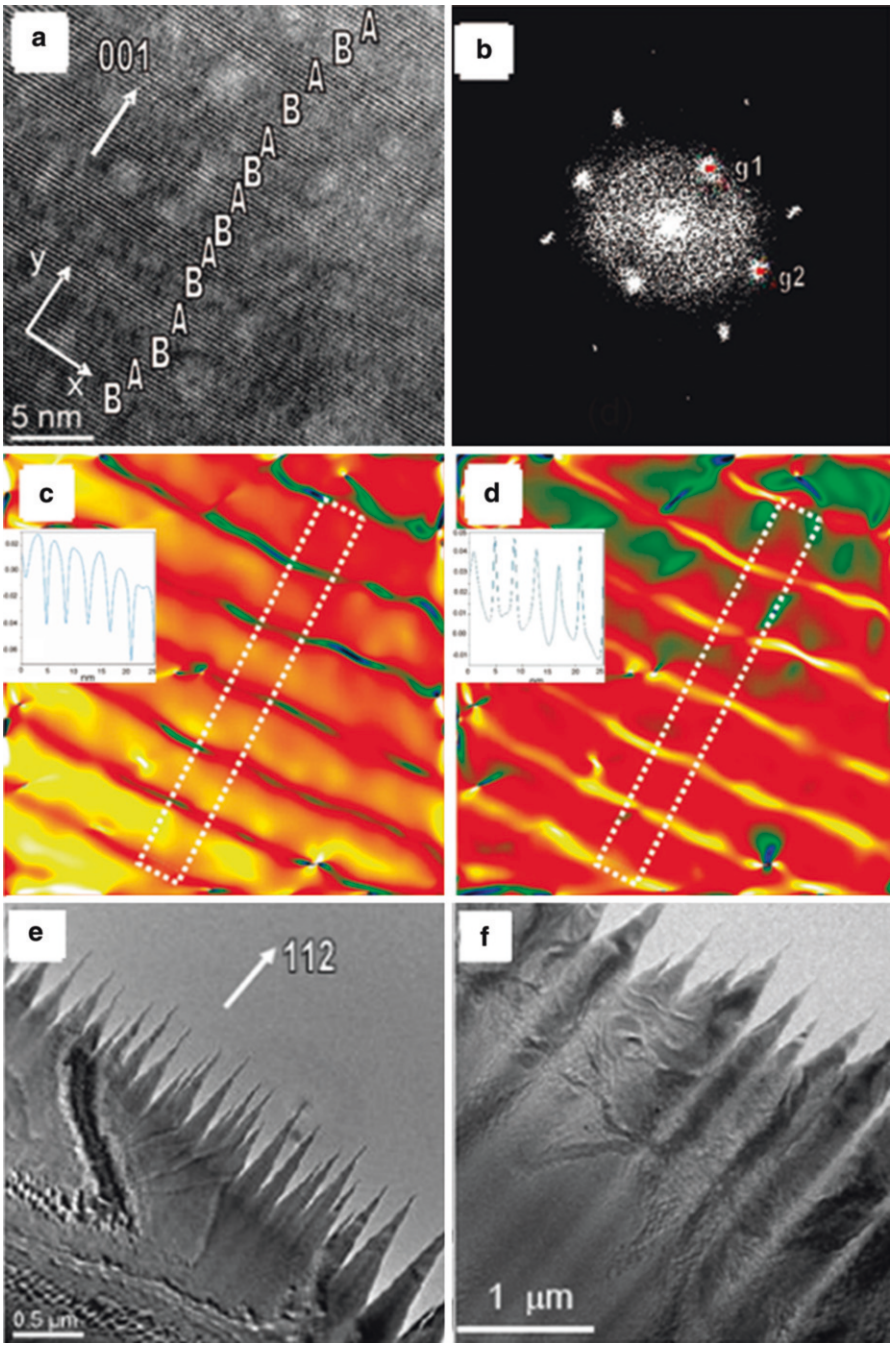


Fig. 10.44 (continued)

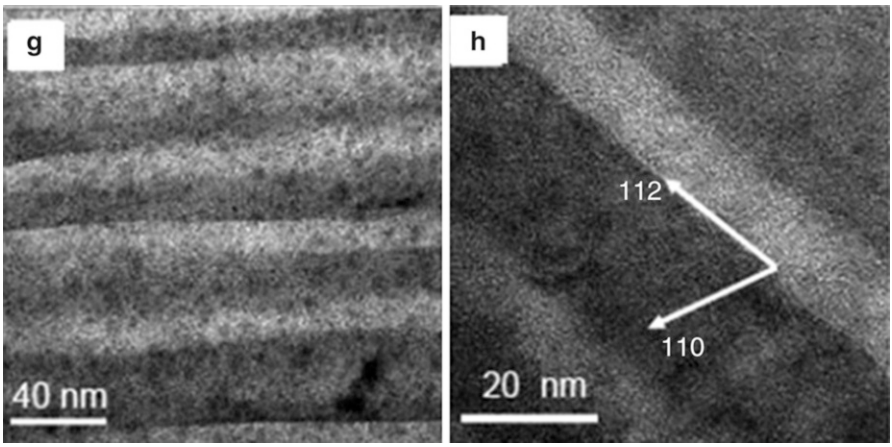


Fig. 10.44 (**a**) TEM image of $NaPb_{13}Sn_5BiTe_{20}$ showing lamella structure labeled as *ABAB*. (**b–d**) Strain mapping for this precipitate: (**b**) power spectrum image. (**c**, **d**) show the strain map profile along the 001 direction (ε_{yy}) and the shear direction (ε_{xy}), respectively. (**e–h**) Different magnification images for $NaPb_{13}Sn_5BiTe_{20}$ with sawtooth shape of lamellar structure [89]

damage, while the other, about 80 nm away from the edge, contains many regular precipitates (2–10 nm) with dark contrast. Interestingly, the $NaPb_{13}Sn_5BiTe_{20}$ sample also contains two different kinds of lamellar structures. An HRTEM lattice image (Fig. 10.45i) of the lamellar structure clearly reveals the first type of lamellar structures: ordered modulated structures labeled sequence ABAB with a (100) interface plane. The secondary type inserted in Fig. 10.45i illustrates one type with sequence CDCDCD. These dark- and bright-contrast lamellar structures, 100–200 nm wide, grow along the (112) plane. EDS showed that the level of Pb is high in regions marked by A and C, while areas denoted by B and D are rich in Sn, implying local nanoscale segregation between the two phases PbTe and SnTe.

Figure 10.46a is an HRTEM image of a $NaPb_{13}Sn_5BiTe_{20}$ sample showing one rhombic-shaped precipitate inserted in the matrix. A line-scanning profile crossing the strong and weak peaks in FFT pattern (Fig. 10.46b) of the whole image in Fig. 10.46a shows no split peaks, signifying that there is minimal mismatch between the matrix and precipitates. Figure 10.46c contains the FFT images of precipitate (red oval) and matrix (blue oval) in Fig. 10.46a, which indicates additional superlattice spots arising from the precipitates. The line profile, encompassing the precipitates and matrix, demonstrates that the peak spot arises only from the precipitate. Therefore, the lattice parameters of precipitates are twice those of the matrix. The precipitates here are probably nominally $NaPb_2BiTe_4$. Figure 10.46d shows the HRTEM lattice image of the $NaPb_{13}Sn_5BiTe_{20}$ sample with inclusions of two different sizes. GPA (Fig. 10.46e) discloses large strains at the boundaries between the matrix and inclusions. The grain size distribution of $NaPb_{18-x}Sn_xBiTe_{20}$ ($x = 5, 9$), shown in Fig. 10.46f, g, are very similar.

Figure 10.47a is an HRTEM image showing the lamellar structure and precipitates. Figure 10.47b is its FFT pattern and line profile across two spots (002) and (220), each of which displays three clear spot splittings. Applying the Lorentzian fit function [107] to all of the split peaks, the out-of-plane lattice parameters of PbTe, SnTe, and the precipitate can be refined as 6.487, 5.984, and 5.660 Å. Similarly, the

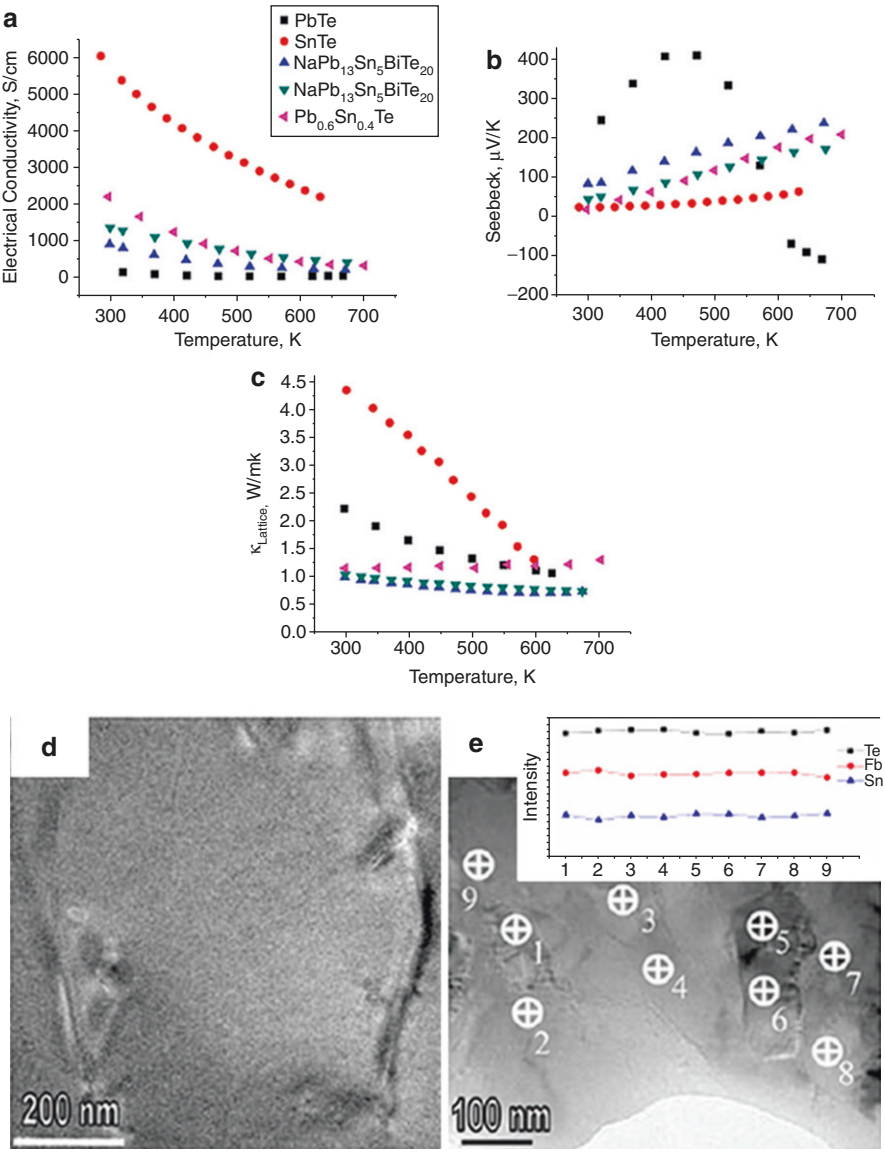


Fig. 10.45 (continued)

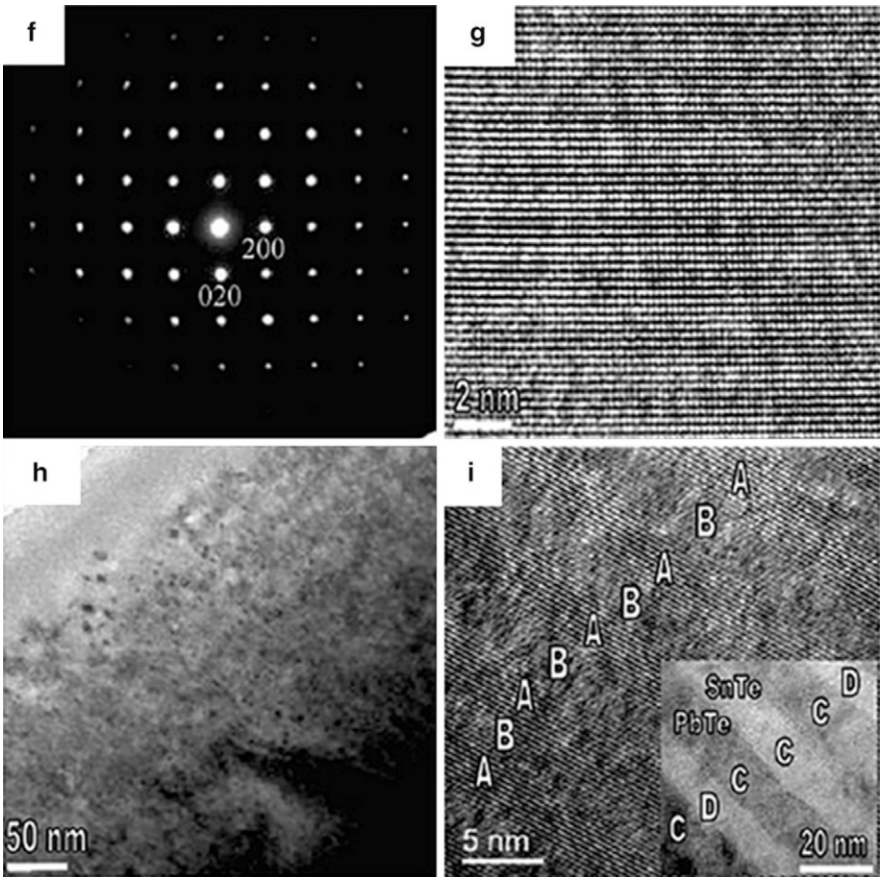


Fig. 10.45 (**a**) σ, (**b**) S, and (**c**) k_{lat} dependence of temperature of five samples, PbTe, SnTe, $Pb_{0.6}Sn_{0.4}Te$, $NaPb_{13}Sn_5BiTe_{20}$, and $NaPb_9Sn_9BiTe_{20}$. Low-magnification TEM images of three samples PbTe (**d**), $Pb_{0.6}Sn_{0.4}Te$ (**e**), and $NaPb_9Sn_9BiTe_{20}$ (**h**). DP (**f**) and HRTEM lattice image (**g**) of sample $Pb_{0.6}Sn_{0.4}Te$. (**i**) Two kinds of lamellar structures of $NaPb_{13}Sn_5BiTe_{20}$ [90]

in-plane values were derived as 6.165, 5.925, and 5.773 Å. Figure 10.47c shows enlarged lattice image in Fig. 10.47a indicating the modulated intensity contrast based on PbTe and SnTe phases. Based on the proposed atomic model (Fig. 10.47d), a simulated HRTEM image (Fig. 10.47c) can match well with the experimental image, confirming the general validity of the proposed atomic structure of the interface. Figure 10.47e is an HRTEM lattice image covering three regions: close to the edge amorphous-like region, the lamellar structure region, and the nonlamellar structure region. Figure 10.47f, g displays strain maps along the 001 and 110 directions, respectively. Correspondingly, three distinct regions show different strain information: For the amorphous region, the irregular contrast represents damage from the ion beam thinning; for the lamellar structure region,

a separation of about 6 % off between PbTe and SnTe along [100] was observed, while uniform contrast along [110]; for the nonlamellar structure region, homogeneous contrast was observed. These findings signify that SnTe is highly distorted at

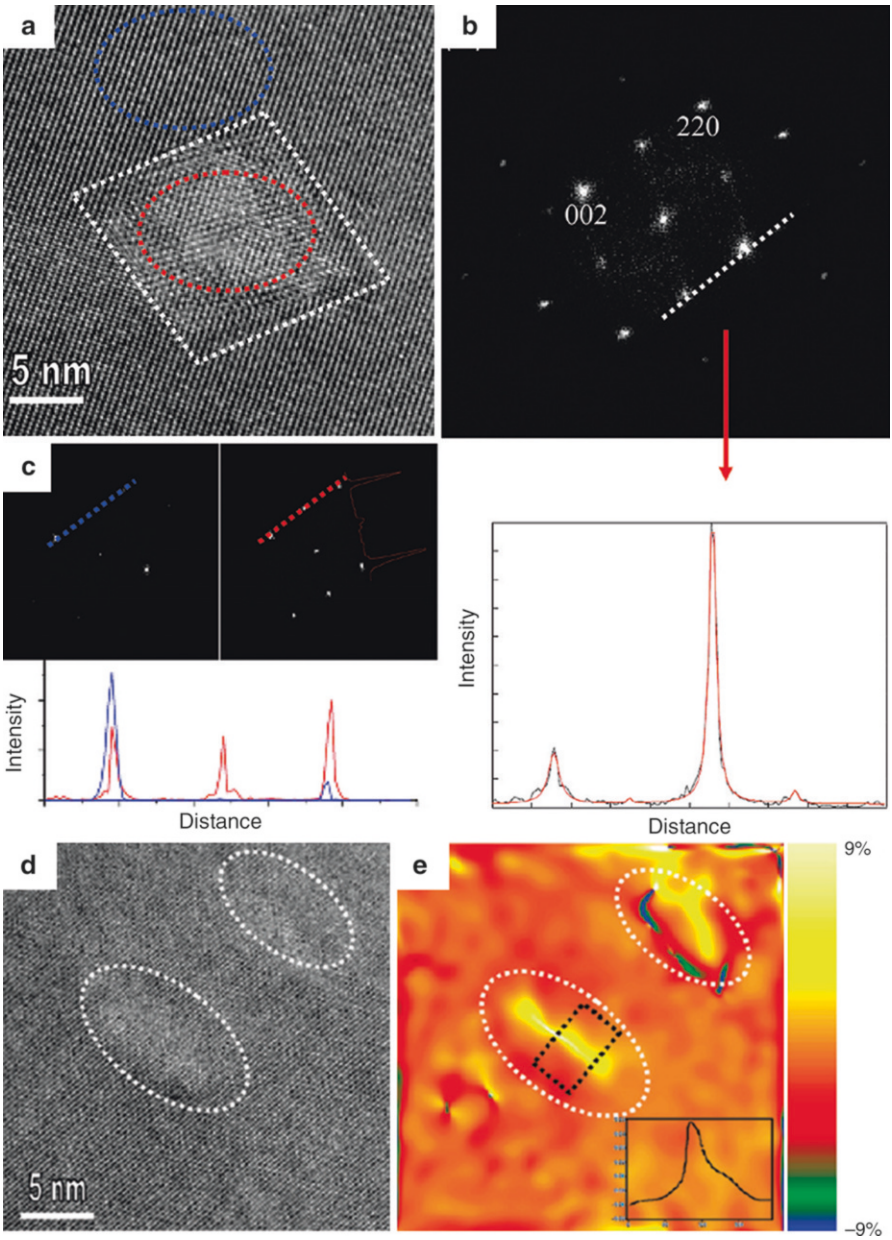


Fig. 10.46 (continued)

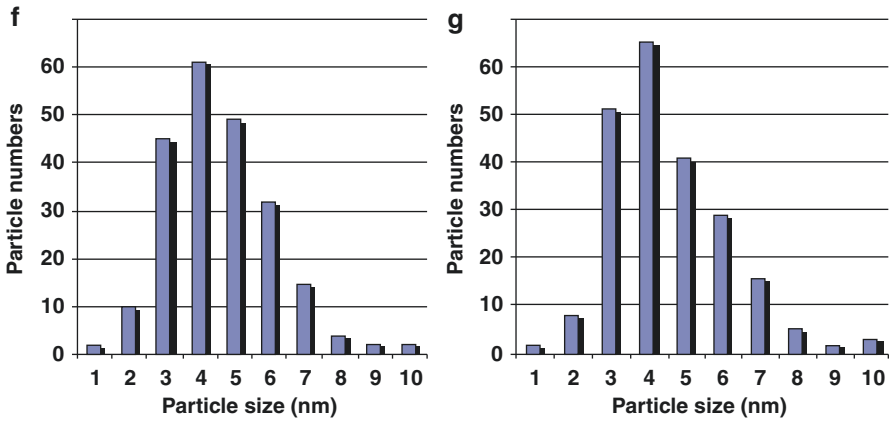


Fig. 10.46 (**a**) HRTEM lattice image of $NaPb_{13}Sn_5BiTe_{20}$ with nanoscale inclusions. (**b**) FFT images of the whole image. (**c**) FFT images of the precipitate and of the matrix and the intensity profile. (**d**) HRTEM lattice image of the nanoscale inclusions in $NaPb_{13}Sn_5BiTe_{20}$. (**e**) The strain distribution of the nanoscale inclusions in $NaPb_{13}Sn_5BiTe_{20}$ and $NaPb_9Sn_9BiTe_{20}$, respectively [90]

the interfaces. At room temperature, PbTe and SnTe have NaCl-type cubic crystal structure, with lattice parameters of 6.462 and 6.331 Å, respectively. Because the interatomic bonding in PbTe is stronger than that in SnTe [108], the in-plane lattice PbTe should be essentially remain fixed in space, while that of SnTe to experience tensile strain. The lattice mismatch parameter along the out-of-plane direction is 5.96 %, which is in close agreement with the experimental data.

5.8 PbTe-Sb_2Te_3TE Compounds

As the TE properties of nanostructured materials should vary on the size, density, and morphology of the nanostructural features, the materials engineering science thus become increasingly important in the development of TE nanomaterials. Snyder's group focused on the partitioning of quenched, metastable phases that then transform into two coexisted phases during a controlled process [109, 110]. By restricting the partitioning to solid-state diffusion at low temperatures, the resulting microstructures are quite fine. Figure 10.48 shows an example of $Pb_2Sb_6Te_{11}$ after quenching and then annealing at 400 °C. A lamellar spacing of 360 nm is observed, including 80-nm PbTe and 280-nm Sb_2Te_3 layer thicknesses. The lamellar spacing can be further controlled from ten nm to several micrometers. The crystallographic relationship between PbTe and Sb_2Te_3 in the lamellar growth is PbTe (111)/Sb_2Te_3 (001) with low lattice mismatch, which leads to coherent interfaces between the lamellae.

In the TE chalcogenide systems, subtle changes in the metal (M)/chalcogen (Te) ratio can cause varying structural transformations. In rock salt structure tellurides, such as PbTe and $AgSbTe_2$, the M/Te is approximately equal to one. The removal

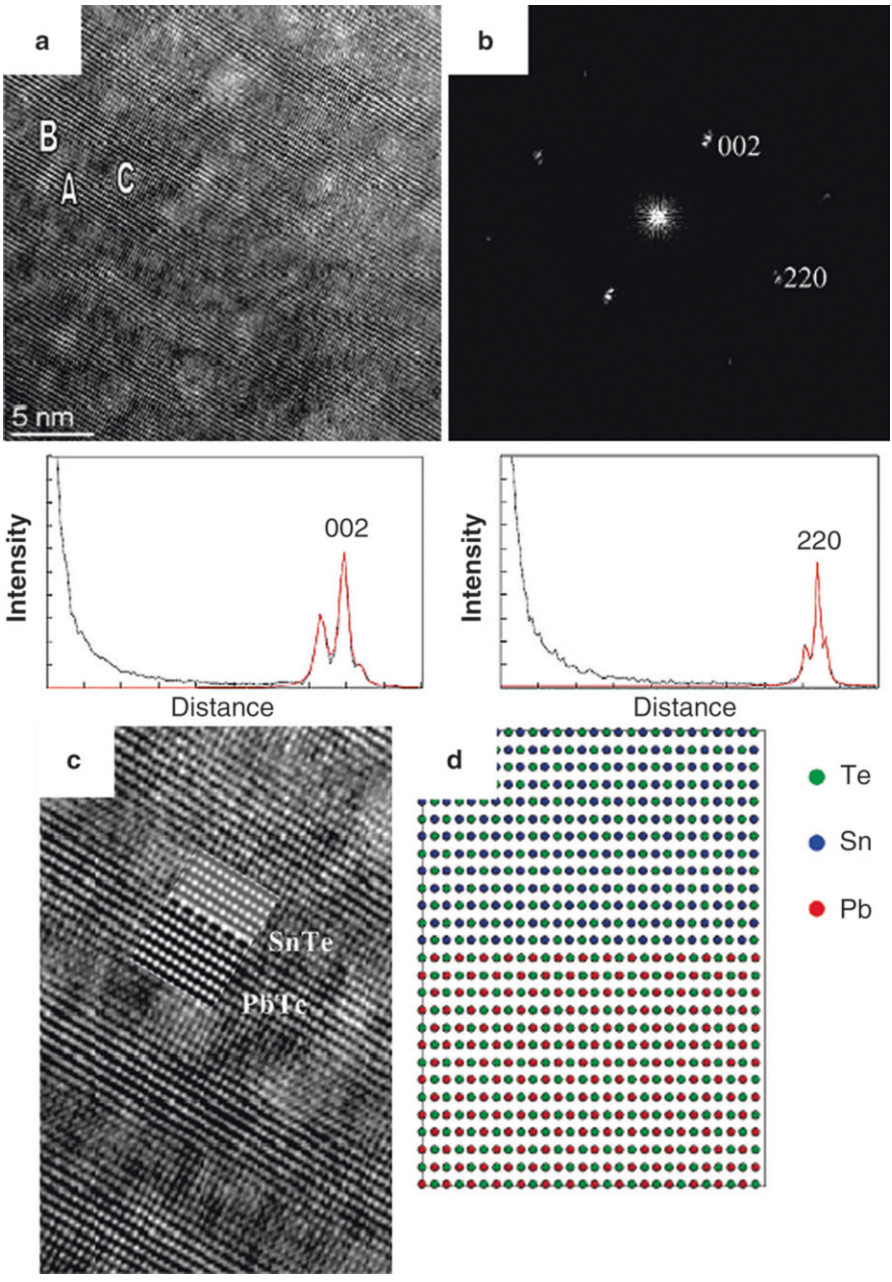


Fig. 10.47 (continued)

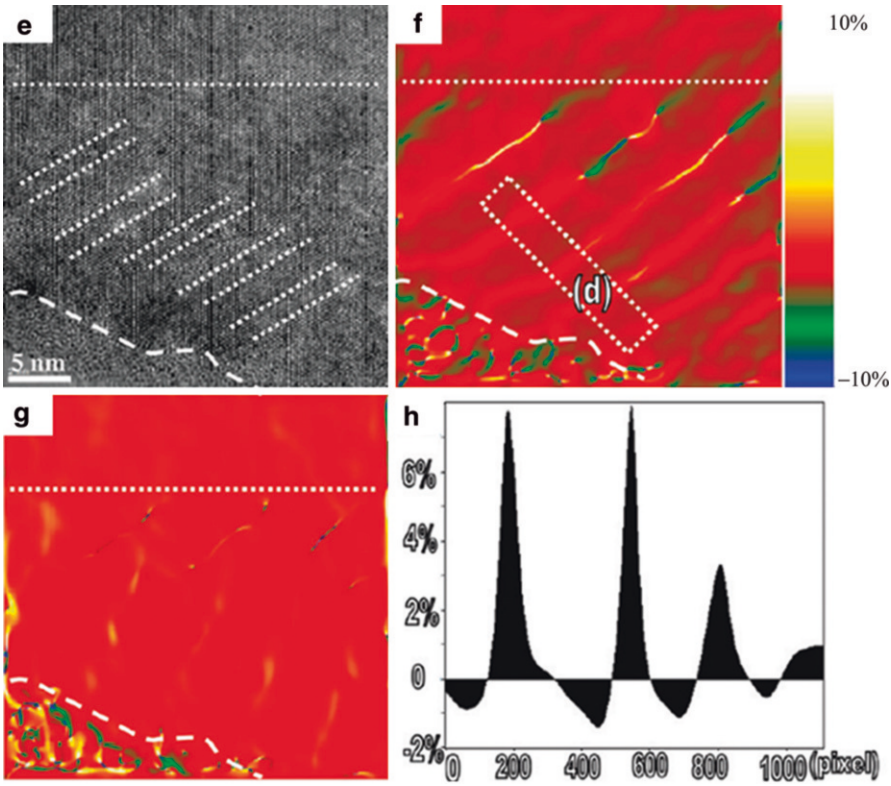


Fig. 10.47 (**a**) HRTEM lattice image of $NaPb_{13}Sn_5BiTe_{20}$ including lamellar structure and precipitates, (**b**) the FFT image of (**a**) and two line-scanning profiles crossing the 002 and 220 peaks, respectively. (**c**) One enlarged lattice image from (**a**). (**d**) Modeling based on SnTe and PbTe, and the simulated image is inserted in (**c**). (**e**) HRTEM image with a nonlamellar structural region, lamellar structural region, and amorphous region. (**f**, **g**) The strain maps along out-of-plane and in-plane, respectively. (**h**) The line-scanning profile of the marked region in (**f**) [90]

of metal planes at regularly spaced intervals results in compounds with M/Te ratios less than unity. The five-layered M_2Te_3 and seven-layered M_3Te_4 compounds are two typical examples [22, 91, 110–112]. The following discussion of these layered crystal structures in the Ag–Sb–Te system provides information needed to detect compounds with intermediate composition between MTe (i.e., PbTe and $AgSbTe_2$), M_2Te_3 (i.e., Sb_2Te_3), and M_3Te_4 (i.e., "$Pb_2Sb_6Te_{11}$") with electron diffraction.

For the traditional rock salt structure PbTe, it is easy to understand. In $AgSbTe_2$, the cations (Ag and Sb) are disordered so that the probability of any cation site containing either Ag or Sb is equal, assuming the composition of $AgSbTe_2$ is stable over a range of compositions. The structure of $AgSbTe_2$ can be represented in terms of the stacking of the close-packed planes as $A\beta C\alpha B\gamma A\beta C\alpha B\gamma\cdots$, where the capitals A, B, and C represent layers of Te atoms and α, β, *and* γ represent layers of metal

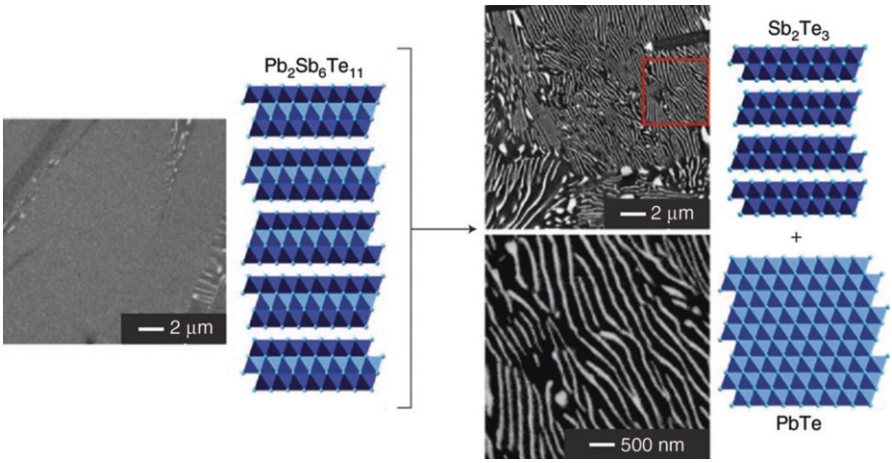


Fig. 10.48 Nanostructured TEs can be formed by the solid-state partitioning of a precursor phase. The metastable $Pb_2Sb_6Te_{11}$ phase (*left*) will spontaneously assemble into lamellae of Sb_2Te_3 and PbTe (*right*). These domains are visible with backscattering SEM, with the *dark regions* corresponding to Sb_2Te_3 and the *light regions* to PbTe. Electron backscattering diffraction reveals that the lamellae are oriented with coherent interfaces, shown schematically (*right*) [22]

atoms (either Ag or Sb). Figure 10.49a shows the stacking viewed along a [1–10] crystallographic direction and its simulated DP. The close-packed planes alternate between Sb/Ag and Te with no interruptions. The corresponding experimental HREM lattice image and electron diffraction of $AgSbTe_2$ in Fig. 10.49d can match the model well.

For Sb_2Te_3, it can also be described by its stacking sequence: $[A\beta C\alpha B]_{5\text{-}layers}[C\alpha B\gamma A]_{5\text{-}layers}[B\gamma A\beta C]_{5\text{-}layers}A\cdots$, which repeats sequences of five close-packed planes separated by a double-Te layer. Based on a rhombohedral unit cell, a [1–120] projection of this structure is shown in Fig. 10.49b. This structure can be regarded as removing one plane of metal atoms every six planes from the rock salt structure and displacing the remaining five-layered sections by 1/3 [1–100] to obtain the above stacking sequence. The five-layered stacking is also obvious in the simulated DP: the appearance of superlattice reflections at 1/5 the distance to the fundamental reflection, 0 0 0 15. A unit cell of Sb_2Te_3 thus contains 15 close-packed planes or three five-layered units. Figure 10.49e shows the experimental HREM lattice image and electron diffraction of $AgSbTe_2$, which can confirm the five-layered model.

Ideally, kinds of compounds with a varied M/Te ratio can be formed by periodically removing a metal plane any n even number of close-packed planes. If a metal plane was removed every 8th close-packed plane ($n = 8$), a seven-layered structure would result (M_3Te_4, i.e., $Pb_2Sb_6Te_{11}$). Figure 10.49c shows the results of seven-layered units by 1/3 [1–100]. The resulting M_3Te_4 structure can be described by its stacking sequence: $A\beta C\alpha B\gamma A_{7\text{-layers}}B\gamma A\beta C\alpha B_{7\text{-layers}}C\alpha B\gamma A\beta C_{7\text{-layers}}A\cdots$. The seven-layered stacking is evident in the simulated DP: the appearance of superlattice reflections at 1/7 the distance to the fundamental reflection, 0 0 0 21.

Figure 10.49f shows the experimental HREM lattice image and electron diffraction of $Pb_2Sb_6Te_{11}$, which can confirm the seven-layered model.

Therefore, intermediate phases PbTe, $AgSbTe_2$, and $Pb_2Sb_6Te_{11}$in the Ag–Sb–Te system can be detected and distinguished simply by counting the number of superlattice reflections in the DP or the stacking sequence of the close-packed planes.

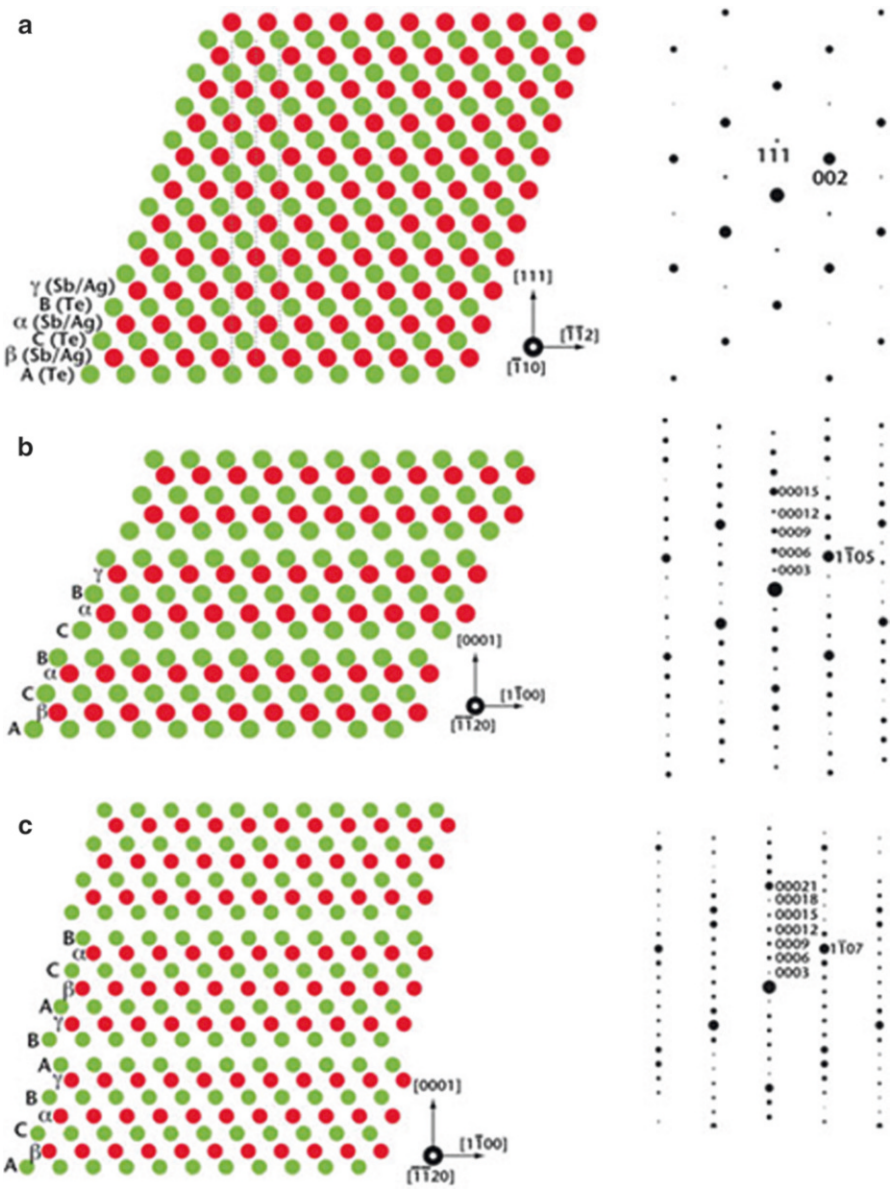


Fig. 10.49 (continued)

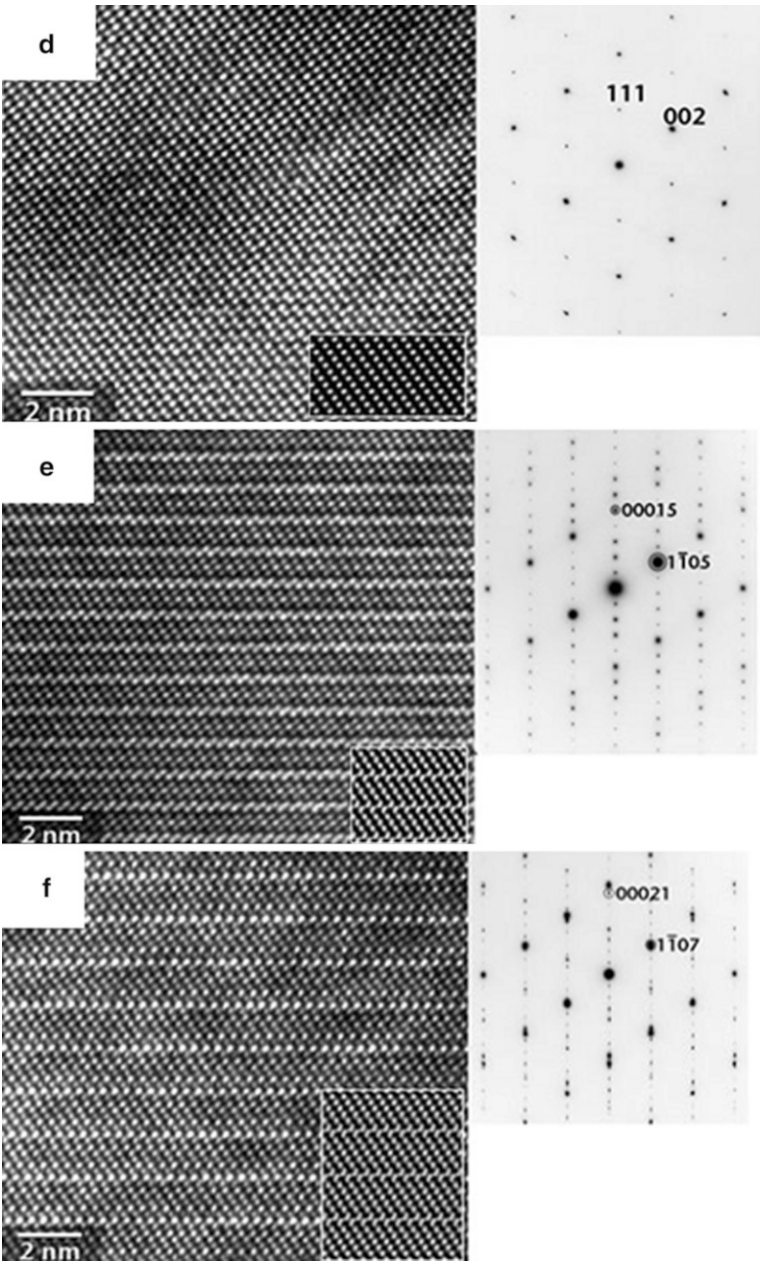


Fig. 10.49 (**a**–**c**) Crystal structures and simulated DPs for (**a**) PbTe or $AgSbTe_2$, (**b**) Sb_2Te_3, and (**c**) $Pb_2Sb_6Te_{11}$ with the viewing directions indicated in each figure. (**d**–**f**) Corresponding HRTEM image and DPs of (**d**) rock salt PbTe or $AgSbTe_2$, (**e**) Sb_2Te_3 and (**f**) $Pb_2Sb_6Te_{11}$ with *inset* simulated images [91]

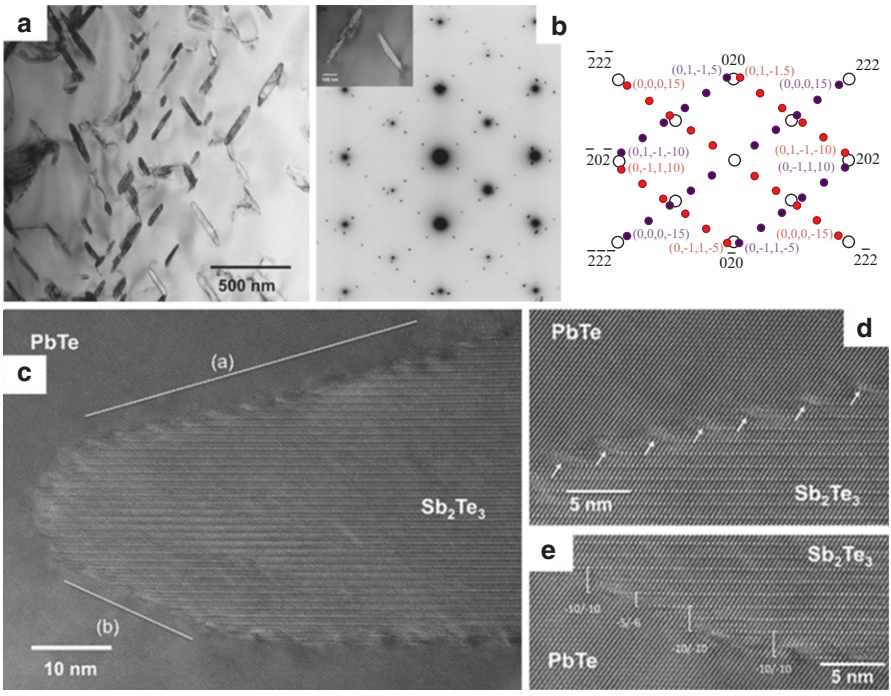


Fig. 10.50 (**a**) TEM micrograph showing Sb_2Te_3 precipitates in the PbTe matrix. (**b**) *Inset* TEM micrograph showing two Sb_2Te_3 precipitates. The DP from these precipitates confirms the orientation relationship discussed in the text. In the indexed schematic the Sb_2Te_3 patterns are indicated by *red* and *violet circles*; PbTe is indicated by *open circles*. (**c**) HRTEM image of Sb_2Te_3 precipitate taken near the tip of a precipitate. Enlargements of regions (**a**, **b**), indicated by the *white lines*, are presented in (**d**) and (**e**). (**d**) Array of +6/+5 disconnections separating $(111)_{PbTe}/(0001)_{Sb2Te3}$ terraces along region (**a**) from (**c**). The *arrows* indicate the positions of the dislocation cores of these defects. (**b**) Three -10/-10 disconnections and a -5/-6 disconnection along region (**b**) of (**b**) [113]

Heinz investigated the interfacial structure of precipitates of Sb_2Te_3 in PbTe. Using HRTEM, the author investigated the structure and arrangement of interfacial disconnections observed in this system. The TEM observations showed nanoscale Sb_2Te_3 precipitates, crystallographically aligned within the PbTe matrix, as shown in Fig. 10.50a. The precipitates exhibit an elongated, platelike morphology. DP (Fig. 10.50b) confirms that the precipitates are aligned with the crystallographic relation $\{111\}_{PbTe}\|(0001)_{Sb2Te3}$ and that the precipitates are with an elongation along the $(0001)_{Sb2Te3}$ planes. Since there are four sets of {111} planes in a cubic structure, the precipitates can form in four crystallographically equivalent orientation variants with aligning habit plane. In a TEM specimen with the matrix oriented along a <110>-type direction (Fig. 10.50a, b), two of the Sb_2Te_3 variants are oriented edge on, while the remaining two are inclined with respect to the imaging direction. The density of interfacial steps is higher near the ends of the precipitates, because there is a more significant departure from the general $\{111\}_{PbTe}\|(0001)_{Sb2Te3}$ crystallographic

relation (Fig. 10.50c). The author concentrated on the regions of interface indicated by the white line on the upper (a) and lower (b) sides of the precipitate in Fig. 10.50c. Enlarged lattice images in Fig. 10.50d, e of the regions of interface indicated by the white line on the upper (a) and lower (b) sides of the precipitate in Fig. 10.50c show arrays of closely spaced $\{111\}_{PbTe}\|(0001)_{Sb2Te3}$ terraces. The above analyses provide insight concerning the roles of these defects in accommodating the large interfacial misfit (6.7 %) in this system and in mediating the transformation from the rock salt to the tetradymite Sb_2Te_3structure [113].

6 Conclusions and Future Perspective

This chapter reviews the recent advances in TE materials, especially PbTe-based TE materials, with a special attention given to the microstructural tradeoffs dictating the ZT values. PbTe TE materials are the champions of high ZT. Our group has synthesized several materials with ZTs above 1.7, and recently as high as 2.2 at 915 K by doping PbTe with Sr and Na, we can control nanostructure formations (to reduce κ_{lat}) while concurrently modifying the electronic structure to significantly enhance the $TES^2\sigma$. The challenge to create high-efficiency TE materials lies in achieving simultaneously high σ, high S, and low κ in the same material. By adding nanostructure to the matrix of the pristine material, the k_{lat} component can be significantly reduced, resulting in dramatic increases in ZT. A different understood method for increasing ZT is to increase the $S^2\sigma$ by increasing the S of material without depressing the σ. The relationship between S and σ is quite complex, but it may be possible to alter one and not the other with band structure engineering.

PbTe-based TE materials contain significant amount of Te, which is a scarce element in the crust of the earth; thus a broad search for more inexpensive alternatives is therefore warranted. PbSe combines several attractive features for potential TE applications such as a favorable electronic valence band structure, lower cost, and higher operation temperatures. S is earth abundant compared to Te and Se, and the Pb is very strongly bound to S, making it environmentally safe. PbS can be proposed as an ideal candidate for widespread application of environmentally stable and affordable TE material system. Complex bulk materials (such as skutterudites, half-Heusler, Stannite) have been explored with high efficiencies, since its intrinsic potential to reduce κ through disorder within the unit cell. TE oxides are expected to play an important role in extensive applications for waste heat recovery, because of their potential advantages over heavy metallic alloys of chemical and thermal robustness. A detailed review about these Te-free-based TE materials will be presented elsewhere.

Recently, Gang Chen and Zhifeng Ren's group proposed some key characteristics for the new generation nanostructuring, called ordered nanocomposites. They explained these characters along size scale from solid solution doping, nanoprecipitates, grain boundaries, and grain shape to engineer the morphology as shown in Fig. 10.51 [114]. (1) Modulation doping means a two-phase coexisting composite with heavily doped minor phase provides carrier, while undoped matrix

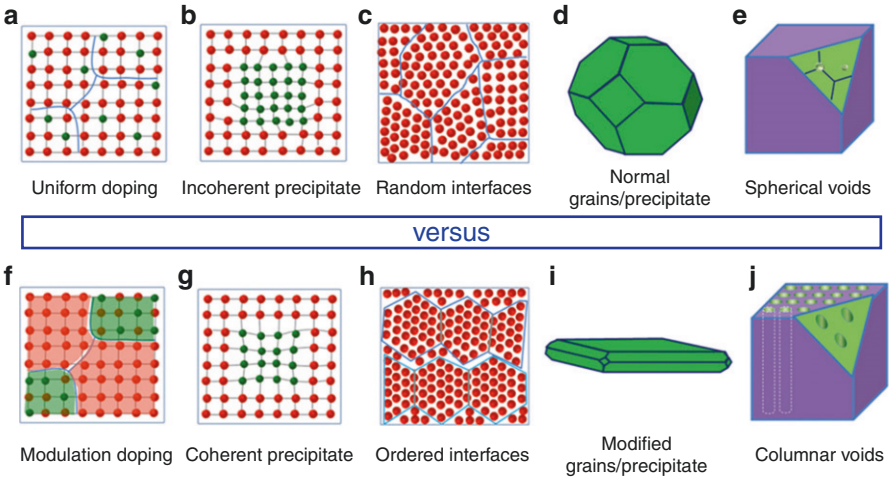


Fig. 10.51 Comparison of various nanostructures between random nanocomposites (**a**–**e**) and ordered nanocomposite (**f**–**j**) from doping atom, nano-inclusions, grain boundaries, and grain shape to void morphology [114]

phase as high-speed transport channel [115]. (2) Coherent interface between nanoprecipitate and the matrix has less deteriorating effect on the carrier mobility, but with strong scattering effect on the phonons [86, 116]. (3) Ordered interfaces such as twin boundary have less impact on transport of electrons but still scatter phonons [117]. (4) Modified grains and precipitates, such as platelike or wire-like, would be a new direction to decouple the transport of phonons and electrons [42]. (5) Ordered nanoscaled holes can reduce the k_{lat} but little impact on the carrier mobility, eventually enhancing the ZT value [118, 119]. Thus, the direction of the TE material in the future should be to design a new system with all these or at least several nanoscaled features together, and a higher ZT value could be expected.

The need for new materials is increasing and the next decade will be critical in the development of this field. Taking into account the difficulty if identifying the "right" compound and optimizing to ZT $>$ 2, long-term sustainable work is necessary, and close collaboration between chemists, physicists, and engineers is necessary to success.

References

1. Hytch MJ, Putaux J-L, Penisson J-M (2003) Measurement of the displacement field of dislocations to 0.03 Å by electron microscopy. Nature 423(6937):270–273
2. Hÿtch MJ, Snoeck E, Kilaas R (1998) Quantitative measurement of displacement and strain fields from HREM micrographs. Ultramicroscopy 74(3):131–146
3. Hytch MJ (1997) Analysis of variations in structure from high resolution electron microscope images by combining real space and Fourier space information. Microsc Microanal Microstruct 8(1):41–58

4. Johnson CL et al (2008) Effects of elastic anisotropy on strain distributions in decahedral gold nanoparticles. Nat Mater 7(2):120–124
5. Johnson CL, Hÿtch MJ, Buseck PR (2004) Nanoscale waviness of low-angle grain boundaries. Proc Natl Acad Sci USA 101(52):17936–17939
6. Hüe F et al (2008) Direct mapping of strain in a strained silicon transistor by high-resolution electron microscopy. Phys Rev Lett 100(15):156602
7. Muller EW, Panitz JA, McLane SB (1968) The atom-probe field ion microscope. Rev Sci Instrum 39(1):83–86
8. Tsong T (1990) Atom probe field ion microscopy. Field emission, and surfaces and interfaces at atomic resolution. Cambridge University Press, Cambridge
9. Seidman DN, Stiller K (2009) An atom-probe tomography primer. MRS Bull 34(10):717–724
10. Miller MK, Forbes R (2009) Atom probe tomography. Mater Charact 60(6):461–469
11. Seidman DN (2007) Three-dimensional atom-probe tomography: advances and applications. Annu Rev Mater Res 37:127–158
12. Kelly TF et al (2007) Atom probe tomography of electronic materials. Annu Rev Mater Res 37:681–727
13. Gault B et al (2010) High-resolution nanostructural investigation of Zn_4Sb_3 alloys. Scr Mater 63(7):784–787
14. World, E.B.f., IEC/OECD, 2008
15. http://en.wikipedia.org/wiki/Energy_conversion_efficiency
16. Liu W-S et al (2011) Thermoelectric property studies on Cu-doped n-type $Cu_xBi_2Te_{2.7}Se_{0.3}$ nanocomposites. Adv Energy Mater 1(4):577–587
17. Poudel B et al (2008) High-thermoelectric performance of nanostructured bismuth antimony telluride bulk alloys. Science 320(5876):634–638
18. Venkatasubramanian R et al (2001) Thin-film thermoelectric devices with high room-temperature figures of merit. Nature 413(6856):597–602
19. Wang XW et al (2008) Enhanced thermoelectric figure of merit in nanostructured n-type silicon germanium bulk alloy. Appl Phys Lett 93(19):193121–193123
20. Joshi G et al (2008) Enhanced thermoelectric figure-of-merit in nanostructured p-type silicon germanium bulk alloys. Nano Lett 8(12):4670–4674
21. Goldsmid HJ, Douglas RW (1954) The use of semiconductors in thermoelectric refrigeration. Br J Appl Phys 5(11):386
22. Snyder GJ, Toberer ES (2008) Complex thermoelectric materials. Nat Mater 7(2):105–114
23. Rowe DM (1995) CRC handbook of thermoelectrics. CRC Press, Boca Raton, FL
24. Zhu GH et al (2009) Increased phonon scattering by nanograins and point defects in nanostructured silicon with a low concentration of germanium. Phys Rev Lett 102(19):196803
25. Yu B et al (2012) Enhancement of thermoelectric properties by modulation-doping in silicon germanium alloy nanocomposites. Nano Lett 12(4):2077–2082
26. Bux SK et al (2009) Nanostructured bulk silicon as an effective thermoelectric material. Adv Funct Mater 19(15):2445–2452
27. Heikes RR, Ure RW (1961) Thermoelectricity: science and engineering. Interscience, New York
28. Heremans JP et al (2008) Enhancement of thermoelectric efficiency in PbTe by distortion of the electronic density of states. Science 321(5888):554–557
29. Hsu KF et al (2004) Cubic $AgPb_mSbTe_{2+m}$: bulk thermoelectric materials with high figure of merit. Science 303(5659):818–821
30. Zhou M, Li J-F, Kita T (2008) Nanostructured $AgPb_mSbTe_{2+m}$ system bulk materials with enhanced thermoelectric performance. J Am Chem Soc 130(13):4527–4532
31. Androulakis J et al (2007) Spinodal decomposition and nucleation and growth as a means to bulk nanostructured thermoelectrics: enhanced performance in Pb1-xSnxTe-PbS. J Am Chem Soc 129(31):9780–9788

32. Ahn K et al (2010) Exploring resonance levels and nanostructuring in the PbTe-CdTe system and enhancement of the thermoelectric figure of merit. J Am Chem Soc 132(14):5227–5235
33. Girard SN et al (2010) In situ nanostructure generation and evolution within a bulk thermoelectric material to reduce lattice thermal conductivity. Nano Lett 10(8):2825–2831
34. Sootsman JR et al (2010) Microstructure and thermoelectric properties of mechanically robust PbTe-Si eutectic composites. Chem Mater 22(3):869–875
35. Sootsman JR et al (2009) High thermoelectric figure of merit and improved mechanical properties in melt quenched PbTe-Ge and PbTe-$Ge_{1-x}Si_x$ eutectic and hypereutectic composites. J Appl Phys 105(8):083718
36. Pei Y et al (2011) High thermoelectric performance in PbTe due to large nanoscale Ag_2Te precipitates and La doping. Adv Funct Mater 21(2):241–249
37. Androulakis J et al (2006) Nanostructuring and high thermoelectric efficiency in p-Type Ag(Pb1 – ySny)mSbTe2 + m. Adv Mater 18(9):1170–1173
38. Pei Y et al (2011) Convergence of electronic bands for high performance bulk thermoelectrics. Nature 473(7345):66–69
39. Poudeu PFP et al (2006) High thermoelectric figure of merit and nanostructuring in bulk p-type $Na_{1-x}Pb_mSb_yTe_{m+2}$. Angew Chem Int Ed 45(23):3835–3839
40. Ohta M et al (2012) Enhancement of thermoelectric figure of merit by the insertion of MgTe nanostructures in p-type PbTe doped with Na_2Te. Adv Energy Mater 2(9):1117–1123
41. Biswas K et al (2011) High thermoelectric figure of merit in nanostructured p-type PbTe-MTe (M = Ca, Ba). Energy Environ Sci 4(11):4675–4684
42. Biswas K et al (2012) High-performance bulk thermoelectrics with all-scale hierarchical architectures. Nature 489(7416):414–418
43. Biswas K et al (2011) Strained endotaxial nanostructures with high thermoelectric figure of merit. Nat Chem 3(2):160–166
44. Lo S-H et al (2012) Phonon scattering and thermal conductivity in p-Type nanostructured PbTe-BaTe bulk thermoelectric materials. Adv Funct Mater 22(24):5175–5184
45. He J et al (2010) Microstructure-lattice thermal conductivity correlation in nanostructured $PbTe_{0.7}S_{0.3}$ thermoelectric materials. Adv Funct Mater 20(5):764–772
46. He J et al (2012) Morphology control of nanostructures: Na-doped PbTe-PbS system. Nano Lett 12(11):5979–5984
47. Girard SN et al (2011) High performance Na-doped PbTe-PbS thermoelectric materials: electronic density of states modification and shape-controlled nanostructures. J Am Chem Soc 133(41):16588–16597
48. He J et al (2012) Strong phonon scattering by layer structured $PbSnS_2$ in PbTe based thermoelectric materials. Adv Mater 24(32):4440–4444
49. Girard SN et al (2012) PbTe-$PbSnS_2$ thermoelectric composites: low lattice thermal conductivity from large microstructures. Energy Environ Sci 5(9):8716–8725
50. Androulakis J et al (2011) Thermoelectrics from abundant chemical elements: high-performance nanostructured PbSe-PbS. J Am Chem Soc 133(28):10920–10927
51. Johnsen S et al (2011) Nanostructures boost the thermoelectric performance of PbS. J Am Chem Soc 133(10):3460–3470
52. Androulakis J et al (2011) High-temperature thermoelectric properties of n-type PbSe doped with Ga, In, and Pb. Phys Rev B 83(19):195209
53. Parker D, Singh DJ (2010) High-temperature thermoelectric performance of heavily doped PbSe. Phys Rev B 82(3):035204
54. Hu Z, Gao S (2008) Upper crustal abundances of trace elements: a revision and update. Chem Geol 253(3–4):205–221
55. Madelung O (2004) Semiconductors: data handbook. Springer, Berlin, Vol. 3
56. Scanlon WW (1959) Recent advances in the optical and electronic properties of PbS, PbSe, PbTe and their alloys. J Phys Chem Solids 8:423–428
57. Mahan GD (1997) Good thermoelectrics. In: Henry E, Frans S (eds) Solid state physics. Academic Press, Elsevier B.V., pp 81–157

58. Zhao L-D et al (2011) High performance thermoelectrics from earth-abundant materials: enhanced figure of merit in PbS by second phase nanostructures. J Am Chem Soc 133(50):20476–20487
59. Zhao L-D et al (2012) Thermoelectrics with earth abundant elements: high performance p-type PbS nanostructured with SrS and CaS. J Am Chem Soc 134(18):7902–7912
60. Cox PA (1989) The elements. Their origin, abundance, and distribution. The elements. Their origin, abundance, and distribution. Oxford University Press, Oxford, UK, 8+ 207 p, ISBN 0-19-855298-X, Price£ 9.95 (paper). ISBN 0-19-855275-0, Price£ 25.00 (cloth). 1989
61. Zhao L-D et al (2012) Raising the thermoelectric performance of p-Type PbS with endotaxial nanostructuring and valence-band offset engineering using CdS and ZnS. J Am Chem Soc 134(39):16327–16336
62. Guo J et al (2012) Development of skutterudite thermoelectric materials and modules. J Elec Materi 41(6):1–7
63. Joshi G et al (2012) Enhancement of thermoelectric figure-of-merit at low temperatures by titanium substitution for hafnium in n-type half-Heuslers $Hf_{0.75-x}Ti_xZr_{0.25}NiSn_{0.99}Sb_{0.01}$. Nano Energ 2(1):82–87
64. Ibáñez M et al (2012) Composition control and thermoelectric properties of quaternary chalcogenide nanocrystals: the case of stannite $Cu_2CdSnSe_4$. Chem Mater 24(3):562–570
65. Snyder GJ et al (2004) Disordered zinc in Zn_4Sb_3 with phonon-glass and electron-crystal thermoelectric properties. Nat Mater 3(7):458–463
66. Li J et al (2012) A high thermoelectric figure of merit $ZT > 1$ in Ba heavily doped BiCuSeO oxyselenides. Energy Environ Sci 5(9):8543–8547
67. Liu Y et al (2005) Preparation of $Ca_3Co_4O_9$ and improvement of its thermoelectric properties by Spark Plasma Sintering. J Am Ceram Soc 88(5):1337–1340
68. Van Nong N et al (2011) Enhancement of the thermoelectric performance of p-type layered oxide $Ca_3Co_4O_{9+\delta}$ through heavy doping and metallic nanoinclusions. Adv Mater 23(21):2484–2490
69. Flahaut D et al (2006) Thermoelectrical properties of $Ca_{1-x}ReMnO_3$ system. J Appl Phys 100(8):084911-084911-4
70. Bérardan D et al (2008) Ge, a promising n-type thermoelectric oxide composite. Solid State Commun 146(1):97–101
71. Hiramatsu H et al (2007) Crystal structures, optoelectronic properties, and electronic structures of layered oxychalcogenides MCuOCh (M = Bi, La; Ch = S, Se, Te): effects of electronic configurations of M3+ ions. Chem Mater 20(1):326–334
72. Liu Y et al (2011) Remarkable enhancement in thermoelectric performance of BiCuSeO by Cu deficiencies. J Am Chem Soc 133(50):20112–20115
73. Zhao LD et al (2010) $Bi_{1-x}Sr_xCuSeO$ oxyselenides as promising thermoelectric materials. Appl Phys Lett 97(9):092118-3
74. Liu J et al (2009) Enhancement of thermoelectric efficiency in oxygen-deficient $Sr_{1-x}La_xTiO_{3-\delta}$ ceramics. Appl Phys Lett 95(16):162110-3
75. Shikano M, Funahashi R (2003) Electrical and thermal properties of single-crystalline (CaCoO) CoO with a CaCoO structure. Appl Phys Lett 82:1851
76. Seebeck TJ (1822) AAWB 289
77. Peltier JC (1834) ACL 371
78. Biswas K et al (2011) High thermoelectric figure of merit in nanostructured p-type PbTe–MTe (M = Ca, Ba). Energy Environ Sci 4(11):4675–4684
79. Ohta M et al (2012) Enhancement of thermoelectric figure of merit by the insertion of MgTe nanostructures in p-type PbTe doped with Na_2Te. Adv Energy Mater 2(9): 1117–1123
80. Zhao LD, Hao HJWS, Wu C, Zhou X, Biswas K, Ohta M, He JQ, Hogan TP, Uher C, Wolverton C, Dravid VP, Kanatzidis MG (2012) Synergistic band structure tailoring and all-scale hierarchical structuring for high performance thermoelectrics (to be submitted)

81. Heremans JP, Thrush CM, Morelli DT (2004) Thermopower enhancement in lead telluride nanostructures. Phys Rev B 70(11):115334
82. Shi X et al (2011) Multiple-filled skutterudites: high thermoelectric figure of merit through separately optimizing electrical and thermal transports. J Am Chem Soc 133(20):7837–7846
83. He J et al (2012) Seeing is believing: weak phonon scattering from nanostructures in alkali metal-doped lead telluride. Nano Lett 12(1):343–347
84. Blum ID et al (2012) Dopant distributions in PbTe-based thermoelectric materials. J Elec Materi 41(6):1583–1588
85. He J et al (2011) Anomalous electronic transport in dual-nanostructured lead telluride. J Am Chem Soc 133(23):8786–8789
86. He J et al (2010) On the origin of increased phonon scattering in nanostructured PbTe based thermoelectric materials. J Am Chem Soc 132(25):8669–8675
87. Yang SH et al (2008) Nanostructures in high-performance $(GeTe)_x(AgSbTe_2)_{100-x}$ thermoelectric materials. Nanotechnology 19(24):245707
88. Wu J et al (2011) Electron-beam activated thermal sputtering of thermoelectric materials. J Appl Phys 110(4):044325
89. Gueguen A et al (2009) Thermoelectric properties and nanostructuring in the p-Type materials $NaPb_{18-x}Sn_xMTe_{20}$ (M = Sb, Bi). Chem Mater 21(8):1683–1694
90. He J et al (2009) Role of self-organization, nanostructuring, and lattice strain on phonon transport in $NaPb_{18-x}Sn_xBiTe_{20}$ thermoelectric materials. J Am Chem Soc 131(49):17828–17835
91. Sugar J, Medlin D (2011) Solid-state precipitation of stable and metastable layered compounds in thermoelectric $AgSbTe_2$. J Mater Sci 46(6):1668–1679
92. Solymar L, Walsh D (2010) Electrical properties of materials. Oxford University Press, USA
93. Ravich IUI, Efimova BA, Smirnov IA (1970) Semiconducting lead chalcogenides, vol 5. Plenum Press, New York
94. Goldsmid HJ (1964) Thermoelectric refrigeration, vol 1. Plenum, New York
95. Williams DB, Carter CB (2009) Transmission electron microscopy: a textbook for materials science. Springer, New York
96. Hayashi K, Kitakaze A, Sugaki A (2001) A re-examination of herzenbergite-teallite solid solution at temperatures between 300 and 700 °C. Mineral Mag 65(5):645–651
97. He J et al (2006) Geometric shadowing from rippled $SrRuO_3/SrTiO_3$ surface templates induces self-organization of epitaxial $SrZrO_3$ nanowires. Phys Rev B 74(20):205410
98. Quarez E et al (2005) Nanostructuring, compositional fluctuations, and atomic ordering in the thermoelectric materials $AgPb_mSbTe_{2+m.}$ The myth of solid solutions. J Am Chem Soc 127(25):9177–9190
99. Androulakis J et al (2006) Coexistence of large thermopower and degenerate doping in the nanostructured material $Ag_{0.85}SnSb_{1.15}Te_3$. Chem Mater 18(20):4719–4721
100. D S.E.a.T (1976) US patent specification 3 945 855
101. Christakudis CC, Plachkova SK, Shelimova LE, Avilov ES (1989) Proceedings of 8th international conference on thermoelectric energy conversion, Nancy, France, July 1989, p 125
102. Cook B et al (2007) In-situ elevated-temperature TEM study of $(AgSbTe_2)_{15}(GeTe)_{85}$. J Mater Sci 42(18):7643–7646
103. Cook BA et al (2007) Nature of the cubic to rhombohedral structural transformation in $(AgSbTe_2)_{15}(GeTe)_{85}$ thermoelectric material. J Appl Phys 101(5):053715–053716
104. Wood C (1988) Materials for thermoelectric energy conversion. Rep Prog Phys 51(4):459
105. Ioffe AF (1956) Semiconductor thermoelements, and thermoelectric cooling. Infosearch, Ltd., London, England
106. Orihashi M et al (2000) Effect of tin content on thermoelectric properties of p-type lead tin telluride. J Phys Chem Solids 61(6):919–923
107. Wu L et al (2009) Nanostructures and defects in thermoelectric $AgPb_{18}SbTe_{20}$ single crystal. J Appl Phys 105(9):094317–094318
108. Gelbstein Y et al (2008) Mechanical properties of PbTe-based thermoelectric semiconductors. Scr Mater 58(4):251–254

109. Ikeda T et al (2007) Self-assembled nanometer lamellae of thermoelectric PbTe and Sb_2Te_3 with epitaxy-like interfaces. Chem Mater 19(4):763–767
110. Ikeda T et al (2007) Solidification processing of alloys in the pseudo-binary PbTe–Sb_2Te_3 system. Acta Mater 55(4):1227–1239
111. Ikeda T et al (2007) Development and evolution of nanostructure in bulk thermoelectric Pb-Te-Sb alloys. J Electron Mater 36(7):716–720
112. Ikeda T, Ravi VA, Snyder GJ (2009) Formation of Sb_2Te_3 widmanstätten precipitates in thermoelectric PbTe. Acta Mater 57(3):666–672
113. Heinz NA et al (2011) Interfacial disconnections at Sb_2Te_3 precipitates in PbTe: mechanisms of strain accommodation and phase transformation at a tetradymite/rocksalt telluride interface. Acta Mater 59(20):7724–7735
114. Liu W et al (2012) Recent advances in thermoelectric nanocomposites. Nano Energ 1(1):42–56
115. Zebarjadi M et al (2011) Power factor enhancement by modulation doping in bulk nanocomposites. Nano Lett 11(6):2225–2230
116. Zhang Y et al (2011) Nanodopant-induced band modulation in $AgPb_mSbTe_{2+m}$-type thermoelectrics. Phys Rev Lett 106(20):206601
117. Yan X et al (2010) Experimental studies on anisotropic thermoelectric properties and structures of n-type $Bi_2Te_{2.7}Se_{0.3}$. Nano Lett 10(9):3373–3378
118. He Y et al (2011) Thermal transport in nanoporous silicon: interplay between disorder at mesoscopic and atomic scales. ACS Nano 5(3):1839–1844
119. Tang J et al (2010) Holey silicon as an efficient thermoelectric material. Nano Lett 10(10):4279–4283

TEM for Characterization of Nanocomposite Oxide Thin Films: A Case Study on Solution-Derived Lanthanum Strontium Manganites

11

Patricia Abellán, César Moreno, Felip Sandiumenge, and Xavier Obradors

Contents

1 Definition of the Topic 538
2 Overview 538
3 Introduction 538
4 Experimental and Analysis Methodologies 541
4.1 The Chemical Solution Deposition Route to Oxide Epitaxial Films 541
4.2 TEM Sample Preparation 543
4.3 TEM Analysis 543
5 Nanocomposites by Spontaneous Phase Separation 545
5.1 Microstructure and Nucleation Control in MOD-Derived Films 545
5.2 Tracking the Microstructural Evolution 547
5.3 Identification of the Nanocomposite Components 550
5.4 Dependence of the Spatial Distribution of Nanocomposite Components on Film Thickness 556
5.5 Effect of Film Thickness on Misfit Strain Relaxation 557
5.6 Strain Measurements 563
6 Nanocomposites by Accommodation of La Excess Content 564
7 Conclusions and Future Perspective 568
References 569

P. Abellán (✉)
Physical Sciences Division, Pacific Northwest National Laboratory, Richland, WA, USA
e-mail: Patricia.AbellanBaeza@pnnl.gov

C. Moreno
International Center for Young Scientist, National Institute for Materials Science, Tsukuba, Ibaraki, Japan
e-mail: MORENOSIERRA.Cesar@nims.go.jp; moreno.cesar@gmail.com

F. Sandiumenge • X. Obradors
Institut de Ciencia de Materials de Barcelona, CSIC, Bellaterra, Spain

C.S.S.R. Kumar (ed.), *Transmission Electron Microscopy Characterization of Nanomaterials*, DOI 10.1007/978-3-642-38934-4_11,
© Springer-Verlag Berlin Heidelberg 2014

1 Definition of the Topic

A transmission electron microscope (TEM) allows for direct observation of interfaces and nanoscale particles embedded in a matrix with atomic spatial resolution. It provides chemical and structural information and allows for local strain mapping by the geometrical phase analysis (GPA) technique combined with high-resolution TEM (HRTEM) imaging. In this chapter we apply these capabilities of TEM to the study of epitaxial nanocomposite manganite thin films formed by spontaneous phase separation using a chemical solution deposition route. A methodology to obtain the most significant structural and chemical features from nanocomposite functional films is described.

2 Overview

Nanocomposite oxide thin film properties are controlled by epitaxial strain – due to lattice mismatch with the substrate and with the secondary phases embedded in the main material matrix – and by interfaces structure and chemistry. Recent relevant examples span from vertically assembled multifunctional nanostructures [1, 2], horizontal – layered – heteroepitaxial systems exhibiting ionic conductivity [3] to superconducting and colossal magnetoresistance nanocomposite films [4–6]. Therefore, the atomic-scale study of interfaces and the investigation of the strain state of thin films and nanostructures are crucial in exploring the structure-function correlations.

While the current main objective in the field of nanocomposite oxide thin films is to develop a simple and low-cost preparation route, in the majority of works, pulsed laser deposition (PLD) is used to fabricate the films. Based on self-assembly, PLD can provide epitaxial composite films in two main nanostructure forms – horizontal and vertical – in a relatively easy way [7]. However, in order to fabricate truly low-cost films, the chemical solution deposition (CSD) route, though less explored, has already provided nanocomposite oxide films with enhanced functionalities [5, 6, 8–11].

The challenge of studying the microstructure at the interface between two materials is typically addressed by electron microscopy. Direct exploration of interfaces is possible in a TEM by means of cross-sectional investigations. The improved experimental resolution and signal-to-noise ratio in images due to advances on spherical aberration correction enables more accurate image interpretation at subnanometer scale resolution [12]. Structural information at a larger scale and local chemical information may also be gained in the TEM using different imaging modes and various spectroscopies. Image processing of the data further provides a local measurement of lattice spacing distances and the possibility of strain mapping [13].

3 Introduction

The ability to assemble different phases to form a nanocomposite thin film has already brought the scientific community to the realization of enhanced functionalities [5, 6, 14]. Some of the most interesting achievements have been the

fabrication of films exhibiting multifunctional properties [15, 16] or even novel functional properties [3] that were not present in neither of the phases in their single oxide thin film form. The final distribution of one material relative to the other one – and thus the strain that one phase produces on the other one – will ultimately determine the nanocomposite film functionalities.

A current major challenge is to fabricate nanocomposite films using lower-cost approaches that would help meeting industry requirements. Interesting routes which are being extensively explored nowadays are mainly based on self-assembly [17]. In particular, the simultaneous growth of two epitaxial phases is receiving much attention in a variety of functional oxide systems [1, 2, 18–22]. This is typically achieved using vapor deposition techniques and the main goal has been to obtain heteroepitaxial nanocomposite thin films with ordered nanostructures [7]. These studies point out that the major parameters determining the topological pattern of the resulting nanostructures are structural compatibility [1, 2] and interface energy [19]. Yang et al. in a more recent work presented a guideline for material selection for self-assembled nanocomposite oxide films [7]. According to these authors, the necessary conditions for the design of heteroepitaxial nanocomposite thin films with periodic nanoscale patterns are that (1) both phases should have the potential to grow epitaxially on the chosen substrate, (2) have similar growth kinetics for a given growth temperature, (3) be the most thermodynamically stable when combined, and (4) their cations should have sufficiently different ionic radii in order to minimize intermixing at the interphase. Following these guidelines, two forms of nanocomposites of epitaxial oxide films can be fabricated: with horizontal- and with vertical-ordered nanostructures. Horizontal heteroepitaxial systems – multilayers – exhibiting ionic conductivity [3] and vertically assembled multifunctional nanostructures [1, 2, 20, 22, 23] are relevant examples achieved by PLD in the last years. An interesting, though less explored, alternative route to preparation of nanocomposites of functional oxide thin films is one that takes advantage of the phenomenon of spontaneous phase separation in materials [5, 6, 8, 9]. The resulting nanostructure is a spontaneous 3D assembly of nanodots within the bulk of an otherwise homogeneous thin film. While these nanocomposite films do not necessarily display an obvious ordered periodic nanoscale pattern, they have already proved to have equally stoning enhanced functionalities. Their preparation, following a solution route, presents a more realistic approach for the scalability of scientific results into industry. In this chapter, we are going to focus on the investigation of CSD-derived nanocomposite oxide films with enhanced functionalities. Besides the usual advantages of using CSD for growing homogeneous thin films, i.e., the possibility of cost-effective high-throughput production [24], here the ease of preparation is also an added value, as precursors and processing conditions are determined for a single phase.

Colossal magnetoresistance (MR) manganites, such as $La_{0.7}Ca_{0.3}MnO_3$ (LCMO) or $La_{0.7}Sr_{0.3}MnO_3$ (LSMO), are interesting candidates for formation of self-assembled nanocomposites because of the possibility of enhancing their magnetotransport properties [6]. Particularly, the main motivation has been to enhance the low-temperature low-field MR (LFMR) or the room temperature MR. This field started with the works of Balcells et al. on the $(LSMO)_x/(CeO_2)_{1-x}$

nanocomposite [25] and Petrov et al. on $(LCMO)_x/(SrTiO_3)_{1-x}$ [26]. Several attempts have been made to enhance the magnetoelectric properties of perovskite manganites by mixture of these CMR materials with insulating, conductive, nonmagnetic, and magnetic secondary phases. Considering only LSMO, the list of secondary phases used for the nanocomposite films is extense and includes TiO_2 [27, 28]; Sb_2O_5 [29, 30]; semiconducting materials such as ZnO [1, 31]; ionic conductors such as ZrO_2 [32]; insulating oxides such as silica, SiO_2 [33], alumina Al_2O_3 [34, 35], CeO_2 [36], polymer polyparaphenylene (PPP) [37], glass [38], $SrTiO_3$ [39], CuO [40], In_2O_3 [41], NiO [42–44], or MgO [45]; other manganites such as $Pr_{0.5}Sr_{0.5}MnO_3$ [46], $Sm_{0.7}Sr_{0.3}MnO_3$ [47], and $ErMnO_3$ [48]; and hard ferromagnetic insulators such as $BaFe_{113}(ZnSn)_{0.7}O_{19}$ [49]. Most of these systems are based on the introduction of either a granular or an amorphous secondary phase within the bulk of the manganite film whose intergrain interface control is not easy. Since the spin-scattering and the spin-polarized tunneling at grain boundaries are the main factors inducing an enhancement of the magnetoresistance properties [50], the capability to grow an epitaxial nanocomposite film is thus crucial for a control of the magnetotransport properties.

The TEM allows for direct observation of the texture of the resulting nanocomposite, mapping local strain and chemistry, and an exploration of the different interfaces of interest with atomic spatial resolution. While X-ray diffraction typically provides information from larger areas than the TEM, results are averaged over the field of view and thus it can fail on diagnosing structure in the suborn range [51]. With TEM, structure can be directly investigated at the atomic scale. As a 3D heteroepitaxy, the vertical and lateral interfaces between the different phases forming a nanocomposite thin film will have a great impact on its performance. Thus, being able to gain direct information of interfaces at the atomic scale is crucial. There are different imaging techniques available that can provide such high spatial resolution. The scanning tunneling microscope (STM) and the atomic force microscope (AFM) can achieve this goal but are limited to structural information on the surface of the material. The TEM, on the other hand, can reveal the internal structure of a material with subnanometer scale resolution. Moreover, further structural and chemical information are available in the TEM using electron diffraction and various spectroscopies. Finally, a technique that allows us to map strain is needed in order to explain most of the property changes in nanocomposite films. While X-ray diffraction and Raman spectroscopy can be used for strain mapping, only TEM meets the spatial resolution requirements for studying nanocomposites of thin films [13]. In fact, the spherical aberration corrected instrument used for most of the results shown in this chapter allows measuring deformations by the geometrical phase analysis (GPA) technique [13] from high-resolution TEM (HRTEM) images to an accuracy of less than 1 pm [52, 53].

In this chapter, we review some recent examples of self-assembled nanocomposites of LSMO thin films formed using CSD. The microstructural transformation of the manganite films occurring with thermal treatment (combination of crystallization temperature and time) and precursor solution concentration (controlling the final film thickness) is explained. In nanocomposite nanostructures, the films misfit relaxation

and the topological distribution of the spontaneously segregated secondary phases are strongly correlated and must be carefully studied. The main steps needed to understand the self-assembled segregation mechanisms are the identification of the different phases formed, their distribution and orientation relative to the LSMO film, as well as a measure of the strain state of the self-segregated manganite film.

4 Experimental and Analysis Methodologies

4.1 The Chemical Solution Deposition Route to Oxide Epitaxial Films

There are three principal categories of CSD routes for electronic oxide thin film technology depending on the compounds (precursors) used in the initial (precursor) solution and their reactivity on the solution preparation conditions: Sol–gel, metalorganic decomposition (MOD), and hybrid processes [54]. The route used in the fabrication of the samples described in this chapter was MOD. A schematic illustration of the generic CSD-MOD route to epitaxial films is found in Fig. 11.1. Detailed reviews on CSD routes can be found in references [24] and [54].

In brief, MOD solution synthesis is performed by dissolving a metalorganic compound to form carboxylate precursor solutions for each metal. Combination of those solutions in the desired stoichiometry yields the composition of the final film. The precursor solutions are deposited on the substrates by spin coating (see Fig. 11.1b) or alternative techniques such as dip-coating or ink-jet printing and let them dry. Then the film is pyrolyzed, which leads to removal of the organic compounds upon heating, yielding an amorphous or polycrystalline inorganic film. Finally, a single-crystal film is obtained from the pyrolyzed film by annealing at higher temperatures. The heat treatment process, which involves steps (c) and (d), used to complete the transformation of the as-deposited film to the final crystalline ceramic can be typically undertaken using either one or two heat treatment steps. The one-step process has been used for the preparation of perovskite films and nanostructures, such as $BaZrO_3$ and $La_{0.7}Sr_{0.3}MnO_3$ [55–59]. It consists of heating the sample directly to the crystallization temperature and thus accomplishes both the removal of the organic constituents and the material crystallization simultaneously. In the two-step process, which has been used for the preparation of other perovskites, such as $YBa_2Cu_3O_7$, the organic removal is carried out at lower temperatures in a step separately from the crystallization performed at higher temperatures [60]. Among other factors such as the spin-coating speed or the solution viscosity, the amount of material in a CSD film is a function of the precursor concentration. Figure 11.2 shows the dependence of the final film thickness on the metal concentration for the LSMO/STO films described here when the same conditions are used for the spin-coated process. Therefore, the final film thickness can be controlled by changing the precursor concentration.

In particular, LSMO thin films were grown by MOD, following a route described elsewhere [57, 58]. Propionate-based precursors containing La, Sr, and Mn in nominal ratio 0.7:0.3:1.0 were dissolved in a propionic acid solvent, filtered and deposited on

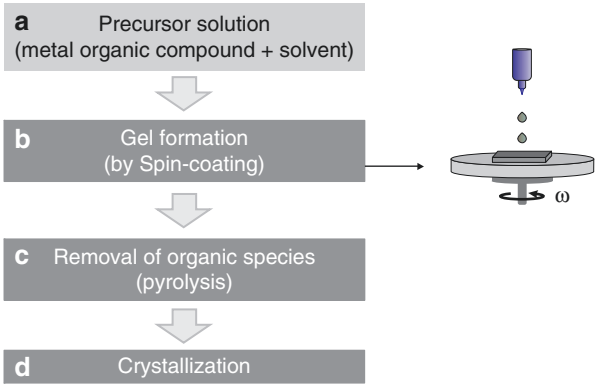


Fig. 11.1 Typical chemical solution deposition process following the metal organic decomposition solution synthesis

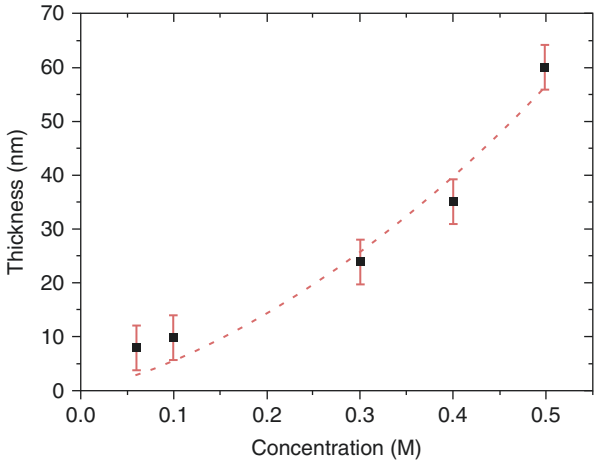


Fig. 11.2 Thickness dependence of LSMO films grown on STO after the growth process. Concentration values are given relative to Mn content

a (001) STO substrate by spin coating. As-deposited precursor films were subsequently submitted to an annealing procedure for 1 h at 900 °C or for 1 h, 6 h, 9 h, or 12 h at 1,000 °C (depending on the investigated film). Final film thicknesses were estimated to be in the range ~20–26 nm by SFM and cross-sectional TEM (see Fig. 11.2). In order to investigate the effect of thickness on samples annealed for 12 h at 1,000 °C, solution concentrations of 0.4 M and 0.5 M, leading to film thicknesses of 35 nm and 60 nm, respectively, were furthermore grown. Films grown from a 0.2 M solution concentration did not fully wet the substrate, as observed by SFM analysis, while saturation of the precursor solution occurred for 0.6 M solution concentration. In order to study the effect of adding an excess of Lanthanum on films microstructure – which would most likely give rise to the introduction of La-rich oxide phases within the manganite thin film – samples annealed for 12 h at 1,000 °C with an addition of 20 mol % and 40 mol % excess of La propionates precursor content in the starting solution were grown.

4.2 TEM Sample Preparation

Cross-sectional and planar view TEM specimens were prepared by using the mechanical tripod polisher technique followed by Ar^+ milling in a Precision Ion Polishing System (PIPS). The tripod technique provides large viewing areas and reduced broad ion beam milling times as compared to other mechanical techniques [61, 62]. Tripod polishing of samples for TEM requires extensive training but allows for high-quality uniformly thin specimens suitable for quantitative analysis. Unlike the typical tripod process [62], a wedge shape of the TEM specimen was purposely avoided. A leveler and a special table consisting on a well-polished plane surface and 3 ft with associated micrometers were used to diagnose whether top and botton specimen surfaces were kept parallel to one another while decreasing sample thickness during mechanical milling so that any deviation could be corrected during the process. The specimen was inspected during all the process using an optical microscope to avoid surface scratches. Once the sample thickness was mechanically milled down to around 20 μm, final milling proceeded by Ar^+ ion bombardment on a PIPS. Low angle (6°–8°) milling and low acceleration voltages (3–5KV) were used to minimize the ion milling damage. Ion bombarding proceeded down to electron transparency.

4.3 TEM Analysis

Diffraction contrast TEM imaging in cross-section specimens and energy dispersive X-ray (EDX) analysis were performed with a 200 KV Jeol JEM – 2011 microscope equipped with an INCA (R-X) EDS microanalysis system and double tilt sample holder. Diffraction contrast TEM imaging in planar view specimens was performed with a 300 kV Philips CM30 microscope equipped with a GATAN 622–600 image intensifier. High-resolution TEM images and EFTEM images were acquired with a 200 KV Cs-corrected F20 – SACTEM Tecnai microscope fitted with an energy filter GIF – Tridiem. HRTEM images were also obtained by using a Jeol 2010 F microscope operated at 200 kV, with a Gatan GIF MSC 600 camera. TEM image analysis was performed using the geometrical phase analysis (GPA) software [13, 63] developed in the Gatan Digital Micrograph environment.

4.3.1 Strain Mapping by Combined GPA and HRTEM

Image processing of high-quality HRTEM images can provide useful local information. In fact, the reason why phase contrast is so widely used to image structures with atomic resolution, despite the difficulties on its interpretation, is its sensitivity. Here, the basis of a method for measuring and mapping the displacements of the atomic columns from a HRTEM image is given. This method consists of a determination of the atomic plane positions in a HRTEM image for a subsequent calculation of the differences on interplanar distances with respect to an ideally free-of-strain reference area. The result is a local displacement field

map. Displacement fields, which may be due, for instance, to epitaxial stress by a secondary phase or by the substrate, typically have a strong influence on the properties of nanostructured thin films and, thus, are necessary information for a full characterization at the nanoscale. Mainly, there are two kinds of techniques for determining displacement fields based, either upon finding the peaks in image contrast and associating them with atomic columns [64] or upon Fourier processing the images to analyze the different lattice fringes separately [13]. Displacements in GPA are measured by the latter. It uses that the intensity, I(**r**), in a HRTEM image, can be written as

$$I(\mathbf{r}) = \sum_g I_g e^{2\pi i \mathbf{g}\cdot\mathbf{r}} \tag{11.1}$$

where **g** are the reciprocal lattice vectors. The GPA method is based on the calculation of the local Fourier components of the lattice fringes, I_g, which are given by

$$I_g = A_g(\mathbf{r}) e^{iP_g(\mathbf{r})} \tag{11.2}$$

These Fourier components have amplitude, $A_g(\mathbf{r})$, and phase, $P_g(\mathbf{r})$, with the phase describing the fringes position. This is what it is called the geometric phase and it is related to the displacement field **u**(**r**) as follows [65]:

$$P_g(\mathbf{r}) = -2\pi \mathbf{g}\cdot\mathbf{u}(\mathbf{r}) \tag{11.3}$$

Thus, the geometric phase depends on the component of the displacement field in the direction of **g**. In order to determine the two-dimensional displacement field, two phase images, $P_{g1}(\mathbf{r})$ and $P_{g2}(\mathbf{r})$, are needed. This is done by the following relation between reciprocal space and real space measurements [13]:

$$\mathbf{u}(\mathbf{r}) = -\frac{1}{2\pi}\left[P_{g1}(\mathbf{r})\mathbf{a}_1 + P_{g2}(\mathbf{r})\mathbf{a}_2\right] \tag{11.4}$$

where $\mathbf{a}_1$ and $\mathbf{a}_2$ are the lattice basis vectors in real space and $\mathbf{g}_1$ and $\mathbf{g}_2$ their corresponding reciprocal lattice vectors.

If the distortion measured in a HRTEM image is due to a mechanical strain, then strain maps can be determined from the deformation maps measured by GPA. The two-dimensional deformation tensor, ε_{ij}, and the local in-plane rigid body rotation, ω_{xy}, can be determined following the classical relations for elasticity theory [66]:

$$\varepsilon_{ij} - \frac{1}{2}\left(\frac{\partial u_i}{\partial x_j} + \frac{\partial u_j}{\partial x_i}\right)$$
$$\omega_{xy} = \frac{1}{2}\left(\frac{\partial u_x}{\partial x} + \frac{\partial u_x}{\partial y}\right)$$

where ε_{ij} is the 2D deformation tensor, with components ε_{xx}, ε_{xy} (shear strain), and ε_{yy}. For strain mapping, the direction x must be defined (y will be automatically taken as the direction perpendicular to x).

In the literature, a wide variety of systems where this technique has been applied can be found, such as quantum dots, nanocrystals, metal multilayers, nanowires, and thin films (see for a review [67]). The use of C_s-corrected instruments for capturing the HRTEM images to be analyzed with GPA presents clear advantages over uncorrected microscopes [53].

In this chapter, when giving a result from GPA, the precision and spatial resolution will also be specified. The precision is defined as the accuracy of the measurements as determined by a statistical treatment, while the spatial resolution is defined as the minimum resolvable distance in the image. An important issue to GPA is that the size of the mask employed for selecting the particular frequency of interest, **g**, in Fourier space determines the spatial resolution of this technique. A larger mask size will make spatial resolution in strain mapping better but, on the other hand, results in an increased noise of the measurement [68]. In practice, the precision is given by the standard deviation of the fluctuations in the measurements [69]. These fluctuations are assumed to be due to noise in the image, and thus, precision is ultimately determined by image noise. The precision of the technique was tested by measuring a continuous displacement field around a dislocation core in Si with an accuracy of 0.03 Å respect to theoretical estimations [63]. On the other hand, spatial resolution is given by the length scale of the fluctuations [69]. The effect that factors such as thin film relaxation in TEM specimens or chemical interdiffusion have on the accuracy of the strain measurements has also been studied [52]. For disentangling the effect of chemical interdiffusion, knowledge of local specimen composition by an independent technique would be highly recommended.

To ensure more reliable strain measurements, an additional post-processing of the image, consisting of the extraction of distortions due to the projector lens (assuming that a C_s-corrector is already used for the objective lens) and the CCD camera was performed. Projection lens and CCD camera distortions were corrected by an automatic routine incorporated in the GPA plug-in that makes use of the experimentally registered camera Ronchigram.

5 Nanocomposites by Spontaneous Phase Separation

5.1 Microstructure and Nucleation Control in MOD-Derived Films

A CSD-derived pyrolyzed film immediately after step (c) in Fig. 11.1 is typically amorphous (although very recently evidence of nanocrystalline as pyrolyzed CeO_2 films has been reported [70]). Crystallization of a specific phase will occur through a process of nucleation of stable seeds and growth, and thus, it can be described with classical crystallization theory [71]. By considering only the forces

that describe the transformation from the amorphous/pyrolyzed film to the crystalline one without taking into account the precise transformation pathway, i.e., from a purely thermo dynamic perspective, a first approximation of the resulting microstructure can be obtained [72]. The main idea in order to prepare highly oriented films is that film processing must proceed so that heterogeneous nucleation at the film-substrate interface determines the final film microstructure. In the extreme case where heterogeneous nucleation at the interface with the substrate is the only nucleation event, then the low-energy epitaxial orientation is established from the initial growth stages. Typically, this is not the case and nucleation simultaneously occurs within the bulk of the film and at the interface with the substrate. In fact, it is important to mention that for typical processing conditions, the crystallization driving force is high enough for surmounting the energy barriers for any nucleation event, even for those energetically less favorable, i.e., homogeneous nucleation. This can lead to film microstructures defined by nucleation and growth processes associated to more than one nucleation event.

In most circumstances, temperature is the processing parameter that most strongly affects nucleation events [72]. As a general rule, it has been observed that (1) higher annealing temperatures typically promote heterogeneous nucleation. Besides temperature, (2) processing parameters such as total and partial pressures, atmosphere, time, or precursor chemistry have also been proven to be key factors for nucleation control [24, 54, 73, 74]. A number of models for the epitaxial growth of CSD-derived thin films concerning factors such as material chemistry as compared to the substrate and lattice matching with the substrate have been proposed. Some main conclusions on these specific concerns can be found in a review on CSD including these models up to 2004 and [54] are that (3) when film and substrate have identical structure and their lattice mismatch is small a 2D layer by layer growth mechanism is favored, and (4) when film and substrate have different structure, then if epitaxial growth occurs, it would follow the Volmer Weber nucleation (island nucleation mechanism).

From a kinetic point of view, on the other hand, the crystallization pathway will differ between systems and will strongly modify the final microstructure. Two main cases of crystallization pathway may be considered: binary oxides and multicomponent oxides. Most of the films of interest to be grown by CSD are multicomponent oxide films, such as the $La_{0.7}Sr_{0.3}MnO_3$ (LSMO) thin films studied in this chapter. For the case of LSMO grown on STO, studies on ultrathin films using the temperature range for growth of LSMO specified in the experimental section [75] showed that LSMO/STO nucleates heterogeneously from the first stages of nucleation. A reason for this must be the very small mismatch between LSMO and STO (less than 1 %). Also, the use of short-chain carboxylate precursors for its synthesis leads to a lower organic content of the precursors to be eliminated during pyrolysis and is yielding excellent results [6, 8, 9, 58]. This strategy, pioneered by Haertling [76] and developed by Hasenkox et al. for colossal magnetoresistive compounds such as LSMO [57], has been followed for growth of LSMO films used in this chapter.

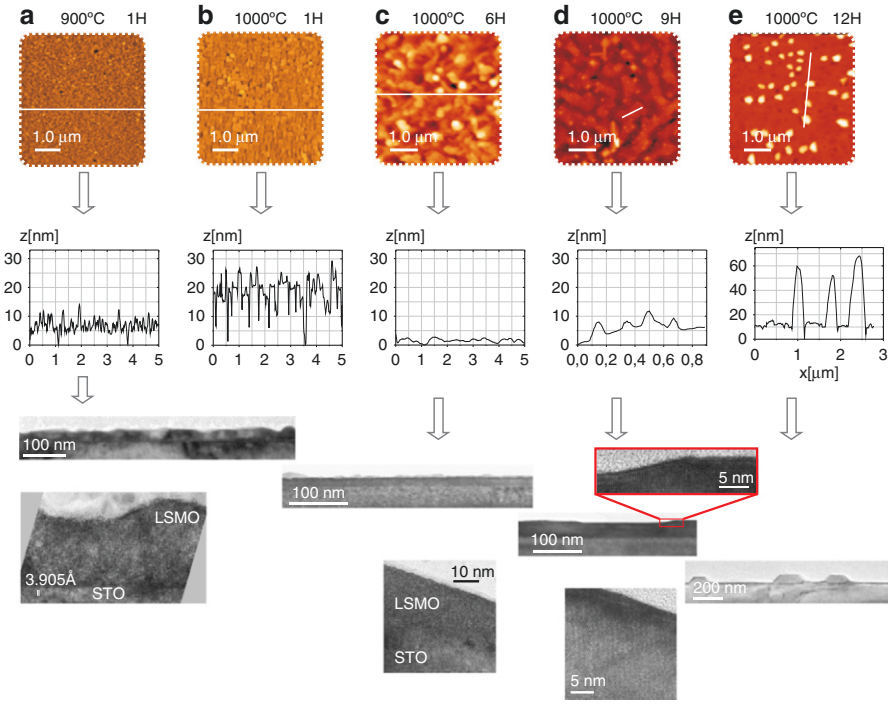


Fig. 11.3 SFM topographic images of the samples grown with different annealing times and temperatures and corresponding line scans. The LSMO films investigated were grown at 900 °C for 1 h (**a**) and at 1,000 °C for 1 h (**b**), for 6 h (**c**), for 9 h (**d**), and for 12 h (**e**). Also, low magnification cross-sectional TEM images are shown, except for (**b**), and HRTEM images showing details of the films' microstructure

5.2 Tracking the Microstructural Evolution

In order to study the effect of thermal treatment on the LSMO film microstructure, different cross-section TEM specimens were investigated. The information obtained by SFM and TEM are used to describe the overall evolution of the films. Figure 11.3 shows SFM topographic images as well as line scans and low magnification cross-section TEM images of LSMO films grown either at 900 °C or at 1,000 °C for different annealing times.

On one hand, the effect of increasing the crystallization temperature from 900 °C (a) to 1,000 °C (b) is an increase on the planarity of the LSMO film. It is observed that processing at 1,000 °C favors the development of parallelepipedic terraces (see Figs. 11.3a, b) and inside each of these areas the surface roughness strongly decreases, as compared to the 900 °C processed film. On the other hand, the effect of longer annealing times on films grown at 1,000 °C consists of a further increased planarity up to 9 h processing time and the development of a nanostructured surface morphology consisting of polygonal-shaped islands with heights h $\sim$ 60 nm and l $\sim$ 200 nm in size, after an annealing process of 12 h.

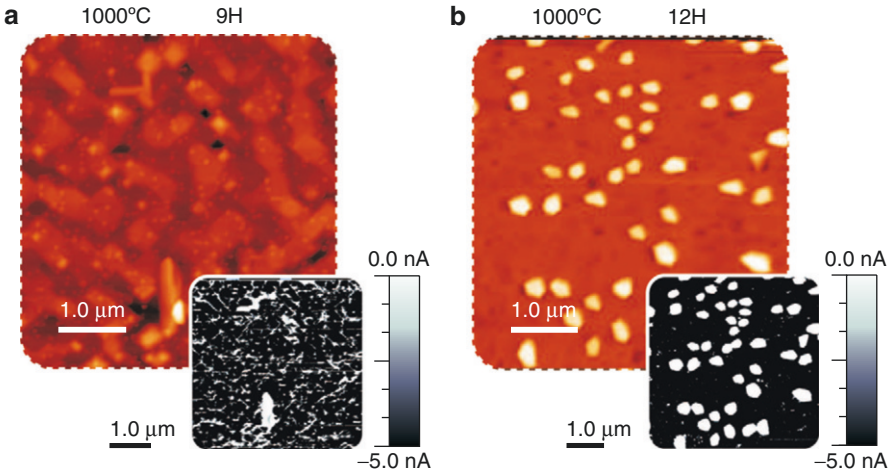


Fig. 11.4 Topographic images of LSMO films for 9 h (**a**) and 12 h (**b**) annealing times and corresponding current maps ($V_{tip} = +2.7$ V, F = 50 nN)

Regarding surface roughness, measured average values were observed to decrease from root mean square values rms ~ 3 nm found after 6 h annealing (c) to below rms ~ 1 nm after 9 h annealing (d). For LSMO thin films grown at 1,000 °C for 9 h, Fig. 11.3d, even though the apparent morphology is that of an atomically flat thin film, nanometric domes (~7–8 nm in height and ~80–100 nm in size) are also observed (see the line scan in (d) taken on a flat surface film terrace). Finally, the nanostructured surface morphology which forms after 12 h of annealing at 1,000 °C is shown in Fig. 11.3e in planar view by SFM and cross-sectional view on the low magnification TEM micrograph. In all the cases, the LSMO film, as revealed by the high-resolution TEM images, presents high crystalline quality. FFT patterns of the HRTEM images can be indexed according to the rhombohedral, $R\bar{3}c$, phase of LSMO, and a cube-on-cube epitaxial relationship of the LSMO film with the substrate is deduced, being consistent with XRD analyses (for 1,000 °C 12 h films, see Fig. 11.12a). A nanoscale electrical analysis of the LSMO films was performed by current SFM (C-SFM). Figure 11.4 shows SFM topographic images of LSMO films grown at 1,000 °C for 9 h (a) and 12 h (b). The insets show the current SFM (C-SFM) images corresponding to the above surfaces. The spatially resolved current images were simultaneously taken with the topographic ones. In the present experiments, a current of 5 nA was measured on the LSMO film which appears as dark contrast. The current measured on the nanometric domes in (a) and on the polyhedral islands in (b) drastically drops to zero, which means that their nature is insulating. Before 9 h of thermal processing, no insulating phases on the surface of the conducting LSMO films were found by C-SFM. Also, as a main result, the islands developed after 12 h of annealing process are measured to be insulating, while the film still exhibits a metallic behavior, as expected for typical LSMO

films. In the following subsections, the microstructure of the *quenched films* corresponding to the intermediate growth stages prior to phase separation (see Fig. 11.3a, c, d) is analyzed.

5.2.1 Annealing at 900 °C During 1 h

These samples exhibit a rough surface (rms ∼ 6 nm), resulting from an apparent undulation (as opposed to a terraced structure) (see Fig. 11.3a). In principle, such an undulation could be associated to a stress relaxation mechanism. However, observations of low magnification images show that the undulations are irregular and nonperiodic, in contrast with the behavior expected for a misfit relaxation mechanism. This suggests that the roughness, at this stage, could be merely a fingerprint of the granular structure of the precursor material. During recrystallization (secondary grain growth), the epitaxial orientation of those grains nucleated on the substrate surface is transmitted through the amorphous or nanocrystalline-disordered matrix towards the top of the film. The detail of the effect of this process on the topography of the film is unknown, but as far as the process involves the disappearance of grains to favor the growth of more favorable ones, it is likely that the mechanism alters the surface of the film. Once a unique orientation is achieved at sufficiently high temperatures, mass transport acts to flatten the film surface in order to reduce the total surface area. This would be appreciated in films annealed for 1 h at 1,000 °C, exhibiting flat surfaces (with local roughness inside terraces of rms ∼1 nm) (see Fig. 11.3b).

5.2.2 Annealing at 1,000 °C During 6 h and 9 h

The microstructure of samples obtained after 6 and 9 h of annealing at 1,000 °C is quite similar. At this stage, high-resolution TEM analysis of the films still does not show any signs of phase segregation. The inset squared in red in Fig. 11.3d shows a magnified image of the termination of one terrace, corresponding to a film grown at 1,000 °C for 9 h. The atomically flat terrace has a total height of ∼2 nm and it is bounded by a planar facet inclined by ∼15° to the surface of the film. A typical feature observed at this quenched state of growth is shown in Fig. 11.5.

These domes are isostructural to the LSMO film. According to their dimensions and the lack of any other features disturbing the film surface planarity, they may correspond to those insulating phases determined by C-SFM. This phase could be a precursor phase for the islands.

5.2.3 Annealing at 1,000 °C During 12 h

In this subsection, the structure and microstructure of the LSMO films which have undergone the spontaneous surface nanostructuration process for extended annealing times (12 h) at 1,000 °C are studied. Typical low magnification images as viewed along [010] for LSMO and STO are shown in Fig. 11.6a.

The film thickness was measured to be ∼24 nm. As shown in the images, islands are pyramidal and well faceted and present heights typically comprised between 20 and 55 nm, some of them being even larger than the film thickness, and a basal width varying from 50 to 200 nm. Larger pyramids are typically truncated by

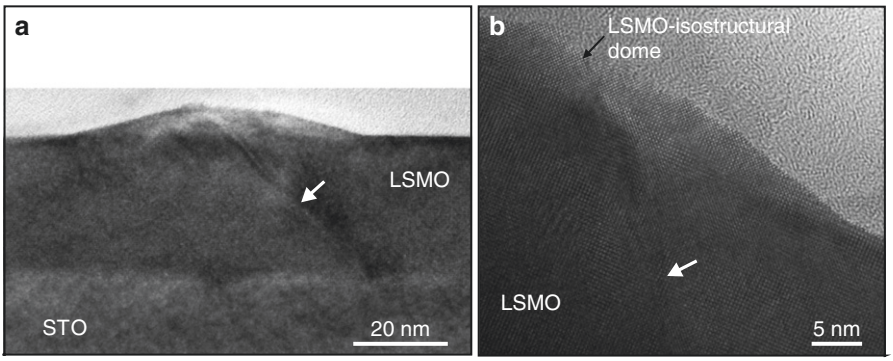


Fig. 11.5 A LSMO-isostructural dome nucleated at the surface of the film

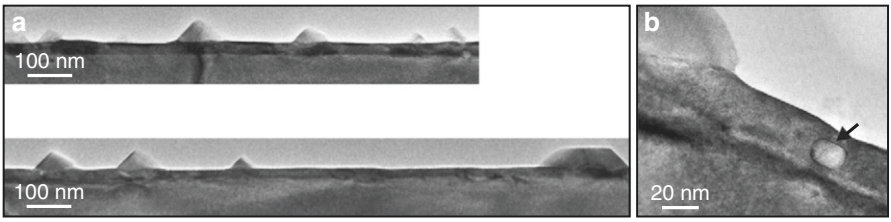


Fig. 11.6 (**a**) Low magnification images showing a general view of the system with several islands. (**b**) A detail showing an inclusion of a third phase embedded in the film

a flat surface. Viewed along this zone axis, island facets form an apparent angle of about 45° with the substrate surface. Moreover, they are observed to penetrate several nanometers into the film, thus thinning the film below the islands and even approaching the substrate in some cases. In addition to the outcropped islands, TEM observations revealed the occurrence of rounded inclusions, about 10–20 nm in diameter embedded within the LSMO film. Figure 11.6b is a low magnification cross-section image including an island and such an inclusion (indicated with an arrow).

5.3 Identification of the Nanocomposite Components

In order to gather high spatial resolution chemical information from such islands and inclusions, energy-filtered TEM imaging (EFTEM) was carried out. Figure 11.7a is the elastic-electron image corresponding to an area including the three phases. The image shows the STO substrate, the LSMO film, and an inclusion in contact with the root of an island, enabling direct comparison between both secondary phases. Images in (b)–(d) are the corresponding La-$M_{5,4}$, Mn-$L_{3,2}$, and Ti-$L_{3,2}$-edge filtered images, respectively, corresponding to the analyzed region in (a). An arrow indicates the location of the rounded

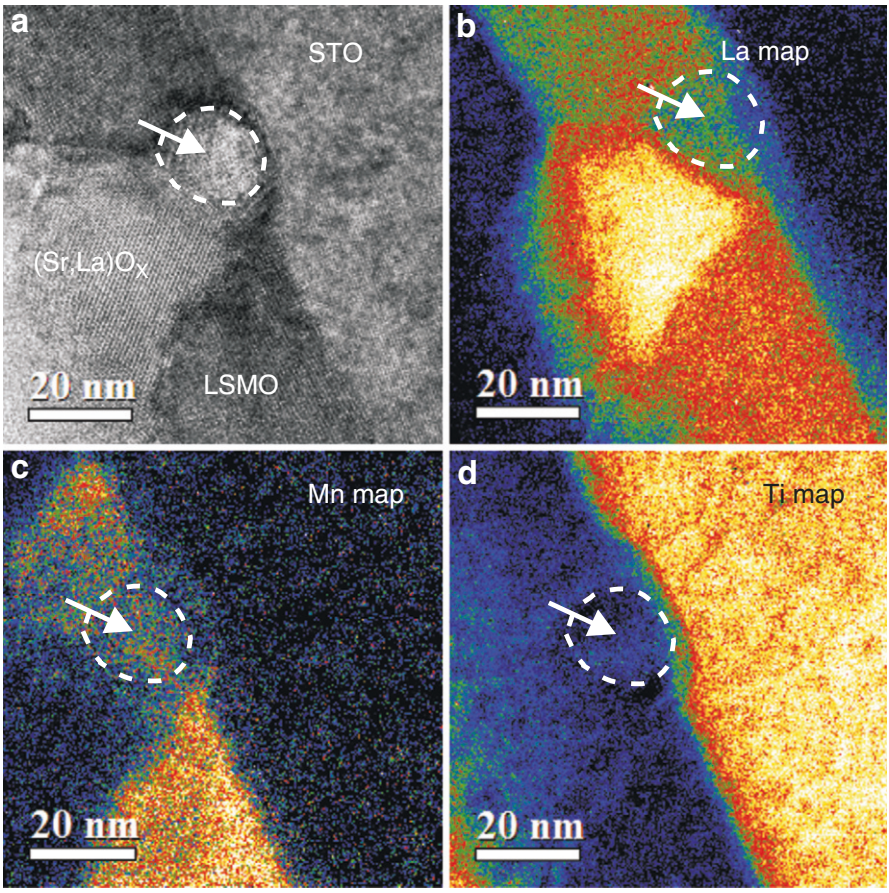


Fig. 11.7 A low magnification TEM image of the three-phase system (**a**) and corresponding EFTEM chemical maps showing the La (**b**), Mn (**c**), and Ti (**d**) distribution [8]. The arrows indicate the presence of an inclusion, with contour marked with a dashed line, under a (Sr, La)O_x island

inclusion in the elastic-electron image and chemical maps. It is observed that the interface between the LSMO film and the STO substrate is chemically sharp within the resolution of the energy-filtered images, which is estimated to be ~1 nm [77]. Our EFTEM analysis points out that no Mn is present in the outcropped islands (see Fig. 11.7c), while they exhibit a content of Lanthanum higher than that of the LSMO film (see Fig. 11.7b). Regarding the inclusions, our measurements indicate that they lack Lanthanum (see Fig. 11.7b). Qualitatively, this is consistent with overall stoichiometric balance considerations.

EFTEM did not yield reliable information about the occurrence of Sr because of the unfavorable energies associated to its edges [78]. Alternatively, the Sr content of the islands was determined by energy dispersive X-ray spectroscopy (EDS),

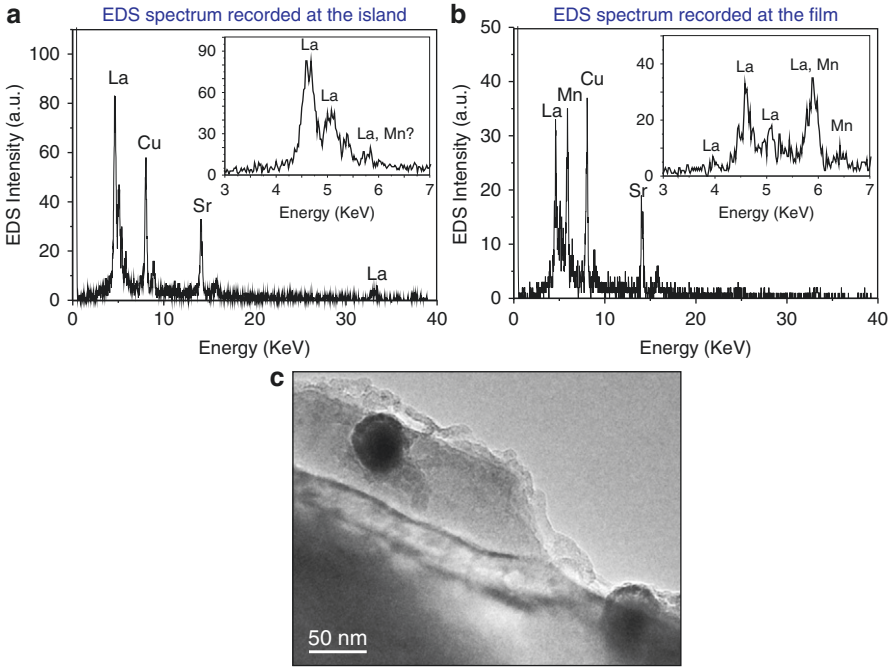


Fig. 11.8 EDX spectra recorded from a (Sr, La)O_x island (**a**) and the LSMO film (**b**). The insets show the part of the spectra running from 3.0 to 7.0 keV. No signal from Mn is observed in (**a**). At the inset in (**a**), damaged areas produced by an overexposure to the e-beam while recording the EDX spectra are observed. These damaged areas allow a measurement of the effective beam spot size for EDX analysis, which is measured to be ∼35 nm

yielding values comprised within the range 20–30 at.% against a perceptual relation of 80–70 at.% of La. EDS measurements taken in the island and LSMO films are shown in Fig. 11.8a, b, respectively. The beam spot size was measured to be ∼35 nm by observation of the damaged area produced by an overexposure to the e-beam (image inset in Fig. 11.8a). An enhancement of the spectra signal emitted from 3-7KeV, where the Mn peaks lies, is shown at the insets. Notice that no spectral signal corresponding to Mn is shown when measuring the island (see Fig. 11.8a), in agreement with EFTEM measurements, while a strong Sr peak is clearly observed in both cases. These results indicate that the islands correspond to an oxide-containing Strontium and Lanthanum (Sr, La)O_x.

It is important to mention that the self-segregation, self-nanostructuration process reported here (1) does not affect the composition and properties of the LSMO films [8] and (2) is found to accommodate large deviations of the La content from the stoichiometric 0.7(La):0.3(Sr):1(Mn) relation in a way that the three-phase system is kept up to a 20 % excess of Lanthanum. Notably, it is found that such additions are not detrimental to the structural homogeneity of the films. Thus, in this study and in terms of microstructure, stoichiometric samples and samples with a La

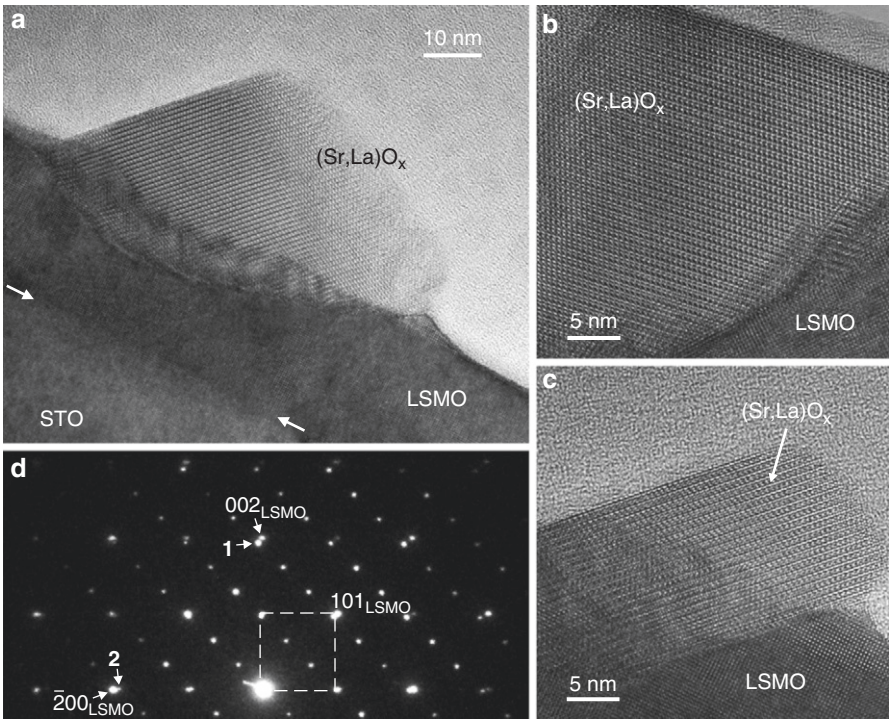


Fig. 11.9 HRTEM images of the (Sr, La)Ox island showing the LSMO/STO [8] (**a**) and LSMO/island (**a**–**c**) LSMO/island interfaces. (**d**) ED pattern taken across the island-LSMO interface illustration the matching distances between both phases [8]. **1** and **2** mark spots originated by the island

excess content up to a 20 % value as compared to the Mn content are considered equivalent to each others. The microstructural effects of further Lanthanum addition on the propionate precursor solution (of ~40 mol % with respect to the Manganese content) are shown in Sect. 6.

5.3.1 (Sr, La)O_x Surface Dots

The major consequence of the high-temperature annealing process is the spontaneous outcropping of (Sr, La)O_x pyramidal islands (see Fig. 11.6). The resulting islands feature a characteristic-layered crystal structure and a well-defined epitaxial relationship with the film. In Fig. 11.9a–c, high-resolution cross-sectional images of three different (Sr, La)O_x islands and their interfaces with the LSMO film are shown. The SAED pattern in Fig. 11.9d was taken across the (Sr, La)O_x island-LSMO film interface [8]. The diffraction spots due to the LSMO film are indicated in the figure with a dashed square. Additional spots belong to the (Sr, La)O_x phase. A spacing list of the different reflections measured from the ED pattern in (d) is provided in Table 11.1. The most significant lattice spacings are 8.37 and 5.41 Å which do not correspond neither

Table 11.1 Spacing list of the different reflections measured from the ED pattern in Fig. 11.9b. The standard deviation for each D-spacing value was ~0.02 Å

Spot	D-spacing (Å)	Degrees to spot 1 (°)
1	4.06	0.0
2	3.98	88.1
3	3.99	92.2
4	4.06	179.9
5	8.37	43.6
6	8.36	135.2
7	5.41	65.0
8	5.43	27.2
9	2.90	–

to the sesquioxide $Sr_{0.2}La_{1.8}O_{2.9}$ [79] nor to any other Sr-La-O reported phase, namely, $Sr_3La_4O_9$, La_4SrO_7, $La_2Sr_2O_5$, and La_2SrO_x [80]. Furthermore, the present structure is different from those for pure La_2O_3, which in ambient air has been found to be chemically unstable and evolve to monoclinic LaO(OH), hexagonal $La(OH)_3$ and other carbon-containing phases [81, 82]. Also, the occurrence of carbon was investigated by EELS (not shown) and it was concluded that no carbon is present in the islands. As shown in Fig. 11.9a–c, the surface dots exhibit planar facets parallel to the {100} and {110} perovskite planes, even when embedded in the LSMO film. This could be attributed to energy minima in the Wulff plot [83] and can be understood considering that the interfaces developed on those planes are semicoherent, with matching distances along $< 100 >$ and $< 110 >$. However, an analysis of the island-film interface by the ED pattern in (d) and the FFTs of the HRTEM images in (a)-(c) reveal that they sustain an epitaxial relationship both perpendicularly and parallel the film. This is indicated in the ED pattern taken across the island-film interface in (d). Matching distances are found to be $d_{\|} \cong 4.06$ Å and $d_{\perp} \cong 4.05$ Å, parallel and perpendicular to the interface, respectively, yielding misfit strains $\varepsilon_{\|} = 4.7$ % and $\varepsilon_{\perp} = 4.5$ %. Spot splitting in both diffraction patterns are better observed for higher-order reflections, as for instance, between the $(002)_{LSMO}$ and $(-200)_{LSMO}$ spots and those labeled **1** and **2** for the island, respectively.

5.3.2 Ruddlesden-Popper Inclusions

The formation of the (Sr, La)O_x islands appears associated with additional segregation of bulk nanodots of a second phase. In the analyzed LSMO [010] zone axis images, these inclusions typically exhibit either cubic-like or tetragonal-like structural projections. As already shown by EFTEM measurements, these nanodots lack Lanthanum (see Fig. 11.7). High-resolution TEM images in Fig. 11.10 show three different inclusions and their corresponding FFT. It is observed that such inclusions hold an epitaxial relationship with the surrounding LSMO matrix. The FFT patterns in Fig. 11.10 cannot be indexed as neither Mn_3O_4 nor MnO. Table 11.2 contains the structural data of the known Sr-Mn-O phases, adapted and completed from [84]. Considering that the

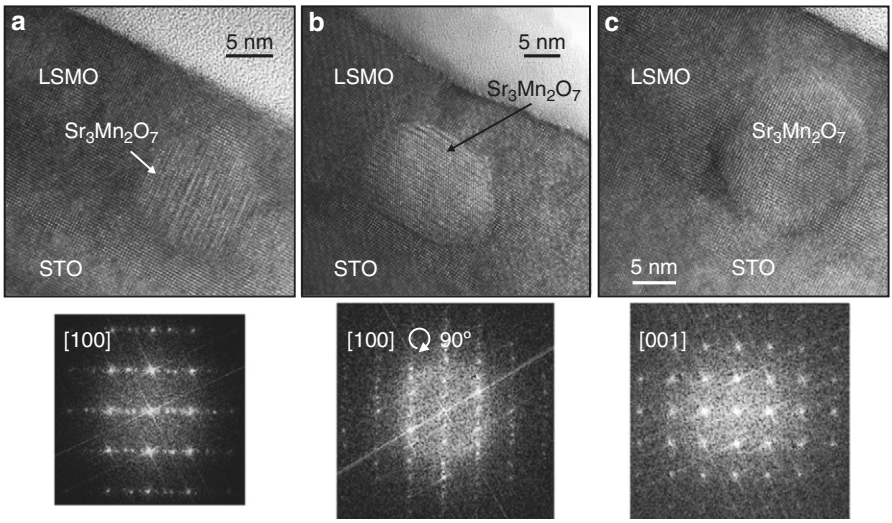


Fig. 11.10 HRTEM images and FFT of three different nano-inclusions found embedded in the film. The structural data is consistent with a kind of tetragonal manganite with a ≈ b ≈ a_p, c ≈ 20 Å. According to this model, (**a**) and (**b**) would correspond to the [100] zone axis; the latter being rotated by 90° compared to the former one, and (**c**) would correspond to the [1] zone axis

Table 11.2 Structural data of the known Sr–Mn–O phases, adapted from [84]

Name	Compos.	Space group	Lattice parameters (Å)
Brownmillerite	$SrMnO_{2.5}$	Pbam or Pba2	a = 5.523, b = 10.761, c = 3.811 [85]
			a = 5.523, b = 10.783, c = 3.815 [86]
4H – $SrMnO_{3-z}$	$SrMnO_{3-z}$	$P6_3/mmc$	a = 5.454, c = 9.092 [87]
			a = 5.443, c = 9.070 [88]
Perovskite	$SrMnO_{3-z}$	Pnma	-[89] a = 3.806 [90]
2:1 R-P phase	Sr_2MnO_4	$R\bar{3}c$ I4/mmm	-[91] a = 3.802, c = 12.519A [92]
L. 3:2 R-P phase	$Sr_3Mn_2O_7$	I4/mmm	a = 3.801, c = 20.060 [93]
			a = 3.828, c = 20.104 [94]
4:3 phase	$Sr_4Mn_3O_{10}$	Cmca	a = 5.443, b = 12.427, c = 12.5 [95]
			a = 5.477, b = 12.466, c = 12.528 [96]
$Sr_7Mn_4O_{15}$	$Sr_7Mn_4O_{15}$	$P2_{1/2}$	a = 6.817, b = 9.621, c = 10.378 [97]
$SrMn_3O_{6-z}$	$SrMn_3O_{6-z}$	Orthorhombic	a = 9.430, b = 11.510, c = 5.060 [98]

observed two types of projection correspond to two major zone axis, namely, [001] and [100] or [010], the lattice parameters derived from the FFT spectra yield lattice parameters ∼3.8 Å and ∼19.7 Å, which interestingly fit with the n = 2 Ruddlesden-Popper (R-P) structure [85], $Sr_3Mn_4O_7$ (see Table 11.2). This phase displays a tetragonal structure with a ≈ b ≈ a_p, c ≈ 20Å and space group I4/mmm. Thus, the FFTs of Fig. 11.10a, b would correspond to the [100] zone axis,

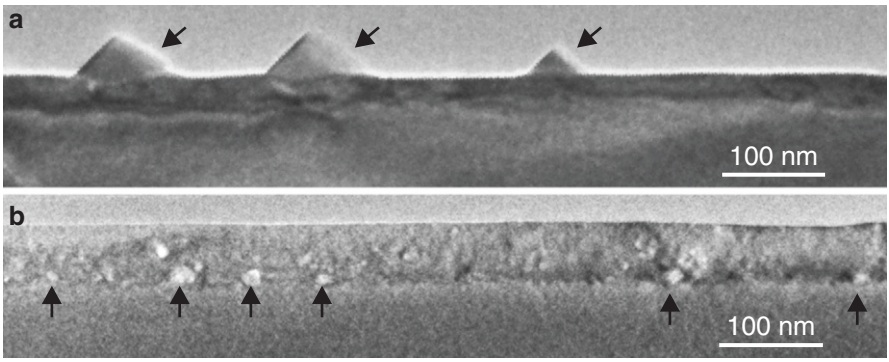


Fig. 11.11 Comparison of cross-sectional TEM views along the [100] direction of the LSMO and the STO for the 24 nm (**a**) and 60 nm (**b**) films [9]. The thinnest film contains (Sr, La)O_x islands (**a**), in contrast to the thickest one where the (Sr, La)O_x phase forms nanodots at the STO-LSMO interface (**b**)

rotated by 90° respect to one another, while (c) would correspond to the [001] $Sr_3Mn_4O_7$ zone axis. As a general behavior, [001] images exhibit rather perfect crystallinity, while [100] or [010] ones may feature strong disorder (see Fig. 11.10a), both in the stacking sequence and in the lateral continuity of atomic layers. In fact, stacking disorder is a common feature in these phases [86]. Formation of this phase is believed to assist the system for stoichiometric balance. On the other hand, this phase does not appear to affect much the LSMO matrix. No dislocations are found at the R-P inclusions/LSMO film interface.

5.4 Dependence of the Spatial Distribution of Nanocomposite Components on Film Thickness

LSMO films were grown using different precursor solution concentration, giving rise to different film's thickness as explained in the experimental methodologies section (see Fig. 11.2). In this section, observations on segregated LSMO thin films grown at 1,000 °C for 12 h, with thicknesses of 24, 35, and 60 nm, are discussed. These films were prepared from precursor solutions with concentrations 0.3 M, 0.4 M, and 0.5 M, respectively. Figure 11.11 compares cross-section TEM images of a 24 nm and a 60 nm film. As indicated by arrows, while the thinnest film (a) has (Sr, La)O_x islands, the thickest one exhibits a flat surface and (Sr, La)O_x nanodots embedded at the LSMO/STO interface (b). A few small islands were also found by SFM and TEM for the 60 nm thick films, such as the one analyzed in Fig. 11.13c, although their occurrence at the film surface was not observed to be the general trend for these films. In contrast to (Sr, La)O_x, the topological distribution of the R-P inclusions was not found to be film thickness dependent, i.e., for thicker films their location remains within the bulk of the LSMO film.

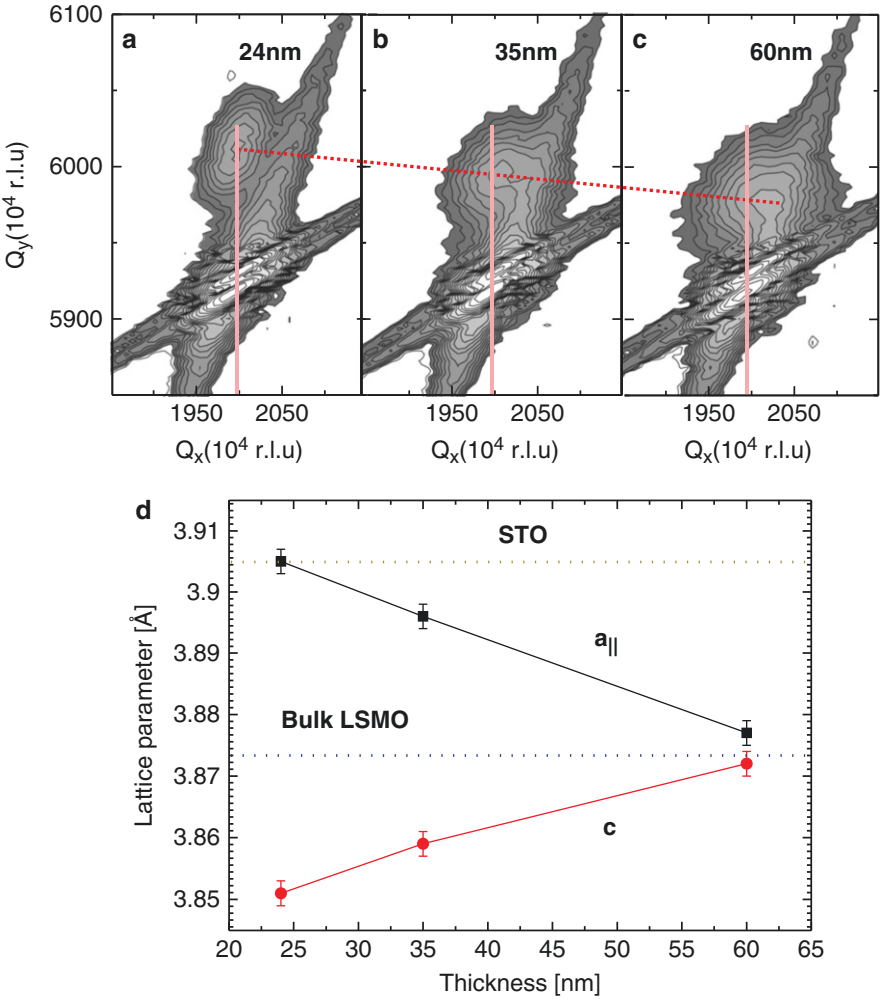


Fig. 11.12 Thickness dependence of the in-plane and out-of-plane LSMO lattice parameters [9]. The reciprocal space maps around the (103) reflections of LSMO and STO for the 24 nm (**a**), 35 nm (**b**), and 60 nm (**c**) thick LSMO films indicate misfit relaxation with increasing film thickness. The thickness dependence of the lattice parameters shows an almost complete relaxation for a thickness of 60 nm (**d**). rlu means "reciprocal lattice units" and $1\text{rlu} = \frac{2}{\lambda}$ with $\lambda = 0.154184$ nm

5.5 Effect of Film Thickness on Misfit Strain Relaxation

The average strain state of the films was investigated by X-ray reciprocal space mapping. In Fig. 11.12, maps around the (103) film and substrate reflections for 24 nm (a), 35 nm (b), and 60 nm (c) LSMO films are shown. The average lattice parameters measured from the X-ray reciprocal space maps are plotted in the graph in Fig. 11.12d. First at all, reciprocal space mapping analysis (see Fig. 11.12a–c)

shows that the separation between the (103)-LSMO and (103)-STO peaks evolves with thickness according to a progressive misfit relaxation. The thickness dependence of the film in-plane and out-of-plane lattice parameters indicates that almost complete relaxation is achieved at 60 nm (d). Therefore, the relaxation of partially segregated films occurs at a smaller thickness (∼60 nm) than nonsegregated ones (>100 nm, see [101–104]), coinciding with a topological redistribution of the (Sr, La)O_x phase from the film surface to the film-substrate interface.

This result suggests that interfacial (Sr, La)O_x decisively contributes to the misfit relaxation of the LSMO composite film. As measured in Sect. 5.5.1, the matching distances along the pseudocubic unit cell in-plane and out-of-plane parameters of LSMO, determined for the (Sr, La)O_x islands, are $d_{\parallel} \sim d_{\perp} \sim 0.403$ nm $> a_{STO}$ ($a_{STO} = 0.3905$ nm [105]). As a consequence, the LSMO film is tensiley strained around the nanodots to a larger extent than at the LSMO/STO interface ($a_{LSMO} = 0.3873$ nm [106]). Therefore, the 0.8 % tensile misfit at the film-substrate interface can be partially relieved by the nucleation of (Sr, La)O_x nanodots whenever the sum of their strain and interfacial energies is smaller than the concomitant reduction in misfit elastic strain energy. In following sections the role of these dots on the plastic relaxation behavior observed for different film thickness when placed at the film surface and at the film-substrate interface will be discussed.

5.5.1 The Role of the (Sr, La)O_x Surface Dots on Plastic Relaxation

As already mentioned, a few (Sr, La)O_x surface dots were observed on the segregated 60 nm thick LSMO film, their number being very low. This contrasts with 24 nm thick LSMO films, for which the main characteristic was the high density of islands at the film surface. Since while nanostructured 24 nm thick films are fully strained and 60 nm thick films are fully relaxed, the presence of the (Sr, La)O_x phase at the film surface does not seem to be an active mechanism for relieving the LSMO/STO misfit strain. In fact, a high density of misfit dislocations along the (Sr, La)O_x/LSMO interface has been observed which indicates a high relaxation degree between islands and film. Selected area ED patterns taken across the surface (Sr, La)O_x dots/LSMO film interface shown in the previous section gave values for the matching distances of the islands to the 24 nm LSMO film of d∼0.405 nm, yielding a theoretical misfit strain of ∼4.6 %. Here, an estimation of the matching distance of the surface (Sr, La)O_x dots to the 60 nm thick LSMO films is done based on a quantitative analysis of HRTEM images by the GPA method, as explained above. Also, the density of interfacial dislocations will be measured for both thicknesses considered here, representing the two extreme cases of misfit relaxation states, i.e., fully relaxed and fully strained. Figure 11.13a, c are HRTEM images showing the (Sr, La)O_x/LSMO interface for the case of the ∼24 nm thick LSMO film and for the case of a 60 nm thick LSMO film, respectively. These two images were analyzed by the GPA method [13, 63].

The phase map of (a) is shown in (b) and was constructed by filtering with $\mathbf{g} = 100$. The reference lattice was chosen at the top part of the island. It is observed an almost homogeneous contrast at the island side, with a slight (notice the darker contrast) phase gradient perpendicular to the growth direction, that could indicate

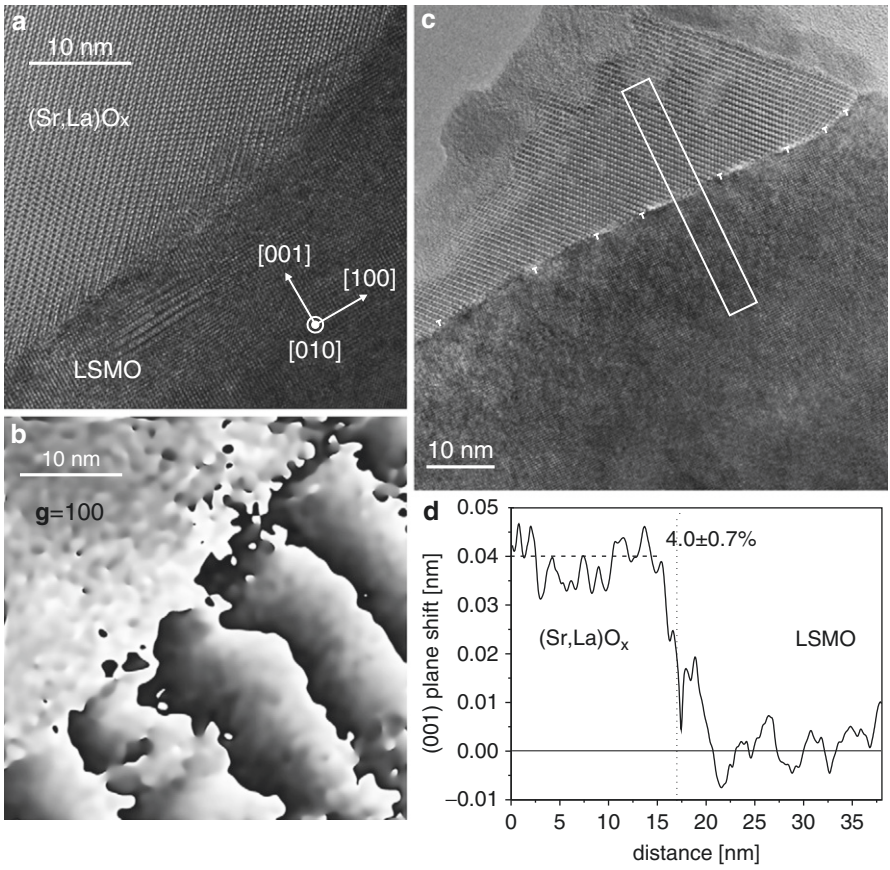


Fig. 11.13 (**a**) HRTEM image showing the interface between a (Sr, La)O_x island and the LSMO film for a nanostructured 24 nm thick film. (**b**) Phase map with $\mathbf{g} = 100$ of image (**a**). The reference lattice has been taken at the island side. (**c**) HRTEM image showing a surface dot/film interface for the case of a nanostructured 60 nm thick LSMO film. Misfit dislocations with Burgers vectors $\mathbf{b} = a_{LSMO}$ [100] are indicated. (**d**) Profile of the deformation of the (001) planes across the film/dot interface measured by quantitative Fourier analysis of the HRTEM micrograph in (**c**). The (Sr, La)O_x lattice planes differ with respect to the LSMO lattice measured along its [001] direction by ~4 % with a variation of 0.7 % respect to the reference lattice taken in the LSMO film. The dotted line in (**d**) indicates the position of the interface plane

either a certain degree of relaxation of the island upon its surface or a small accumulated error in the phase map as measured by GPA. The 2π phase shift, imaged as black to white change in color, corresponds to misfit dislocations on the LSMO side. A mean distance between dislocations for the case of the 24 nm thick LSMO phase beneath the island of ~10.06 nm is thus measured.

For the case of 60 nm thick samples, dislocations with Burgers vector $\mathbf{b} = a$ [86] are also found and are indicated in the HRTEM image in (c). Their spacing appears nonhomogeneous with mean dislocations spacing of ~10.05 nm,

as measured from (d). Thus, in terms of misfit relaxation, the effect of the islands on the film surface appears to be the same for the 24 nm and for the 60 nm thick LSMO films. Figure 11.13 shows a profile of the local displacement of the (001) planes measured across the (Sr, La)O_x/LSMO interface from the micrograph in (c). The change in the spacing of the (001) lattice planes of the LSMO and the corresponding lattice planes in the (Sr, La)O_x structure, as going from the LSMO film to the island, is measured to be a $(4.0 \pm 0.7)\%$ (a positive measured value indicates a compressive deformation state of the island lattice with respect to the reference LSMO lattice structure). The reference lattice for this measurement was taken in the LSMO film, in an area far away from the interface. The nominal lattice parameter values for bulk LSMO will be considered for an estimation of the matching distance of the islands to the dot from the lattice plane variation measured by the GPA method. Note that the 60 nm thick LSMO films are observed to be fully relaxed, and thus, its lattice parameters could be considered to be very close to nominal bulk values. With all these considerations, the matching distance of the (Sr, La)O_x phase to the 60 nm thick film is measured to be $d(Sr, La)Ox,\| \sim 0.403 \pm 0.003$ nm, which is consistent with the measured matching distances measured for the case of the 24 nm thick film from ED patters (see Fig. 11.9). From the fact that the density of dislocations at the surface dots/LSMO interface is the same for the fully relaxed and for the fully strained segregated LSMO films and the consistency in the matching distances measured for both systems, it can be deduced that the effect of the islands on the misfit strain of the film underneath them is negligible.

Notice that in Fig. 11.13a there is a small area in the LSMO side right under the (Sr, La)O_x nanoisland displaying a layered-type structure. This nanometric area with tetragonal-like contrast instead of the typical cubic-like observed for the rhombohedral LSMO structure is not related to a specific strain state of the film. It is due to the release of oxygen during electron irradiation giving rise to a reversible phase transition that occurs in situ during observation of the films in the TEM [107].

5.5.2 The Role of the (Sr, La)O_x Inclusions on Plastic Relaxation

Figure 11.14 shows examples of interfacial nanodots, (a) and (d). As for the case of the (Sr, La)O_x islands, the (Sr, La)O_x inclusions are faceted along the $\{100\}_{LSMO}$ and $\{110\}_{LSMO}$ perovskite planes, suggesting local minima in the interface energy for these orientations [83, 108]. Strikingly, in (a) the (Sr, La)O_x nanodot is partially embedded in the STO substrate. The mechanism leading to this configuration is not clearly understood. In the images, the LSMO/STO interface has been indicated by arrows. On one hand, the lateral displacement induced in the neighboring LSMO lattice by a (Sr, La)O_x (SLO when written as a subscripts/superscripts below) nanodot is

$$B = \varepsilon^{LSMO/SLO} \cdot D \tag{11.5}$$

where $\varepsilon^{LSMO/SLO} = \frac{(d_{SLO} - a_{LSMO})}{a_{LSMO}}$ and D is the diameter of the nanodot projected onto the interface (see Fig. 11.15a for a definition of the magnitudes). Thus, if a nanodot's size equals

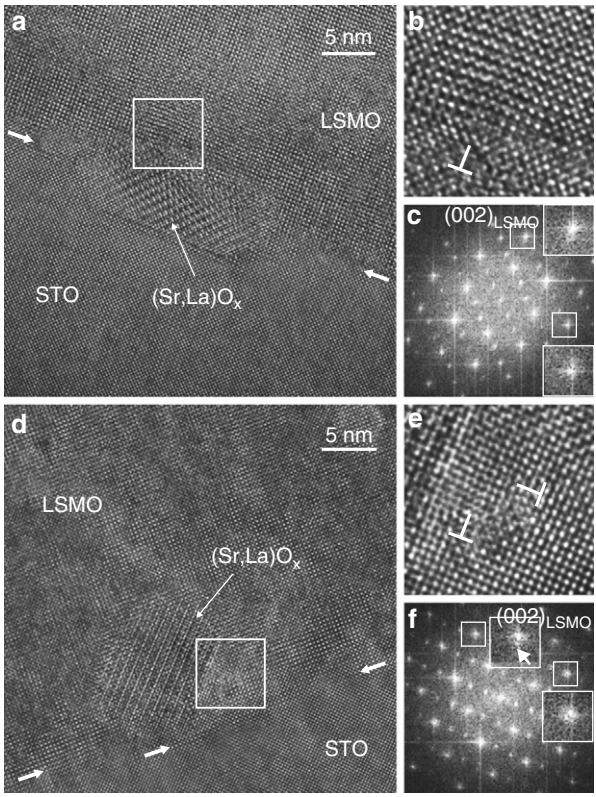


Fig. 11.14 HRTEM images showing two different nanodots are presented (**a**) and (**d**) [9]. Three different types of dislocations are found (**a**)–(**f**). The interfaces between the film and the substrate are indicated with arrows. Digitally magnified views of the areas indicated with solid squares in (**a**) and (**d**) are shown in (**b**) and (**e**), respectively. The presence of dislocations is signaled and the distortion introduced by the dislocations in the LSMO structure can be observed. The FFTs of the same areas are shown in (**c**) and (**f**). A splitting of the STO-inclusion spot in (**f**) indicates a larger lattice parameter in the case of the inclusion

$$D_{eq} = \frac{|\mathbf{b}|}{\varepsilon^{LSMO/SLO}} \tag{11.6}$$

then it would induce a compensating strain around it equivalent to a misfit dislocation with a Burgers vector **b**. The matching distances of interfacial (Sr, La)O_x are measured to be smaller than those of (Sr, La)O_x islands. They also vary from one nanodot to another and so their effect on the local strain release of the LSMO film. A quantitative analysis of different nanodot images using the geometrical phase analysis method indicates that the displacements measured from images (a) and (d), for instance, are B $\sim$ 0.23 nm and $\sim$0.48 nm, respectively.

Figure 11.16b shows the displacement field map of the $(100)_{LSMO–STO}$ planes of a (Sr, La)O_x nanodot in (a). Also in this case, the nanodot appears partially embedded in the substrate. The reference was chosen in an area of the STO substrate. The profile of these relative in-plane interplanar shifts as measured across the (Sr, La)O_x nanodot/STO substrate interface is shown in (c). The as-measured in-plane matching distance of the (Sr, La)O_x is $d_{SLO} \sim (a_{STO} + 0.014)$nm = 0.405 nm (see figure). Since the projected nanodot diameter is about D$\sim$15 nm, thus the overall displacement induced by this particular nanodot on the LSMO film is

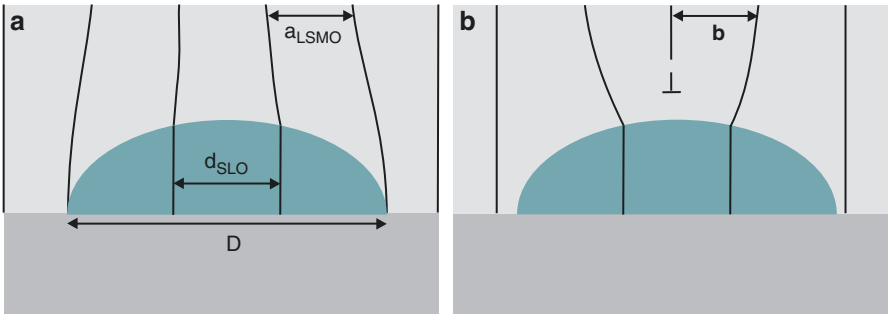


Fig. 11.15 Schematic drawing illustrating the misfit accommodation mechanism by interfacial nanodots [9]

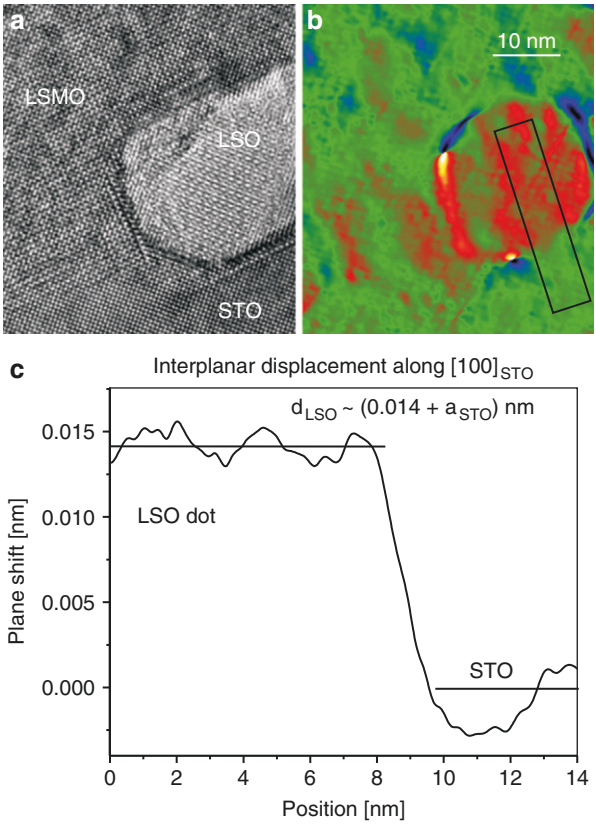


Fig. 11.16 (**a**) HRTEM image of a (Sr, La)O_x nanodot viewed along the [100] zone axis of the LSMO and STO. (**b**) Deformation map for the $(010)_{LSMO/STO}$ reflections taking as a reference the STO substrate. (**c**) Profile averaged over the boxed area in the deformation map

B ~ 0.65 nm. It should be pointed out that the misfit compensating effect of the interfacial nanodots is only efficient within a slab of LSMO adjacent to the interface. Analysis of the high-resolution TEM images shown in Fig. 11.14a, d indicates, however, that once nucleated, such nanodots constitute preferential

nucleation sites for dislocations with Burgers vectors $\mathbf{b} = a_{LSMO}$ [010] (see Fig. 11.14b) and $\mathbf{b}_1 = \frac{1}{2}a_{LSMO}$ [$0\bar{1}\bar{1}$] and $\mathbf{b}_2 = \frac{1}{2}a_{LSMO}$ [$0\bar{1}1$], yielding misfit components $\mathbf{b}_1 + \mathbf{b}_2 = a_{LSMO}$ [010] (see Fig. 11.14e), with the extra plane residing in the LSMO film. The misfit accommodation mechanism is sketched in Fig. 11.15. Such dislocations compensate (totally or partially) the displacement B induced by the nanodots, thus relaxing the misfit strain through the entire volume of the composite film. Note that beyond a size corresponding to $B > |\mathbf{b}|$, the cost in elastic and interface energies for interfacial nucleation would be no longer compensated by a reduction of the film elastic strain energy, thus explaining the observed large discrepancy between the island and nanodot sizes. In other words, while, in energy terms, there is a reason for the nanodots to keep their sizes below a certain value, the islands could continue growing by coalescence or any other active mechanism, since there is no apparent energy limitation for it.

5.6 Strain Measurements

The precise local effect of these inclusions on the LSMO matrix has also been investigated by quantitative Fourier analysis of the HRTEM images. Figure 11.17a is a HRTEM micrograph of the (Sr, La)Ox inclusion located right above the LSMO/STO interface line. An area in the STO substrate was chosen as the averaged reference lattice. Figures 11.17c, d are the phase images corresponding to image (a) and constructed with the Fourier components $\mathbf{g} = 101$, (c), and $\mathbf{g} = -\bar{1}01$, (d). Note that in the substrate side, the contrast is kept constant, while the change from black to white contrast in the LSMO side under the presence of the inclusion means a phase change of 2π, as indicated in the images, which indicates the presence of a dislocation. As observed in the phase maps, the dislocation introduced by the inclusion has an effect on the LSMO phase within more than tens of nanometer range. Figure 11.17b is a profile of the symmetric ε_{xx} component of the deformation matrix calculated from the phase maps in (c) and (d), across the LSMO/STO interface near the particle. The mean measured value of lattice deformation relative to the STO substrate along the interface plane (x-direction) is $\varepsilon_{xx} = (-0.8 \pm 0.2)\%$ (a negative sign stands for a tensile deformation state of the LSMO film as compared to the reference STO lattice). Since the reference was taken in the substrate side, then, ideally, assuming that chemical inhomogeneities do not occur and that the measured lattice spacing at the substrate side is an ideal undistorted spacing, thus $\varepsilon_{xx} = \frac{a_{LSMO} - a_{STO}}{a_{STO}} \approx -0.8\%$ with a_{LSMO} and a_{STO} being the nominal lattice parameters of LSMO and STO, respectively. Therefore, in this specific area, the local measurement of the parameter mismatch indicates that the LSMO in-plane parameter becomes fully relaxed 6–7 nm away from the interface with the substrate.

These local nanostrain variations induced around the interfacial (Sr, La)O_x and bulk RP inclusions were correlated with an increase by more than a factor of 2 in the magnetoresistance of these nanocomposite thin films [9]. Furthermore, these nanostructured films were used as templates for the growth of superconducting

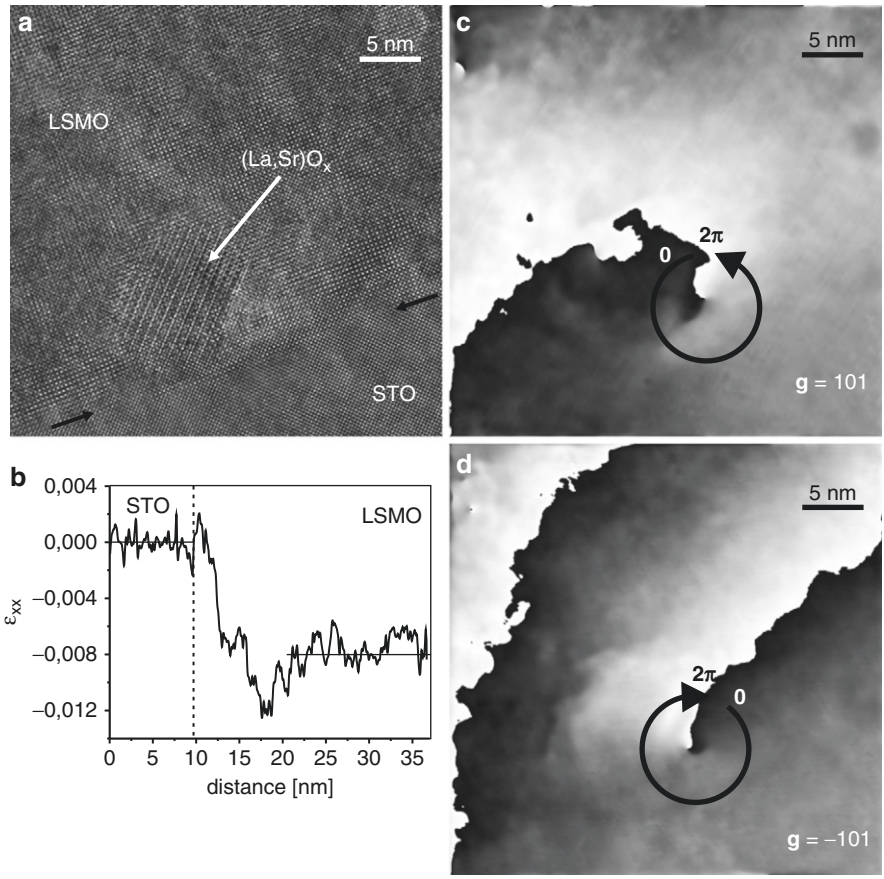


Fig. 11.17 (**a**) HRTEM image showing a (Sr, La)O_x inclusion in the 60 nm thick film located just above the interface with the substrate (**b**) Deformation profile across the LSMO/STO near the particle in image (**a**). A mean deformation value of $\varepsilon_{xx} = (-0.8 \pm 0.2)\%$ was measured. For obtaining the relative deformation map, the STO was chosen as the reference lattice and phase maps were constructed using the 101, in (**c**), and −101, in (**d**), Fourier components. The profile indicates that the LSMO film is fully relaxed 6–7 nm away from the STO-LSMO interface plane near the (Sr, La) O_x interfacial dot

$YBa_2Cu_3O_{7-x}$ films, resulting in an enhanced critical current of the high T_C superconductor [109], as well as to develop a methodology to reach multilevel resistive states at nanoscale for low-cost memories [110].

6 Nanocomposites by Accommodation of La Excess Content

A simple strategy for the controlled fabrication of nanocomposite films by CSD is to grow the films using the synthesis conditions for a single phase – which in our case is

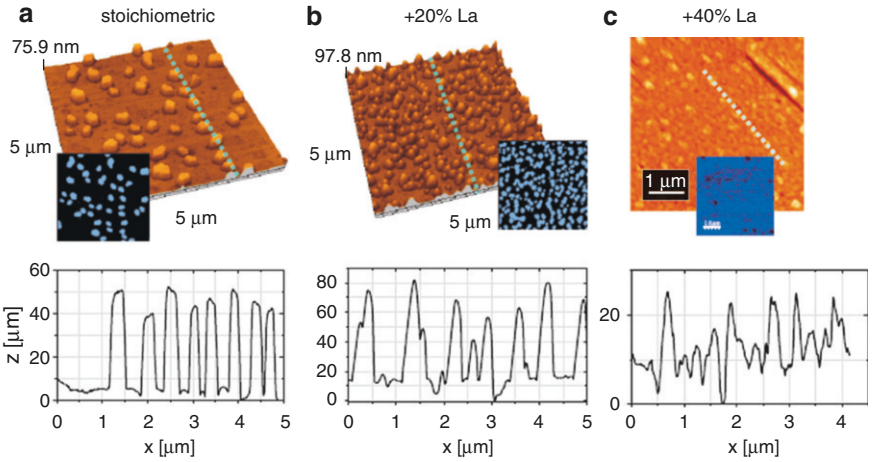


Fig. 11.18 Topographic SFM images as a function of La content. Topographic SFM images (5μm × 5μm), *insets* are binarized areas in (**a**)–(**b**) and current map in (**c**) and profile across several nanodots on the LSMO film surface for films displaying different islands concentration and sizes. (**a**) Stoichiometric LSMO films; (**b**)–(**c**) LSMO films grown with 20 mol % and 40 mol % excess of La propionates precursor content in the starting solution, respectively

the LSMO – but adding an excess of one of the metalorganic compounds in the precursor solution. In this section, the effect of Lanthanum content on the microstructure of LSMO films grown with the particular thermal annealing conditions for inducing self-segregation (1,000 °C during 12 h) on STO substrates is investigated. As explained bellow, when the La excess content achieves the 40 %, it is accommodated by formation of La-rich inclusions embedded in the epitaxial LSMO thin film matrix. The presence of these new phases may also influence the growth process of the film and induce misorientation of some LSMO grains within the nanocomposite films.

The general surface topography of the films was previously characterized by SFM for different La contents. In Fig. 11.18 are SFM topographic images showing 5 μm × 5 μm areas of the final segregated LSMO film grown from a stoichiometric (a) precursor solution, from a solution with a 20 % excess of Lanthanum content (b) and from a precursor solution with a 40 % excess of La. As it is shown, a conducting LSMO film with a surface distribution of (Sr, La) O_x dots is found also for additions up to a 20 % La. The density and size of the islands is found to be directly related to the increase of Lanthanum concentration [8]. When the excess of La propionate precursor solution achieves the 40 mol %, no insulating nanodots are found at the film surface anymore.

Figure 11.19 is a low magnification TEM image of the composite film grown with 40 % excess of Lanthanum in the precursor solution. Film thickness oscillates from 26 to 35 nm and image contrast is observed to change from place to place along the film. This suggests that the film is composed by different phases and/or orientations of the same phase. EFTEM images of the area shown in the low magnification TEM image in Fig. 11.20a (see Fig. 11.20b, c) show

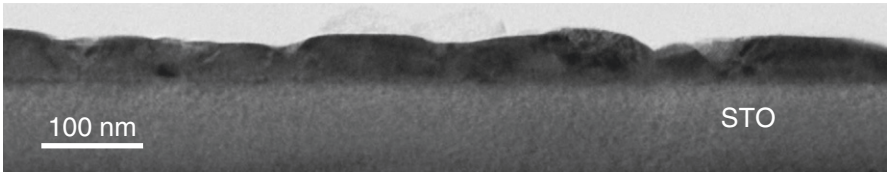


Fig. 11.19 Cross-section low magnification TEM image showing an overview of LSMO/STO system for a 40 % excess of La LSMO film [6]. Note that image contrast changes from place to place within the film, indicating the presence of different grains

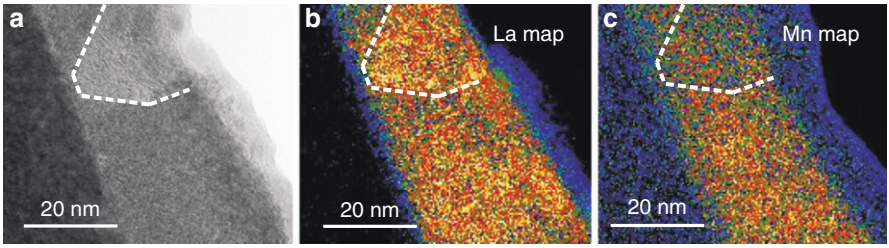


Fig. 11.20 (**a**) Low magnification TEM image of the film with a 40 % La addition and the corresponding La – $M_{5,4}$-edge, (**b**), and Mn – $L_{3,2}$edge, (**c**), filtered images [6]

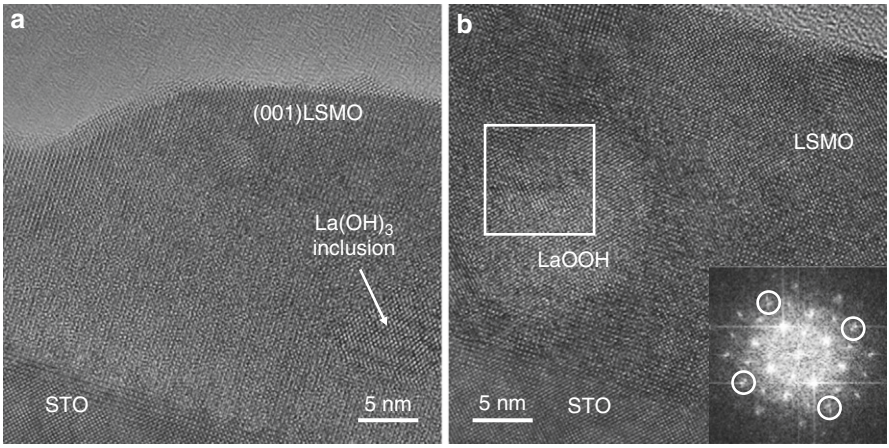


Fig. 11.21 HRTEM images showing different inclusions with crystal structure consistent with the hexagonal $La(OH)_3$ (**a**) and with the monoclinic LaO(OH) (**b**) phases [6]

that there are areas with enriched La and poor Mn contents. These different particles appear all along the film and their sizes run from a few nanometers to the entire film thickness. An identification of the different phases encountered in the composite film was performed by analysis of HRTEM images taken at different places along the film. In Fig. 11.21a, a HRTEM image of such

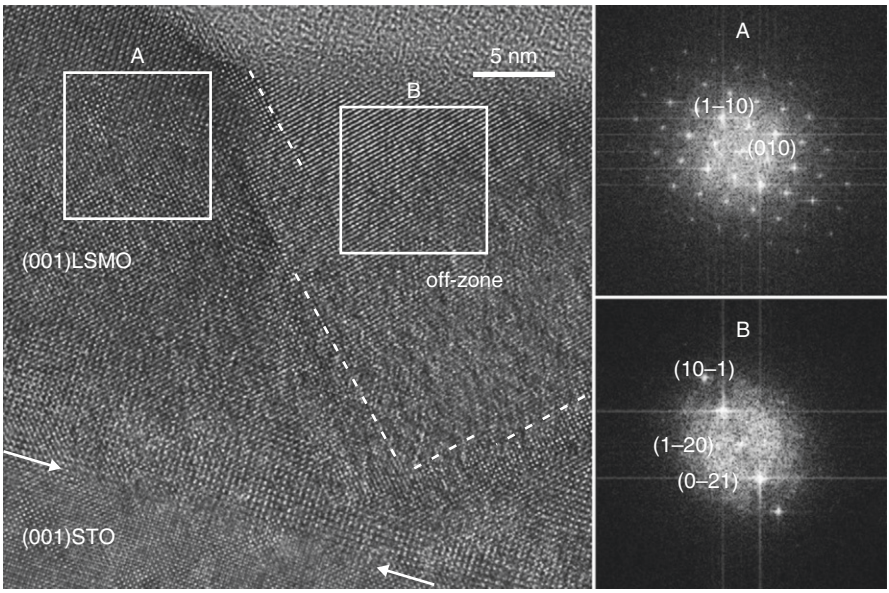


Fig. 11.22 Cross-section HRTEM image exhibiting a misoriented LSMO grain (FFT in *B*) with grain thickness being almost that of the epitaxial LSMO film (FFT in *A*) [6]

inclusions embedded in the LSMO film is shown. The corresponding FFT spectrum is consistent with the hexagonal $La(OH)_3$ phase. According to previous works, this phase is most likely derived from the hexagonal La_2O_3 phase after reaction in air [81]. Also, inclusions exhibiting a FFT spectrum consistent with the monoclinic LaO(OH) phase, as seen along the [001] and/or [101] zone axis, are observed. In Fig. 11.21b, one of these inclusions is shown; it presents a high degree of mosaicity and structural disorder. This form of La hidroxide has been reported to be a common product of a reaction from the cubic La_2O_3 when exposed to air [81, 82, 111]. Hence, TEM analysis revealed a massive presence of these two La-O phases. Most likely, hexagonal and cubic La_2O_3 were formed during film synthesis and reacted with air moisture to form hydroxides when preparing the TEM sample. Besides the large number of La-rich inclusions found in the film, misoriented LSMO grains were also observed. Figure 11.22 is a HRTEM image showing one such misoriented LSMO grains. The interface with the STO substrate is indicated with white arrows for clarity. The two domains shown in the image are coherent along the (1–10) planes, indicating that this is a common plane to both orientations. Rotation occurs along an axis normal to the (1–10) planes, i.e., along the [1–10] axis. The FFT patterns on the right-hand side correspond to the [001] zone axis of the LSMO phase obtained from A and to a disoriented grain near the [212] zone axis in grain B. This latter zone axis is at 48° from the [001] zone axis. From the image features and the FFT pattern, the grain observed in B could be around 3°–5° away from that zone axis.

Careful electrical measurements of these nanocomposites were carried out following a methodology which rules out extrinsic effects due to contact resistance

or extrinsic Joule self-heating [112] and due to the existence of misoriented grains of LSMO or segregated secondary phases. It was concluded that the films present enhanced magnetoresistance in a whole range of temperatures [6].

7 Conclusions and Future Perspective

In this chapter, the mechanism for the creation of an epitaxial nanocomposite CSD-derived film by spontaneous phase separation has been investigated using TEM.

We have discussed how to apply TEM for a systematic analysis of the microstructure evolution with some processing parameters, an identification of the different phases in the nanocomposite films based on both a microstructural and chemical characterization at the nanoscale and an investigation of the strain state of the different phases. The systems studied for this purpose have been self-nanostructured $La_{0.7}Sr_{0.3}MnO_3$ thin films grown on (001) $SrTiO_3$. For the results discussed in this chapter, a variety of TEM and spectroscopic techniques in the TEM have been used, namely, bright field TEM, selected area ED, EFTEM, EDX, and HRTEM. Combination of HRTEM imaging and the GPA method has also been performed. Based on the phase separation of two crystallographically dissimilar structures, diffusion towards the surface of the film of the minority phase may occur spontaneously leading to the formation of self-assembled islands. The two crystalline phases investigated here have been LSMO and an unknown insulating (Sr, La)Ox phase which appear by TEM to be faceted along the $\{100\}_{LSMO}$ and $\{110\}_{LSMO}$ perovskite planes. Simultaneously to the formation of the (Sr, La)O_x phase, rounded inclusions of a Ruddlesden-Popper phase are formed, most likely due to stoichiometry balance of the LSMO film. The development of the nanostructure does not take place before 9–10 h of annealing at 1,000 °C without any signature on the strain state of the films, thus indicating that the driving force for phase exsolution must be thermodynamic.

These self-nanostructured LSMO films are shown to fully plastically relax at a thickness of 60 nm, about six times larger than the equilibrium critical thickness predicted for systems exhibiting pure dislocation mechanisms. It is argued that the actual critical thickness in the present system is determined by a subtle balance between elastic energy and the chemical energy associated with chemical disorder before the nanostructure is developed. A novel and efficient misfit relaxation mechanism for LSMO thin films on STO substrates based on the thermodynamically induced self-assembled segregation of secondary phases has been investigated. The effect of an excess of Lanthanum content in the precursor solution has been investigated. The Lanthanum excess is accommodated by the formation of La-rich inclusions embedded in the LSMO thin film matrix. An enhanced magnetoresistance of these films is explained by the presence of such inclusions and misoriented LSMO grains induced during the growth process of the films. Currently, an emerging field in electron microscopy is the development of in situ imaging and spectroscopic capabilities for the study of nanomaterials under tunable conditions. The use of environmental stages and holders designed to fit in any

TEM [113–115] allows us to apply all the technological advances in TEM to the study of nanocomposite oxide thin films at the temperatures relevant for applications, as well as at specific atmospheres. Using hermetically sealed windowed cells, localized gas conditions are created around the sample, without interfering in the high-vacuum conditions inside the microscope column. In this way, a direct relation between microstructure and functionality can be achieved. In this chapter, a whole microstructural characterization of the nanocomposites films has been presented. However, analysis of the films was performed under high-vacuum conditions – inside the microscope column – and at around room temperature. The study of nanocomposite oxide thin films and, in particular, the correlation between microstructure and their new functionalities would strongly benefit of the use of environmental cells and/or heating holders when performing the investigation of the films.

Acknowledgments A portion of this work was performed at the Pacific Northwest National Laboratory, which is operated by Battelle Memorial Institute for the US Department of Energy under Contract No. DE-AC05-76RL01830. C. Moreno thanks financial support from the Japanese Ministry for Education, Culture, Sports, Science, and Technology (MEXT) through ICYS program. P. Abellan acknowledges FPU grant from Spanish MICINN. This work was supported by the Ministerio de Ciencia e Innovation (MAT2008-01022), Consolider NANOSELECT (CSD2007-00041), Generalitat de Catalunya (2009 SGR 770 and Xarmae), and the European Union (HIPERCHEM, NESPA).

References

1. MacManus-Driscoll JL, Zerrer P, Wang H, Yang H, Yoon J, Fouched A, Yu R, Blamire MG, Jia QX (2008) Strain control and spontaneous phase ordering in vertical nanocom-posite heteroepitaxial thin films. Nat Mater 7(4):314–332
2. Zheng H, Wang J, Lofland SE, Ma Z, Mohaddes-Ardabili L, Zhao T, Salamanca- Riba L, Shinde SR, Ogate SB, Viehland D, Jia Y, Schlom DG, Wutting M, Roytburd A, Ramesh R (2004) Multiferroic $BaTiO_3$ – $CoFe_2O_4$ nanostructures. Science 303(5658):661–663
3. Garcia-Barriocanal J, Rivera-Calzada A, Varela M, Sefriouri Z, Iborra E, Leon C, Pennycook SJ, Santamaria J (2008) Colossal ionic conductivity at interfaces of epitaxial ZrO_2: Y_2O_3/$SrTiO_3$ heterostructures. Science 321(5889):676–680
4. Kang S, Goyal A, Li J, Gapud AA, Martin PM, Heatherly L, Thompson JR, Christen DK, List FA, Paranthaman M, Lee DF (2006) High-performance high-Tc superconducting wires. Science 311(5769):1911–1914
5. Llordes A, Palau A, Gazquez J, Coll M, Vlad R, Pomar A, Arbiol J, Guzman R, Ye S, Rouco V, Sandiumenge F, Ricart S, Puig T, Varela M, Chateigner D, Vanacken J, Gutierrez J, Moshchalkov V, Deutscher G, Magen C, Obradors X (2012) Nanoscale strain-induced pair suppression as a vortex-pinning mechanism in high-temperature superconductors. Nat Mater 11:329–336
6. Moreno C, Abellan P, Sandiumenge F, Casanove M-J, Obradors X (2012) Nanocomposite lanthanum strontium manganite thin films formed by using a chemical solution deposition. Appl Phys Lett 100(2):023103
7. Yang H, Meng Q, Zhao R et al (2011) Self-assembled nanocomposite oxide films: design, fabrication, and properties. In: Reddy B (eds) Advances in nanocomposites – synthesis, characterization and industrial applications. Intech, New York, ISBN 978-953-307-165-7, pp 947–966（Chap 40）

8. Moreno C, Abellan P, Hassini A, Ruyter A, del Pino Perez A, Sandiumenge F, Casanove M-J, Santiso J, Puig T, Obradors X (2009) Spontaneous outcropping of self-assembled insulating nanodots in solution-derived metallic ferromagnetic $La_{0.7}Sr_{0.3}MnO_3$ films. Adv Funct Mater 19:2139–2146
9. Abellan P, Moreno C, Sandiumenge F, Obradors X, Casanove M-J (2011) Misfit relaxation of $La_{0.7}Sr_{0.3}MnO_3$ thin films by a nanodot segregation mechanism. Appl Phys Lett 98(4):041903
10. Martinez-Julian F, Ricart S, Pomar A, Coll M, Abellan P, Sandiumenge F, Casanove M-J, Obradors X, Puig T, Pastoriza-Santos I, Liz-Marzan LM (2011) Chemical solution approaches to $YBa_2Cu_3O_7$-Au nanocomposites superconducting thin films. J Nanosc Nanotechnol 11(4):3245–3255
11. Obradors X, Puig T, Palau A et al (2011) Sandiumenge in: nanostructured superconductors with efficient vortex pinning, Section 3.10. In: Andrews D, Scholes G, Wiederrecht G (eds) Comprehensive nanoscience and technology. Elsevier, Oxford, pp 303–349
12. Urban KW (2009) Is science prepared for atomic-resolution electron microscopy? Nat Mater 8:260–262
13. Hytch MJ, Snoeck E, Kilaas R (1998) Quantitative measurement of displacement and strain fields from HREM micrographs. Ultramicroscopy 74:131–146, http://www.hremresearch.com
14. Ramesh R, Spaldin NA (2007) Multiferroics: progress and prospects in thin films. Nat Mater 6:21–29
15. Ueda K, Tabata H, Kawai T (1998) Ferromagnetism in $LaFeO_3$ – $LaCrO_3$ superlattices. Science 280:1064–1066
16. Ohtomo A, Muller DA, Grazul JL et al (2002) Artificial charge-modulation atomic-scale perovskite titanate superlattices. Nature 419:378–380
17. Guiton BS, Davies PK (2007) Nano-chessboard superlattices formed by spontaneous phase separation in oxides. Nat Mater 6:586–591
18. Moshnyaga V, Damaschke B, Shapoval O, Belenchuk A, Faupel J, Lebedev OI, Verbeeck J, Van Tendeloo G, Miicksch M, Tsurkan V, Tidecks R, Samwer K (2003) Structural phase transition at the percolation threshold in epitaxial $(La_{0.7}Ca_{0.3}MnO_3)_{1-x}$:$(MgO)_x$ nanocomposite films. Nat Mater 2:247–252
19. Zheng H, Zhan Q, Zavaliche F, Sheburne M, Straub F, Cruz MP, Chen L-Q, Dahmen U, Ramesh R (2006) Controlling self-assembled perovskite-spinel nanostructures. Nano Lett 6(7):1401–1407
20. Yang H, Wang H, Yoon J, Wang Y, Jain M, Feldmann DM, Dowden PC, MacManus-Driscoll JL, Jia Q (2009) Vertical interface effect on the physical properties of self-assembled nanocomposite epitaxial films. Adv Mater 21:3794–3798
21. Yang H, Wang H, Maiorov B et al (2009) Self-assembled multilayers and enhanced superconductivity in $(Y\,Ba_2Cu_3O_{7-x})_{0.5}$: $(BaZrO_3)_{0.5}$ nanocomposite films. J Appl Phys 106:093914
22. Cantoni C, Gao Y, Wee SH, Specht ED, Gazquez J, Meng J, Pennycook SJ, Goyal A (2011) Strain-driven oxygen deficiency in self-assembled, nanostructured, composite oxide films. ACS Nano 5(6):4783–4789
23. Murakami M, Fujino S, Lim S-H, Salamanca-Riba LG, Wuttig M, Takeuchi I, Varughese B, Sugaya H, Hasegawa T, Lofland SE (2006) Microstructure and phase control in Bi-Fe-O multiferroic nanocomposite thin films. Appl Phys Lett 88(11):112505
24. Lange FF (1996) Chemical solution routes to single-crystal thin films. Science 273(5277):903–909
25. Balcells L, Carrillo AE, Martinez B, Fontcuberta J (1999) Enhanced field sensitivity close to percolation in magnetoresistive $La_{2/3}Sr_{1/3}MnO_3/CeO_2$ composites. Appl Phys Lett 74(26):4014–4016
26. Petrov DK, Krusin-Elbaum L, Sun JZ, Feild C, Duncombe PR (1999) Enhanced magnetoresistance in sintered granular manganite/insulator systems. Appl Phys Lett 75(7):995–997
27. Kameli P, Salamati H, Eshraghi M, Mohammadizadeh MR (2005) The effect of TiO_2 doping on the structure and magnetic and magnetotransport properties of $La_{0.75}Sr_{0.25}MnO_3$ composite. J Appl Phys 98(4):043908

28. Gaur A, Varma GD (2007) Electrical and magnetotransport properties of $La_{07}Sr_{033}MnO_3$/TiO_2 composites. Cryst Res Technol 42(2):164–168
29. Miao JH, Yuan SL, Ren GM, Xiao X, Yu GQ, Wang YQ, Yin SY (2007) Electrical transport and magnetoresistance properties in (1–x)$La_{2/3}Ca_{1/3}MnO_3$/xSb_2O_5 composites. Mater Sci Eng 136(1):67–71
30. Miao JH, Yuan SL, Ren GM, Xiao X, Yu GQ, Wang YQ, Yin SY (2006) Enhancement of room temperature magnetoresistance in (1–x)$La_{0.65}Ca_{0.33}MnO_3$/xSb_2O_5 composites. J Phys D: Appl Phys 39(14):2897–2901
31. Kang BS, Wang H, Manus-Driscoll JL et al (2006) Low field magnetotransport properties of $(La_{0.7}Sr_{0.3}MnO_3)_{(0.5)}$: $(ZnO)_{(0.5)}$ nanocomposite films. Appl Phys Lett 88(19): 192514–192516
32. Lu WJ, Sun YP, Zhu XB, Song WH, Du JJ (2006) Low-field magnetoresistance in $La_{0·8}Sr_{0·2}MnO_3$/ZrO_2 composite system. Mater Lett 60(27):3207–3211
33. Huang YH, Yan CH, Wang S, Luo F, Wang ZM, Liao CS, Xu GX (2001) Chemical synthesis of $La_{0.7}Sr_{0.3}MnO_3$/silica homogeneous nanocomposites. J Mater Chem 11(12):3296–3299
34. Yan L, Kong LB, Yang T, Goh WC, Tan CY, Ong CK, Rahman MA, Osipowicz T, Ren MQ (2004) Enhanced low field magnetoresistance of Al_2O_3–$La_{0.7}Sr_{0.3}MnO_3$ composite thin films via a pulsed laser deposition. J Appl Phys 96(3):1568–1571
35. De Andres A, Taboada S, Colino JM, Ramirez R, Garcia-Hernandez M, Martinez JL (2002) Low field magnetoresistance at the metal-insulator transition in epitaxial manganite thin films. Appl Phys Lett 81(2):319–321
36. Valencia S, Castano O, Fontcuberta J, Martinez B, Balcells L (2003) Enhanced low field magnetoresistive response in $(La_{2/3}Sr_{1/3}MnO_3)(x)/(CeO_2)(1–x)$ composite thick films prepared by screen printing. J Appl Phys 94(4):2524–2528
37. Gil LK, Baca E, Moran O, Quinayas C, Bolanos G (2008) Influence of polyparaphenylene on the magnetotransport of manganite/polymer composites. Physica B 403(10–11): 1813–1818
38. Gupta S, Ranjit R, Mitra C, Raychaudhuri P, Pinto R (2001) Enhanced room-temperature magnetoresistance in $La_{0.7}Sr_{0.3}MnO_3$ – glass composites. Appl Phys Lett 78(3):362364
39. Shlyakhtin OA, Shin KH, Oh Y-J (2002) Enhancement of low field magnetoresistance by chemical interaction in bulk composites $La_{0.7}Sr_{0.3}MnO_3$/$SrMeO_3$ (Me = Ti, Zr). J Appl Phys 91:7403–7405
40. Freitas JCC, Victor RA, Orlando MTD, Takeuchi AY, Oliveira IS, Bonagamba TJ (2008) Evidence for magnetic phase separation in $La_{0.86}Sr_{0.14}Mn_{1–x}Cu_xO_{3+\delta}$; manganites from NMR and magnetic measurements. J Phys Condens Matter 20(9):095214
41. Shim IB, Lee BW, Kim CS (2002) Influence of the indium oxide addition on low field magneto resistance behavior in the $La_{2/3}Sr_{1/3}$ MnO_3 granular composite thin films. J Magn Magn Mater 239(1–3):279–281
42. Eshraghi M, Salamati H, Kameli P (2007) The effect of NiO doping on the structure, magnetic and magnetotransport properties of $La_{0.8}Sr_{0.2}MnO_3$ composite. J Alloys Compd 437(1–2):22–26
43. Eshraghi M, Salamati H, Kameli P (2006) Structural, magnetic and transport properties of $La_{0.8}Sr_{0.2}MnO_3$/xNiO composites. J Phys Condens Matter 18(35):8281–8294
44. Gaur A, Varma GD (2006) Magnetoresistance behaviour of $La_{0.7}Sr_{0.3}MnO_3$/NiO composites. Solid State Commun 139(6):310–314
45. Koster SA, Moshnyaga V, Samwer K, Lebedev OI, van Tendeloo G, Shapoval O, Belenchuk A (2002) Doping of interfaces in $(La_{0.7}Sr_{0.3}MnO_3)_{1–x}$: $(MgO)_x$ composite films. Appl Phys Lett 81(9):1648–1650
46. Liu JM, Yuan GL, Sang H, Wu ZC, Chen XY, Liu ZG, Du YW, Huang Q, Ong CK (2001) Low-field magnetoresistance in nanosized $La_{0.7}Sr_{0.3}MnO_3$/$Pr_{0.5}Sr_{0.5}MnO_3$ composites. Appl Phys Lett 78(8):1110–1112

47. Yan CH, Luo F, Huang YH, Li XH, Wang ZM, Liao CS, Zhao HW, Shen BG (2002) Enhanced room temperature magnetoresistance in $La_{0.7}Sr_{0.3}MnO_3/Sm_{0.7}Sr_{0.3}MnO_3$ nanocomposites. J Appl Phys 91:7406–7408
48. Dey P, Nath TK, Goswami MLN et al (2007) Room temperature ferroelectric and ferromagnetic properties of multiferroics $xLa_{0.7}Sr_{0.3}MnO_3$-(1–x)$ErMnO_3$ (weight percent x = 0.1, 0.2) composites. Appl Phys Lett 90(16):162510–162512
49. Huang Q, Li J, Huang XJ, Ong CK, Gao XS (2001) Effect of magnetic coupling on the magnetoresistive properties in $La_{0.67}Sr_{0.33}MnO_3/BaFe_{11.3}(ZnSn)_{0.7}O_{19}$ composites. J Appl Phys 90(6):2924–2929
50. Salamon, Myron B, Jaime M (2001) The physics of manganites: structure and transport. Rev Mod Phys 73(3):583–628
51. Molina L, Knoth K, Engel S, Holzapfel B, Eibl O (2006) Chemically deposited $La_2Zr_2O_7$ buffer layers for YBCO-coated conductors: film growth and microstructure. Supercond Sci Technol 19:1200–1208
52. Hytch MJ, Houdellier F (2007) Mapping stress and strain in nanostructures by high-resolution transmission electron microscopy. Microelectron Eng 84(3):460–463
53. Houdellier F, Hytch M, He F et al (2008) Aberration correction with the SACTEM-toulouse: from imaging to diffraction. In P Hawkes (ed) Advances in imaging and electron physics, vol 153, 1st edn. Academic/Elsevier, Boston, pp 225–259 (Chap 6).
54. Schwartz RW, Schneller T, Waser R (2004) Chemical solution deposition of electronic oxide films. C R Chimie 7(5):433–461
55. Gibert M, Puig T, Obradors X (2007) Growth of strain-induced self-assembled $BaZrO_3$ nanodots from chemical solutions. Surf Sci 601(13):2680–2683
56. Obradors X, Puig T, Pomar A, Sandiumenge F, Piñol S, Mestres N, Castaño O, Coll M, Cavallaro A, Palau A, Gazquez J, Gonzalez JC, Gutierrez J, Roma N, Ricart S, Moreto JM, Rossell MD, van Tendeloo G (2004) Chemical solution deposition: a path towards low cost coated conductors. Supercond Sci Technol 17(8):1055
57. Hasenkox U, Mitze C, Waser R, Arons RR, Pommer J, Guntherodt G (1999) Chemical solution deposition of epitaxial $La_{1-x}(Ca, Sr)_xMnO_3$ thin films. J Electroceram 3(3):255–260
58. Hassini A, Pomar A, Gutierrez J, Coll M, Roma N, Moreno C, Ruyter A, Puig T, Obradors X (2007) Atomically flat MOD $La_{0.7}Sr_{0.3}MnO_3$ buffer layers for high critical current $YBa_2Cu_3O_7$ TFA films. Supercond Sci Technol 20:S230
59. Zabaleta J, Jaafar M, Abellan P, Monton C, Iglesias-Freire O, Sandiumenge F, Ramos CA, Zysler RD, Puig T, Asenjo A, Mestres N, Obradors X (2012) Nanoscale magnetic structure and properties of solution-derived self-assembled $La_{0.7}Sr_{0.3}MnO_3$ islands. J Appl Phys 111, 024307 (2012)
60. Castaño O, Cavallaro A, Palau A, Gonzalez JC, Rossell M, Puig T, Sandiumenge F, Mestres N, Piñol S, Pomar A, Obradors X (2002) High quality $YBa_2Cu_3O_7$ thin films grown by trifluoroacetates metalorganic deposition. Supercond Sci Technol 16(1):45–53
61. Williams DB, Carter CB (1996/2009) Transmission electron microscopy, a textbook for materials science, 2nd edn. Springer, New York
62. Eberg E, Monsen AF, Tybell T, Van Helvoort ATJ, Holmestad R (2008) Comparison of TEM specimen preparation of perovskite thin films by tripod polishing and conventional ion milling. J Electron Microsc 57(6):175–179
63. Hytch MJ, Putaux J-L, Penisson J-M (2003) Measurement of the displacement field of dislocations to 0.03 A by electron microscopy. Nature 423(6937):270–273
64. Bierwolf R, Hohenstein H, Philipp F, Brandt O, Crook GE, Ploog K (1993) Direct measurement of local lattice distortions in strained layer structures by HREM. Ultramicroscopy 49(1–4):273–285
65. Hytch MJ (1997) Analysis of variations in structure from high resolution electron microscope images by combining real space and Fourier space information. Microsc Microanal Microstruct 8(1):41–57

66. Hirth JP, Lothe J (1992) Theory of dislocations, 2nd edn. Krieger, Malabar
67. Hytch MJ (2001) In: stress and strain in epitaxy: theoretical concepts measurements and applications. Elsevier, Amsterdam, p 201
68. Rouviere J-L (2008) The use of the geometrical phase analysis to measure strain in nearly periodic images. In: 15th conference on microscopy of semiconducting, 2007, vol 120, p 199
69. Hytch MJ (2006) GPA for digital micrograph. GPA phase manual 1.0. HREM Research Inc. Saitama
70. Roure P, Farjas J, Camps J, Ricart S, Arbiol J, Puig T, Obradors X (2011) Decomposition processes and structural transformations of cerium propionate into nanocrystalline ceria at different oxygen partial pressures. J Nanopart Res 13(9):4085–4096
71. Thompson CV (1990) Grain growth in thin films. Annu Rev Mater Sci 20:245–268
72. Schwartz RW (1997) Chemical solution deposition of perovskite thin films. Chem Mater 9(11):2325–2340
73. Chen H, Zalamova K, Pomar A, Granados X, Puig T, Obradors X (2010) Nucleation and growth rate influence on microstructure and critical currents of TFA-$YBa_2Cu_3O_7$ under low-pressure conditions. J Mater Res 25:2371–2379
74. Gibert M, Abellan P, Martinez L, Roman E, Crespi A, Sandiumenge F, Puig T, Obradors X (2011) Orientation and shape selection of self-assembled epitaxial $Ce_{1-x}Gd_xO_{2-y}$ nanostructures grown by chemical solution deposition. Cryst Eng Comm 13:6719–6727
75. Zabaleta Llorens J (2012) Growth and advanced characterization of solution-derived nanoscale La0.7Sr0.3MnO3 heteroepitaxial systems. PhD thesis ICMAB-CSIC, Autonomous University of Barcelona, Physics Department, Bellaterra
76. Haertling GH (1991) Plzt thin films prepared from acetate precursors. Ferroelectrics 116(1):51–63
77. Mitome M, Bando Y, Golberg D, Kurushima K, Okura Y, Kaneyama T, Naruse M, Honda Y (2004) Nanoanalysis by a high-resolution energy filtering transmission electron microscope. Microsc Res Tech 63(3):140–148
78. Walther T (2003) Electron energy-loss spectroscopic profiling of thin film structures: 0.39 nm line resolution and 0.04 eV precision measurement of near-edge structure shifts at interfaces. Ultramicroscopy 96(3–4):401–411
79. Foex M (1961) Properties of some solid solutions and compounds with lanthanum oxide base. Bull Soc Chim France 1:109–117
80. JCPDS-International Centre for Diffraction Data (2001) Power diffraction files, JCPDS-ICDD Card Nos. 01-072-0893 (Sr3La4O9), 00-022-1430 (La4SrO7), 00-022-1431 (La2Sr2O5), 00-0420343 (La2SrOx) International Center for Diffraction Data, Swarthmore
81. Nieminen M, Putkonen M, Niinist ö L (2001) Formation and stability of lanthanum oxide thin films deposited from ft-diketonate precursor. Appl Surf Sci 174:155–165
82. Wilk GD, Wallace RM, Anthony JM (2001) High-k gate dielectrics: current status and materials properties considerations. J Appl Phys 89(10):5254–5275
83. Russell KC (1980) Nucleation in solids: the induction and steady state effects. Adv Coll Interf Sci 13:205–318
84. Grundy AN, Hallstedt B, Gauckler LJ (2004) Assessment of the Sr-Mn-O system. J Phase Eq Diff 25(4):311–319
85. Caignaert V, Nguyen N, Hervieu M, Raveau B (1985) $Sr_2Mn_2O_5$, an oxygen-defect perovskite with Mn(III) in square pyramidal coordination. Mater Res Bull 20(5):479485
86. Mori T, Inoue K, Kamegashira N, Yamaguchi Y, Ohoyama K (2000) Neutron diffraction study of $Sr_2Mn_2O_5$. J Alloys Compd 296(1–2):92–97
87. Kuroda K, Ishizawa N, Mizutani N, Kato M (1981) The crystal structure of a – $SrMnO_3$. J Solid State Chem 38(3):297–299
88. Battle PD, Gibb TC, Jones CW (1988) The structural and magnetic properties of $SrMnO_3$: a reinvestigation. J Solid State Chem 74(1):60–66
89. Tichi RS, Goodenough JB (2002) Oxygen permeation in cubic $SrMnO_3$-δ. J Solid State Sci 4(5):661–664

90. Negas T, Roth RS (1970) The system $SrMnO_{3-x}$. J Solid State Chem 1(3–4):409–418
91. Balz D, Plieth K (1955) The structure of potassium nickel fluoride, K_2NiF_4. Z Elektrochem 59(6):545–551
92. Tesuka K, Inamura M, Hinatsu Y, Shimojo Y, Morii Y (1999) Crystal structures and magnetic properties of $Ca_{2-x}Sr_xMnO_4$. J Solid State Chem 145(2):705–710
93. Mizutani N, Kitazawa A, Ohkuma N, Kato M (1970) Synthesis of strontium-manganese double oxides. Kogyo Kagaky Zasshi 73(6):1097–1103
94. Mitchell JF, Millburn JE, Medarde M, Short S, Jorgensen JD, Fernandez-Diaz MT (1998) $Sr_3Mn_2O_7$: Mn^{4+} parent compound of the n = 2 Layered CMR manganites. J Solid State Chem 141(2):599–603
95. Fabry J, Hybler J, Jirak Z, Jurek K, Maly K, Nevriva M, Petricek V (1988) Preparation and the crystal structure of a new manganate, $Sr_4Mn_3O_{10}$. J Solid State Chem 73(2):520–523
96. Floros N, Hervieu M, van Tendeloo G, Michel C, Maignan A, Raveau B (1998) The layered manganate $Sr_{4-x}Ba_xMn_3O_{10}$: synthesis, structural and magnetic properties. J Solid State Sci 2(1):1–9
97. Vente JF, Plaisier JR, Ijdo DJV, Kamenev KV (2000) Preparation and crystallographic properties of $Sr_{7-x}(Ca/Ba)_xMn_4O_{15}$. Mater Res Bull 35(14–15):2437–2444
98. Negas T (1973) The $SrMnO_{3-X} - Mn_3O_4$ system. J Solid State Chem 7(1):85–88
99. Ruddlesden SN, Popper P (1985) The compound $Sr_3 Ti_2O_7$ and its structure. Acta Crystallogr 11:54–55
100. Seshadri R, Hervieu M, Martin C, Maignan A, Domenges B, Raveau B, Fitch A (1997) Study of the layered magnetoresistive perovskite $La_{1.2}Sr_{1.8}Mn_2O_7$ by high-resolution electron microscopy and synchrotron x-ray powder diffraction. Chem Mater 9(8):1778–1787
101. Maurice J-L, Pailloux F, Barthelemy A, Durand O, Imhoff D, Lyonnett R, Rocher A, Contour J-P (2003) Strain relaxation in the epitaxy of $La_{2/3}Sr_{1/3}MnO_3$ grown by pulsed-laser deposition on $SrTiO_3$ (001). Philos Mag 83(28):3201–3224
102. Lebedev OI, Van Tendeloo G, Amelinckx S, Hu HL, Krishnan KM (2000) High-resolution electron microscopy study of strained epitaxial $La_{0.7}Sr_{0.3}MnO_3$ thin films. Philos Mag A 80(3):673–691
103. Casanove M-J, Roucau C, Baules P, Majimel J, Ousset J-C, Magnoux D, Bobo J-F (2002) Growth and relaxation mechanisms in $La_{0.66}Sr_{0.33}MnO_3$ manganites deposited on $SrTiO_3$ (001) and MgO(0001). Appl Surf Sci 188(1–2):19–23
104. Ranno L, Llobet A, Tiron R, Favre-Nicolin E (2002) Strain-induced magnetic anisotropy in epitaxial manganite films. Appl Surf Sci 188(1–2):170–175
105. Brous J, Fankuchen I, Banks E (1953) Rare earth titanates with a perovskite structure. Acta Crystallogr 6:67–70
106. Hammouche A, Siebert E, Hammou A (1989) Crystallographic, thermal and electrochemical properties of the system $La_{1-x}Sr_xMnO_3$ for high temperature solid electrolyte fuel cells. Mater Res Bull 24(3):367–380
107. Zhang M, Ma XL, Li DX, Lu HB, Chen ZH, Yang GZ (2005) Abnormal lattice expansion and double periodicity in $La_{0.7}Sr_{0.3}MnO_3$ thin films under electron irradiation. J Mater Res 20(7):1778–1784
108. Sutton AP, Balluf RW (1995) S: interfaces in crystalline materials. Clarendon, Oxford
109. Gutierrez J, Puig T, Gibert M, Moreno C, Roma N, Pomar A, Obradors X (2009) Anisotropic c-axis pinning in interfacial self-assembled nanostructured trifluoracetate- $YBa_2Cu_3O_{7-x}$ films. Appl Phys Lett 94(17):172513
110. Moreno C, Munuera C, Valencia S, Kronast F, Obradors X, Ocal C (2010) Reversible resistive switching and multilevel recording in $La_{0.7}Sr_{0.3}MnO_3$ thin films for low cost nonvolatile memories. Nano Lett 10(10):3828–3835
111. Gonzalez-Rovira L, Sanchez-Amaya JM, Lopez-Haro M, Hungria AB, Boukha Z, Bernal S, Botana FJ (2008) Formation and characterization of nanotubes of $La(OH)_3$ obtained using porous alumina membranes. Nanotechnology 19(49):495305

112. Moreno C, Munuera C, Perez del Pino A, Gutierrez J, Puig T, Ocal C, Obradors X, Ruyter A (2009) Absence of self-heated bistable resistivity in $La_{0.7}Sr_{0.3}MnO_3$ films up to high current densities. Phys Rev B 80(9):094412
113. Butler EP, Hale KF (1981) Dynamic experiments in the electron microscope, vol 9. North-Holland, Amsterdam
114. Creemer JF, Helveg S, Hoveling GH, Ullmann S, Molenbroek AM, Sarro PM, Zandbergen HW (2008) Atomic-scale electron microscopy at ambient pressure. Ultramicroscopy 108(9):993–998
115. Mehraeen S, Mackeown JT, Deshmukh PV, Evans JE, Abellan P, Xu P, Reed BW, Taheri ML, Fischione PE, Browning ND (2013) A (S)TEM gas cell holder with localized laser heating for in-situ experiments. Microsc Microanal 19:470–478

TEM Characterization of Metallic Nanocatalysts

12

Dong Su

Contents

1 Definition of the Topic 577
2 Overview 578
3 Introduction 578
4 Experimental and Instrumental Methodology 580
4.1 Imaging: TEM and STEM 580
4.2 Spectroscopy: EELS and EDS 580
4.3 Nanodiffraction and CBED 581
4.4 Electron Beam Effect 581
5 Key Research Findings 582
5.1 Structural and Chemical Characterization of Metallic Nanocatalysts 582
5.2 In Situ Environmental TEM Study on Nanocatalysts 601
6 Conclusions and Future Perspective 613
References 614

1 Definition of the Topic

Transmission electron microscopy (TEM) techniques, including scanning transmission electron microscopy (STEM); X-ray energy-dispersive spectroscopy (EDS); electron energy-loss spectroscopy (EELS); selected area (SA), nano-beam (NB), and convergent-beam (CB) electron diffraction (ED); electron tomography (ET); and electron holography, are powerful in characterizing metallic nanocatalysts at both high spatial resolution (~0.05 nm) and high energy resolution (~0.1 eV). This chapter will review recently published results on the relationship between the structure and catalytic properties of metallic catalysts from the prospective of electron microscopy. As there already exist excellent books and reviews giving insights into the different

D. Su
Center for Functional Nanomaterials, Brookhaven National Laboratory, Upton, NY, USA
e-mail: dsu@bnl.gov

C.S.S.R. Kumar (ed.), *Transmission Electron Microscopy Characterization of Nanomaterials*, DOI 10.1007/978-3-642-38934-4_12,
© Springer-Verlag Berlin Heidelberg 2014

TEM techniques [1–6], this chapter will avoid in-depth discussions on electron microscopy techniques and tune its focus toward the application of (S)TEM on metallic nanocatalysts, especially on key issues of structural and chemical characterization; it will also introduce the recent developments in in situ environmental TEM techniques. I sincerely hope that this chapter would be of help to those researchers who come from a background of materials or chemistry and who are interested in the application of TEM characterization. Within such limited space, this chapter could not be exhaustive in covering all TEM-related publications, but would instead put an emphasis on those works published in the last 5 years that are of significant value.

2 Overview

Metallic nanoparticles (NPs) and nanostructured catalysts have traditionally played a critical role in guaranteeing the effectiveness of industrial heterogeneous catalysis [7–11]. The design and synthesis of new nanocatalysts will require fundamental understanding of the relationship between their catalytic properties (activity, stability, selectivity, etc.) and their structure. The need to optimize the catalysts' properties can only be realized by precise control over size, shape, composition, and morphology. The recent development of the aberration correction system has enabled us to probe materials with greatly improved spatial resolution. In addition, atomic-resolution spectroscopic mapping techniques can help researchers understand not only the local structural information but also the elemental and valence information of the materials. I would emphasize the practical applications of these techniques and provide readers with knowledge of the status quo of the state-of-the-art electron microscopy applied to the study of nanocatalysts. After a brief introduction (Sect. 3), I would first review the new developments (Sect. 4) in the TEM techniques for nanoscience: imaging – TEM and STEM; spectroscopy – EDS and EELS; and nanodiffraction/convergent-beam electron diffraction (CBED). Furthermore, the field-emission electron beam source used in the modern TEM may produce ultrahigh beam intensity over the TEM sample, and a discussion on electron beam effect, which might induce a structural change in the metallic samples, will be included. In the second part of key research findings (Sect. 5), I will first introduce some recent publications on the characterization of the metallic nanoparticles in terms of size, crystallography, elemental distribution, facets, and shape control (Sect. 5.1). Then I will review the recent progress in in situ environmental TEM study (Sect. 5.2). Finally, I would summarize this chapter and present future prospects and perspectives on the TEM study of nanocatalysts (Sect. 6).

3 Introduction

Catalytic reactions occur on the surface of individual particles of nanocatalysts. Existing in a range of sizes, shapes, facets, compositions (for multimetallic particles), and phases, nanoparticles have many complicated factors controlling their overall

catalytic properties collectively [10, 11]. Therefore, understanding how to optimize these factors to achieve the desired catalytic properties is the ultimate goal for both industrial and academic researchers. To achieve this goal, one can isolate one factor from the others by studying the chemical reaction of a well-defined bulk surface, and different surface characterization techniques (Scanning tunneling microscopy (STM), X-ray photoelectron spectroscopy (XPS), Low energy electron diffraction (LEED)), etc.) have been used for this purpose. But in most cases, these surface-sensitive techniques need an ultrahigh vacuum (UHV) experiment which differs from the reaction conditions. In addition, using a well-controlled bulk surface may be too simplistic as compared to the complex system of nanocatalysts, for example, they differ dramatically in surface strain, possible reaction sites, and surface chemistry. To solve the first problem, researchers have been striving to operate the characterization techniques in ambient conditions and to develop real-time techniques. As for the second problem, researchers are trying to build model catalyst systems with monodisperse particle size and well-controlled shapes or facets to bridge the gap between surface science and industrially applicable nanocatalysts. On the other hand, the study of model catalysts may give useful feedback to the theory based on surface science. Researchers have proposed the following strategy for the catalysis work:

$$\text{Surface science} \longleftrightarrow \text{Model nanocrystal} \longleftrightarrow \text{Real catalyst}$$

Obviously, to make this a successful strategy, the atomic-resolution characterization techniques and theory/simulation are essential. This chapter will cover the TEM work on the latter two parts in the past several years.

For industrial applications of catalysts, cost is a very important factor that needs to be considered. Since noble metals are widely used for catalysts and for different reactions, catalysts can get slowly corroded; therefore, reducing the amount of noble metals is one of the key problems to be solved for commercial catalysts. One approach to solve this problem is to synthesize a core–shell structure of a bimetallic catalyst, where, at the core, cheap metals are used to reduce the loading of noble metals. For example, in proton exchange membrane fuel cells (PEMFCs), which convert the chemical energy of hydrogen to electricity, the Pt-based core–shell structural electrocatalysts have been developed to reduce the cost and improve the oxygen reduction rate [12]. For other chemical reactions, researchers may improve the properties of catalysts by tuning the composition ratios. Again, the development of nanocomposite heterogeneous catalysts for an improved catalytic activity, selectivity, and durability demands the understanding of its composition, phase, structure, and surface chemistry at the atomic level.

For the ex situ characterization of catalysts, there are several aspects of information that transmission electron microscopy can provide: morphology and size distribution (by TEM/STEM imaging), phase/crystallography (by TEM/STEM, diffraction, and spectroscopy), compositional distribution (by STEM-EELS and STEM-EDS), and chemical information (valence and oxidation states, by EELS). In addition, in situ TEM techniques (imaging and spectroscopy) may give real-time information for either gas or liquid reactions.

4 Experimental and Instrumental Methodology

4.1 Imaging: TEM and STEM

The main goal of electron microscopy imaging is to achieve a resolution exceeding the resolution of the light microscope, since a high-energy electron has a much shorter wavelength. For example, the wavelength of a 200-kV electron is about 0.00251 nm. There are mainly two modes in which TEM works: TEM and STEM. In the TEM mode, a parallel electron beam illuminates the specimen and the interfered image diffraction patterns are formed on the screen. In the STEM mode, the electron beam is focused on a small probe and detectors are used to collect either transmitted or scattered electrons to form images while scanning the electron probe on the sample. STEM-BF imaging offers information similar to TEM-BF imaging. If we collect the STEM-DF signal using a high-angle annular dark-field (HAADF) detector, then the contrast of the image is approximately dependent on the atomic number Z (Z-contrast imaging). The contrast of HRTEM normally needs the help of image simulation to be correctly interpreted, while the contrast of HAADF imaging can be directly interpreted from the mass-thickness (Z-contrast). In addition, using STEM, one can control the electron probe in the area of interest and, therefore, study the local chemistry by EELS or EDS, which provides huge opportunities for the study of nanocatalysts. Since there are already excellent books on transmission electron microscopy [1–3], we would not go into more details about TEM but only discuss some case studies of its application for metallic catalysts.

4.2 Spectroscopy: EELS and EDS

When a high-energy electron beam passes through a thin specimen, it interacts with both the nuclei and the electrons surrounding the nuclei via Coulomb interaction. An inelastic scattering event may happen between the fast electrons and the electron cloud. The fast electrons which lost energy to the atom electrons will give the EELS spectroscopy. In the mean time, the electrons in the inner shell of the atom may absorb a certain amount of energy and excite the conduction band. A hole will be left in that shell and consequently an outer shell electron will transmit to the inner shell with electromagnetic radiation in the form of an X-ray photon (or the excitation of another electron, an Auger electron). EDS is the spectroscopy of the X-ray emitted by the outer electrons.

For compositional analysis, both EELS and EDS can provide local chemical identification, combining with a high spatial resolution of STEM. Generally speaking, EDS is sensitive to heavy elements and easy to be quantified, while EELS is sensitive to light elements and needs special care for quantitative analysis [1, 5, 6]. In the case of metallic nanoparticles, EELS has better detection efficiency when the nanoparticle's size is small (approximately less than 10 nm). However, with the development of highly efficient EDS detectors, which offer maximum collection efficiency with a solid angle of 0.9 srad, elemental mapping using EDS has become

more efficient in the present time. Another important advantage of EELS is that it has a better energy resolution, that is, 0.1 eV, for microscopes with a monochromatic electron source, compared with the resolution of 120 eV for EDS. With this resolution, it is possible to probe the local chemical states (valence, oxidation state, charge transfer) through the near-edge structure of EELS (ELNES), which is an analog to the fine structure of X-ray absorption spectroscopy (XAS) but with a spatial resolution of less than 1 nm.

4.3 Nanodiffraction and CBED

Electron microdiffraction is an efficient tool for extracting information of crystalline structures from submicron regions of materials [6]. Information of defects, strain, and crystal symmetry could be retrieved from regions as small as of nanometer scale. With the sub-nanometer electron probe of the aberration-corrected STEM, it is possible to have the CBED pattern within one unit cell. A combination of STEM and CBED techniques, STEM-CBED, which records the CBED patterns for each pixel during the electron beam scanning, is a promising approach to retrieve information of crystal symmetry, lattice distortion, and elemental distribution from one single scan [13].

4.4 Electron Beam Effect

The electron beam used in a transmission electron microscope (TEM) can cause temporary or permanent change in the surface or bulk structure of a specimen [14, 15]. The electron beam damage can be monitored by either imaging or spectroscopy [16]. We can catalog the damaging effects to the effects from both elastic scattering and inelastic scattering. For metallic materials, the charge induced by incident electrons is delocalized and there is no charge accumulation process. So, the inelastic process (radiolysis effect) is suppressed and elastic scattering plays the dominant role. E_d is the energy transfer that is required for atomic displacement. Only if the energy transferred from the incident electron to the atom is larger than E_d, the atom in the specimen can be displaced (damaged). On the other hand, the elastic process (knock-on effects) involves only certain transfer of energy and momentum from fast electrons to atoms through an elastic collision (not all kinetic energy of fast electrons can be transferred to the atom). The total damage rate depends on acceleration voltage, the atomic number Z, the electron beam dose, and the composition/geometry of the sample [14, 15, 17]. For metallic nanoparticles, the corner atoms may have less bonding with the neighboring atoms; thus, the nanoparticles are observed to be easily damaged compared to the bulk materials. In practice, lowering the electron beam intensity and shortening illustration time (dose rate and dose, respectively) are the two choices to avoid the electron beam damage. In some cases, the electron beam can promote the phase transitions of nanoparticles, and this change can be monitored from the change in either TEM/STEM images or EELS [16, 18].

5 Key Research Findings

5.1 Structural and Chemical Characterization of Metallic Nanocatalysts

Information about the structure and elemental distribution is crucial in understanding the catalytic function of nanoparticles. To take full advantage of the available TEM techniques, it is important to utilize different techniques, which provides a combination of different types of information, to correctly solve intricate scientific problems. In the following text, I will introduce the main approaches for the structural and chemical characterization.

5.1.1 Size Distribution, Phase, and Surface Defects

For heterogeneous catalysts, the catalytically active phase, usually the metal particles, is residing on the surface of the catalyst support, and catalytic reactions often occur on the surface. Therefore, in order to maximize the contact between the catalyst and reactants, it is crucial to increase the surface area of the catalyst. In this regard, we can either incorporate high-surface-area porous catalyst support or develop nanosized catalysts which have close metal–support interaction. During catalytic reactions, metal particles are subject to sintering (agglomerating into large particles) and thus lose their activity. Therefore, controlling the size distribution of nanocatalysts is an efficient way to improve the activity. The particle size (assuming the particle is crystalline in nature) can be calculated from X-ray diffraction by using line-broadening fitting with Scherrer equation, and such results are usually averaged over the entire sample. In comparison, TEM/STEM images provide more localized information, and from TEM/STEM images at proper magnification, one can retrieve the size distribution directly by simply counting the particles with different sizes.

As shown in Fig. 12.1, the size distribution of ZrO_2 NPs are counting from the HAADF images, matching the average particles size estimated from XRD. When counting the particles, different shaped models (such as sphere, square, and oval) can be applied, as soon as they are used for all counting [19]. Software or scripts could be very helpful when counting a large number of particles, such as ImageJ [20]. From the size distribution, the statistical analysis can be performed based on different models. For example, the average number (d), surface (d_s), and volume (d_v) of nanoparticles can be retrieved from the TEM/STEM image using the following equations [21]:

$$d = \frac{\sum_i d_i}{n}; \qquad d_s = \frac{\sum_i d_i^3}{\sum_i d_i^2}; \qquad d_v = \frac{\sum_i d_i^4}{\sum_i d_i^3}$$

In the case of Au nanoparticles on TiO_2 and Al_2O_3 used for the water−gas shift (WGS) reaction, the reaction rate can be correlated with the average Au particle size (d) with a simple power law, as shown in Fig. 12.2. For particles with regular geometries, the surface sites (surface, perimeter, or corner) vary with particle sizes. According to Ref. [22], the WGS reaction rate per total mole of Au for each catalyst

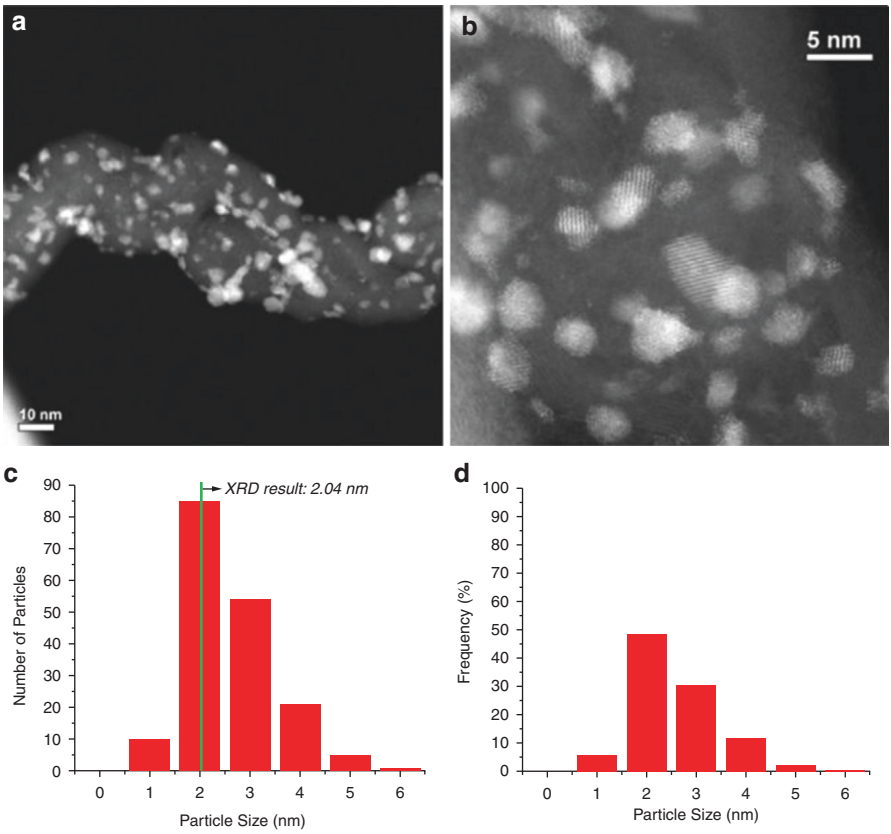


Fig. 12.1 (**a**, **b**) HAADF-STEM images of ZrO_2 nanoparticles on multiwall carbon nanotubes (MWCNT) at different magnifications. (**c**) Particle size number distribution based on several HAADF-STEM images at different regions on the same sample, in comparison to the XRD fitting result (marked with a *green line*). (**d**) Particle size number distribution in frequency (%) (Reprinted with permission from [19], Copyright (2012) American Chemical Society)

is considered to be a sum of rates of the corner sites (in contact with the support), the rest of the perimeter sites (in contact with the support), and the rest of the surface sites (not in contact with the support), according to the following equation:

$$r = \sum [x_c(d)R_c + x_p(d)R_p + x_s(d)R_s]$$

where r is the WGS reaction rate per total mole of Au and x_c(d), x_p(d), and x_s(d) are the fractions of corner, perimeter, and surface sites calculated from a truncated cuboctahedral geometry, respectively. R_c, R_p, and R_s are the turnover rates. From the experimental results of reaction rates for different particle sizes, one can determine that the dominant active sites of Au/Al_2O_3 and Au/TiO_2 catalysts are the low coordinated perimeter and corner sites [22].

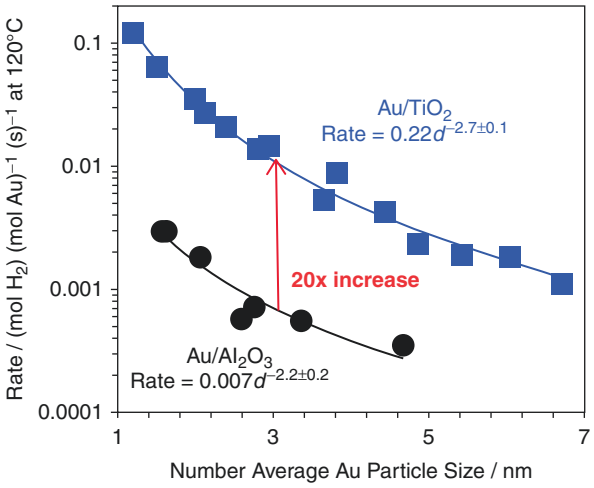


Fig. 12.2 Rate per total mole of Au calculated at 120 °C, 6.8 % CO, 21.9 % H_2O, 8.5 % CO_2, and 37.4 % H_2 for Au/Al_2O_3 (●) and Au/TiO_2 catalysts (■) versus average Au particle size. The vertical dimensions of the points represent the 15 % error associated with rate measurement (Reprinted with permission from [22], Copyright (2012) American Chemical Society)

In the presence of multiple phases or phase transitions, the phase (composition and space group) information is important to understand the nature of catalysts. While EDS and EELS are used to identify the composition, selected area diffraction patterns (SAED) can be used to identify the phases. Within a selected area aperture normally larger than 100 nm (depending on the hardware of the microscope), the selected area diffraction patterns (SAED) are recorded with a CCD camera. As shown in Fig. 12.3, from the SAED of a bimetallic nanoparticle (NP) with a gold octahedron core and a palladium epitaxial shell, two sets of rings are observed [23]. The different radii of the diffraction rings indicate the different lattice parameters of Au core and Pd shell.

Another common method to identify the phase of nanoparticles is to directly measure the lattice constants using atomic-resolution TEM/STEM imaging. As shown in Fig. 12.4, Pt alloy and SnO_2 nanoparticles can be distinguished from their different lattice constants [24]. Remembering that the constants measured from the TEM/STEM images could have a large error depending on the imaging conditions, a calibration with a known structure would be necessary for precise investigation of the phases in the materials. In particular, in HAADF-STEM imaging, there are additional errors of the measured lattice constants from the scanning distortion and sample drifting, although the HAADF-STEM has the Z-contrast feature. A statistical estimation of the scanning distortion is necessary if one tries to quantitatively address the lattice constants directly. Extracted from either SAED patterns or HRTEM imaging, the lattice parameters need to be compared with the standard lattice constants which are from the crystal structure database of bulk materials. It should be noted that there might be a difference of a few percentage between the lattice parameters from nanocrystals and that from bulk materials.

Because of the errors from scanning distortion and sample drifting, the lattice constants measured from HRSTEM imaging are less precise than those acquired

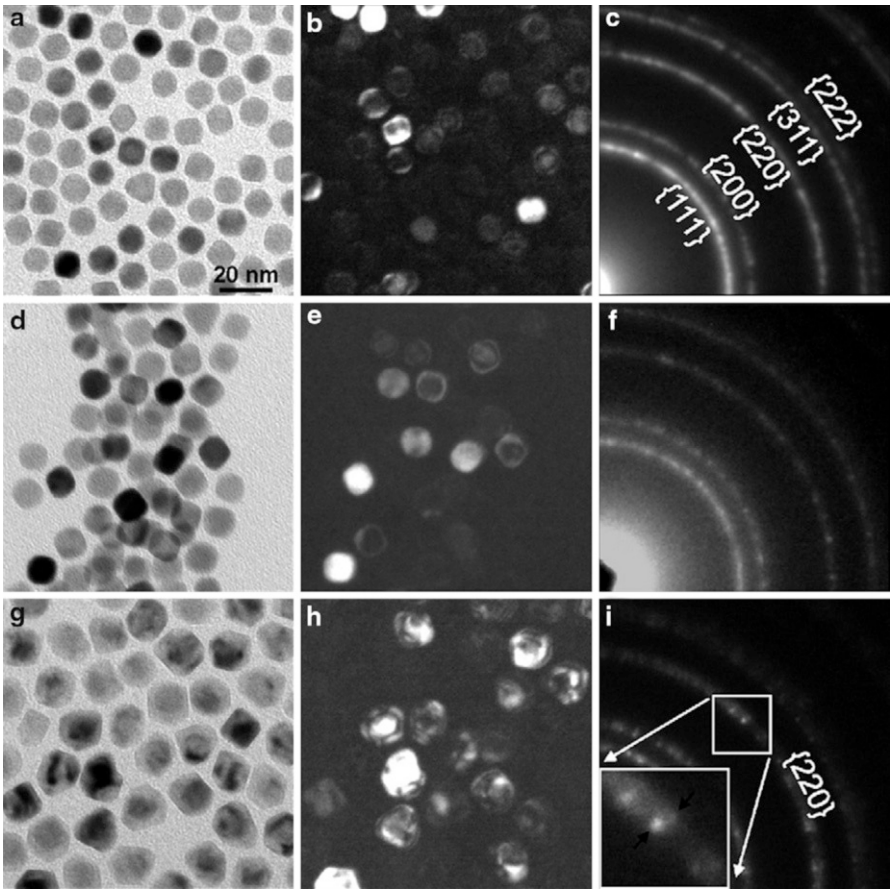


Fig. 12.3 Low-magnification bright-field (*left*) and dark-field (*middle*) TEM images and their corresponding diffraction patterns (*right*) for Au seeds (**a**–**c**) and one layer Pd-coated (**d**–**f**) and ~2 nm Pd-coated (**g**–**i**) bimetallic nanoparticles (Reprinted with permission from [23], Copyright (2010) American Chemical Society)

from HRTEM imaging. For HRTEM imaging, it is possible to retrieve the local lattice distortion (down to 0.03 Å) by geometry phase analysis (GPA) [25, 26]. Figure 12.5 is an example that shows how to quantitatively address the strain field of 17-nm Au fivefold-twinned nanoparticles [26]. Starting from the aberration-corrected HRTEM images, Johnson et al. measured the internal rigid-body rotation of the lattice and the intrinsic strains in the particle. The results show that elastic anisotropy is critical for understanding the strain distributions and the internal structures in the Au decahedral nanoparticles. Since the internal structure of complex structured nanoparticles will determine their growth and stability as well as affect their surface structures, the GPA method may help the researcher obtain the quantitative information for HRTEM/STEM imaging.

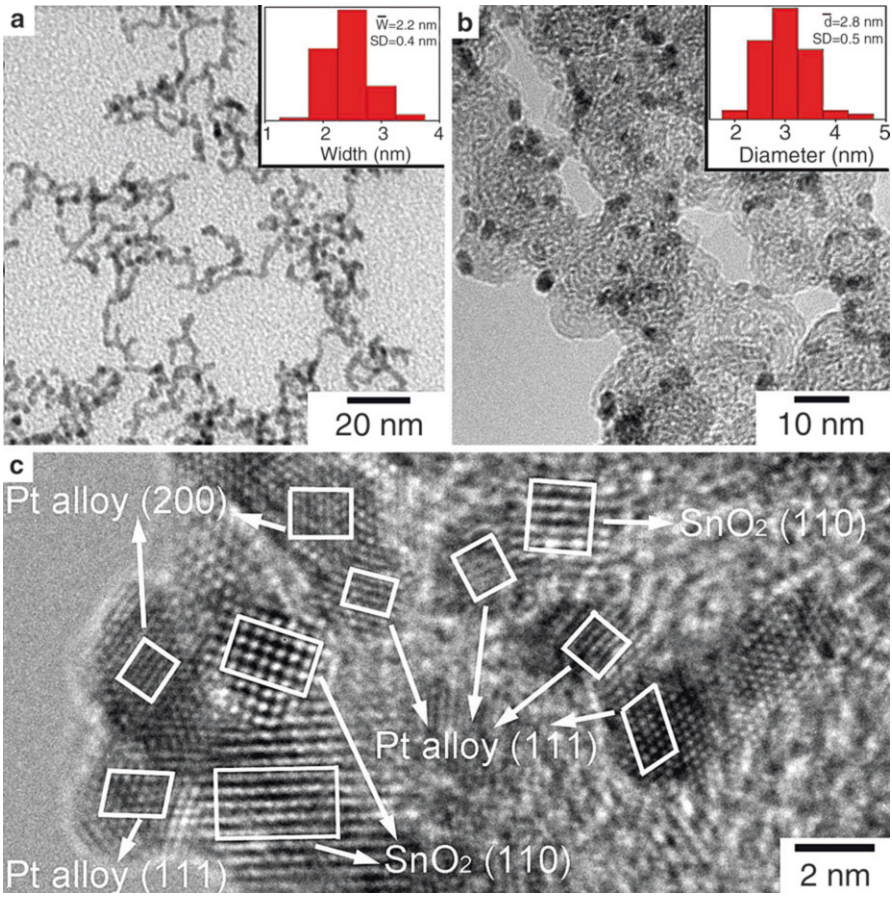


Fig. 12.4 TEM images of (**a**) as-made unsupported $Pt_{52}Rh_{12}Sn_{36}$ and (**b**, **c**) carbon-supported $Pt_{52}Rh_{12}Sn_{36}$ catalyst after thermal treatment (Reprinted from [24] with permission from Royal Society of Chemistry)

Surface defects, including stacking faults and dislocations, may change the electronic structure of surface electrons and then contribute to the activity. For the nanoparticles with Au core and Pd shell [23], HRTEM images along the <110> zone axis reveal the existence of stacking faults at the {111} plane. Shockley partial dislocations (SPDs) are also observed at the interface between Au core and Pd shell to release the strain from the lattice mismatch between Au and Pd. It is found that for the NPs coated with more Pd (>2 nm), the stacking faults still exist, but no SPDs are found. This may be due to the diffusion of Au atoms into the Pd shell layers to eliminate the SPDs. After being annealed at 523 K, the SPD disappeared, possible due to the interdiffusion between Au and Pd (Fig. 12.6).

It was shown above that by combining TEM/STEM imaging and the diffraction pattern, one can investigate the size distribution, phase, and surface defects. Basic

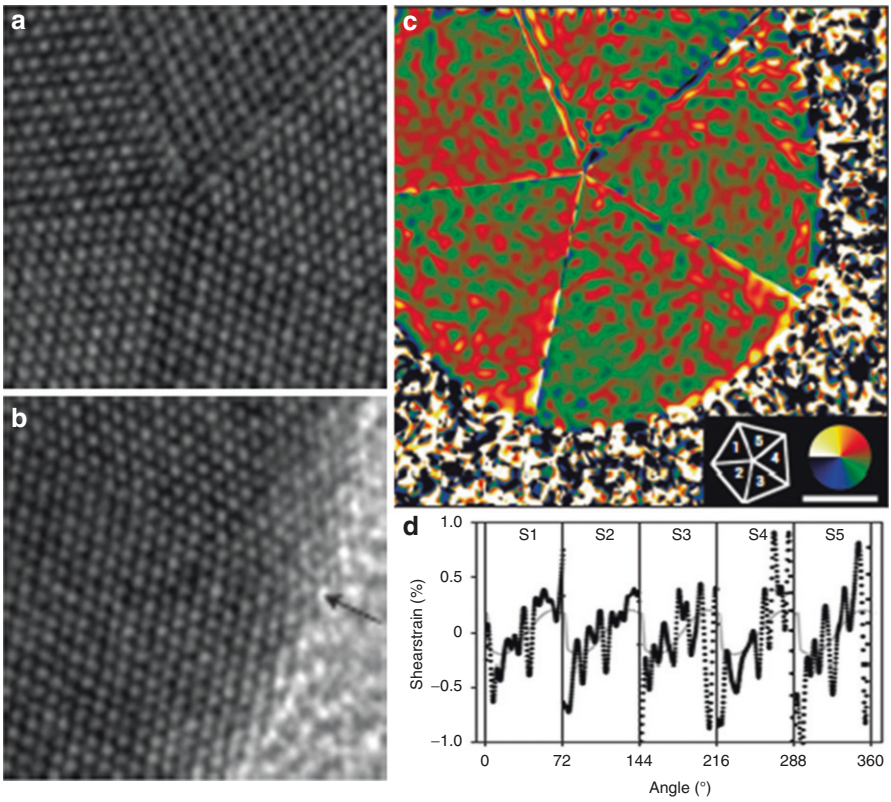


Fig. 12.5 (**a**, **b**) HRTEM images from a core and edge of a 17-nm-radius defect-free decahedral Au nanoparticle, respectively (along <110>). (**c**) The shear-strain map shows the shear gradient across each segment of the decahedral particle. (**d**) The tangential profiles of the measured shear (experimental data: *black circles*) and the shear determined from the finite-element calculations (anisotropic cylinder: *gray solid line*); the numbering *S1–S5* refers to the schematic diagram in the inset in (**c**) (Reprinted from [26] with permission from the Nature Publishing Group)

knowledge on the crystallography, space group theory, and the defect theory is necessary for performing the analysis. However, the information we have above is from a 2D image. Sometimes, we would like to know the 3D feature of the nanoparticles by tilting the sample. In the next part, I will introduce the image reconstruction and electron tomography methods to retrieve the 3D information of nanoparticles.

5.1.2 Shape: From 2D to 3D

As pointed out in previous publications [27–36], the shape of a nanocrystal enables control of its properties and eventually improvement of its usefulness for a given application. Controlling the exposed facets of nanoparticles has long been pursued by many researchers. It is acknowledged that the TEM/STEM images represent a 2D projection of a 3D objective through a dynamical interference process. Although

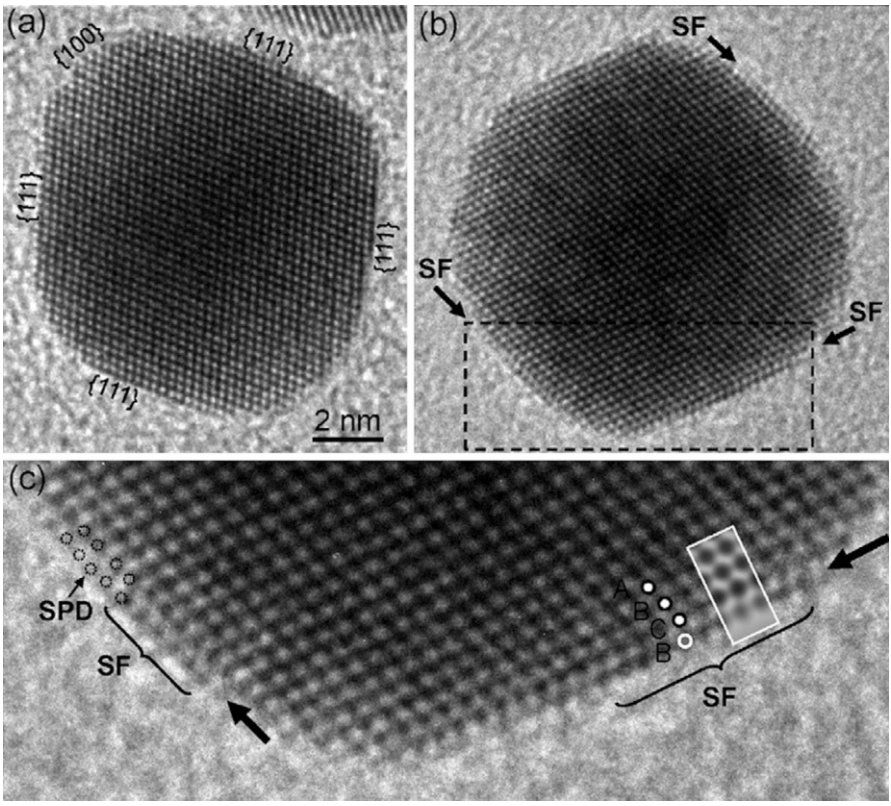


Fig. 12.6 HRTEM images of (**a**) a Au seed and (**b**) a bimetallic nanoparticle coated with a single atomic layer of Pd. (**c**) Magnified HRTEM image of the enclosed rectangular area in (**b**)

the process of electron beam scattering is much more complicated than the process of optical microscopy, after proper data analysis (reconstruction), the 3D morphology (shape, orientation, facet, etc.) of nanoparticles with a regular shape can be directly determined from HRTEM imaging from one or several projections. Exit wave reconstruction allows one to reconstruct the 3D structure from a series of HRTEM images with different focus. For example, as shown in Fig. 12.7 [37], Wang et al. studied the periodic shell structure and surface reconstruction of metallic FePt nanoparticles with an icosahedral structure using HRTEM with focal series reconstruction. Based on the exit wave phase image (Fig. 12.7a) from about 20 lattice images, they constructed an icosahedron model by multiple twinning (MT) of tetrahedrons from ⟨112⟩ to ⟨110⟩ and ⟨111⟩. Figure 12.7c, d shows the simulated images based on the shell growth model and the model relaxed by energy minimization, respectively, both of which prove that the particle is an icosahedral MT particle. With the help of Molecular dynamics (MD) simulation, their results also suggested that the presence of the Pt-enriched shell around the FePt core explains the

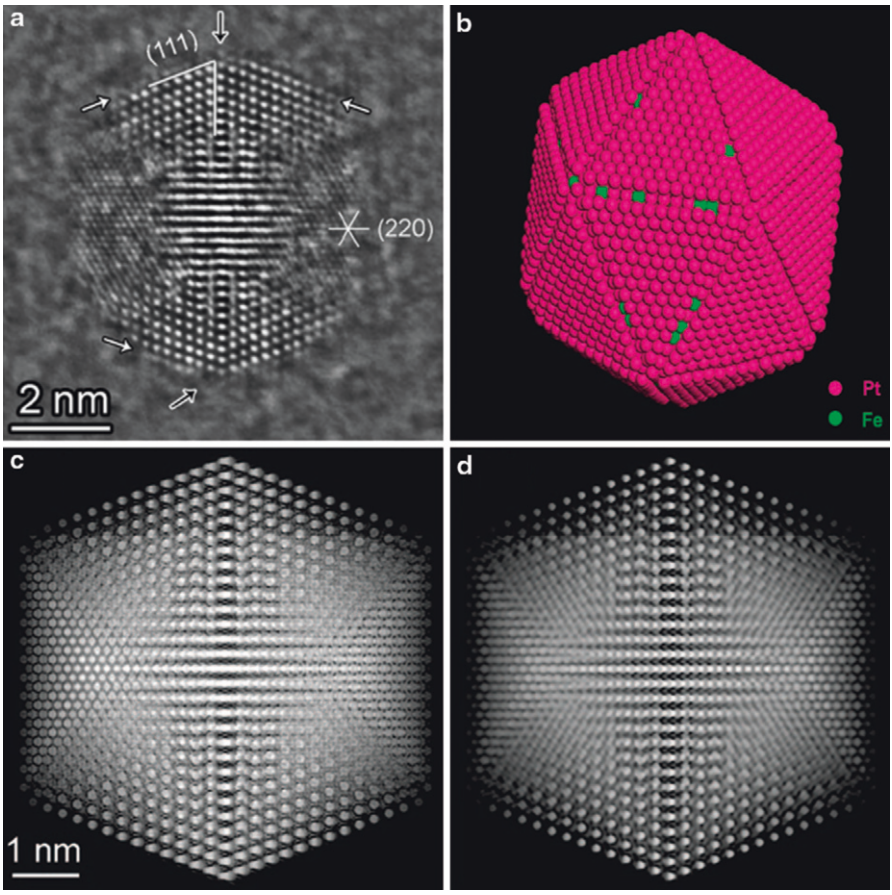


Fig. 12.7 Icosahedron structures of the FePt nanoparticle. (**a**) Experimental exit wave phase image of the same representative FePt nanoparticle. (**b**) Proposed shell growth icosahedron model with 10,179 randomly distributed Fe and Pt atoms. *Red* and *green* circles represent Fe and Pt atoms, respectively. (**c**) Simulated phase image. (**d**) Simulated phase image from the MT model relaxed by energy minimization (Reprinted with permission from [37], Copyright (2009) American Chemical Society)

environmental stability of the magnetic icosahedron and strongly reduces the exchange coupling between neighboring particles [37, 38].

Besides HRTEM imaging, STEM imaging can also be helpful in addressing the 3D morphology [39]. Since the contrast of HAADF-STEM image is directly related to the atomic number Z of the specimen, in the growth of bimetallic nanoparticles, for example, it is possible to distinguish Au cores from Ag shells. As shown in Fig. 12.8, different polyhedrons are produced in the same reaction from a spherical gold seed. These particular {111}-faceted particle shapes are all related in that they consist of 2, 5, and 20 tetrahedral subunits, respectively, separated by twin boundaries [39]. As the bimetallic nanostructures grew, they successively developed twin

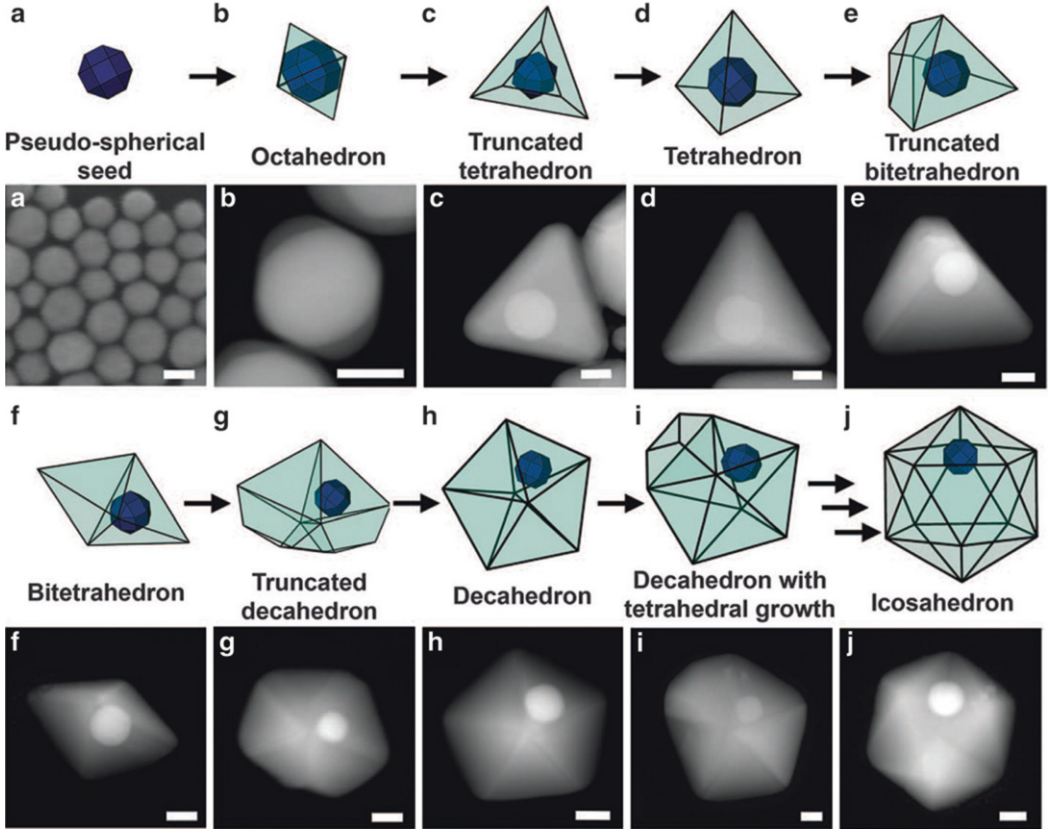


Fig. 12.8 (continued)

structures to form multiply twinned nanoparticles from single-crystalline seeds. Clearly, the STEM investigation performed by Langille et al. reveals the elemental distribution during the growth, benefiting from Z-contrast imaging.

As the spatial resolution of STEM imaging reaches the sub-Angstrom level, it is possible to reveal the 3D structure at atomic resolution. For example, from only two projections, it is possible to reconstruct the 3D structure of a silver nanoparticle embedded in an aluminum matrix at atomic resolution [40]. As shown in Fig. 12.9, Van Aert et al. took HRSTEM images on one single Ag particle from $[10\bar{1}]$ and [100] zone axes, respectively. From each zone axis, the number of atoms on each column is determined from the fitting of Gaussian mixture models. Therefore, a 3D model of Au atoms can be constructed as shown in Fig. 12.10.

TEM 3D electron tomography (ET) has been used for structural biology and crystallography since the 1960s [41]. Recently, electron tomography using Z-contrast imaging in STEM has become highly useful in the study of crystalline inorganic nanomaterials in 3D. Comparing to the TEM-ET, STEM (HAADF)-ET effectively suppresses phase and diffraction contrast, providing image intensities that vary with the projected mass-thickness [42–49]. In order to perform 3D ET, a large number of projections (100–150) are needed and the samples must be rotated at a step of 1°–2° to create a single- or dual-axis tomography tilt series, excepted for a special ET approach is introduced by Ref. [46] using the STEM confocal imaging. The stability of the microscope, the sample tolerance to the electron beam, and the data analysis are important to achieve high spatial resolution of ET. Current resolutions of ET systems are in the 1–20 nm range, depending on the above factors. Figure 12.11 shows the application of ET on a Pt−Co nanocatalyst before and after electrochemical aging. In their study [48], a carbon-coated gold TEM indexed grid is chosen as the working electrode. Pt−Co particles loaded on carbon-black supports are dropped on the TEM grid. The same areas are measured with electron tomography before and after electrochemical aging. By overlaying the reconstructions before and after the aging, one can directly visualize the particle movement and coalescence, as shown in Fig. 12.11(c–f). It is found that the coarsening events were mainly attributed to coalescence but not Ostwald ripening. Obviously, ET is a very useful method which allows us to track, in 3D, the trajectories and morphologies of a nanocatalyst during the reaction.

For Fischer–Tropsch (FT) synthesis, an industrial reaction that converts syngas (a mixture of hydrogen and carbon monoxide) to liquid fuel, the initial reduction of

Fig. 12.8 Models and representative STEM images depicting the proposed growth pathway of a single-crystalline seed in this plasmon-mediated reaction. (**a**) STEM image of the pseudo-spherical single-crystalline Au seeds. (**b**–**j**) STEM images of bimetallic particles with (**b**) octahedral, (**c**) truncated tetrahedral, (**d**) tetrahedral, (**e**) truncated bitetrahedral, (**f**) bitetrahedral, (**g**) truncated decahedral, (**h**) decahedral, (**i**) decahedral with an additional tetrahedral growth, and (**j**) icosahedral morphologies, which were all observed as products of the same reaction. Scale bars: 25 nm. See Fig. S7 for models of a more detailed growth scheme from (**i**) to (**j**) (Reprinted from [39] with permission from the American Association for the Advancement of Science)

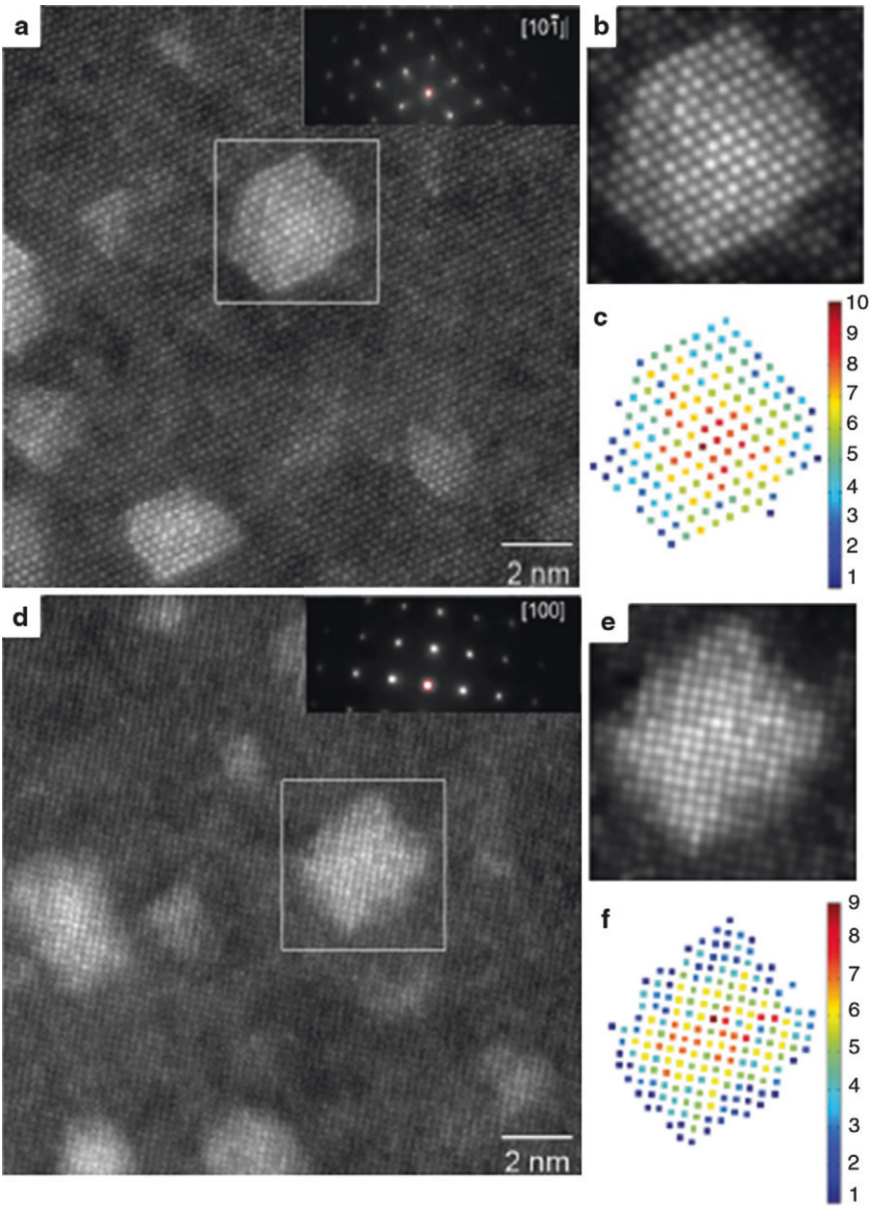


Fig. 12.9 Quantification of HAADF-STEM images. (**a**) Experimental HAADF-STEM image of nanosized Ag clusters embedded in an Al matrix in $[10\bar{1}]$ zone-axis orientation, together with the corresponding electron diffraction pattern. (**b**) Refined model of the *boxed* region in (**a**). (**c**) Number of Ag atoms per column. (**d**) Experimental HAADF-STEM image in [100] zone-axis orientation, together with the corresponding electron diffraction pattern. (**e**) Refined model of the *boxed* region in (**d**). (**f**) Number of Ag atoms per column (Reprinted from [40] with permission from the Nature Publishing Group)

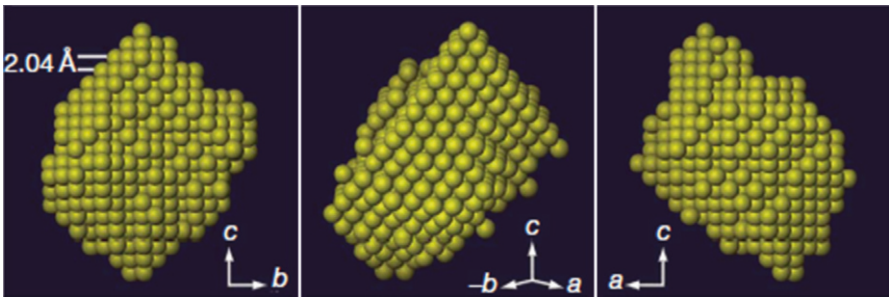


Fig. 12.10 The computed 3D reconstruction of the Ag nanocluster viewed along three different directions (Reprinted from [40] with permission from the Nature Publishing Group)

oxide nanoparticles into metallic catalysts is critical. Xin et al. studied the structure of initial CoO_x/SiO_2 nanocomposites using ET [50]. After recording 73 ADF-STEM images of a single CoO_x/SiO_2 nanoporous particle from −72° to 72° at a 2° interval, the 3D structure of the material was reconstructed as shown in Fig. 12.12. The porous structure is expected to be beneficial to facilitating the infiltration of gas molecules at reaction conditions.

In most cases, the spatial resolution of ET is still larger than 2 nm. To observe further details of the nanocatalysts, one needs to combine ET with other techniques. As shown in Fig. 12.13, morphology and composition are derived from high-resolution STEM image and EELS line scan results, respectively, indicating that the majority of the core material is polycrystalline cobalt monoxide with a trace amount of Co_3O_4 [50]. Electron tomography has much higher spatial resolution than both conventional lensless X-ray microtomography and the newly developed synchrotron-based scanning transmission X-ray tomography. With the anticipation of improved spatial resolution in the near future, a 3D atomic-resolution ET would be the ideal approach for the investigation of the shape, facets, and size distribution for nanocatalysts.

Metal nanoparticles/clusters dispersed on the surface of a porous carrier are widely used in the catalyst industry. In this application, quantitative information on the 3D nanospatial distribution of the metal particles is indispensable to understand the stability of supported nanoparticles as well as the catalytic performance. 3D electron tomography is an ideal tool to solve this problem. As shown in Fig. 12.14, for CuZn nanoparticles on meso-structured silica (SBA-15) used for the industrial production of methanol from synthesis gas ($CO/CO_2/H_2$), ET can reveal not only the hexagonal arrangement of the catalyst mesopores but also the size, shape, and location of the individual Cu nanoparticles [51]. With an image analysis, it is found that frequently occurring events, and probably corrugation of the pore walls, add to the stabilization of the shape. In the above case, the stability of the supported catalysts depends not only on the individual properties of the catalytic nanoparticles, such as the particle size, but also on the collective properties, such as their relative spatial location.

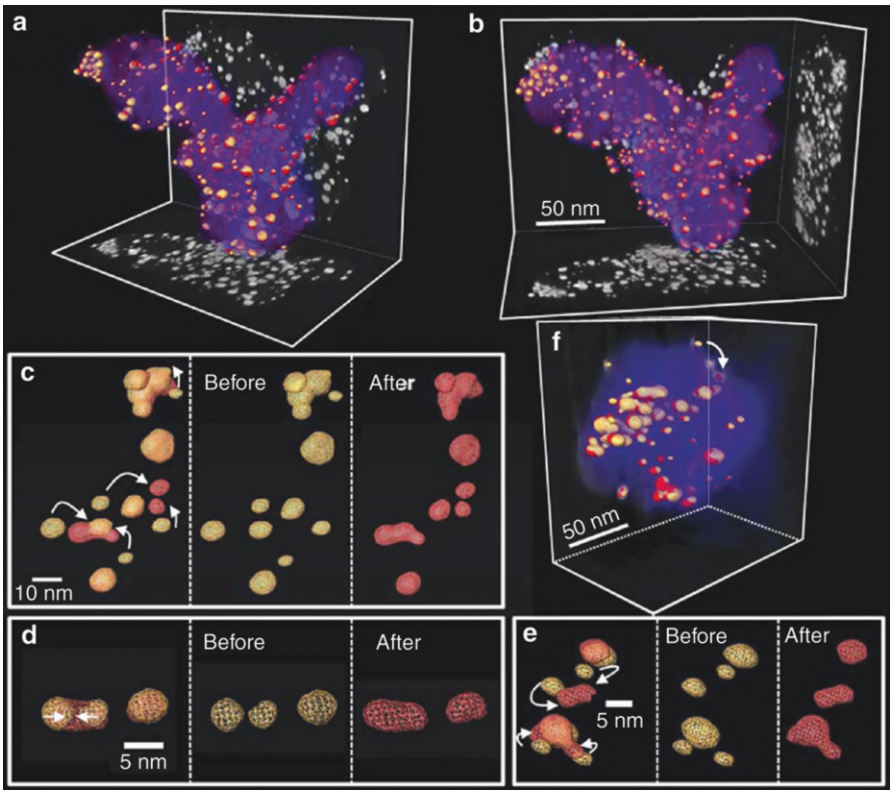


Fig. 12.11 One-to-one correspondence of nanocatalyst particles before (*gold*) and after (*red*) electrochemical aging, and the same color scheme is used in all figures. (**a**) A 3D reconstruction of nanocatalyst particles, on the carbon support (*violet*) with projected 2D images shown on each side. (**b**) Alternate viewing angle. (**c**–**e**) Several instances of nanocatalyst particle coalescence and migration, with particle positions indicated by *arrows*. (**f**) One example of cropped volume from (**a**, **b**), showing how one nanocatalyst particle moves into the positive curvature (valley) from the negative curvature (summit) of the catalyst support. The *arrow* points out the trajectory of the particle movement. *Violet shading* is the carbon support (Reprinted with permission from [48], Copyright (2012) American Chemical Society)

5.1.3 Elemental Distribution by STEM techniques

The elemental distribution can affect the performance of nanocatalysts, that is, the core–shell noble catalysts [52–68]. As mentioned in the previous part (Sect. 4.1), the STEM working mode allows one to control the electron probe to probe the local area. Therefore, by combining with the spectroscopy methods (EDS or EELS), one can retrieve the chemical information of the materials at an atomic scale (at 2D) [54–65]. On the other hand, the contrast of HAADF-STEM imaging is propositional to the atomic number Z and, thus, can provide the information of elemental distribution for the two elements with a large difference in Z. In the atomic-resolution STEM image in Fig. 12.15, two Pd(core)–Pt(shell) nanoparticles with

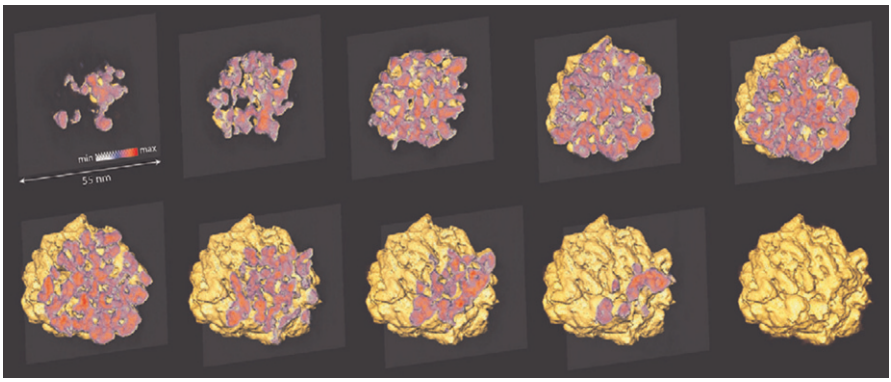


Fig. 12.12 3D tomographic reconstruction of an as-prepared CoO_x/SiO_2 nanocomposite. The progressing cross sections and the isosurfaces visualize the internal structures of the porous CoO_x core (Reprinted with permission from [50], Copyright (2012) American Chemical Society)

one and four Pt layers, respectively, are imaged using a Hitachi-2700C dedicated STEM with a CEOS probe corrector [54]. With the help of image simulation, one can identify the thickness of the layer as well as the structure of the nanoparticles. However, this reconstruction by HRSTEM imaging would only work when the shape of the nanoparticles is regular and so a reasonable model can be built. Otherwise, the thickness may also yield a change of contrast.

In the general case of the multimetallic nanocatalysts, one should use the high-resolution STEM-EELS or STEM-EDS method to probe the elemental distribution. With the modern STEM system, it is possible to simultaneously collect the ADF signals from the ADF detector and particular elemental signals from the EELS/EDS detector. By scanning the electron probe on the nanocatalyst, with the modes of line profile (1D) or mapping (2D), one can obtain the elemental distribution. Obviously, the spatial resolution of the line profile or mapping is decided by the step of scanning or the probe size whichever is bigger. The signal-to-noise ratio (SNR) of the final mapping depends on the collection time, energy dispersion, and electron beam current for a certain EELS/EDS detector. However, the increase in the collection time and electron beam current will increase the electron beam damage on the specimen. The experimental parameters for STEM-EELS/STEM-EDS collection as well as the method of STEM-EELS or STEM-EDS need to be carefully chosen according to the element of interest, the sample geography (size, support, shape, etc.), and the acceleration voltage of the microscope. The first case we show here is of the 4-nm $Fe_{43}Pt_{37}Au_{20}$ nanoparticles (NP) developed for the purpose of promoting formic acid oxidation reaction (FAOR) [55]. Synthesized from a high-temperature solution-phase reaction, monodisperse binary FePt NPs have the chemically disordered face-centered cubic (fcc) structure, in which Fe and Pt atoms randomly occupy the fcc crystal lattice. After being further annealed, the fcc structure can be converted into the chemically ordered face-centered tetragonal (fct) structure, in which Fe and Pt atoms form alternating atomic layers stacked

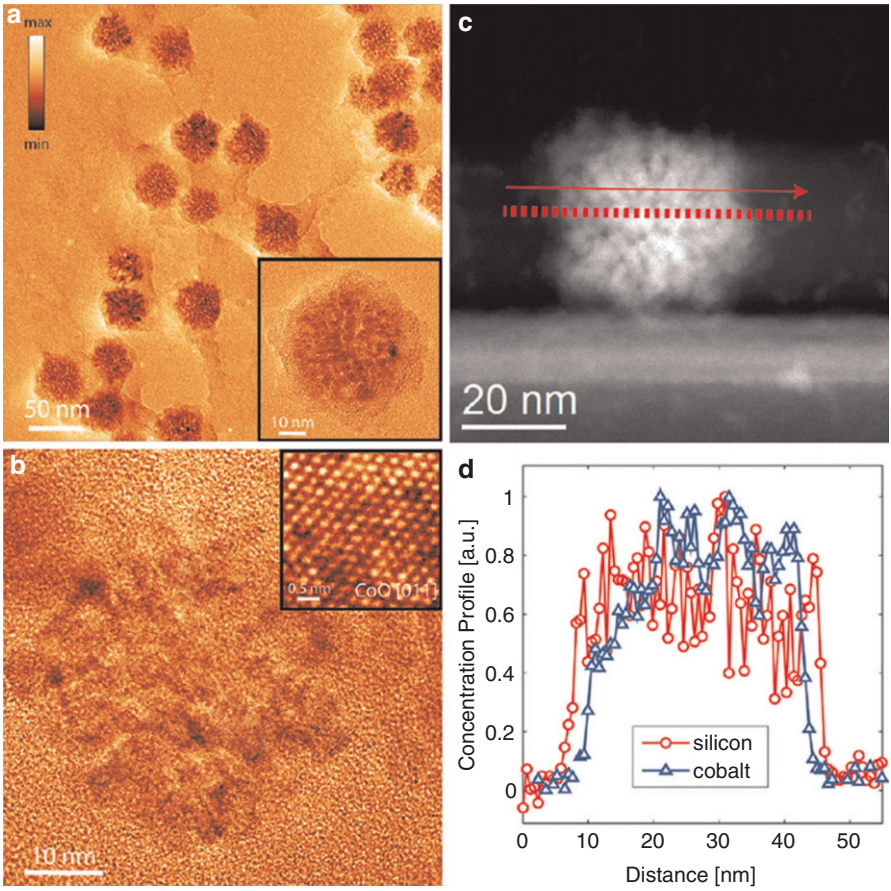


Fig. 12.13 Morphology and composition of as-prepared CoO_x/SiO_2 nanocomposites. (**a**) Bright-field TEM image of the nanocomposites. (**b**) High-resolution TEM image of a CoO_x/SiO_2 particle. (**c**) ADF-STEM image of a CoO_x/SiO_2 nanocomposite. The EELS line profile was recorded along the *dashed line*. (**d**) Extracted silicon and cobalt concentrations along the line profile in (**c**). Silicon concentration was integrated from the Si $L_{2,3}$ edges. Cobalt concentration was integrated from the Co $L_{2,3}$ edges (Reprinted with permission from [50], Copyright (2012) American Chemical Society)

along one specific direction. In addition, the presence of Au in FePtAu facilitates FePt structural transformation from fcc to fct, with Au segregating on the fct-FePt surface. It would be interesting to know the elemental distributions for FePtAu NPs. These NPs are directly dispersed on the ultrathin carbon Cu grid for TEM. These 2D mappings at 48 × 48 pixels were collected with an energy dispersion of 0.5 eV/ch and a 1.3 Å electron probe at ~70 pA using a Hitachi-STEM at 200 kV, as shown in Fig. 12.16a–h [55]. The distribution of Fe for fcc and fct NPs is identified from their EELS Fe $L_{2,3}$ edges as well as the simultaneous ADF signals which represent the collective signals from Au, Pt, and Fe. It is found that Fe in the fcc structure is

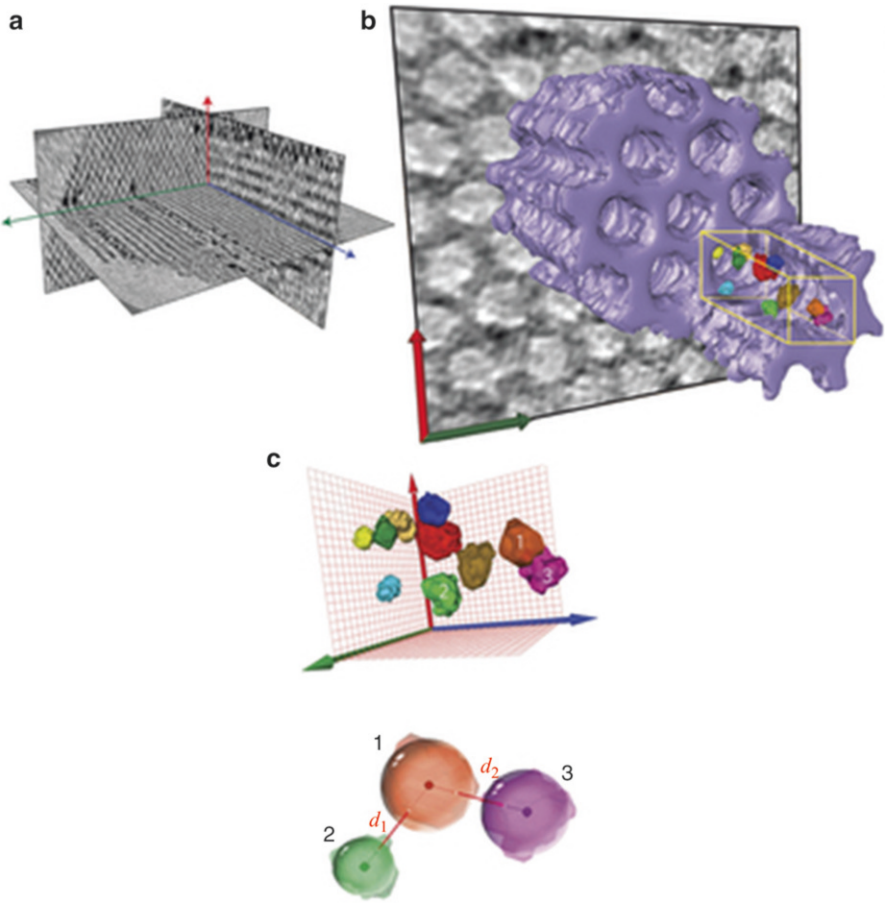


Fig. 12.14 (**a**) Orthogonal cross sections through the 3D reconstructed tomogram of a representative particle of a nanostructured catalyst. The SiO_2 pore walls are *gray* and the metal nanoparticles appear as *black spots*. (**b**) 3D-rendered volume obtained by image segmentation showing the hexagonal arrangement of the catalyst mesopores as well as details of the internal corrugation of the silica pore walls. One of the reconstructed mesopores has been partially sectioned to visualize the individually segmented Cu nanoparticles. (**c**) 3D view of the isolated Cu nanoparticles extracted from the volume indicated with a *yellow frame* in (**b**). The approximation of the metal particles by volume-equivalent spheres centered at their center of gravity and the derivation of surface-to-surface interparticle distances are schematically depicted (Reprinted from [51] with permission from the Nature Publishing Group)

uniformly distributed, and, in contrast, Fe is concentrated in the core region in the fct NP [55]. Since the core-loss signals ($M_{4,5}$) of Pt (2,122 eV) and Au (2,206 eV) are too close and overlapped, we apply a STEM-EDS line scan on these NPs, confirming that Au alloys uniformly with Fe and Pt in the fcc NPs (Fig. 12.16i), but in the fct structure it diffuses out and concentrates around the shell (Fig. 12.16j). Composed of a surface rich of Au in fct NPs, this material has a mass activity of

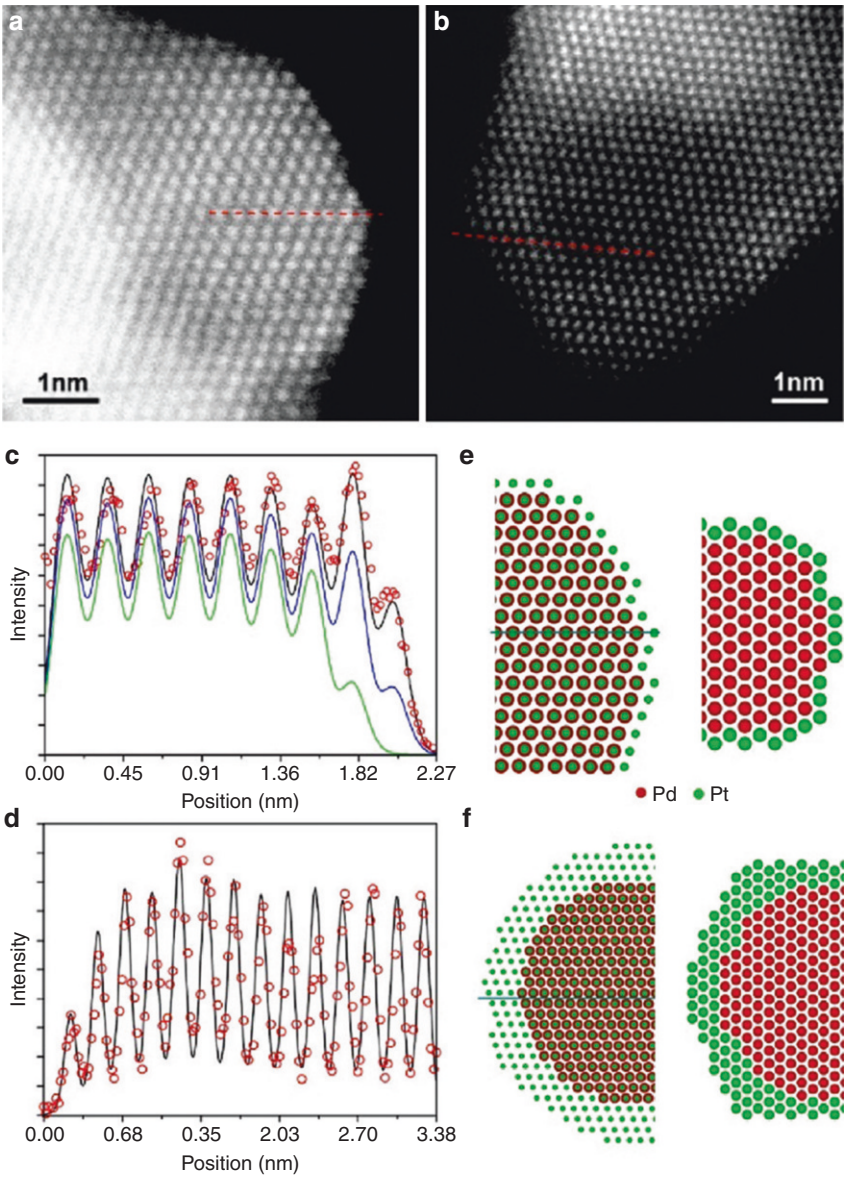


Fig. 12.15 (**a**, **b**) HAADF-STEM images of the Pd(core)–Pt(shell) nanoparticles with one and four Pt layers, respectively. (**c**, **d**) Intensity profiles from the scan lines in (**a**) and (**b**), and the best fits (*black lines*), based on the structure models shown in (**e**) and (**f**) for Pd particles with one and three to four Pt surface layers, respectively. (**e**) Projection of the one-Pt-layer core–shell structure model along the [101] direction (*left*), and the atomic arrangement (*right*) of the (1-1-1) plane at the position indicated by the *line* on the *left*. (**f**) Projection of the structure model with four Pt layers on the STEM image plane (*left*) and the arrangement of atoms in the vertical columns along the scan line (*right*) (Reprinted with permission from [54], Copyright (2009) American Chemical Society)

2809.9 mA/mg Pt and retains 92.5 % of this activity after a 13-h stability test which is superior to other Pt, FePt, and FePtAu NPs.

In another case of the Pt_3Co electrocatalyst, the STEM-EELS method is applied to address the change of elemental distribution after voltage cycling [56]. Using an aberration-corrected Nion STEM with a 1–1.4 Å electron probe at 100 kV, distributions of Pt and Co can be obtained from 2D mappings with 64 × 64 pixels or more. In this mapping, it was found by using a multivariate curve resolution (MCR) method that the minor Pt N edge (518 eV) can be used to map Pt with an enhanced SNR. As shown in Fig. 12.17, the as-received Pt_3Co NPs have a Pt shell of 0.6 nm. After 30,000 voltage cycles, the thickness of the Pt shell increases to 2.3 nm while the average Pt–Co particle size increases from 3.7 to 5.1 nm. After a statistical measurement of the elemental distribution before and after voltage cycling, it is concluded that both Ostwald ripening and coalescence are significant contributors to the reduced surface area/mass of Pt with approximately half of the larger particles having undergone coalescence.

The interface between catalysts and support is believed to be important since the electronic structure originating at cluster–support interfaces can significantly affect the kinetics of catalytic reactions [69, 70]. Using STEM-EELS, one can directly probe the local electronic structure at the interface. Figure 12.18 demonstrates the application of STEM-EELS for the characterization of interfacial charge transfer between these Au NPs and their [−110] TiO_2 support [70]. Ti L edges of Fig. 12.18d (green) show restoration of the interfacial Ti atoms to an electronic state resembling that of bulk TiO_2 (Ti^{4+}). It is suggested that calculation of the integrated area under the curve provides a quantitative measurement of charge transfer from the substrate to the nanoparticles at the Au–TiO_2 interface.

5.1.4 Other TEM Techniques

In this part, I would introduce two TEM techniques that have not been discussed above, high-resolution secondary electron microscopy (SEM) imaging and diffractive imaging, which are less popular for studying metallic nanocatalysts because their technical requirement is demanding. However, these techniques may provide some unique information and may be of potential importance to characterize nanocatalysts.

STEM-SEM has been used to image nanoparticles since the late 1980s [71, 72]. However, no atomic-resolution STEM-SEM images had been collected until the invention and development of aberration correction in recent years. Spherical-aberration correction allows a reduction of the probe diameter and an increase in the probe current concurrently by increasing the numerical aperture of the lens. Figure 12.19 shows a pair of SEM and ADF images of Pd particles on a carbon support, taken by the Hitachi-2700C STEM in Brookhaven National Laboratory, which has a SEM detector as well as an ADF detector equipped in the column [73]. It is observed that the SEM image offers a better 3D view of the area. As shown in Fig. 12.20, individual uranium atoms are seen from the STEM-SEM image of uranium oxide nanocrystal sample. A STEM-SEM image has a comparable spatial resolution with the simultaneously taken ADF-STEM images, although it has high noise. A possible mechanism for atomic-scale SEM imaging is proposed [74]. Although the

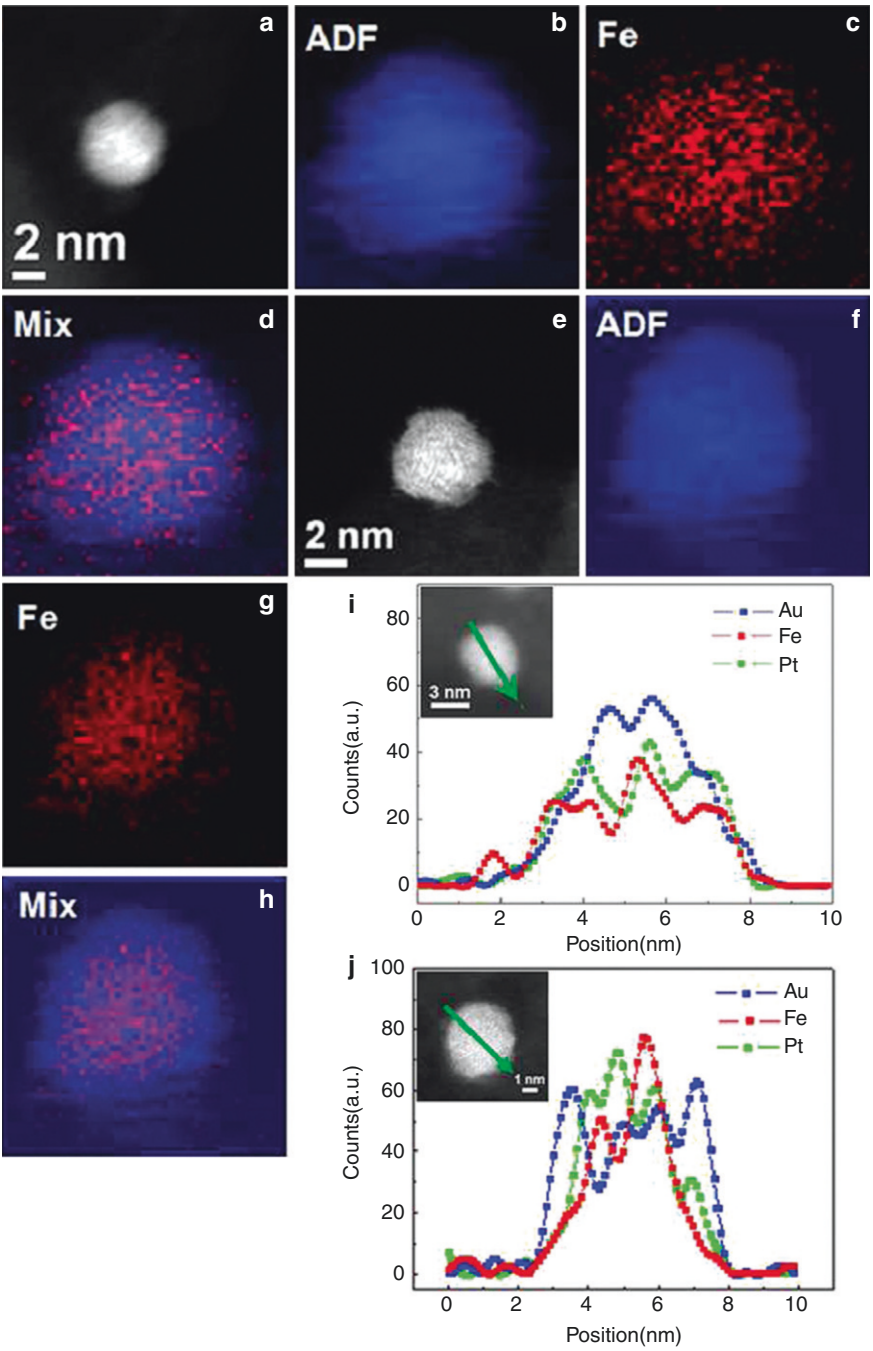


Fig. 12.16 (**a**) STEM imaging and (**b**–**d**) simultaneous 2D STEM-EELS mapping from a representative fcc-$Fe_{43}Pt_{37}Au_{20}$ NP. (**e**) STEM imaging and (**f**–**h**) simultaneous 2D

technique is still under development, the ultrahigh-resolution SEM technique potentially could be important for identifying the surface structure of nanoparticles.

Diffractive imaging has the potential to succeed in the structure determination of single nanoparticles using an electron probe. The principle of diffractive imaging is based on coherent diffraction of an isolated object and recording of diffraction patterns at a spatial frequency (f) smaller than the reciprocal of the object size ($1/S$) [75]. In the diffraction pattern, the oversampling increases the amount of information about the object recorded. In principle, if the smallest spatial frequency that can be recorded in an experiment is $1/L$, where L is the coherence length, the maximum oversampling ratio will be $(L/S)^n$. To increase the spatial resolution, one can incorporate the information from a TEM image and its corresponding diffraction pattern to obtain a higher-spatial-resolution image. As shown in Fig. 12.21, Huang et al. has demonstrated the spatial resolution improved from 3.3 to 0.78 Å in a 7-nm CdS particle [76]. This method is promising to achieve an ultrahigh resolution for imaging the 3D atomic structure of single nanoparticles, with the help of diffraction patterns.

5.2 In Situ Environmental TEM Study on Nanocatalysts

In this section, I would like to introduce the environmental TEM approaches to study the gas and liquid reactions in situ developed in recent years.

5.2.1 In Situ Environmental Reaction in TEM: Gas Reaction

The study on the reaction at the gas–solid interface in situ with TEM would give the direct mechanistic information on how catalysts work [50, 77–85]. This has been a long-standing goal and challenge for the TEM community [77, 78]. One challenge is, since the high-energy electron beam requires a high vacuum in TEM, when the gas is introduced into the specimen area, the high vacuum of TEM still needs to be retained. There are two methods to solve this problem technically: by using differentially pumped vacuum systems and by using windowed cells. The details of these two approaches can be found in Refs. [81] and [86]. Figure 12.22a shows a schematic diagram of a differentially pumped TEM column [81]. The function of differentially pumped vacuum systems is to keep a high vacuum at the electron source while the gas is pumped into the sample area. Between the electron source and the specimen area, there are three turbo pumps working to keep the pressure difference between them. A pressure difference as high as of the order of 10^6 can be reached by the FEI-Titan environmental TEM (E-TEM). Figure 12.22b shows a picture of a differentially pumped vacuum system. Obviously, the integrated pump system would increase the complexity of the TEM

Fig. 12.16 (continued) STEM-EELS mapping from a representative fct-$Fe_{43}Pt_{37}Au_{20}$ NP. (**i**, **j**) STEM-EDS line scans crossing fcc-$Fe_{43}Pt_{37}Au_{20}$ (**i**) and fct-$Fe_{43}Pt_{37}Au_{20}$ (**j**) NPs. The *insets* show the scanned NPs (Reprinted with permission from [55], Copyright (2012) American Chemical Society)

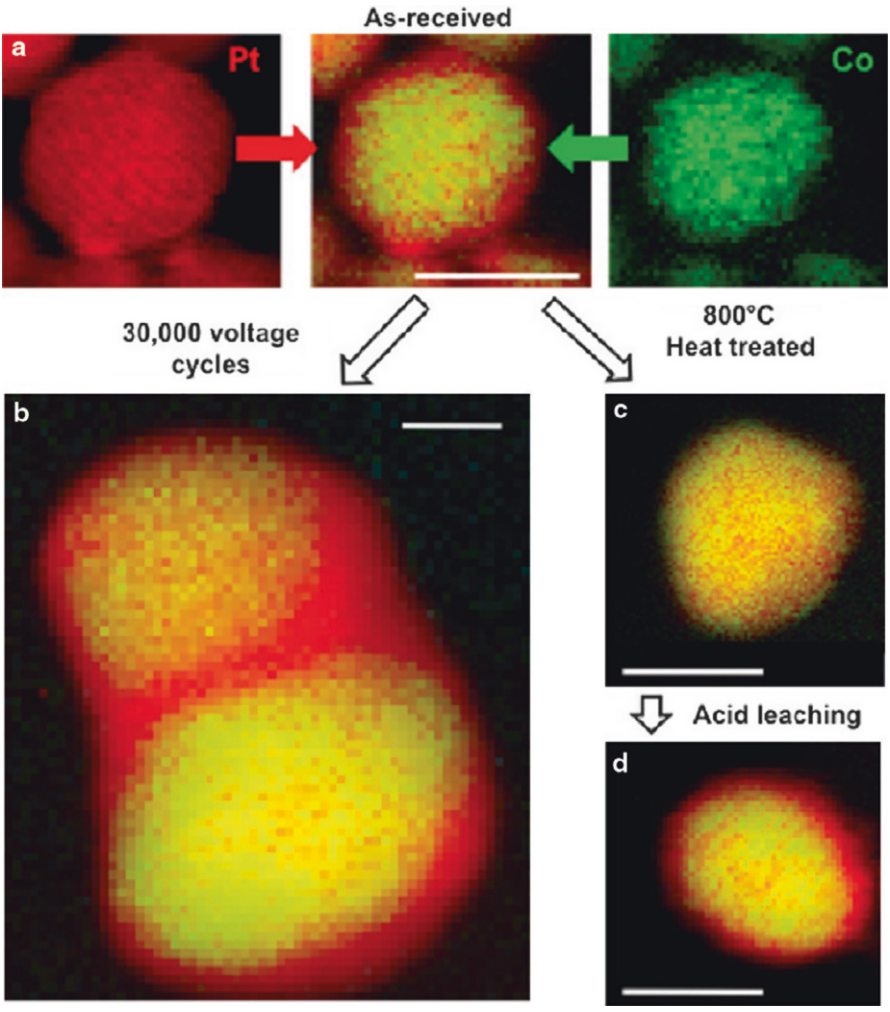


Fig. 12.17 Typical EELS spectroscopic images of Pt−Co nanoparticles for the chemical and electrochemical processes studied here. The relative Pt concentration is shown in *red* and the Co concentration in *green*, and so *yellow* indicates a Pt−Co alloy. The *stripes* in the Pt image of (**a**) are <111> lattice planes viewed at a slight mistilt. (**a**) As-received, showing a 0.6-nm Co-free shell, (**b**) after 30-K voltage cycles, showing a coalescence of two smaller Pt−Co nanoparticles surrounded by a Co-free shell ~2−3-nm thick, (**c**) after heat treatment of the as-received material, leading to a uniform Co distribution and no Co-free shell, and (**d**) after acid-leaching the heat-treated sample, where a Co-free shell similar to that of the starting material (**a**) has returned. The scale bar for each image is 5 nm (Reprinted with permission from [56], Copyright (2012) American Chemical Society)

system, and vibration introduced by the gas flow or the pump system may reduce the spatial resolution. Even with these drawbacks, the current E-TEM can reach an atomic resolution at high temperature and gas atmosphere of a few thousand pascals.

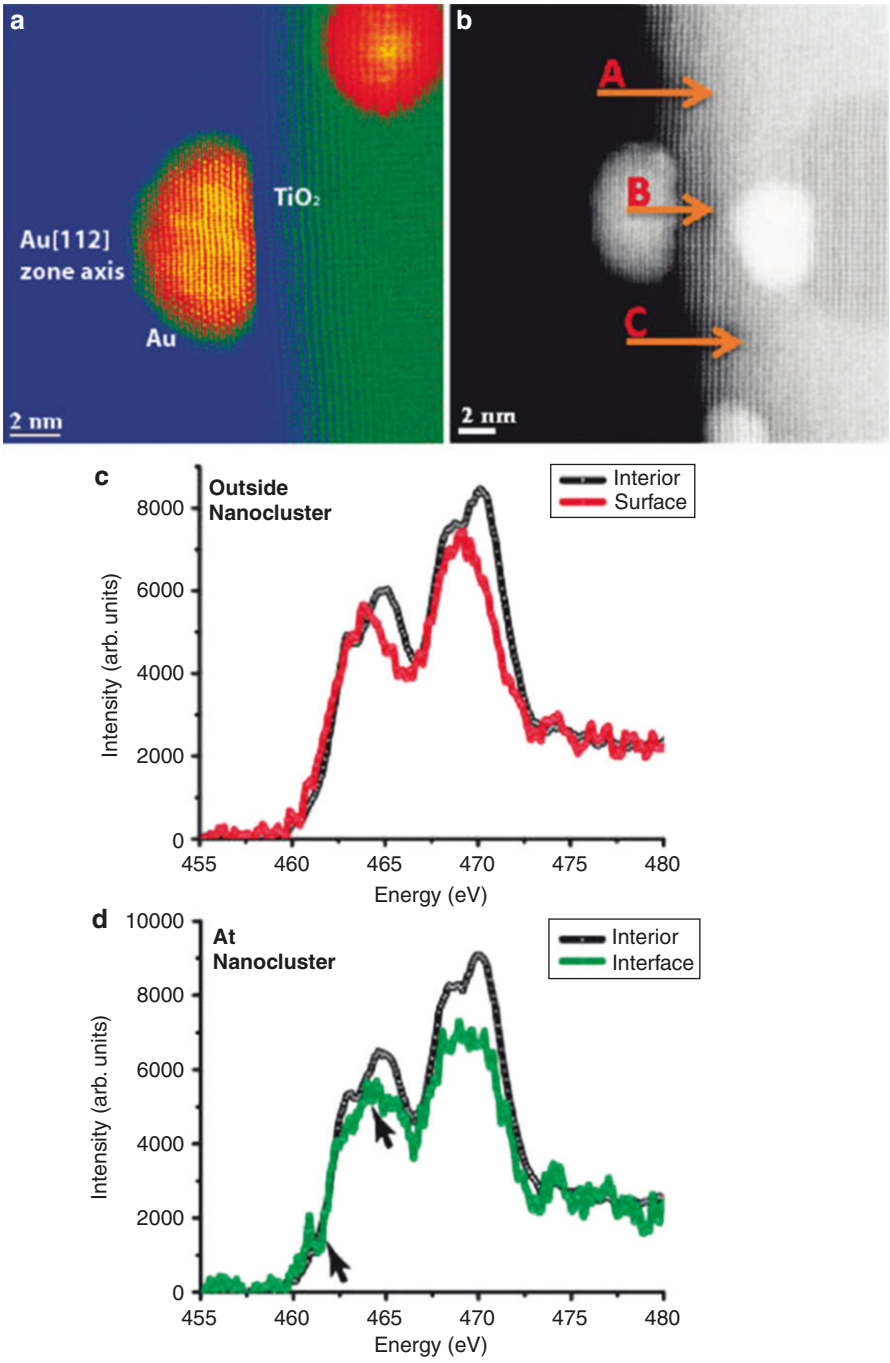


Fig. 12.18 (**a**, **b**) Au nanoclusters on (−110) TiO_2. (**c**, **d**) EELS spectra for the regions (*arrows*) scanned in (**b**) (Reprinted with permission from [70], Copyright (2010) American Chemical Society)

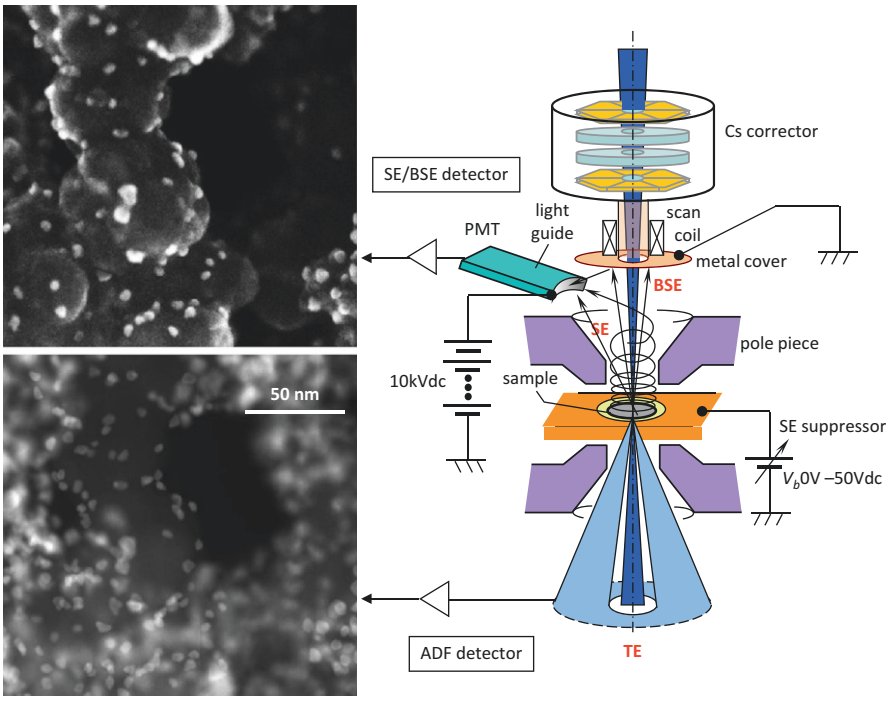


Fig. 12.19 Overview of the experimental setup for the simultaneous acquisition of SEM and STEM images. (**a**) The image pair (raw data) of Pd nanoparticles on a carbon support. The SEM image using secondary electrons (SEs) and BSEs is at the *top* and the STEM image using transmitted electrons (TEs) with an ADF detector is at the *bottom*. (**b**) A schematic of the instrument. *PMT* photomultiplier tube (Reprinted from [73] with permission from the Nature Publishing Group)

For the CoO_x/SiO_2 nanocomposite system [50], annealing at 300 °C in the vacuum of TEM would not change the morphology of the particles (Fig. 12.23). After annealing for 1.75 h in 15 mtorr H_2 gas, significant changes in morphology have been observed. With the increase in the temperature, the nanocomposites keep getting deoxidized – $CoO_x \rightarrow$Co metal, as determined from the Co $L_{2,3}$ edges of EELS – and the size of particles also increases. At 600 °C, the cobalt oxides convert to metallic cobalt completely. The surface-to-volume ratio and the reduction fraction can be calculated from the experimental data further to find the optimal reduction temperature for this experiment. It needs to be noted that the electron beam damage at high temperature and ambient environment would be more severe than that at normal imaging conditions. To minimize or completely exclude the beam effect, one needs to reduce the illustration time and beam intensity and perform a control experiment at room temperature or without gas. Apart from this, E-TEM allows the researchers to study the chemical reaction at high spatial resolution and obtain unique information about their materials.

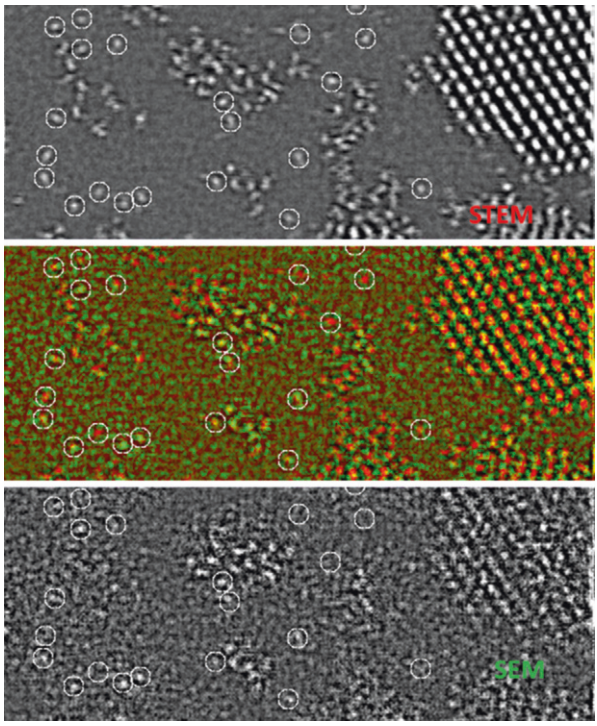


Fig. 12.20 Secondary electron image of U atoms: Uranium single atoms (*circled*) and small clusters imaged simultaneously using a scanning probe to produce forward scattering (*top*) and backward scattering (*bottom*). *Center panel* shows superimposition of the two in *red* (STEM) and *green* (SEM). Spots (*red*) present in ADF but absent in SEM are presumed to be on the bottom of the substrate. Profiles of single-atom spots show that the Full width at half maximum (FWHM) in the ADF image is 0.08 nm, whereas that in the SEM image is <0.1 nm (Reprinted from [73] with permission from the Nature Publishing Group)

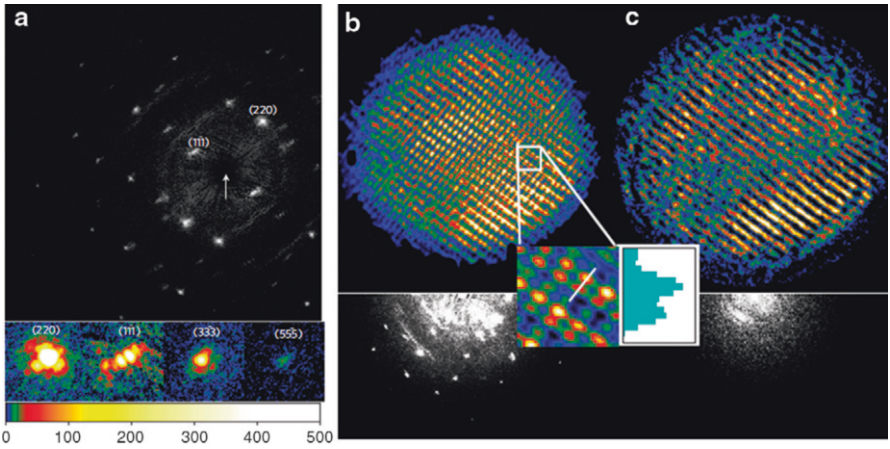


Fig. 12.21 (**a**) Part of an electron diffraction pattern after background subtraction of a CdS nanocrystal of 7 nm diameter in the [112] cubic orientation. The intensity distributions of selected diffraction spots are shown below. The index is based on the hexagonal wurtzite structure of CdS. (**b**) The reconstructed image using information from the starting image (**c**) and the diffraction pattern of (**a**) and its power spectrum (*bottom*). (**c**) Starting electron image with lattice fringe contrast (*top*) and its power spectrum (*bottom*) (Reprinted from [76] with permission from the Nature Publishing Group)

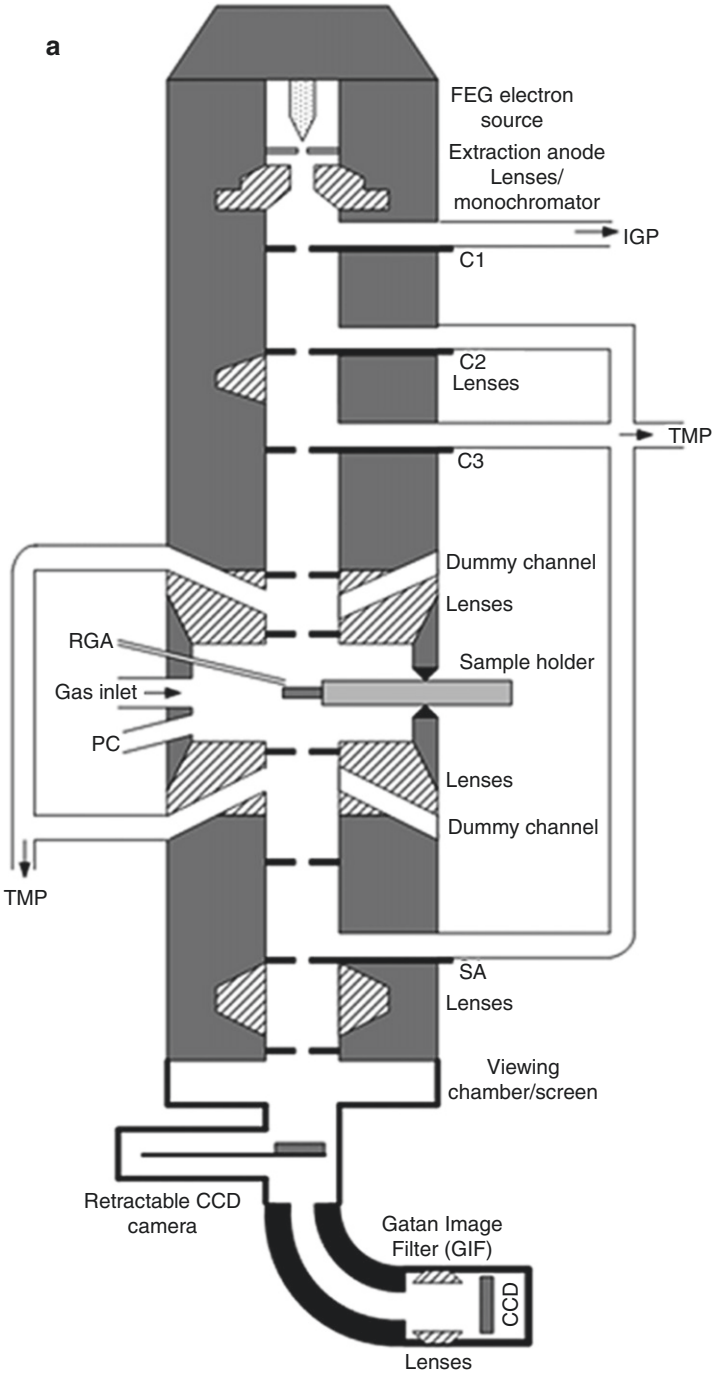


Fig. 12.22 (continued)

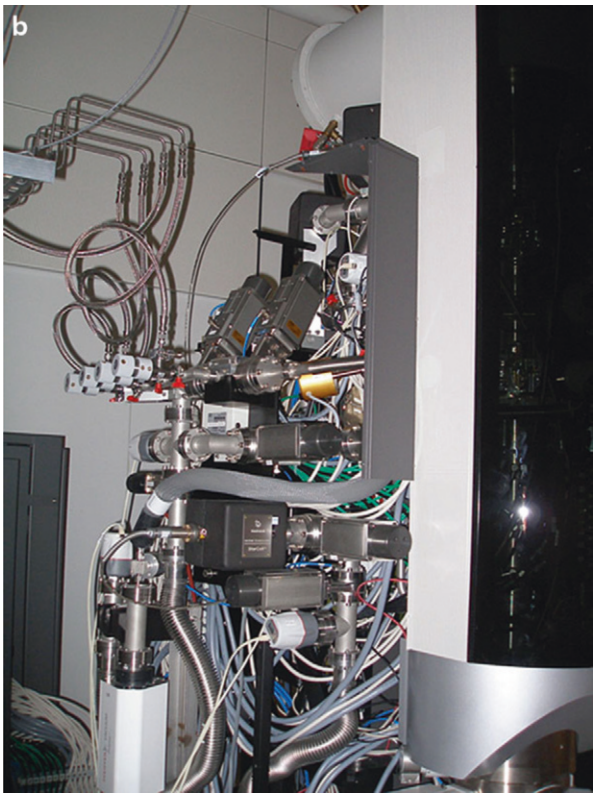


Fig. 12.22 (**a**) Schematic diagram of a differentially pumped TEM column. C1, first condenser aperture; *FEG* field-emission gun, *IGP* ion getter pump, *TMP* turbo molecular pump, *RGA* residual gas analyzer, *PC* plasma cleaner, *SA* selected area aperture (Reprinted from [81] with permission from Elsevier B.V.) (**b**) A picture of the differential pump of the FEI-Titan environmental TEM (with a CEOS aberration correction system) in the Center for Functional Nanomaterials, Brookhaven National Laboratory

In general, one needs to be cautious because the information of E-TEM is obtained at a gas pressure of a few millibars instead of at ambient pressure in which condition many nanomaterials are synthesized. As mentioned above, using a windowed cell attached in the holder can also be used to study the gas–solid reaction at higher pressure than E-TEM. Based on the microelectromechanical system (MEMS) technique, Creemer et al. have demonstrated the design of a "nanoreactor," as shown in Fig. 12.24 [86]. In this nanoreactor, 10-nm SiN_x films are used for the top/bottom windows. This nanoreactor allows researchers to heat the sample to 500 °C and expose it to 1.2 bar of H_2. At those experimental condition, they have achieved a spatial resolution of 0.18 nm for Cu particles on ZnO using a Philips CM300ST FEG. Various

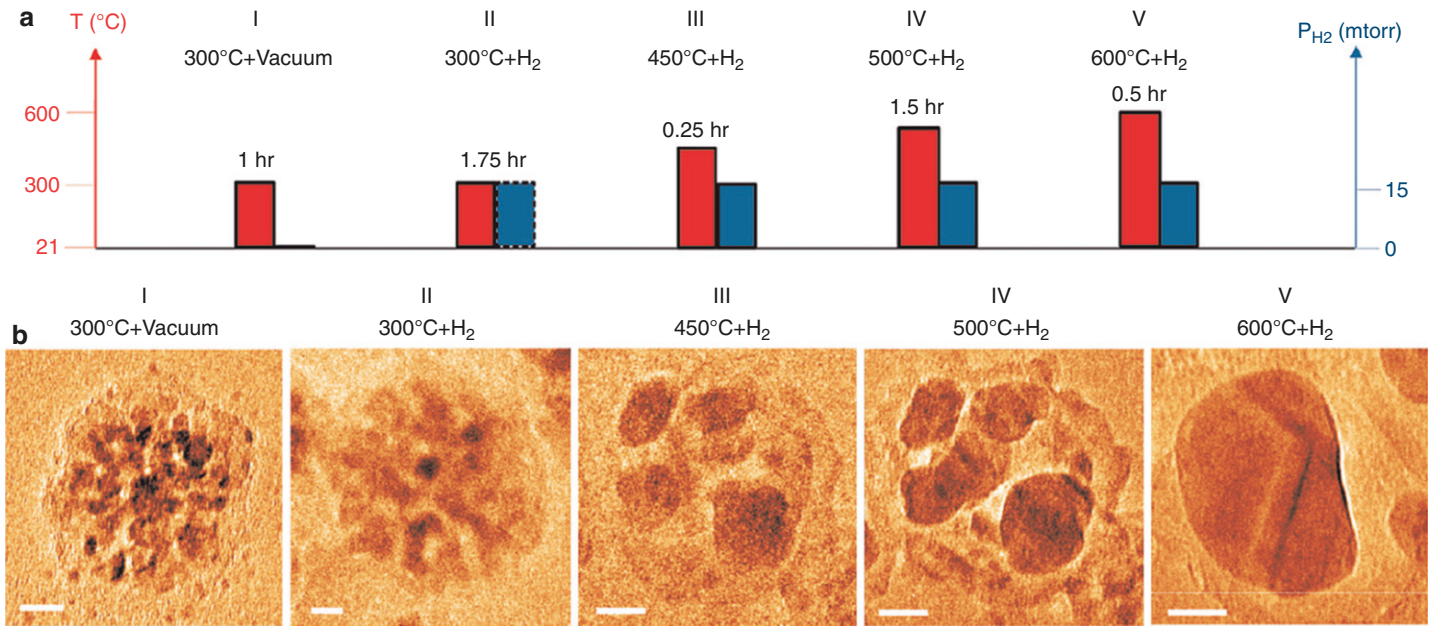


Fig. 12.23 In situ observation of structural changes of Co/CoO_x catalysts at different reduction conditions. (**a**) Heating and H_2 gas environmental conditions and their durations. (**b**) In situ TEM images of the nanocomposites under the corresponding environmental treatments. Scale bars: 10 nm (Reprinted with permission from [50], Copyright (2012) American Chemical Society)

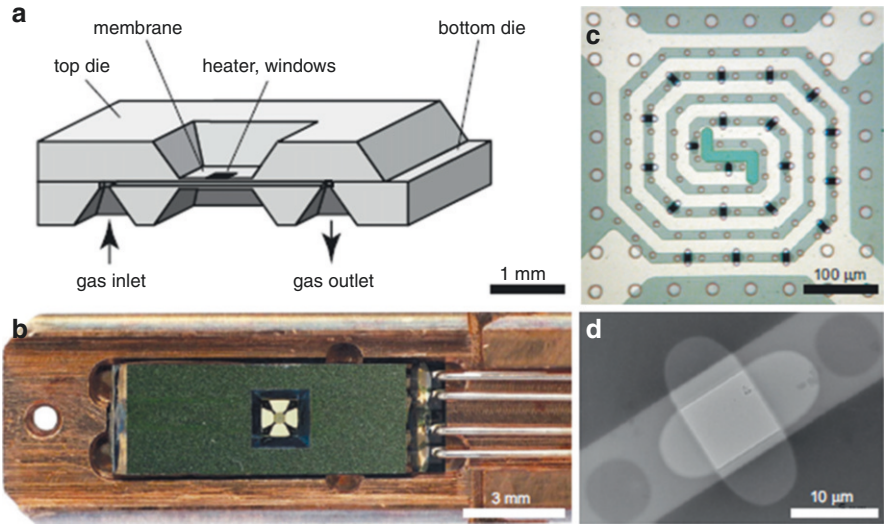


Fig. 12.24 Illustration of the nanoreactor device: (**a**) Schematic cross section of the nanoreactor. (**b**) Optical image of the TEM holder with the integrated nanoreactor and the four electrical probe contacts. (**c**) Optical close-up of the nanoreactor membrane. The *bright spiral* is the Pt heater. The *small ovaloids* are the electron-transparent windows. The *circles* are the SiO_2 spacers that define the minimum height of the gas channel. (**d**) A low-magnification TEM image of a pair of superimposed 10-nm-thick windows. Their alignment creates a highly electron-transparent (*bright*) square through which high-resolution TEM imaging can be performed (Reprinted from [86] with permission from Elsevier B.V.)

designs of a pressure gas cell are still under development. It is also believed that new insights and results using this approach will impact a variety of fields, especially heterogeneous catalysis.

5.2.2 In Situ Environmental Reaction in TEM: Liquid Reaction

The use of electron microscopy in studying liquid reactions has experienced a surge of interest and at the same time encountered a lot of technical challenges. In order to realize liquid-phase reactions, an open environmental chamber approach can be implemented in the TEM experiment. However, it is difficult to control the thickness of the liquid phase accurately in the open chamber, that is, a liquid film thinner than ~1 µm as required for nanometer-scale resolution in TEM. To solve this problem, the liquid cells have been designed with the newly developed thin-film and microfabrication techniques [87–95]. Thin carbon foils and graphene sheets have been used as membranes, and thin (10–100 nm) SiN_x films supported on silicon microchips are increasingly popular. The design by Zheng et al. is shown in Fig. 12.25, and in this design, the window thickness itself may limit the resolution [88, 91]. The formation of bubbles in the liquid layer may cause problems. Uncontrolled bubble formation may be alleviated by flowing the liquid

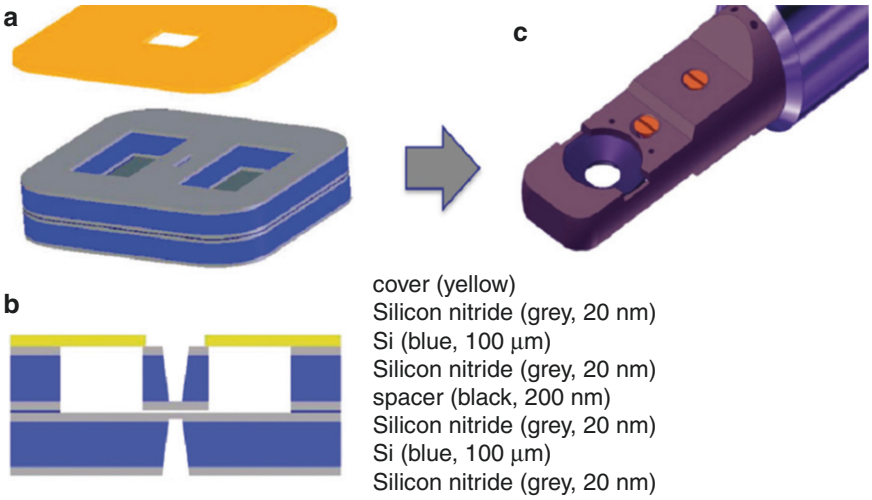


Fig. 12.25 (**a**) 3D view. Lateral dimensions of the liquid cell: 2.6 × 2.6 mm and 3 mm diagonally; reservoirs: 0.6 × 1.2 × 0.1 mm; electron-transparent window: 1 × 50 μm; cover: 0.6 × 0.6 mm for the hole and its outer dimensions are the same as the liquid cell. (**b**) Cross-sectional view of the plane marked in (**a**). (**c**) The TEM holder holding the liquid cell (Reprinted with permission from [91], Copyright (2012) American Chemical Society)

through the cell, and the reduced liquid thickness in a bubble actually improves the resolution [87]. Although presenting unsolved problems, such liquid cells enable researchers to observe the growth of metallic nanocrystals at atomic resolution, induced either by electron beam or heating [89, 90].

The time sequence of TEM images in Fig. 12.26a–h shows the growth dynamics of the attachment process of iron oxyhydroxide (Fe chemical formula) nanoparticles [89]. It is observed that the surfaces of two adjacent particles make transient contact at multiple points and orientations before finally attaching to each other and growing together. These results imply that, in ceramics, the strong, highly direction-specific interactions drive crystal growth via oriented attachment.

The growth of Pt_3Fe nanowires from nanoparticles has been studied within a liquid cell as shown in Fig. 12.27 [90]. A solvent mixture of pentadecane and oleylamine (7:3 vol/vol) or a mixture of pentadecane, oleylamine, and oleic acid (6:3:1 vol/vol/vol) is used for the comparison of surfactant effects. Three distinct stages of growth can be identified. During the first stage, many small nanoparticles are formed. Subsequently, the second stage of growth is dominated by nanoparticles forming nanoparticle chains. In the final stage, adjacent nanoparticles within the chain come in contact with each other, forming a neck while surfactant molecules are excluded. The liquid cell technique enables direct observation of the dynamic growth of nanoparticles/nanorods in solution using TEM. Studying the mechanism of nanocrystal growth provides fundamental understanding of the nanostructures and paves the way to rational design of nanocatalysts with controlled properties.

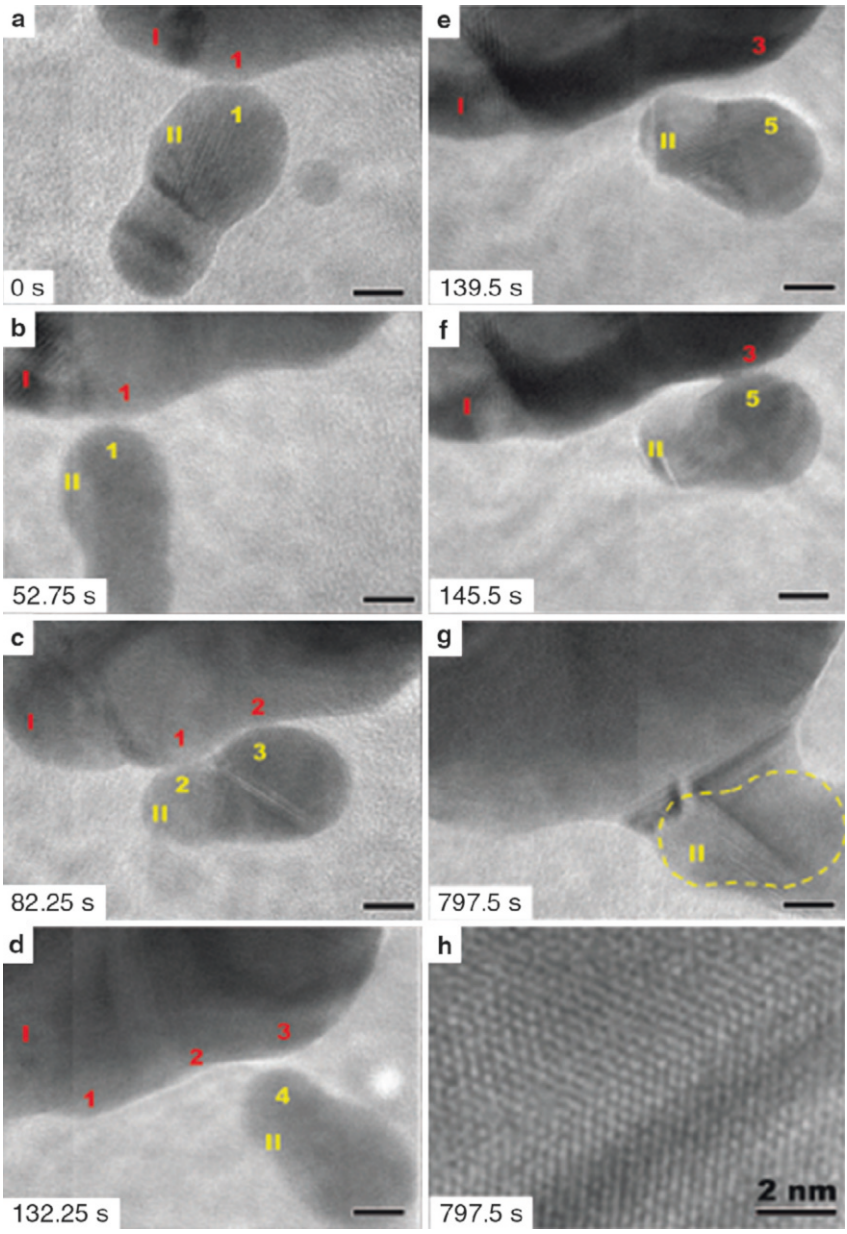


Fig. 12.26 (**a**–**g**) Time sequence of images showing typical dynamics of the attachment process. The surfaces of particles I and II made transient contact at many points and orientations (points *1-1*, *1-2*, *2-3*, and *3-4*) before finally attaching and growing together (points *3-5*). (**h**) High-resolution image of interface in (**g**) showing a twin structure (an inclined twin plane). The *yellow dashed line* in (**g**) shows the original boundary of the attached particle (Reprinted from [89] with permission from American Association for the Advancement of Science)

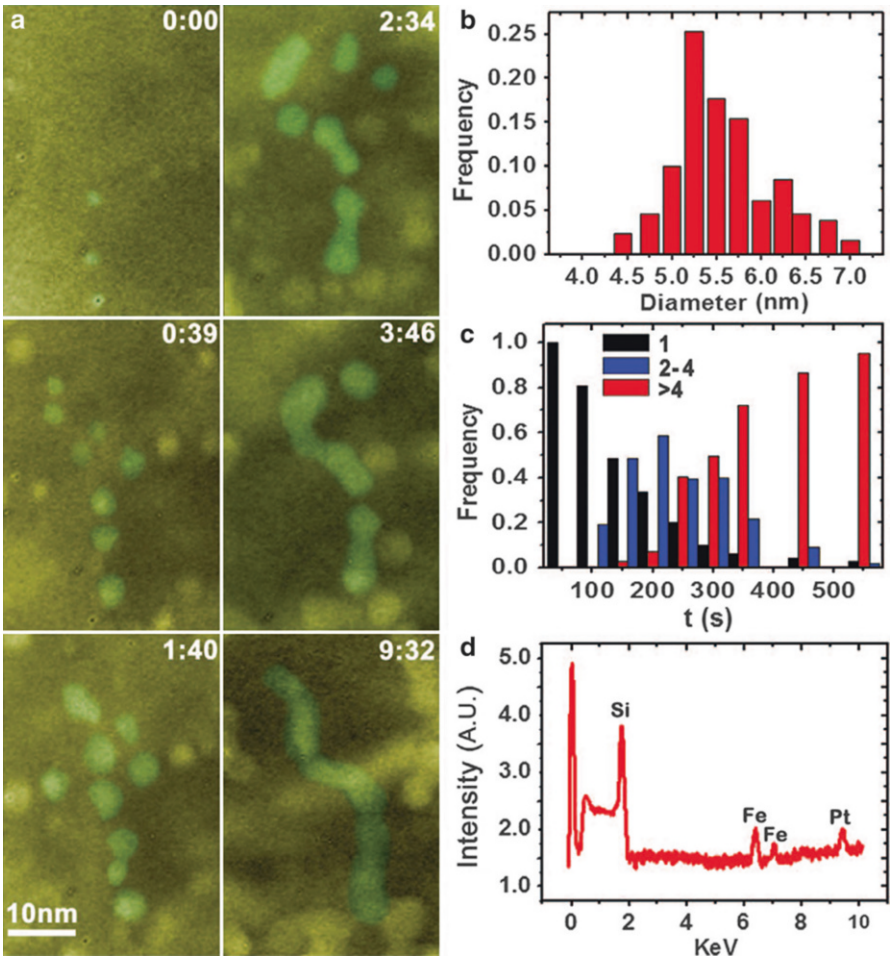


Fig. 12.27 The growth of Pt_3Fe nanowires in a liquid cell during exposure to the electron beam. A solvent mixture of pentadecane and oleylamine (7:3 vol/vol) was used. (**a**) Sequential color TEM images showing the evolution from the initial nucleation and growth in the molecular precursor solution to a later stage of nanowire formation by shape-directed nanoparticle attachment. Specific nanoparticles that contributed to the nanowire formation are highlighted in *green*. Time is displayed as minutes:seconds. The initial time is arbitrary. (**b**) Histograms of the particle size distribution when nanoparticle attachment begins. (**c**) Statistics of the length of nanoparticle chain as a function of time. Data are collected in a time window from 1 min 40 s to 9 min 32 s corresponding to (**a**). (**d**) EDS spectra of Pt_3Fe nanowires obtained ex situ from the same liquid cell. The observed Si signal is from the silicon nitride membrane (Reprinted from [90] with permission from American Association for the Advancement of Science)

However, quantitative data acquisition is the key challenge for the electron microscopy of liquids, in particular if we hope to use the technique to understand the fine details of static structures and to test models for dynamic processes. Equally important is the need for a more rigorous understanding of electron

beam–liquid/precursor interactions. With the advance of the liquid cell techniques, numerous exciting developments can be expected in the near future. For example, based on the liquid cell technique, other spatial environmental cells have been developed or are being developed, such as the electrochemical cell, which allows researchers to study the electrochemical reactions for various fields in energy research [93]. Of course, besides the TEM techniques (diffraction, HRTEM), STEM and EELS techniques are also being developed for E-TEM [85, 95].

6 Conclusions and Future Perspective

Suffice it to say that the invention and development of the aberration correction system has been the most prominent progress in the field of electron microscopy in the past decade, without which the techniques introduced in this chapter, structural and chemical characterization and in situ environmental TEM, would not have blossomed. As Dr. Urban once put – "Is science prepared for atomic-resolution electron microscopy?" – a lot of attention needs to be called to this fast-growing technique [96]. For the TEM study on metallic nanocatalysts, the aberration correction technique would bring the spatial resolution and the temporal resolution to a whole new level, which would allow our researchers to understand the materials and catalytic reactions in more depth. Consequently, significant achievements are to be expected. In the mean time, other branches of electron microscopy have also advanced at a fast pace, although they are not covered in this chapter. These techniques have also had an impact on the characterization of metallic catalysts: (1) The "soft" TEM/STEM, with the help of the aberration-correction techniques, which has been expanded to low acceleration energy (~30–80 kV) in order to image carbon-based materials, organic materials, and even gas molecules [97–99]. (2) High spatial resolution valence-EELS technique for plasmonics study: we could achieve both high spatial resolution and high energy resolution on the plasmonics properties of metallic nanoparticles. Hot spots can be directly observed from the VEELS mapping [100, 101]. (3) Ultrafast TEM techniques, including dynamical TEM and 4D TEM approaches, with a temporal resolution ~10 ns [102–106].

For the future perspectives, there is no doubt that the electron microscopy techniques will keep excelling in achieving high resolutions (spatial, energy, and temporal), becoming more quantitative and easy to operate. To solve the problems raised by the practical or theoretical study of nanocatalysts, one needs to combine all possible TEM techniques to probe the questions in hand and find the answers from the massive information (sometimes, controversial information) collectively and thoughtfully. The application-oriented approaches will still be the main stream of TEM study on the catalysis field. It will require the researchers to have the knowledge of both catalysis and electron microscopy. The more knowledge one is equipped with, both extensively and intensively, the broader the horizon they would possess when applying this knowledge to their work. On the other hand, to prevent the results with controversy which could lead to misinterpretation, one needs to (1) understand the strengths and drawbacks of each experimental method,

for example, what could induce errors during the experiments, and (2) understand the electron beam effect and compare the results with control experiments.

During the development of electron microscopy, we have also noticed the trend from 2D (imaging) to 3D (tomography), and now even 4D (tomography + elemental mapping). The 5D (3D tomography + elemental mapping + in situ) is under its way, while a similar approach has been proposed for X-ray microscopy [107]. This trend has its roots in the technical development in electron microscopy, engineering, and electronics. From a different angle, the expansion of the TEM techniques to ambient environment and other promptive conditions, such as heating/cooling and charging, may offer more opportunities to study not only the static structure and chemistry but also dynamical responses of the nanocatalysts. In summary, TEM would play an increasingly important role in the field of heterogeneous catalysis in the future.

Acknowledgments I would like to thank Drs. Eric Stach, Huolin Xin, Haimei Zheng, Fang Lu, and Ms. Changchang Liu for the helpful discussions. This research at the Center for Functional Nanomaterials, Brookhaven National Laboratory, is supported by the U.S. Department of Energy, Office of Basic Energy Sciences, under Contract No. DE-AC02-98CH10886.

References

1. Williams DB, Carter CB (2009) Transmission electron microscopy: a textbook for materials science, 2nd edn. Springer, New York
2. Pennycook SJ, Nellist PD (eds) (2011) Scanning transmission electron microscopy: image and analysis. Springer, New York
3. Hawkes P, Spence JCH (eds) (2007) Science of microscopy. Springer, New York
4. Egerton RF (2011) Electron energy-loss spectroscopy in the electron microscope, 3rd ed. Springer, New York
5. Goldstein J (2003) Scanning electron microscopy and X-ray microanalysis. Kluwer, Holland
6. Spence JCH, Zuo JM (1992) Electron microdiffraction. Plenum, New York/London
7. Scott SL, Crudden CM, Cathleen M, Jones CW, Christopher W (eds) (2003) Nanostructured catalysts. Springer, New York
8. Bell AT (2003) The impact of nanoscience on heterogeneous catalysis. Science 299:1688–1691
9. Davis M (Chair), Tilley D (Co-Chair) (2003) NSF workshop report on "future directions in catalysis: structures that function on the nanoscale," NSF Headquarters, Arlington, 19–20 June 2003
10. Datye AK (2003) Electron microscopy of catalysts: recent achievements, and future prospects. J Catal 216:144–154
11. Jin R (2012) The impacts of nanotechnology on catalysis by precious metal nanoparticles. Nanotechnol Rev 1:31–56
12. Zhang J, Vukmirovic MB, Xu Y, Mavrikakis M et al (2005) Controlling the catalytic activity of platinum-monolayer electrocatalysts for oxygen reduction with different substrates. Angew Chem Int Ed 44:2132–2135
13. Pantel R, Clement L, Rouviere JL, Kwakman L (2003) Strain measurements at a NiSi/Si interface using STEM-CBED: a quantification method for stress relaxation during TEM lamella preparation. Microsc Microanal 9(suppl 2):866–867
14. Egerton RF, Li P, Malac M (2004) Radiation damage in the TEM and SEM. Micron 35:399–409

15. Egerton RF, McLeod R, Wang F, Malac M (2010) Basic questions related to electron-induced sputtering in the TEM. Ultramicroscopy 110:991–997
16. Su D, Wang F, Ma C, Jiang N (2013) Engineering nano-composite $Li_4Ti_5O_{12}$ anodes via scanning electron-probe fabrication. Nano Energy 2:343–350
17. Jiang N, Zhou S, Su D, Qiu J (2012) Do Eu dopants prefer the precipitated LaF3 nanocrystals in glass ceramics? Phys Status Solidi RRL 6(12):487–489
18. Zheng H, Rivest JB, Miller TA, Sadtler B et al (2011) Observation of transient structural-transformation dynamics in a Cu_2S nanorod. Science 333:206–209
19. Liu C, Lee S, Dong S, Lee B et al (2012) Controlling the particle size of ZrO_2 nanoparticles in hydrothermally stable ZrO_2/MWCNT composites. Langmuir 28(49):17159–17167
20. Abramoff MD, Magalhaes PJ, Ram SJ (2004) Image processing with ImageJ. Biophotonics Int 11(7):36–42
21. Shekhar M, Wang J, Lee W, Akatay MC et al (2012) Counting Au catalytic sites for the water–gas shift reaction. J Catal 293:94–102
22. Shekhar M, Wang J, Lee W, Williams WD et al (2012) Size and support effects for the water–gas shift catalysis over gold nanoparticles supported on model Al_2O_3 and TiO_2. J Am Chem Soc 134:4700–4708
23. Ding Y, Fan F, Tian Z, Wang ZL (2010) Atomic structure of Au-Pd bimetallic alloyed nanoparticles. J Am Chem Soc 132:12480–12486
24. Du W, Wang Q, LaScala CA, Zhang L et al (2011) Ternary PtSnRh–SnO_2 nanoclusters: synthesis and electroactivity for ethanol oxidation fuel cell reaction. J Mater Chem 21:8887–8892
25. Hytch MJ, Snoeck E, Kilaas R (1998) Quantitative measurement of displacement and strain fields from HREM micrographs. Ultramicroscopy 74:131–146
26. Johnson CL, Snoeck E, Ezcurdia M, Rodriguez-Gonzalez B et al (2008) Effects of elastic anisotropy on strain distributions in decahedral gold nanoparticles. Nat Mater 7:120–124
27. Xia Y, Xiong Y, Lim B, Skrabalak SE (2009) Shape-controlled synthesis of metal nanocrystals: simple chemistry meets complex physics? Angew Chem Int Ed 48:60–103
28. Zheng Y, Tao J, Liu H, Zeng J et al (2011) Facile synthesis of gold nanorice enclosed by high-index facets and its application for CO oxidation. Small 7(16):2307–2312
29. Wang C, Tian W, Ding Y, Ma Y et al (2010) Rational synthesis of heterostructured nanoparticles with morphology control. J Am Chem Soc 132:6524–6529
30. Wang ZL (2000) Transmission electron microscopy of shape-controlled nanocrystals and their assemblies. J Phys Chem B 104:1153–1175
31. Lim B, Xiong Y, Xia Y (2007) A water-based synthesis of octahedral, decahedral, and icosahedral Pd nanocrystals. Angew Chem Int Ed 46:9279–9282
32. Lu F, Zhang Y, Zhang L, Zhang Y et al (2011) Truncated ditetragonal gold prisms as nanofacet activators of catalytic platinum. J Am Chem Soc 133:18074–18077
33. Wang J, Ma C, Choi Y, Su D et al (2011) Kirkendall effect and lattice contraction in nanocatalysts: a new strategy to enhance sustainable activity. J Am Chem Soc 133:13551–13557
34. Wang F, Li C, Sun L-D, Wu H et al (2011) Heteroepitaxial growth of high-index-faceted palladium nanoshells and their catalytic performance. J Am Chem Soc 133:1106–1111
35. Cheong S, Watt JD, Tilley RD (2010) Shape control of platinum and palladium nanoparticles for catalysis. Nanoscale 2:2045–2053
36. Henning AM, Watt J, Miedziak PJ, Cheong S et al (2013) Gold–palladium core–shell nanocrystals with size and shape control optimized for catalytic performance. Angew Chem Int Ed 52:1477–1480
37. Wang R, Dmitrieva O, Farle M, Dumpich G et al (2009) FePt icosahedra with magnetic cores and catalytic shells. J Phys Chem C 113:4395–4400
38. Wang R, Dmitrieva O, Farle M, Dumpich G et al (2008) Layer resolved structural relaxation at the surface of magnetic FePt icosahedral nanoparticles. Phys Rev Lett 100:017205–017208
39. Langille MR, Zhang J, Personick ML, Li S et al (2012) Stepwise evolution of spherical seeds into 20-fold twinned icosahedra. Science 337:954–957

40. Van Aert S, Batenburg KJ, Rossell MD, Erni R et al (2011) Three-dimensional atomic imaging of crystalline nanoparticles. Nature 470:374–377
41. Koning RI, Koster AJ (2009) Cryo-electron tomography in biology and medicine. Ann Anat 191:427–445
42. Midgley PA, Weyland M, Thomas JM, Johnson BFG (2001) Z-contrast tomography: a technique in three-dimensional nanostructural analysis based on Rutherford scattering. Chem Commun 10:907–908
43. Jinschek JR, Batenburg KJ, Calderon HA, Kilaas R et al (2008) 3-D reconstruction of the atomic positions in a simulated gold nanocrystal based on discrete tomography: prospects of atomic resolution electron tomography. Ultramicroscopy 108:589–604
44. Florea I, Demortiere A, Petit C, Bulou H et al (2012) Electron tomography and 3D molecular simulations of platinum nanocrystals. Nanoscale 4:5125–5131
45. Arslan I, Yates TJV, Browning ND, Midgley PA (2005) Embedded nanostructures revealed in three dimensions. Science 309:2195–2198
46. Xin HL, Muller DA (2009) Aberration-corrected ADF-STEM depth sectioning and prospects for reliable 3D imaging in S/TEM. J Electron Microsc 58(3):157
47. Scott MC, Chen C-C, Mecklenburg M, Zhu C et al (2012) Electron tomography at 2.4-Å resolution. Nature 483:444–448
48. Yu Y, Xin HL, Hovden R, Wang D et al (2012) Three-dimensional tracking and visualization of hundreds of Pt−Co fuel cell nanocatalysts during electrochemical aging. Nano Lett 12:4417–4423
49. Arslan I, Stach EA (2012) Seeing atoms in three dimensions. Nat Mater 11:911–912
50. Xin HL, Pach EA, Diaz RE, Stach EA (2012) Revealing correlation of valence state with nanoporous structure in cobalt catalyst nanoparticles by in situ environmental TEM. ACS Nano 6(5):4241–4247
51. Prieto G, Zecevic J, Friedrich H, de Jong KP et al (2013) Towards stable catalysts by controlling collective properties of supported metal nanoparticles. Nat Mater 12:34–39
52. Yang H (2011) Platinum-based electrocatalysts with core–shell nanostructures. Angew Chem Int Ed 50:2674–2676
53. Sasaki K, Naohara H, Choi YM, Cai Y et al (2012) Highly stable Pt monolayer on PdAu nanoparticle electrocatalysts for the oxygen reduction reaction. Nat Commun 3:1115. doi:10.1038/ncomms2124
54. Wang JX, Inada H, Wu L, Zhu Y et al (2009) Oxygen reduction on well-defined core-shell nanocatalysts: particle size, facet, and Pt shell thickness effects. J Am Chem Soc 131:17298–17302
55. Zhang S, Guo S, Zhu H, Su D et al (2012) Structure-induced enhancement in electrooxidation of trimetallic FePtAu nanoparticles. J Am Chem Soc 134:5060–5063
56. Xin HL, Mundy JA, Liu Z, Cabezas R et al (2012) Atomic-resolution spectroscopic imaging of ensembles of nanocatalyst particles across the life of a fuel cell. Nano Lett 12:490–497
57. Sasaki K, Naohara H, Cai Y, Choi YM et al (2010) Core-protected platinum monolayer shell high-stability electrocatalysts for fuel-cell cathodes. Angew Chem Int Ed 49:8602–8607
58. Wang D, Yu Y, Xin HL, Hovden R et al (2012) Tuning oxygen reduction reaction activity via controllable dealloying: a model study of ordered Cu3Pt/C intermetallic nanocatalysts. Nano Lett 12:5230–5238
59. Mazumder V, Chi M, More KL, Sun S (2010) Synthesis and characterization of multimetallic Pd/Au and Pd/Au/FePt core/shell nanoparticles. Angew Chem Int Ed 49:9368–9372
60. Mazumder V, Chi M, More KL, Sun S (2010) Core/shell Pd/FePt nanoparticles as an active and durable catalyst for the oxygen reduction reaction. J Am Chem Soc 132:7848–7849
61. Xu J, Wilson AR, Rathmell AR, Howe J et al (2011) Synthesis and catalytic properties of Au-Pd nanoflowers. ACS Nano 8:6119–6127

62. Du W, Wang Q, Saxner D, Aaron Deskins N et al (2011) Highly active iridium/iridium-Tin/Tin oxide heterogeneous nanoparticles as alternative electrocatalysts for the ethanol oxidation reaction. J Am Chem Soc 133:15172–15183
63. Du W, Su D, Wang Q, Frenkel AI et al (2011) Promotional effects of bismuth on the formation of platinum-bismuth nanowires network and the electrocatalytic activity toward ethanol oxidation. Crystal Growth Design 11(2):594–599
64. Du W, Deskins NA, Su D, Teng X (2012) Iridium − ruthenium alloyed nanoparticles for the ethanol oxidation fuel cell reactions. ACS Catal 2:1226–1231
65. Gong K, Su D, Adzic RR (2010) Platinum-monolayer shell on $AuNi_{0.5}Fe$ nanoparticle core electrocatalyst with high activity and stability for the oxygen reduction reaction. J Am Chem Soc 132:14364–14366
66. Kuttiyie KA, Sasaki K, Choi Y, Su D et al (2012) Nitride stabilized PtNi core−shell nanocatalyst for high oxygen reduction activity. Nano Lett 12(12):6266–6271
67. Johnston-Peck AC, Scarel G, Wang J, Parsons GN et al (2011) Sinter-free phase conversion and scanning transmission electron microscopy of FePt nanoparticle monolayers. Nanoscale 3:4142–4149
68. Johnston-Peck AC, Tracy JB (2012) Phase transformation of alumina-coated FePt nanoparticles. J Appl Phys 111:07B522
69. Wieckowski A, Savinova ER, Constantinos VG (2003) Catalysis and electrocatalysis at nanoparticle surfaces, 1st edn. CRC, New York
70. Sanchez SI, Small MW, Sivaramakrishnan S, Wen J et al (2010) Visualizing materials chemistry at atomic resolution. Anal Chem 82:2599–2607
71. Liu J, Cowley JM (1988) High resolution SEM in a STEM instrument. Scanning Microsc 2:65–81
72. Bleloch AL, Howie A, Milne RH (1989) High resolution secondary electron imaging and spectroscopy. Ultramicroscopy 31:99–110
73. Zhu Y, Inada H, Nakamura K, Wall J (2009) Imaging single atoms using secondary electrons with an aberration-corrected electron microscope. Nat Mater 8:808–812
74. Inada H, Su D, Egerton RF, Konno M et al (2011) Atomic imaging using secondary electrons in a scanning transmission electron microscope: experimental observations and possible mechanisms. Ultramicroscopy 111:865–876
75. Miao JW, Charalambous P, Kirz J, Sayre D (1999) Extending the methodology of X-ray crystallography to allow imaging of micrometre-sized non-crystalline specimens. Nature 400:342–344
76. Huang WJ, Zuo JM, Jiang B, Kwon KW et al (2009) Sub-ångström-resolution diffractive imaging of single nanocrystals. Nat Phys 5:129–133
77. Sharma R (2001) Design and applications of environmental cell transmission electron microscope for in situ observations of gas–solid reactions. Microsc Microanal 7:494–506
78. Gai PL (2002) Developments in in situ environmental cell high-resolution electron microscopy and applications to catalysis. Topics Catal 21(4):161–173
79. Hansen PL, Wagner JB, Helveg S, Rostrup-Nielsen JR (2002) Atom-resolved imaging of dynamic shape changes in supported copper nanocrystals. Science 295:2053–2055
80. Hansen TW, Wagner JB, Dunin-Borkowski RE (2010) Aberration corrected and monochromated environmental transmission electron microscopy: challenges and prospects for materials science. Mater Sci Technol 26(11):1338–1344
81. Wagner JB, Cavalca F, Damsgaard CD, Duchstein LDL et al (2012) Exploring the environmental transmission electron microscope. Micron 43:1169–1175
82. Gai PL, Boyes ED (2012) In situ TEM measurement methods. Charact Mater :1–11
83. Ciston J, Si R, Rodriguez JA, Hanson C et al (2011) Morphological and structural changes during the reduction and reoxidation of CuO/CeO_2 and $Ce_{1-x}Cu_xO2$ nanocatalysts: in situ studies with environmental TEM, XRD, and XAS. J Phys Chem C 115: 13851–13859

84. Chenna S, Banerjee R, Crozier PA (2011) Atomic-scale observation of the Ni activation process for partial oxidation of methane using in situ environmental TEM. Chem Cat Chem 3:1051–1059
85. Chenna S, Crozier PA (2012) Operando transmission electron microscopy: a technique for detection of catalysis using electron energy-loss spectroscopy in the transmission electron microscope. ACS Catal 2:2395–2402
86. Creemer JF, Helveg S, Hoveling GH, Ullmann S (2008) Atomic-scale electron microscopy at ambient pressure. Ultramicroscopy 108:993–998
87. de Jonge N, Ross FM (2011) Electron microscopy of specimens in liquid. Nat Nanotechnol 5:695–704
88. Zheng H, Smith RK, Jun Y-W, Kisielowski C et al (2009) Observation of single colloidal platinum nanocrystal growth trajectories. Science 324:1309–1312
89. Li D, Nielsen MH, Lee JRI, Frandsen C et al (2012) Direction-specific interactions control crystal growth by oriented attachment. Science 336:1014–1018
90. Liao H-G, Cui L, Whitelam S, Zheng H (2012) Real-time imaging of Pt_3Fe nanorod growth in solution. Science 336:1011–1014
91. Xin HL, Zheng H (2012) In situ observation of oscillatory growth of bismuth nanoparticles. Nano Lett 12:1470–1474
92. Yuk JM, Park J, Ercius P, Kim K et al (2012) High-resolution EM of colloidal nanocrystal growth using graphene liquid cells. Science 336:61–64
93. Williamson MJ, Tromp RM, Vereecken PM, Hull R et al (2003) Dynamic microscopy of nanoscale cluster growth at the solid–liquid interface. Nat Mater 2:532–536
94. Woehl TJ, Evans JE, Arslan I, Ristenpart WD et al (2012) Direct in situ determination of the mechanisms controlling nanoparticle nucleation and growth. ACS Nano 6:8599–8610
95. Jungjohanna KL, Evans JE, Aguiara JA, Arslan I et al (2012) Atomic-scale imaging and spectroscopy for in situ liquid scanning transmission electron microscopy. Microsc Microanal 18:621–627
96. Urban K (2009) Is science prepared for atomic-resolution electron microscopy? Nat Mater 8:260–262
97. Suenaga K, Koshino M (2010) Atom-by-atom spectroscopy at graphene edge. Nature 468:1088–1090
98. Krivanek OL, Chisholm MF, Nicolosi V, Pennycook TJ et al (2010) Atom-by-atom structural and chemical analysis by annular dark-field electron microscopy. Nature 464:571–574
99. Yoshida H, Kuwauchi Y, Jinschek JR, Sun K et al (2012) Visualizing gas molecules interacting with supported nanoparticulate catalysts at reaction conditions. Science 335:317–319
100. Nelayah J, Kociak M, Stephan O, Javier Garcia De Abajo F et al (2007) Mapping surface plasmons on a single metallic nanoparticles. Nat Phys 3:348–353
101. Scholl JA, Koh AL, Dionne JA (2012) Quantum plasmon resonances of individual metallic nanoparticles. Nature 483:421–428
102. Zewail AH, Thomas JM (2009) 4D Electron microscopy. Imperial College Press, London
103. Zewail AH (2010) Four-dimensional electron microscopy. Science 328:187–193
104. Kim JS, LaGrange T, Reed BW, Taheri ML et al (2008) Imaging of transient structures using nanosecond in situ TEM. Science 321:1472–1475
105. Reed BW, LaGrange T, Shuttlesworth RM, Gibson DJ et al (2010) Solving the accelerator-condenser coupling problem in a nanosecond dynamic transmission electron microscope. Rev Sci Instrum 81:053706
106. Yurtsever A, van der Veen RM, Zewail AH (2012) Subparticle ultrafast spectrum imaging in 4D electron microscopy. Science 335:59–64
107. Burmans ILC, Weckhuysen BM (2012) Heterogeneities of individual catalyst particles in space and time as monitored by spectroscopy. Nat Chem 4:873–886

3D Electron Microscopy Applied to Nanoscience

13

Ileana Florea, Ovidiu Ersen, and Charles Hirlimann

Contents

1 Definition of the Topic 619
2 Overview 620
3 Introduction 620
4 Experimental and Instrumental Methodology 625
4.1 Tomography Requirements, Artifacts 625
4.2 Reconstruction Algorithms 626
4.3 TEM Tomography 627
4.4 Z-Contrast Tomography 628
4.5 Analytical Tomography 629
4.6 Data Treatment Procedure 630
4.7 Resolution in Analytical Tomography 632
5 Key Research Findings 633
5.1 Short Review of the Previous Works 633
5.2 Quantitative 3D-TEM 634
5.3 Analytical 3D-TEM 647
6 Conclusions and Perspective 653
References 654

1 Definition of the Topic

Nanotechnologies and nanosciences underwent an enhanced development for more than a quarter of a century now, while in the meantime the specific techniques necessary to characterize nano-objects and nanostructures have been lagging behind. It is the aim of this contribution to demonstrate, through highlighting examples, that recent progress in the use of electron microscopy techniques based

I. Florea • O. Ersen (✉) • C. Hirlimann
Institut de Physique et Chimie des Matériaux de Strasbourg (IPCMS), UMR 7504 CNRS – Université de Strasbourg, Strasbourg, France
e-mail: ersen@ipcms.unistra.fr

C.S.S.R. Kumar (ed.), *Transmission Electron Microscopy Characterization of Nanomaterials*, DOI 10.1007/978-3-642-38934-4_13,
© Springer-Verlag Berlin Heidelberg 2014

on tomography permitted to fulfill the gap between the development of new materials and structures and their characterization. Progress came out from the development of simple but stringent software that allowed performing precise 3D reconstruction of objects at the nanoscale. A special focus is put here on two new techniques: quantitative 3D tomography and analytical 3D tomography. The former technique has given access to quantitative measurement of specific parameters in nano – objects and – structures such as specific surfaces, porosities, specific volume, and long distance order while the latter based on electron energy loss spectroscopy details the 3D chemical composition of these objects and structures on a 5 nm scale.

2 Overview

The change in physical and chemical properties that occurs in materials when they are downsized is at the very heart of the strong interest in nanoscaled objects. A deep understanding of these properties is an absolute need on a fundamental level but is also strongly needed in order to turn them into an advantage when developing innovative devices. If one wants to overcome an empirical use of nanomaterials in new applications, there is a strong need for developing new tools able to correlate their characteristics to their chemical and physical properties.

Inside this frame we will show that a large variety of electron microscopy modes can be adapted to a 3D study of nanomaterials and that each mode brings up advantages of its own. Adapting various modes to the tomographic analysis of materials is not an easy task though. Various difficulties need to be overcome such as large magnification required, large amounts of data needing to be collected and processed, and new processes needed for combining various bit of information collected on a single sample. Coupling the tomography techniques with classical electron microscopy modes like high-resolution microscopy, for example, has permitted obtaining a larger and better description of nano-objects of interest from the point of view of their morphology, their crystal structure, and chemical composition.

To be able to explore the potential of various modes of electron tomography, specific families of samples have had to be chosen that would exemplify their specific interest, but also the difficulties needing to be overcome in their use. The various materials that have been studied have been chosen for the large interest that has been shown in the communities of nanosciences and nanotechnologies and for their potential interest in the field of catalysis.

3 Introduction

In the last few years, a major challenge has been the quest of nano-objects or nanostructured materials which are at the forefront in societal concerns such as

communication technologies, energy, or health. One of the specific interests of nanomaterials stems from the enhanced influence of their surface with respect to the bulk, providing striking changes in the electronic, magnetic, or catalytic properties, for instance. An optimization of these properties requires a close control of the synthesis process and characterization tools at the cutting edge to investigate accurately surface characteristics (geometry, surface to volume ratio, chemical composition, etc.). Basically, such investigations are crucial in most of the fields where surface chemistry plays a key role, like for instance in catalysis.

Various analysis techniques such as X-ray reflectivity, spectroscopic ellipsometry, SAXS, or GISAXS are currently used to get physical and chemical information on the structure, morphology, or chemical composition as well [1, 2]. Unfortunately, they only give access to an averaged view of the analyzed objects, so that to avoid fluctuation effects; near-field imaging techniques such as STM, AFM, or TEM are very often used for a precise characterization at the atomic scale. Their limit however lies in their limitation to the exploration of very tiny surfaces with an as small as possible curvature. Therefore an extrapolation of the information they give access to is highly risky. A very remarkable 3D spectroscopic technique with atomic resolutions is the atom probe tomography [3] that requires a tip-shaped sample. It unfortunately only informs one, in a destructive manner, about a small working volume (few tens of nanometers) and, in addition, it requires generally a conductive or, at least, semiconductive specimen, which can be sometimes considered as a limiting factor.

Investigating the artificial nanomaterials that are nowadays developed requires new tools or methodologies to be implemented in order to explore the morphology, the structure, the chemical composition, or the magnetic properties in the three dimensions of space. A well appropriate technique is the electron tomography (or 3D-TEM) giving access to such information with a nanometer resolution [4–6]. When looking at a transparent and structured object, an observer does spontaneously rotate the object in order to get an understanding of the structure. This gives the general principle on which tomography is based: recording of images at various angles given by some wave transmitted through the object of interest which wavelength limits the ultimate reachable resolution. Tomography is therefore very general and light; sounds, neutrons, X rays, etc., can be used depending on the size and nature of the objects being studied. Electron microscopes, as they provide electrons with wavelengths in the picometer range, are ideally suited for performing 3D imaging using the tomographic technique and solve details at the nanometer scale. Electron tomography is based on the recording of series of images of an object that is rotated inside the electron microscope. As soon as 1917, Johann Radon described a mathematical transformation that connects the 3D Cartesian space to its projection onto a cylinder [7]. For a given incidence, the Radon transform of a 2D function $f(x,y)$ is given by the following integral function:

$$P_\theta(x') = \int_{-\infty}^{\infty}\int_{-\infty}^{\infty} f(x,y)\delta(x\cos(\theta) + y\sin(\theta) - x')dx\ dy$$

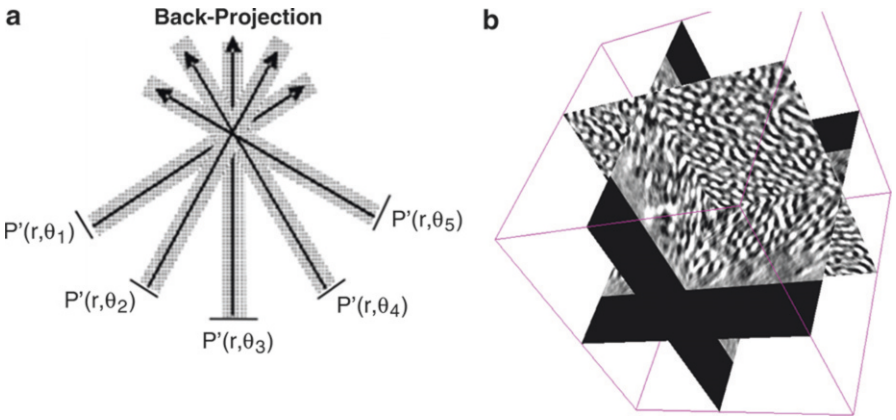


Fig. 13.1 Reconstruction of the 3D volume of an object from a set of projected images P′: (**a**) Back projection of the set of equivalent pixels from the projected images yielding one 3D voxel. (**b**) Illustration of the reconstruction of one plane inside the reconstructed 3D voxel matrix

For tomographic purposes, $f(x,y)$ is the 2D intensity distribution of the projected image of an object; it needs to be proportional to the matter density encountered by the electron beam under incidence. As the Radon transform can be uniquely inverted, from the transmission images of an object recorded at various incidence angles, a 3D image of the object can be constructed. When using digital recorders, as in nowadays microscopes, integral calculation needs to be transposed to discrete series and sums. Inversion of the Radon projection can be understood as the projection of the intensity recorded at position (x,y) along a segment orthogonally protruding from the projection. The corresponding 3D intensity is then given by the sum of the intensities at the intersection of all the equivalent segments from the series of projections. The reconstruction is improved by limiting the segment length to the expected volume of the object. This process is named weighted back projection [8].

On a practical point of view, tomography is performed by first recording a set of projection images for a limited number of incidence angles. For mechanical reasons, a sample cannot be rotated around a 360° like in the human body X-ray scanning technique. The most usual angle intervals lie in the range ±80°. Each recorded image collects a projection in the observation plane of the quantity of interest like the mass or the chemical composition. In a second step, the Radon function is inverted yielding a 3D matrix that describes the sample in the real space. In order to improve the reconstruction process, a self-coherent method is used that compares the Radon projections of the matrix with the experimental ones in a convergent process (see Fig. 13.1). The 3D voxel matrix reached at the end of the process is the starting point from which quantitative or chemical analysis can then be performed. A 3D imaging of the object of interest can be extracted from the matrix by recognizing, through contrast measurements, the interface between vacuum and matter. From this image, porosity, for example, can be quantitatively determined.

Low-resolution electron tomography was first developed for biology studies [9] but, thanks to large improvements in the electron microscopes resolution and in the ability to process larger and larger data fluxes, it has become a powerful tool for studying nanomaterials. The development of new 2D-analyzing modes in electron microscopy has even paved the way to more specialize and efficient 3D analyses of nanomaterials.

As previously explained, because of strong interactions between the electron beam of a microscope and the sample under study, various signals obtained using various imaging modes can be used in electron tomography yielding an increased sensitivity on the shape, the density, or the chemical nature of the studied objects for example. The bright-field transmission electron microscopy (BF-TEM) technique, mostly developed for biological applications, is fast and easy to implement [10–12] but not really suited for crystalline materials, because the diffraction contrast and Fresnel fringes can induce sizeable artifacts during the 3D reconstruction step. Indeed, tomographic recording requires the image intensity to be characterized by a monotonic variation with the mass and thickness of the sample. When recording 2D images in the BF-transmission electron microscopy mode, this requirement is not always fulfilled, due to electron diffraction by crystalline structures inside the studied object for specific recording angles of incidence. As a consequence, the use of BF-TEM in the materials field has long been restricted to the study of amorphous materials such as polymers [13] or mesoporous crystals [14].

For the 3D analysis of crystalline materials, the use of the annular dark field (ADF) imaging technique in the scanning TEM mode (STEM) constitutes an attractive alternative. For high collection angles in the ADF mode (HAADF), the contribution of Bragg diffracted electrons by crystalline structures is strongly weakened and the recorded signal is predominantly incoherent, improving in this way the projection requirement for the tomography. It is worth mentioning here that the STEM-HAADF incoherent mode is also known as the Z-contrast 3D mode, since the contrast in the initial images depends mainly on the thickness and local atomic number [15, 16]. If 3D analytical information is needed, it can indirectly be obtained through the dependence on the atomic number of the tomographic signal. Unfortunately in a large number of materials the atomic numbers of their constituent elements are very close one to the other making STEM-HAADF tomography not efficient.

However the only real way to perform 3D chemical analytical mapping over a few hundreds of nanometers is to perform tomography in the energy-filtered TEM (EFTEM) mode. This new technique has an impressive potential since it combines the ability of the usual electron tomographic imaging to collect 3D information at a nanoscale spatial resolution and the chemical selectivity of the EFTEM imaging. More precisely, it combines the tilt-series approach (reconstruction of a volume from a series of projections) with the image acquisition in energy-filtered imaging mode. From a discerning choice of energy windows collecting the core losses of the ionization edges for the elements of interest, one can record chemically selective 2D images for a given orientation of the sample. The modus operandi is repeated for

each tilt angle giving projections series of the spatial distribution of the elements that are further used to deduce the 3D elemental map. Up to now this powerful combination did not received much attention in the field of materials because the most interesting recording modes, namely, HAADF-STEM and EFTEM, are rather difficult to operate in the tomographic procedure. The development of this way of doing chemical analysis at the nanometer scale has been further slowed down by the following needs: (i) achieving high magnifications for reaching high spatial resolutions, (ii) processing of largely increased data quantities, (iii) combining, for a unique object, data from different nature, and (iv) selecting samples that can stand the increased irradiation exposition durations caused by the necessary multi-energy recordings.

Analytical electron tomography suffers several technical difficulties needing to be overcome. One of its main drawbacks stems very basically from the weak signals recorded in the elemental projections given by inelastically scattered electrons that account for only about 1 % of the incident electrons. Besides, the background of the spectrum coming from other inelastic interactions is much higher than the chemical signal of the core edges. As a consequence, using the pre-edge part of the spectrum to subtract the background is only approximate and the extracted signal may be questionable. In addition, some other practical issues and limiting factors are to be emphasized:

- Residual diffraction contrast may be observed in the energy-filtered images for crystalline materials; using incoherent illumination can merely reduce them.
- For increasing thickness, the probability for incident electrons to interact more than once with the sample rapidly rises. This so-called multi-scattering effect can dramatically modify the intensity distribution on the filtered images, thus breaking the projection requirement [17]. This effect is negligible as a first approximation when the sample thickness is smaller than the effective inelastic mean free path in any point of the specimen and for all angular positions of the tilt series. Accordingly, nonuniform average thickness over the sampled angular range has to be cautiously considered.
- The low signal to noise ratio (SNR) in elemental projections due to the statistical noise in filtered images, and to the uncertainty on the background extrapolation, as well, is another limiting factor. It is closely dependent on the thickness-integrated concentration of the element at various locations of the sample. A satisfactory compromise when performing a quantitative analysis consists in the comparison of the 3D elemental maps of some of the elements present in the specimen when they are spatially separated.
- Finally, the alignment of the projections needed for the reconstruction is a crucial step since it provides generally the actual resolution limitation. Owing to the low SNR in 2D elemental maps, the traditional cross-correlation algorithm used for electron tomography cannot be applied; in addition the lack of identifiable natural markers (not visible in this imaging mode) makes it impossible to use a fine alignment procedure. The unique way to properly align the elemental projections makes use of the alignment performed from Zero Loss tilt series recorded along with electron-loss series; these shape-sensitive images formed by elastically

scattered electrons (99 % of incident electrons) exhibit a higher SNR, suitable for traditional alignment procedures.

Provided that all the elemental projections do fulfill the projection requirement for tomography and that considerable attention is attached to the above issues, achieving nanoscale resolution in 3D analysis has become a realistic target, as illustrated in this paper.

4 Experimental and Instrumental Methodology

4.1 Tomography Requirements, Artifacts

The first requirement for performing electron tomography is about the images recorded as tilt series; they need to be real projections of the sample. To reach this requirement, the sample must experience a parallel electron beam for all tilt angles, meaning that the imaging field depth must always be larger than the sample thickness. Depending on the recording conditions, the imaging field depth may vary from a few tens of nanometers to a few hundreds of nanometers. The imaging setup needs to be adapted to the geometry of the sample.

It is also required for proper tomographic recording that the intensities recorded on collected images be proportional to the signal of interest integrated along the thickness of the sample in each point. As signals of interest, one can consider the mean density, the atomic number, the chemical nature, the amplitude of plasmon oscillations, and more. This requirement is certainly not fulfilled when studying crystalline materials that diffract electrons in the parallel TEM mode, giving rise to parasitic diffraction contrasts in the recorded images. This inconvenience can be partly overcome when using a scanning mode like STEM for which electrons scattered at large angles can be collected on annular detectors. When large collection angles are used, coherent diffraction effects do disappear and only incoherent electrons are collected that fulfill the proportionality requirement.

Multiple electron scattering is also at the origin of degradations in the elemental images but will be looked at the time when EFTEM tomography will be examined.

Very generally, two main artifacts have to be taken into account when reconstructing an object of interest using electron tomography (see Fig. 13.2). The number of recorded projection images being limited to a discrete set of records gives rise to the so-called “star” artifacts that can degrade the quality of the reconstructed voxel matrix of the object. A second artifact comes out from the limited value of the maximum angular rotation of the sample that creates a blind volume (so-called “missing wedge”) for which no record is available. As a result, the reconstructed space metric varies when going from the electron beam direction to an orthogonal direction: distances are enlarged in the direction of the beam and the spatial resolution is degraded. These two artifacts are strongly attenuated when using a self-coherent reconstruction technique as already mentioned earlier.

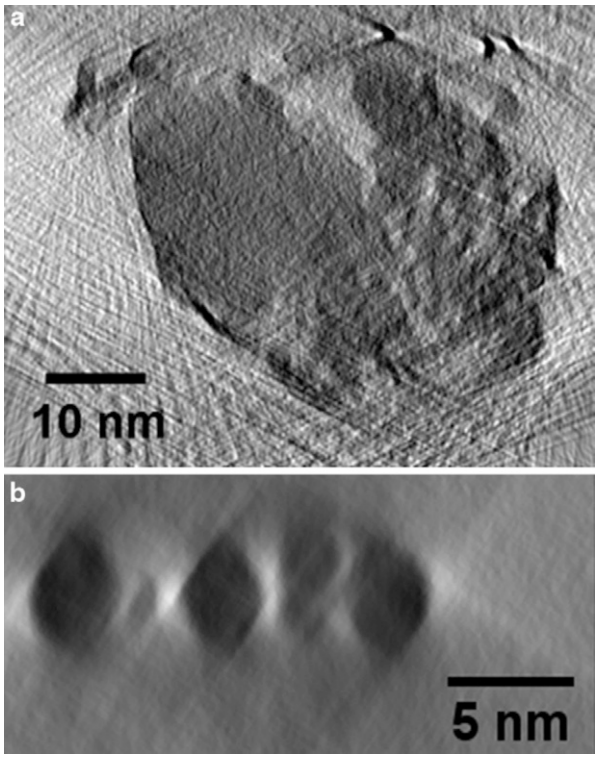


Fig. 13.2 Illustration of two typical artifacts observable in TEM electron tomography: (**a**) "Star" artifacts due to a discrete sampling of the object. (**b**) Elongation of the reconstructed volume caused by a limited sampling range

4.2 Reconstruction Algorithms

Two main ways can be used to reconstruct the sample space from its recorded projections. The first one relies on the fact that the recorded intensity values constitute a 3D representation of the reciprocal space of the sample: each projection of the sample is univocally related to a Fourier central slice that is orthogonal to the projection direction. A Fourier transform of this reciprocal space univocally yields a reconstruction of the real space of the sample. Fourier calculations, even when "fast" ones, are tedious calculations, but even worse the reciprocal space recorded through electron tomography is made out of point values that are not evenly distributed nor periodically distributed leading therefore to really "heavy" Fourier calculations. It is therefore simpler to perform the reconstruction calculations in the direct space using the weighted back-projection method already mentioned above. In this method the intensity of one pixel on one projection image is "painted" on a straight-line segment orthogonal to the image at the position of the pixel. The operation is repeated for each equivalent pixel in the full set of images and at the point where the segment does intersect an intensity value is set to be the sum of the intensities on each back-projecting segment. The obtained intensity is associated to a voxel (3D pixel) that therefore contains the value of the parameter of

interest at some point of a 3D matrix mapping the 3D space. In order to optimize the back-projection process, a window that contains the size of the sample is applied to the straight-line segment on which the projection is applied.

The quality of the reconstruction of the object of interest improves as the number of recorded projection increases according to a widening of the angular span of the rotation and of the number of angular steps. In order to get a most regularly distribution of points in the reconstruction matrix, it is important to correct for the nonlinear cosine dependence of the projections by nonlinearly varying the tilt angle of the sample according to a cosine function [18].

The overall process can be strongly improved by applying self-coherent algorithms that limit the artifacts generated by the finite number of recorded projections and do improve the signal to noise ratio. In these algorithms projected images are calculated from the reconstruction matrix and compared with the original images. A least squares comparison technique allows reaching a stable matrix in a convergent process. Most of the algorithms are based on the filtered retro-projection technique and the most popular ones are the simultaneous iterative reconstruction techniques (SIRT) and the algebraic reconstruction technique (ART). A good literature can be found that discusses the stability and the reliability of the algorithms [19, 20].

The introduction of electronic tomography in the material science field has led to the development of even more powerful reconstruction algorithms taking advantage of the discrete nature of the reconstructed volume by fixing the number of grey levels used for the reconstruction to the exact number of component known to be present in the sample under study [21, 22]. These techniques are especially well suited for studying homogenous samples or heterogeneous samples made out of homogeneous parts; they apply very well to chemical reconstruction calculations when using EFTEM tomography. The main advantage of the discrete reconstruction technique in that latter case relies on the fact that the segmentation of the data can be performed at the time of the calculation of the volume then highly simplifying the analysis of the data.

To push down the resolution, new reconstruction algorithms are being elaborated that do take into account the discrete (atomic) nature of the matter for analyzing high-resolution projected images and do model atomic positions along specific symmetry lines.

4.3 TEM Tomography

In the following presented experimental results, projected images were acquired by means of a probe corrected for spherical aberration (Cs) in a JEOL 2100F transmission electron microscope with a field emission gun operating at 200 kV. The acquisition software, plugged in the Digital Micrograph software, provides an automated acquisition process of the tilt series by varying the tilt angle step-by-step and by controlling the defocusing and the specimen drift at each tilt angle. In addition, it allows the automatic adjustment of the focal point of the beam

in order to ensure that the focus is maintained on the tilted specimen. The tilt series of bright-field (BF) images were recorded with a 2048×2048 pixel cooled CCD detector having a pixel size of about 0.25 nm and a 1 s exposure time for each record. The angular interval sampled during the acquisition was between 70° and -70°, with a tilt increment given by a 2° Saxton scheme, giving a total of 90 images. Once the acquisition of the tilt series was completed, the images were first roughly aligned using a cross-correlation algorithm. A refinement of this initial alignment was then obtained with the IMOD software [23] where 5 nm gold beads deposited on the membrane supporting the specimen were used as fiducial markers. The volume reconstructions were computed using algebraic reconstruction techniques (ART) implemented in the TomoJ software with a number of iterations not exceeding 20 before reaching stability. Visualization and quantitative analysis of the final volumes were carried out using Slicer and ImageJ softwares [24, 25].

4.4 Z-Contrast Tomography

The experimental data for tomography in the Z-contrast mode were acquired with the same aberration-corrected microscope under the same conditions as above. The acquisition of STEM (HAADF and BF) tilt series was performed in the scanning mode, simultaneously using a circular centered detector for the BF and an annular detector for the HAADF, with a 10 cm camera length corresponding to inner and outer semiangles for the HAADF detector of 60 and 160 mrad, respectively. Using a 100 μm condenser, aperture provides a probe diameter of approximately 0.12 nm and a current density of about 0.5 pA/Å^2. The focusing depth of the electron beam during the STEM acquisitions was estimated to be about 20 nm, thus ensuring that the nanoparticle under study was fully inside the focal volume. The acquisition software, plugged into the Digital Micrograph software, automatically increased by discrete increment the tilt angle of the sample holder, simultaneously controlling the defocusing and the specimen drift at each tilt angle. In addition, it allowed the automatic tuning of the focus of the beam in order to keep the focal point onto the tilted specimen. An image was recorded for each position of the sample holder, and the exposure time for each pixel in the images was set to 40 μs, giving an acquisition time of 10 s for a typical 1024×1024 BF or HAADF image. The pixel size in both images was 0.07 nm. Using a high-tilt sample holder from the GATAN Company, HAADF and BF tilt series were simultaneously acquired with angles spanning from +70° to −70°. The tilt increment was set to 2° with a nonlinear variation according to the Saxton scheme [18] starting with an increment of 2° at 0° tilt. In this scheme, the tilt increment depends on the cosine of the tilt angle, in order to fill the Fourier space more evenly by making the tilt increment smaller at high tilt angles. As a result the total number of recorded projections was 99 and the total recording time was 2:30 h.

Once the acquisition of the tilt series was completed, the images were first roughly aligned using a cross-correlation algorithm. A refinement of this initial alignment and a precise determination of the tilt axis direction were then obtained

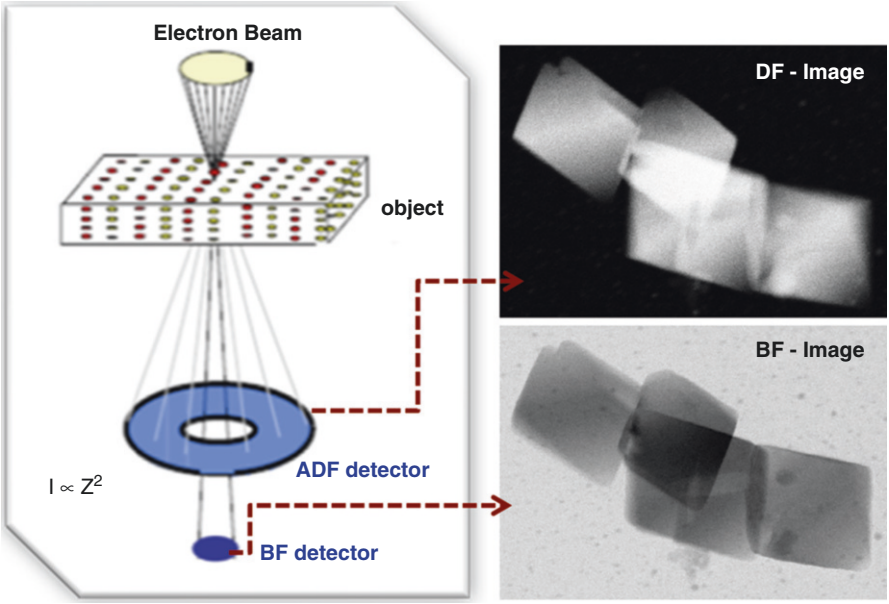


Fig. 13.3 Correlation between BF-STEM and ADF-STEM

using the IMOD software where the centers of the nanoparticles used as references were used as fiducial markers. To do so, the centers of the nanoparticles were determined from the BF images where their borders are better defined. Since the HAADF and BF tilt series were acquired simultaneously, the alignment deduced for the BF tilt series could be applied to the HAADF tilt series (see Fig. 13.3). The spatially correlated BF-STEM and HAADF-STEM reconstructions were computed using algebraic reconstruction techniques (ART) implemented in the TomoJ software with a number of iterations not exceeding 20. Visualization and quantitative analysis of the final volumes were carried out using Slicer and ImageJ softwares. To obtain the 3D models corresponding to the surfaces of the studied objects, a data segmentation procedure based on a simple selection of the voxels as a function of their intensities was used.

4.5 Analytical Tomography

One of the recent breakthroughs in nanoscience has been the development of 3D chemical analysis at the nanometer scale based on analytic tomography. At first, simple acquisition processes were used in which only two filtered images were recorded in the more convenient EFTEM mode for each element. This approach was used to investigate relative changes in the distribution of biological elements in a specimen (e.g., phosphorous) [26]. But this way rapidly shown as being inadequate for reliably construct 3D elemental maps that can be obtained only if the

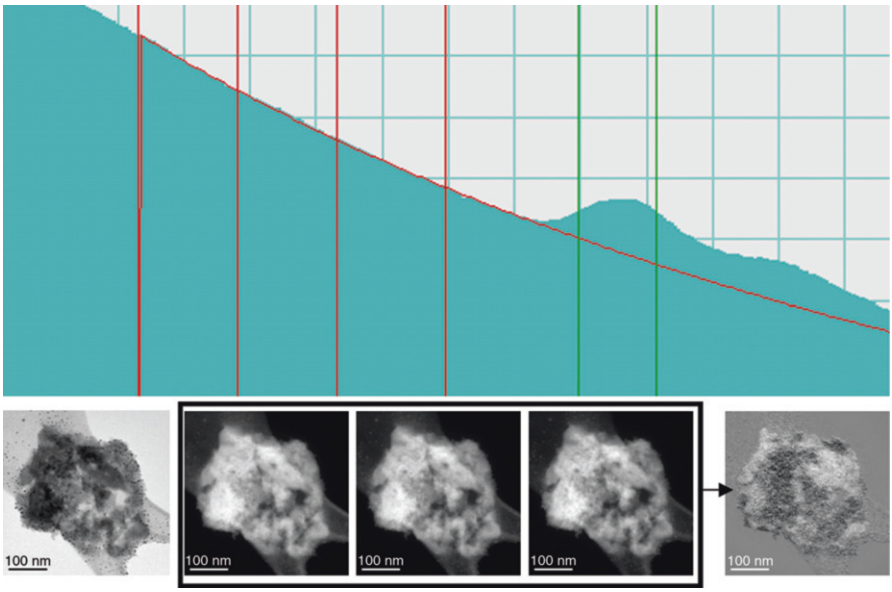


Fig. 13.4 Illustration of the acquisition of the filtered images in analytical tomography. For each tilted position of the sample, three images are recorded: one on the energy loss edge of interest and two on the scattering background allowing for its subtraction from the total signal. A Zero Loss image (*right*) is recorded during the same session. This Zero Loss image has a larger signal to noise ratio than the energy-filtered ones and it is also fully correlated to them. Previous to these recordings, a full spectrum (*green*) of the sample must be recorded that allows allocating the actual energy losses

intensity of the signal in the recorded projections is strictly proportional to the thickness and the concentration of the chemical element [27]. By using only two experimental filtered images, namely, the pre-edge and the post-edge, jump-ratio spectroscopic images can be obtained, but they reproduce a very approximate linear projection relationship. It has then been early recognized that at least three filtered images for each element are necessary to properly extrapolate the background and extract quantitative chemical signals [28, 29]. Although this lengthens the duration of the recording sessions, it offers a good assessment of the background and elemental projections with a rather good accuracy. As a consequence, this has become the recommended approach to achieve reliable 3D analytical maps (see Fig. 13.4). This full set of recordings is performed as many times as the number of elements of interest.

4.6 Data Treatment Procedure

After the acquisition process of the tilt series, the preprocessing steps and the reconstruction procedure were performed using the IMOD and TOMOJ/EFTETJ

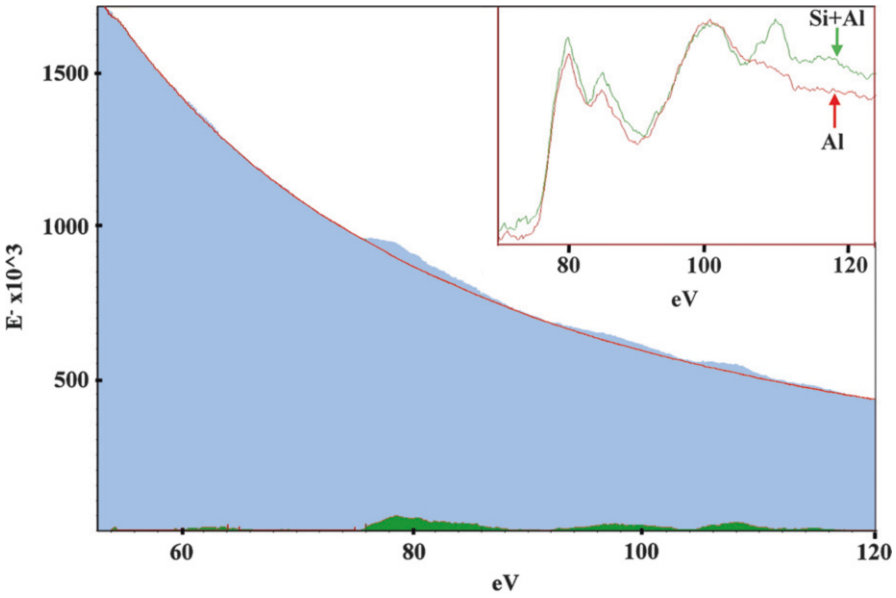


Fig. 13.5 Typical EELS spectrum (*light blue*) recorded in the vicinity of the L_{23} edge of Al (energy position: 79 eV), used as a signature for Al_2O_3 and the L_{23} edge of Si (105 eV), used as a signature for SiO_2 for a model sample made out of a mechanical mixture of silica and alumina. The *green* spectrum results from the subtraction of the background (*red line*). The inset (*upper right*) compares this latter spectrum with a reference spectrum for pure alumina, allowing thus to separate the chemical signals of the two components

software [30]. For each element of interest, the background is extrapolated from the two low-energy images and then subtracted from the elemental energy loss image in order to be left only with the signal of interest. A 2D elemental projection is reached that way for each tilt angle. This procedure is only rigorous when there is no element mixing in the sample, as in the case illustrated in Fig. 13.5.

To align the Zero Loss tilt series containing images with a high contrast and a good SNR, the standard alignment tools have been used: a cross-correlation algorithm followed by a fine tuning of the alignment using gold fiducial markers. The as-deduced alignment parameters were then used to align the tilt series of elemental projections, leading to spatially correlated series of projections. Once the alignment procedure was completed, a shape-sensitive reconstruction and the elemental volumes were computed using iterative algorithms from the tilt series of the Zero Loss and elemental projections. This procedure yields high-fidelity reconstructions by reducing the artifacts due to a limited maximum tilt angle and a limited number of projections and allows to preserve the original intensities, a crucial criterion for performing a quantitative analysis. Once the reconstructions were computed, the external shape and the porous structure of

the sample were extracted from the shape-sensitive volume that is characterized by a high SNR. To perform the "skin" calculation of the sample, a segmentation procedure was applied selecting the dark voxels of the reconstructed volume that correspond to the material and assigning them a unique intensity. Using then a surface rendering process, the surface of the object was obtained. It can be displayed in 3D for a global visualization of the analyzed aggregate or used for subsequent quantitative analysis. In addition, in analytical tomography, the knowledge of the external morphology and porous structure of the analyzed object is particularly beneficial, since it allows for extracting from the elemental volumes only the voxels corresponding to the material. Therefore we have shown that, making use of the object morphology through the simultaneous recording of classical tomography inside the same reference frame as for the elemental reconstructions, it is possible to solve one of the practical difficulties of analytical tomography, i.e., the shape determination of the analyzed object. This is done at the price of a longer recording session. Once the inner part of the specimen has been extracted from the two elemental reconstructions, a simple selection criterion can be used to attribute a given location to one of the elements. It is based on the direct comparison of the intensities, voxel by voxel, which were averaged in circular regions 5 pixels in diameter, in order to reduce the statistical noise present in the elemental reconstructions. The last step consists in a quantitative combined analysis of the elemental volumes, allowing the determination, for instance, of the amount of each element inside the analyzed grain or on its surface. Note that a relative 3D map can be also deduced, by superposing, with different colors, the intensities of the considered elemental 3D maps.

4.7 Resolution in Analytical Tomography

The spatial resolution of the 3D elemental maps generally depends on (i) the recording parameters (pixel size, maximum tilt angle, number of projections) and the data processing (accuracy of the image alignment, algorithm used for the reconstruction) and (ii) the resolution in the 2D elemental projections. They are referred to as R_{tomo} and R_{2D}, respectively. In first approximation, this 3D analytical resolution can be estimated as follows: $R_{3D} = (R_{2D}{}^2 + R_{tomo}{}^2)^{1/2}$, where R_{tomo} is the resolution of the tomographic approach and R_{2D} the 2D analytical (EFTEM) resolution. The resolution of the latter is limited by the inelastic interaction transfers by the optics of the column and is close to 1 nm for the existing TEM equipment. This leads to a theoretical 3D resolution in EFTEM mode of about 1.5 nm. In practice, a crucial parameter is the signal to noise ratio (SNR) in the elemental projections. Increasing the resolution without keeping the SNR in the 2D elemental maps to acceptable values leads to uninterpretable elemental volumes, even if the redundancy of information coming from a series of projections induces an improvement of the SNR in the computed volumes [31].

5 Key Research Findings

To be able to explore the potential application of various modes of electron tomography, specific families of samples have had to be chosen that would exemplify their specific interest but also the difficulties that needed to be overcome in their use. The various materials that are presented here have been chosen for the large interest they aroused in the communities of nanosciences and nanotechnologies and for their potential interest in the field of catalysis.

5.1 Short Review of the Previous Works

Electron tomography has long been used in the second half of the last century as a powerful instrument for studying the details of the morphology and the inner structures of living cells; this does not require very high resolution to be achieved. Work from Baumeister et al. [32] is nowadays a very good reference for electron tomography as long as biological studies are concerned.

By contrast the use of electron tomography in the field of materials only took place at the very beginning of the present century. As a result of the high technological maturity of the electron microscopy techniques at the time, its use in the field very rapidly reached a high degree of sophistication. Advantage has immediately been taken of the various working modes available in electron microscopy to gain as much 3D information on nano-objects and nanostructures as could be reached. For example it has rapidly appeared that analytical tomography could be used to perform chemical analysis at the nanometer scale. Teams around Professor de Jong (Utrecht University) and Professor Midgley (Cambridge University) have been indisputable pioneers of the field. The first team studied, as soon as in the year 2000, porous zeolites of interest for catalysts support [33]. They used the same techniques as the ones previously used in the field of biology, recording set of tilted projections using transmission electron microscopy (TEM) in the bright-field (BF) mode. They based their reconstructed 3D images on the simple filtered retroprojection technique.

Related to the HAADF-STEM tomography, since the inspiring experiments carried out by Midgley et al. [16], this incoherent mode was applied on several occasions to the 3D characterization of nanocrystals, such as, for instance, magnetite nanocrystals [34], cerium oxide [35], gold [21], palladium, or platinum nanoparticles [36]. The morphology and the surface crystallography were unambiguously solved for all these particles, which generally have a size larger than 10 nm. Bimetallic nano-alloys were also investigated, either isolated such as FePd or CoPt or physically attached to a support, as for instance CdSe on carbon nanotubes [37].

The team from Cambridge, simultaneously with a group with Professor Günter Möbus (Sheffield University), first combined electron tomography with electron energy loss spectroscopy (EELS) to tentatively perform chemical analysis [16, 38]. Using ad hoc model samples, they could reach down a 10 nm spatial resolution.

Furthermore, by applying EFTEM tomography at energy losses corresponding to core levels (core-loss EFTEM), several pioneering works were performed up to now. On the one hand, some of these works report its first implementations in the material fields [39] and the further progress in the experimental settings and data treatment, as well as its limitations compared to other tomographic modes. On the other hand, some other works were devoted to the application of this technique for obtaining reliable 3D chemical information by mapping calcium or phosphorous concentrations in biological specimens [40] to localize at 3D carbon in carbonaceous nano-composites, to reach information on the oxidation degree at the surface of a SiC nanograin, to separate at the nanoscale the 3D distributions of silica and alumina within a porous grain of heterogeneous catalyst support, to solve the spatial distribution of Y_2O_3 nanoparticles within a FeAl matrix, and to obtain reliable chemical maps of the different components in semiconductor devices.

Very recently, a pioneering work was devoted to the 3D characterization of a semiconductor nano-object using the STEM-EELS mode. Such measurements require a specific rotation holder, and are recommended for pillar-shaped sample, limiting the application to well-defined nano-objects. It is important to point out that, due to low signal intensities, longer lasting acquisition times are needed, and as a consequence the irradiation damages may become dramatic for sensitive samples. In addition, the acquisition of a collection of EELS spectra in the STEM mode may suffer from pixel-to-pixel drifts.

In the field of nanomaterials reference, the team led by Professor Van Tendeloo (Antwerpen) has also performed pioneering studies, exploring discrete tomography [21] and tomography with atomic resolution [41].

5.2 Quantitative 3D-TEM

5.2.1 Porosity

Quantitative measurement of the porosity of meso- and microporous materials is indubitably one major contribution of electron tomography in the field of nanomaterial sciences. Characterization of this family of materials needs to acquire the ability for measuring the quality of the porosity (open or closed porosity), mean size of the pores, total open surface of the pores, specific surface of the material, and ratio of the porous volume to the total volume. For bulk materials, chemisorption of nitrogen or mercury can give access to some of these parameters through heavy modeling of the geometry of the pores and their connections. These techniques cannot be applied to nano-objects, and electron tomography is, in that case, a must that even gives direct information not needing any modeling. Due to limited spatial resolutions, though, tomography misses the smallest porosities of a sample (typically less than 1 nm) and is therefore quantitatively incomplete. Most of the porous materials are amorphous or poorly crystallized in nature so that they do not give rise to coherent diffraction under electronic irradiation; therefore TEM tomography can be applied with no trouble.

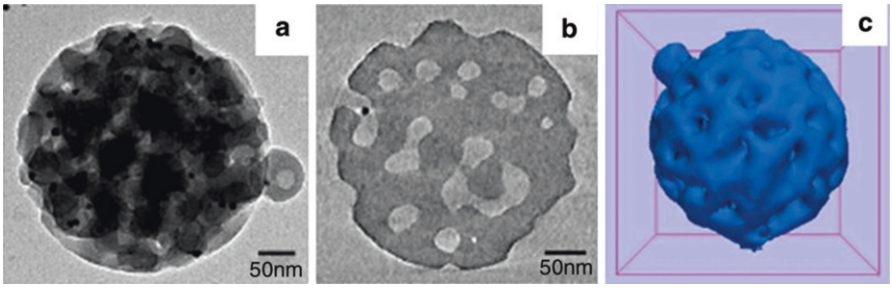


Fig. 13.6 3D-TEM imaging of a mesoporous zeolite. (**a**) Classical 2D-TEM projection of a 350 nm particle, (**b**) cross-section of the reconstructed object, showing the closed porosity of the nano-object, (**c**) 3D modeling of the sample, defined by using a segmentation algorithm based on grey level intensities of the voxels in the 3D matrix

As an illustration of the application of the electron tomography technique to the quantitative characterization of a catalyst support, we present in the following a study of mesoporous zeolite. A usual 2D-TEM projection of one of the nanoparticles clearly exhibits its porosity (Fig. 13.6a). But information about its open or closed character cannot be determined from such an image. On the contrary by using the 3D reconstructed volume of the sample, it was possible to access and to measure the total volume of the pores as well as their exposed surface. The main information that was reached though was the opened nature of the porosity that can be clearly observed on 2D cross-sections of the reconstructed object (see Fig. 13.6b) [12].

5.2.2 3D Localization of NPs on a Support

Determining the localization of nanoparticles on a support is highly relevant to electron tomography. The functionalities of nanomaterials and nano-object made up from a number of constituting elements are highly dependent on their relative positions or their position on some substrate. A good example is given by heterogeneous catalysts consisting of an active phase made of nanoparticles scattered on a physical support which catalytic properties are strongly dependant on the existence of an open access to the catalytic particles. Even the proper particles properties may depend on their localization on a substrate when this localization controls their size for example. Confinement of a material inside a nanometric cavity has been observed to favor the development of new metastable phases.

Studying spatial distribution of nanoparticles on their support has been at the heart of our team activity at the starting of electron tomographic experiments. In cases when the recording contrast between the nanoparticles and their support is high enough, like for metal nanoparticles on a light support, and when coherent diffraction is only of a low intensity level, then bright-field TEM can be an adequate mode to be combined with the tomographic approach. In the following paragraphs, we will present some of the studies that have been done in order to illustrate the use of the electron tomography technique for the study of composed materials.

Palladium Particles Imbedded Inside a Carbon Nanotube. 2D analysis of nanoparticles imbedded in a porous or structured substrate does not give access to the knowledge of whether these particles lay "inside" or "outside" the support, while 3D reconstruction gives direct qualitative information on the relative position of particles on various substrates; these reconstructions even allow a precise quantization of the information. Demonstration of the interest of 3D electron tomography for localizing nanoparticles (NP) on a surface was performed using metal particles (Pt, Pd, PtRu, etc.) embedded in various support like, for example, mesoporous SBA15 [12], porous zeolites [42], and pure or doped carbon nanotubes (CNT) [43]. All these artificial combinations were aimed at studying the effect of confinement on physical and chemical properties of nanoparticles.

A first example is given by the study of the combination of palladium nanoparticles imbedded in carbon nanotubes simulation of a pollutant "sponge" [43]. Figure 13.7 below shows longitudinal (Fig. 13.7b–e) and transversal (Fig. 13.7f) through cuts of the reconstructed volume of such a system as well as the modeling of the object (Fig. 13.7g). A statistical study of the Pd particles allows quantifying their mean diameter to be close to 4 nm. A direct counting of the palladium particles showed that 50 % of these particles were inside the carbon nanotube while the other half remained on the outside. Furthermore this study showed the much more complex than expected structure of the object: an organic residue layer shows up on both the inner and outer surface of the nanotube. These layers strongly indicate the good quality of the wetting process that occurred during the sample preparation, moreover highlighting the hydrophilic nature of the CNT surfaces that were functionalized with OH functions for that purpose.

Particles Scattered on a Plane Surface. Plane surfaces are of prime importance in nanosciences as they characterize many materials because they can present specific structures like steps and terraces at various scales as well as different chemical properties depending on the dangling atoms lying at the surface. These physical and chemical structures on plane surfaces are key parameters that govern the physical and chemical properties of nanoparticles deposited on these surfaces. It is therefore of utter importance to be able to quantify the position of nanoparticles on plane surfaces before starting any kind of modeling.

Along this line we have the 2D spatial distribution of palladium nanoparticles on delta phase-layered alumina [44] as well as the localization of platinum nanoparticles deposited on ultrafine graphite (few layer graphene, FLG) exhibiting a very large number of steps and terraces on its edges [45]. In the latter case, we could even study the temperature stability of the particles on the surface by combining the tomography procedure with in situ high-resolution imaging and molecular dynamics simulations.

We will now focus on a system made of hybrid epitaxial layers like P3HT polymer–CdSe, Au, and Pt NPs. These layered materials spontaneously grow by alternating crystallized and amorphous layers, the nanoparticles resting in the latter. These materials have potential applications as photovoltaic light collectors with an extended spectral width. As the position of the nanoparticles inside the polymer layers contributes to the control of the electrical transport properties of any

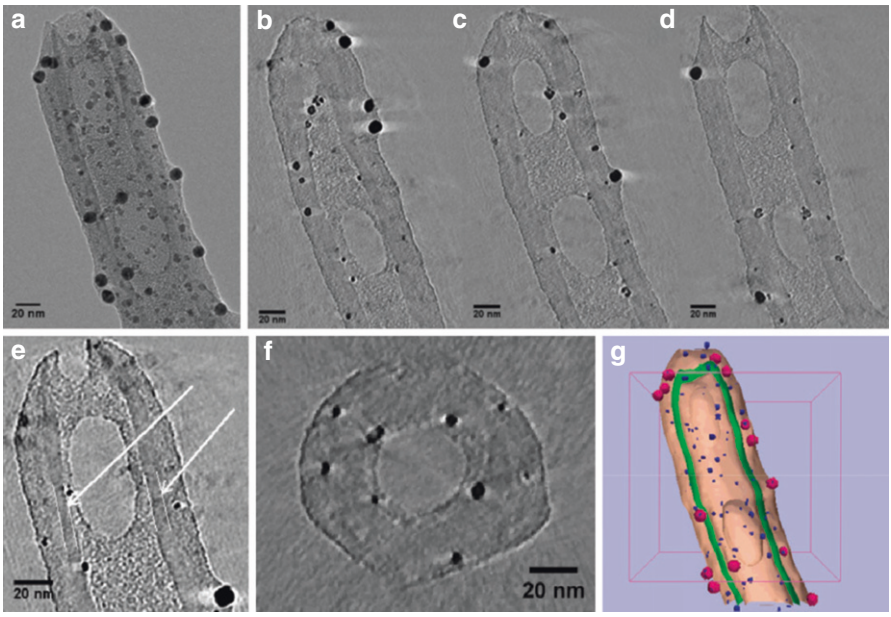


Fig. 13.7 (**a**) Typical 2D-TEM image from the tilt series used to reconstruct the volume of a CNT that has been immersed into a suspension of Pd nanoparticles (*blue dots*). (**b–d**) Transverse sections through the reconstructed volume exhibiting the location of the Pd particles along the carbon nanotube. (**e**) Longitudinal section at higher magnification highlighting the presence inside the CNT channel and on its outer surface of an amorphous phase that is a residue of the ethanol used as a solute during the sample preparation. (**f**) Transverse section perpendicular to the tube axis (which is parallel to the tilt axis) showing the good wetting of the inner tube wall by the liquid-like phase coming from ethanol solute. (**g**) Modeling of the various surfaces that characterize the sample. The *red* particles are the 5 nm gold nanoparticles used for the precise alignment of the tilted projection series. The carbon nanotube itself is shown in *green*. The *pink color* symbolizes the amorphous material that has been deposited at the time of preparation of the sample. This reconstruction clearly demonstrates that 3D analysis of such a sample permits to discriminate between inner and outer palladium particles

potential device, there is a strong need for being able to characterize the distribution of these particles. 3D quantitative electron tomography is the only tool presently available that permits determining the topology of the distribution of particles inside a volume. Fig. 13.8 presents results that have been obtained for P3HT–CdSe hybrid film. The main result is that the distribution density of the nanoparticles inside the amorphous layers of the layered structure is not uniform but exhibits a vertical segregation process. This segregation process has been interpreted as the result of the difference in "solubility" of the nanoparticles in the semicrystalline polymer phase and the solvent used in the epitaxial process.

Nanoparticles Localized on a Curved Surface. In the course toward always smaller electronic devices, metal and semiconductor nanostructures are ongoing a booming growth. Charge doping, size effects, and surface and interface structures

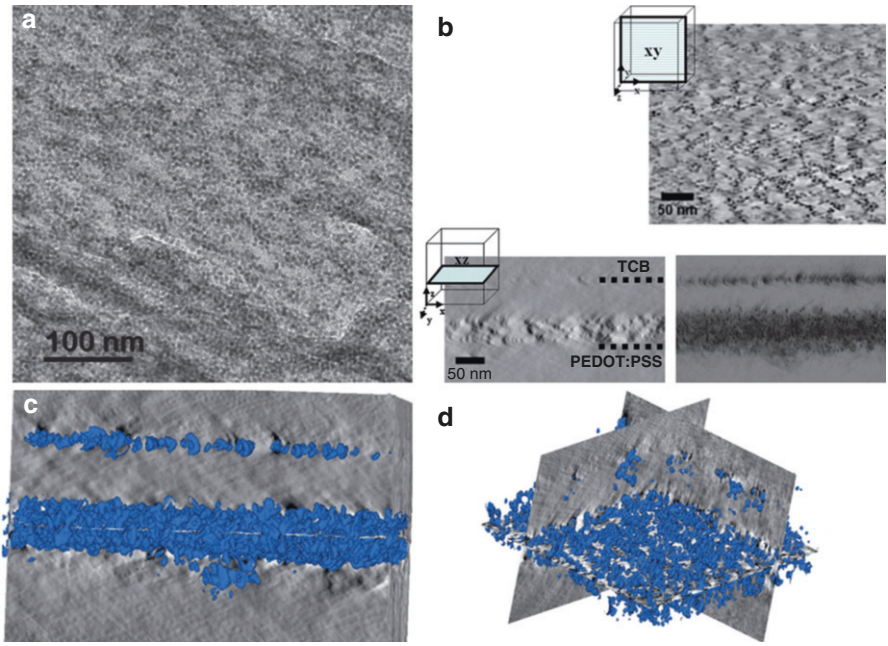


Fig. 13.8 Tomographic analysis of the P3HT–CdSe hybrid film (1:1 in weight). (**a**) A bright-field TEM image extracted from the tilt series used to calculate the volume of the hybrid film. (**b**) *Top*: example of a longitudinal slice extracted from the reconstructed volume. *Bottom left*: typical cross-section at a chosen location. *Bottom right*: sum of cross-sectional images along one direction in the plane of the film showing the bilayer structure and the surface decoration of the top P3HT layer. (**c**, **d**) 3D modeling of the CdSe nanocrystals (in *blue*) illustrating the 3D distribution of CdSe NCs in the film

are highly relevant parameters needing to be studied at a nanometer scale. Considering, Si or Ge nano-wires for example, one of the many potential bricks of future electronic devices, they are generally grown using gold nanoparticles caps acting as a catalyst. This method is detrimental to the conduction properties of the final wire as gold residues end onto the surface of the wire or even diffuse inside the wire at the time of its growth. It is the aim of the following study (see Fig. 13.9) to allocate the gold distribution in a silicon nano-wire grown according to the catalytic method [46]. Electron tomography of a gold-grown nano-wire has evidenced a complex but interesting conduction structure. The axial part of the wire exhibits the natural intrinsic conductance of the constituting semiconductor, while the outer part, strongly gold doped, exhibits an extrinsic conductance. As a natural consequence, the interface between the two regions acts as a Schottky junction. The overall conductivity of the wire was separately determined using conductive-tip AFM measurements.

Other tomographic measurements have been performed on InGaN/GaN heterostructures formed as semiconducting nano-wires that have potential applications as electroluminescent diodes. In these structures the electrical and therefore

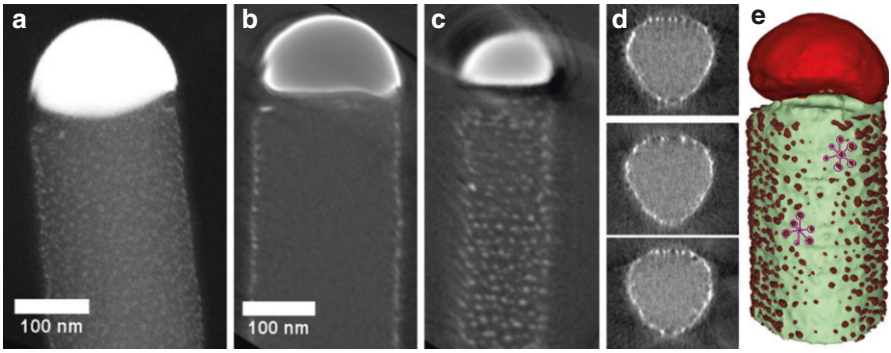


Fig. 13.9 Nano-wire Au/Si: (**a**) Typical HAADF-STEM image of the nano-wire where the *white dots* correspond to the Au-rich regions: they correspond to NW catalyst droplet and to the catalyst residues along the nano-wire. (**b**, **c**) Longitudinal and (**d**) transversal slices showing that the Au nanoparticles are localized on the outer surface of the nano-wire. (**e**) Modeling of the nano-wire; the sketch illustrates two Au nanoparticles and their neighbors

the light emitting properties can be adjusted by varying the indium composition as well as the size of nanoparticles clusters present in the bulk of the material. Again, electron microscopy is a choice tool for studying these clusters, and our studies along this line are still underway.

5.2.3 Faceted Nanoparticles

Despite the coherent diffraction that occurs when looking at crystallized nanoparticles, it is of very high importance to be able to characterize the morphology of small crystals and even more important to get information on their surface crystallization degree. This is because the catalytic activity of a particle as well as the selectivity of the chemical reaction it controls are totally dependent on the shape and symmetry of the exposed surfaces. Therefore the contribution of electron tomography in this field is its ability to provide full 3D descriptions of the facets and crystalline planes in general of nanocrystals; this knowledge can in turn give guidance to the chemists in charge of the growing of the particles. Looking at crystals with a high-order symmetry axis parallel to the projection direction can collect this information, when the characterization is performed using 2D electron microscopy. This technique, however, strongly depends on the good fortune of having a set of crystals with the proper orientation to permit recording of all the high-symmetry directions yielding a full characterization of the crystalline sample. 3D tomography on the contrary directly gives access to the full characterization of a unique crystal giving furthermore access to a possible study of the symmetries as a function of the nanocrystal size.

CeO_2 Nanoparticles; Model-Based Image Segmentation. We have recently performed a surface study of cerium oxide (ceria, CeO_2) nanoparticles [47] that are considered as interesting potential support for oxygen storage [48]. The ceria nanocrystals were grown by a solvothermal synthesis process assisted by

microwave heating [49]. Adjusting accurately the synthesis parameters (e.g., duration and heating temperature) allowed the preparation of ceria nanoparticles with different morphologies and consequently adjustable properties in terms of reactivity and selectivity to a given reactant. More precisely, cubic and octahedral nanoparticles as well as nanorods with various sizes can be obtained. On each of these families, we have performed a full geometrical characterization, quantifying the truncations and facets they exhibit (see Fig. 13.10). Each tomographic study has been directly related to high-resolution studies of the same nano-object with the same orientation used for the recording of the tilt series.

As an illustration of one of these studies, we choose here to discuss objects that do exhibit triangular shapes on their 2D projections and that only 3D tomography could help solving their actual shape. Fig. 13.11a illustrates several typical images from the tilt series acquired simultaneously in BF and HAADF modes. Their simple observation suggests that at first sight, the NPs are not identical from a morphological point of view. However, comparing the acquired BF and HAADF images to some theoretical images obtained by projecting the structure of an ideal crystal, the NPs can be roughly associated to octahedrons or to other close geometrical shapes. Their 3D representations are obviously required in order to definitely determine their exact shape. By analyzing in a combined manner the results obtained by tomography and high resolution (in TEM or in STEM) microscopy, we were able to asses that the four nanoparticles have similar shapes with external surfaces made of eight identical triangles. In addition, the angles between two adjacent triangles were systematically measured, and values close to the geometrical angles between {111} planes in a crystal were systematically found. That allowed us to definitely assign the morphology of NPs to a shape close to an octahedron. Finally, a more detailed analysis of the reconstructed volumes allowed us also to observe that the apexes of the bipyramid and two of the corners of the basal plane are rounded, while the other corners are faceted introducing thus two well-indentified {110} minor facets. The 3D quantification allowed us to precisely determine the amounts of the two types of facets, i.e., 98 % for the {111} planes and 2 % for the {110} ones.

Molecular Dynamics-Assisted Shape Modeling. Progress in both the development of aberration-corrected optics for electron microscopes as in the development of more sophisticated software for recording and analyzing data makes it today quite feasible to reach a 1 nm spatial resolution in tomographic reconstructions. As a consequence it is now certainly possible to precisely study the external shape of objects sized only a few nanometers, and because of the very limited amount of atoms in the object, it becomes possible to take advantage of molecular dynamics calculation to check that the obtained shape is a stable one or not [36].

To illustrate this point, we present here a study of 5 nm-sized platinum nanoparticles making, for the first time ever, use of molecular dynamics calculations. Two series of tilted projections of a set of platinum nanocrystals have been simultaneously recorded in both the HAADF and BF modes using scanning transmission STEM. The 3D image reconstruction was performed using the HAADF

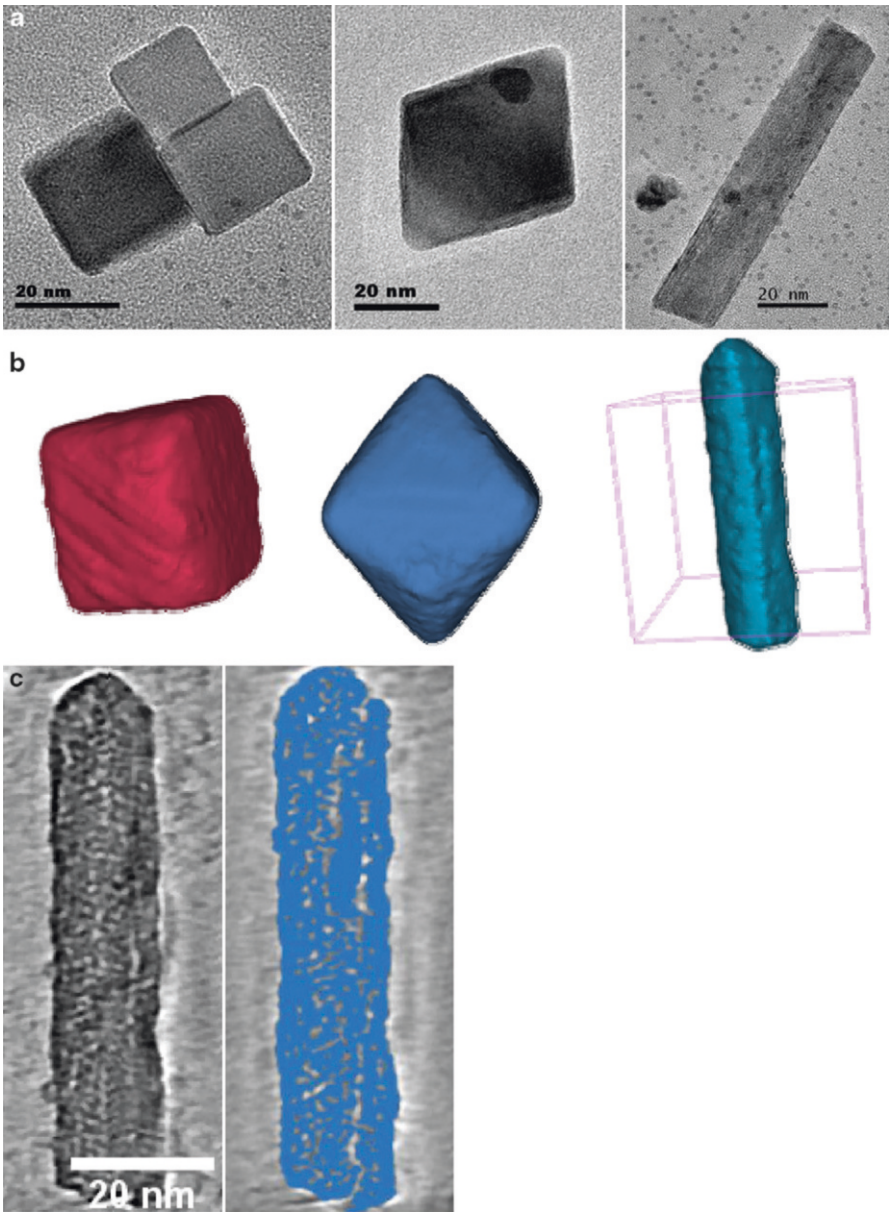


Fig. 13.10 (**a**) Three different CeO_2 morphologies obtained using a green chemistry synthesis; (**b**) their corresponding 3D models obtained by tomography; (**c**) longitudinal slices extracted from the 3D voxel matrix of the nanorod illustrating the presence of a porous structure inside the rod

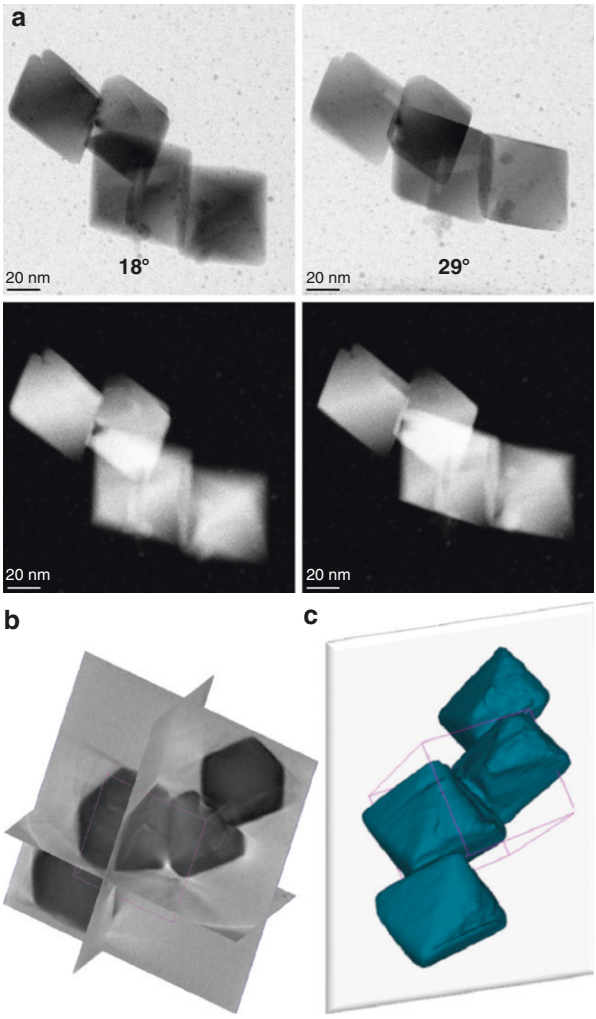


Fig. 13.11 (**a**) Typical BF and HAADF images acquired simultaneously in the STEM mode on a collection of four CeO_2 nanocrystals with a polyhedral shape, extracted from the corresponding tilt series at the angles 18° and 29°. The two tilt series were subsequently used to calculate two spatially correlated volume reconstructions. (**b**) Orthogonal slices through the BF-reconstructed volume obtained for this assembly of CeO_2 nanoparticles with a polyhedral shape. (**c**) 3D representations of the four nanoparticles oriented individually to present the same global appearance; they have been obtained by applying a classical data segmentation process to the sub-volumes extracted from the computed reconstruction

series in order to avoid coherent scattering but using the high quality alignment of the BF images series for which the edges of the material samples are sharper due to a better SNR. Iterative algorithms have been used in the course of the reconstruction of the 3D object, the resulting shape being compared to a general 3D model. As a result the best representation has been recognized as being a truncated octahedral shape rather than a simple octahedron or a cube-octahedron that are other possible stable shapes. Checking of this empirical result has been performed through molecular dynamics calculations in which starting from a spherical nano-object or from an octahedron, one performs repeated numerical annealing of the object up to the point where a stable object appears [50]. Both these calculations led to a truncated octahedron with large {111} facets with a hexagonal symmetry in full

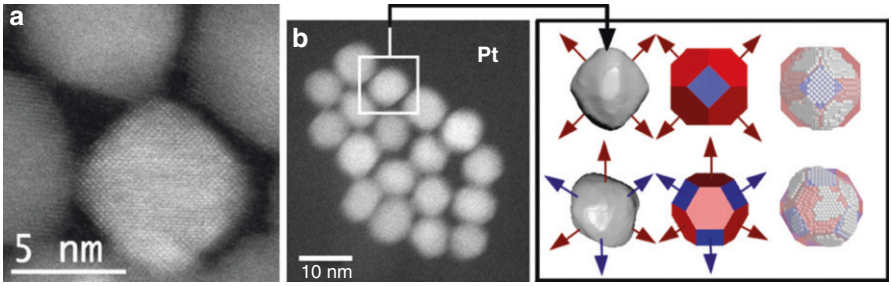


Fig. 13.12 (**a**) HAADF image acquired on a representative Pt nanoparticle. (**b**) Illustration of the selection of the NP on which a detailed analysis of the reconstruction has been realized. A combined analysis of the results obtained by electron tomography and by molecular dynamic simulations allowed us to demonstrate that the morphology of the NP is close to a truncated octahedron (see more details in Ref. [36])

agreement with the experimental determination of the sample shape. Starting from a cube-octahedron shape, the calculation yielded a truncated octahedron having small {111} triangular facets, not compatible with the experimental results.

Molecular dynamics calculations being based on the minimization of the energy of the atoms constituting the object of interest, the calculations yielded a very interesting side result: an atomic modeling of the sample. This has been reached by taking into account the translational periodicity of the atomic lattice of the crystal. From this atomic modeling, the surface atoms have been identified and then a measure of the relative amount of facets has been made that stands as 50 % of {111} facets and 15 % of {100} facets (Fig. 13.12).

5.2.4 Long-Range Ordering

2D or 3D organization can be performed or self-organization can take place within populations of objects. Long-range periodically ordered assemblies are generally studied through the diffraction of appropriate wavelengths and short-range ordered assemblies through scattering of waves. Organized populations are important in that they add new collective properties to the intrinsic properties of their constituents. When dealing with organized populations of nano-objects, electron tomography is a very appropriate tool for accessing order properties of these assemblies: (i) measures are directly performed in the real space thus escaping the phase reference problem of the diffractive techniques, (ii) a unique measure simultaneously gives access to information at both the scale of the individual objects as well as at the scale of their structure, and (iii) a unique measure addresses all structures – ordered at long- and short-range, disordered, and all their possible combination.

3D Meta-Crystals. The first example of this application of electron tomography to ordered assemblies of nano-objects is on the self-assembly of platinum nanocrystals as a meta-crystal [51]. The individual Pt nanoparticles used in this study are the ones already discussed above that exhibited a truncated octahedral morphology having a 5 nm main length. We performed a tomographic analysis of

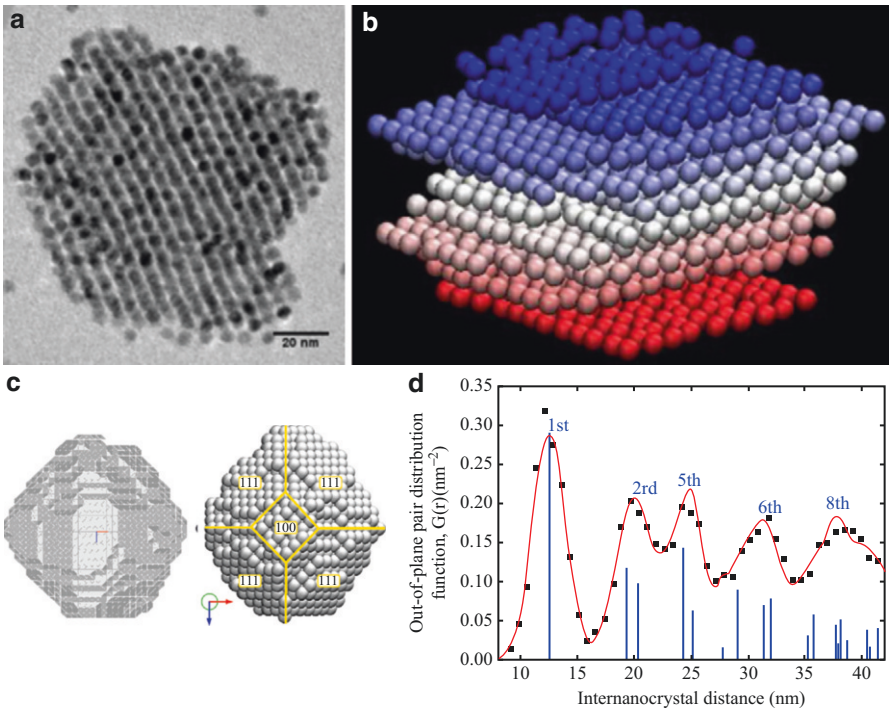


Fig. 13.13 (**a**) Typical BF-TEM image from the tilt series used to reconstruct the volume of a fragment of a meta-crystal, corresponding to 0° tilt angles. (**b**) Reconstructed 3D image of the meta-crystal. The colors indicate the different monolayers in the assembly. (**c**) *Left*: reconstruction of one of the constituent nano-objects. *Right*: atomic reconstruction of these constituting objects clearly shows the symmetry of facets. (**d**) The out-of-plane pair distribution functions (PDF). The *black square* symbols represent the experimental PDFs, the *blue lines* represent the PDFs for a slightly distorted fcc structure, while the *red curve* is a fit of PDF for the experimental structures

a meta-crystal fragment having a ten-layer thickness and a few hundred nanometers for the lateral sizes (see Fig. 13.13a). From the reconstructed image of the meta-crystal, the 3D position of the center of gravity of the Pt nanocrystals in the structure has been measured giving a description of the meta-crystal lattice in the real space. Quantitative information on the lattice has been gained through the calculation of pair correlation functions (PDF) of the inter-object distances. These calculations were performed both in-plane and out-of-plane. Such a correlation function is shown on Fig. 13.13d. It exhibits nice sharp correlation peaks indicating a well-ordered meta-crystal. The qualitative analysis of the calculated lattice suggests a fcc structure for the meta-crystal, but the mean lattice parameters extracted from the in-plane and out-of-plane correlation functions clearly demonstrate that a tetragonal distortion must be taken into account. On the long-range scale, the order parameter of the meta-crystal has been also measured, from the intensity decrease of the neighboring nanocrystals peaks in

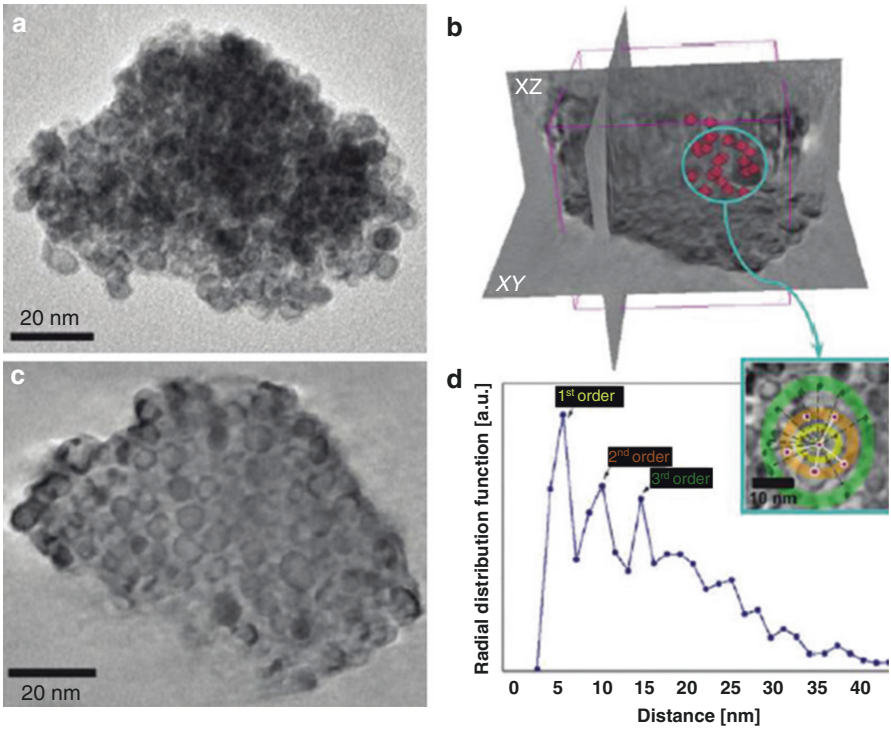


Fig. 13.14 Electron tomographic study of CoPt core–shell pellets: (**a**) Electron microscopy micrograph of the region considered for the tomographic acquisition. (**b**) 3D representation of the reconstructed volume with the nanoparticles centers marked by red spheres. (**c**) XY section through the reconstructed volume. (**d**) Radial distribution of the nanoparticles as a function of the distance between the nanoparticles in the pellet

the correlation functions, to be 250 nm. Another side result gained through this tomographic study is the very low-size dispersion of the synthesized Pt crystals that allows a long-range order as large as 250 nm.

A similar quantitative tomography study has been performed on CoPt core–shell nano-objects. These platinum-coated cobalt particles were compressed as to form pellets [52] (see Fig. 13.14). From the reconstructed image, the 3D spatial distribution of the core–shell objects was measured as in the meta-crystal case. By analyzing the pair distribution correlation function (Fig. 13.14d), one can only clearly observe the first three neighbors indicating that for this sample, only short-range order applies that was measured to be only a few tens of nanometers with constituent particles with the same-size particles as in the Pt meta-crystal.

Stacking Faults in a Periodically Ordered Mesoporous Material. The material FDU12 is a porous material which porosity is made of connected periodically distributed voids on a fcc lattice at the nanometer scale. Quantitative tomography is again efficient for studying this spectacular case of inverted meta-crystal [53].

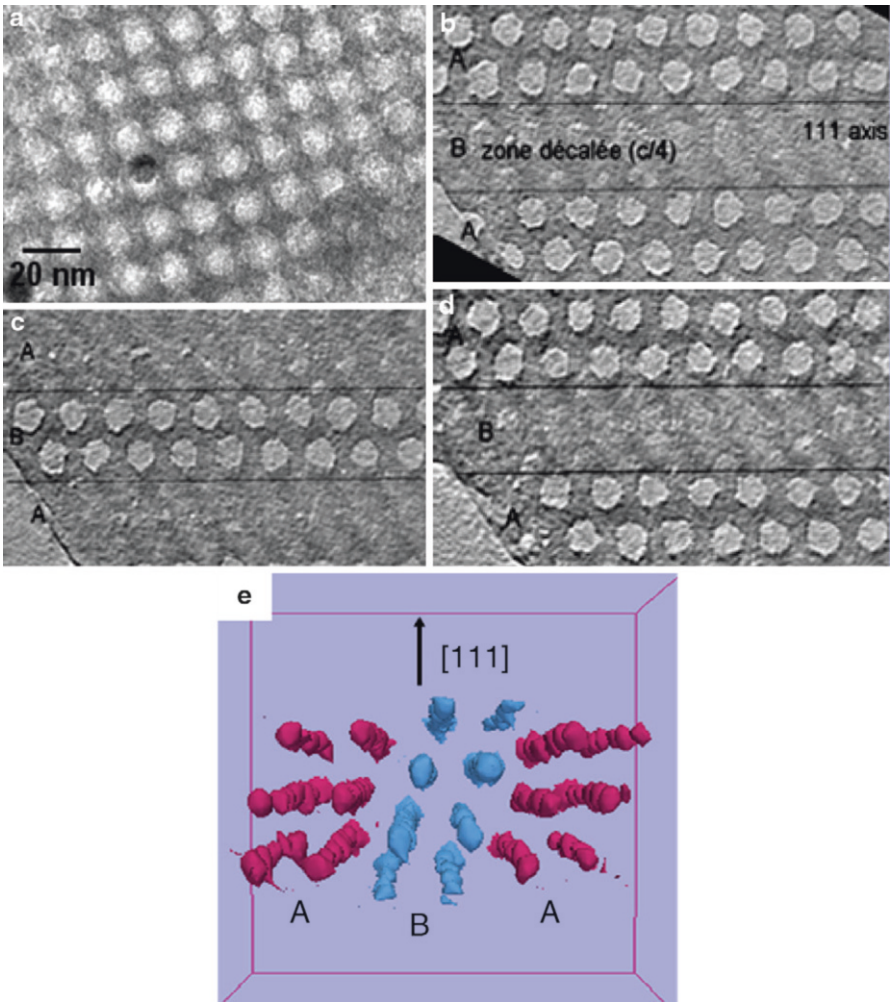


Fig. 13.15 (**a**) Typical TEM image from the tilt series used to reconstruct the volume of the FDU-12 mesoporous silica, showing the presence of an ordered network of spherical cages. (**b**–**d**) Three (111) sections separated by half of the d_{111} distance; (**e**) Views of the modeling along the [1–2 1] axis

Only the lattice parameter or the space group of the structure can be deduced from the simple observation of a 2D-TEM projection of the object (Fig. 13.15a). Tomographic analysis of the object provides much more direct and precise information about the organization of the voids in the real space. Fig. 13.15b–e clearly shows a stacking fault in the ordering of the porosity voids of the sample under study: along the [111] direction of the lattice, two (111) planes are clearly shifted by half the value of the lattice parameter. The interesting part is that this kind of defect never appears in the corresponding crystal lattices.

5.2.5 Combined Analysis of Various Reconstructions

This part of the chapter is devoted to the demonstration that quantitative electron microscopy is unavoidable as soon as complex mixtures of nanostructures and nano-objects are concerned as the one encountered in realistic process and device development. This is a very basic situation in the field of heterogeneous catalysis, for example, in which actives phases are mainly shaped as nanoparticles that need to be supported in such a way that the overall catalytic activity of the combination is enhanced when compared to the activity of the constituents. Reactants must freely access the active part of the catalysts, and the product of the reactions must not remain confined at the place they were produced. In such studies if the contrast between the various phases is large enough for giving a good SNR then TEM in the bright-field mode is the tool of choice for performing electron tomography because of its simplicity. This assumes that diffraction contrast can be neglected. Such a situation can be seen in the study of small metal nanoparticles lying on or being embedded in a light support. If the diffraction contrast cannot be neglected, an incoherent mode like high-angle annular dark field is needed STEM-HAADF and STEM-BF. To reach good enough SNR, it then becomes necessary to use scanning transmission microscopy that enhances the recorded signals. HAADF though is more sensitive to heavy elements and if one faces a sample combining light and heavy elements, it is then necessary to record images in the bright-field mode so that one ends with STEM-HAADF and STEM-BF. That way the two sets of records are totally correlated and a precise comparison can be performed between the two 3D reconstructions of the object of interest.

As an example we present a complex structure made of two metal, cobalt and ruthenium nanoparticles as catalysts impregnated in a semiconducting support exhibiting a bimodal porosity. Typically this actual catalysts combination has been studied using HAADF for imaging the metal nanoparticles and comparing with the morphology of the support that has been deduced from the bright-field reconstruction. As a result we could determine that the Co nanoparticles were confined at the entrance of the small pores of the bimodal porosity of the SiC support while, on the contrary, Ru was selectively localized inside the large pores (Fig. 13.16).

5.3 Analytical 3D-TEM

5.3.1 Validation of the Methodology

Validation of the 3D analytical tomography using energy-filtered transmission electron tomography has been performed on a model material made of a 50–50 % mixture of amorphous alumina (Al_2O_3) and silica (SiO_2) which preparation method has been described elsewhere [31]. Fig. 13.5 above shows a typical electron energy loss spectrum that has been recorded in the vicinity of the L_{23} edge of Al (energy position: 79 eV), used as a signature for Al_2O_3 and the

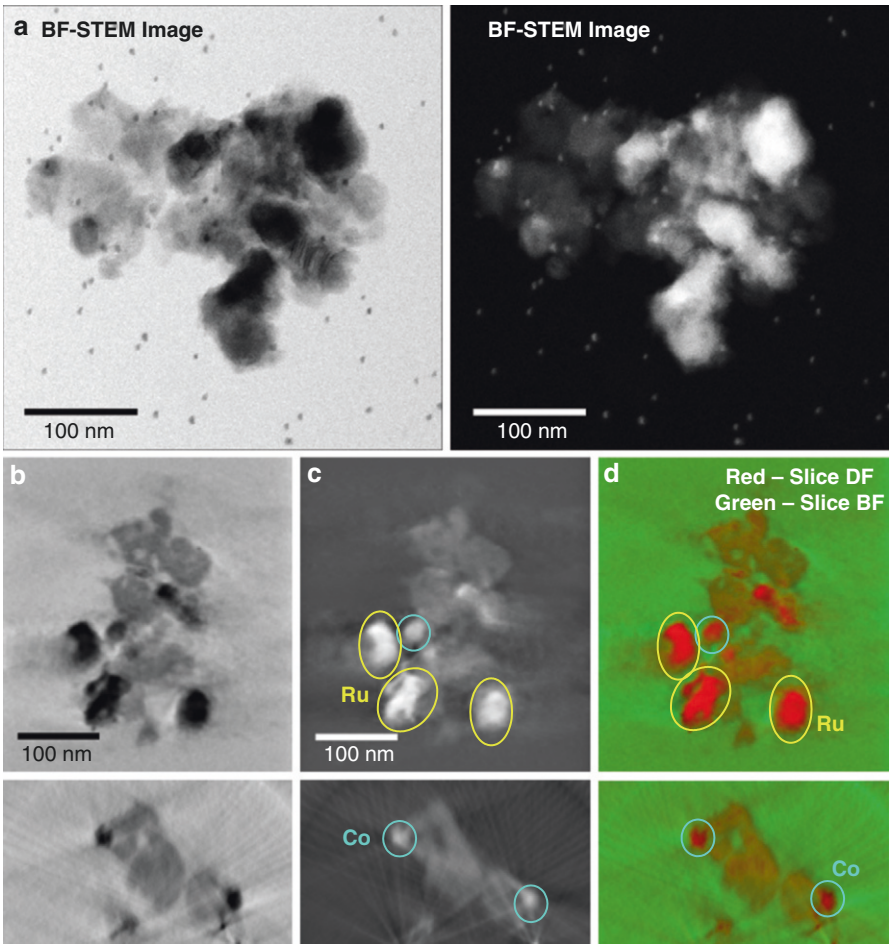


Fig. 13.16 Combined STEM tomographic analysis on a silicon carbide (SiC)–cobalt (Co)- and ruthenium (Ru)-supported nanoparticles. (**a**) STEM-BF and STEM-HAADF images extracted from the two tilt series recorded simultaneously in STEM that were subsequently used to reconstruct the two complementary HAADF et BF volumes spatially correlated. (**b**) Ortho-slices through the STEM-BF reconstruction. (**c**) Same for the STEM-HAADF reconstruction, but here Co and Ru can be differentiated by the contrast. (**d**) Combined representation of the two reconstructed volumes obtained by superposing the HAADF volume in *red* and the BF volume in *green*

L_{23} edge of Si (105 eV), used as a signature for SiO_2. Tilt-series images were recorded with the energy of the electrons filtered around the two energy loss edges, from which 3D reconstruction of the sample was performed for the two elements. Fig. 13.17 below illustrates the final elemental images: the two chemical components, AL_2O_3 and SiO_2, can clearly be distinguished and a quantitative analysis of their content perfectly retrieves their 50–50 % proportion.

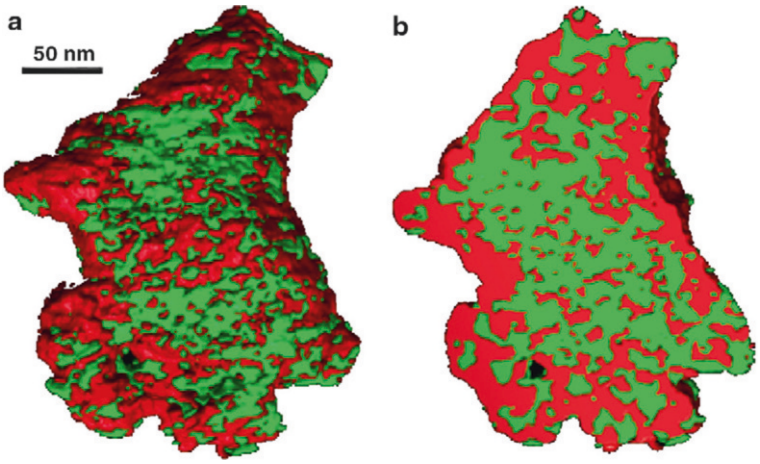


Fig. 13.17 Illustration of the capability of analytic 3D tomographic imaging for a catalyst sample made out of a mixture of silica and alumina. (**a**) Reconstruction of the external surface of the sample allowing the distinction of the two chemical components. (**b**) Cut through the 3D analytical reconstruction showing the inner composition of the sample. The upper limit of the chemical resolution in this low-contrast mixture is 5 nm! The *red color* represents the Al_2O_3 distribution and the *green color* gives the SiO_2 distribution

5.3.2 Nitrogen-Doped Carbon Nanotubes

Once the methodology of analytical tomography has been validated, it was immediately applied to real cases studies. The first one was focused onto the morphological effect induced by the doping of carbon nanotubes with nitrogen. Among the different types of doped carbon nanotubes, the nitrogen-doped carbon nanotubes (N-CNTs) have received an increasing scientific interest during the past decade due to the fact that nitrogen incorporation strongly modifies the chemical and physical properties of the pure carbon nanotubes. In this general framework, the first goal of this study was to determine the spatial localization of the nitrogen atoms within the structure of highly doped N-CNTs (about 20 %N). In this type of tubes, the insertion of nitrogen atoms changes the classical tubular morphology in a bamboo-like one, with successive arches closing progressively along the tube. Previous 2D EELS-analyses [54, 55] have shown that the carbon atoms of the graphitic plans that compose the arches are partially substituted by nitrogen atoms. From a morphological point of view, a traditional TEM analysis of highly doped N-CNTs shows the presence of two types of arches: (i) transversal arches, perpendicular to the walls and containing a rather high density of crystallographic defects, and (ii) rounded arches, thicker and with less defects. Based on these previous findings, one of our purposes was to individually solve the nitrogen concentration within the two types of arches. To obtain such information, a classical 2D analysis in the spectroscopic EELS mode is certainly not sufficient, due to the 3D morphology of the tube. As a consequence, the setup of the tomographic approach in TEM coupled with the EFTEM analytical mode is once again unavoidable.

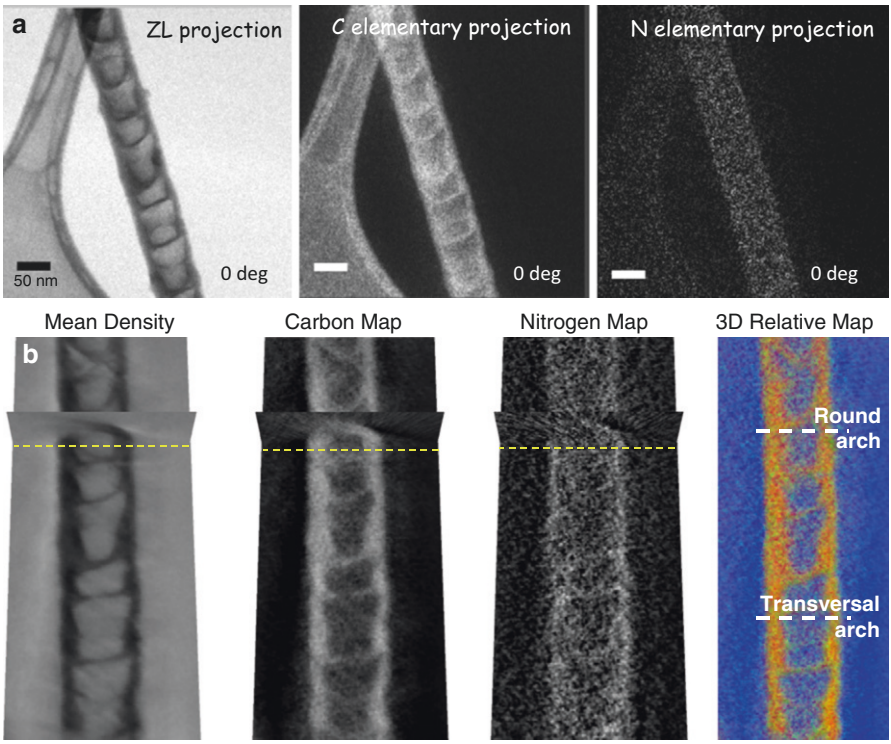


Fig. 13.18 3D analytical study of the nitrogen distribution in multiwall nitrogen-doped carbon nanotubes (N-CNTs). (**a**) Three typical images extracted at 0° tilt from the spatially correlated tilt series of as-recorded Zero Loss images (*left*) and 2D elemental maps of carbon (*middle*) and nitrogen (*right*); the last two images have been calculated by the decomposition method described in the experimental part using as input the series of EFTEM images. (**b**) Longitudinal slices extracted at the same depth and orientation from the shape-sensitive reconstruction (*left*), C and N 3D elemental maps (*middle*), and C-to-N 3D relative map (*right*). The last one was obtained by superposing the two elemental 3D maps with different colors, nitrogen in *green* and carbon in *red*. Note that the two types of arches are present within the analyzed area, transversal arches, and rounded ones

From experimental point of view, three tilt series of 2D images have been used: the first one corresponds to the Zero Loss recording and the two others are the tilt series of elemental maps for carbon and nitrogen. The last images have been deduced by using the "three-windows" method from the corresponding filtered images acquired on the K-ionization edges of carbon and nitrogen. Three spatially correlated volumes were then obtained: the sensitive-shape volume and the two elemental reconstructions (see Fig. 13.18). Their superposition has given rise to a 3D relative map that can be analyzed slice by slice. Related to the localization of the nitrogen atoms, we can observe that the transversal arches are rather concentrated in nitrogen, while the rounded ones contain less nitrogen. Indeed, by analyzing slice by slice, the 3D relative map, one can observe that the green color, associated to nitrogen, is less pronounced on the rounded arches

than on the transversal ones. In addition, another interesting finding obtained from this tomographic analysis is related to the modification of the tube morphology. More exactly, by analyzing the reconstructed volumes in cross-section, one can easily observe that the morphology of the tube changes in a prism at the vicinity of the transversal arches, where the N concentration is relatively high [56].

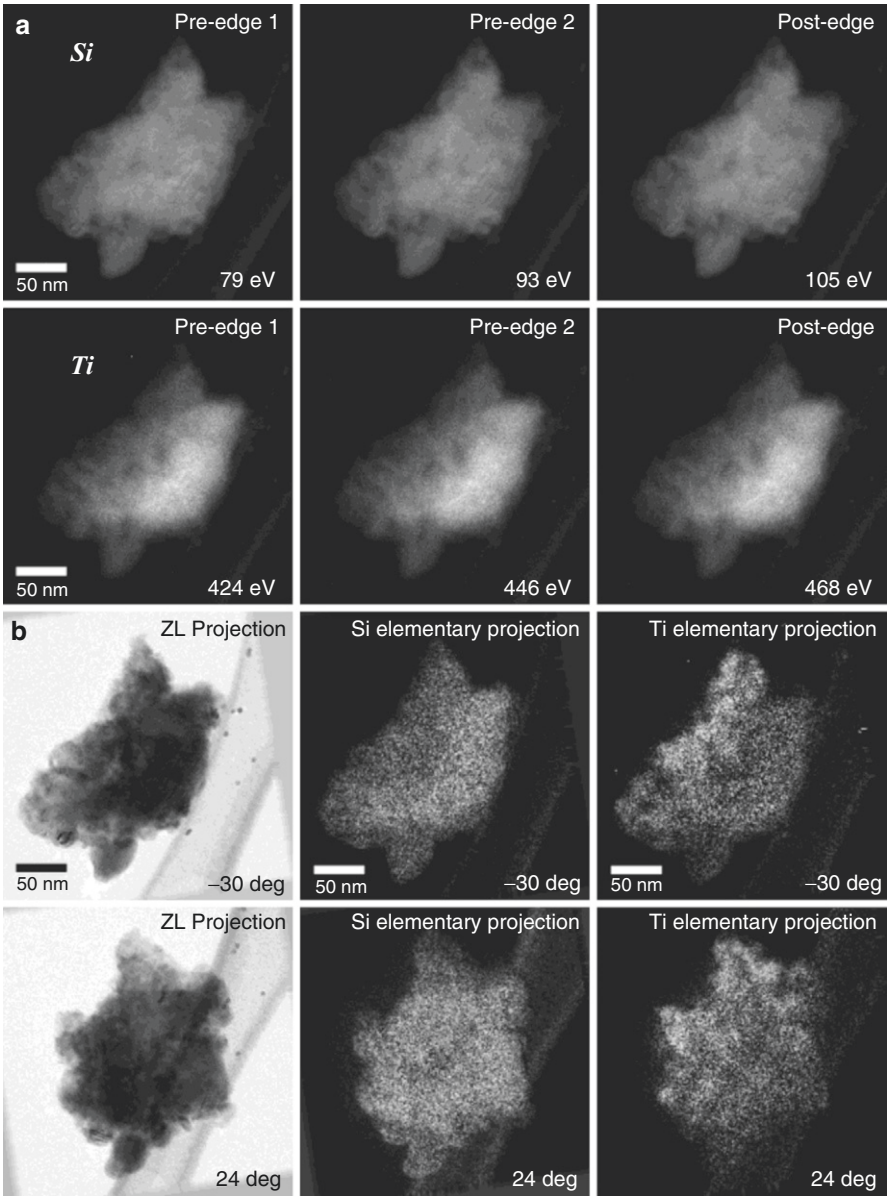


Fig. 13.19 (continued)

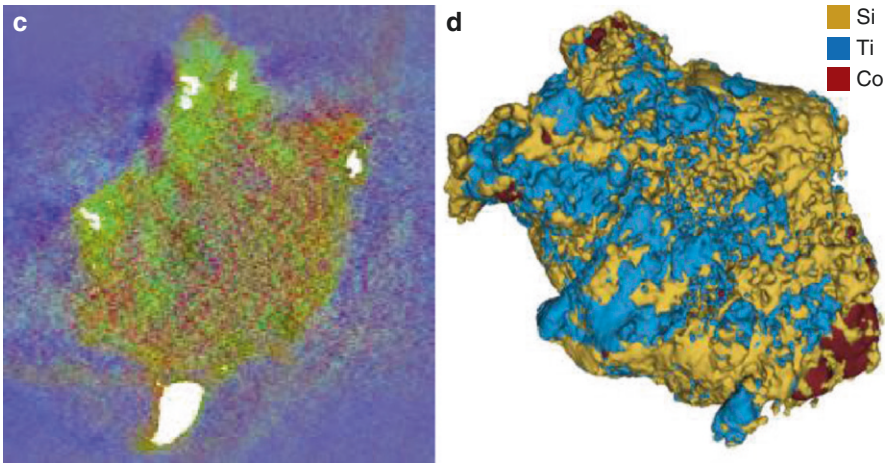


Fig. 13.19 (**a**) Energy-filtered TEM images acquired at 0° tilt: three EFTEM images ("pre-edge 1," "pre-edge 2," and "post-edge") at the Si-$L_{2,3}$ edge and three corresponding ones to Ti-$L_{2,3}$ edge. (**b**) Two typical images extracted for the tilt angles of −30° and 24° from the spatially correlated tilt series of as-recorded Zero Loss images (*left*) and 2D elemental maps of Si (*middle*) and Ti (*right*) calculated by the three-windows method. (**c**) Slice extracted from the 3D relative map of 10Co/TiO_2-SiC, obtained by superposing the volumes of Ti (*green*), Si (*red*), and Co (*white*). The catalyst was calcined at 350 °C for 2 h followed by a reduction under H_2 at 300 °C for 6 h. (**d**) 3D model of the sample where the *yellow color* represents the SiO_2 distribution, the *blue color* gives the TiO_2 distribution, and the *red color* gives the localization of the Co nanoparticle within the zeolite structure

This observation is in agreement with the theoretical calculations performed by Kutana et al. [57] which have shown that the insertion of nitrogen in the graphitic structure of carbon nanotubes can induce a triangularization of the tube in cross-section.

5.3.3 Co/TiO_2-SiC Catalyst

Mixed titanium oxide and silicon carbide material has received much attention as a potential catalyst support. Indeed, when Co nanoparticles are deposited on such nanometric support, an enhancement of the catalytic performances and a higher stability were observed for the Co/TiO_2-SiC catalyst comparing to Co/SiC. This was associated to a better dispersion of Co nanoparticles on TiO_2-doped SiC support, which could be explained by a relatively high Co-TiO_2 interaction. In order to obtain reliable information on the relative distribution of SiC and TiO_2, as well as on the precise localization of cobalt on the two components, we have performed a 3D-TEM analytical study on a typical catalyst grain, summarized in Fig. 13.19. To calculate the elemental 2D maps of TiO_2 and SiC compounds, we have considered in EFTEM the L_{23} absorption edge of Ti as the signature of its oxide and the L_{23} silicon absorption edge as the signature of the carbide. Note that the energy positions of edges for Si (99 eV) and Ti (456 eV) do not overlap as it was the case in the previous

study of the silica–alumina mixture (see Sect. 5.3.1), making thus easier the extraction of the corresponding chemical signals. We showed that the TiO_2 is relative well distributed within the bimodal porosity of beta-SiC (Fig. 13.19). In addition, the characteristics of cobalt nanoparticles depend on the phase they are in contact, small nanoparticles on TiO_2 and bigger nanoparticles close to SiC. From a more general point of view, for such catalysts, the quantification of the relative amount of the components at the surface of the grains is of utter importance for understanding/improving the catalysis activity yield.

6 Conclusions and Perspective

Strangely enough nanomaterials have received huge attention for decades now, while the means for fully characterizing objects and structures at the nanoscale were paid much less efforts. We have shown in this chapter that the full 3D characterization of this type of materials can be performed through quantitative tomography and analytical tomography.

Quantitative tomography allows one to perform qualitative and quantitative characterizations of porosities inside nano-objects; it is the only technique being able to tell whether nano-objects lay inside or outside a hollow structure. Moreover, by construction it is well adapted to precise morphological studies like the faceting of nanocrystals. On a slightly larger scale, quantitative tomography can even characterize short- and "long"-range orders. It was shown that a large number of recording modes could be combined together in order to optimize the collection of data necessary for achieving a specific study.

Combining electron energy loss spectroscopic technique to 3D tomography leads to in analytical tomography performing chemical analysis at the nanoscale. A highly representative example has been given through the study of nitrogen-doped carbon nanotubes that could establish a strong correlation between the doping level and the morphology of the object. Even though analytical tomography is achieved by means of a rather volume-selective technique, it eventually gives a suitable picture of the surface properties with chemical selectivity. The close correspondence between morphology and chemical composition provides a powerful tool to analyze materials at the forefront in catalysis, nanoelectronics, therapy, or imaging, and accordingly, it should significantly impact these fields in the future.

Recent advances in electron-based instrumentation, in particular the development of new aberration correctors, enable nowadays performing true atomic-resolution tomography in two different ways: with a probe corrector allowing reducing the depth of field in STEM mode and therefore recording series of confocal images. Atomic resolution will also be reached in high-resolution TEM mode when combining this mode with a reconstruction algorithm using the constraint that the object is composed of atoms. With respect to the spatial resolution inferred in analytical mode (slightly below 5 nm), further advances in instrumentation and analysis software are expected to decrease its value. Note however that the ultimate limit, dictated by the beam-sample inelastic interaction, is of the order of 1 nm.

Finally, it is worth noticing that beyond the analytical information in 3D at the nanoscale, this technique is well adapted to highlight various structural and chemical information from the studied nanomaterials.

References

1. Fan J, Yu C, Gao F, Lei J, Tian B, Wang L, Luo Q, Tu B, Zhou W, Zhao D (2003) Cubic mesoporous silica with large controllable entrance sizes and advanced adsorption properties. Angew Chem Int Ed 42:3146–3150
2. Matos JR, Kruk M, Mercuri LP, Jaroniec M, Zhao L, Kamiyama T, Terasaki O, Pinnavaia TJ, Liu Y (2003) Ordered mesoporous silica with large cage-like pores: structural identification and pore connectivity design by controlling the synthesis temperature and time. J Am Chem Soc 125:821–829
3. Blavette D, Bostel A, Sarrau JM, Deconihout B, Menand A (1993) An atom probe for three – dimensional tomography. Nature 363:432–435
4. Friedrich H, de Jongh PE, Verkleij AJ, de Jong KP (2009) Electron tomography for heterogeneous catalysts and related nanostructured materials. Chem Rev 109:1613–1629
5. Möbus GB, Inkson J (2007) Nanoscale tomography in materials science. Mater Today 10:18–25
6. Midgley PA, Dunin-Borkowski RE (2009) Electron tomography and holography in materials science. Nat Mater 8:271–280
7. Radon J (1917) Uber die Bestimmung von Funktionnen durch ihre integralwerte längs gewwisser Mannigfaltigkeiten. Ber Saechs Akad Wiss Leipzig Math-Phys Kl69:262
8. Zeng GL (2001) Image reconstruction – a tutorial. Comput Med Imaging Graph 25:97–103
9. Kremer RJ, Mastronarde DN, McIntosh JR (1996) Computer visualization of three-dimensional image data using Imod. J Struct Biol 116:71–76
10. Koster AJ, Ziese U, Verkleij AJ, Janssen AH, de Jong KP (2000) Three dimensional transmission electron microscopy a novel imaging and characterization technique with nanometer scale resolution for materials science. J Phys Chem B 104:9368–9370
11. Ersen O, Werckmann J, Houllé M, Ledoux MJ, Pham-Huu C (2007) 3D Electron microscopy study of metal particles inside multiwalled carbon nanotubes. Nano Lett 7:1898–1907
12. Ersen O, Hirlimann C, Drillon M, Werckmann J, Tihay F, Pham-Huu C, Crucifix C, Schultz P (2007) 3D-TEM characterization of nanometric objects. Solid State Sci 9:1088–1098
13. Roiban L, Hartmann L, Fiore A, Djurado D, Chandezon F, Reiss P, Legrand J-F, Doyle S, Brinkmann M, Ersen O (2012) Mapping the 3D distribution of CdSe nanocrystals in highly oriented and nanostructured hybrid P3HT-CdSe films grown by directional epitaxial crystallization. Nanoscale 4(22):7212–7220
14. Florea I, Houlle M, Ersen O, Roiban L, Deneuve A, Janowska I, Nguyen P, Pham-Huu C (2009) Selective deposition of palladium nanoparticles inside the bimodal porosity of β-SiC investigated by electron tomography. J Phys Chem C 113:17711–17719
15. Midgley PA, Weyland M, Thomas JM, Johnson BFG (2001) Z Contrast tomography: a technique in three-dimensional nanostructural analysis based on Rutherford scattering. Chem Commun 10:907–908
16. Midgley PA, Weyland M (2003) 3D Electron microscopy in the physical sciences the development of Z-contrast and EFTEM tomography. Ultramicroscopy 96:413–431
17. Jarausch K, Thomas P, Leonard DN, Twesten R, Booth CR (1984) Four-dimensional STEM-EELS: enabling nano-scale chemical tomography. Ultramicroscopy 13:57–70
18. Saxton W, Baumeister W, Hahn M (2009) Three-dimensional reconstruction of imperfect two-dimensional crystals. Ultramicroscopy 109:326–337
19. Gordon R, Bender R, Herman G (1970) Algebraical reconstruction technique (ART) for three-dimensional electron microscopy and X-rays photography. J Theor Biol 24:471

20. Gilbert P (1972) Iterative methods for the three-dimensional reconstruction of an object from projections. J Theor Biol 36:105–117
21. Batenburg KJ, Bals S, Sijbers J, Kübel C, Midgley PA, Hernandez JC, Kaiser U, Encina ER, Coronado EA, Van Tendeloo G (2009) 3D imaging of nanomaterials by discrete tomography. Ultramicroscopy 109:730
22. Roelandts T, Batenburg KJ, Biermans E, Kubel C, Bals S, Sijbers J (2012) Accurate segmentation of dense nanoparticles by partially discrete electron tomography. Ultramicroscopy 114:96
23. Mastronarde DN (1997) Dual-axis tomography: an approach with alignment methods that preserve resolution. J Struct Biol 120:343–352
24. http://rsb.info.nih.gov/ij/docs/intro.html
25. http://www.slicer.org/
26. Aronova MA, Kim YC, Harmon R, Sousa AA, Zhang A, Leapman RD (2007) Three-dimensional elemental mapping of phosphorus by quantitative electron spectroscopic tomography, (QuEST). J Struct Biol 160:35–48
27. Jin-Phillipp NY, Koch CT, van Aken PA (2011) Toward quantitative core-loss EFTEM tomography. Ultramicroscopy 111:1255–1261
28. Gass MH, Koziol KKK, Windle AH, Midgley PA (2006) Four-dimensional spectral tomography of carbonaceous nanocomposites. Nano Lett 6(3):376–379
29. Möbus G, Inkson BJ (2001) Three dimensional reconstruction of buried nanoparticles by element sensitive tomography based on inelastically scattered electrons. Appl Phys Lett 79:1369–1371
30. Messaoudi C, Boudier T, Sanchez Sorzano C, Marco S (2007) TomoJ: tomography software for three-dimensional reconstruction in transmission electron microscopy. Bioinformatics 6:288
31. Roiban L, Sorbier L, Pichon C, Bayle-Guillemaud P, Werckmann J, Drillon M, Ersen O (2012) 3D Chemistry of multiphase nanomaterials by EFTEM tomography. Microsc Microanal 18(5):1118–1128
32. Medalia V, Weber I, Frangakis AS, Nicastro D, Gerisch G, Baumeister W (2002) Macromolecular architecture in eukaryotic cells visualized by cryoelectron tomography. Science 298:1209
33. Koster AJ, Ziese U, Verkleij AJ, Janssen AH, de Jong KP (2000) Three dimensional transmission electron microscopy: a novel imaging and characterization technique with nanometer scale resolution for materials science. J Phys Chem B 104:9368
34. Buseck P, Dunin-Borkowski RE, Devouard B, Frankel RB, McCartney MR, Midgley PA, Posfai M, Weyland M (2001) Magnetite morphology and life on Mars. Proc Natl Acad Sci U S A 98:13490–13495
35. Kaneko K, Inoke K, Freitag B, Hungria AB, Midgley P, Hansen TW, Zhang J, Ohara S, Adschiri T (2007) Structural and morphological Characterization of Cerium Oxide Nanocrystals Prepared by Hydrothermal synthesis. Nano Lett 7:421–425
36. Florea I, Demortiere A, Petit C, Bulou H, Hirlimann C, Ersen O (2012) Electron tomography and 3D molecular simulations of platinum nanocrystals. Nanoscale 4:5125
37. Hungria AB, Juarez BH, Klinke C, Weller H, Midgley PA (2008) 3-D Characterization of CdSe Nanoparticles attached to carbon nanotubes. Nano Res 1:89–97
38. Möbus G, Inkson BJ (2001) Three dimensional reconstruction of buried nanoparticles by element sensitive tomography based on inelastically scattered electrons. Appl Phys Lett 79:1369
39. Florea I, Ersen O, Arenal R, Ihiawakrim D, Messaoudi C, Chirazi K, Janowska I, Pham-Huu C (2012) 3D analysis of the morphology and spatial distribution of nitrogen in nitrogen-doped carbon nanotubes by energy-filtered transmission electron microscopy tomography. J Am Chem Soc 134:9672–9680
40. Leapman RD, Kocsis E, Zhang G, Talbot TL, Laquerriere P (2004) Three-dimensional distributions of elements in biological samples by energy-filtered electron tomography. Ultramicroscopy 100(2):115–125

41. van Aert S, Batenburg KJ, Rossel MD, Erni R, Van Tendeloo G (2011) Three-dimensional atomic imaging of crystalline nanoparticles. Nature 470:374
42. Florea I, Houlle M, Ersen O, Roiban L, Deneuve A, Janowska I, Nguyen P, Pham C, Pham-Huu C (2009) Selective deposition of palladium nanoparticles inside the bimodal porosity of β-SiC investigated by electron tomography. J Phys Chem C 113:17711–17719
43. Ersen O, Werckmann J, Houlle M, Ledoux M-J, Pham-Huu C (2007) 3D Electron microscopy study of metal particles inside multi-walled carbon nanotubes. Nano Lett 7:1907–1998
44. Roiban L, Sorbier L, Pichon C, Pham-Huu C, Drillon M, Ersen O (2012) 3D-TEM investigation of the nanostructure of the δ-Al_2O_3 catalyst support decorated with Pd nanoparticles. Nanoscale 4:946
45. Moldovan SM, Bulou H, Dappe YJ, Janowska I, Bégin D, Pham-Huu C, Ersen O (2012) On the evolution of Pt nanoparticles on few-layer graphene supports in the high-temperature range. J Phys Chem C 116(16):9274–9282
46. Borowik Ł, Florea I, Deresmes D, Ersen O, Hourlier D, Mélin T (2012) Surface and intrinsic conduction properties of Au-catalyzed Si nanowires. J Phys Chem C 116:6601
47. Florea I, Feral-Martin C, Majimel J, Ihiawakrim D, Hirlimann C, Ersen O (2013) 3D tomographic analyses of CeO_2 nanoparticles. J Cryst Growth Des 13:1110–1121
48. Trovarelli A (1996) Catalytic Properties of Ceria and CeO_2-Containing Materials. Catal Rev Sci Eng 38:439–520
49. Nikoobakht B, El-Sayed MA (2003) Preparation and growth mechanism of gold nanorods (NRs) using seed-mediated growth method. Chem Mater 15:1957–1962
50. Strickland-Constable RF (1968) Kinetics and mechanism of crystallization from the fluid phase and of the condensation and evaporation of liquids. Academic, London
51. Florea I, Demortière A, Petit C, Bulou H, Hirlimann C, Ersen O (2012) 3D quantitative analysis of platinum nanocrystal superlattices by electron tomography. ACS Nano 6:2574
52. Bigot J-Y, Kesserwan H, Halté V, Ersen O, Moldovan MS, Kim TH, Jang J-T, Cheon J (2012) Magnetic properties of annealed core–shell CoPt nanoparticles. Nano Lett 12:1189
53. Ersen O, Parmentier J, Solovyov L, Drillon M, Pham-Huu C, Werckmann J, Schultz P (2008) Direct observation of stacking faults and pore connections in ordered cage-type mesoporous silica FDU-12 by electron tomography. J Am Chem Soc 130:16800
54. Ayala P, Arenal R, Ru M, Rubio A, Pichler T (2010) The doping of carbon nanotubes with nitrogen and their potential applications. Carbon 48(3):575–586
55. Arenal R, De la Pena F, Stephan O, Walls M, Tence M, Loiseau A, Colliex C (2008) Extending the analysis of EELS spectrum-imaging data, from elemental to bond mapping in complex nanostructures. Ultramicroscopy 109:32
56. Florea I, Ersen O, Arenal R, Ihiawakrim D, Messaoudi C, Chirazi K, Janowska I, Pham-Huu C (2012) 3D analysis of the morphology and spatial distribution of nitrogen in nitrogen-doped carbon nanotubes by energy-filtered transmission electron microscopy tomography. J Am Chem Soc 134:9672–9680
57. Kutana A, Giapis KPS (2009) First-principles study of chemisorption of oxygen and aziridine on graphitic nanostructures. J Phys Chem C 113:14721–14726

Transmission Electron Microscopy of 1D-Nanostructures

14

Teresa Ben, Rabie Fath Allah, David L. Sales, David González, and Sergio I. Molina

Contents

1 Definition of the Topic 657
2 Overview 658
3 Introduction 658
4 Experimental and Instrumental Methodologies 660
4.1 General Characterization Techniques 660
4.2 Column-to-Column Compositional Quantification of III–V Semiconductors 660
4.3 Strain Field Maps Simulation for Heteroepitaxial Systems by Finite Element Method (FEM) 664
5 Key Research Findings 664
5.1 Results on ZnO Nanowires Grown on CdTe (111) Substrate 664
5.2 Results on ZnO nanorods grown on Si (111) substrate 669
5.3 Results on Ternary III-N NWs Grown by Catalyst-Free PAMBE 676
5.4 Results on $InAs_xP_{1-x}$ Quantum Wires Deposited by MBE on InP Substrate 682
6 Conclusions and Future Perspective 693
References 695

1 Definition of the Topic

In this chapter, we review results obtained by conventional and advanced electron microscopy related techniques of complex 1-D nanostructures such as spontaneous core–shell $Al_xGa_{1-x}N$/GaN (0001) nanowires, ZnO/Si(111) nanorods, ZnO/CdTe (111) nanowires, and $InAs_xP_{1-x}$/InP(001) quantum wires.

T. Ben (✉) • R. Fath Allah • D.L. Sales • D. González • S.I. Molina
Departamento de Ciencia de los Materiales e I. M. y Q. I. Facultad de Ciencias, Universidad de Cádiz, Puerto Real, Cádiz, Spain
e-mail: teresa.ben@uca.es

C.S.S.R. Kumar (ed.), *Transmission Electron Microscopy Characterization of Nanomaterials*, DOI 10.1007/978-3-642-38934-4_14,
© Springer-Verlag Berlin Heidelberg 2014

2 Overview

With the aim to improve the design and potential use of 1D-nanostructures as functional materials, structural and compositional changes of these nanostructures must be correlated with the growth conditions. The process temperature, deposition time, diffusivity of participant specimens, the buffer or intermediate layer characteristics grown previously to the nanomotives, etc., can influence strongly on the final behavior of these systems. In this sense, techniques such as conventional and high-resolution electron microscopy imaging and energy dispersive X-ray and electron energy loss spectroscopies are valuable tools for the analysis of their morphology, crystalline structure, and composition.

In this work, we apply these techniques to examine a number of 1D-nanostructures formed by ZnO, $AlGa_xN_{1-x}$ or $InAs_xP_{1-x}$. In the case of chemical bath pre-deposited ZnO/Si nanorods, we analyze the role of the buffer layer and how it influences the vapor phase transport deposition process subsequently carried out. We also determine the compositional and morphological changes of ZnO nanowires' manufacture by the thermal oxidation of Zn films on CdTe substrate. On the other hand, we study the defect-free core–shell structures spontaneously formed in $Al_xGa_{1-x}N$ nanowires grown by plasma-assisted molecular beam epitaxy on GaN substrate and the complex chemical composition gradient along the wire axis for both core and shell blocks. Finally, we analyze the nucleation, the compositional and morphology evolution of single and stacked layers of self-assembled InAs/InP quantum wires formed through the Stranski-Krastanov transition by molecular beam epitaxy. For this work, the determination of high-resolution compositional maps extracted by aberration – corrected Z-contrast imaging combined with strain field map obtained by finite element methods have been especially successful.

3 Introduction

1D-nanostructures, such as horizontal quantum wires (QWRs), and vertical nanowires (NWs) and nanorods, have received steadily growing interest for the two last decades due to their unique and fascinating properties. Although the density-of-states (DOS) of 1D-nanostructures cannot be described by a series of Dirac's deltas, as quantum dots, it has an $E^{1/2}$ dependence which leads to peaks at each new quantized state [1]. Moreover, their 1D confined transport, considerable mechanical properties, and a large surface area/volume ratio play key roles. Since the first lasing experiments from semiconductor nanowires, covering from UV all the way to IR [2], many devices have been produced and now are spanning. These devices include solar cells [3, 4] and other optoelectronic devices [5, 6], piezoelectric nanogenerators to power battery-free wireless nanodevices [7, 8], and even a real platform to interface with living cells [9].

The growth of vertical 1D-nanostructures is governed by different strategies, e.g., nanorods and nanowires that are perpendicular or almost perpendicular to the substrate, and that have been produced by metallic catalytic and self-catalytic vapor–liquid–solid mechanism [10, 11], by vapor-solid condensation by Gibbs energy reduction [12] such as molecular beam epitaxy technique [13], by vertical evolution on hydrothermal deposition of seeds with the same materials [14], etc. In addition to vertical nanowires, surface quantum wires (formed parallel to the substrate) can be formed as a consequence of the anisotropic strain appearing during their formation by epitaxial growth [15].

Efficient applications of 1D nanostructures require the fine-tuning of composition, size distribution, and density. The control of these parameters is also needed for the understanding of growth mechanisms. Electron beam–related techniques include a series of powerful standard or advance tools that contribute to improve the design of semiconducting nanostructures. In this sense, conventional transmission electron microscopy (CTEM) and high-resolution electron microscopy (HREM) produce micrographs that are related to the 3D structure of these nanostructures. One-dimensional nano-objects and their internal defect structures can be imaged at near-atomic resolution [16, 17]. Furthermore, TEM is really versatile, combining within an instrument the complementary capabilities of imaging, diffraction, and spectroscopy at high spatial resolution. Parallel studies can often be executed simultaneously on the same region of interest, providing a huge variety of information required to solve material science problems. The last 30 years have witnessed dramatic advances in electron microscope technologies, leading to the wide spread availability of techniques such as high-angle annular dark-field scanning transmission electron microscopy (HAADF-STEM) imaging, atom-scale elemental composition determination by energy dispersive X-ray analysis (EDX)[18], and electron energy loss spectroscopy (EELS)[19, 20], all realized in STEM mode. Undoubtedly, the most significant advance toward atomic scale imaging has been the rapid emergence of aberration correctors for the optic column [21–24] for S/TEM imaging mode. This development has made possible the achievement of sub-Angstrom (i.e., <0.1 nm) point-to-point resolution [25–27]. Atom-scale imaging is crucial for the characterization of advanced functional materials [28] and so is also central for the advance of nanotechnology.

In this book chapter, we review the work carried out on (i) ZnO nanorods deposited on Si substrate by a three-step method, by combining chemical bath deposition (CBD) and vapor phase transport (VPT), (ii) ZnO nanowires (NWs) formed by thermal oxidation of Zn films on CdTe substrate, (iii) catalyst-free $Al_xGa_{1-x}N$ NWs grown by plasma-assisted molecular beam epitaxy (PAMBE) on GaN (0001) substrate, and (iv) $InAs_xP_{1-x}$ quantum wires (QWRs) formed by molecular beam epitaxy (MBE) on InP (001). Several techniques were applied for each material in order to better extract chemical or structural information, in particular from TEM and HRTEM, low- and high-resolution HAADF-STEM and EDX and EEL spectroscopies.

4 Experimental and Instrumental Methodologies

4.1 General Characterization Techniques

Most of the structural and compositional features were studied from micrographs collected by CTEM, HRTEM, and HAADF imaging in STEM mode for the last case, while the nanoprobe analyses of local proportions of atomic elements were measured by EDX and EELS also made in the same mode. These imaging experiments were carried out using a JEOL 1200-EX and a JEOL 2010F microscope operating at 120 and 200 kV, respectively. High-resolution aberration-corrected Z-contrast images were taken at 100 kV using a dedicated VG Microscopes HB501UX STEM with a Nion aberration corrector. EDX spectra were recorded using an Oxford Instruments EDX detector, and the module INCAPentaFET-x3 and EELS experiments were developed with a Gatan Imaging Filter (GIF) and a Gatan ENFINA spectrometer. XTEM specimens were prepared using mechanical thinning and Ar^+ milling in a Gatan Precision Ion Polishing System (model 656-low voltage). Additionally, we also carried out the analysis of rods and wires scraped off the substrate and dispersed on a lacey carbon-coated copper grid. For some samples, especially when the nanomotive density is high as is the case of $Al_xGa_{1-x}N$ nanowires, microstructural analysis was also carried out on the NW which were sonicated in hexane solution and dispersed onto TEM grids.

4.2 Column-to-Column Compositional Quantification of III–V Semiconductors

Chemical composition is a crucial attribute of functional materials. Specifically in the case of nanostructured heteroepitaxial lasers, chemical composition of the nano-objects constituting their active layers strongly influences the emission energy of the final device. Normally, the real composition differs from nominal (i.e., from the desired one, for which the growth process is set up) [29]. Segregation and inter-diffusion occurring during upper confining layer growth are two important processes in this scenario. Not only real or effective composition is required, but also the compositional distribution. In this sense, Shumway et al. quantified that a difference of 10 at.% of In (from 50 % to 60 %) in InGaAs/GaAs quantum dots (QDs) produces a wavelength redshift of around 20-40 meV [30]. This strong effect justifies the effort on developing new methodologies for compositional analysis at the nanoscale.

EDX and EELS are common analytical techniques based on electron–matter interaction. Although these techniques have greatly improved in recent years [31, 32], they still have some limitations, namely (i) the intrinsic electron probe broadening effect, (ii) lower energy resolution, and (iii) the need for high acquisition times, and hence a high stability (i.e., radiation resistant materials, extreme stability of the microscope setup, hydrocarbons free sample surfaces, etc.). It is therefore worthy to look for another compositional sensitive signal, requiring less acquisition time with high resolution.

HAADF images provide significant information on the position of atomic columns in a crystal with sub-Angstrom resolution (when the microscope is equipped with aberration correctors), requiring a low acquisition time (high-quality images in less than 16 s). Furthermore, contrast in HAADF images is approximately proportional to the square of the average atomic number of the atomic column. Therefore, this technique is also called *Z-contrast imaging*. Several works in literature show qualitative compositional mapping with high resolution from Z-contrast images of various material systems [33, 34].

In this section, a method to quantitatively determine with atomic column spatial resolution the composition of a semiconducting ternary alloy is presented. The method is based on the analysis of local integrated intensities from aberration-corrected Z-contrast images, and was first presented in Ref. [35]. It is necessary to use a set of reference samples of known composition to quantify the relationship between the Z-contrast intensity with the thickness and composition of material analyzed, although this might be skipped in some special cases [36]. To detail the steps and significant potential of this method, it was applied in previous works to an $InAs_xP_{1-x}$ alloy. A series of $InAs_xP_{1-x}$ epilayers grown on InP (001) by MBE were used as reference samples. STEM images were recorded using a HAADF detector in the dedicated aberration-corrected VG HB501 microscope, with probe size of 0.13 nm.

Three MBE samples consisting on a $InAs_xP_{1-x}$ epilayers grown on InP(001) substrates were considered. The As molar fraction was precisely measured by High-Resolution X-Ray Diffraction, giving $x = 0.27, 0.59$, and 0.87, respectively for each sample. Specimens for Z-contrast imaging were produced for cross-sectional view by mechanical thinning and Ar^+ ion milling in such a way that clean surfaces in the region of interest were produced The thickness of each analyzed region was determined from the analysis of the corresponding spatially resolved low-loss EELS signal, by using the mean free path determined for each x composition of the three $InAs_xP_{1-x}$/InP reference samples, according to the method described in Ref. [37].

A characterization procedure was defined to ensure (i) the reproducibility of the study, (ii) the minimization of radiation damage, and (iii) the minimization of errors by deposition of hydrocarbons during the observation. After HAADF images are acquired, they are processed to extract chemical information:

The starting point is a HAADF image from the $InAs_xP_{1-x}$/InP interface with atomic column resolution and known composition (x) and thickness (t), as the one shown in Fig. 14.1a. HAADF detectors normally register a background signal even if the sample is not being imaged. Then, the first step is to subtract the mean value of the detector black level, which depends on the detector gain and might differ from one microscope session to another. Next, pixels with the local intensity maxima associated to In atomic columns (higher Z) are detected on the image. For this, the peak finding tool of the *Strain Determination Software* is used [38]. Once these maxima intensity pixels are located, it is straightforward, with the help of image processing software, to measure the intensities integrated within a selected area of the projected unit cell, as shown in Fig. 14.1b. In this case, the number of pixels that an $InAs_xP_{1-x}$ unit cell occupies in the 500,000x image is 18×13 pixels. Taking into account the crystal orientation, and dimensions of the unit cell, pixels that

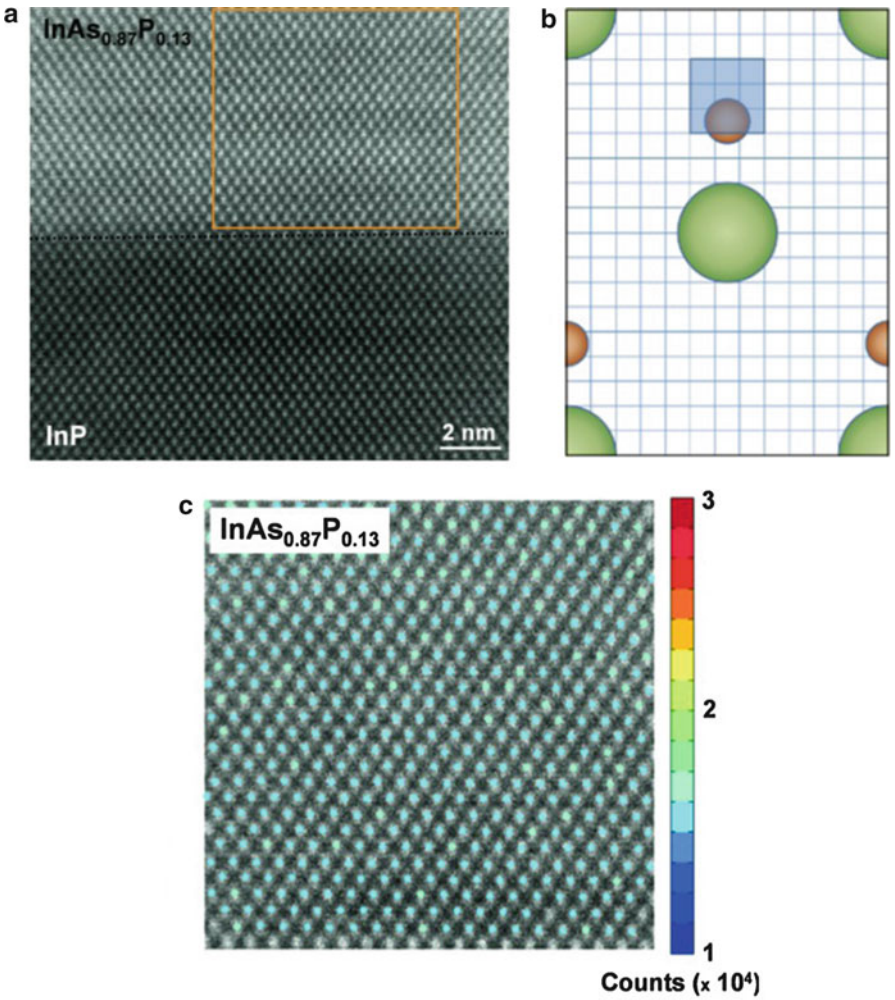


Fig. 14.1 (**a**) Raw data high-resolution aberration-corrected Z-contrast image taken along [110] from the $InAs_{0.8}7P_{0.13}$/InP interface. (**b**) Area selected (*blue square* of 9 pixels) for each element of the group V column to integrate intensities and calculate R ratios, drawn on the projected unit cell. Projected positions of In and group V atomic columns are represented with *red* and *green color circles*. (**c**) Integrated intensities in the area selected in (**b**) superimposed on the high-resolution Z-contrast image from which were determined for each analyzed group V column. Note that intensity distribution is very homogeneous throughout the whole analyzed image

correspond to the position of the anion are localized within the image. These pixels will be, in principle, more sensitive to the change of x (arsenic molar fraction) in an $InAs_xP_{1-x}$ alloy with variable composition.

The resulting integrated intensities of an $InAs_{0,87}P_{0,13}$ region are shown superimposed on the experimental image in the Fig. 14.1c. The integrated intensities for each pair of In-AsP columns are shown in this figure by a colored circle

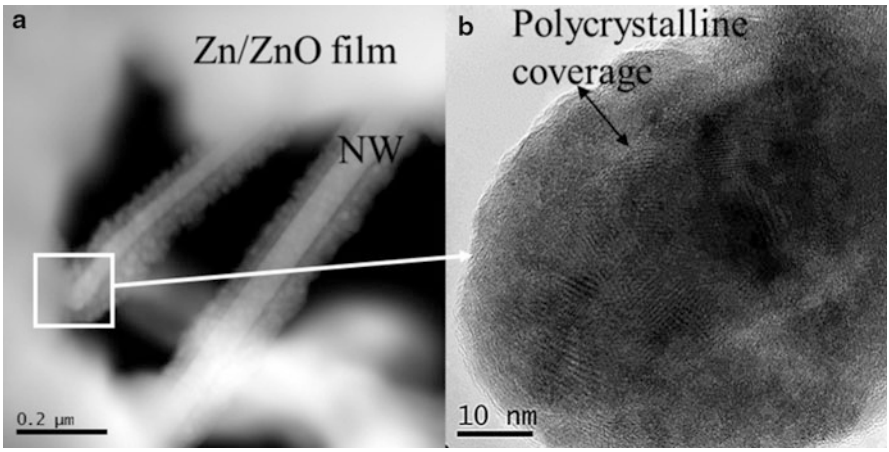


Fig. 14.2 (**a**) HAADF-STEM image showing several ZnO nanowires of sample A1 for which shorter oxidation times are used. (**b**) HRTEM image of the rod highlighted in the *square* in (**a**)

located in the brightest pixel, near the center of the projected position of the In atomic column. The integration area used is the one marked with a blue box in Fig. 14.1b. It is noted that the dispersion of the value is very low. This process is repeated for an InP area of the same image. Finally, two integrated intensity mean values, one for the $InAs_{0,87}P_{0,13}$ ($I_{s0,87}$) and one for the InP (*Io*), are determined. Defining the normalized integrated intensity parameter as given in Eq. 14.1, the quotient $R_e(0,87)$ is deduced, which defines the image in Fig. 14.1a.

$$R_e(x) = I_{sx}/I_0 \tag{14.1}$$

The error is minimized in this way, as the specimen thickness variations and other local fluctuations – that may contribute to the intensity values – are small within the area covered by a single HAADF image.

The selected integration area for the analysis has to be (i) linearly dependent on the As content, (ii) independent of specimen thickness, and (iii) independent on the surrounding atomic columns so that the signal is essentially due to the contribution of As and P from the selected atomic column. These three aspects were evaluated in several integration areas, the marked one in Fig. 14.1b resulting the most satisfying.

The same procedure for measuring integrated intensities of hundreds of anion–cation column pairs was performed in regions of different specimen thickness in the three reference samples (different x). Then, R_e quotients for certain x are obtained averaging the normalized integrated intensity values from different thickness areas of the same reference sample. The maximum observed standard deviation of $R_e(x)$ due to the specimen thickness was 1.5 %. The $R_e{-}x$ plot shows a clear linear dependency (see Fig. 14.2 of Ref. [35]). A fitting equation with a correlation coefficient of 0.9974 is obtained.

Thus, by measuring the values of R_e according to the procedure in a heterogeneous $InAs_xP_{1-x}$ alloy, it is possible to determine the composition, atomic column to atomic column, simply from the linear regression equation relating Re−x in the calibration samples.

4.3 Strain Field Maps Simulation for Heteroepitaxial Systems by Finite Element Method (FEM)

FEM calculations leading to elastic-energy profiles in 3D in heteroepitaxial systems can be carried out by setting an initial strain condition on the nanostructure [39, 40]. The input for simulations of the three-dimensional (3D) strain can be built by using a structural and compositional model. For the study of samples presented in this book chapter, an accurate 3D model was defined taking into account the elastic parameters, composition, and boundary conditions of the materials extracted from the STEM-EELS and high-resolution Z-contrast results.

An initial condition is set up by straining the material a specific amount in the three perpendicular directions of the model and finally the elastic-energy distribution can be obtained by allowing the system to relax. The system evolves up to a final relaxed state following the Hooke's law for the anisotropic elasticity theory. This is done by the commercial FEM solver Comsol Multiphysics code 3.0.

5 Key Research Findings

5.1 Results on ZnO Nanowires Grown on CdTe (111) Substrate

Nanowires and nanorods composed of oxide materials such as zinc oxide (ZnO) are resulting very promising as consequence of the direct band gap of 3.37 eV [41] and large exciton binding energy, 60 meV of this oxide [42], which enables the observation of excitonic emission at room temperature. Because of this, their generation is finding a wide range of applications such as ultraviolet (UV) light-emitting devices [43], nanogenerators [7], rectifying diodes [44], sensors [45], electron emitters [46], and even in medical applications and environmental science [47].

Most of techniques to manufacture ZnO NWs require operating at low pressures and high temperatures (800–1,400 °C) except the hydrothermal synthesis route [14, 48–50]. In this last case, despite its the easy implementation, the growth rate [3] and the optical quality of the resulted ZnO nanostructures are generally poorer than those grown by the other techniques [51, 52] and the size and shape reproducibility of as-grown nanostructures are lower. In this work, we described a detailed structural and compositional study of the parameters affecting the growth of the ZnO NWs on CdTe substrates, a potential candidate for photovoltaic applications [53]. This work represents a deeper study on some preliminary results previously reported on this new technique, [54] which opens new possibilities for the effective

cost production of high-quality NWs on alternative substrates at relatively low temperature.

ZnO nanowires analyzed were prepared following a two-step process: (i) a Zn metal film layer was evaporated at a temperature of 800 °C for different deposition times on top of the CdTe substrate maintained close to room temperature. (ii) Subsequently, a further oxidation step was performed in air at 500 °C for different times; more details of the preparation technique can be found elsewhere [55].

5.1.1 Structural and Compositional Characterization of ZnO Nanowires Grown Through Thermal Oxidation of Metallic Zinc Films on CdTe Substrates

In order to shed light on the growth mechanism of these ZnO nanowires, a series of three samples were grown, changing the experimental conditions. The effect of the oxidation time on the nanowires properties was studied by comparing samples A1, A2 and A3 grown under similar Zn metal film deposition conditions, (3 min, 800 °C), but with different oxidation times (1, 18 and 188 h respectively). In order to study the effect of the Zn metal thickness (in order words the available Zn), sample B was prepared with a more prolonged Zn evaporation time (5 min) and oxidiced during a time similar to sample A2.

Figure 14.2a is a HAADF-STEM image showing several ZnO NWs of sample A1 for which shorter oxidation times are used. The early stages of the nanowires formation can be seen, where the NWs appear as a fine filamentary structure surrounded by a sheath of granular aspect. Typically, the measured NWs have total diameters (including the sheath thickness participation) in the range of 30–120 nm and relatively short length (<1 μm). HRTEM carried out on these nanowires (see Fig. 14.2b) revealed a NW core with an intermediate crystalline quality, and a polycrystalline sheath.

As the oxidation time increases, NWs grow longer using the Zn film as precursor source and new nucleation sites are formed, so the NWs density becomes higher. The NWs are found to be around 50–80 nm in diameter and up to several micrometers in length. However, for high oxidation times (see SEM results on sample A3 in Ref. [55]), the NWs formation seems to be inhibited and even inverted, we observed in this case only poor areas or damaged NWs.

At longer Zn evaporation times (sample B), NWs appear quite straight with diameters in the range of 15–25 nm being much thinner compared to NWs grown under the same oxidation time and relatively shorter Zn evaporation time. Figure 14.3 shows a CTEM image of a NW example of sample B scrapped from the substrate. Figure 14.3b is an HRTEM image of two NWs of same sample recorded along the pole 0001 showing an excellent crystalline quality.

The Fast Fourier Transform (FFT) (inset in Fig. 14.3b) confirms the wurtzite structure of NWs grown along the <11-20> direction. There are no evidences of structural defects such as planar defects [56], dislocations [57], or different phases or precipitates inside the NWs. The entire NW exhibits a homogeneous HAADF-STEM contrast, indicating uniform composition (see Fig. 14.3c). By observing both images, we can confirm that the Zn film thickness seems to influence positively the

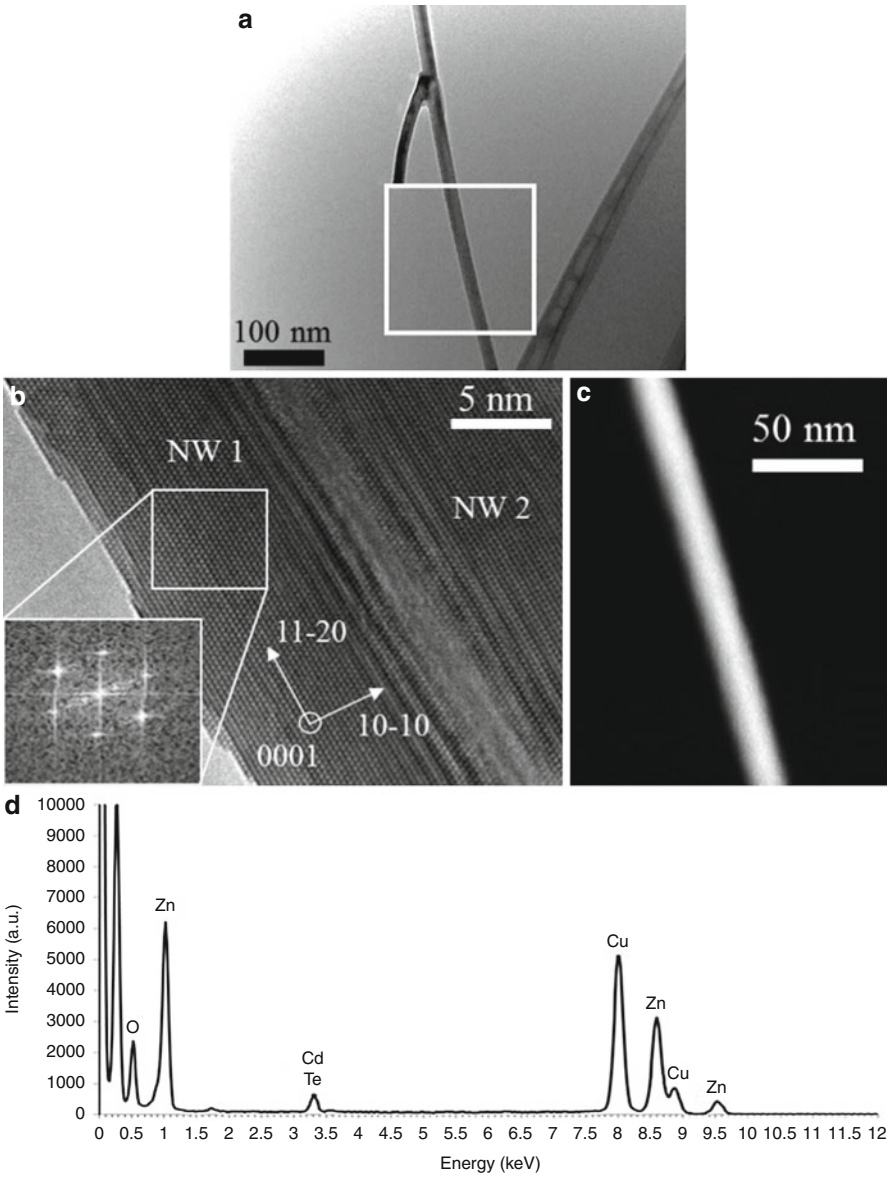


Fig. 14.3 (**a**) and (**b**) CTEM and HRTEM images of some NWs of sample B. The inset of (**b**) shows the FFT of the zone highlighted by the *square*. (**c**) HAADF-STEM image of an area of a NW shown in (**a**), (**d**) EDX spectrum of a the *bottom* area of a NW of sample B which displays the presence of Cd in a nanowire made up principally by ZnO

development of the nanostructure growth during the oxidation process. Additionally, EDX analyses performed on sample B (see an example in Fig. 14.3d) showed that the NWs are constituted mainly by Zn and O, although low signals from Cd and Te also were detected. In particular, Cd, with a very low atomic percentage composition (about 2 %), was found in the lower zone of these NWs, but not in the top.

5.1.2 Catalytic Effect of Substrate Elements on the Development of ZnO Nanowires

Martinez et al. have not appreciated any nanowires formation on GaSb substrates under similar growth conditions [58] to our case. Then the CdTe substrate must have an effect favoring the formation of ZnO NWs. EDX analyses demonstrated the presence of Cd and Te in the bottom of the NWs, these data indicate the additional presence of mainly Cd atoms on the ZnO seeding layer and its incorporation to the bottom of the NWs.

In this context, in order to analyze the substrate element role, Z-contrast imaging and EDX spectroscopy (as shown in Fig. 14.4) were performed simultaneously on sample B to identify spatially the composition in the region near the interface of the substrate CdTe with the ZnO film. Brighter agglomerations were observed as a separate phase in the lower zones of ZnO films (indicated by circles in the Fig. 14.4a). EDX profile analyses performed along the area indicated by the arrow in Fig. 14.4b (see an example in Fig. 14.4c) revealed these brighter areas as Cd. In general, despite the very long oxidation times, these profiles showed the presence of heterogeneously distributed Cd into ZnO layer with maximum values around the first hundred nanometers. Similarly, Zn has been detected in the CdTe substrate. That reveals the intermixing of the liquid Zn with the substrate components.

Because to redox list order, Zn must be oxidized nearly completely before Cd oxidation. This fact explains the presence of Cd in short and intermediate oxidation time, when the film is not completely oxidized and metallic Zn is still present to prevent Cd oxidation. The absence of atomic Cd in samples oxidized for such long times is probably due to their oxidation to form a new CdO phase. The loss of Cd phase [55] and the destruction and impoverishment of the quality of the NWs for very long oxidation times seem to be correlated. This could be also at the origin of the better NW formation (in terms of longer and thinner NWs) on sample B if one assumes that a higher Zn thickness would prevent better the Cd from oxidizing.

In the light of these results, we suggest a growth mechanism in which the Zn, Cd, and Te react after being thermally activated by the oxidation temperature. Zn melts at the surface forming drops that act as seeds for the NW formation. The growth takes place through a vapor-solid (VS) mechanism, in which the liquid phase is involved only in the nucleation and the Zn vapor assumes the growth [59]. The fact that the oxidation temperature (500 °C) is superior than the melting point of Zn (419.53 °C) suggests that Zn liquid phase is involved in the NW nucleation. This NW nucleation takes place in a local atmosphere slightly rich in Zn, Cd, and Te (to a less extent, because of its lower volatility). The existence of Cd in sample B, with a thicker Zn metallic film, let us to assume that the substrate element contribution is not only

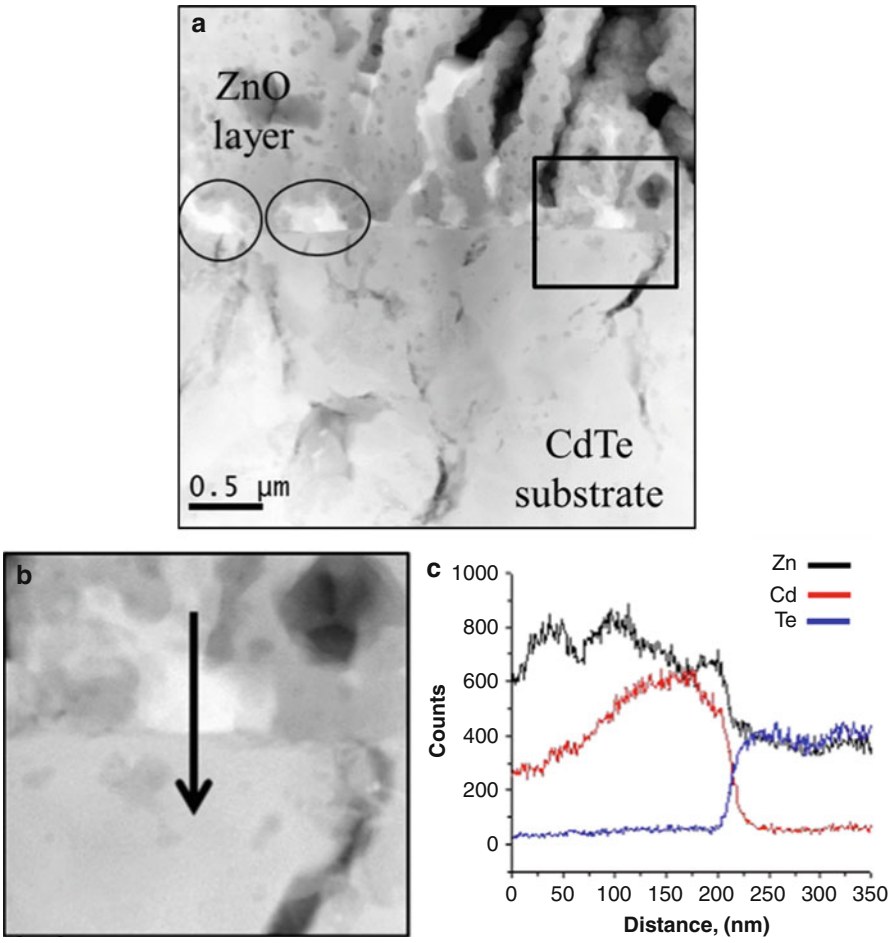


Fig. 14.4 (**a**) Z-contrast image showing the region near the interface of the CdTe substrate and the ZnO film of sample B. (**b**) Same region at higher magnification where the *arrow* indicates where the EDX profile was taken. (**c**) Zn, Cd, and Te elemental EDX profiles taken along the material accumulation of brighter contrast showed in figure (**b**)

provided as material crossing the Zn metallic film, but also as gas through the growth chamber during the oxidation step since during the deposition of the Zn metal film, the substrate does not increase its temperature enough. Although the temperature to obtain vapor from solid Cd-Te is very high, the formation of a Cd-Te atmosphere has been already reported under vacuum conditions and evaporation temperatures ranging from 400 °C to 510 °C [60]. In our case, the oxidation is carried out at atmospheric pressure, where the different vapor pressures for both components (1 kPa for Cd and 100 Pa for Te) at the oxidation temperature of 500 °C ensure a slightly higher Cd enrichment of the local atmosphere.

For low and intermediate oxidation times, the elements of the substrate migrate from the surface of the substrate, and in some way benefit the formation of ZnO NWs as the oxidation time increases; however, for very long oxidation times, all Zn metals are exhausted and this migration let to a new cubic CdO phase apparition, which apparently implies the collapse of Zn metal supplies and the end of the NW growth. The exact role of the Cd elements in the ZnO growth is difficult to explain at the present, additional studies are needed for this purpose.

5.2 Results on ZnO nanorods grown on Si (111) substrate

The CBD growth processes carried out on pre-seeded substrates with ZnO crystallites can overcome various limitations of the simple solution-phase route, as the seed layer can provides a dense network of nucleation sites with a high degree of texture, on diverse substrates, which enhances subsequent growth of vertically aligned ZnO nanorods [3, 61]. Furthermore, high-quality deposits can be achieved by high temperature growth processes such as VPT [7]. In order to combine the easiness and the benefits of the scale-up of the low temperature methods (CBD) with the high-quality products obtained with the evaporation and condensation processes (VPT), a catalyst-free technique, compatible with a variety of substrate types, has been developed. This method combines CBD methods to create a thin (~200–300 nm) c-axis aligned buffer layer which is suitably robust for VPT deposition. While in practice, the VPT growth of aligned nanorods on a CBD-derived buffer layer is a relatively simple process, there are several aspects of the specific mechanisms that influence this process and its control is needed. In this work, we focused on the structural and compositional changes during the VPT deposition of aligned nanorods on CBD-derived buffer layer using silicon substrates. In addition, we also examined in detail the morphological changes and partial degradation of the underlying buffer layer during the high temperature deposition.

To grow highly oriented ZnO nanorods, the first step of growth method was performed to create a thin seed layer of aligned ZnO crystallites (CBD_1) which will act as nucleation sites during the subsequent ZnO rod growth. For this, Zn $(CH_3COO)_2$ in ethanol solution was deposited by consecutive drops on the substrate Si(111), subsequently annealed at 350 °C in air for 30 min. Secondly, the pre-seeded substrates were submerged in an equimolar solution of $Zn(NO_3)_2$ and $C_6H_{12}N_4$ at RT. After this, the solution was heated to 90 °C and maintained at this temperature for 30 min to create aligned CBD ZnO nanorods (CBD_2) (referenced as sample C). Finally, VPT growth step was used, where the material source for the carbothermal reduction was prepared with a fixed amount of ZnO powder mixed with graphite (referenced as sample D). Samples with the CBD rods were placed directly above the powder source in a horizontal tube furnace and heated to 925 °C under flow of argon, the growth methods details can be found in references [14] and [62]. Study of effect of the temperature was analyzed in intermediate steps using samples E and F, for the CBD_1 step without and with heating, respectively, and finally using sample G for CBD_2 step with annealing, without Zn source contribution.

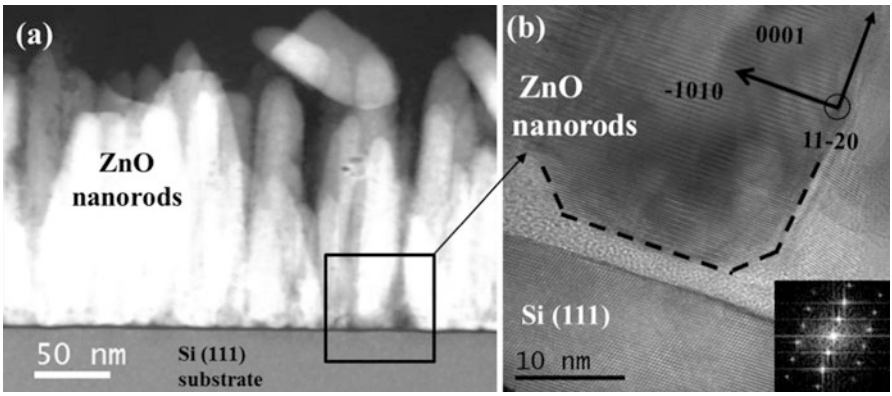


Fig. 14.5 (**a**) HAADF-STEM image of ZnO nanorods of sample C. (**b**) HRTEM image of the rod selected by a the *square* inside (**a**) (Adapted from, with permission from [65]. Copyright (2011) American Chemical Society)

5.2.1 Development of ZnO Nanorods on Si(111) Using the Three Step Method: Structural and Compositional Characterization

As we have commented, the growth process is divided into three distinct stages. Firstly a thin seed layer by CBD_1 is formed on the substrate, followed by annealing. Secondly, a denser NW layer is grown on this seed layer by CBD_2. Figure 14.5a shows a cross-sectional HAADF-STEM image of a CBD_2 sample (sample C). The formed nanorods are clearly visible as brighter vertical columns on substrate Si(111). CBD rods appear to grow in a spatially confined mode due to the high density of seeds forcing good vertical alignment during the rod formation [63]. HRTEM mode (see an example in Fig. 14.5b), revealed a relatively good crystalline quality and hexagonal wurtzite ZnO crystal structure with lattice constant of $c \approx 5.2$ Å, in good agreement with the standard values of bulk ZnO [64].

In the third stage, well-aligned ZnO nanorods are deposited by VPT onto the CBD buffer layer. Several analyses for a VPT process performed on sample D were carried to identify the supersaturation effects on the CBD nanorods. Figure 14.6a shows a CTEM image of sample D where well-developed ZnO nanorods arrays are observable. The VPT rods appear much larger than CBD rods (full length 1–3 μm versus 180 nm $\pm$ 10 for CBD rods) with a modified morphology, standing out the conic base. In this respect, VPT rods present two clearly different areas, a conical base (260 nm $\pm$ 40), and above it an upper section of homogeneous diameter and with a diamond-like facetted tip. HRTEM images (see an example in Fig. 14.6b) revealed also a very good crystalline quality with well-defined atomic planes, indicating the good crystalline quality of Zn deposited by VPT. Because of the low surface energy of the basal plane, ZnO is well known to normally grow with a c-axis preferred orientation, leading to a growth in the <0001> families directions [66]. The corresponding FFT (inset of Fig. 14.6b) confirms this fact, and proves the wurtzite structure of VPT rods as is the case of CBD rods. However, in VPT syntheses, the growth direction depends on many factors such as the crystal

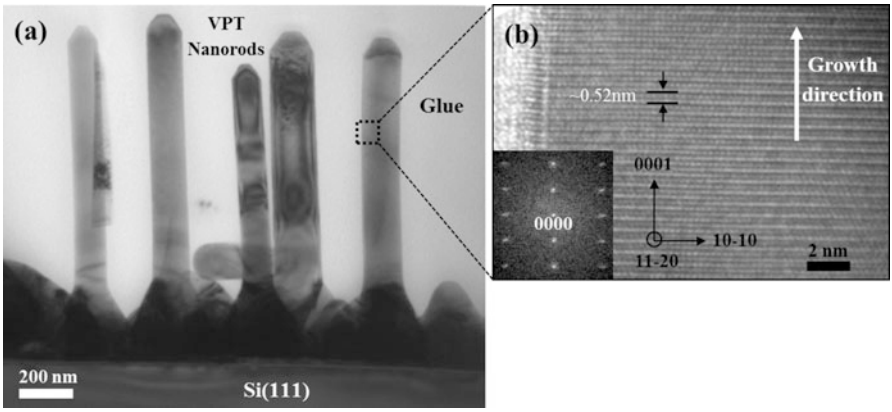


Fig. 14.6 (**a**) Cross-sectional TEM image of ZnO nanorods in sample D. (**b**) HRTEM image confirming the high crystalline quality of the rods; inset shows the FFT recorded along the [11-20] zone axis, confirming the wurtzite structure and c-axis orientation of the nanorods (Adapted from [67])

orientation and flatness of the substrate and hence, a well-aligned and c-oriented array of ZnO nanorods is not always achieved. However, in our case, the preferential c-alignment is confirmed by HRTEM micrographs.

On the other hand, VPT samples showed the appearance of a complex interface between the rod bases and the substrate Si(111). HAADF-STEM image of Fig. 14.7a is an example showing an intermediate layer composed of two different regions with three clear interfaces. Based on the Z number related intensities, we appreciate a sharp and darker layer just over the crystalline silicon substrate which can be associated with amorphous material or material of lower Z number. Over the darker layer appears another thicker, brighter, and heterogeneous layer. For a better understanding of the interface origin, EELS analyses have been combined with Z-contrast images. The simultaneously acquisition of two signals, whose are sensitive to the composition, allowed us to verify "in situ" and with nanometric precision the results by two different routes and thus to discriminate wrong spectra due to incidental probe or sample drift during the analysis. The peak corresponding to Si-L edge (Fig. 14.7b), detected in the area labeled by number 3 in Fig. 14.7a, shows obvious changes in the shape as well as in position compared to the Si peak corresponding to the substrate Si (labeled by 4 in the same figure). Note that this is the same area where O-K peak starts to appear (see Fig. 14.7c); hence, the area in question should be a SiO_2 layer. The oxygen signal appears also in the area 2 and 1 although with less intensity in this last layer, the oxygen reaches a steady value corresponding to the onset of the ZnO nanorod. However, the Zn-L signal begins before the O-K signal has reached this steady state (see point 2 of Fig. 14.7c), i.e., before the onset of the ZnO nanorod. In this area, corresponding to the first brighter layer in the HAADF-STEM image, the Zn-L edge signal does not vary significantly, but the O-K signal of the recorded spectra does experience a progressive redshift when we move from the adapting layer to nanorod base (inset of

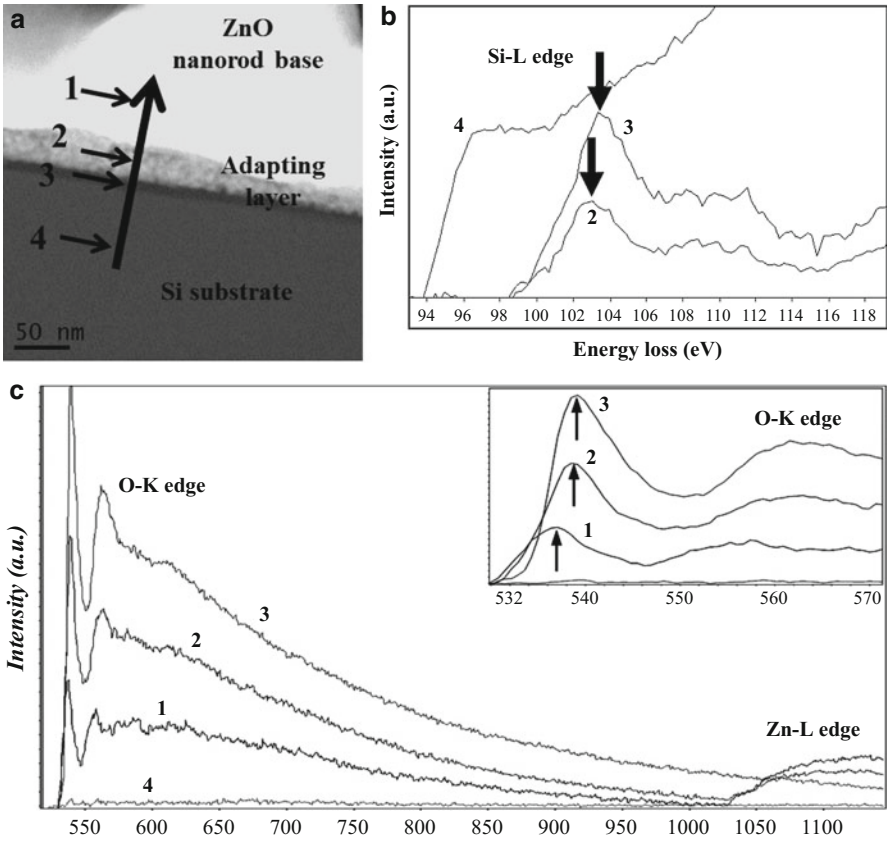


Fig. 14.7 (**a**) HAADF-STEM image of the Si substrate/nanorod interface region of sample D. The points 1–4 correspond to the ZnO rod base, $Zn_xSi_{1-x}O_y$, SiO_2 layers, and Si substrate, respectively. (**b**) Si-L signals of individual low-loss EEL spectra recorded from several points, which are labeled in (**a**). (**c**) Individual core-loss EEL spectra for this area (Reproduced from [67] with the permission of the copyright owner)

Fig. 14.7c). Moreover, in this region, the Si-L edge experiences a slight change toward decreasing energies when comparing against the darker with the brighter layer (point 3 compared to point 2). This energy change can be explained by a ZnO/SiO_2 alloy with a band gap between the two original compounds.

The nanorods/substrate interface experienced chemical and structural alterations; it is well-known that at high temperatures, silicon substrates can be oxidized, forming oxide layers in addition to the native oxide initially present; hence, it is easy to understand that darker layer is composed by SiO_2. On other hand, the chemical nature of the brighter layer seems to be more complex to interpret; however, we think that in addition to ZnO polycrystalline particles immersed in an amorphous SiO_2 matrix, the brighter layer must also contain new zinc silicate species supposedly formed in such conditions [68]. The energy changes of Si-L

transitions are sensitive to band gap variations; as we have seen, the Si-L energy corresponding to brighter layer (point 2 in Fig. 14.7c) is located between the Si-L energy for Si (point 4) and SiO_2 (point 3): The compound formed in the area in question must have a band gap located between these two elements. These results suggest that the area observed an additional compound is formed in the amorphous SiO_2 matrix. As we mentioned, in particular new zinc silicate species could have been formed where the oxidation state of Si and Zn atoms remains constant. Although there are different compounds combining Zn-Si-O [69], Zn_2SiO_4 (Willemite), is the most thermodynamically stable intermediate compound according to the diagram of ZnO-SiO_2 and it can be formed at 770 °C. In the literature, we found that the band gap of Zn_2SiO_4 ternary (5.5 eV) is located in between the band gap of Si (~1.1 eV)[70] and SiO_2 (~9 eV) [71]. Besides this, FFT reconstructions of HRTEM images for several SiO_2-ZnO interfaces confirm the existence of spots with interplanar spacing in agreement with the values for Zn_2SiO_4 crystals, suggesting reactions between ZnO and SiO_2 to form inclusions of Zn_2SiO_4 phase.

5.2.2 Effect of Experimental Parameters on the Growth of ZnO Nanorod Arrays Grown by a Three-Step Catalyst-Free Method

Effect of the High VPT Temperature on the ZnO Seed Layers

Daragh and coauthors have reported previously that ZnO seed layer formed during CBD_1 was not sufficiently appropriate for the direct deposition in high temperatures [14]. They observed that the seed layer suffered significant alterations; the growth was mainly confined to the edges of the substrate with little or no growth in the center. To understand the growth mechanism, the temperature effect has been studied separately on ZnO seed layer grown by CBD_1. Figure 14.8a, b show CTEM and HAADF_STEM images of a ZnO seed layer before (sample E) and after (sample F) annealing at 925 °C, respectively. Prior to the annealing, the CBD_1 layer formed by ZnO nanocrystals [72] appears with a uniform thickness of several tens of nanometers. Note that the diffraction pattern (see inset of Fig. 14.8a), recorded from mainly seed layer but also from substrate, consists of concentric rings, one for each diffracting plane, which refers to the polycrystalline nature of seed layer. Next the thermal treatment induced the formation of an amorphous layer of relatively uniform thickness directly above the substrate, whose thickness ranges between 25 and 50 nm, into which small particles with different sizes are embedded (Fig. 14.8b). Analyses performed by HRTEM images on the same area (Fig. 14.8c) revealed that the particles are crystalline. No evolution to nanorods has been detected as consequence of the process. Additionally, certain density reduction of the nanoparticles is appreciated after the thermal process. At last, EELS spectra showed element signals that indicate again of new Zn-Si-O phase.

All results lead us to conclude that the annealing treatment caused dramatic effects on the ZnO crystallites, leading to a severe reduction of available nucleation sites, which deactivated any potential subsequent growth. The growth of the layer silicate together with the appearance of Zn_2SiO_4 phase seems to be an obstacle disabling in some way the smaller seeds to develop the nucleation sites and subsequent growth of ZnO nanorods.

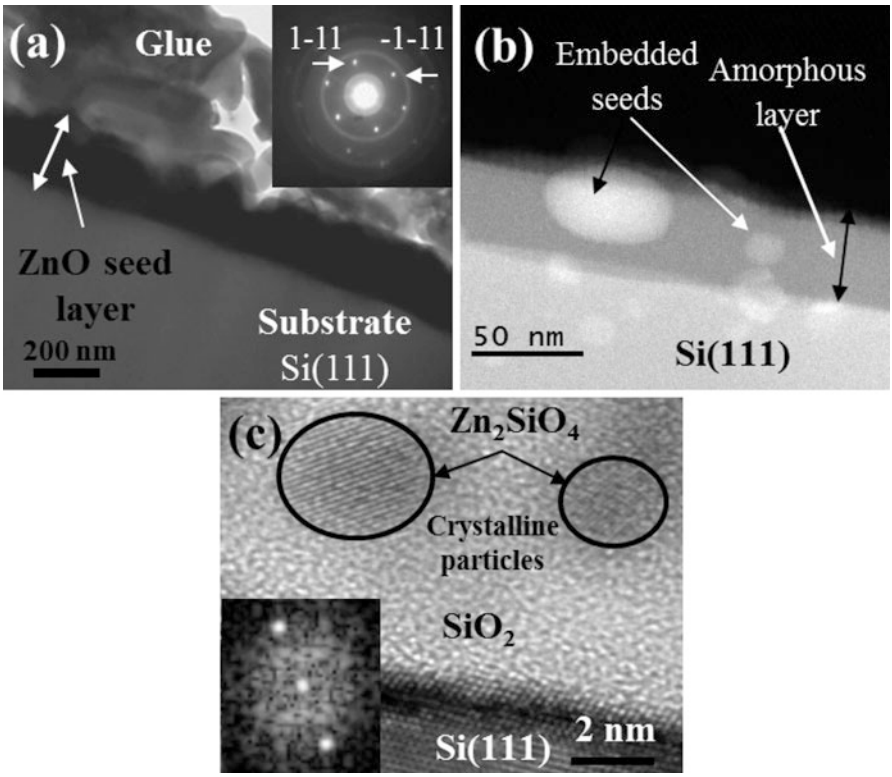


Fig. 14.8 (**a**) CTEM images of a ZnO seed layer before annealing at 925 °C (sample E), (**b**) HAADF- STEM image of the sample after annealing (sample F), (**c**) HRTEM image detailing the area between the Si substrate and SiO_2 layer showing crystalline particles embedded within an amorphous layer; the inset shows the FFT of the particle highlighted in the *square* region in image (**c**) displaying spots associated with planes of Zn_2SiO_4

Effect of the High VPT Temperature on the CBD Rods

The possibility of growing nanorods directly from annealed ZnO seed layers was discarded. Next the following study examines the temperature effect on the CBD_2 nanorods. A sample similar to C was annealed (referenced below as sample G) at temperatures typically reached during the VPT process under identical conditions, and nevertheless without the Zn source. Figure 14.9a shows a HAADF-STEM image of some ZnO nanorods of sample G, which was annealed at 925 °C. Radical changes in the morphology of these nanowires can be clearly appreciated if we compare the sample C after annealing. The CBD nanorods initially with sharp features lost the hexagonal shape during the annealing treatment, many of them merge with other neighboring nanorods to form thicker irregularly structures (compare Figs. 14.9a and 14.5a).

We suggest that the huge morphology transformation may be is due to partial sublimation of ZnO from CBD NWs and their subsequent transport along the

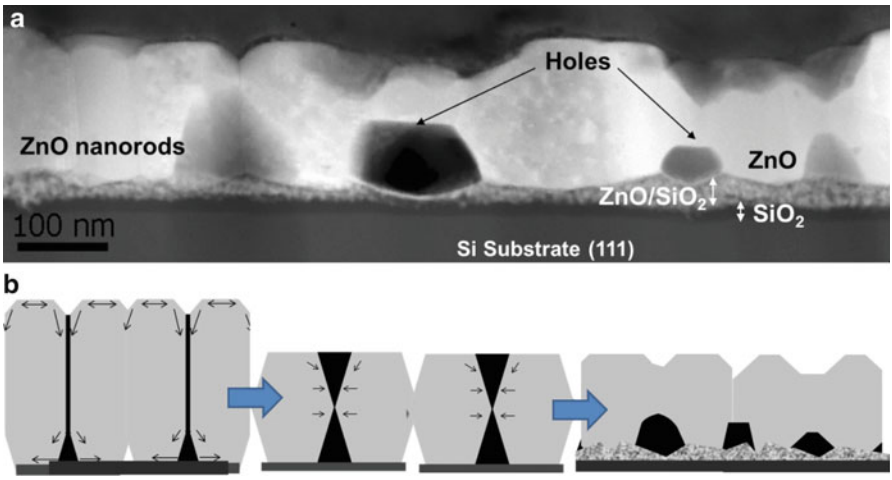


Fig. 14.9 (**a**) Cross-sectional HAADF-STEM image of the substrate/rods interface showing the adapting layer of annealed C-type sample (sample G). (**b**) Schematic representation illustrating the morphological changes among samples during the annealing

longitudinal direction of the nanorod. Because of the anisotropic nature of the wurtzite structure [73, 74], the etching and the sublimation rate of ZnO vary depending on the different faces of the ZnO crystal. Furthermore, Leonard and coauthors reported that the presence of impurities adsorbed on surfaces such as H_2O molecules can vary the surface free energy of ZnO at high temperatures and also attenuate the initial sublimation rate of the different crystal face [73]. However Ntep et al. [75] reported a contradictory outcome affirming that the presence of water in the gas mixture favors the process of sublimation. In any case, the nanorods that have been analyzed here were grown by a CBD process; hence, water and other impurities of the surface could be certainly present. Different facets of ZnO can undergo sublimation at different rates, and the reported temperatures necessary to induce the sublimation are really achieved in our experiments.

By comparing the morphological changes observed in the VPT rods, they were much less significant compared to the CBD_2 annealed rods; this fact may indicate that the high supersaturation levels of Zn source, which is typical of a VPT process, counteract the annealing effects. In other words, the sublimation consequences and the magnitude of morphological and structural changes are restricted in VPT nanorods with respect to simply annealed ones.

Regardless of the exact path of such morphological changes, Zn and O belonging to the nanowire CBD should be considered as a key point. We suggest that being thermally activated, the mentioned adatoms acquire sufficient kinetic energy to sublimate and diffuse from the top and prismatic facets to the pyramidal ones during the VPT/annealing growth, leading to the partial fusion of several nanorods and the formation of diamond-shaped structures. Figure 14.9b shows a schematic representation illustrating the morphological changes of sample C after annealing

at 925 °C. The structural changes are even more complex. Some authors reported melting points of ZnO nanostructures much lower than the "bulk" material [76–78]; in fact, the phenomenon is poorly understood. Despite the conflicting references found in the literature about the influence of the melting point on the ZnO nanostructures, we believe that, based on our observations, the structural and morphological transformations of VPT and CBD nanorods are mainly due to the partial sublimation, diffusion, and to the re-deposition of ZnO on nanostructures.

5.3 Results on Ternary III-N NWs Grown by Catalyst-Free PAMBE

The growth of one-dimensional semiconductor nanostructures, such NWs, nanobelts, and nanorings, has reached a considerable state of maturity, thanks to the research efforts made in the last decade. Up to now, extensive research has been mostly carried out in binary alloys, especially in wide-bandgap materials, such as ZnO [79, 80] and GaN [81]. Although the bandgap tailoring via the use of ternary alloys could be necessary for multi-color light-emitting nanowire-based devices, much less attention has been paid to these materials, probably because of the complexity in obtaining high-quality ternary NWs [82]. Thus, the lack of composition homogeneity, the presence of crystal defects, or size oscillations is common during the growth of such structures [83, 84].

Among them, the formation of radial phase separation structures must not be construed as a setback, but rather as an opportunity. Indeed, many reports have demonstrated that the core–shell nanostructures are promising systems that exhibit exceptional physical properties and extend their functional properties. It is well admitted that coaxial geometry in NWs gives rise to enhanced emission efficiency [85] and advantages for nano-FETs, such as a capacitance enhancement compared to standard planar gates [86]. Additionally, it could offer new approaches in the NW device strategy, as strain engineering of the band gap energy [87] or piezoelectric engineering to separate photon-generated electron–hole pairs in the core [88]. It is well know the possibility of a higher carrier/excitonic confinement for the core–shell structures in AlGaN NWs, which permits tunable emission from 365 to 600 nm with high quantum efficiencies [89]. Besides it other attractive advantage of this structures lies in the fact of they could resemble a properly optical fiber due to the difference in the refractive index between the core and the shell blocks [90].

In general, core–shell structures are synthesized in two steps. Firstly, the nanowire core is developed by any of the nanowire growth methods, i.e., metal organic chemical vapor deposition (MOCVD); secondly, these cores are overgrown by the same or another technique such as pulse laser deposition [85]. Another method to create the core–shell structure is to play with the ratio between the axial and radial growth of the NW. It is more straightforward that the materialization of auto-assembled coaxial nanostructures are supposed to make a step forward in the development of core–shell structures [91]. However, to compete with the coaxial two-step methods, the auto-assembled coaxial methods should offer a perfect control over the thickness and composition of both core and shell blocks.

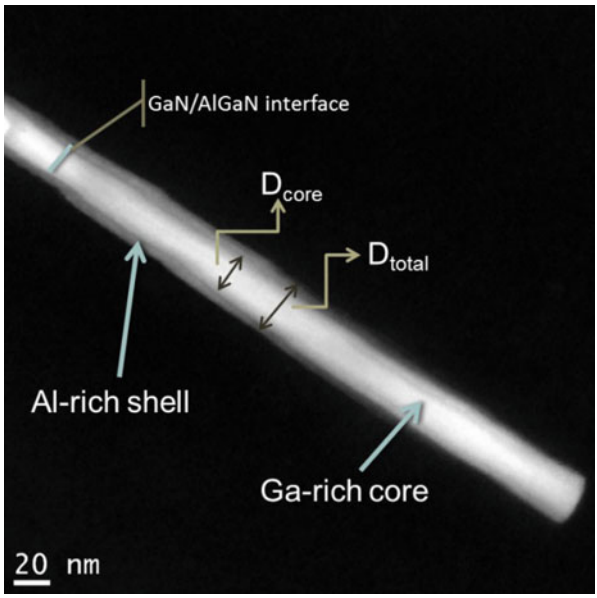


Fig. 14.10 HAADF-STEM images of an $Al_{0.23}Ga_{0.77}N$/GaN NW. A core–shell structure is showed, with diameter variations along the growth direction and an apex that is almost free of shell

In this work, we use transmission electron microscopy–related techniques to analyze the structure and composition of $Al_xGa_{1-x}N$ sections in catalyst-free GaN NW grown by PAMBE. A spontaneous core–shell structure is evinced along the whole NW that has been analyzed in detail. Hence, knowledge of the exact composition and radius of both the core and shell blocks along the structure is essential to assess the quality of these auto-assembled coaxial AlGaN NWs. Moreover, the roughness and coherence state of the interface, which could act as a natural mirror, are also examined.

When GaN was deposited directly by PAMBE on Si (111) at 790 °C, reflection high-energy electron diffraction pattern (RHEED) gradually evolved from a (7 × 7) streaky feature to a ring-like pattern, indicating a disorientation of the grown layer. Continuing GaN deposition, a pattern corresponding to a hexagonal structure appeared overlapping with a faint ring-like pattern. GaN NWs were then deposited under N-rich atmosphere. Finally, a 300 nm-$Al_xGa_{1-x}N$ section was grown on the top of GaN NW. More details of growth method can be found in Ref. [92]. Several core–shell structures were analyzed; however, in this report, only results focused on a sample whose nominal Al content is 0.23 are presented.

5.3.1 Development of Core–Shell $Al_xGa_{1-x}N$/GaN Nanowires: Structural and Compositional Characterization

Figure 14.10 shows an HAADF-STEM image of a single nanowire of sample H where the electron beam is disposed perpendicular to the growth direction. Indeed, a clear contrast of the bright inner core in comparison with a dark outer shell is observed and this fact appears in all of the investigated $Al_xGa_{1-x}N$ sections. This dark shell layer, presumably richer of lighter atoms, entirely wraps a core of heavier atoms not only in the ternary $Al_xGa_{1-x}N$ zone but also in the GaN nanowire

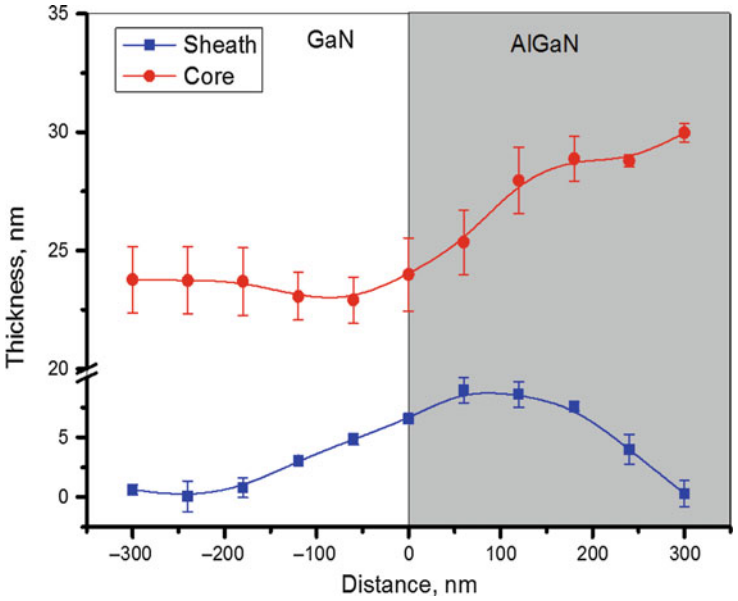


Fig. 14.11 Thickness profiles of the shell, core, along the growth direction

basement. Better yet, a sharp interface along the NW which separates core and shell regions is unmistakably shown and this fact helps us to measure both the core and shell thickness with a nanometer-precision. The measured cores have the diameters (D_{core}) in the range of 20–30 nm, whereas the shell thickness (d_{shell}) is in the range of 8–9 nm near the GaN/$Al_xGa_{1-x}N$ interfaces in the axial direction (indicated by the arrow in Fig. 14.10). However, the d_{shell} is not regular along the $Al_xGa_{1-x}N$ region, reaching the maximum close to the GaN/$Al_xGa_{1-x}N$ interface. Additionally, the shell does not rudely finish near the $Al_xGa_{1-x}N$/GaN interface, but it continues down surrounding the GaN base. The shell prolongation over the GaN slowly declines up to almost 300 nm beneath the GaN/$Al_xGa_{1-x}N$ interface. Far away this point, there is no evidence of a shell that covers the GaN close to the substrate. Additionally, the so-called D_{core} shifts form a constant value along the growth direction, with a sluggish but continuous increase up to the apex.

These trends are showed in the averages curve graph of Fig. 14.11 where we have used an average multiple curve method to interpolate on the curves of several nanowires. The shell reaches a maximum thickness around 80 nm from the GaN/$Al_xGa_{1-x}N$ interface although the nanowire diameter maximum appears at the half of the $Al_xGa_{1-x}N$ region.

At this point, it is important to check if this shell is a special feature of the nanowire growth mechanism involved in ternary III-N alloys or it is an undesirable consequence of a post-growth deposition during the TEM sample preparation or exploration. The latter is usually due to adsorption of organic material at the surface giving rise to an amorphous layer that surrounds the sample.

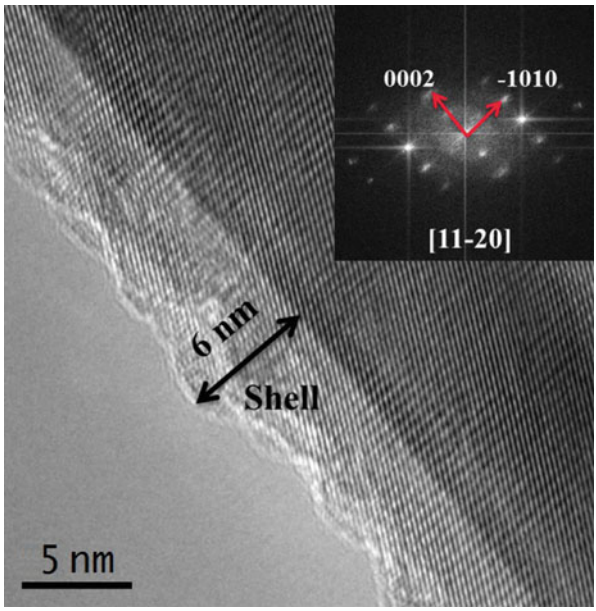


Fig. 14.12 HRTEM image of the edge of a nanowire taken along <11-20> zone axis. The core and shell exhibit perfect crystal coherence without crystalline defects

Figure 14.12 shows a HRTEM image at the edge of nanowire taken at medium height of the $Al_xGa_{1-x}N$ region along the 11-20 pole. In the micrograph, the shell presents a crystal structure pattern identical to the core zone where an abrupt change of the column contrast is evinced alongside the growth direction. In spite of the cylindrical geometry of the nanowire, this feature cannot be attributed to a thickness-contrast effect since the nanowire diameter is lower than the extinction distances. In this case, the inner region that evinces a darker contrast regarding the shell is produced by higher concentration of atoms with higher atomic scattering factors, i.e., higher atomic number *Z*. Therefore, the huge contrast variance implies a strong difference in the Ga/Al balance between the core and the shell regions giving rise to a poor Al content core and a rich Al content shell. Nevertheless, it is more important to notice the continuity in the crystal structure from the core to the shell. The shell exhibits a pseudomorphic relationship regarding the core at the interface and this feature follows up to the lateral surface. There is no evidence of disorientation or other crystalline defects as grain boundaries or misfit dislocations.

Considering that only two atoms are brought into play to meet stoichiometrically to nitrogen, we have analyzed the distribution Ga and Al along the NW. For this, a number of EDS point measurements higher than ten were made along eight NWs. In the following, taken into account that variability in composition, morphology, and elemental distribution that occurs in the NW, we only show the outcomes obtained by using the average multiple curve methodology over six NWs. Initially, we have made EDS point measurements in the center of the NW. Figure 14.13 plots the corresponding EDS measurements showing that the Al composition in $Al_xGa_{1-x}N$ segment gradually declines along the NW length and that Ga composition correspondingly increases.

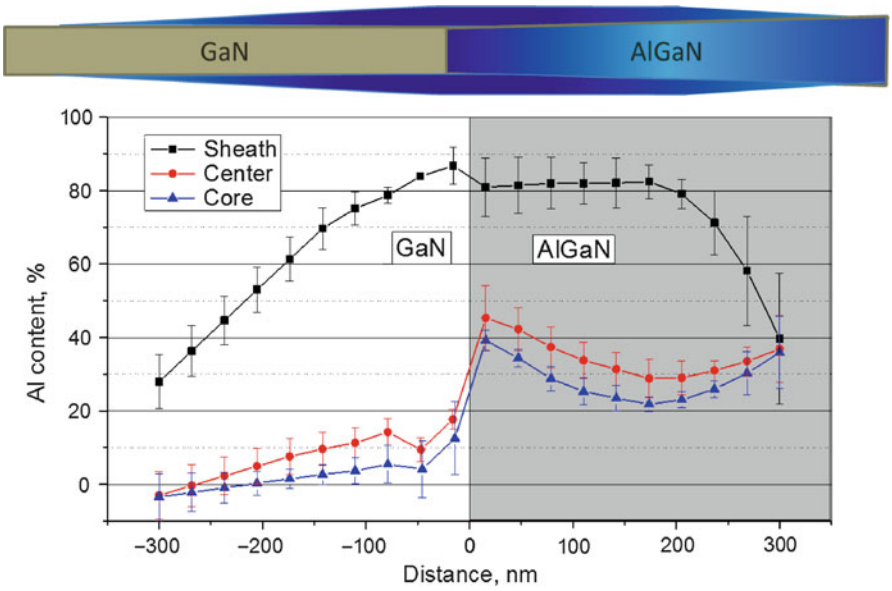


Fig. 14.13 Average axial EDS profiles of NWs from sample with $Al_{0.23}Ga_{0.77}N$/GaN NWs that are located at the center and edge regions. A scheme of the core/shell structure of $Al_xGa_{1-x}N$ showing the thickness and composition distribution is shown above the graph

However, the Al content undergoes a rise at the apex in the majority of the studied NWs. The measured Al compositions (x) were in the range of 0.28–0.45 at the center of the NW base with an average measurement of 0.33 in the $Al_xGa_{1-x}N$ region. The NW composition was somewhat higher than the nominal composition of $x = 0.25$ expected from NW calibration growths. Nevertheless, the average composition including the GaN base is 0.23 that it is close to the predicted one using growth rate considerations. These changes in the Al content in $Al_xGa_{1-x}N$ NWs point out to the strong dependence upon the diffusive transport of adatoms along the NW sidewalls toward the apex.

However, as the composition balance between core and shell regions must be so different and the shell thickness contribution on the whole diameter is so high, it is necessary to separate both contributions to depict a clear image of the Al distribution along the radius of the NW. For this, EDS spot measurements were made in the shell region, x_{shell}, at the same height used in the measurements of the nanowires centers x_{center} where their full diameter is defined as D_{dot}. Additionally, thickness measurements of the core and shell were carried out simultaneously [93]. If we consider that a gradient of composition along the diameter does not occur, the EDS profile (not shown here) across the diameter follows typical thickness dependence. We can estimate the composition inside the core x_{core} as:

$$x_{core} = \frac{x_{center}.D_{tot} - x_{shell}.2d_{shell}}{d_{core}} \tag{14.2}$$

According to Eq. 14.2, Fig. 14.13 plots the shell and estimated core compositions along the NW. First, it highlights the high values of X_{shell} regarding the X_{core} ones reaching an average composition of 0.82 along the NW. This composition is maintained almost constant in $Al_xGa_{1-x}N$ segment up to 2/3 of the NW height, and it only decreases when approaching the apex. This trend matches with the shell thickness decline, affecting the Al content experimental estimation, which explains the increment in the error bars of the measurements in the top of the NWs. The Al content oscillates in the range of 0.21–0.39 along the nanowire with an integrated average value of 0.27 ± 0.05.

The scheme on Fig. 14.13 depicts the morphology and composition distribution of the auto-assembled coaxial $Al_xGa_{1-x}N$ NW (not a scale). A shell of very rich Al content (near 90 %) surrounds not only the $Al_xGa_{1-x}N$ region but also the GaN basement. Although x_{shell} is almost constant along the $Al_xGa_{1-x}N$ region (with a sudden fall near to the apex), the thickness profile resembles a gentle hill with a peak in the $Al_xGa_{1-x}N$ area being null in the apex and at 300 nm under the $Al_xGa_{1-x}N$/GaN interface. The $Al_xGa_{1-x}N$ core diameter increases slightly as it grows but the Al core content changes in a different way, decaying from a maximum content at the $Al_xGa_{1-x}N$/GaN interface along the growth direction and rising near to the apex.

The formation of core–shell structures with a Ga richer core and poorer shell in an element is explained by the differences between adatom diffusion lengths. It is well known that the Al diffusion length is less than the Ga diffusion length. Al has a higher activation energy for migration, giving a diffusion length that is at least a factor of 4 lower compared to Ga [94].

Therefore, Al will deposit on the NW sidewalls and an accumulation of Al would be expected around the outside of the NW [83, 93]. This lateral deposition leads to a radial growth that is not homogenous although it evinces almost a constant percentage of Al, about 90 %. Although first $Al_xGa_{1-x}N$ layers have additional contribution from Al atoms diffusing from the lateral sidewall, under the interface, in top areas of wires, these atoms cannot reach anymore the new c-plane forming; in other words, there is no additional contribution. Because of this, as the NW height increases, the Al composition inside the core evidently declines (and Ga composition correspondingly increases) since limited amounts of Al as compared to Ga would be able to reach the top of the NWs to contribute to axial growth. This fact is in agreement with the Al composition decay observed up to 200 nm from the GaN/$Al_xGa_{1-x}N$ interface.

However, from this point, a change in the trend of the core/shell structure occurs. Firstly, the shell thickness ebbs up to almost nothing at the apex as well as its Al content undergoes a continuous decrease to fit the core composition. At the same time, the core increases its Al content besides its diameter suggesting the lateral contribution to the NW growth increases. There is not a clear separation of rich/poor phases giving place to an only alloy with a composition higher to the predicted one. Up to now, there is not a clear explanation for this behavior. The classical models point out that the lateral growth comes from adatoms in the substrate, which climb along the whole NW length to deposit at the apex [95, 96]. Nevertheless, we think it should evince an aluminum track near at the base but we do not observe it.

We suggest that this structural inhomogeneity could be attributed to the shadow effect in the MBE growth induced by the proximity of the neighbor NWs, implying that the deposition at the wire sidewall becomes less important as the wires are getting longer, since being shadowed and taking into account the lower chemical potential of the front growth of the NWs, fewer of the incident adatoms can be adsorbed at the bottom zones and the nanowire sidewalls close to the apex. Now the impinging flux contribution overcomes the lateral one and takes over the NW growth. As a result, most of Al atoms are preferentially deposited on top surface and remain in the c-plane. This fact causes the disappearance of the shell as can be observed in the analyzed sample.

Lower activation energy for migration of Al adatoms would imply a higher adatom diffusion lengths and the chance of not getting stuck to the shell and reach the apex. The formation of a longer shell richer in Al atoms could enhance the Al diffusion or reducing the sticking coefficient of Ga adatoms [97]. In any case, the consequence is the disappearance of the core–shell structure by means of widening of the core diameter. The fabrication of longer core/shell wires of $Al_xGa_{1-x}N$ is a good chance to improve the optical properties, but it needs to overcome two main problems: the gradual decay of the core composition along the growth direction and the sharpened of the shell up to [53] total vanishing around 300 nm from the interface. The exact comprehension of the mechanism involved in the formation and annihilation of the core/shell structures will allow us to design suitable growth routes to obtain axial wires with both thickness and composition controlled. Further researches are in progress to elucidate the role of the growth parameters in the development of core–shell structures.

5.4 Results on $InAs_xP_{1-x}$ Quantum Wires Deposited by MBE on InP Substrate

As mentioned in Sect. 3, the ideal density-of-states (DOS) function for 1-D nanostructures presents peaks at each new quantized state. This phenomenon has important consequences for technological applications like nano-lasers. InAs/InP horizontal QWRs have received special attention because of their potential emission within the two important optical telecom windows 1.3 and 1.5 μm [98, 99]. Furthermore, they exhibit efficient optical emission at even 1.6 μm [12].

These QWRs are formed instead of quantum dots due to a strong stress anisotropy built up during the growth process, due to the distortion of As-In bonds along [110] direction and As–As dimerization along [110] [15], which leads to a stress relaxation that takes place mainly along the [110] direction, resulting in elongated nanostructures along the perpendicular one (i.e., [110]).

As it is the case for quantum dots [100, 101], the epitaxial growth of QWR embedded in a matrix offers possibility of engineering a few of their optical properties by tailoring their strain status (strain engineering). The stress field induced by the confining layer is considered as a decisive factor for the emission energy of these nanostructures [101].

Design and development of epitaxial quantum nanostructures devices requires a precise control of their morphology, composition, and organization degree. In this sense, the growth of stacked layers is a common approach to improve the spatial distribution and size homogeneity of self-assembled nanostructures [102–104]. For stacked systems, the number of active nanostructures increases and thus, the quantum efficiency escalates, saturation gain effects being avoided in case of laser devices [105]. Growth parameters such as the spacer layer chemical composition [106], its thickness, the substrate temperature [107], and material deposition [108, 109] are some factors that determine the spatial and compositional distribution of nano-objects in single and stacked layers [87].

A considerable effort has been devoted to learning about the nucleation and evolution of nanostructures grown by the Stranski–Krastanov (SK) mode. Moreover, when these nanostructures are buried under capping layers, inhomogeneous strain fields are produced, which propagate toward the spacer layer surface, thus achieving a vertical correlation with the next nanostructures forming on the surface depending both on the buried nanostructures size and the spacer layer thickness [102, 109]. The development and implementation of methods to extract this information at the nanoscale, and in some cases at the atomic scale, should help us to know and relate their characteristics with their functional properties.

In this chapter section, we review results obtained by CTEM, high-resolution phase-contrast (HRTEM) and aberration-corrected Z-contrast electron microscopy techniques, in coordination with Peak Finding Methods (Peak Finding [110] and Peak Pairs [38]), Finite Elements Analysis (FEA), and Electron Energy Loss (EEL) Spectroscopy. They are applied to first characterize the morphological and compositional evolution of the QWRs from the initial formation stages and into the growth process and with that to measure the above mentioned structural attributes at nanoscale and atomic scale. Secondly, STEM measurements on InAsP QWRs coupled to elasticity calculations by finite element methods (FEM) are used to predict their preferred nucleation site on single and stacked layers.

A first group of samples (series I) consists of the growth by MBE of 2.3 (sample I1), 2.5 (sample I2), and 2.7 (sample I3) InAs monolayers (ML) on InP(001) were analyzed. InAs was deposited on the substrate at 0.5 ML per second (ML s^{-1}), at 480 °C of the substrate temperature and under As_4 beam equivalent pressure of 4×10^{-6} mbar. Then QWRs were buried under 20-nm thick InP layer for allowing optical measurements. Details of growth are reported elsewhere [111].

Additionally, a second samples series (named as S) were studied. In this case, several stacked layers consisting of self-assembled 2.5 MLs InAs QWRs were spaced by InP whose thickness was selected between 3 and 20 nm. The substrate temperature during the spacer deposition was fixed at 380 (named as series SL) and 515 °C (named as series SH). Further growth details are shown in Ref. [107].

5.4.1 Nucleation and Evolution of InAs/InP(001) Quantum Wires

Self-assembly, through the SK growth mode, is recognized as one of the most remarkable method to optimize the 3D growth of heteroepitaxial InAs/InP QWRs. In this case, nanostructures spontaneously undergo a transition to 3D growth when

the accumulated biaxial stress exceeds a given value and after a critical thickness is attained [15]. The epitaxial growth in heterostructures, with reticular misfit of 3.2 %, led the coupled structure to be relaxed by providing the surface energy needed to create these nano-objects. Each new nanostructure evolutes and self-orders on the surface depending on the stress provided by the other buried wires previously formed. The growth onset clearly is influenced by the substrate temperature, the surface stress of the dimers present in the reconstructed surfaces, and the presence of surface steps.

Nucleation: Steps as Preferential Nucleation Sites of Single QWR Layers

Surface steps at growth front surface play an important role during epitaxial growth. Their influence on the growth process, morphology, strain–stress distribution, and materials functionality has been widely reported [112–119]. This is also the case for horizontal QWRs. Atomic force microsocpy (AFM) images show a growth front surface consiting of one-atom high steps both in stages just before and during the QWRs formation [111]. These, with a linear density of $4.2 \cdot 10^4$ steps/cm, divide the surface into terraces. The scenario at the very initial growth stage of the wires shows that most of them are located at upper terraces and by the steps, and when the step follows the wires orientation (i.e., [110]), they are placed on both terraces with a greater portion placed on the upper ones.

To estimate the impact of a superficial step on the growth of InAs/InP heteroepitaxies, FEM models of the growth front surface were created. Then, the strain–stress state after deposition of the firsts InAs monolayers on a superficial InP step was simulated following the anisotropic elastic theory. Figure 14.14 depicts the [110] component of the strain associated to the one-atom high InP step covered by an InAs wetting layer. The upper terrace has higher positive strain values than the lower one, even when just a monolayer of InAs is deposited (Fig. 14.14a). When the InP step is covered with two MLs or more, an increase of the negative strain is observed at the lower terrace (see Fig. 14.14b). Strain values are higher on areas closer to the step edge in all the considered scenarios. These general statements are also valid for $InAs_xP_{1-x}$ wetting layers instead of pure InAs, and even when the diatomic step moves across the InP surface during growth with respect to its original position.

Positive in-plane strain means that InP broadens somewhat its lattice parameter, lowering the chemical potential for (i.e., favoring) the deposition of InAs on this portion of the surface, compared with pseudomorphical InAs growth on a flat InP surface. This result suggests that upper terraces are preferential nucleation sites for QWRs, where 2D-3D transition takes place. Similar mechanism should be expected with any other material system with reticular misfit between nano-objects and substrate [120, 121].

This suggestion is reinforced after analyzing cross-sectional Z-contrast images of the QWRs placed on interfacial steps. The regions of the wires just on the upper terrace show higher intensity, which means higher As content [122]. Therefore, it can be affirmed that these wires are formed over regions where in-plane strain was high. This also explains the non-symmetrical distribution normally found in horizontal QWRs, which will also be shown next in this chapter [123, 124].

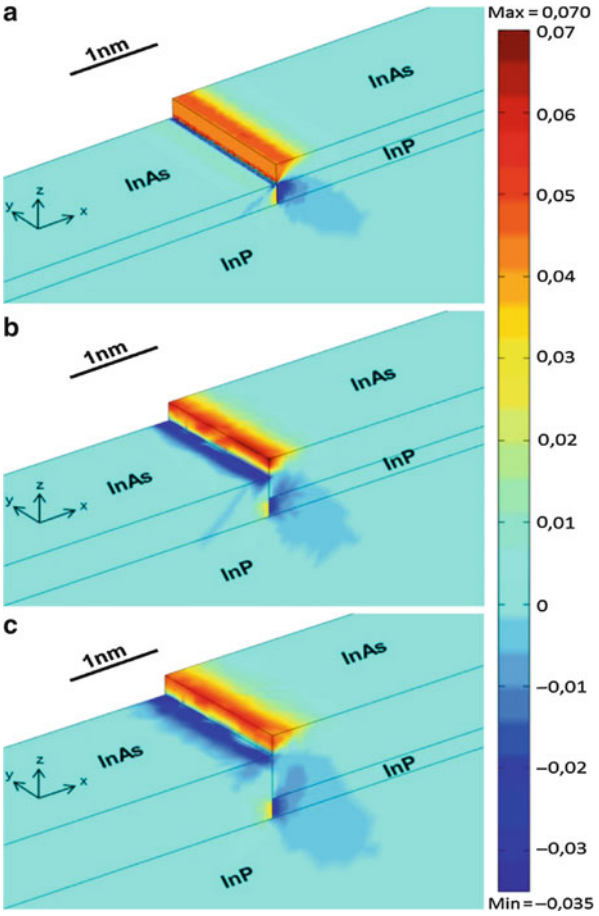


Fig. 14.14 Strain along [110] calculated by anisotropic elasticity theory in a wetting layer of InAs epitaxially grown on an InP diatomic step. The InAs layer is one (**a**), two (**b**), or three monolayers thick (**c**). Positive strain values (*hot colors*) are present on upper terrace surface with respect to the relaxed substrate (*cold colors*), favoring the further InAs deposition as a consequence of the reduced chemical potential for nucleation

Figure 14.15 shows a high-resolution Z-contrast image of a QWR grown on InP (001) substrate using MBE conditions away from the initial stages of the formation of nano-objects (further details in [107]). The wire is covered with InP to avoid oxidation. This image was taken of a region with constant sample thickness using a VG-HB603U STEM microscope with a Nion aberration corrector. The probe size is 0.07 nm full width at half-maximum (FWHM). Rich As regions appear brighter in the image, while a decrease in intensity is due to the presence of P. The shape and compositional distribution of the QWR is clearly identified in this image with atomic column spatial resolution. The substrate–wire interface is highlighted with a dotted line in Fig. 14.15 (right). The chemical information present in this Z-contrast image allows the localization of a diatomic step within this interface below the QWR. A clear difference in contrast is observed between the In (brighter) and the $As^{+}P$ (dimmer) atomic columns. Note that pure P columns are barely detectable in the left image of Fig. 14.15 but they are not observable in the color rendering of the magnified image (right). In this way, the presence of the faint

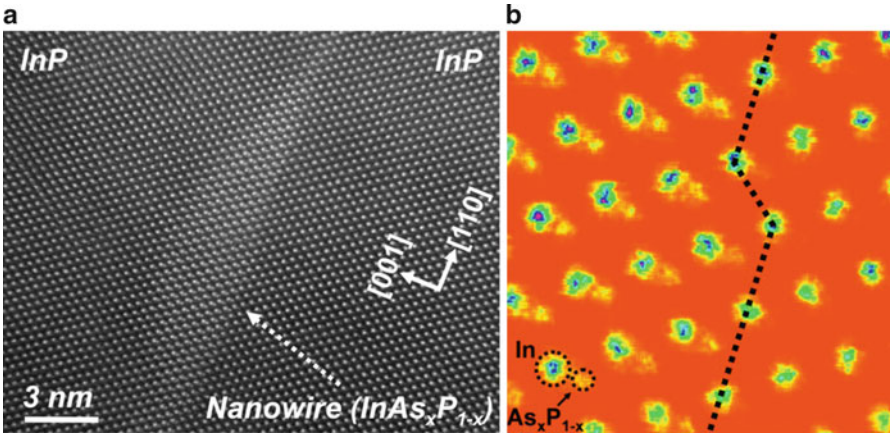


Fig. 14.15 (**a**) Z-contrast image (raw data) of an InP capped InAs(P) nanowire grown by solid source molecular beam epitaxy on (001) InP substrate. This image enables the two fcc sublattices of In (brighter contrasts) and $As^{+}P$ atoms constituting the zinc-blende structure of the $InAs_xP_{1-x}$ disordered alloy to be directly distinguished. Stronger intensities are observed in the projected positions of the $InAs_xP_{1-x}$ atomic columns. (**b**) Color low pass filtered high-resolution Z-contrast image obtained from a magnified region of the central part of the InAs(P)/InP wire interface. The existence of a diatomic step is clearly visible on the *dotted line* (Reprinted with permission from [122]. Copyright [2007], AIP Publishing LLC)

column clearly delineates the outline of the nanowire and the presence of the interfacial step. The existence of brighter intensities in the atomic columns of the nanowire located on the upper terrace of the diatomic step clearly confirms the presence of an As-rich region at this location. This locates the site of the original nucleation on the upper terrace and supports the strain-induced nucleation previously established from strain calculations.

QWRs Growth: From Elongated Islands to Mature QWRs

Once the 3D nano-objects are nucleated, they start to gradually grow along [110] direction up to completely covering the whole surface. During this process, wires not only change by elongating along this specific direction, but also experience variations of their cross-sectional shape. Additionally, the InAs(P) wetting layer also undergoes remarkable changes.

The most remarkable morphological modification is the one from a flat two-dimensional structure toward a three-dimensional one, also called in literature as "2D-3D transition." During the MBE growth, this transition is traditionally observed by changes of the RHEED pattern. This is a spontaneous and almost instantaneous process which occurs after a small variation of the growth conditions, and when the wetting layer has achieved its critical thickness [125]. Nevertheless, for some material systems, 3D nanostructures may appear on the growth surface before the RHEED pattern changes, and alternative methods with higher sensibility are needed. The one based on the detection of laser deflection on a cantilever shape cut sample has been successfully used to evaluate, in situ and in real time, the elastic

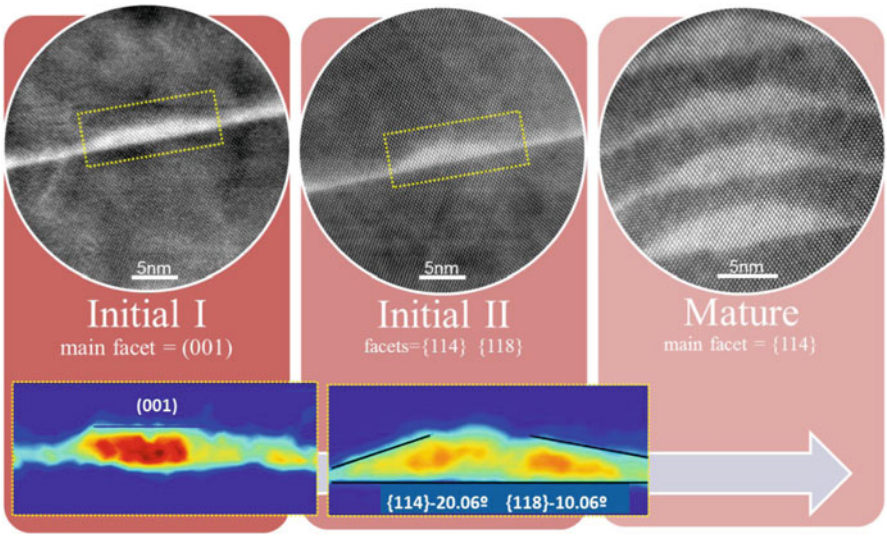


Fig. 14.16 Z-contrast images and their maps of integrated intensities around As–P columns of samples I2 (*left*), I3 (*middle*), and mature stacked QWR layers, example of sample SL (*right*) from a sample grown with similar MBE conditions. Higher values of integrated intensity denote higher As content (Partially reproduced from Ref. [124])

relaxation of multiple III–V systems due to the 2D-3D transition [108, 111, 126]. With the aim of evaluating the wires growth at their initial stages, three samples (I1, I2, I3) with different elastic relaxation states, measured with the last mentioned method, were analyzed. Accordingly, the first sample corresponds to the onset of the elastic relaxation process due to the spontaneous self-assembling of QWRs, and the last sample to the well-developed QWRs. The growth conditions are reported in Ref. [111] and [124].

AFM images acquired in Madrid Institute of Microelectronics and published in Ref. [111] show important changes on the QWR length and density when only a 0.2 ML of InAs was increased. QWRs length changes from 185 $\pm$ 50 nm in the 2.5 ML sample (I2) to several microns in the 2.7 ML one (I3). Changes on cross-sectional QWRs shape are clearly observable in high-resolution Z-contrast images of Fig. 14.16, where maps of the integrated intensity around As–P columns (bottom colored images) – determined from the high-resolution Z-contrast images as described in paragraph 2.2 – display that (001) is the main facet of the nano-objects at their very initial stage of formation; however, it is gradually reduced in favor of {114} or {118}. It is clearly observable from this analysis the compositional asymmetry of the nanowires since their initial steps of growth, which has a strong effect on the final arrangement, composition, and strain of the nanowires.

Three-dimensional models built by FEA explain the facets evolution in terms of variation of the elastic energy. Simulations of the elastic energy on the growth front surface have been carried out, also solving the anisotropic elastic theory equations by FEM. The size, shape, and composition of the 1D- nanostructures and the wetting

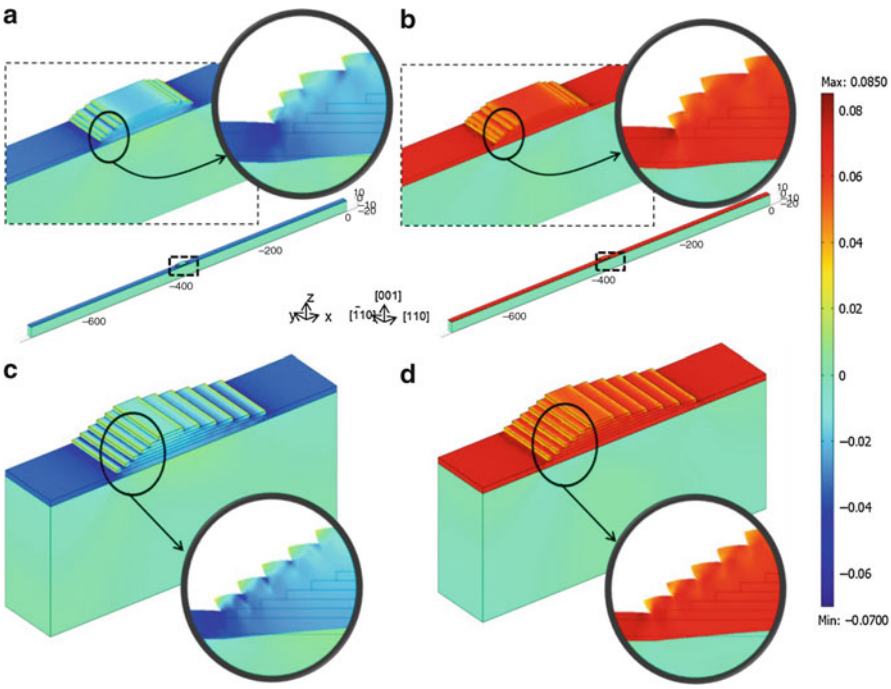


Fig. 14.17 Simulated strain for initial QWRs corresponding to samples I2 ((**a**) and (**b**)) and I3 ((**c**) and (**d**)). (**c**) and (**d**) represent the strain component in the growth direction and (**a**) and (**b**) in-plane direction. Details of the deformed shape multiplied by a factor of 10 are also shown in *circles* (Reproduced from [124] with the permission of the copyright owner)

layers beside them have been modeled on the basis of Z-contrast high-resolution images, with enough sensitivity to define those aspects with atomic column resolution, and EELS spectrum images of buried nanostructures of interest (see examples of HAADF-STEM images in Fig. 14.16). For the boundary conditions set up, a 3D wire was built and the symmetries were then incorporated into the calculations to represent the entire sample. The InAs deposited was compressively strained (3.2 % is the lattice misfit value between both materials). Anisotropic behavior and values at 300 K are assumed for elastic constants of InAs and InP [127]. All the nodes of symmetry planes are fixed against displacement in the directions normal to these planes, and all nodes on the bottom of the substrate are fixed against rigid body shift in the z direction.

Figure 14.17 shows the colored maps where the strains in an in-plane direction (ε_{xx}) and in the growth direction (ε_{zz}) are plotted on the 3D models representing the nanowires with 2.5 and 2.7 ML of InAs, I2 and I3, respectively. Note that the strain value displayed is related to the lattice parameter of each material in bulk. As expected for pseudomorphic InAs grown on InP, positive strain along the [001] direction is found in the InAs layer due to tetragonal distortion. It can be noticed that ε_{zz} is higher for the wetting layer than inside wires, due to the extra relaxation parallel to the hetero-interfaces experimented by 3D shaped nanoobjects.

The strain component parallel to the surface at the sides of the QWR results in a lower compressive deformation with respect to the wetting layer. Thus, the lattice parameter is higher (i.e., closer to bulk InAs) in this area, being more favorable to new InAs incorporation in terms of strain energy. In contrast, the border between the QWR and the wetting layer shows an in-plane lattice parameter more similar to relaxed InP, so the InAs would grow highly compressed in this place. These areas of the surface with higher chemical potential present less probability of further InAs deposition, and hence more superficial diffusion of As outward.

In order to determine the chemical potential distribution along the surface now forming, several terms must be taken into account, i.e., elastic energy stored in the material, surface energy, chemical potential component associated to the entropy of mixing of the formed alloy, or the chemical potential in an unstressed surface [128, 129]. By analyzing the influence of all parameters, we deduce that the major contribution is the two first terms, the elastic energy and surface energy. The chemical potential energy is confirmed to be minima in concave surface regions and on (001) facets and maxima around the QWR perimeter where it joins the WL, favoring diffusion of arsenic atoms from these edges toward both the QWR outside for the nucleation of new wires and to the QWR top. The later means the wire undergoes a height increase, a reduction of its (001) facets, and a definition of the {114} [128] (mainly) and {118} lateral facets, as experimentally observed in HAADF-STEM images of Fig. 14.16.

Stacking of $InAs_xP_{1-x}$/InP QWR: Strain Field Transmission and Prediction of Nucleation Sites for the Growth of the Upper Wires

The InP capped $InAs_xP_{1-x}$ nanowires underneath each new stacked layer of nanowires produce inhomogeneous strain fields that propagate toward the capping layer surface where the next nanostructures is to be formed, controlling the distribution of the strain at the InP growth surface. By combining in situ stress measurements and transmission electron microscopy, the effect of this field has been already reported and the wire growth explained by considering stress-driven mass transport and P/As exchange [110].

Compositionally sensitive XTEM image of Fig. 14.18a, taken from a low capping temperature (380 °C) sample (SL-type sample) with 20-nm thick spacer layers, shows randomly distributed nanowires. In contrast, Fig. 14.18b illustrates ordered stacked nanowires. This last image corresponds to a heterostructure of the same type but with 5-nm thick spacer layers. They are arranged along a direction that forms $\alpha = 9°$ with the [001] vertical direction. A thinner capping layer is however needed to orderly arrange the stacked wires if the growth temperature of the capping layer is 515 °C (SH-type sample). In this case, similar arrangement is only found for 3 nm of thickness and the stacking angle α is about 16°, as it is displayed in Fig. 14.18c.

In order to establish the behavior of stacked InAs QWRs layers, two approaches have been applied to InAs/InP single and stacked QWRs (to both sample series SL and SH): (i) plot experimental strain field maps from HRTEM images using Peak Finding Methods and (ii) calculate the strain field by solving the anisotropic elastic

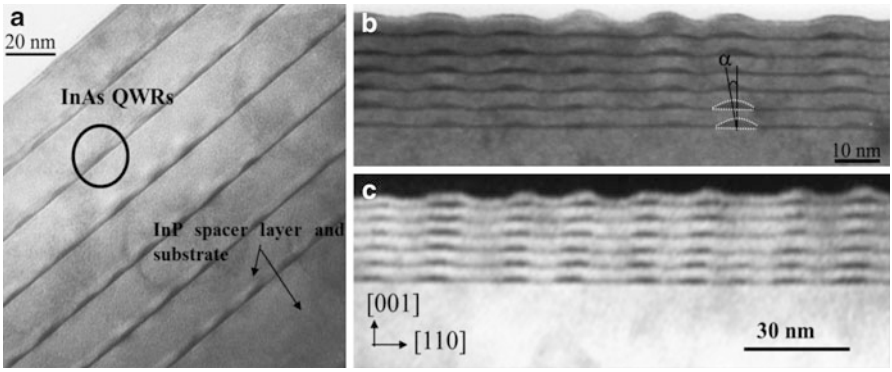


Fig. 14.18 CTEM images of stacked InAs QWRs, (**a**) sample type LT with a 20-nm thick spacer layer, (**b**) with a 5-nm thick spacer layer (angle a is shown on this image), and (**c**) sample type HT with a 3-nm thick spacer layer

theory equations by Finite Elements Analysis (FEA) using a compositional model of the studied nano-objects. Inputs for this compositional model are given by both spatially resolved EELS and aberration-corrected high-resolution Z-contrast images. For this, similar boundary conditions for the 3D strain model are also set up.

Experimental contour plots strain field maps of the [001] component of the strain field show similar strain maxima (5–7 %) for SL and SH samples series (examples are reported in Ref. [130, 131]). In general, we have measured an asymmetric strain field through the InP spacer layer and an off-centered that means the maximum strain is not in the wire center, which is associated to the existence of an inhomogeneous composition distribution in the wires, as it was previously shown for initial QWRs. This fact leads to the generation of a new wire in a preferential region slightly closer but tilted with respect to the growth [001] direction. A reduced size is measured in nanowires grown with higher temperature capping layers [107]. This is due to the enhancement of the As/P exchange process during wire capping, which is enhanced at higher temperatures. That size reduction generates weaker strain fields, requiring thinner spacer to preserve the vertical ordering.

Figures 14.19a, b display the As distribution in a QWR of sample SH buried under a 3 nm thick spacer layer determined by using high-resolution Z-contrast imaging at atomic scale. We have quantified the integrated intensities around each dumbbell as illustrated in Fig. 14.1c. Figure 14.19a displays the distribution of integrated intensities superimposed over the original Z-contrast image of the object. Higher values of these integrated intensities correspond to higher As content. The resulting interpolated normalized intensities are represented in Fig. 14.19b. An enrichment of As toward the inner part of the wire is evinced from the Z-contrast image. The full process including simulation to analyze possible artifact of the Z-contrast images is detailed in Ref. [123, 124]. On the other hand, Fig. 14.19c shows a As map obtained by EELS corresponding to a stacked wire type SL buried under 5-nm thick spacer layer. Similar As content maximum is detected. The size

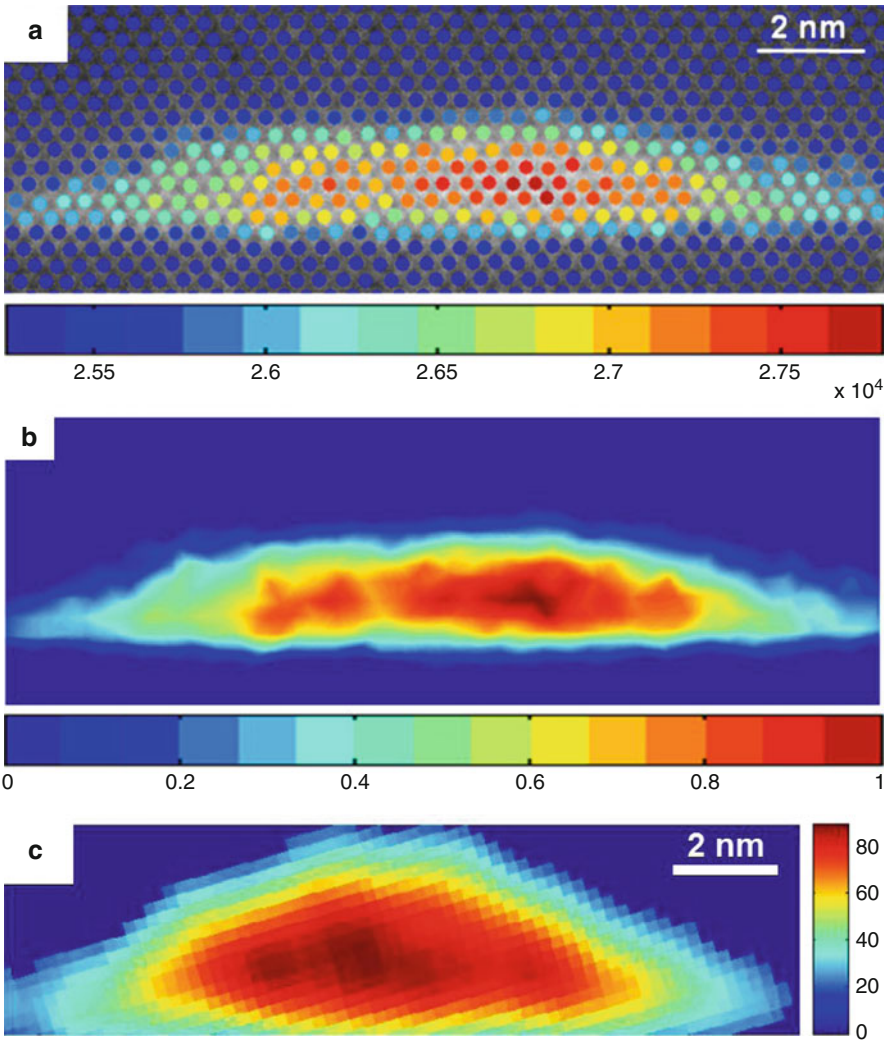


Fig. 14.19 (**a**) Areal integrated intensities for each atomic dumbbell are shown overlapped on the original Z-contrast image on the [110] projection of the sphalerite structure for a NW with a 3-nm thick spacer layer deposited at high temperature. (**b**) Interpolated normalized intensities from integrated intensities shown in (**a**). Intensities are normalized assigning 0 to the minimum and 1 to the maximum intensity. (**c**) Arsenic compositional map of other wire buried at low temperature, determined from EELS spectra (Reproduced from [121] and [132] with the permission of the copyright owner)

reduction is corroborated in case of SH samples by comparing (a/b) and (c) images. Once again the EELS map shows the existence of an As compositional asymmetry in the wire, which is the main reason for the inhomogeneous strain field map experimentally observed from HRTEM images. If the As compositional

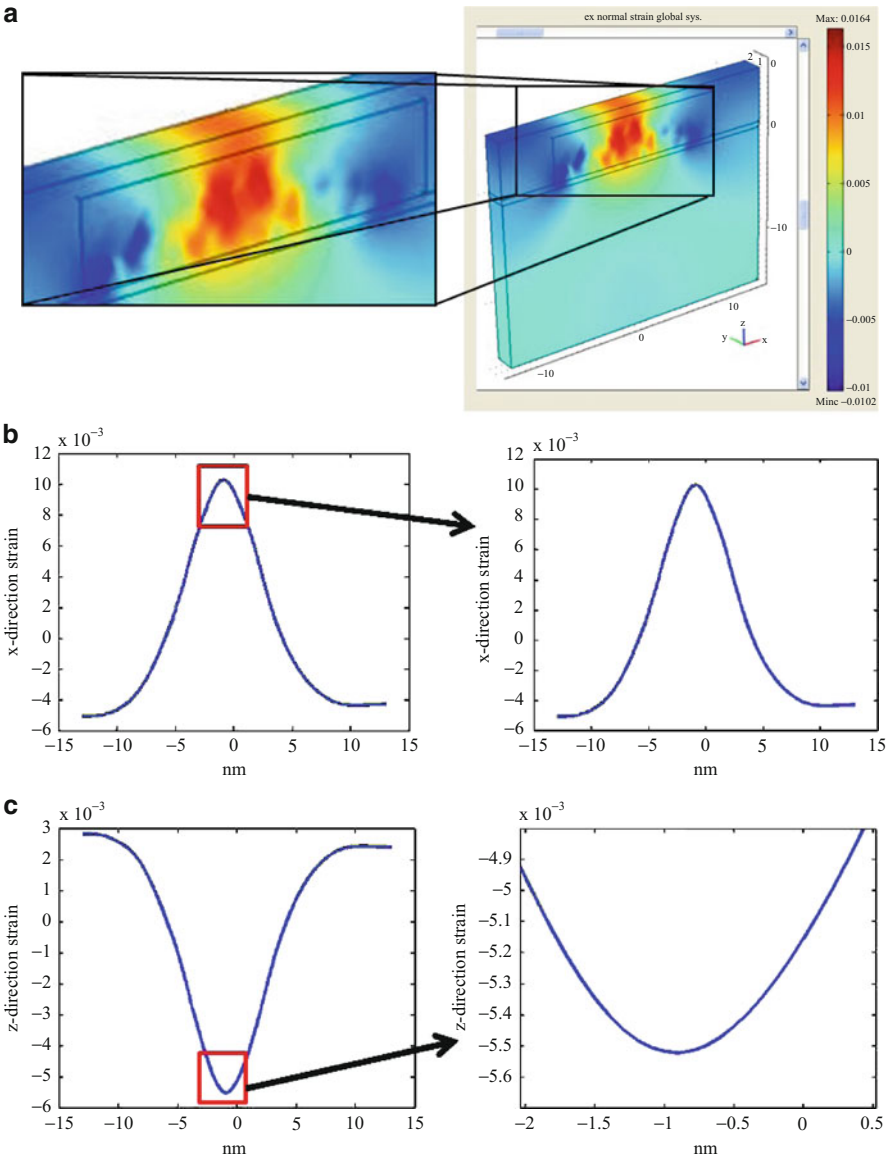


Fig. 14.20 (**a**) 3D representation of the x (i.e., [110] component) of the strain (ε_{xx}) obtained by finite element calculations. Profiles of the ε_{xx} and ε_{zz} (i.e., [001] component of the strain) values versus x obtained at the surface of the 5-nm thick InP capping layer are shown in (**b**) and (**c**), respectively. The 0 nm point in the abscissa axis corresponds to the center of the wire underneath. x = [110]; y = [110]; z = [001] (Reproduced from [132] with the permission of the copyright owner)

distribution in the wires were perfectly symmetrical, the strain field generated on the InP capping layer would have a maximum value just on top of the center of this wire. As we will show in the following, this compositional asymmetry in the wires has a strong influence on the position of the subsequent wires in the stacked wire layers, since it can motivate a displacement of the ε_{xx} maximum and the ε_{zz} minimum to another zone slightly shifted from the top of the center of the wire underneath, and hence the nucleation of the upper stacked wire will be somewhat displaced with respect to the symmetrical case.

To picture the strain influence on the stacked layer growth, composition distributions obtained by analysis of EEL spectra and HAADF images for samples here analyzed have been used as inputs to simulate the strain and stress maps caused by wires of both samples (we show on case next). Following similar approach regarding the location of the chemical potential at the growth surface to section before, a successful prediction of the nucleation sites for stacked wires in upper layer and stacking angles of the studied nanostructures is obtained from the definition of the sites where the stacked InAs wires grow with minimum strain energy.

Figure 14.20 depicts the resulting strain components determined by introducing the realistic (asymmetrical) compositional model of the wire represented in Fig. 14.19. Three-dimensional plot of the in-plane component is represented in Fig. 14.20a. By observing graphs in Fig. 14.20b, c, we can confirm the existence of the predicted displacement of the ε_{xx} maximum and the ε_{zz} minimum to another zone slightly farther away from the top of the center of the wire underneath. The absolute displacement value corresponds to an angle of 9.8° between [001] and the straight line joining the position of the critical strains point at the growth surface of the 5 nm InP capping layer with the center of the base of the studied wire in the first layer (see angle definition in Fig. 14.18b). That is in good agreement with the values of α experimentally observed (the average experimental value of α is 9°). The α angle determined by finite element calculations for the sample type SH with spacer layer thickness of 3 nm is 16.7°, which is also close to the experimental angle ($\alpha = 16°$) already mentioned before. That is a demonstration of the usefulness of this approach for the location of the preferential sites for the strain-influenced epitaxial growth of stacked nanowires.

6 Conclusions and Future Perspective

In this chapter, we summarize the studies carried out on several 1D nanostructures formed by metal oxide, III-nitrides, and III–V semiconductors. For this work, the combination of conventional and aberration-corrected high-resolution electron microscopy imaging, energy dispersive X-ray and electron energy loss spectroscopies, and experimental and simulated strain field mapping has demonstrated to be a successful tool for the determination of the nanostructures' behavior through the morphology, crystalline structure, and nanoscale compositional analysis.

TEM analyses have demonstrated the thermal oxidation in air at 500 °C of Zn metal films deposited on top of a CdTe substrate could be a very simple method to

grow <11-20> ZnO nanowires. Their study showed that the oxidation and Zn evaporation times affected the morphology and the crystal quality of NWs. Moreover, the Cd coming from the substrate plays the role of a catalyst, promoting the growth of the ZnO NWs from the oxidation of a Zn metallic layer. The intermediate oxidation times and thicker Zn films lead to the best formation of the NWs, i.e., longer nanowires with a high structural quality; however, their growth can be reverted by high oxidation times.

We have also analyzed and characterized by S/TEM microscopy techniques, EDX and EEL spectroscopy, different vertical ZnO nanorods arrays grown along the [0001] direction by a novel three-step catalyst-free method that is independent of the substrate nature. The combination of VPT growth process on CBD buffer layers resulted in well-aligned ZnO nanorods of excellent crystalline quality. VPT nanorods underwent huge morphology changes compared to CBD ones, with chemical and structural alterations at the nanorods–substrate interface. The structural and morphological transformations of VPT and CBD nanorods are mainly due to the partial sublimation, diffusion, and to the re-deposition of ZnO on nanostructures.

Furthermore, a TEM study on the structural and compositional properties of spontaneous single crystalline GaN/$Al_xGa_{1-x}N$ nanowire heterostructures is presented. The results showed the formation of core–shell radial structures, where the $Al_xGa_{1-x}N$ segment is surrounded by a spontaneously formed Al-rich $Al_xGa_{1-x}N$ shell. The shell appears not only along these sections but also on the top area of the GaN NW basement. The complex chemical composition is attributed to the low mobility of Al atoms in comparison with Ga atoms. Indeed, all the wires have a maximum core Al content close to the GaN–AIGaN interface which decreases exponentially with the NW height. Nevertheless, this trend changes in the longer NWs, giving rise to an increase both of the Al content and the diameter of the core. The formation and the structure that evolves along the NW are explained by the Al/Ga surface mobility differences and the shadow effect of the neighboring NWs.

Finally, high-resolution phase-contrast and Z-contrast electron microscopy techniques, in coordination with Peak Finding Methods, FEM and EEL spectroscopy, have been proved as a powerful tool to predict the preferential sites of nucleation of stacked $InAs_xP_{1-x}$/InP wires by finding the growth surface zones where the chemical potential is minimized. Good agreement is found between the predicted and experimental locations of the preferential sites for wire nucleation. Furthermore, we have shown that the combined application of these techniques contributes to explain the formation of initial stage and the arrangement of horizontal InAs single and stacked quantum wires grown by MBE on InP (001). In particular, experimental results confirm that: (i) Preferential sites for the nucleation of single strained nanowires lie on the upper terrace surface close to the step edge, where maximum stress relief occurs during the initial stages just before the 2D–3D transition taking place. (ii) Self-assembled InAs/InP nanowires evolve during their formation in such a way that (001) is the main facet in the initial stages of growth, which gradually becomes replaced by {114} and {118} facets, ending with the formation of mature QWRs with {114} facets. During this evolution process, the height of the QWRs increases

whereas their width reduces. (iii) An inhomogeneous strain field appears in stacked InAs quantum wires caused mainly by the asymmetric As distribution in the initial steps of growth. (iv) The presence of such strain in the growth front is of great relevance in the definition of the sites for the growth of the new stacked wires. This fact also has strong influence on the wire sizes and the arrangement control for the optimization of the design of devices based on InAs/InP semiconductor materials.

Acknowledgments Financial support from Spanish projects (MAT2010-15206, TEC2011-29120-C05-03 and CONSOLIDER INGENIO 2010 CSD2009-00013), Junta de Andalutia (P09-TEP-5403, PAI research groups TEP-120 and TEP-946), and the European Science Foundation (COST Action MP0805) are gratefully acknowledged. TEM measurements were carried out at DME-SCCYT-UCA. The authors would like to thank their collaborators and coauthors of the articles reviewed here (O. Martinez, J.L. Plaza, E. Dieguez, J.G. Lozano, J. Mass, D. Byrne, E. McGlyn, B. Twamley, M. O. Henry, P.L. Galindo, J. Pizarro, D. Fuster, L. González, Y. González, S. Kret, R. Songmuang, M. H. Gass, P. J. Goodhew, M. Varela, S. J. Pennycook). Authors belong to the Institute of Electron Microscopy and Materials, which is in interim stage of creation.

References

1. Manasreh O (2012) Introduction to nanomaterials and devices. Wiley, New York
2. Duan XF, Huang Y, Agarwal R, Lieber CM (2003) Single-nanowire electrically driven lasers. Nature 421(6920):241–245
3. Law M, Greene LE, Johnson JC, Saykally R, Yang PD (2005) Nanowire dye- sensitized solar cells. Nat Mater 4(6):455–459
4. Levy-Clement C, Tena-Zaera R, Ryan MA, Katty A, Hodes G (2005) CdSe-sensitized p-CuSCN/nanowire n-ZnO heterojunctions. Adv Mater 17(12):1512–1525
5. Tomioka K, Motohisa J, Hara S, Hiruma K, Fukui T (2010) GaAs/AlGaAs core multishell nanowire-based light-emitting diodes on Si. Nano Lett 10(5):1639–1644
6. Hochbaum AI, Chen R, Delgado RD, Liang W, Garnett EC, Najarian M, Majumdar A, Yang P (2008) Enhanced thermoelectric performance of rough silicon nanowires. Nature 451(7175):163–167
7. Wang ZL, Song JH (2006) Piezoelectric nanogenerators based on zinc oxide nanowire arrays. Science 312(5771):242–246
8. Wang X, Song J, Liu J, Wang ZL (2007) Direct-current nanogenerator driven by ultrasonic waves. Science 316(5821):102–105
9. Patolsky F, Timko BP, Yu G, Fang Y, Greytak AB, Zheng G, Lieber CM (2006) Detection, stimulation, and inhibition of neuronal signals with high-density nanowire transistor arrays. Science 313(5790):1100–1104
10. Wu YY, Yang PD (2001) Direct observation of vapor–liquid-solid nanowire growth. J Am Chem Soc 123(13):3165–3166
11. Choi HJ (2012) Vapor–liquid-solid growth of semiconductor nanowires. Springer, Berlin/Hiedelberg
12. Utama MIB, Zhang J, Chen R, Xu X, Li D, Sun H, Xiong Q (2012) Synthesis and optical properties of II–VI1D nanostructures. Nanoscale 4(5):1422–1435
13. Calarco R, Meijers RJ, Debnath RK, Stoica T, Sutter E, Luth H (2007) Nucleation and growth of GaN nanowires on Si(111) performed by molecular beam epitaxy. Nano Lett 7(8):2248–2251
14. Byrne D, McGlynn E, Kumar K, Biswas M, Henry MO, Hughes G (2010) A study of drop-coated and chemical bath-deposited buffer layers for vapor phase deposition of large area, aligned, zinc oxide nanorod arrays. Cryst Growth Des 10(5):2400–2408

15. González L, Garcia JM, Garcia R, Briones F, Martinez-Pastor J, Ballesteros C (2000) Influence of buffer-layer surface morphology on the self-organized growth of InAs on InP (001) nanostructures. Appl Phys Lett 76(9):1104–1106
16. Ding Y, Wang ZL (2009) Structures of planar defects in ZnO nanobelts and nanowires. Micron 40(3):335–342
17. Bougerol C, Songmuang R, Camacho D, Niquet YM, Mata R, Cros A, Daudin B (2009) The structural properties of GaN insertions in GaN/AlN nanocolumn heterostructures. Nanotechnology 20(29):295706–295710
18. Gudiksen MS, Lauhon LJ, Wang J, Smith DC, Lieber CM (2002) Growth of nanowire superlattice structures for nanoscale photonics and electronics. Nature 415(6872):617–620
19. Jarausch K, Thomas P, Leonard DN, Twesten R, Booth CR (2009) Four-dimensional STEM-EELS: Enabling nano-scale chemical tomography. Ultramicroscopy 109(4):326–337
20. Du GH, Yuan ZY, Van Tendeloo G (2005) Transmission electron microscopy and electron energy-loss spectroscopy analysis of manganese oxide nanowires. Appl Phys Lett 86(6):063113–063115
21. Urban K, Kabius B, Haider M, Rose H (1999) A way to higher resolution: spherical-aberration correction in a 200 kV transmission electron microscope. J Electron Microsc 48(6):821–826
22. Krivanek OL, Dellby N, Lupini AR (1999) Towards sub-angstrom electron beams. Ultramicroscopy 78(1–4):1–11
23. Rose H (1994) Correction of aberrations, a promising means for improving the spatial and energy resolution of energy-filtering electron-microcopes. Ultramicroscopy 56(1–3): 11–25
24. Haider M, Rose H, Uhlemann S, Schwan E, Kabius B, Urban K (1998) A spherical-aberration-corrected 200 kV transmission electron microscope. Ultramicroscopy 75(1):53–60
25. O'Keefe MA (2008) Seeing atoms with aberration-corrected sub-Angstrom electron microscopy. Ultramicroscopy 108(3):196–209
26. Muller DA (2009) Structure and bonding at the atomic scale by scanning transmission electron microscopy. Nat Mater 8(4):263–270
27. Pennycook SJ, Varela M, Hetherington CJD, Kirkland AI (2006) Materials advances through aberration-corrected electron microscopy. MRS Bull 31(1):3643
28. Varela M, Findlay SD, Lupini AR, Christen HM, Borisevich AY, Dellby N et al (2004) Spectroscopic imaging of single atoms within a bulk solid. Phys Rev Lett 92(9): 095502–095505
29. Galluppi M, Frova A, Capizzi M, Boscherini F, Frigeri P, Franchi S, Passaseo A (2001) Atomic equilibrium concentrations in (InGa)As quantum dots. Appl Phys Lett 78(20):3121–3123
30. Shumway J, Williamson AJ, Zunger A, Passaseo A, DeGiorgi M, Cingolani R, Catalano M, Crozier P (2001) Electronic structure consequences of In/Ga composition variations in self-assembled $In_xGa_{1-x}As$/GaAs alloy quantum dots. Phys Rev B 64(12):125302–125313
31. Eee H, Nellist PD, Lozano-Perez S, Ozkaya D (2010) Towards quantitative analysis of core-shell catalyst nano-particles by aberration corrected high angle annular dark field STEM and EDX. J Phys Conf Ser 241(1):012067–012070
32. Allen LJ, D'Alfonso AJ, Findlay SD, LeBeau JM, Lugg NR, Stemmer S (2010) Elemental mapping in scanning transmission electron microscopy. J Phys Conf Ser 241(1):012061–012067
33. Carlino E, Modesti S, Furlanetto D, Piccin M, Rubini S, Franciosi A (2003) Atomic resolution composition analysis by scanning transmission electron microscopy high-angle annular dark-field imaging. Appl Phys Lett 83(4):662–664
34. Zhi D, Midgley PA, Dunin-Borkowski RE, Joyce BA, Pashley DW, Bleloch AL, Goodhew PJ (2005) Growth and overgrowth of Ge/Si quantum dots: an observation by atomic resolution HAADF-STEM imaging. In: Tsybeskov L, Lockwood DJ, Delerue C,

Ichikawa M (eds) Group-IV semiconductor nanostructures 2005. MRS Society, Warrandale, pp 105–110
35. Molina SI, Sales DL, Galindo PL, Fuster D, González Y, Alen B, González L, Varela M, Pennycook SJ (2009) Column-by-column compositional mapping by Z- contrast imaging. Ultramicroscopy 109(2):172–176
36. Hernandez-Maldonado D, Herrera M, Alonso-González P, González Y, González L, Gazquez J et al (2011) Compositional analysis with atomic column spatial resolution by 5th-order aberration-corrected scanning transmission electron microscopy. Microsc Microanal 17(4):578–581
37. Egerton RF (1986) Electron energy-loss spectroscopy in the electron microscope. Plenum Press, New York
38. Galindo PL, Kret S, Sanchez AM, Laval JY, Yanez A, Pizarro J, Guerrero E, Ben T, Molina SI (2007) The peak pairs algorithm for strain mapping from HRTEM images. Ultramicroscopy 107(12):1186–1193
39. Gatti R, UhHk F, Montalenti F (2008) Intermixing in heteroepitaxial islands: fast, self-consistent calculation of the concentration profile minimizing the elastic energy. New J Phys 10(8):083039–083049
40. Liu GR, Jerry SSQ (2002) A finite element study of the stress and strain fields of InAs quantum dots embedded in GaAs. Semicond Sci Technol 17(6):630–643
41. Ozgur U, Alivov YI, Liu C, Teke A, Reshchikov MA, Dogan S, Avrutin V, Cho SJ, Morkoc H (2005) A comprehensive review of ZnO materials and devices. J Appl Phys 98(4):041301–041403
42. Ellmer K, Klein A, Rech B (2008) Transparent conductive zinc oxide: basics and applications in thin film solar cells. Springer, London
43. Bagnall DM, Chen YF, Zhu Z, Yao T, Koyama S, Shen MY, Goto T (1997) Optically pumped lasing of ZnO at room temperature. Appl Phys Lett 70(17):2230–2232
44. Lao CS, Liu J, Gao P, Zhang L, Davidovic D, Tummala R, Wang ZL (2006) ZnO nanobelt/nanowire schottky diodes formed by dielectrophoresis alignment across Au electrodes. Nano Lett 6(2):263–266
45. Rout CS, Hari Krishna S, Vivekchand SRC, Govindaraj A, Rao CNR (2006) Hydrogen and ethanol sensors based on ZnO nanorods, nanowires and nanotubes. Chem Phys Lett 418(4–6):586–590
46. Pradhan D, Kumar M, Ando Y, Leung KT (2008) One-dimensional and twodimensional ZnO nanostructured materials on a plastic substrate and their field emission properties. J Phys Chem C 112(18):7093–7096
47. Li Z, Yang R, Yu M, Bai F, Li C, Wang ZL (2008) Cellular level biocompatibility and biosafety of ZnO nanowires. J Phys Chem C 112(51):20114–20117
48. Yang J, Zheng J, Zhai H, Yang X, Yang L, Liu Y, Lang J, Gao M (2010) Oriented growth of ZnO nanostructures on different substrates via a hydrothermal method. J Alloys Compd 489(1):51–55
49. Lockman Z, Pet Fong Y, Wai Kian T, Ibrahim K, Razak KA (2010) Formation of selfaligned ZnO nanorods in aqueous solution. J Alloys Compd 493(1–2):699–706
50. Xu S, Ding Y, Wei Y, Fang H, Shen Y, Sood AK, Polla DL, Zhong LW (2009) Patterned growth of horizontal ZnO nanowire arrays. J Am Chem Soc 131(19):6670–6671
51. Yao B, Feng L, Cheng C, Loy MMT, Wang N (2010) Tailoring the luminescence emission of ZnO nanostructures by hydrothermal post-treatment in water. Appl Phys Lett 96(22):223105–223107
52. Hsu YF, Xi YY, Djurisic AB, Chan WK (2008) ZnO nanorods for solar cells: hydrothermal growth versus vapor deposition. Appl Phys Lett 92(13):133507–133509
53. Bosio A, Romeo N, Mazzamuto S, Canevari V (2006) Polycrystalline CdTe thin films for photovoltaic applications. Progr Cryst Growth Char Mater 52(4):247–279
54. Plaza JL, Martinez O, de Dios S, Olvera J, Dieguez E (2009) New method for fabricating ZnO nanowires deposited onto CdTe substrates. J Cryst Growth 312(1):64–67

55. Martinez O, Hortelano V, Jimenez J, Plaza JL, de Dios S, Olvera J et al (2011) Growth of ZnO nanowires through thermal oxidation of metallic zinc films on CdTe substrates. J Alloys Compd 509(17):5400–5407
56. Ding Y, Kong XY, Wang ZL (2004) Doping and planar defects in the formation of singlecrystal ZnO nanorings. Phys Rev B 70(23):235408–235414
57. Ding Y, Wang ZL (2004) Structure analysis of nanowires and nanobelts by transmission electron microscopy. J Phys Chem B 108(33):1228012291
58. Martínez O, Plaza JL, Mass J, Capote B, Diéguez E, Jiménez J (2007) Luminescence of pure and doped ZnO films synthesised by thermal annealing on GaSb single crystals. Superlattices Microst 42(1–6):145–151
59. Zanotti L, Zha M, Calestani D, Comini E, Sberveglieri G (2005) Growth of tin oxide nanocrystals. Cryst Res Technol 40(10–11):932–936
60. Ali A, Shah NA, Aqili AKS, Maqsood A (2006) Impact of evaporation rates of Cd and Te on structural, morphological, optical, and electrical properties of CdTe thin films deposited by a two-sourced evaporation technique. Cryst Growth Des 6(9):2149–2154
61. Govender K, Boyle DS, Kenway PB, O'Brien P (2004) Understanding the factors that govern the deposition and morphology of thin films of ZnO from aqueous solution. J Mater Chem 14(16):2575–2591
62. Byrne D, McGlynn E, Henry MO, Kumar K, Hughes G (2010) A novel, substrate independent three-step process for the growth of uniform ZnO nanorod arrays. Thin Solid Films 518(16):4489–4492
63. Greene LE, Law M, Tan DH, Montano M, Goldberger J, Somorjai G, Yang P (2005) General route to vertical ZnO nanowire arrays using textured ZnO seeds. Nano Lett 5(7):1231–1236
64. Lide DR (1992) CRC handbook of chemistry and physics. CRC, Boca Raton, p 2560
65. Byrne D, Fath Allah R, Ben T, González Robledo D, Twamley B, Henry MO, McGlynn E (2011) Study of morphological and related properties of aligned zinc oxide nanorods grown by vapor phase transport on chemical bath deposited buffer layers. Cryst Growth Des 11(12):5378–5386
66. Kim SS, Lee B-T (2004) Effects of oxygen pressure on the growth of pulsed laser deposited ZnO films on Si(001). Thin Solid Films 446(2):307–312
67. Fath Allah R, Byrne D, Ben T, González D, McGlynn E, Garcia R (2012) Effect of high temperature VPT conditions on the development of aligned ZnO nanorod arrays grown by a three step catalyst-free method. J Nano Lett 3(2):1–8
68. Lim YS, Park JW, Kim MS, Kim J (2006) Effect of carbon source on the carbothermal reduction for the fabrication of ZnO nanostructure. Appl Surf Sci 253(3):1601–1605
69. Xu XL, Guo CX, Qi ZM, Liu HT, Xu J, Shi CS, Chong C, Huang WH, Zhou YJ, Xu CM (2002) Annealing effect for surface morphology and luminescence of ZnO film on silicon. Chem Phys Lett 364(1–2):57–63
70. Karazhanov SZ, Ravindran P, Fjellvag H, Svensson BG (2009) Electronic structure and optical properties of $ZnSiO_3$ and Zn_2SiO_4. J Appl Phys 106(12):123701–123707
71. DiStefano TH, Eastman DE (1971) The band edge of amorphous SiO_2 by photoinjection and photoconductivity measurements. Solid State Commun 9(24):2259–2261
72. Ashfold MNR, Doherty RP, Ndifor-Angwafor NG, Riley DJ, Sun Y (2007) The kinetics of the hydrothermal growth of ZnO nanostructures. Thin Solid Films 515(24):8679–8683
73. Leonard RB, Searcy AW (1971) The variation of vaporization rates with orientation for basal planes of zinc oxide and cadmium sulfide. J Appl Phys 42(10):4047–4054
74. Iwanaga H, Yoshiie T, Yamaguchi T, Shibata N (1979) Crystal growth and sublimation in II–VI compounds along their polar axis. J Cryst Growth 47(5–6):703–711
75. Ntep JM, Barbé M, Cohen-Solal G, Bailly F, Lusson A, Triboulet R (1998) ZnO growth by chemically assisted sublimation. J Cryst Growth 184–185:1026–1030
76. Su X, Zhang Z, Zhu M (2006) Melting and optical properties of ZnO nanorods. Appl Phys Lett 88(6):061913–061915

77. Yan Z, Ma Y, Wang D, Wang J, Gao Z, Wang L, Yu P, Song T (2008) Impact of annealing on morphology and ferromagnetism of ZnO nanorods. Appl Phys Lett 92(8):081911–081913
78. Yan Z, Zhu K, Chen W-P (2008) ZnO quasibicrystals formed by thermal annealing. Appl Phys Lett 92(24):241912–241914
79. Wang N, Cai Y, Zhang RQ (2008) Growth of nanowires. Mater Sci Eng R Reports 60(1–6):1–51
80. Heo YW, Norton DP, Tien LC, Kwon Y, Kang BS, Ren F, Pearton SJ, LaRoche JR (2004) ZnO nanowire growth and devices. Mater Sci Eng R Rep 47(1–2):1–47
81. Hersee SD, Sun X, Wang X (2006) The controlled growth of GaN nanowires. Nano Lett 6(8):1808–1811
82. Fan HJ, Yang Y, Zacharias M (2009) ZnO-based ternary compound nanotubes and nanowires. J Mater Chem 19(7):885–900
83. Fakhr A et al (2010) Dependence of InGaP nanowire morphology and structure on molecular beam epitaxy growth conditions. Nanotechnology 21(16):165601–165607
84. Songmuang R, Ben T, Daudin B, González D, Monroy E (2010) Identification of III-N nanowire growth kinetics via a marker technique. Nanotechnology 21(29):295605–295608
85. Hayden O, Greytak AB, Bell DC (2005) Core-Shell nanowire light-emitting diodes. Adv Mater 17(6):701–704
86. Lauhon LJ, Gudiksen MS, Wang D, Lieber CM (2002) Epitaxial core-shell and coremultishell nanowire heterostructures. Nature 420(69–11):57–61
87. Sköld N, Karlsson LS, Larsson MW, Pistol M-E, Seifert W, Tragardh J, Samuelson L (2005) Growth and optical properties of strained GaAs-$Ga_xIn_{1-x}P$ core-shell nanowires. Nano Lett 5(10):1943–1947
88. Boxberg F, Sondergaard N, Xu HQ (2010) Photovoltaics with piezoelectric core-shell nanowires. Nano Lett 10(4):1108–1112
89. Qian F, Gradečak S, Li Y, Wen C-Y, Lieber CM (2005) Core/multishell nanowire heterostructures as multicolor, high-efficiency light-emitting diodes. Nano Lett 5(11):2287–2291
90. Choi H-J, Johnson JC, He R, Lee S-K, Kim F, Pauzauskie P, Goldberger J, Saykally RJ, Yang P (2003) Self-organized GaN quantum wire UV lasers. J Phys Chem B 107(34):8721–8725
91. Li Y, Xiang J, Qian F, Gradečak S, Wu Y, Yan H, Blom DA, Lieber CM (2006) Dopant-free GaN/AlN/AlGaN radial nanowire heterostructures as high electron mobility transistors. Nano Lett 6(7):1468–1473
92. Songmuang R, Landre O, Daudin B (2007) From nucleation to growth of catalyst-free GaN nanowires on thin AlN buffer layer. Appl Phys Lett 91(25):251902–251904
93. Lim SK, Tambe MJ, Brewster MM, Gradečak S (2008) Controlled growth of ternary alloy nanowires using metalorganic chemical vapor deposition. Nano Lett 8(5):1386–1392
94. Shitara T, Neave JH, Joyce BA (1993) Reflection high-energy electron diffraction intensity oscillations and anisotropy on vicinal AlAs(001) during molecular-beam epitaxy. Appl Phys Lett 62(14):1658–1660
95. Schubert L, Werner P, Zakharov ND, Gerth G, Kolb FM, Long L, Gosele U, Tan TY (2004) Silicon nanowhiskers grown on $<111>$ Si substrates by molecular-beam epitaxy. Appl Phys Lett 84(24):4968–4970
96. Debnath RK, Meijers R, Richter T, Stoica T, Calarco R, Luth H (2007) Mechanism of molecular beam epitaxy growth of GaN nanowires on Si(111). Appl Phys Lett 90(12):123117–123119
97. Iliopoulos E, Moustakas TD (2002) Growth kinetics of AlGaNfilms by plasma-assisted molecular-beam epitaxy. Appl Phys Lett 81(2):295–297
98. Canet-Ferrer J, Munoz-Matutano G, Fuster D, Alen B, González Y, González L, Martinez-Pastor JP (2011) Localization effects on recombination dynamics in InAs/InP self-assembled quantum wires emitting at 1.5 μm. J Appl Phys 110(10):103502–103507
99. Atlasov KA, Karlsson KF, Deichsel E, Rudra A, Dwir B, Kapon E (2007) Site- controlled single quantum wire integrated into a photonic-crystal membrane microcavity. Appl Phys Lett 90(15):153107–153119

100. Seravalli L, Minelli M, Frigeri P, Allegri P, Avanzini V, Franchi S (2003) The effect of strain on tuning of light emission energy of InAs/InGaAs quantum-dot nanostructures. Appl Phys Lett 82(14):2341–2343
101. Chuang SL (1991) Efficient band-structure calculation of strained quantum-wells. Phys Rev B 43(12):9649–9661
102. Tersoff J, Teichert C, Lagally MG (1996) Self-organization in growth of quantum dot superlattices. Phys Rev Lett 76(10):1675–1678
103. Alen B, Martinez-Pastor J, González L, Garcia JM, Molina SI, Ponce A, Garcia R (2002) Size-filtering effects by stacking InAs/InP (001) self-assembled quantum wires into multilayers. Phys Rev B 65(24):241301–241304
104. Skolnick MS, Mowbray DJ (2004) Self-assembled semiconductor quantum dots: fundamental physics and device and applications. Ann Rev Mater Res 34:181–218
105. Ryzhii V, Khmyrova I, Mitin V, Stroscio M, Willander M (2001) On the detectivity of quantum-dot infrared photodetectors. Appl Phys Lett 78(22):3523–3525
106. Cui K, Robinson BJ, Thompson DA, Botton GA (2010) Stacking pattern of multilayer InAs quantum wires embedded in $In_0.5_3Ga_0.4_{7-x}Al_xAs$ matrix layers grown lattice-matched on InP substrate. J Cryst Growth 312(19):2637–2646
107. Fuster D, González MU, González L, González Y, Ben T, Ponce A, Molina SI, Martinez-Pastor J (2004) Size control of InAs/InP(001) quantum wires by tailoring P/As exchange. Appl Phys Lett 85(8):1424–1426
108. Fuster D, González MU, González L, González Y, Ben T, Ponce A, Molina SI (2004) Stacking of InAs/InP(001) quantum wires studied by in situ stress measurements: role of inhomogeneous stress fields. Appl Phys Lett 84(23):4723–4725
109. Xie QH, Madhukar A, Chen P, Kobayashi NP (1995) Vertically self-organized InAs quantum box islands on GaAs(100). Phys Rev Lett 75(13):2542–2545
110. Kret S, Ruterana P, Rosenauer A, Gerthsen D (2001) Extracting quantitative information from high resolution electron microscopy. Phys Status Solidi (b) 227(1):247–295
111. Fuster D, Alén B, González L, González Y, Martínez-Pastor J, González MU, García JM (2007) Isolated self-assembled InAs/InP(001) quantum wires obtained by controlling the growth front evolution. Nanotechnology 18(3):035604035609
112. Blunier S, Zogg H, Maissen C, Tiwari AN, Overney RM, Haefke H, Buffat PA, Kostorz G (1992) Lattice and thermal misfit dislocations in epitaxial CaF_2/Si(111) andBaF_2-CaF_2/Si (111) structures. Phys Rev Lett 68(24):3599–3602
113. Hannon JB, Shenoy VB, Schwarz KW (2006) Anomalous spiral motion of steps near dislocations on silicon surfaces. Science 313(5791):1266–1269
114. Kaganer VM, Ploog KH (2001) Energies of strained vicinal surfaces and strained islands. Phys Rev B 64(20):205301–205314
115. Kukta RV, Peralta A, Kouris D (2002) Elastic interaction of surface steps: effect of atomic-scale roughness. Phys Rev Lett 88(18):186102–186105
116. Liu F, Tersoff J, Lagally MG (1998) Self-organization of steps in growth of strained films on vicinal substrates. Phys Rev Lett 80(6):1268–1271
117. Voorhees PW (2006) Step dances on silicon. Science 313(5791):1247–1249
118. Wollschläger J, Pietsch H, Klust A (1998) Competition between terrace and step nucleation: epitaxy of CaF_2 on vicinal Si(111) studied by atomic force microscopy. Appl Surf Sci 130–132:29–35
119. Bai LG, Tersoff J, Liu F (2004) Self-organized quantum-wire lattice via step flow growth of a short-period superlattice. Phys Rev Lett 92(22):225503–225506
120. Molina SI, Sanchez AM, Beltran AM, Sales DL, Ben T, Chisholm MF et al (2007) Incorporation of sb in InAs/GaAs quantum dots. Appl Phys Lett 91(26): 263105–263107
121. Xu MC, Temko Y, Suzuki T, Jacobi K (2005) On the location of InAs quantum dots on GaAs (001). Surf Sci 589(1–3):91–97

122. Molina SI, Varela M, Sales DL, Ben T, Pizarro J, Galindo PL, Fuster D, González Y, González L, Pennycook SJ (2007) Direct imaging of quantum wires nucleated at diatomic steps. Appl Phys Lett 91(14):143112–143114
123. Molina SI, Varela M, Ben T, Sales DL, Pizarro J, Galindo PL, Fuster D, González Y, González L, Pennycook SJ (2008) A method to determine the strain and nucleation sites of stacked nano-objects. J Nanosci Nanotechnol 8(7):3422–3426
124. Sales DL, Varela M, Pennycook SJ, Galindo PL, González L, González Y, Fuster D, Molina SI (2010) Morphological evolution of InAs/InP quantum wires through aberration-corrected scanning transmission electron microscopy. Nanotechnology 21(32):325706–325713
125. Jesson DE, Munt TP, Lou C (2004) Critical thickness for nanostructure self-assembly during Stranski-Krastanow growth. Jpn J Appl Phys 43(10):7230–7231
126. Silveira JP, Briones F (1999) In situ observation of reconstruction related surface stress during molecular beam epitaxy (MBE) growth of III–V compounds. J Cryst Growth 201–202:113–117
127. Levinstein RS, Shur M (1996) Handbook series on semiconductor parameters. World Scientific, London
128. Liu P, Zhang YW, Lu C (2003) Three-dimensional finite-element simulations of the self-organized growth of quantum dot superlattices. Phys Rev B 68(19):195314–195321
129. Biasiol G, Kapon E (1999) Mechanism of self-limiting epitaxial growth on nonplanar substrates. J Cryst Growth 201–202:62–66
130. Ben T, Molina SI, García R, Fuster D, González MU, González L, González Y, Kret S (2005) Quantitative measurements of the inhomogeneous strain field of stacked self-assembled InAs/InP(001) quantum wires by the Peak Finding Method. In: Cullis AG, Hutchison JL (eds) Microscopy of semiconducting materials. Springer, Berlin/Heidelberg, pp 299–302
131. Ben T, Sales D, Pizarro J, Galindo P, Fuster D, González Y, González L, Varela M, Pennycook S, Molina S (2008) Experimental and simulated strain field maps in stacked quantum wires. Microsc Microanal 14(Suppl 2):344–345
132. Molina SI, Ben T, Sales DL, Pizarro J, Galindo PL, Varela M, Pennycook SJ, Fuster D, González Y, González L (2006) Determination of the strain generated in InAs/InP quantum wires: prediction of nucleation sites. Nanotechnology 17(22):5652–5658

Erratum to: TEM Characterization of Biological and Inorganic Nanocomposites

Penghe Qiu, Lin Wang, and Chuanbin Mao

Owing to an unfortunate oversight the name of the third author, Chuanbin Mao, was misspelled in this chapter.

The online version of the original chapter can be found at
http://dx.doi.org/10.1007/978-3-642-38934-4_1

C.S.S.R. Kumar (ed.), *Transmission Electron Microscopy Characterization of Nanomaterials*, DOI 10.1007/978-3-642-38934-4_15,
© Springer-Verlag Berlin Heidelberg 2014

Index

A
Aberration-corrected STEM, 380–381, 383
Abnormal bone mineralization, 8
Advanced atomic analysis at atomic scale
  bonding mapping, 396–399
  Ca_2FeCoO_5, coordination state, 398–399
  multiwalled C nanotube, 396–397
  oxidation state in Mn_3O_4, 397–398
Algebraic reconstruction technique (ART)
  HAADF-STEM, 627
  reconstruction algorithms, 627
  volume reconstructions, TEM tomography, 628
Analytical 3D-TEM
  Co/TiO_2-SiC catalyst, 652–653
  nitrogen-doped carbon nanotubes, 649–652
  validation, methodology, 647–649
Analytical mode, STEM/TEM
  EDXS, 339–341
  EELS, 341–342
Analytical tomography
  EFTEM mode, 629
  filtered images, acquisition, 630
  limiting factors, 624
  low signal to noise ratio, 624
  multi-scattering effect, 624
  residual diffraction contrast, 624
  resolution, 632
  technical difficulties, 624
Anisotropic soft-X-ray emission
  graphite and hexagonal BN, 317
  intensity distributions, 319–320
  K-emission spectra, BN, 320, 321
  schematic diagram, emission intensity, 317–318
  single-crystalline graphite, 318–319
Annular bright field (ABF) imaging, 376, 386–389
Annular dark field (ADF) imaging technique
  coherence effects, 387
  3D electron microscopy, nanosciences, 623
  grain boundary regions, 388
  images of projected YH_2 structure, 388–389
  interfacial misfit dislocations, 389, 390
  set up, 384, 386
  $SrTiO_3$, 386–387
Aragonite platelets, 10
AS1411, 32, 33
Atomic force microscope (AFM), 141, 161, 197, 244, 684, 687
Atomic resolution, nanostructures
  effects, 125
  electro-optical design, 126
  K-edges, of GaAs, 126, 127
  L-edges, of GaAs, 126, 128
  localization distance, 126, 127
Atom probe tomography (APT)
  composition analyses, 481, 482
  thermoelectric nanomaterials, 431–434
$Au@Cu_2O$ nanoparticles
  HAADF approach, 260–261
  HRTEM imaging, 267–268
Au distribution in Si and GaAs
  catalytic contamination, 401
  diffusion, 399–400
  interstitials, 399–400
  twin boundary, 401

B
Backscattered electron image, CZTS, 74, 75
Bacterial flagella templates, 19, 21
Bacteriophage templates, 17–19
Ball models, CZTS, 63, 64
Band gap
  PbTe, 468
  strain engineering, 676
  thin film photovoltaic materials, 45
  variations, 673

C.S.S.R. Kumar (ed.), *Transmission Electron Microscopy Characterization of Nanomaterials*, DOI 10.1007/978-3-642-38934-4,

© Springer-Verlag Berlin Heidelberg 2014

Bimetallic core-shell and alloy nanoparticles, 252, 254–255
Bio-inorganic nanocomposites, 2
  externally introduced inorganic nanoparticles, 27, 31–34
  naturally occurring bio-inorganic nanocomposites, 6–12
  negative staining, 5
  positive staining, 4–5
  synthetic inorganic nanomaterials, 13–19, 21–27
  ultramicrotome, 3–4
Biotemplates, 2, 13, 21–27, 35
Boron
  allotropes, 301
  crystal structure, rhombohedral B, 302
  DOS, 304–305
  intensity comparison, 303
  metal hexaborideMB$_6$ structure, 304, 306
  rhombohedral crystal structure, 302
  spectrum of rhombohedral B, 302–303
  structure of metal hexaboride MB$_6$, 304, 306
Boron@boron oxides nanowires, elemental mapping
  EELS spectrum, 272–273
  spatial distribution of boron and oxygen, 273–274
Bound rubber, 141, 145, 146, 158, 171, 172
Brick-and-mortar-assembled structure, 10
Bright field (BF) imaging, 92, 97, 98, 108. *See also* Dark field (DF) imaging
Bright-field transmission electron microscopy (BF-TEM)
  biological applications, 623
  images, 338, 352

C

Cadmium telluride (CdTe)
  chlorine activation, 52
  Joule heating, 227, 228
  planar defects, 53, 54
  sphalerite structure, 53, 55
  sulfur diffusion, 54–55
  superstrate CdS/CdTe cell, 52, 53
Calcium carbonate–based bio-inorganic nanocomposites
  aragonite platelets, 10
  sea urchin spine, 10–11
Carbon
  1D-, 2D-, 3D-C$_{60}$, 308–309
  π*-resonance excitation, 310
  single-crystalline diamond, graphite, and fcc monomer-C$_{60}$, 307–308
  types of structures, 306–307
Carbon black network structure
  carbon black-filled NR compounds, 145–146
  CB aggregate distance, 146, 148
  3D-TEM images, 146, 147
  fractions of cross-linked, branched and isolated chains, 149–151
  nanofiller aggregate network, 149, 150
  skeletonized network structure, 147, 149
  volume resistivity, 146–148
Carbon black/rubber interaction layer visualization
  AFM phase image, 161, 162
  coefficient of thermal expansion, 167
  3D images, 163
  storage modulus, 164–166
  volume fractions, 164
  volume ratios, 164, 165
Carbon K-emission spectra
  1D-, 2D-, 3D-C$_{60}$, 308–309
  diamond, graphite, and fcc monomer-C$_{60}$, 307–308
  π*-resonance excitation, 310
  types of structures, 306–307
Catalytic nanomaterials. *See* Metallic nanocatalysts
Cathodoluminescence (CL)
  description, 44
  inorganic solar cells, 72–75
^{13}C CP MAS NMR spectra, PK/PA polymer alloy, 184, 185
CdTe-and Cu(In,Ga)Se$_2$ (CIGS), 48
  CIGS/Mo interface, 56, 58
  CL spectra, 59, 61–62
  grain boundary distribution, 59, 61
  grain size, 57, 60
  sodium in, 62, 63
  three-stage evaporation process, 57, 59
Ceramic matrix nanocomposites (CMNC), 335. *See also* Titanium nitride (TiN)
Chaperonin, 22
Charge coupled device (CCD), 100, 101
Charge transfer (CT) state, 50, 51
Chemical analysis at atomic scale
  $Bi_{0.5}Sr_{0.5}MnO_3$ structure, 393–394
  cations distribution in $Ba_{0.03}Sr_{0.97}TiO_3$, 393, 396
  C nanotubes with La and Er inclusions, 394, 396
  $SrTiO_3$/$LaVO_3$ multilayer system, 393, 395

Chemical analysis techniques, 44
Chemical solution deposition (CSD) route, oxide epitaxial films
  LSMO thin films, 541–542
  MOD solution synthesis, 541
  thickness dependence, 542
Clusters, semiconductor nanomaterials
  anatase TiO_2 nanorod, 122
  CdTe tetrapod, 119, 120
  coherent electron diffraction imaging, 121–123
  multiple-twinning model, 121
  nano-diffraction pattern, 124
  phase-retrieved diffractive image, 124–125
  Shannon's theorem, 123
Coefficient of thermal expansion (CTE), 167
Cold welding, 229–231
Collagen–apatite bio-inorganic nanocomposites., 6–8
Column-to-column compositional quantification, III-V semiconductors
  HAADF-STEM image, ZnO nanowires, 663
  $InAs_xP_{1-x}$/InP interface, HAADF, 661–662
  integrated intensities, 662–663
  limitations, 660
  MBE, 661
  segregation and interdiffusion, 660
  Z-contrast imaging, 661
Convergent beam electron diffraction (CBED), 100
  LACBED, 117–118
  whole pattern, 116–118
Core-multishell semiconductor nanowires, elemental mapping, 274–275
Core-shell $Al_xGa_{1-x}N$/GaN nanowires
  diffusion, 681–682
  EDS profiles, 679–680
  HAADF-STEM image, 677
  HRTEM image, 679
  morphology and composition distribution, 680–681
  thickness profiles, 678
Core-shell nanomaterials
  classes of, 245–246
  diffraction contrast imaging, 248–252, 254, 255, 260
  elemental mapping, 270–275
  HAADF approach, 260–266
  HRTEM imaging, 267–272
  statistical data analysis, 244–245
  synthesis of, 246–247
  TEM technique, 247–248
Coster-Kronig transition, 290, 296, 311, 313
Co/TiO_2-SiC catalyst analytical 3D-TEM, 652–653
Cryo-TEM examination, negatively stained collagen fibril, 7
Curing
  compounding recipes, 154, 155
  3D-TEM images, 157–159
  elongation ratio, 161, 162
  image analysis technique, 158
  interparticle distance determination, 158
  network images, 160, 161
  residual elongation ratios, 156
  two-step curing process, 155–156
  volume resistivity *vs.* residual elongation ratios, 156
$Cu_2ZnSn(S,Se)_4$ (CZTS), 49
  ball models, 63, 64
  IBM hydrazine solution route, 65, 67
  phase decomposition, 64, 66
  STEM-EELS analysis, 63–65

D
Dark field (DF) imaging, 97, 111. *See also* Bright field (BF) imaging
Data treatment procedure
  EELS spectrum, 631
  preprocessing steps, 630
  skin calculation, 632
  Zero Loss tilt series, 631
Deformation twinning, 10
1D filamentous biological templates
  bacteriophage templates, 17
  tobacco mosaic virus templates, 14, 16–17
3D electron microscopy, nanosciences
  analytical 3D-TEM, 647–653
  analytical tomography, 624, 629, 630, 632
  annular dark field imaging, 623
  artifacts, tomography requirements, 625–626
  artificial nanomaterials, 621
  bright-field transmission electron microscopy, 623
  data treatment procedure, 630–632
  definition, 619–620
  2D intensity distribution, 621–622
  3D voxel matrix, 622
  electron tomography, 621
  energy-filtered TEM, 623–624
  faceted nanoparticles, 639–643
  long-range ordering, 643–646

3D electron microscopy, nanosciences (*cont.*)
low-resolution electron tomography, 623
overview of, 620
quantitative 3D-TEM, 634–646
radon projection, 622
reconstruction algorithms, 626–627
reconstructions, combined analysis, 647
short review, previous works, 633–634
STEM-HAADF tomography, 623
TEM tomography, 627–628
Z-contrast tomography, 628–629
Density functional theory (DFT), 106, 119
Diatoms, 12
Diffraction contrast imaging, core-shell nanomaterials
bimetallic nanoparticles, 252, 254–255
hollow core-shell nanomaterials, 254–260
silica coatings, 248–252
Dipole transition, 289, 294, 302
Donolato's EBIC method, 72
Double-display phage system, 19
Double Schottky barrier, 68

E
EELS
advanced atomic analysis at atomic scale, 396–399
advantages, 393
chemical analysis at atomic scale, 393–396
electronic structure and electronic transitions, schematic drawing of, 288–289
energy-dispersive X-ray spectroscopy (EDS), 291
inner-shell electron excitation, 289
photoelectron emission spectroscopy (PES), 290
valence electron excitation, 288–289
wavelength-dispersive X-ray spectroscopy (WDS), 291
EELS and SXES spectrum
Al, 322, 323
BN, 322, 324
Mg, 321–322
Electrical conductivity/Seebeck, TE coefficient measurements, 443–444
Electron diffraction, semiconductor nanomaterials
experiments, 92–93, 100
symmetries in, 116–11
Electrical pulsing, nanowires, 224–227
Electrochemistry, in situ TEM
charging-discharging effects, 232
SnO_2, 232–234
Electron-beam-induced current (EBIC) method, 72
Electron coherent diffraction imaging (EDI), 100, 122–125, 133
Electron energy-loss magnetic chiral dichroism (EMCD), 128–129, 131
Electron energy-loss near edge structure (ELNES), 129, 131
Electron energy-loss spectroscopy (EELS)
advanced atomic analysis at atomic scale, 396–399
advantages, 393
atomic resolution, nanostructures, 125–128
chemical analysis at atomic scale, 393–396
electronic structure and transitions, 288–289
energy-dispersive X-ray spectroscopy (EDS), 291
inner-shell electron excitation, 289
photoelectron emission spectroscopy (PES), 290
PK/PA polymer alloy, 181–182
semiconductor nanomaterials, 101–103
valence electron excitation, 288–289
wavelength-dispersive X-ray spectroscopy (WDS), 291
Elemental mapping, 270–271
boron@boron oxides nanowires, 272–274
core-multishell semiconductor nanowires, 274–275
Energy crisis and energy conversion efficiency, TE nanomaterials
examples, 435
nuclear energy, 436
recycling lost waste heat, 433, 436
renewable energy, 434–435
significance and scale, 434
Energy dispersive X-ray spectroscopy (EDXS)
effects, 125
electro-optical design, 126
K-edges, of GaAs, 126, 127
semiconductor nanomaterials experiments, 100–101
Energy-filtered TEM (EFTEM) mode, 102, 623–624, 629

Energy-loss magnetic chiral dichroism, 131, 132
Experimental and instrumental methodology, TE
APT, 445
electrical conductivity/Seebeck, 443–444
SEM, 444
synthesis, 443
TEM, 444–445
thermal conductivity, 444
X-ray diffraction, 443
Ex situ TEM techniques, nanowires and nanorods
Co_3O_4, 201–203
copper nanowires, CuPd and CuPt, 204–205
hollow nanowires, 202
Kirkendall effect, 205–208
oriented attachment, 212–216
PbS, 199–200
structural defects, in silicon nanowires, 208–212
TiO_2, 202
vapor–liquid–solid mechanism, 199
zinc, 201
Extension for higher-energy region
drawback, 327
energy dispersion, 324
indium-tin-oxide, 325–326
$KNbO_3$, 325–326
multilayer-coated grating, 325
Externally introduced inorganic nanoparticles
biodegradation behavior, 27–31, 33
cell internalization, 32–34

F
Faceted nanoparticles, quantitative 3D-TEM
CeO_2 nanoparticles, 639–641
modeling, 640, 642–643
molecular dynamics-assisted shape
False-color crystal-phase amplitude maps, 115, 116
Fermi edge, 294–296
Figure of merit (ZT). *See* ZT
Fill factor (FF), 46
Finite element analysis, 664
Fischer–Tropsch (FT) synthesis, 591, 593
Fish scale, 8, 9
Flagella, 14, 19–21
Focused ion beam (FIB) milling, 95
Fresnel contrast method, 76–77

G
Gas reaction, E-TEM
column, 606–607
CoO_x/SiO_2 nanocomposite system, 604, 608
Geometric phase analysis (GPA)
Bragg peaks, 431
displacement measurement, 429–430
fast Fourier transformation, 429
HRTEM, 428–429
image processing, 429
mean dilatation, 430
quantitative method, 431
rotation, 430
strain tensor, 430
Grain boundaries
ab initio simulations, 71
band bending profile, 69
electronic band structure, 67, 68
luminescence spectrum, 70
Na diffusion, 70
numerical simulations, 69

H
Head-to-head approach, cold welding, 229, 231
Heating of nanowires and in situ TEM
electrical pulsing, 224–227
electron beam, 224, 225
Joule heating, 227
Heat treatment, carbon black
characteristics, 154
cross-linked point densities, 153
3D-TEM images, 152–153
Heteroepitaxial systems, strain field maps simulation by FEM, 664
High-angle annular dark-field (HAADF) imaging
Au@Ag, 261–262
Au@Cu_2O nanoparticles, 260–261
dealloyed Pt-Ni, 264, 265
3D electron microscopy, nanosciences, 623
drawbacks, 385
heterostructure interfaces, 384–386
Pd@Au and Au@Pd, 263–264
Pt@Ag particles, 264, 266
semiconductor nanomaterials, 98–99
set up, 383, 384
uncorrected *vs.* aberration-corrected systems, 384, 385
High energy-resolution EELS. *See* Electron energy-loss spectroscopy (EELS)

High-resolution transmission electron microscopy (HRTEM) imaging, 428
Au@Cu_2O nanoparticles, 267–268
core-shell $Al_xGa_{1-x}N$/GaN nanowires, 679
dumbbell identification, 404
geometric phase analysis, 428–429
LAST(T), 505–509
nanorods, ZnO growth on Si (111) using three step method, 670
PbTe/CdTe core-shell nanoparticles, 268–270
PbTe/CdTe nanoparticles, 268–270
PbTe, doped, 446, 448–450
PbTe + XTe, 458
polarity assignment, semiconductor nanowires, 404
Pt@Pd core-shell nanoparticles, 270, 272
Pt@Pd nanoparticles, 270, 272
semiconductor nanomaterials imaging experiments, 98
strain mapping, 543–545
TiN-Ag nanocomposites, 352
ZnSe/GaAs heterostructure, 109
Zn/ZnO core-shell nanobelts, 269–271
Zn/ZnO nanobelts, 269–271
Hollow core-shell nanomaterials
$\alpha Fe_2O_3/SiO_2$ nanotemplates, 259–260
formation process of V_2O_3-SnO_2 composite, 258
monodisperse latex and silica spheres, 254
Ostwald ripening processes, 256–257
rattle-type carbon-alumina particle formation, 258
V_2O_5-SnO_2 double-shelled nanocapsules, 255–256
Hydrophilic silica VN–3, 168
Hydroxyapatite–collagen nanocomposites, in bone and fish scales, 6–8

I

Impact resistance, 142, 143, 189
In-line holography, 76–77
Inorganic solar cells
CIGS devices, 48–49
grain boundaries, 67–71
material issues in, 52, 55, 56, 62, 63, 66
recombination velocity, 72–75
In situ environmental TEM (E-TEM) study
gas reaction, 601–602, 604, 607–609
liquid reaction, 609–612
In situ TEM techniques, heating nanowires
electrical pulsing, 224–227
electron beam, 224
In situ TEM techniques, nanowires
electrochemistry, 232–234
elemental analysis, Si-Ge heterojunction, 220
mechanical and electrical characterization, 228–232
nucleation, 221
oriented attachment growth, 221–222
video imaging, 217–218
VLS and VSS growth mechanisms, 216–218
$InAs_xP_{1-x}$ quantum wires deposition
nucleation and evolution, 683–693
spatial distribution and size homogeneity, 683
Stranski-Krastanov (SK) mode, 683
stress field, 682
Iron oxide nanoparticles (IONPs), 28–30

J

Joule heating, nanowires, 227, 228

K

K-emission
beryllium, 295–296
boron, 301–306
carbon, 306–310
lithium, 294–296
Keyhole coherent electron diffraction imaging (KEDI), 125
Kirkendall effect
CeO_2 nanotubes, 206–207
$Cr_2Te_4O_{11}$, 207
description, 205
Sn-SnO_2 nanotubes, 205, 206
Te nanowires, 207–209
$ZnAl_2O_4$, 208, 210

L

Large angle convergent beam electron diffraction (LACBED) pattern, 117–118
Laser ablation, 200

LAST(T), TE nanomaterials
Ag–Sb-rich chains, 505–508
DP, 505–509
HRTEM images, 505–509
κ lowering, 508
microstructural base, 501
microstructurs, 510, 512, 513
temperature dependence, 510–512
XRD patterns, 504
ZT, 504
L-emission
Co, 311–312
Mg and Al, 296–297
Mn, 311
radiative electronic transition, 299–300
Ti, 312–313
$TiSi_2$, 300–301
Liquid reaction, E-TEM
carbon foils and graphene sheets, 609
3D view, 609, 610
growth, Pt_3Fe nanowires, 610, 612
time sequence, 610, 611
Load-displacement curve, 184, 185
Local-electrode atom-probe (LEAP) tomograph, 432, 433
Long-range ordering, quantitative 3D-TEM
3D meta-crystals, 643–645
stacking faults, periodically ordered mesoporous material, 645–646

M

Manganites. *See* Nanocomposite oxide thin films
Maryna umbrellata, 11–12
Material issues
CdTe, 52–55
CIGS, 56–62
CZTS, 63–66
M-emission
Cu, 298
Gd, Tb, Dy, Ho, Er, Tm and Yb compounds, 314, 316
integrated intensity ratio, 316, 318
La, Ce, Pr, Nd, Sm and Eu compounds, 314–315
schematic level drawing with decay processes, 315, 317
Mesoporous silica nanoparticles (MSNPs), 27–28
Metallic nanocatalysts
definition, 577–578
EELS and EDS, spectroscopy, 580–581
electron beam effect, 581
elemental distribution, STEM techniques, 594–600, 602, 603
ex situ characterization, 579
industrial applications, 579
nanodiffraction and CBED, 581
overview of, 578
phase, 583–585
shape, 587–594
in situ environmental TEM study, 601, 602, 604, 606, 609, 613
size distribution, 582
STEM-SEM, 604, 605
strategy, 579
structural and chemical characterization, 582
surface defects, 586–588
TEM and STEM, imaging, 580
Metallic nanocatalysts elemental distribution in STEM/TEM
core–shell noble catalysts, 594–595, 598
Fe distribution, 596–597, 600
Pt_3Co electrocatalyst, 599, 602
signal-to-noise ratio, 595
STEM-EELS, 599, 603
Metal matrix nanocomposites (MMNC), 336
Metal-organic chemical vapor deposition (MOCVD), 274, 676
Microstructural evolution tracking
annealing, 549–550
LSMO films, topographic images, 548
SFM topographic images, 547, 549
Microstructure and nucleation control
CSD-derived pyrolyzed film, 545
kinetic point of view, 546
temperature, 546
Middle-angle bright field (MABF), 389–391
Misfit strain relaxation, film thickness effect
density of dislocations, 560
displacement, 560
LSMO composite film, 558
plastic dislocation, 560–563
thickness dependence, 557–558
Molecular beam epitaxy (MBE), 94, 107, 129
Multiple order twinning polarity driven growth, GaAs on Si, 410–415
Multiple twinning (MT), 588

N
Nacre, 8
Nanocomposite materials
  classification, 335
  CMNC, 335 (*see also* Titanium nitride (TiN))
  MMNC, 336
  PMNC, 336, 356–363
  schematic diagram, distribution-dispersion relation, 334–335
  TEM/STEM methods, 336–339, 342–346
Nanocomposite oxide thin films
  colossal magnetoresistance manganites, 539–540
  definition, 538
  fabricate approach, 539
  GPA and HRTEM, strain mapping, 543–545
  La excess content accommodation, 564–568
  microstructural transformation, 540–541
  oxide epitaxial films, chemical solution deposition route, 541–542
  spontaneous phase separation, 545–564
  TEM, 543–545
Nano-diffraction pattern (n-DP), 100, 123, 124
Nanofiller filled rubber vulcanizate, 140, 145
Nanofiller network structure, 140, 143
Nanoparticles
  Au@Cu_2O, 260, 261, 267, 268
  bimetallic core-shell and alloy, 252, 254–255
  PbTe/CdTe, HRTEM imaging, 268–270
  Pt@Pd core-shell, HRTEM imaging, 270, 272
Nanoparticles, 3D localization
  functionalities, 635
  nanoparticles localization, curved surface, 637–639
  nanoparticles spatial distribution, 635
  nano-wire Au/Si, 638, 639
  palladium particles, carbon nanotube, 636, 637
  particles scattered, plane surface, 636–637
  P3HT–CdSe hybrid film, 638
Nanorods. *See also* Nanowires and nanorods
  CBD methods, 669
  high VPT temperature effect on, 673, 674, 676
  using three step method, 670–672
Nanostructured semiconductors. *See* Semiconductor nanomaterials
1D-Nanostructures
  applications, 659
  III-V semiconductors, 660–663
  $InAs_xP_{1-x}$ quantum wires deposition, MBE on InP, 682, 683, 693
  strain field maps simulation, heteroepitaxial systems by FEM, 664
  ternary III-N grown by catalyst-free PAMBE, 677–682
  ZnO nanorods growth, Si (111), 669–676
  ZnO nanowires growth, CdTe (111), 664–669
Nanowires
  boron@boron oxides, elemental mapping, 272–274
  core-shell $Al_xGa_{1-x}N$/GaN, 677–682
  ZnO growth, CdTe (111), 664–669
Nanowires and nanorods
  ex situ TEM techniques, 199–205, 208, 212, 216
  HAADF imaging, 198
  in situ TEM techniques, 216–218, 220–222, 224–234
Naturally occurring bio-inorganic nanocomposites
  calcium carbonate, 10–11
  hydroxyapatite–collagen, 6–8
  silica, 11–12
Negative staining, 5, 14, 26
NISSAN ARC-AK method, 144
Nitrogen-doped carbon nanotubes, analytical 3D-TEM, 649–652

O
Optical transparent polymers, 142
Organic bulk heterojunction solar cells
  bright-field electron tomography, 79, 80
  charge transfer state, 50
  mean electron energy loss spectrum, 80, 81
  operating principles, 50
  principal component analysis, 80
  thermal annealing, 51
Oriented aggregation, nanowire
  CdS nanowires, 213–214
  growth mechanism, 212
  pearl chain structures, 213
  Sb_2O_3 coaxial nanowires, 215–216
  silver sulfide, 214–215
Osteoporosis, 8

P
Partial dislocation emission, 10
PbTe/CdTe core-shell nanoparticles, 268–270

PbTe, doped
crystallographic directions, 446
HRTEM studies, 446, 448–450
microstructural features, 446
Na/K doped p-type, 445–446
PbTe + PbX
APT, 481, 483
A-site substitution, 468
displacement layers, 481, 485
GPA analysis, 481, 482
high-density stacking faults, 485–487
lattice mismatch, 474–479
low-magnification STEM image, 487
low-magnification TEM images, 468, 471, 476, 479
Moiré fringes, 18, 477
precipitate, 478–480
p-type dopant element Na role, 478
SEM images, 483–485
in situ nanostructure formation, 468, 470, 473
spinodal decomposition, 470–471
TEM investigations, 483, 485, 486
thermopower, 468–470
PbTe-Sb2Te3TE compounds
chalcogenide systems, 523
interfacial structure of precipitates, 528–530
nanostructured TEs, 523, 526
rock salt structure, 525–528
PbTe + X
Bi sample precipitate, 491
Burger's circuit, 490–491
low-magnification TEM images, 493–494
Pb-and Sb-rich precipitates, 494–495
Pb/Sb codoped system, 492
pherical-like precipitates, 488, 489
phonons scattering, 487–488
platelet-like precipitates, 488, 489
SEM images, 496–497
$S^2\sigma$ enhancement, 492–493
PbTe + XTe
atomic-scale doping/substitution, 453–455
Cd substitution, 464, 466–467
HRTEM images, 458
MgTe, 463–465
nanostructures, 453
PbTe–BaTe bulk TE system, 456–458, 460
phonon blocking and charge transmitting, 448–449
phonons, 461–463
precipitates and matrix boundaries, 460, 461
SPS, 456
SrTe, 451–453
temperature dependence, 450, 451
Photovoltaic (PV) materials
barrier height, 76–78
device operation, 46–48
inorganic solar cells (*see* Inorganic solar cells)
organic solar cells, 50, 51, 79–81
thin films, 44–45
Polarity assignment, semiconductor nanowires
CBED, 404
EELS, 404–405
electronic and optoelectronic properties, 415, 417–419
GaN on diamond, 408–409
HRTEM, 404
with medium and high atomic number atoms, 405–406
model, 407–408
multiple order twinning polarity driven growth, GaAs on Si, 410–412
polarity, 402
polytypes, 403
single ZnTe nanowires,-tripods, and-tetrapods formation, 411, 413–417
STM, 405
twin boundaries, 402, 404
ZnO, ABF technique, 406–407
Polyketone/polyamid (PK/PA) polymer alloy
^{13}C CP MAS NMR spectra, 184, 185
DSC curves, 178, 179
EELS, 181–182
grass transition phenomenon, 179–181
load-displacement curve, 184, 185
mass fraction, 187
maximum stress and displacement, 186
moisture absorption rates, 177, 178
phase inversion, 183
SAXS, 183–184
TEM images, 181–182
weight ratio, 176, 177
wet test specimens, 177
Polymeric nano-composites
carbon black network structure, 145–151
carbon black/rubber interaction layer visualization, 161–167
3D-TEM, 143–144
polyketone/polyamid alloy, 176–187
silica-filled cured NR, optical properties, 168–172, 174–176
Zn removal from rubber vulcanizates, 144–145

Polymer matrix nanocomposites (PMNC), 336. *See also* Polymer matrix nanocomposites
  applications, 356–357
  inorganic nanofiller, 356
  synthesis, 357–358
  ZrO_2 dispersion, 358–363
Porosity
  characterization, 634
  mesoporous zeolite, 635
  quantitative measurement, 634
Positive staining, 4–5
Protein cages, 13–15
Pt@Pd core-shell nanoparticles, 270, 272

Q
Quantitative 3D-TEM
  faceted nanoparticles, 639–643
  long-range ordering, 643–646
  NPs, 3D localization, 635–639
  porosity, 634–635
  reconstructions, combined analysis, 647
Quantum dots (QDs), 19, 90, 268, 545, 658, 682
Quantum wires, $InAs_xP_{1-x}$ on InP, MBE
  nucleation and evolution, 683–689
  spatial distribution and size homogeneity, 683
  Stranski-Krastanov (SK) mode, 683
  stress field, 682
Quasi-neutrality level, 67

R
Radiation spectrum, 45, 47
Recombination velocity
  cathodoluminescence, 72–75
  electron-beam-induced current, 72
Reconstruction algorithms
  algebraic reconstruction technique, 627
  Fourier transform, 626
  quality, 627
  simultaneous iterative reconstruction techniques, 627

S
SALT, TE nanomaterials
  Ag-free system, 512
  disperse precipitates, 515–517
  electrical transport properties, 517, 520–521, 523
  lamellar structure and precipitates, 520–523, 525
  nanocrystal domains, 514, 515
  nanoscale lamellar features, 514, 515
  temperature dependence, 512, 514
  TE nanomaterials, 512, 514
Sample preparation,semiconductor nanomaterials
  complexity, 96–97
  FIB, 95
  thickness, 95
Scanning transmission electron microscopy (STEM). *See also* TEM/STEM methods
  metallic nanocatalysts elemental distribution, 594–600, 602, 603
  schematic diagram, 382, 383
  semiconductor nanowires, 382, 384, 386, 389–392, 623
Sea urchin (SU) spine, 10–11
Second generation photovoltaics, 48
Sectioning, 4
Selected area electron diffraction (SAED), 205
Self-assembled hierarchically structured biotemplates, 21–23
Semiconductor nanomaterials
  clusters, 119–125
  electron diffraction, 92–93, 100, 116–118
  imaging experiments, 91, 92, 97–99
  sample preparation, 95–97
  spatial resolution, 91
  spectroscopic experiments, 93–94, 100–103
  strain effect, 114–116
  TEM result simulation, 103–107
  TEM/STEM, heterostructures, 107–114
Semiconductor nanowires
  aberration-corrected STEM, 380–381, 383
  Au distribution in Si and GaAs, 399–401
  cross-sectional STM, 377
  dumbbell identification, 402–419
  EELS, 393–399
  elemental mapping, core-multishell, 274–275
  Ga in AlN barriers, core-shell nanowires, 402, 403
  low-and high-magnification, 377–378
  STEM special modes, 382, 384–392
  STM image, 377–379
  twin boundary crossing and high-resolution XSTM image, 378

III-V semiconductors
HAADF-STEM image, ZnO nanowires, 663
InAsxP1-x/InP interface, HAADF, 661–662
integrated intensities, 662–663
limitations, 660
MBE, 661
segregation and interdiffusion, 660
Z-contrast imaging, 661
Shockley partial dislocations (SPDs), 586
Shockley-Read-Hall (SRH) recombination, 68
Silica-coated core-shell nanomaterials
advantages, 248
Au@SiO_2 nanoparticles, 248–249
$CoFe_2O_4$-SiO_2 core-shell nanoparticles, 249–250
Fe_3O_4/SiO_2/Au/porous-SiO_2 composite colloids, 251
porous silica protected Fe_3O_4/SiO_2/Au composite structures, 249, 251
Si nanowire lithiation on stainless steel substrate, 252, 253
Silica-filled cured NR, optical properties
chain density × chain length vs. silica loading, 175
diffuse transmittance, 168, 170, 174
diffusion transmittance and haze vs. chain density × chain length, 175, 176
3D-TEM images, 170, 171
haze, 168, 170
optical transparency, 168, 169
Silica-filled cured NR, rearrangement and destruction, network
curing, 154–161
heat-treatment, 151–154
recipes of, 168, 169
shield effect, 168, 170
visualization of network structures, 172–174
volume resistivity, 172
Silica, in plants and microorganisms, 11–12
Silica–pili bio-inorganic nanocomposites, 23
Silicon nanowires
HAADF-STEM images, 212
internal structure, 209, 211
Simultaneous iterative reconstruction techniques (SIRT), 627
Small-angle X-ray scattering (SAXS), 183–184
Soft-X-ray emission spectroscopy (SXES)
advantage and disadvantage, 290
anisotropic emission, 317–321
extension for higher-energy region, 324–327
multichannel plate with CCD detector, 294
schematic representation of optics, 292
ver.1, 292–293
ver.6, 292–293
Special transmission electron microscope, techniques
atom probe tomography, 431–433
geometric phase analysis, 428–431
Spectroscopic experiments, 93–94
EELS, 101–103
energy-dispersive X-rays, 100–101
Spontaneous phase separation, nanocomposite oxide thin films
microstructural evolution tracking, 547–550
microstructure and nucleation control, 545–546
misfit strain relaxation, film thickness effect, 557, 558, 560–563
nanocomposite components identification, 550–556
spatial distribution dependence, 556
strain measurements, 563–564
Stacking faults (SFs), 107–109
Strain effect, in semiconductor nanomaterials, 114–116
STEM. See Scanning Transmission Electron Microscopy
STEM special modes
ABF, 386–389
HAADF, 382, 384–386
image simulation, 390–392
MABF, 389–391
schematic diagram, 382, 383
STEM technique, elemental distributions
core–shell noble catalysts, 594–595, 598
Fe distribution, 596–597, 600
Pt3Co electrocatalyst, 599, 602
signal-to-noise ratio, 595
STEM-EELS, 600, 603
Surface rendering, 143, 632
Synthetic inorganic nanomaterials
bacterial flagella templates, 19, 21
1D filamentous biological templates, 14–20
DNA-based biotemplates, 23–27
protein cages, 13–15
self-assembled structure, 21–23

T
TAGS
TE nanomaterials, 497–501
XRD patterns, 501–503
TEM. *see also* Transmission Electron Microscopy
analysis, 543–545
sample preparation, 543
strain mapping, GPA and HRTEM, 543–545
TEM in scanning (STEM) mode. *See* Scanning transmission electron microscopy (STEM)
TEM/STEM methods
analytical 3D-TEM, 624, 629, 630, 632, 647–653
diffraction mode, 338–339
energy-filtered TEM, 623–624
imaging mode, 338
nonrelativistic and relativistic wavelength, 337
scanning mode, 339
schematic diagram of, 336–337
tomographic mode, 342–346
TEM technique
amplitude contrast, 247
elemental mapping, 247–248
HRTEM image, 247
Z-contrast image, 247
Ternary III-N grown by catalyst-free PAMBE
core-shell AlxGa1-xN/GaN nanowires, 677–682
MOCVD, pulse laser
deposition, 676
reflection high-energy electron diffraction pattern, 677
Thermoelectric (TE) nanomaterials
definition, 428
description, 431
detector measurement, 432
dual-beam focused ion beam, 432–434
energy crisis and energy conversion efficiency, 433–436
experimental and instrumental methodology, 443–445
LAST(T), 501, 504–513
local-electrode atom-probe, 432, 433
nanostructures comparision, 431
PbTe, doped, 445, 446, 448–450
PbTe + PbX, 18, 468–471, 473–487
PbTe-Sb2Te3TE Compounds, 523, 525–530
PbTe + X, 487–497
PbTe + XTe, 448–458, 460–467
SALT, 512, 514
sample preparation, 432
special transmission electron microscope techniques, 428–433
TAGS, 497
TE materials, 436–439
ZT, 439–443
Thermomechanical analysis (TMA), 179–180
Thin-film photovoltaics, 44–45
III-V semiconductors, column-to-column compositional quantification
HAADF-STEM image, ZnO nanowires, 663
$InAs_xP_{1-x}$/InP interface, HAADF, 661–662
integrated intensities, 662–663
limitations, 660
MBE, 661
segregation and interdiffusion, 660
Z-contrast imaging, 661
TiN-Ag nanocomposites
bright-field TEM images, 352
dc arc-plasma method, schematic diagram, 351
formation mechanism, schematic diagram, 353, 355
HRTEM images, 352
semitransparent reconstructed volume, 353–354
STEM-HAADF images, 353
tilt series of STEM-HAADF images, 353–354
Titanium nitride (TiN)
application of, 349
fabrication of, 349–351
properties, 348–349
TiN-Ag nanocomposites, 351–355
Tobacco mosaic virus (TMV) templates, 14, 16–17
Tomographic mode, TEM/STEM
absence of images and missing wedge, schematic diagram, 344
angular range-image quality relation, 344–345
3D-ET method, 342–343
3D reconstructed volume of Al alloys, 346
elongation factor, 344

number of projections-image quality relation, 344–345
relative specimen thickness increases,345–346
resolution, 343
schematic diagram, overlapped structure, 343
Total electronic structure analysis
Al-Ni-Co, 322, 323
DOS of bands, 320
EELS and SXES spectrum, 321–324
Trans-activating transcriptional activator (TAT) peptide, 31

U
Ultramicrotome, 3–4
Ultrasoft-X-ray emission spectra
Be K-emission spectrum, 295–296
Cu $M_{2,3}$-emission spectrum, 298
Li K-emission spectrum, 294–296
Mg and Al L-emission spectra, 296–297
$M_{2,3}$-emission spectrum of Cu, 298

V
Valence electron spectroscopy
boron K-emission spectra, 301–306
carbon K-emission spectra, 306–310
EELS, 288–291
L-emission spectra, 311–312
M-emission intensity, 314–318
total electronic structure analysis, 320–324
ultrasoft-X-ray emission spectra (*see also* Soft-X-ray emission spectroscopy (SXES)), 294–298
Van Roosbroeck model, 73
Vapor–liquid–solid (VLS) mechanism, 199
GaN, 221
Ge nanowires, 216–218
Vapor–solid–solid (VSS) mechanism
Ge nanowires, 216–218
Si-Ge heterojunction nanowire, 220
Video imaging, 197, 217
Viscoelasticity, 141, 188

W
Water-gas shift (WGS) reaction, 582–583
Whole pattern (WP), CBED diffraction, 117–118

X
X-ray absorption near edge structure (XANES), 129
X-ray magnetic circular dichroism (XMCD), 128–129, 131

Y
Young's modulus, 229

Z
Z-contrast tomography. *See also* High-angle annular dark-field (HAADF) imaging
BF-STEM *vs.* ADF-STEM, 629
pixel size, 628
Saxton scheme, 628
tilt increment, 628
visualization and quantitative analysis, 629
Zero Loss tilt series, 631
ZnO growth, CdTe (111)
applications, 664
catalytic effect, substrate elements, 667–669
thermal oxidation, metallic zinc films, 665–667
ZnO growth on Si (111)
CBD rods, 674–676
cross-sectional TEM image, 671
EEL spectra, 671–672
HAADF-STEM image, 670
HRTEM mode, 670
ZnO seed layers, 673–674
ZnO nanorods growth, Si (111)
CBD methods, 669
three-step catalyst-free method, 673–676
using three step method, 670–673
ZnO nanowires growth, CdTe (111)
applications, 664
catalytic effect, substrate elements, 667–669
thermal oxidation of metallic zinc films, 665–667
ZnSe/GaAs heterostructure
HAADF images, 109–112
HRTEM image, 109
staking faults, 107, 108
ZnS nanowires, 17–19
Zn/ZnO core-shell nanobelts, 269–271

ZrO_2 dispersed PMNC
advantages, 358
3D reconstructed volume, 360–361
fabrication, 358
grain diameters, histograms of, 361
interparticle distances, histograms of, 362
light scattering, 362–363
refractive indexes, 363
sample comparison, 358
schematic diagram, 359–360
STEM-HAADF images, pillar-shaped specimens, 359–360
transmittance and transparencies, 358–359
ZT
enhancement methods, 441–443
TE nanomaterials, 439–441